CODEN: JASMAN

THE JOURNAL of the Acoustical Society of America

ISSN: 0001-4966

Vol. 101, No. 3 March 1997

(Continued)

CONTENTS—*Continued from preceding page*

(Continued)

CONTENTS—*Continued from preceding page*

(Continued)

CONTENTS—*Continued from preceding page*

ERRATA

CUMULATIVE AUTHOR INDEX

NOTES CONCERNING ARTICLE ABSTRACTS

1. The number following the abstract copyright notice is a Publisher Item Identifier (PII) code that provides a unique and concise identification of each individual published document. This PII number should be included in all document delivery requests for copies of the article.
2. PACS numbers are for subject classification and indexing. See June and December issues for detailed listing of acoustical classes and subclasses.
3. The initials in brackets following the PACS numbers are the initials of the JASA Associate Editor who accepted the paper for publication.

ACOUSTICAL NEWS—USA

Elaine Moran
Acoustical Society of America, 500 Sunnyside Boulevard, Woodbury, New York 11797

Editor's Note: *Deadline dates for news items and notices are 2 months prior to publication.*

Preliminary notice: 133rd Meeting of the Acoustical Society of America

The 133rd meeting of the Acoustical Society of America (ASA) will be held Monday through Friday, 16–20 June 1997 at the Penn State Conference Center on the campus of the Pennsylvania State University, State College, Pennsylvania. Registration will begin Sunday, 15 June, at 2:00 p.m.

The Acoustical Society Meeting is being held jointly with NOISE-CON '97, 15–17 June 1997. While the two technical programs are independent, NOISE-CON sessions on Monday and Tuesday, 15–16 June, will be held at the Penn State Conference Center. Attendees of the ASA meeting who wish to attend both meetings can register for a slightly modified registration fee. NOISE-CON '97 attendees will attend a reception on Sunday and receive proceedings of the meeting. For information about the technical program refer to the ASA Home Page at http://asa.aip.org/. For information about accommodations, facilities, leisure activities, etc., refer to the conference homepage at http://www.acs.psu.edu/asa97.html

Technical program

The technical program will consist of lecture and poster sessions. Technical sessions will be scheduled Monday through Friday, 16–20 June. The following special sessions are planned for invited and contributed papers:

Subjects	*Sponsoring Technical Committees/ Groups*
Acoustical measurements of coastal ocean processes	Acoustical Oceanography
Bioacoustics communications	Animal Bioacoustics
Bioacoustics sensing of the environment	Animal Bioacoustics
Low-frequency bioacoustics	Animal Bioacoustics
Acoustics of large spaces (arenas and stadiums)—poster session	Architectural Acoustics
Sound reinforcement of large spaces (arenas and stadiums)—poster session	Architectural Acoustics
Human vibration exposure	Bioresponse to Vibration/ Biomedical Ultrasound
Take fives: Sharing ideas for teaching acoustics	Education in Acoustics
Undergraduate research poster session	Education in Acoustics
Loudspeakers: Past, present, and future	Engineering Acoustics
Modeling and predictive capabilities for transducers	Engineering Acoustics
New transducer materials	Engineering Acoustics
Sensor self-noise	Engineering Acoustics/Noise
Directional microphones and other approaches for improving speech intelligibility	Engineering Acoustics/Speech Communication/ Signal Processing in Acoustics
Acoustics of bells	Musical Acoustics
Convergence of music cognition and musical theory	Musical Acoustics
Lip reed and brass instruments	Musical Acoustics
Role of musical acoustics in teaching engineering acoustics, mathematics, and engineering	Musical Acoustics/Education in Acoustics
Combined exposure to noise and other hazards	Noise
Product noise labeling issues	Noise
(Joint sessions with NOISE-CON are listed below)	
Auditory system plasticity and perceptual learning	Psychological and Physiological Acoustics
Physiological and psychological aspects of modulation processing	Psychological and Physiological Acoustics
Model based signal processing for acoustic propagation	Signal Processing in Acoustics
Signal processing for condition based maintenance	Signal Processing in Acoustics/ Noise
Active classification of structures	Structural Acoustics and Vibration
Time domain modeling of plate and shell vibration	Structural Acoustics and Vibration/ Musical Acoustics
Prediction for dynamic systems with evolving damage	Structural Acoustics and Vibration/ Signal Processing in Acoustics
Chaos and predictability in long-range sound propagation	Underwater Acoustics
Synthetic aperture sonar	Underwater Acoustics
Time-reversed acoustic propagation	Underwater Acoustics/Physical Acoustics/Signal Processing in Acoustics
Joint special sessions: Noise, Architectural Acoustics, and NOISE-CON '97	
Consumer product sound quality	Power plant noise
Engineering controls for mining noise	Reaction to low level environmental noise
Design for low noise and quality control	Room noise criteria
Noise in school classrooms	Speech intelligibility in rooms

Distinguished lectures

Two ASA Distinguished Lectures are planned for this meeting. George Izenour will present a lecture titled ''Toward Dynamic Theatre Design for the Twenty-First Century—An Approach to Better Seeing and Hearing in Multiuse and Multiform Theatres for Music, Opera, and Drama.'' Mathias Fink will present a lecture titled ''Time-Reversed Ultrasound.''

Tutorial lecture, short courses, hot topics

The Tutorials Committee has planned a Tutorial Lecture on Medical Ultrasonic Imaging and two short courses—one on ''Smart Structures and MicroElectroMechanical Systems (MEMS)'' and the other on ''Design of Acoustic Materials.'' See the following articles in this news section for further details. A ''Hot Topics'' session sponsored by the Tutorial Committee is also planned.

Joint sessions with NOISE-CON '97

NOISE-CON '97, the 1997 National Conference on Noise Control Engineering, will be held at the Pennsylvania State University in State College, Pennsylvania on 15–17 June. NOISE-CON '97 is being sponsored as a joint meeting by the Acoustical Society of America (ASA) and Institute of Noise Control Engineering (INCE) in conjunction with the ASA meeting at Penn State. The theme of NOISE-CON is Frontiers of Noise Control. Three frontiers are being emphasized: active control, vibration analysis for machinery health monitoring, and numerical methods for noise control. Technical papers in other areas of noise control engineering will also be presented. The NOISE-CON Announcement and Call for Papers appeared in *The Journal of the Acoustical Society of America*, Vol. 100, No. 4, pp. 1916–1917, October 1996, and can also be found on the World Wide Web at http://users.aol.com/noisecon97/nc97_cfp.html.

 0001-4966/97/101(3)/1205/4/$10.00

On Sunday, 15 June, the NOISE-CON technical sessions and a NOISE-CON reception will be held at the Nittany Lion Inn on the Penn State campus. On 16–17 June, all NOISE-CON technical sessions will be held at the Penn State Conference Center in conjunction with ASA sessions. Bus transportation from selected hotels in State College to the Penn State Conference Center will be provided.

Individuals may register for the Acoustical Society meeting alone, NOISE-CON alone, or may pay a joint registration fee to attend both meetings. Registration for NOISE-CON alone or for both meetings includes attendance at the technical sessions to be held at the Nittany Lion Inn on Sunday, 15 June, the technical sessions to be held at the Penn State Conference Center on 16–17 June, the reception at the Nittany Lion Inn on 15 June, and a copy of the NOISE-CON Conference Proceedings.

Student transportation subsidies

A student transportation subsidies fund has been established to provide limited funds to students to partially defray transportation expenses to meetings. Students presenting papers who propose to travel in groups using economical ground transportation will be given first priority to receive subsidies, although these conditions are not mandatory. No reimbursement is intended for the cost of food or housing. The amount granted each student depends on the number of requests received. To apply for a subsidy, submit a written proposal to be received by 15 April: Elaine Moran, ASA, 500 Sunnyside Blvd., Woodbury, NY 11797, 516-576-2360, FAX: 516-576-2377, E-mail: asa@aip.org. The proposal should indicate your status as a student, whether you have submitted an abstract, whether you are a member of ASA, method of travel, whether you will travel alone or with other students, names of those traveling with you, and approximate cost of transportation.

Students meet members for lunch

The Education Committee has established a program for students to meet with members of the ASA over lunch. Students should sign up at the registration desk at the meeting. Members who wish to participate should contact James Sabatier, Tel.: 601-232-5404, E-mail: sabatier@olemiss.edu prior to the meeting. Participants are responsible for cost of their own meal.

Plenary session, awards, fellows' luncheon and social events

Complimentary buffet socials with cash bar will be held early on Tuesday and Thursday evenings. The Plenary Session will be held on Wednesday afternoon where Society awards will be presented and recognition of Fellows will be announced. A Fellows' Luncheon will be held on Thursday; ASA Fellows may purchase tickets for this luncheon at the meeting.

Exhibits

An equipment exhibition for the joint meeting will be held at the Penn State Conference Center, 16–18 June. The exhibition will include active noise control systems, computer-based instrumentation, sound level meters, sound intensity systems, signal processing systems, devices for noise control, and acoustical materials. Organizations interested in exhibiting should contact: Richard Peppin, 5012 Macon Rd., Rockville, MD 20852, Tel.: 301-984-3375; E-mail: rpeppin@asme.org

Paper copying service

Authors are requested to provide one paper copy of their projection material and/or paper(s) to the Paper Copies Desk in the Registration area upon arrival. The copy should be material on one side only on 8-1/2×11 inch or A4 paper suitable for photocopy reproduction. Copies of available papers will be made for a nominal charge.

Technical tours

Technical tours have been arranged to various University laboratories and nearby companies. A schedule of tours and sign-up sheets will be available at the meeting.

Registration

Registration will begin Sunday afternoon, 15 June, at 2:00 p.m. at both the Penn State Conference Center and the Nittany Lion Inn. Registration Monday through Friday, 16–20 June, will be held at the Penn State Conference Center only. Checks or travelers checks in U.S. funds drawn on U.S. banks and Visa, MasterCard, and American Express credit cards will be accepted for payment of registration. The registration fee is $150 for members of the Acoustical Society of America. The registration fee is $195 for nonmembers and $35 for Emeritus members of ASA (Emeritus status preapproved by ASA) and accompanying persons. One-day registration is available at $75 for members and $100 for nonmembers. A nonmember who pays the $195 nonmember registration fee and simultaneously applies for Associate Membership in the Acoustical Society of America will be exempt from dues payment for the first year of membership (1997). Invited speakers who are members of the Acoustical Society of America are expected to pay the registration fee, but nonmember invited speakers who participate in the meeting for one day only may register without charge. Nonmember invited speakers who wish to participate in the meeting for more than one day will be charged the member registration fee of $150, which will include a one-year membership in the ASA upon completion of an application form at the meeting. There is no fee for students with active student identification cards.

Members who desire to attend the NOISE-CON '97 meeting will pay an additional registration fee of $50 for a total ASA/NOISE-CON registration fee of $200. A schedule of fees for those desiring to attend the NOISE-CON meeting and take advantage of above mentioned fees will be pro-rated accordingly upon registration.

Assistive listening devices

Anyone planning to attend the meeting who will require the use of an assistive listening device, is requested to advise the Society in advance of the meeting by writing to: Acoustical Society of America, 500 Sunnyside Boulevard, Woodbury, NY 11797.

Accompanying persons program

Accompanying persons are welcome. A Hospitality Room will be open near the conference rooms where information will be available on a wide variety of activities available in Central Pennsylvania. The room will be open from 4:00 to 6:00 p.m. Sunday, 15 June, and 8:00 to 11:00 a.m. daily Monday through Friday. A full-day trip is planned to the Woolrich Woolen Mill Factory and Outlet and to historic Curtain Village on Tuesday. A trip is planned to an Amish Open-Air Market on Wednesday, 18 June. Because of limited space, reservations should be made before the meeting and up to Monday evening, 16 June, by writing to Mrs. G. Hayek, ASA Meeting, 227 Hammond Building, Penn State University, University Park, PA 16802.

Air transportation

The University Park Airport serving State College is served by United Airlines, U.S. Air, and Northwest Airlines with a total of 38 flights a day. The airport designation for State College is SCE.

Ground transportation

State College, PA is located on U.S. 322 and is 15 miles south of I-80, Exits 24 or 25. The State College airport is 5 miles from town. The airport is served by car rental agencies: National, Hertz, and Avis. The limousine shuttle between the airport and the hotels costs $6.00 per person.

Hotel accommodations

The Penn State Conference Center Hotel is the site for the meeting. A block of rooms for single and double accommodations has been reserved here and at the hotels in State College. Please make your reservations directly, and more important, as early as possible. Contact the hotel of your choice and ask for one of the rooms being held for either the **ACOUSTICAL SOCIETY OF AMERICA or NOISE-CON 97** program at Penn State. To obtain the group rate, please, make your reservation prior to **12 May 1997**. After that date, all rooms will be released.

Shuttle bus service will be provided between The Penn State Conference Center and the Residence Halls and all the hotels (except for the

Sleep Inn). Most hotels will provide shuttle service from the University Park/State College Airport, provided that you notify them of your need when making your hotel reservation.

1. PENN STATE CONFERENCE CENTER HOTEL $95-Single
Penn State Research Park $105-Double
215 Innovation Blvd.
University Park, PA 16802
Phone: (814) 863-5000/800-893-4602

2. NITTANY LION INN $95-Single
200 W. Park Ave. $105-Double
University Park, PA 16802
Phone: (814) 231-7500/800-233-7505

3. PENN STATE RESIDENCE HALLS $24-Single
126 Johnston Commons $36-Double
University Park, PA 16802
Phone: (800) 778-8006

Rooms at the Campus Residence Halls are available for double or single occupancy, without private baths but with male and female bathroom facilities on each floor. All rooms are nonsmoking.

4. ATHERTON HOTEL $95-Single
125 S. Atherton St. $105-Double
State College, PA 16801
Phone: (814) 231-2100/800-832-0132

5. BEST WESTERN STATE COLLEGE INN $55-Single
Atherton Street at Branch Road Double
State College, PA 16801
Phone: (814) 237-8005/800-635-1177

6. COURTYARD BY MARRIOTT $89-Single
1730 University Drive Double
State College, PA 16801
Phone: (814) 238-1881/800-321-2211

7. DAYS INN PENN STATE $68-Single
240 S. Pugh Street $78-Double
State College, PA 16801
Phone: (814) 238-8454/800-258-DAYS

8. HAMPTON INN HOTEL $70-Single
1101 E. College Ave. Double
State College, PA 16801
Phone: (814) 231-1590/800-426-7866

9. THE HOLIDAY INN PENN STATE $58-Single
1450 S. Atherton St. Double
State College, PA 16801
Phone: (814) 238-3001

10. SLEEP INN OF STATE COLLEGE $45-Single
111 Village Drive Double
State College, PA 16801
Phone: (814) 235-1020
(NOT INCLUDED IN SHUTTLE SERVICE)

11. BED AND BREAKFAST RESERVATION SERVICE OF STATE COLLEGE
Call Mon–Fri, 8:30–11:30 EST
for information (814) 238-1484

Room sharing

ASA will compile a list of those who wish to share a hotel room and its cost. To be listed, send your name, telephone number, gender, smoker or nonsmoker, by 5 May 1997 to the Acoustical Society of America, Attn.: Room Sharing, 500 Sunnyside Boulevard, Woodbury, NY 11797, e-mail: asa@aip.org. The responsibility for completing any arrangements for room sharing rests solely with the participating individuals.

Tutorial lecture to be presented at State College meeting

A Tutorial Lecture on Medical Ultrasonic Imaging will be presented by James G. Miller, Dept. of Physics, Washington University, St. Louis, MO, at 7:00 p.m. on Monday, 16 June.

This is the twenty-fourth in a continuing series of Tutorial Lectures presented at Society meetings to foster a broader understanding and appreciation by our members for acoustical research in areas other than their own field of interest.

A complete set of notes summarizing the lecture will be available to attendees at the lecture room before the session. To insure receiving the notes, you should register for this Tutorial lecture in advance. Attendees who have not preregistered will receive notes only until the available supply is exhausted. Notes will not be mailed.

To partially defray the cost of the lecture a registration fee is charged. The fee is $15 for registration received by 2 June and $25 thereafter including on-site registration at the meeting. The fee for students with current ID's is $7.50 for registration received by 2 June and $12.50 thereafter, including on-site registration at the meeting. Payment may be made by check or money order in U.S. funds drawn on a U.S. bank or by Visa, MasterCard, or American Express credit card. To register send your name, address, and payment to the Acoustical Society of America, 500 Sunnyside Blvd., Woodbury, NY 11797, Tel: 516-576-2360; Fax: 516-576-2377; E-mail: asa@aip.org

ABSTRACT

Medical Ultrasonic Imaging. James G. Miller (Department of Physics, Washington University, St. Louis, MO 63130)

Diagnostic ultrasound has become a standard tool in the delivery of health care. Although some work was carried out at least as early as the 1940s, medical imaging with ultrasound grew from a modest novelty in the early 1970s to become the widely used and still rapidly growing diagnostic modality of today. In this tutorial lecture the use of ultrasonic imaging will be illustrated with the aid of video tapes and large screen projection of representative diagnostic studies. Some of the physics and engineering underlying the generation of clinical images will be reviewed at an intuitive, non-mathematical level. The advantages and limitations of ultrasound in comparison with alternative diagnostic modalities will also be highlighted. Specific applications used to diagnose heart disease will provide opportunities to illustrate ultrasonic imaging of the beating heart. Real-time two-dimensional ultrasonic images of the heart will be shown with superimposed color encoded visualizations of Doppler-based estimates of blood flow in the cardiac chambers, which have become the standard for the diagnosis and management of most forms of heart disease.

Short courses to be presented at 133rd meeting in State College, Pennsylvania

Two short courses will be offered at the 133rd meeting in State College, PA. Both courses will be held at the Penn State Conference Center on Friday and Saturday, 20 and 21 June. Please refer to article titled ''Preliminary notice: 133rd Meeting of the Acoustical Society of America'' in this news section for details on hotel accommodations.

Short Course on Smart Structures and Microelectromechanical Systems (MEMS)

Objective

In recent years, the field of sensing and control of noise and vibration in underwater structures, civil structures, aircraft and helicopters with electronic materials such as piezoelectric and ferroelectric ceramics, films and polymers, and MEMS (MicroElectroMechanical Systems) devices attracts researchers from various disciplines. The objective of this course, thus, is to provide an interdisciplinary flavor with an introduction of smart materials, smart electronics, and MEMS to design and develop cost effective, lightweight and reliable microsensors, microprocessors and actuators for noise suppression and vibration reduction in aircraft cabins, control of radiated noise in underwater structures, flow induced noise in helicopters, etc.

Instructors

Vijay Varadan and Vasundara Varadan are Alumni Distinguished Professors of Engineering Science and Mechanics and Electrical Engineering and Co-Directors of the Center for the Engineering of Electronic and Acoustic Materials at the Pennsylvania State University.

Program

Friday, 20 June	1:00 p.m. to 5:00 p.m.
Saturday, 21 June	9:00 a.m. to 12:00 noon

Instructional materials

Each participant will receive a copy of course notes/viewgraphs prepared by the instructors.

Short Course on Design of Acoustic Materials

Objective

In this course, the phrase ''acoustic materials'' includes both the viscoelastic material used and the configuration the viscoelastic material is used in. Thus, there are two parts to the course: the first part is on intrinsic viscoelastic material properties and how these properties are related to molecular structure, and the second part is on the use of these materials in a configuration to enhance sound absorption or decoupling, such as a coating of the material with inclusions, or a wedge of the material in air. The ''design'' includes both the molecular or chemical arrangement and the physical arrangement such as the thickness of the viscoelastic layer and the size of the cavities. The goal of the course is to provide sufficient background to design an acoustic material for a wide variety of applications, involving both water-borne and air-borne sound.

Instructors

Bruce Hartmann is Head of the Polymer Science Group at the Carderock Division of the Naval Surface Warfare Center and has 30 years experience in relating the molecular structure of polymers to their acoustic properties.

Jacek Jarzynski is Professor in the George W. Woodruff School of Mechanical Engineering at Georgia Institute of Technology. He has 30 years experience in measurements of viscoelastic properties of polymers and in performance measurements and design of acoustic coatings.

Program

Friday, 20 June	2:00 p.m. to 5:00 p.m. Intrinsic Material Properties
Saturday, 21 June	9:00 a.m. to 12:00 noon Performance of Acoustic Coatings 2:00 p.m. to 3:15 p.m. Further Intrinsic Material Properties 3:45 p.m. to 5:00 p.m. Case Studies

Instructional materials

Each participant will receive a copy of course notes/viewgraphs prepared by the instructors and a diskette containing a MATLAB multi-layer program.

Registration

The registration fee for each course is $250 and covers attendance, instructional materials and coffee breaks. Only those who have registered by 2 June will be guaranteed receipt of instructional materials. There will be a $50 discount for reservations made prior to 2 May. Full refunds will be made for cancellations prior to 2 June. Any cancellation after 2 June will be charged a $25.

To register send your name, address, and the course for which you are registering to Acoustical Society of America, Short Course Registration, 500 Sunnyside Blvd., Woodbury, NY 11797, Tel: 516-576-2360; FAX: 516-576-2377; E-mail: asa@aip.org. Payment may be made by check or money order in U.S. funds drawn on a U.S. bank or by Visa, Mastercard, or American Express credit card.

USA Meetings Calendar

Listed below is a summary of meetings related to acoustics to be held in the U.S. in the near future. The month/year notation refers to the issue in which a complete meeting announcement appeared.

1997

13–16 April	23rd International Symposium on Acoustical Imaging, Boston, MA [Sidney Lees, Bioengineering Dept., Forsyth Dental Ctr., 140 Fenway, Boston, MA 02115; FAX: 617-262-4021; E-mail: slees@forsyth.org]. *7/96*
12–14 May	Third AIAA/CEAS Aeroacoustic Conference, Atlanta, GA [Dr. Stephen Engelstad, Lockheed Martin Aeronautical Systems, D/73-47, Z/0-685, Marietta, GA 30063, Tel.: 770-494-9178; FAX: 770-494-3055; E-mail: sengelstad@fs2.mar.1mco.com].
15–20 June	Eighth International Symposium on Nondestructive Characterization of Materials, Boulder, CO [Debbie Harris, The Johns Hopkins University, Ctr. for Nondestructive Evaluation, 102 Maryland Hall, 3400 N. Charles St., Baltimore, MD 21218, Tel.: 410-516-5397; FAX: 410-516-7249, E-mail: cnde@jhuvms.hcf.jhu.edu].
15–17 June	NOISE-CON 97, State College, PA [Institute of Noise Control Engineering, P.O. Box 320, Arlington Branch, Poughkeepsie, NY 12603, Tel.: 914-891-1407; FAX: 914-463-0201.]
16–20 June	133rd meeting of the Acoustical Society of America, State College, PA [ASA, 500 Sunnyside Blvd., Woodbury, NY 11797, Tel.: 516-576-2360; FAX: 516-576-2377; Email: asa@aip.org, WWW: http://asa.aip.org].
9–13 July	International Clarinet Association, Texas Tech Univ., Lubbock, TX [Keith Koons, Music Department, Univ. of Central Florida, P.O. Box 161354, Orlando, FL 23816-1354, Tel.: 407-823-5116; E-mail: kkoons@pegasus.cc.ucf.edu].
7–11 Sept.	American Academy of Otolaryngology—Head and Neck Surgery, San Francisco, CA [American Academy of Otolaryngology—Head and Neck Surgery, One Prince St., Alexandria, VA 22314 Tel.: 703-836-4444; FAX: 703-683-5100].
22-24 Sept.	Second Biennial Hearing Aid Research and Development Conference, Bethesda, MD [National Institute of Deafness and Other Communication Disorders, Tel.: 301-970-3844; FAX: 301-907-9666; E-mail: hearingaid@tascon.com]. Deadline for abstracts is 15 March.
19–22 Oct.	Workshop on Applicatons of Signal Processing in Audio and Acoustics, New Paltz, NY [Jont B. Allen, AT&T Labs Research, Room 2D-553, 600 Mountain Ave., Murray Hill, NJ 07974; Tel.: 908-582-3157; E-mail: jba@research.att.com; WWW: http://www.icsi.berkeley.edu/waspaa97/]. Deadline for summaries is 15 April.
1–5 Dec.	134th meeting of the Acoustical Society of America, San Diego, CA [ASA, 500 Sunnyside Blvd., Woodbury, NY 11797, Tel.: 516-576-2360; FAX: 516-576-2377; E-mail: asa@aip.org, WWW: http://asa.aip.org].

1998

22–26 June	135th meeting of the Acoustical Society of America/16th International Congress on Acoustics, Seattle, WA [ASA, 500 Sunnyside Blvd., Woodbury, NY 11797, Tel.: 516-576-2360; FAX: 516-576-2377; E-mail: asa@aip.org, WWW: http://asa.aip.org].
13–17 Sept.	American Academy of Otolaryngology—Head and Neck Surgery, San Francisco, CA [American Academy of Otolaryngology—Head and Neck Surgery, One Prince St., Alexandria, VA 22314, Tel.: 703-836-4444; FAX: 703-683-5100].
12–16 Oct.	136th meeting of the Acoustical Society of America, Norfolk, VA [ASA, 500 Sunnyside Blvd., Woodbury, NY 11797, Tel.: 516-576-2360; FAX: 516-576-2377; E-mail: asa@aip.org, WWW: http://asa.aip.org].

REVIEWS OF ACOUSTICAL PATENTS

Daniel W. Martin
7349 Clough Pike, Cincinnati, Ohio 45244

The purpose of these acoustical patent reviews is to provide enough information for a Journal reader to decide whether to seek more information from the patent itself. Any opinions expressed here are those of reviewers as individuals and are not legal opinions. Printed copies of United States Patents may be ordered at $3.00 each from the Commissioner of Patents and Trademarks, Washington, DC 20231. [S0001-4966(97)04603-1]

Reviewers for this issue:

GEORGE L. AUGSPURGER, *Perception Incorporated, Box 39536, Los Angeles, California 90039*
HARVEY H. HUBBARD, *325 Charleston Way, Newport News, Virginia 23606*
SAMUEL F. LYBARGER, *101 Oakwood Road, McMurray, Pennsylvania 15317*
ROBERT C. WAAG, *University of Rochester Medical Center, 601 Elmwood Avenue, Rochester, New York 14642*

5,510,578

43.38.Ja AUDIO LOUDSPEAKER CABLE ASSEMBLY

John H. Dunlavy, Colorado Springs, CO
23 April 1996 (Class 174/128.1); filed 30 June 1995

The patent asserts that loudspeaker cables do matter, that the characteristic impedance of most cables is several times that of a typical loudspeaker load, and that the resulting impedance mismatch causes ringing, blurring, and other audible distortion. The problem is solved by bundling together multiple pairs of insulated wire, ''...wherein the impedance of said cable assembly is within the impedance range of said loudspeaker.''—GLA

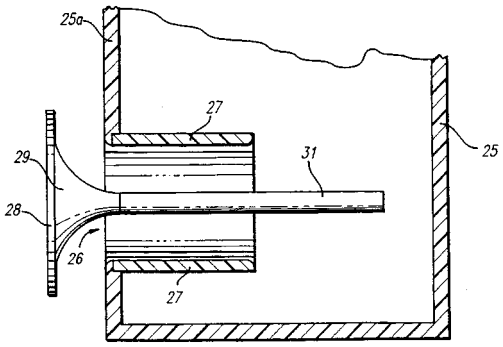

5,517,570

43.38.Ja SOUND REPRODUCING ARRAY PROCESSOR SYSTEM

Stephen F. Taylor, assignor to Taylor Group of Companies
14 May 1996 (Class 381/18); filed 14 December 1993

The patent includes 19 pages of illustrations to help describe a system for recording and reproducing sound via ''audio pixels.'' In essence, it is an implementation of Tom Holman's dictum that the best way to make sound come from a certain location is to put a loudspeaker there. A system intended for use with video games utilizes eight audio channels for the sound pixel array plus four high-frequency signals fed to super-tweeters and three low-frequency signals for subwoofers.—GLA

5,517,573

43.38.Ja PORTED LOUDSPEAKER SYSTEM AND METHOD WITH REDUCED AIR TURBULENCE

Matthew S. Polk and Colin B. Campbell, assignors to Polk Investment Corporation
14 May 1996 (Class 381/159); filed 23 August 1994

The popularity of high-power subwoofers has prompted considerable research into the aerodynamics of loudspeaker vent design. When driven at high velocities, air in the vent becomes increasingly turbulent, producing all sorts of nasty effects that loudspeaker designers would prefer not to deal with. In one version the system takes the form of a permanently open poppet valve to promote a more laminar air flow.—GLA

5,537,479

43.38.Ja DUAL-DRIVER BASS SPEAKER WITH ACOUSTIC REDUCTION OF OUT-OF-PHASE AND ELECTRONIC REDUCTION OF IN-PHASE DISTORTION HARMONICS

Kenneth W. Kreisel and Lester M. Field, assignors to Miller and Kreisel Sound Corporation
16 July 1996 (Class 381/96); filed 29 April 1994

Loudspeaker designers have recently rediscovered the 1950s method of mounting paired woofers Janus style, one facing forward and the other back, to reduce even-order distortion. The patented system utilizes motional

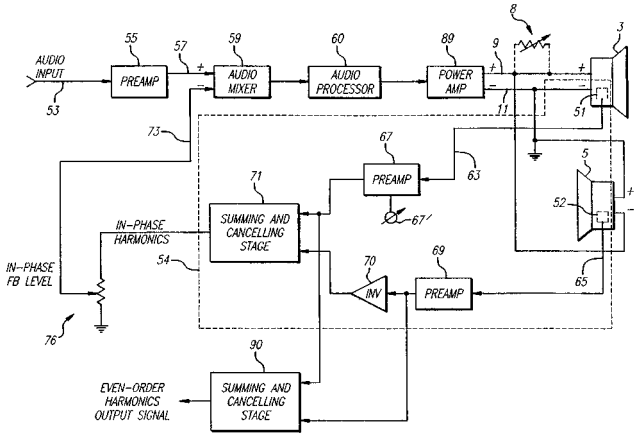

 0001-4966/97/101(3)/1219/6/$10.00

feedback from each woofer, which is then electronically summed and cancelled to suppress odd-order harmonics. Interesting and clever.—GLA

5,553,148

43.38.Ja APPARATUS AND METHOD FOR PRODUCING VIBRATORY SENSATIONS TO ACCOMPANY AUDIBLE SOUNDS IN A PROPERLY PHASED RELATIONSHIP

Ben Werle, Woodland Hills, CA
3 September 1996 (Class 381/24); filed 20 June 1994

It had never occurred to this reviewer that ''body-sonic'' type chairs are subject to phase distortion. The apparatus utilizes a gel pack as a kind of tactile upholstery interposed between the driving transducers and the user. Signals to the transducers are delayed electronically, ''...to allow sound waves from a speaker to reach the ears of the listener at the same time that the vibrations are provided to the body of the listener.''—GLA

5,557,680

43.38.Ja LOUDSPEAKER SYSTEM FOR PRODUCING MULTIPLE SOUND IMAGES WITHIN A LISTENING AREA FROM DUAL SOURCE LOCATIONS

Thomas A. Janes, Cincinnati, OH
17 September 1996 (Class 381/27); filed 19 April 1995

Left, center, and right channels are reproduced from two loudspeaker cabinets. Left and right loudspeakers face forward. Two more loudspeakers are angled in to generate a phantom center image.—GLA

5,509,080

43.38.Lc BASS CLIPPING CIRCUIT

John H. Roberts, assignor to Peavey Electronics Corporation
16 April 1996 (Class 381/98); filed 14 March 1994

A very simple clipping circuit is incorporated into tone control circuitry, allowing full bass boost for low-level signals but flattening frequency response at high levels.—GLA

5,459,786

43.38.Si LOUDSPEAKER TELEPHONE DEVICE COMPRISING A NOVEL NOISE SUPPRESSING CIRCUIT

Yutaka Tomiyori and Tadashi Eguchi, assignors to NEC Corporation
17 October 1995 (Class 379/390); filed in Japan 19 February 1991

When a loudspeaker telephone is used in a noisy environment there is a tendency for the system to lock up in the transmit mode. The patent adds a simple compander to limit the microphone's output level when it exceeds a specified threshold, allowing the signal from the other station to actuate the receive mode.—GLA

5,513,265

43.38.Si MULTI-CHANNEL ECHO CANCELLING METHOD AND A DEVICE THEREOF

Akihiro Hirano, assignor to NEC Corporation
30 April 1996 (Class 381/66); filed in Japan 31 May 1993

The patent relates to large teleconferencing installations which may employ a number of microphone-loudspeaker stations at each location. Because delay paths vary continuously as various microphones and loudspeakers are switched on and off, an adaptive echo-cancelling filter tends to become large, slow, and confused. The patent describes a three-step scheme to speed up the process, including ''...a step of cancelling the echoes from mixed signals in which the echoes are mixed by subtracting the echo replicas from the mixed signals.''—GLA

5,553,147

43.38.Vk STEREOPHONIC REPRODUCTION METHOD AND APPARATUS

Joseph E. M. Pineau, assignor to One, Incorporated
3 September 1996 (Class 381/24); filed 11 May 1993

If conventional left and right stereophonic signals are reproduced from essentially the same point in space (e.g., small, back-to-back loudspeakers), then the Haas effect is circumvented and a listener can be almost anywhere. Hmm. What about mixing the signals electrically and using only one loudspeaker?—GLA

5,407,034

43.50.Gf NOISE DAMPED BRAKE PAD ASSEMBLY

Edward J. Vydra *et al.*, assignors to Pre Finish Metals, Incorporated
18 June 1995 (Class 188/73.37); filed 31 January 1994

This patent relates particularly to disk brakes and brake pad assemblies to inhibit brake squeal or noise. A brake pad assembly is designed to have a damping structure, including a viscoelastic material disposed between the backing plate and the friction lining pad, and firmly attached to each. The viscoelastic material inhibits noise generation by absorbing or damping the noise-creating vibrations of the friction lining pad.—HHH

5,414,230

43.50.Gf SILENCER ARRANGEMENT FOR COMBUSTION ENGINES

Joris A. M. Nieuwendijk *et al.*, assignors to U. S. Philips Corporation
9 May 1995 (Class 181/206); filed in European Patent Office 23 September 1992

This patent relates to the reduction of exhaust noise from an internal combustion engine of the type used in automotive vehicles. A conventional passive acoustic silencer is used to suppress the high-frequency noise. Inputs

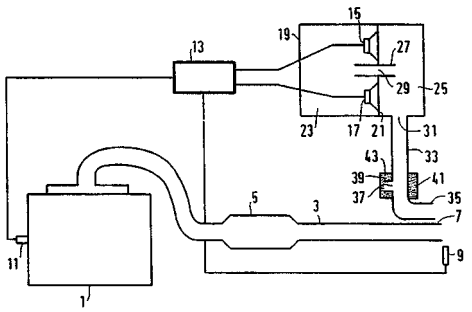

from an external microphone and a tachometer are applied to an active control unit which drives a pair of loudspeakers coupled to a Helmholtz resonator for low-frequency noise control.—HHH

5,539,163

43.50.Gf LIGHTWEIGHT LOW PROFILE SOUND WALL PANEL

Peter L. Anderson *et al.*, assignors to the Reinforced Earth Company
23 July 1996 (Class 181/210); filed 28 April 1994

This patent relates to sound barriers for use along highways, railways, airports, and industrial areas. A new acoustic barrier panel is identified which consists of a center slab sandwiched between two outside slabs with grout curtains interposed. All slabs are formed from Durisol which is made from Portland Cement with long, thin, specially treated wood shavings as aggregate. The resulting surfaces are absorptive, thus reducing the adverse effects of reverberation between parallel walls.—HHH

5,568,404

43.50.Nm METHOD AND SYSTEM FOR PREDICTING SOUND PRESSURE LEVELS WITHIN A VEHICLE DUE TO WIND NOISE

Gary S. Strumolo, assignor to Ford Motor Company
22 October 1996 (Class 364/558); filed 24 October 1994

This patent describes in admirable detail a Wind Noise Modeller which is ''an analytical tool to predict interior SPL at the driver's ear due to wind noise.'' It is a programmable digital computer system for (a) storing data representing the geometry of an automotive vehicle part (e.g., window) susceptible to vibration by the turbulent air flow outside the window; (b) storing data representing noise spectra for external ''vortex, reattached and turbulent boundary layer flows;'' and (c) computing sound pressure level data within the vehicle at driver and passenger ear positions. The patent is a monograph on the subject from the standpoint of aeroacoustics.—DWM

5,566,573

43.58.Fm CAPACITIVE ACOUSTIC WAVE DETECTOR AND METHOD OF USING SAME

William T. Yost, assignor to United States National Aeronautics and Space Administration
22 October 1996 (Class 73/643); filed 27 September 1994

''A capacitor having two substantially parallel conductive faces is acoustically coupled to a conductive sample end such that the sample face is one end of the capacitor. A non-contacting dielectric may serve as a spacer between the two conductive plates. The formed capacitor is connected to an LC oscillator circuit such as a Hartley oscillator circuit producing an output

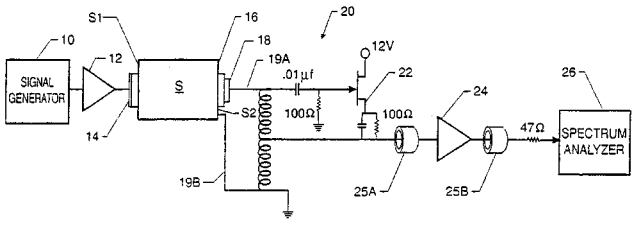

frequency which is a function of the capacitor spacing. This capacitance oscillates as the sample end coating is oscillated by an acoustic wave generated in the sample by a transmitting transducer. The electrical output can serve as an absolute indicator of acoustic wave displacement.''—DWM

5,549,658

43.66.Ts FOUR-CHANNEL COCHLEAR SYSTEM WITH A PASSIVE, NON-HERMETICALLY SEALED IMPLANT

Robert V. Shannon *et al.*, assignors to Advanced Bionics Corporation and House Ear Institute
27 August 1996 (Class 607/57); filed 27 October 1994

The patent shows four implanted receiver coils driven by an external processor having four driver coils, each of which matches an implanted coil in position. The driver coils may be located above the ear in a wearable assembly. One end of each receiver coil goes to a different position along the cochlea and the processor sequentially activates the implanted electrodes using a continuous interleaved sampling system (CIS).—SFL

5,553,151

43.66.Ts ELECTROACOUSTIC SPEECH INTELLIGIBILITY ENHANCEMENT METHOD AND APPARATUS

Hyman Goldberg, San Diego, CA
3 September 1996 (Class 381/68.4); filed 15 June 1994

The patent shows a hearing aid amplifier feedback circuit that controls gain at two levels to better fit the hearing loss characteristics of a user. A first level detector adjusts the system gain for low-level input signals; the

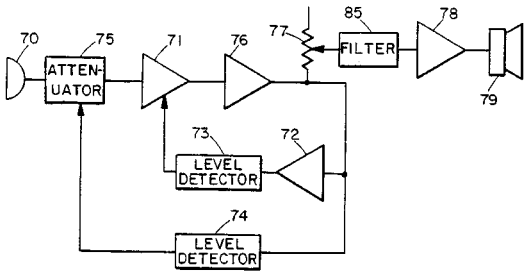

second level detector controls high-level input signals. Results are stated to be superior to those obtained with a single feedback system.—SFL

5,554,096

43.66.Ts IMPLANTABLE ELECTROMAGNETIC HEARING TRANSDUCER

Geoffrey R. Ball, assignor to Symphonix
10 September 1996 (Class 600/25); filed 8 April 1994

This patent is a continuation-in-part of Pat. 5,546,654. The present patent shows a small moving-coil transducer that is attached to an ossicle of the middle ear. Input to the transducer is shown as a subcutaneous pickup

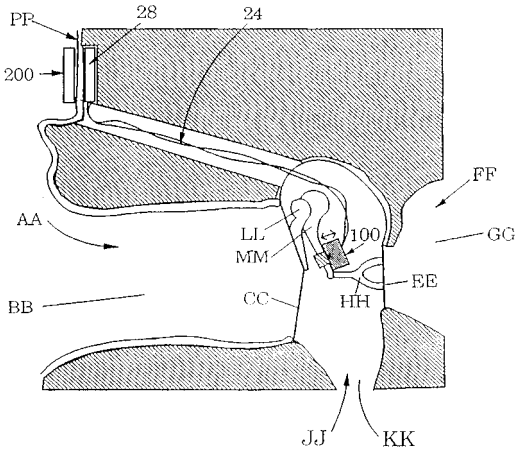

driven from an external sound transducer unit outside the skin opposite the pickup unit.—SFL

5,554,188

43.66.Ts UNIVERSAL MIDDLE EAR PROSTHESIS

Anthony Prescott, assignor to XOMED, Incorporated
10 September 1996 (Class 623/10); filed 11 April 1995

A middle ear prosthesis designed to substitute for missing ossicles is shown. The prosthesis has two parts. One end has a somewhat enlarged tip, rounded on the edges, and designed for contact with the eardrum. The other, smaller, end fits against the footplate of the stapes. One end of the smaller

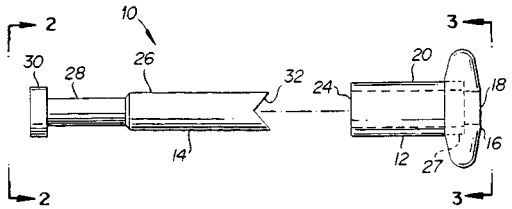

part fits into a hole in the larger end, permitting the adjustment of length. When the malleus and incus are missing, the hole in the larger end can be fitted over the head of the stapes.—SFL

5,557,673

43.66.Ts AUDITORY ASSISTANCE APPARATUS AND METHOD

Boris Ginzburg, assignor to AVR Communications
17 September 1996 (Class 379/443); filed 25 October 1994

The patent shows a means of reducing stray magnetic field interference when using the telecoil of a hearing aid. Two coils with cores are arranged coaxially and spaced a short distance apart. The outputs of the coils are out of phase for stray fields, but do not affect the function of the telecoil when their axes are located at right angles to those of the desired signals.—SFL

5,558,618

43.66.Ts SEMI-IMPLANTABLE MIDDLE EAR HEARING DEVICE

Anthony J. Maniglia, Hunting Valley, OH
24 September 1996 (Class 600/25); filed 23 January 1995

The patent shows an implanted hearing prosthesis in which a high coercivity permanent magnet enclosed in a hermetically sealed case is

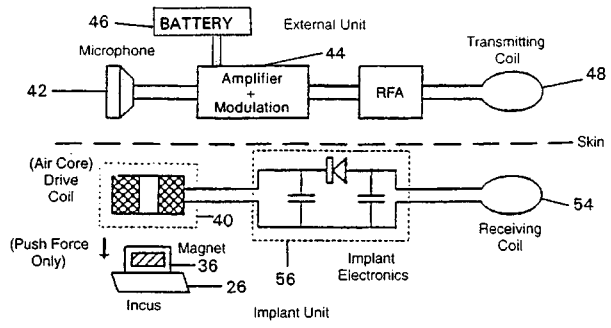

affixed to one of the ossicles and caused to vibrate by an adjacent enclosed coil. Several arrangements as well as circuitry are shown.—SFL

5,551,090

43.66.Vt EAR PROTECTING APPARATUS

Janet M. Thompson, Edgewater, FL
3 September 1996 (Class 2/209); filed 20 April 1995

A hearing protector on a headband is shown that has an annular mem-

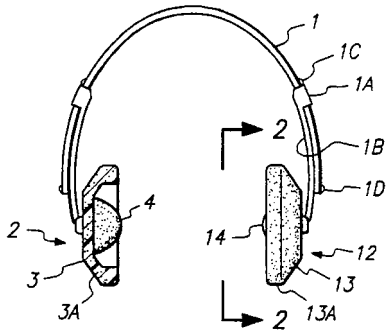

ber surrounding the pinna and a central projecting portion that presses against the opening of the auditory canal.—SFL

5,557,077

43.66.Vt HEARING PROTECTOR PLUG

Bengt G. Berg, assignor to Bilsom AB
17 September 1996 (Class 181/135); filed in Sweden 19 April 1991

The patent discloses the use of a distributed detectable material in powder form, particularly iron powder, for the manufacture of hearing protector earplugs. The purpose is to allow the recovery and removal of lost earplugs, with particular application in the food industry.—SFL

5,567,895

43.75.Gh SOUND REVERBERATOR MOUNTED IN A SOUND BOX OF A STRING MUSICAL INSTRUMENT

Roberto Aspri and Claude Mauffette, both of Montreal, Quebec, Canada
22 October 1996 (Class 84/294); filed 12 July 1995

For guitars or other string instruments having enclosures behind the strings, this patent proposes an internal spring **18** connected at its free end by transfer member **21** to the bridge across which strings **13** are stretched, for the purpose of adding reverberation at the frequencies of string tone. The stored vibrational energy in the spring is radiated through the spring terminations from the body of the instrument. An internal damper **39**, controlled

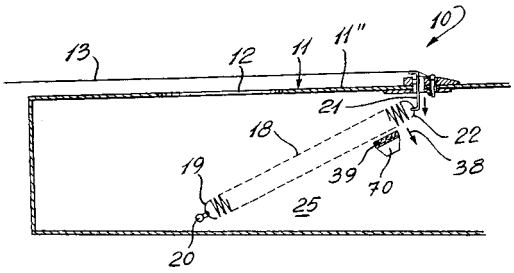

from outside the instrument, contacts the spring when it is ''off.'' The reviewer, who invented a similarly reverberant loudspeaker [Patent 2,853,145 reviewed J. Acoust. Soc. Am. **31**, 266 (1959)], anticipates that the guitarist will need to handle the guitar carefully, in order to avoid inadvertent mechanical excitation of the springs.—DWM

5,567,896

43.75.Gh STRING INSTRUMENT WITH SOUND AMPLIFICATION

Peter Gottschall, Uttenweiler, Germany
22 October 1996 (Class 84/294); filed in Switzerland 23 December 1994

Within the resonant air space of this guitar is a securely supported plate **19** that is downwardly inclined relative to the belly **5**, in order to divide the interior space into two chambers connected together at the free edge **25**

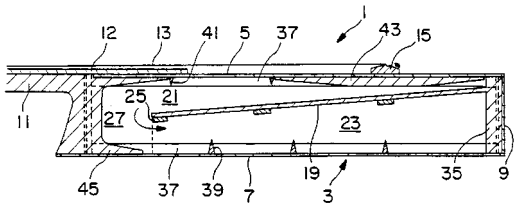

of the plate **19**. The partitioning of the interior space is said to improve resonance of the acoustical resonator.—DWM

5,567,902

43.75.Mn METHOD AND APPARATUS FOR OPTICALLY SENSING THE POSITION AND VELOCITY OF PIANO KEYS

Thomas E. Kimble and David R. Wade, assignors to Baldwin Piano and Organ Company
22 October 1996 (Class 84/658); filed 6 January 1995

''An electronic keyboard musical instrument is provided having optical emitters and detectors both positioned beneath each of the instrument's keys, whereby optical energy is emitted upon the bottom reflective surface of the key and the reflected light is detected. The distance between the optoelectric sensor and the bottom of the key is detected by the light detector which produces an analog output signal and, by measuring the time between a first and second threshold crossing, the key's velocity can be determined. ...Electronics in the keyboard instrument sequentially scan each of the output voltages produced by their corresponding light detectors so that a single microprocessor can measure all of the key position values. ...The time interval between threshold crossings can be determined, which in turn is used to determine the velocity of each key as it is being depressed. Once the velocity is known, the volume for that key's particular musical tone can be controlled by a sound engine, as well as its other characteristics, such as timbre, attack, and envelope.''—DWM

5,563,360

43.75.Tv AUTOMATIC PERFORMANCE APPARATUS CAPABLE OF REPETITIVE PERFORMANCE OF SPECIFIED PORTION

Hiromu Miyamoto and Hiroyuki Iwase, assignors to Yamaha Corporation
8 October 1996 (Class 84/609); filed in Japan 25 December 1992

The apparatus ''automatically repeats a certain specified tune sequence of a musical tune or automatically starts playing from a specified point in a musical tune sequence.'' It is under the control of central processing unit **1**. Read-only memory **2** stores control programs and pattern data for the CPU **1**, and read-and-write memory **3** is a work area for the CPU, and serves as a temporary memory for storing computed results and pattern and song data

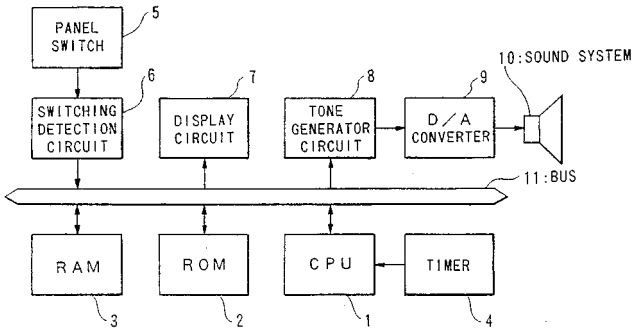

programmed by the user. Since many musical pieces start with an introduction and finish with an ending, between which are repeated passages, this system allows the selection of two points in the musical sequence to define a passage for repetitive performance, effecting a storage saving and providing performance flexibility.—DWM

5,567,901

43.75.Tv METHOD AND APPARATUS FOR CHANGING THE TIMBRE AND/OR PITCH OF AUDIO SIGNALS

Brian C. Gibson *et al.*, assignors to IVL Technologies Limited
22 October 1996 (Class 84/603); filed 18 January 1995

It is well known that the perceived timbre of the same complex waveform differs greatly when the fundamental frequency is greatly changed. Consequently, when a tone wave is sampled at a first rate for storage, then read out at a second rate to change the musical pitch, the tone spectrum needs to be scaled to retain a consistent perceived timbre. According to the patent, the digital method and apparatus patented here make it possible to control the tone spectrum while holding frequency constant, or to control frequency while maintaining the same spectral envelope.—DWM

5,550,902

43.80.Qf REMOTE STETHOSCOPE SIGNAL PROCESSING SYSTEM

C. Richard Abbruscato, assignor to American TeleCare, Incorporated
27 August 1996 (Class 379/106); filed 17 August 1994

The patent shows an electronic stethoscope having its low-frequency output shifted up into a frequency band transmitted by a conventional telephone line. At the doctor's end, the signals are shifted down to their original frequencies and converted to sound for the doctor's analysis. At the doctor's end, stethoscope band filters may be provided to permit more accurate diagnosis.—SFL

5,557,681

43.80.Qf ELECTRONIC STETHOSCOPE

Samuel L. Thomasson, Gilbert, AZ
17 September 1996 (Class 381/67); filed 24 September 1993

The device shown is a hand-held rectangular unit with the pickup microphone mounted in a resilient collar at one end. The microphone is coupled to an active filter having a continuously adjustable bandwidth and center frequency. The controls for these adjustments are located on one side of the case; a gain control is located on the opposite side. The output signal from the active filter passes through a filter having a frequency response inverse to that of the human ear, and is amplified and delivered to earphones.—SFL

5,515,857

43.80.Qf ULTRASONIC DIAGNOSTIC APPARATUS

Hiroyuki Tsujino and Eiichi Shiki, assignors to Kabushiki Kaisha Toshiba
14 May 1996 (Class 128/661.1); filed in Japan 9 June 1993

A velocity profile is formed in this apparatus by using either the average velocity or the maximum velocity of bloodflow at a number of positions along each of two orthogonal directions, one of which extends across

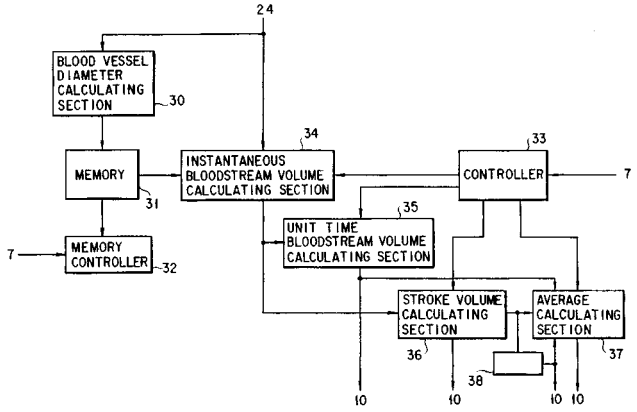

the blood vessel. Bloodflow volume is calculated from the velocity profile and the vessel diameter. This permits reduction of error caused by vessel pulsation.—RCW

5,517,996

43.80.Qf ULTRASONIC DIAGNOSTIC APPARATUS

Kazutaka Okada *et al.*, assignors to Hitachi Medical Corporation
21 May 1996 (Class 128/660.07); filed in Japan 21 April 1994

This apparatus contains individual memories to store signal waveforms that are applied to excite transducer elements. The waveforms are formed through computer processing. This permits the utlrasonic wave that is produced by the stored waveforms to be controlled desirably.—RCW

5,520,184

43.80.Qf ULTRASONIC DIAGNOSTIC METHOD AND AN ULTRASONIC DIAGNOSTIC APPARATUS FOR CARRYING OUT THE SAME

Taibo Ri, assignor to GE Yokogawa Medical Systems, Limited
28 May 1996 (Class 128/661.01); filed in Japan 2 April 1992

This system is designed to enhance real-time performance, enlarge the field of view, and improve signal-to-noise ratio. In the system a main lobe and grating lobes are formed to scan sections of the field of view separately. Echoes received along the direction of the main lobe and echoes received along the direction of the grating lobes are processed to form image sections. The sections are then combined to form an image that spans the entire field of view.—RCW

5,514,086

43.80.Sh MULTIPIECE ULTRASONIC PROBE FOR LIPOSUCTION

Tulio Parisi and R. Kemp Massengill, assignors to Sonique Surgical Systems, Incorporated
7 May 1996 (Class 604/22); filed 22 September 1994

The tip of this probe is mostly plastic to prevent the propagation of ultrasonic waves to the distal end of the apparatus, and thus limits unwanted damage caused by an excessively hot tip. The tip can be reusable or permanently connected, and can have a metal jacket covering the lateral surface to assist in penetration of fatty tissue. One or more openings may be included in the tip for aspiration of fatty tissue.—RCW

5,515,853

43.80.Vj THREE-DIMENSIONAL DIGITAL ULTRASOUND TRACKING SYSTEM

Wayne L. Smith *et al.*, assignors to Sonometrics Corporation
14 May 1996 (Class 128/660.06); filed 28 March 1995

This system uses a network of piezoelectric transducers and digital counters to determine the propagation delay between the activation of one transducer and reception by another transducer. By alternating between transmit and receive modes, the system finds and tracks the position of each transducer in three dimensions.—RCW

5,526,816

43.80.Vj ULTRASONIC SPECTRAL CONTRAST IMAGING

Marcel Arditi, assignor to Bracco Research S. A.
18 June 1996 (Class 128/662.02); filed in European Patent Office 22 September 1994

The different frequency-dependent scattering property of ultrasonic contrast agents that contain microbubbles is used to separate spectral response from tissue that does not contain contrast agent, and then the different responses are combined in a way that enhances the contrast response relative to the tissue background.—RCW

5,529,070

43.80.Vj ACQUISITION AND DISPLAY OF ULTRASONIC IMAGES FROM SEQUENTIALLY ORIENTED IMAGE

Larry J. Augustine and Phillip Keller, assignors to Advanced Technology Laboratories
25 June 1996 (Class 128/660.07); filed 27 September 1994

A sequence of images of planes that includes the position of each plane is produced. The positional information is developed from accelerometers or transmitters located within the ultrasonic scanhead. Spatially related images are shown by displaying one image plane in the plane of the display and a second image plane projected in relation thereto.—RCW

Sonic effervescence: A tutorial on acoustic cavitation[a)]

Robert E. Apfel
Yale University, New Haven, Connecticut 06520-8286

(Received 19 July 1996; revised 19 September 1996; accepted 11 October 1996)

This article on acoustic cavitation is a revision of a tutorial lecture presented at the Acoustical Society of America meeting in Austin, Texas, on 28 November 1994. The general approach adopted here differs from a review article in stressing the overarching themes that come under the category of acoustic cavitation, rather than being an encyclopedic reference on the topic. When possible, specific order-of-magnitude estimates have been given so that the reader can better understand the particular phenomena being described. The basic physics is discussed, and applications are reviewed with the goal of putting them in a useful context. © *1997 Acoustical Society of America.* [S0001-4966(97)04902-3]

PACS numbers: 43.10.Ln, 43.25.Yw, 43.35.Ei [DWM]

INTRODUCTION

The objective of this tutorial article is to give the reader a semi-quantitative appreciation for the physical phenomena and many applications that fall under the term: acoustic cavitation. Because of the required brevity of this effort, much is left out, and, therefore, the reader is asked to forgive omissions of content and attribution which are found, instead, in the comprehensive review articles and books listed in the bibliography.

Cavitation can be defined as any stimulated bubble activity. The stimulation may be due to flow, decompression, acoustic waves, sudden deposition of electromagnetic or ionizing radiation, or heat. The activity can refer to bubble inception or dynamics.

Acoustic cavitation is just acoustically induced bubble activity. In general, we should assume that the activity is observable to the extent that we can measure the activity or the effect of that activity. When the collapse of a bubble is capable of producing high fluid velocities, shock waves, and/or jetting phenomena, the cavitation is called ''inertial,'' because the kinetic energy stored in the liquid is imparted to the bubble, and dominates the motion. This designation is typical of bubbles that grow to more than twice their original size in one or two acoustic cycles. For a more gentle cavitation in which the size changes in each acoustic cycle are relatively small, the term ''noninertial'' cavitation has been deemed appropriate. Here, the restoring force of the internal gas is important in the cycle-to-cycle motion. These designations, inertial and noninertial, are considered more appropriate than the terms ''transient'' and ''stable'' cavitation, which have been used to describe the same phenomena.[1]

A. Cavitation as the great energy concentrator

Sound waves are, in general, of relatively low energy density. For instance, even a progressive sound wave in water of pressure amplitude of five atmospheres (0.5 MPa) has an energy density of only about 50 Joules per cubic meter, which, on a per molecule basis is about six orders of magnitude below the thermal energy per molecule of water at room temperature. But that same five-atmosphere sound wave at a frequency of 3 MHz (typical of diagnostic ultrasound) can cause a bubble with an initial radius of 1 micron to grow to a radius of about 3 microns. This nearly empty gas bubble will collapse in about 0.3 microseconds depositing into a fraction of a cubic micron about 3 ten-thousandths of an erg, which, for purposes of comparison with ionizing radiation, is over 100 million electron volts. The nearly adiabatic bubble collapse will lead to almost nine orders of magnitude of enhancement in the energy per molecule, producing internal gas pressures of hundreds to thousands of atmospheres and temperatures of thousands of degrees Kelvin. It is no wonder that sound and ultrasound can be used to catalyze chemical reactions, in a process called sonochemistry. An example of the energy concentrating effects of acoustic cavitation is given in Table I.

B. Context of related bubble phenomena

Acoustic cavitation shares much with other bubble phenomena. Inception mechanisms and the role of impurities (cavitation ''nuclei'') are similar, and dynamical effects can be similar. The early work of Harvey is noteworthy in this context.[2] Consider the factors that can influence the growth or collapse of a spherical bubble in a fluid.

1. Boiling

When the temperature of a liquid is high enough that the vapor pressure exceeds the ambient pressure, then boiling may take place. But if no pre-existing nuclei are present and if there is no free surface (one in contact with a gas or vapor), then bubbles must originate at the submicroscopic scale; at this scale, one can see from the bubble equilibrium equation that the inward stress due to surface tension can be large. Liquids will ''superheat'' significantly before boiling occurs. For instance, we have shown that water drops moving slowly in hot oil can be superheated at atmospheric pressure to 279.5 °C before bursting into the vapor phase.[3]

This superheat limit will not be achieved in the presence of sufficiently energetic ionizing radiation, as Donald Glaser

[a)]Based on a tutorial given at a fall meeting of the Acoustical Society of America, Austin, Texas, 28 November 1994 [J. Acoust. Soc. Am. **96**, 3233(A) (1994)].

TABLE I. Example of energy concentration (3-MHz sound wave, 5-atmosphere pressure amplitude).

	Initial	Final
Radius	1 micron	3 microns, max size to 0.14 microns, min. size
Internal pressure	1 atmosphere	4140 atmospheres
Internal temperature	20 °C	2900 °C
Energy density	1 MeV/micron^3	383 MeV/micron^3

demonstrated in 1952 in his invention of the ''bubble chamber,'' an instrument that has played a major role in the advancement of elementary particle physics. Apfel has shown that certain liquid drop materials, chosen to be superheated at room temperature, could be immersed in a gel in order to form a sensitive radiation detector composition, with applications in radiation safety and medicine.

2. Bends

As with boiling, the pressure on the inside of the bubble plays an essential role in bubble formation in gas-supersaturated liquids. The ''bends'' refers to the effects of gas bubble formation in living systems. These bubbles usually form when a gas-saturated tissue is decompressed. The growth of gas bubbles is, in general, much slower than vapor bubble growth in boiling for the same pressure differential, because in the latter case one is dealing with evaporation from the bubble wall interface, whereas in case of the motion of noncondensable gases, such as air, gas diffusion through the liquid controls rate processes.

A human diver saturated at 2.5 atmospheres gauge pressure, corresponding to a water depth of about 25 meters, could face fatal consequences if decompressed to the surface without adequate time for dissolved gas to come out of tissues. It appears that there are numerous sites for bubble nucleation in moderately supersaturated tissue.

3. Beer

The opening of a beer or a soft drink can often lead to the formation of bubbles, in much the same way as bubbles form in a rapidly decompressed diver. Pouring a soft drink or beer into a glass or plastic container with or without ice can result in quite different behavior. With a plastic cup, ice, or a dirty glass surface, bubbles will be nucleated on the available surfaces. With a clean glass, the water will tend to wet the glass, and the smooth surface is less likely to produce bubbles. Do you think it is better from the point of view of not nucleating too many bubbles, to add the ice before or after the drink is in the glass?

4. Bark

How does water get from the roots of a tree to the leaves? With some redwoods, that distance is 365 feet. Transpiration of water at the leaves leads to a capillary action that works to lift the water. But this is a pump that is lifting water

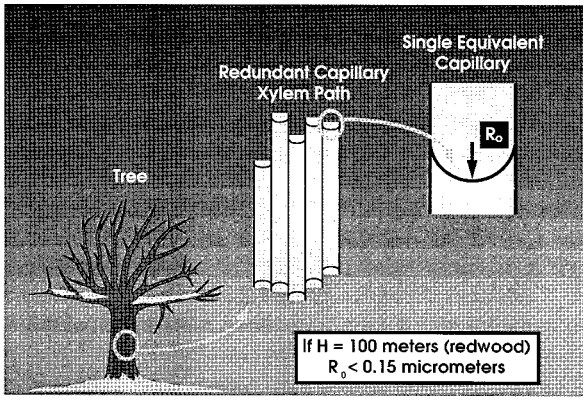

FIG. 1. Transpiration of water from the pores of leaves atop a redwood tree can, by capillary action, draw water from the roots. A negative pressure of up to 11 atmospheres must be sustained in the xylem path, and the pores at the point of transpiration must have a radius of less than 0.15 μm.

that is at atmospheric pressure at the base of the tree. With a redwood, that might imply that the xylem path for carrying water and nutrients near the top of the tree is subjected to a negative pressure (positive tension) of about 11 atmospheres (Fig. 1). Bubbles may be nucleated by disease or even cosmic rays. A tension of 11 atmospheres on a bubble nuclei of radius 0.15 μm will cause the nuclei to grow.

Some of the highly redundant xylem paths can be blocked by bubbles. But with disease and/or serious freezing, it is possible that too many paths can be interrupted, and a tree can die.

5. ''Boats'' (hydrodynamic)

Hydrodynamic cavitation occurs when the flow past an object leads to a pressure reduction, according to Bernoulli's law, that is measured by the product of one half the liquid density and the square of the flow velocity. For water, for example, a pressure reduction of one atmosphere corresponds to a velocity of about 14 meters per second (31 miles per hour). Hydrodynamic cavitation is common on ship propellers, sometimes leading to the erosion of propeller edges and surfaces and to substantial cavitation noise (Fig. 2).[4] Special shaping and materials can ameliorate these effects.

FIG. 2. Bubble generation on a propeller tip, from Strasberg, Ref. 4.

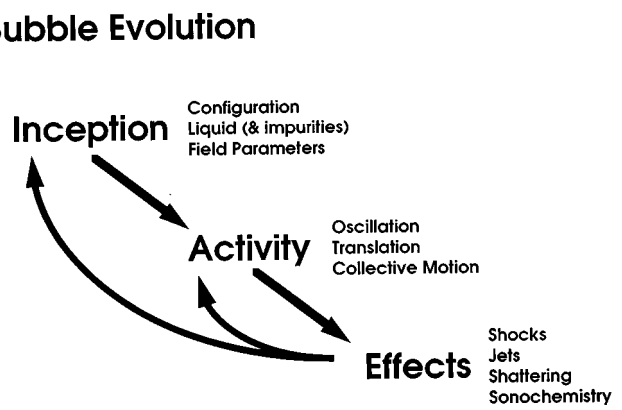

FIG. 3. Bubbles evolve in an acoustic field through stages of inception, bubble activity, and effects due to bubble motion. Each phase may affect the others.

C. History and literature

Bubbles attract and amuse. It is no wonder that this subject has a long and revered history. The books and chapters on cavitation listed in the references are a rich source of information on the historical development of this ever-intriguing field of interest to both experimentalists and theorist. It is also no surprise why theoreticians have tackled the problem of bubble dynamics; for what could be a better starting point than the spherical symmetry that bubbles (at least small ones) afford.

We have already provided one result that follows quickly from the equations describing the motion of a spherical void in an incompressible, inviscid liquid. That was the collapse time for a bubble of a given initial size (e.g., 3 μs for a bubble reaching a maximum radius of 3 μm). We also estimated the energy of collapse as the product of the bubble volume and the ambient pressure, leaving out the contribution due to surface tension, which is okay for bubbles that are a few microns in radius or larger.

I. RELEVANT PARAMETERS

In trying to summarize the vast amount of literature on acoustic cavitation, we can categorize bubble dynamics by the relative amplitude of bubble motion (low, medium, and high) and by the importance of certain fluid parameters which will influence bubble motion. The following parameters come into our computations.

Liquid and gas (and not only water): Density, viscosity, compressibility, diffusion constant, surface tension (and other surface properties if surfactants or contaminants are present), vapor pressure, expansivity, thermal conductivity, specific heat, inner gas properties, dissolved gases and impurities.

Thermodynamic variables: External pressure, temperature, heat balance.

Acoustic variables: Acoustic pressure, frequency or waveform (spectrum), duty cycle, pulse shape and width.

The processes involved in cavitation involve bubble inception, bubble activity, and the effects due to bubble motion, as illustrated in the schematic of Fig. 3.

II. INCEPTION

A. Introduction

Cavitation inception or nucleation refers to the threshold conditions to initiate observable bubble activity. That activity refers to the motion or dynamics of the bubble or bubbles in a particular environment (e.g., near or far from solid surfaces). That activity can produce observable effects, such as radiation forces, acoustic streaming, shock waves, fluid jetting, enhanced chemical reactions, thermal effects (fusing), surface erosion, etc.

B. Homogeneous nucleation thresholds—Tensile strength of liquids

When no pre-existing bubbles or pockets of gas are present in a liquid, it may be necessary to create a bubble *ab initio* in order to cavitate a liquid. Theory predicts, for instance, that a tension of over 1000 atmospheres may be necessary to initiate a bubble in pure, nuclei-free, room temperature water.[5] Figure 4 illustrates the use of the Kelvin equation to estimate the initial bubble size for nucleation at a negative pressure of 1000 atmospheres. Experiments are difficult to perform, not only because it is difficult to produce such a pure sample, but also because it is difficult to produce such large tensile stresses in a liquid. Clever approaches which examine the melting of ice inclusions in solids have produced tensions comparable to the theoretical predictions,[6] and Greenspan and Tschiegg have demonstrated acoustic cavitation thresholds in pure water in excess of 250 atmospheres.[7] This is remarkable given that slightly impure water may only withstand acoustic tensile stresses of a few atmospheres.

Acoustic levitation of a drop in an immiscible host liquid allows one to examine the strength of very small samples, many of which may be free of gaseous nuclei. In

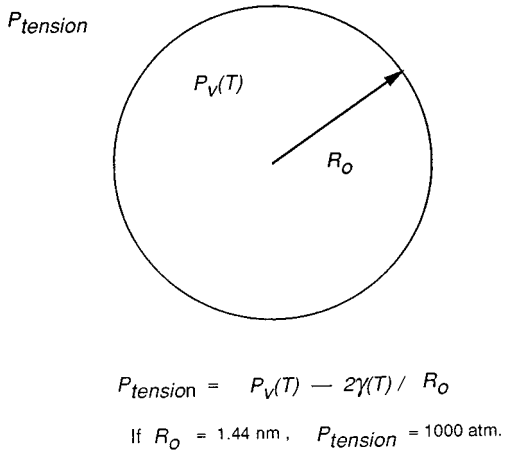

FIG. 4. For a negative pressure of 1000 atmospheres in water, the spontaneous formation of a bubble of radius 1.44 nm is required according to the Kelvin equation.

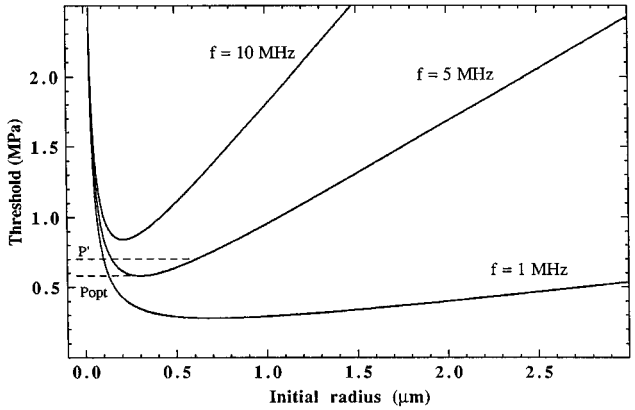

FIG. 5. Calculations of the threshold for inertial cavitation in water at three frequencies, after Apfel and Holland, Ref. 10.

this way, Apfel has measured tensile strengths of organic liquids in good agreement with predictions of homogeneous nucleation theory.[8]

C. Heterogeneous nucleation thresholds

When there are pre-existing nuclei, thresholds for bubble inception can be much lower, even approaching the vapor pressure of the liquid. Blake predicted the minimum acoustic pressure to cause a free, spherical gas bubble to overcome surface tension stresses and to grow unstably.[9] His results assume low acoustic frequencies and negligible viscosity. When the frequency is sufficiently high, the liquid inertia can delay the bubble growth for a long enough duration as to exceed the tensile phase. Thus, the acoustic pressure must be greater in order to overcome these inertial forces during the tensile phase. These inertial effects are especially important in raising thresholds at megahertz frequencies associated with diagnostic ultrasound. Figure 5 illustrates the calculations of Apfel and Holland showing the heterogeneous threshold versus bubble size.[10] For small sizes the Blake mechanism dominates. For larger bubbles, liquid inertia dominates.

D. Mote-induced cavitation; cavitation nuclei

Since free gas bubbles in pure liquids are inherently unstable (they will either dissolve or, if the liquid is supersaturated with gas, they will grow), free bubbles are unlikely to act as nuclei in liquids that have been given time to ''settle down.'' Gas can, however, be trapped in the crevices of solid particles (Fig. 6). Depending on the size of these particles and the wetability of the liquid, it will take a certain minimum acoustic pressure to induce these gas pockets to grow. For sufficiently small crevices (10 microns or less), surface tension remains a dominant factor. For larger crevices, gas saturation and prior history of the liquid are most important.

In the body, crevices may not be the only mechanism for bubble stabilization. Semi-impermeable organic skins can coat bubbles. Injectable bubbles based on this stabilization principle are used as bubble contrast agents for ultrasound imaging[11] and may also be used as cavitation seeds in therapeutic uses of ultrasound.

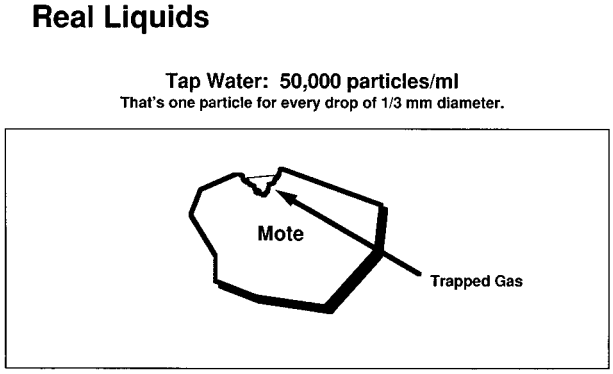

FIG. 6. Schematic of gas pocket trapped in a crevice of a hydrophobic particle (mote). Tap water containing 50 000 motes/ml corresponds to one mote for each drop of 1/3 mm diameter.

E. Radiation-induced

As with superheated liquids used in bubble chambers to follow the paths of elementary particles, tensilely stressed liquids will also form bubbles initiated by radiation of the right type and of sufficient energy. Greenspan and Tschiegg performed a comprehensive set of measurements of thresholds for radiation-induced cavitation in organic liquids and water. Fast neutrons, for example will reduce the threshold to a few atmospheres for some organic liquids, but, for water, the threshold drops to only about 50 atmospheres.[12]

Superheated drop detectors are a new class of bubble chamber in which drops of a volatile liquid are immersed in a gel. For instance, Freon®-12 drops in an aqueous gel at room temperature are superheated by over 50 °C. These will ''pop'' when exposed to neutrons. Since superheat and tension both produce the metastable state, it is not unexpected to find that acoustic waves can increase the sensitivity of these superheated drop suspensions.[13]

III. REGIMES OF DYNAMICS

A. Introduction

Depending on the conditions of the liquid, the size of initial bubbles, and the acoustical conditions, bubbles can experience a wide range of phenomena, including (a) radial motion ranging from small to high amplitude (with the consequent radiation of waves ranging from pure sine waves, to shock waves to broad band noise), (b) shape oscillations ranging from steady-state quadrupole oscillations, to high amplitude jetting and bubble fission, (c) single bubble translation due to radiation forces, and (d) multiple bubble effects due to secondary wave scattering.

B. Low amplitude (free and forced)

The resonance frequency of a symmetrically pulsating bubble (called volume pulsations) is attributed to the stiffness of the internal noncondensable gas resonating against the effective inertia of the surrounding liquid. For bubbles that are more than 10 micron in diameter, one can get the resonance frequency of a bubble at atmospheric pressure in

Bubble Diameter	Resonance Frequency	Relevance
1 mm	3 kHz	Underwater Propagation, Noise in the Ocean, Ultrasonic Cleaning
Human Hair (80 μm)	40 kHz	
Red Blood Cell (4 μm)	1 MHz	Diagnostic and Theraputic Ultrasound
Cell Nucleus x 10	30 MHz	

FIG. 7. The resonance size of bubbles at an ambient pressure of one atmosphere for a given frequency, with typical occurrences.

water (in Hz) by dividing 326 by the bubble radius in centimeters. Different resonance frequencies for different size bubbles are shown in Fig. 7.

Bubbles are damped by three primary mechanisms: Thermal losses, viscous losses, acoustic radiation. Over different frequency regimes, each of these can be more or less important.

C. High amplitude (nonlinear acoustics all the way to chaos)

But bubble motion is not entirely linear. One reason is that the gas ''spring'' is only linear for small amplitude motion. As the amplitude increases, harmonics ($2f_0$, $3f_0$, etc.), subharmonics ($f_0/2$, $f_0/3$, etc.) and ultraharmonics (e.g., $3f_0/2$) can be observed,[14] as seen in Fig. 8.

One can interpret some of this behavior in terms of the general approach of nonlinear dynamics. That is, one can find a threshold for bifurcations and the approach to chaos in bubble dynamics when the pressure amplitude of this nonlinear oscillator is increased to greater values as illustrated in the predictions of Kamath and Prosperetti (Fig. 9).[15]

For bubbles that do not oscillate about an equilibrium position but rather grow in a cycle or two to a much larger size, the collapse is violent and impulsive in character. If the viscosity is sufficiently high or the bubble is sufficiently small so that surface tension is important, then the collapse can retain a nearly spherical shape, and bubble rebound is expected. During the rebound, as much as 70% of the energy can radiate away as sound. Since most of the action takes place in a very small fraction of the acoustic cycle, the acoustic spectrum of the radiated sound energy tends to be very broad; that is, there is a white noise spectrum.

D. Radially symmetric (and shock waves)

From the simple analysis by Rayleigh of the collapse of a void in an incompressible liquid, we know that the bubble wall achieves sonic velocity when the bubble has collapsed to about 1/30 of its original diameter.[16] Of course, this does not take into account surface tension, which will be important when bubbles are in the micron size range or smaller, or the compressibility of either the inner gas or outer liquid. When sonic velocities are approached, compressibility becomes more important. A rarefaction wave will be launched. More importantly, when the wall motion is suddenly decelerated by the trapped gas, a strong pressure wave is

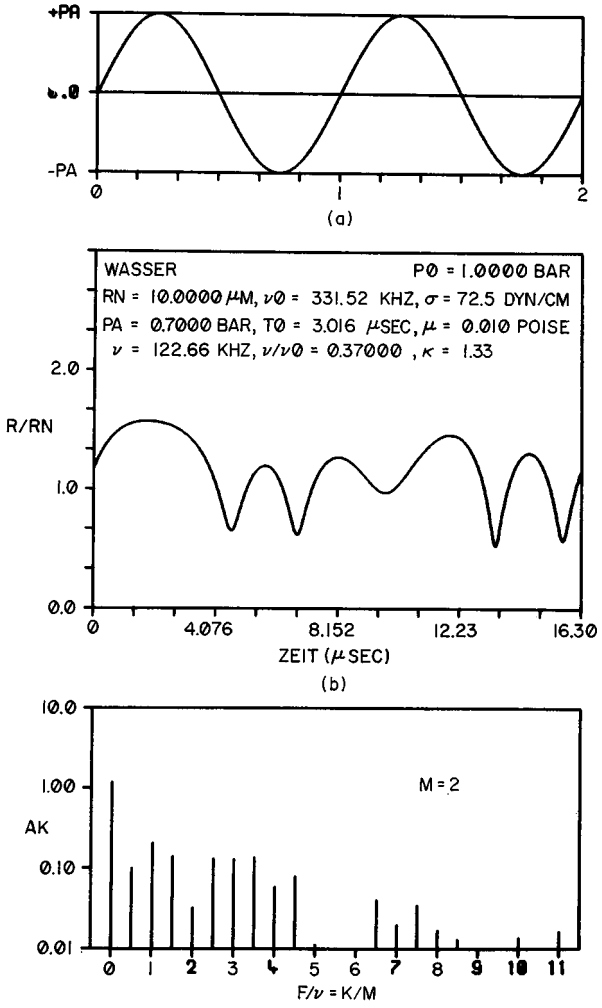

FIG. 8. Predicted nonlinear oscillations of bubbles showing radius versus time and spectral content, after Lauterborn, Ref. 14.

launched. If this is strong enough, shock waves will be generated. But with spherical spreading, these shock waves do not retain their strength very far from the bubble. The biggest effect, therefore, may be in bubble-bubble interactions, in which bubble shattering sometimes occurs.

There is good evidence that suggests that there is a also

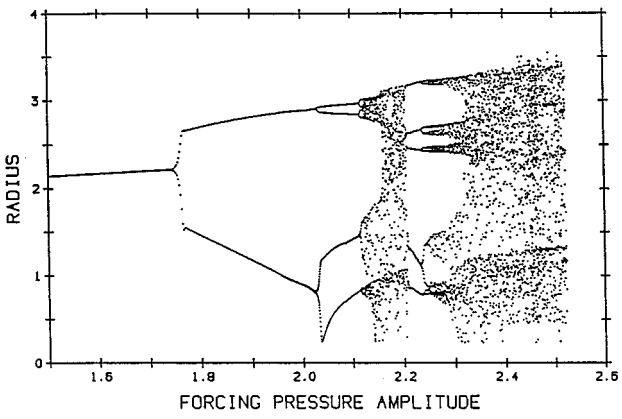

FIG. 9. Nonlinear dynamics of bubbles, after Kamath and Prosperetti, Ref. 15.

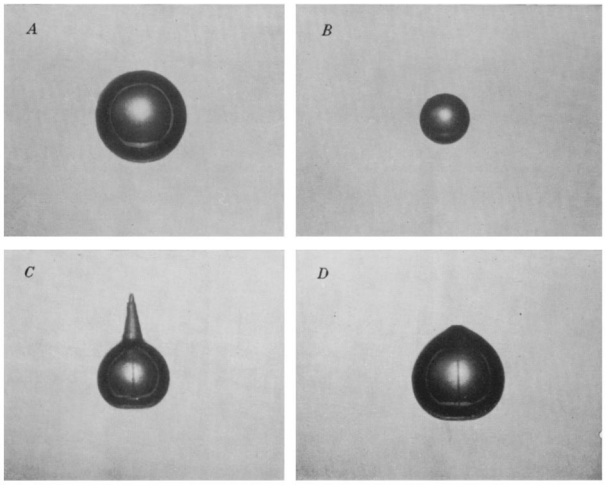

FIG. 10. Photo of jet formation from bubble collapse near a solid boundary, after Benjamin and Ellis, Ref. 17.

a shock wave that is radiated into the bubble when the speed of sound in the gas is exceeded. This situation is discussed later when effects such as sonoluminescence are discussed.

E. Shape deformation and jets

Normally, if effects are to be felt, surfaces must be in the near vicinity. And if a bubble collapses in the vicinity of these surfaces, whether they be solid, another liquid, or gas (free surface or another bubble), then the bubble collapse will not remain symmetrical. From simple hydrodynamic arguments, one can see that fluid rushing inward during the rapid collapse of a bubble will be forced from an initial radial direction if the bubble is near a solid surface. This asymmetric flow deforms the bubble, which then further distorts the flow. A powerful jetting can ensue, as shown in the accompanying photographic sequence of a bubble collapsing near a solid surface (Fig. 10).[17]

The role of these jets in effects is discussed later.

F. Surface instabilities

A surface that continues to grow in size tends to reduce the irregularities in the surface shape. A surface that is forced to decrease in size, tends to buckle like a compressed beam. In the case of a growing bubble, spherical symmetry is encouraged. In the case of a collapsing bubble, small perturbations in the shape may grow. Moreover, surface perturbations grow when a gas-liquid interface accelerates in the direction of the liquid, which is common in bubble collapse. This is called the Rayleigh–Taylor instability, and is related to flow and surface parameters.

The photographic sequence of Fig. 11 shows the explosive growth of a vapor bubble (originating from a superheated drop), and its subsequent collapse. Notice that the growth is a smoothing process, and the collapse leads to instabilities. Surface tension works against these perturbations, because the greater the radius of curvature of the surface, the greater the acoustic stress working to eliminate the perturbations.[18]

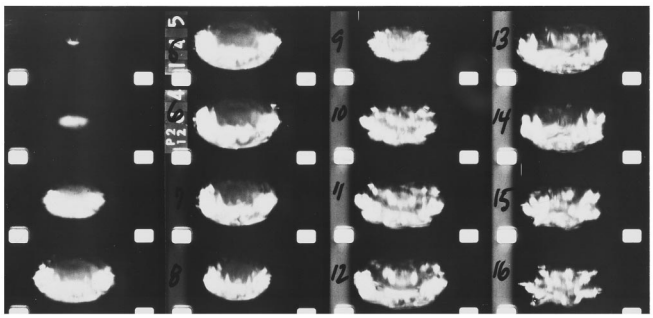

FIG. 11. Vaporization of a superheated drop, leading to symmetrical growth and unstable collapse, after Harbison and Apfel, Ref. 18.

Surface waves of wavelength λ, propagate around a bubble with a velocity of $V=(2\pi\sigma/\rho\lambda)^{1/2}$. Note that these waves are dispersive (depending on frequency). For a spherical bubble of radius R, if one trip around the sphere corresponds to the acoustic period, we have a shape resonance of the lowest order (the quadrupole mode). For instance, for a 1-mm-diam bubble, the quadrupole resonance frequency associated with alternating oblate and prolate shapes is 342 Hz, whereas for a 1-cm-diam bubble, the result is 11 Hz (i.e., this resonance frequency goes inversely as the 3/2 power of the diameter).

A different type of surface instability occurs when a surface (whether curved or flat) is subjected to a high intensity sound field. In this case, the sound field itself interacts with the perturbed surface; at a given threshold intensity, instabilities will grow, and the surface will shatter into small pieces (mixing gas and liquid). This principle can be used for emulsification, as discussed in Sec. VII having to do with applications of cavitation.

G. Effects inside the bubble

When heat conduction cannot keep up with the increase of temperature in a rapidly collapsing bubble, then the motion can be modeled as adiabatic, with pressure increasing as the 3γ power of the inverse bubble radius, and with temperature increasing to the $3(\gamma\text{-}1)$ power. (γ is the ratio of specific heats.) An example of this energy concentration is given in Table I.

H. Effects outside the bubble (radiation: sound and light)

One can learn something about the cavitation process based on the sound and light that emanates from cavitating bubbles. As we have seen, harmonics, subharmonics, and ultraharmonics give some evidence of the nonlinear nature of the phenomena and the amplitude of bubble motion. White noise in the spectrum indicates violent collapse. The three sound spectra given in Fig. 12 indicate growing broadband emission with increasing acoustic amplitude.[19]

When light is emitted, there is strong evidence for high internal bubble temperatures, and chemical processes are possible, at least internally. Additional discussion of this phenomenon is given below.

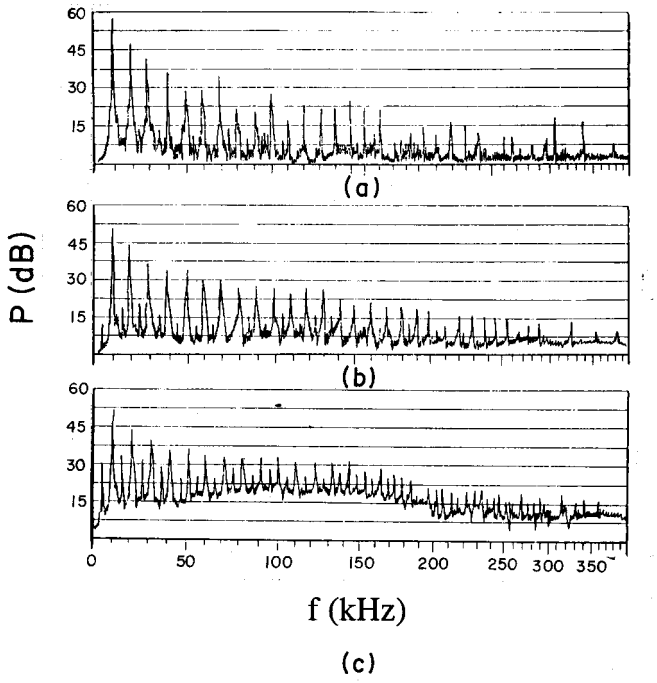

FIG. 12. Sound emissions from radiating bubbles. Discrete frequencies (corresponding to bubble modes) in the spectrum are apparent even for low-pressure amplitudes. At higher pressures, broad band radiation from inertial cavitation becomes more apparent (after Rosenberg, Ref. 19).

IV. BUBBLE TRANSLATION AND OTHER MOTIONS IN A SOUND FIELD

A. Introduction

A sound wave can exert a force on a bubble or other inclusion in a fluid due to the fact that the fundamental fluid equations from which the linearized sound wave equation is derived are essentially nonlinear. The force is just the integral of the pressure over an area. This is equivalent to the time average of the product of bubble volume (which is time varying) and the acoustic pressure gradient. [$F = \langle V(t)\text{grad } P\rangle$.] Notice that since both the volume and pressure gradient are time varying, the time average of their product may have a nonzero component. Physically, the bubble moves in pressure and particle velocity gradients while at the same time the bubble size is changing. This combination leads to a rectified effect that forces the bubble to move in a given direction.

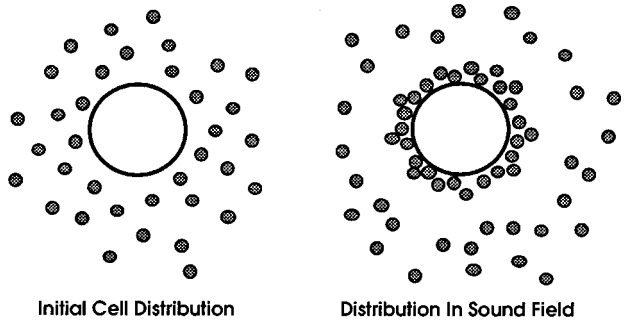

FIG. 13. Schematic illustrating how a radiating bubble will draw particles (e.g., blood cells) toward it due to acoustic radiation forces.

B. Motion in progressive wave field: Primary forces

When a bubble finds itself in a plane progressive wave sound field, it will move in the direction of the progressive wave. A pulsating bubble produces a pressure field that varies as the inverse of the distance from the bubble. In such a diverging field, particles will be attracted to the bubble. For example, red blood cells have been observed to gather around resonating bubbles trapped in the pores of hydrophobic, Nucleopore™, membranes, as schematically illustrated in Fig. 13.

C. Motion in a standing wave field

In a standing wave field, the motion of a bubble will depend on the size of the bubble in relation to its resonance size. For a bubble smaller than resonance size, the bubble size decreases as the acoustic pressure increases; in this case, bubbles move toward a position of spatial pressure maximum (velocity node) in the standing wave field. For bubbles greater than resonance size, the bubble is growing as the pressure increases (in the same way as a mass moves in opposite phase to the forcing in a spring-mass system driven above resonance); here, the bubble moves away from the pressure maximum and toward a velocity maximum.

For particles or liquid drops, the motion depends on the compressibility and density contrasts of the inclusion as compared to the host medium. For bubbles of smaller than resonance size and for drops that are far more compressible than the surrounding medium's compressibility (e.g., oil drops), there is migration toward the pressure maximum in the field, with the inclusion ending up at a position above or below that position depending on its density assuming the field variation is vertical (in the Earth's gravitation field). For solid particles with lower compressibility than the surrounding medium, and for bubbles larger than resonance size, migration is toward the acoustic pressure minimum in the standing wave. This potential differentiation based on these factors make possible separation of materials in a standing wave field.

D. Secondary fields and forces, e.g., bubble–bubble effects

When two bubbles in a sound field are within a few diameters of each other, then they may attract each other. During the rarefaction part of cycle, bubbles expand; flow between bubbles causes a pressure reduction (Bernoulli principle), and bubbles move toward each other. During compression phase, bubbles contract, and fluid that was forced out from between bubbles now flows back. This too induces Bernoulli effect, since pressure is reduced no matter what the direction of the flow. Thus, the net effect averaged over one complete cycle is bubble attraction.

The form of attracting force for two bubbles of volume V_1 and V_2 separated by R is, for the case of wavelength long compared to the separation, $F = AV_1V_2 \div R^{2\cdot}$ This, of course, reminds us of gravitational and electrostatic forces, which are yet to be unified by physicists in any Grand Unified Theory. Is this just a coincidence, or is there some deeper reason for the same form for the force?[20]

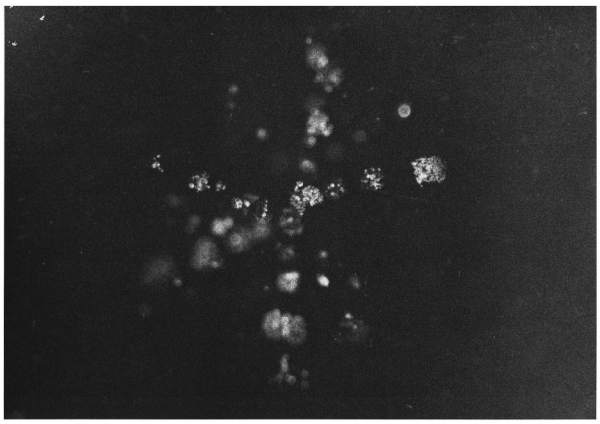

FIG. 14. Stroboscopic image, after Crum, Ref. 21, of bubble ''comets'' moving radially from an acoustic pressure maximum in an acoustic standing wave field.

E. Radiation pressure and the resonance size of bubbles

This difference in behavior of bubbles above and below resonance size in a sound field produces interesting cavitational phenomena. When observing cavitation from a continuous wave source with a frequency under 100 kHz, one sees darting, cometlike cavities moving away from a particular spot (see Fig. 14 from Crum[21]). Hissing and pinging sounds are often heard. What is happening is that very small bubbles, below resonance size, are growing by rectified diffusion (that is, more gas passes into the bubble in expansion than leaves during contraction, leading to a net gas increase each cycle); simultaneously, they move toward pressure maxima in the sound field due to acoustic radiation forces, as discussed above; at the pressure maxima, they continue to grow and perhaps coalesce with other bubbles until a bubble of resonance size is reached. Very high amplitude motion ensues, accompanied by short broad band ''clicks'' and some additional growth, at which point the bubble's phase relative to the sound field is reversed and the bubble is driven away from the sound pressure maximum. It continues, however, to grow and collapse as it translates toward a region of low acoustic pressure. With each collapse, the bubble may shatter, and then reform as it grows again, giving a comet like appearance. If this bubble hits a container surface, a pinging sound may be heard. Bubbles, larger than resonance size adhering to wall or transducer surfaces may oscillate with relative large amplitude, radiating both pure and broadband emissions.

In the steady state, this procession of inward-moving small bubbles and of outward-moving comets is referred to as ''streamers.'' Sometimes, the process has a period quality to it, which is called cyclic cavitation.

V. BUBBLE DETECTION

To detect cavitation one can employ direct or indirect measures. Direct measures refer, for example, to optical or acoustic observations that allow one to determine, or at least infer, the dynamic character of the bubble motion in real time (with only a delay for the interrogating wave to reach the receiver). For instance, a shadow image of a bubble can be picked up with a photo diode. For extremely fast phenomena, such as cyclic sonoluminescence, high speed photomultiplier tubes have been used. Commonly, hydrophones monitor the acoustic pressure in a given region due to bubble activity in another region, giving information on amplitude, phase, and frequency content of bubble emissions. Such information can provide data on the amplitude and scale of bubble activity.

There are a wide variety of indirect measures for cavitation, including erosion of solid surfaces, chemical assays (e.g., iodine release), histological analysis of tissues, etc. Since these methods are indirect, often involving the effects of cavitation on systems, one must infer the kind of bubble activity that created the effect. Sometimes one cannot be sure that the effect was due to bubbles; for instance, thermal effects can also produce bioeffects in tissue, which can, in some instances, be confused with mechanically induced effects.

VI. ESSENTIALS OF APPLICATIONS OF ACOUSTIC CAVITATION

A. Introduction

Acoustic cavitation may be a desirable or undesirable effect of the use of high-intensity sonic or ultrasonic waves. In the ocean, for instance, it may be a limiting factor in the range of long range sonar applications.

B. Macrosonics (cleaning, sonochemistry, etc.)

Bubbles driven into activity by acoustic waves act as sources of pressure variation and fluid motion. For instance, a bubble driven at its resonance frequency will lead to high oscillatory fluid velocity. Such fluid motion can increase heat, momentum, and mass transport. Gas diffusion, for example, will increase so that an evacuated liquid can be outgassed more quickly in the presence of an intense sound field. A chemical reaction that depends on the surface area of a solid material in a fluid, will be aided by oscillatory fluid motion which will convect away unfavorable gradients of chemical reactants.

High fluid velocities occur at cavitation centers, which also are the places where dirt and other impurities form on surfaces. This situation is, of course, favorable for ultrasonic cleaning. Whether in large scale industrial cleaning at 20 kHz, or in the fine scale cleaning required of microchips at 1 MHz, the type of cavitation must produce fluid velocities for scrubbing the surface without powerful inertial cavitation, which might actually pit or otherwise damage the surface below the dirt. The addition of solvents and surfactants, in appropriate amounts, can aid the process. For instance, adding a solvent of high vapor pressure can soften cavitation, since the pressure inside the bubble is cushioned by the vapor of the solvent; at the same time, the surface tension lowering characteristic of surfactants aids in wetting solids and helps the acoustically induced fluid motion to clean effectively.

When flow and macrosonics are combined, one can achieve a variety of phenomena. For instance, flow itself over an edge can produce broadband sound. If the edge is part of a resonant chamber (as with a flute), then particular

frequencies are enhanced. In a liquid flow over an edge, one can also get a pressure reduction. Combine this with an orifice, and one can produce a sonic or ultrasonic atomizer of liquids. Or the acoustics in such systems can be produced by a standard piezoelectric transducer. In any event, dc flow (which can produce hydrostatic pressure reduction via Bernoulli's principle) coupled with ac pressure variation enables a wide range of possibilities when cavitation is produced.

C. Bubbles in the ocean

Bubbles in the ocean act as sources of sound. Some of these bubbles come from wave motion, some from rain drops entraining gas as they enter the water surface, and some from cool, gas-saturated water becoming supersaturated as it warms. These bubbles contribute to the overall sound level in the oceans. Sound encountering these bubbles is attenuated and is slowed because the effective elasticity modulus of the medium is reduced. Since sound refracts toward regions of lower sound velocity, it will bend toward the ocean surface where bubbles are most prevalent.

Underwater explosions not only generate shock waves from the immediate chemical explosion but also from a large amplitude acoustic wave that follows the oscillation period of the bubble, accompanying the explosion. Also, when the initial positive pressure pulse of the explosion hits the free ocean surface, it will reflect as a rarefaction, often leading to a high amplitude, long-duration tension that creates a large bubble just beneath the surface; these bubbles will rise due to their buoyancy and burst at the surface.

Surface reflected rarefactions also can occur in the body from high intensity sources of therapeutic or diagnostic ultrasound, as discussed below.

Long-range sonar transmission requires high acoustic pressures of low frequency. The deeper the sound source, the higher the acoustic pressure attainable without cavitation. Pressurized sonar domes can produce an analogous effect near the surface, but their limited size and pressure means that cavitation represents an ultimate limitation on long-range sonar propagation.

D. Bubbles and bioacoustics

Ultrasound in the body is used for diagnostic and therapeutic applications. Diagnostically, the primary applications are imaging and flow assessment (the latter through doppler modalities); the frequency range is typically from 2 to 15 MHz, the lower frequencies for deeper penetration as in fetal examination and the higher frequencies for shallow penetration with high resolution, such as in the eye.

Current clinical diagnostic ultrasound equipment produces peak acoustic pressure amplitudes of 10 to 50 atmospheres (1 to 5 MPa). These have been shown to produce cavitation *in vitro*, and recently tests suggest that bubbles can be produced *in vivo*, as well. The problem in such observations is that the bubbles that are produced are on the scale of one micrometer, and they survive for about a microsecond. Given the large number of scattering objects in the body

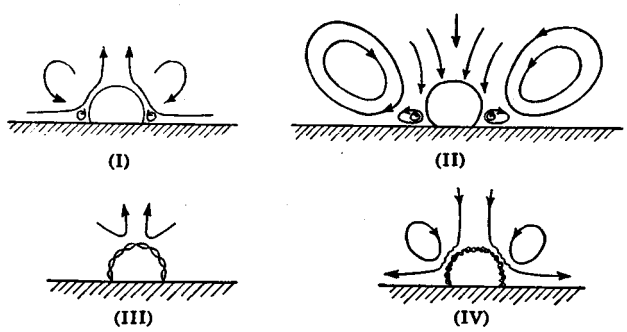

FIG. 15. Streaming (flow) patterns near oscillating bubble, after Elder, Ref. 23.

(e.g., millions of blood cells of 4 micron diameter), finding the bubble in the body is akin to finding a needle in a haystack.

But even if bubbles did form and collapse in the body, would there be any reason for concern? Here, the issue is the amount of bubble activity and its consequences. For instance, bubble activity in rat lung tissue insonified at diagnostic levels produces extravasation of blood vessels and visible damage on the lung surface.[22] Could bubble activity at the submicron level induce mutation of dividing fetal cells? As we have shown earlier, bubbles of this size deposit an energy comparable to ionizing radiation. Yet, there is no evidence for diagnostically induced mutation of fetal cells.

Therapeutic applications of ultrasound usually are in the frequency range of 0.1 to 5 MHz, and employ continuous waves or long pulses with duty cycles in excess of 25%, although for shock-wave lithotripsy, a sequence of single cycle pulses is used. At duty cycles above 10% or 20%, acoustic absorption with the consequent rise in temperature is possible, and applications for producing hypothermia exist. (This is useful in some cancer treatment therapies.) In such a regime, bubbles produced by the ultrasound can undergo a noninertial cavitation in which a bubble will continue to oscillate about its equilibrium radius.

Unconstrained bubbles may grow by rectified diffusion to resonant size and then may undergo much stronger oscillations, in effect turning into inertial cavitation. If constrained near or at resonance, the amplitudes of relatively stable cavitation bubbles can be great enough to induce fluid flow and to promote radiation forces on nearby particles. Elder,[23] for example, observed such bubble induced effects, plotting the nature of the acoustically-induced radiation pressure and fluid ''microstreaming'' (Fig. 15). At low frequencies, in the 10s of kilohertz range, such streaming can produce shear stresses sufficient to cause the breaking of cell membranes, which has found use in ultrasonic cell disrupters. Nyborg and colleagues have observed the attraction of blood cells to resonantly driven bubbles in hydrophobic Nucleopore membranes (Fig. 13). The implications of this work to separation science are obvious, though practical, cost-effective applications in this area have yet to be developed.

Recently, new applications in medicine for high amplitude ultrasound have been proposed. For instance, an ultrasonic horn that is terminated with a long, ball-tipped wire

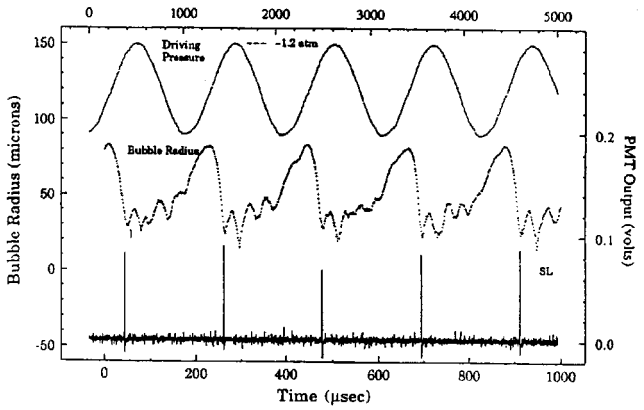

FIG. 16. Bubble radius and light output vs time for a sonoluminescencing bubble, after Gaitan and Crum, Ref. 26.

and driven at about 20 kHz can be introduced into blood vessels, and the cavitation created at the ball tip can remove plaque from clogged arteries. At the same frequency, high molecular weight drugs have been driven through the skin, aided by acoustic cavitation, in a process called transdermal drug delivery.[24] A continuous wave, 4-MHz transmitter can be inserted in the male rectum and placed so that it disrupts prostate tissue; this ''debulking'' can relieve urinary flow insufficiency. And extracoporeal lithotripter pulses of 10s to 100s of MPa positive pressure and perhaps 10-MPa rarefaction pressures, normally used to shatter kidney stones as an alternative to surgery, are being tested to see if they can enhance the effectiveness of drug take-up in the body.

In addition, micron scale bubbles have been stabilized with semi-permeable lipid skins.[10] When injected in the body, these bubbles can act as ultrasound contrast agents or as the seeds for inducing cavitation in order to promote some therapeutic effect.

E. Investigative tool (sonoluminescence, bubble–bubble interactions)

Because inertial collapse of bubbles is associated with high internal pressures, exceeding hundreds of atmospheres, and high temperatures of several thousand degrees Kelvin, it is not surprising to expect light emission from this hot, dissociated gas. Prior to 1990, this ''sonoluminescence'' was examined as a function of several variables to determine its physical origin. Most of the evidence pointed to a thermal mechanism. For instance, it was found that dissolved gases of lower thermal conductivity led to greater sonoluminescence, all other things being equal. It was also found that if the liquid had a higher vapor pressure (which could be achieved by adding some alcohol to water), then the light emissions were diminished, presumably because the bubble collapse was cushioned by the higher internal gas pressure.

Some experiments added chemicals, such as Luminol®,[25] which produced a chemically induced luminescence in the presence of intense sound. But in all of these chemi- and sonoluminescence experiments, control of the position and regularity of the phenomena were limited.

Then, in 1989, University of Mississippi graduate student Felipe Gaitan, working under the supervision of Lawrence Crum, reported that he had found a unique regime of parameters for his cavitation experiments that permitted a bubble to emit a single pulse of light synchronously with each acoustic cycle, as illustrated in Fig. 16.[26] Key elements of this discovery were using a liquid of low gas concentration, so that the collapsing vapor bubble would achieve a sufficient collapse velocity to cause the residual dissolved gas to heat to luminescence temperatures. Also, to maintain the bubble cycle after cycle, without shattering, the initial bubble had to be small enough (on the scale of microns) so that surface tension stresses could maintain the bubble's spherical shape for a significant part of the collapse phase. The acoustic pressure also had to be chosen carefully. The acoustic field plays the role both of holding the bubble against buoyancy forces and of driving it sufficiently hard to produce the repetitive sonoluminescence pulses. The frequency of these early experiments was between 21 and 25 kHz. Subsequent experiments by others have extended this frequency range up to about 60 kHz and down to about 10 kHz.

Seth Putterman of UCLA visited Gaitan and Crum and recognized that some extremely interesting physics might be going on inside the collapsing bubble. Putterman's research team then performed some groundbreaking experiments in which the time history and spectra of the light pulses, the dynamics of the bubbles, and the sensitivity of the phenomena to a wide variation of experimental parameters were examined. They determined, for instance, that the light pulses had a duration of less than 50 picoseconds, that the pulse synchronicity was steady to within 50 ps, that the efficiency of light emission is high, and that the light emission was broadband, with no distinct spectral lines.[27]

Current work by several groups suggests that a shock wave inside the bubble is responsible for the time history of luminescence, although there are almost as many theories of light generation as there are theorists. Much work continues not only on understanding this fascinating field of sonophysics, but also determining whether there are practical applications of this new knowledge.

F. Sonochemistry

One well-established application of inertial cavitation is called sonochemistry. The field has spanned the first observations of sonically induced chemical changes dating back to the 1920s, to the first substantial practical applications of this effect beginning in the 70s and 80s. Suslick and his colleagues have examined both the underlying phenomena and the practical applications of sonochemistry.[28] For instance, they have measured light spectra to determine internal temperatures of cavitating bubbles in excess of 5000 K. These temperatures are sufficient, for example, to melt metal. At much lower temperatures this cavitation can accelerate chemical reactions (which require from tenths to tens of electron volts per molecule). Common in this regime is the production of free radicals which can catalyze reactions. Intense fields can, through shock waves and jetting, break long chain polymers as part of a process to synthesize block copolymers.

Increases in heterogeneous chemical reaction rates of tenfold are not unusual, with reactions with metals such as magnesium, lithium and zinc being common. One remarkable observation by Suslick and his colleagues was the sonochemical deposition of volatile organometallics to produce amorphous iron powder. It is assumed that the process requires cooling rates on the order of one million degrees Kelvin per second, which is only possible in a dynamic process that involves sufficiently low thermal inertia, which is possible with fine particles.[29]

Sonochemistry for producing and enhancing chemical processes is still at an early stage. The benefits of high energy concentration (up to 12 orders of magnitude) is both a benefit and a limitation. For when sound energy is focused in one small region, it is not able to process the rest of the material. That is, its effect is felt at points in the medium. One solution is to raise the energy of application and to use flow and scanning to distribute these hot spots. But there is a limit here because the liquid heats up as well. The thermal effects may not be desirable, or if they are, can be achieved without ultrasound. Therefore, it appears that sonochemistry may offer its best opportunities in ''high value added'' processes.

VII. CONCLUDING REMARKS

Acoustic cavitation is an enormously broad area of study of relevance in a wide variety of practical processes; it can be a tool for fundamental scientific studies spanning enormous scales of size and energy. This tutorial exercise, which strives to give a broad overview and provide enough numbers to put the reader in the right ballpark of the phenomena associated with cavitation, has only scratched the surface. Major reviews of work on cavitation, in general, and acoustic cavitation, in particular, complement the present work.[30–36] In these reviews, one can find listed primary references to many of the topics discussed in this brief tutorial (and also to many not mentioned!)

[1] National Council on Radiation Protection, NCRP Report #66, draft report, W. Nyborg.
[2] See, for example, E. N. Harvey, D. Barnes, W. McElroy, A. Whitely, D. Pease, and K. Copper, ''Bubble formation in animals,'' J. Cellular Comp. Physiol. **24**, 1–34 (1944).
[3] R. E. Apfel, ''Water superheated to 279.5 °C at atmospheric pressure,'' Nature **238**, 63–64 (1972).
[4] M. Strasberg, ''Propeller cavitation noise after 35 years of study,'' ASME Symposium on ''Noise and Fluids Engineering,'' Nov. 1977, pp. 89–99.
[5] M. Volmer and A. Weber, Z. Phys. Chem. **119**, 277 (1926); W. Doring, *ibid.* **36**, 371 (1937).
[6] E. Roedder, Science **155**, 1413–1417 (1967).
[7] M. Greenspan and C. E. Tschiegg, ''Radiation-induced acoustic cavitation; apparatus and some results,'' J. Res. Natl. Bur. Stand. Sec. C **71**, 299–311 (1967).
[8] R. Apfel, Sci. Am. **227**, 58–71 (Dec. 1972).
[9] F. G. Blake, Technical Memo 12, Acoustics Research Laboratory, Harvard University, Cambridge, Massachusetts, Sept. 1949.
[10] R. E. Apfel and C. K. Holland, ''Gauging the likelihood of cavitation from short-pulse, low-duty cycle diagnostic ultrasound,'' Ultrasound Med. Biol. **17**, 179–185 (1991).
[11] H. J. Bleeker, K. K. Shung, and J. L. Barnhart, ''Ultrasonic characterization of Albunex™, a new contrast agent,'' J. Acoust. Soc. Am. **87**, 1792–1797 (1990).
[12] M. Greenspan and C. E. Tschiegg, J. Res. Natl. Bur. Stand. Sec. C **71**, 299 (1967).
[13] R. Apfel, Nucl. Instrum. Methods **162**, 603–608 (1979).
[14] W. Lauterborn, J. Acoust. Soc. Am. **59**, 283 (1976).
[15] V. Kamath and A. Prosperetti, ''Numerical integration methods in gas-bubble dynamics,'' J. Acoust. Soc. Am. **85**, 1538–1548 (1989).
[16] Lord Rayleigh, ''On the pressure developed in a liquid during the collapse of a spherical cavity,'' Philos. Mag. **34**, 94–98 (1917).
[17] T. B. Benjamin and A. T. Ellis, Philos. Trans. R. Soc. London, Ser. A **260**, 221 (1966).
[18] J. Harbison and R. Apfel, J. Acoust. Soc. Am. **57**, 1371–1373 (1975).
[19] L. Rosenberg, *High Intensity Ultrasonic Fields* (Plenum, New York, 1971), p. 248.
[20] R. Apfel, Am. J. Phys. **53**, 66 (1985).
[21] L. A. Crum and D. A. Nordling, J. Acoust. Soc. Am. **52**, 294 (1972).
[22] C. Holland, X. Zheng, R. Apfel, J. Alderman, L. Fernandez, and K. Taylor, Ultrasound Med. Biol. (in press).
[23] S. A. Elder, ''Cavitation microstreaming,'' J. Acoust. Soc. Am. **31**, 54–64 (1958).
[24] S. Mitragotri, D. Blankschtein, and R. Langer, ''Ultrasound-medicated transdermal protein delivery,'' Science **269**, 850–853 (1995).
[25] K. Negishi, ''Experimental studies on sonoluminescence and ultrasonic cavitation,'' J. Phys. Soc. Jpn. **16**, 1450–1465 (1961).
[26] D. F. Gaitan, L. A. Crum, C. C. Church, and R. A. Roy, ''Sonoluminescence and bubble dynamics from a single, stable cavitation bubble,'' J. Acoust. Soc. Am. **91**, 3166–3183 (1992).
[27] B. P. Barber and S. J. Putterman, Nature (London) **352**, 318 (1991).
[28] K. S. Suslick, Science **247**, 1430–1445 (1990).
[29] K. S. Suslick, Science **247**, 1067–1069 (1990).
[30] H. G. Flynn, ''Physics of Acoustic Cavitation in Liquids,'' in *Physical Acoustics*, edited by W. P. Mason (Academic, New York, 1964), Vol. 1, Pt. B, pp. 57–172.
[31] E. A. Neppiras, ''Acoustic Cavitation,'' Phys. Rep. **61**, 159–251 (1980).
[32] R. E. Apfel, ''Acoustic Cavitation,'' in *Ultrasonics*, edited by P. Edmonds (Academic, New York, 1981), Vol. 19.
[33] A. Prosperetti, ''Bubble dynamics: A review and some results,'' Appl. Sci. Res. **38**, 145–164 (1982).
[34] F. R. Young, *Acoustic Cavitation* (McGraw-Hill, London, 1989).
[35] T. G. Leighton, *The Acoustic Bubble* (Academic, London, 1994).
[36] NCRP Report 74 (on exposure criteria and biological effects of ultrasound), prepared by committee headed by W. Nyborg, National Center for Radiological Protection, Bethesda, MD, 1983.

Reflection of a plane sound wave from a semi-infinite periodic transversely isotropic set of layers

Evgeni L. Shenderov
Research and Development Institute ''Morfizpribor,'' 46 Chkalovski pr., St. Petersburg, 197376, Russia

(Received 22 July 1995; accepted for publication 14 October 1996)

A novel method is presented to calculate the reflection coefficient of sound from a semi-infinite periodic system of elastic layers. Each layer may consist of sublayers, and may be either isotropic, or transversely anisotropic. The reflection coefficient is given in an explicit form for alternating solid and liquid layers at an oblique incidence of a sound wave as well as for all solid layers at normal incidence. For all solid layers at oblique incidence a quadratic matrix equation with respect to the input impedance matrix is obtained. The method of solving this equation and the coefficients of a transfer matrix for transversely isotropic layers are presented in the Appendices. Resonance properties of the system of layers follow from the results of computations of the frequency and angular dependencies. © *1997 Acoustical Society of America.* [S0001-4966(97)01503-8]

PACS numbers: 43.20.Bi, 43.20.Fn, 43.35.Cg, 43.30.Dr [ANN]

INTRODUCTION

Studies of the acoustical properties of layered media are of interest to researchers in architectural acoustics, hydroacoustics, geophysics, and the design of layered composite materials. An approach to this problem founded on the application of transfer matrix methods has been applied in numerous papers (see Refs. 1–9). Furthermore, in recent years many investigators have studied anisotropic layers. Many fiber-reinforced plastics may be described as either orthotropic or transversely isotropic materials. If the fibers are aligned in two perpendicular principal directions in the plane of the layer, then one can consider such material as orthotropic. The elastic properties of the orthotropic material are described by nine elastic constants. If the fibers are aligned in many different directions then the elastic properties of the layer are the same in all directions in the plane of the layer but differ from the properties in the normal plane. In this case the material is transversely isotropic. The elastic properties of the transversely isotropic material are described by five elastic constants. However, four constants are enough for calculation of reflection and transmission coefficients (see Appendix A). Note that if a plane wave is incident on the orthotropic layer in one of the principal directions, then all expressions for the reflection and transmission coefficients coincide with those of the transversely isotropic layer. Therefore, the case of the transversely isotropic layer is the most significant.

The general properties of the transfer matrix for an anisotropic layer were established in Ref. 10. In particular, it was proved that the determinant of the transfer matrix is equal to 1. The coefficients of the transfer matrix for an orthotropic layer are presented in Ref. 11. The value λ_{xzxz} in this paper should be changed to λ_{xxzz}. The coefficients of the transfer matrix for the transversely isotropic layers are listed in Ref. 12, however with typographical errors. The corrected coefficients are listed below in Appendix A.

Methods which combine Floquet theory with the transfer matrix approach have been used for obtaining dispersion equations in periodically layered composites.[6,13–21] Here we follow another approach to compute the reflection coefficient and input impedance for semi-infinite periodically layered media. A very simple solution of this problem for alternating solid and liquid layers at an oblique incidence of the sound wave has been obtained. This solution is also valid for all solid layers at normal incidence of the wave. The solution is more complicated for all solid layers at an oblique incidence of the wave, but it has been reduced to solving several standard equations. In principle this approach enables us to compute the reflection coefficient for any anisotropic material, but in this paper we restrict our analysis to transversely isotropic materials and, in particular, to isotropic materials.

This paper is organized as follows: Section I is devoted to a calculation of the reflection coefficient and input impedance for a system of semi-infinite periodic layers. In Sec. I A we present a simple method to determine the properties of semi-infinite periodic structures. In Sec. I B we apply this method to determine the reflection coefficient for a structure with intermediate liquid layers having common properties with the outer medium. In Sec. I C this method is extended to intermediate liquid layers with properties differing from those of the outer medium. These results are also applicable to solid intermediate layers at normal incidence of a sound wave. A general case dealing with all solid layers at an oblique incidence is considered in Sec. I D. The coefficients of the transfer matrix for a transversely isotropic layer are listed in Appendix A. The solutions of a quadratic matrix equation and a quartic equation with complex coefficients are presented in Appendices B and C.

I. THEORY

A. General approach

Let us consider a semi-infinite stack of layers. The solid or liquid layers form periodically repeating subsets [Fig. 1(a)]. To illustrate the suggested method, let us consider a semi-infinite chain of elements [Fig. 2(a)]. It is necessary to obtain the input impedance. It is easy to see that the properties of the chain will not change if it is cut at the points c,d.

 0001-4966/97/101(3)/1239/11/$10.00

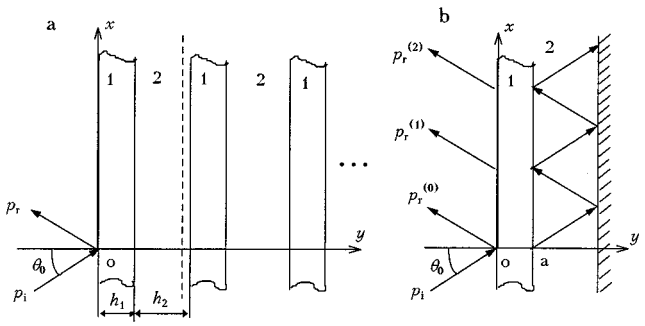

FIG. 1. Reflection of sound from a system of layers. (a) semi-infinite stack of the layers; (b) equivalent system with partial waves.

The remaining right-hand part of the chain is semi-infinite like the original chain. Due to this, the input impedance Z at points c,d is the same as that at points a,b. Then one can replace the semi-infinite chain in Fig. 2(a) with the finite circuit in Fig. 2(b). The unknown impedance is to be found in the left- and right-hand sides of this circuit. One obtains a quadratic equation with respect to Z

$$Z=Z_1+\frac{ZZ_2}{Z+Z_2}. \tag{1}$$

This equation has two roots

$$Z=(Z_1/2)\pm\sqrt{(Z_1/2)^2+Z_1Z_2}.$$

To choose the sign, one can assume Z_1,Z_2 to have real values. If there are no sources of energy, then $Z_1,Z_2>0$. Because of Z having to be positive, it is necessary to choose the plus sign.

We have applied this simple idea to the system in Fig. 1(a). Let us cut this system at the dash line. The right-hand side of the system will coincide with the original system and the reflection coefficients for these systems should be the same. Then we obtain the finite set [Fig. 1(b)]. There may be three particular cases. If the properties of the liquids in the half-space and in even layers are the same, one can just consider the reflection coefficient. If they are different, it is necessary to first find the input impedance and then the reflection coefficient. If the even layers are solid then instead of a single normal input impedance one should consider an input impedance matrix.

B. The same liquid media in the half-space and in the even layers

For the first particular case we shall suppose that the reflection and transmission coefficients for layer 1 (or the stack of layers 1) are known. The expressions for these coefficients are given in Appendix A. In this case one can obtain the reflection coefficient immediately without having to find the input impedance. The simplest way is to use the method dealing with sequentially reflected and transmitted waves. The incident and the reflected waves are

$$p_i=\exp[ik_0(x\ \sin\ \theta_0+y\ \cos\ \theta_0)], \tag{2a}$$

$$p_r=A_L\ \exp[ik_0(x\ \sin\ \theta_0-y\ \cos\ \theta_0)], \tag{2b}$$

where A_L is the reflection coefficient for the whole system, and $k_0=\omega/c_0$ is the wave number in the half-space. Time dependence is taken as $\exp(-i\omega t)$. The partial reflected waves shown in the Fig. 1(b) may be written as the following expressions:

$$\begin{aligned}
p_r^{(0)}&=A\ \exp[ik_0(x\ \sin\ \theta_0-y\ \cos\ \theta_0)],\\
p_r^{(1)}&=B_1^2A_Lu\ \exp[ik_0(x\ \sin\ \theta_0-y\ \cos\ \theta_0)],\\
p_r^{(2)}&=B_1^2A_L^2Au^2\ \exp[ik_0(x\ \sin\ \theta_0-y\ \cos\ \theta_0)],\\
p_r^{(3)}&=B_1^2A_L^3A^2u^3\ \exp[ik_0(x\ \sin\ \theta_0-y\ \cos\ \theta_0)],
\end{aligned} \tag{3}$$

where $u=\exp(2ik_0h_2\cos\theta_0)$, A is the reflection coefficient for layer 1, $B_1=B\exp(ik_0h_1\cos\theta_0)$, and B is the transmission coefficient for layer 1. Taken into account here is that, according to the definition, the transmission coefficient is the ratio of sound pressures at the same point in the transmitted and incident waves. Therefore, we take sound pressures in the transmitted waves at point a and refer their phases to the origin O. Phases of all reflected waves in Eqs. (3) also are referred to the point O.

The sum of the partial reflected waves in Eqs. (3) should be equal to the reflected wave Eq. (2b). So one obtains

$$A_L=A+B_1^2A_Lu\sum_{j=0}^{\infty}(A_LAu)^j.$$

After summation over the terms of the geometric progression one can write

$$A_L=A+B_1^2\frac{A_Lu}{1-AA_Lu}. \tag{4}$$

This equation is similar to Eq. (1). The unknown reflection coefficient A_L appears both in the left- and right-hand sides. Of the two solutions of this quadratic equation one must choose the following expression:

$$\begin{aligned}
A_L=\{&1-(B_1^2-A^2)u\\
&-\sqrt{[1-(B_1^2-A^2)u]^2-4A^2u}\}/(2Au).
\end{aligned} \tag{5}$$

The minus sign before the square root provides for the correct behavior in the limit $A\to0$, $B\to1$. In this case one obtains the true solution $A_L\to0$.

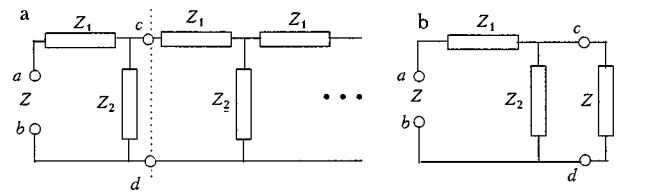

FIG. 2. Electric circuit, (a) Semi-infinite chain; (b) equivalent circuit.

C. Different liquid media in the half-space and in the even layers at oblique incidence of a plane wave (or all solid layers at normal incidence)

If the liquid media in the half-space and in the even layers are different, it is impossible to take the same values

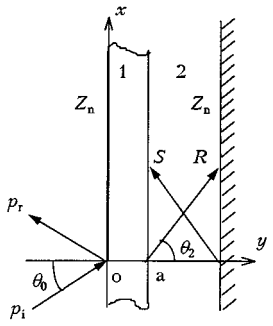

FIG. 3. Equivalent system for different media in the half-space and in the even layers.

of reflection coefficients at the boundaries $y=0$ and $y=h_1+h_2$. In this case it is necessary to first obtain the input impedance at boundary $y=0$.

In accordance with the approach outlined in Sec. I A let us cut the system along the dash line. The input impedance of the right-hand side must be the same as for the whole system. Thus, one obtains the simple system shown in Fig. 3. The input normal impedance at the boundary $y=0$ is a ratio of total sound pressure and normal component of particle velocity at this boundary

$$Z_n=p^{(0)}/\nu_y^{(0)}|_{y=0}=-\sigma_{yy}^{(0)}/\nu_y^{(0)}|_{y=0}. \tag{6}$$

The quantity $\sigma_{yy}^{(0)}$ is the normal component of stress tensor at the boundary $y=0$. The input normal impedance at the boundary $y=h_1+h_2$ is

$$Z_n=p^{(2)}/\nu_y^{(2)}|_{y=h_1+h_2}. \tag{7}$$

Here and below the superscripts (0), (1), (2) are related to boundaries $y=0$, $y=h_1$, $y=h_1+h_2$, respectively. These impedances should be equal one to another. Then

$$p^{(2)}/\nu_y^{(2)}|_{y=h_1+h_2}=-\sigma_{yy}^{(0)}/\nu_y^{(0)}|_{y=0}. \tag{8}$$

The waves in region 2, shown in Fig. 3, are the sums of all partial waves in Fig. 1(b). The amplitudes R and S of these waves are unknown.

One can describe the properties of solid layer 1 by a transfer matrix $\mathbf{A}_1$ with the elements a_{jk} $(j,k=1\cdots4)$. Layer 1 may be an arbitrary set of sublayers. In this case the matrix $\mathbf{A}_1$ is a product of the matrices for all layers (beginning with the last sublayer).

Boundaries $y=0$ and $y=h_1$ should be free of tangential stresses $\sigma_{xy}^{(0)}$ and $\sigma_{xy}^{(1)}$. One can write the relationship between the components of velocities and elements of the stress tensor at the boundaries of layer 1 as

$$\begin{aligned}
\nu_x^{(1)}&=a_{11}\nu_x^{(0)}+a_{12}\nu_y^{(0)}+a_{13}\sigma_{yy}^{(0)},\\
\nu_y^{(1)}&=a_{21}\nu_x^{(0)}+a_{22}\nu_y^{(0)}+a_{23}\sigma_{yy}^{(0)},\\
\sigma_{yy}^{(1)}&=a_{31}\nu_x^{(0)}+a_{32}\nu_y^{(0)}+a_{33}\sigma_{yy}^{(0)},\\
0&=a_{41}\nu_x^{(0)}+a_{42}\nu_y^{(0)}+a_{43}\sigma_{yy}^{(0)}.
\end{aligned} \tag{9}$$

Coefficients a_{jk} are listed in Appendix A. Eliminating $\nu_x^{(0)}$ from the second, third, and fourth equations, we obtain the relationship between the normal components of velocities of particles and the normal stresses:

$$\nu_y^{(1)}=M_{22}\nu_y^{(0)}+M_{23}\sigma_{yy}^{(0)}, \tag{10a}$$

$$\sigma_{yy}^{(1)}=M_{32}\nu_y^{(0)}+M_{33}\sigma_{yy}^{(0)}, \tag{10b}$$

$$M_{22}=a_{22}-a_{42}a_{21}/a_{41},\quad M_{23}=a_{23}-a_{21}a_{43}/a_{41}, \tag{11a}$$

$$M_{32}=a_{32}-a_{42}a_{31}/a_{41},\quad M_{33}=a_{33}-a_{31}a_{43}/a_{41}. \tag{11b}$$

Notice that for normal incidence the indeterminacy 0/0 arises in Eqs. (11). In this case we have

$$M_{22}=a_{22},\quad M_{23}=a_{23},\quad M_{32}=a_{32},\quad M_{33}=a_{33}. \tag{11c}$$

The sound-pressure p_2 in the region 2 is a sum of pressures in two waves with unknown amplitudes R and S. Each of these waves is a sum of all partial waves in layer 2, shown in Fig. 1(b) and propagating in the same direction. Then

$$\begin{aligned}
p_2=&R\ \exp[ik_2(x\ \sin\ \theta_2+y\ \cos\ \theta_2)]\\
&+S\ \exp[ik_2(x\ \sin\ \theta_2-y\ \cos\ \theta_2)].
\end{aligned} \tag{12}$$

Wave numbers k_0 and k_2 are related to each other by Snell's law

$$k_0\ \sin\ \theta_0=k_2\ \sin\ \theta_2. \tag{13}$$

One can write down the normal components of velocity at the boundaries $y=h_1$ and $y=h_1+h_2$ as a normal derivative of sound-pressure p_2

$$\begin{aligned}
\nu_y^{(1)}=&\frac{1}{Z_2}\left[R\ \exp(iP_1)-S\ \exp(-iP_1)\right]\\
&\times\exp(ik_0x\ \sin\ \theta_0),
\end{aligned} \tag{14a}$$

$$\begin{aligned}
\nu_y^{(2)}=&\frac{1}{Z_2}\left[R\ \exp(i(P_1+P_2))-S\ \exp(-i(P_1+P_2))\right]\\
&\times\exp(ik_0x\ \sin\ \theta_0),
\end{aligned} \tag{14b}$$

with $Z_2=\rho_2c_2/\cos\ \theta_2$, $P_1=k_2h_1\cos\ \theta_2$, and $P_2=k_2h_2\times\cos\ \theta_2$. Taking a ratio of Eqs. (10a) and (10b) and using definition (6), one gets

$$\frac{\sigma_{yy}^{(1)}}{\nu_y^{(1)}}=\frac{M_{32}-M_{33}Z_n}{M_{22}-M_{23}Z_n}. \tag{15}$$

At boundary $y=h_1$ we have $\sigma_{yy}^{(1)}=-p_2|_{y=h_1}$. From Eqs. (12), (14a), and (15) one finds

$$\frac{R\ \exp(iP_1)+S\ \exp(-iP_1)}{R\ \exp(iP_1)-S\ \exp(-iP_1)}=\frac{M_{33}Z_n/Z_2-M_{32}/Z_2}{M_{22}-M_{23}Z_n}. \tag{16}$$

In accordance with our general approach the input impedance at boundary $y=h_1+h_2$ should be equal to the input impedance of the whole system. The ratio of sound pressure and normal component of velocity of particles at this boundary may be derived from Eqs. (12) and (14b):

$$\frac{R\ \exp[i(P_1+P_2)]+S\ \exp[-i(P_1+P_2)]}{R\ \exp[i(P_1+P_2)]-S\ \exp[-i(P_1+P_2)]}=\frac{Z_n}{Z_2}. \tag{17}$$

Eliminating this ratio from Eqs. (16) and (17) we obtain the quadratic equation with respect to the impedance Z_n

$$aZ_n^2+bZ_n+c=0, \tag{18a}$$

where

$$a=M_{33}i\ \sin\ P_2-Z_2M_{23}\ \cos\ P_2,$$

$$b=(M_{23}Z_2^2-M_{32})i\ \sin\ P_2+(M_{22}-M_{33})Z_2\ \cos\ P_2,$$

$$c=M_{32}Z_2\ \cos\ P_2-Z_2^2M_{22}i\ \sin\ P_2.$$

This equation is similar to Eq. (1) with respect to the input impedance of the electric circuit shown in Fig. 2. To choose one of the two solutions, we shall consider the case $P_2=0$ at normal incidence. The system of layers becomes a semi-infinite medium with $Z_n=\rho_1c_1$. We have $a=-Z_2M_{23}$, $b=0$, $c=Z_2M_{32}$. In this case we can use the well-known values of the coefficients: $M_{22}=M_{33}=a_{22}=a_{33}=\cos P_1$, $M_{23}=a_{23}=-i\sin P_1/(\rho_1c_1)$, $M_{32}=a_{32}=-i\rho_1c_1\sin P_1$. The true solution $Z_n=\rho_1c_1$ would result if the plus sign before a square root is used. Hence,

$$Z_n=(-b+\sqrt{b^2-4ac})/(2a). \tag{18b}$$

The reflection coefficient is

$$A_L=\frac{Z_n-Z_0}{Z_n+Z_0}, \tag{19}$$

where $Z_0=\rho_0c_0/\cos\theta_0$. This result is valid for liquid even layers and arbitrary odd layers (or for stacks of the sublayers 1, including anisotropic layers) at oblique incidence of a plane wave. This result is also valid for all solid layers at normal incidence of the wave.

D. All solid layers at oblique incidence of a plane wave

Let us consider a semi-infinite system consisting of solid layers. Each layer in turn may consist of thinner layers. The properties of layers are defined by the transfer matrices $\mathbf{A}_1$ and $\mathbf{A}_2$. The components of velocities and the stress tensor at the input boundary $y=0$ and at the boundary $y=h_1+h_2$ are related by the transfer matrix $\mathbf{A}=\mathbf{A}_2\mathbf{A}_1$,

$$\begin{bmatrix}\nu_x^{(2)}\\ \nu_y^{(2)}\\ \sigma_{yy}^{(2)}\\ \sigma_{xy}^{(2)}\end{bmatrix}=\mathbf{A}\begin{bmatrix}\nu_x^{(0)}\\ \nu_y^{(0)}\\ \sigma_{yy}^{(0)}\\ \sigma_{xy}^{(0)}\end{bmatrix}. \tag{20}$$

Let stresses $\sigma_{yy}^{(0)},\sigma_{xy}^{(0)}$ be given on boundary $y=0$. Then the relationship between stresses and velocities at this boundary can be written down as the matrix product

$$\begin{bmatrix}\sigma_{yy}^{(0)}\\ \sigma_{xy}^{0}\end{bmatrix}=\mathbf{Z}\begin{bmatrix}\nu_x^{(0)}\\ \nu_y^{(0)}\end{bmatrix}, \tag{21}$$

where

$$\mathbf{Z}=\begin{bmatrix}z_{11} & z_{12}\\ z_{21} & z_{22}\end{bmatrix} \tag{22}$$

is an unknown matrix, defined as the input impedance matrix at boundary $y=0$. Let us cut the system along the dash line shown in Fig. 1(a). In accordance with our approach we state that the properties of the system would not change if one period was deleted. Therefore, the matrix defining the input impedance at boundary $y=h_1+h_2$ should be the same as the impedance matrix at boundary $y=0$. Then one can write

$$\begin{bmatrix}\sigma_{yy}^{(2)}\\ \sigma_{xy}^{(2)}\end{bmatrix}=\mathbf{Z}\begin{bmatrix}\nu_x^{(2)}\\ \nu_y^{(2)}\end{bmatrix}. \tag{23}$$

Let us separate the 2×2 matrices in the product (20). We obtain

$$\mathbf{v}^{(2)}=\mathbf{B}_{11}\mathbf{v}^{(0)}+\mathbf{B}_{12}\mathbf{s}^{(0)},$$

$$\mathbf{s}^{(2)}=\mathbf{B}_{21}\mathbf{v}^{(0)}+\mathbf{B}_{22}\mathbf{s}^{(0)}, \tag{24}$$

where

$$\mathbf{v}^{(0)}=\begin{bmatrix}\nu_x^{(0)}\\ \nu_y^{(0)}\end{bmatrix},\quad \mathbf{v}^{(2)}=\begin{bmatrix}\nu_x^{(2)}\\ \nu_y^{(2)}\end{bmatrix},$$

$$\mathbf{s}^{(0)}=\begin{bmatrix}\sigma_{yy}^{(0)}\\ \sigma_{xy}^{(0)}\end{bmatrix},\quad \mathbf{s}^{(2)}=\begin{bmatrix}\sigma_{yy}^{(2)}\\ \sigma_{xy}^{(2)}\end{bmatrix},$$

$$\mathbf{B}_{11}=\begin{bmatrix}a_{11} & a_{12}\\ a_{21} & a_{22}\end{bmatrix},\quad \mathbf{B}_{12}=\begin{bmatrix}a_{13} & a_{14}\\ a_{23} & a_{24}\end{bmatrix},$$

$$\mathbf{B}_{21}=\begin{bmatrix}a_{31} & a_{32}\\ a_{41} & a_{42}\end{bmatrix},\quad \mathbf{B}_{22}=\begin{bmatrix}a_{33} & a_{34}\\ a_{43} & a_{44}\end{bmatrix}.$$

From Eqs. (21) and (23) and the first equation of the system (24), one obtains

$$\mathbf{s}^{(2)}=\mathbf{Z}\mathbf{v}^{(2)}=\mathbf{Z}(\mathbf{B}_{11}\mathbf{v}^{(0)}+\mathbf{B}_{12}\mathbf{s}^{(0)})$$

$$=\mathbf{Z}(\mathbf{B}_{11}\mathbf{v}^{(0)}+\mathbf{B}_{12}\mathbf{Z}\mathbf{v}^{(0)}). \tag{25}$$

In a similar way from the second equation of the system (24), one obtains

$$\mathbf{s}^{(2)}=\mathbf{B}_{21}\mathbf{v}^{(0)}+\mathbf{B}_{22}\mathbf{Z}\mathbf{v}^{(0)}. \tag{26}$$

Now we equate Eqs. (25) and (26) and obtain

$$(\mathbf{Z}\mathbf{B}_{12}\mathbf{Z}+\mathbf{Z}\mathbf{B}_{11}-\mathbf{B}_{22}\mathbf{Z}-\mathbf{B}_{21})\mathbf{v}^{(0)}=0. \tag{27}$$

This equation should be satisfied for arbitrary values of $\mathbf{v}^{(0)}$. Therefore,

$$\mathbf{Z}\mathbf{B}_{12}\mathbf{Z}+\mathbf{Z}\mathbf{B}_{11}-\mathbf{B}_{22}\mathbf{Z}-\mathbf{B}_{21}=0, \tag{28}$$

a quadratic matrix equation with respect to the matrix $\mathbf{Z}$. In contrast to Eq. (1), the unknown value is a matrix and not a number. Solution of Eq. (28) is presented in Appendix B. With knowledge of matrix $\mathbf{Z}$ it is possible to find the reflection coefficient A_L. At boundary $y=0$ the tangential stress should be zero, i.e., $\sigma_{xy}^{(0)}=0$. From Eq. (21) it follows that

$$\sigma_{yy}^{(0)}=Z_{11}\nu_x^{(0)}+Z_{12}\nu_y^{(0)},$$

$$0=Z_{21}\nu_x^{(0)}+Z_{22}\nu_y^{(0)}. \tag{29}$$

The conditions of continuity of normal stress and normal velocity at boundary $y=0$ may be written as

$$\nu_y^{(0)}=\left.\frac{1}{i\omega\rho_0}\frac{\partial p}{\partial y}\right|_{y=0}=\frac{\cos\ \theta_0}{\rho_0c_0}\ (1-A_L)\exp(ik_0x\ \sin\ \theta_0),$$

$$\sigma_{yy}^{(0)}=-p|_{y=0}=-(1+A_L)\exp(ik_0x\ \sin\ \theta_0). \tag{30}$$

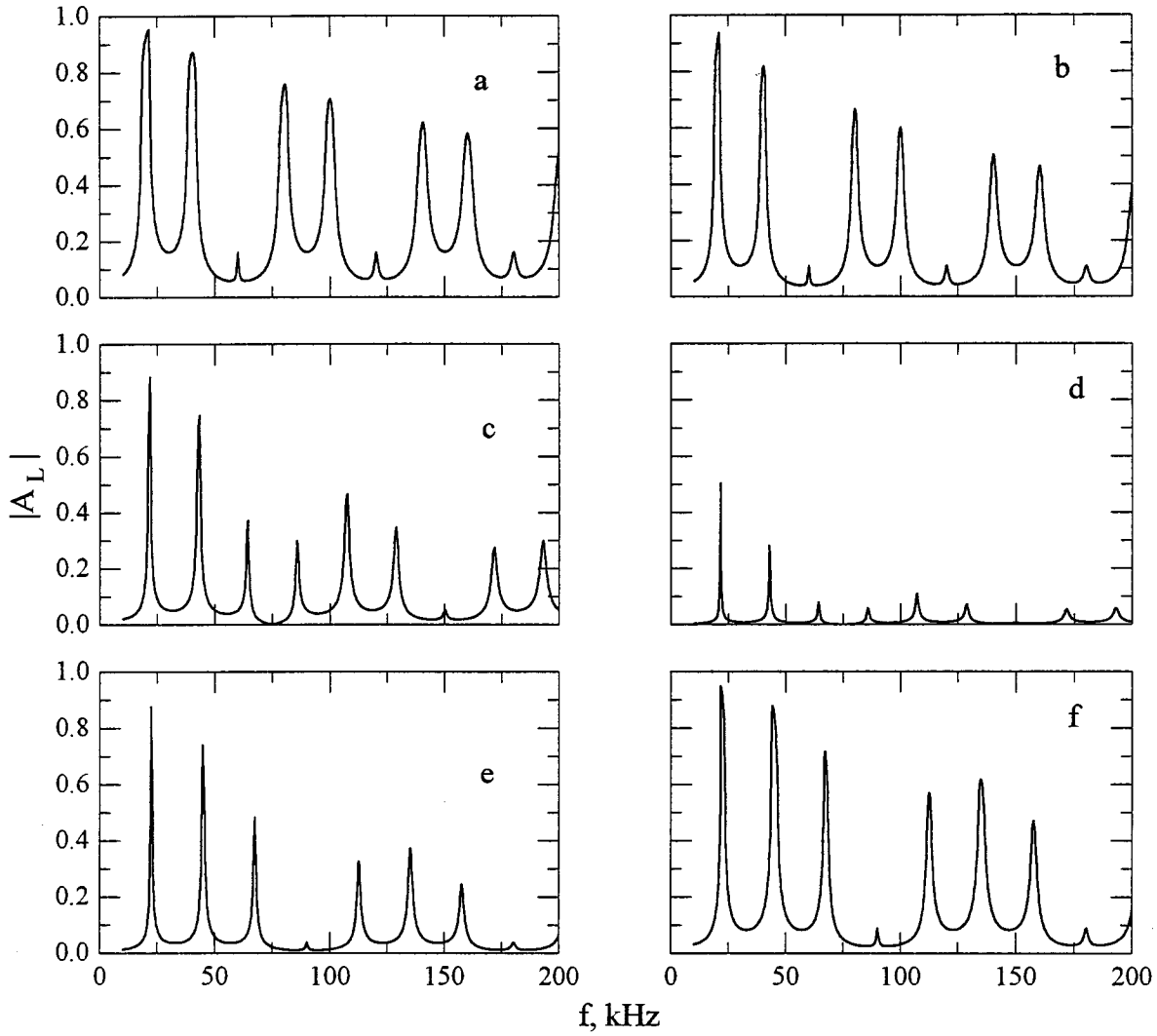

FIG. 4. Reflection coefficient from a stack of layers with low acoustical contrast in water at normal incidence of a sound wave. The densities and the velocities are given below in kg/m^3, m/s, respectively. $\rho_0=\rho_2=1000$, $c_0=c_2=1500$, $h_1=0.01$ m, $h_2=0.025$ m, $\eta=0.04$. (a) $\rho_1=900$, $c_1=1200$; (b) $\rho_1=1000$, $c_1=1200$; (c) $\rho_1=900$, $c_1=1500$; (d) $\rho_1=1000$, $c_1=1500$; (e) $\rho_1=900$, $c_1=1800$; (f) $\rho_1=1000$, $c_1=1800$.

Eliminating $\nu_x^{(0)}$ from Eqs. (29) and taking into account boundary condition (30), one can find the reflection coefficient as Eq. (19), where

$$Z_n=(Z_{11}Z_{22}-Z_{12}Z_{21})/Z_{21}, \tag{31}$$

and $Z_0=\rho_0 c_0/\cos\theta_0$. The value $Z_n=p/\nu_y^{(0)}|_{y=0}$ is the normal input impedance.

II. RESULTS OF COMPUTATIONS

The results of computation of the reflection coefficient at normal incidence of a wave for layers with low acoustical contrast in water are shown in Fig. 4. The absorption of sound in layers 1,3,... has been taken into account. During computations of the reflection coefficients A and the transmission coefficients B we introduced a complex velocity of sound in these layers $\overline{c}_1^2=c_1^2(1-i\eta)$, where $\eta=0.04$. A bar denotes a complex value.

The frequency dependence of the reflection coefficient involves a system of resonances. Narrow and high resonances arise at frequencies for which the equality

$$B_1^2-A^2\cong u^{-1} \tag{32}$$

is satisfied. Exact equality may take place only for layers without losses. Coefficients A and B_1 in this case satisfy identity $|B_1^2-A^2|=1$. Therefore, at these frequencies

$$\arg(B_1^2-A^2)+\arg u=2\pi n,\quad n=0,1,2,\ldots\ . \tag{33}$$

However, even if this condition is satisfied, but there exists a half-wave resonance of layers 1,3,... ($k_1h_1=\pi m$), then the high maxima fail to appear at these frequencies. As an example one can see in Fig. 4 that there are intervals where the high maxima are absent.

If $k_2h_2=\pi m$, then $u=1$ at normal incidence of the wave. This case corresponds to in-phase summation of all reflected waves. All layers 1,3,... may be connected together as if $h_2=0$, and we obtain a semi-infinite medium. Then the reflection coefficient at these frequencies should be the same as for semi-infinite media.

Note that in the case $\rho_1=1000$ kg/m^3, $c_1=1500$ m/s, i.e., when $\rho_0=\rho_1=\rho_2$, $c_0=c_1=c_2$, the reflection coefficient is not exactly equal to zero. [Fig. 4(d)]. One can explain this

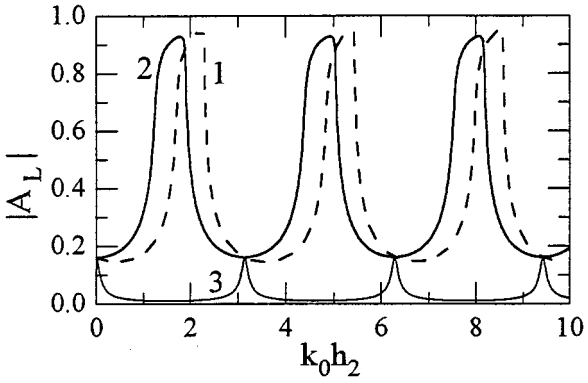

FIG. 5. Dependency of the reflection coefficient on wave thickness k_0h_2. ρ_1=900 kg/m^3, c_1=1200 m/s; h_1=0.01 m, ρ_0, ρ_2, c_0, c_2 the same as in Fig. 4. 1−f=21.4 kHz, 2-f=30 kHz, 3−f=60 kHz.

phenomenon if one takes into account that the loss coefficients in layers 1,3,... are not zero. Hence, the complex velocities of sound in these layers are not equal to those in layers 2,4,..., and the reflection coefficients from the layers with odd numbers are not exactly equal to zero. But in this case the transmission coefficients for low-loss layers are about 1. Then waves reflected from deep inner layers spread out with a slight decrease of their amplitudes. If there is in-phase addition of such waves, the amplitude of the wave reflected from the stack of layers may be great even for layers with very low acoustical contrast.

Dependencies of the reflection coefficient on wave thickness of layers 2 (Fig. 5) also have resonances. It is necessary to note that if $k_0h_2=\pi n$, n=0,1,2,... (i.e., layers 2 are absent or the half-wave resonance exists), then the reflection coefficient is equal to that of a semi-infinite medium with parameters of layers 1 (in this example $|A_L|$=0.163 for all curves).

The angular dependencies of the reflection coefficient are also of the resonance kind (Fig. 6). Maxima of the curves arise at the angles for which condition (32) is satisfied. The width of the first maximum is strongly dependent on the velocity of sound in the layers. The higher the frequency, the

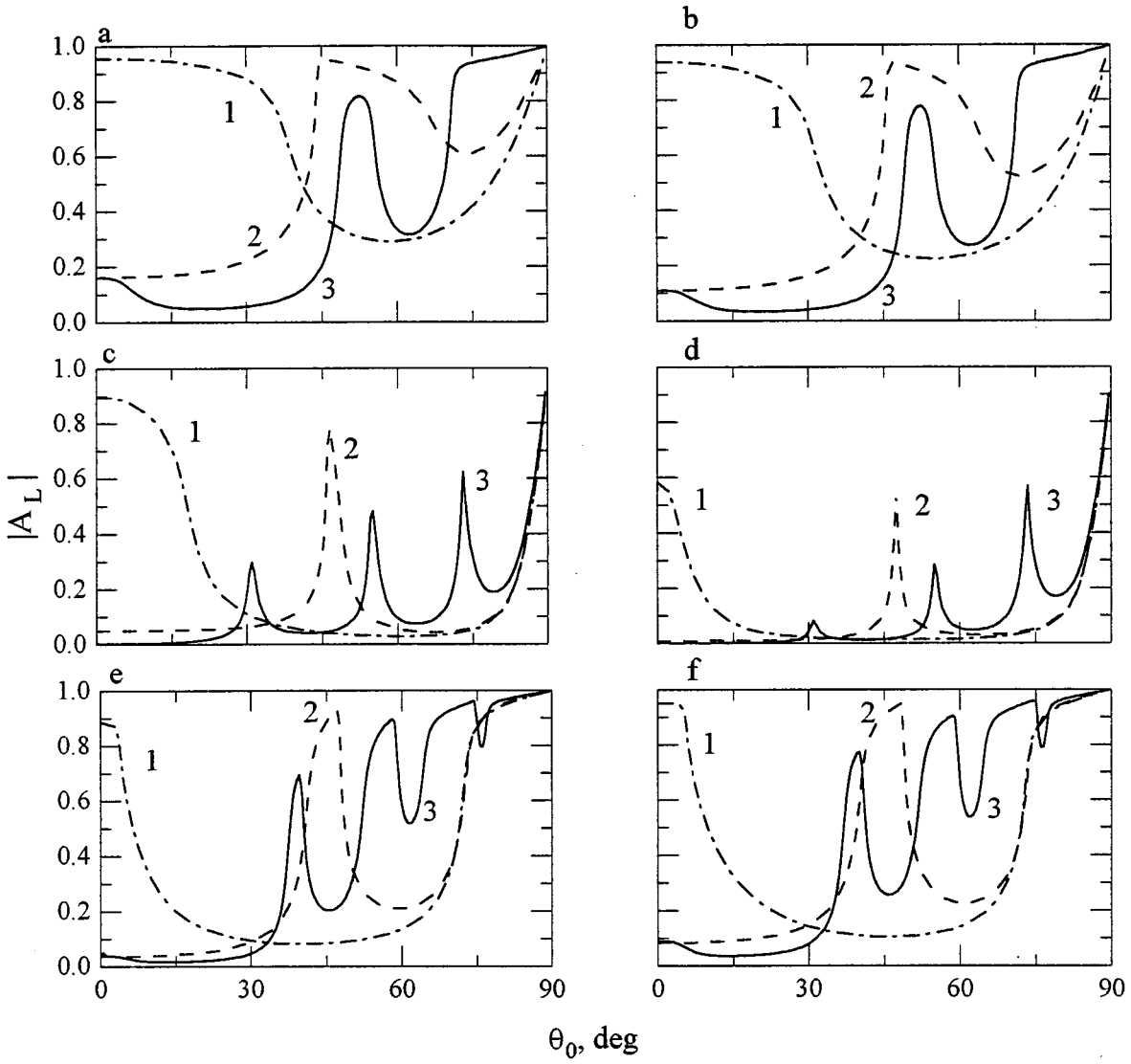

FIG. 6. Reflection coefficient as a function of angle of incidence of a plane wave. (a)–(f) correspond to the values of ρ_1,c_1 given in Fig. 4. Curve 1 in each picture is related to the frequencies of the first resonance in the corresponding picture of Fig. 4; curve 2 is related to the frequency of the minimum value of $|A_L|$, located between the first and the second resonances; curve 3 is related to the half-wave resonance of layers 1.

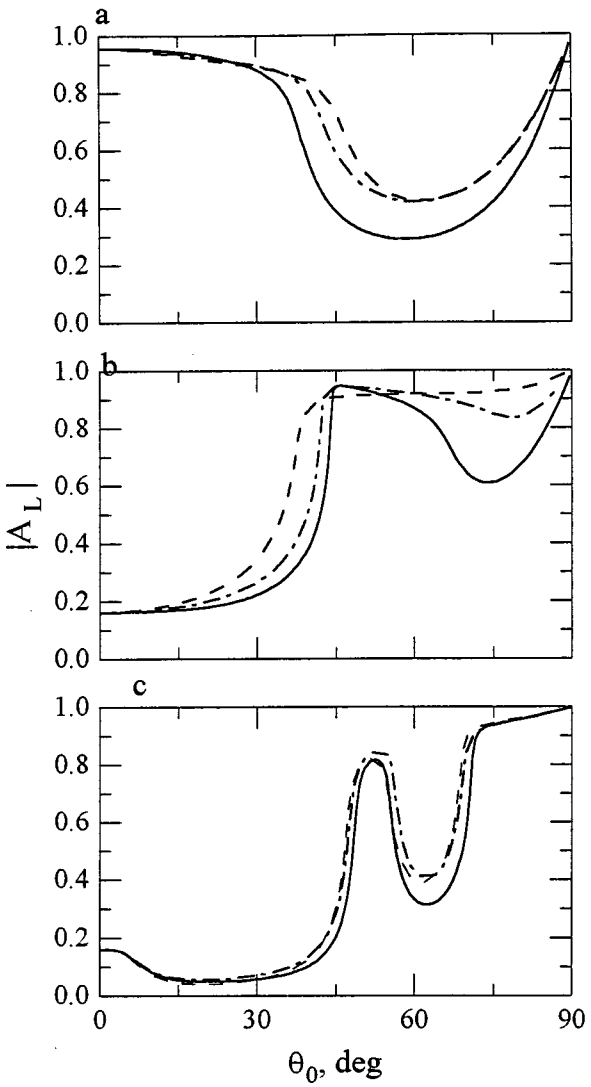

FIG. 7. Reflection coefficient as a function of angle of incidence for different values of the Poisson coefficient of layers 1. $h_1=h_2=0.01$ m, $\eta=0.04$, $\rho_1=900$ kg/m^3, $c_{11}=c_{33}=2.916\times10^9$ Pa. Pictures (a)–(c) are related to the frequencies of the first resonance in the Fig. 4(e), $f=22.146$ kHz, of the first minimum, $f=32.952$ kHz, and to the half-wave resonance of the layers 1, $f=90$ kHz, respectively. Solid lines: $\nu=0.5$ (liquid layers 1, $c_{44}=0$, $c_{13}=2.916\times10^9$ Pa), dot-and-dash lines: $\nu=0.45$ ($c_{44}=2.651\times10^8$ Pa, $c_{13}=2.386\times10^9$ Pa), dash lines: $\nu=0.4$ ($c_{44}=4.86\times10^8$ Pa, $c_{13}=1.944\times10^9$ Pa).

more maxima occur on the curves.

Figure 7 illustrate dependencies of the reflection coefficient on the rigidity of the material of layers 1. The curves computed for the Poisson coefficient $\nu=0.5$ correspond to liquid layers, i.e., other values of ν correspond to solid layers. The increase of rigidity affects significantly the curve's behavior at the intermediate angles of incidence of a sound wave and has no effect at normal incidence and at very acute angles. In the last case the reflection coefficient is about 1 even for layers with very low acoustical contrast.

The results obtained by solving matrix equation (28) for solid layers are shown in Figs. 8 and 9. If the losses in layers 1 are very little, then flat-top curves are observed. To explain this behavior, one may invoke Eq. (19). If the input impedance has a real part then the reflection coefficient depends on

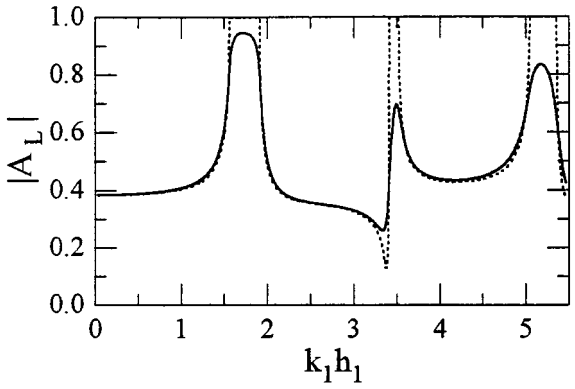

FIG. 8. Dependency of the reflection coefficient on wave thickness k_1h_1 at normal incidence. Layers 1 and 2 are transversely isotropic plastics, $h_1=h_2$. Layers 1: $\rho=1700$ kg/m^3, $c_{11}=2.2\times10^{10}$ Pa, $c_{33}=0.9\times10^{10}$ Pa, $c_{13}=0.6\times10^{10}$ Pa, $c_{44}=3\times10^9$ Pa. Layers 2: $\rho=1000$ kg/m^3, $c_{11}=1.0\times10^{10}$ Pa, $c_{33}=0.8\times10^{10}$ Pa, $c_{13}=0.4\times10^{10}$ Pa, $c_{44}=2\times10^9$ Pa. Solid line: coefficients of losses of all layers for c_{11} and c_{33} are 0.02, for c_{13} and c_{44} they are 0.03. Dash line: all coefficients of losses are 1×10^{-9}.

the value of this impedance. A propagating wave occurs in this case. But if the input impedance is purely imaginary then the magnitude of complex value of A_L does not depend on the input impedance and is equal to 1. In this case there are no waves carrying energy from left to right. If layers 1 or 2 have losses (solid line in Fig. 8), then the input impedance cannot be purely imaginary and the maxima are less than 1. Figure 9 illustrates angular dependencies of $|A_L|$ at a low frequency and at the frequency of the first maximum in Fig. 8. Even at the low frequency (solid line in Fig. 9) the curves are not smooth. It may be noted that there is a sharp maximum at $\theta_0=25°$. This angle corresponds to the angle where the reflection coefficient has a maximum for isolated layers with the same elastic parameters. Such a maximum is explained by interaction of a bending wave in the layer (nonsymmetrical with respect to a middle plane of the layer) with a symmetrical one.

III. CONCLUSION

A novel method for analyzing the reflection properties of a semi-infinite periodic stack of layers is presented. The

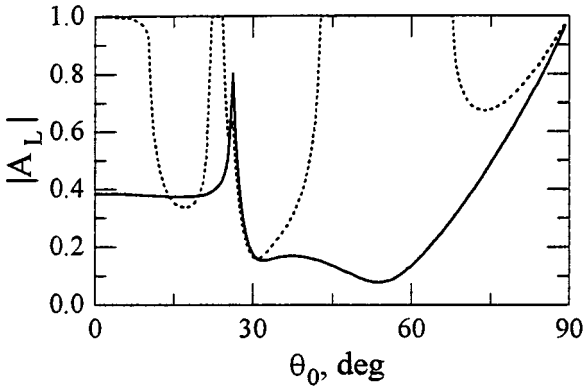

FIG. 9. Angular dependencies of the reflection coefficient. Parameters of materials are given under Fig. 8. Solid line: $k_1h_1=0.1$, dash line: $k_1h_1=1.7$. Losses are 1×10^{-9}.

layers may be either isotropic or transversely isotropic. With liquid even layers at oblique incidence of a sound wave or solid at normal incidence, and the even layers having the same parameters as the outer liquid, the reflection coefficient may be found in an explicit form as a solution of a quadratic equation. A quadratic equation with respect to the input normal impedance is derived for the case of liquid even layers which have parameters different from those of the outer liquid. These results are valid for liquid even layers at oblique incidence of a sound wave or for the solid even layers at normal incidence. And for a system consisting of all solid layers at oblique incidence of a wave, a quadratic matrix equation with respect to the impedance matrix is obtained. The solution of the equation is performed in terms of eigenvalues of a matrix related to the transfer matrix of a two-layered system.

Frequency and angle dependencies of the reflection coefficient have some resonance maxima, which may be explained by in-phase addition of partial reflected waves. At some frequencies the amplitude of the reflected wave may be great even for layers with low acoustical contrast.

ACKNOWLEDGMENTS

The author wishes to thank Dr. G. C. Gaunaurd for his constant encouragement and attention, A. G. Gamin for his help in computation, Dr. V. V. Fock and Professor D. P. Kouzov for discussions of the solution of the matrix equation, and Julia Verzhbinsky for incalculable help during all stages of preparation of this paper. The research described in this publication was made possible in part by Grant No. NVB000 from the International Science Foundation and Grant No. NVB300 from the Russian Government.

APPENDIX A: REFLECTION AND TRANSMISSION COEFFICIENTS FOR A SYSTEM OF ISOTROPIC OR TRANSVERSELY ISOTROPIC LAYERS

The formulae given below are valid for isotropic and transversely isotropic layers as well as for orthotropic layers in the plane of symmetry. The properties of transversely isotropic media may be described either by the physical elasticity constants c_{11}, c_{33}, c_{12}, c_{13}, c_{44}, or by technical constants (Young's modulus and Poisson coefficients) E_1, E_3, G_1, G_3, ν_1, ν_3. Indexes 1 and 3 are related to the plane of the layer and the normal plane, respectively. There are five independent values because the shear modulus in the plane of layer is related to the Young's modulus and the Poisson coefficient in this plane as $G_1=E_1/[2(1+\nu_1)]$. Value c_{44} is the shear modulus in the normal plane. This value for layered plastics is often spoken of as the modulus of interlayer shear. To compute the reflection and transmission coefficients, it is necessary to have only four of the five elasticity constants.

The physical and technical constants are interrelated by the following equations:[22]

$$c_{11}=\frac{E_1(1-\nu_3^2E_1/E_3)}{(1+\nu_1)m},\quad c_{33}=E_3(1-\nu_1)/m,$$

$$c_{44}=G_3,\quad c_{12}=\frac{E_1(\nu_1+\nu_3^2E_1/E_3)}{(1+\nu_1)m},$$

$$c_{13}=E_1\nu_3/m,\quad m=1-\nu_1-2\nu_3^2E_1/E_3,\qquad (A1)$$

$$G_1=(c_{11}-c_{12})/2=E_1/(2(1+\nu_1)).$$

To go over to isotropic layers (see Refs. 23 and 24) one can put $c_{11}=c_{33}=\lambda+2\mu$, $c_{44}=\mu$, $c_{12}=c_{13}=\lambda$, where λ and μ are Lamé constants. Reflection coefficient A and the transmission coefficient B for a system of layers, separating two different liquid media, are (see Ref. 12 with corrections)

$$A=\frac{(M_{22}Z_2/Z_0+M_{32}/Z_0)-(M_{33}+M_{23}Z_2)}{(M_{22}Z_2/Z_0+M_{32}/Z_0)+(M_{33}+M_{23}Z_2)},$$

$$B=\frac{2(M_{33}M_{22}-M_{32}M_{23})Z_2/Z_0}{(M_{22}Z_2/Z_0+M_{32}/Z_0)+(M_{33}+M_{23}Z_2)}\qquad (A2)$$

$$\times\exp(-iR),$$

where $Z_0=\rho_0c_0/\cos\theta_0$, $Z_2=\rho_2c_2/\cos\theta_2$ are the impedances of the media on the front and back sides of the system and

$$M_{22}=A_{22}-A_{21}A_{42}/A_{41},\quad M_{23}=A_{23}-A_{21}A_{43}/A_{41},$$
$$M_{32}=A_{32}-A_{31}A_{42}/A_{41},\quad M_{33}=A_{33}-A_{31}A_{43}/A_{41}.\qquad (A3)$$

Value R in the exponent depends on the definition of the transmission coefficient. If it is defined as a ratio of sound pressures in the transmitted wave at a point behind the system and in the incident wave at a point on the front side (i.e., if the system is removed) then $R=0$. If it is defined as ratio of sound pressures in the transmitted and incident waves at the same point behind the system, then its value depends on the location of a boundary of media 0 and 2 if the system is removed. If this boundary is located on the front side of the system, then $R=k_2H\cos\theta_2$; if it is located on the rear side, then $R=k_0H\cos\theta_0$, where H is the total thickness of the system, $k_0=\omega/c_0$, $k_2=\omega/c_2$. The coefficients A_{jk} are elements of the transfer matrix $\mathbf{A}_{\text{system}}$ of the system. This matrix is determined as a matrix product of all transfer matrices in the stack beginning from the last layer

$$\mathbf{A}_{\text{system}}=\mathbf{A}_n\mathbf{A}_{n-1}\cdots\mathbf{A}_1.\qquad (A4)$$

Here $\mathbf{A}_1$ is the matrix for the layer situated on the size of the incident wave. It is useful to note that the matrix product must be written down as in Eq. (A4), but not in the form $\mathbf{A}_1\mathbf{A}_2\cdots\mathbf{A}_n$. The changed order does not affect the transmission coefficient but results in erroneous values of the reflection coefficient for a nonsymmetrical set of absorbing layers. For a nonsymmetrical loss-free set one obtains the true magnitude and wrong phase of the reflection coefficient.

The coefficients of the transfer matrix for each layer are given by

$$a_{11}=(-\nu f_2m_L\cos P+f_1m_T\cos Q)/s_1,$$

$$a_{12}=i(\nu f_4m_L\sin P-f_3m_T\sin Q)/s_2,$$

$$a_{13}=-\nu_Lm_Lm_T(\cos P-\cos Q)/s_1,$$

$$a_{14}=i\nu_L(m_L\sin P-m_T\sin Q)/s_2,$$

$$a_{21}=i(-\nu f_2\sin P+f_1\sin Q)/s_1,$$

$$a_{22}=(\nu f_4\cos P-f_3\cos Q)/s_2,$$

$$a_{23}=i\nu_L(-m_T \sin P+m_L \sin Q)/s_1,$$

$$a_{31}=f_1f_2(\cos P-\cos Q)/(\nu_T s_1),$$

$$a_{32}=i(-f_1f_4 \sin P+f_2f_3 \sin Q)/(\nu_T s_2),$$

$$a_{41}=i(f_2f_3 \sin P-f_1f_4 \sin Q)/(\nu_T s_1),$$

$$a_{24}=a_{13}, \quad a_{33}=a_{22}, \quad a_{34}=a_{12}, \quad a_{42}=a_{31},$$

$$a_{43}=a_{21}, \quad a_{44}=a_{11},$$

where

$$\nu=\nu_L/\nu_T, \quad P=(\omega h/\nu_L)\cos \theta_L,$$

$$Q=(\omega h/\nu_T)\cos \theta_T,$$

$$s_1=c_{33}(m_T \cos \theta_L-\nu m_L \cos \theta_T),$$

$$s_2=c_{44}(m_T\nu \cos \theta_T-m_L \cos \theta_L),$$

$$f_1=c_{13}m_L \sin \theta_L+c_{33} \cos \theta_L,$$

$$f_2=c_{13}m_T \sin \theta_T+c_{33} \cos \theta_T,$$

$$f_3=c_{44}(m_L \cos \theta_L+\sin \theta_L),$$

$$f_4=c_{44}(m_T \cos \theta_T+\sin \theta_T),$$

Values ν_L, ν_T are the velocities of quasi-longitudinal and quasi-shear waves, respectively, $\nu_L=c_0 \sin \theta_L/\sin \theta_0$, $\nu_T=c_0 \sin \theta_T/\sin \theta_0$, where θ_L and θ_T are the angles of refraction for these waves and can be written as

$$\sin \theta_{L,T}=\sin \theta_0[(-d_2\pm \sqrt{d_2^2-4c_{33}c_{44}d_1})/(2d_1)]^{1/2}, \tag{A5}$$

with

$$d_1=A_1^2 \sin^4 \theta_0-(A_2 \sin^2 \theta_0-\rho_M c_0^2)(A_3 \sin^2 \theta_0+\rho_M c_0^2),$$

$$d_2=c_{33}(A_2 \sin^2 \theta_0-\rho_M c_0^2)-c_{44}(A_3 \sin^2 \theta_0+\rho_M c_0^2)-A_1^2 \sin^2 \theta_0,$$

$$A_1=c_{13}+c_{44}, \ A_2=c_{11}-c_{44},$$

$$A_3=c_{33}-c_{44}, \ A_4=c_{33}+c_{44}.$$

The plus and minus signs in Eqs. (A5) and (A6) are related to ν_L and ν_T, respectively, and ρ_M is the layer density. Reciprocal relationships describing the dependencies of ν_L and ν_T on the direction of propagation are given by

$$\nu_{L,T}^2=\{(A_2-A_3)\sin^2 \theta_{L,T}+A_4\pm[((A_2+A_3)\sin^2 \theta_{L,T}-A_3)^2+(2A_1 \sin \theta_{L,T} \cos \theta_{L,T})^2]^{1/2}\}/(2\rho_M). \tag{A6}$$

Values m_L and m_T are the tangents of angles between the normal axis and the directions of displacements of particles for quasi-longitudinal and quasi-shear waves

$$m_{L,T}=-\frac{(c_{13}+c_{44})\sin \theta_{L,T} \cos \theta_{L,T}}{c_{11} \sin^2 \theta_{L,T}+c_{44} \cos^2 \theta_{L,T}-\rho_M \nu_{L,T}^2}.$$

APPENDIX B: SOLUTION OF A QUADRATIC MATRIX EQUATION

Let us consider the quadratic matrix equation

$$\mathbf{XAX}+\mathbf{XB}+\mathbf{CX}+\mathbf{D}=\mathbf{0}, \tag{B1}$$

where $\mathbf{X},\mathbf{A},\mathbf{B},\mathbf{C}$ are square matrices. Let us premultiply this equation by $\mathbf{A}$ and represent the third term as $\mathbf{CA}^{-1}\mathbf{AX}$. Denoting for a while $\mathbf{Y}=\mathbf{AX}$, we obtain $\mathbf{Y}^2+\mathbf{YB}+\mathbf{ACA}^{-1}\mathbf{Y}+\mathbf{AD}=\mathbf{0}$, or $(\mathbf{Y}+\mathbf{ACA}^{-1})(\mathbf{Y}+\mathbf{B})+\mathbf{AD}-\mathbf{ACA}^{-1}\mathbf{B}=\mathbf{0}$. After substitution $\mathbf{U}=\mathbf{Y}+\mathbf{B}$ we obtain the equation

$$\mathbf{U}^2+\mathbf{HU}+\mathbf{G}=\mathbf{0}, \tag{B2}$$

where $\mathbf{H}=\mathbf{ACA}^{-1}-\mathbf{B}$, $\mathbf{G}=\mathbf{AD}-\mathbf{ACA}^{-1}\mathbf{B}$. Matrices $\mathbf{U}$ and $\mathbf{X}$ are related as

$$\mathbf{X}=\mathbf{A}^{-1}(\mathbf{U}-\mathbf{B}). \tag{B3}$$

Note that the solution of the common quadratic equation, understood in a matrix sense, namely, $\mathbf{U}=(-\mathbf{H}\pm\sqrt{\mathbf{H}^2-\mathbf{4G}})/2$, does not satisfy Eq. (B2) because after substitution in the equation we obtain a nonzero difference $\mathbf{H}\sqrt{\mathbf{H}^2-\mathbf{4G}}-\sqrt{\mathbf{H}^2-\mathbf{4G}}\mathbf{H}$.

Let us multiply Eq. (B2) by an arbitrary vector $\mathbf{x}$. Eigenvalues λ of the matrix $\mathbf{U}$ satisfy the equation $\mathbf{Ux}=\lambda\mathbf{x}$. So Eq. (B2) becomes

$$(\lambda^2\mathbf{I}+\lambda\mathbf{H}+\mathbf{G})\mathbf{x}=\mathbf{0},$$

where $\mathbf{I}$ is the identity matrix. This system of equations has a nontrivial solution if

$$\det(\lambda^2\mathbf{I}+\lambda\mathbf{H}+\mathbf{G})=0. \tag{B4}$$

This equation is of order $2n$, where n is the order of the matrix. After numerical solution of this equation we find $2n$ values: $\lambda^{(1)}, \lambda^{(2)},...,\lambda^{(2n)}$. The characteristic equation of the matrix $\mathbf{U}$ is

$$\det(\mathbf{U}-\lambda\mathbf{I})=\mathbf{0}. \tag{B5}$$

Let us consider a solution of Eq. (B2) for a 2×2 matrix. In this case Eq. (B5) is a quadratic equation. Any quadratic equation can be written down as

$$\lambda^2-(\lambda_1+\lambda_2)\lambda+\lambda_1\lambda_2=0, \tag{B6}$$

where λ_1, λ_2 satisfy Eq. (B4), i.e., $\lambda_1\lambda_2$ are any pair of the values $\lambda^{(1)}$, $\lambda^{(2)}$, $\lambda^{(3)}$, $\lambda^{(4)}$. In accordance with the Hamilton–Cayley theorem, any square matrix satisfies its own characteristic equation. Therefore, matrix $\mathbf{U}$ should satisfy the following equation

$$\mathbf{U}^2-(\lambda_1+\lambda_2)\mathbf{U}+\lambda_1\lambda_2\mathbf{I}=0. \tag{B7}$$

Eliminating $\mathbf{U}^2$ from Eqs. (B2) and (B7) we obtain the solution

$$\mathbf{U}=-((\lambda_1+\lambda_2)\mathbf{I}+\mathbf{H})^{-1}(\mathbf{G}-\lambda_1\lambda_2\mathbf{I}). \tag{B8}$$

To choose the appropriate pair λ_1, λ_2 out of six possible pairs of the values $\lambda^{(1)}$, $\lambda^{(2)}$, $\lambda^{(3)}$, $\lambda^{(4)}$, it is useful to consider an infinite system of the layers. In this case it follows from Floquet's theorem that all values of velocities and stresses at the boundaries $y=0$ and $y=h_1+h_2$ are interrelated as $\nu_x^{(2)}=\exp(i\kappa(h_1+h_2))\nu_x^{(0)}$, $\nu_y^{(2)}=\exp(i\kappa(h_1+h_2))\nu_y^{(0)}$ etc., where κ is the real or complex wave number of a normal

wave. Upon substituting these values in Eq. (20), one obtains a homogeneous system of equations. Hence, $\det[\mathbf{A}-\exp(i\kappa(h1+h2)\mathbf{I}]=0$. This is a quartic equation with respect to $\exp(i\kappa(h_1+h_2))$. We can verify that this equation coincides with Eq. (B4). Therefore roots λ and $\exp(i\kappa(h_1+h_2))$ are interrelated as $\lambda^{(\alpha)}=\exp[i\kappa^{(\alpha)}(h_1+h_2)]$, $\alpha=1,2,3,4$. The true physical solution would result if $\mathrm{Im}\,\kappa^{(\alpha)}\geqslant 0$ with an equality possible only if the layers are loss free. Therefore, one should choose such values of $\lambda^{(\alpha)}$ that $|\lambda^{(\alpha)}|\leqslant 1$. If some values of $|\lambda^{(\alpha)}|$ are about 1, then some roots may be chosen erroneously (because of existence of finite accuracy of computations). To avoid these errors, it is always useful to specify some value of loss in the layers, even a small one. Then the above condition will become a strict inequality $|\lambda^{(\alpha)}|<1$, and the uncertainty does not arise.

This method can also be applied to matrices of a higher order. Let us consider Eq. (B2), where all matrices have the order 3×3. Such matrices can appear in 3D problems. In this case Eq. (B4) is a sextic equation and has six roots. It is necessary at first to match the order of a quadratic matrix equation (B2) and the order of a cubic characteristic equation (B5). Let us multiply Eq. (B2) by $\mathbf{U}$. Then we obtain a cubic equation

$$\mathbf{U}^3+\mathbf{H}\mathbf{U}^2+\mathbf{G}\mathbf{U}=0. \tag{B9}$$

The characteristic equation (B6) of matrix $\mathbf{U}$ can be written down as a cubic equation

$$\lambda^3-q_1\lambda^2+q_2\lambda-q_3=0,$$

where $q_1=\lambda_1+\lambda_2+\lambda_3$, $q_2=\lambda_1\lambda_2+\lambda_2\lambda_3+\lambda_1\lambda_3$, $q_3=\lambda_1\lambda_2\lambda_3$. Here λ_1, λ_2, λ_3 are any 3 of the six roots of Eq. (B4). In accordance with the Hamilton–Cayley theorem, $\mathbf{U}$ should satisfy the equation

$$\mathbf{U}^3-q_1\mathbf{U}^2+q_2\mathbf{U}-q_3\mathbf{I}=0. \tag{B10}$$

Eliminating $\mathbf{U}^3$ from Eqs. (B9) and (B10), we obtain a new quadratic equation

$$(q_1\mathbf{I}+\mathbf{H})\mathbf{U}^2+(-q_2\mathbf{I}+\mathbf{G})\mathbf{U}+q_3\mathbf{I}=0. \tag{B11}$$

Eliminating $\mathbf{U}^2$ from Eqs. (B2) and (B11), we obtain the solution of the quadratic equation (B2) for the 3×3 matrices:

$$\mathbf{U}=(\mathbf{H}^2+q_1\mathbf{H}-\mathbf{G}+q_2\mathbf{I})^{-1}(q_3\mathbf{I}-q_1\mathbf{G}-\mathbf{H}\mathbf{G}). \tag{B12}$$

There are $\binom{6}{3}=20$ combinations of values λ_1, λ_2, λ_3 from the 6 roots of Eq. (B4). These roots are related to six normal waves. Three of them propagate at acute angles with respect to the y axis, and the rest propagate at obtuse angles. Since all sources of sound are situated on the left-hand side, only the waves propagating at acute angles with respect to the y axis can exist. Hence, there is only one combination of roots $\lambda_1,\lambda_2,\lambda_3$ which gives the true solution of the physical problem. Appropriate roots satisfy conditions $|\lambda_j|\leqslant 1$, $j=1,2,3$. In a general case for matrices of order $n\times n$ there are $\binom{2n}{n}$ solutions of Eq. (B2).

APPENDIX C: SOLUTION OF A QUARTIC EQUATION

The roots of an equation with complex coefficients $\lambda^4+a_1\lambda^3+a_2\lambda^2+a_3\lambda+a_4=0$ are given by

$$\lambda^{(1),(2)}=\left[-(a_1+d)/2 \pm \sqrt{\left(\frac{a_1+d}{2}\right)^2-4\left(c+\frac{a_1c-a_3}{d}\right)}\,\right]\Big/\,2,$$

$$\lambda^{(3),(4)}=\left[-\left(\frac{a_1-d}{2}\right) \pm \sqrt{\left(\frac{a_1-d}{2}\right)^2-4\left(c-\frac{a_1c-a_3}{d}\right)}\,\right]\Big/\,2,$$

$$c=u+a_2/6,\quad d=\sqrt{8c+a_1^2-4a_2},$$

$$u=(-q+\sqrt{q^2+p^3})^{1/3}\epsilon_j+(-q-\sqrt{q^2+p^3})^{1/3}\epsilon_k,$$

$$j,k=1,2,3,$$

$$p=(a_1a_3-4a_4)/12-a_2^2/36,$$

$$q=-a_2^3/216+a_2(a_1a_3-4a_4)/48+(a_4(4a_2-a_1^2)-a_3^2)/16,$$

$$\epsilon_1=1,\quad \epsilon_2=(-1+i\sqrt{3})/2,\quad \epsilon_3=(-1-i\sqrt{3})/2.$$

The factors ϵ_j and ϵ_k are introduced to choose the appropriate branches of the cubic roots. It is necessary to choose such a combination ϵ_j, ϵ_k that the cubic equation $u^3+3pu+2q=0$ is satisfied. There are three such combinations out of nine possible pairs ϵ_j, ϵ_k.

[1] D. L. Folds and C. D. Loggins, ''Transmission and reflection of ultrasonic waves in layered media,'' J. Acoust. Soc. Am. **62**, 1102–1109 (1977).

[2] P. R. Stepanishen and B. Strozeski, ''Reflection and transmission of acoustic wideband plane waves by layered viscoelastic media,'' J. Acoust. Soc. Am. **71**, 9–21 (1982).

[3] L. M. Brekhovskikh, *Waves in Layered Media* (Academic, New York, 1960).

[4] E. L. Shenderov, *Wave Problems in Hydroacoustics* (Sudostroenie, Leningrad, 1972. [English translation: Joint Publications Research service, Report JPRS-58146 (433p.), Feb. 1973. National Technical Information Service, Springfield, VA 22151.]

[5] P. Cervenka and P. Challande, ''A new efficient algorithm to compute the exact reflection and transmission factors for plane waves in layered absorbing media (liquids and solids),'' J. Acoust. Soc. Am. **89**, 1579–1589 (1991).

[6] J. W. Dunkin, ''Computation of modal solutions in layered, elastic media at high frequencies,'' Bull. Seismol. Soc. Am. **55**, 335–358 (1965).

[7] M. Castaings and B. Hosten, ''Delta operator technique to improve the Thomson–Haskell method stability for propagation in multilayered anisotropic absorbing plates,'' J. Acoust. Soc. Am. **95**, 1931–1941 (1994).

[8] K. P. Scharnhorst, ''Properties of acoustic and electromagnetic coefficients and transfer matrices of multilayered plates,'' J. Acoust. Soc. Am. **74**, 1883–1887 (1983).

[9] J. S. Sastry and M. L. Munjal, ''A transfer matrix approach for evaluation of the response of a multilayer infinite plate to a two-dimensional pressure excitation,'' J. Sound. Vib. **182**, 109–128 (1995).

[10] A. H. Nayfeh, ''The general problem of elastic wave propagation in multilayered anisotropic media,'' J. Acoust. Soc. Am. **89**, 1521–1531 (1991).

[11] F. I. Solyanik, ''Transmission of plane waves through layered media consisting from anisotropic plates,'' Akust. Zh. **23**, 933–938 (1977). [English Transl.: Sov. Phys. Acoust. **23**, (1977).]

[12] E. L. Shenderov, ''Transmission of sound through transversely-isotropic plate,'' Akust. Zh. **30**, 122–129 (1984). [English Transl.: Sov. Phys. Acoust. **30**, (1984).]

[13] A. M. B. Braga and G. Herrmann, ''Floquet waves in anisotropic periodically layered composites,'' J. Acoust. Soc. Am. **91**, 1211–1227 (1991).

[14] K. E. Gilbert, ''A propagator matrix method for periodically stratified media,'' J. Acoust. Soc. Am. **73**, 137–142 (1982).

[15] M. Schoenberg, ''Wave propagation in alternating fluid/solid layers,'' Wave Motion **6**, 303–320 (1984).

[16] W. M. Karunasena, R. L. Bratton, S. K. Datta, and A. H. Shah, ''Elastic wave propagation in laminated composite plates,'' ASME J. Eng. Mater. Tech. **113**, 43, 413–424 (1991).
[17] W. L. Mochan and M. del Castillo-Mussot, ''Effect of plasma waves on the optical properties of metal-insulator superlattices,'' Phys. Rev. B **35**, 1088–1098 (1987).
[18] R. Esquivel-Sirvent and G. H. Cocoletzi, ''Band structure for the propagation of elastic waves in superlattice,'' J. Acoust. Soc. Am. **95**, 86–90 (1995).
[19] P. J. Shull, D. E. Chimenti, and S. K. Datta, ''Elastic guided waves and the Floquet concept in periodically layered plates,'' J. Acoust. Soc. Am. **95**, 99–108 (1994).
[20] T. J. Delph and G. Herrmann, ''Harmonic wave propagation in a periodically layered, infinite elastic body: Plane strain, analytical results,'' J. Appl. Mech. **46**, 113–119 (1978).
[21] T. J. Delph, G. Herrmann, and R. K. Kaul, ''Harmonic wave propagation in periodically layered, infinite elastic body: Antiplane strain,'' J. Appl. Mech. **5**, 343–349 (1978).
[22] S. G. Lekhnitski, *Theory of Elasticity of an Anisotropic Body* (Nauka, Moskva, 1977, in Russian).
[23] W. T. Thompson, ''Transmission of elastic waves through a stratified medium,'' Appl. Phys. **21**, 89–93 (1950).
[24] N. A. Haskell, ''The dispersion of surface waves in multilayered media,'' Bull. Seismol. Soc. Am. **43**, 17–34 (1953).

Sound propagation in an irregular two-dimensional waveguide

Mark Spivack
Department of Applied Mathematics and Theoretical Physics, The University of Cambridge, CB3 9EW, England and Smith Institute, Surrey Research Park, Guildford, Surrey GU2 5YP, England

(Received 4 October 1995; revised 23 September 1996; accepted 31 October 1996)

A method is presented for the numerical calculation of a scalar wave propagating along a two-dimensional rough-sided or irregular waveguide. In this situation the wave becomes multiply scattered, with simultaneous interaction at the two boundaries. The field can be expressed in terms of a pair of coupled integral equations; these are derived and solved in an approach based on the parabolic integral equation method, which assumes that all energy is carried in a forward direction. An extended formulation encompassing backscatter is also derived, and a method given for its treatment. This paper serves in part to explain the computational results presented in B. J. Uscinski, ''High-frequency propagation in shallow water,'' J. Acoust. Soc. Am. **98**, 2702–2707 (1995). [S0001-4966(97)03703-X]

PACS numbers: 43.20.Fn, 43.20.Mv, 43.30.Hw [ANN]

INTRODUCTION

In many acoustic and electromagnetic applications, waves propagate along irregular or rough-sided waveguides,[1–5] becoming scattered progressively as they impinge upon the boundaries. This is an important mechanism, for example, for sound propagation in shallow water and ice, or electromagnetic waves in ducts and dielectric layers. The surfaces often vary randomly on a scale comparable with a wavelength; this gives rise to a high degree of multiple scattering, which is enhanced by the low angles of incidence. The field can be expressed exactly in terms of boundary integrals; these give rise to a pair of coupled integral equations whose treatment is difficult both numerically and analytically.

In the simpler case of a single boundary (i.e., a rough half-space) the analogous low grazing angle problem has been treated successfully using parabolic integral equation method.[6–8] Under the approximation that all energy is forward scattered, the full wave equation is replaced by the parabolic equation, an appropriate Green's function derived, and the exact boundary integral formulation replaced by the parabolic integral equations. (These equations allow for waves traveling only in the direction away from the source, but an extended description taking into account multiple backscatter has been derived.[9])

The same approach can be applied to the present problem,[4] giving rise to a set of coupled equations, again within the approximation that forward scatter predominates. The first purpose of this note is to explain the treatment of the coupled system, and to show how the parabolic form allows fast and efficient solution. The method is implemented here for the case in which both surfaces have pressure release boundary conditions. The system is first discretized with respect to range, giving a pair of coupled matrix equations in the unknown vertical derivatives of the field along the two surfaces. The ''one-way'' form of the equations allows the system to be solved progressively from the left, say. This requires only $O(N^2)$ operations, where N is the number of points used in the discretization. The advantages can be seen when the pair of matrix equations are rewritten formally in terms of a single ''matrix operator'' $\mathscr{M}$, whose entries are themselves 2×2 matrices; this matrix operator is lower triangular, and can therefore be inverted efficiently. Computational examples are given below for a Gaussian beam traveling at various angles with respect to the horizontal.

One drawback is that backscatter, the relevant quantity in applications such as detection and imaging, is precluded by this description as it stands. The second aim of the paper is to extend the method to include direct and indirect backscatter components. The one-way Green's function is replaced by an analogous two-way form; the resulting equations thereby include components of the field scattered back toward the source. In this form the equations do not directly yield a lower triangular system, so that the computational advantage is initially lost, but the solution can be expressed as a series in which each term is again lower triangular. It is explained below how this system may be treated in a way similar to that above.

The problem is formulated in Sec. I, and the implementation of the numerical solution given in Sec. II, with computational examples. In Sec. III an extended form of the equations is derived taking backscatter into account, and it is explained how these equations may be treated similarly.

I. FORMULATION OF PROBLEM

Consider a two-dimensional waveguide with boundaries varying irregularly about the horizontal direction, as shown schematically in Fig. 1. We will as far as possible follow the conventions of previous papers.[6,8] The derivation of equations is similar to that for the case of a single surface (irregular half-space)[6,7] and details will be kept to a minimum here. Let x be the horizontal and z the vertical axis, and denote the upper and lower surfaces by $h_1(x)$, $h_2(x)$ respectively. We consider time-harmonic solutions p of the wave equation $(\nabla^2+k^2)p=0$, with wave number k. Then p can be considered as the sum

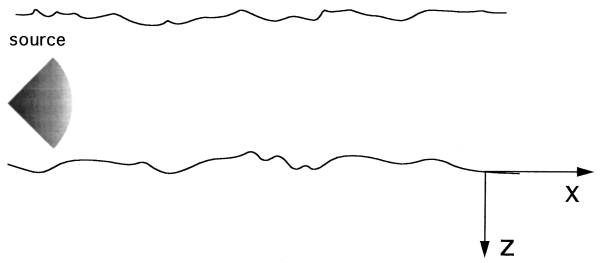

FIG. 1. Schematic view of the scattering geometry.

$$p = p_{\text{inc}} + p_s$$

of an incident field p_{inc} and a scattered component p_s due to the presence of the surfaces. It will be assumed that angles of propagation and scatter are small with respect to the horizontal, so the field has a rapidly varying phase component $\exp(ikx)$. This can be factored out, and the reduced wave ψ introduced,

$$\psi = p\ \exp(-ikx).$$

Then ψ obeys the parabolic or one-way wave equation

$$\psi_x + 2ik\psi_{zz} = 0, \tag{1}$$

and we can write

$$\psi = \psi_{\text{inc}} + \psi_s, \tag{2}$$

where the reduced forms ψ_{inc}, ψ_s of the incident and scattered fields are defined similarly. Now the parabolic form of the Green's function can be derived for wave equation (1). This is given by

$$G_p(x,z;x',z') = \begin{cases} \dfrac{1}{2}\sqrt{i/2\pi k}\sqrt{\dfrac{1}{x-x'}}\exp\left[\dfrac{ik(z-z')^2}{2(x-x')}\right] & \text{for } x'<x \\ 0, \quad \text{otherwise}. \end{cases} \tag{3}$$

By analogy with the Helmholtz equations, and as for previous applications of the parabolic integral equation method to a rough half-space, the field at a point r inside the waveguide can be expressed as an integral across the bounding surfaces:

$$\psi_s(\mathbf{r}) = \psi_{\text{inc}} + \int_S \left[G(\mathbf{r};\mathbf{r}')\ \frac{\partial\psi}{\partial z}(\mathbf{r}') - \frac{\partial G}{\partial z}(\mathbf{r};\mathbf{r}')\psi(\mathbf{r}') \right] dx', \tag{4}$$

where $\mathbf{r}' = (x', S(x'))$, and S is the union of the surfaces h_1 and h_2.

For convenience we will henceforth specialize to the case of pressure release surfaces. The method is equally applicable when either or both surfaces obey Neumann boundary conditions. (See concluding remarks for discussion of more general cases.) In this case Eq. (4) becomes

$$\psi_s(\mathbf{r}) = \int_{h_1+h_2} G(\mathbf{r};\mathbf{r}')\ \frac{\partial\psi}{\partial z}(\mathbf{r}')dx'. \tag{5}$$

Taking limits as $\mathbf{r}$ tends, respectively, to the upper and to the lower surfaces, and applying the boundary conditions, we obtain two coupled integral equations for the unknown values of the quantity $\partial\psi/\partial z$ along each of the two surfaces. It is convenient to regard these as separate functions of the single coordinate x, and accordingly we define

$$\psi^1(x) = \frac{\partial\psi}{\partial z}(x, h_1(x)), \qquad \psi^2(x) = \frac{\partial\psi}{\partial z}(x, h_2(x)). \tag{6}$$

The coupled integral equations for ψ^1, ψ^2 can then be written

$$\psi_{\text{inc}}(\mathbf{r}_2) = \int_0^x [G(\mathbf{r}_2;\mathbf{r}_2')\psi^2(x') - G(\mathbf{r}_2;\mathbf{r}_1')\psi^1(x')]dx',$$
$$\psi_{\text{inc}}(\mathbf{r}_1) = \int_0^x [G(\mathbf{r}_1;\mathbf{r}_2')\psi^2(x') - G(\mathbf{r}_1;\mathbf{r}_1')\psi^1(x')]dx', \tag{7}$$

where

$$\mathbf{r}_1 = (x, h_1(x)),\ \ \mathbf{r}_1' = (x', h_1(x')), \qquad \mathbf{r}_2 = (x, h_2(x)),\ \ \mathbf{r}_2' = (x', h_2(x')). \tag{8}$$

The main task is to invert this set of coupled equations to find the field derivatives ψ^1, ψ^2 along the surfaces. These may then be substituted into Eq. (5) to yield the value of the field in the waveguide.

For computational purposes we will take as a source a Gaussian beam, centered at a point $(0,z_0)$, say, whose principal direction is at some small angle θ to the horizontal. This gives rise to an incident field

$$E_{\text{inc}}(x,z) = \frac{w}{\sqrt{w^2 + 2ix/k}}\exp\left[-\frac{2z^2 + ikSw^2(Sx - z)}{2(w^2 + 2ix/k)} \right], \tag{9}$$

where $S = \sin(\theta)$, and w is the width of the beam.

II. SOLUTION

In this section the numerical solution of the integral equations will be explained, and computational examples given.

A. Numerical implementation

The numerical treatment is similar in many respects to that of the corresponding rough half-space problem (described elsewhere[6]), so we concentrate here on the additional complications introduced by the coupling of the equations. Some care is required in treating the integrands, which contain weak (i.e., integrable) singularities.

Following previous treatments we discretize Eqs. (7) with respect to range x introducing, say, N equally spaced points $\{x_n\}$, $n = 1,\ldots,N$. The first of Eqs. (7), for example, is written as a sum of subintervals

$$\psi_{\text{inc}}(\mathbf{r}_2) = \sum_{j=1}^{n-1} \int_{x_j}^{x_{j+1}} [G(\mathbf{r}_2;\mathbf{r}_2')\psi^2(x') - G(\mathbf{r}_2;\mathbf{r}_1')\psi^1(x')]dx', \tag{10}$$

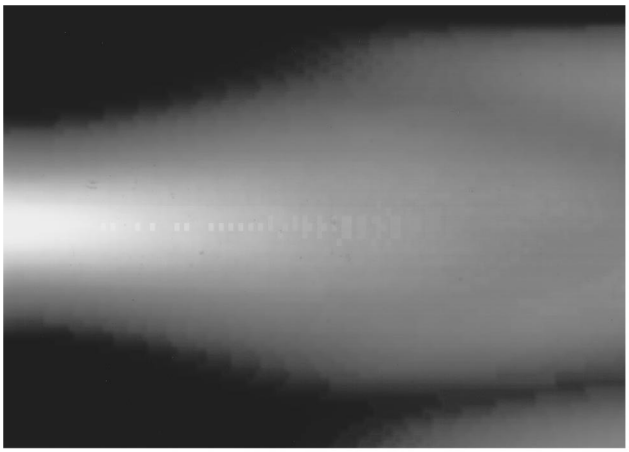

FIG. 2. Amplitude of the wave due to a horizontally traveling Gaussian beam, in a regular flat-sided waveguide.

where $\mathbf{r}_2=(x_n,h_2(x_n))$, $\mathbf{r}_1'=(x',h_1(x'))$, and $\mathbf{r}_2'=(x',h_2(x'))$. We may assume that the unknown functions ψ^1, ψ^2 vary sufficiently slowly to be treated as constant over each of the subintervals (x_j,x_{j+1}), and can therefore be taken outside the integral. Writing $X_n=(x_{n+1}+x_n)/2$, we then replace ψ^1, ψ^2, and the incident field along the surfaces by vectors:

$$\begin{aligned} a_n&=\psi_{\text{inc}}[x_n,h_1(x_n)],\\ b_n&=\psi_{\text{inc}}[x_n,h_2(x_n)],\\ c_n&=\psi^1(X_n),\quad d_n=\psi^2(X_n). \end{aligned} \tag{11}$$

Equations (7) then become

$$\begin{aligned} a_n&=\sum_{j=1}^{n-1}[S_{j,n}c_j+T_{j,n}d_j],\\ b_n&=\sum_{j=1}^{n-1}[S'_{j,n}c_j+T'_{j,n}d_j], \end{aligned} \tag{12}$$

where

$$\begin{aligned} S_{j,n}&=\int_{x_{j-1}}^{x_j}(\mathbf{r}_1;\mathbf{r}_1')dx',\\ T_{j,n}&=-\int_{x_{j-1}}^{x_j}G(\mathbf{r}_1;\mathbf{r}_2')dx',\\ S'_{j,n}&=\int_{x_{j-1}}^{x_j}G(\mathbf{r}_2;\mathbf{r}_1')dx',\\ T'_{j,n}&=-\int_{x_{j-1}}^{x_j}G(\mathbf{r}_2;\mathbf{r}_2')dx', \end{aligned} \tag{13}$$

and

$$\begin{aligned} &\mathbf{r}_1=(x_n,h_1(x_n)),\quad \mathbf{r}_1'=(x',h_1(x')),\\ &\mathbf{r}_2=(x_n,h_2(x_n)),\quad \mathbf{r}_2'=(x',h_2(x')). \end{aligned} \tag{14}$$

Note that, by expanding the integrand in each interval about the endpoint x_j, the integrals (13) can be carried out analytically and expressed in terms of Fresnel integrals. This becomes particularly important when the x values of the arguments of the Green's function are close (especially at large vertical separation), because $G(x,z;x',z')$ has a weak singularity as $x'\to x$. Further details can be found in Ref. 6.

The equations are now in a form which can be solved by induction, or progressively from the left. At each stage the calculation reduces to a pair of simultaneous linear equations for the values of c_n,d_n at a single range step x_n, say.

Step 1:

For $n=1$, Eqs. (12) give:

$$\begin{aligned} a_1&=S_{11}c_1+T_{11}d_1,\\ b_1&=S'_{11}c_1+T'_{11}d_1. \end{aligned} \tag{15}$$

Multiplying the first by S'_{11}, the second by S_{11}, and subtracting, this gives the solutions for the field derivative at the initial range step

$$\begin{aligned} d_1&=\frac{S_{11}b_1-S'_{11}a_1}{S_{11}T'_{11}-S'_{11}T_{11}},\\ c_1&=(a_1-T_{11}d_1)/S_{11}. \end{aligned} \tag{16}$$

Step 2:

Assume that c_j,d_j are known for $j=1,\ldots,n-1$. Then Eqs. (12) can be written in the form

$$\begin{aligned} a_n-\sum_{j=1}^{n-1}[S_{jn}c_j+T_{jn}d_j]&=S_{nn}c_n+T_{nn}d_n,\\ b_n-\sum_{j=1}^{n-1}[S'_{jn}c_j+T'_{jn}d_j]&=S'_{nn}c_n+T'_{nn}d_n. \end{aligned} \tag{17}$$

This is solved to find c_n,d_n, exactly as for $n=1$: Write

$$\begin{aligned} X_n&=a_n-\sum_{J=1}^{n-1}[S_{jn}c_j+T_{jn}d_j],\\ Y_n&=b_n-\sum_{J=1}^{n-1}[S'_{jn}c_j+T'_{jn}d_J]. \end{aligned} \tag{18}$$

Then we obtain

$$\begin{aligned} d_n&=\frac{S_{n,n}Y_n-S'_{n,n}X_n}{S_{nn}T'_{nn}-S'_{nn}T_{nn}},\\ c_n&=\frac{X_n-T_{nn}d_n}{S_{nn}} \end{aligned} \tag{19}$$

as required. This is carried out progressively up to the maximum range x_N.

B. Computational examples

The scheme described above can be applied both to regular and irregular waveguides. In the following examples, the vertical scale is exaggerated, approximately by a factor of 10, so that on a true scale the figures would be stretched horizontally. Figure 2 shows the amplitude of the total field in a regular flat-sided waveguide, due to a Gaussian beam traveling horizontally i.e., with principal direction parallel to the mean surface direction. The source is at the left, and the field vanishes on both surfaces. (This is visible at the lower surface which corresponds to the lower edge of the plot; the

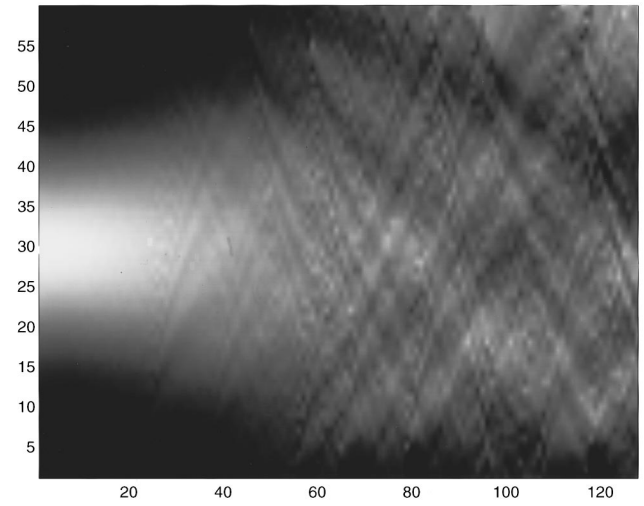

FIG. 3. Amplitude of the total (i.e., incident plus scattered) wave, for the same incident field as in Fig. 2 where the surfaces are now rough. The horizontal scale size L of each surface is approximately $\lambda/4$ where λ is the wavelength.

top of the graph extends up to slightly below the upper waveguide surface.) An example is shown in Fig. 3 of the field resulting when the surfaces are rough; here the scattering has largely destroyed the deterministic interference pattern. The surface correlation length, L, is about a quarter of a wavelength. Figure 4 shows a calculation for surfaces with the same rms height, but with scale sizes L about four times as large, i.e., of the order of a wavelength.

Figures 5 and 6 show similar configurations, but here the beam is at a nonzero angle θ to the horizontal. Again the disruption of the flat waveguide pattern is clear.

The parabolic equation method which we apply requires low angles of propagation and scatter, i.e., less than around 15° to the x direction. It is difficult to translate this into a precise limitation on the form of the rough surfaces, because a general solution for the scattered field is unavailable. However, the method should yield reasonably accurate results provided that the maximum average angles of slope relative to the direction of incidence are less than 15°.

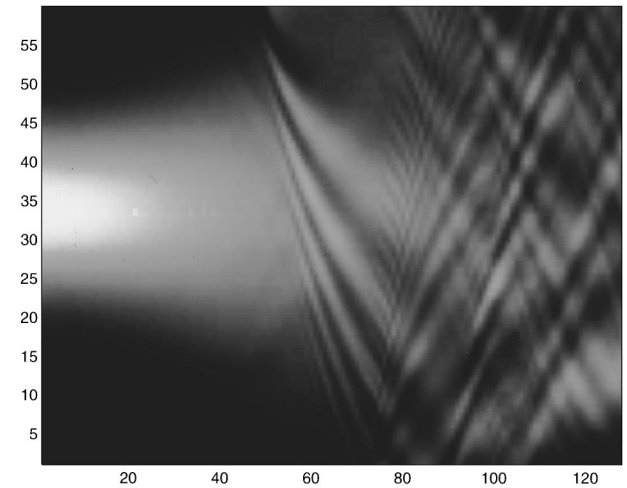

FIG. 4. Similar plot to Fig. 3, buth with scale sizes L four times as large.

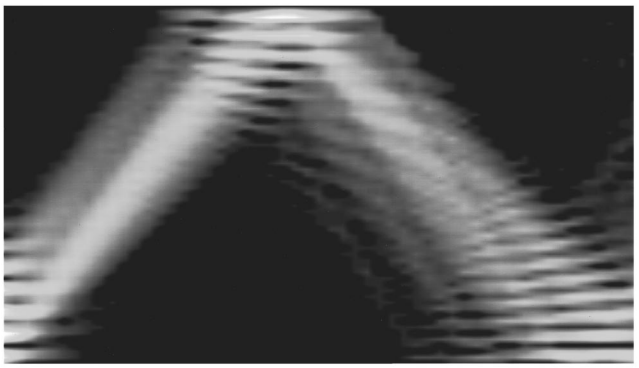

FIG. 5. Amplitude of the wave in a flat-sided waveguide, due to a Gaussian beam traveling at an angle $\theta=0.2$.

III. MULTIPLE BACKSCATTER

In many circumstances, particularly in detection and imaging, the principal quantity required is power scattered back towards the source, and the above purely forward scatter calculation is not sufficient. In this section we formulate a method which takes account of backscatter, although numerical implementation will not be carried out here.

The above discretized solution is first expressed in more formal terms, in order to simplify the eventual backscatter calculation.

Define vectors $\mathbf{A}=(A_1,\ldots,A_N)$, $\mathbf{C}=(C_1,\ldots,C_N)$ of length N, whose elements are themselves two-dimensional vectors,

$$A_n=(a_n,b_n), \quad C_n=(c_n,d_n), \tag{20}$$

where a_n, b_n, c_n, d_n are given by (11). Thus, in effect $\mathbf{A}$, $\mathbf{C}$ are functions of x. Define the 2×2 matrices M_{jk} by

$$M_{jk}=\begin{pmatrix} S_{jk} & T_{jk} \\ S'_{jk} & T'_{jk} \end{pmatrix}. \tag{21}$$

Then Eq. (15) becomes

$$A_1=M_{11}C_n,$$

Eq. (17) is

$$A_n-\sum_{j=1}^{n-1}[M_{jn}C_j]=M_{nn}C_n,$$

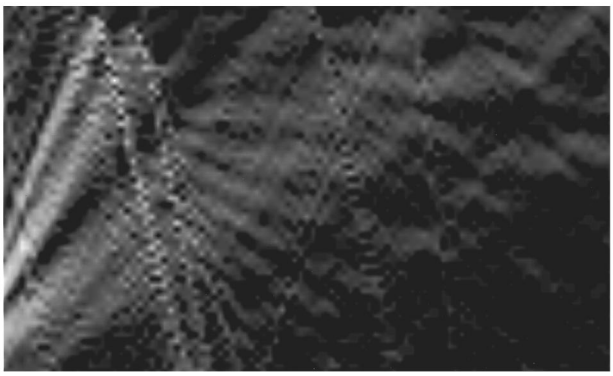

FIG. 6. Amplitude of the wave in a rough-sided waveguide, due to a Gaussian beam traveling at an angle $\theta=0.2$.

and so on. As is easily checked, we thus obtain the matrix operator equation

$$\mathbf{A}=\mathscr{M}\mathbf{C}, \tag{22}$$

where $\mathscr{M}$ is a lower-triangular matrix operator whose entries are themselves the 2×2 matrices M_{jk}, for $j\leqslant k$. This is simply a convenient way of writing the coupled system of Eqs. (12).

The solution of (22) can formally be written

$$\mathbf{C}=\mathscr{M}^{-1}\mathbf{A}. \tag{23}$$

This expresses the discretized forms of the unknown functions ψ^1, ψ^2 in terms of the known incident field, and Eqs. (12)–(19) show how the inversion of $\mathscr{M}$ may be carried out in practice.

The next step is to derive extended governing equations, making use of the *two-way* parabolic form of the Green's function $\mathscr{G}$, given by[9]

$$\mathscr{G}(x,z;x',z')$$
$$=\begin{cases}\dfrac{1}{2}\sqrt{\dfrac{i}{2\pi k}}\sqrt{\dfrac{1}{x-x'}}\exp\left[\dfrac{ik(z-z')^2}{2(x-x')}\right], & x'<x\\ \dfrac{1}{2}\sqrt{\dfrac{i}{2\pi k}}\sqrt{\dfrac{1}{x'-x}}\exp\left[\dfrac{ik(z-z')^2}{2(x'-x)}\right] & \\ \quad\times\exp[2ik(x'-x)], & x\geqslant x.\end{cases}$$

The factor $\exp[2ik(x'-x)]$ arises for $x'\geqslant x$ because we are solving for the reduced wave ψ. Using the new Green's function we can then derive extended forms of Eqs. (4) and (7):

$$\psi(\mathbf{r})=\int_S\left[\mathscr{G}(\mathbf{r};\mathbf{r}')\,\frac{\partial\psi}{\partial z}(\mathbf{r}')-\frac{\partial\mathscr{G}}{\partial z}(\mathbf{r};\mathbf{r}')\,\psi(\mathbf{r}')\right]dx', \tag{24}$$

where again $\mathbf{r}'=[x',S(x')]$, and S is the union of the surfaces h_1 and h_2. Taking the limit as r approaches the surface gives rise as before to coupled integral equations:

$$\psi_{\rm inc}(\mathbf{r}_2)=\int_0^\infty[\mathscr{G}(\mathbf{r}_2;\mathbf{r}_2')\psi^2(x')-\mathscr{G}(\mathbf{r}_2;\mathbf{r}_1')\psi^1(x')]dx',$$
$$\psi_{\rm inc}(\mathbf{r}_1)=\int_0^\infty[\mathscr{G}(\mathbf{r}_1;\mathbf{r}_2')\psi^2(x')-\mathscr{G}(\mathbf{r}_1;\mathbf{r}_1')\psi^1(x')]dx'. \tag{25}$$

The key difference in these equations is that, since $\mathscr{G}$ no longer vanishes for $x'>x$, integration is across the whole surface and therefore allows for left-traveling wave components. These equations may be discretized exactly as before. Omitting the details, this eventually results in a matrix operator equation, analogous to (22):

$$\mathbf{A}=\mathscr{P}\mathbf{C}, \tag{26}$$

with formal solution

$$\mathbf{C}=\mathscr{P}^{-1}\mathbf{A}, \tag{27}$$

where $\mathscr{P}$ is now a full matrix, whose entries are 2×2 matrices, which is simply the sum of $\mathscr{M}$ with an upper-triangular part $\mathscr{Q}$:

$$\mathscr{P}=\mathscr{M}+\mathscr{Q}. \tag{28}$$

It can be shown that, in the regime here in which most energy is scattered to the right, $\mathscr{Q}$ has the effect of a small perturbation. The inverse of $\mathscr{P}$ can thus be expanded in a series about $\mathscr{M}^{-1}$:

$$\mathscr{P}^{-1}=[1-\mathscr{M}^{-1}\mathscr{Q}+(\mathscr{M}^{-1}\mathscr{Q})^2-\cdots]\mathscr{M}^{-1} \tag{29}$$

and solution (27) can be approximated by truncating this and substituting in (27):

$$\mathbf{C}\cong[1-\mathscr{M}^{-1}\mathscr{Q}]\mathscr{M}^{-1}\mathbf{A}. \tag{30}$$

This expresses the solution of the extended system as the forward-going result (27) plus a correction accounting for backscatter via the action of the operator $\mathscr{Q}$. Here $\mathscr{Q}$ simply acts by matrix multiplication, and so (30) requires the inversion only of the same ''lower-triangular'' coupled system represented by $\mathscr{M}$, which has been described earlier.

IV. DISCUSSION

The paper has described the efficient solution for a scalar wave propagating along a rough-sided waveguide, a problem requiring the evaluation of a pair of coupled integral equations. Results have been presented for the purely forward scattered component, and the extension to backscatter of the governing equations and their numerical treatment have been explained.

This approach is computationally convenient and makes possible the numerical investigation of other questions which have not been discussed here, such as field statistics when the surfaces are randomly rough (see Refs. 5 and 11). One such question concerns the mean scattered field $\langle\psi_s\rangle$: It can be shown that the effect of surface roughness upon the mean field is equivalent to the solution for a *flat* waveguide, in which the reflection coefficient of each surface is replaced by an effective one, R_e say, depending on the surface statistics and the depth δ of the waveguide. However, R_e in general is not known, and some studies approximate it by the coefficient for the *isolated* rough surface, as in the rough half-space solution. It can be argued[10] that this holds in the limit of large δ (specifically when $\delta\gg kL^2$, due to the evolution of the wave on propagation across the waveguide). This is clear from Eq. (7); when δ becomes large the cross terms $G(\mathbf{r}_2;\mathbf{r}_1')$, $G(\mathbf{r}_1;\mathbf{r}_2')$ oscillate rapidly, and the two equations approximately decouple. This issue is also discussed by Voronovich[11] in terms of the ''skip distance,'' which depends upon the horizontal wavenumber and is in some sense a more refined estimate. It appears that these two measures in fact reflect separate mechanisms for decorrelation.

The method can be extended in principle to waveguides with penetrable surfaces, where the boundary conditions can no longer be expressed in terms of reflection coefficients independent of frequency. In the related vector wave case, for example in an elastic layer adjoining a fluid half-space, additional mechanisms come into play such as mode conversion ($P-S$, etc.) at the interfaces, and leakage of energy outside the layer. Such complications are less easy to treat with this approach because the angles of scattering due to wave conversion may easily exceed the limits imposed by the parabolic wave equation.

ACKNOWLEDGMENTS

The author holds the Smith Institute Research Fellowship in the Department of Applied Mathematics and Theoretical Physics in the University Cambridge, and is grateful to B. J. Uscinski and D. Berman for numerous discussions related to this work and to the referee for helpful comments.

[1] L. M. Brekhovskikh, *Elastic Waves in Layered Media,* Applied Mathematics and Mechanics, Vol. 16 (Academic, New York, 1980).
[2] T. W. Dawson and J. A. Fawcett, ''A boundary integral equation method for acoustic scattering in a waveguide with nonplanar surfaces,'' J. Acoust. Soc. Am. **87**, 1110–1125 (1990).
[3] A. S. Starkov, ''Normal mode propagation in a waveguide with an irregular section,'' Sov. Phys. Acoust. **36**, 419–423 (1990).
[4] B. J. Uscinski, ''High-frequency propagation in shallow water,'' J. Acoust. Soc. Am. **98**, 2702–2707 (1995).
[5] D. H. Berman, ''The mean acoustic field in layered media with rough interfaces,'' J. Acoust. Soc. Am. **98**, 542–551 (1995).
[6] M. Spivack, ''A numerical approach to rough surface scattering by the parabolic equation method,'' J. Acoust. Soc. Am. **87**, 1999–2004 (1990).
[7] E. Thorsos, ''Rough surface scattering using the parabolic wave equation,'' J. Acoust. Soc. Am. Suppl. 1 **82**, S103 (1987).
[8] M. Spivack, ''Moments and angular spectrum for rough surface scattering at grazing incidence,'' J. Acoust. Soc. Am. **97**, 745–753 (1995).
[9] M. Spivack, ''Backscatter at low grazing angles from rough surfaces,'' J. Acoust. Soc. Am. (submitted).
[10] J. D. Sheard and M. Spivack, ''Wave scattering in a rough elastic layer adjoining a fluid half-space,'' J. Acoust. Soc. Am. **97**, 72–83 (1995).
[11] A. G. Voronovich, *Wave Scattering from Rough Surfaces* (Springer-Verlag, Berlin, 1994).

Elastic wave band gaps and defect states in two-dimensional composites

M. M. Sigalas
Ames Laboratory and Department of Physics and Astronomy, Iowa State University, Ames, Iowa 50011

(Received 10 December 1995; revised 20 July 1996; accepted 15 October 1996)

Using the plane-wave expansion method, we study the propagation of elastic waves through two-dimensional (2-D) periodic composites which exhibit full band gaps for all the polarizations and directions of the displacements. Defect states created inside those band gaps are also studied by disturbing the periodicity of the lattice. Systems exhibiting such kinds of states can be used as acoustical filters. © *1997 Acoustical Society of America.* [S0001-4966(97)06003-7]

PACS numbers: 43.20.Gp, 43.20.Jr, 43.20.Mv [JEG]

INTRODUCTION

In the last few years, there has been considerable interest in the existence of band gaps in the band structure of acoustic (AC) and elastic (EL) waves propagating in periodic composite materials.[1–19] One motivation for these studies is the better understanding of wave localization in inhomogeneous media.[1–19] The attention to the acoustic and elastic waves in connection with gaps or localization is not only due to their possible applications (such as acoustical filters and transducers)[20,21] but to their rich physics as well: EL waves are full vector waves with a different velocity of propagation between the longitudinal and the transverse component. In the EL and AC wave equation there is a term proportional to the mass density variation which may cause the appearance of novel behavior. Furthermore, AC and EL waves in structures exhibiting localized eigenwaves (i.e., mobility gaps) offer themselves for an accurate experimental investigation of open questions regarding the problem of disorder induced localization.

Although the properties of elastic and acoustic waves propagating in layered media (1-D) have been studied for over 30 years,[4,6,8,9] studies of 2-D and 3-D systems started more recently. The study of acoustic and elastic wave propagation in periodic binary composites consisting of spheres embedded in a host (3-D) or from cylinders embedded in a host (2-D), shows that gaps can exist under rather extreme conditions.[5,11,13,15,16] These conditions concern mainly the density and velocity contrast of the components of the composite, the volume fraction of one of the two components, the lattice structure, and the topology;[15,16] they are realized in a Be or Si or SiO_2 matrix with embedded Au or Pb spheres placed periodically in an fcc lattice.[16] More recently,[17] wide band gaps have been found in polymer matrix composites with scatterers of high-density material (such as steel, Ni, Pb, Cu, etc.) forming fcc, bcc, or sc structures. It has been shown that the existence of these wide gaps can be analyzed and predicted by using the single scattering results.[17] For 2-D square lattice, full band gaps have been found only in Au cylinders in a Be host.[11] However, the 2-D hexagonal lattices have proven more favorable for the creation of the gaps; in particular, rods from Mo, Al_2O_3, Fe, and steel embedded in Lucite host exhibit relatively wide gaps.[15] Vasseur *et al.* studied numerically the elastic band structure of 2-D commercially available composite materials such as epoxy reinforced C or glass fibers, and they found several extremely large complete band gaps in those systems.[22] Langlet *et al.* used the finite element method to study the propagation of acoustic waves in passive periodic materials.[23] From the experimental point of view, Kinra and Ker have measured the phase velocity of longitudinal waves through 3-D periodic polymer matrix composites as a function of frequency.[3] More recently, Martinez-Sala *et al.* measured the attenuation of sound in a minimalistic sculpture consisting of steel cylinders in air and they found a full band gap.[24]

In the present paper, we study 2-D periodic composites consisting of cylinders embedded in a different matrix material (Sec. II). Using a supercell, we then study defects states appearing inside the band gaps (Sec. III). These states are created by changing the radius of one cylinder in the supercell. Possible applications of those systems as acoustical filters are also discussed.

I. THEORY

For a locally isotropic medium, the elastic wave equation is[25]

$$\frac{\partial^2 u^i}{\partial t^2}=\frac{1}{\rho}\left\{\frac{\partial}{\partial x_i}\left(\lambda\frac{\partial u^l}{\partial x_l}\right)+\frac{\partial}{\partial x_l}\left[\mu\left(\frac{\partial u^i}{\partial x_l}+\frac{\partial u^l}{\partial x_i}\right)\right]\right\}, \tag{1}$$

where u^i is the ith component of the displacement vector $\mathbf{u}(\mathbf{r})$, $\lambda(\mathbf{r})$, and $\mu(\mathbf{r})$ are the Lamé coefficients, and $\rho(\mathbf{r})$ is the density.

For the case of 2-D structures consisting of infinite cylinders parallel to the z axis (in that case ρ, λ, μ are independent of the z coordinate) and for wave propagation in the x,y plane [this means that $\mathbf{u}(\mathbf{r})=\mathbf{u}(x,y)$], Eq. (1) splits into two independent wave equations.[11,12] The first one, which is a scalar equation, describes the displacement along the z axis:

$$-\omega^2 u^z=\frac{1}{\rho}\,\boldsymbol{\nabla}(\mu\boldsymbol{\nabla}u^z). \tag{2}$$

The second set of equations, in which a mixing of longitudinal and transverse modes occurs, describes the displacement vectors in the x,y plane and they have the same form as Eq. (1), but with $i,l=x,y$.[11,12]

The coefficients $\lambda(\mathbf{r})$, $\mu(\mathbf{r})$ and $\rho(\mathbf{r})$ are periodic functions of $\mathbf{r}$:

$$f(\mathbf{r}+\mathbf{R})=f(\mathbf{r}) \tag{3}$$

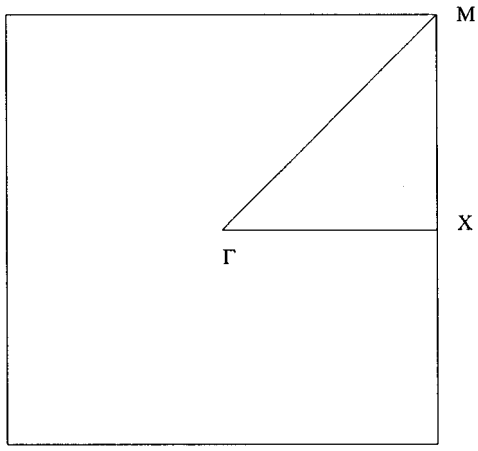

FIG. 1. The first Brillouin zone for a 2-D square lattice.

for all vectors $\mathbf{R}=n_1\mathbf{a}_1+n_2\mathbf{a}_2$, where n_1 and n_2 are integers, $\mathbf{a}_1=(a,0,0)$ and $\mathbf{a}_2=(0,a,0)$ are the unit vectors and a is the lattice constant of a 2-D square lattice. $f(\mathbf{r})$ stands for $\lambda(\mathbf{r})$, $\mu(\mathbf{r})$, and $1/\rho(\mathbf{r})$. Because of its periodicity $f(\mathbf{r})$ can be expanded in a 2-D Fourier series:[26]

$$f(\mathbf{r})=\sum_{\mathbf{G}} f_{\mathbf{G}}e^{\mathbf{Gr}}, \tag{4}$$

where the summation extends over all the reciprocal vectors **G** defined by the relation

$$\mathbf{G}=m_1\mathbf{b}_1+m_2\mathbf{b}_2, \tag{5}$$

with m_1, m_2 integers and $\mathbf{b}_1=(2\pi/a)(1,0,0)$, $\mathbf{b}_2=(2\pi/a)(0,1,0)$.

As a result of the common periodicity of all the coefficients in Eq. (1), its eigensolutions, according to the Floquet–Bloch theorem,[26] can be chosen so as to satisfy the relation

$$\mathbf{u}(\mathbf{r})=e^{i\mathbf{kr}}\mathbf{u}_{\mathbf{k}}(\mathbf{r}), \tag{6}$$

where **k** is restricted within the first Brillouin zone (BZ) (see Fig. 1) and $\mathbf{u}_{\mathbf{k}}(\mathbf{r})$ is a periodic function of **r** like the $1/\rho$, λ, μ. Consequently, $\mathbf{u}_{\mathbf{k}}(\mathbf{r})$ can be expanded in Fourier series according to Eq. (4). Thus we have

$$\mathbf{u}(\mathbf{r})=\sum_{\mathbf{G}} \mathbf{u}_{\mathbf{k}+\mathbf{G}}e^{i(\mathbf{k}+\mathbf{G})\mathbf{r}}. \tag{7}$$

Substituting (4) and (7) in (1) we obtain

$$\begin{aligned}\omega^2 u^i_{\mathbf{k}+\mathbf{G}}=\sum_{\mathbf{G}'}\Bigg\{&\sum_{l,\mathbf{G}''}\rho^{-1}_{\mathbf{G}-\mathbf{G}''}[\lambda_{\mathbf{G}''-\mathbf{G}'}(\mathbf{k}+\mathbf{G}')_l(\mathbf{k}+\mathbf{G}'')_i\\ &+\mu_{\mathbf{G}''-\mathbf{G}'}(\mathbf{k}+\mathbf{G}')_i(\mathbf{k}+\mathbf{G}'')_l]u^l_{\mathbf{k}+\mathbf{G}'}\\ &+\sum_{\mathbf{G}''}\Bigg[\rho^{-1}_{\mathbf{G}-\mathbf{G}''}\mu_{\mathbf{G}''-\mathbf{G}'}\sum_j(\mathbf{k}+\mathbf{G}')_j(\mathbf{k}\\ &+\mathbf{G}'')_j\Bigg]u^i_{\mathbf{k}+\mathbf{G}'}\Bigg\},\end{aligned} \tag{8}$$

while Eq. (2) becomes

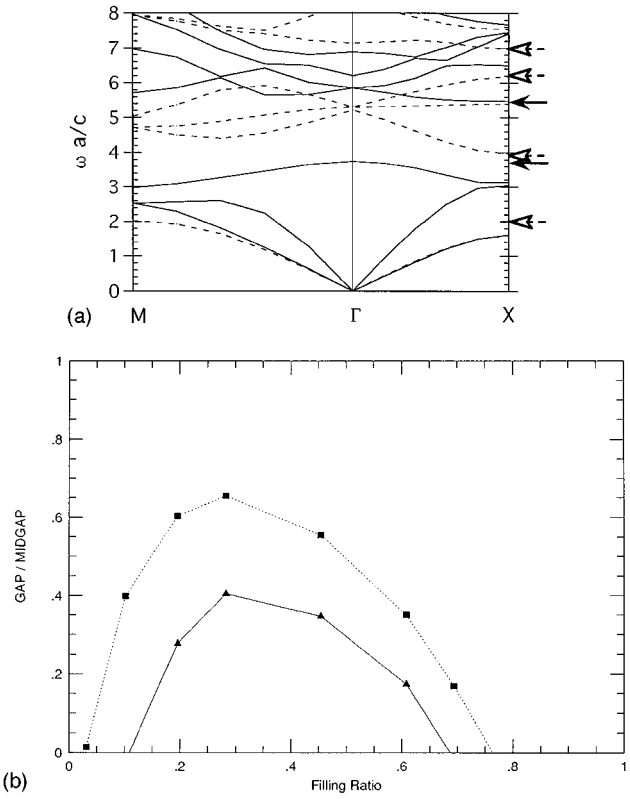

FIG. 2. (a) Elastic wave band structure for a 2-D square periodic composite consisting of Pb cylinders in epoxy matrix. The filling ratio of the cylinders is 0.283; ω is the frequency, a is the lattice constant, and c is the transverse wave velocity in the epoxy (c_{to}). Solid and open arrows indicate the edges of the full band gaps for waves described by Eqs. (1) and (2), respectively. (b) Gap over midgap frequency versus the filling ratio of the cylinders for the same system. In both panels, solid and dotted lines correspond to waves described by Eqs. (1) and (2), respectively.

$$\omega^2 u^z_{\mathbf{k}+\mathbf{G}}=\sum_{\mathbf{G}',\mathbf{G}''}\rho^{-1}_{\mathbf{G}-\mathbf{G}''}\lambda_{\mathbf{G}''-\mathbf{G}'}(\mathbf{k}+\mathbf{G}')(\mathbf{k}+\mathbf{G}'')u^z_{\mathbf{k}+\mathbf{G}'}. \tag{9}$$

Keeping N reciprocal vectors, **G**, in the previous sum and substituting in Eqs. (1) and (2), we get $2N\times 2N$ and $N\times N$ matrix eigenvalue equations, respectively. The number N is increased until the desired convergence is achieved. For a given **k** in the first BZ an infinite number of eigensolutions are obtained, each characterized by a natural number n (besides **k**). The corresponding eigenfrequency is $\omega_{\mathbf{k}n}$. Usually one plots the $\omega_{\mathbf{k}n}$ vs **k** for $n=1,2,3,...$, as the tip of **k** is varied along straight segments in the first BZ. A spectral gap (or stop band) corresponds to a region in the ω axis to which no $\omega_{\mathbf{k}n}$ (for any **k** and n) belongs.

II. PERIODIC STRUCTURES

Figure 2(a) shows the band structure of EL waves propagating through a 2-D square lattice consisting of Pb cylinders embedded into an epoxy matrix; the filling ratio of the cylinders is 0.283. For the z component of **u** [Eq. (2); see dotted lines in Fig. 2(a)], there is a wide gap between the first and the second band with gap over midgap ratio, $\Delta\omega/\omega_g=0.64$; there is also a smaller gap between the fourth and fifth bands with $\Delta\omega/\omega_g=0.12$. For the x and y components of **u** [Eq. (1);

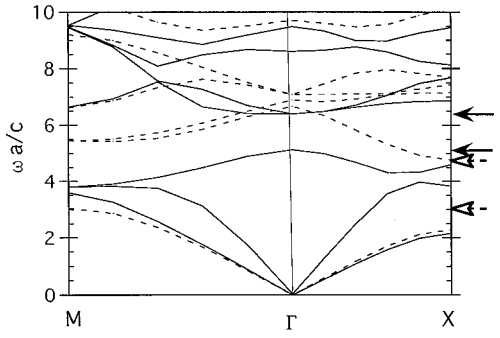

FIG. 3. Elastic wave band structure for a 2-D square periodic composite consisting of epoxy cylinders in the Pb matrix. The filling ratio of the cylinders is 0.739; ω is the frequency, a is the lattice constant, and c the transverse wave velocity in the Pb (c_{to}). Solid and open arrows indicate the edges of the full band gaps for waves described by Eqs. (1) and (2), respectively.

see solid lines in Fig. 2(a)], there is only one gap between the third and fourth bands with $\Delta\omega/\omega_g=0.37$. A complete band gap for all the displacements and k directions exists in that particular case with $\Delta\omega/\omega_g=0.06$.

The case shown in Fig. 2(a) has actually the wider gaps we can get for this particular system. As it is shown in Fig. 2(b), $\Delta\omega/\omega_g$ has its maximum value for filling ratios at around 0.3. The gap of the u^z displacements is always bigger and appears in a wider range of filling ratios than the gap of the u^x and u^y displacements.

For a system consisting of epoxy cylinders in the Pb matrix, there are no complete band gaps for all the displacements and the directions. However, there are band gaps for each one of Eqs. (1) and (2). In particular, for a system with filling ratio of the epoxy cylinders $f=0.739$ (Fig. 3), there is a gap for the u^z displacements between the first and second bands (dotted lines in Fig. 3) with $\Delta\omega/\omega_g=0.44$, while the gap for the u^x and u^y displacements is between the third and fourth bands (solid lines in Fig. 3) with $\Delta\omega/\omega_g=0.22$.

By using steel cylinders in epoxy matrix, even wider band gaps can be created. For cylinders with filling ratio 0.4 (which is its optimum value), there are actually two complete band gaps (for all the displacements and directions) with $\Delta\omega/\omega_g=0.44$ and 0.33 for the first and second band gaps. In general, plastics as matrix material and high density scatterers favor the appearance of band gaps.[17,22]

III. DEFECT STATES

In the following, we study defects in 2-D periodic square structures. We use a supercell consisting of M by M unit cells with one cylinder of radius r in each unit cell. A defect is created by changing the radius, r_d, of one of the cylinders. We concentrate in systems constructed from Pb and epoxy because we can achieve good convergence with small values of N. In particular, using just $N=100$ plane waves, we have a convergence better than 5%. Note that the computer time depends on $(M^2N)^3$. We expect qualitatively similar results for any other combinations of materials such as steel and epoxy.

Figure 4 shows the results of a supercell calculation for Pb rods with filling ratio $f=0.283$ and $M=3$. For $r_d<r$, there is a nondegenerate defect band emerging from the lower edge of the gap and moving toward the upper edge of the gap as r_d decreases. In the case where one of the cylin-

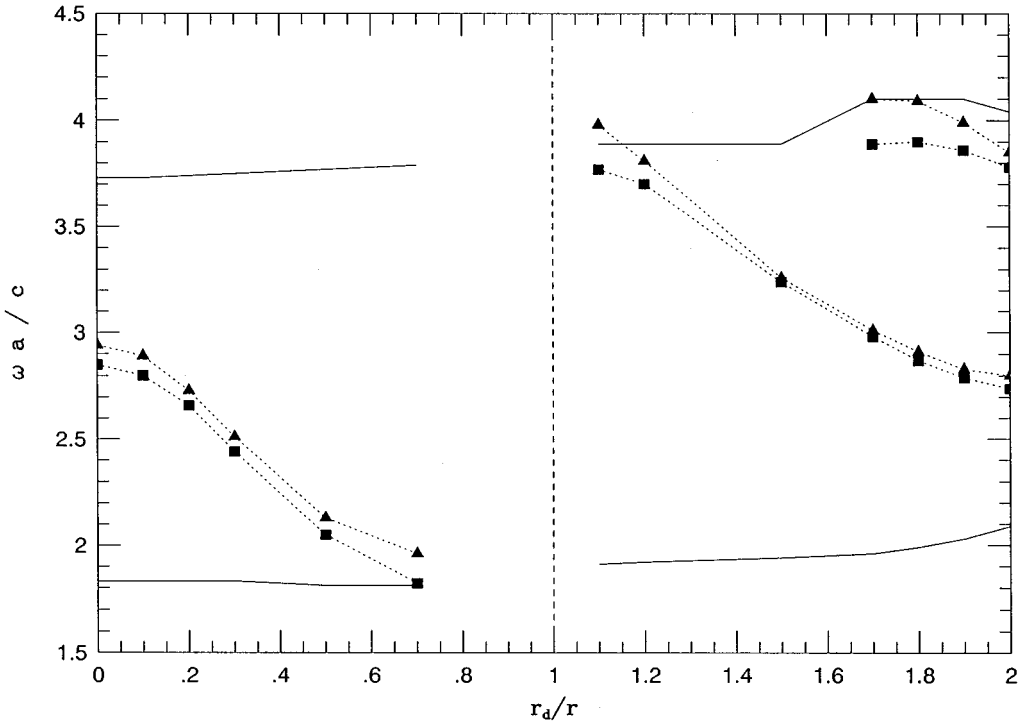

FIG. 4. The frequencies of the defect modes as a function of the defect radius, r_d, for a supercell with $M=3$ and a 2-D composite similar to the one described in Fig. 2(a). The waves described by Eq. (2). Squares (triangles) show the lower (upper) edge of the particular defect band. Solid lines show the edges of the band gap.

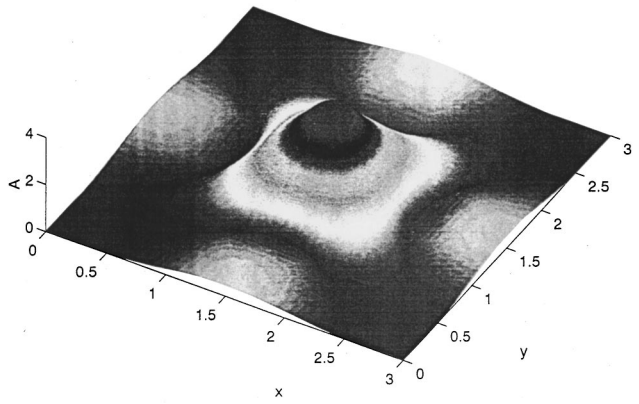

FIG. 5. The amplitude A of the u_z at Γ point for a defect state shown in Fig. 4 with $r_d/r=0.3$.

ders is completely removed ($r_d=0$), the defect band is centered a little above the midgap frequency at around $\omega a/c=2.9$.

We also studied how the results depend on M. The results indicate that although the midband frequency ω_d of the defect band remains the same, the width of the defect band, $\Delta\omega_d$, depends strongly on the size of the supercell. In particular, for $r_d=0.5$, the width of the defect band is $\Delta\omega_d a/c=0.08$ and 0.03 and the midband frequency is $\omega_d a/c=2.09$ and 2.14 for $M=3$ and 4, respectively. The wavefunction which corresponds to that defect state is well-localized around the defect. However, there is an overlap between the wavefunctions localized at neighboring defects. This actually causes the widening of the defect band. The closer the defects, the wider is the width of the defect band. For the same reason, the defect band emerges earlier inside the gap as M increases. Since the system is 2-D, one expects that a defect is created with the smallest amount of disorder. The reason we do not see that in the present case is due to the finite size of the supercell.

For $r_d>r$ (Fig. 4), a double degenerate defect band emerges from the upper edge of the gap moving towards the lower edge as r_d increases. For $r_d/r>1.7$, a second double degenerate defect band appears from the upper edge of the gap.

We can figure out how well localized is a particular defect state by studying its wavefunction. Figure 5 shows the z component of the displacement vector at Γ point for a case shown in Fig. 4 with $r_d/r=0.3$. A supercell with $M=3$ has been used. The wave is basically localized around the defect which is located at the middle of the supercell. The maximum amplitude of u^z at (3/2, 3/2) (the center of the supercell) is 7.5 and 110 times higher than its amplitude at (3/2, 0) and (0,0), respectively.

The situation is more complicated for a system consisting of epoxy cylinders with $f=0.75$ embedded in the Pb matrix (Fig. 6). In that case, defect bands emerge from both the lower and the upper edges of the gap as r_d decreases. In particular, a nondegenerate defect band emerges from the lower edge of the gap; its midband frequency is almost constant ($\omega a/c=3.1$) for $r_d/r<0.5$. A single and a double degenerate defect state emerges from the upper edge of the gap. While the nondegenerate state is moving rapidly toward the midgap frequency ($\omega a/c=4$), the double degenerate state remains close to the upper edge of the gap and actually moves toward the upper edge for small values of r_d. The defect

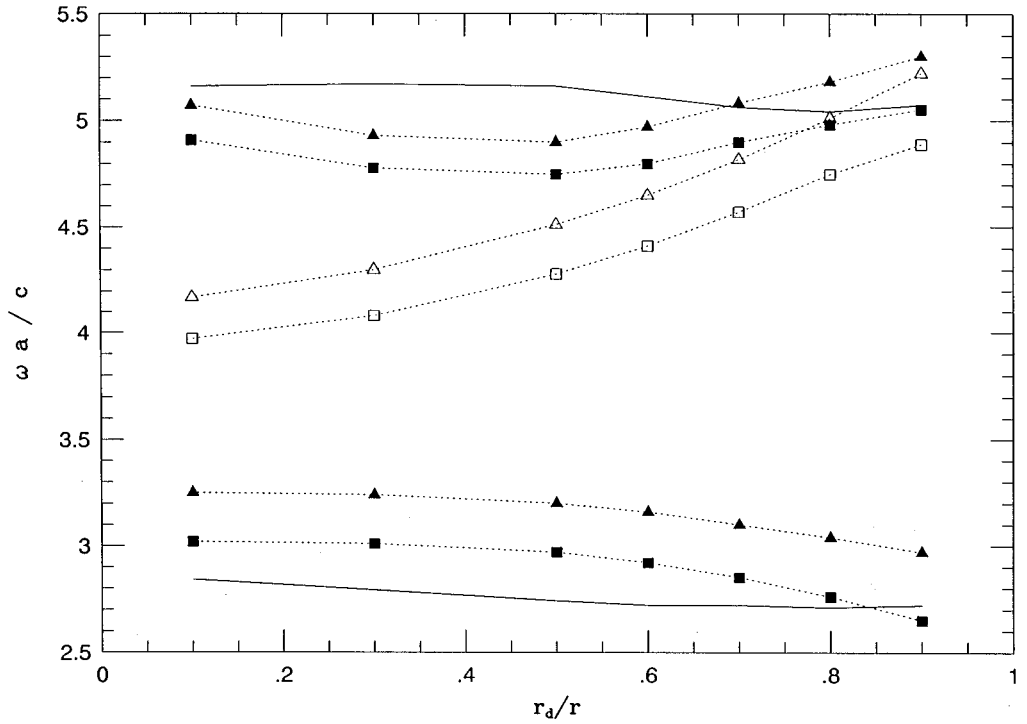

FIG. 6. The frequencies of the defect modes as a function of the defect radius, r_d, for a supercell with $M=3$ and a 2-D composite similar to the one described in Fig. 3. The waves described by Eq. (2). Squares (triangles) show the lower (upper) edge of the particular defect band. Solid lines show the edges of the band gap.

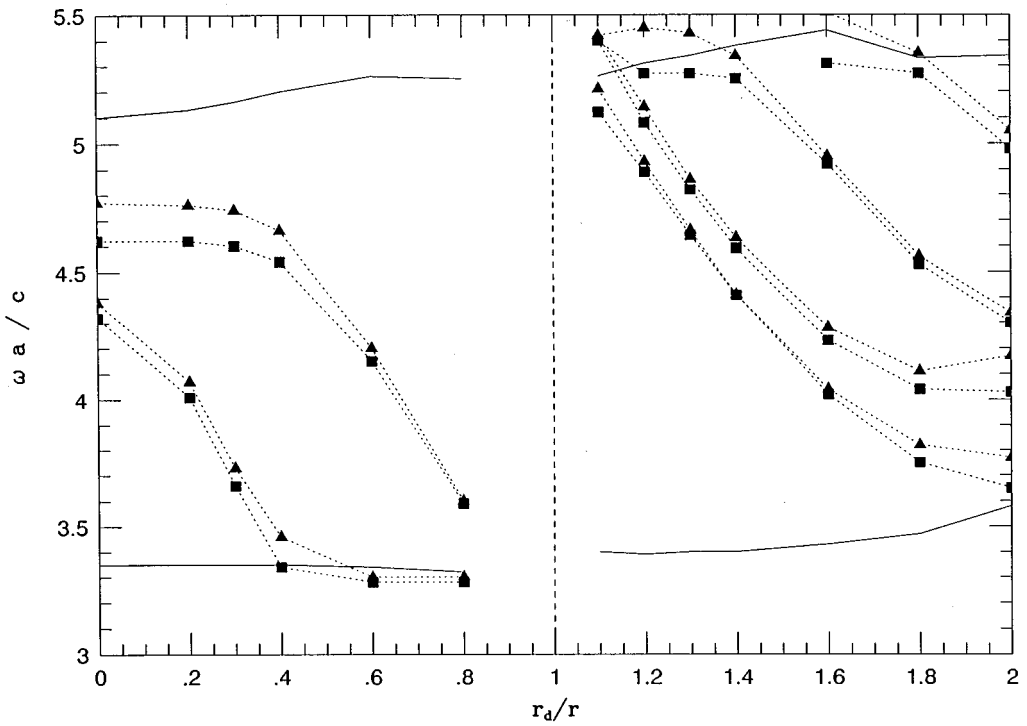

FIG. 7. The frequencies of the defect modes as a function of the defect radius, r_d, for a supercell with $M=3$ and a 2-D composite similar to the one described in Fig. 2(a). The waves described by Eq. (1). Squares (triangles) show the lower (upper) edge of the particular defect band. Solid lines show the edges of the band gap.

bands in that case are wider than the cases in Fig. 4, indicating that the defect states are not as well localized as in the cases studied in Fig. 4.

Although Eqs. (1) and (2) are quite different, the general trends of the defect states are similar for both equations. In particular, Fig. 7 shows the behavior of the defect states for a system consisting of Pb cylinders with $f=0.26$ in epoxy matrix (identical to the systems studied in Fig. 4) and for the u^x and u^y displacements [Eq. (1)]. Similarly, with the scalar waves described by Eq. (2), defect states emerge from the lower (upper) edge of the gap as the defect radius, r_d, decreases (increases). However, there are considerable differences regarding the number of the defect states appearing inside the gap. There are single and double degenerate defect bands emerging from the lower edge of the gap for $r_d/r<1$, while there are two single and two double degenerate defect bands emerging from the upper edge of the gap for $r_d/r>1$.

The amplitude of u^x is shown in Fig. 8. The defect radius is $r_d/r=0.8$. The amplitude of u^y can be found by interchanging the x and y axes in Fig. 8. The ratio of the amplitude at (3/2, 7/4) and (0, 7/4) points is 4.7. Comparing the amplitudes in Figs. 5 and 8, we conclude that the wave is more well localized in the case of Fig. 5. Note that the defect state shown in Fig. 8 appears at around $\omega a/c=3.6$. So, it is inside the complete band gap (for all the polarizations and directions). Systems exhibiting such kinds of defect states can be used as narrow bandpass acoustical filters.

Previous studies of lattice vibrations in crystals containing ''isotope'' impurities[27] show that a lighter impurity mass tends to split off a discrete eigenfrequency above the upper bound of the continuum. On the other hand, a heavier impurity mass creates a discrete level below the optical branch. This behavior is quite similar with the behavior of the defect states in systems containing Pb cylinders in epoxy matrix. As we pointed earlier, for both Eqs. (1) and (2), defects emerge from the lower (upper) edge of the gap as the defect radius, r_d, decreases (increases). By decreasing (increasing) r_d, the average density (which is equivalent to the mass in the lattice model) decreases (increases). Similar behavior has been also observed in periodic dielectric materials.[28,29] By removing (adding) dielectric material from those structures defect states split off from the lower (upper) edge of the gap. However, in the case of epoxy cylinders in the Pb matrix (Fig. 6), there are defect states emerging from both the upper and lower edges. Note that in the lattice model and the periodic dielectric materials, there is only one parameter which varies (the mass or the dielectric constant). In the present cases

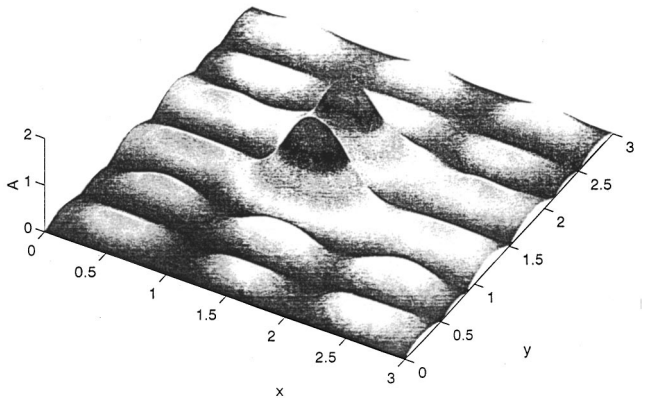

FIG. 8. The amplitude, A, of the u_x at Γ point for a defect state shown in Fig. 7 with $r_d/r=0.8$.

though, there are more than one parameter, the density and the Lame coefficients. This is probably the reason we find that different behavior.

IV. CONCLUSIONS

Supercell calculations performed using the plane-wave method have been used to study defect modes of elastic waves in 2-D composites. The composites are arrays of cylinders placed in an infinite elastic background. Defects are created by changing the radius, r_d, of one cylinder in supercell.

For 2-D cases, elastic waves can be described by two independent wave equations; a scalar equation [Eq. (2)] involving the u^z deformations and a vector wave equation [Eq. (1)] involving the u^x and u^y deformations. For Pb cylinders in an epoxy matrix and for both Eqs. (1) and (2), defect modes emerge from the lower (upper) edge of the gap as r_d decreases (increases). Qualitatively similar trends have been found in models of lattice vibrations in crystals with mass impurities and in periodic dielectric materials with defects. However, for epoxy cylinders in the Pb matrix, there are defect modes emerging from both the upper and lower edges of the gap as r_d decreases. As in the case of periodic dielectric structures,[28–30] systems having such kind of defect modes can be used as high-Q narrow bandpass acoustical filters.

ACKNOWLEDGMENT

Ames Laboratory is operated by the U.S. Department of Energy by Iowa State University under Contract No. W-7405-Eng-82.

[1] P. Sheng, Ed., *Scattering and Localization of Classical Waves in Random Media* (World Scientific, Singapore, 1990).
[2] See the proceedings of the NATO ARW, *Photonic Band Gaps and Localization*, edited by C. M. Soukoulis (Plenum, New York, 1993).
[3] V. K. Kinra and E. L. Ker, Int. J. Solids Structures **19**, 393 (1983).
[4] W. M. Ewing, W. S. Jardetsky, and F. Press, *Elastic Waves in Layered Media* (McGraw-Hill, New York, 1967).
[5] M. M. Sigalas and E. N. Economou, J. Sound Vib. **158**, 377 (1992).
[6] J. P. Dowling, J. Acoust. Soc. Am. **91**, 2539 (1992).
[7] L. Ye, G. Cody, M. Zhou, P. Sheng, and A. N. Norris, Phys. Rev. Lett. **69**, 3080 (1992).
[8] M. M. Sigalas and C. M. Soukoulis, Phys. Rev. B **51**, 2780 (1995).
[9] R. James, S. M. Woodley, C. M. Dyer, and V. F. Humphrey, J. Acoust. Soc. Am. **97**, 2041 (1995).
[10] M. S. Kushwaha, P. Halevi, L. Dobrzynski, and B. Djafari-Rouhani, Phys. Rev. Lett. **71**, 2022 (1993).
[11] M. M. Sigalas and E. N. Economou, Solid State Commun. **86**, 141 (1993).
[12] M. M. Sigalas and E. N. Economou, J. Appl. Phys. **75**, 2845 (1994).
[13] E. N. Economou and M. M. Sigalas, in *Photonic Band Gaps and Localization*, edited by C. M. Soukoulis (Plenum, New York, 1993), pp. 317–338.
[14] E. N. Economou and M. M. Sigalas, Phys. Rev. B **48**, 13 434 (1993).
[15] M. M. Sigalas, E. N. Economou, and M. Kafesaki, Phys. Rev. B **50**, 3393 (1994).
[16] E. N. Economou and M. M. Sigalas, J. Acoust. Soc. Am. **95**, 1734 (1994).
[17] M. Kafesaki, M. M. Sigalas, and E. N. Economou, Solid State Commun. **96**, 285 (1995).
[18] M. S. Kushwaha and P. Halevi, Appl. Phys. Lett. **64**, 1085 (1994).
[19] M. S. Kushwaha, P. Halevi, G. Martinez, L. Dobrzynski, and B. Djafari-Rouhani, Phys. Rev. B **49**, 2313 (1994).
[20] W. A. Smith and B. A. Auld, IEEE Trans. Ultrason. Ferroelectr. Freq. Control **38**, 40 (1991).
[21] B. A. Auld, Y. A. Shui, and Y. Wang, J. Phys. (France) Colloq. **45**, (1984).
[22] J. O. Vasseur, B. Djafari-Rohani, L. Dobrzynski, M. S. Kushwaha, and P. Halevi, J. Phys., Condens. Matter. **6**, 8759 (1994).
[23] P. Langlet, A.-C. Hladky-Hennion, and J.-N. Decarpigny, J. Acoust. Soc. Am. **98**, 2792 (1995).
[24] R. Martinez-Sala, J. Sancho, J. V. Sanchez, V. Gomez, J. Llinares, and F. Meseguer, Nature (London) **378**, 241 (1995).
[25] L. D. Landau and E. M. Lifshitz, *Theory of Elasticity* (Pergamon, London, 1959).
[26] C. Kittel, *Introduction to Solid State Physics* (Wiley, New York, 1986).
[27] E. N. Economou, *Green's Functions in Quantum Physics* (Springer-Verlag, Berlin, 1979).
[28] E. Yablonovitch, T. J. Gmitter, R. D. Meade, A. M. Rappe, K. D. Brommer, and J. D. Joannopoulos, Phys. Rev. Lett. **67**, 3380 (1991).
[29] R. D. Meade, K. D. Brommer, A. M. Rappe, and J. D. Joannopoulos, Phys. Rev. B **44**, 13772 (1991).
[30] E. Ozbay, G. Tuttle, M. Sigalas, C. M. Soukoulis, and K. M. Ho, Phys. Rev. B **51**, 13961 (1995).

A statistical analysis for an inverse acoustic problem in estimating spatially varying sound velocity

Cheng-Hung Huang and Duen-Min Wang
Department of Naval Architecture and Marine Engineering, National Cheng Kung University, Tainan, Taiwan, Republic of China

(Received 31 July 1996; revised 10 October 1996; accepted 15 October 1996)

A simple inverse acoustic algorithm using the Levenberg–Marquardt method is developed to estimate the sound velocity field as a function of depth from the transient measurements of the wave displacement at some suitable locations. The inverse calculations are performed based on the simulated exact and inexact measurement data to show the validity of the present study. Moreover, statistical analysis will also be considered here to determine both the best measurement position and the 99% confidence bounds. Results show that the accuracy of the estimated sound velocity and its sensitivity to the measurement errors depend on the number of measurement data, as well as the measured positions. The reliable inverse solutions can be obtained only when these two factors are chosen properly. © *1997 Acoustical Society of America.* [S0001-4966(97)05903-1]

PACS numbers: 43.20.Hq, 43.20.Ye, 43.20.Px [JEG]

LIST OF SYMBOLS

C	sound velocity vector
$E(\cdot)$	expected value
f	boundary intensity
g	source intensity
J	Jacobian matrix
u	estimated wave displacement vector
Y	measured wave displacement vector

Greek letters

δ	Dirac delta function
Ω	sum of least square norm
ρ	density
μ	damping coefficient
ω	random number
σ	standard deviation

INTRODUCTION

The direct acoustic wave problem involves the determination of the wave field within the specified domain when the initial condition, boundary condition, water density, and sound speed are given. On the other hand, in the present study the inverse problem is concerned with the determination of sound velocity as a function of depth from the knowledge of transient wave displacement measurements taken within the domain.

Various methods of solving inverse acoustic problems regarding the estimation of sound velocity have been discussed in the literature.[1–4] However, most of the above references are very mathematically involved, and none of them discusses the inverse solutions from the viewpoint of statistics analysis, and this may be one of the most important items in inverse problems.

The present work addresses the development of a simple but efficient method, the Levenberg–Marquardt algorithm,[5] for estimating sound speed as well as performing the statistical analysis. This method combines the Newton's and steepest-descent methods and has the advantage of fast convergence. It has proven to be a powerful algorithm in various types of inverse calculations.[6–9] In order to include the effects, such as measurement errors, the number of measurement data, and the measured positions, to the inverse solutions, a statistical analysis is performed to derive the standard deviation of the unknown sound velocity; thus, 99% confidence bounds for the estimated sound velocity can be determined.

I. THE DIRECT PROBLEM

We consider a one-dimensional acoustic wave equation where the density ρ is assumed to be a constant and the sound velocity $C(z)$ is a function of depth. Initially, the wave displacement and velocity are equal to zero; when time $t>0$, the boundaries at $z=0$ and $z=L$ are subjected to a boundary impulse function at $t=t_j$ with intensity f and complete reflect boundary conditions, respectively. Moreover, there also exists an instantaneous point source at $z=z_g$ and $t=t_i$ with intensity g inside the domain.

The mathematical formulation of this problem is given as

$$\frac{\partial^2 u}{\partial t^2}=C^2(z)\,\frac{\partial^2 u}{\partial z^2}+\rho g\,\delta(z-z_g)\,\delta(t-t_i)$$

$$\text{in } 0<z<L,\quad t>0, \tag{1a}$$

$$u_z(0,t)=f\,\delta(t-t_j)/\lambda(0),\quad \text{at } z=0,\quad t>0, \tag{1b}$$

$$u_z(L,t)=0\quad \text{at } z=L,\quad t>0, \tag{1c}$$

$$u(z,0)=0\quad \text{for } t=0,\quad 0\leqslant z\leqslant L, \tag{1d}$$

$$u_t(z,0)=0\quad \text{for } t=0,\quad 0\leqslant z\leqslant L, \tag{1e}$$

 0001-4966/97/101(3)/1262/7/$10.00

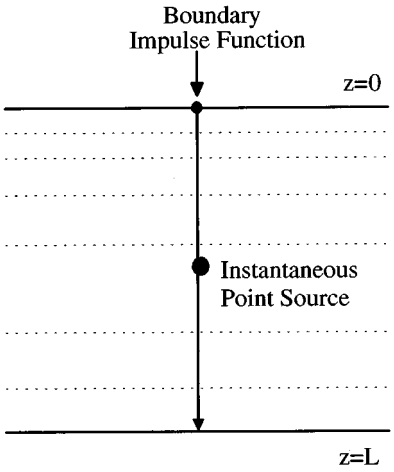

FIG. 1. Geometry and coordinates.

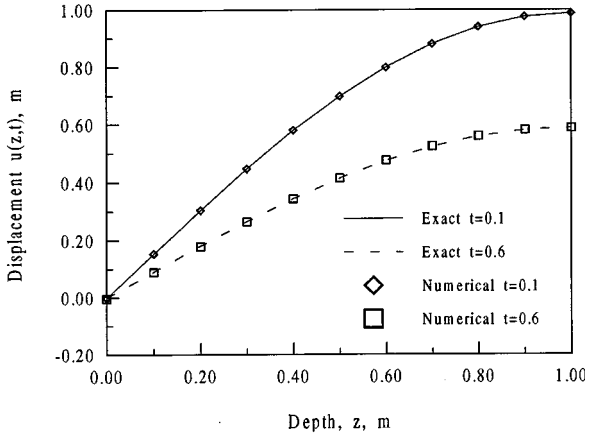

FIG. 2. The comparison of analytical and WAM solutions.

where $\lambda(0)=C^2(0)\rho(0)$. Figure 1 shows the geometry and coordinates.

The direct problem considered here is concerned with the determination of the wave displacement $u(z,t)$ when the density ρ, sound speed $C(z)$, and the boundary and initial conditions are known.

The weighted average method (WAM)[10] is adopted here due to its simplicity to solve this one-dimensional acoustic problem. In order to show the accuracy of WAM in solving the direct problem (1), the following demonstrated problem is first solved numerically:

$$\frac{\partial^2 u}{\partial z^2}=\frac{\partial^2 u}{\partial t^2} \quad 0<z<1, \quad t>0, \tag{2a}$$

$$u_z(0,t)=\frac{\pi}{2}\cos\frac{\pi}{2}t \quad \text{at } z=0, \quad t>0, \tag{2b}$$

$$u(1,t)=\cos\frac{\pi}{2}t \quad \text{at } z=1, \quad t>0, \tag{2c}$$

$$u(z,0)=\sin\frac{\pi}{2}z \quad \text{for } t=0, \quad 0\leqslant z\leqslant 1, \tag{2d}$$

$$u_t(z,0)=0 \quad \text{for } t=0, \quad 0\leqslant z\leqslant 1; \tag{2e}$$

and its analytical solution can be shown as

$$u(z,t)=\cos\frac{\pi}{2}t\,\sin\frac{\pi}{2}z. \tag{3}$$

The numerical results are then compared with the analytical solutions obtained from Eq. (3) and shown in Fig. 2. The accuracy of using WAM in the present test case is thus proved. This result provides us greater confidence in using WAM to solve the direct problem equation (1).

II. THE INVERSE PROBLEM

For the inverse problem, the sound velocity $C(z)$ is regarded as being unknown, but everything else in Eq. (1) is known. In addition, the wave displacement readings taken at some appropriate locations are considered available.

We assumed that M sensors are used to record the displacement information $Y(z_m,t_n)=Y_{mn}$, where $m=1$ to M and $n=1$ to N, to identify $C(z)$ in the inverse calculations over the time period t_N; also, during this t_N, N measurement data can be obtained by each sensor.

Solution of the problem (1) with sound velocity $C(z)$ unknown can be recast as a problem of optimum control, i.e., choose the control parameters $C(z)=C_k$, which minimize the following sum of the least-squares norm Ω:

$$\Omega(C_k)=\sum_{n=1}^{N}\sum_{m=1}^{M}[Y_{mn}-u_{mn}(C_k)]^2, \quad k=1 \text{ to } K,$$
$$=G^TG, \tag{4}$$

where

N = the number of measured data;
M = the number of sensors;
K = the number of discreted grid points in the z direction (or the number of unknown parameters);
$\mathbf{C}=C_k$
$=\{C_1,C_2,C_3,\ldots,C_K\}$
$=\{C_{z=z_1},C_{z=z_2},C_{z=z_3},\ldots,C_{z=z_K}\}$;
= the estimated sound velocity vector;
$\mathbf{Y}=Y_{mn}$
$=\{Y_{11},Y_{12},\ldots,Y_{1N},Y_{21},\ldots,Y_{2N},\ldots,Y_{MN}\}$
$=\{Y_{z=z_1,t=t_1},Y_{z=z_1,t=t_2},\ldots,Y_{z=z_1,t=t_N},$
$Y_{z=z_2,t=t_1},\ldots,Y_{z=z_2,t=t_N},\ldots,Y_{z=z_M,t=t_N}\}$
= the measured displacement vector;
$\mathbf{u}=u_{mn}$
$=\{u_{11},u_{12},\ldots,u_{1N},u_{21},\ldots,u_{2N},\ldots,u_{MN}\}$
$=\{u_{z=z_1,t=t_1},u_{z=z_1,t=t_2},\ldots u_{z=z_1,t=t_N},u_{z=z_2,t=t_1},$
$\ldots,u_{z=z_2,t=t_N},\ldots,u_{z=z_M,t=t_N}\}$
= the calculated (or estimated) displacement vector using the estimated sound velocity $\mathbf{C}$;

and

$$\mathbf{G}=\mathbf{Y}-\mathbf{u}.$$

Equation (4) is minimized with respect to the estimated parameters to obtain

$$\sum_{n=1}^{N}\sum_{m=1}^{M}\left[\frac{\partial u_{mn}}{\partial C_k}\right][Y_{mn}-u_{mn}]=0; \quad k=1 \text{ to } K. \tag{5}$$

Equation (5) is linearized by expanding $u_{mn}(c_k)$ in the Taylor series and retaining the first-order terms. Then, a damping parameter μ is added to the resulting expression to improve convergence, leading to the Levenberg–Marquardt method[5] given by

$$(\mathbf{F}+\mu\mathbf{I})\Delta\mathbf{C}=\mathbf{D}, \tag{6a}$$

where

$$\mathbf{F}=\mathbf{J}^T\mathbf{J}, \tag{6b}$$

$$\mathbf{D}=\mathbf{J}^T\mathbf{G}, \tag{6c}$$

$$\Delta\mathbf{C}=\mathbf{C}^{p+1}-\mathbf{C}^p. \tag{6d}$$

Here, the superscript p and T represent the iteration index and transport matrix, respectively, $\mathbf{I}$ is the identity matrix, and $\mathbf{J}$ denotes the Jacobian matrix defined as

$$\mathbf{J}\equiv\frac{\partial\mathbf{u}}{\partial\mathbf{C}^T}. \tag{7}$$

The Jacobian matrix defined by Eq. (7) is determined by perturbing the unknown parameters C_k one at a time and computing the resulting change in displacement from the solution of the direct problem, Eq. (1).

Equation (6a) is now written in a form suitable for iterative calculation as

$$\mathbf{C}^{p+1}=\mathbf{C}^p+(\mathbf{J}^T\mathbf{J}+\mu\mathbf{I})^{-1}\mathbf{J}^T(\mathbf{Y}-\mathbf{u}). \tag{8}$$

When $\mu=0$, Newton's method is obtained; as $\mu\to\infty$, the steepest-descent method is obtained. For fast convergence the steepest-descent method is applied first, then the value of μ is decreased. Finally, Newton's method is used to obtain the inverse solution. The algorithm of choosing this damping value μ is described in detailed in Ref. 5, so they are not repeated here.

Some suitable initial guesses of the sound velocity distribution are necessary in the present algorithm. Here, we always choose the surface sound speed $C(0)$ as the initial guess values.

III. STOPPING CRITERION

If the problem contains no measurement errors, the traditional check condition is specified as

$$\Omega(C_k)<\epsilon^2, \tag{9}$$

where ϵ is a small specified number. However, the observed displacement data may contain measurement errors. Therefore, we do not expect the least-squares norm equation (4) to be equal to zero at the final iteration step. Following the experience of Alifanov,[11] we use the discrepancy principle as the stopping criterion, i.e., we assume that the wave displacement residuals may be approximated by

$$\mathbf{Y}-\mathbf{u}\approx\sigma, \tag{10}$$

where σ is the stand deviation of the measurements, which is assumed to be a constant. Substituting Eq. (10) into Eq. (4), the following expression is obtained for ϵ:

$$\epsilon^2=MN\sigma^2. \tag{11}$$

Then, the stopping criterion is given by Eq. (9) with ϵ determined from Eq. (11).

IV. THE STATISTICAL ANALYSIS

Statistical analysis is important in determining the accuracy of the computed inverse solution. In this section we develop the confidence bounds analysis for the estimated sound velocity $C(z)$ by assuming independent, constant-variance errors. The variance–covariance matrix of the estimated parameter vector $\mathbf{C}$ is defined as[12]

$$\text{var–cov}(\mathbf{C})\equiv E[[\mathbf{C}-E(\mathbf{C})][\mathbf{C}-E(\mathbf{C})]^T], \tag{12}$$

where $\mathbf{C}=\mathbf{C}(\mathbf{Y})$ is the unknown sound speed vector, $\mathbf{Y}$ is the measured displacement vector, $E(\cdot)$ denotes the statistical expected value (averaging) operator, and superscript T refers to the transport. Equation (12) is a nonlinear system for the determination of the variance-covariance matrix.

The right-hand side of Eq. (12) is then linearized by expanding $\mathbf{C}$ and $E(\mathbf{C})$ in the Taylor series and neglecting the higher-order terms. We obtain

$$\text{var–cov}(\mathbf{C})=\left[\frac{\partial\mathbf{C}}{\partial\mathbf{Y}^T}\right]E[\mathbf{Y}-E(\mathbf{Y})][\mathbf{Y}-E(\mathbf{Y})]^T]\left[\frac{\partial\mathbf{C}^T}{\partial\mathbf{Y}}\right]. \tag{13}$$

For independent displacement measurements with constant variance σ^2, we have[12]

$$E[[\mathbf{Y}-E(\mathbf{Y})][\mathbf{Y}-E(\mathbf{Y})]^T]=\sigma^2\mathbf{I}. \tag{14}$$

Introducing Eq. (14) into Eq. (13), the variance–covariance matrix becomes

$$\text{var–cov}(\mathbf{C})=\sigma^2\left[\frac{\partial\mathbf{C}}{\partial\mathbf{Y}^T}\right]\left[\frac{\partial\mathbf{C}^T}{\partial\mathbf{Y}}\right]. \tag{15}$$

To express the right-hand side of Eq. (15) in Jacobian terms, the method of chain rule is applied and the high-order terms are neglected. After some length manipulations, the following equation is obtained:

$$\text{var–cov}(\mathbf{C})=\sigma^2\left\{\left[\frac{\partial\mathbf{u}^T}{\partial\mathbf{C}}\right]\left[\frac{\partial\mathbf{u}}{\partial\mathbf{C}^T}\right]\right\}^{-1}. \tag{16}$$

Here, the Jacobian matrix and its transport are evaluated from the results of the direct problem by perturbing the sound velocity parameters.

If we assume independent errors, the nondiagonal elements in the variance–covariance matrix vanish and can be written in explicit form as

$$\text{var–cov}(\mathbf{C})=\begin{bmatrix}\sigma_{C_1}^2 & 0 & \cdots & 0\\ 0 & \sigma_{C_2}^2 & & \vdots\\ \vdots & & \ddots & 0\\ 0 & \cdots & 0 & \sigma_{C_K}^2\end{bmatrix}, \tag{17}$$

then a comparison of Eqs. (16) and (17) gives the standard deviation of the estimated parameters $\sigma_{\mathbf{C}}$ as

$$\sigma_{\mathbf{C}}=0\sqrt{\text{diag}\left\{\left[\frac{\partial\mathbf{u}^T}{\partial\mathbf{C}}\right]\left[\frac{\partial\mathbf{u}}{\partial\mathbf{C}^T}\right]\right\}^{-1}}, \tag{18}$$

where σ is standard deviation of the measurements.

If we now assume a normal distribution for the measurement errors, the 99% confidence bounds are determined as[6]

$$\{\mathbf{C}-2.576\sigma_{\mathbf{C}}\leqslant\mathbf{C}_{\text{mean}}\leqslant\mathbf{C}+2.576\sigma_{\mathbf{C}}\}=99\%. \tag{19}$$

This expression defines the approximate statistical confidence bounds for the estimated sound velocity vector **C**, i.e., the estimated values of the parameters are expected to lie between these two bounds with a 99% confidence.

V. RESULTS AND DISCUSSION

To illustrate the accuracy of the present approach in predicting sound velocity $C(z)$ with inverse analysis, in each numerical experiment study here we will first examine the inverse analysis by using the simulated exact wave displacement measurement from some appropriate measured locations. To study the effect of measurement errors on the unknown sound velocity, the measured displacement containing measurement errors are simulated in the following manner

$$Y_{\text{measured}}=Y_{\text{exact}}+\omega\sigma, \tag{20}$$

where σ is the standard deviation of measurement errors. For normally distributed errors with 99% confidences, ω lies within the bounds $-2.576<\omega<2.576$. The values of ω are calculated randomly by the International Mathematical and Statistical Libraries (IMSL) subroutine DRNNOR.[13] The measured displacement data simulated by Eq. (20) are then used to estimate the unknown sound velocity by the Levenberg–Marquardt algorithm.

We now present the inverse solutions of the following three numerical experiments by varying the location of impulse source function, the sensor's number, and its position, and the number of measured wave displacement data. Then the inverse solutions are analyzed by the statistical analysis.

A. Example 1

In the first test example we assume that the physical quantities appeared in Eq. (1) are taken as

$$L=1200\ \text{m},\quad u_t(z,0)=0,\quad u(z,0)=0$$

$$g=0,\quad f\delta(t-0.1)/\lambda(0)=-0.0001,$$

which implies that the only boundary impulse function is placed at $z=0$.

The exact sound velocity function is assumed as

$$C(z)=1400-100\sin(2\pi z/1200)\ \text{m/s},$$
$$0\leqslant z<1200\ \text{m}. \tag{21}$$

When the above information is substituted into Eq. (1) and solved by WAM, the errorless measurement data $Y(z,t)_{\text{exact}}$ at measured position z and time t can be obtained. Here, the finite difference increments in time and space are chosen as $dz=60$ m and $dt=0.1$ s and the weighted function that was used in WAM is taken as 0.25.

To check the validity of the inverse algorithm, the simulated exact wave displacements ($\sigma=0$) measured on the surface $z=0$, as shown in Fig. 3, are used in the inverse analysis to determine $C(z)$. Figure 4 indicates the estimated sound speed with $\sigma=0$ when the measurement time are chosen as 3, 5, and 7 s, i.e., the corresponding number of measurement data are $N=30$, 50, and 70, respectively. Indeed, the inverse solutions for these three cases are all agree with the exact values very well.

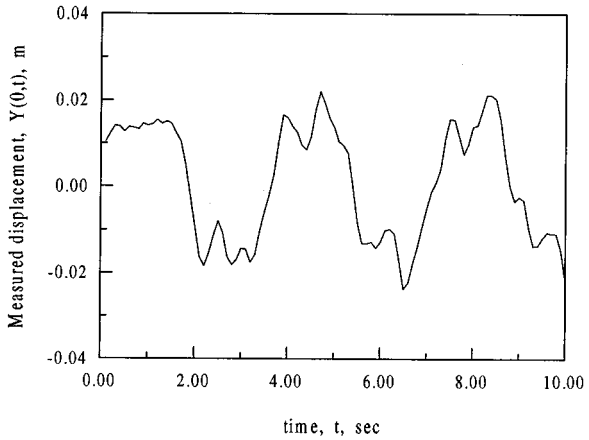

FIG. 3. The measured wave displacement with $\sigma=0$ at $z=0$ for example 1.

Next let us take a close look at the relative error of the estimated $C(z)$. Here, the relative error is defined as

$$\left[\sum_{k=1}^{K}\left|\frac{C_k-\hat{C}_k}{C_k}\right|\right]\div K\times 100\%, \tag{22}$$

where C_k denotes the exact value of sound velocity, $\hat{C}_k$ represents the estimated value, and K is the number of estimated parameters. The relative error for $N=30$ and 70 are calculated based on Eq. (22) and their values are obtained as 3.66×10^{-2}% and 1.0×10^{-6}%, respectively. This implies that the accuracy of the inverse solutions are improved as the number of measurements are increased. This phenomenon can also be seen from Fig. 5 where it represents the relation between the number of measurement data N and the ratio of the standard deviation $\overline{\sigma_C}/\sigma$ at different measured positions. Here $\overline{\sigma_C}$ is the average standard deviation of the estimated sound speed and is defined as

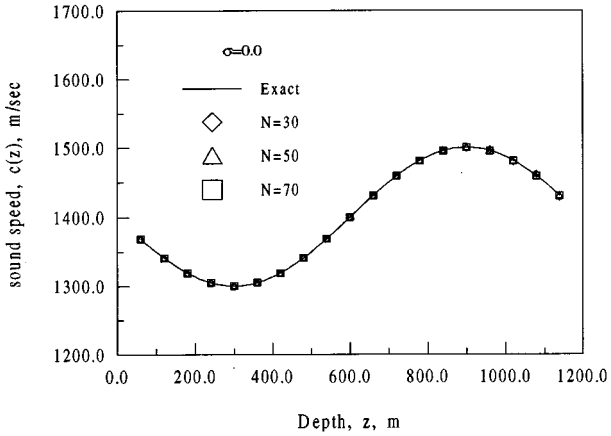

FIG. 4. The comparisons of exact and estimated $C(z)$ with $\sigma=0$ in example 1 by varying the number of measurements N.

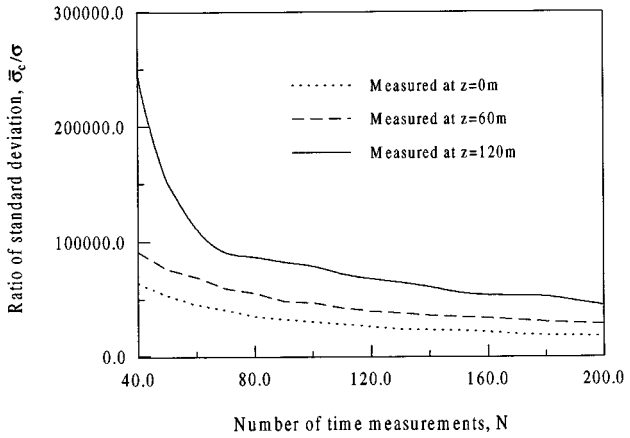

FIG. 5. The relation of $\overline{\sigma_C}/\sigma$ and N by varying the measured positions in example 1.

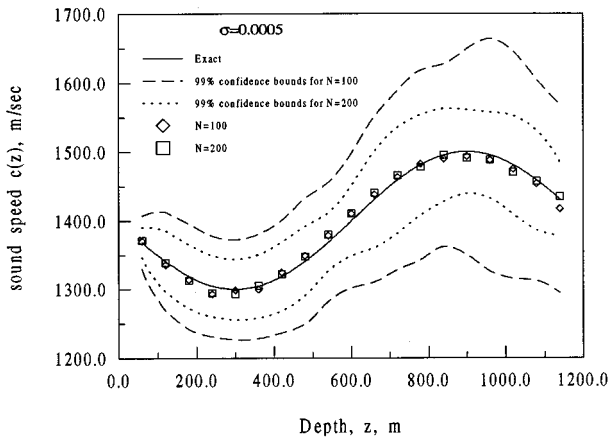

FIG. 6. The exact and estimated $C(z)$ and their confidence bounds with $\sigma=0.0005$ in example 1 by varying the number of measurements N.

$$\overline{\sigma_c}=\sum_{k=1}^{K}\sigma_{c_k}\Big/K, \tag{23}$$

where σ_{C_k} is obtained from Eq. (15).

Figure 5 reveals that when the measured data N are not sufficient, the value of $\overline{\sigma_C}/\sigma$ is large and the estimated results are unreliable since the band of 99% confidence bounds become very wide while a narrower band is desired. As N is increased, the ratio of $\overline{\sigma_C}/\sigma$ will approach to a fixed number; this also implies that we do not need a very large number of the measured data. Moreover, the ratio $\overline{\sigma_C}/\sigma$ at a different measured position for the same N occurs at a great discrepancy; for instance, when $N=40$, the ratio of $\overline{\sigma_C}/\sigma$ at measured positions $z=0$, 60, and 120 m are about 7×10^4, 9×10^4, and 2.5×10^5, respectively, when the only impulse function is placed on $z=0$.

This indicates that when the measured position is chosen at $z=0$ (the same as the location of boundary impulse function), one could obtain the most reliable inverse solution. The reason for this is that when the positions of the sensor and impulse function are the same, as time $t>0$, the sensor can detect the wave displacement immediately and all measurement data become ''effective.'' However, when the measured position is different from the location of the impulse function, the wave displacement can be recorded by the sensor at its position only after the effect of impulse function reaches it; this means some data will become ''invalid.'' Those ''invalid'' data are increased as the distance between boundary impulse function and measured position is increased.

Next, in order to study the effects of the measurement errors, some random errors with standard deviation $\sigma=0.0005$ are introduced into the exact displacement Y_{exact} in accordance with Eq. (20). This error represents about a 2% error of the average measured displacement. Figure 6 shows the exact and estimated sound velocity as well as their 99% confidence bounds for $N=100$ and 200, respectively. From Fig. 6 we learned that the confidence bounds for $N=200$ are narrower than for $N=100$. This implies that the inverse solution for $N=200$ is more reliable than for $N=100$.

Thus far we have concentrated on only one sensor, i.e., $M=1$. Will the results of inverse solutions be improved by utilizing multiple sensors? To answer this matter, let us consider the inverse solution that was obtained by adding one more sensor at $z=600$ m with 10-s measurement time, i.e., $M=2$ and $N=100$. Under this situation 100 data will be recorded by each sensor, i.e., a total of 200 measured data will be used in the inverse calculations. Figure 7 shows the comparison of the estimated results and their 99% confidence bounds for $M=1$ (sensor was placed at $z=0$) and $M=2$ (sensors were placed at $z=0$ and 600 m). It is as expected that the confidence bounds for $M=2$ are narrower than for $M=1$. However, when the case of $M=2$ is compared with the case of $N=200$ in Fig. 6 (these two cases are all using 200 measured data to perform the inverse calculation), it is obvious that the confidence bounds for the latter case is narrower than for the former case; this means that the inverse solutions for one sensor measurement can be better than for two sensors measurement, provided that the measuring time period is increased.

B. Example 2

In this illustrated example we choose a more rigorous test example, i.e., a step function to describe the variation of sound velocity:

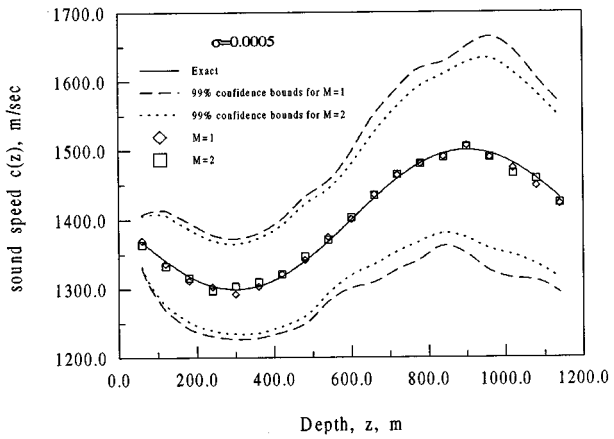

FIG. 7. The exact and estimated $C(z)$ and their confidence bounds with $\sigma=0.0005$ in example 1 by varying the number of sensor M.

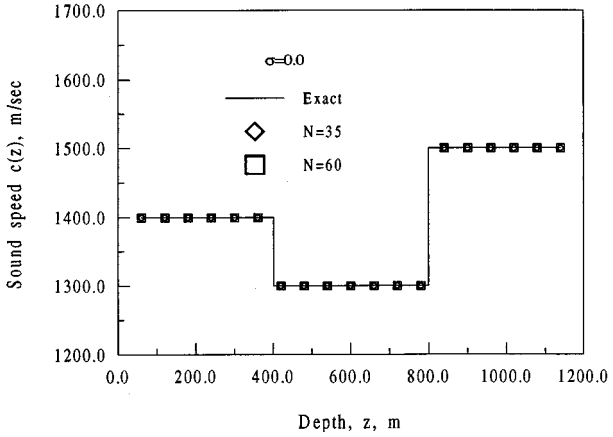

FIG. 8. The comparisons of exact and estimated $C(z)$ with $\sigma=0$ in example 2 by varying the number of measurements N.

$$C(z)=\begin{cases}1400 \text{ m/s}, & 0\leqslant z<400 \text{ m}\\ 1300 \text{ m/s}, & 400\leqslant z<800 \text{ m}\\ 1500 \text{ m/s}, & 800\leqslant z<1200 \text{ m};\end{cases} \tag{24}$$

the other dimension and finite difference parameters are the same as those were used in example 1.

Figure 8 shows the comparison of the exact and estimated $C(z)$ using one sensor measured at $z=0$ with $N=35$ and 60 when $\sigma=0$. Indeed, the estimated $C(z)$ agrees very well with the exact value, and when the number of measured data are increased, the accuracy of the inverse solutions are improved since the relative errors based on Eq. (19) are calculated as 6.8×10^{-3}% and 1.0×10^{-6}% for $N=35$ and 60, respectively.

When the standard deviation of the measurement error is taken as $\sigma=0.0003$ (about 1% error of the average measured displacement), the exact and estimated $C(z)$ and their confidence bounds are shown in Fig. 9 for $N=100$ and 200. The relative error for $N=100$ and 200 are obtained as 9.4×10^{-1}% and 2.9×10^{-1}%, respectively. Again, a narrower 99% confidence bounds is obtained when $N=200$.

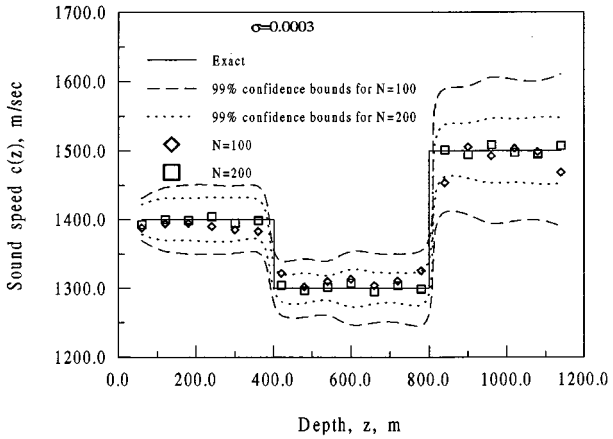

FIG. 9. The exact and estimated $C(z)$ and their confidence bounds with $\sigma=0.0003$ in example 2 by varying the number of measurements N.

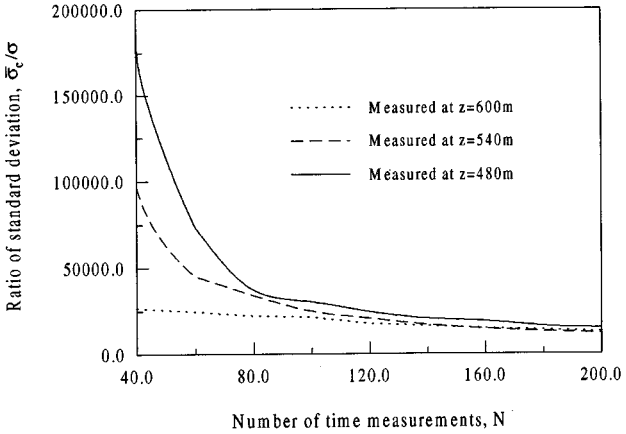

FIG. 10. The relation of $\overline{\sigma_C}/\sigma$ and N by varying the measured positions in example 3.

C. Example 3

In the previous two examples, the boundary impulse function is always placed on the surface $z=0$, and we concluded that when the positions of the sensor and the impulse source function are the same, the best inverse solution can be recasted.

To prove this matter more rigorous with numerical experiment, in the third example we assume $f=0$ and $\rho g\,\delta(t-0.1)\,\delta(z-600)=10$, which implies that a source impulse function (or instantaneous point source) is now placed in the middle of the domain. The sound velocity for this example is chosen as

$$C(z)=1400+100\sin(2\pi z/1200) \text{ m/s},\qquad 0\leqslant z<1200 \text{ m}, \tag{25}$$

and the other dimension and finite difference parameters are the same as those were used in examples 1 and 2, except for f and g.

As the same procedure in obtaining Fig. 5 was performed again, the relation of N and $\overline{\sigma_C}/\sigma$ for this example is shown in Fig. 10. It can be seen form Fig. 10 that when the distance between the sensor's position and the impulse function's location are increased, the ratio of $\overline{\sigma_C}/\sigma$ is also increased for the same number of time measurements N, especially when N is not sufficient enough. The reason for this matter is the same as was discussed in example 1.

Figure 11 indicates the estimated results and their 99% confidence bounds with $\sigma=0.0005$ when the locations of the sensor and impulse function are placed at $z=600$ m for $N=100$ and 200. Similar results as before were obtained, i.e., when N is increased the band of confidence bounds become narrower and more reliable inverse solutions are yielded.

Finally, from all the cases study here, we conclude that the number of sensors, the distance between the sensor and impulse function, as well as the number of measured data, play an important role in estimating the unknown sound velocity $C(z)$ for the inverse acoustic problem. Only when those factors are controlled properly can the best inverse solutions be recasted.

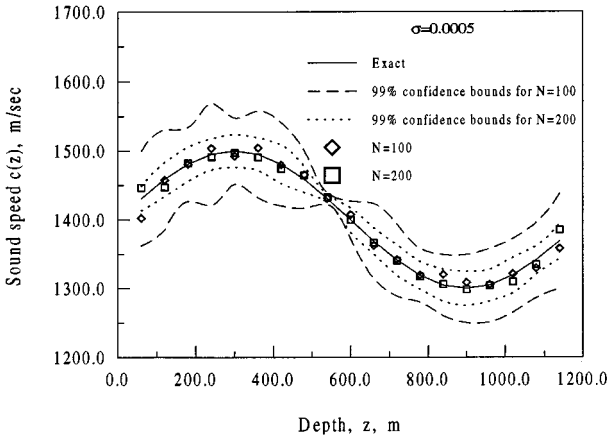

FIG. 11. The exact and estimated $C(z)$ and their confidence bounds with $\sigma=0.0005$ in example 3 by varying the number of measurements N.

VI. CONCLUSION

An inverse acoustic problem with statistical analysis in estimating the unknown sound velocity as a function of depth has been developed successfully based on the Levenberg–Marquardt algorithm.

When assuming no measurement errors, the exact inverse solution can be recast by the present algorithm with only a small number of iterations as long as the ''effective'' measured data are sufficient; the accuracy of the inverse solution is increased as the number of measured data are increased.

Under the circumstance that the measurement errors are included, the 99% confidence bounds and standard deviation for the estimated parameters are determined from a statistical analysis.

[1] A. Bartoloni, C. Lodovici, and F. Zirilli, ''Inverse problem for a class of one-dimensional wave equation with piecewise constant coefficients,'' J. Optim. Theory Appl. **76**, 13–32 (1993).

[2] V. K. Kinra, P. T. Jaminet, C. Zhu, and V. R. Lyer, ''Simultaneous measurement of the acoustical properties of a thin-layered medium: The inverse problem,'' J. Acoust. Soc. Am. **95**, 3059–3074 (1994).

[3] Y. M. Chen, ''A numerical algorithm for solving inverse problems of two-dimensional wave equations,'' J. Comput. Phys. **50**, 193–208 (1983).

[4] M. Moghaddam and W. C. Chew, ''Simultaneous inversion of compressibility and density in the acoustic inverse problem,'' Inverse Probl. **9**, 715–730 (1993).

[5] D. M. Marquardt, ''An algorithm for least-squares estimation of nonlinear parameters,'' J. Soc. Ind. Appl. Math. **11**, 431–441 (1963).

[6] C. H. Huang and M. N. Ozisik, ''A direct integration approach for simultaneously estimating temperature dependent thermal conductivity and heat capacity,'' Num. Heat Trans. A **20**, 95–110 (1991).

[7] G. P. Flach and M. N. Ozisik, ''Inverse heat conduction problem of simultaneously estimating spatially varying thermal conductivity and heat capacity per unit volume,'' Num. Heat Trans. **16**, 249–266 (1989).

[8] A. J. Silva Neto and M. N. Ozisik, ''An inverse problem of estimating thermal conductivity, optical thickness and single scattering albedo of a semi-transparent medium,'' in *The First Conference in a Series on Inverse Problems in Engineering*, June 13–18, Palm Coast, Florida, edited by N. Zabaras, K. A. Woodbury, and M. Raynaud (United Engineering Trustees, Inc., 1993), pp. 267–273.

[9] C. H. Huang and M. C. Huang, ''Inverse problem in determining the normal and tangential drag coefficients of marine cables,'' J. Ship Res. **38**, 296–301 (1994).

[10] G. D. Smith, *Numerical solution of Partial Differential Equations: Finite Different Methods* (Clarendon, Oxford, 1985).

[11] O. M. Alifanov, ''Solution of an Inverse Problem of Heat Conduction by Iteration Methods,'' J. Eng. Phys. **26**, 471–476 (1972).

[12] R. W. Farebrother, *Linear Least Squares Computations* (Marcel Dekker, New York, 1988).

[13] IMSL Library Edition 10.0, User's Manual: Math Library Version 1.0, IMSL, Houston, TX, 1987.

A boundary diffraction wave model for a spherically focused ultrasonic transducer

Lester W. Schmerr, Jr.
Center for NDE and Department of Aerospace Engineering and Engineering Mechanics, Iowa State University, Ames, Iowa 50011

Alexander Sedov
Department of Mechanical Engineering, Lakehead University, Thunder Bay, Ontario P7B 5E1, Canada

Terence P. Lerch
Center for NDE and Department of Aerospace Engineering and Engineering Mechanics, Iowa State University, Ames, Iowa 50011

(Received 18 April 1995; revised 20 September 1996; accepted 26 September 1996)

A model of a spherically focused piston transducer is developed in terms of boundary diffraction waves. The model represents the radiated pressure in terms of a direct wave and a one-dimensional edge wave integral. This decomposition allows the efficient calculation of the transducer beam in a form previously available only for a planar transducer. Numerical results for the simulation of the entire wave field of a transducer are given to illustrate the effectiveness of the formulation. © *1997 Acoustical Society of America.* [S0001-4966(97)04703-6]

PACS numbers: 43.20.Ks, 43.20.Tb, 43.38.Ar, 43.35.Yb [JEG]

INTRODUCTION

The transducers used in ultrasonic testing typically contain piezoelectric crystals that are mounted in a housing. Planar (unfocused) transducers have a flat crystal that radiates a beam of sound into the adjacent medium while spherically focused transducers contain an acoustic lens between the crystal and the adjacent medium that concentrates the sound beam, producing high sensitivity and spatial resolution. When making quantitative measurements with such transducers, it is often necessary to characterize the significant pressure variations in the sound beam using models. For a planar probe radiating into a fluid, the model most commonly used is the Rayleigh–Sommerfeld theory for a piston source. Harris[1] summarizes a variety of expressions that have been used for calculating the sound beam of a planar piston probe, all of which are special forms of the basic Rayleigh–Sommerfeld integral. In 1947, O'Neil[2] showed how the Rayleigh–Sommerfeld theory could also be adopted to develop an approximate model for a spherically focused probe radiating into a fluid and gave explicit expressions for the on-axis pressure and the pressure in the plane of the geometrical focus. The O'Neil theory treated the focused transducer as a piston (constant velocity) source on a spherical surface and, therefore, did not model an acoustic lens directly. Schlengermann,[3,4] however, has developed a focused probe model that does incorporate the lens explicitly and has also given explicit on-axis pressure expressions. In the paraxial approximation the O'Neil and Schlengermann models predict identical on-axis expressions if the corresponding geometrical focal lengths of the two models are adjusted properly.[5] Thus the absence of an explicit lens in the O'Neil model is not likely to be significant. Recently, a number of numerical and experimental studies have also shown that the O'Neil model agrees very well with both more exact focused probe models and with experiments.[6–8] Thus the O'Neil model does appear to be a good basis for characterizing spherically focused transducers.

O'Neil[2] only gave completely exact analytical expressions for the on-axis pressure of the spherically focused probe. To use the model fully, however, one must be able to also efficiently calculate off-axis pressure values anywhere in the transducer wave field and particularly near the ''true'' focus where the fields are most significant. For the planar probe, one of the most efficient formulations for evaluating the pressure at general off-axis points involves the exact integration over one of the coordinates of the original 2-D Rayleigh–Sommerfeld integral, producing a direct plane-wave term and an integral around the transducer edge (edge wave term) that can be readily evaluated numerically.[9,10] This same direct/edge wave formulation can also be obtained directly using boundary diffraction wave theory.[11] Although Penttinen and Luukkala[12] obtained direct/edge wave expressions for an impulsively excited spherically focused probe, to date a similar formulation for a focused transducer has not been found for the O'Neil theory at a fixed frequency. In Ref. 8 Madsen *et al.* did reduce the original 2-D integrals of O'Neil into a direct wave and line integral terms for the harmonic wave case. However, the expressions in Ref. 8 included terms on the periphery of a certain subregion of the transducer face, so that they were not purely of a direct wave/edge wave type as found in the planar case. Also, Marchand and Wolf[11] presented boundary diffraction wave expressions for a focused probe, but their results were not based on the O'Neil model and they did not reduce their general results to explicitly evaluated forms. Since the submission of this work, a closely related derivation of direct wave/edge wave formulation for a focused transducer has appeared.[15] However, unlike the present work, that derivation relied on a Kirchhoff–Huygens representation similar to

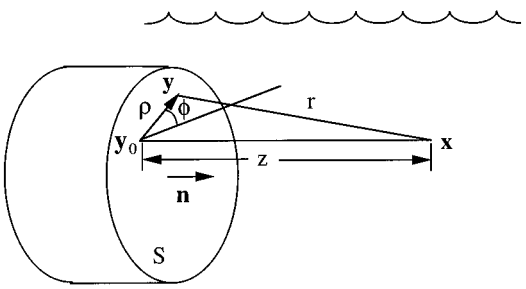

FIG. 1. Geometry for a planar transducer radiating into a fluid.

that of Marchand and Wolf.[11] There are, of course, other approaches for efficiently solving for the transducer radiation field. For example, Chen *et al.*[13] recently evaluated the response of a spherically focused transducer using Bessel function expansions. However, a direct/edge wave decomposition expresses the response in terms of wave terms having an explicit physical meaning and can serve as the basis for more general problems, such as the radiation through an interface at oblique incidence,[14] which are difficult to solve with series expansion methods.

Here, we will show, using the theory of O'Neil, that a direct/edge wave formulation can be obtained for a spherically focused probe at a fixed frequency that is a direct extension of the planar probe case. This formulation will be given both in terms of completely coordinate-free boundary diffraction wave theory expressions, and explicitly in terms of transducer-centered coordinates, as used for the planar transducer.[9] In fact, these expressions will be shown to reduce directly to the planar transducer case as the geometrical focal length goes to infinity and, in the paraxial approximation, will be shown to also yield the well-known approximation for the behavior of the off-axis pressure in the geometrical focal plane.[2] The efficiency of numerically evaluating these expressions will be demonstrated by computing the full wave-field responses for a specific spherically focused transducer example.

I. BOUNDARY DIFFRACTION WAVE MODEL FOR A PLANAR TRANSDUCER

Since the theory developed here for the spherically focused transducer relies on a direct extension of the methods used previously for unfocused probes, we will first discuss some of the important aspects of the planar case. For a planar piston probe radiating into a fluid, the Rayleigh–Sommerfeld integral gives the pressure p at an arbitrary point $\mathbf{x}$ in the fluid in the form (Fig. 1)

$$p(\mathbf{x},\omega) = -i\omega\rho v_0/2\pi \int_S \frac{\exp(ikr)}{r}\, dS, \tag{1}$$

where ω is the circular frequency, ρ and c are the density and wave speed of the fluid, respectively, $k=\omega/c$ is the wave number, $r=|\mathbf{x}-\mathbf{y}|$ is the distance from a point $\mathbf{x}$ in the fluid to an arbitrary point $\mathbf{y}$ on the transducer face S, and v_0 is the spatially uniform velocity of the transducer surface. To further evaluate the integral in Eq. (1) we drop a line from $\mathbf{x}$ to a point $\mathbf{y}_0$ on the plane of the transducer where the line is perpendicular to that plane (see Fig. 1). Then, we have to consider separately the following three cases: (1) the line intersects the transducer plane at a point $\mathbf{y}_0$ which lies within the active surface S of the transducer, (2) the intersection point $\mathbf{y}_0$ lies outside S, and (3) $\mathbf{y}_0$ lies directly on the edge C of the transducer. In all these cases, we can set up a set of polar coordinates (ρ,ϕ) centered at $\mathbf{y}_0$ as shown and write $dS=\rho\, d\rho\, d\phi$. However, since $r = \sqrt{\rho^2+z^2}$, we also can write $dS=r\, dr\, d\phi$ so that the r integration can be done exactly to yield

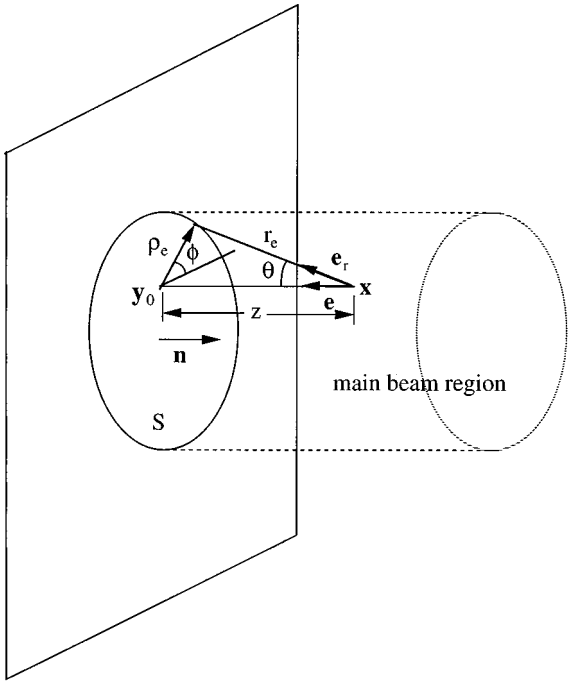

FIG. 2. Case one: Geometrical terms when the pressure is evaluated at a point $\mathbf{x}$ inside the main beam of a planar transducer.

$$p(\mathbf{x},\omega) = -\frac{\rho c v_0}{2\pi} \int \exp(ikr)\Big|_{r_{\min}}^{r_{\max}} d\phi, \tag{2}$$

where the values of $r_{\min}$ and $r_{\max}$ must now be determined for each case.

A. Case 1: Point x in the main beam

When point $\mathbf{x}$ is within the cylindrical ''main beam'' region (Fig. 2) formed by extending the edge of the transducer face S in the z direction, point $\mathbf{y}_0$ will lie within S, and ρ and r are single-valued functions of ϕ. In this case $r_{\min}=z$, $r_{\max} = r_e(\phi) = \sqrt{\rho_e^2(\phi)+z^2}$, where ρ_e is the radius from $\mathbf{y}_0$ to the edge. Then we find

$$p(\mathbf{x},\omega) = \rho c v_0 \left[\exp(ikz) - 1/2\pi \int_0^{2\pi} \exp(ikr_e) d\phi \right], \tag{3}$$

where the first term in Eq. (3) is the direct plane wave and the integral term represents the edge wave contribution.

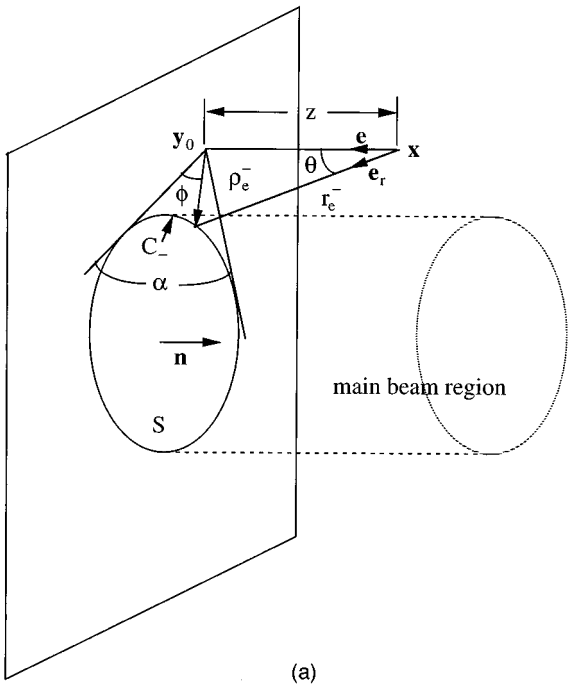

(a)

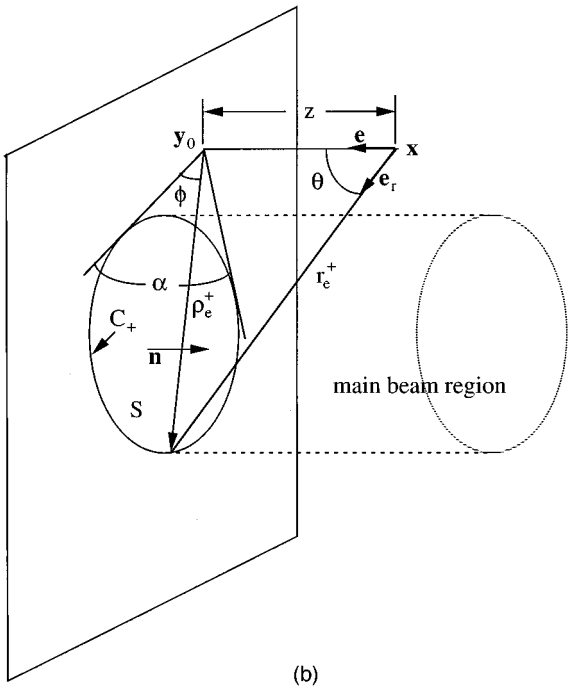

(b)

FIG. 3. (a) Case two: Geometrical terms when the pressure is evaluated at a point **x** outside the main beam of a planar transducer and the integration is over C_- on the transducer edge. (b) Case two: Geometrical terms when the pressure is evaluated at a point **x** outside the main beam of a planar transducer and the integration is over C_+ on the transducer edge.

B. Case 2: Point x outside the main beam

When **x** is outside the main beam, point $\mathbf{y}_0$ lies outside S, and ρ and r are no longer single-valued functions of ϕ. However, if we let $r_{\min} = r_e^-(\phi) = \sqrt{[\rho_e^-(\phi)]^2 + z^2}$ on C_- and $r_{\max} = r_e^+(\phi) = \sqrt{[\rho_e^+(\phi)]^2 + z^2}$ on C_+ [Fig. 3(a) and (b)], we have

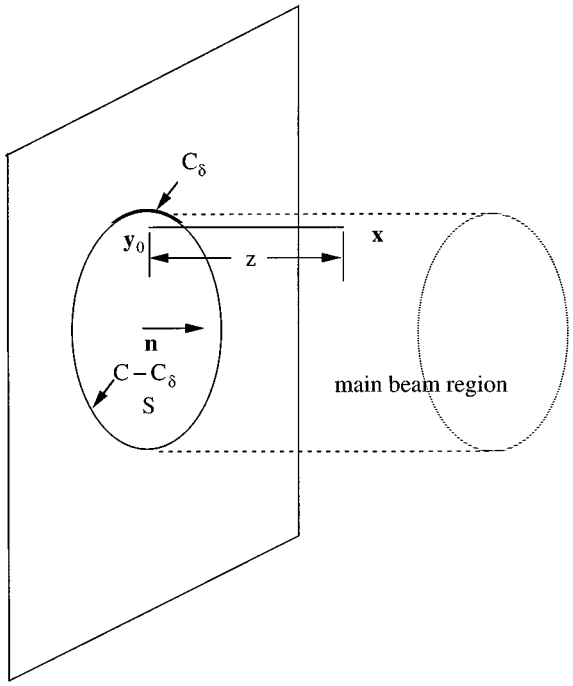

FIG. 4. Case three: Geometry definition for considering the limit as point **x** goes to the edge of the main beam of a planar transducer from the inside of the main beam region.

$$p(\mathbf{x},\omega) = \rho c \nu_0 \left[1/2\pi \int_0^{\alpha} \exp(ikr_e^-) d\phi - 1/2\pi \int_0^{\alpha} \exp(ikr_e^+) d\phi \right]. \quad (4)$$

Equation (4) contains only edge wave integrals. The first integral is a clockwise integral over C_- while the second integral is a counterclockwise integral over C_+. Thus, if both integrals are taken counterclockwise, we can rewrite Eq. (4) as

$$p(\mathbf{x},\omega) = -\rho c \nu_0 / 2\pi \int_C \exp(ikr_e) d\phi, \quad (5)$$

where $r_e = r_e^-$ on C_-, $r_e = r_e^+$ on C_+ and $C = C_+ + C_-$. Note that in the same fashion we can rewrite Eq. (3) for case 1 as

$$p(\mathbf{x},\omega) = \rho c \nu_0 \left[\exp(ikz) - 1/2\pi \int_C \exp(ikr_e) d\phi \right]. \quad (6)$$

C. Case 3: Point x on the edge of the main beam

Since the pressure is continuous as point **x** goes to the edge of the main beam either from the outside (case 2) or inside (case 1) of the main beam region (and as point $\mathbf{y}_0$ correspondingly goes to the edge C), we can obtain this limit from either Eq. (5) or Eq. (6). Consider Eq. (6). If we write this expression as (Fig. 4)

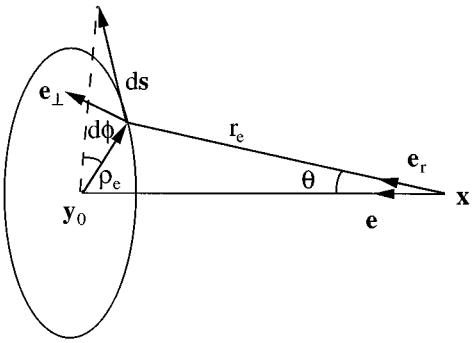

FIG. 5. Geometrical terms for defining the angle differential $d\phi$ in the coordinate-invariant form of Eq. (12).

$$p(\mathbf{x},\omega)=\rho c\nu_0\Bigg[\exp(ikz)-1/2\pi\int_{C-C_\delta}\exp(ikr_e)d\phi - 1/2\pi\int_{C_\delta}\exp(ikr_e)d\phi\Bigg], \tag{7}$$

then when $\mathbf{y}_0$ goes to a point on C_δ, the angle ϕ varies approximately over a range of π on C_δ where $\exp(ikr_e)\cong\exp(ikz)$, so that the last integral in Eq. (7) is equal to $-\exp(ikz)/2$ as $\delta\to 0$. Also the first integral becomes in that limit the principal value integral

$$P\int_C\exp(ikr_e)d\phi=\lim_{\delta\to 0}\int_{C-C_\delta}\exp(ikr_e)d\phi,$$

giving

$$p(\mathbf{x},\omega)=\rho c\nu_0\Bigg[\exp(ikz)/2-1/2\pi\int_C\exp(ikr_e)d\phi\Bigg]. \tag{8}$$

The same limit is obtained if instead we start from outside the main beam and use Eq. (5) instead.

D. General results for a planar probe

We can combine Eqs. (5), (6), and (8) into a single form valid for any location $\mathbf{x}$ as

$$p(\mathbf{x},\omega)=\rho c\nu_0\Bigg[\Theta\ \exp(ikz)-1/2\pi\int_C\exp(ikr_e)d\phi\Bigg], \tag{9}$$

where

$$\Theta=\begin{cases}1 & \text{for } \mathbf{y}_0 \text{ in } S\\ 1/2 & \text{for } \mathbf{y}_0 \text{ on } C\\ 0 & \text{for } \mathbf{y}_0 \text{ outside } S\end{cases} \tag{10}$$

and the integral is implicitly understood to be interpreted in the principal value sense when $\mathbf{y}_0$ is on C.

Equation (9) is the expression of the original Rayleigh–Sommerfeld integral in the form of a direct wave/edge wave combination. It is written explicitly in terms of the angle ϕ as measured from $\mathbf{y}_0$. We can, however, transform this expression into a coordinate invariant boundary diffraction wave form.[11] To see this, let $\mathbf{e}$ and $\mathbf{e}_r$ be the unit vectors as shown in Figs. 2 and 3(a) and (b). Then it follows that (see Fig. 5)

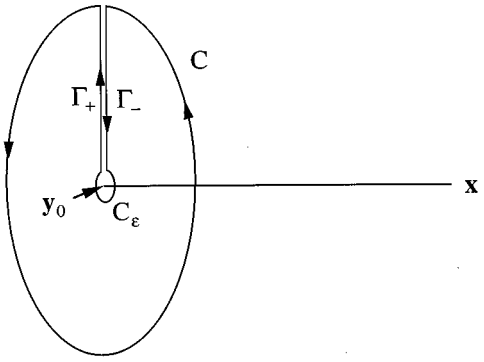

FIG. 6. Definition of the extended integration path C_r for expressing the pressure wave field of a planar transducer solely in terms of boundary diffraction waves [Eq. (14)].

$$\frac{1}{r_e}\frac{(\mathbf{e}_r\times\mathbf{e})\cdot d\mathbf{s}}{1-(\mathbf{e}_r\cdot\mathbf{e})^2}=\frac{1}{r_e}\frac{\sin\theta\mathbf{e}_\perp\cdot d\mathbf{s}}{1-\cos^2\theta}=\frac{\mathbf{e}_\perp\cdot d\mathbf{s}}{\rho_e}=d\phi, \tag{11}$$

where $\mathbf{e}_\perp$ is a unit vector in the plane of the transducer perpendicular to the radius from $\mathbf{y}_0$ to $\mathbf{y}$. Since $\mathbf{e}=-\mathbf{n}$, where $\mathbf{n}$ is the unit normal to the transducer, we have

$$d\phi=\frac{1}{r_e}\frac{(\mathbf{n}\times\mathbf{e}_r)\cdot d\mathbf{s}}{1-(\mathbf{n}\cdot\mathbf{e}_r)^2} \tag{12}$$

and placing this result into Eq. (9), we find

$$p(\mathbf{x},\omega)=\rho c\nu_0\Bigg[\Theta\ \exp(ikz) - \frac{1}{2\pi}\int_C\frac{\exp(ikr_e)}{r_e}\frac{(\mathbf{n}\times\mathbf{e}_r)\cdot d\mathbf{s}}{1-(\mathbf{n}\cdot\mathbf{e}_r)^2}\Bigg]. \tag{13}$$

The edge wave integral in Eq. (13) is the same boundary diffraction wave term found by Marchand and Wolf[11] using a combination of integral representation theorems and Stokes' theorem. The direct wave term also can be written as a boundary diffraction wave if we extend the edge integral C to include a small line integral C_ϵ around $\mathbf{y}_0$ (Fig. 6). Since the integrals on Γ_+ and Γ_- cancel and the integral on C_ϵ evaluates to just the direct wave term, we find

$$p(\mathbf{x},\omega)=-\frac{\rho c\nu_0}{2\pi}\int_{C_r}\frac{\exp(ikr_e)}{r_e}\frac{(\mathbf{n}\times\mathbf{e}_r)\cdot d\mathbf{s}}{1-(\mathbf{n}\cdot\mathbf{e}_r)^2}, \tag{14}$$

where $C_r=C+\lim_{\epsilon\to 0}C_\epsilon$.

The boundary diffraction waveform in Eq. (13) is both general and convenient. It is valid for an arbitrarily shaped planar piston transducer and has reduced the 2-D surface integration of the original Rayleigh–Sommerfeld integral to merely a 1-D line integration. For a circular transducer of radius a, the edge wave integral can be expressed in terms of polar coordinates (ρ_0,ψ) measured from the center of the transducer (Fig. 7), where

$$\frac{1}{r_e}\frac{(\mathbf{n}\times\mathbf{e}_r)\cdot d\mathbf{s}}{1-(\mathbf{n}\cdot\mathbf{e}_r)^2}=\frac{a\cos\gamma\,d\psi}{\rho_e}=\frac{a(a-\rho_0\cos\psi)d\psi}{a^2+\rho_0^2-2a\rho_0\cos\psi} \tag{15}$$

and

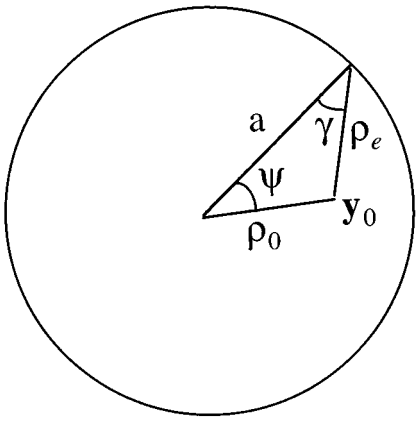

FIG. 7. Geometry terms for expressing the pressure wave field of a plane circular transducer of radius a in terms of transducer-centered coordinates.

$$r_e(\psi)=\sqrt{a^2+\rho_0^2+z^2-2a\rho_0\cos\psi}, \tag{16}$$

giving, explicitly,

$$p(\rho_0,z,\omega)=\rho c\nu_0\left[\Theta\ \exp(ikz)-1/2\pi \times\int_0^{2\pi}\frac{\exp[ikr_e(\psi)]a(a-\rho_0\cos\psi)d\psi}{a^2+\rho_0^2-2a\rho_0\cos\psi}\right]. \tag{17}$$

The efficiency of using this formulation to evaluate the wave field of various planar probes has been previously demonstrated.[9] As shown in the next section, a similar formulation is also possible for the spherically focused case.

II. BOUNDARY DIFFRACTION WAVE MODEL FOR A SPHERICALLY FOCUSED TRANSDUCER

Although the individual results presented in the last section for the planar transducer are not new, combining them in this manner allows directly their generalization to the spherically focused transducer model of O'Neil. To show this, we first note that the O'Neil model also uses the Rayleigh–Sommerfeld integral of Eq. (1) but where S is a radiating spherical surface and ν_0 is the spatially uniform radial velocity on this surface. Consider, now a spherically focused transducer of radius a and geometrical focal length R_0. The distance, h, from the back to the front surface is then given by $h=R_0-\sqrt{R_0^2-a^2}$ (Fig. 8). If from an arbitrary point $\mathbf{x}$ in the fluid we drop a line through the geometrical focus to the surface S as shown in Fig. 8, we can write the area element $dS=R_0\sin\eta\,d\eta\,d\beta$, where the angle β (not shown) is in a plane perpendicular to this line. Applying the law of cosines to triangle ABC, we have $R^2=2R_0^2-2R_0^2\cos\eta$, which when differentiated gives $R\,dR=R_0^2\sin\eta\,d\eta$. Using this result in the expression for dS, we find $dS=R\,dR\,d\beta$. But, from triangle ABC, it also follows that $R=2R_0\cos\xi$ and, from triangle ABD,

$$r^2=R^2+R_0^2(1-q_0^2)-2RR_0(1-q_0)\cos\xi,$$

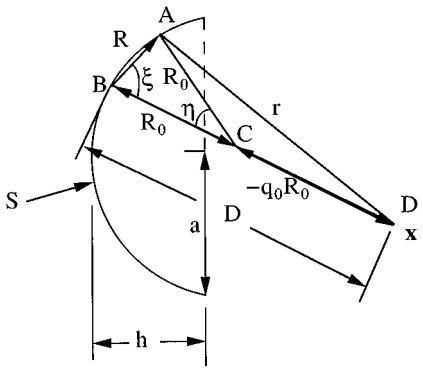

FIG. 8. Geometry for evaluating the pressure wave field of a spherically focused transducer of radius a and focal length R_0.

where $q_0=1-D/R_0$ is the normalized distance from the geometrical focus, so that we also have $r^2=R^2q_0+R_0^2(1-q_0)^2$ which can be differentiated on both sides to give $r\,dr=R\,dR\,q_0$. Thus the area element dS is found to be also expressible as

$$dS=r\,dr\,d\beta/q_0, \tag{18}$$

which is the generalization of the result found previously for the planar transducer. In fact, if we let $R_0\to\infty$, then $q_0\to1$, $\beta\to\phi$ and we do recover our previous result. Thus, as in the planar case, we can perform the integration on r to obtain

$$p(\mathbf{x},\omega)=-\frac{\rho c\nu_0}{2\pi q_0}\int\exp(ikr)\Big|_{r_{\min}}^{r_{\max}}d\beta, \tag{19}$$

and we must again consider three cases.

A. Case 1: Point x in the main beam

For the spherically focused probe the ''main beam'' is the region inside the cone formed by extending the normals from the active face of the transducer into the surrounding medium (Fig. 9). If point $\mathbf{x}$ is in this main beam then point $\mathbf{y}_0$ (where the line through the geometrical focus from $\mathbf{x}$ intersects S) is on the face of the transducer and $r_{\min}=D$ and $r_{\max}=r_e$, where r_e is the distance from $\mathbf{x}$ to the transducer edge. We then find

$$p(\mathbf{x},\omega)=\frac{\rho c\nu_0}{q_0}\left[\exp(ikD)-1/2\pi\int_0^{2\pi}\exp(ikr_e)d\beta\right], \tag{20}$$

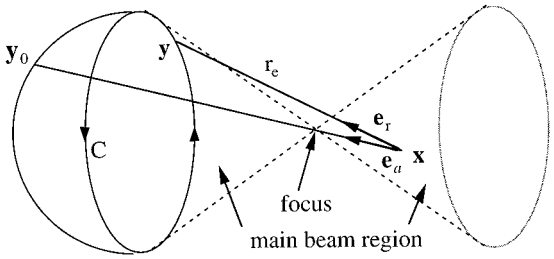

FIG. 9. Case 1: Geometrical terms when the pressure is evaluated at a point $\mathbf{x}$ inside the main beam of a spherically focused transducer.

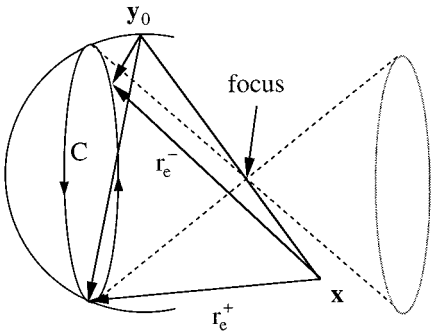

FIG. 10. Case 2: Geometrical terms when the pressure is evaluated at a point **x** outside the main beam of a spherically focused transducer.

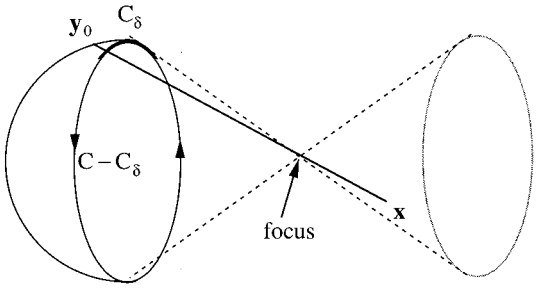

FIG. 11. Case 3: Geometry definition for considering the limit as point **x** goes to the edge of the main beam of a spherically focused transducer from the inside of the main beam region.

which shows the existence again of a direct wave and edge wave term. In this case, however, the direct wave is a spherically converging wave when **x** is between the transducer face and the geometrical focus, and a diverging spherical wave when **x** is beyond that focus, as predicted by ray theory. Although the factor q_0 does cause this direct wave to become infinitely large at the geometrical focus, this infinity is canceled by that of the edge wave term and the entire pressure expression in Eq. (20) is everywhere finite and well-behaved.

B. Case 2: Point x outside the main beam

If point **x** is outside the main beam then point $\mathbf{y}_0$ lies on the continuation of the spherical transducer surface outside the transducer edge (Fig. 10) and r_e is no longer a single-valued function of β, as in the corresponding planar case. Thus, breaking the edge up into two parts, as before, we have

$$p(\mathbf{x},\omega)=\frac{\rho c v_0}{2\pi q_0}\left[\int_{C_-}\exp(ikr_e^-)d\beta - \int_{C_+}\exp(ikr_e^+)d\beta\right], \tag{21}$$

which, as in the planar case, can be put into the compact form

$$p(\mathbf{x},\omega)=\frac{-\rho c v_0}{2\pi q_0}\left[\int_{C}\exp(ikr_e)d\beta\right], \tag{22}$$

where $C=C_+ + C_-$ and the integration is in a counterclockwise sense for the entire edge.

C. Case 3: Point x on the edge of the main beam

When the point **x** lies on edge of the main beam, we can again obtain the pressure expression as the limit of either case 1 or case 2. Following the planar probe discussion, from case 1 we can write Eq. (20) as (Fig. 11)

$$p(\mathbf{x},\omega)=\frac{\rho c v_0}{q_0}\left[\exp(ikD)-\frac{1}{2\pi}\int_{C-C_\delta}\exp(ikr_e)d\beta - \frac{1}{2\pi}\int_{C_\delta}\exp(ikr_e)d\beta\right]; \tag{23}$$

however, on C_δ $r_e \cong D$ and the range of β is from 0 to π, so we find

$$p(\mathbf{x},\omega)=\frac{\rho c v_0}{q_0}\left[\frac{\exp(ikD)}{2}-\frac{1}{2\pi}\int_{C}\exp(ikr_e)d\beta\right]. \tag{24}$$

D. General results for a spherically focused probe

Combining all three cases from Eqs. (20), (22), and (24), the entire transducer wave field is then finally given by

$$p(\mathbf{x},\omega)=\frac{\rho c v_0}{q_0}\left[\Theta\ \exp(ikD)-\frac{1}{2\pi}\int_{C}\exp(ikr_e)d\beta\right], \tag{25}$$

which can be compared with the planar result [Eq. (9)] and reduces to that result if we let $R_0\to\infty$.

It is also possible to put Eq. (25) into a general boundary diffraction waveform as done for the planar case. To see this, consider the geometry of case 1 in Fig. 9 where $\mathbf{e}_a$ and $\mathbf{e}_r$ are unit vectors pointing from **x** to $\mathbf{y}_0$ and **x** to **y**, respectively. As

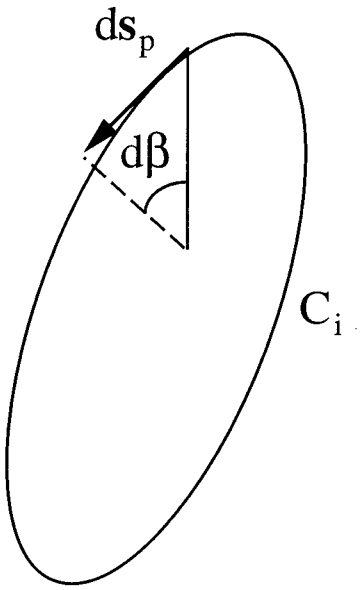

FIG. 12. The relationship between the angle $d\beta$ and the vector displacement $d\mathbf{s}_p$ on C_i, the image of the edge C in a plane perpendicular to $\mathbf{e}_a$.

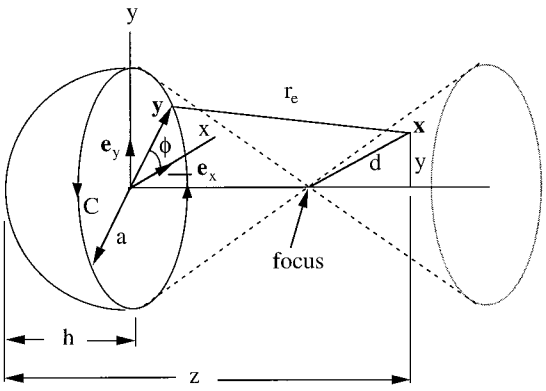

FIG. 13. Geometry terms for expressing the pressure wave field of a spherically focused transducer of radius a and focal length R_0 in terms of transducer-centered coordinates.

point **y** moves along the edge C through the vector displacement **ds**, in the plane P that is perpendicular to the line from **x** to $\mathbf{y}_0$ we have on C_i (Fig. 12)

$$d\mathbf{s}_p = d\mathbf{s} - (d\mathbf{s}\cdot\mathbf{e}_a)\mathbf{e}_a, \tag{26}$$

where C_i is the image of C in this plane and $\mathbf{ds}_p$ is the component of **ds** in this plane. From the results of the planar transducer case [Eq. (12)] it follows that in plane P we have

$$d\beta = \frac{1}{r_e}\frac{(\mathbf{e}_r\times\mathbf{e}_a)\cdot d\mathbf{s}_p}{1-(\mathbf{e}_r\cdot\mathbf{e}_a)^2}. \tag{27}$$

Placing Eq. (26) into Eq. (27) then gives

$$d\beta = \frac{1}{r_e}\frac{(\mathbf{e}_r\times\mathbf{e}_a)\cdot[d\mathbf{s}-(d\mathbf{s}\cdot\mathbf{e}_a)\mathbf{e}_a]}{1-(\mathbf{e}_r\cdot\mathbf{e}_a)^2} = \frac{1}{r_e}\frac{(\mathbf{e}_r\times\mathbf{e}_a)\cdot d\mathbf{s}}{1-(\mathbf{e}_r\cdot\mathbf{e}_a)^2}, \tag{28}$$

since $\mathbf{e}_r\times\mathbf{e}_a$ is perpendicular to $\mathbf{e}_a$. This result is also valid for cases 2 and 3, so, using the fact that $\mathbf{e}_a=-\mathbf{n}$ where **n** is the unit normal to the transducer surface, Eq. (25) then becomes

$$p(\mathbf{x},\omega) = \frac{\rho c v_0}{q_0}\left[\Theta\ \exp(ikD) - \frac{1}{2\pi}\int_C \frac{\exp(ikr_e)}{r_e}\frac{(\mathbf{n}\times\mathbf{e}_r)\cdot d\mathbf{s}}{1-(\mathbf{n}\cdot\mathbf{e}_r)^2}\right], \tag{29}$$

which is the generalization of Eq. (13) to the spherically focused case. We could also put this result entirely into a boundary diffraction waveform as before to obtain

$$p(\mathbf{x},\omega) = \frac{-\rho c v_0}{2\pi q_0}\left[\int_{C_r}\frac{\exp(ikr_e)}{r_e}\frac{(\mathbf{n}\times\mathbf{e}_r)\cdot d\mathbf{s}}{1-(\mathbf{n}\cdot\mathbf{e}_r)^2}\right]. \tag{30}$$

We now will use the coordinate invariant form of Eq. (29) to express the edge wave integral in terms of coordinates centered in a plane perpendicular to the central transducer axis (Fig. 13), as done for the planar case. Letting

$$\begin{aligned} d\mathbf{s} &= -a\ \sin\phi\, d\phi\,\mathbf{e}_x + a\ \cos\phi\, d\phi\,\mathbf{e}_y,\\ \mathbf{x} &= (z-h)\mathbf{e}_z + y\mathbf{e}_y,\\ \mathbf{y} &= a\ \cos\phi\,\mathbf{e}_x + a\ \sin\phi\,\mathbf{e}_y, \end{aligned} \tag{31}$$

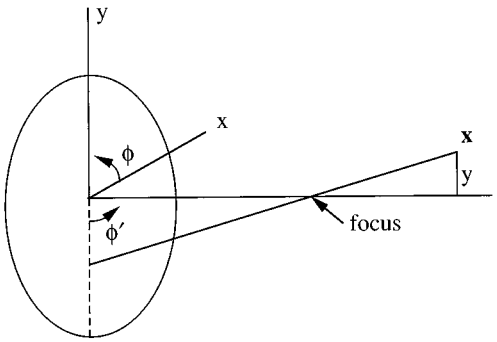

FIG. 14. The relationship between the angle ϕ, measured from the positive x axis, and the angle ϕ', measured from the negative y axis.

where $y=|y|$ for $D>R_0$ and $y=-|y|$ for $D<R_0$, after some considerable algebra one obtains

$$p(y,z,\omega) = \frac{-\rho c v_0}{(d/R_0)}\left\{\Theta\ \exp[ik(R_0+d)] + \frac{a\sqrt{y^2+(z-R_0)^2}}{2\pi}\times\int_0^{2\pi}\frac{\exp(ikr_e)[|y|\sin\phi(h-R_0)-a|z-R_0|]d\phi}{[|y|\sin\phi(h-R_0)-a|z-R_0|]^2+y^2R_0^2\cos^2\phi}\right\} \tag{32}$$

and all the quantities appearing in Eq. (32) are defined in terms of the variables y, z, a, R_0 as follows:

$$\begin{aligned} d &= \begin{cases}\sqrt{(z-R_0)^2+y^2} & D>R_0\\ -\sqrt{(z-R_0)^2+y^2} & D<R_0,\end{cases}\\ r_e &= \sqrt{a^2+y^2-2ay\ \sin\phi+(z-h)^2},\\ h &= R_0-\sqrt{R_0^2-a^2}. \end{aligned} \tag{33}$$

E. Special cases

Equation (32) also reduces to our previous result for the planar case in the limit as $R_0\to\infty$ with y and z fixed since in this limit, we have

$$-d/R_0\to 1,$$

$$R_0+d\to z,$$

$$r_e\to\sqrt{a^2+y^2-2ay\ \sin\phi+z^2},$$

and the edge wave term in Eq. (32) becomes

$$\frac{-a}{2\pi}\int_0^{2\pi}\frac{\exp(ikr_e)[a+|y|\sin\phi]d\phi}{a^2+y^2+2a|y|\sin\phi}.$$

The angle ϕ here is not the same as the angle ψ in the planar case which was measured from the radius in the plane from the center of the transducer to $\mathbf{y}_0$ (Fig. 14) but if we let $\phi=\phi'+3\pi/2$ we have $\sin\phi=\cos\phi'$ so that finally Eq. (32) reduces to

$$p(y,z,\omega)=\rho c\nu_0\left\{\Theta\ \exp(ikz)-1/2\pi \times\int_0^{2\pi}\frac{\exp(ikr_e)a[a-|y|\cos\ \phi']d\phi'}{a^2+y^2-2a|y|\cos\ \phi'}\right\}, \tag{34}$$

with $r_e=\sqrt{a^2+|y|^2-2a|y|\cos\ \phi'+z^2}$ which is identical to Eq. (17) of the planar case if we simply let $\phi'=\psi$ and $|y|=\rho_0$. Note that obtaining Eq. (34) involved a change of limits on ϕ' from $(-3\pi/2,\pi/2)$ to $(0,2\pi)$ which is permissible since

$$\int_\alpha^{2\pi+\alpha} f(\cos\ \phi')d\phi'=\int_0^{2\pi} f(\cos\ \phi')d\phi'$$

for any function f and angle α.

One important special case of Eq. (32) is the expression for the off-axis pressure on a plane passing through the geometrical focus and perpendicular to the transducer central axis. In this plane $\Theta=0$ except at the single point on the axis and $z=R_0$ so that Eq. (32) becomes

$$p(R_0,y,\omega)=\frac{\rho c\nu_0 aR_0}{2\pi y}\int_0^{2\pi}\frac{\sin\ \phi\sqrt{R_0^2-a^2}\ \exp[ik\sqrt{R_0^2+y^2-2ay\ \sin\ \phi}]d\phi}{R_0^2-a^2\ \sin^2\ \phi}, \tag{35}$$

which is an exact result (subject, of course, to the approximations inherent in the O'Neil model). In the paraxial approximation, however, where $R_0\gg y,a$ we find

$$p(R_0,y,\omega)=\frac{\rho c\nu_0 a\ \exp(ik\overline{R_0})}{2\pi y}\int_0^{2\pi}\sin\ \phi \times\exp[-ikay\ \sin\ \phi/\overline{R_0}]d\phi, \tag{36}$$

where $\overline{R_0}=\sqrt{R_0^2+y^2}$ and the integral can be evaluated as a Bessel function to obtain

$$p(R_0,y,\omega)=-i\omega\rho\nu_0 a^2\frac{\exp(ik\overline{R_0})}{\overline{R_0}}\frac{J_1(kay/\overline{R_0})}{(kay/\overline{R_0})}, \tag{37}$$

which was also given by O'Neil.[2]

III. NUMERICAL RESULTS

For a specific example, Eq. (32) was used to calculate the wave field of a 5-MHz, 1/2-in.-diam, 4-in. focal length transducer. Figure 15 shows a full 2-D cross-sectional plot of the magnitude of the normalized pressure, $|p/\rho c\nu_0|$, for this transducer. As can be seen, the direct and edge waves interfere, producing a near-field structure of maxima and minima similar to those seen in the planar case, with the whole pattern being compressed near the focus. The values of the normalized pressure from this plot on the transducer axis are shown in Fig. 16. On the axis, of course, the integral in Eq. (32) can also be done analytically to give the same form obtained by O'Neil:

$$p(z,\omega)=\frac{\rho c\nu_0}{q_0}[\exp(ikz)-\exp(ikr_e)]. \tag{38}$$

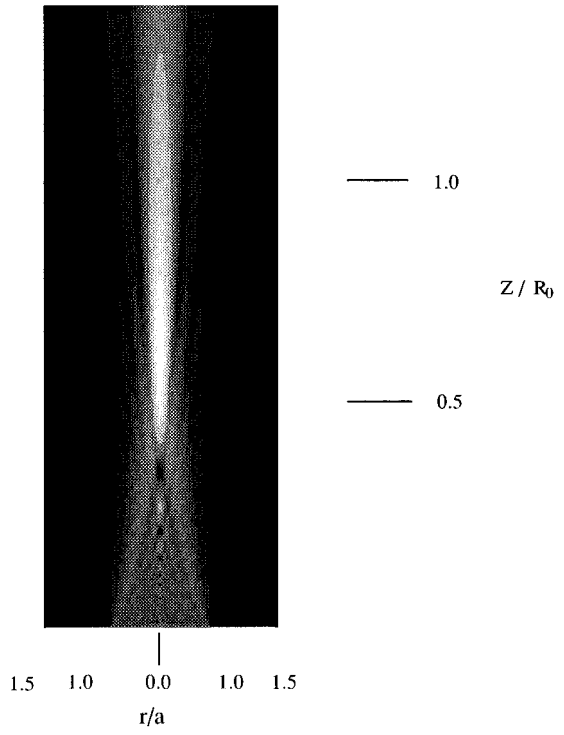

FIG. 15. A two-dimensional cross-sectional plot showing the magnitude of the normalized pressure wave field of a 5-MHz, 1/2-in. diam, 4-in. focal length transducer.

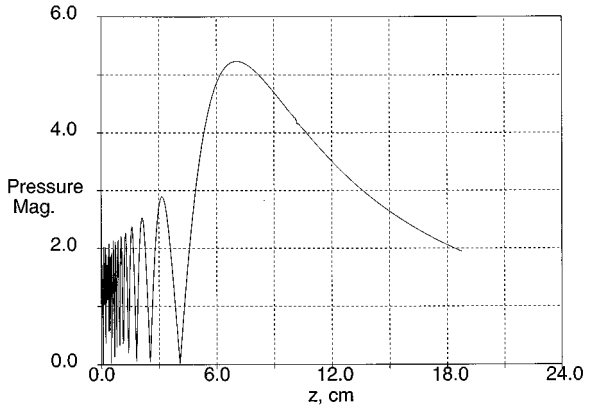

FIG. 16. The magnitude of the normalized pressure versus the on-axis distance for a 5-MHz, 1/2-in.-diam, 4-in. focal length transducer.

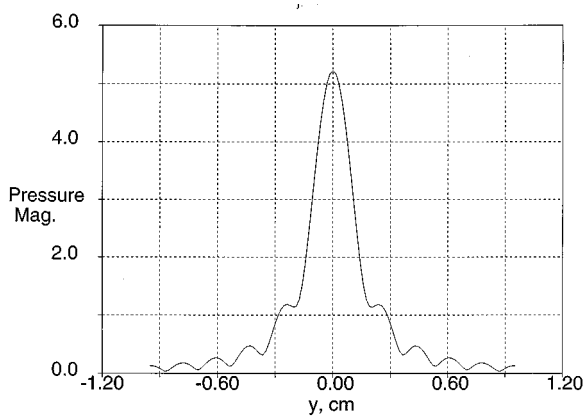

FIG. 17. The magnitude of the normalized pressure versus distance from the transducer axis in a plane perpendicular to the transducer axis at the ''true'' focus (location of maximum on-axis pressure) for a 5-MHz, 1/2-in.-diam, 4-in. focal length transducer.

If we define the true focus position to be where this on-axis response reaches its maximum value, Fig. 16 shows that this location typically occurs closer to the transducer face than the geometrical focus. Figures 17 and 18 also show the magnitude of the normalized pressure distribution across the central axis of the transducer at the axial position of the true focus and the geometrical focus, respectively. While the latter result can be accurately described by Eq. (37), the results at the true focus and all other locations in the transducer wave field must be determined numerically from Eq. (32).

IV. SUMMARY

A model for a spherically focused transducer has been given in terms of boundary diffraction waves. The model is a natural extension of an equivalent form which has been known for some time for the planar transducer and generalizes previously known expressions for special cases (on-axis pressure and the field in the geometrical focal plane) to the entire transducer wave field. The model can be used as an efficient tool for characterizing the sound beam of spherically focused probes.

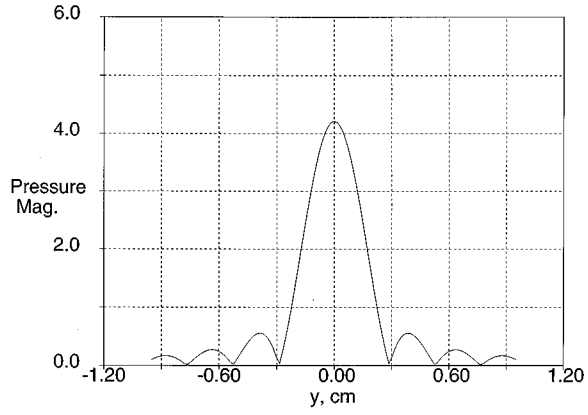

FIG. 18. The magnitude of the normalized pressure versus distance from the transducer axis in a plane perpendicular to the transducer axis at the geometrical focus for a 5-MHz, 1/2-in.-diam, 4-in. focal length transducer.

ACKNOWLEDGMENTS

L. W. Schmerr and T. P. Lerch were supported in this work by the Center for NDE, Iowa State University. A. Sedov has been supported by the Natural Sciences and Engineering Research Council of Canada.

[1] G. R. Harris, ''Review of transient field theory for a baffled planar piston,'' J. Acoust. Soc. Am. **70**, 10–20 (1981).
[2] H. T. O'Neil, ''Theory of focusing radiators,'' J. Acoust. Soc. Am. **21**, 516–526 (1949).
[3] U. Schlengermann, ''Schallfeldausbildung bei ebenen ultraschallquellen mit fokussierenden linsen,'' Acustica **30**, 291–300 (1974).
[4] U. Schlengermann, ''The characterization of focussing ultrasonic transducers by means of single frequency analysis,'' Mater. Eval. **38**, 73–79 (1980).
[5] T. P. Lerch, L. W. Schmerr, and A. Sedov, ''Characterization of spherically focussed transducers using an ultrasonic measurement model approach,'' Research in NDE, **8**, 1–21 (1996) .
[6] M. F. Hamilton, ''Comparison of three transient solutions for the axial pressure in a focused sound beam,'' J. Acoust. Soc. Am. **92**, 527–532 (1992).
[7] F. Coulouvrat, ''Continuous field radiated by a geometrically focused transducer: Numerical investigation and comparison with an approximate model,'' J. Acoust. Soc. Am. **94**, 1663–1675 (1993).
[8] E. L. Madsen, M. M. Goodsitt, and J. A. Zagzebski, ''Continuous waves generated by focused radiators,'' J. Acoust. Soc. Am. **70**, 1508–1517 (1981).
[9] J. A. Archer-Hall and D. Gee, ''A single integral computer method for axisymmetric transducers with various boundary conditions,'' NDT Int. **13**, 95–101 (1980).
[10] D. A. Hutchins and G. Hayward, ''Radiated fields of ultrasonic transducers,'' in *Physical Acoustics: Ultrasonic Measurement Methods*, edited by R. N. Thurston and A. D. Pierce (Academic, New York, 1990), Vol. 19, pp. 1–80.
[11] E. W. Marchand and E. Wolf, ''Boundary diffraction wave in the domain of the Rayleigh-Kirchhoff diffraction theory,'' J. Opt. Soc. Am. **52**, 761–767 (1962).
[12] A. Pennttinen and M. Luukkala, ''The impulse response and pressure nearfield of a curved ultrasonic radiator,'' J. Phys. D **9**, 1547–1557 (1976).
[13] X. Chen, K. Q. Schwarz, and K. J. Parker, ''Radiation pattern of a focused transducer: a numerically convergent solution,'' J. Acoust. Soc. Am. **94**, 2979–2991 (1993).
[14] L. W. Schmerr, A. Sedov, and T. Lerch, ''Modeling the radiation of focused and unfocused ultrasonic transducers through planar interfaces,'' in *Review of Progress in Quantitative Nondestructive Evaluation*, edited by D. O. Thompson and D. E. Chimenti (Plenum, New York, 1995), Vol. 14A, pp. 1061–1066.
[15] A. T. de Hoop, S. Zeroug, and S. Kostek, ''Transient analysis of the transmitting properties of a focused acoustic transducer with an arbitrary rim,'' J. Acoust. Soc. Am. **98**, 1767–1777 (1995).

Time-domain simulation of the influence of close barriers on sound propagation to the environment

D. Botteldooren[a)]
Department of Information Technology, Acoustics Group, University of Gent, St. Pietersnieuwstraat 41, 9000 Gent, Belgium

(Received 8 May 1995; accepted for publication 15 October 1996)

A time-domain numerical model for studying the influence of close barriers on sound levels at a large distance from a source is proposed. It is a combination of a near-field simulation with a near-field to far-field transform based on the Helmholtz–Kirchhof integral. The near-field simulation is based on a finite-difference time-domain type discretization of a well chosen volume around sources and near objects. The numerical accuracy of the model is studied theoretically and experimentally for a particular sound field. The simulation example is a large power station transformer surrounded by barriers. The evaluation of sound levels in the highly multimodal environment is not trivial. It is performed in small frequency bands around the frequency of the typical pure tones emitted by the source. © *1997 Acoustical Society of America.* [S0001-4966(97)06103-1]

PACS numbers: 43.20.Rz, 43.28.Bj, 43.50.Gf [JEG]

INTRODUCTION

For environmental noise prediction the attenuation of sound caused by the screening effect of objects is mostly calculated using semiempirical formulas.[1] Alternatively ray-tracing is often used. These approaches give good results as long as the wavelength corresponding to the main frequency in the sound spectrum is small compared to the size of the screening objects and compared to the typical distance between source and barrier. At low-frequency wave behavior has to be taken into account more accurately. In this paper a model is introduced that is especially appropriate when many screens surround de sound sources. The main interest is in finding sound pressure levels at a large distance. The influence of wind and temperature gradients, ground interaction, and air absorption will not be included in the calculation. The influence of these phenomena on sound propagation can be estimated afterwards using standard calculation procedures.[2]

Previously, other authors have used the boundary element numerical approximation of the frequency domain linear acoustic-wave equations to study the problem described above.[3] In this paper a time-domain simulation is preferred. Time domain has a few interesting advantages. When calculating the influence of close screens on environmental sound propagation, one is interested in the spectral transfer function from the source to a limited number of points at a large distance. A single-frequency calculation is not sufficient even if the source emits a pure tone. One of the reasons for this is that sound velocity can change considerably due to temperature changes for outdoor propagation. This can lead to an important shift of the sharp resonance peaks observed at low frequency. A good design should therefore take into account also the behavior at a frequency close to the frequency of the sound source. It is known that a time-domain simulation can be very efficient for calculating the transfer functions mentioned above. Time domain also allows to study the behavior of sound fields generated by relatively broadband noise sources directly. Finally time-domain models allow to study transient noise phenomena and the influence of moving objects and sources directly.

The time-domain wave equations can be discretized both on the boundaries of the simulation domain (boundary elements) or in the whole domain (finite elements, finite differences, finite volumes). The choice between the two approaches fundamentally depends on efficiency of data storage. In closed or almost closed spaces, containing many boundaries, volume discretization is more efficient. In open space, boundary discretization is clearly more efficient. For the problems at hand typically an almost closed space between sources and barriers is found together with the open radiation space. Therefore a good choice would be to glue a volume discretization to a boundary discretization at a more or less arbitrary closed surface. As it turns out the feedback of the boundary elements on the arbitrary interface is not necessary to obtain a sufficiently accurate model. By neglecting the boundary element feedback storage requirement can be reduced considerably as is the CPU time requirement.

The simulation model introduced in this paper combines a finite-difference time-domain volume discretization in a limited simulation region with a far-field calculation based on the time-domain Kirchhoff–Helmholtz integral theorem.[4] Accuracy seems sufficient for the problems at hand if a simple radiating boundary condition is used to describe free space. The model that is obtained is sufficiently accurate and yet reasonably efficient to make it a useful computer-aided engineering tool for the design of close noise barriers. This paper will focus on the model and its accuracy. A practical example will illustrate the use.

[a)]Electronic mail: dick.botteldooren@intec.rug.ac.be

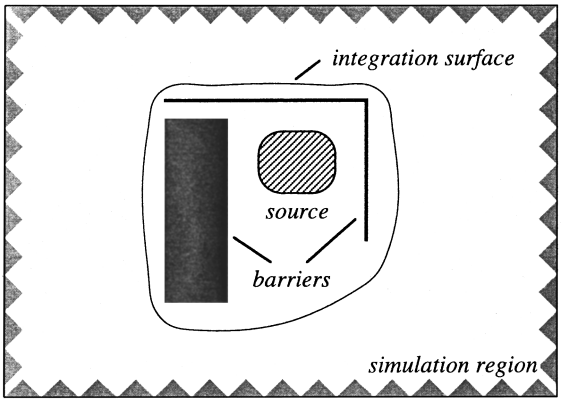

FIG. 1. Illustration of volume discretization region and far-field integration surface.

I. NUMERICAL FORMULATION

As mentioned in the Introduction a time-domain numerical model is used. A simulation region around the sources, surrounding all possible close barriers and buildings is chosen (Fig. 1). In this region a volume discretization of the acoustical wave equations is used. The approach used in this paper is sometimes called a first-order finite-element time-domain technique or a finite-volume time-domain approach. In the special case where a Cartesian grid is used for discretization the method is mostly labeled finite-difference time-domain (FDTD). Henceforth the volume discretization technique will be called FDTD, also if non-Cartesian grid formulations are used. Details on the volume discretization method used in this work can be found elsewhere.[5]

Basic features of the approach are summarized as follows. Sound pressure p and particle velocity $\mathbf{v}$ are both used as unknown variables. The discretization grids for both quantities are staggered in such a way that second-order accuracy in the approximation to the derivatives is guaranteed. Time iteration follows a leap-frog mechanism: pressure is calculated from previous particle velocity values and particle velocity is calculated in turn from previous pressure values. In a Cartesian grid $(\delta x, \delta y, \delta z)$ and with time step δt, the discrete set of unknown quantities is noted $p^{[l]}(i,j,k)$ and $v_x^{[l+0.5]}(i+\frac{1}{2},j,k), v_y^{[l+0.5]}(i,j+\frac{1}{2},k)$, and $v_z^{[l+0.5]}(i,j,k+\frac{1}{2})$. The time iteration is stable as long as the time step δt remains smaller than a stability limit depending on the spatial discretization. Appropriate formulations for sources and material boundary conditions can be found in Refs. 5 and 7. In Ref. 10 the FDTD formulation was extended to include vibrating plates.

The boundary of the volume discretization region should approximate a free-field radiation condition as accurately as possible. Several types of descriptions for the free-radiation condition are used.[6] The most accurate approach takes into account the whole boundary while calculating acoustical field just inside this boundary. However, the drawback of this approach is a large CPU time consumption and a severe memory requirement. In this paper a very simple first-order approach is chosen instead. The radiating boundary is simply described by a boundary impedance equal to $\rho_0 c$, the characteristic impedance in air. The numerical error introduced by this choice is estimated to be of the order of 2 dB as will be demonstrated in Sec. II. The error is more important when sound reaches the boundary at grazing incidence. It introduces larger errors in the numerical sound field near corners of the simulation region and at low frequencies.

From the FDTD simulation described above, sound pressure and particle velocities are obtained in the staggered grid. To calculate the sound pressure $p(\mathbf{r},\tau)$ at a large distance from these data, a direct discretization of the time-domain Kirchhoff–Helmholtz integral is used:[4]

$$p(\mathbf{r},\tau)=\frac{\rho_0}{4\pi}\oint\frac{\partial}{\partial t}\frac{v_n(\mathbf{r}_s,\tau-R/c)}{R}\,dS + \frac{1}{4\pi c}\oint\mathbf{e}_R\cdot\mathbf{n}_s\left(\frac{\partial}{\partial t}+\frac{c}{R}\right)\frac{p(\mathbf{r}_s,\tau-R/c)}{R}\,dS, \quad (1)$$

where the integration is over a closed surface including all sources and scattering obstacles (Fig. 1); $R=|\mathbf{r}-\mathbf{r}_s|$ is the distance from a point $\mathbf{r}_s$ on the integration surface to the point $\mathbf{r}$ at large distance, outside the closed surface; v_n is the component of the particle velocity orthogonal to the integration surface and pointing outward; $\mathbf{e}_R$ is the unit vector $(\mathbf{r}-\mathbf{r}_s)/R$, and $\mathbf{n}_s$ denotes the unit vector, orthogonal to the surface and pointing outward.

First the spatial discretization of (1) is considered. To facilitate this discretization, the closed integration surface is chosen to be built up from parts of grid surfaces for pressure p used in the volume discretization. Because of the staggered grid, particle velocity v is not defined on these grid surfaces. To obtain v_n, a linear interpolation is used.

The time discretization is more complicated. Sound pressure p is known at $t=l\,\delta t$ in the volume discretization schema, while sound particle velocities are known at $t=(l+0.5)\,\delta t$. In the integration (1) these quantities are needed at $t=\tau-R/c$, where R is the distance from the point $\mathbf{r}$ to the integration point $\mathbf{r}_s$. This time changes over the integration surface and generally does not correspond to integer or half-integer multiples of δt. A linear interpolation is again necessary. Time derivatives are approximated using a central finite difference schema.

To simplify the formulations, it is assumed that the volume discretization grid is Cartesian (at least near the integration surface) and that the integration surface is a beam bounded by the planes $x=i_-\delta x$, $x=i_+\delta x$, $y=j_-\delta y$, $y=j_+\delta y$, $z=k_-\delta z$, $z=k_+\delta z$. This leads to the semidiscrete form of Eq. (1):

$$p(\mathbf{r},\tau)=\frac{\rho_0}{4\pi}\left\{\sum_{j,k}\left(\frac{\gamma_{i_+,j,k}\delta y\,\delta z}{2R\,\delta t}\,w_x(i_+,j,k;\mathbf{r};\tau)-\frac{\gamma_{i_-,j,k}\delta y\,\delta z}{2R\,\delta t}\,w_x(i_-,j,k;\mathbf{r};\tau)\right)+\cdots\right\}$$
$$+\frac{1}{4\pi c}\left\{\sum_{j,k}\left(\begin{array}{l}\gamma_{i_+,j,k}R_x\delta y\,\delta z\left\{\dfrac{q_1(i_+,j,k;\mathbf{r};\tau)}{R\,\delta t}+\dfrac{cq_2(i_+,j,k;\mathbf{r};\tau)}{R^2}\right\}\\ -\gamma_{i_-,j,k}R_x\delta y\,\delta z\left\{\dfrac{q_1(i_-,j,k;\mathbf{r};\tau)}{R\,\delta t}+\dfrac{cq_2(i_-,j,k;\mathbf{r};\tau)}{R^2}\right\}\end{array}\right)+\cdots\right\}, \tag{2}$$

where the continuation mark indicates similar terms for the y and z directions; the summation over j and k runs from j_- to j_+ and from k_- to k_+, respectively; R_x is equal to $(x-i_-\delta x)$ or to $(x-i_+\delta x)$. The coefficients $\gamma_{i,j,k}$ are 1 on the surfaces of the beam, 1/2 on the edges, and 1/3 in the corners. In (2) two new sets of variables w and q are introduced. They are defined as

$$\begin{aligned}w_x(i,j,k;\mathbf{r};\tau)=\eta_{l_1}&\{v_x^{[l_1+1.5]}(i-\tfrac{1}{2},j,k)\\&+v_x^{[l_1+1.5]}(i+\tfrac{1}{2},j,k)\}+(1-2\,\eta_{l_1})\\&\times\{v_x^{[l_1+0.5]}(i-\tfrac{1}{2},j,k)+v_x^{[l_1+0.5]}(i+\tfrac{1}{2},j,k)\}\\&-(1-\eta_{l_1})\{v_x^{[l_1-0.5]}(i-\tfrac{1}{2},j,k)\\&+v_x^{[l_1-0.5]}(i+\tfrac{1}{2},j,k)\}\end{aligned} \tag{3}$$

and

$$q_1(i,j,k;\mathbf{r};\tau)=\eta_{l_2}p^{[l_2+1]}(i,j,k)+(1-2\,\eta_{l_2})\times p^{[l_2]}(i,j,k)-(1-\eta_{l_2})p^{[l_2-1]}(i,j,k), \tag{4a}$$

$$q_2(i,j,k;\mathbf{r};\tau)=\eta_{l_1}p^{[l_1+1]}(i,j,k)+(1-\eta_{l_1})p^{[l_1]}(i,j,k), \tag{4b}$$

where the time interpolation is based on l_1 and l_2 as defined in

$$\begin{aligned}&l_1=\mathrm{int}\left[\frac{\tau}{\delta t}-\frac{R}{c\,\delta t}\right];\quad \eta_{l_1}=\frac{\tau}{\delta t}-\frac{R}{c\,\delta t}-l_1,\\&l_2=\mathrm{int}\left[\frac{\tau}{\delta t}-\frac{R}{c\,\delta t}+\frac{1}{2}\right];\eta_{l_2}=\frac{\tau}{\delta t}-\frac{R}{c\,\delta t}+\frac{1}{2}-l_2,\\&R=\sqrt{(x-i\,\delta x)^2+(y-j\,\delta y)^2+(z-k\,\delta z)^2}.\end{aligned} \tag{5}$$

In (5) ''int[ ]'' denotes the integer part of the expression in brackets.

When deriving (2), it was assumed that the pressures and particle velocities are defined in the center of the volume discretization cells. The distance R changes during integration over a grid cell. A more accurate approach could take this into account. It can be seen that this would influence mainly the time variables l_1 and l_2 if the point is located at a large distance.

A possible approach to solve (2) would be to store $p^{[l]}$ and $\mathbf{v}^{[l+0.5]}$ in all grid cells on the closed integration surface for all l and calculate $p(\mathbf{r},\tau)$ after the time simulation. However, this requires a considerable amount of storage. Therefore the summation in (2) is inverted and solved during simulation time stepping. The first step in deriving the inverted procedure is to split the time axes for $p(\mathbf{r},\tau)$ in intervals of length δt, thus obtaining $p(\mathbf{r},m\,\delta t)$. Choosing the time interval equal to the volume simulation time step δt simplifies calculations but is not strictly required. During time iteration of the volume numerical method, values of $p^{[l]}(i,j,k)$ and $\mathbf{v}^{[l+0.5]}(i,j,k)$ are obtained at a certain time $l\,\delta t$. These values contribute to far-field pressure at a future time τ in the summation in (2), because R is assumed constant over the cell. From (2) it can be seen that volume simulation results in a certain grid cell, obtained at time $l\,\delta t$ contribute to far-field pressure at $\tau=(l+0.5)\,\delta t+R/c$, $\tau=l\,\delta t+R/c$, $\tau=(l-0.5)\,\delta t+R/c$, $\tau=(l-1)\,\delta t+R/c$, $\tau=(l-1.5)\,\delta t+R/c$, and $\tau=(l-2)\,\delta t+R/c$. For each of these τ, contributions are added to the corresponding interval m of the far-field time axes.

The length of the far-field pressure array can be limited to the time interval of length $(R_{\max}-R_{\min})/c+3\,\delta t$ where contributions from the closed surface integration can be expected. $R_{\min}$ denotes the shortest distance from the closed surface to $\mathbf{r}$ and $R_{\max}$ denotes the largest distance. Finally, the time interpolation given in Eq. (4) is neglected in the inverted procedure. This corresponds to putting $\eta=0$ in this equation.

II. ACCURACY CONSIDERATIONS

It is very hard to obtain analytical expressions for the numerical accuracy of the calculation schema proposed in this paper. The numerical error is the sum of the numerical error caused by the volume simulation and the numerical error introduced by the far-field integration. The first error includes contributions caused by the FDTD approach itself and inaccuracy in the description of the boundary conditions. All numerical errors tend to interact strongly and depend on the specific near field. In this section some indication of the expected numerical error is obtained from analytical considerations and from a comparison of a simulated far-field pressure of a point source to known results.

When a pure-tone plane-wave traveling in free space, is modeled using FDTD, each time step introduces a numerical error. The amplitude of the pure tone is reconstructed exactly, but a phase error is introduced. For a propagation vector $\mathbf{k}(k_x,k_y,k_z)$, the FDTD phase change φ_{FDTD} per time step δt in a Cartesian grid, relates to the exact value of the phase $\varphi=j\,\omega\,\delta t$ as[7]

$$\frac{\varphi_{\mathrm{FDTD}}}{\varphi}=\frac{2\arcsin\{c\,\delta t\sqrt{\Sigma_\alpha[\sin^2(k_\alpha\delta\alpha/2)/\delta\alpha^2]}\}}{c\;\delta t\sqrt{\Sigma_\alpha k_\alpha^2}}, \tag{6}$$

where the summation index α runs over x, y, and z. The phase error depends quadratically on frequency. It introduces dispersive propagation and changes the waveform of propagating pulses. The phase error also depends on propagation

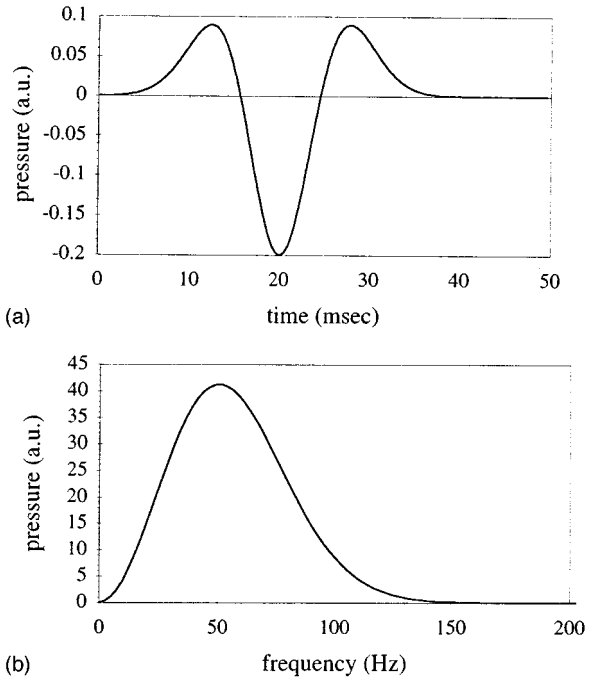

FIG. 2. (a) Source pressure pulse; (b) Source pulse spectrum.

direction. In a Cartesian grid, it is smaller for propagation in the (1,1,1) direction. The phase error also increases when δt decreases below the stability limit. In many applications of FDTD, the phase error is not as important as an amplitude error. However, in calculating the far-field integral (2), phase errors can be translated into amplitude errors because interacting sound waves propagate a different distance in the FDTD-simulation region where the numerical phase error is introduced and a different distance outside the integration surface, where no phase error is introduced.

A second source of numerical error is the poor description of the radiating boundary condition. For the applications described in this paper a boundary impedance $Z=\rho_0 c$ is used. Especially near edges and corners of the simulation region this introduces an important error. The frequency dependency of the inaccuracy can be estimated from a second-order approximation as proposed in Ref. 8. The boundary impedance corresponding to this second-order approximation is given by

$$Z=\frac{\rho_0 c}{1-\kappa c/2\, j\omega}, \tag{7}$$

where κ is the curvature of the surface. When the curvature is high compared to the wavelength of the sound, this impedance differs considerably from $\rho_0 c$. Since the error originates at edges, destructive and constructive interference can occur near certain points in the volume simulation region. At a given point in the simulation region, an error that is oscillating as a function of frequency and increasing at low frequency, is expected.

The numerical error introduced by using the discrete approximation in Eq. (2) to the exact equation (1) is of the order of magnitude of the errors introduced by the volume discretization. However, this numerical error does not accumulate during time simulation and is therefore not an important contribution to the total numerical error.

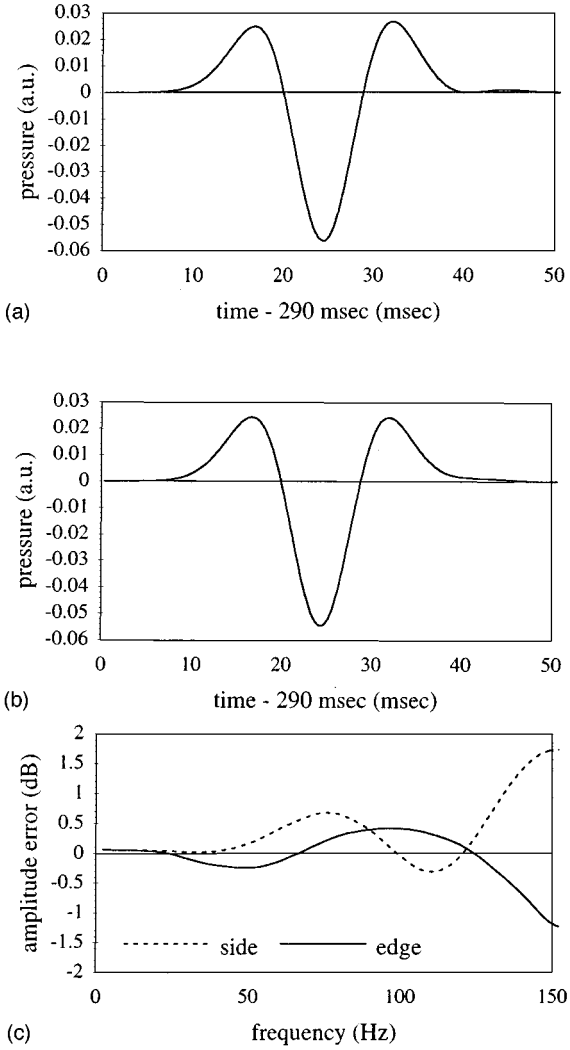

FIG. 3. Pressure pulse 100 m from the source in direction of edge of the integration surface (a) and in direction of a side (b); (c) corresponding spectral amplitude error.

To evaluate the global numerical error introduced by the proposed model, the far-field sound pressure generated by a point source is simulated. The volume discretization region is a square box with a side of 10 m. A Cartesian square grid (0.2 m, 0.2 m, 0.2 m) is used for the FDTD discretization and the integration surface is a 4-m square box around the source. In the center of the box a pressure pulse is added to the initially quiet environment. The pressure pulse and the corresponding spectrum are shown in Fig. 2. The sound pressure is calculated at 100-m distance from the source using the numerical method described in this paper. Figure 3(a) and (b) shows the pulse observed at this distance in the direction orthogonal to the side of the box and in the direction of the edge of the box. In Fig. 3(a) and (b) the influence of numerical dispersion is clearly observed. Since numerical error is expected to be frequency dependent, it is shown as a function of frequency in Fig. 3(c). The error increases with frequency up to about 2 dB at 150 Hz. The upper frequency

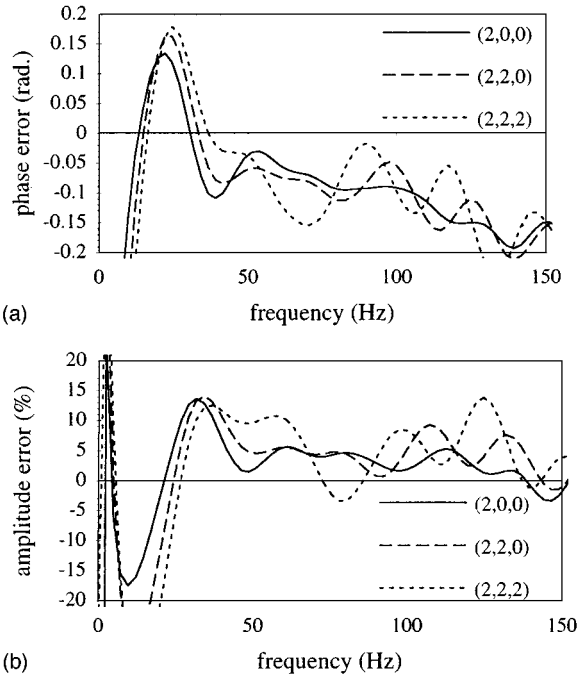

FIG. 4. Phase (a) and relative amplitude (b) numerical error due to the FDTD approximation observed at three places along the cubic integration surface of 4-m side.

limit is choosen 150 Hz since this is a practical upper limit for accurate FDTD simulations in this grid. The influence of several parameters of the simulation on the numerical error was investigated. Some of the conclusions are summarized in the rest of this section.

The numerical error is a combination of the FDTD inaccuracy and the inaccuracy in solving (2). To evaluate the FDTD part of the error, the numerical error on the simulated pressure at three positions on the integration surface is plotted in Fig. 4. Both amplitude and phase errors are shown. The oscillating behavior is due to the inaccuracy in the description of the radiating boundary condition. The increase at low frequency is believed to be caused mainly by the poor description of the radiating boundary condition in the corners of the simulation region. The increase in phase error at high frequency due to the FDTD discretization itself is only slightly observable below 150 Hz. As predicted theoretically, this error depends on direction and is not pronounced in the amplitude. A comparison of this near-field error to the far-field numerical error of Fig. 3(c) shows that errors attributed to the poor boundary condition seem to average out in the far-field integration. The typical oscillating behavior is indeed not observed. It is expected that the FDTD-discretization phase error in combination with the numerical integration causes most of the high-frequency error in the far field.

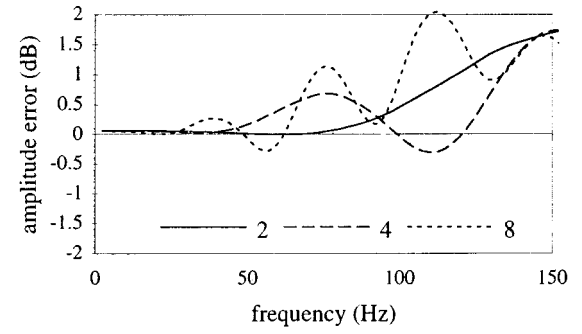

FIG. 5. Amplitude numerical error on the simulated pressure at 100-m distance for three sizes of the cubic integration surface.

The choice of the integration surface influences the far-field numerical error considerably. This is illustrated in Fig. 5. Square boxes with side 2 m, 4 m, and 8 m are used as integration surfaces. The larger box causes a larger numerical error, that is oscillating with frequency more rapidly. The oscillation period in the error is proportional to the size of the integration surface. This behavior is explained by an increasing phase error between different contributions to the integration, when sound waves propagate further in the volume discretization region. If the near sound field is focused on a smaller part of the integration surface, the far field is expected to be obtained more accurately.

To confirm the above conclusions on the cause of the far-field numerical error, the spatial discretization step is changed. Increasing the discretization to (0.4 m, 0.4 m, 0.4 m) cells causes the numerical error to increase by a factor of 2 in most of the frequency range of interest. If the integration surface is not changed the oscillation period in the error does not change. Reducing the time discretization step δt below the stability limit increases the numerical error slightly. This is consistent with the fact that the FDTD-discretization phase error given in Eq. (6) increases more slowly with decreasing δt than with increasing δx, δy, and δz.

It should be kept in mind that the considerations in this section on numerical error introduced by the model used in this paper, only apply to a limited number of special cases. The results provide, however, useful guidelines for estimating the numerical error in more complicated examples as the one described below.

III. EXAMPLE

As an example the study of the low-frequency noise emitted by a power station transformer is described. The existing transformer and the close noise barriers surrounding it are shown in Fig. 6. The direction of critical environmental noise observation points is also indicated. These points are located at a distance of 500 m from the transformer. Experimental data on the existing situation are scarce. Specific noise levels due to the transformer cannot be identified in the observation points because other noise sources in the power station also contribute at exactly the same frequency. Near-field intensity measurements can only be performed along the sides of the transformer and not above it because of security risks related to the high voltages. The sound powers obtained from intensity measurements are not very accurate because the pure tones emitted at low frequency make the near-field vector intensity spatial distribution strongly fluctuating.

The purpose of the part of the study used as an example in this paper was to try to relate far-field sound pressure levels at 50 Hz and at 100 Hz to the measured near-field sound power emitted from the open side of the transformer

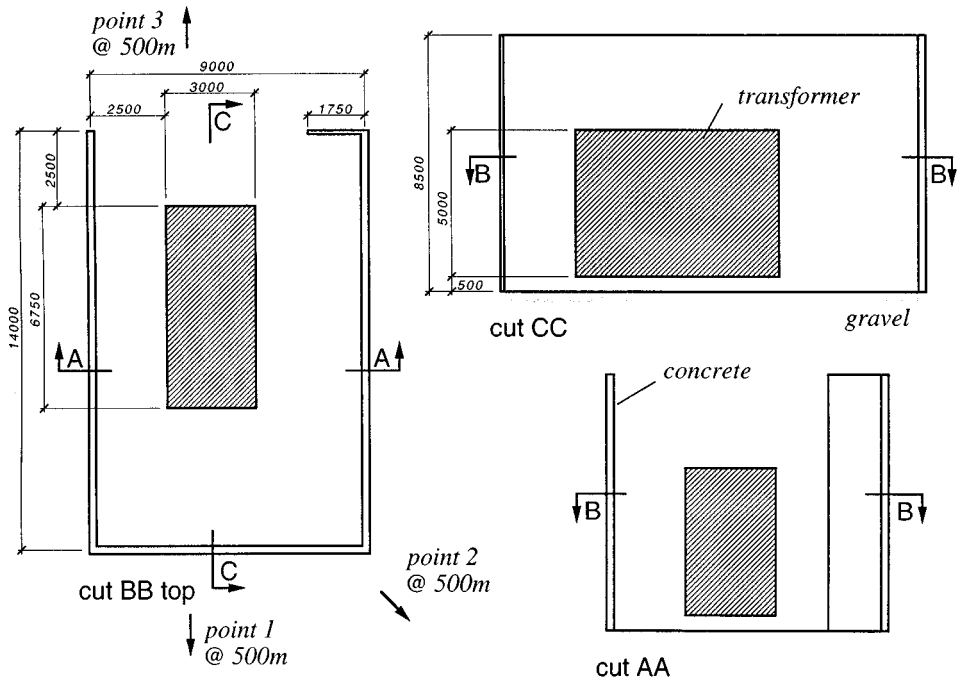

FIG. 6. Layout of the transformer and surrounding barriers used as a calculation example.

box. The influence at higher frequency is calculated using high-frequency approximations. A numerical model of the transformer and its near surrounding can be found that is sufficiently accurate to relate near-field partial power to far-field sound pressure level. It is, however, impossible to predict power levels directly without going into much greater detail of the construction of the transformer. The model will allow to estimate the influence of possible changes to the close surroundings on specific emission in the observation points. Influence of ground impedance, air absorption, wind and temperature gradients are not included in this calculation. These influences can be added afterwards based on international guidelines.

The volume discretization uses a Cartesian grid with cells (0.2 m, 0.2 m, 0.2 m). The structure in Fig. 6 is discretized. The source is represented by vibrating side panels of the transformer. Air loading of these panels is neglected. For calculating near pressure and intensity field distributions, sinusoidal excitation of these panels is used. In the context of this paper only pulse excitation of the form $v(t)=(t-t_0)\exp[-(t-t_0)^2/\sigma]$ is used. Resulting far-field pressure pulses are then transformed to frequency domain using FFT. Other excitations such as recorded signals could also be useful.

The sound power propagating through the front opening is used as a reference to relate simulations to measurements, as described above. To calculate this sound power the orthogonal component of the vector intensity can be summed over all grid cells in the opening and integrated in time.[9] This accurate method for obtaining the power can only be used for specific time signals. It is also useful for predicting the vector intensity distribution and helping to understand measurement results. Spectral sound power can be obtained more efficiently, but less accurately, by adding sound intensity spectra in a limited number (12) of observation points in the opening. The intensity spectra are obtained from pulse response as described above. Figure 7 shows the difference between spectral intensity level L_{IS} through the front opening and plate excitation velocity level. Various resonances can be observed.

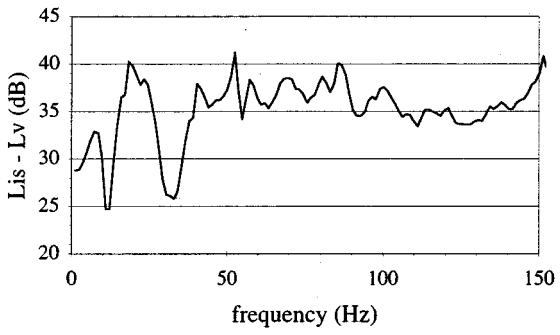

FIG. 7. Difference between the level of the sound intensity emitted through the side opening of the box surrounding the transformer and the transformer surface velocity level.

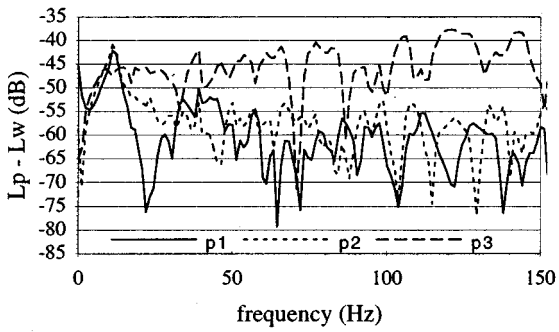

FIG. 8. Spectral difference between sound pressure level at the observation points p1, p2, and p3 and the sound power emitted through the side opening.

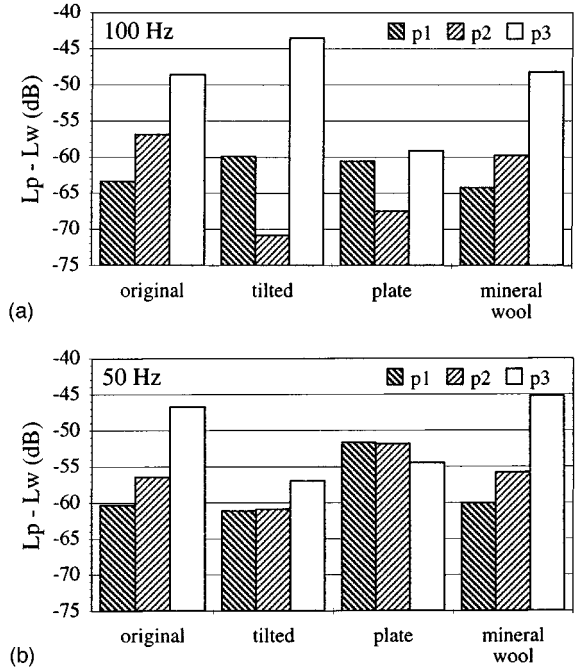

FIG. 9. Difference between sound pressure level in the observation points and sound power emitted through the side opening for the four situations described in the text: (a) in a 5-Hz band around 100 Hz, (b) in a 5-Hz band around 50 Hz.

Given the frequency considered and the dimension of the structure involved, a highly multimodal behavior of the sound pressure is expected. The calculated attenuation spectra in Fig. 8 are indeed very peaked, which confirms this expectation. Although the transformer emits pure tonal sound at low frequency, the sharp spectral peaks around a source frequency cannot be used for the prediction of sound pressure levels. One of the reasons for this is that the frequency of the resonances is determined by a typical ratio of structure dimension to wavelength and not by the frequency itself. When the speed of sound changes the resonance peaks shift. An expectable temperature change from 0° to 30 °C roughly corresponds to a frequency shift of 5 Hz around the frequency of interest. Instead of changing the speed of sound and recalculating expected immission at 50 and 100 Hz, it is preferred to look at immission in a 5-Hz frequency band around this frequency for a given speed of sound. The result is expected to be similar. The quantity to be studied is the average sound level in this frequency band or the maximum level, dependent on the design strategy. By averaging over the frequency band, the influence of small spectral shifts caused by the numerical phase error is also reduced.

As an illustration of the numerical method, immission levels in the three evaluation points at 500 m distance are given in Fig. 9 for four possible construction changes of the barriers:

(1) the original structure;
(2) the wall in the direction of the second immission point is tilted by 10°;
(3) the vertical opening is closed with a 2 mm steel plate;
(4) the concrete walls are covered with a thin layer of mineral wool.

To implement the absorption of the concrete wall and the mineral wool layer, a boundary impedance is used as described in Ref. 7. The approximate impedance corresponding to concrete is $Z=18\,000+8e6/j\omega$. The impedance of the mineral wool layer is approximated by $Z=600+3e6/j\omega$. To implement the transmission behavior of the steel plate, a FDTD approximation of the linear equations describing the behavior of a thin bending plate is used. Details on the implementation are described elsewhere.[10]

Some of the effects seen in Fig. 9 could be expected. The influence of tilting one of the parallel walls in the direction of observation point 2, clearly reduces sound levels in that direction. Some increase in sound levels in the other directions is expectable. The important decrease of immission in the 50-Hz band in the observation point 1, which is in the direction of the vertical opening, can only be explained by taking into account wave behavior accurately. The metal plate covering the vertical opening, clearly reduces immission in the direction of points 2 and 3. An increase, which is caused by reflection on the plate, can be expected in point 1. Only the 50-Hz immission in point 2 does not behave as expected from this basic knowledge. The absorbing material influences immission less than could be expected at first sight. However, changes in absorption coefficient are very small at the low frequency considered and the phase shift that is introduced in the boundary material can cause changes that are difficult to predict.

The attenuation in Fig. 9, which is labeled original, was also compared to sound levels obtained by ray-tracing. The commercial model that was used,[11] allowed to include an approximate description of diffraction at the edges and interference. When interference is omitted the commercial ray-tracing model gives noise levels that are typically 2 to 8 dB lower. Including interference in the ray-tracing model does not give usable results. It seems the ray-tracing interference is calculated for the central frequency of the octave bands and thus behaves as abruptly as can be expected from Fig. 8.

IV. CONCLUSIONS

A numerical model for calculating the influence of close noise barriers on sound emission to the environment is introduced. The time-domain simulation is based on a volume discretization in the source and barrier region and on a numerical evaluation of the far-field pressure from the Kirchhoff–Helmholtz integral. The accuracy of this approach is sufficient for environmental noise prediction and for the evaluation of the impact of changes in the barrier construction. Yet the model is efficient enough to be run on a modern workstation. The example studied is a large power station transformer surrounded by noise barriers. To take into account external influences on sound propagation such as temperature changes, the sound spectra are averaged over small spectral bands. The influence of construction changes on the immission in three points at 500-m distance at 50 and 100 Hz is predicted.

ACKNOWLEDGMENT

Dr. D. Botteldooren is a senior research assistant with the Belgian National Fund for Scientific Research (NFWO).

[1] G. S. Anderson and U. J. Kurze, ''Outdoor sound propagation,'' in *Noise and Vibration Control Engineering*, edited by L. L. Beranek and I. L. Vér (Wiley, New York, 1992).
[2] ISO/DIS 9613-2, ''Attenuation of sound during propagation outdoors'' (ISO, Geneva, 1992).
[3] H. Antes, in *Boundary Element Methods in Acoustics*, edited by R. D. Ciskowski and C. A. Brebbia (Elsevier, London, 1991).
[4] A. D. Pierce, *Acoustics* (McGraw-Hill, New York, 1981).
[5] D. Botteldooren, ''Acoustical Finite Difference Time Domain Simulation in a Quasi-Cartesian Grid,'' J. Acoust. Soc. Am. **95**, 2313–2319 (1994).
[6] K. S. Kunz and R. J. Luebbers, *The Finite Difference Time Domain Method for Electromagnetics* (CRC, Boca Raton, FL, 1993).
[7] D. Botteldooren, ''FDTD-Simulation of low-frequency room acoustic problems,'' J. Acoust. Soc. Am. **98**, 3302–3308 (1995).
[8] L. F. Kallivokas and J. Bielak, ''Time-domain analyses of transient structural acoustics problems based on the finite element method and a novel absorbing boundary element,'' J. Acoust. Soc. Am. **94**, 3480–3492 (1993).
[9] D. Botteldooren, ''FDTD-Study of the Influence of Close Noise Barriers on Sound Propagation,'' accepted for ICA '95, Trondheim, Norway.
[10] D. Botteldooren, ''Finite Difference Time Domain Study of Acoustical Cavities with Vibrating Plate Boundaries,'' Proc. Internoise 93 (Leuven), 1577–1581 (1993).
[11] *Raynoise* (NIT, Leuven, Belgium).

Lamb waves in piezoelectric focused radiator as a reason for discrepancy between O'Neil's formula and experiment

D. Cathignol
INSERM, Unité 281, 151 Cours Albert Thomas, 69424 Lyon Cedex 03, France

O. A. Sapozhnikov
Department of Acoustics, Physics Faculty, Moscow State University, Moscow 119899, Russia

J. Zhang
Bâtiment 502, GEMPPM, INSA de Lyon, 69621 Villeurbanne, France

(Received 20 December 1995; revised 17 September 1996; accepted 18 September 1996)

One of the well-known methods of ultrasound focusing is the use of a transducer having the form of a concave spherical cap. In the theoretical analysis O'Neil's formula is widely used, which describes acoustic pressure on the axis of the transducer under the assumption that normal velocity of its surface is uniform. Usually, it is believed that modern piezoelectric focused sources are very close to this theoretical model. The paper presented describes results of experimental investigation which showed that there exists a significant disagreement between the observed acoustic field and that predicted by the theory of O'Neil. Two types of measurements have been made to clarify this problem. The acoustic pressure field of a focused piezoceramic transducer (with aperture diameter of 100 mm, radius of curvature of 100 mm, resonance frequency of 1 MHz) has been measured in a water tank using a miniature hydrophone. In addition, the radiator surface vibration has been studied in air using an optical interferometric technique. Theoretical analysis and the measurements show that the disagreement between the theory and the experiment is due to Lamb waves, which originate at the radiator edge, propagate along the piezoceramic plate without significant attenuation, and thus radiate additional acoustic perturbations. © *1997 Acoustical Society of America.* [S0001-4966(97)05003-0]

PACS numbers: 43.20.Rz, 43.20.Bi, 43.20.Px, 43.38.Fx [JEG]

INTRODUCTION

Focused acoustic fields are extensively used in various applications, the best known examples being medicine, acoustical microscopy, and nondestructive techniques. One of the effective methods of focusing is to employ a transducer in the form of a concave spherical cap. No exact theory exists describing acoustic field of such curved radiators. Widely used is the Rayleigh integral approach, which is a mathematical formulation of Huygens' principle. This theory is exact for planar radiators mounted in an infinite rigid baffle, but for curved transducers it is only an approximation due to secondary diffraction and boundary effects. Using the Rayleigh integral as the base, Williams[1] and O'Neil[2] considered the focused radiator in the form of an axisymmetric spherical cap with uniform distribution of normal velocity on its surface. The result of O'Neil[2] was a solution for acoustic pressure along the transducer axis. More recently, similar solutions were obtained using other approximations,[3] but it is unlikely that they are more exact than the O'Neil solution. O'Neil's formula is quite attractive for its simplicity:

$$p = \frac{p_0 e^{-i\omega t}}{1 - z/F}\,(e^{ikz} - e^{ikR_{\max}}), \tag{1}$$

where p is axial acoustic pressure, $p_0 = \rho c u_0$, u_0 is the normal velocity amplitude on the radiator surface, ρ and c are the density and sound velocity of the medium, ω is the frequency, $k = \omega/c$ is the wave number, z is the distance along the axis, F is radius of the radiator curvature, $R_{\max} = F\sqrt{1 + (1 - z/F)^2 - 2(1 - z/F)\cos\alpha_{\max}}$ is the distance between observation point and the radiator edge, where $\alpha_{\max}$ is the half-aperture angle of the radiator.

Modern piezoceramic focused sources are usually very close to the acoustic source of the O'Neil model. Indeed, the shape of the ceramic cap can be made spherical with high accuracy. The piezoelectric parameters of the radiator plate can be made fairly uniform, so it may be hoped that its vibration is also uniform.

Numerous measurements have been performed with spherical focused sources, which confirmed qualitatively the validity of Eq. (1). Several experiments have been carried out to verify O'Neil's formula quantitatively.[4–8] It appeared that pressure distribution in the focal plane was similar to its theoretical representation. But, as far as the axial pressure field is concerned, the discrepancy between formula (1) and experiment was noticeable. Specifically, instead of theoretical zeros of pressure [see Eq. (1)] only local minima were observed; levels of local maxima differed from their theoretical values and extrema coordinates were also different. Two explanations of this discordance are possible. It may be thought that it is caused by the approximate nature of the Rayleigh integral. Another explanation deals with peculiarities of the experiment: A realistic radiator may not be entirely adequate for its theoretical model.

An important feature of acoustic source which is supposed in theoretical papers[1,2] is the uniformity of the normal velocity distribution along the radiator surface. It is to be

noted that piezoelectric radiators are assumed to vibrate uniformly not only in Refs. 1 and 2, but in the majority of papers associated with computing of acoustic radiation pattern of such transducers. This seems to be fairly reasonable, especially when the piezoceramic plate thickness is much smaller than its diameter. Indeed in this case, an applied electrical field, being normal to the radiator surface, mainly excites the thickness vibrational mode, which corresponds to the uniform (''pistonlike'') velocity distribution.

Some experimental work has been performed to verify the piston model. To do this, plane circular piezoelectric radiators were tested in pulsed regime.[9–15] The on-axis field has been usually employed for comparison of theory and experiment because of its simple theoretical presentation. According to the theory, the pressure signal consists of two time-separated components: One represents the plane wave from the radiator surface (''direct wave''); another is associated with acoustic perturbations coming from the radiator edge (''edge wave''). However, in the measurements of the ultrasonic radiation performed with the hydrophone probe and Schlieren systems, anomalous behavior has been found: Apart from the direct and edge waves, additional pulses were observed. This extra radiation, generally referred to as ''head wave'' and not predicted by the piston model, has been attributed to radiation from some elastic waves traveling along the faces of transducers. On thick plates, this wave exhibited the characteristics of a surface wave (Rayleigh type),[9,11,12] while on thin plates it exhibited those of a plate wave (Lamb type).[10,13–15] These elastic waves originate at the radiator rim, where a nonuniformity of the driving electric field and corresponding piezoelectric stress exist.

It is to be noted, that all papers mentioned[9–15] are on plane transducers. The effect of Lamb waves in a focused source has not been studied yet. Some new peculiarities may appear here because of possible focusing of the head waves.

The role of Lamb waves for continuously excited piezoceramic transducers has not been investigated to the same extent as that for pulsed sources. We are familiar only with experiments on this point with small piezoceramic elements, when the transversal dimensions of the radiator were comparable with its thickness.[16] The measurements demonstrated severe deviations from the piston theory predictions, consisting mainly in the occurrence of parasitic sidelobes in the radiation pattern. It was shown that these lobes were due to parasitic zero-order Lamb waves propagating in the transducer and radiating into the fluid medium. If the piezoceramic plate diameter is many times higher than its thickness, the Lamb waves may seem to be negligible as compared with the usual piston vibrational mode. Indeed, the thickness oscillation in a piezoelectric transducer is usually a resonant one, whereas the Lamb waves are not (the corresponding resonance frequency is very low). Moreover, the thickness mode is excited at the entire transducer volume, while the Lamb wave sources occupy a very small volume near the radiator rim. On the other hand, an acoustic field under continuous excitation is Fourier transform of the corresponding pulse response. Therefore, the effect of Lamb waves in pulsed regime, observed by authors of Refs. 9–15, may be also noticeable under continuous excitation.

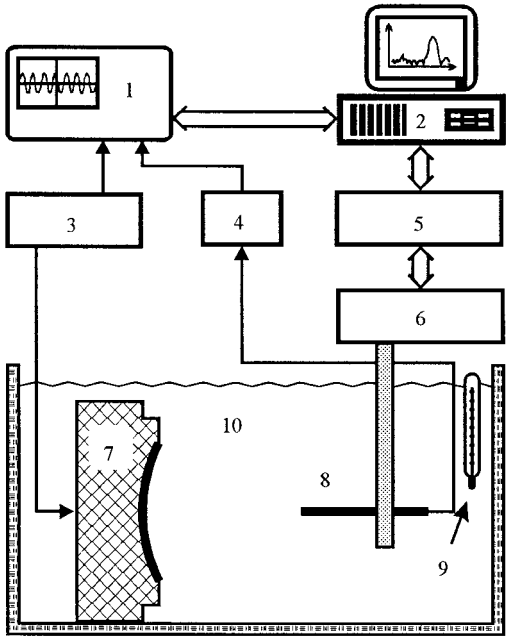

FIG. 1. The experimental design for acoustic pressure measuring in water. 1: Oscilloscope; 2: computer; 3: pulse generator; 4: preamplifier; 5: stepper controller; 6: x-y-z micropositioning system; 7: focused transducer; 8: needle hydrophone; 9: thermometer; and 10: water tank.

This paper presents results of an experimental and theoretical investigation of Lamb wave effect on acoustic field radiated by focused piezoceramic transducer, both in pulsed and continuous regimes. The acoustic pressure pattern of a focused radiator has been measured in a water tank using a miniature hydrophone (Sec. I). Noticeable deviations from the expression (1) have been detected. Theoretical analysis of the leaky waves is performed in Sec. II, which explains the peculiarities of the acoustical experiment. In addition, the radiator surface vibration has been studied with the help of an optical interferometer. The corresponding results are described in Sec. III, showing that Lamb waves do exist in the piezoceramic plate.

I. ACOUSTICAL MEASUREMENTS

A. Experimental apparatus

The experimental design is shown in Fig. 1. A focused transducer was placed in a $0.75\times0.6\times0.5$-m water tank filled with degassed and distilled water. The transducer was driven with pulse bursts over a frequency range 0.6–1.4 MHz using an 8116A Hewlett–Packard generator. The pressure field was sampled by a needle hydrophone with a 0.25-mm active element diameter [Specialty Engineering Associates (SEA), PZTZ44]. The hydrophone was connected to an oscilloscope (Tektronix 2430A) via a preamplifier (SEA, A17DB). An x-y-z micropositioning system was used to move the hydrophone in three orthogonal directions with an accuracy of 0.01 mm (Micro-Controle, France). This system was controlled by an IBM/PC486 computer with the help of a stepper controller. The computer was used also to record the hydrophone signal transferred from the oscilloscope.

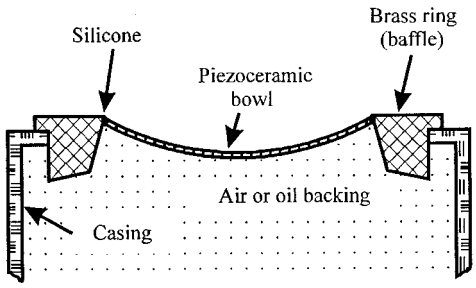

FIG. 2. The transducer mounting.

The transducer mounting is depicted in Fig. 2. The radiator was a spherical cap made from PZT P1-60 piezoelectric ceramics, with a curvature radius of $F=100$ mm and an aperture diameter also of $d=100$ mm (Quartz & Silice, France). The mechanical resonance frequency of the air-backed transducer was 1 MHz. The bowl was flush-mounted in a thick brass ring, which acted as a rigid baffle. A gap of 0.2 mm between this ring and the bowl side wall was filled with silicone cement. The walls of the brass ring were made nonparallel to avoid possible resonances in it. The casing of the transducer was a hermetic box filled with air or oil. A transformer was used to match electrically the tone burst generator and the radiator.

B. Experimental procedure

To verify expression (1), one needs a precise positioning of the hydrophone on the radiator axis, henceforth referred to as an acoustical axis. To do this, the following procedure was used.

(1) The axis of radiator symmetry was oriented approximately along the z axis of the micropositioning system (we refer to this as a mechanical axis henceforth).
(2) Pressure distribution was measured along the mechanical axis. This curve had a lot of maxima and minima and looked like the corresponding O'Neil curve (1).
(3) Two points on the z axis were chosen, with coordinates z_1 and z_2. One corresponded to some pressure maximum near the radiator, another to a pressure maximum near the focal point. Pressure amplitude distributions were measured near the axis in two x-y planes $z=z_1$ and $z=z_2$ with spatial resolution of 0.1 mm. The equipressure curves in each plane were drawn in the monitor screen. They typically had a circular form: This was indicative of good axial symmetry of the radiator. As the mechanical axis differed from the acoustical one, the centers of the equipressure circles were not usually positioned at the origin of the x-y plane, i.e., they had nonzero coordinates.
(4) These coordinates (x_1,y_1) and (x_2,y_2) were determined for each plane with an accuracy of about 0.1 mm, which was much less than wavelength $\lambda\approx 1.5$ mm. Therefore, by this strategy, the coordinates (x_1,y_1,z_1) and (x_2,y_2,z_2) of two points of the acoustical axis were found, i.e., the position of the whole axis became known.
(5) Special software then enabled the hydrophone to be scanned along this axis.

As the hydrophone displacement along the axis was determined by the micropositioning system with high accuracy, to find the hydrophone position with respect to the radiator it was sufficient to measure the distance between the receiver and the transmitter only at one point on the axis. This was done by measuring the time passing between the tone burst front emission and reception, and using the value of the sound velocity at the temperature of water. The accuracy of this measurement was better than 0.3 mm.

To simulate continuous wave (cw) behavior, a gated sine wave was used to drive the transducer. The gate of the oscilloscope was adjusted so as to sample the signal after cw behavior had been established, but before any reflections had returned from possible reflectors (a mounting of the hydrophone, back sides of the tank, etc.). The peak-to-peak hydrophone voltage was used to characterize the acoustic pressure amplitude.

C. Possible weak points of the experimental apparatus and their verification

To test the validity of the O'Neil formula (1), experimental conditions need to be very close to the theoretical model. Some questions might come to mind about the properties of the radiator, the medium, and the hydrophone.

It will be recalled that (a) the radiator should be a spherical one, and (b) the normal velocity distribution on its surface should be uniform. Numerical calculations on the basis of the Rayleigh integral showed that even slight nonsphericity of the radiator surface resulted in a significant perturbation of the axial acoustic pressure. This is why the shape of the bowl was specially tested: Coordinates of about 600 uniformly distributed points of the radiator surface were measured (SMV, France). It appeared that all of these points lay with an accuracy of 10 μ on the same sphere of 100-mm radius. More difficult was to verify the uniformity of normal velocity distribution. No direct methods exist to measure a surface velocity in liquid in continuous regime. The bowl we used was previously tested in pulsed regime,[8] pulse amplitude distribution along the radiator surface appeared to be very uniform.

Nonlinear acoustical effects in water could also influence the pressure field. To avoid this, the voltage applied to the transducer was kept fairly low. The pressure amplitudes near the radiator surface were less than 0.1 bar, which is well below those required to yield significant nonlinear effects.[17] No deviations from sinusoidal waveforms were observed on the oscilloscope.

The signal of the hydrophone necessarily included variations from the actual pressure because of the fact that it was not a perfect point receiver. To be sure that the hydrophone spatial resolution was high enough, we measured its directivity pattern at 0.5, 1, and 2 MHz. No nonuniformity of this pattern was noticed up to the directivity angle of 90°; i.e., the effective diameter of the hydrophone was much less than the wavelength. This allowed us to measure the pressure with sufficient resolution.

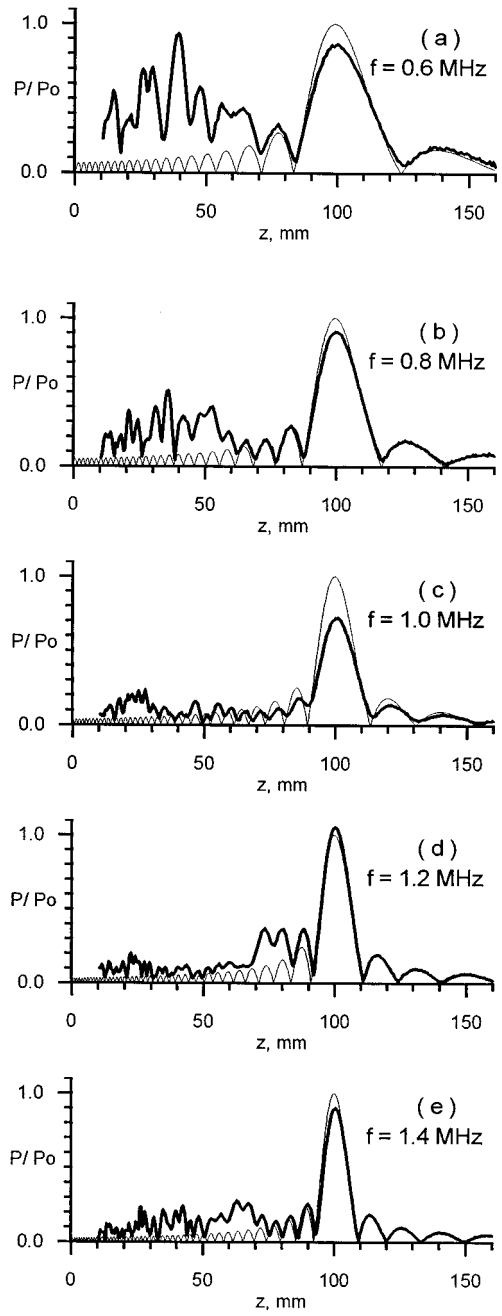

FIG. 3. Experimental results for pressure amplitude distribution along the axis of transducer symmetry (thick lines), compared with the corresponding results of the O'Neil theory (thin lines). The pressure amplitude P is normalized by its theoretical maximum P_0. Curves (a)–(e) correspond to different frequency values $f=0.6$–1.4 MHz.

D. Experimental results for continuous waves

Axial distribution of the sinusoidal wave amplitude was measured over the axial distance z range of 10 mm$\leqslant z\leqslant$160 mm at various frequencies. Some typical curves are plotted in Fig. 3(a)–(e) by thick lines. The thin lines in each figure correspond to the theoretical O'Neil expression (1). Acoustic pressure amplitude is normalized by its initial value p_0. To do this, the associated hydrophone signal was normalized by its corresponding initial value U_0. The measurement of U_0 was taken in a pulsed regime (see Sec. I E).

From Fig. 3 the following can be concluded:

(1) Severe frequency-dependent discrepancy between the experiment and the O'Neil theory is observed at distances $z<F$. Additional peaks are observed, some as large as the usual focal peak (see, for example, the curve of 0.6 MHz).
(2) If the axial coordinate z is approximately equal to or greater than the geometrical focal length F, the measured curves differ little from the theoretical ones for all frequencies, excepting those close to the resonance frequency 1 MHz.
(3) If the frequency is of approximately resonance one, the measuring curves in the focal region are greatly distorted. The theoretical zeros of the acoustic pressure are not observed in the experiment.

This clearly demonstrates that the acoustic field radiated from actual focused sources differs from that associated with the O'Neil formula (1). In some cases, however, this discrepancy is very slight. As an example, Fig. 4 presents the structure of the acoustic pressure field measured at 0.8 MHz (thick lines: the experiment, thin lines: O'Neil theory). All curves are normalized by the maximum amplitude $p_{\max}$. Figure 4(a) shows the axial amplitude distribution near the geometrical focal point. The two curves accord very closely. The agreement between the theory and experiment is even better for transversal distribution at the focal plane [see Fig. 4(b)]. The thin curve here is plotted on the basis of corresponding expression from the O'Neil paper:[2]

$$p/p_{\max}=(2/\zeta)\sum_{n=0}^{\infty}(-1)^n(h/a)^{2n}J_{2n+1}(\zeta),$$

$$\zeta=(1-i/kx)\cdot ka\ \sin\theta\approx ka\ \sin\theta,$$

where $h=F(1-\cos\alpha_{\max})$ is the depth of the concave surface, $a=F\sin\alpha_{\max}$ is the radiator radius, x is the distance between the observation point and the center of the focused source, θ is the angle between the radiator axis and the direction of observation, $J_{2n+1}(\zeta)$ is a Bessel function. This series converge very rapidly, so only the first term is usually used. The second term is also accounted in Fig. 4(b), though the corresponding correction is very small.

The same measurements as described above have been performed when the radiator was oil-backed. No noticeable difference in the results has been detected.

E. Measurements in pulsed regime

To gain greater insight into why Eq. (1) does not account for the experiment, in addition to the described experiments, the axial acoustic signal was examined in the pulsed regime. In doing this, the transducer was excited by voltage pulse of duration 0.5 μs. The hydrophone response was measured at various distances. Figure 5 describes the corresponding results for $z=10$ mm. The curve of Fig. 5(a) presents the voltage pulse applied to the radiator. Figure 5(c) shows the hydrophone signal. It consists of two time separated parts. The former looks like a damped transient oscillation. The latter part of the signal is more irregular. Figure 6 shows analogous signals at $z=15$, 20, and 25 mm. The measurements show that the front pulse has the same waveform at all

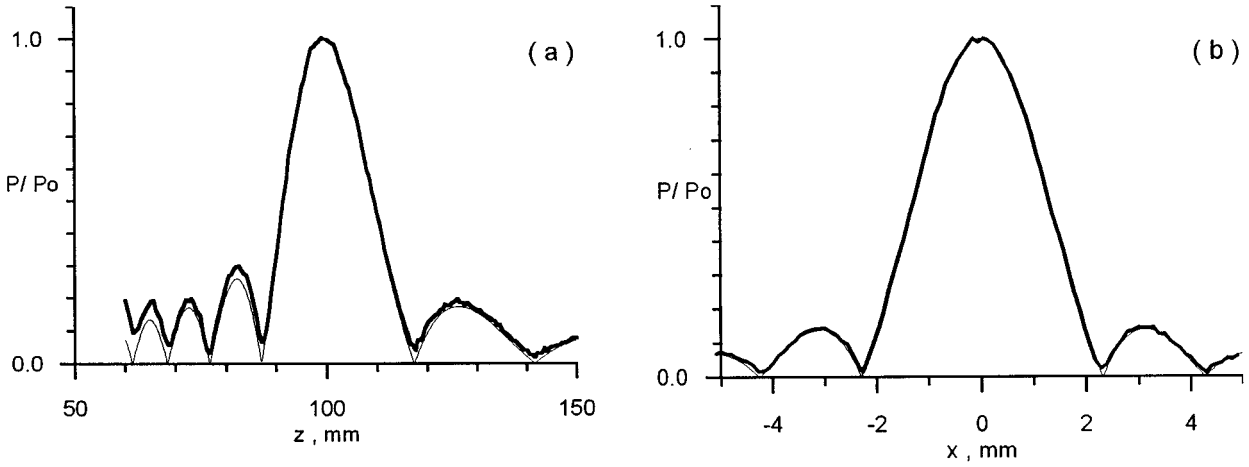

FIG. 4. Acoustic field pattern at $f=0.8$ MHz (thick lines: the experiment; thin lines: the theory). (a) Axial distribution, (b) transversal distribution in the focal plane ($z=100$ mm). In the latter case, the theoretical and the experimental curves are difficult to distinguish. The pressure amplitude P for each curve is normalized by its own maximum $P_{\max}$.

distances, the oscillation frequency is equal to the resonance frequency of the radiator, the number of oscillation periods is approximately given by the quality factor ($Q\approx 10$) of the transducer, the peak pressure of this pulse p_+ depends on the distance as $p_+(z)=\text{const}/(1-z/F)$, and its front always appears at the moment $t=z/c$. All this means is that the first part of the hydrophone signal describes the direct (spherical) wave. According to the O'Neil formula (1), the direct wave should be followed by the edge wave, which is a delayed inverted replica of the direct one. It is to be noted also that the edge wave arrival time should be $t=R_{\max}/c$. This predicted structure of the hydrophone response is plotted in Fig. 5(b). The direct wave is shown by a thick line, the edge wave by a thin one. When this result is compared with that of Fig. 5(c), it is apparent that there are some significant distinctions

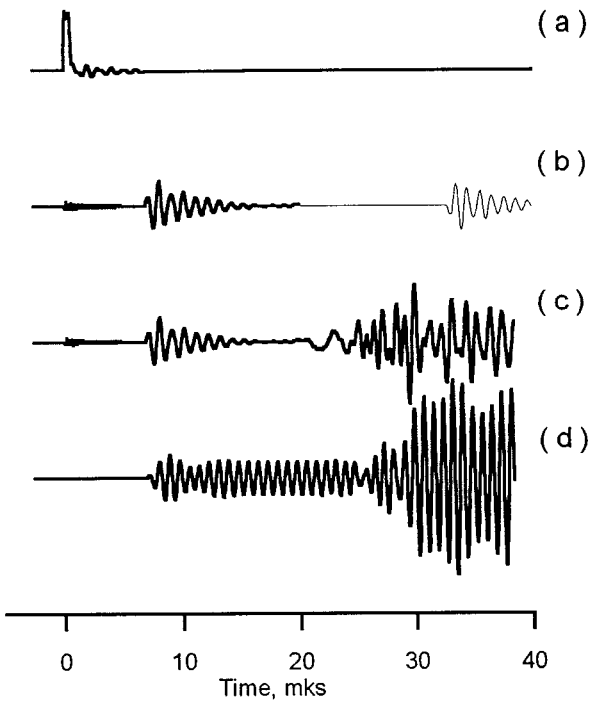

FIG. 5. Waveforms in transient regime at $z=10$ mm: (a) voltage applied to the transducer in pulsed regime; (b) the initial part of the hydrophone signal in pulsed regime (thick line) combined with its delayed inverted replica (thin line), the total curve corresponds to the O'Neil theory; (c) the hydrophone signal in pulsed regime; (d) the hydrophone signal associated with sinusoidal transducer excitation starting at time $t=0$. As is seen from the waveform (c), the curve (d) at time interval 15 μs$<t<$20 μs presents the direct wave in continuous regime.

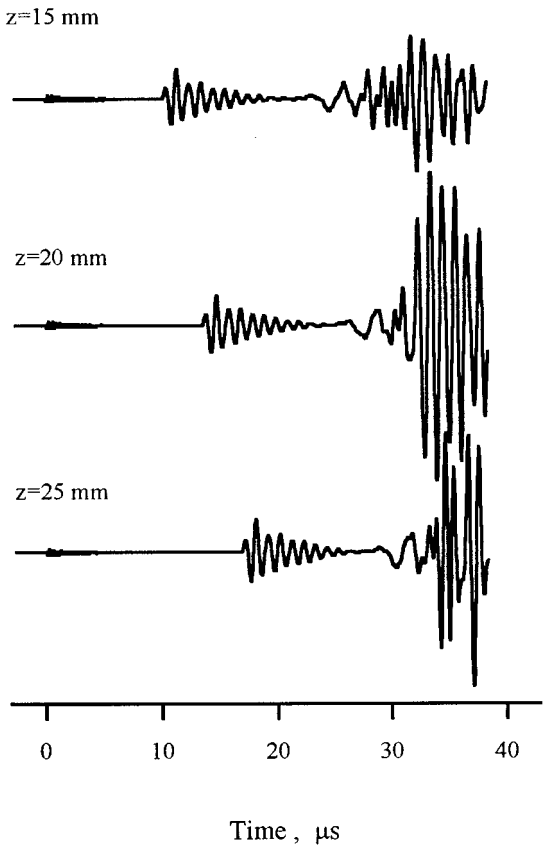

FIG. 6. Hydrophone signal in pulsed regime [the same as in Fig. 5(c)] at different distances z. The weak signal starting at $t=0$ is due to electrical coupling between the radiator and the hydrophone.

between the theoretical and the experimental wave profiles (see also Fig. 6): (a) the experimental ''edge'' perturbation appears much earlier than predicted; (b) in the experiment ''edge'' wave peak-to-peak value is much higher than that of the direct wave, whereas in theory they are equal; (c) observed ''edge'' perturbation has a fairly complicated waveform with frequency modulation inside it, with its front consisting of low-frequency oscillations. The peculiarity (a) means that the experimental ''edge'' wave is not in fact the edge one. It originates from some source situated closer (as compared with the edge) to the axis. The properties (b) and (c) signify that this source is frequency dependent. This conclusion followed also from the measurements in continuous regime (see the previous section).

An important by-product of the transient pressure measurements is the possibility of deducing a value of the hydrophone signal corresponding to pressure $p_0=\rho c u_0$, which enters into the O'Neil formula (1). One can see that p_0 is, in fact, the direct-wave amplitude on the radiator surface. It cannot be measured in the continuous regime as the direct wave always interferes with the edge one. On the other hand, under pulsed excitation, these two waves are time separated; i.e., there exists a time interval, when the direct pulse has passed but the edge pulse has not reached the hydrophone. In Fig. 5(c) this is 15 μs$<t<$20 μs. According to the general properties of linear systems, only the direct wave should exist at the mentioned time interval, with the transient process finished here. This is confirmed by the experiment [Fig. 5(d)]. Consequently, the hydrophone signal U_d corresponding to the direct-wave amplitude at a given distance z can be easily measured with high accuracy. The hydrophone signal U_0 associated with pressure p_0 can then be calculated from value U_d by the expression $U_0=U_d\cdot(1-z/F)$. The experimental curves of Fig. 3 have been plotted using the value of U_0 measured by the method described.

II. THEORETICAL ANALYSIS OF THE TRANSDUCER BEHAVIOR IN VIEW OF LAMB WAVES

According to Sec. I C, the experimental situation seemed to be very close to that of the O'Neil model. However, the significant disagreement observed between the measurement and the theory indicates that some factor was not taken into account in the theory. As was discussed in Introduction, this may be Lamb wave traveling along the transducer face. In this section, the effect of Lamb waves on the acoustic field of the focusing source is considered theoretically.

A. The effect of Lamb waves in continuous regime

Lamb waves are guided elastic perturbations propagating in solid plates with soft faces. As is usually the case with waveguides, different modes may propagate. Some of them are primary shear and others are primary longitudinal, but both components are involved in satisfying the boundary conditions on the surfaces of the plate. The dispersion of Lamb wave velocity may be studied using the well-known Rayleigh–Lamb equation.[18,19] Reference 20 gives the dispersion curves for the five lowest-order modes propagating in a PZT-4 ceramics, whose physical properties are very similar

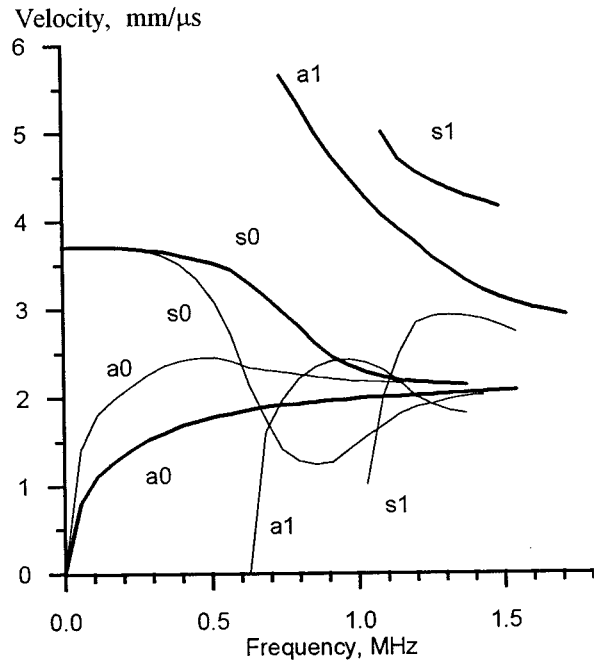

FIG. 7. Dispersion curves for different Lamb modes. Thick lines correspond to the phase velocity, thin lines to the group velocity.

to those of the P1-60 type ceramics used in our experiments.[16] The corresponding phase and group velocities for the piezoceramic plate under investigation are plotted in Fig. 7 against the frequency. When considering Lamb waves, distinction is made between symmetrical (s_n) and antisymmetrical (a_n) modes, where n is a non-negative integer, known as the order of the mode. At low frequencies, only two Lamb waves s_0 and a_0 can exist, representing quasilongitudinal and flexural waves, respectively. The former is similar to an ordinary longitudinal wave, but some transversal displacement takes place and the wave velocity is slightly lower than that of the longitudinal wave c_1. The flexural wave a_0 is much slower. With the increase of frequency, the phase velocities of these two modes become equal to the Rayleigh wave velocity c_R. Unlike the zeroth-order modes, the higher-order modes s_1, a_1, s_2, a_2, etc., can propagate in the plate only if the frequency exceeds some corresponding critical values. For very large frequencies, their phase velocities tend to those of transverse bulk c_t. In the case of the radiator, the external plate face has a mechanical contact with water which should perturb the Lamb wave propagation. But, owing to severe mechanical impedance mismatch between the ceramics ($Z=32\times10^6$ kg/m^2 s) and water ($Z=1.5\times10^6$ kg/m^2 s), the induced change in the phase velocity is negligible.

More important is the reverse process of the plate wave influence on the surrounding liquid. It can be seen that if the Lamb wave phase velocity $c_{\rm ph}$ exceeds the speed of sound in water c, this wave becomes a leaky wave, i.e., acoustic signals are generated into the liquid. The corresponding acoustic pressure field p_L can be calculated on the basis of the Rayleigh integral:

$$p_L=\rho c\,\frac{ik}{2\pi}\int u_L\,\frac{e^{ikR}}{R}\,dS, \tag{2}$$

where ρ and c are density and sound velocity of water, $k=\omega/c$ is a wave number, the integral is taken along the radiator surface, u_L is the surface normal velocity, R is a distance between an observation point and a surface element dS. One can write for the velocity u_L: $u_L=u_L^{(0)}\cdot\exp(ik_L\xi-\delta\xi)\cdot G(\xi)$, where $u_L^{(0)}$ is the normal velocity at the radiator edge, ξ is a distance from the edge in the direction of radiator center, $k_L=\omega/c_{\rm ph}$ is Lamb wave number, δ is the Lamb wave dissipation factor, G is a geometrical factor accounting for Lamb wave convergence. Only the converging wave is allowed for here, as the Lamb wave propagating outward from the center does not radiate leaky waves in the direction of the radiator axis. Let α be an angle coordinate of surface point in the spherical coordinate system with its origin at the center of the radiator curvature. The $\xi=F(\alpha_{\max}-\alpha)$ and $G=\sin\alpha_{\max}/\sin\alpha$, where F is a radius of the radiator curvature. In addition, on the axis one has

$$R=F\sqrt{1+(1-z/F)^2-2(1-z/F)\cos\alpha}.$$

The Rayleigh integral (2) then gives

$$p_L=\rho c u_L^{(0)}\cdot ikF\,\sin\alpha_{\max}\cdot\int_0^{\alpha_{\max}}d\alpha\,\frac{\exp(ikF\alpha_{\max}\sin\varphi-\delta F\alpha_{\max}+\delta F\alpha+ikF\cdot\Phi(\alpha))}{\sqrt{1+(1-z/F)^2-2(1-z/F)\cos\alpha}},$$

where

$$\Phi(\alpha)=\sqrt{1+(1-z/F)^2-2(1-z/F)\cos\alpha}-\alpha\cdot\sin\varphi,$$

φ is the Snell–Descartes angle: $\varphi=\arcsin(c/c_{\rm ph})$.

The easiest to express from this is the pressure p_L at the center of the radiator curvature:

$$p_L(z=F)=\rho c u_L^{(0)}\cdot ikF\,\sin\alpha_{\max}\cdot[\exp(ikF\alpha_{\max}\sin\varphi-\delta F\alpha_{\max})-1]/(ikF\,\sin\varphi-\delta F).$$

It is interesting to compare an amplification factor $K_L=|p_L|/(\rho c u_L^{(0)})$ with an amplification factor for the focused radiator with uniform velocity distribution:

$$K=\frac{|p(z=F)|}{\rho c u_0}=kF(1-\cos\alpha_{\max}); \tag{3}$$

the latter expression follows from O'Neil formula (1).[2] If, say, $\varphi=\delta=0$, then $K_L/K=\alpha_{\max}\mathrm{ctg}(\alpha_{\max}/2)\approx 2$. More difficult is to calculate the axial pressure field at $0<z<F$. As $kF\gg 1$, it is possible to use the method of stationary phase for asymptotic evaluation of the integral. The stationary phase angle $\alpha=\alpha_{\rm st}$ is found from an equation $\Phi'(\alpha_{\rm st})=0$, which gives

$$\alpha_{\rm st}=\arccos[(\sin^2\varphi+\cos\varphi\sqrt{(1-z/F)^2-\sin^2\varphi})/(1-z/F)]$$

or, alternatively, $z=F(1-\sin\varphi/\sin(\varphi+\alpha_{\rm st}))$. Simple geometrical consideration shows that surface point with an angle coordinate $\alpha_{\rm st}$ emits an acoustic wave in the direction of an observation point with a coordinate z exactly at the Snell–Descartes angle φ. If $\varphi+\alpha_{\rm st}>\pi/2$, two stationary phase angles $\alpha_{\rm st}^{(1)}$ and $\alpha_{\rm st}^{(2)}=\pi-2\varphi-\alpha_{\rm st}^{(1)}$ exit for the corresponding observation point. Following the method of stationary phase, an expression for the acoustic pressure modulus can be obtained:

$$|p_L|\approx D\cdot\frac{\rho c u_L^{(0)}\cdot\sqrt{2\pi kF}\cdot\sin\alpha_{\max}\cdot\exp(\delta F\alpha_{st}-\delta F\alpha_{\max})}{\sqrt{\cos\varphi\cdot\sqrt{(1-z/F)^2-\sin^2\varphi}\cdot|\sqrt{(1-z/F)^2-\sin^2\varphi}-\cos\varphi|}}. \tag{4}$$

Here, factor D depends on z, φ, and $\alpha_{\max}$. If $\varphi<\pi/2-\alpha_{\max}$, then $D=1$ for $0<z<z_1$, $D=2$ for $z_1<z<z_2$, and $D=0$ for $z>z_2$; if $\varphi>\pi/2-\alpha_{\max}$, then $D=1$ for $0<z<z_1$, $D=0$ for $z>z_1$, where $z_1=F\cdot[1-\sin\varphi/\sin(\varphi+\alpha_{\max})]$ and $z_2=F\cdot(1-\sin\varphi)$. It can be seen from Eq. (4) that acoustic pressure increases indefinitely when $z\to z_0=0$ and $z\to z_2$, which is meaningless. The problem at $z=z_0$ is associated with misuse of the geometrical approximation for Lamb waves near the radiator center. As for the infinity of pressure at the point $z=z_2$, it appears because of $\Phi''(\alpha_{\rm st})=0$, which shows that the use of the form of the stationary phase method is incorrect in this case. The next order of approximation of the method gives a finite value for the pressure amplitude at the point $z=z_2$:

$$|p_L(z_2)|\approx\rho c u_L^{(0)}\cdot\sin\alpha_{\max}\cdot\frac{2\pi(kF)^{2/3}\cdot\exp\left[-\delta F\left(\alpha_{\max}+\varphi-\frac{\pi}{2}\right)\right]}{\cos\varphi\cdot(-1/3)!}\cdot\left(\frac{2}{9\sin\varphi}\right)^{1/3}, \tag{5}$$

where $(-1/3)!=\Gamma(2/3)=1.354...$. Note that the point $z=z_2$ is unattainable if $\varphi<\pi/2-\alpha_{\max}$ as the singularity lies off the

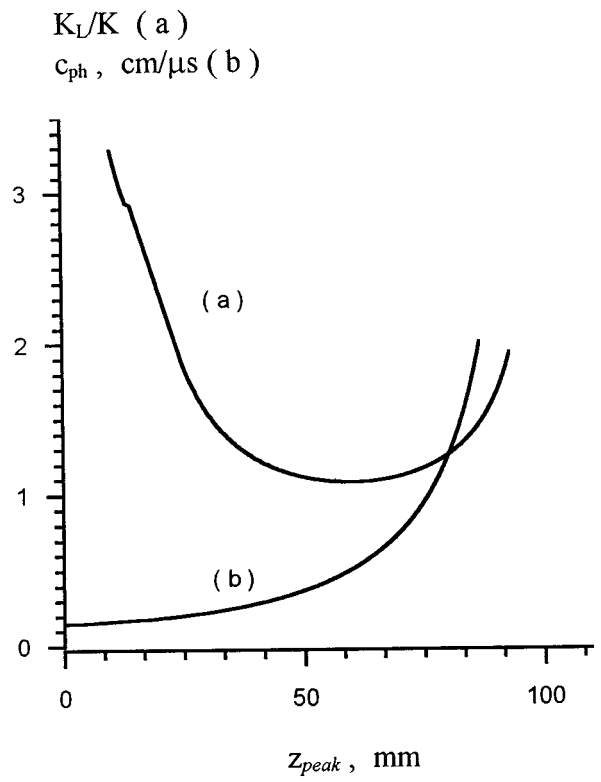

FIG. 8. On the theoretical explanation of peculiarities of experimental axial pressure distribution (see Fig. 3). Curve (a) presents the ratio K_L/K vs the peak position, where K_L is the amplification factor for Lamb waves, and K the amplification factor for the pistonlike focused source. Curve (b) shows Lamb wave phase velocity vs z_{peak}.

region $\alpha_{\text{st}}<\alpha_{\max}$. In this case, the peak of the pressure corresponds to an equality $\alpha_{\text{st}}=\alpha_{\max}$. The net result is the following expression for axial pressure peak p_{peak} and its coordinate z_{peak}: If $\varphi>\pi/2-\alpha_{\max}$, then $z_{\text{peak}}=z_2$ and $p_{\text{peak}}=|p_L(z_2)|$ from Eq. (5); if $\varphi<\pi/2-\alpha_{\max}$, then $z_{\text{peak}}=z_1$ and $p_{\text{peak}}=|p_L(z_1)|$ from Eq. (4) with $D=1$, $\alpha=\alpha_{\text{st}}$.

Let us compare the maximum value of the amplification factor $K_L=p_{\text{peak}}/(\rho c u_L^{(0)})$ and the factor K of Eq. (3). Figure 8(a) shows a ratio K_L/K as a function of the peak coordinate z_{peak} at 1 MHz. The factor δ is supposed to be negligible. The corresponding value of the Lamb wave phase velocity c_{ph} is also plotted in this figure by the curve (b). Note that the ratio K_L/K is always greater than unity. Hence, acoustic waves emitted by Lamb vibrational mode are amplified on the axis even better than those radiated by the thickness vibrational mode, especially at small distances. The inclusion of Lamb wave decay will not noticeably change this result unless wave frequency is not very close to a critical frequency: severe impedance mismatch between the ceramics and the water causes the factor $\delta F\alpha_{\max}$ to be small. Note also that according to Eqs. (3)–(5), the ratio K_L/K increases with decreasing frequency. Figure 8 shows that the difference between the O'Neil theory and the experiment (Fig. 3) may be explained if Lamb waves cause a change of about 10% in surface normal velocity at the edge of the radiator.

The curve (b) in Fig. 8 depicts Lamb wave phase velocity c_{ph} vs z_{peak}. Together with Fig. 7, it allows one to consider how the peak coordinate z_{peak} depends on frequency. Several peaks can exist according to the number of Lamb modes excited. The experimental frequency range 0.6 MHz$\leqslant f\leqslant$1.4 MHz is of interest. The mode a_0 there has a nearly constant phase velocity of about 2 mm/μs. The corresponding value of z_{peak} is 25 mm. This peak has been actually observed at all frequencies (see Fig. 3). The mode s_0 changes its phase velocity from 3.5 mm/μs at $f=0.6$ MHz to 2 mm/μs at $f=1.4$ MHz, so z_{peak} should change from 48 to 25 mm. This peculiarity is also seen in Fig. 3. The antisymmetrical mode a_1 is excited at $f>0.6$ MHz, its velocity at 0.6 MHz$<f<$0.8 MHz is rather high, so the corresponding peak should be situated near the focal point $z=F$. Experimental curves of Fig. 3, however, are not disturbed there. Consequently, the mode a_1 radiates very weak, if any, acoustic waves into water. This is no surprise, since this mode appears at its critical frequency as a standing shear wave with zero surface normal velocity. The last of the possible Lamb modes is the symmetrical one s_1. It exists starting from thickness resonance $f=1$ MHz, where its phase velocity tends to infinity. The O'Neil curve at this frequency is really disturbed near the focal point, whereas at lower frequencies it is not (Fig. 3). It is particularly remarkable also that the corresponding experimental peak is shifted in the direction of the radiator when frequency increases. This is in accordance with theoretical decrease of s_1 mode phase velocity.

B. The analysis of the transient axial pressure signal

The radiator behavior in pulsed regime is rather complex; however, one of the important parameters of the transient acoustic field on the radiator axis can be analyzed in a simple manner. This is an arrival time t_{fr} of the ''head wave'' front. The path of this signal consists of two parts: The signal originates at the radiator rim, then propagates along the piezoceramic plate with a velocity c_*, and, after that, it travels through water with sound velocity c. If so, the corresponding arrival time can be written as $t=\xi/c_*+R/c$, where $\xi=F(\alpha_{\max}-\alpha)$ is the signal path length in the piezoceramic plate, R is the path length in water, and α an angle coordinate of the radiator point from where the acoustic wave in water is originated; we use here the same notations as in Sec. II A. The value of time t depends on the angle α. The acoustic pulse front is associated with the fastest signal, so the corresponding angle α_* is found from the condition $t'(\alpha_*)=0$. It can readily be seen that it is the same as the condition $\Phi'(\alpha_{\text{st}})=0$ from the previous section, if only α_{st} is replaced by α_*. Therefore, the leaky wave corresponding to the signal front is radiated at Snell–Descartes angle $\varphi=\arcsin(c/c_{\text{ph}})$. The arrival time takes the form

$$\frac{ct_{fr}}{F}=\cos\varphi-\sqrt{\left(1-\frac{z}{F}\right)^2-\sin^2\varphi}+\sin\varphi\cdot\left\{\alpha_{\max}-\arccos\left[\frac{\sin^2\varphi}{1-z/F}+\cos\varphi\sqrt{1-\frac{\sin^2\varphi}{(1-z/F)^2}}\right]\right\}.$$

Figure 9 shows the z dependence of the arrival time t_{fr} for different values of plate-wave velocity c_* together with corresponding experimental points (crosses). It can be seen that the experimental arrival time corresponds to the velocity c_*

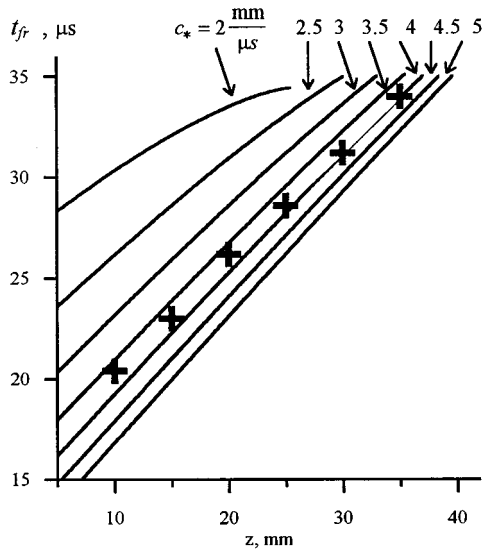

FIG. 9. Theoretical z dependence of the arrival time t_{fr} for different values of Lamb wavefront velocity c_*, compared with corresponding experimental results (crosses).

lying in the range from 3.5 to 4 mm/μs. This velocity is in a sense a maximum signal velocity in the piezoceramic plate, i.e., it should be of about the maximum group velocity of plate waves. According to Fig. 7, $c_*=3.7$ mm/μs (group velocity of the mode s_0 at low frequencies), which is in good agreement with Fig. 9.

The fact that the low-frequency Lamb wave s_0 is the fastest one also explains another peculiarity of the transient signal noted in Sec. I E: the experimental pressure waveform is frequency modulated, with its front consisting of low-frequency oscillations (see Fig. 6).

The theoretical results of this section give an insight into why there is a discrepancy between the O'Neil theory and experiment. All measured peculiarities of the axial pressure field are attributable to a nonuniformity in normal velocity distribution on the radiator surface. This nonuniformity results from Lamb waves originating at the radiator edge and propagating along the piezoceramic plate to its center.

III. OPTICAL INTERFEROMETRIC DETECTION OF LAMB WAVES

The theoretical analysis made in the previous section seems to be sufficient to account for all peculiarities of the acoustical measurements. However, it may be decided that this way of explanation has little force, as only secondary effects of Lamb waves were shown to be in agreement with measurements. The existence of Lamb waves in the radiator in such an approach was, in fact, an hypothesis. To be certain that Lamb waves do travel along the radiator, additional experiments on direct observation of these waves have been performed using a laser interferometric vibrometer.

A. Experimental setup

As has been seen from the Rayleigh integral (2), detection of normal velocity of the radiator surface is of particular interest. Normal displacement can be measured using optical interferometry. As well as the direct and absolute measurements, this method offers high resolution, both spatial (0.1 mm) and temporal (10^{-8} s). The idea of the technique is to measure the phase difference between a fixed reference beam and an optical beam which has been reflected from the surface under study. For small displacements (10 nm or less), the output signal of the interferometer varies linearly with the value of the surface displacement. The method is widely used in studies of surface vibration in air. But, unfortunately, a problem exists when the surface is immersed in a liquid, as is the case of the radiator at hand. The fact is that liquids are characterized by strong acousto-optic interaction.[21] An acoustic wave radiated by the surface changes the refractive index in the medium, so an additional phase-shift appears for the signal optical beam propagating in the liquid, as large as that caused by the surface displacement itself. In principle, one can allow for this additional phase shift if the structure of the acoustic field is known. For example, if this is a plane wave (associated with a uniform vibration of an infinite plane surface), the effect of the acousto-optic interaction can be accounted for simply by use of an effective refractive index rather than the true value.[22] But the plane-wave case is an abstraction. In studies of a real surface vibration, two situations are possible when the normal velocity distribution is not known in advance. If this distribution is smooth at each point of the surface, then the plane-wave model can be used as a good approximation. The assumption of the plane-wave propagation has been applied, for example, to calibration of membrane hydrophones.[22] A completely different situation arises if the normal velocity distribution along the surface varies over distances of the order of the acoustic wavelength. The acoustic field in this case is far from being a plane wave. As a result, the effect of acousto-optic interaction can hardly be predicted. Such is indeed the case of the piezoceramic radiator under investigation. Consequently, one can conclude that it is impossible to measure the vibration of the radiator face when it is immersed in water.

It should be noted, however, that the rear (convex) face of the piezoceramic bowl is not contacting liquid unless oil backing is being used (see Fig. 2). One could thus study the radiator vibration by applying the optical interferometric technique for this surface. On the other hand, the external and internal radiator faces vibrate in the same manner, because the piezoceramic plate is curved slightly and the acoustical impedance of ceramics is much higher than that of water and air. If so, the measurement procedure can be simplified by interchanging the roles of the faces: the internal radiator surface can be brought into contact with liquid, and the external one into contact with air. This is the case of an oil-backed transducer residing in air. The acoustical impedance of machine oil ($Z=1.3\times10^6$ kg/m^2 s) is very close to that of water ($Z=1.5\times10^6$ kg/m^2 s), so there is little difference whether water or oil is used. It is essential that the thickness of the oil should be large enough to provide free-space condition. In the described experiment, it was 150 mm, being equal to the corresponding size of the transducer casing (Fig. 2), so the impact of the acoustic wave reflected from the casing onto the piezoceramic bowl vibration could easily be avoided through the use of a proper temporal gate;

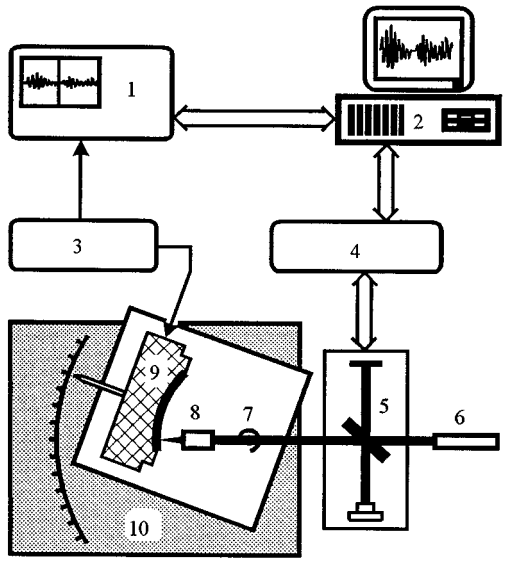

FIG. 10. The experimental setup for studying of the radiator surface vibration 1: Oscilloscope; 2: computer; 3: pulse generator; 4: interferometer controller; 5: optical interferometer; 6: laser; 7: rotatable support; 8: optical objective; 9: transducer; and 10: table.

in addition, the reflected wave has been damped thanks to attenuation in the oil.

A block diagram of the system is shown in Fig. 10. The optical interferometer was of Michelson type, with an He-Ne laser being used as a light source. The transducer casing was rigidly attached to a support, a rectangular plate made from plastic PVC. The support lay on a solid table and could slide over it, rotating about a fixed axis. This axis passed through the center of the radiator curvature. Both the table and the interferometer were clamped to an optical bench to avoid the influence of environmental vibration. The signal optical beam was oriented horizontally at a level of the radiator curvature center, with it intersected the axis of the support rotation. A lens was used to focus the beam at the radiator surface with a focal diameter of about 0.1 mm. The surface point the laser beam was focused at could be easily changed simply by the turning support through the corresponding angle α. The angle $\alpha=0°$ was associated with the radiator center. Changing α from $\alpha=0°$ to $\alpha=30°$, the angular distribution of the radiator surface displacement could be studied.

The interferometer was operated from its controller. The amount of reflected light had been accounted for just before the surface displacement was detected. The controller data were processed by a computer. The transducer was excited in the same manner as was described in Sec. I A.

B. Experimental results at continuous excitation

To investigate the radiator behavior in continuous regime, a gated sine wave can be used (see Sec. I B). The electrical pulses of 200 μs duration and 8 V amplitude were employed to excite the transducer. The surface displacement measurements were performed after 100 μs from the pulse beginning, because at this time, on the one hand, the optical interferometer signal had been stabilized and, on the other hand, parasitic signals corresponding to acoustic waves reflected from the casing had not returned. The displacement temporal profile was registered for different values of the observation angle α. These data made it possible to calculate the displacement amplitude and phase. Figure 11 shows these characteristics measured at frequency 1 MHz. It is to be noted that the amplitude distribution is not at all piston-like [Fig. 11(a)]. This effect is most pronounced at the radiator center, where Lamb waves focus and so the amplitude is many times higher than its mean value. The phase distribution [Fig. 11(b)] is more uniform, though irregularities exist near the center and edge of the radiator.

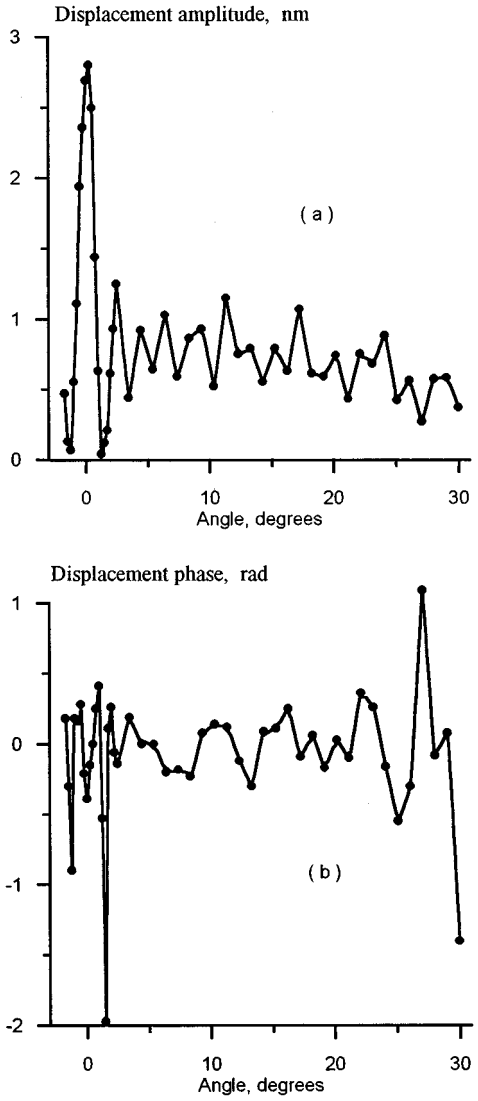

FIG. 11. Amplitude (a) and phase (b) of the radiator surface displacement versus angle coordinate at $f=1$ MHz. Angle 0° corresponds to the transducer center, angle 30° to its edge.

C. Experimental results at pulsed excitation

To study the transient radiator behavior, electric excitation pulses consisting of five periods of 1 MHz sinusoid were applied to the transducer. The pulse amplitude was 8 V. As well as in continuous regime, temporal displacement profile was recorded for different points of the radiator surface. Typical waveforms are presented in Fig. 12. The displace-

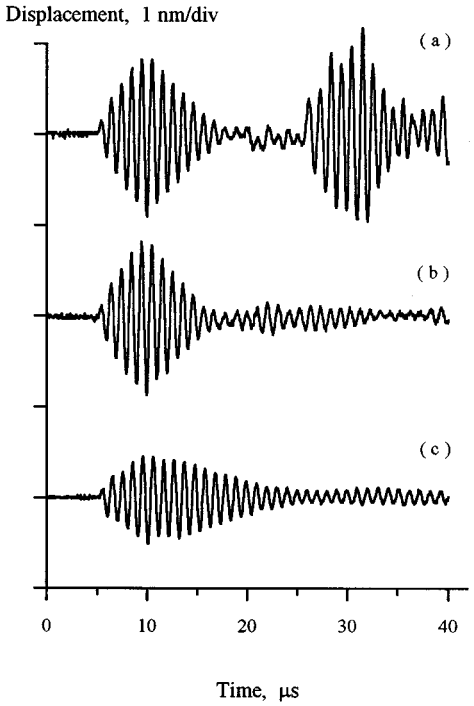

FIG. 12. Radiator surface vibration in pulsed regime. Angle coordinate of the corresponding points is 0° (a), 15° (b), and 30° (c).

ment signal consisted of a head pulse followed by a long irregular tail. The head pulse started immediately after the beginning of electrical excitation and had nearly the same profile for all observation points, whereas the tail changed essentially from point to point. Far from the radiator center peak value of the tail signal was of about 10%–30% of the head pulse peak. A picture of the signal changed noticeably near the center. The head and tail became time-separated, with tail front delay, and tail peak value increased as the center was approached. All this clearly demonstrated the wave character of the tail signal, with these waves being originated at the edge of the radiator. As was the case in the acoustical measurements (Fig. 6), the beginning of the tail consisted of low-frequency oscillations (the profile of $\alpha=0°$ in Fig. 12). The observed tail front delay was 15 μs, which corresponded to the plate-wave velocity of about 3.5 mm/μs. This value is in good accordance with the properties of Lamb waves.

The head pulse was obviously due to the radiator thickness vibration. The variation of its peak value was small, which indicated that the piezoelectric properties of the radiator were fairly uniform. This can be seen in Fig. 13, which presents a characteristic displacement A_0 versus angle α, where A_0 is the difference between the second maximum and the first minimum of the signal. This result for the radiator in hand was previously obtained using pulsed acoustical measurements.[8]

Apart from measurements with oil backing, the air-backed radiator vibration was also tested. Figure 14 compares the corresponding displacement at the radiator center. It can be seen that the head pulse was somewhat amplified when the oil had been poured off the transducer casing. The tail signals in these two cases differed significantly. Under

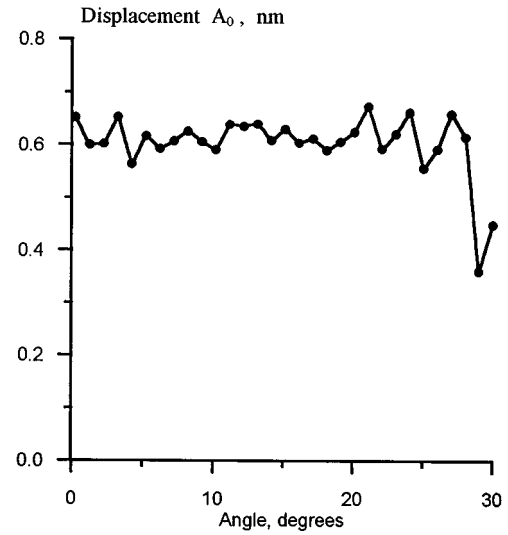

FIG. 13. Displacement A_0 vs angle coordinate, where A_0 is the difference between the second maximum and the first minimum of the waveforms shown in Fig. 12.

the oil-backing, the tail duration was about 100 μs, whereas for the air-backed radiator it was more than 1 ms. The tail pulse resembled as a train of pulses, which could be associated with Lamb waves echoes: plate wave, originating at the edge, converging to the center, then diverging again toward the edge, etc. It is to be noted that the Lamb wave amplitude at the center was damped only by a factor of 2 when the oil-backing was used instead of air-backing (Fig. 14). This

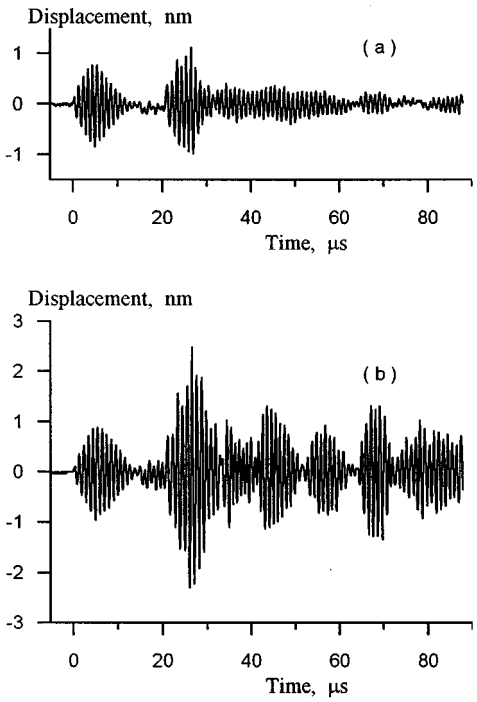

FIG. 14. Comparison of the radiator surface vibration with oil-backing (a) and without any backing (b). The curves correspond to the radiator center displacement in pulsed regime.

indicates that Lamb wave attenuation in a single pass along the bowl was moderate.

IV. CONCLUDING REMARKS

The experimental results presented in Sec. III show that Lamb waves do exist in the piezoceramic plate. Their amplitude is more than 10%–30% of the thickness displacement amplitude, especially near the radiator center. It turned out also that these waves propagate in the plate without significant attenuation, even if the radiator face contacts with liquid. Therefore, the assumptions used in the theory of Sec. II are reasonable and thus the peculiarities of the acoustical measurements (Sec. I) are explained by Lamb waves.

ACKNOWLEDGMENTS

This work was initiated by stimulating discussions on the subject matter with Professor J. Naze Tjøtta. We would like to thank also Mr. Y. Theillère for his technical assistance, and to express our appreciation to Dr. J. Y. Chapelon and Dr. J. C. Baboux for several constructive suggestions. The research was supported by the Institut National de la Santé Et de la Recherche Medicale (INSERM), France, when one of the authors (O. Sapozhnikov) was a Foreign Researcher in Unit 281. Partial support was also provided by the Russian Foundation for Basic Research (Grant No 95-02-04663a).

[1] A. O. Williams, Jr., ''Acoustic intensity distribution from a ''piston'' source.—II. The concave piston,'' J. Acoust. Soc. Am. **17**, 219–227 (1946).
[2] H. T. O'Neil, ''Theory of focusing radiators,'' J. Acoust. Soc. Am. **21**, 516–526 (1949).
[3] M. F. Hamilton, ''Comparison of three transient solutions for the axial pressure in a focused sound beam,'' J. Acoust. Soc. Am. **92**, 527–532 (1992).
[4] E. L. Madsen, M. M. Goodsitt, and J. A. Zagzebski, ''Continuous waves generated by focused radiators,'' J. Acoust. Soc. Am. **70**, 1508–1517 (1981).
[5] B. G. Lucas and T. G. Muir, ''The field of a focusing source,'' J. Acoust. Soc. Am. **72**, 1289–1296 (1982).
[6] H. D. Mair and D. A. Hutchins, ''Axial focusing by phased concentric annuli,'' in *Progress in Underwater Acoustics: Proceedings of the Twelfth International Congress on Acoustics*, edited by H. M. Merklinger (Plenum, New York, 1987), pp. 619–626.
[7] L. R. Gavrilov, V. N. Dmitriev, and L. V. Solontsova, ''Use of focused ultrasonic receivers for remote measurements in biological tissues,'' J. Acoust. Soc. Am. **83**, 1167–1179 (1988).
[8] L. Texier, ''Etude de la fragmentation des calculs biliaires en lithotritie extracorporelle. Comparaison expérience-théorie des diagrammes de rayonnement de transducteurs fortement et faiblement focalisés, respectivement en régime linéaire et nonlinéaire,'' Thèse de Doctorat, Université Paris VI (1993).
[9] M. R. Layton, E. F. Carome, H. D. Hardy, and J. A. Bucaro, ''Effects of diffraction on stress pulse propagation,'' J. Acoust. Soc. Am. **64**, 250–256 (1978).
[10] A. J. Hayman and J. P. Weight, ''Transmission and reception of short ultrasonic pulses by circular and square transducers,'' J. Acoust. Soc. Am. **66**, 945–951 (1979).
[11] J. C. Baboux, F. Lakestani, and M. Perdrix, ''Pulsed ultrasonic field of a thick transducer,'' in *Ultrasonic International 79 Conference Proceedings, IPC Sci. Tech.* (Guildford, United Kingdom, 1979), pp. 462–467.
[12] J. C. Baboux, F. Lakestani, and M. Perdrix, ''Theoretical and experimental study of the contribution of radial modes to the pulsed ultrasonic field radiated by a thick piezoelectric disk,'' J. Acoust. Soc. Am. **75**, 1722–1731 (1984).
[13] R.-I. Yu. Kazhis and A. P. Mashonis, ''Analysis of transient processes in a radially vibrating piezoelectric disk,'' Sov. Phys. Acoust. **33**, 70–72 (1987).
[14] X. Jia, J. Berger, and G. Quentin, ''Experimental investigation of Lamb waves on pulsed piezoelectric transducers and their ultrasonic radiation into liquids,'' J. Acoust. Soc. Am. **90**, 1181–1183 (1991).
[15] E. Riera-Franco de Sarabia, A. Ramos-Fernandez, and F. Rodriguez-Lopez, ''Temporal evolution of transient transverse beam profiles in near-field zones,'' Ultrasonics **32**, 47–56 (1994).
[16] B. Delannoy, C. Bruneel, F. Haine, and R. Torguet, ''Anomalous behavior in the radiation pattern of piezoelectric transducers induced by parasitic Lamb wave generation,'' J. Appl. Phys. **51**, 3942–3948 (1980).
[17] O. V. Rudenko and S. I. Soluyan, *Theoretical Foundations of Nonlinear Acoustics* (Plenum, New York, 1977), pp. 15–29.
[18] H. Lamb, ''On waves in an elastic plate,'' Proc. R. Soc. London, Ser. A **93** (1917).
[19] I. A. Viktorov, *Rayleigh and Lamb waves* (Plenum, New York, 1967).
[20] E. S. Furgason and V. L. Newhouse, ''Convolution and correlation using nonlinear interactions of Lamb waves,'' IEEE Trans. Sonics Ultrason. **20**, 360–364 (1973).
[21] C. V. Raman and K. S. Venkataraman, ''Determination of the adiabatic piezo-optic coefficient of liquids,'' Proc. R. Soc. London, Ser. A **171**, 137–147 (1939).
[22] D. R. Bacon, ''Primary calibration of ultrasonic hydrophones using optical interferometry,'' IEEE Trans. Ultrason. Ferroelectr. Freq. Control **35**, 152–161 (1988).

Analytical method for describing the paraxial region of finite amplitude sound beams

Mark F. Hamilton
Department of Mechanical Engineering, The University of Texas at Austin, Austin, Texas 78712-1063

Vera A. Khokhlova and Oleg V. Rudenko
Department of Physics, Moscow State University, Moscow, Russia 119899

(Received 15 February 1995; accepted for publication 29 October 1996)

A special analytical method, which combines the parabolic approximation (KZ equation) with nonlinear geometrical acoustics, is developed to model nonlinear and diffraction effects near the axis of a finite amplitude sound beam. The corresponding system of nonlinear equations describing waveform evolution is derived. For the case of an initially sinusoidal wave radiated by a Gaussian source, an analytic solution of the coupled equations is obtained for the paraxial region of the beam. The axial solution is expressed in both the time and frequency domains, and is analyzed in detail for both unfocused and focused beams in their preshock regions. Harmonic propagation curves are compared with finite difference solutions of the KZ equation, and good agreement is obtained for a variety of parameter values. [S0001-4966(97)05602-6]

PACS numbers: 43.25.Jh, 43.25.Cb [MAB]

INTRODUCTION

Considerable attention is currently being devoted to modeling the propagation and focusing of intense sound beams. This attention is due in large part to applications in medicine and other ultrasound technologies. In related theoretical analyses, it is necessary to take into consideration nonlinear phenomena such as harmonic generation, waveform distortion, and shock formation. These nonlinear phenomena occur simultaneously and thus compete with the linear processes associated with diffraction. For example, whereas finite amplitude effects may be increased because of focusing, the corresponding strong diffraction introduces phase shifts between the nonlinearly generated harmonics, leading to broadening of the shock front and thus tending to offset nonlinearity.

As demonstrated in previous numerical investigations,[1,2] all of the aforementioned processes, when acting together, can substantially alter the waveform and spectrum of a finite amplitude sound beam in comparison with the distortion of one-dimensional waves, i.e., plane or converging spherical waves. Owing to the complexity of nonlinear interactions in diffracting sound beams, analytical investigations can be realized only through the use of special asymptotic methods.

The underlying idea of the method used here dates back to the era of classical optics.[3] It is known that the paraxial approach can be used to investigate collimated light beams. This approach is based on the approximation of the real surface of a lens, mirror, or other optical elements by a paraboloid. A solution for the wave field can then be found as a series expansion in r/a, where r is the transverse coordinate and a is the characteristic dimension of the light source. This paraxial approach has been applied successfully to problems in laser physics[4] and nonlinear optics.[5] As only quasiharmonic waves were considered, it was possible to separate and expand independently the amplitude and eikonal functions of the optical signal, and a highly accurate analytic solution was thus obtained.[6]

A similar approach was suggested by Rudenko *et al.*[7] to investigate finite amplitude sound beams. In contrast with problems in nonlinear optics, acoustical nonlinearity leads to substantial broadening of the frequency spectrum because of the comparatively weak dispersion associated with typical acoustical media. It is therefore impossible to consider only one particular harmonic component, and to separate the amplitude and eikonal function. Instead, description of the entire nonlinearly distorted waveform is required. Specifically, one can seek a solution of the nonlinear equations describing the sound-pressure waveform p in terms of the following expansion:

$$p(r,z,t')=p_0(z,t')+\frac{r^2}{2a^2}\,p_2(z,t')+\frac{r^4}{4a^4}\,p_4(z,t')+\cdots . \tag{1}$$

Here, r is distance from the axis of the beam (axial symmetry is assumed), z the axial coordinate, $t'=t-z/c_0$ the retarded time, c_0 the sound speed, and a the characteristic source radius. It is evident that the expansion is valid only near the axis, where $r^2/a^2 \ll 1$. This limitation is unimportant if only the region very near the axis is of interest. Analytical results obtained with this method describe, for example, axial waveform distortion in a diffracting beam radiated by an axisymmetric harmonic source.[7] As is well known, the rarefaction phase is smoothed and extended, the compression phase is shortened and sharpened, and the peak positive pressure may be considerably greater than its initial value.[1] These phenomena are related to the harmonic phase shifts introduced by diffraction. The process of higher harmonic generation is delayed in time with respect to the phase of the fundamental frequency component, which results in asymmetric waveform distortion.

However, the direct expansion in Eq. (1) imposes a strong restriction on the obtained results. Truncating the series at two or three terms leads to the appearance of a new small parameter $z/z_0 \ll 1$, where $z_0 = \omega_0 a^2/2c_0$ is the characteristic diffraction length for a beam with angular frequency ω_0. Thus, whereas the expansion accounts for strong nonlinearity, it can account for only weak diffraction effects. An analogous approach has been used for focused beams.[8] It was shown that another small parameter appears, $z/d \ll 1$, where d is the focal length. It is therefore impossible to use the described approach for investigation of the focal region.

The restrictions on z corresponding to the expansion in Eq. (1) are due to wavefront curvature associated with diffraction and focusing. Note that the phase in Eq. (1) is based on a retarded time for plane waves. As shown in the present paper, introduction of an explicit phase term that accounts for wavefront curvature in the linear approximation leads to substantially improved nonlinear solutions based on an expansion similar to Eq. (1).

In particular, to describe a converging beam one may introduce a retarded time that accounts for wavefront curvature following the method of nonlinear geometrical acoustics (NGA).[6] This method is effective for describing the nonlinear distortion of a wave propagating from the source toward the focal point, but it cannot describe the strong diffraction effects in the focal region. Nevertheless, a variety of problems solved by the NGA method (e.g., self-refraction of focused pulses containing shocks,[9] and finite amplitude wave propagation through inhomogeneous media[10]) demonstrate the power of the NGA methodology.

In the present article, an analytical method is developed which combines the advantages of the paraxial and NGA approaches. As an example of how to apply this method, implicit time domain solutions and explicit frequency domain solutions are derived for beams radiated by both unfocused and focused Gaussian sources. Attention is restricted here to the preshock region. Results presented elsewhere[11] illustrate properties exhibited by the solution for strong nonlinearity, especially differences with the multivalued solutions predicted for simple waves.

I. BASIC EQUATIONS AND METHODOLOGY

We start with the KZ (Khokhlov–Zabolotskaya) equation in cylindrical coordinates,[1]

$$\frac{\partial}{\partial t'}\left(\frac{\partial p}{\partial z}-\frac{\beta p}{\rho_0 c_0^3}\frac{\partial p}{\partial t'}\right)=\frac{c_0}{2}\left(\frac{\partial^2 p}{\partial r^2}+\frac{1}{r}\frac{\partial p}{\partial r}\right), \tag{2}$$

where β is the coefficient of nonlinearity and ρ_0 is the ambient density of the fluid. Equation (2) can be rewritten in the dimensionless form

$$\frac{\partial}{\partial \tau}\left(\frac{\partial P}{\partial \sigma}-NP\frac{\partial P}{\partial \tau}\right)=\frac{1}{4G}\left(\frac{\partial^2 P}{\partial R^2}+\frac{1}{R}\frac{\partial P}{\partial R}\right), \tag{3}$$

where

$$P=p/p_p, \quad \sigma=z/d, \quad R=r/a, \quad \tau=\omega_0 t', \tag{4}$$

and where p_p characterizes the peak sound pressure at the source. The two dimensionless constants in Eq. (3) are ratios of the characteristic focusing, nonlinearity, and diffraction lengths:

$$N=d/\overline{z}, \quad G=z_0/d, \tag{5}$$

where $\overline{z}=\rho_0 c_0^3/\beta p_p \omega_0$ is the shock formation distance for a plane wave with peak source pressure p_p. The parameter N characterizes the nonlinearity in the beam, and G characterizes the small-signal focusing gain.

We seek a solution of Eq. (3) in the form

$$P=P(R,\sigma,\theta), \tag{6}$$

where the retarded time τ has been replaced with the new quantity

$$\theta=\tau-\psi(R,\sigma). \tag{7}$$

Here, ψ is a definite function that is known *a priori*. It is assumed to have no singularities and be sufficiently smooth that a unique and well-defined transformation can be made between the original variables (R,σ,τ) and the new ones $[R,\sigma,\theta(R,\sigma,\tau)]$. Substitution of Eq. (6) into Eq. (3) yields

$$\frac{\partial}{\partial \theta}\left\{\frac{\partial P}{\partial \sigma}-NP\frac{\partial P}{\partial \theta}+\frac{1}{4G}\left(P\nabla_\perp^2\psi+2\frac{\partial P}{\partial R}\frac{\partial \psi}{\partial R}\right)-\left[\frac{\partial \psi}{\partial \sigma}+\frac{1}{4G}\left(\frac{\partial \psi}{\partial R}\right)^2\right]\frac{\partial P}{\partial \theta}\right\}=\frac{1}{4G}\nabla_\perp^2 P, \tag{8}$$

where

$$\nabla_\perp^2=\frac{\partial^2}{\partial R^2}+\frac{1}{R}\frac{\partial}{\partial R}. \tag{9}$$

Note that the terms in the square brackets are similar to those in the ''eikonal'' equation of geometrical acoustics for the phase function ψ.[6] It is convenient to consider these terms separately by introducing the following notation:

$$Q=4G\frac{\partial \psi}{\partial \sigma}+\left(\frac{\partial \psi}{\partial R}\right)^2. \tag{10}$$

Equation (8) can now be rewritten in the form

$$\frac{\partial}{\partial \theta}\left[\frac{\partial P}{\partial \sigma}-NP\frac{\partial P}{\partial \theta}+\frac{1}{4G}\left(P\nabla_\perp^2\psi+2\frac{\partial P}{\partial R}\frac{\partial \psi}{\partial R}\right)-\frac{Q}{4G}\frac{\partial P}{\partial \theta}\right]=\frac{1}{4G}\nabla_\perp^2 P. \tag{11}$$

Known analytic solutions of the KZ equation, obtained in limiting cases, provide a means of choosing an appropriate expression for ψ, and therefore Q through Eq. (10), to use when solving Eq. (11) for a specific nonlinear problem.

Consider, for example, the linear solution of Eq. (3) for a converging spherical wave with uniform amplitude:[6]

$$P=\frac{1}{1-\sigma}S\left(\tau+\frac{GR^2}{1-\sigma}\right), \quad N=0, \tag{12}$$

where $S(\tau)$ is an arbitrary time waveform. The dependence of the phase on the transverse coordinate R approximates the spherical curvature of the wave in the paraxial region. From comparison with Eq. (7) we identify the eikonal

$$\psi = \frac{GR^2}{\sigma - 1}, \tag{13}$$

the substitution of which into Eq. (10) gives $Q=0$. Substitution of these expressions for ψ and Q into Eq. (11) with the right-hand side set equal to zero yields a partial differential equation for the pressure P in the nonlinear geometrical acoustics approximation, i.e., for very short wavelengths. Analysis of this case may be found in Ref. 6. However, since Eqs. (11) and (13) are singular in the focal plane, $\sigma=1$, there is little practical reason to solve the resulting system if one is interested in propagation of the wave through the focus.

Better guidance for the selection of ψ is provided by linear theory for diffracting Gaussian beams. In the paraxial region, an appropriate source condition for a focused Gaussian beam is

$$P = e^{-R^2} \sin(\tau + GR^2), \quad \sigma = 0. \tag{14}$$

The linear solution of Eq. (3) that satisfies Eq. (14) can be written as

$$P = \frac{1}{f}\, e^{-R^2/f^2} \sin\, \theta, \quad N = 0, \tag{15}$$

where

$$f(\sigma) = \sqrt{(1-\sigma)^2 + (\sigma/G)^2}, \tag{16}$$

θ is defined by Eq. (7) with

$$\psi = GR^2 f'/f - \eta, \tag{17}$$

where $f' = df/d\sigma$,

$$\eta(\sigma) = \frac{1}{G} \int_0^\sigma \frac{d\sigma'}{f^2(\sigma')} \tag{18}$$

$$= \arctan\left(\frac{\sigma/G}{1-\sigma}\right) + \pi H(\sigma - 1), \tag{19}$$

and H is the Heaviside unit step function. Both the amplitude and characteristic beamwidth described by Eq. (15) are determined completely by the function f in Eq. (16). Equation (15) is a well-known linear solution in both the quasi-optic theory of diffraction[6] and in acoustics,[12] and it describes all stages of focused Gaussian beam propagation—its convergence and divergence, as well as the field structure in the focal region. Substituting Eq. (17) into Eq. (10) and taking into account the relation $f^3 f'' = G^{-2}$, which follows from Eq. (16), one obtains

$$Q = -\frac{4}{f^2}\left(1 - \frac{R^2}{f^2}\right). \tag{20}$$

We now consider Eq. (11), subject to the source condition given by Eq. (14), and with ψ and Q defined by Eqs. (17) and (20), respectively. Unlike Eq. (13), Eq. (17) is not singular in the focal plane. Consequently, the coefficients in Eq. (11) have no singularities. In the linear approximation ($N=0$), the solution of Eq. (11) is Eq. (15), as must be the case because Eqs. (10) and (11) combined are equivalent to Eq. (3). It is therefore sensible to define ψ in the same way to seek a nonlinear solution of Eq. (11) that corresponds to radiation of a beam from a focused Gaussian source.

Following the approach in Ref. 7, we shall seek a paraxial solution of Eq. (11) in the form

$$P = P_0(\sigma,\theta) + \frac{R^2}{2} P_2(\sigma,\theta) + \frac{R^4}{4} P_4(\sigma,\theta) + \cdots . \tag{21}$$

In contrast with the direct expansion in Eq. (1), the modified expansion in Eq. (21) depends on the phase variable ψ through θ. Consequently, phase errors connected with truncation of the expansion are reduced. As discussed above, the source condition determines an appropriate choice for ψ.

The example we choose for illustration of our methodology is radiation from a focused Gaussian source, using the functions ψ and Q defined in Eqs. (17) and (20). In Sec. II, we derive coupled equations for P_0 and P_2, the solutions for which are obtained in the Appendix. Solutions for radiation from unfocused Gaussian sources are obtained as a limiting case.

II. FOCUSED GAUSSIAN BEAMS

Here we seek a solution of Eq. (3) in the form of Eq. (21), and which satisfies the source condition in Eq. (14). We therefore solve Eq. (11) with ψ defined as in Eq. (17), Q as in Eq. (20).

It is convenient to rewrite Eq. (11) with the terms in ψ expressed as explicit functions of $f(\sigma)$ and R. On the basis of Eq. (17) we obtain the relations

$$\frac{\partial \psi}{\partial R} = \frac{2GRf'}{f}, \quad \nabla_\perp^2 \psi = \frac{4Gf'}{f}. \tag{22}$$

Equation (11) thus becomes, with Q defined by Eq. (20),

$$\frac{\partial}{\partial \theta}\left[\frac{\partial P}{\partial \sigma} - NP\,\frac{\partial P}{\partial \theta} + \frac{f'}{f}\left(P + R\,\frac{\partial P}{\partial R}\right) + \frac{1}{Gf^2}\left(1 - \frac{R^2}{f^2}\right)\frac{\partial P}{\partial \theta}\right] = \frac{1}{4G}\,\nabla_\perp^2 P. \tag{23}$$

Substitution of Eq. (21) into Eq. (23) produces a sequence of coupled equations. We shall restrict our consideration to the first two of these equations, at orders R^0 and R^2:

$$R^0\text{:}\quad \frac{\partial}{\partial \theta}\left[\frac{\partial P_0}{\partial \sigma} - NP_0\,\frac{\partial P_0}{\partial \theta} + \frac{f'}{f}\,P_0 + \frac{1}{Gf^2}\,\frac{\partial P_0}{\partial \theta}\right] = \frac{P_2}{2G}, \tag{24}$$

$$R^2\text{:}\quad \frac{\partial}{\partial \theta}\left[\frac{\partial P_2}{\partial \sigma} - N\,\frac{\partial (P_0 P_2)}{\partial \theta} + 3\,\frac{f'}{f}\,P_2 - \frac{2}{Gf^4}\,\frac{\partial P_0}{\partial \theta} + \frac{1}{Gf^2}\,\frac{\partial P_2}{\partial \theta}\right] = \frac{2P_4}{G}. \tag{25}$$

Equations (24) and (25) contain three unknown functions (P_0, P_2, P_4), and therefore an additional condition is required to close the system.

We choose to impose a condition on P_4 that is consistent with the expansion of the linear solution, Eq. (15). Expansion of Eq. (15) as in Eq. (21) yields

$$P_0 = \frac{1}{f} \sin\, \theta, \quad P_2 = -\frac{2}{f^3} \sin\, \theta, \quad P_4 = \frac{2}{f^5} \sin\, \theta, \tag{26}$$

which satisfy Eqs. (24) and (25) for $N=0$. Now let

$$P_4 = -\frac{2}{f^4}\frac{\partial^2 P_0}{\partial \theta^2}, \tag{27}$$

which satisfies Eqs. (26). Use of Eq. (27) to eliminate P_4 from Eq. (25) yields

$$R^2\colon\ \frac{\partial}{\partial\theta}\left[\frac{\partial P_2}{\partial\sigma} - N\frac{\partial(P_0P_2)}{\partial\theta} + 3\frac{f'}{f}P_2 + \frac{2}{Gf^4}\frac{\partial P_0}{\partial\theta} + \frac{1}{Gf^2}\frac{\partial P_2}{\partial\theta}\right] = 0. \tag{28}$$

Equations (24) and (28) provide a closed nonlinear system for P_0 and P_2.

To solve Eqs. (24) and (28) it is convenient to introduce a new time variable θ_1 and function F, defined as follows:

$$\theta_1 = \theta - \eta,\ \ P_2 = 2G\frac{\partial F}{\partial\theta_1}. \tag{29}$$

Comparison with Eqs. (7) and (17) reveals that

$$\theta_1 = \tau - GR^2 f'/f, \tag{30}$$

and therefore $\theta_1 = \tau$ along the axis of the beam. In terms of the new variables, Eqs. (24) and (28) reduce to

$$\frac{\partial}{\partial\theta_1}\left(\frac{\partial P_0}{\partial\sigma} - NP_0\frac{\partial P_0}{\partial\theta_1} + \frac{f'}{f}P_0 - F\right) = 0, \tag{31}$$

$$\frac{\partial^2}{\partial\theta_1^2}\left(\frac{\partial F}{\partial\sigma} - NP_0\frac{\partial F}{\partial\theta_1} + 3\frac{f'}{f}F + \frac{P_0}{G^2f^4}\right) = 0, \tag{32}$$

which after integration with respect to θ_1 yield

$$\frac{\partial P_0}{\partial\sigma} - NP_0\frac{\partial P_0}{\partial\theta_1} + \frac{f'}{f}P_0 - F = \phi_1(\sigma), \tag{33}$$

$$\frac{\partial F}{\partial\sigma} - NP_0\frac{\partial F}{\partial\theta_1} + 3\frac{f'}{f}F + \frac{P_0}{G^2f^4} = \phi_2(\sigma) + \theta_1\phi_3(\sigma). \tag{34}$$

The integration functions ϕ_i are determined by noting that the time average of the pressure must be zero,[1] i.e., $P=0$. We therefore have $P_0=0$ and $P_2=0$. From the second of Eqs. (29) it follows that the auxiliary function F can have an arbitrary time-averaged value and produce the same solution for the off-axis term P_2. It is convenient to choose F such that $F=0$, for which $\phi_1=0$. As all terms on the left-hand side of Eq. (34) are periodic in time, we must also have $\phi_3=0$.

Equations (33) and (34) can now be rewritten in the following canonical form:

$$\left(\frac{\partial}{\partial\sigma} - NP_0\frac{\partial}{\partial\theta_1}\right)\begin{pmatrix} P_0 \\ F\end{pmatrix} = \begin{pmatrix} F - (f'/f)P_0 \\ -3(f'/f)F - P_0/(G^2f^4) + \phi_2\end{pmatrix}. \tag{35}$$

Equation (35) is a system of quasilinear differential equations with the same principal part,[13] an analytic solution of which can be derived.

III. ANALYTIC AXIAL SOLUTIONS

Subject to the source condition $P_0=\sin\tau$ at $\sigma=0$ [from Eqs. (14) and (21)], and with the requirement $P_0=0$ for all σ, Eq. (35) yields the axial solution (see the Appendix)

$$P_0 = \frac{1}{f}\sin(\theta_0 + \eta) + \Delta, \tag{36}$$

where θ_0 is defined by the implicit relation

$$\theta_0 = \tau + g\ \sin(\theta_0 + \phi) + \delta. \tag{37}$$

Equations (36) and (37) depend on the following quantities, several of which were defined earlier but are repeated here for convenience:

$$f = \sqrt{(1-\sigma)^2 + (\sigma/G)^2}, \tag{38}$$

$$g = N\left(\frac{\eta^2 + \ln^2 f}{1 + G^{-2}}\right)^{1/2}, \tag{39}$$

$$\eta = \arctan\left(\frac{\sigma/G}{1-\sigma}\right) + \pi H(\sigma - 1), \tag{40}$$

$$\phi = \arctan\left(\frac{G\eta + \ln f}{\eta - G\ \ln f}\right), \tag{41}$$

$$\Delta = (g/2f)\sin(\eta - \phi), \tag{42}$$

$$\delta = NG\int_0^\eta f^2(\eta')\Delta(\eta')\,d\eta'. \tag{43}$$

The relation $f(\eta) = (\cos\eta + G\sin\eta)^{-1}$ is used to calculate the integral in Eq. (43).

Implicit solutions in the form of Eq. (36) may become multivalued for σ sufficiently large, which corresponds to the existence of shocks. The shock formation distance along the axis of the beam is derived by calculating the smallest value of σ for which $\partial P_0/\partial\tau = \infty$. The condition for shock formation is found to be $g=1$, which yields the following transcendental equation for the shock formation distance σ_s:

$$\eta^2(\sigma_s) + \ln^2 f(\sigma_s) = N^{-2}(1 + G^{-2}). \tag{44}$$

For $\sigma > \sigma_s$, weak shock theory can be used to correct the solution.[14,15] Attention is restricted in the present article to the preshock region, $\sigma < \sigma_s$.

For the preshock region, standard techniques[16] can be used to obtain the following explicit Fourier series expansion of Eq. (36):

$$P_0(\sigma,\tau) = \frac{1}{2}\sum_{n=1}^{\infty} C_n(\sigma)e^{jn\tau} + \text{c.c.},\ \ \sigma < \sigma_s, \tag{45}$$

where the spectral coefficients are defined by

$$C_n = \frac{e^{jn(\phi+\delta)}}{jnf}\left[e^{j(\eta-\phi)}J_{n-1}(ng) + e^{-j(\eta-\phi)}J_{n+1}(ng)\right], \tag{46}$$

J_n is the Bessel function of the first kind, c.c. designates complex conjugates of the preceding terms, and $C_n^* = C_{-n}$. An equivalent form of Eq. (45) is

$$P_0(\sigma,\tau)=\sum_{n=1}^{\infty} B_n(\sigma)\sin[n\tau+\zeta_n(\sigma)],\quad \sigma<\sigma_s, \tag{47}$$

where

$$B_n=\frac{1}{nf}\,[J_{n-1}^2(ng)+J_{n+1}^2(ng)$$
$$+2J_{n-1}(ng)J_{n+1}(ng)\cos 2(\eta-\phi)]^{1/2}, \tag{48}$$

$$\zeta_n=n(\phi+\delta)+\arg\, Z_n, \tag{49}$$

and

$$Z_n=(2/g)J_n(ng)\cos(\eta-\phi)$$
$$+j[J_{n-1}(ng)-J_{n+1}(ng)]\sin(\eta-\phi). \tag{50}$$

The magnitudes $B_n=|C_n|$ are the harmonic amplitudes, relative to the peak source pressure p_p, along the axis of the beam. The phase shifts $\zeta_n=\arg C_n+\pi/2$ are caused by diffraction.

IV. LIMITING CASES

Before investigating Eqs. (36) and (47) in detail, we first consider several asymptotic forms of the solutions.

A. Geometrical acoustics ($\omega_0\to\infty$)

In the limit $\omega_0\to\infty$ we have $G\to\infty$, Eqs. (40)–(43) vanish, and with $f\to 1-\sigma$, $g\to\ln(1-\sigma)^{-N}$, Eq. (36) reduces to

$$P_0=\frac{1}{1-\sigma}\,\sin[\tau+(1-\sigma)\ln(1-\sigma)^{-N}P_0]. \tag{51}$$

Equation (51) is the solution of the lossless generalized Burgers equation for a converging spherical wave.[15,17] The expression for the shock formation distance, Eq. (44), reduces in this case to the explicit result

$$\sigma_s=1-e^{-1/N}. \tag{52}$$

Since $\sigma_s<1$ is obtained for any finite value of N, shock formation always occurs before the focus. The geometrical acoustics limit of Eq. (47) is

$$P_0=\frac{1}{1-\sigma}\sum_{n=1}^{\infty}\frac{2J_n[n\,\ln(1-\sigma)^{-N}]}{n\,\ln(1-\sigma)^{-N}}\sin n\tau, \tag{53}$$

which is the spherical-wave generalization of the well-known Fubini solution.[15]

B. Unfocused beams ($d\to\infty$)

In the limit $d\to\infty$ (and therefore $G\to 0$), another length scale must be chosen for normalizing the physical parameters. The Rayleigh distance z_0 is chosen and the following new definitions for the axial coordinate and nonlinearity parameter are introduced:

$$\sigma=z/z_0,\quad N=z_0/\overline{z}. \tag{54}$$

In terms of Eqs. (54), with P, R, and τ still defined by Eqs. (4), the dimensionless form of the KZ equation becomes, in place of Eq. (3),

$$\frac{\partial}{\partial\tau}\left(\frac{\partial P}{\partial\sigma}-NP\,\frac{\partial P}{\partial\tau}\right)=\frac{1}{4}\left(\frac{\partial^2 P}{\partial R^2}+\frac{1}{R}\,\frac{\partial P}{\partial R}\right). \tag{55}$$

The boundary condition for an unfocused Gaussian source is, instead of Eq. (14),

$$P=e^{-R^2}\,\sin\,\tau,\quad \sigma=0. \tag{56}$$

Solutions (36) and (47) remain the same, but Eqs. (38)–(43) reduce to the following:

$$f=\sqrt{1+\sigma^2}, \tag{57}$$

$$g=N\sqrt{\eta^2+\ln^2 f}, \tag{58}$$

$$\eta=\arctan\,\sigma, \tag{59}$$

$$\phi=\arctan(\eta^{-1}\,\ln\,f\,), \tag{60}$$

$$\Delta=(g/2\,f\,)\sin(\eta-\phi), \tag{61}$$

$$\delta=N\int_0^{\eta} f^2(\eta')\Delta(\eta')\,d\eta', \tag{62}$$

with $f(\eta)=\sec\,\eta$. The shock formation distance is still defined by $g=1$, which yields in place of Eq. (44)

$$\arctan^2\,\sigma_s+\ln^2\sqrt{1+\sigma_s^2}=N^{-2}. \tag{63}$$

This relation for the shock formation distance was proposed originally by Rudenko *et al.*[18] on the basis of quasilinear theory [a factor of 4 was omitted in front of $\arctan^2\,\delta$ in Eq. (11) of Ref. 18, as well as in Eq. (4.4) on p. 225 of Ref. 15]. Coulouvrat[19] subsequently recovered the same relation from his renormalized Gaussian beam solution.

The appropriate geometrical acoustics limit is also obtained for the case of unfocused beams. With $\omega_0\to\infty$, Eqs. (59)–(62) vanish and we have $f\to 1$, $g\to z/\overline{z}$, which yields the plane wave result $P_0=\sin(\tau+\sigma P_0)$. Here $\sigma=g$, and the shock formation distance is thus $\sigma_s=1$.

C. Quasilinear solutions ($\bar{z}\to\infty$)

The quasilinear limit ($N\to 0$) is obtained by expanding either Eq. (36) or (47) in powers of N, which to lowest order for the nth harmonic component yields

$$P_0^{(n)}=\frac{(ng/2)^{n-1}}{n!\,f}\,\sin[n\tau+\eta+(n-1)\phi]. \tag{64}$$

For the fundamental and second harmonic components, Eq. (64) reduces to

$$P_0^{(1)}=\frac{1}{f}\,\sin(\tau+\eta), \tag{65}$$

$$P_0^{(2)}=\frac{g}{2\,f}\,\sin(2\tau+\eta+\phi). \tag{66}$$

Equations (65) and (66) are the familiar quasilinear axial solutions of the KZ equation for both focused [with Eqs. (38)–(41)] and unfocused[15,18] [with Eqs. (57)–(60)] Gaussian beams.

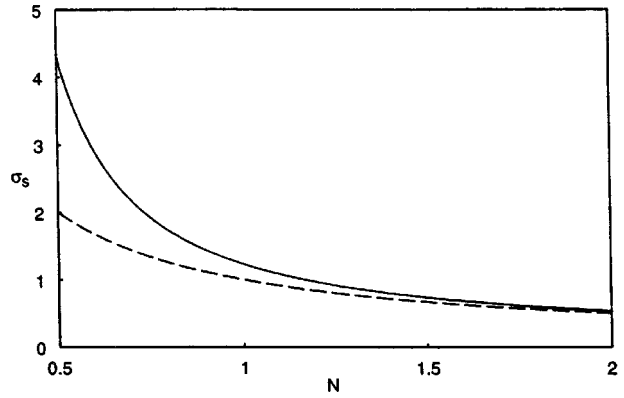

FIG. 1. Shock formation distance for an unfocused beam. Solid line is obtained from Eq. (63), and dashed line is the result for a plane wave.

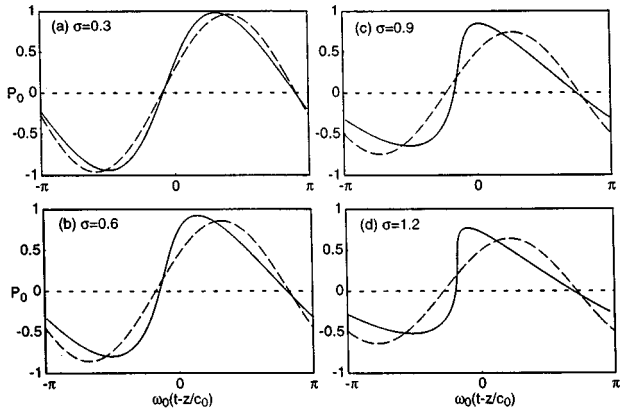

FIG. 3. Waveforms in an unfocused beam with $N=1$. Solid lines are calculated with Eq. (36), and dashed lines are linear theory given by Eq. (65).

V. RESULTS

The properties of Eqs. (36) and (47) are investigated below for both unfocused and focused beams. As noted above, attention is restricted to the preshock region, $\sigma<\sigma_s$.

A. Unfocused beams

The results presented in this section are obtained by substituting Eqs. (57)–(62) into Eqs. (36) and (47). The axial coordinate $\sigma=z/z_0$ defines location in relation to the Rayleigh distance, and therefore $\sigma\simeq 1$ separates the near from far-field regions of the beam. For $N=z_0/\overline{z}$ sufficiently greater than unity, shock formation is expected to occur in the near field, where the wavefronts are approximately planar. Shown in Fig. 1 is a graph of the shock formation distance σ_s predicted by Eq. (63). The dashed asymptote is the plane-wave result $\sigma_s=1/N$. For $N\gtrsim 1.5$, the shock formation distance for a Gaussian beam is approximated well by the result for plane waves.

In Fig. 2 are presented propagation curves for the first three harmonic amplitudes along the axis of a beam with $N=1$, for which $\sigma_s=1.23$. The solid lines are $B_n(\sigma)$, and the dashed lines are finite difference solutions of the KZ equation, obtained with the computer code described by Naze Tjøtta *et al.*[20] The agreement between the analytical and numerical results is comparable to that obtained in the preshock region by Coulouvrat,[19] with his renormalized solution evaluated for the same source condition (see Fig. 8 of Ref. 19, in which δ is equivalent to σ in the present article). The corresponding waveforms at selected axial locations, calculated with Eq. (36), are presented in Fig. 3, where the dashed lines are the linear theory given by Eq. (65).

The familiar waveform asymmetry depicted in Fig. 3 is due to the combined effects of diffraction and nonlinearity, and it may be characterized by the ratio of the peak positive pressure $P_+=f^{-1}+\Delta$ to the peak negative pressure $P_-=f^{-1}-\Delta$. The following expression is obtained for this ratio:

$$\frac{P_+}{P_-}=\frac{2+g\ \sin(\eta-\phi)}{2-g\ \sin(\eta-\phi)}. \tag{67}$$

Equation (67) is plotted in Fig. 4 for different values of N (the curve for $N=1$ is terminated at $\sigma=1.23$, the shock formation distance). For all values of N, the asymmetry increases most rapidly in the near field of the beam.

To examine more closely the accuracy of the analytic solution, comparisons are made in Figs. 5 and 6 with finite difference solutions of the KZ equation for $N=0.2$ and $N=0.5$, out to $\sigma=4$. The predicted shock formation distance for $N=0.5$ is $\sigma_s=4.3$, and therefore all results presented in the two figures pertain to the preshock region. The solid lines in Fig. 5 are the magnitudes B_n (expressed in decibels, i.e.,

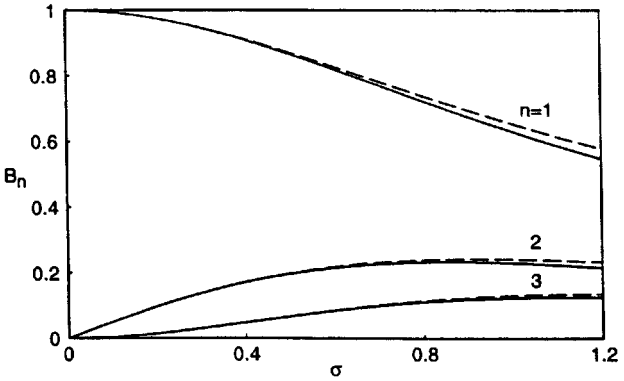

FIG. 2. Harmonic propagation curves for an unfocused beam with $N=1$. Solid lines are obtained from Eq. (48), and dashed lines are finite difference solutions.

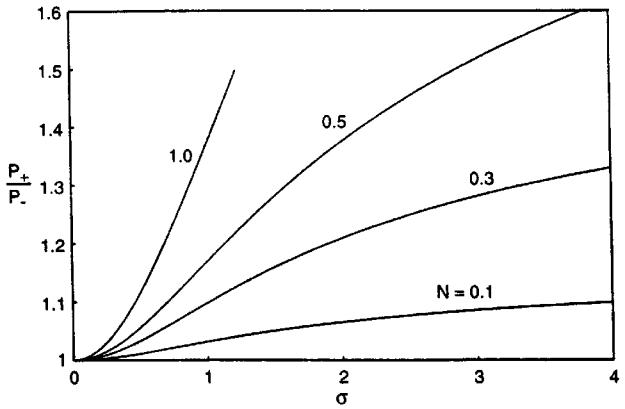

FIG. 4. Ratio of peak positive to peak negative pressure in waveforms of unfocused beams, calculated with Eq. (67).

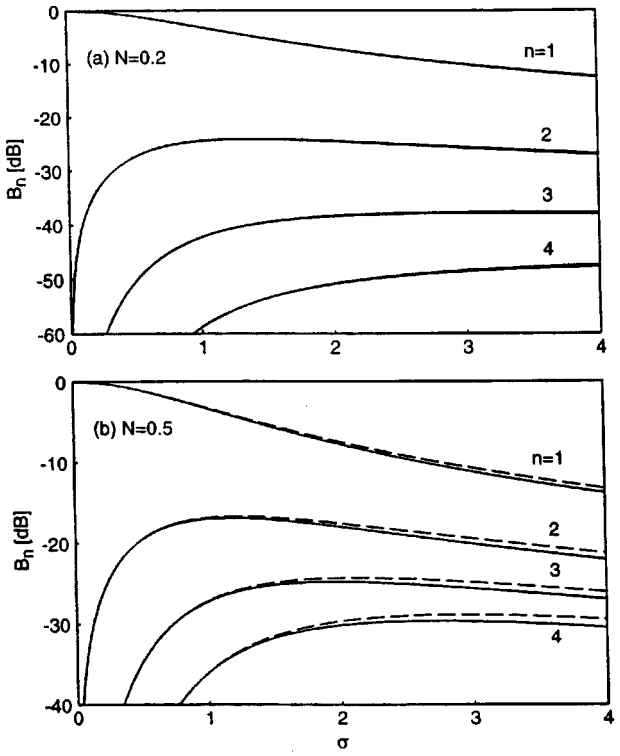

FIG. 5. Harmonic propagation curves for an unfocused beam. Solid lines are obtained from Eq. (48), and dashed lines are finite difference solutions.

$20 \log_{10} B_n$), in Fig. 6 they are the phases ζ_n (in degrees), and the dashed lines in both figures are the corresponding numerical solutions. For $N=0.2$ the analytic and numerical solutions are virtually indistinguishable.

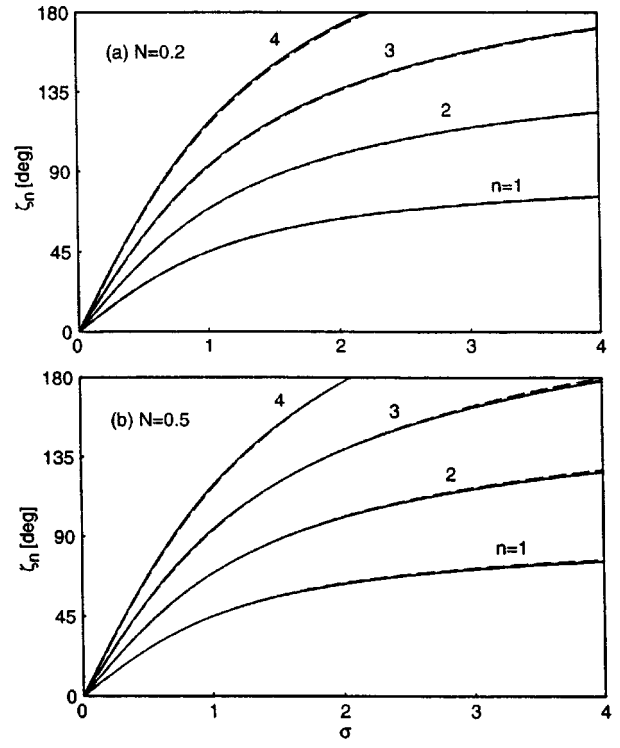

FIG. 6. Phases associated with the harmonic propagation curves in Fig. 5, with solid lines obtained from Eq. (49).

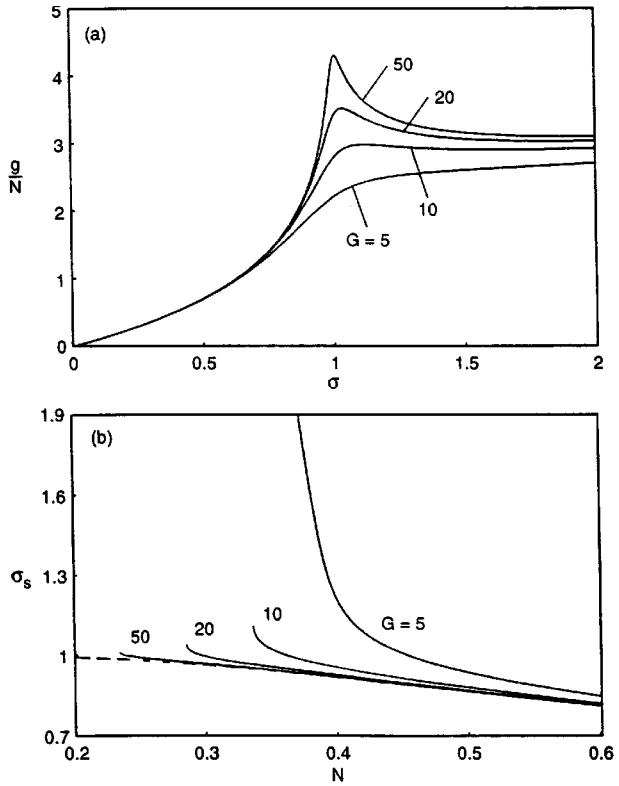

FIG. 7. (a) Distortion parameter, calculated with Eq. (39), and (b) shock formation distance, calculated with Eq. (44), for a focused beam. Dashed line is the result for a converging spherical wave, Eq. (52).

B. Focused beams

All elements of the solutions for focused beams are provided in Sec. III. We begin the discussion once again by investigating the condition for shock formation. Depending on the value of G, the function $\sigma_s(N)$ may not be monotonic, in contrast with the case of unfocused beams (recall Fig. 1). We therefore consider first the behavior of the function $g(\sigma)$, which characterizes waveform distortion in the beam. Specifically, g varies from zero for the undistorted wave at the source, to unity at the point of shock formation. Equation (39) was used to generate the graphs of g/N in Fig. 7(a), for several focusing gains G. For $G=5$ (weak focusing), g increases monotonically from zero to infinity, and therefore setting $g=1$ and varying N in Fig. 7(a) yields a unique value for the shock formation distance σ_s, which is plotted in Fig. 7(b). Now consider a large focusing gain, $G=50$, and let $N=0.25$. Shock formation in this case corresponds to where the curve for $G=50$ in Fig. 7(a) first crosses the line $g/N=4$, which occurs at $\sigma \simeq 1$. For larger values of N (smaller values of g/N), shock formation occurs ever closer to the source, following the curve for $G=50$ in Fig. 7(b). However, for a smaller value of N, e.g., $N=0.20$, the curve for $G=50$ in Fig. 7(a) does not cross the line $g/N=5$ (the condition for shock formation in this case) in the focal region, although it eventually crosses that line very far from the source. We ignore this latter situation (i.e., shock formation far beyond the focus) when plotting the results in Fig. 7(b), which is the reason for the termination of the curves for $G \geqslant 10$.

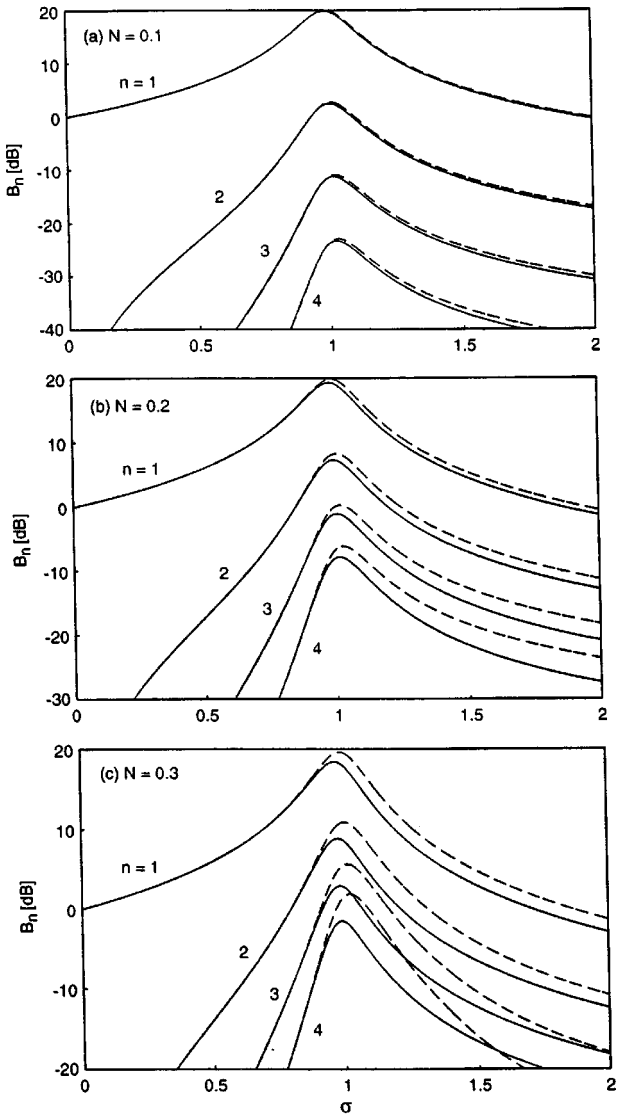

FIG. 8. Harmonic propagation curves for a focused beam with $G=10$. Solid lines are obtained from Eq. (48), and dashed lines are finite difference solutions.

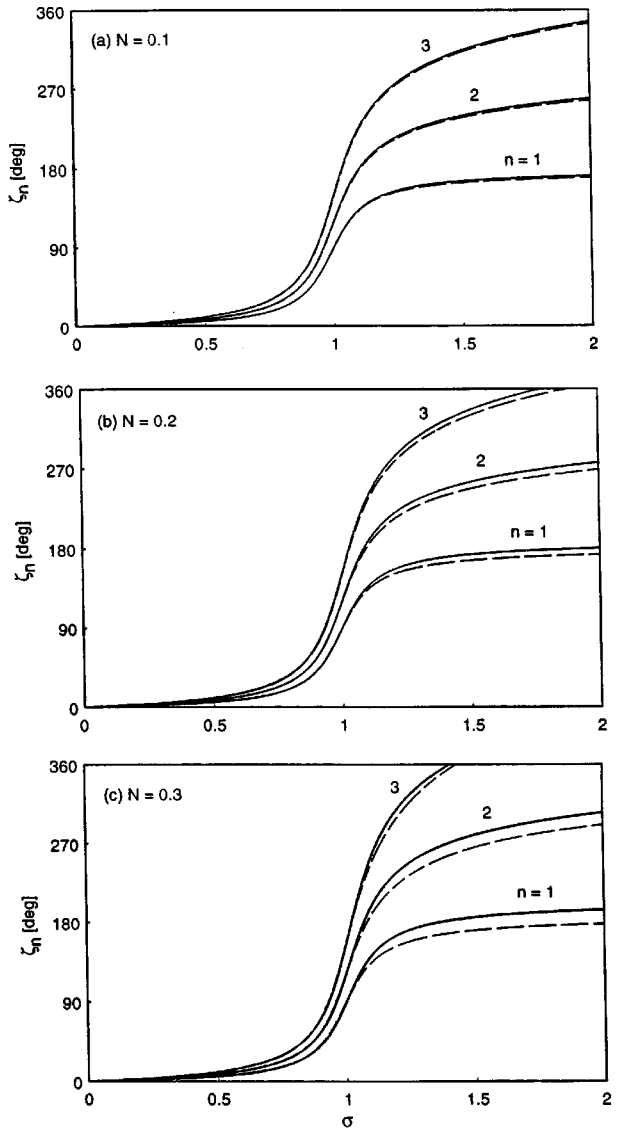

FIG. 9. Phases associated with the harmonic propagation curves in Fig. 8, with solid lines obtained from Eq. (49).

For large values of G the effect of diffraction on shock formation is reduced, and the curves for σ_s approach the dashed line in Fig. 7(b), which is the shock formation distance for a converging spherical wave, given by Eq. (52). Figure 7(a) indicates that for large focusing gains, the waveform can ''undistort'' (i.e., g decreases) just after passing through the focus.

Propagation curves for the harmonic amplitudes B_n and phases ζ_n are plotted as solid lines in Figs. 8 and 9, respectively, for $G=10$ and for three values of N. For comparison, finite difference solutions[21] of the KZ equation are again plotted as dashed lines. The shock formation distance for the largest nonlinearity considered, $N=0.3$, is $\sigma_s=5.25$. In this case, g attains a local maximum value of 0.89 at $\sigma=1.1$, after which it decreases slightly as the wave leaves the focal region, before increasing again to unity at $\sigma=\sigma_s$. Although the analytic predictions of the phases in Fig. 9 are in good agreement with the numerical results for all values of N, the predicted harmonic amplitudes in Fig. 8 are somewhat underestimated, beginning in the focal region, for $N=0.2$ and $N=0.3$. However, agreement in the prefocal region is excellent in all cases.

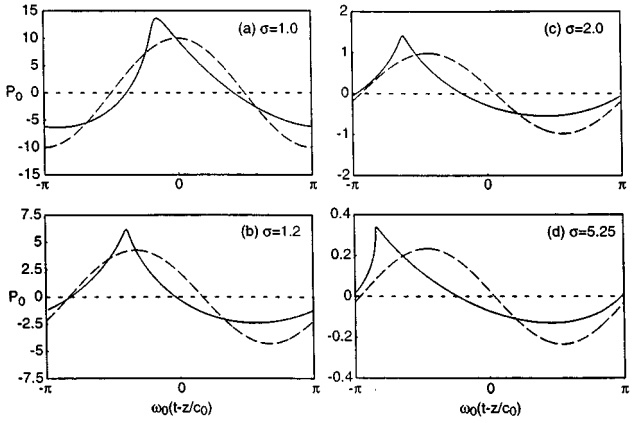

FIG. 10. Waveforms in a focused beam with $N=0.3$ and $G=10$. Solid lines are calculated with Eq. (36), and dashed lines are linear theory given by Eq. (65).

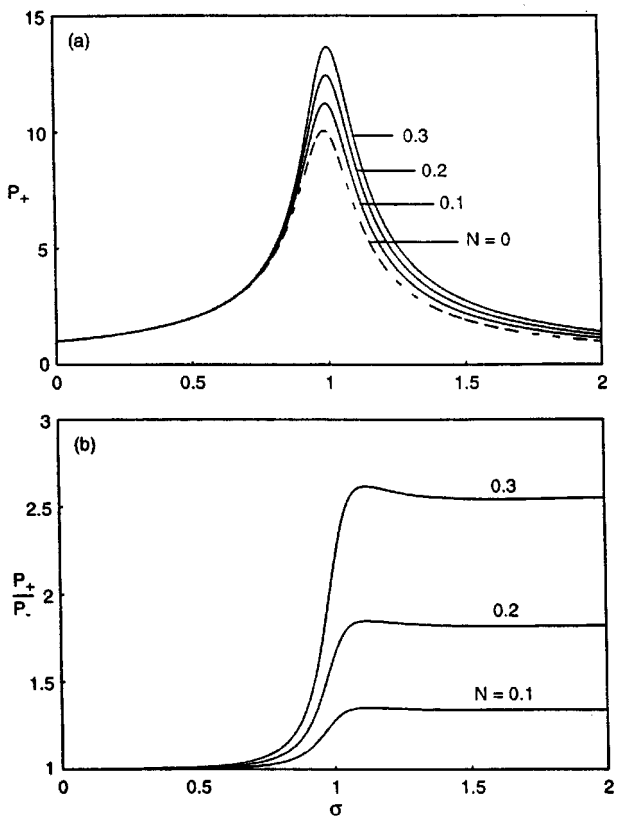

FIG. 11. (a) Peak positive pressure, $P_+ = f^{-1} + \Delta$, and (b) ratio of peak positive to peak negative pressure, calculated with Eq. (67), for waveforms in focused beams with $G = 10$.

The waveforms shown with solid lines in Fig. 10 correspond to the case $N = 0.3$ in Figs. 8 and 9, and the dashed lines are linear theory. As discussed in relation to the behavior of the distortion function g beyond the focus, the waveform steepening is slightly less at $\sigma = 1.2$ and $\sigma = 2$ than at the focus, $\sigma = 1$. Figure 10(d) shows the waveform at the shock formation distance.

Figure 11(a) reveals that, for $G = 10$, finite amplitude effects can increase substantially the peak waveform pressure $P_+ = f^{-1} + \Delta$ in comparison with the small signal amplitude, e.g., by 36% at the focus for $N = 0.3$. The waveform asymmetry may again be characterized by Eq. (67), which is graphed in Fig. 11(b) for several values of N. For the cases considered, the asymmetry increases rapidly as the wave passes through the focus, after which the asymmetry remains relatively constant up to shock formation.

VI. CONCLUSION

A new analytical method for investigating directive sound beams of finite amplitude has been presented. This modified paraxial approach combines the advantages of both nonlinear geometrical acoustics and the quasi-optical theory of diffraction. In contrast with the usual paraxial approach, here we express the acoustic pressure p as a function of the eikonal ψ before performing a power series expansion in terms of $(r/a)^2$, and greater accuracy is thus achieved. Gaussian beam solutions obtained following this approach reduce to several known analytical results, e.g., in the geometrical acoustics and quasilinear limits.

Although only periodic signals were considered in the present work, the analysis can be extended to include transient signals. Waveforms containing shocks, also not considered here, can be investigated by incorporating weak shock theory.

ACKNOWLEDGMENTS

The authors are grateful to M. A. Averkiou and I. R. S. Makin for assistance with the finite difference calculations. This work was supported in part by the North Atlantic Treaty Organization in cooperation with the National Science Foundation, by the International Science Foundation, by the Office of Naval Research, and the National Institutes of Health under Grant No. DK43881.

APPENDIX: SOLUTION OF EQ. (35)

The method of characteristics[13] is used to obtain an exact solution of Eq. (35) for P_0, Eq. (36), and F. The solution for the off-axis term P_2 can then be obtained from Eq. (29). The equations for the characteristics of Eq. (35) are

$$\frac{dP_0}{d\sigma} + \frac{f'}{f} P_0 = F, \tag{A1}$$

$$\frac{dF}{d\sigma} + 3\frac{f'}{f} F = -\frac{P_0}{G^2 f^4} + \phi_2, \tag{A2}$$

$$\frac{d\theta_1}{d\sigma} = -NP_0. \tag{A3}$$

Equations (A1) and (A2) can be rewritten in the more convenient forms

$$f^2 \frac{d}{d\sigma}(fP_0) = f^3 F, \tag{A4}$$

$$f^2 \frac{d}{d\sigma}(f^3 F) = -f\frac{P_0}{G^2} + f^5 \phi_2. \tag{A5}$$

In terms of η, which satisfies the relation [recall Eq. (18)]

$$\frac{d\eta}{d\sigma} = \frac{1}{Gf^2}, \tag{A6}$$

and following introduction of the new quantities

$$A = fP_0, \quad B = f^3 F, \quad \Phi = Gf^5 \phi_2, \tag{A7}$$

Eqs. (A4) and (A5) reduce to

$$\frac{dA}{d\eta} = GB, \tag{A8}$$

$$\frac{dB}{d\eta} = -\frac{A}{G} + \Phi(\eta). \tag{A9}$$

Differentiation of Eq. (A8) and use of Eq. (A9) to eliminate B yields

$$\frac{d^2 A}{d\eta^2} + A = G\Phi. \tag{A10}$$

We may write the general solution of Eq. (A10) as

$$A = C_1 \sin\ \eta + C_2 \cos\ \eta + G \int_0^{\eta} \Phi(\eta') \sin(\eta - \eta')\, d\eta'. \tag{A11}$$

The solution for B is obtained directly from Eq. (A8):

$$B = \frac{1}{G}\left[C_1 \cos\ \eta - C_2 \sin\ \eta + G \int_0^{\eta} \Phi(\eta') \cos(\eta - \eta')\, d\eta' \right]. \tag{A12}$$

Combining Eqs. (A3) and (A6) yields

$$\frac{d\theta_1}{d\eta} = -NGfA. \tag{A13}$$

Substituting Eq. (A11) into Eq. (A13) and integrating, we obtain for the third characteristic equation

$$\theta_1 = \theta_0 - NG\left[\int_0^{\eta} f(\eta')(C_1 \sin\ \eta' + C_2 \cos\ \eta')\, d\eta' + G \int_0^{\eta} f(\eta') \int_0^{\eta'} \Phi(\eta'') \sin(\eta' - \eta'')\, d\eta'\ d\eta'' \right]. \tag{A14}$$

To evaluate the unknowns in Eqs. (A11), (A12), and (A14), we first impose the source condition corresponding to Eqs. (14) and (21):

$$P_0 = \sin\ \theta_1, \quad \sigma = 0. \tag{A15}$$

With $f(0)=1$ and $\eta(0)=0$ we obtain at $\sigma=0$, from Eqs. (26) and (29), $\theta=\theta_1$, $P_0=\sin\ \theta_1$, and $F=G^{-1}\cos\ \theta_1$. We therefore have

$$A(0) = \sin\ \theta_0, \quad B(0) = G^{-1} \cos\ \theta_0, \tag{A16}$$

where the substitution $\theta_1=\theta_0$ has been made, based on Eq. (A14) with $\eta=0$.

Application of the boundary conditions to Eqs. (A11) and (A12) thus yields

$$C_1 = \cos\ \theta_0, \quad C_2 = \sin\ \theta_0. \tag{A17}$$

The solution $P_0=A/f$ can now be expressed as in Eq. (36),

$$P_0 = \frac{1}{f} \sin(\theta_0 + \eta) + \Delta, \tag{A18}$$

where

$$\Delta = \frac{G}{f} \int_0^{\eta} \Phi(\eta') \sin(\eta - \eta')\, d\eta'. \tag{A19}$$

Equation (A14) assumes the parametric form

$$\theta_0 = \theta_1 + NG \int_0^{\eta} f(\eta')(\sin\ \theta_0 \cos\ \eta' + \cos\ \theta_0 \sin\ \eta')\, d\eta' + \delta, \tag{A20}$$

where δ is given by Eq. (43). The integral over η'' in Eq. (A14) was eliminated by using the definition for Δ in Eq. (A19). Noting that $f(\eta)=(\cos\ \eta + G \sin\ \eta)^{-1}$, we may perform the integration in Eq. (A20) to obtain

$$\theta_0 = \theta_1 + \frac{NG}{1+G^2}\left[(\eta - G \ln f\ ) \sin\ \theta_0 + (G\eta + \ln f\ ) \cos\ \theta_0 \right] + \delta \tag{A21}$$

$$= \theta_1 + g \sin(\theta_0 + \phi) + \delta, \tag{A22}$$

where g and ϕ are defined by Eqs. (39) and (41), respectively. The time variables θ_1 and τ are related according to Eqs. (30) and (A6) as

$$\theta_1 = \tau + \frac{R^2}{2} \frac{d}{d\eta}\left(\frac{1}{f^2} \right). \tag{A23}$$

Equation (A22) reduces to Eq. (37) on axis, because $\theta_1=\tau$ for $R=0$.

We must also require the time average of the pressure to vanish,[1] i.e.,

$$\overline{P_0} = \frac{1}{2\pi} \int_{2\pi} P_0\ d\tau = 0 \tag{A24}$$

for all σ. An explicit expression for Δ can then be obtained from Eq. (A24). Substitution of Eq. (A18) into Eq. (A24) and use of Eq. (A22) to write

$$d\theta_1 = [1 - g\ \cos(\theta_0 + \phi)]\, d\theta_0 \tag{A25}$$

yields, following integration, Eq. (42) for Δ. It can also be shown that

$$\Phi = Nf/2 \tag{A26}$$

by performing the same integration but using Eq. (A20) to write

$$d\theta_1 = \left[1 - NG \int_0^{\eta} f(\eta') \cos(\theta_0 + \eta')\, d\eta' \right] d\theta_0, \tag{A27}$$

and then comparing the result with Eq. (A19).

Using Eqs. (29) and (A7), we can write the solution for the off-axis term in the form

$$P_2 = \frac{2G}{f^3} \frac{\partial B}{\partial \theta_1}, \tag{A28}$$

and evaluate it using Eqs. (A12) and (A25) to obtain

$$P_2 = -\frac{2 \sin(\theta_0 + \eta)}{f^3 [1 - g\ \cos(\theta_0 + \phi)]}. \tag{A29}$$

As required, Eq. (A29) reduces for $N \to 0$ to the corresponding small-signal result in Eq. (26).

The solutions for P_0, given by Eq. (A18), and P_2, given by Eq. (A29), are written in parametric form via Eq. (A22), and they can be used to analyze the paraxial region of the beam. Consider, for example, the evolution of the beamwidth defined according to the following definition of mean intensity:

$$I \equiv \frac{1}{2\pi} \int_{2\pi} P^2(\tau)\, d\tau$$

$$= \frac{1}{2\pi}\left(\int_{2\pi} P_0^2 \, d\tau + R^2 \int_{2\pi} P_0 P_2 \, d\tau + \cdots \right). \tag{A30}$$

Now define I_0 to be the axial value of the intensity and rewrite Eq. (A30) as

$$I = I_0\left(1 - 2\frac{R^2}{R_c^2} + \cdots \right), \tag{A31}$$

where we interpret R_c as a characteristic beamwidth:

$$R_c^2(\eta) = -2\frac{\int_{2\pi} P_0^2 \, d\tau}{\int_{2\pi} P_0 P_2 \, d\tau}. \tag{A32}$$

The beamwidth is defined such that in the linear approximation, calculation using the expressions in Eqs. (26) yields $R_c = f$, in accordance with Eq. (15). An approximation of the finite amplitude beamwidth is obtained by substituting Eqs. (A18) and (A29) into Eq. (A32) and performing the integrations with the use of Eq. (A25) to find

$$R_c^2(\eta) = f^2 - 2\Delta^2. \tag{A33}$$

Equation (A33) indicates that the intensity beamwidth becomes narrower with increasing nonlinearity N.

[1] N. S. Bakhvalov, Ya. M. Zhileikin, and E. A. Zabolotskaya, *Nonlinear Theory of Sound Beams* (American Institute of Physics, New York, 1987).

[2] T. S. Hart and M. F. Hamilton, ''Nonlinear effects in focused sound beams,'' J. Acoust. Soc. Am. **84**, 1488–1496 (1988).

[3] M. Born and E. Wolf, *Principles of Optics* (Pergamon, New York, 1980), 6th ed.

[4] H. Kogelnik and T. Li, ''Laser beams and resonators,'' Appl. Opt. **5**, 1550–1567 (1966).

[5] S. A. Akhmanov, A. P. Sukhorukov, and R. V. Khokhlov, ''Self-focusing and diffraction of light in a nonlinear medium,'' Sov. Phys. Usp. **10**, 609–652 (1967).

[6] M. B. Vinogradova, O. V. Rudenko, and A. P. Sukhorukov, *Theory of Waves* (Moscow, Nauka, 1990), 2nd ed. (in Russian).

[7] O. V. Rudenko, S. I. Soluyan, and R. V. Khokhlov, ''Nonlinear theory of paraxial sound beams,'' Sov. Phys. Dokl. **20**, 836–837 (1976).

[8] O. V. Rudenko, S. I. Soluyan, and R. V. Khokhlov, ''Paraxial beams in a nonlinear medium: Analytical solutions,'' *Abstracts of 7th ISNA*, edited by A. H. Nayfeh and J. E. Kaiser (Blacksburg, Virginia, 1976), pp. 25–28.

[9] A. G. Musatov, O. V. Rudenko, and O. A. Sapozhnikov, ''Nonlinear refraction and nonlinear absorption in the focusing of high-intensity pulses,'' Sov. Phys. Acoust. **38**, 274–282 (1992).

[10] O. V. Rudenko, A. K. Sukhorukova, and A. P. Sukhorukov, ''Equations of high-frequency nonlinear acoustics for inhomogeneous media,'' Acoust. Phys. (formerly Sov. Phys. Acoust.) **40**, 264–268 (1994).

[11] M. F. Hamilton, O. V. Rudenko, and V. A. Khokhlova, ''New method for calculating the paraxial region of intense acoustic beams,'' Acoust. Phys. (formerly Sov. Phys. Acoust.) **43**, 48–53 (1997).

[12] B. K. Novikov, O. V. Rudenko, and V. I. Timoshenko, *Nonlinear Underwater Acoustics* (Acoustical Society of America, New York, 1987).

[13] R. Courant and D. Hilbert, *Methods of Mathematical Physics* (Wiley, New York, 1962), Vol. II, pp. 139–145.

[14] D. T. Blackstock, ''Connection between the Fay and Fubini solutions for plane sound waves of finite amplitude,'' J. Acoust. Soc. Am. **39**, 1019–1026 (1966).

[15] O. V. Rudenko and S. I. Soluyan, *Theoretical Foundations of Nonlinear Acoustics* (Plenum, New York, 1977).

[16] F. H. Fenlon, ''Derivation of the multiple frequency Bessel–Fubini series via Fourier analysis of the preshock time waveform,'' J. Acoust. Soc. Am. **53**, 1752–1754 (1973).

[17] K. A. Naugol'nykh, S. I. Soluyan, and R. V. Khokhlov, ''Spherical waves of finite amplitude in a viscous thermally conducting medium,'' Sov. Phys. Acoust. **9**, 42–46 (1963).

[18] O. V. Rudenko, S. I. Soluyan, and R. V. Khokhlov, ''Confinement of a quasiplane beam of periodic perturbations in a nonlinear medium,'' Sov. Phys. Acoust. **19**, 556–559 (1974).

[19] F. Y. Coulouvrat, ''An analytical approximation of strong nonlinear effects in bounded sound beams,'' J. Acoust. Soc. Am. **90**, 1592–1600 (1991).

[20] J. Naze Tjøtta, S. Tjøtta, and E. H. Vefring, ''Propagation and interaction of two collimated finite amplitude sound beams,'' J. Acoust. Soc. Am. **88**, 2859–2870 (1990).

[21] J. Naze Tjøtta, S. Tjøtta, and E. H. Vefring, ''Effects of focusing on the nonlinear interaction between two collinear finite amplitude sound beams,'' J. Acoust. Soc. Am. **89**, 1017–1027 (1991).

Application of the Foldy–Wouthuysen transformation to the reduced wave equation in range-dependent environments

Daniel Wurmser and Gregory J. Orris
United States Naval Research Laboratory, Washington, DC 20375-5200

Roger Dashen[a)]
Physics Department, University of California, San Diego, La Jolla, California 92037

(Received 4 November 1994; accepted for publication 13 September 1996)

The Foldy–Wouthuysen transformation can be used to reduce the relativistic Klein–Gordon equation to the nonrelativistic Schrödinger equation. This technique is modified and applied to the problem of wave propagation through media with a range-dependent index of refraction. The forward and backward propagating components of the field are decoupled order-by-order to produce a perturbative expansion of the range-dependent parabolic equation. The result includes energy-conserving correction terms that can be associated with a rapid fluctuation of energy between forward and backward propagating solutions of the Helmholtz equation. The approach selects out physical processes which accumulate over the entire range of propagation, distinguishing them from effects which depend solely on the initial and final values of the index of refraction and its derivatives. It is also shown that the corresponding backscatter mechanism is fundamentally nonperturbative, so that the parabolic equation technique as applied to the problem of propagation through range-dependent media generates an asymptotic expansion of the exact solution. This procedure has been applied to long-distance low-frequency propagation through a sound channel with internal waves. For this application, the expansion parameters are typically very small, so the propagation distances must be very large for the effect to be detectable. [S0001-4966(97)02203-0]

PACS numbers: 43.30.Bp [MBP]

INTRODUCTION

Much effort has been expended to enhance wave propagation models to increase their speed of execution while properly accounting for range-dependent environments. The parabolic equation (PE) technique, based on the parabolic approximation of the Helmholtz equation, has had much success at modeling short-to-moderate-range propagation in range-dependent environments. In ocean acoustics, for example, the PE has proven to be capable of including such effects as internal waves, range dependence of the sound speed, and variable bathymetry.[1–3] It would seem that wave propagation, where the wave speed in the medium is assumed to depend weakly on both spatial and temporal variables, is ideally suited to current PE techniques. Yet, for extremely long-range modeling, the PE technique cannot account for all of the effects observed experimentally.[4] Generally, these discrepancies have been attributed to incomplete or incorrect environmental knowledge. We believe that the PE may have a fundamental missing piece of physics, and that an upper bound must be placed on the effects associated with it before a massive effort to revise environmental parameters is undertaken. Thus, within this paper the physical consequences of the parabolic approximation in range-dependent environments will be revisited.

The main physical effect associated with wave propagation through weakly range-dependent environments is refraction. There are many causes of range dependence in the index of refraction. For example, internal gravity waves and changing temperature profiles in the oceans causes both range and time dependence of the acoustic index of refraction. Within these contexts, refraction can be intuitively, although not necessarily quantitatively, understood using concepts from geometrical and physical wave mechanics. One of the key features of refraction is that the physical processes involved apply over scales greater than a wavelength.[5–9] In this paper we show that there exists another type of physical effect associated with wave propagation through range-dependent environments. To lowest order, the cumulative effect of this new phenomenon on wave propagation can be accounted for by rescaling the phase speed c according to the transformation formula

$$c \rightarrow c - \frac{1}{8k_0^2}\frac{\partial^2 c}{\partial x^2}, \tag{1}$$

where k_0 is the reference wave number, usually taken at the source location, and $\partial^2 c/\partial x^2$ is the second derivative of the local phase speed, in the preferred direction of propagation. Because of its simplicity, this prescription can be used with existing techniques including wide-angle PEs with little modification to the model. Immediately we can estimate the size of the effect by considering the most likely ocean-acoustic scenario where Eq. (1) might make a difference—long-range propagation through variable sound-speed profiles caused by internal waves. Taking the corresponding horizontal length scale to be of approximately 500 m, the nominal reference wave number of 1500 m/s and the size of

[a)]Deceased.

the fluctuation to be $\mathcal{O}(1)$ m/s,[10] and assuming a sound-speed fluctuation that is roughly sinusoidal, we find $\delta c \approx 1/f^2$, where f is the propagation frequency. While this effect must be small (the effects of larger fronts or eddys will of course be larger, yet the total number of such interactions is much smaller), the cumulative effect could be large enough to be measured. As will be demonstrated the associated effect is minimal for continuous wave problems of interest, however, we suspect that examples involving pulse propagation will be more strongly affected. (Due to size constraints we will leave this conjecture to be proven in another paper.)

Our analysis is built upon the observation that the parabolic approximation to the Helmholtz equation belongs to the same class of second-order partial differential equations as the Schrödinger equation of quantum mechanics.[1,9] In essence, the PE approximates the Helmholtz equation for a propagating wave field in much the same way that the nonrelativistic Schrödinger equation approximates the relativistic Klein–Gordon equation, although the Helmholtz equation is of elliptic type and the Klein–Gordon equation is of hyperbolic type: Both are reductions of more complicated and thus more difficult to solve differential equations to parabolic ones. Formally, forward time-propagation of a quantum mechanical field obeying the Klein–Gordon equation corresponds to forward range propagation of a scalar field representing the solution to the Helmholtz equation. Similarly, the backward time-propagating solutions of the quantum mechanical field correspond to backward range-propagation of the scalar field. The interpretation of the backward time-propagating Klein–Gordon field is that these solutions are antiparticles. Despite the lack of existence of antiparticles in real matter, their existence still affects real matter, most notably through the particle charge and mass. In light of this deep physical relationship between the forward and backward time-propagating waves in quantum mechanics, there must be a similar relationship between all field equations that are reducible to parabolic form. Within this paper we address this type of interpretation of solutions to the Helmholtz equation by drawing analogies to their quantum mechanical counterparts. Similar to the first uses of the Schrödinger equation, traditional parabolic equations and their methods of solution treat the forward propagating solution as if it must conserve energy independent of the backward propagating solution. These two solutions are always assumed to be decoupled from one another, except for strong interactions with the environment that cause scattering. Hence the effort to find correction terms to the acoustic PE that would conserve energy.

Deeper insights into how the PE approximates the Helmholtz equation can emerge from the analogy between quantum field theory and classical wave propagation in random media. Most significantly, relativistic quantum field theory suggests a technique for generating higher-order parabolic equations which include range-dependent effects. For example, the Schrödinger equation, complete with relativistic corrections, can be derived using a transformation method that operates in a spinor space,[11] where one component is the forward propagating solution and the other is the backward propagating solution. This transformation is known as a Foldy–Wouthuysen transformation.[9,12–14] The advantage to using this transformation is that it provides an order-by-order prescription for decoupling the forward and backward propagating solutions of the Klein–Gordon equation and consequently, as applied to classical field theory, the Helmholtz equation. This iterative procedure performed on the wave field resembles the procedure known as renormalization of the quantum field: With each iteration, terms with an undesirable characteristic, in this case coupling between forward and backward propagation, are shifted to the next higher-order PE approximation. This procedure manifestly leads to additional corrections to the forward propagating portion of the field which can be identified with phase changes of the field. These new correction terms can be identified as the classical equivalent of the relativistic quantum mechanical effect known as *Zitterbewegung.*[15–17] The physical consequences of this phenomenon are as follows: Averaged over the scale of a wavelength, no energy is transferred into backward propagation by this phenomenon, yet there is an interference between the forward and backward propagating components of the field. One effect is that the wavefronts no longer occupy specific locations, but are smeared in the direction of propagation, over spatial scales that are approximately $\delta x \sim 1/(2k_0)$. The effect on the physical system, as suggested by Eq. (1), is that this effect bears a superficial resemblance to classical refraction, but the underlying physics is genuinely different.

The formalism makes no provision for problems involving strong backscatter. This will implicitly been assumed to be negligible. Strong backscatter can result if the index of refraction varies greatly on the order of a wavelength. Phenomena of this type are best modeled using the perturbative expansion known as the Born series.[18,19] If scattering is significant, parameters for the expansion generated by the Foldy–Wouthuysen procedure will be large, allowing us to conclude that the picture implicit in the Born series is fundamentally incompatible with the PE approximation, as has previously been pointed out by Fishman and McCoy.[9,20] Nevertheless, for many problems of interest including long-distance wave propagation in most physical systems involving weak range dependence, the assumption that there are no regions of strong backscatter is a valid one and will be made throughout the remainder of this paper.

Another type of backscatter is compatible with the physical assumptions made in this paper. Its quantum mechanical analog is that of a charged particle propagating through an external electric field. This particle will transfer energy from the particle to the antiparticle components of the field via a process known as particle-pair production.[21–23] As has been recognized previously in the probabilistic literature, this process is the backscattering mechanism which corresponds to the physical assumptions that underlie the PE.[24–26] For example, in the acoustic problem, range dependence of the sound speed plays a role very similar to that of the external electric field in quantum field theory. It follows that the parabolic equation is an asymptotic expansion of the exact solution that fails to include energy-transferring backscatter at any order. This has previously been commented on by Taylor and Fishman,[27,28] implying that for any PE approximation

we are left with the unphysical prospect of conserving the energy of both the forward and backward propagating solutions independently.

A picture of the physical implications of a weakly range-dependent index of refraction can be put onto a more solid footing by systematically using the Foldy–Wouthuysen transformation and analyzing the results through appropriate analogies to established relativistic quantum mechanical cases. This effort will center around the observation that new classical phenomena can occur when the index of refraction is range dependent. The related energy-conserving corrections to the PE can now be recognized as a consequence of the fact that range dependence couples forward and backward propagating solutions, but, in this case, no energy is permanently transferred into the backward propagating solution. Instead, the coupling imparts a certain fuzziness to the forward propagating wavefront by redistributing the energy in a frequency-dependent manner.

We point out that the problem could also have been attacked from a formal mathematical point of view. Indeed, a great deal of work has been done in the mathematical physics community concerning the reduction of the second-order Helmholtz equation to the first order. For example, within this context it was discovered that pseudo-partial differential operator equations reduce to first-order systems that can subsequently be decoupled in orders of the smoothness.[27] The Foldy–Wouthuysen procedure turns out to be a special case of this procedure. For the range-independent case, this was demonstrated by Fishman and McCoy,[9,20] Fishman,[28] and Fishman *et al.*[29] The asymptotic character of the expansion, in particular, was examined by Fishman.[28] This paper therefore represents the coming together of two strands of research: The physical, based on the intuition that range dependence and coupling between forward propagation and backscatter are somehow related, and the formal, based on the realization that the proper factorization of the Helmholtz equation must ultimately emerge from a systematic study of approximate wave theories.

In the next section we derive a vector formulation of the Helmholtz equation and discuss the relationship between pseudo-Hermitian operators and energy conservation. In Sec. III we first develop the concept of the Foldy–Wouthuysen transformation and then apply it to a range-independent case. The bulk of this section though, is devoted to the range-dependent case. At the end of Sec. III we derive the main result of the paper. In Sec. IV we apply Eq. (1) to an ocean with internal waves. We describe the internal wave spectrum and how a large internal wave field is constructed. There it is shown that the size of the effect of the new Foldy–Wouthuysen correction term to the PE is in general very small for continuous-wave work. We believe that it can have larger implications on signal processing techniques that rely heavily on relative phase information. Last, we conclude with a brief discussion of the results.

I. VECTOR FORMULATION OF THE HELMHOLTZ EQUATION

Points in space are labeled by a Cartesian coordinate system with x the range coordinate. We will denote the two-dimensional vector transverse to the range by $\mathbf{x}_\perp=(y,z)$. This coordinate system is preferable for the formal work to be pursued in this paper, although cylindrical or spherical coordinates can also be used. The result in cylindrical coordinates, in the far-field limit, is mathematically identical to that obtained when the Cartesian coordinate system is used, provided that the radial coordinate r is substituted for x, the wave function is rescaled by a factor $1/\sqrt{r}$, and nonpropagating terms proportional to $1/r$ are dropped.

A. Converting a second-order differential equation to first order

The wave field is assumed to propagate according to the wave equation through a time-independent environment and is monochromatic with radial frequency ω. So the pressure is given by

$$P(x,\mathbf{x}_\perp,t)=\mathrm{Re}[A(x,\mathbf{x}_\perp)e^{-i\omega t}], \tag{2}$$

where $A(x,\mathbf{x}_\perp)$ is a solution of the Helmholtz equation

$$\frac{\partial^2 A}{\partial x^2}+\nabla_\perp^2 A+k_0^2 n^2(x,\mathbf{x}_\perp)A=0. \tag{3}$$

The wave number k_0 is given by $k_0=\omega/c_0$, with c_0 a reference phase speed usually taken to be the phase speed at the source location. Also, in Eq. (3), $n(x,\mathbf{x}_\perp)$ is the index of refraction and is spatially dependent.

The second-order differential equation for the scalar field, A, is reduced to a first-order equation for a vector field $\vec{\Phi}$. The components of $\vec{\Phi}$ must be linear combinations of A and its first derivative $\partial A/\partial x$. Following Bjorken and Drell,[30] we define

$$\vec{\Phi}=\begin{pmatrix}\theta\\ \chi\end{pmatrix}, \tag{4}$$

where the functions θ and χ are given by

$$\theta=\frac{1}{2}\left(A+\frac{i}{k_0}\frac{\partial A}{\partial x}\right), \tag{5a}$$

$$\chi=\frac{1}{2}\left(A-\frac{i}{k_0}\frac{\partial A}{\partial x}\right). \tag{5b}$$

This choice of reduction (i.e., the choice of θ and χ) is not an exact splitting of the solution to the Helmholtz equation into forward and backward propagating waves for transversally dependent media (see, e.g., Ref. 31). The physical identification between these forward and backward propagating waves is accomplished through a splitting in terms of the inverse of the square-root Helmholtz operator. However, that formulation still leaves the forward and backward components coupled for range-dependent environments. Our effort will be focused on finding the modification (i.e., extra terms) which may be added to the one-way PE that correctly accounts for the cumulative effects of propagation in range-dependent environments. Thus, it is not the natural choice for the work presented here. We are interested in making the connection between the forward and backward propagating components (these must be to first approximation decoupled in weakly range-dependent environments), which includes the correct physics. It is straightforward to show that Eqs. (5)

are the correct splitting in the homogeneous free-field case where there is a uniform phase speed c_0 everywhere. There the vector $\vec{\Phi}$ represents purely outgoing plane waves (i.e., $A \propto e^{+ik_0 x}$), where it follows that

$$\vec{\Phi} \propto \begin{pmatrix} 0 \\ \chi(\mathbf{x}) \end{pmatrix}. \tag{6}$$

Similarly the backward propagating vector in a range-independent, homogeneous environment (i.e., $A \propto e^{-ik_0 x}$) would be represented as

$$\vec{\Phi} \propto \begin{pmatrix} \theta(\mathbf{x}) \\ 0 \end{pmatrix}. \tag{7}$$

Using the definitions for θ and χ the Helmholtz equation can be rewritten as

$$ik_0\left(\frac{\partial\theta}{\partial x} - \frac{\partial\chi}{\partial x}\right) = \nabla_\perp^2(\theta+\chi) + k_0^2 n^2(\theta+\chi). \tag{8}$$

Manipulating the definitions of θ and χ in Eq. (5), we also have an equation of constraint

$$ik_0\left(\frac{\partial\theta}{\partial x} + \frac{\partial\chi}{\partial x}\right) = k_0^2(\theta-\chi). \tag{9}$$

Adding and subtracting Eqs. (8) and (9), expressing the answers in matrix form, and defining $\mu \equiv \frac{1}{2}(1-n^2)$, we have in matrix-differential operator form of the field equation for $\vec{\Phi}$,

$$i\,\frac{\partial\vec{\Phi}}{\partial x} = [k_0\,\boldsymbol{\eta} + \hat{\Lambda}\,\boldsymbol{\eta} + \hat{\Lambda}\,\boldsymbol{\sigma}]\vec{\Phi}, \tag{10}$$

where the differential operator $\hat{\Lambda}$ is defined as

$$\hat{\Lambda} \equiv \frac{\nabla_\perp^2}{2k_0} - \mu k_0, \tag{11}$$

and the matrices $\boldsymbol{\eta}$ and $\boldsymbol{\sigma}$ are

$$\boldsymbol{\eta} \equiv \begin{pmatrix} 1 & 0 \\ 0 & 1 \end{pmatrix}, \tag{12a}$$

$$\boldsymbol{\sigma} \equiv \begin{pmatrix} 0 & 1 \\ -1 & 0 \end{pmatrix}. \tag{12b}$$

The operator $\hat{\mathbf{O}} \equiv \hat{\Lambda}\,\boldsymbol{\sigma}$ is henceforth called the odd operator. It has two very important properties: (1) $\boldsymbol{\sigma}^2 = -\mathbf{I}$, and (2) it is off-diagonal and thus couples the components of $\vec{\Phi}$. By contrast, the operator $\hat{\mathbf{E}}$, henceforth known as the even operator and defined by $\hat{\mathbf{E}} \equiv \hat{\Lambda}\,\boldsymbol{\eta}$, is diagonal, and does not couple θ and χ. We now have reduced the Helmholtz equation to the Hamiltonian form,

$$i\,\frac{\partial\vec{\Phi}}{\partial x} = \hat{\mathbf{H}}(\hat{\Lambda})\vec{\Phi}, \tag{13}$$

where

$$\hat{\mathbf{H}}(\hat{\Lambda}) \equiv k_0\,\boldsymbol{\eta} + \hat{\mathbf{E}} + \hat{\mathbf{O}}. \tag{14}$$

Equation (13) is the Helmholtz equation rewritten in vector form, and is not a unique way of recasting the Helmholtz equation as a first-order matrix equation.[32] There are a number of methods for taking the square root of an operator, with the Dirac operator being a prime example.[33–35] However, unlike Eq. (13), the Dirac equation introduces a superfluous nonphysical degree of freedom corresponding to quantum mechanical spin, which is not present in the classical scalar wave equation. Levers found a nonobvious family of splittings, using the algebraic methods associated with relativistic quantum mechanics [specifically the algebra of what is known as SU(2), or the special unitary group of degree 2], which are linear in the transverse differential operator, and hence is analogous to the Dirac construction.[36] Even for the exact splittings which can thus be constructed, none diagonalize in the transversely inhomogeneous limit. These systems of equations coupling the wave field components always remain coupled in this limit, and, thus, do not correspond to the physically independent left- and right-traveling waves in a transversely inhomogeneous environment.

B. Energy conservation and pseudo-Hermitian operators

To address the issue of energy conservation one must show that the Hamiltonian operator $\hat{\mathbf{H}}(\hat{\Lambda})$ is pseudo-Hermitian and that $\vec{\Phi}$ is related to the energy flux. The former property implies that the energy is conserved at all ranges. The concept of pseudo-Hermiticity is, of course, a generalization of the familiar property of operators called Hermiticity which we review in Appendix A. The definition of a pseudo-Hermitian operator is similar to that of a Hermitian operator: the matrix-differential operator $\hat{\boldsymbol{\alpha}}$ is pseudo-Hermitian if $(\boldsymbol{\eta}\hat{\boldsymbol{\alpha}})^\dagger = \boldsymbol{\eta}\hat{\boldsymbol{\alpha}}$, where $\boldsymbol{\eta}$ is defined by Eq. (12). A pseudo-Hermitian operator is essentially a Hermitian operator with the unit matrix replaced by $\boldsymbol{\eta}$. The physical significance of using $\boldsymbol{\eta}$ instead of the unity matrix, **1**, lies in the fact that the energy associated with the two components of $\vec{\Phi}$ propagates in different directions. Since $\hat{\Lambda}$ and $\boldsymbol{\eta}$ are Hermitian, $\boldsymbol{\sigma}$ is anti-Hermitian (i.e., $\boldsymbol{\sigma}^\dagger = -\boldsymbol{\sigma}$) and $\boldsymbol{\eta}\boldsymbol{\sigma} = -\boldsymbol{\sigma}\boldsymbol{\eta}$, it follows that $\hat{\mathbf{H}}$ as defined by Eq. (14) is also pseudo-Hermitian.

One of the implications of the fact that $\hat{\mathbf{H}}$ is pseudo-Hermitian is that we can define the quantity

$$\mathscr{T}(x) \equiv \int \vec{\Phi}^\dagger \boldsymbol{\eta} \vec{\Phi}\, d\mathbf{x}_\perp\,. \tag{15}$$

Differentiating $\mathscr{T}$ by x we see

$$\frac{\partial\mathscr{T}}{\partial x} = \int \left(\vec{\Phi}^\dagger \boldsymbol{\eta}\,\frac{\partial\vec{\Phi}}{\partial x} + \frac{\partial\vec{\Phi}^\dagger}{\partial x}\,\boldsymbol{\eta}\vec{\Phi}\right) d\mathbf{x}_\perp\,. \tag{16}$$

However, because the operator $\boldsymbol{\eta}$ is pseudo-Hermitian,

$$i\int \vec{\Phi}^\dagger \boldsymbol{\eta}\,\frac{\partial\vec{\Phi}}{\partial x}\, d\mathbf{x}_\perp = \int \vec{\Phi}^\dagger \boldsymbol{\eta}\hat{\mathbf{H}}\vec{\Phi}\, d\mathbf{x}_\perp \tag{17a}$$

$$= \int (\boldsymbol{\eta}\hat{\mathbf{H}}\vec{\Phi})^\dagger \vec{\Phi}\, d\mathbf{x}_\perp \tag{17b}$$

$$= -i\int \frac{\partial\vec{\Phi}^\dagger}{\partial x}\,\boldsymbol{\eta}\vec{\Phi}\, d\mathbf{x}_\perp\,. \tag{17c}$$

Thus

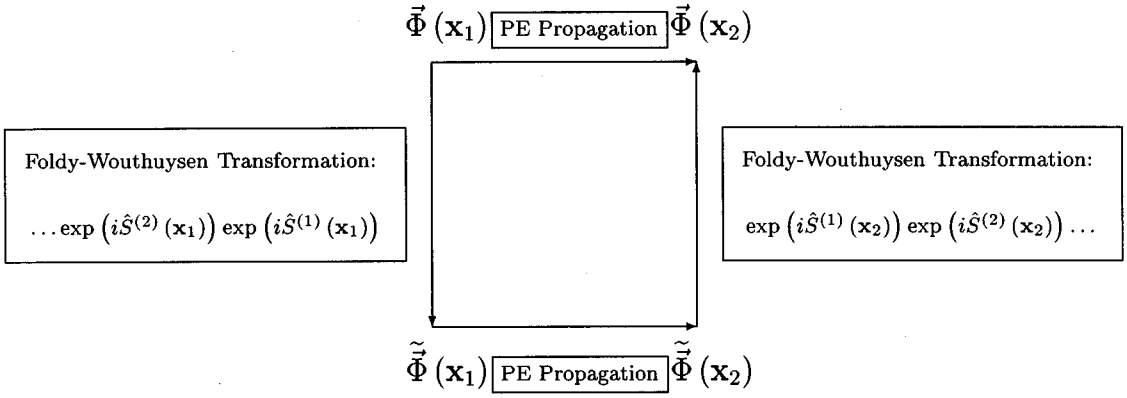

FIG. 1. The strategy to be employed is diagrammed above. The Foldy–Wouthuysen transformation is used to reformulate the problem such that forward- and backward-propagating solutions are decoupled. The problem is solved in transformed space. For many applications, propagation effects dominate, and it is possible to drop the contribution from the transformations at the endpoints.

$$\frac{\partial \mathscr{T}}{\partial x} = 0. \tag{18}$$

To see that this equation is an expression of total energy conservation, i.e., that the forward and backward propagating components of the field are both included, Eq. (15) is reexpressed as

$$\mathscr{T} = \int (\theta^* \theta - \chi^* \chi)\, d\mathbf{x}_\perp \tag{19a}$$

$$= \frac{i}{2k_0} \int \left[A^* \frac{\partial A}{\partial x} - \left(\frac{\partial A}{\partial x}\right)^* A \right] d\mathbf{x}_\perp . \tag{19b}$$

This represents the energy flux through the $\mathbf{x}_\perp$ plane. For the acoustic case we can rewrite this as

$$\mathscr{T}(x) = -2\rho c_0 \int \left(\frac{\mathrm{Im}(A^* \boldsymbol{\nabla} A)}{2\rho\omega} \cdot \hat{x} \right) d\mathbf{x}_\perp \tag{20a}$$

$$= -2\rho c_0 \int \hat{S}_{\mathrm{ave}} \cdot \hat{\mathbf{x}}\, d\mathbf{x}_\perp , \tag{20b}$$

where $\vec{S}_{\mathrm{ave}}$ is the time-averaged energy flux and ρ is the density.[37] It follows that $\mathscr{T}$ is proportional to the total downrange flow of energy. Since it is the same for all values of the range, there are no energy sources or sinks, and we have shown that the pseudo-Hermiticity of $\hat{\mathbf{H}}$ guarantees energy conservation. Furthermore, the physical significance of the quantity $\vec{\Phi}^\dagger \boldsymbol{\eta} \vec{\Phi}$, taken as a function of the position $\mathbf{x}$, has been established: It is the time-averaged energy density flux in the direction of the range $\hat{x}$.

II. THE FOLDY–WOUTHUYSEN TRANSFORMATION

A. Canonical transformations

We seek a canonical transformation that will decouple the forward and backward propagating solutions, while preserving the equation of motion.[38,39] (See Fig. 1.) The transform will be of the form, $\vec{\Phi} \rightarrow \tilde{\vec{\Phi}}$, $\hat{\mathbf{H}} \rightarrow \tilde{\hat{\mathbf{H}}}$.

$$i \frac{\partial \vec{\Phi}}{\partial x} = \hat{\mathbf{H}} \vec{\Phi} \rightarrow i \frac{\partial \tilde{\vec{\Phi}}}{\partial x} = \tilde{\hat{\mathbf{H}}} \tilde{\vec{\Phi}}. \tag{21}$$

The Foldy–Wouthuysen transformation is one of a class of transforms that has precisely the correct properties. More importantly it diagonalizes $\hat{\mathbf{H}}$ (i.e., $\tilde{\hat{\mathbf{H}}}$ is diagonal), while the components of $\tilde{\vec{\Phi}}$ ($\tilde{\theta}$ and $\tilde{\chi}$) represent decoupled backward and forward propagating solutions, respectively.

Technically, the Foldy–Wouthuysen transformations are implemented only at the beginning and end of propagation (henceforth these will be referred to as endpoints). However, there exists an alternate formulation of the problem such that the effects associated with these transformations take the form of additional energy conserving terms in the Hamiltonian. The lowest-order contribution of this type turns out to be the result discussed by Schurman *et al.*[6] In Appendix B we briefly examine the ''endpoint'' contribution of Schurman *et al.* within the context and formalism presented in this paper. This term also follows from the requirement that the solution of the range-dependent PE must still satisfy the wave equation. Since the two formulations are equivalent, the contribution from the additional term in the Hamiltonian must cancel during propagation, the final result depending only on the expansion parameters evaluated at the endpoints. Nevertheless, the direct argument based on consistency between the wave equation and the PE provides no indication of this fact. As we shall show below, the main advantage of the approach based on the Foldy–Wouthuysen transformation is the clear separation between propagation and endpoint effects.

The range-dependent effects, of which we are most interested, accumulate as the wave field propagates over large distances, thus the contributions at the endpoints can be neglected, provided that $r/L \gg 1$ where L is the fluctuation length scale of the phase speed in the environment. To insure that these endpoint contributions are as small as possible, only energy-conserving transformations are allowed. This is so that the transformations at the endpoints are not needed to put energy back into the system and so they can be ignored. This requirement implies that the transformation must be pseudo-unitary (i.e., if $\vec{\Phi} = U \tilde{\vec{\Phi}}$, then $U^\dagger \boldsymbol{\eta} U = \boldsymbol{\eta}$), which in turn guarantees that the total energy flux remains equal to $\mathscr{T}$. For this to be true $\tilde{\hat{\mathbf{H}}}$ must be pseudo-Hermitian; $\tilde{\hat{\mathbf{H}}}$ is also

Hermitian, because $\tilde{\tilde{\mathbf{H}}}$ is diagonal, and so the equations for the components of $\tilde{\tilde{\Phi}}$ are decoupled, implying that each component must independently conserve energy.

To see that the endpoint contributions can be ignored we consider the case of long-range propagation. The effects associated with the diagonalization of $\hat{\mathbf{H}}$ can be more important than the refraction effects which can be associated with the contribution at the endpoints. This can be seen by considering the following argument: Let an arbitrary translational operator equation have the form

$$i\,\frac{\partial A}{\partial x}=\hat{\mathbf{H}}A. \tag{22}$$

Formally, the solution to Eq. (22) can be written as

$$A(x)=\hat{R}\left[\exp\left(i\int_{x_0}^{x}\hat{\mathbf{H}}\,dx\right)\right]A(x_0), \tag{23}$$

where $\hat{R}$ is a range-ordering operation similar to the time-ordering operator in quantum field theory.[40–42] Energy conservation forces $\hat{\mathbf{H}}$ to behave like a real (as opposed to complex) number. Suppose $\hat{\mathbf{H}}$ can be written as $\hat{\mathbf{H}}=\hat{\mathbf{H}}_0+\delta\hat{\mathbf{H}}$, where $\delta\hat{\mathbf{H}}$ is very small compared to $\hat{\mathbf{H}}_0$. Generally, the effects of the added term $\delta\hat{\mathbf{H}}$ will be negligibly small. Note, however, that formally the solution to Eq. (13) is exp $(i\hat{\mathbf{H}}x)$. In essence, canonical transformations of $\hat{\mathbf{H}}$ are in the phase of an exponential, and that its contribution grows with increasing propagation distance. Meanwhile the effects of $\hat{\mathbf{H}}_0$ (which is where the endpoint contributions can be found) are constrained.[6] The perturbation can become significant for long-range propagation. This is a desirable result since it is well known that the PE method without new range-dependent terms works very well in most applications. By contrast, the effect of range refraction remains very small for long-distance sound propagation in the ocean, since it does not accumulate in this way.

The physical nature of the endpoint contribution can best be appreciated by considering the simple problem of a plane wave traversing parallel layers, each characterized by a constant, nondispersive sound speed. Neglecting energy lost to backscatter, the series of layers can be replaced by a single interface between the initial and final half-spaces. This may be observed in propagation over a single strong or sudden change in the index of refraction.[5,6] However, the endpoint contributions are generally negligible for long-range propagation, including instances where a number of changes are traversed, provided that the final index of refraction is roughly similar to that at the source.

B. Range-independent index of refraction

We now illustrate the Foldy–Wouthuysen technique by examining the case where there is no range dependence in the index of refraction (i.e., μ can depend on $\mathbf{x}_\perp$, but it is independent of x). The corresponding Foldy–Wouthuysen transformation is

$$\tilde{\tilde{\Phi}}=e^{i\hat{S}}\vec{\Phi}, \tag{24}$$

where

$$\hat{S}=\boldsymbol{\eta}\boldsymbol{\sigma}\Theta(\hat{\Lambda})=\begin{pmatrix}0 & 1\\ 1 & 0\end{pmatrix}\Theta(\hat{\Lambda}), \tag{25a}$$

$$\Theta(\hat{\Lambda})=-\frac{i}{2}\tanh^{-1}\frac{\hat{\Lambda}}{k_0+\hat{\Lambda}}. \tag{25b}$$

Here, $\hat{S}$ can be obtained heuristically by invoking an analogy to rotations about coordinate axes commonly used in quantum mechanics, while the value of Θ given in Eq. (25) comes from the requirement that off-diagonal elements of $\tilde{\tilde{\mathbf{H}}}$ must be zero.[43]

Requiring $\partial\hat{\Lambda}/\partial x=0$ implies that $\tilde{\tilde{\mathbf{H}}}=e^{i\hat{S}}\hat{\mathbf{H}}e^{-i\hat{S}}$ and, from the definition of $\hat{\mathbf{H}}$ given by Eq. (14), it follows that $e^{i\hat{S}}\hat{\mathbf{H}}=\hat{\mathbf{H}}e^{-i\hat{S}}$. Finally, this leads to

$$\tilde{\tilde{\mathbf{H}}}=\hat{\mathbf{H}}e^{-2i\hat{S}}=\boldsymbol{\eta}\mathbf{k}_0\sqrt{1+\frac{2\hat{\Lambda}}{k_0}}. \tag{26}$$

For a forward propagating wave, we have

$$\tilde{\tilde{\Phi}}=\begin{pmatrix}0\\ \tilde{\chi}\end{pmatrix}, \tag{27}$$

where

$$-i\,\frac{\partial\tilde{\chi}}{\partial x}=k_0\sqrt{1+\frac{2\hat{\Lambda}}{k_0}}\,\tilde{\chi}. \tag{28}$$

Since the operator on the right-hand side of Eq. (28) is independent of x and this is an eigenvalue equation, it follows that $\tilde{\chi}$ must be an eigenfunction of the differential operator $\hat{\Lambda}$. Therefore the transformation at the endpoints

$$A=\theta+\chi=(1\quad 1)e^{-iS(\hat{\Lambda})}\begin{pmatrix}0\\ \tilde{\chi}\end{pmatrix} \tag{29}$$

is just rescaling by a constant, where A also satisfies Eq. (28). This is the standard PE for a range-independent index of refraction first introduced by Tappert.[1] Expanding the square-root operator in $\hat{\Lambda}/k_0$, we have

$$-i\,\frac{\partial A}{\partial x}=\frac{\nabla_\perp^2}{2k_0}A+k_0(1-\mu)A, \tag{30}$$

and with $A\propto e^{ik_0x}$, we recover the basic lowest-order PE. Thus for a range-independent index of refraction, the Foldy–Wouthuysen transformation recovers the various well-known forms of the parabolic equation. Assuming μ to be slowly varying, $\partial\mu/\partial x$ is a second-order correction. This implies that the first-order result of Eq. (30) is also applicable to the more general case of a range-dependent index of refraction.

C. The general range-dependent problem

A perturbative solution to the range-dependent problem will now be obtained by repeated applications of the Foldy–Wouthuysen transformation. The expansion parameter is the dimensionless operator $\hat{\Lambda}_0=\hat{\Lambda}/k_0$. The range dependence is assumed to be small and slowly varying, so the operator $k_0^{-1}\partial\hat{\Lambda}_0/\partial x=-k_0^{-1}\partial\mu/\partial x$ is $\mathcal{O}(\hat{\Lambda}_0^2)$. In observing the definitions $\hat{\mathbf{O}}\equiv\hat{\Lambda}\boldsymbol{\sigma}$ and $\hat{\mathbf{E}}\equiv\hat{\Lambda}\boldsymbol{\eta}$, we see that these operators are

now of the same order of smallness. This implies that even on a formal level, some care must be taken in transferring the results of the previous subsection.

To generate the expansion, a succession of transformations is used, each having the form $\tilde{\tilde{\Phi}}=e^{i\hat{S}}\vec{\Phi}$. With each iteration, $\hat{S}$ is of increasing order in $\hat{\Lambda}_0$, and the transformation is designed to diagonalized $\tilde{\tilde{\mathbf{H}}}$ to that order. Henceforth, numeral supercripts will denote the order of $\hat{S}$ and of the diagonalized part of $\tilde{\tilde{\mathbf{H}}}$. The corresponding $\tilde{\Phi}$, $\hat{\mathbf{O}}$, and $\hat{\mathbf{E}}$ will also be labeled in this way. For example, $\tilde{\tilde{\Phi}}^{(1)}=e^{i\hat{S}}\vec{\Phi}$ obeys the equation

$$i\,\frac{\partial\tilde{\tilde{\Phi}}^{(1)}}{\partial x}=\tilde{\tilde{\mathbf{H}}}^{(1)}\tilde{\tilde{\Phi}}^{(1)}, \tag{31}$$

where $\tilde{\tilde{\mathbf{H}}}^{(1)}=k_0\boldsymbol{\eta}+\hat{\mathbf{E}}^{(1)}+\hat{\mathbf{O}}^{(1)}$ is diagonalized to $\mathcal{O}(\hat{\Lambda}_0)$.

Substituting for $\tilde{\Phi}$ in the original equation of motion Eq. (13), we have the result

$$0=e^{i\hat{S}^{(1)}}\left(\hat{\mathbf{H}}-i\,\frac{\partial}{\partial x}\right)e^{-i\hat{S}^{(1)}}\tilde{\tilde{\Phi}}^{(1)}. \tag{32}$$

From a theorem given by Bjorken and Drell,[13] and using $\hat{\mathbf{H}}=\mathcal{O}(\mathbf{1})$ and $\hat{S}^{(1)}=\mathcal{O}(\hat{\Lambda}_0)$, we have

$$\begin{aligned}e^{i\hat{S}^{(1)}}\hat{\mathbf{H}}e^{-i\hat{S}^{(1)}}=\hat{\mathbf{H}}&+i[\hat{S}^{(1)},\hat{\mathbf{H}}]-\tfrac{1}{2}[\hat{S}^{(1)},[\hat{S}^{(1)},\hat{\mathbf{H}}]]\\&-\frac{i}{3!}[\hat{S}^{(1)},[\hat{S}^{(1)},[\hat{S}^{(1)},\hat{\mathbf{H}}]]]\\&+\frac{1}{4!}[\hat{S}^{(1)},[\hat{S}^{(1)},[\hat{S}^{(1)},[\hat{S}^{(1)},\hat{\mathbf{H}}]]]]\\&+\mathcal{O}(\hat{\Lambda}_0^5),\end{aligned} \tag{33}$$

with the familiar commutator notation

$$[\hat{A},\hat{B}]=\hat{A}\circ\hat{B}-\hat{B}\circ\hat{A},$$

and

$$\begin{aligned}e^{i\hat{S}^{(1)}}\,\frac{\partial}{\partial x}\,e^{i\hat{S}^{(1)}}=\frac{\partial}{\partial x}&-i\,\frac{\partial\hat{S}^{(1)}}{\partial x}+\frac{1}{2}\left[\hat{S}^{(1)},\,\frac{\partial\hat{S}^{(1)}}{\partial x}\right]\\&+\frac{i}{3!}\left[\hat{S}^{(1)},\left[\hat{S}^{(1)},\,\frac{\partial\hat{S}^{(1)}}{\partial x}\right]\right]+\mathcal{O}(\hat{\Lambda}_0^5).\end{aligned} \tag{34}$$

By analogy to the range-independent calculation, the correct choice for $\hat{S}^{(1)}$ is

$$\hat{S}^{(1)}=-\frac{i\boldsymbol{\eta}\hat{\mathbf{O}}}{2k_0}. \tag{35}$$

Now the expression for $\tilde{\tilde{\mathbf{H}}}^{(1)}$ can be obtained by comparison to Eq. (31), and using $\boldsymbol{\eta}\hat{\mathbf{O}}=-\hat{\mathbf{O}}\boldsymbol{\eta}$, $\boldsymbol{\eta}\hat{\mathbf{E}}=\hat{\mathbf{E}}\boldsymbol{\eta}$, $\boldsymbol{\eta}^2=\mathbf{1}$, and Eq. (14).

Since $\hat{\mathbf{E}}/k_0$, $\hat{\mathbf{O}}/k_0=\mathcal{O}(\hat{\Lambda}_0)$ and the anticommutation properties of $\hat{\mathbf{O}}$ and $\boldsymbol{\eta}$, where the anticommutation operation is defined as

$$\{\hat{A},\hat{B}\}=\hat{A}\circ\hat{B}+\hat{B}\circ\hat{A},$$

imply that $i[\hat{S}^{(1)},\hat{\mathbf{H}}]=-\hat{\mathbf{O}}+\mathcal{O}(\hat{\Lambda}_0^2)$. Thus all other new terms such as those proportional to $[\hat{S}^{(1)},[\hat{S}^{(1)},\hat{\mathbf{H}}]]$ or $\partial\hat{S}^{(1)}/\partial\chi$ are second order or higher. Thus, by construction, the Foldy–Wouthuysen transformation cancels the odd first-order terms, and replaces them with new terms of higher order. This result depends only on the definition of $\hat{S}$ and the anticommutation relation $\{\boldsymbol{\eta},\hat{\mathbf{O}}\}=0$. The procedure can be repeated order-by-order, with the order of the remaining odd terms increasing with each iteration. As can be seen from the following argument, the anticommutation relation will always be met.

We will begin with the Hamiltonian $\hat{\mathbf{H}}$ and apply repeated transformations of the sort just discussed. The transformed Hamiltonian will consist of terms whose matrix part is constructed from products of $\boldsymbol{\eta}$'s and $\boldsymbol{\sigma}$'s. Since $\boldsymbol{\sigma}^{2n}=(-1)^n\mathbf{1}$, $\boldsymbol{\eta}^{2n}=\mathbf{1}$, and $\{\boldsymbol{\sigma},\boldsymbol{\eta}\}=0$, the matrix part of the odd operators will be either $\boldsymbol{\eta}\boldsymbol{\sigma}$ or $\boldsymbol{\sigma}$ while that of the even operators will be $\boldsymbol{\eta}$ or $\mathbf{1}$. It follows that the odd operators all anticommute with $\boldsymbol{\eta}$. The anticommutation relation, together with the iterative nature of the procedure, also insures that energy will be conserved no matter how many times the procedure is repeated. Before iteration, $\hat{\mathbf{H}}$ and therefore $\hat{\mathbf{O}}$ are pseudo-Hermitian ($\hat{\mathbf{O}}^{\dagger}\boldsymbol{\eta}=\boldsymbol{\eta}\hat{\mathbf{O}}$), which, using the anticommutation relation, also implies that $\hat{S}=-i\boldsymbol{\eta}\hat{\mathbf{O}}/2k_0$ is pseudo-Hermitian. Thus, $e^{i\hat{S}}$ is pseudo-unitary and the transformation preserves energy conservation. The new Hamiltonian and consequently the new odd operator $\hat{\mathbf{O}}$ is therefore once again pseudo-Hermitian, and the process can be repeated. In this way, we have provided an order-by-order prescription for diagonalizing the Hamiltonian. This implies that the true coupling between forward and backward propagating fields (i.e., backscatter) is of higher order than any finite order of perturbation theory, and that the perturbative expansion constructed in this way must be asymptotic.

Dropping terms of $\mathcal{O}(\hat{\Lambda}_0^5)$ and higher, we expand each of the commutators found in Eqs. (33) and (34). After substituting $\hat{S}^{(1)}$ as given by Eq. (35), we obtain

$$i[\hat{S}^{(1)},\,\hat{\mathbf{H}}]=-\hat{\mathbf{O}}+\frac{\boldsymbol{\eta}}{2k_0}[\hat{\mathbf{O}},\hat{\mathbf{E}}]+\frac{1}{k_0}\,\boldsymbol{\eta}\hat{\mathbf{O}}^2, \tag{36a}$$

$$-\frac{1}{2}[\hat{S}^{(1)},[\hat{S}^{(1)},\hat{\mathbf{H}}]]=-\frac{\boldsymbol{\eta}\hat{\mathbf{O}}^2}{2k_0}-\frac{1}{8k_0^2}[\hat{\mathbf{O}},[\hat{\mathbf{O}},\hat{\mathbf{E}}]]-\frac{\hat{\mathbf{O}}^3}{2k_0^2}, \tag{36b}$$

$$-\frac{i}{3!}[\hat{S}^{(1)},[\hat{S}^{(1)},[\hat{S}^{(1)},\hat{\mathbf{H}}]]]=\frac{\hat{\mathbf{O}}^3}{6k_0^2}-\frac{\boldsymbol{\eta}\hat{\mathbf{O}}^4}{6k_0^3}, \tag{36c}$$

$$\frac{1}{4!}[\hat{S}^{(1)},[\hat{S}^{(1)},[\hat{S}^{(1)},[\hat{S}^{(1)},\hat{\mathbf{H}}]]]]=\frac{\boldsymbol{\eta}\hat{\mathbf{O}}^4}{24k_0^3}, \tag{36d}$$

$$-\frac{\partial\hat{S}^{(1)}}{\partial x}=\frac{i\boldsymbol{\eta}\,\dfrac{\partial\hat{\mathbf{O}}}{\partial x}}{2k_0}, \tag{36e}$$

$$\frac{i}{2}\left[\hat{S}^{(1)},\,\frac{\partial\hat{S}^{(1)}}{\partial x}\right]=-\frac{i}{8k_0^2}\left[\hat{\mathbf{O}},\,\frac{\partial\hat{\mathbf{O}}}{\partial x}\right], \tag{36f}$$

where the odd fourth-order term

$$-\frac{\boldsymbol{\eta}}{48k_0^2}[\hat{\mathbf{O}},[\hat{\mathbf{O}},[\hat{\mathbf{O}},\hat{\mathbf{E}}]]] \tag{37}$$

in Eq. (36c) and the term $\frac{1}{6}[\hat{S}^{(1)},[\hat{S}^{(1)},\partial S^{(1)}/\partial x]]$ in Eq. (34), which can be shown to be equivalent to

$$\frac{1}{6}\left[\hat{S}^{(1)},\left[\hat{S}^{(1)},\frac{\partial \hat{S}^{(1)}}{\partial x}\right]\right]=-\frac{i\boldsymbol{\eta}}{24k_0^3}\left[\hat{\mathbf{O}},\left[\hat{\mathbf{O}},\frac{\partial \hat{\mathbf{O}}}{\partial x}\right]\right], \tag{38}$$

have been dropped. This is because the next Foldy–Wouthuysen transformation will remove these odd terms, replacing them with terms of fifth order and higher, which is of higher order than concerns us here. Therefore, to obtain the diagonalized Hamiltonian to $\mathcal{O}(\hat{\Lambda}_0^4)$, we can use the results from Bjorken and Drell without modification.[43] However, we have to be careful to make sure we include all relevant terms during the next stage of the diagonalization procedure. Strictly speaking, the order counting in Ref. 13 is different from that which must be used for the PE.

Inserting Eqs. (36a)–(36f) into Eqs. (33) and (34) we derive the $\mathcal{O}(\Lambda_0^2)$ result:

$$\tilde{\tilde{\mathbf{H}}}^{(1)}=k_0\boldsymbol{\eta}+\hat{\mathbf{E}}^{(1)}+\hat{\mathbf{O}}^{(1)}+\mathcal{O}(\hat{\Lambda}_0^5), \tag{39a}$$

$$\hat{\mathbf{E}}^{(1)}=\boldsymbol{\eta}\left(\frac{\hat{\mathbf{O}}^2}{2k_0}-\frac{\hat{\mathbf{O}}^4}{8k_0^3}\right)+\hat{\mathbf{E}}-\frac{1}{8k_0^2}[\hat{\mathbf{O}},[\hat{\mathbf{O}},\hat{\mathbf{E}}]] -\frac{i}{8k_0^2}\left[\hat{\mathbf{O}},\frac{\partial \hat{\mathbf{O}}}{\partial x}\right], \tag{39b}$$

$$\hat{\mathbf{O}}^{(1)}=\frac{\boldsymbol{\eta}}{2k_0}[\hat{\mathbf{O}},\mathbf{E}]-\frac{\hat{\mathbf{O}}^3}{2k_0^2}+\frac{i\boldsymbol{\eta}}{2k_0}\frac{\partial \hat{\mathbf{O}}}{\partial x}. \tag{39c}$$

The above procedure is iterated to eliminate odd terms which are second order in $\hat{\Lambda}_0$. The second Foldy–Wouthuysen transformation is

$$\hat{S}^{(2)}=-\frac{i\boldsymbol{\eta}\hat{\mathbf{O}}^{(1)}}{2k_0}+\mathcal{O}(\hat{\Lambda}_0^3), \tag{40a}$$

$$\tilde{\tilde{\mathbf{H}}}^{(2)}=\tilde{\tilde{\mathbf{H}}}^{(1)}+i[\hat{S}^{(2)},\tilde{\tilde{\mathbf{H}}}^{(1)}]-\tfrac{1}{2}[\hat{S}^{(2)},[\hat{S}^{(2)},\tilde{\tilde{\mathbf{H}}}^{(1)}]] -\frac{\partial \hat{S}^{(2)}}{\partial x}+\mathcal{O}(\hat{\Lambda}_0^5). \tag{40b}$$

$$=k_0\boldsymbol{\eta}+\hat{\mathbf{E}}^{(1)}+i[\hat{S}^{(2)},\hat{\mathbf{E}}^{(1)}]+\frac{i}{2}[\hat{S}^{(2)},\hat{\mathbf{O}}^{(1)}] +\frac{i\boldsymbol{\eta}}{2k_0}\partial\hat{\mathbf{O}}\partial x^{(1)}+\mathcal{O}(\hat{\Lambda}_0^5), \tag{40c}$$

where the result $[\hat{S}^{(2)},k_0\boldsymbol{\eta}]=i\hat{\mathbf{O}}^{(1)}$ was used to simplify $\tilde{\tilde{\mathbf{H}}}^{(2)}$. Simplifying the commutators, we now have

$$\tilde{\tilde{\mathbf{H}}}^{(2)}=k_0\boldsymbol{\eta}+\hat{\mathbf{E}}^{(2)}+\hat{\mathbf{O}}^{(2)}+\mathcal{O}(\hat{\Lambda}_0^5), \tag{41a}$$

$$\hat{\mathbf{E}}^{(2)}=\hat{\mathbf{E}}^{(1)}+\frac{\boldsymbol{\eta}(\hat{\mathbf{O}}^{(1)})^2}{2k_0}, \tag{41b}$$

$$\hat{\mathbf{O}}^{(2)}=\frac{\boldsymbol{\eta}}{2k_0}[\hat{\mathbf{O}}^{(1)},\hat{\mathbf{E}}^{(1)}]+\frac{i\boldsymbol{\eta}}{2k_0}\frac{\partial \hat{\mathbf{O}}^{(1)}}{\partial x}. \tag{41c}$$

Now, we apply the Foldy–Wouthuysen transformation yet again,

$$\hat{S}^{(3)}=-\frac{i\boldsymbol{\eta}\hat{\mathbf{O}}^{(2)}}{2k_0}+\mathcal{O}(\hat{\Lambda}_0^4), \tag{42}$$

and obtain

$$\tilde{\tilde{\mathbf{H}}}^{(3)}=k_0\boldsymbol{\eta}+\hat{\mathbf{E}}^{(2)}+i[\hat{S}^{(3)},\hat{\mathbf{E}}^{(2)}]-\frac{\partial S^{(3)}}{\partial x}+\mathcal{O}(\hat{\Lambda}_0^5), \tag{43}$$

with the last two terms of $\tilde{\tilde{\mathbf{H}}}^{(3)}$ being $\mathcal{O}(\hat{\Lambda}_0^4)$. The only effect of the next Foldy–Wouthuysen transformation will be to push such terms up to higher order. Finally have

$$\tilde{\tilde{\mathbf{H}}}^{(4)}=k_0\boldsymbol{\eta}+\hat{\mathbf{E}}^{(2)}+\mathcal{O}(\hat{\Lambda}_0^5), \tag{44}$$

where

$$\hat{\mathbf{E}}^{(2)}=\boldsymbol{\eta}\left(\frac{\hat{\mathbf{O}}^2}{2k_0}-\frac{\hat{\mathbf{O}}^4}{8k_0^3}\right)+\hat{\mathbf{E}}-\frac{1}{8k_0^2}[\hat{\mathbf{O}},[\hat{\mathbf{O}},\hat{\mathbf{E}}]] -\frac{i}{8k_0^2}\left[\hat{\mathbf{O}},\frac{\partial \hat{O}}{\partial x}\right]+\frac{\boldsymbol{\eta}}{8k_0^3}\left(-[\hat{\mathbf{O}},\hat{\mathbf{E}}]^2 -i\left\{\frac{\partial \hat{\mathbf{O}}}{\partial x},[\hat{\mathbf{O}},\hat{\mathbf{E}}]\right\}+\frac{\partial \hat{\mathbf{O}}^2}{\partial x}\right)+\mathcal{O}(\hat{\Lambda}_0^5). \tag{45}$$

Using the definitions $\hat{\mathbf{E}}=\hat{\Lambda}\boldsymbol{\eta}$ and $\hat{\mathbf{O}}=\hat{\Lambda}\boldsymbol{\sigma}$ and substituting them into Eq. (45) gives

$$[\hat{\mathbf{O}},\hat{\mathbf{E}}]^2=4\hat{\Lambda}^4, \tag{46a}$$

$$\left\{\frac{\partial \hat{\mathbf{O}}}{\partial x},[\hat{\mathbf{O}},\hat{\mathbf{E}}]\right\}=2\boldsymbol{\eta}\left[\hat{\Lambda}^2,\frac{\partial \hat{\Lambda}}{\partial x}\right], \tag{46b}$$

$$\frac{\partial \hat{\mathbf{O}}}{\partial x}=-\frac{\partial \hat{\Lambda}^2}{\partial x}. \tag{46c}$$

Substituting these results into Eq. (45), we have

$$\tilde{\tilde{\mathbf{H}}}^{(4)}=\boldsymbol{\eta}k_0\left(1+\frac{\hat{\Lambda}}{k_0}-\frac{\hat{\Lambda}^2}{2k_0^2}+\frac{\hat{\Lambda}^3}{2k_0^3}-\frac{5\hat{\Lambda}^4}{8k_0^4}-\frac{1}{8k_0^4}\left(\frac{\partial \hat{\Lambda}}{\partial x}\right)^2\right) +\frac{i}{8k_0^2}\left[\hat{\Lambda},\frac{\partial \hat{\Lambda}}{\partial x}\right]-\frac{i}{4k_0^3}\left[\hat{\Lambda}^2,\frac{\partial \hat{\Lambda}}{\partial x}\right]+\mathcal{O}(\hat{\Lambda}_0^5), \tag{47}$$

where $\hat{\Lambda}\equiv\nabla_\perp^2/2k_0-\mu k_0$. For a range-independent index of refraction $\partial\hat{\Lambda}/\partial x\to 0$, and we recover an expansion of $\tilde{\tilde{\mathbf{H}}}=\boldsymbol{\eta}k_0\sqrt{1+2\hat{\Lambda}/k_0}$. It is also seen that if μ has no transverse dependence, then the commutator terms in Eq. (47) would vanish, however the extra noncommutator terms containing $\partial\hat{\Lambda}/\partial x$ would, in general, not vanish.

For the diagonal Hamiltonian $\tilde{\tilde{H}}$, the pure forward and backward propagating solutions, $\tilde{\Phi}\propto\binom{0}{1}$ and $\tilde{\Phi}\propto\binom{1}{0}$, respectively, remain of the same vector form as they propagate. For these solutions, $\boldsymbol{\eta}$ can be replaced by $\mp\mathbf{1}$, so that the energy flux is proportional to $\tilde{\Phi}^\dagger\tilde{\Phi}$. Following the same reasoning as before, it follows that the range propagation operator must be unitary and $\tilde{\tilde{\mathbf{H}}}$ must be Hermitian. Being diagonal and Hermitian, it remains pseudo-Hermitian as well. Using the

expression for $\tilde{\tilde{\mathbf{H}}}^{(4)}$ given in Eq. (47), the fact that it is Hermitian can also be verified directly by inspection. The third-order term $(i/8k_0^2)[\hat{\Lambda}, \partial\hat{\Lambda}/\partial x]$ is analogous to *Zitterbewegung* in the quantum mechanical problem. It is possible to interpret a term of this sort as being the consequence of interference between the forward and backward propagating solutions of the field equations. This effect is essentially a classical mechanical analog of a relativistic quantum mechanical particle's field containing components of both positive and negative energy solutions.[15,16] For relativistic quantum mechanical particles the interference between the positive (particle) and negative (antiparticle) energy solutions occurs at an extremely high frequency and thus the effect can only be measured at correspondingly small length scales. The net effect is that the location of the wavefront (in the quantum mechanical case this could, for instance, be the field corresponding to the particle's location) is not well defined and similar terms of higher order can then be interpreted as corresponding to multiple short-ranged fields oscillating about the wavefront.

When $\hat{\Lambda}$ depends on x, it is a true matrix-differential operator, and the transformations at the endpoints can therefore no longer be considered trivial rescalings. Nevertheless, for propagation over long distances through a fluctuating range-dependent media, it is reasonable to neglect these endpoint contributions when calculating the long-distance effects of propagation. In particular, consider the problem of long distance low-frequency propagation in the ocean. These pseudo-unitary transformations at the endpoints differ from unity by $(1/k_0)(\partial\mu/\partial x)$ or some higher-order range derivative of μ. At 50 Hz, the acoustic wavelength is 30 m, and the change in the sound speed over such a distance is negligible. Similar terms associated with propagation are only significant when the effect accumulates over very large distances.

D. Further simplification

It is possible to apply a variation of the Foldy-Wouthuysen transformation to rearrange terms without changing the order of the diagonalized part of the Hamiltonian. For the Hamiltonian defined in Eq. (47), choose

$$\hat{S}^{(4,1)} = \frac{\boldsymbol{\eta}}{8k_0^2}\frac{\partial\hat{\Lambda}}{\partial x} + \mathcal{O}(\hat{\Lambda}_0^3). \tag{48}$$

where $\hat{S}^{(4,1)}$ corresponds to a Hamiltonian which is diagonal to $\mathcal{O}(\hat{\Lambda}_0^4)$, while $\hat{S}$ is diagonal only to $\mathcal{O}(\hat{\Lambda}_0)$. Because $\hat{S}^{(4,1)}$ is diagonal and Hermitian, the transformation $e^{i\hat{S}^{(4,1)}}$ is unitary, diagonal, and pseudo-unitary, so energy conservation considerations discussed in the previous section will not be affected by the transformation. Now, we have

$$\tilde{\tilde{\mathbf{H}}}^{(4,1)} = \tilde{\tilde{\mathbf{H}}}^{(4)} + i\left[\hat{S}^{(4,1)}, \boldsymbol{\eta}\left(k_0 + \hat{\Lambda} - \frac{\hat{\Lambda}^2}{2k_0}\right)\right] - \frac{1}{2}[\hat{S}^{(4,1)}, [\hat{S}^{(4,1)}, \boldsymbol{\eta}k_0]] - \frac{\partial\hat{S}^{(4,1)}}{\partial x} + \mathcal{O}(\hat{\Lambda}_0^5) \tag{49a}$$

$$= \boldsymbol{\eta}k_0\left(\left[1 + \frac{\hat{\Lambda}}{k_0} - \frac{\hat{\Lambda}^2}{2k_0^2} + \frac{\hat{\Lambda}^3}{2k_0^3} - \frac{5\hat{\Lambda}^4}{8k_0^4}\right] - \frac{1}{8k_0^3}\frac{\partial^2\hat{\Lambda}}{\partial x^2} - \frac{1}{8k_0^4}\left(\frac{\partial\hat{\Lambda}}{\partial x}\right)^2\right) - \frac{3i}{16k_0^3}\left[\hat{\Lambda}^2, \frac{\hat{\Lambda}}{\partial x}\right] + \mathcal{O}(\hat{\Lambda}_0^5). \tag{49b}$$

Applying another Foldy–Wouthuysen transformation with

$$\hat{S}^{(4,2)} = \frac{-3\boldsymbol{\eta}}{16k_0^3}\frac{\partial(\hat{\Lambda}^2)}{\partial x} \tag{50a}$$

$$= \frac{-3\boldsymbol{\eta}}{16k_0^3}\left\{\hat{\Lambda}, \frac{\partial\hat{\Lambda}}{\partial x}\right\} + \mathcal{O}(\hat{\Lambda}_0^4), \tag{50b}$$

the transformed Hamiltonian becomes

$$\tilde{\tilde{\mathbf{H}}}^{(4,2)} = \tilde{\tilde{\mathbf{H}}}^{(4,1)} + i[\hat{S}^{(4,2)}, \boldsymbol{\eta}(k_0 + \hat{\Lambda})] - \frac{\partial\hat{S}^{(4,2)}}{\partial x} + \mathcal{O}(\hat{\Lambda}_0^5) \tag{51a}$$

$$= \boldsymbol{\eta}k_0\left(\left[1 + \frac{\hat{\Lambda}}{k_0} - \frac{\hat{\Lambda}^2}{2k_0^2} + \frac{\hat{\Lambda}^3}{2k_0^3} - \frac{5\hat{\Lambda}^4}{8k_0^4}\right] - \frac{1}{8k_0^3}\frac{\partial^2\hat{\Lambda}}{\partial x^2} + \frac{1}{4k_0^4}\left(\frac{\partial\hat{\Lambda}}{\partial x}\right)^2 + \frac{3}{16k_0^4}\left\{\hat{\Lambda}, \frac{\partial^2\hat{\Lambda}}{\partial x^2}\right\}\right) + \mathcal{O}(\hat{\Lambda}_0^5) \tag{51b}$$

The last step in Eqs. (51) is the most important result of this paper. The term in the brackets can be formally written as $\sqrt{1+2\hat{\Lambda}/k_0}$, following the common practice of defining the function of an operator by the Taylor series expansion. Wide angle PEs based on the Padè approximation are essentially numerically efficient ways of obtaining high orders of perturbation theory, but are formally equivalent to it. This implies that the results here apply to procedures based on these techniques as well. It can also be shown that, to the order obtained here, the result is independent of the choice of k_0. To third order, we may use the straightforward substitution

$$\mu \to \mu - \frac{1}{8k_0^2}\frac{\partial^2\mu}{\partial x^2}. \tag{52}$$

To this order, this is equivalent to rescaling the sound speed

$$c \to c - \frac{1}{8k_0^2}\frac{\partial^2 c}{\partial x^2}, \tag{53}$$

which is indeed Eq. (1).

The transformation $\hat{S}^{(4,1)}$, roughly speaking, substitutes a dependence on $\partial^2\mu/\partial\mathbf{x}_\perp\,\partial x$ with one on $\partial^2\mu/\partial x^2$. Disturbingly, these terms are zero at different spatial locations. However, the apparent discrepancy disappears after closer scrutiny. If $\partial^2\mu/\partial x^2 = 0$ and $\partial^2\mu/\partial\mathbf{x}_\perp\,\partial x \neq 0$, then μ is proportional to the range. However, if μ increases linearly with the range, then the endpoint transformation can no longer be ignored. On the other hand, if $\partial^2\mu/\partial\mathbf{x}_\perp\,\partial x = 0$, then $\partial^2\mu/\partial x^2$ is

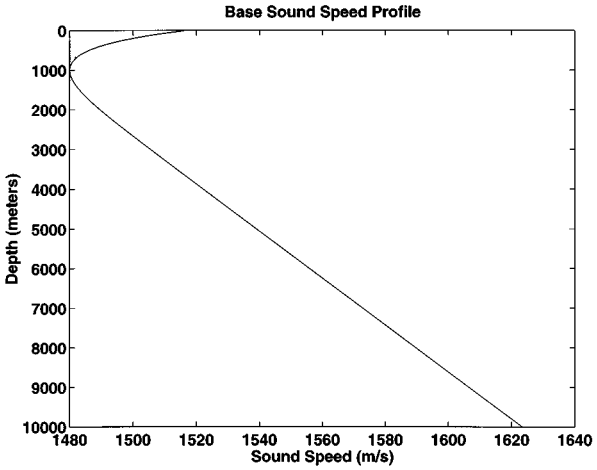

FIG. 2. The Munk sound-speed profile used for these models, with the constant parameters $B=1$ km, $-z_1=1$ km, and $\epsilon=5.7\times10^{-3}$. The base sound speed profile is the dominant depth dependence of the spatially dependent sound speed profile. The axis of the SOFAR channel (here at 1 km in depth) will be maintained throughout propagation.

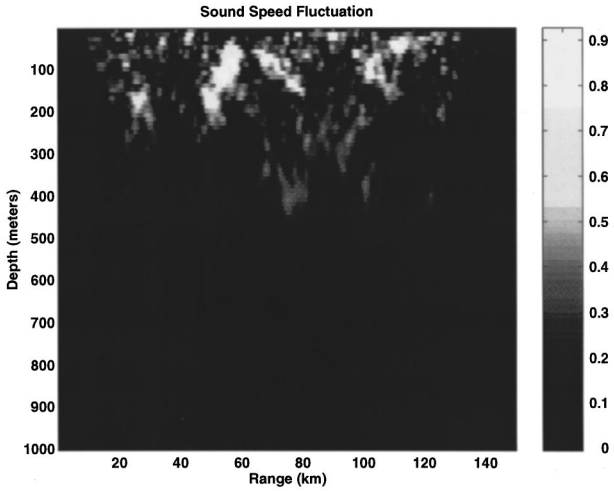

FIG. 4. A realization of the internal wave field in which it can be seen that the perturbations of the sound speed profile is limited to that region close to the surface, where the amplitudes of the eigenmodes of the internal wave field are relatively large. This grayscale map shows the most intensely fluctuating part of the sound speed at approximately ±1 meter-per-second.

a function of the range only. It is easy to verify that the solution corresponding to the transformation of the Hamiltonian $\hat{\mathbf{H}}\rightarrow\hat{\mathbf{H}}+f(x)$ differs from the original solution by the overall phase $\exp[-i\int f(x)\,dx]$. The phase change is the same for all $\mathbf{x}_\perp$, and the effect is trivial, since there is no associated field structure.

III. EXAMPLE

To determine the effects of Eq. (51) via Eq. (53) we propagate the acoustic field in three different environments: (1) a range-independent Munk sound-speed profile, (2) an environment consisting of only an internal wave field, and (3) the internal wave field and the effective sound speed calculated using Eq. (53). As has already been discussed, the main effect of Eq. (51) will be to change the phase of the acoustic field. While eventually a phase error will propagate in to a difference in the transmission loss, the main effect of Eq. (51) on the wavefront is expected to make it less sharply defined, because the effect is frequency dependent.

Internal gravity waves in the ocean have horizontal scales from 500 m to approximately 50 km and vertical scales from 10 to 1000 m.[10] These scales along with the relative size of the perturbations in the sound speed they induce ($\sim$1 m/s), make acoustic propagation in the ocean a likely physical environment where the effects of Eq. (51) will be of importance. The exact spatial dependence of an internal wave field cannot be known over the long distances required to see the effects of Eq. (51). Typically one assumes that the spatial dependence of internal waves can be represented by a random field. Using the Garrett–Munk theory of internal waves,[10,44–46] one creates such a random wave field

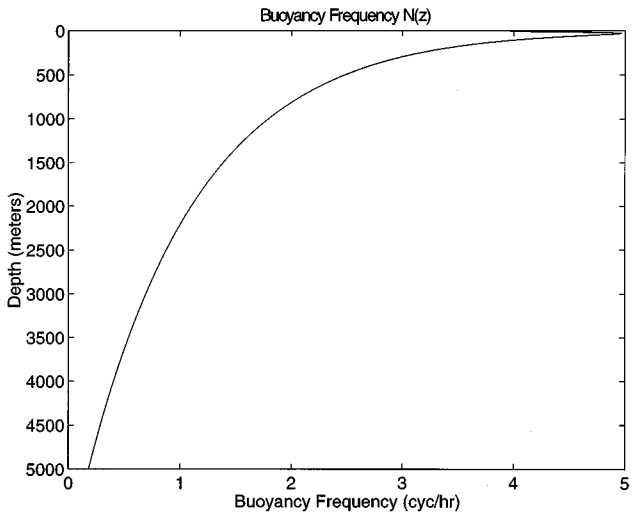

FIG. 3. The buoyancy frequency as given by Eq. (62). This is modeled on the buoyancy frequency measured in the SLICE-89 experiment, with the value N ($z_{\text{ref}}=250$ m)$=3$ cycles/h.

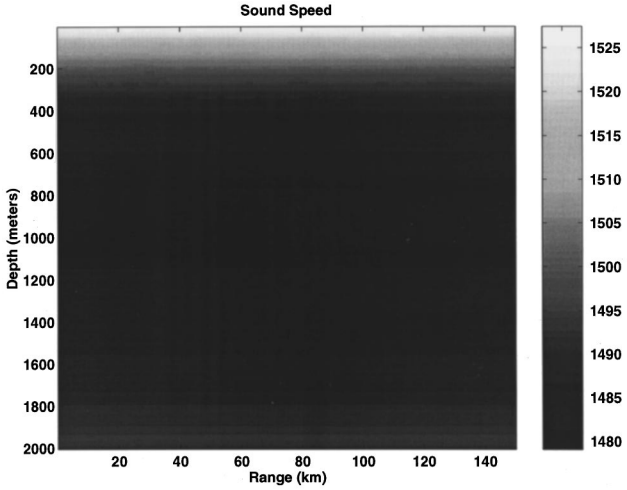

FIG. 5. A typical realization of the sound speed, including the effects of the internal wave field, as calculated by Eq. (57). The depth of the water column extends down to 9000 m. Only the first 2000 m is shown here, because it is this top layer that is affected most by the internal waves. The sound speed given by this grayscale map is in meters-per-second.

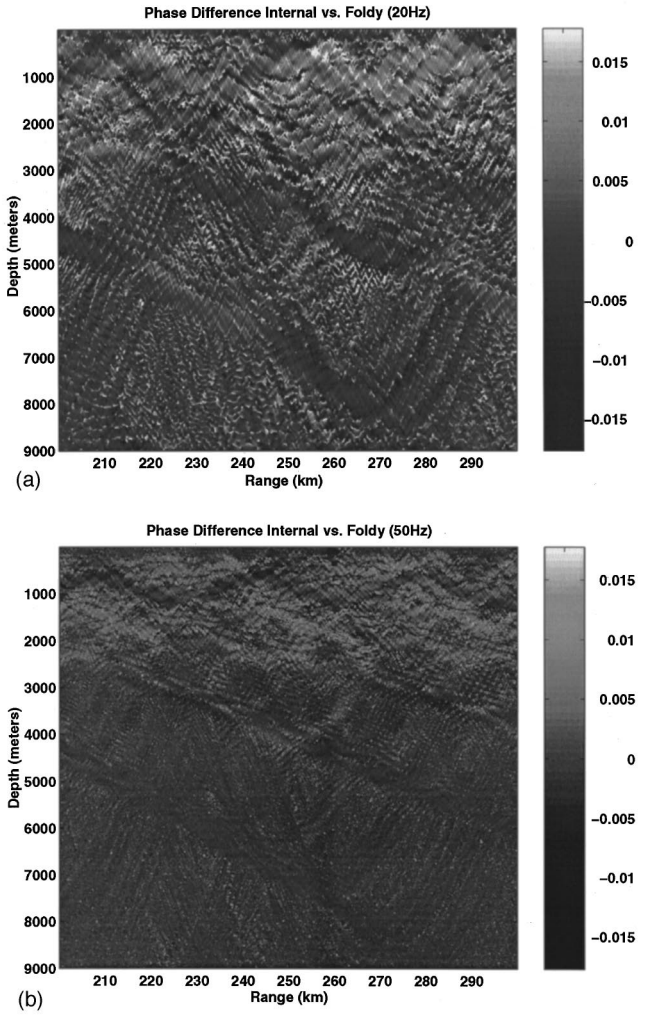

FIG. 6. The relative phase difference between propagating using the internal wave field and the Foldy–Wouthuysen correction term. The phases have been determined using Eq. (71) on the field calculated using a modified version of RAM. The phase difference is shown for the ranges between 200 and 300 km. The dynamic range of the plot is equivalent to $\pm 1°$, and is plotted in radians. The frequency dependence of the correction term is self-evident, with the higher frequency [50 Hz, (b)] having a much smaller phase difference than the lower frequency [20 Hz, (a)].

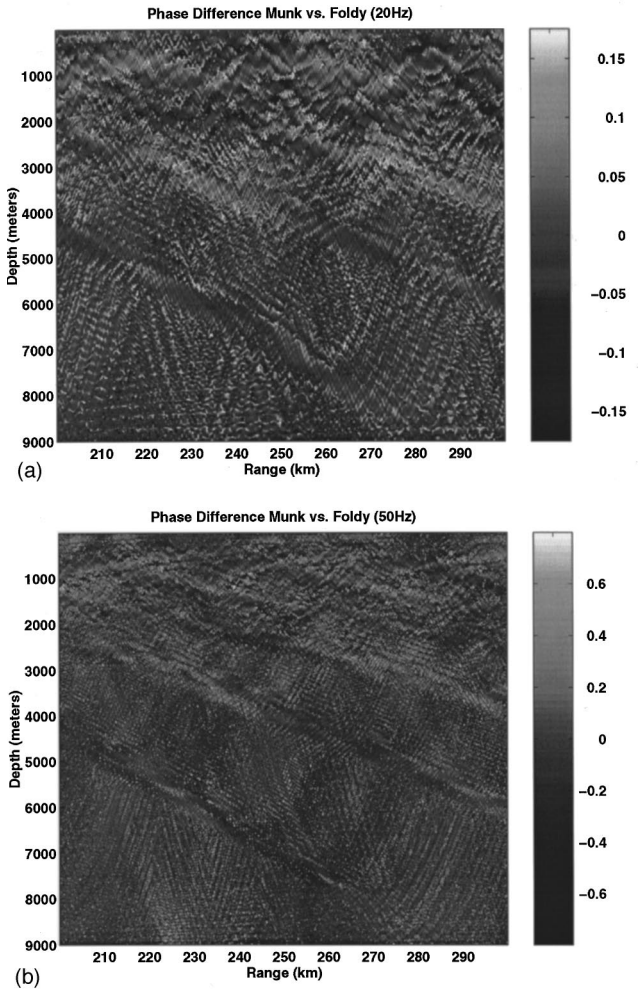

FIG. 7. The relative phase difference of the field propagated through the Munk sound-speed profile (see Fig. 2) and the field including both the internal waves and the Foldy–Wouthuysen correction of Eq. (51) as given by Eq. (53). The phases for each field are calculated using Eq. (71) and are subtracted and are plotted in radians. The dynamic range for the 20-Hz case (a) is $\pm 10°$, while the dynamic range for the 50-Hz case (b) is $\pm 45°$, this being a function of the fact that the effects of the internal waves alone are much greater for higher frequencies.

which is related to the physics of the internal waves through its spectral density and the local normal modes of the internal waves. This theory was used to create such a range-dependent sound-speed profile through which propagation was modeled using the PE propagation code RAM.[2]

The time evolution of internal waves is considerably longer ($\sim$ minutes) than the interaction time that a single pulse has with the range-dependence ($\sim 10^{-6}$ s). This implies that to test the effects of Eq. (51) on propagation using the PE, we may consider the sound speed of the ocean to be a frozen realization of a random field representing the perturbations of the sound-speed profile caused by internal gravity waves, superimposed on top of a Munk profile.[47] Thus, in the examples shown below, the form of the sound-speed profile of the underlying stratified ocean is based on the Munk profile.[10,47] This profile is of the form

$$c_{\text{Munk}} = c_0(1 + U_0(z)), \tag{54}$$

where $U_0(z)$ is the functional form of the deviation of the sound speed as a function of depth, reflecting the effects of vertical stratification common in temperate waters. $U_0(z)$ is usually represented functionally as

$$U_0(z) = \epsilon(e^{\eta(z)} - \eta(z) + 1), \tag{55}$$

$\eta(z)$ containing the depth dependence of the sound speed is given by

$$\eta(z) = (z - z_1)/\tfrac{1}{2}B, \tag{56}$$

with the constants B, $-z_1$, and ϵ chosen to be 1 km, 1 km, and 5.7×10^{-3}, respectively. The resulting sound-speed profile is plotted in Fig. 2, where it can be seen that the axis of the SOFAR channel is at 1 km.

The effects of internal gravity waves upon the sound-speed profile will be to add a range-dependent term, $\xi(\mathbf{x},t)$, to Eq. (54). Thus the full spatially dependent sound-speed profile is

$$c(\mathbf{x},t) = c_0(1 + U_0(z) + \xi(\mathbf{x},t)), \tag{57}$$

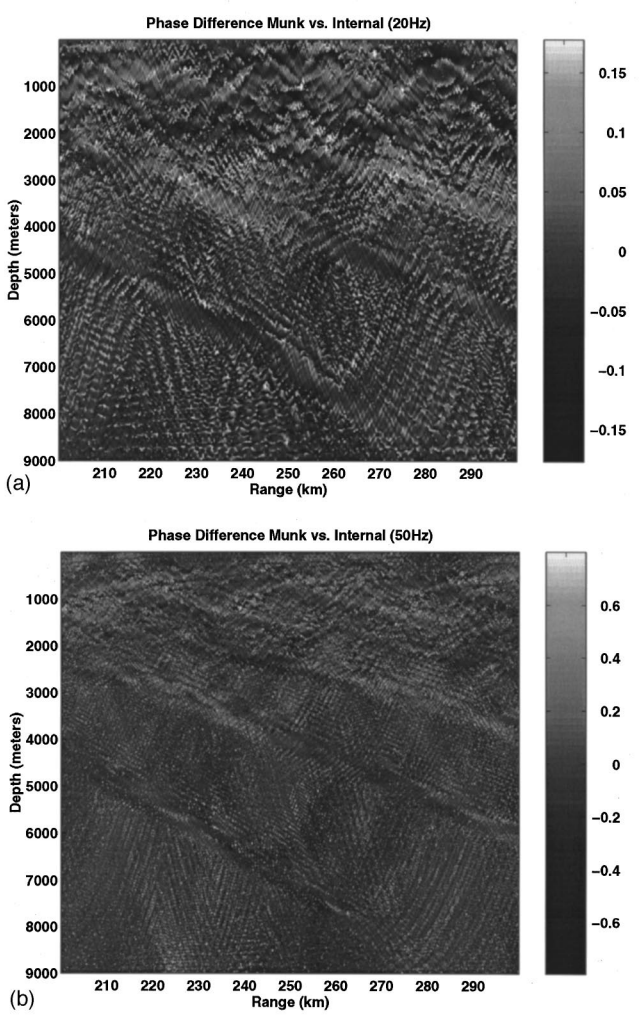

FIG. 8. The relative phase difference of the field propagated through the Munk sound-speed profile (see Fig. 2) and the field including the internal only. The phases for each field are calculated using Eq. (71) and are subtracted and are plotted in radians. The dynamic range for the 20-Hz case (a) is $\pm 10°$, while the dynamic range for the 50-Hz case (b) is $\pm 45°$, this being a function of the fact that the effects of the internal waves alone are much greater for higher frequencies.

where $\xi(\mathbf{x},t)$ is given by

$$\xi(\mathbf{x},t)=\left(\frac{\partial U(z)}{\partial z}\right)_P \zeta(\mathbf{x},t). \tag{58}$$

Here $(\partial U(z)/\partial z)_P$ is the fractional potential gradient of the sound speed, and $\zeta(\mathbf{x},t)$ is the vertical displacement of the internal gravity wave field.[10,48]

The normal modes of the internal waves are found by first considering horizontal plane wave solutions to the Navier–Stokes equations in the Boussinesq approximation, i.e., solutions proportional to $\exp(ik_x x+ik_y y-i\omega t)$.[10,49,50] In this approximation the eigenmodes of the linear internal gravity wave displacements are given by the second-order differential eigenvalue equation,[10,44–46,48]

$$\frac{\partial^2 W_j(k,z)}{\partial z^2}+k^2\left(\frac{N^2(z)-\omega_j^2(k)}{\omega_j^2(k)-\omega_i^2}\right)W_j(k,z)=0. \tag{59}$$

We point out that in Eq. (59), the eigenvalues $[\omega_j^2(k)]$ are dependent on the magnitude of the horizontal wave number $k=\sqrt{k_x^2+k_y^2}$, the depth-dependent local buoyancy frequency $N(z)$,

$$N(z)=\sqrt{-\frac{g}{\rho}\frac{\partial \rho}{\partial z}}, \tag{60}$$

and the local inertial frequency, ω_i,

$$\omega_i=2\Omega \sin \lambda, \tag{61}$$

where Ω and λ in Eq. (61) are the frequency of the rotation of the Earth and the latitude, respectively. We arbitrarily set $\lambda=30°$, so that $\omega_i=1/24$ cycles/h.

The buoyancy frequency used for these examples is modeled on that used by Colosi *et al.*[48] In that work, the buoyancy frequency was an average of several measurements taken during the SLICE-89, experiment. Our functional form is normalized such that $N(z_{\text{ref}})=3$ cycles/h, for $z_{\text{ref}}=250$ m. The functional form of $N(z)$ used in these examples is

$$N(z)=7.5\exp\left(\sqrt{\frac{z}{250}}\log\frac{3}{7.5}\right)-4\exp\left(-\frac{z}{10}\right), \tag{62}$$

and plotted in Fig. 3.

To solve Eq. (59) for the eigenmodes, $W_j(k,z)$, a finite difference approximation of the partial differential equation is used. This procedure leads to a generalized algebraic eigenvalue problem, which can be solved using the QZ algorithm.[51,52] The choice of using this method over that of the usual WKB method is that it produces a more accurate representation of the internal wave field in the upper ocean, near the surface, where the effects of Eq. (53) are expected to be the greatest. The solution vectors, $W_j(k,z)$, are orthonormal with respect to weighted inner product[48]

$$\int_0^\infty dz(N^2(z)-w_i^2)W_i(k,z)W_j(k,z)=\delta_{i,j}. \tag{63}$$

The displacement of a particular parcel of fluid can be described as the real part of a sum of the internal wave normal modes multiplied by a random field,

$$\zeta(r,z,t)=\zeta_0\ \text{Re}\left\{\int_{k_{\min}}^{k_{\max}}dk\int_0^{2\pi}d\theta\sum_{j=1}^{j_m}\tilde{G}_j(k,\theta)W_j(k,z)\times\exp[ikx\cos\theta-i\omega_j(k)t]\right\}, \tag{64}$$

where θ is the angle between the direction of propagation and a group of incoming internal plane waves. ζ_0 is set so that it is equal to $\langle\zeta(z_{\text{ref}})\rangle=5$ m. The values of $k_{\min}$ and $k_{\max}$ were taken to be the largest and smallest scales of the internal wave field, respectively, i.e., $k_{\min}=1/50$ cycles/km and $k_{\max}=2$ cycles/km. Finally, in Eq. (64), $\tilde{G}_j(k,\theta)$ are complex Gaussian random functions. The Garett–Munk theory requires that these functions are normalized such that

$$\sum_{j=1}^{\infty}\int_0^\infty dk\ G_j(k)=1, \tag{65}$$

where the spectral density $G_j(k)$ given by[10,44,48]

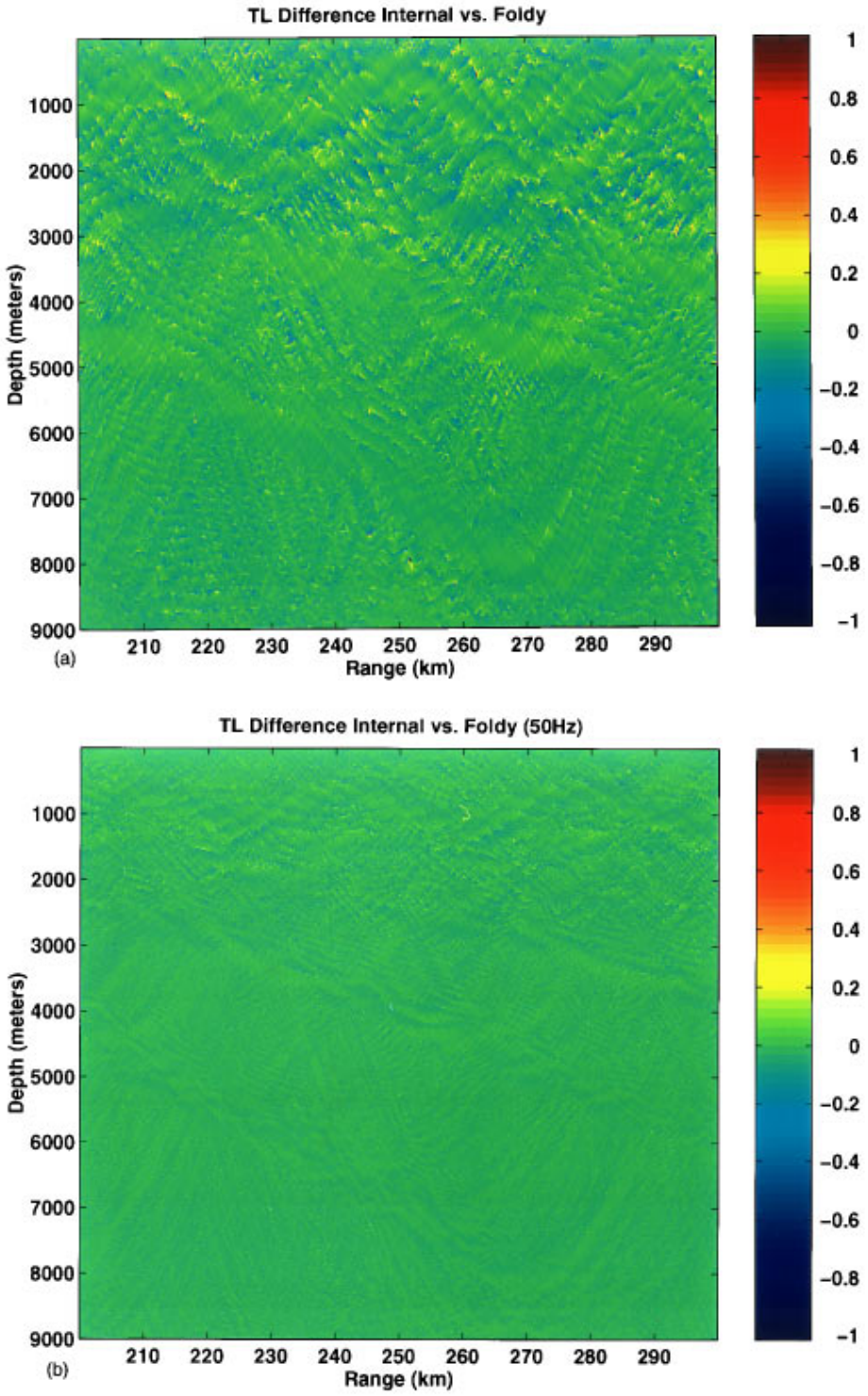

FIG. 9. The relative transmission loss difference between propagating using the internal wave field and the Foldy–Wouthuysen correction term. The difference is shown for the ranges between 200 and 300 km. The dynamic range of the plot is equivalent to ±1 dB. The frequency dependence of the correction term is self-evident, with the higher frequency of 50 Hz (b) having a much smaller difference than the lower frequency 20 Hz (a).

$$G_j(k) = \frac{8}{\pi^2} \frac{j_*}{j^2 + j_*^2} \frac{k^2 k_j}{(k^2 + k_j^2)^2}, \tag{66}$$

and is related to the random Gaussian functions $\tilde{G}_j(k,\theta)$ through the relation

$$\langle |\tilde{G}_j(k,\theta)|^2 \rangle = \int_{k-\delta k/2}^{k+\delta k/2} dk' G_j(k'). \tag{67}$$

The parameter j_* is set to 3, and the mode-dependent parameter k_j is

$$k_j = \frac{\pi j \omega_i}{n_0 B}, \tag{68}$$

where $n_0 B = 4.5$ km-cycles/hr.

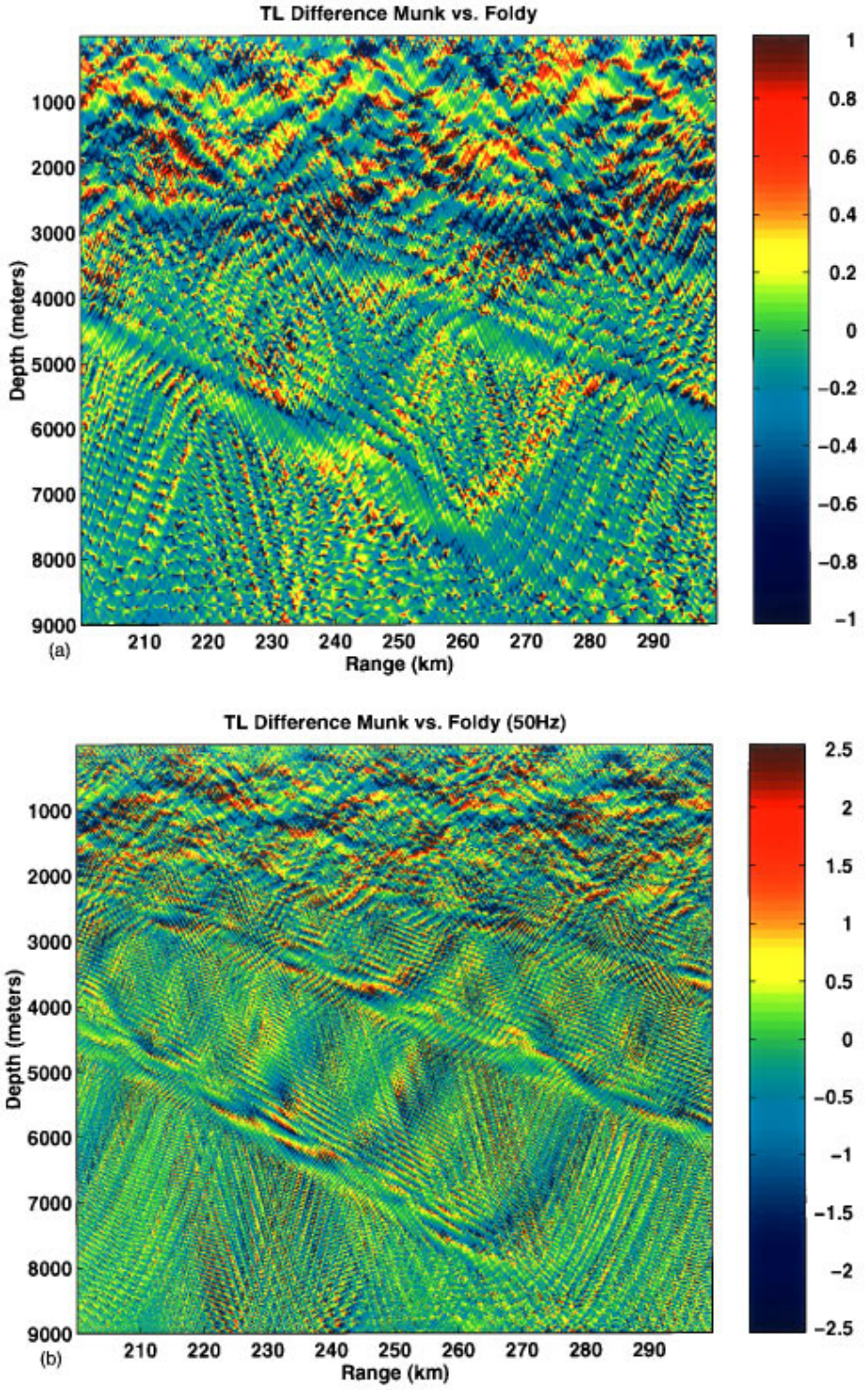

FIG. 10. The relative transmission loss difference between propagating through a Munk profile and one including the internal wave field and the Foldy–Wouthuysen correction term. The difference is shown for the ranges between 200 and 300 km. The dynamic range of the plot is equivalent to ±1 dB for the 20-Hz case (a) and is ±2.5 dB for the 50-Hz case (b).

Once the vertical eigenmodes are determined, it is a relatively straightforward process to determine the internal wave field, up to the largest length scale $1/k_{\min}$, in our case 50 km, using Eq. (64). To extend the vertical displacement field due to the internal waves, we create different realizations by choosing new random variables $\tilde{G}_j(k,\theta)$ and use hat functions to glue the different realizations together. In essence, given the nth realization $\zeta_n(r)$ of vertical displacements for $0 \leqslant r \leqslant 50$ km, then the total field $\zeta(r,z,t)$ is

$$\zeta(r,z,t) = \sum_{n=1}^{N} \zeta_n(r_{n-1},z,t)\,\phi_n(r,z,t); \quad r_n = \frac{n}{2k_{\min}}, \tag{69}$$

where the nth hat function ϕ_n is defined by

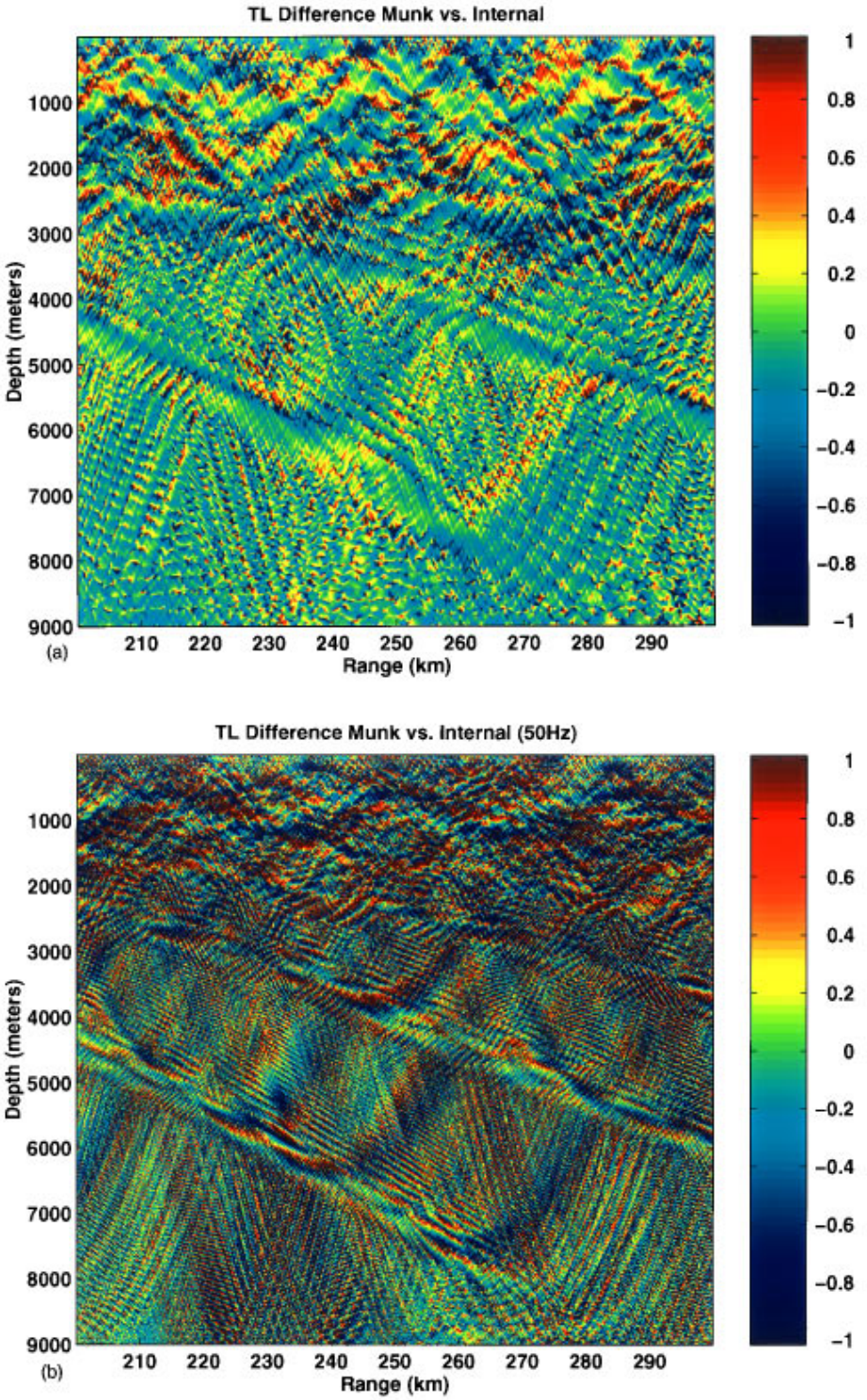

FIG. 11. The relative transmission loss difference between propagating through a Munk profile and one including only internal waves. The difference is shown for the ranges between 200 and 300 km. The dynamic range of the plot is equivalent to ± 1 dB for the 20-Hz case (a) and is ± 2.5 dB for the 50-Hz case (b).

$$\phi_n(r,z,t)=\begin{cases}\dfrac{r-r_{n-1}}{r_n-r_{n-1}}, & r_{n-1}\leqslant r\leqslant r_n,\\ \dfrac{r_{n+1}-r}{r_{n+1}-r_n}, & r_n\leqslant r\leqslant r_{n+1}.\end{cases} \tag{70}$$

A realization of the total sound-speed field was calculated and a portion of it is shown in Fig. 5. The perturbations in the sound speed due to internal waves, as shown in Fig. 4, were added to the Munk profile, shown in Fig. 2, to create Fig. 5. As can be seen from this figure, the profile is still strongly similar to the basic Munk profile, allowing us to use the waveguide properties of the SOFAR channel to model propagation over long distances without the field interacting with the boundaries. To further minimize the interaction of the field with the boundaries, we have chosen a water depth

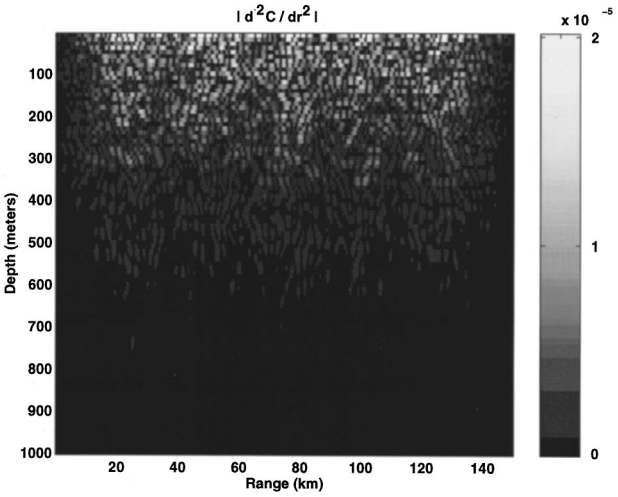

FIG. 12. Plotted here is the magnitude of the second derivative of the sound-speed profile with respect to range. The maximum magnitude of this term is of the order of 2×10^{-5} m^{-2} s^{-1}. This is the frequency-independent portion of the Foldy–Wouthuysen correction term, as given by Eq. (53). This shows that the Foldy–Wouthuysen term, Eq. (53), is extremely small, and thus unlikely to affect propagation of cw fields, except at extremely low frequencies.

of 9000 m and set the attenuation in the sediment to the arbitrarily high value of 10 dB/λ.

The propagation was modeled through each environment out to a range of 500 km using RAM. A portion of the phase difference as a function of range is plotted in Fig. 6. In this plot we have subtracted the phase of the field, found from the formula

$$\text{Phase} = \arctan\left(\frac{\text{Im}(A)}{\text{Re}(A)}\right), \tag{71}$$

by propagating the acoustic field using the internal wave field from that found by using the effective sound speed of Eq. (53). The results are plotted in radians, with a dynamic range of $\pm1°$. The frequency dependence is self-evident, with the higher frequency (50 Hz) showing much less effect than the lower frequency (20 Hz).

By considering Figs. 7 and 8, we conclude that the main effect of the inclusion of the Foldy–Wouthuysen correction term on propagation through an internal wave field is not the Foldy–Wouthuysen term itself, but the direct effects of the internal waves. This is emphasized in Figs. 9–11, where there is only a single dB difference in the transmission loss between the internal wave case and the Foldy–Wouthuysen case, while there is a much large deviation between the Munk profile and the other two cases. This is not surprising considering the size of the correction as can be seen in Fig. 12. However, upon Fourier synthesis of a complete pulse, the wavefront is likely to be blurred more by the Foldy–Wouthuysen correction term than for just internal waves alone. This is provided the frequencies are low enough ($\leqslant$50 Hz).

IV. CONCLUSIONS AND DISCUSSION

Foldy–Wouthuysen transformations have been used to diagonalize the scalar wave propagation Hamiltonian. This transformation clearly separates range-dependent effects which accumulate during propagation from those which cancel everywhere except at the endpoints. The former come from virtual oscillations (a concept developed within this context in Appendix C) between forward- and backward-propagating fields. To third order these virtual oscillations can be modeled using an effective phase speed, obtained by subtracting a term proportional to the second derivative of the phase speed in the medium. This perturbative theory is designed to describe effects which accumulate during propagation through range-dependent media that with length scales much larger that the wavelength of the propagating wave field. This has been applied to long distance, low-frequency propagation through a sound channel with internal waves. For this application, the expansion parameters are typically very small, so the propagation distances must be very large for the effect to be significant.

We have demonstrated that for an ocean with internal waves perturbing the sound speed profile using the Garrett–Munk theory and at a frequency of 20 Hz, effects are immediate but small, and they grow with range, out to the limit of the modeled propagation (500 km). Although, for the same internal wave field, and at a frequency of 50 Hz, little effect can be seen. This being a direct result of the fact that Eq. (53) is a function of (frequency)$^{-2}$. Nevertheless, phase errors did occur for even those frequencies, leading us to conclude that applications of the PE to such things as pulse propagation, tomography, signal processing, and matched-field processing, which rely heavily on relative phases of a received field, could be severely affected by the addition (or neglect) of this new effect.

APPENDIX A: PROPERTIES OF HERMITICIAN MATRIX OPERATORS

We denote the Hermitian conjugate of the vector function $\vec{\Phi}$ (**R**) is its transpose and complex conjugate as

$$\vec{\Phi}^\dagger = (\vec{\Phi}^*)^t.$$

To extend the concept of Hermiticity to an operator $\hat{\boldsymbol{\alpha}}$ it is necessary to define the bilinear operation,

$$\int (\vec{\Phi}^\dagger \hat{\boldsymbol{\alpha}} \vec{\Phi})\, d^2x, \tag{A1}$$

where it is assumed that $\hat{\alpha}$ operates to the right. The Hermitian conjugate $\hat{\alpha}^\dagger$, which operates to the left, is defined by the equation

$$\int (\vec{\Phi}^\dagger \hat{\boldsymbol{\alpha}}^\dagger \vec{\Phi}) d^2x = \int ((\hat{\boldsymbol{\alpha}} \vec{\Phi})^\dagger \vec{\Phi})\, d^2x. \tag{A2}$$

The Hermitian conjugate of a matrix operator is the transpose and complex conjugate of the matrix, while for matrix-differential operators containing powers of the differential operator $(\boldsymbol{\nabla}_\perp)^n$ it is necessary to integrate by parts, picking up a minus sign for every power, for a total change of sign of $(-1)^n$. It follows from these definitions that the Hermitian conjugate of a product is the product of the Hermitian conjugates in reverse order [i.e., $(\hat{\alpha}\hat{\beta})^\dagger = \hat{\beta}^\dagger \hat{\alpha}^\dagger$]. The bilinear operation defined by Eq. (A1) is required specifically so that

the concept of Hermiticity can be extended to the differential operator $\nabla_\perp$.

APPENDIX B: THE CONTRIBUTIONS FROM THE ENDPOINTS

We now turn to a brief examination of the contribution at the endpoints. This is done for the purpose of comparing our formalism with the results of Schurman *et al.*[6] For the problem to which our work is primarily addressed: that of long distance, low-frequency propagation in the ocean, the endpoint correction is not expected to be an important effect. The effect associated with the endpoints and hence called the ''endpoint correction,'' is important in the presence of a single strong front, where there is little propagation history, and cumulative effects are unimportant, but differences between the initial and final sound speed are significant.

Technically, the Foldy–Wouthuysen transformations themselves contribute only at the endpoints, yet there exists an alternate formulation of the problem such that the effects associated with these transformations take the form of additional energy-conserving terms in the Hamiltonian. The lowest-order contribution of this type turns out to be the result discussed by Schurman *et al.* This term also follows from the requirement that the solution of the range-dependent PE must still satisfy the wave equation as well. Since the two formulations are equivalent, the contribution from the additional term in the Hamiltonian must cancel during propagation, the final result depending only on the expansion parameters evaluated at the endpoints. Note that the direct argument based on consistency between the wave equation and the PE provides no indication of this fact. An important advantage of the approach based on the Foldy–Wouthuysen transformation is the clear separation between propagation and endpoint effects.

Consider the range-dependent problem through second order:

$$\vec{\Phi}\big|_{\mathbf{x}_2} = e^{-i\hat{S}^{(1)}} e^{-i\hat{S}^{(2)}} \tilde{\vec{\Phi}}^{(2)}\big|_{\mathbf{x}_2}. \tag{B1}$$

From Glauber's identity[53]

$$e^A e^B = e^{A+B} e^{(1/2)[A,B]} \tag{B2}$$

this becomes

$$\vec{\Phi}\big|_{\mathbf{x}_2} = e^{-i(\hat{S}^{(1)}+\hat{S}^{(2)})} \vec{\Phi}^{(2)}\big|_{\mathbf{x}_2} + \mathcal{O}(\hat{\Lambda}_0^3) \tag{B3}$$

and

$$i\,\frac{\partial \vec{\Phi}}{\partial x}\bigg|_{\mathbf{x}_2} = \left(\frac{\partial \hat{S}^{(1)}}{\partial x}\,\vec{\Phi} + e^{-i(\hat{S}^{(1)}+\hat{S}_2^{(2)})} i\,\frac{\partial \tilde{\vec{\Phi}}^{(2)}}{\partial x}\right)\bigg|_{\mathbf{x}_2} + \mathcal{O}(\hat{\Lambda}_0^3) \tag{B4a}$$

$$= \left(\frac{\partial \hat{S}^{(1)}}{\partial x}\,\vec{\Phi} + e^{-i(\hat{S}^{(1)}+\hat{S}^{(2)})} \tilde{\tilde{H}}^{(2)} \tilde{\vec{\Phi}}^{(2)}\right)\bigg|_{\mathbf{x}_2} + \mathcal{O}(\hat{\Lambda}_0^3). \tag{B4b}$$

For a pure forward propagating wave,

$$\tilde{\vec{\Phi}}^{(2)}\big|_{\mathbf{x}_2} = \begin{pmatrix} 0 \\ \tilde{\chi}^{(2)} \end{pmatrix}\bigg|_{\mathbf{x}_2} \tag{B5}$$

and $\tilde{\tilde{\mathbf{H}}}^{(2)} = \boldsymbol{\eta}\hat{H}_s^{(2)} + \mathcal{O}(\hat{\Lambda}_0^3)$ [where the scalar Hamiltonian is defined by $\hat{H}_s^2 \equiv k_0(1+\hat{\Lambda}_0 - (1/2)\hat{\Lambda}_0^2)$] can be replaced by $\tilde{\tilde{\mathbf{H}}}^{(2)} = -\mathbf{1}\hat{H}_s^{(2)}$. Therefore, for this special case, the transformation $e^{-i(\hat{S}_2^1+\hat{S}_2^{(2)})}$ and the Hamiltonian commute to $\mathcal{O}([\hat{\Lambda}_0, \partial\hat{\Lambda}_0/\partial x]) = \mathcal{O}(\hat{\Lambda}_0^3)$ and we have

$$i\,\frac{\partial \vec{\Phi}}{\partial x}\bigg|_{\mathbf{x}_2} = \left(\frac{\partial \hat{S}^{(1)}}{\partial x}\,\vec{\Phi} - \hat{H}_s^{(2)}\mathbf{1}\vec{\Phi}\right)\bigg|_{\mathbf{x}_2} + \mathcal{O}(\hat{\Lambda}_0^3). \tag{B6}$$

Using

$$(1 \quad 1)\vec{\Phi}\big|_{\mathbf{x}_2} = A\big|_{\mathbf{x}_2} \tag{B7}$$

and

$$(1 \quad 1)\,\frac{\partial \hat{S}}{\partial x}\bigg|_{\mathbf{x}_2} = (1 \quad 1)\,\frac{i\boldsymbol{\eta}\boldsymbol{\sigma}}{2}\,\frac{\partial \mu}{\partial x_2}\bigg|_{\mathbf{x}_2} \tag{B8a}$$

$$= \frac{i}{2}\,\frac{\partial \mu}{\partial x_2}\,(1 \quad 1)\bigg|_{\mathbf{x}_2} \tag{B8b}$$

to obtain

$$-i\,\frac{\partial A}{\partial x}\bigg|_{\mathbf{x}_2} = \left(\hat{H}_s^{(2)} - \frac{i}{2}\,\frac{\partial \mu}{\partial x}\right)A\bigg|_{\mathbf{x}_2} + \mathcal{O}(\hat{\Lambda}_0^3), \tag{B9}$$

we have essentially the same as Eq. (9) of Schurman *et al.*[6] To show this we must first assume that the range derivative of μ is not treated as an extra order in the perturbative expansions. Substituting

$$\hat{H}_s^{(2)} = k_0(1+\hat{\Lambda}_0) + \mathcal{O}(\hat{\Lambda}_0^2) \tag{B10}$$

into Eq. (B9), dropping the $\mathbf{x}_2$ notation, and multiplying by $2k_0$, we have

$$0 = 2ik\,\frac{\partial A}{\partial x} + \frac{k}{k_0}\,\nabla_\perp^2 A + 2kk_0(1-\mu)A - ik\,\frac{\partial \mu}{\partial x}\,A + \mathcal{O}(\hat{\Lambda}_0^2). \tag{B11}$$

Now, note that

$$k = k_0(1-\mu) + \mathcal{O}(\hat{\Lambda}_0^2), \tag{B12a}$$

$$\frac{\partial k}{\partial x} = -k_0\,\frac{\partial \mu}{\partial x} + \mathcal{O}(\hat{\Lambda}_0^2) = -k\,\frac{\partial \mu}{\partial x} + \mathcal{O}(\hat{\Lambda}_0^2), \tag{B12b}$$

$$k\nabla_\perp^2 = k_0\nabla_\perp^2 + \mathcal{O}(\hat{\Lambda}_0^2), \tag{B12c}$$

so we have

$$0 = 2ik\,\frac{\partial A}{\partial x} + \nabla_\perp^2 A + \left(i\,\frac{\partial k}{\partial x} + 2k^2\right)A. \tag{B13}$$

This correction was found by Schurman *et al.*[6] to be particularly useful for modeling fronts where there is a monotonic change in the sound speed profile. This is a sensible result, since this is precisely the sort of situation where one would not expect to be able to neglect the contribution from the endpoints.

The new term can be deduced from the requirement that A obey the full wave equation as well as the PE. Let

$$\hat{\mathbf{H}}_{\text{eff}} \equiv \hat{H}_s^{(2)} - \frac{i}{2}\frac{\partial \mu}{\partial x} \tag{B14a}$$

$$= k_0(1+\hat{\Lambda}_0) + \frac{i}{2}\frac{\partial \hat{\Lambda}_0}{\partial x} \tag{B14b}$$

and apply the chain rule as well as Eq. (B9) to $i\partial(\hat{\mathbf{H}}_{\text{eff}} A)/\partial x$, obtaining to $\mathcal{O}(\hat{\Lambda}_0^2)$,

$$\left[-\frac{\partial^2}{\partial x^2} + ik_0 \frac{\partial \hat{\Lambda}_0}{\partial x} \right] A = -i\hat{\mathbf{H}}_{\text{eff}} \frac{\partial A}{\partial x} = \hat{\mathbf{H}}_{\text{eff}}^2 A, \tag{B15a}$$

which reduces to the wave equation. Note that the term $-(i/2)\partial\mu/\partial x$ must be present in $\hat{\mathbf{H}}_{\text{eff}}$ so that the right-hand side of the equation has a term corresponding to the term $ik_0\ \partial\hat{\Lambda}_0/\partial x$ found on the left-hand side. It is significant that a straightforward argument of this sort for determining corrections to the PE due to range dependence fails to provide a clear distinction between cumulative effects associated with propagation, and endpoint effects.

APPENDIX C: VIRTUAL OSCILLATIONS

The concept of virtual oscillations within the context of this work can be developed as follows. First, recall the prescription $\mu \to \mu - 1/(8k_0^2)\ \partial^2\mu/\partial x^2$. Now, consider a coordinate shift $x \to x + \delta x$ and expand $\mu(x+\delta x)$. We have

$$\mu(x+\delta x) = \mu(x) + \frac{\partial \mu}{\partial x}\ \delta x + \frac{1}{2}\frac{\partial^2 \mu}{\partial x^2}\ (\delta x)^2, \tag{C1}$$

and treating δx as a random fluctuation to be averaged over, we have

$$\langle \mu(x+\delta x)\rangle = \mu(x) + \frac{\partial \mu}{\partial x}\ \langle \delta x\rangle + \frac{1}{2}\frac{\partial^2 \mu}{\partial x^2}\ \langle (\delta x)^2\rangle. \tag{C2}$$

Comparing the prescription $\mu \to \mu - 1/(8k_0^2)\partial^2\mu/\partial x^2$, we conclude that the fluctuation has average $\langle \delta x\rangle = 0$ and mean square displacement is then

$$\langle (\delta x)^2\rangle = -\frac{1}{4k_0^2}, \tag{C3}$$

corresponding to fluctuations on the order $\delta x \sim i/(2k_0)$. The quantity is imaginary because it is associated with an evanescent wave phenomenon (not to be confused with the evanescent portion of the propagating field's wave number spectrum). Incorporating the boundary term $(i/2)\partial\mu/\partial x$ given in Eq. (B9), we are left with the simple prescription $\mu(x) \to \mu(x + i/(2k_0))$ (i.e., a small shift of x into the complex plane). Consequently, no energy flows from the forward- into the backward-propagating fields (or vice versa). This is what is meant by a virtual oscillation between the fields. Furthermore, higher-order terms correspond to virtual fluctuations into multiple backward-propagating fields. The diagonalization procedure also serves to push strong backscatter (as opposed to virtual backscatter) to its natural place at infinite order in perturbation theory.

The oscillations between forward- and backward-propagating fields have the attributes of a harmonic oscillator. The transformations used to simplify the diagonal representations of the Hamiltonian can be understood as translations of the zero point of the harmonic oscillator. The crucial quantity characterizing both the virtual fluctuations and the true backscatter is $\partial^2\mu/\partial x^2$, which corresponds to the spring constant of the oscillator. For true backscatter, the oscillator is not bound, and the spring constant is negative, and thus can never be analyzed using perturbation theory. For virtual oscillations, such as those being examined here, the analogous oscillator is bound, the spring constant positive, small fluctuations remain small, and perturbation theory is appropriate.

[1] F. D. Tappert, ''The parabolic approximation method,'' in *Wave Propagation and Underwater Acoustics*, edited by J. B. Keller and J. S. Papadakis (Springer-Verlag, New York, 1977), Vol. 70, pp. 224–287.
[2] M. D. Collins, ''Ram User's Guide,'' Tech. Rep., Naval Research Laboratory, Washington, DC (1995).
[3] M. D. Collins, ''A split-step Padé solution for the parabolic equation method,'' J. Acoust. Soc. Am. **93**, 1736–1742 (1993).
[4] B. E. McDonald, M. D. Collins, W. A. Kuperman, and K. D. Heaney, ''Comparison of data and model predictions for the Heard Island acoustic transmissions,'' J. Acoust. Soc. Am. **96**, 2357–2370 (1994).
[5] F. D. Tappert and D. Lee, ''A range refraction parabolic equation,'' J. Acoust. Soc. Am. **76**, 1797–1803 (1984).
[6] I. W. Schurman, W. L. Siegman, and M. J. Jacobson, ''An energy-conserving parabolic equation incorporating range refraction,'' J. Acoust. Soc. Am. **89**, 134–144 (1990).
[7] M. B. Porter, F. B. Jensen, and C. M. Ferla, ''The problem of energy conservation in one-way models,'' J. Acoust. Soc. Am. **89**, 1058–1067 (1991).
[8] M. D. Collins and E. K. Westwood, ''A higher-order energy-conserving parabolic equation for range-dependent ocean depth, sound speed, and density,'' J. Acoust. Soc. Am. **89**, 1068–1075 (1991).
[9] L. Fishman and J. J. McCoy, ''Derivation and application of extended parabolic wave theories: I. The factorized Helmholtz equation,'' J. Math. Phys. (N.Y.) **25**, 287–293 (1984).
[10] S. Flatté, R. Dashen, W. Munk, K. Watson, and F. Zachariasen, *Sound Transmission Through a Fluctuating Ocean* (Cambridge U.P., London, 1979).
[11] J. D. Bjorken and S. D. Drell, *Relativistic Quantum Mechanics* (McGraw-Hill, New York, 1962).
[12] L. L. Foldy and S. A. Wouthuysen, ''On the Dirac theory of spin 1/2 particles and its nonrelativistic limit,'' Phys. Rev. **78**, 29–36 (1950).
[13] J. D. Bjorken and S. D. Drell, *Relativistic Quantum Mechanics* (McGraw-Hill, New York, 1964), pp. 46–62.
[14] P. Roman, *Advanced Quantum Theory* (Addison–Wesley, Reading, MA, 1965), pp. 133–139.
[15] C. Itzykson and J.-B. Zuber, *Quantum Field Theory* (McGraw-Hill, New York, 1980), p. 62.
[16] J. J. Sakurai, *Advanced Quantum Mechanics* (Benjamin/Cummings, Menlo Park, CA, 1984), pp. 117–119.
[17] J. D. Bjorken and S. D. Drell, *Relativistic Quantum Mechanics* (McGraw–Hill, New York, 1964), p. 38.
[18] B. E. McDonald, ''Echoes from vertically striated subresonant bubble clouds: A model for ocean surface reverberation,'' J. Acoust. Soc. Am. **89**, 617–622 (1991).
[19] F. S. Henyey, ''Acoustic scattering from ocean micro-bubble plumes in the 100 Hz to 2 kHz region,'' J. Acoust. Soc. Am. **90**, 399–405 (1991).
[20] L. Fishman and J. J. McCoy, ''Factorization, path integral representations, and the construction of direct and inverse wave propagation theories,'' IEEE Trans. Geosci. Remote Sens. **GE-22**, 682–692 (1984).
[21] J. J. Sakurai, *Advanced Quantum Mechanics* (Benjamin/Cummings, Menlo Park, CA, 1984), pp. 229–231.
[22] C. Itzykson and J.-B. Zubėr, *Quantum Field Theory* (McGraw–Hill, New York, 1980), pp. 185–195.
[23] J. D. Bjorken and S. D. Drell, *Relativistic Quantum Mechanics* (McGraw-Hill, New York, 1964), p. 90ff.
[24] T. Levitan, ''Creation of mass processes and perturbation theory,'' Can. J. Math. **3**, 456–467 (1973).
[25] M. L. Silverstein, ''Markov processes with creation of particles,'' Z.

Wahrscheinlichkeitstheor. Verwandte Geb. **9**, 235–257 (1968).
[26] M. Nagasawa, ''Markov process with creation and annihilation,'' Z. Wahrscheinlichkeitstheor. Verwandte Geb. **14**, 49–60 (1969).
[27] M. E. Taylor, *Pseudodifferential Operators* (Princeton U.P., Princeton, NJ, 1981).
[28] L. Fishman, ''Exact and operator rational approximate solutions of the Helmholtz, Weyl composition equation in underwater acoustics—the quadratic profile,'' J. Math. Phys. **33**, 1887–1914 (1982).
[29] L. Fishman, J. J. McCoy, and S. C. Wales, ''Factorization and path integration of the Helmholtz equation: Numerical algorithms,'' J. Acoust. Soc. Am. **81**, 1355–1376 (1987).
[30] J. D. Bjorken and S. D. Drell, *Relativistic Quantum Mechanics* (McGraw-Hill, New York, 1964), pp. 199–207.
[31] L. Fishman, ''One-way wave propagation methods in direct and inverse scalar wave propagation modeling,'' Radio Sci. **28**, 865–876 (1993).
[32] S. T. McDaniel, ''Parabolic approximations for underwater sound propagation,'' J. Acoust. Soc. Am. **58**, 1178–1185 (1975).
[33] J. J. Sakurai, *Advanced Quantum Mechanics* (Benjamin/Cummings, Menlo Park, CA, 1984), Ch. 3.
[34] J. D. Bjorken and S. D. Drell, *Relativistic Quantum Mechanics* (McGraw-Hill, New York, 1964), Chap. 1.
[35] C. Itzykson and J.-B. Zuber, *Quantum Field Theory* (McGraw-Hill, New York, 1980), Ch. 2.
[36] R. G. Levers, ''Spinning the Helmholtz equation,'' in *Computational Acoustics—Wave Propagation*, edited by D. Lee, R. L. Sternberg, and M. H. Schultz (North Holland, Amsterdam, 1988), pp. 287–293.
[37] L. D. Landau and E. M. Lifshitz, *Fluid Mechanics*, Vol. 6 of *Course of Theoretical Physics* (Pergamon, New York, 1987), 2nd ed., Eqs. 64.6 and 64.5.
[38] H. Goldstein, *Classical Mechanics* (Addison–Wesley, Reading, MA, 1980), 2nd ed.
[39] D. Creamer, F. Henyey, R. Schult, and J. Wright, ''Improved linear representation of surface waves,'' J. Fluid Mech. **205**, 135–161 (1989).
[40] J. D. Bjorken and S. D. Drell, *Relativistic Quantum Fields* (McGraw-Hill, New York, 1964).
[41] C. Itzykson and J.-B. Zuber, *Quantum Field Theory* (McGraw-Hill, New York, 1980), pp. 123–124.
[42] J. J. Sakurai, *Advanced Quantum Mechanics* (Benjamin/Cummings, Menlo Park, CA, 1984), pp. 207–208.
[43] J. D. Bjorken and S. D. Drell, *Relativistic Quantum Mechanics* (McGraw-Hill, New York, 1964), p. 47.
[44] C. Garrett and W. Munk, ''Space-time scales of internal waves,'' Geophys. Fluid Dyn. **2**, 225–264 (1972).
[45] C. Garrett and W. Munk, ''Oceanic mixing by breaking internal waves,'' Deep Sea Res. **19**, 823–832 (1972).
[46] C. Garrett and W. Munk, ''Space-time scales of internal waves: A progress report,'' J. Geophys. Fluid Dyn. **80(3)**, 291–297 (1975).
[47] W. H. Munk, ''Sound channel in an exponentially stratified ocean, with application to SOFAR,'' J. Acoust. Soc. Am. **55**, 220–226 (1974).
[48] J. A. Colosi, S. M. Flatté, and C. Bracher, ''Internal-wave effects on 1000-km oceanic acoustic pulse propagation: Simulation and comparison with experiment,'' J. Acoust. Soc. Am. **96**, 452–468 (1994).
[49] S. H. Lamb, *Hydrodynamics* (Dover, New York, 1932).
[50] J. Lighthill, *Waves in Fluids* (Cambridge, U.P., Cambridge, 1985).
[51] G. H. Golub and C. F. V. Loan, *Matrix Computations* (Johns Hopkins U.P., Baltimore, 1989), 2nd ed.
[52] E. Anderson, Z. Bai, C. Bischof, J. Demmel, J. Dongara, J. D. Croz, A. Greenbaum, S. Hammarling, A. McKenney, S. Ostrouchov, and D. Sorensen, *LAPACK Users' Guide* (SIAM, Philadelphia, 1992).
[53] A. Messiah, *Quantum Mechanics* (Wiley, New York, 1958), Vol. I, p. 442.

A hybrid split-step/finite-difference PE algorithm for variable-density media

David Yevick
Department of Electrical Engineering, Queen's University, Kingston, Ontario K7L 3N6, Canada

David J. Thomson
Defence Research Establishment Atlantic, Esquimalt Defence Research Detachment, CFB Esquimalt, PO Box 17000 STN FORCES, British Columbia V9A 7N2, Canada

(Received 23 January 1996; accepted for publication 2 October 1996)

Although variations in the density, ρ, are naturally incorporated into finite-difference parabolic equation (PE) solvers, split-step PE algorithms traditionally account for density changes by adding to the refractive index terms containing derivatives of ρ. As a consequence, geoacoustic density profiles that contain step discontinuities at layer interfaces must be smoothed appropriately before these extra terms can be evaluated. In this paper, a new hybrid method is proposed for treating density inhomogeneities in the split-step PE. This approach involves splitting the differential operator into density-independent and density-dependent components. While the former terms may be evaluated with the split-step Fourier technique, the influence of density changes is handled through a finite-difference procedure. Such an algorithm can be easily implemented in recently proposed hybrid split-step/finite-difference and split-step/Lanczos PE solvers. [J. Acoust. Soc. Am. **96**, 396–405 (1994)]. [S0001-4966(97)03302-X]

PACS numbers: 43.30.Bp [MBP]

INTRODUCTION

Both split-step and finite-difference marching algorithms are widely used to solve parabolic equations (PEs) that are derived from approximations to the exact, one-way wave equation of underwater sound propagation. However, while each numerical procedure is easily adapted to treat propagation in a constant-density ocean, the modifications needed to accommodate variable-density media differ for the two cases. In the finite-difference formalism, a so-called ''homogeneous'' procedure results if the density is taken to be uniform on both sides of a jump discontinuity (typically, the ocean bottom) and continuity conditions for both the pressure and particle velocity are imposed by appropriately modifying the equations describing the field in the vicinity of the interface.[1,2] Alternatively, in the ''heterogeneous'' procedure, a finite-difference approximation is applied directly to the relevant, density-dependent, transverse differential operator.[3–6] Neither of these procedures can be applied directly in the split-step Fourier algorithm. Instead, a change of variables is invoked to transfer the influence of density variations from the depth-dependent differential operator to the refractive index, allowing the separation of the propagator into a sum of a constant-coefficient, transverse derivative term and a position-space term which includes an effective index of refraction.[7,8] This term, however, contains density derivatives so that any jump discontinuities in the geoacoustic density profile must be smoothed by convolution with an appropriate analytic function.[6,9–12] In any given application, the accuracy of this approach is related to the width chosen for the smoothing function transition region, typically set to equal λ_0/π,[9] where λ_0 is an appropriate reference acoustic wavelength.

To avoid the above complications in the variable-density, split-step PE, we propose in this paper an alternative hybrid technique that does not rely on a smoothing parameter and that can be easily introduced into existing, widely used split-step codes.[13–15] In particular, we separate the effects of the nonuniform density by splitting the propagator into density-independent and density-dependent components. The former can be treated in the standard manner with the split-step scheme. The latter components, which appear as corrections to either the standard or wide-angle propagation operator, are instead implemented with the aid of finite-difference methods. Specifically, by applying the Crank–Nicolson procedure to the [1,1]-Padé approximant of the variable-density propagator, the correction term only gives rise to a single extra tridiagonal system of equations at each range step in addition to the computations associated with the split-step algorithm. The proposed formalism can be incorporated naturally into the hybrid split-step/finite difference and split-step/Lanczos procedures developed previously,[16] considerably extending their range of applicability.

The remainder of this paper is organized as follows. First, we introduce our new operator-splitting into standard and higher-order PE approximations that are amenable to the split-step algorithm. We then propose a finite-difference solution method for the variable-density component of the total propagator. We test this procedure for two shallow-water test cases which exhibit large density-dependent effects and present a comparison both with the traditional PE method using a smoothed density jump and with reference solutions computed using a wave number integration code. Finally, we discuss and summarize our theoretical and numerical results.

I. THEORETICAL METHOD

A. Fundamental equations

To construct the relevant one-way propagation equation for a medium with varying density $\rho(z)$, we consider a region $0<z<z_b$ between the surface $(z=0)$ and bottom

$(z=z_b)$ of a stratified ocean with sound speed and absorption designated by $c(z)$ and $\alpha(z)$ respectively. We assume a uniform half-space in $z>z_b$ with values c_b, α_b and ρ_b. If changes in the pressure field $P(r,z,\phi,t)$ with respect to the azimuthal coordinate ϕ in a cylindrical coordinate system (r,ϕ,z) produced by a harmonic $(\omega=2\pi f)$ point source located at $(r,z)=(0,z_s)$ are slow compared to the fluctuations in the (r,z)-plane, then P may be approximated along any radial by $P(r,z,t)=p(r,z)\exp(-i\omega t)$. For $r>0$, and for a density function which (locally) is solely dependent on the depth coordinate z, the complex pressure $p(r,z)$ then satisfies the two-dimensional scalar Helmholtz equation

$$\frac{1}{r}\frac{\partial}{\partial r}\left(r\frac{\partial p}{\partial r}\right)+\rho\frac{\partial}{\partial z}\left(\frac{1}{\rho}\frac{\partial p}{\partial z}\right)+k_0^2N^2p=0, \tag{1}$$

where $N(z)=n(z)+i\alpha(z)/k_0$, $n(z)=c_0/c(z)$ is the refractive index and $k_0=\omega/c_0$ is an arbitrary reference wave number. Then, if we define

$$\psi(r,z)=p(r,z)\exp(-ik_0r)\sqrt{k_0r} \tag{2}$$

we may describe outgoing propagating waves in the far-field $(k_0r\gg1)$ by the ''one-way'' evolution equation[9,17]

$$\frac{\partial\psi}{\partial r}=ik_0(Q-1)\psi, \tag{3}$$

whose formal solution is given by

$$\psi(r+\Delta r,z)=\exp\{ik_0\Delta r(Q-1)\}\psi(r,z). \tag{4}$$

Here the quantity Q denotes the pseudo-differential operator

$$Q=\sqrt{N^2+k_0^{-2}\rho\frac{\partial}{\partial z}\left(\rho^{-1}\frac{\partial}{\partial z}\right)}. \tag{5}$$

Since the exact square-root operator Q is difficult to evaluate numerically, efficient computational schemes for implementing the exponential propagator in Eq. (4) are obtained from approximations to Q which lead to diagonally banded operators. While finite-difference representations for the full variable-density operator appearing in Eq. (4) can be developed in a straightforward way,[5,6] to handle density variations in the context of the split-step algorithm, it is instead customary to introduce the change of variable $\tilde{\psi}=\sqrt{\rho}\psi$.[7,8,12] Then, instead of Eq. (4), we obtain

$$\tilde{\psi}(r+\Delta r,z)=\exp\{ik_0\Delta r(\tilde{Q}-1)\}\tilde{\psi}(r,z). \tag{6}$$

where $\tilde{Q}$ is

$$\tilde{Q}=\sqrt{\tilde{N}^2+k_0^{-2}\frac{\partial^2}{\partial z^2}} \tag{7}$$

and $\tilde{N}$ is the ''effective'' index of refraction defined by

$$\tilde{N}^2=N^2+\frac{1}{2k_0^2}\sqrt{\rho}\frac{\partial}{\partial z}\left(\frac{1}{\rho\sqrt{\rho}}\frac{\partial\rho}{\partial z}\right). \tag{8}$$

As a result of the presence of derivatives of ρ in the expression for $\tilde{N}$, any step discontinuities contained in standard geoacoustic density profiles must first be smoothed appropriately. Thus, a discontinuous jump in density from ρ_1 to ρ_2 at the depth $z=\zeta$ is replaced by an analytic function of the form[9]

$$\rho(z)=\rho_1+\tfrac{1}{2}(\rho_2-\rho_1)\{1+\tanh[(z-\zeta)/L]\}, \tag{9}$$

where L defines the width of the transition region and is generally chosen such that $k_0L\approx2$. Multiple density jumps can be handled effectively using digital filter techniques based on Eq. (9).[11]

B. Propagator approximations

We now derive a split-step propagation procedure for variable density profiles based on Eq. (4) which does not require smoothing of the density profile. Our method is derived by extending the standard split-step method. That is, we first introduce the notation

$$\varepsilon=N^2-1, \tag{10}$$

$$\mu=\frac{1}{k_0^2}\frac{\partial^2}{\partial z^2}, \tag{11}$$

and

$$\gamma=-\frac{1}{k_0^2\rho}\frac{\partial\rho}{\partial z}\frac{\partial}{\partial z}, \tag{12}$$

and expand the right-hand side of Eq. (5) in the binomial series,

$$\begin{aligned}Q&=\sqrt{1+\varepsilon+\mu+\gamma}\\&=1+\sum_{j=1}^{\infty}\binom{\frac{1}{2}}{j}(\varepsilon+\mu+\gamma)^j\\&=1+\tfrac{1}{2}(\varepsilon+\mu+\gamma)-\tfrac{1}{8}(\varepsilon+\mu+\gamma)^2+\tfrac{1}{16}(\varepsilon+\mu+\gamma)^3\\&\quad+\cdots.\end{aligned} \tag{13}$$

If the norm of $N^2-1+k_0^{-2}\partial_{zz}-k_0^{-2}\rho^{-1}\rho_z\partial_z$ applied to the propagating field is sufficiently small, then the series equation (13) can be truncated after the second term to yield

$$Q_0=1+\tfrac{1}{2}(\varepsilon+\mu+\gamma). \tag{14}$$

This approximation leads to the standard, narrow-angle parabolic equation of underwater acoustics.[9,16,17] Substituting Eq. (14) into Eq. (4) yields the propagator

$$\exp\{\tfrac{1}{2}i\delta(\varepsilon+\mu+\gamma)\}\approx\underbrace{\exp\{\tfrac{1}{2}i\delta\gamma\}}_{\text{density}}\underbrace{\exp\{\tfrac{1}{2}i\delta\mu\}}_{\text{diffraction}}\underbrace{\exp\{\tfrac{1}{2}i\delta\varepsilon\}}_{\text{lens}}, \tag{15}$$

in which δ denotes $k_0\Delta r$. Because the individual operators defined in Eqs. (10)–(12) do not commute, replacing this exponential of the sum by the product of the exponentials is correct only to terms that are linear in Δr. For constant-density profiles $(\gamma=0)$, the right-hand side of Eq. (15) reduces to a form that can be implemented directly by the split-step algorithm. In general, however, $\gamma\neq0$, and the evaluation of the density propagator requires special treatment. Following the hybrid solution approach of our previ-

ous work,[16] we propose to evaluate the lens and diffraction propagators using the split-step method while we apply a finite-difference technique to the density operator. It should be noted that if both the density and refractive index profiles contain discontinuities, it is essential to observe the ordering of the density, diffraction and lens operators as given on the right-hand side of Eq. (15). Otherwise, the large derivatives of the field generated by the lens operator will not be smoothed through subsequent diffraction and absorption in the diffraction step prior to application of the density operator. In this case, the derivative terms in the density operator will convert the high-frequency lens components into low-order modes, causing large errors in the propagating field.

We now demonstrate that our procedure can be simply extended to accommodate higher-order variable-density split-step PEs. Such equations incorporate additional terms of the binomial series in Eq. (13). For example, the one-term, rational-linear approximation Q_1, originally introduced by Claerbout[18]

$$Q_1=\frac{1+\frac{3}{4}(\varepsilon+\mu+\gamma)}{1+\frac{1}{4}(\varepsilon+\mu+\gamma)}=Q_0-\tfrac{1}{8}(\varepsilon+\mu+\gamma)^2+\cdots, \tag{16}$$

agrees with the first three terms of the series expansion of Q including the six cross terms involving the three operators ε, μ, and γ. Even when $\gamma=0$, the remaining cross-terms preclude the direct use of the split-step algorithm. The [1,1]-Padé approximant derived from this so-called rational-linear approximation, and from its n-term Padé series extension Q_n, can however be implemented easily using finite-difference techniques.[5,6,19]

Alternatively, retaining all terms in Eq. (13) that do *not* involve cross products of ε, μ, and γ leads to [6,16]

$$Q_1'=-2+\sqrt{1+\varepsilon}+\sqrt{1+\mu}+\sqrt{1+\gamma}. \tag{17}$$

Substituting Eq. (17) into Eq. (4) and neglecting terms of $O(\Delta r^2)$ yields

$$\begin{aligned}\exp\{i\delta(Q_1'-1)\}&=\exp\{i\delta(-3+\sqrt{1+\varepsilon}+\sqrt{1+\mu}+\sqrt{1+\gamma})\}\\&\approx\underbrace{\exp\{-i\delta+i\delta\sqrt{1+\gamma}\}}_{\text{density}}\underbrace{\exp\{-i\delta+i\delta\sqrt{1+\mu}\}}_{\text{diffraction}}\\&\quad\times\underbrace{\exp\{-i\delta+i\delta\sqrt{1+\varepsilon}\}}_{\text{lens}}.\end{aligned} \tag{18}$$

When $\gamma=0$, the above wide-angle, split-operator approximation to the propagator can again be implemented by the split-step Fourier algorithm.[6,20,21] For variable-density media, however, we can still use a hybrid solution procedure, where, in addition to the split-step operations, the separate density propagator is evaluated with finite-difference techniques, in much the same way as we have treated an analogous operator arising in electric field propagation.[22] Clearly, when the conditions underlying Eq. (14) are satisfied, the narrow-angle propagator in Eq. (15) can be obtained from the wide-angle propagator in Eq. (18) by expanding the exponentials. As before, to maintain numerical stability, the operator ordering given on the right-hand side of Eq. (18) should be preserved.

Following the approach used in Ref. 16, the split-operator approximation to Eq. (17) may be improved by successively introducing higher-order cross-terms containing Q, namely

$$Q_n'=Q_1'+\sum_{j=2}^{n}\binom{\frac{1}{2}}{j}[(\varepsilon+\mu+\gamma)^j-\varepsilon^j-\mu^j-\gamma^j]=Q_1'-\underbrace{\tfrac{1}{8}[(\varepsilon+\mu+\gamma)^2-\varepsilon^2-\mu^2-\gamma^2]+\tfrac{1}{16}[(\varepsilon+\mu+\gamma)^3-\varepsilon^3-\mu^3-\gamma^3]+\cdots}_{n-1\ \text{terms}}. \tag{19}$$

In practice, only the lowest-order contributions can be evaluated simply by finite-difference techniques. Higher-order corrections involving products of third and higher-order derivatives with spatially varying functions are more easily analyzed in the context of the Lanczos formalism.[16,23]

A specific hybrid form for the wide-angle, split-step PE derived from the variable-density operator Q_2' can be obtained by substituting Eq. (17) and Eq. (19) with $n=2$ into Eq. (4). The resulting propagator can be written

$$\begin{aligned}\exp\{i\delta(Q_2'-1)\}&=\exp\{i\delta(Q_1'-1)-\tfrac{1}{8}i\delta[\varepsilon(\mu+\gamma)+(\mu+\gamma)\varepsilon+\mu\gamma+\gamma\mu]\}\\&\approx\exp\{i\delta(Q_1'-1)\}\underbrace{\exp\{-\tfrac{1}{8}i\delta[\varepsilon(\mu+\gamma)+(\mu+\gamma)\varepsilon+\mu\gamma+\gamma\mu]\}}_{\text{cross-terms}}.\end{aligned} \tag{20}$$

The propagator containing Q_1' may then be generated using the hybrid split-step/finite-difference procedure suggested by Eq. (18). The remaining propagator in Eq. (20), which depends on the lowest-order cross-terms, can also be implemented by finite-difference methods. For $\gamma\neq0$, this hybrid procedure involving $\exp\{i\delta(Q_2'-1)\}$ thus requires two Padé approximant propagators in addition to the operations required by the split-step algorithm.

II. NUMERICAL IMPLEMENTATION

We now consider the computational aspects associated with the variable-density propagators introduced in the previous section. Beginning with Eq. (18), we recall that the first two propagators generated by the operator Q_1' can be evaluated with the split-step algorithm. In particular, the lens component, which depends on ε, may be applied through an element-by-element vector multiplication in z-space while the diffraction component, which depends on μ, is implemented similarly in k_z-space, the Fourier transform domain of z. In practice, these Fourier transforms (and their inverses) are carried out using the fast Fourier transform (FFT) algorithm, yielding[6,16,20,21,24]

$$\psi(r+\Delta r',z)\approx\exp\{i\,\delta(N-2)\}\cdot \mathrm{FFT}^{-1}[\exp\{i\,\delta\sqrt{1-k_z^2/k_0^2}\}\cdot \mathrm{FFT}[\psi(r,z)]]. \tag{21}$$

Here $r+\Delta r'$ is used to denote a density-independent state intermediate to r and $r+\Delta r$. When $\gamma\neq 0$, the third propagator, which depends on density through γ, can be handled by Padé approximant methods. Specifically, this component can be approximated by the unitary, z-space representation

$$\exp\{-i\,\delta+i\,\delta\sqrt{1+\gamma}\}\approx\frac{1+\frac{1}{4}(1+i\,\delta)\,\gamma}{1+\frac{1}{4}(1-i\,\delta)\,\gamma} \tag{22}$$

which generates the finite-difference system of equations

$$\{1+\tfrac{1}{4}(1-i\,\delta)\,\gamma\}\psi(r+\Delta r,z)=\{1+\tfrac{1}{4}(1+i\,\delta)\,\gamma\}\psi(r+\Delta r',z). \tag{23}$$

A suitable approximation for $\gamma\psi$ can be obtained from the heterogeneous finite-difference representation of the transverse derivative expression containing the variable ρ[6]

$$\mu'\psi(r,z)=\frac{\rho}{k_0^2}\frac{\partial}{\partial z}\left(\rho^{-1}\frac{\partial\psi(r,z)}{\partial z}\right)\approx\frac{\rho_-\psi(r,z-\Delta z)-\rho_0\psi(r,z)+\rho_+\psi(r,z+\Delta z)}{k_0^2\Delta z^2}, \tag{24}$$

where the variables

$$\rho_\pm=\frac{2\rho(r,z)}{\rho(r,z)+\rho(r,z\pm\Delta z)} \tag{25}$$

and

$$\rho_0=\rho_-+\rho_+ \tag{26}$$

have been introduced. When ρ is constant, Eq. (24) reduces to the standard second-order difference form for the operator μ. Since $\mu'\equiv\mu+\gamma$, a finite-difference approximation for $\gamma\psi$ can be obtained by forming

$$\gamma\psi(r,z)\equiv(\mu'-\mu)\psi(r,z)\approx[(\rho_--1)\psi(r,z-\Delta z)-(\rho_0-2)\psi(r,z)+(\rho_+-1)\psi(r,z+\Delta z)]/(k_0^2\Delta z^2). \tag{27}$$

TABLE I. Geoacoustic profile for the Bucker case.

Depth (m)	Sound speed (m s^{-1})	Density (g cm^{-3})	Attenuation dB λ^{-1}
0	1500	1.0	0.0
120	1498	1.0	0.0
240	1500	1.0	0.0
240	1505	2.1	0.0
1024	1505	2.1	0.0
2048	1505	2.1	0.5

The fourth exponential operator associated with Q_2' in Eq. (20) can be represented by the Padé approximant

$$\exp\{-\tfrac{1}{8}i\,\delta(\varepsilon\mu'+\mu'\varepsilon+\mu\gamma+\gamma\mu)\}\approx\frac{1-\frac{1}{16}i\,\delta(\varepsilon\mu'+\mu'\varepsilon+\mu\gamma+\gamma\mu)}{1+\frac{1}{16}i\,\delta(\varepsilon\mu'+\mu'\varepsilon+\mu\gamma+\gamma\mu)}. \tag{28}$$

If $\gamma=0$, the representation in Eq. (28) reduces to the same hybrid form that was introduced in Ref. 16, and thus leads to a tridiagonal system of equations. When $\gamma\neq 0$, however, the finite-difference evaluation of $\mu\gamma\psi$ and $\gamma\mu\psi$ involves the operator $\partial^3/\partial z^3$ which leads to a higher-order system. To circumvent this complication, we choose to neglect third-order contributions to the propagating field. From Eq. (24), we further observe that the terms involving $\varepsilon\mu'\psi$ and $\mu'\varepsilon\psi$ can be approximated by the finite-difference expressions

$$\varepsilon\mu'\psi(r,z)\approx\varepsilon(r,z)\frac{\rho_-\psi(r,z-\Delta z)-\rho_0\psi(r,z)+\rho_+\psi(r,z+\Delta z)}{k_0^2\Delta z^2} \tag{29}$$

and

$$\mu'\varepsilon\psi(r,z)\approx[\rho_-\varepsilon(r,z-\Delta z)\psi(r,z-\Delta z)-\rho_0\varepsilon(r,z)\psi(r,z)+\rho_+\varepsilon(r,z+\Delta z)\psi(r,z+\Delta z)]/(k_0^2\Delta z^2). \tag{30}$$

Substituting the above formulas into the Padé approximant of the operator for Eq. (28) and applying the Crank–Nicolson procedure leads to a tridiagonal system of equations.[6,25]

III. NUMERICAL RESULTS

In this section, we demonstrate our numerical implementation of the split-operator, variable-density procedure for two shallow-water propagation examples. In the first of these, attributed to Bucker and given in Table I, the geoacoustic profile contains jump discontinuities in both sound speed and density along the ocean bottom at $z=240$ m. This Bucker profile has previously been employed by a number of authors to establish the ability of their PE solvers to accommodate density variations.[1,2,11] Although the small ε-contrast results in only a small number of normal modes with real propagation wave numbers, the large γ-contrast yields a significant number of virtual modes close to the real

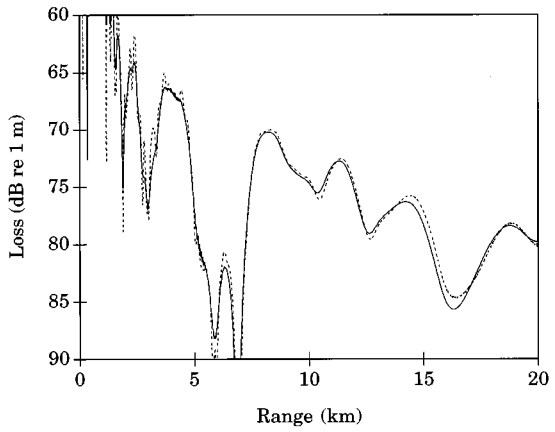

FIG. 1. Transmission loss versus range for the Bucker profile and a receiver depth of 90 m. Dashed line: SAFARI. Solid line: Split-step PE using $\widetilde{Q}$ with $k_0L=2$.

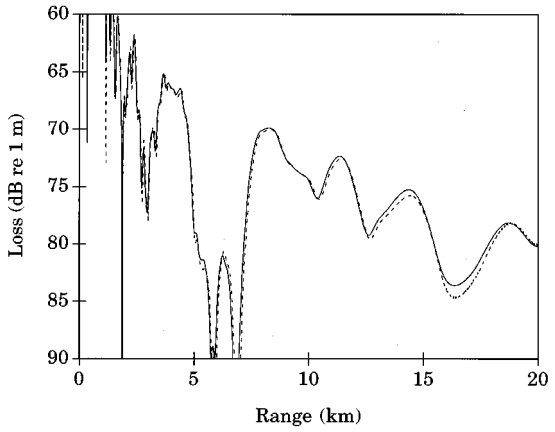

FIG. 3. Transmission loss versus range for the Bucker profile and a receiver depth of 90 m. Dashed line: SAFARI. Solid line: Hybrid split-step/finite-difference PE using a one-term Padé approximation to the density component of Q_1'.

wave number axis (see Ref. 12, pp. 249–251). To suppress reflections from the edge of the PE computational window, a linearly increasing attenuation is introduced between depths of $z=1024$ m and $z=2048$ m. A 100-Hz acoustic source is located at $z=30$ m. Reference solutions for this problem, computed for receivers at $z=90$ m and $z=240$ m, were obtained using the spectral integration model SAFARI.[26]

Before presenting our hybrid split-step/finite-difference results, we exhibit in Figs. 1 and 2, for the shallow and deep receiver respectively, traditional split-step PE calculations for the Bucker profile obtained by smoothing the density jump appearing in the operator $\widetilde{Q}$ according to Eq. (9).[9,11] In our calculations, we employed a range step size of $\Delta r=10$ m, a depth step size of $\Delta z=2$ m, and a value of $c_0=1500$ m s^{-1}. Further, as mentioned in Ref. 12 (p. 385), it is necessary to multiply $\widetilde{\psi}$ by $\sqrt{\rho}$ before computing transmission loss. For the recommended value of the smoothing parameter $k_0L=2$, the split-step PE produces reasonable results, although the transmission losses at ranges $r<5$ km lack the detailed structure evident in the reference solution. The quality of the PE results in Fig. 2 for the deep receiver is gratifying, considering that this depth is within the transition region of the smoothed density profile. It is worthwhile pointing out that PE codes based solely on finite-difference solvers can readily handle this problem. In fact, for the same values of Δr, Δz and c_0, the transmission loss curve obtained using the Claerbout approximation in Eq. (16) (not shown here) agrees with the SAFARI curve shown to within a linewidth at all ranges.

Next, we apply the hybrid procedures of the previous section to this test case. The PE calculations shown in Figs. 3 and 4 were obtained by combining a split-step evaluation of the γ-independent terms of Eq. (18) with a finite-difference solution for the γ-dependent term according to Eq. (27). It is seen that for both receiver depths, our hybrid approach both reproduces the detailed structure of the SAFARI result at ranges $r<5$ km and maintains satisfactory accuracy at longer ranges. The long-range behavior is not improved by incorporating the next higher-order operator Q_2', which suggests that the errors implicit in the operator splitting associated with Eq. (20) generates the major source of approximation error in our calculations. On the other hand, including the Q_2' higher-order terms greatly reduces

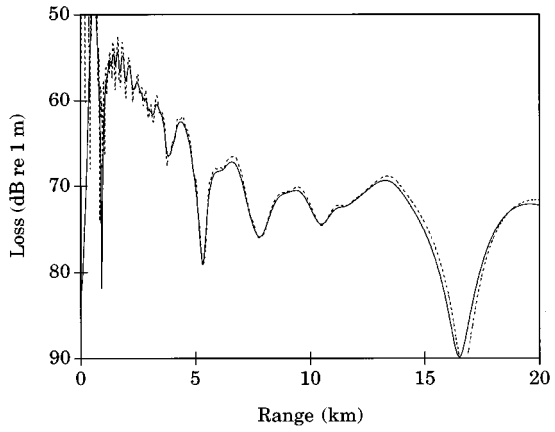

FIG. 2. Transmission loss versus range for the Bucker profile and a receiver depth of 240 m. Dashed line: SAFARI. Solid line: Split-step PE using $\widetilde{Q}$ with $k_0L=2$.

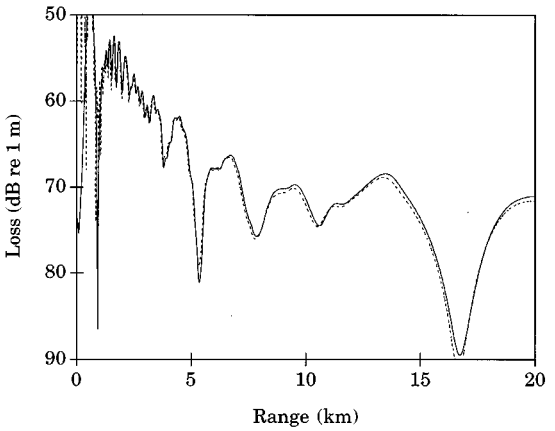

FIG. 4. Transmission loss versus range for the Bucker profile and a receiver depth of 240 m. Dashed line: SAFARI. Solid line: Hybrid split-step/finite-difference PE using a one-term Padé approximation to the density component of Q_1'.

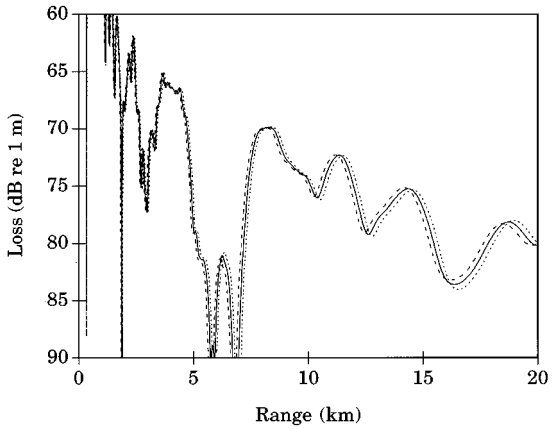

FIG. 5. Hybrid split-step/finite-difference PE predictions for the Bucker profile at a receiver depth of 90 m using a one-term Padé approximation to the density-dependent component of Q_1'. Dotted line: $c_0=1480$ m s^{-1}. Solid line: $c_0=1500$ m s^{-1}. Dashed line: $c_0=1520$ m s^{-1}.

the sensitivity of the hybrid procedure to variations in reference sound speed c_0. This feature is illustrated in Figs. 5 and 6, which show the variations in transmission losses at the shallow receiver depth for three values of c_0 for the hybrid procedure based on the operators Q_1' and Q_2', respectively. The dependence of the Q_1' solutions on c_0 shown in Fig. 5 is removed when the higher-order terms of Q_2' are included (all three transmission loss curves in Fig. 6 overlay one another). Note that such a behavior mirrors a similar decrease in sensitivity to c_0 in a previous model of a leaky surface duct[16] and would therefore be expected to extend to the smoothed density technique of Eq. (9) as well.

The geoacoustic profile for the second example, given in Table II, corresponds to the deep-end section of the lossy wedge test case introduced as one of the ASA range-dependent benchmark problems.[27] Jump discontinuities in sound speed, density and absorption occur along the sloping wedge interface, i.e., the line z (m)$=200-50r$ (km). The coordinates of the apex of the wedge are $z=0$ m and $r=4$ km. Additionally, an absorbing layer with linearly increasing attenuation is inserted between the depths $z=512$ m and

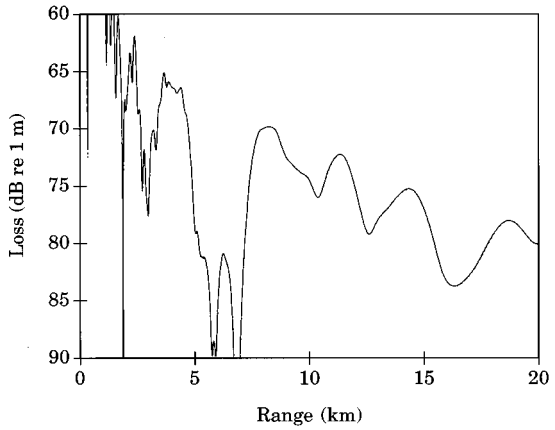

FIG. 6. Hybrid split-step/finite-difference PE predictions for the Bucker profile at a receiver depth of 90 m using one-term Padé approximations to the density-dependent components of Q_2'. Dotted line: $c_0=1480$ m s^{-1}. Solid line: $c_0=1500$ m s^{-1}. Dashed line: $c_0=1520$ m s^{-1}.

TABLE II. Deep-end geoacoustic profile for ASA wedge case.

Depth (m)	Sound speed (m s^{-1})	Density (g cm^{-3})	Attenuation dB λ^{-1}
0	1500	1.0	0.0
200	1500	1.0	0.0
200	1700	1.5	0.5
512	1700	1.5	0.5
1024	1700	1.5	5.0

$z=1024$ m.[6,28] A 25-Hz acoustic source, positioned at $z=100$ m, in the proximity of a node of the second lowest-order mode, excites both of the other propagating modes while the receivers are located at $z=30$ m and $z=150$ m.

The widespread practice of approximating a range-dependent waveguide by a sequence of range-independent sections and then marching the outgoing field according to a simple range-updating procedure is known to violate conservation of energy at the vertical interfaces between sections.[29] Although energy-conserving,[30] two-way,[31] and sloping[32,33] PEs have been introduced to ameliorate this problem, we will here apply standard one-way PE techniques with a range step size of $\Delta r=5$ m, a depth step size of $\Delta z=1$ m, and a value of $c_0=1500$ m s^{-1}. Reference solutions are calculated with a finite-difference PE based on a two-term Padé approximation for the operator Q_2.

The transmission losses for the split-step operator $\tilde{Q}$ and hybrid split-step/finite-difference operator Q_1' are shown in Figs. 7 to 10. For both receiver depths, the results obtained using the hybrid operator Q_1' [observing the order of the propagators in Eq. (18)] agree better with the reference curves generated using Q_2 than the results obtained with the traditional split-step approach based on $\tilde{Q}$. The smaller range shifts observed in the multipath interference structure in Figs. 8 and 10 further suggest that the hybrid PE formulation leads to a wider-angle capability than the traditional split-step PE.

Unfortunately, introducing successive higher-order terms in the operator Q_2' yields appreciable errors in comparison to the results shown in Figs. 8 and 10. Evidently, the

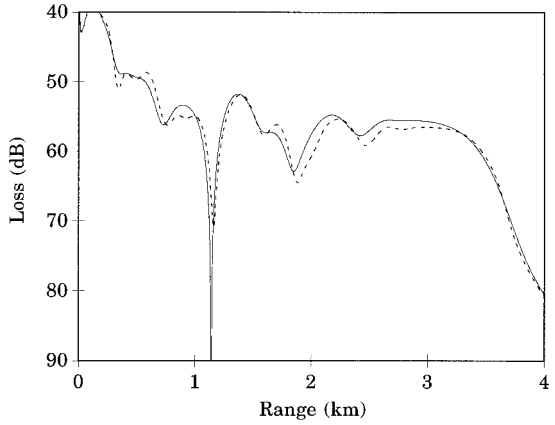

FIG. 7. Transmission loss versus range for the ASA wedge and a receiver depth of 30 m. Dashed line: Finite-difference PE using the two-term Padé approximation Q_2. Solid line: Split-step PE using $\tilde{Q}$ with $k_0L=2$.

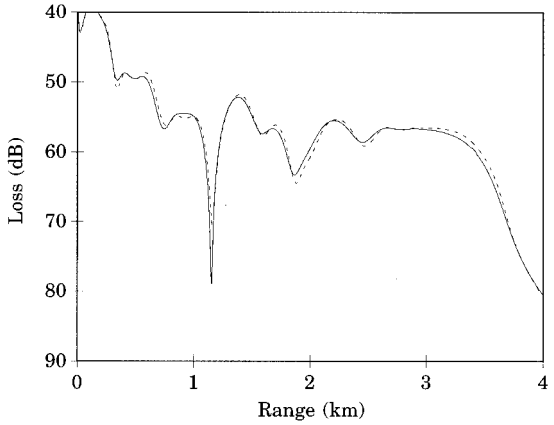

FIG. 8. Transmission loss versus range for the ASA wedge and a receiver depth of 30 m. Dashed line: Finite-difference PE using the two-term Padé approximation Q_2. Solid line: Hybrid split-step/finite-difference PE using a one-term Padé approximation to the density component of Q_1'.

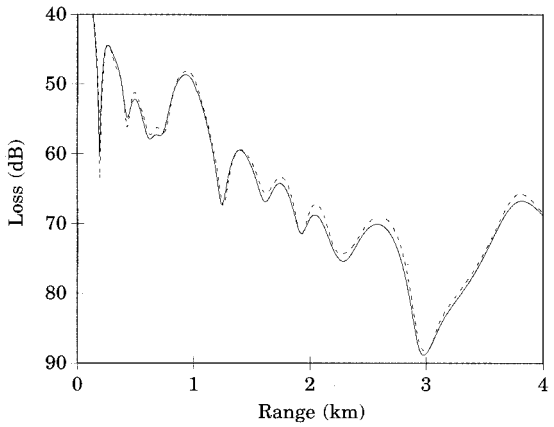

FIG. 10. Transmission loss versus range for the ASA wedge and a receiver depth of 150 m. Dashed line: Finite-difference PE using the two-term Padé approximation Q_2. Solid line: Hybrid split-step/finite-difference PE using a one-term Padé approximation to the density component of Q_1'.

correction terms of Eqs. (28)–(30) introduce significant high-frequency components into the acoustic field at the vicinity of the large sound speed discontinuity along the sea-bottom interface which cannot be adequately propagated by our operator approximation. Future research may, however, lead to a procedure for circumventing this difficulty. Similar effects are expected to appear as well in a related split-step approximation, recently introduced for acoustic thermometry applications.[34] As this formulation requires a non-linear transformation of the sound speed profile applicable to media in which the sound speed varies smoothly with depth, numerical difficulties are expected in shallow-water scenarios where realistic geoacoustic discontinuities must be incorporated. On the other hand, for sufficiently smooth profiles such as those of Ref. 34, both the transformation method and the procedure based on hybrid operator Q_2' should dramatically reduce the degree of sensitivity to the value of c_0 as demonstrated in Refs. 16 and 23 for both the leaky surface-duct and Bucker profiles.

Finally, regarding the computational efficiency of the hybrid split-step/finite-difference approach, the operator Q_1' requires solving a system of tridiagonal equations in addition to the multiplications and additions inherent in Eq. (21). As a result, the runtime for our scalar code is about 20% greater than that associated with the standard split-step PE for the examples presented above.

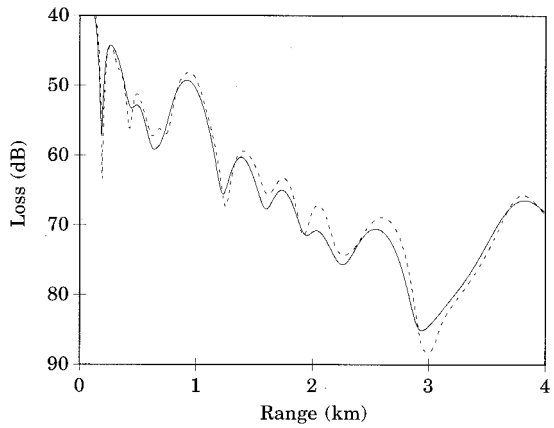

FIG. 9. Transmission loss versus range for the ASA wedge and a receiver depth of 150 m. Dashed line: Finite-difference PE using the two-term Padé approximation Q_2. Solid line: Split-step PE using $\tilde{Q}$ with $k_0 L = 2$.

IV. CONCLUSIONS

In this paper, we have advanced a hybrid split-step technique for modeling acoustic propagation in the presence of nonuniform density profiles. Our method separates the propagation operator into a product of the standard density-independent terms and a new density-dependent contribution which can be evaluated separately by finite-differencing. For the examples shown, the accuracy of the resulting method exceeds that of the standard procedure for including density variations into the split-step propagation technique. Moreover, because our algorithm does not rely on an empirically determined smoothing function, geoacoustic media that contain density jumps are incorporated in a natural way. Unfortunately, as a result of the additional operator splitting, some precision is necessarily sacrificed with respect to the standard full finite-difference technique. In wide-angle problems involving nearly constant sound-speed and density profiles, however, the increased accuracy afforded by the split-step approach should more than offset the error inherent in the operator splitting. Further, in such profiles, hybrid split-step/finite difference and split-step/Lanczos procedures can be employed to reduce significantly the reference sound-speed dependence of the results. We thus believe that the hybrid method introduced here provides a practical alternative to treating density variations in existing split-step codes, particularly for shallow-water applications.

ACKNOWLEDGMENTS

Financial support for one of us (DY) was provided through the scientific research Contract No. W7708–4–1214/01–XSA with the Defence Research Establishment Pacific (now Esquimalt Defence Research Detachment, a Division of the Defence Research Establishment Atlantic). The same author would like to acknowledge the National Re-

search Council of Canada, the Ontario Center for Materials Research, BNR and Corning Glass for continued funding.

[1] S. T. McDaniel and D. Lee, ''A finite-difference treatment of interface conditions for the parabolic wave equation,'' J. Acoust. Soc. Am. **71**, 855–858 (1982).
[2] D. Lee and S. T. McDaniel, ''Ocean acoustic propagation by finite-difference methods,'' Comput. Math. Appl. **14**, 305–423 (1987).
[3] A. R. Mitchell, *Computational Methods in Partial Differential Equations* (Wiley, New York, 1969), Chap. 2, pp. 22–32.
[4] K. R. Kelly, R. W. Ward, S. Treitel, and R. M. Alford, ''Synthetic seismograms: a finite-difference approach,'' Geophysics **41**, 2–27 (1976).
[5] M. D. Collins, ''Higher-order and elastic parabolic equations for wave propagation in the ocean,'' in *Computational Acoustics—Vol. 3*, edited by D. Lee, A. Cakmak, and R. Vichnevetsky (North-Holland, New York, 1990), pp. 167–184.
[6] D. J. Thomson, ''Wide-angle parabolic equation solutions to two range-dependent benchmark problems,'' J. Acoust. Soc. Am. **87**, 1514–1520 (1990).
[7] P. G. Bergman, ''The wave equation in a medium with a variable index of refraction,'' J. Acoust. Soc. Am. **17**, 329–333 (1946).
[8] L. M. Brekhovskikh, *Waves in Layered Media* (Academic, New York, 1980), 2nd ed., Chap. III, pp. 161–162.
[9] F. D. Tappert, ''The parabolic approximation method,'' in *Wave Propagation and Underwater Acoustics*, edited by J. B. Keller and J. S. Papadakis (Springer-Verlag, New York, 1977), Chap. 5, pp. 224–287.
[10] F. D. Tappert and L. Nghiem-Phu, ''Modeling of pulse response functions of bottom-interacting sound using the parabolic equation method,'' in *Ocean Seismo-Acoustics*, edited by T. Akal and J. M. Berkson (Plenum, New York, 1986), pp. 129–137.
[11] B. H. Maranda and D. J. Thomson, ''A digital filter approach for treating density variations in the split-step algorithm of underwater acoustics,'' in *IEEE Pacific Rim Conference on Communications, Computers and Signal Processing, 4–5 June 1987, Victoria, BC, Conference Proceedings* (IEEE, New York, 1987), pp. 342–345.
[12] F. B. Jensen, W. A. Kuperman, M. B. Porter, and H. Schmidt, *Computational Ocean Acoustics* (AIP Press, New York, 1994), pp. 384–385.
[13] F. B. Jensen and M. G. Martinelli, ''The SACLANTCEN parabolic equation model (PAREQ),'' SACLANT Undersea Research Centre, La Spezia, Italy (1985).
[14] E. S. Holmes and L. A. Gainey, ''The Navy Standard Parabolic Equation Model, Broadband PE, and PE Workshop II,'' in *PE Workshop II: Proceedings of the Second Parabolic Equation Workshop*, edited by S. A. Chin-Bing, D. B. King, J. A. Davis, and R. B. Evans (Naval Research Laboratory, US Government Printing Office, 1993), pp. 175–213.
[15] K. B. Smith and F. D. Tappert, ''UMPE: The University of Miami Parabolic Equation Model, Version 1.0,'' Marine Physical Laboratory Tech. Memo. **432**, May 1993.
[16] D. Yevick and D. J. Thomson, ''Split-step/finite-difference and split-step/Lanczos algorithms for solving alternative higher-order parabolic equations,'' J. Acoust. Soc. Am. **96**, 396–405 (1994).
[17] J. A. Davis, D. White, and R. C. Cavanagh, ''NORDA Parabolic Equation Workshop, 31 March–3 April 1981,'' Tech. Note 143, Naval Ocean Research and Development Activity, NSTL Station, MS, 1982.
[18] J. F. Claerbout, ''Coarse grid calculations of waves in inhomogeneous media with application to delineation of complicated seismic structure,'' Geophysics **35**, 407–418 (1970).
[19] M. D. Collins, ''Benchmark calculations for higher-order parabolic equations,'' J. Acoust. Soc. Am. **87**, 1535–1538 (1990).
[20] M. D. Feit and J. A. Fleck, ''Light propagation in graded-index optical fibers,'' Appl. Opt. **17**, 3990–3998 (1978).
[21] D. J. Thomson and N. R. Chapman, ''A wide-angle split-step algorithm for the parabolic equation,'' J. Acoust. Soc. Am. **74**, 1848–1854 (1983).
[22] D. Yevick, J. Yu, W. Bardyszewski, and M. Glasner, ''Stability issues in vector electric field propagation,'' Photon. Technol. Lett. **7**, 656–658 (1995).
[23] D. Yevick and B. Hermansson, ''Convergence properties of wide-angle techniques,'' Photon. Technol. Lett. **6**, 1457–1460 (1994).
[24] F. D. Tappert and R. H. Hardin, ''Computer simulation of long-range ocean acoustic propagation using the parabolic equation method,'' in *Proceedings of the 8th International Congress on Acoustics* (Goldcrest, London, 1974), Vol. 2, p. 452.
[25] B. Hermansson, D. Yevick, W. Bardyszewski, and M. Glasner, ''The unitarity of split-operator finite difference and finite-element methods: Application to longitudinally varying semiconductor rib waveguides,'' IEEE J. Light. Technol. **7**, 1866–1874 (1990).
[26] H. Schmidt, ''SAFARI Seismo-Acoustic Fast field Algorithm for Range-Independent environments,'' SACLANT Undersea Research Centre, San Bartolomeo, Italy, Rep. SR-113, 1988.
[27] F. B. Jensen and C. M. Ferla, ''Numerical solutions of range-dependent benchmark problems in ocean acoustics,'' J. Acoust. Soc. Am. **87**, 1499–1510 (1990).
[28] D. Yevick, J. Yu, and Y. Yayon, ''Optimal absorbing boundary conditions,'' J. Opt. Soc. Am. A **12**, 107–110 (1995).
[29] M. B. Porter, F. B. Jensen, and C. M. Ferla, ''The problem of energy-conservation in one-way models,'' J. Acoust. Soc. Am. **89**, 1058–1067 (1991).
[30] M. D. Collins and E. K. Westwood, ''A higher-order energy-conserving parabolic equation for range-dependent ocean depth, sound speed, and density,'' J. Acoust. Soc. Am. **89**, 1068–1075 (1991).
[31] M. D. Collins and R. B. Evans, ''A two-way parabolic equation for acoustic backscattering in the ocean,'' J. Acoust. Soc. Am. **91**, 1357–1368 (1992).
[32] D. Lee and W. L. Siegmann, ''Finite difference treatment of irregular interfaces: An error analysis,'' J. Comp. Acoust. **3**, 1–14 (1995).
[33] G. H. Brooke, D. J. Thomson, and P. M. Wort, ''A sloping-boundary condition for efficient PE calculations in range-dependent acoustic media,'' J. Comp. Acoust. **4**, 11–27 (1996).
[34] F. D. Tappert, J. L. Spiesberger, and L. Boden, ''New full-wave approximation for ocean acoustic travel time predictions,'' J. Acoust. Soc. Am. **97**, 2771–2782 (1995).

Narrow-band source localization in the presence of internal waves for 1000-km range and 25-Hz acoustic frequency

Paul J. Book[a] and L. W. Nolte[b]
Department of Electrical Engineering, Box 90291, Duke University, Durham, North Carolina 27708-0291

(Received 24 January 1996; accepted for publication 30 October 1996)

The effects of internal waves on low-frequency (25 Hz) narrow-band source localization performance are investigated at a very long range (1000 km). Sound-speed perturbations induced by internal waves obeying the Garrett–Munk spectral model are incorporated into the normal mode solution to the wave equation using the adiabatic approximation. Sensitivity of source localization on the internal wave modal content is examined. For the entire range of signal-to-noise ratios (SNR) and degrees of internal-wave field structure, the optimal uncertain field processor (OUFP) provides both the signal processing algorithm as well as the limitations on source localization performance. For high SNR, the localization errors are local and the performance level of the OUFP is predicted by the hybrid Cramer–Rao lower bound (CRLB). In fairly structured internal-wave environments, significant performance gains are made optimally localizing the source. Under very random internal-wave environments, the environmental variability limits the performance of all signal processing algorithms. © *1997 Acoustical Society of America.* [S0001-4966(97)03803-4]

PACS numbers: 43.30.Wi, 43.60.Gk [MBP]

INTRODUCTION

This paper quantifies the performance and limitations of low-frequency (25-Hz) narrow-band source localization in the presence of internal-wave variability at a very long range (1000 km) in the deep ocean. On time scales under 12 h, much of the variability in the ocean is caused by internal waves. Colosi *et al.* explored the significant effects of internal waves on long-range pulse propagation.[1] Environmental mismatch is known to have a significant effect on the performance of source localization using matched field processing. Jackson and Ewart have investigated the degrading effects of internal waves on Bartlett ambiguity surfaces for a high-frequency narrow-band source at short ranges.[2]

By incorporating environmental uncertainty into the matched field processing technique *a priori*, current processors are made more robust and perform better in mismatched environments.[3–5] In this paper, internal-wave characteristics are optimally incorporated *a priori* into a Bayesian source localization processor, known as the optimum uncertain field processor (OUFP). The limits of localization performance as well as the optimum signal processing algorithm to achieve those limits are computed for the entire range of signal-to-noise ratios (SNR). At low SNR the source localization errors are scattered globally and the performance limits are computed using the OUFP. At high SNR most localization errors are local; i.e., there is primarily a shifting of the correct peak in the matched field ambiguity surface. For high SNR the Cramer–Rao lower bound (CRLB) can be used to predict the theoretical limits on the source localization error.

Sound-speed perturbations induced by internal waves obeying the Garrett–Munk spectrum[1,6,7] are incorporated into the normal mode solution of the wave equation using the adiabatic approximation. Colosi has found that internal waves cause significant modal coupling for a 75-Hz source at multi-megameter ranges.[6] The source frequency chosen in this work is 25 Hz and the modal coupling was found not to be as significant as with the 75 Hz source. The modal content of the pressure field is still accurately preserved with the adiabatic assumption. The adiabatic approximation is also chosen because it provides a fast method of computing pressure waves containing small sound-speed perturbations and, more importantly, allows for analytical computations of source localization limits. Consequently, these results are taken with the assumption that the adiabatic approximation is valid.

A general description of the localization problem and the specific models and processors that are implemented are discussed in Sec. I. Once the models and processors are implemented, numerical simulations are performed in Sec. II. Finally, Sec. III concludes with a discussion of the results.

I. PROBLEM DESCRIPTION

Very-long-range source localization is performed in a deep ocean containing an uncertain internal wave (Fig. 1). The ocean model is described in Sec. II A and the sound-speed perturbations caused by internal waves obeying the Garrett–Munk spectrum are discussed in Sec. I A. The acoustic source generates a continuous sinusoidal wave with a known frequency and has a complex amplitude distribution described *a priori*. The acoustic wave propagation of this source is simulated by the normal mode solution to the wave equation using KRAKEN and the adiabatic approximation.[8,9] The details of incorporating internal-wave-induced sound-speed perturbations into the normal mode solution to the wave equation using the adiabatic approximation are in Sec. I B. A fully spanning vertical receiver array is used to sample the acoustic pressure field. The optimum uncertain field processor (OUFP) computes the localization limits of this

[a]Electronic mail: pbook@ee.duke.edu
[b]Electronic mail address: lwn@ee.duke.edu

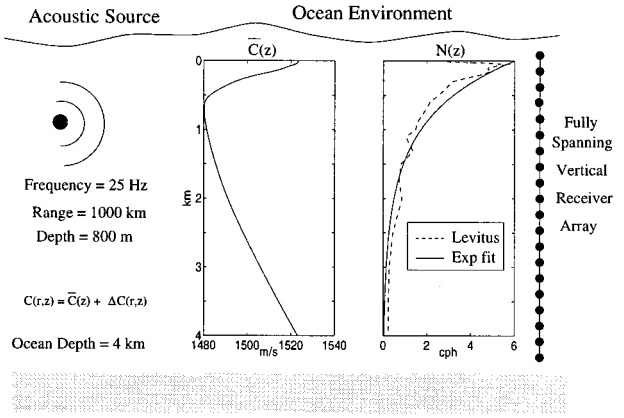

FIG. 1. Deep ocean source localization problem with average sound velocity profile, $C(z)$, and buoyancy frequency, $N(z)$.

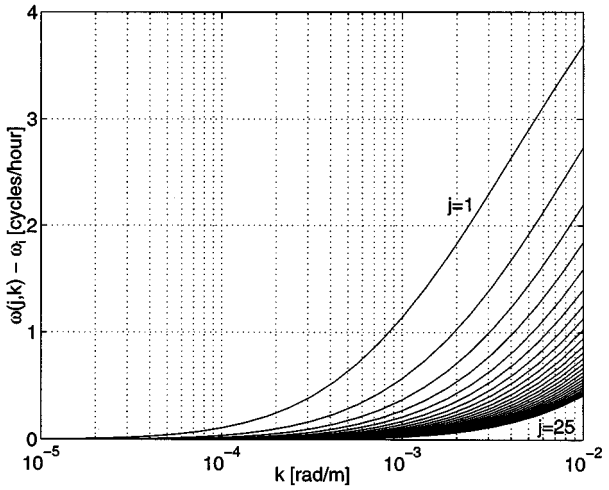

FIG. 2. Dispersion curves for the internal wave modes.

acoustic source in this ocean containing an uncertain internal wave. The localization performances of the Bartlett processor, the minimum variance (MV) beamformer, and the minimum variance beamformer with environmental perturbations constraints (MV-EPC) are compared with the OUFP. The matched-field processor is also implemented and provides the upper bound on source localization when the ocean environment is known. Section I C contains details of the processors. These processors are compared using the probability of correct localization. Under high SNR conditions, the localization errors for all processors are local and the square root of the mean squared (rms) error on the estimates is also used to compare the processors. When the localization errors are local, the theoretical limit on source localization error can be calculated analytically using the Cramer–Rao lower bound (CRLB), which is discussed in Sec. I D.

A. Ocean model

The ocean is range-dependent with a constant depth of 4 km. The range-dependent sound-speed profile model consists of a known range-independent average plus a range-dependent perturbation due to an internal wave $[C(r,z)=C(z)+\Delta(r,z)]$. The average sound-speed profile, $C(z)$, is computed by converting temperature and salinity profiles from Kauai (159.46°W, 22.44°N) to Point Sur (122.00°W, 36.25°N) using Del Grosso's sound speed equation (Fig. 1). The temperature and salinity profiles are provided by Levitus and NOAA.[10] The average buoyancy frequency, $N(z)=\sqrt{-(g/\rho)(\partial p/\partial z)}$, is also computed using the oceanographic toolbox from Woods Hole Oceanographic Institution. An exponential fit $[N(z)=N_0e^{-z/B}$, where $N_0=6$ cycles/h is the extrapolated surface frequency and $B=800$ m] is applied to the average buoyancy frequency.

1. Garrett–Munk internal-wave model

Perturbations in density stratification cause internal waves. Garrett and Munk have developed an internal-wave spectrum which appears to be a first-order description of deep water internal waves.[1,7] Reviewing this model briefly, the vertical displacements of the propagating modes of internal waves are described by

$$\frac{\partial^2 W(j,k,z)}{\partial z^2}+k^2\left(\frac{N^2(z)-\omega^2(j,k)}{\omega^2(j,k)-\omega_i^2}\right)W(j,k,z)=0, \qquad (1)$$

where j is the discrete mode number of the internal wave $(j=1,2,3,\ldots,j_n)$, k (rad/m) is the horizontal spatial frequency of the internal wave, and z (m) is depth. $W(j,k,z)$ (m) is the magnitude of the vertical displacement with boundary conditions of $W(j,k,0)=W(j,k,z_{\text{bottom}})=0$. Also, ω_i (cycles/h)$=2$ sin (latitude)/24 cycles/hour is the inertial (temporal) frequency and is included to account for the Coriolis force. When the latitude is 30°, $\omega_i=\frac{1}{24}$ cycles/h. $\omega(j,k)$ (cycles/h) is the (temporal) frequency of the internal-wave mode. The dispersion curves are shown in Fig. 2. These internal-wave eigenmodes are orthogonal and normalized by

$$\int_0^{z_{\text{bottom}}}(N^2(z)-\omega_i^2)W(j,k,z)W(j',k,z)dz=\delta(j-j'). \qquad (2)$$

After projecting the total internal-wave displacement onto a two-dimensional ocean slice, the normalized vertical displacement, $\zeta(r,z,t)$, is expressed as a superposition of modes with random complex amplitudes:

$$\zeta(r,z,t)=\zeta_0 N_\sigma\sum_{j=1}^{j_n}\sum_{k=k_1}^{k_n}\sum_{\theta=\theta_1}^{\theta_n}W(j,k,z)\sigma(j,k)\times\text{Re}\{\text{AIW}(j,k,\theta)e^{i[k\cos(\theta)r-\omega(j,k)t]}\}, \qquad (3)$$

where the complex amplitudes of the internal-wave modes, $\text{AIW}(j,k,\theta)$, are independent complex Gaussians with zero mean and unit variance [i.e., $\overline{AIW}(j,k,\theta)=0$ and $\langle\text{AIW}(j,k,\theta)^2\rangle=1$]. The angles between the internal-wave modes and the ocean slice, θ, have independent uniform distributions $(0\leqslant\theta<2\pi)$. The internal-wave field is to have a specific rms displacement, $\zeta_0=\zeta(z_{\text{ref}})$ rms$=7.3$ m, at a depth z_{ref} where $N(z_{\text{ref}})=3$ cycles/h. Using the average buoyancy frequency along the path from Kauai to Point Sur, $z_{\text{ref}}=550$ m and $N_0B=6$ cycles/h$\times$800 m. To properly normalize the vertical displacement

$$N_\sigma^{-2}=\sum_{j=1}^{j_n}\sum_{k=k_1}^{k_n}\sum_{\theta=\theta_1}^{\theta_n}W^2(j,k,z_{\text{ref}})\sigma^2(j,k)\,\frac{1}{2}, \qquad (4)$$

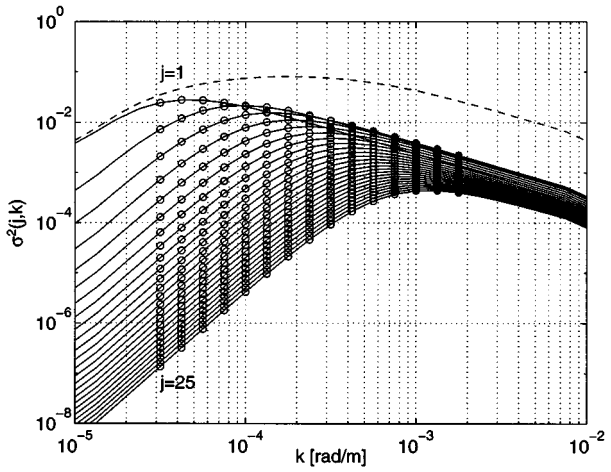

FIG. 3. $\sigma^2(j,k)$ for $j=1,2,...,25$, dashed curve is $\Sigma_{j=1}^{25}\sigma^2(j,k)$.

$$\sigma^2(j,k)=\int_{k-\Delta}^{k+\Delta}\frac{j_*}{j^2+j_*^2}\frac{\hat{k}^2k(j)}{(\hat{k}^2+k^2(j))^2}\,d\hat{k},$$
$$k(j)=\frac{\pi j\omega_i}{N_0B}, \tag{5}$$

and $j_*=3$. The Garrett–Munk spectrum is normalized by

$$\sum_{j=1}^{j_n}\sum_{k=k_1}^{k_n}\sum_{\theta=\theta_1}^{\theta_n}\sigma^2(j,k)=1 \tag{6}$$

rather than Eq. (4) to permit a fairly structured internal wave (i.e., $j_n=2$). The internal-wave energy is distributed according to the Garrett–Munk spectrum (Fig. 3). These internal-wave displacements are converted into a perturbation in sound speed by[7]

$$\Delta C(r,z,t)=\left(\frac{d\overline{C}(z)}{dz}\right)_{\text{potential}}\zeta(r,z,t)$$
$$=GN^2(z)\overline{C}(z)\zeta(r,z,t), \tag{7}$$

where $G=1.25$ s^2/m which is empirically determined (Fig. 4). Then,

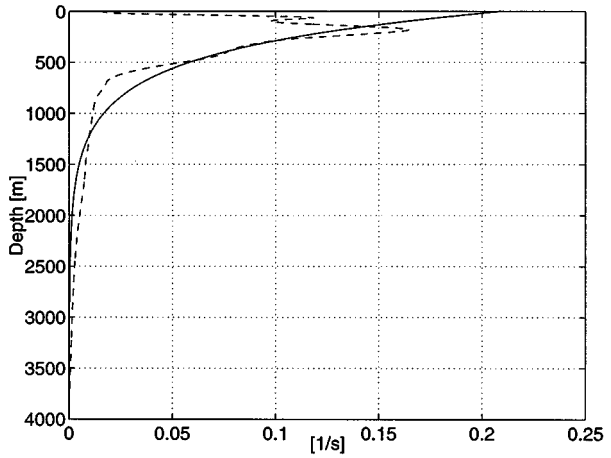

FIG. 4. Factor to convert vertical displacement, $\zeta(r,z,t)$, to a perturbation in sound speed, $\Delta C(r,z,t)$. Solid curve is $GN^2(z)C(z)$ and $(dC(z)/dz)_{\text{potential}}$ is dashed.

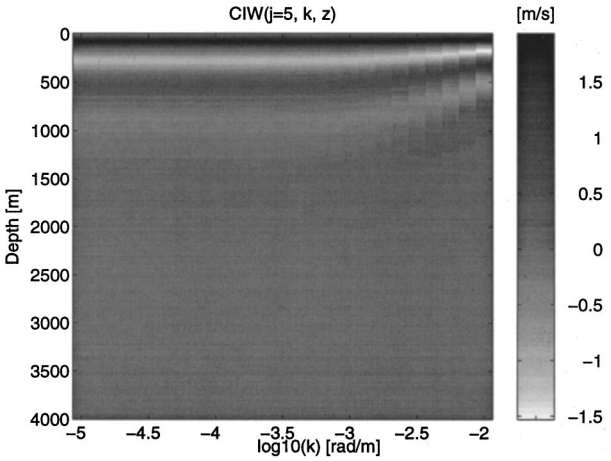

FIG. 5. CIW $(j=5,k,z)$ is approximately constant over k for $2\times10^{-5}\leqslant k\leqslant2\times10^{-3}$ rad/m.

$$\Delta C(r,z,t)=\sum_{j=1}^{j_n}\sum_{k=k}^{k_n}\sum_{\theta=\theta_1}^{\theta_n}\text{CIW}(j,k,z)\sigma(j,k)$$
$$\times\text{Re}\{\text{AIW}(j,k,\theta)e^{i[k\cos(\theta)r-\omega(j,k)t]}\}, \tag{8}$$

where

$$\text{CIW}(j,k,z)=GN^2(z)\overline{C}(z)\zeta_0N_\sigma W(j,k,z). \tag{9}$$

According to the Garrett–Munk spectrum, most of the internal-wave energy is contained over the spatial frequencies $2\times10^{-5}\leqslant k\leqslant2\times10^{-3}$ rad/m (Fig. 3). The corresponding temporal frequencies for these spatial frequencies are $\frac{1}{24}\leqslant\omega(j,k)-\omega_i\leqslant2$ cycles/h (Fig. 2); thus, the ocean is assumed to be frozen. Also, $\text{CIW}(j,k,z)$ is approximately constant over k for these spatial frequencies (Fig. 5); therefore, $\text{CIW}(j,k,z)\simeq\text{CIW}(j,z)$ and

$$\Delta C(r,z)=\sum_{j=1}^{j_n}\sum_{k=k_1}^{k_n}\sum_{\theta=\theta_1}^{\theta_n}\text{CIW}(j,z)\sigma(j,k)$$
$$\times\text{Re}\{\text{AIW}(j,k,\theta)e^{ik\cos(\theta)r}\}. \tag{10}$$

B. Propagation model—normal mode with adiabatic approximation

Acoustic pressures are calculated by solving the wave equation using the normal mode method. This method determines the eigenvalues and eigenfunctions that solve the wave equation and satisfy the boundary conditions. The boundary conditions for this deep ocean are a perfectly rigid bottom and a pressure-release surface. For an isotropic point source with a known frequency f (Hz), the result is a Sturm–Liouville problem for which the acoustic wave numbers, k_m, are all distinct and the acoustic modes, $\Phi_m(z)$, form a complete orthonormal set. KRAKEN, the normal mode program written by Michael B. Porter, is used to compute these acoustic wave numbers and modes.[8,9] Once the wave numbers and modes are computed, the acoustic pressure field generated by a source located at (r_s,z_s) is

$$p(z;r_s,z_s)=p_0\sum_{m=1}^{M}\Phi_m(z_s)\Phi_m(z)\frac{e^{ik_mr_s}}{\sqrt{k_mr_s}}, \tag{11}$$

where z is the depth of the receiver, p_0 is the pressure of the source at $r_s=1$ m, and M is the number of propagating acoustic modes. Normal modes are generally applied to range-independent problems; however, they can also be extended to range-dependent oceans. A range-dependent ocean can be approximated by dividing the range axis into a number of range-independent intervals. The solution can be constructed by using the range-independent normal mode solution and interface conditions (continuity of pressure and normal velocity). In a range-dependent ocean, a common assumption is that the modes couple adiabatically, that is, they do not transfer energy to other modes. After the adiabatic approximation is made, the pressure field becomes

$$p(z;r_s,z_s)=p_0\sum_{m=1}^{M}\Phi_m(z_s,r_s)\Phi_m(z)\,\frac{e^{i\int_0^{r_s}k_m(r)dr}}{\sqrt{k_m(r_s)r_s}}. \tag{12}$$

Using first-order perturbation theory, the range-integrated wave numbers are approximated by

$$\int_0^{r_s}k_m(r)dr\simeq\int_0^{r_s}k_m+\delta k_m(r)dr=k_m r_s+\int_0^{r_s}\delta k_m(r)dr \tag{13}$$

where[5]

$$\delta k_m(r)=\frac{-(2\pi f)^2}{k_m}\int_0^{\infty}\frac{|\Phi_m(z)|^2}{\overline{C^3}(z)}\,\Delta C(r,z)dz. \tag{14}$$

After substituting Eq. (10) into Eq. (14) and simplifying,

$$\int_0^{r_s}\delta k_m(r)dr=\sum_{j=1}^{j_n}\Delta k_m(j)G(j), \tag{15}$$

where

$$\Delta k_m(j)=\frac{-(2\pi f)^2}{k_m}\int_0^{\infty}\frac{|\Phi_m(z)|^2}{\overline{C^3}(z)}\,\mathrm{CIW}(j,z)dz \tag{16}$$

and

$$G(j)=\sum_{k=k_1}^{k_n}\sum_{\theta=\theta_1}^{\theta_n}\sigma(j,k)\mathrm{Re}\left\{\mathrm{AIW}(j,k,\theta)\,\frac{e^{ik\cos(\theta)r_s}-1}{ik\cos(\theta)}\right\}. \tag{17}$$

To verify the validity of the adiabatic approximation, the acoustic pressure wave is also calculated using the standard parabolic equation (PE). The standard PE is[9]

$$\frac{\delta\psi(r,z)}{\delta r}-\frac{ik_0(n^2(r,z)-1)}{2}\,\psi(r,z)+\frac{i}{2k_0}\,\frac{\delta^2\psi(r,z)}{\delta z^2}=0, \tag{18}$$

where $k_0=2\pi f/c_0$, c_0 is a representative sound speed, $n(r,z)=c_0/c(r,z)$. A modal starter is used as the initial condition,

$$\psi(0,z)=\psi_0\sum_{m=1}^{M}\frac{\Phi_m(z_s)\Phi_m(z)}{\sqrt{k_m}}, \tag{19}$$

and the solution is marched in range by

$$\psi(r+\Delta r,z)=\exp\left(\frac{ik_0(n^2(r,z)-1)\Delta r}{2}\right)\times\mathcal{F}^{-1}\left\{\exp\left(-\frac{ik_z^2\Delta r}{2k_0}\right)\mathcal{F}\{\psi(r,z)\}\right\}, \tag{20}$$

which is the split-step Fourier algorithm. The boundary conditions of the acoustic propagation are a reflecting ocean surface and an absorbing bottom. The reflecting surface is modeled numerically by using a discrete sine transform, applied separately to real and imaginary parts of the field. The use of the sine transform ensures the upper boundary condition $\psi(r,0)=0$ is satisfied. The absorption layer is modeled with a complex index of refraction of the form

$$n^2(r,z)=n^2_{\mathrm{water}}(r,z)+i0.01\,\exp(-0.3(z-z_{\mathrm{absorb}})^2). \tag{21}$$

Using a mode starter allows $\psi(r,z)$ to be separated into its original acoustic modes by

$$\psi(r,z)=\sum_{m=1}^{M}A(r,m)\Phi_m(z)$$

or

$$A(r,m)=\int_0^{z_{\mathrm{absorb}}}\psi(r,z)\Phi_m(z)dz. \tag{22}$$

If no internal wave is present, $\Delta C(r,z)=0$ and $\overline{A(r,m)}$ is computed. Rather than comparing actual modal phase, $\angle A(r,m)$, it is helpful to compare the modal phase perturbations,

$$\Delta\angle A(r,m)=\angle A(r,m)-\angle\overline{A(r,m)}. \tag{23}$$

With the adiabatic assumption,

$$|A(r,m)|\simeq|A(r=0,m)|=\psi_0\,\frac{\Phi_m(z_s)}{\sqrt{k_m}} \tag{24}$$

and the modal phase perturbations, $\Delta\angle A(r,m)$, are calculated by Eq. (15). Once $\psi(r,z)$ is calculated the acoustic pressure is calculated by

$$p(r,z)=p_0\,\frac{\psi(r,z)}{\sqrt{r}}\,e^{ik_0r}. \tag{25}$$

C. Processors

For all the numerical simulations, the Bartlett processor, optimum uncertain field processor (OUFP), and matched-field Processor are implemented to estimate the location of the source. The Bartlett processor assumes the average sound-speed profile is the actual sound-speed profile. This processor is very simple to implement, extremely fast, and quite robust when only small sound-speed perturbations are present. The OUFP incorporates environmental uncertainties, i.e., the internal waves, into the signal processing algorithm and optimally estimates the location of the source. The matched-field processor knows the exact realization of the internal-wave field and provides the upper bound on source localization when the environment is known. When multiple snapshots are simulated, the minimum variance (MV) beamformer and the minimum variance beamformer with environ-

mental perturbations constraints (MV-EPC) are also implemented.[4,5] Further details of each processor are presented in Secs. I C 1–5. The probability of correct localization is the most general and robust performance measure to compare these processors. Under high SNR conditions, the localization errors for all processors are local and the rms error on the estimates also provides an effective comparison for these processors.

1. The optimum uncertain field processor

The optimum uncertain field processor (OUFP), developed by Richardson and Nolte,[3,4] incorporates environmental uncertainty into acoustic source localization by using a Bayesian approach to parameter estimation. Using prior probability distributions of the uncertain source location, propagation, and array parameters, the OUFP calculates $p_{\mathbf{S}|\mathbf{r}}(\mathbf{S}|\mathbf{r})$, the *a posteriori* probability density function of the source location, given the received signal $\mathbf{r}$.

The OUFP assumes the ocean is modeled as a deterministic linear system, allowing the computation of replica fields. It also assumes the signal emitted by the acoustic source, $s(t)=\mathrm{Re}\{A\sqrt{2}e^{i2\pi ft}\}$, is a narrow-band sinusoid with a known frequency f (Hz). The signal observed at the array of receivers is

$$\mathbf{r}(t)=A\mathbf{s}(\hat{\mathbf{S}},\hat{\Psi},t)+\mathbf{n}(t), \tag{26}$$

where $\hat{\mathbf{S}}$ is the actual source position and $\hat{\Psi}$ is the actual ocean environment. The frequency transform of the received signal is of the form

$$\mathbf{P}(\mathbf{r})=A\mathbf{H}(\hat{\mathbf{S}},\hat{\Psi})+\mathbf{N}, \tag{27}$$

where $\mathbf{H}(\hat{\mathbf{S}},\hat{\boldsymbol{\Psi}})$ is the acoustic transfer function of the narrow-band source located at $\hat{\mathbf{S}}$ in the ocean $\hat{\boldsymbol{\Psi}}$. The elements of $\mathbf{P}(\mathbf{r})$ are computed from the discretized time-domain received signal, $r_z[l]$, by

$$P_z=\frac{1}{L}\sum_{l=1}^{L} r_z[l]e^{-i2\pi fTl}, \tag{28}$$

where L is the number of snapshots in time and T is the sampling time. The observation, $\mathbf{P}(\mathbf{r})$, is assumed to contain additive zero-mean complex Gaussian noise, $\mathbf{N}$, with a spatial covariance matrix of $\mathbf{Q}$. In this work the noise is assumed to be isotropic consequently, $\mathbf{Q}=\sigma_N^2\mathbf{I}$. Once the amplitude, A, of the narrow-band source is assumed to be a zero-mean complex Gaussian with variance σ_A^2, the OUFP is determined to be

$$p_{\mathbf{S}|\mathbf{r}}(\mathbf{S}|\mathbf{r})=C(\mathbf{r})p_{\mathbf{S}}(\mathbf{S})\int_{\Psi}\frac{1}{E(\mathbf{S},\boldsymbol{\Psi})+1}\times\exp\left(\frac{\frac{1}{2}|R(\mathbf{r},\mathbf{S},\boldsymbol{\Psi})|^2}{E(\mathbf{S},\boldsymbol{\Psi})+1}\right)p_{\boldsymbol{\Psi}|\mathbf{S}}(\boldsymbol{\Psi}|\mathbf{S})\,d\boldsymbol{\Psi}, \tag{29}$$

where $C(\mathbf{r})$ is a normalization constant chosen to make $p_{\mathbf{S}|\mathbf{r}}(\mathbf{S}|\mathbf{r})$ a proper probability density function; $\int_S p_{\mathbf{S}|\mathbf{r}}(\mathbf{S}|\mathbf{r})\,d\mathbf{S}=1$. $\mathbf{S}$ contains the uncertain source location parameters (range and depth). The *a priori* knowledge of the source position, $p_{\mathbf{S}}(\mathbf{S})$, is assumed to be uniform. $\boldsymbol{\Psi}$ contains the uncertain environmental parameters,

$$E(\mathbf{S},\boldsymbol{\Psi})=\delta_A^2\mathbf{H}^{\dagger}(\mathbf{S},\boldsymbol{\Psi})\mathbf{Q}^{-1}\mathbf{H}(\mathbf{S},\boldsymbol{\Psi})=\frac{\sigma_A^2}{\sigma_N^2}\mathbf{H}^{\dagger}(\mathbf{S},\boldsymbol{\Psi})\mathbf{H}(\mathbf{S},\boldsymbol{\Psi}). \tag{30}$$

and

$$R(\mathbf{r},\mathbf{S},\boldsymbol{\Psi})=\delta_A\mathbf{H}^{\dagger}(\mathbf{S},\boldsymbol{\Psi})\mathbf{Q}^{-1}\mathbf{P}(\mathbf{r})=\frac{\sigma_A}{\sigma_N^2}\mathbf{H}^{\dagger}(\mathbf{S},\boldsymbol{\Psi})\mathbf{P}(\mathbf{r}). \tag{31}$$

At the receiver, the

$$\mathrm{SNR}=E(\hat{\mathbf{S}},\hat{\Psi})=\frac{\sigma_A^2}{\sigma_N^2}\mathbf{H}^{\dagger}(\hat{\mathbf{S}},\hat{\Psi})\mathbf{H}(\hat{\mathbf{S}},\hat{\Psi}). \tag{32}$$

A brute force numerical integration is done when $\boldsymbol{\Psi}$ contains very few uncertain environmental parameters. When many uncertain environmental parameters are present, the integration over $\boldsymbol{\Psi}$ can be very efficiently computed using a recently proposed Monte Carlo technique.[4]

2. The Bartlett processor

The Bartlett processor uses only the mean environment, $\overline{\Psi}$, to localize the source. The ambiguity surface is computed by[9]

$$Z_B(\mathbf{S})=\frac{|\mathbf{H}^{\dagger}(\mathbf{S},\overline{\Psi})\mathbf{P}(\mathbf{r})|^2}{\mathbf{H}^{\dagger}(\mathbf{S},\overline{\Psi})\mathbf{H}(\mathbf{S},\overline{\Psi})}. \tag{33}$$

3. The matched-field processor

When the actual environment, $\hat{\boldsymbol{\Psi}}$, is completely known Eq. (29) reduces to

$$p_{\mathbf{S}|\mathbf{r}}(\mathbf{S}|\mathbf{r})=C(\mathbf{r})p_{\mathbf{S}}(\mathbf{S})\frac{1}{E(\mathbf{S},\hat{\Psi})+1}\exp\left(\frac{\frac{1}{2}|R(\mathbf{r},\mathbf{S},\hat{\Psi})|^2}{E(\mathbf{S},\hat{\Psi})+1}\right). \tag{34}$$

4. The minimum variance beamformer

The minimum variance (MV) beamformer effectively incorporates the cross-spectral density matrix of array outputs to suppress the ambiguous beampattern sidelobes associated with the Bartlett processor. The cross-spectral density matrix, $\mathbf{R}=E\{\mathbf{P}(\mathbf{r})\mathbf{P}^{\dagger}(\mathbf{r})\}$, is computed from the multiple independent snapshots. In each snapshot, $\mathbf{P}_i(\mathbf{r})=A_i\mathbf{H}(\hat{\mathbf{S}},\hat{\boldsymbol{\Psi}})+\mathbf{N}_i$, the source location $\hat{\mathbf{S}}$ and the ocean environment $\hat{\boldsymbol{\Psi}}$ remain constant while the signal component A_i and the noise $\mathbf{N}_i$ are independent complex Gaussians. The ambiguity surface for the MV beamformer is computed by

$$Z_{\mathrm{MV}}(\mathbf{S})=\frac{\mathbf{H}^{\dagger}(\mathbf{S},\overline{\Psi})\mathbf{H}(\mathbf{S},\overline{\Psi})}{\mathbf{H}^{\dagger}(\mathbf{S},\overline{\Psi})\mathbf{R}^{-1}\mathbf{H}(\mathbf{S},\overline{\Psi})}. \tag{35}$$

5. The minimum variance beamformer with environmental perturbation constraints

The minimum variance beamformer with environmental perturbation constraints (MV-EPC) achieves robustness by employing constraints designed to maintain the beamformer response over a range of perturbations of the environmental parameters $\boldsymbol{\Psi}$.[4,5] $\boldsymbol{\Psi}$ is modeled as a random vector and the

columns of the constraint matrix $\mathbf{C}(\mathbf{S})$ are the wavefronts corresponding to different realizations ψ_i of $\mathbf{\Psi}$, i.e.,

$$\mathbf{C}(\mathbf{S})=[\mathbf{H}(\mathbf{S},\psi_1),\mathbf{H}(\mathbf{S},\psi_2),\ldots,\mathbf{H}(\mathbf{S},\psi_K)]. \tag{36}$$

For moderate environmental uncertainty, the column space of $\mathbf{C}(\mathbf{S})$ is approximately low rank and is spanned by the largest eigenvectors of the signal correlation matrix

$$\mathbf{R_S}(\mathbf{S})=E\{\mathbf{H}(\mathbf{S},\mathbf{\Psi})\mathbf{H}^{\dagger}(\mathbf{S},\mathbf{\Psi})\}\simeq\mathbf{U}\mathbf{\Lambda}\mathbf{U}^{\dagger}, \tag{37}$$

where $\mathbf{U}\mathbf{\Lambda}\mathbf{U}^{\dagger}$ is a reduced rank approximation of $\mathbf{R_s}(\mathbf{S})$ such that $\mathbf{U}$, with orthonormal columns, has rank J much less than the number of sensors and Λ is a diagonal matrix of the J largest eigenvalues of $\mathbf{R_s}(\mathbf{S})$. Finally, the ambiguity surface for the MV-EPC is computed by

$$Z_{\mathrm{MV-EPC}}(\mathbf{S})=\mathbf{e}_1^{\dagger}(\mathbf{U}^{\dagger}\mathbf{R}^{-1}\mathbf{U})^{-1}\mathbf{e}_1, \tag{38}$$

where $\mathbf{e}_1=[1,0,...,0]^{\dagger}$.

D. The Cramer–Rao lower bound

The Cramer–Rao lower bound (CRLB) can be used to predict the theoretical limit on source localization errors in high SNR. These predictions are only valid when the estimation errors are local, which occurs in the high SNR region only. The CRLB does not provide an algorithm to localize the acoustic source, but rather analytically computes the local limitations on source range and depth estimates attainable by any processor. By incorporating the normal mode solution (along with the adiabatic approximation) to the wave equation and a fully spanning receiver array, Narasimhan and Krolik have computed the CRLB for estimating the range of a narrow-band acoustic source.[11] The Fisher information matrix for source range estimates is

$$\mathbf{J}_{r_s}=\mathrm{SS}\begin{bmatrix} \mathrm{Re}\{\mathbf{k}\}^{\dagger}\mathbf{J}_{\mathbf{\Phi\Phi}}\,\mathrm{Re}\{\mathbf{k}\}+\dfrac{\partial\mathbf{h}^{\dagger}}{\partial r_s}\,\mathbf{J}_{\mathbf{hh}}\,\dfrac{\partial\mathbf{h}}{\partial r_s} & \mathrm{Re}\{\mathbf{k}\}^{\dagger}\mathbf{J}_{\mathbf{\Phi\Phi}}\mathbf{\Delta k} \\ \mathbf{\Delta k}^{\dagger}\mathbf{J}_{\mathbf{\Phi\Phi}}\,\mathrm{Re}\{\mathbf{k}\} & \mathbf{\Delta k}^{\dagger}\mathbf{J}_{\mathbf{\Phi\Phi}}\mathbf{\Delta k}\end{bmatrix} +\begin{bmatrix}0 & 0\\ 0 & \mathbf{R}_G^{-1}\end{bmatrix}, \tag{39}$$

where SS is the number of independent snapshots of the observation, $\mathbf{k}$ is an $M\times 1$ column vector of the acoustic wave numbers, $\mathbf{\Delta k}$ is an $M\times j_n$ modal phase perturbation matrix defined by Eq. (16),

$$\mathbf{J}_{\mathbf{\Phi\Phi}}=\frac{2(\sigma_A^2/\sigma_N^2)^2}{1+(\sigma_A^2/\sigma_N^2)\mathbf{h}^{\dagger}\mathbf{h}}\,(\mathbf{h}^{\dagger}\mathbf{h}\,\mathrm{diag}(\mathbf{h}^2)-\mathbf{h}^2(\mathbf{h}^2)^{\dagger}), \tag{40}$$

$$\mathbf{J}_{\mathbf{hh}}=\frac{2(\sigma_A^2/\sigma_N^2)^2}{1+(\sigma_A^2/\sigma_N^2)\mathbf{h}^{\dagger}\mathbf{h}}\left(\mathbf{h}^{\dagger}\mathbf{h}\mathbf{I}+\frac{1-(\sigma_A^2/\sigma_N^2)\mathbf{h}^{\dagger}\mathbf{h}}{1+(\sigma_A^2/\sigma_N^2)\mathbf{h}^{\dagger}\mathbf{h}}\,\mathbf{h}\mathbf{h}^{\dagger}\right), \tag{41}$$

$$\mathbf{R}_G=\mathrm{diag}(\langle G(j)^2\rangle), \tag{42}$$

$\mathbf{h}$ is an $M\times 1$ column vector of the modal amplitudes whose elements are defined by

$$h_m=\frac{\Phi_m(z_s)e^{-\mathrm{Im}\{k_m\}r_s}}{\sqrt{k_m r_s}}\quad\text{and}\quad h_m^2=\frac{\Phi_m^2(z_s)e^{-2\,\mathrm{Im}\{k_m\}r_s}}{k_m r_s}. \tag{43}$$

The variance of the source range localization error is given by the first diagonal element of $\mathbf{J}_{r_s}^{-1}$. Three CRLBs are computed here: (1) the unperturbed bound for the known ocean, (2) the hybrid bound for the ocean containing an internal-wave obeying the Garrett–Munk internal wave spectrum, and (3) the perturbed bound for a completely random ocean. To achieve the unperturbed bound, the exact realization of the internal-wave field must be known making $\langle G(j)^2\rangle=0$ and the range of the source, r_s the only unknown parameter. For the hybrid and perturbed bound, the unknown parameters are the range of the source, r_s, as well as the range-integrated internal wave coefficients, $G(j)$ in Eq. (17). The hybrid bound uses the spectrum as *a priori* information on $G(j)$ and computes $\langle G(j)^2\rangle$ from realizations of Eq. (17). The perturbed bound assumes no *a priori* information on the spectrum of the internal-wave making $\langle G(j)^2\rangle=\infty$.

The CRLB is also extended to provide the theoretical limit on depth estimates. The Fisher information matrix for source depth estimates is,

$$\mathbf{J}_{z_s}=SS\,\frac{\partial\mathbf{h}^{\dagger}}{\partial z_s}\,\mathbf{J}_{\mathbf{hh}}\,\frac{\partial\mathbf{h}}{\partial z_s}. \tag{44}$$

The variance of the source depth localization error is given by $\mathbf{J}_{z_s}^{-1}$. The depth of the source, z_s, and the range-integrated internal-wave coefficients, $G(j)$, are unknown parameters. Notice the bound is not a function of $\langle G(j)^2\rangle$. When using the normal mode solution with the adiabatic approximation, sound-speed perturbations cause modal phase perturbations. These modal phase perturbations do not cause ambiguity in depth estimations. Consequently, depth estimates are only a function of source location and SNR, not sound-speed perturbations.

II. SIMULATIONS AND RESULTS

For all numerical simulations a 25-Hz source is placed 1000 km in range ($r_s=1000$ km) and 800 m in depth ($z_s=800$ m) which is on the channel axis. This source is placed in an ocean containing a known range-independent sound-speed profile, $C(z)$, with a random range-dependent sound-speed perturbation, $\Delta C(r,z)$, due to internal waves. Both fairly structured internal-wave and very random internal-wave environments are considered. For the fairly structured internal-wave environment, the number of discrete propagating acoustic modes is much greater than the number of propagating internal-wave modes. With the 25-Hz source in this range-independent profile, 23 acoustic modes propagate; therefore, to simulate a fairly structured internal-wave environment, only two discrete modes of the internal wave propagate (i.e., $j_n=2$). For a very random internal wave, the number of propagating internal-wave modes is greater than the number of propagating acoustic modes. Realizations of the very random internal-wave are computed using 25 ($j_n=25$) discrete modes. In both fairly structured and very random internal wave environments, each discrete internal-wave mode propagates at 15 known spatial frequencies spaced logarithmically between 2×10^{-5} and 2×10^{-3} rad/m (Fig. 3) and at 25 uniformly spaced random angles. The complex amplitudes, AIW (j,k,θ), of each discrete internal-

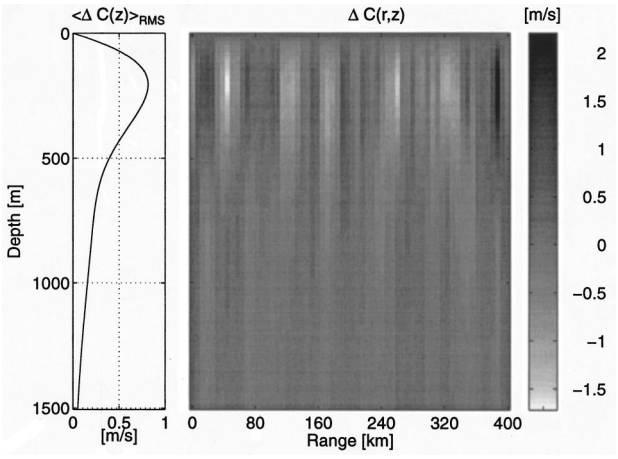

FIG. 6. Sound-speed perturbations, $\Delta C(r,z)$, and the corresponding $\langle \Delta C(z) \rangle_{\text{rms}}$ caused by a realization of a fairly structured internal wave.

wave mode at each spatial frequency and propagating angle are random. The sound-speed perturbations, $\Delta C(r,z)$, along with the corresponding rms levels, $\langle \Delta C(z) \rangle_{\text{rms}}$, caused by a realization of a fairly structured internal-wave field are shown in Fig. 6. A very random internal-wave field causes sound-speed perturbations and rms levels similar to those in Fig. 7. The validity of the adiabatic approximation is verified in Sec. II A. When localizing the source, the acoustic wave propagation of this source in this ocean is simulated by the normal mode solution to the wave equation using KRAKEN and the adiabatic approximation.[8,9] The acoustic pressure field is sampled with a fully spanning array of receivers to allow modal filtering. The processors use the complex modal coefficients to localize the source. The location of the source is estimated to be at the maximum of the ambiguity surface. The internal-wave effects on the estimations of the depth and range of the source are investigated independently. The processors estimate the source depth in Sec. II B and source range in Secs. II C and II D.

A. Verifying the adiabatic approximation with PE

Using the standard PE wave equation to simulate the acoustic propagation, the evolution of the modal power and phase perturbations as a function of range are computed for the 25-Hz source in an ocean containing a very random internal-wave field. With the PE wave equation, the actual modal amplitudes are computed with Eq. (22) and the actual modal phase perturbations are calculated by Eq. (23). With the adiabatic approximation in the PE wave equation, the modal amplitudes are estimated with Eq. (24) and phase perturbations are estimated with Eq. (15). In this numerical simulation, Eq. (20) is implemented with $c_0=1480$ m/s, $\Delta r=50$ m, and a 512-point sine transform. Figure 8 shows one realization of the modal power evolution, $|A(r,m)|^2$, and the modal phase perturbations, $\Delta A(r,m)$, for the strongest seven modes [$m=1$ (strongest in amplitude), 4, 5, 9, 8, 14, 3] out to 1000 km. The modes of the 25-Hz source are not as couple as those of the 75-Hz source investigated in Fig. 3 of Ref. 6. The modes of the 25-Hz source show some coupling, but the approximation is fairly accurate. The adiabatic approximation provides great computational benefits, both numerically and analytically, and reasonably portrays the actual modal content of the pressure field; consequently, the adiabatic approximation is made when localizing the acoustic source.

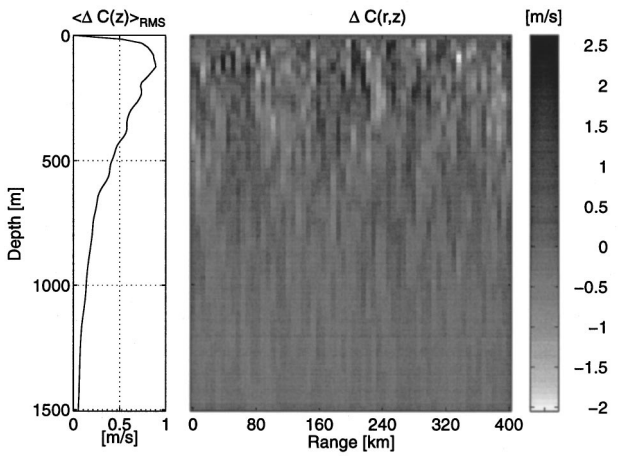

FIG. 7. Sound-speed perturbations, $\Delta C(r,z)$, and the corresponding $\langle \Delta C(z) \rangle_{\text{rms}}$ caused by a realization of a very random internal wave.

B. Depth estimations

When searching for the depth, the range of the source is assumed known. The Bartlett processor, OUFP, and matched-field processor are implemented to estimate the depth of the source in a very random internal-wave ($j_n=25$) environment. Each processor attempts to estimate the depth of the source by searching over 101 depth locations spaced logarithmically around the actual source depth of 800 m between 100 and 1500 m. The ambiguity surfaces are smooth and for simulation purposes the log-spaced search grid reduces the search space of the processors while retaining the local estimation error that is predicted by the CRLB. The integration in the OUFP is done using the Monte Carlo method with 300 internal-wave realizations. One hundred independent internal-wave realizations are simulated in computing the performance curves for each processor. These performance curves are computed for SNRs from 0–40 dB. Recalling that $\text{SNR}=(\sigma_A^2/\sigma_N^2)\mathbf{H}^{\dagger}(\hat{\mathbf{S}},\hat{\boldsymbol{\Psi}})\mathbf{H}(\hat{\mathbf{S}},\hat{\boldsymbol{\Psi}})$, the SNR is adjusted by fixing the amplitude of the source to σ_A and adding the zero mean complex Gaussian noise with the appropriate variance σ_N^2. The depth of the source is estimated to be at the maximum of the ambiguity plot. A depth estimate is considered correct if it is within 10 m of the actual depth (i.e., 800 ± 10 m). The size of the correct localization window (20 m) is chosen to be approximately four times the standard deviation predicted by the CRLB at 20 dB.

The probability of a correct depth localization for each processor is shown in Fig. 9(a). The performance of the OUFP is comparable to the performance of matched-field processor, implying that source depth estimates are fairly insensitive to internal-wave mismatch. Under high SNR conditions, the rms error of the depth estimates is used to further evaluate the performance of each processor. The rms error of the depth estimates for each processor and the theoretical CRLB are shown in Fig. 9(b). Under low SNR, global errors are present and the CRLB does not predict them, therefore, the thresholding phenomena occurs at SNR$\simeq$14 dB. Even

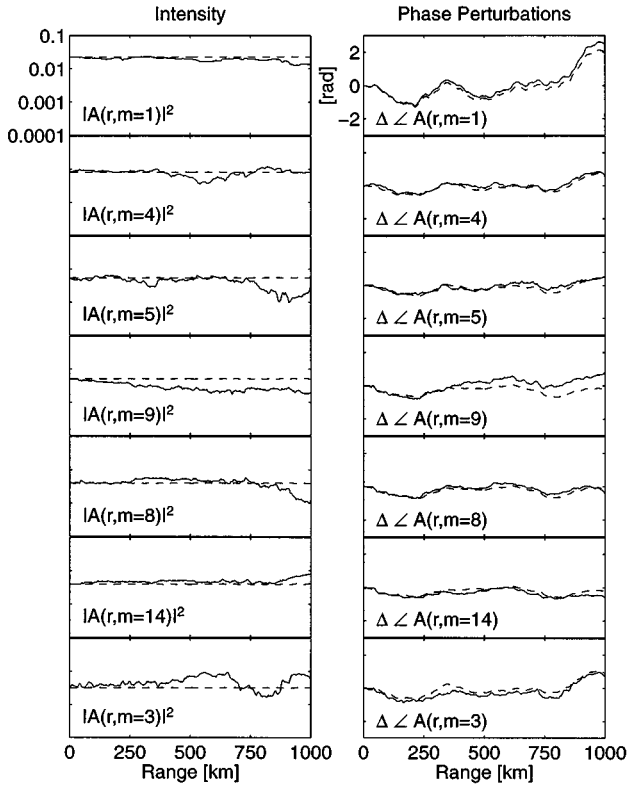

FIG. 8. Modal power and phase perturbations from a simulated propagation. Actual PE results are plotted with solid lines and the PE results using the adiabatic approximation are plotted with dashed lines. The modes are sorted in decreasing strength (1 is strongest) according to Eq. (24).

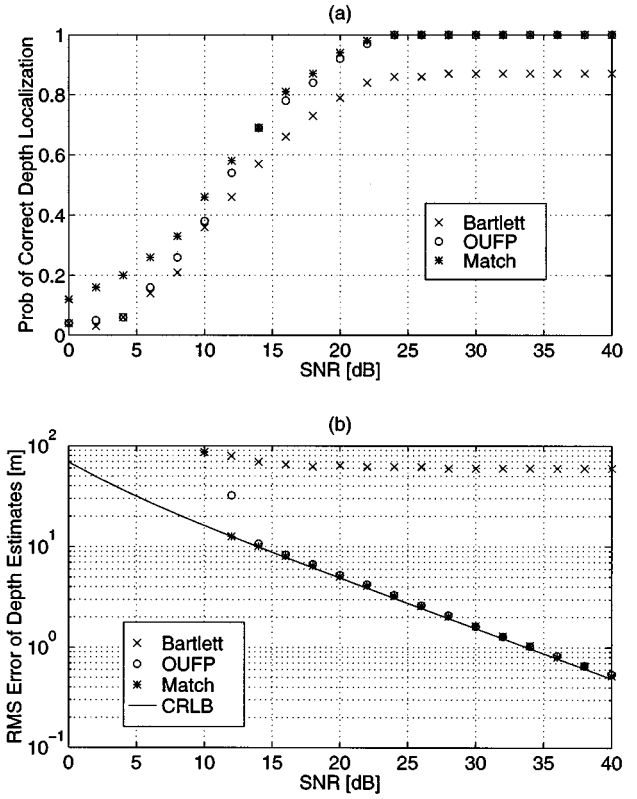

FIG. 9. Processor performance in very random internal-wave environments shown as (a) probability of correct depth localization, and (b) rms error of depth estimates.

under high SNR, the Bartlett processor continues to have global errors and does not achieve the performance level predicted by the CRLB. This continues to reveal the sensitivity of environmental mismatch on source localization using matched field processing when the assumed mean ocean is not the actual ocean. The OUFP and the matched-field processor perform on the CRLB.

When estimating the depth of the source, most of the significant information lies in the modal amplitudes. In using normal modes and the adiabatic approximation, the internal-wave-induced sound-speed perturbations cause modal phase perturbations. Since depth estimates are insensitive to modal phase perturbations, all processors tend to accurately estimate the depth of the source. This does not imply that internal waves have no effect on source depth estimations. It does reveal that internal waves have little effect on source depth estimations when using normal modes and the adiabatic approximation.

C. Range estimations

Now the range of the source is unknown and the depth is known. The Bartlett processor, OUFP, and matched-field processor are implemented to estimate the range of the source in both fairly structured internal-wave ($j_n=2$) and very random internal-wave ($j_n=25$) environments. Each processor searches over 101 range locations spaced logarithmically around the actual source range of 1000 km between 900 and 1100 km. The range of the source is estimated to be at the maximum of the ambiguity plot. A range estimate is considered correct if it is within 500 m of the actual range (i.e., 1000 km$\pm$500 m). The size of the correct localization window was chosen to be approximately four times the standard deviation predicted by the hybrid CRLB at 20 dB. The gridding of the possible source locations as well as the size of the correct localization window should be considered when evaluating correct localization statistics. Again, 100 independent internal waves of each type are simulated in computing the performance curves for each processor. These performance curves are computed for SNRs from 0–40 dB and the SNR of each observation is set by fixing the amplitude of the source to σ_A and adding the zero mean complex Gaussian noise with variance σ_N^2.

When computing the OUFP for the fairly structured internal-wave ($j_n=2$) environment, a brute force integration is performed by assuming $G(j)$ is Gaussian and using 75 discrete samples over ± 3.5 standard deviations for both values of j (i.e., $j=1,2$). The performance of each processor in the fairly structured internal-wave environment is shown in Fig. 10(a) as the probability of correct range localization and in Fig. 10(b) as the rms error on range estimates. The unperturbed CRLB, the hybrid CRLB, and the perturbed CRLB are also shown in Fig. 10(b). For low SNR, the rms error of range estimates for all processors is a function of the search window, which should be infinite, since the errors are no longer local. The CRLB only predicts the local error associated with the source localization; however, under low SNR, global errors are present. This thresholding phenomena occurs at SNR$\simeq$14 dB. For high SNR, the Bartlett processor is uncertainty limited and does not improve with increasing

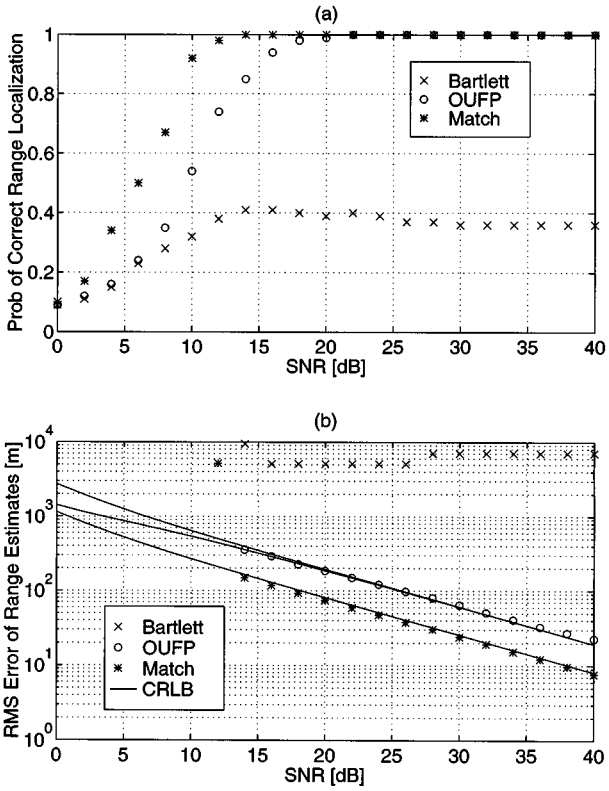

FIG. 10. Processor performance in fairly structured internal-wave environments shown as (a) probability of correct range localization, and (b) rms error of range estimates.

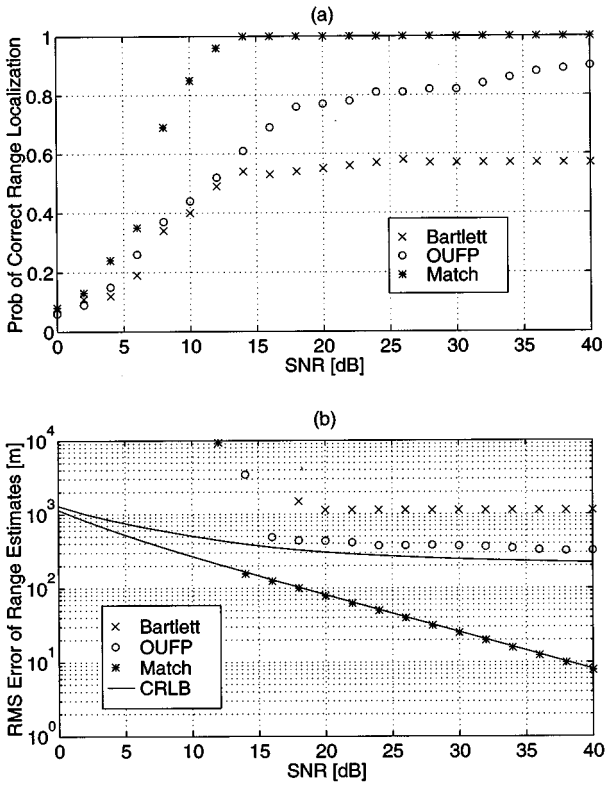

FIG. 11. Processor performance in very random internal-wave environments shown as (a) probability of correct range localization, and (b) rms error of range estimates.

SNR. The range estimates of the OUFP improve with increasing SNR. The OUFP attains the same performance level predicted by the hybrid CRLB. In this fairly structured internal-wave environment, the hybrid CRLB theoretically predicts the accuracy of range estimates and the OUFP is the signal processing algorithm that achieves this performance bound. As expected, the performance of the matched-field processor, which has complete knowledge of each internal-wave realization, lies on the unperturbed CRLB.

For the very random internal wave ($j_n=25$), the OUFP uses 5000 internal-wave realizations in the Monte Carlo numerical integration. The performance of each processor in the very random internal-wave environment is shown in Fig. 11(a) as the probability of correct range localization and in Fig. 11(b) as the rms error of the range estimates. Figure 11(b) also contains the unperturbed CRLB and the hybrid CRLB. The perturbed CRLB diverges and, therefore, is not plotted for the very random internal-wave environment. Just as in the fairly structured internal-wave environment, the source range estimates predicted by the CRLB are only accurate for high SNR (>14 dB). A very accurate integration over the environment $\mathbf{\Psi}$ is necessary for the performance of the OUFP to exactly achieve the accuracy predicted by the hybrid CRLB. Again, the performance of the matched-field processor lies along the unperturbed CRLB. As the internal-wave field becomes more random, all processors are limited by this environmental uncertainty and, therefore, the improvement in processor performance becomes less significant.

D. Range estimations with multiple snapshots

Now the processors have multiple independent snapshots to estimate the range of the source. In addition to the Bartlett processor, OUFP, and matched-field processor, the MV beamformer and the MV-EPC are implemented. The same fairly structured internal-wave ($j_n=2$) and very random internal-wave ($j_n=25$) environments are considered. Each processor estimates the range of the source by searching over the same 101 range locations spaced logarithmically around 1000 km between 900 and 1100 km. Once again, the range of the source is estimated to be at the maximum of the ambiguity plot and a range estimate is considered correct if it is within 500 m of the actual range (i.e., 1000 km$\pm$500 m). One hundred independent internal-wave realizations, each with 100 independent snapshots, are simulated to compute the performance of each processor. In each independent snapshot of the observation, the environment $\mathbf{\Psi}$ is constant and the SNR is set by independently sampling the zero mean complex Gaussian amplitude with variance σ_A^2 of the source and adding the zero mean complex Gaussian noise with variance σ_N^2.

When computing the OUFP for the fairly structured internal wave ($j_n=2$), a brute force integration is performed by assuming $G(j)$ is Gaussian and taking 75 discrete samples over ± 3.5 standard deviations for both values of j (i.e., $j=1,2$). The MV-EPC uses the same discretized set of internal-wave realizations to estimate the range of the source. The performance of each processor using the 100 independent snapshots in the fairly structured internal-wave environ-

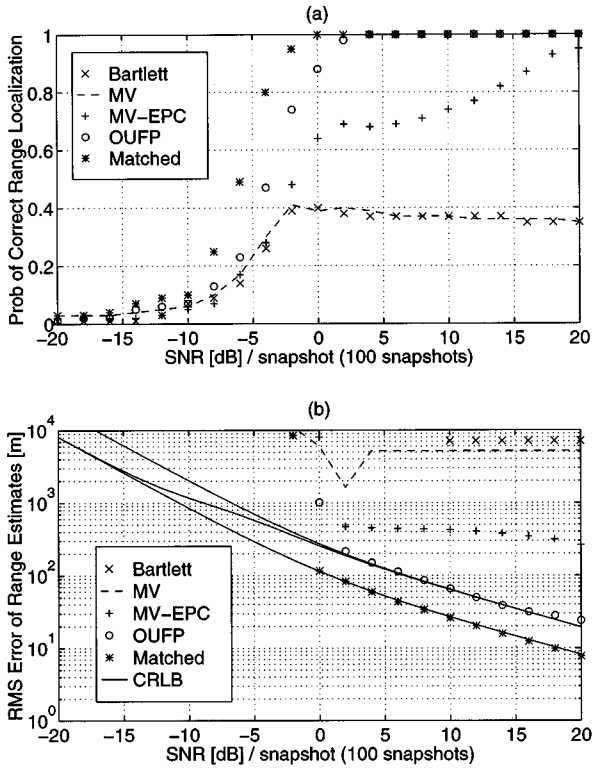

FIG. 12. Processor performance using 100 independent snapshots in fairly structured internal-wave environments shown as (a) probability of correct range localization, and (b) rms error of range estimates.

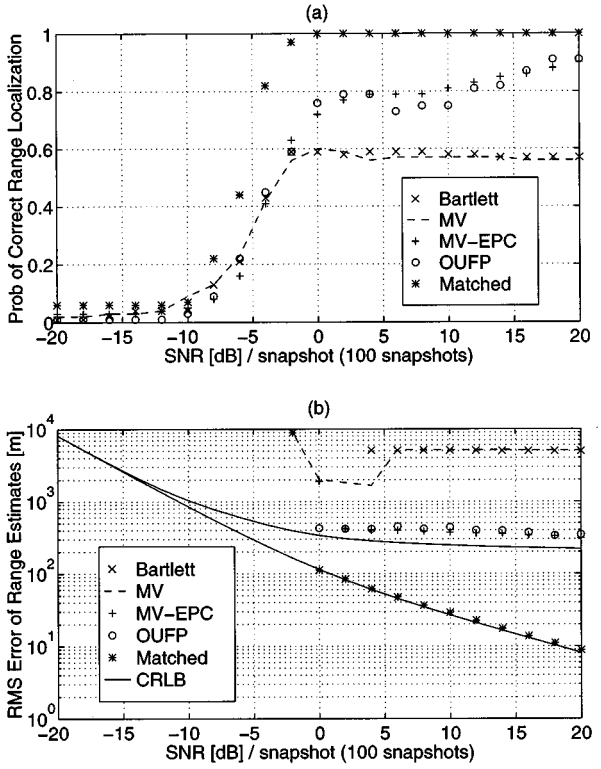

FIG. 13. Processor performance using 100 independent snapshots in very random internal-wave environments shown as (a) probability of correct range localization, and (b) rms error of range estimates.

ments is shown in Fig. 12(a) as the probability of correct range localization and in Fig. 12(b) as the rms error of range estimates. The thresholding phenomena occurs at SNR $\simeq$0 dB per snapshot. Using multiple independent snapshots, the effective SNR is increased. Had the snapshots been dependent or completely correlated, the snapshots can be coherently averaged and the expected SNR increase will be 20 dB because σ_A^2/σ_N^2 would be increased by 20 dB [10 log(SS) (dB)]. With 100 independent snapshots, the effective SNR increase is approximately 14 dB. The Bartlett processor and MV beamformer perform identically. Because the source is estimated at the maximum of the ambiguity surface, sidelobe suppression is not an issue. The OUFP performs along the theoretical limit predicted by the hybrid CRLB. For the fairly structured internal-wave environment, the OUFP performs significantly better than the MV-EPC. The matched-field processor performs along the unperturbed CRLB as expected.

For the very random internal wave (j_n=25), the OUFP uses 5000 internal-wave realizations in the Monte Carlo numerical integration. The OUFP and the MV-EPC use the same set of 5000 internal-wave realizations to estimate the range of the source. The performance of each processor using the 100 independent snapshots in the very random internal-wave environment is shown in Fig. 13(a) as the probability of correct range localization and in Fig. 13(b) as the rms error of range estimates. Just as in the fairly structured internal-wave case, the effective SNR is increased with multiple independent snapshots and the thresholding phenomena occurs at SNR$\simeq$0 dB per snapshot. Again, the performance of the OUFP corresponds with the accuracy predicted by the hybrid CRLB. The MV-EPC also performs along the hybrid CRLB, thus proving to be an effective processor in very random internal-wave environments. Again, the matched field processor performs along the unperturbed CRLB. Significant processor gains are achieved in random, but fairly structured, environments. As the environment becomes completely random, this environmental uncertainty limits all processors.

III. CONCLUSIONS

By optimally incorporating *a priori* internal-wave characteristics into the OUFP, the limits on localizing a narrowband acoustic source in the presence of internal waves have been determined, as well as the signal processing algorithm that achieves those limits. This has been done as a function of the modal content of the internal-wave field and for a wide range of signal-to-noise ratios. The probability of correct localization is the most robust method of computing these limitations when global localization errors are present. When the source localization errors are local, which occurs at high SNR, the rms error of the estimate provides a finer error measurement. The CRLB provides an effective analytical prediction of source localization limitations at high SNR, but does not predict global localization errors which occur in low SNR conditions.

When estimating the depth of the source in high SNR, the OUFP and matched-field processor perform along the CRLB. The internal wave has a small effect on source depth estimates, when using normal modes and the adiabatic ap-

proximation model. However, the internal wave does have a significant effect when estimating the source range. By knowing the ocean environment, the matched-field processor computes the upper bound on performance and, in high SNR conditions, performs along the theoretical unperturbed CRLB. In both the fairly structured and very random internal-wave environments, the OUFP is the signal processing algorithm that computes the limits on range estimates which is predicted by the CRLB for high SNR. When using multiple snapshots to estimate the range of the source, the effective SNR is increased; however, the performance of the Bartlett processor does not improve with this effective SNR increase. In the fairly structured internal-wave environment, the OUFP performs significantly better than the MV-EPC, which also incorporates this environmental variability, making the concept of optimally localizing the source very important. Under very random internal-wave environments, the MV-EPC proves to be an effective processor by performing as well as the OUFP. Under these very random internal-wave conditions, the environmental variability limits the performance of all signal processing algorithms. However, the OUFP provides both a signal processing algorithm as well as the limits on source localization performance as a function of environmental uncertainties and a wide range of signal-to-noise ratios.

ACKNOWLEDGMENTS

John Colosi provided valuable assistance in teaching the proper use of the Garrett–Munk internal-wave model, and for that the authors thank him. Support for this work has been provided by the Office of Naval Research (Ocean Acoustics, Code 321 OA).

[1] J. Colosi, S. Flatte, and C. Bracher, ''Internal-wave effects on 1000 km oceanic acoustic pulse propagation: Simulation and comparison with experiment,'' J. Acoust. Soc. Am. **84**, 452–467 (1994).
[2] D. R. Jackson and T. E. Ewart, ''The effect of internal waves on matched-field processing,'' J. Acoust. Soc. Am. **96**, 2945–2955 (1994).
[3] A. M. Richardson and L. W. Nolte, ''*A posteriori* probability source localization in an uncertain sound speed, deep ocean environment,'' J. Acoust. Soc. Am. **89**, 2280–2284 (1991).
[4] J. A. Shorey, L. W. Nolte, and J. L. Krolik, ''Computationally efficient Monte Carlo estimation algorithms for matched field processing in uncertain ocean environments,'' J. Comput. Acoust. **2**, 285–314 (1994).
[5] J. L. Krolik, ''Matched-field minimum variance beamforming in a random ocean channel,'' J. Acoust. Soc. Am. **92**, 1408–1419 (1992).
[6] J. A. Colosi and S. M. Flatte, ''Mode coupling by internal waves for the multi-megameter acoustic propagation in the ocean,'' J. Acoust. Soc. Am. **100**, 3607–3620 (1996).
[7] S. M. Flatte, R. Dashen, W. Munk, K. Watson, and F. Zacariasen, *Sound Transmission through a Fluctuating Ocean* (Cambridge U.P., Cambridge, 1979).
[8] M. B. Porter and E. L. Reiss, ''A numerical method for ocean acoustic normal modes,'' J. Acoust. Soc. Am. **76**, 244–252 (1984).
[9] F. Jensen, W. Kuperman, M. Porter, and H. Schmidt, *Computational Ocean Acoustics* (American Institute of Physics, New York, 1994).
[10] S. Levitus, *Climatological Atlas of the World Ocean* (National Oceanic and Atmospheric Administration, Rockville, MD, 1982).
[11] S. Narasimhan and J. L. Krolik, ''Fundamental limits on acoustic source range estimation performance in uncertain ocean channels,'' J. Acoust. Soc. Am. **97**, 215–226 (1995).

Conversion of a Stoneley wave at the extremity of a fluid loaded plate

R. Briers,[a] O. Leroy, and G. N. Shkerdin[b]
Interdisciplinary Research Center, K. U. Leuven Campus Kortrijk, B-8500 Kortrijk, Belgium

(Received 29 April 1996; accepted for publication 20 November 1996)

A theoretical model, based on mode theory, is presented in order to study the behavior of the Stoneley wave when it reaches the extremity of a thick plate immersed in a liquid. The superposition of two phenomena is established: the first one being the simple forward diffraction of the Stoneley wave in the liquid and the second one being its conversion into two generalized Rayleigh waves which propagate on the same plane as the incident Stoneley wave or along the vertical end face of the solid support. The theoretical analysis is in good agreement with the experimental observations of Tinel [Ph.D. Thesis, Université Le Havre, France (1991)]. © *1997 Acoustical Society of America.* [S0001-4966(97)00203-8]

PACS numbers: 43.35.Cg [HEB]

INTRODUCTION

The existence of waves propagating along a liquid/solid interface has been shown by Stoneley[1] and Scholte[2] who complemented the historical works of Rayleigh. These waves are usually called generalized Rayleigh wave and Stoneley or Scholte–Stoneley wave. The generalized Rayleigh wave re-emits energy in the liquid while the Stoneley wave is trapped along the interface and does not experience radiation loss.

The generalized Rayleigh wave has already been the subject of many studies and its influence has been shown in the reflection of acoustic beams at a liquid/solid interface.[3,4] Systematic studies of the Stoneley wave are much more recent.[5–9] In this paper, we present a theoretical study of the conversion of a Stoneley wave reaching the extremity of its solid support. We study the forward diffraction in the liquid as well as the conversion into a generalized Rayleigh wave by reflection at the end face of a plate.

The theoretical analysis is based on a mode theory[10,11] that was developed earlier to investigate the validity of a liquid wedge for the generation of a Stoneley wave. In Sec. I we construct the complete and orthogonal set of acoustic modes (radiation modes and eigenmodes) for a liquid/plate/liquid structure. In Sec. II this procedure is repeated for a homogeneous liquid structure. In Sec. III we expand the scattered and mode-converted waves that arise when a Stoneley wave interacts with the end face of a fluid loaded plate into these orthogonal sets of acoustic modes. Expressing the appropriate boundary conditions, a system of complex integral equations in the unknown expansion coefficients of the scattered and mode converted acoustic fields is derived. This system of equations is solved by the method of successive approximations. Finally, in Sec. IV, numerical calculations illustrate the results of the theoretical analysis for different materials.

I. THE ORTHOGONAL SET OF ACOUSTIC MODES FOR A LIQUID/PLATE/LIQUID STRUCTURE

A. The continuous spectrum of radiation modes

Consider a solid plate of thickness $2d$ surrounded by a liquid. We assume that the liquid on top of the plate is identical to the liquid beneath it. The solid plate is characterized by its density ρ_1, its longitudinal sound velocity v_d, and its transverse sound velocity v_s. The liquid has density ρ and longitudinal sound velocity v. We assume all acoustic waves to be propagating in the (y,z) plane and to be uniform along the direction perpendicular to the plane of incidence. According to the fundamentals of mode theory the set of all acoustic modes that can exist in the liquid/plate/liquid structure consists of a discrete spectrum of eigenmodes and a continuous spectrum of radiation modes. By eigenmodes we always mean the surface waves (or guided waves) supported by the investigated structure. To define the notion radiation mode one usually supposes a located-at-infinity $(y=\pm\infty)$ acoustic source. A plane wave emerging from the source is reflected at and transmitted through the plate, and generate longitudinal and transversal waves inside the plate. A radiation mode represents simultaneously the incident, reflected, transmitted, and in-plate generated waves. A radiation mode thus describes the resulting radiation field (or superposition) of these waves in the liquid and in the plate. For what concerns the continuous spectrum of radiation modes, one must distinguish, from the beginning, two different types of modes.

On one hand, there are radiation modes, generated by plane waves incident from the liquid above the plate [hereafter called type 1 modes, see Fig. 1(a)], which are described by the displacement field

$$\mathbf{u}^1=\boldsymbol{\nabla}(\varphi_i+\varphi_R), \quad d<y, \tag{1}$$

$$\mathbf{u}^1=\boldsymbol{\nabla}(\varphi_{D^-}+\varphi_{D^+})+\boldsymbol{\nabla}\times(\boldsymbol{\psi}_{S^-}+\boldsymbol{\psi}_{S^+}), \quad -d<y<d, \tag{2}$$

$$\mathbf{u}^1=\boldsymbol{\nabla}\varphi_T, \quad y<-d. \tag{3}$$

The potential functions are represented by

[a]Postdoctoral fellow of the Flemish Institute for the Encouragement of the Scientific and Technological Research in Industry (I.W.T.).
[b]Permanent address: Institute of Radioengineering and Electronics, Russian Academy of Sciences, Moscow, Russia.

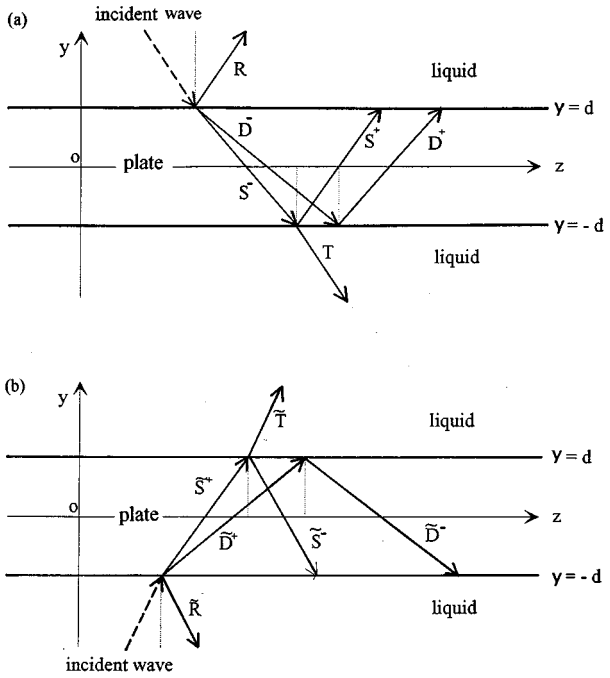

FIG. 1. (a) The excitation of type 1 radiation modes. (b) The excitation of type 2 radiation modes.

$$\varphi_i = A\ \exp[i(-k_y y + k_z z - \omega t)],$$
$$\varphi_R = AR\ \exp[i(k_y y + k_z z - \omega t)],$$
$$\varphi_{D^\pm} = AD^\pm\ \exp[i(\pm k_{dy} y + k_z z - \omega t)], \tag{4}$$
$$\boldsymbol{\psi}_{S^\pm} = AS^\pm\ \exp[i(\pm k_{sy} y + k_z z - \omega t)]\mathbf{e}_x,$$
$$\varphi_T = AT\ \exp[i(-k_y y + k_z z - \omega t)],$$

whereby the wave vector components satisfy the dispersion relations

$$k_y^2 + k_z^2 = k^2 = \left(\frac{\omega}{v}\right)^2,$$
$$k_{dy}^2 + k_z^2 = k_d^2 = \left(\frac{\omega}{v_d}\right)^2, \tag{5}$$
$$k_{sy}^2 + k_z^2 = k_s^2 = \left(\frac{\omega}{v_s}\right)^2.$$

Here, A is an arbitrary amplitude, ω is the circular frequency, and $\mathbf{e}_x$ is a unit vector along the x axis. The corresponding components of the stress tensor T_{ij} follow from Hooke's law

$$T_{ij} = \lambda\,\delta_{ij}\sum_k S_{kk} + 2\mu S_{ij}, \tag{6}$$

λ and μ are the Lamé constants, δ_{ij} is the Kronecker symbol, and S_{ij} is the strain tensor. Six boundary conditions are to be fulfilled: continuity of the normal displacements at $y = \pm d$ and continuity of the normal and the shear stresses at $y = \pm d$. These conditions result in a system of six linear equations in the six unknown reflection and transmission coefficients R, $D^\pm$, $S^\pm$, T of which the solutions take the form:

$$R = -\frac{\exp(-2ik_y d)}{2}\left[\frac{\Delta_s^*}{\Delta_s} + \frac{\Delta_a^*}{\Delta_a}\right], \tag{7}$$

$$D^\pm = \frac{2k_z^2 - k_s^2}{2k_s^2}\exp(-ik_y d)\left[\frac{1}{i\,\cos(k_{dy}d)\Delta_s} \mp \frac{1}{\sin(k_{dy}d)\Delta_a}\right], \tag{8}$$

$$S^\pm = -\frac{k_z k_{dy}}{k_s^2}\exp(-ik_y d)\left[\frac{\tan(k_{dy}d)}{i\,\sin(k_{sy}d)\Delta_s} \mp \frac{\cot(k_{dy}d)}{\cos(k_{sy}d)\Delta_a}\right], \tag{9}$$

$$T = -\frac{\exp(-2ik_y d)}{2}\left[\frac{\Delta_s^*}{\Delta_s} - \frac{\Delta_a^*}{\Delta_a}\right], \tag{10}$$

where

$$\Delta_a = -\frac{k_{dy}}{k_y}\cot(k_{dy}d) + i\,\frac{\rho_1}{\rho}\left[\frac{(k_s^2 - 2k_z^2)^2}{k_s^4} + \frac{4k_{sy}k_{dy}k_z^2}{k_s^4}\tan(k_{sy}d)\cot(k_{dy}d)\right], \tag{11}$$

$$\Delta_s = \frac{k_{dy}}{k_y}\tan(k_{dy}d) + i\,\frac{\rho_1}{\rho}\left[\frac{(k_s^2 - 2k_z^2)^2}{k_s^4} + \frac{4k_{sy}k_{dy}k_z^2}{k_s^4}\cot(k_{sy}d)\tan(k_{dy}d)\right]. \tag{12}$$

On the other hand, radiation modes can also be generated by plane waves incident from the liquid under the plate [hereafter called type 2 modes, see Fig. 1(b)]. They are described by the displacement field

$$\mathbf{u}^2 = \boldsymbol{\nabla}\varphi_{\tilde{T}}, \quad d < y, \tag{13}$$
$$\mathbf{u}^2 = \boldsymbol{\nabla}(\varphi_{\tilde{D}^-} + \varphi_{\tilde{D}^+}) + \boldsymbol{\nabla}\times(\boldsymbol{\psi}_{\tilde{S}^-} + \boldsymbol{\psi}_{\tilde{S}^+}), \quad -d < y < d, \tag{14}$$
$$\mathbf{u}^2 = \boldsymbol{\nabla}(\tilde{\varphi}_i + \varphi_{\tilde{R}}), \quad y < -d. \tag{15}$$

The potential functions are represented by

$$\tilde{\varphi}_i = A\ \exp[i(k_y y + k_z z - \omega t)],$$
$$\varphi_{\tilde{R}} = AR\ \exp[i(-k_y y + k_z z - \omega t)],$$
$$\varphi_{\tilde{D}^\pm} = A\tilde{D}^\pm\ \exp[i(\pm k_{dy} y + k_z z - \omega t)], \tag{16}$$
$$\boldsymbol{\psi}_{\tilde{S}^\pm} = A\tilde{S}^\pm\ \exp[i(\pm k_{sy} y + k_z z - \omega t)]\mathbf{e}_x,$$
$$\varphi_{\tilde{T}} = A\tilde{T}\ \exp[i(k_y y + k_z z - \omega t)].$$

The reflection and transmission coefficients $\tilde{R}$, $\tilde{D}^\pm$, $\tilde{S}^\pm$, $\tilde{T}$ are given by expressions (7)–(10) for R, $D^\pm$, $S^\pm$, T with the substitution $\Delta_a \rightarrow (-\Delta_a)$.

A radiation mode can be labeled by its wave vector component k_z. As shown in a previous paper,[10] two radiation modes are orthogonal if their corresponding k_z components are different. Consequently, for the same value of k_z, modes of type 1 and of type 2 are not orthogonal, although both modes have a completely different nature which makes it

necessary to construct linear combinations of the types 1 and 2 that are orthogonal. Performing a similar orthogonalization procedure[10] as for a liquid/solid structure leads to the following two (new) orthogonal types of radiation modes (noted by r_s and r_a):

$$\mathbf{u}^{r_s}=\mathbf{u}^1+\mathbf{u}^2, \tag{17}$$

$$\mathbf{u}^{r_a}=\mathbf{u}^1-\mathbf{u}^2. \tag{18}$$

More explicitly, radiation modes of the type r_s, called symmetrical radiation modes, are described by the displacement components:

if $d<y$:

$$u_y^{r_s}=-Ak_y\cos[k_y(y-d)-\varphi_s], \tag{19}$$

$$u_z^{r_s}=-iAk_z\sin[k_y(y-d)-\varphi_s]; \tag{20}$$

if $-d<y<d$:

$$u_y^{r_s}=Ak_y\cos\varphi_s\left[\frac{2k_z^2-k_s^2}{k_s^2}\frac{\sin(k_{dy}y)}{\sin(k_{dy}d)}-\frac{2k_z^2}{k_s^2}\frac{\sin(k_{sy}y)}{\sin(k_{sy}d)}\right], \tag{21}$$

$$u_z^{r_s}=-i\frac{Ak_yk_z\cos\varphi_s}{k_{dy}}\left[\frac{2k_z^2-k_s^2}{k_s^2}\frac{\cos(k_{dy}y)}{\sin(k_{dy}d)}+\frac{2k_{dy}k_{sy}}{k_x^2}\frac{\cos(k_{sy}y)}{\sin(k_{sy}d)}\right]; \tag{22}$$

if $y<-d$:

$$u_y^{r_s}=Ak_y\cos[k_y(y+d)+\varphi_s], \tag{23}$$

$$u_z^{r_s}=iAk_z\sin[k_y(y+d)+\varphi_s], \tag{24}$$

with

$$\varphi_s(k_y)=\arccos\left[\frac{(k_{dy}/k_y)\tan(k_{dy}d)}{|\Delta_s|}\right]. \tag{25}$$

For these modes, $u_y^{r_s}$ is antisymmetrical and $u_z^{r_s}$ is symmetrical with respect to $y=0$ so that the particle motion in the middle of the plate is purely z oriented. We must remark that from here on, we dropped the factor $\exp[i(k_zz-\omega t)]$ in the expansions of the displacement fields.

Radiation modes of the type r_a, called antisymmetrical radiation modes, are described by the displacement components:

if $d<y$:

$$u_y^{r_a}=-Ak_y\cos[k_y(y-d)-\varphi_a], \tag{26}$$

$$u_z^{r_a}=-iAk_z\sin[k_y(y-d)-\varphi_a]; \tag{27}$$

if $-d<y<d$:

$$u_y^{r_a}=Ak_y\cos\varphi_a\left[\frac{2k_z^2-k_s^2}{k_s^2}\frac{\cos(k_{dy}y)}{\cos(k_{dy}d)}-\frac{2k_z^2\cos(k_{sy}y)}{\cos(k_{sy}d)}\right], \tag{28}$$

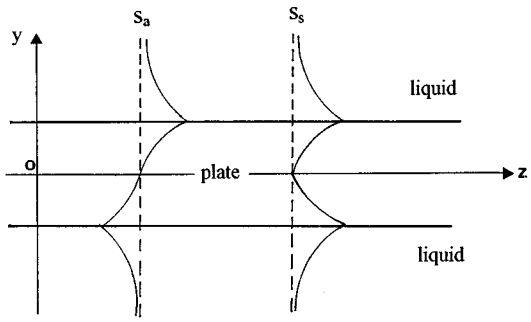

FIG. 2. The displacement amplitude of a symmetrical (s_s) and an antisymmetrical (s_a) Stoneley eigenmode of a liquid/plate/liquid structure.

$$u_z^{r_a}=i\frac{Ak_yk_z\cos\varphi_a}{k_{dy}}\left[\frac{2k_z^2-k_s^2}{k_s^2}\frac{\sin(k_{dy}y)}{\cos(k_{dy}d)}+\frac{2k_{dy}k_{sy}}{k_s^2}\frac{\sin(k_{sy}y)}{\cos(k_{sy}d)}\right], \tag{29}$$

if $y<-d$:

$$u_y^{r_a}=-Ak_y\cos[k_y(y+d)+\varphi_a], \tag{30}$$

$$u_z^{r_a}=-iAk_z\sin[k_y(y+d)+\varphi_a], \tag{31}$$

with

$$\varphi_a(k_y)=\arccos\left[-\frac{k_{dy}\cot(k_{dy}d)}{k_y|\Delta_a|}\right]. \tag{32}$$

For these modes, $u_y^{r_a}$ is symmetrical and $u_z^{r_a}$ is antisymmetrical with respect to $y=0$ so that the particle motion in the middle of the plate is purely y oriented. We remark that in expressions (21), (22), (28), and (29) the components k_{dy} and k_{sy} can be imaginary and in that case the trigonometric functions must be replaced by hyperbolic functions.

B. The discrete spectrum of eigenmodes

A fluid loaded plate can support two eigenmodes (see Fig. 2), a symmetrical and an antisymmetrical Stoneley wave (denoted by s_s and s_a) (see Ref. 12 for a more detailed description). They are the counterparts of the Stoneley wave on an elastic half-space bounded by a liquid.

Implementation of the boundary conditions along the upper and lower side of the plate results in the following displacement field $\vec{u}^{s_a}$ for the symmetrical Stoneley wave:

if $d<y$:

$$u_y^{s_s}=iBk_y\exp[-k_y(y-d)], \tag{33}$$

$$u_z^{s_s}=Bk_z\exp[-k_y(y-d)]; \tag{34}$$

if $-d<y<d$:

$$u_y^{s_s}=2iB\frac{k_yk_z^2}{k_s^2}\left[\left(\frac{k_s^2}{2k_z^2}-1\right)\frac{\sinh(k_{dy}y)}{\sinh(k_{dy}d)}+\frac{\sinh(k_{sy}y)}{\sinh(k_{sy}d)}\right], \tag{35}$$

$$u_z^{s_s}=2B\,\frac{k_y k_z^2}{k_s^2}\left[\frac{(k_z-k_s^2/2k_z)}{k_{dy}}\,\frac{\cosh(k_{dy}y)}{\sinh(k_{dy}d)}-\frac{k_{sy}}{k_z}\,\frac{\cosh(k_{sy}y)}{\sinh(k_{sy}d)}\right]; \tag{36}$$

if $y<-d$:

$$u_y^{s_s}=-iBk_y\,\exp[k_y(y+d)], \tag{37}$$

$$u_z^{s_s}=Bk_z\,\exp[(k_y(y+d)]. \tag{38}$$

The characteristic equation for the symmetrical Stoneley wave from which k_z can be found is

$$k_{dy}k_s^4\,\tanh(k_{dy}d)+4\,\frac{\rho_1}{\rho}\,k_y k_z^2\left[-k_{dy}k_{sy}\,\frac{\tanh(k_{dy}d)}{\tanh(k_{sy}d)}+\left(k_z-\frac{k_s^2}{2k_z}\right)^2\right]=0. \tag{39}$$

The antisymmetrical Stoneley wave is described by the displacement field $\mathbf{u}^{s_a}$:

if $d<y$:

$$u_y^{s_a}=iBk_y\,\exp[-k_y(y-d)], \tag{40}$$

$$u_z^{s_a}=Bk_z\,\exp[-k_y(y-d)], \tag{41}$$

if $-d<y<d$:

$$u_y^{s_a}=2iB\,\frac{k_y k_z^2}{k_s^2}\left[\left(\frac{k_s^2}{2k_z^2}-1\right)\frac{\cosh(k_{dy}y)}{\cosh(k_{dy}d)}+\frac{\cosh(k_{sy}y)}{\cosh(k_{sy}d)}\right], \tag{42}$$

$$u_z^{s_a}=2B\,\frac{k_y k_z^2}{k_s^2}\left[\frac{k_z-\left(\frac{k_z^2}{2k_z}\right)}{k_{dy}}\,\frac{\sinh(k_{dy}y)}{\cosh(k_{dy}d)}-\frac{k_{sy}}{k_z}\,\frac{\sinh(k_{sy}y)}{\cosh(k_{sy}d)}\right], \tag{43}$$

if $y<-d$:

$$u_y^{s_a}=iBk_y\,\exp[k_y(y+d)], \tag{44}$$

$$u_z^{s_a}=-Bk_z\,\exp[(k_y(y+d)]. \tag{45}$$

The characteristic equation for the antisymmetrical Stoneley wave from which k_z can be found is

$$k_{dy}k_s^4\,\frac{1}{\tanh(k_{dy}d)}+4\,\frac{\rho_1}{\rho}\,k_y k_z^2\left[-k_{dy}k_{sy}\,\frac{\tanh(k_{sy}d)}{\tanh(k_{dy}d)}+\left(k_z-\frac{k_s^2}{2k_z}\right)^2\right]=0. \tag{46}$$

To summarize, the orthogonal set of acoustic modes for a liquid/plate/liquid structure consists of two eigenmodes and two different types of radiation modes. Two acoustic modes of the set, labeled by the wave vector components $k_z^{(1)}$ and $k_z^{(2)}$, are orthogonal in the sense of[10]

$$\int_{-\infty}^{+\infty}\sum_{k=y,z}[T_{kz}^{\alpha}(k_z^{(1)})u_k^{\beta *}(k_z^{(2)})-T_{kz}^{\beta *}(k_z^{(2)})u_k^{\alpha}(k_z^{(1)})]dy = N\delta_{\alpha\beta}\delta(k_z^{(1)}-k_z^{*(2)})$$

(general orthogonality condition), (47)

or

$$\int_{-\infty}^{+\infty}[T_{yz}^{\alpha *}(k_z^{(1)})u_y^{\beta}(k_z^{(2)})-T_{zz}^{\beta}(k_z^{(2)})u_z^{\alpha *}(k_z^{(1)})]dy = N_1\delta_{\alpha\beta}\delta(k_z^{(1)}-k_z^{*(2)})+N_2\delta_{\alpha\beta}\delta(k_z^{(1)}+k_z^{*(2)})$$

(simplified orthogonality condition). (48)

An asterisk denotes the complex conjugation. N, N_1, N_2 are normalization constants. These relations express that even when two modes have the same k_z components but are of a different type ($\alpha\neq\beta$), they are orthogonal ($\alpha,\beta=r_a$, r_s, s_a, s_s). For eigenmodes, one must replace the delta function by the Kronecker symbol. The simplified orthogonality condition may not be handled for modes propagating in opposite direction[10] (i.e., $k_z^{(1)}=-k_z^{(2)}$).

II. THE ORTHOGONAL SET OF ACOUSTIC MODES FOR A HOMOGENEOUS LIQUID STRUCTURE

Strictly speaking, one can, in a homogeneous liquid structure, also distinguish two kinds of radiation modes, respectively, represented by plane waves emerging from $y=+\infty$:

$$\mathbf{u}=B\mathbf{k}\;\exp(-ik_y y+ik_z z) \tag{49}$$

and plane waves emerging from $y=-\infty$:

$$\mathbf{u}=B\mathbf{k}\,\exp(ik_y y+ik_z z). \tag{50}$$

Adding and subtracting the displacement fields given by Eqs. (49) and (50), results in two orthogonal types of radiation modes:

the symmetrical ones, for which

$$u_y^{r_s}=Bk_y\,\sin(k_y y),\quad u_z^{r_s}=-iBk_z\,\cos(k_y y); \tag{51}$$

and the antisymmetrical ones, for which

$$u_y^{r_a}=Bk\,\cos(k_y y),\quad u_z^{r_a}=iBk_z\,\sin(k_y y). \tag{52}$$

III. CONVERSION OF A STONELEY WAVE AT THE END OF A PLATE

We apply the mode theory to the configuration sketched in Fig. 3. This configuration is formed by a liquid/plate/liquid structure and a homogeneous liquid structure. When an incident Stoneley wave, propagating at the upper side of the plate, reaches the extremity of the plate, scattering and mode conversion occur. All scattered and mode converted waves can be expanded in the complete and orthogonal set of acoustic modes which is specific for the structure to which they belong.

In the liquid/plate/liquid structure ($z<0$) the most complete representation for the total acoustic field ($\mathbf{u}_2^{\text{tot}}$) is a superposition of three fields which we can expand as

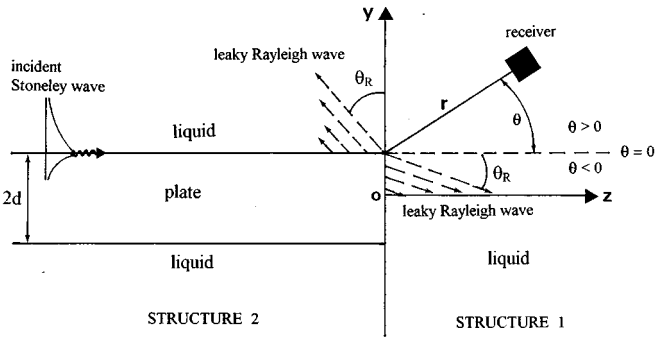

FIG. 3. Configuration for the scattering and mode conversion of a Stoneley wave at the edge of a fluid loaded thick plate.

$$\mathbf{u}_2^i(\mathbf{r}) = \sum_m C^i_{s_m}\mathbf{u}_2^{s_m}(\mathbf{r}) \quad \text{(incident Stoneley wave)}, \tag{53}$$

$$\mathbf{u}_2^r(\mathbf{r}) = \int_0^{+\infty}\sum_m C^r_{r_m}(k_{y,2})\mathbf{u}_2^{r_m}(k_{y,2};\mathbf{r})dk_{y,2} \quad \text{(reflected bulk wave)}, \tag{54}$$

$$\mathbf{u}_2^{\text{ston}}(\mathbf{r}) = \sum_m C^r_{s_m}\mathbf{u}_2^{s_m}(\mathbf{r}) \quad \text{(reflected Stoneley wave)}, \tag{55}$$

while in the homogeneous liquid structure ($z>0$) we only have a transmitted bulk wave ($\mathbf{u}_1^t$) so that

$$\mathbf{u}_1^{\text{tot}}(\mathbf{r}) = \mathbf{u}_1^t(\mathbf{r}) = \int_0^{+\infty}\sum_m C^t_{r_m}(k_{y,1})\mathbf{u}_1^{r_m}(k_{y,1};\mathbf{r})dk_{y,1}. \tag{56}$$

Similar mode expansions have to be used for the stress tensor components, i.e.,

$$T^i_{kl,2}(\mathbf{r}) = \sum_m C^i_{s_m}T^{s_m}_{kl,2}(\mathbf{r}), \tag{57}$$

$$T^r_{kl,2}(\mathbf{r}) = \int_0^{+\infty}\sum_m C^r_{r_m}(k_{y,2})T^{r_m}_{kl,2}(k_{y,2};\mathbf{r})dk_{y,2}, \tag{58}$$

$$T^{\text{ston}}_{kl,2}(\mathbf{r}) = \sum_m C^r_{s_m}T^{s_m}_{kl,2}(\mathbf{r}), \tag{59}$$

$$T^t_{kl,1}(\mathbf{r}) = \int_0^{+\infty}\sum_m C^t_{r_m}(k_{y,1})T^{r_m}_{kl,1}(k_{y,1};\mathbf{r})dk_{y,1}. \tag{60}$$

The subscripts 1 and 2 are always used to distinguish between quantities belonging to the structures 1 and 2. In these field representations one must substitute the displacement field $\mathbf{u}_i^m$ of, respectively, a symmetrical ($m=s$) and an antisymmetrical ($m=a$) radiation mode in structure i ($i=1,2$) by, respectively, expressions (19)–(24) and expressions (26)–(31), while the displacement field $\mathbf{u}_2^{s_m}$ of, respectively, a symmetrical and an antisymmetrical (Stoneley) eigenmode in the liquid/plate/liquid structure has to be substituted by, respectively, expressions (33)–(38) and expressions (40)–(45). The incident and reflected Stoneley wave are thus expanded in a symmetrical and antisymmetrical eigenmode of the liquid/plate/liquid structure. Each integral is taken over the continuous spectrum of radiation modes. The sum following the integral serves as a reminder that the contributions of the different types of radiation modes must be added. To cross the whole spectrum of radiation modes one lets vary the y component of the wave vector from zero up to infinity. The corresponding z component of the wave vector is then real or purely imaginary. In this way we include propagating radiation modes (k_z is real) as well as nonpropagating (or evanescent) radiation modes (k_z is purely imaginary).

The expansion coefficients $C^i_{s_m}$ for the incident Stoneley wave may be assumed to be known. To find the unknown expansion coefficients $C^r_{r_m}$, $C^t_{r_m}$, and $C^r_{s_m}$ we proceed as follows.

From the boundary conditions along the separation plane ($z=0$) between both structures

$$u^{\text{tot}}_{y,1} = u^{\text{tot}}_{y,2} \quad \forall y \epsilon [-d,d], \tag{61}$$

$$u^{\text{tot}}_{z,1} = u^{\text{tot}}_{z,2} \quad \forall y, \tag{62}$$

$$T^{\text{tot}}_{yz,1} = T^{\text{tot}}_{yz,2} \quad \forall y, \tag{63}$$

$$T^{\text{tot}}_{zz,1} = T^{\text{tot}}_{zz,2} \quad \forall y, \tag{64}$$

follow the four equalities

$$\int_{-\infty}^{+\infty}[T^{\text{tot}}_{zz,1}u^{r_m*}_{z,1}(k'_{y,1}) - T^{r_m*}_{yz,1}(k'_{y,1})u^{\text{tot}}_{y,1}]_{z=0}\,dy = \int_{-\infty}^{+\infty}[T^{\text{tot}}_{zz,2}u^{r_m*}_{z,1}(k'_{y,1}) - T^{r_m*}_{yz,1}(k'_{y,1})u^{\text{tot}}_{y,2}]_{z=0}\,dy, \quad m=s,a, \tag{65}$$

$$\int_{-\infty}^{+\infty}[T^{\text{tot}}_{yz,1}u^{r_m*}_{y,1}(k'_{y,1}) - T^{r_m*}_{zz,1}(k'_{y,1})u^{\text{tot}}_{z,1}]_{z=0}\,dy = \int_{-\infty}^{+\infty}[T^{\text{tot}}_{yz,2}u^{r_m*}_{y,1}(k'_{y,1}) - T^{r_m*}_{zz,1}(k'_{y,1})u^{\text{tot}}_{z,2}]_{z=0}\,dy, \quad m=s,a, \tag{66}$$

with $u^{r_m}_{y,1}$, $u^{r_m}_{z,1}$, $T^{r_m}_{yz,1}$, and $T^{r_m}_{zz,1}$ components of a fixed symmetrical or antisymmetrical radiation mode (marked by $k'_{y,1}$) belonging to structure 1. Using the simplified orthogonality condition (48) we find the integral equations

$$C^t_{r_m}(k_{y,1}).\mathscr{K}^{r_m r_m}_{11}(k_{y,1}) = C^i_{s_m}K^{s_m r_m}_{21}(k_{y,1}) + \int_0^{+\infty}C^r_{r_m}(k_{y,2}) \times K^{r_m r_m}_{21}(k_{y,1};k_{y,2})dk_{y,2}, \quad m=s,a, \tag{67}$$

$$C^t_{r_m}(k_{y,1}).\mathscr{T}^{r_m r_m}_{11}(k_{y,1}) = C^i_{s_m}I^{s_m r_m}_{21}(k_{y,1}) + \int_0^{+\infty}C^r_{r_m}(k_{y,2}) \times I^{r_m r_m}_{21}(k_{y,1};k_{y,2})dk_{y,2}, \quad m=s,a, \tag{68}$$

TABLE I. Values of medium constants used for the calculations.

Medium	Longitudinal velocity v_d [m/s]	Transverse velocity v_s [m/s]	Density ρ [kg/m^3]
Aluminum	6350	3100	2800
Brass	4280	2245	8100
Steel	5720	3160	7800
Pyrex glass	5570	3440	2230
Water	1460	⋯	1000

with

$$K_{11}^{r_m r_m}=\mathscr{K}_{11}^{r_m r_m}\delta(k_{y,1}-k'_{y,1}),\quad I_{11}^{r_m r_m}=\mathscr{I}_{11}^{r_m r_m}\delta(k_{y,1}-k'_{y,1}).$$

Here, $I_{ij}^{\alpha\beta}$ and $K_{ij}^{\alpha\beta}$ are defined as the so-called overlap integrals

$$I_{ij}^{\alpha\beta}=\int_{-\infty}^{+\infty}[T_{yz,i}^{\alpha}(k_{y,i})u_{y,j}^{\beta *}(k_{y,j}) - T_{zz,j}^{\beta *}(k_{y,j})u_{z,i}^{\alpha}(k_{y,i})]_{z=0}\,dy, \tag{69}$$

$$K_{ij}^{\alpha\beta}=\int_{-\infty}^{+\infty}[T_{zz,i}^{\alpha}(k_{y,i})u_{z,j}^{\beta *}(k_{y,j}) - T_{yz,j}^{\beta *}(k_{y,j})u_{y,i}^{\alpha}(k_{y,i})]_{z=0}\,dy, \tag{70}$$

which describe the interactions that take place in the separation plane $z=0$ between a radiation mode (or eigenmode) of the type α in structure i and a radiation mode of the type β in structure j ($\alpha,\beta=r_s,r_a,s_s,s_a$; $i,j=1,2$). We remark that overlap integrals between symmetrical and anti-symmetrical modes are identically zero.

The energy carried by the incident Stoneley wave is mainly located in the liquid. At the edge of the plate most of its energy will be transformed into the transmitted bulk wave. Therefore we neglect in a zeroth-order approximation the reflected bulk wave $[C_{r_m}^{r}(k_{y,2})=0]$. Since the overlap integrals $I_{11}^{r_m r_m}$ and $K_{11}^{r_m r_m}$ are equal and since the overlap integrals $I_{21}^{s_m r_m}$ and $K_{21}^{s_m r_m}$ are of the same order of magnitude, the symmetrical ($C_{r_s}^{t}$) and antisymmetrical ($C_{r_a}^{t}$) expansion coefficients for the transmitted bulk wave take the form

$$C_{r_m}^{t}(k_{y,1})=C_{s_m}^{i}\frac{K_{21}^{s_m r_m}(k_{y,1})}{\mathscr{K}_{11}^{r_m r_m}(k_{y,1})} =\pm C_{s_m}^{i}\frac{B_2^{s_m}}{B_1^{r_m}}\,i\,\frac{2}{\pi}\,\frac{\rho_1}{\rho}\,\frac{k_{z,2}^{s_m}}{k_{z,1}}\,[M_{12}^{r_m s_m}(k_{y,1})]^{*},\quad m=s,a. \tag{71}$$

The minus sign must be used for the antisymmetrical expansion coefficient ($m=a$). $B_1^{r_m}$ and $B_2^{s_m}$ are the arbitrary amplitudes of a radiation mode in structure 1 and of a Stoneley eigenmode in structure 2. The z component of the wave vector of a Stoneley eigenmode in structure 2, $k_{z,2}^{s_m}$, must be calculated from the transcendent equation (39) if $m=s$ or from Eq. (46) if $m=a$. The evaluation of the overlap integrals $K_{21}^{s_m r_m}$ is a complicated and longwinded procedure. The cumbersome expressions for the functions $M_{12}^{r_m s_m}$ ($m=s,a$) are given in the Appendix.

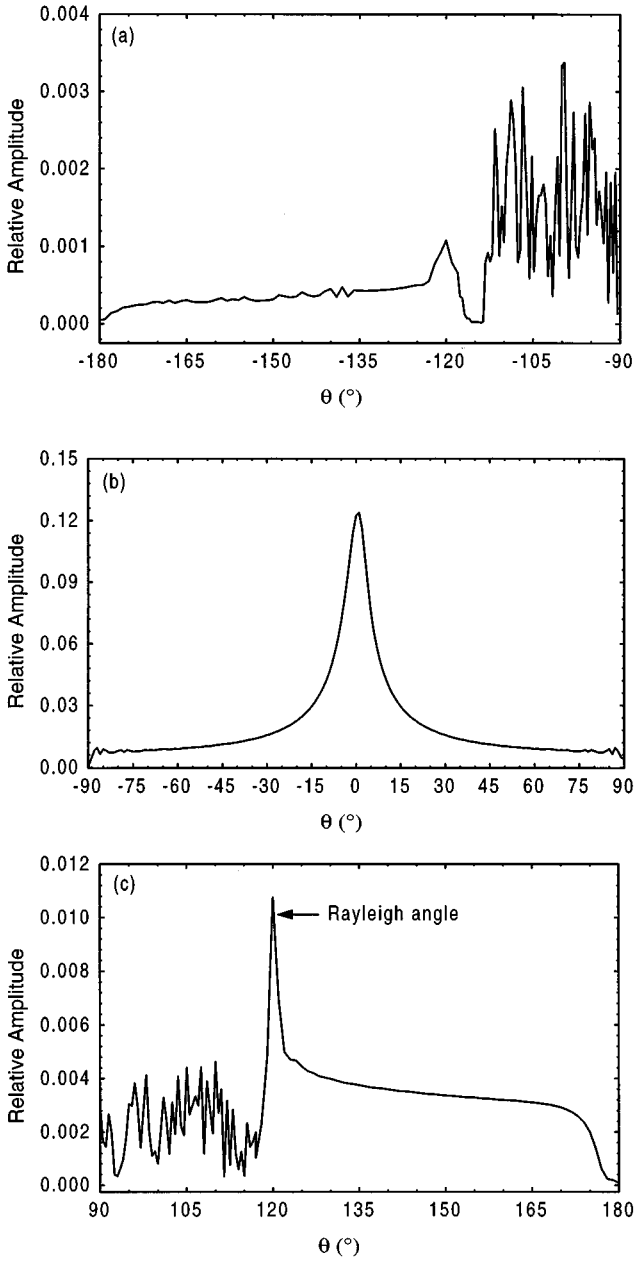

FIG. 4. Scattering of a 5-Mhz Stoneley wave at the end of a water loaded aluminum plate of 1-cm thickness. Theoretically calculated relative amplitude of the (a) reflected bulk wave beneath the plate, (b) transmitted bulk wave in the water, (c) reflected bulk wave above the plate in the direction θ of the receiver ($r=15$ cm).

In (A1)–(A2), the first term represents the contribution to the overlap integral $K_{21}^{s_m r_m}$ from the integration over the liquid, while all other terms arise from the integration over the plate. Physically, the function $M_{12}^{r_m s_m}$ describes the interactions that occur between the radiation modes of structure 1 and the Stoneley eigenmodes of structure 2.

To obtain a first-order approximation for the expansion coefficients $C_{r_m}^{r}$ for the reflected bulk wave we now work out equalities (65)–(66) for the components $u_{y,2}^{r_m}(k'_{y,2})$, $u_{z,2}^{r_m}(k'_{y,2})$, $T_{yz,2}^{r_m}(k'_{y,2})$, and $T_{zz,2}^{r_m}(k'_{y,2})$ of a fixed symmetrical and antisymmetrical radiation mode (marked by $k'_{y,2}$) belonging to structure 2, yielding the four integral equations

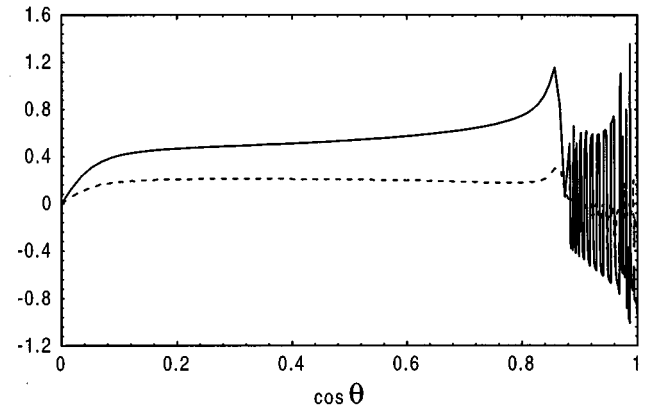

FIG. 5. The real part (solid line) and imaginary part (dashed line) of the symmetrical expansion coefficient $(C^r_{r_s} B^{r_s}_2 k)/(C^i_{s_s} B^{s_s}_2)$ [see Eq. (3.71)] as a function of the cosine of the mode angle θ (water/aluminum/water structure).

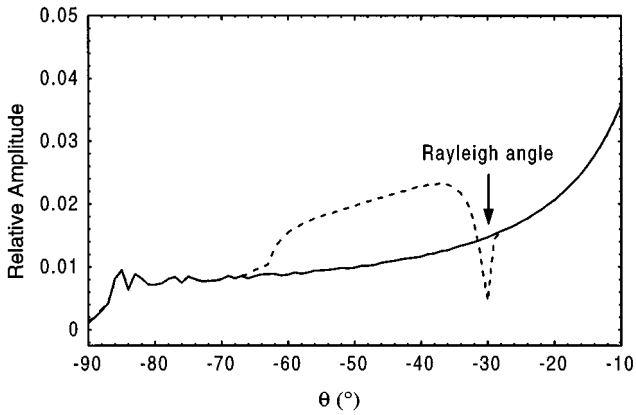

FIG. 7. Scattering of a 5-MHz Stoneley wave at the end of water loaded aluminum plate of 1-cm thickness. Correction (dashed line) to the zeroth-order approximation (solid line) for the relative amplitude of the transmitted bulk wave in the direction θ of the receiver ($r=15$ cm).

$$C^r_{r_m}(k_{y,2}).\mathscr{K}^{r_m r_m}_{22}(k_{y,2}) = \int_0^{+\infty} C^t_{r_m}(k_{y,1}) K^{r_m r_m}_{12}(k_{y,1};k_{y,2})\,dk_{y,1}, \quad m=s,a, \quad (72)$$

$$-C^r_{r_m}(k_{y,2}).\mathscr{T}^{r_m r_m}_{22}(k_{y,2}) = \int_0^{+\infty} C^t_{r_m}(k_{y,1}) I^{r_m r_m}_{12}(k_{y,1};k_{y,2})\,dk_{y,1}, \quad m=s,a, \quad (73)$$

with $K^{r_m r_m}_{22} = \mathscr{K}^{r_m r_m}_{22}\delta(k_{y,2} - k'_{y,2})$. Subtracting the integral equations, we have

$$C^r_{r_m}(k_{y,2}) = \frac{1}{2.\mathscr{K}^{r_m r_m}_{22}} \int_0^{+\infty} C^t_{r_m}(k_{y,1})[K^{r_m r_m}_{12}(k_{y,1};k_{y,2}) - I^{r_m r_m}_{12}(k_{y,1};k_{y,2})]\,dk_{y,1}, \quad m=s,a. \quad (74)$$

Substituting $C^t_{r_m}(k_{y,1})$ by the zeroth-order approximation (71) and evaluating the overlap integrals $K^{r_m r_m}_{22}$, $K^{r_m r_m}_{12}$, and $I^{r_m r_m}_{12}$, we finally find

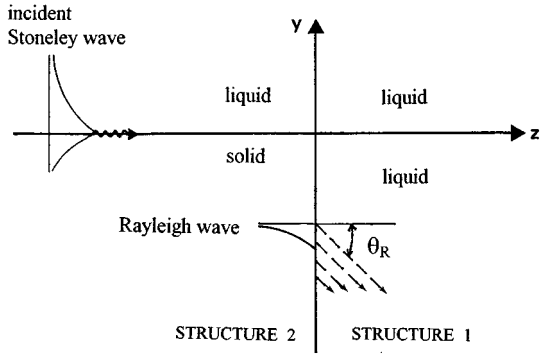

FIG. 6. An alternative configuration to resolve the leaky Rayleigh wave in transmission.

$$C^r_{r_m}(k_{y,2}) = \pm C^i_{s_m} \frac{B^{s_m}_2}{B^{r_m}_2}\, i\, \frac{1}{\pi^2}\, \frac{\rho_1}{\rho}\, \frac{k^{s_m}_{z,1}}{k_{z,2}} \int_0^{+\infty} [M^{r_m s_m}_{12}(k_{y,1})]^* \times \left[\frac{k^*_{z,2}}{k_{z,1}} R^{r_m r_m}_{12}(k_{y,1};k_{y,2}) - N^{r_m r_m}_{12}(k_{y,1};k_{y,2})\right] dk_{y,1}, \quad m=s,a. \quad (75)$$

The minus sign must be used for the symmetrical expansion coefficient. The detailed expressions for the functions $R^{r_m r_m}_{12}$ and $N^{r_m r_m}_{12}$ appearing in the integrand of Eq. (75) are summed up in the Appendix equations (A3)–(A17).

The symbol P in expressions (A7) and (A8) stands for ''principal value.'' The first term in the expressions for the functions $R^{r_m r_m}_{12}$ and $N^{r_m r_m}_{12}$ arises from the integration over the liquid (the so-called delta approximation) while all other terms arise from the integration over the plate. Physically these functions incorporate the interactions that occur between the radiation modes of the structures 1 and 2.

First-order approximations for the expansion coefficients $C^r_{s_m}$ for the reflected Stoneley wave are found by repeating the above described procedure with the components $u^{s_m}_{y,2}$, $u^{s_m}_{z,2}$, $T^{s_m}_{yz,2}$, and $T^{s_m}_{zz,2}$ of a symmetrical and antisymmetrical Stoneley eigenmode of structure 2. The resulting integral equations now take the form [see the similarity with the integral equations (74)]

$$C^r_{s_m} = \frac{1}{2K^{s_m s_m}_{22}} \int_0^{+\infty} C^t_{r_m}(k_{y,1})[K^{r_m s_m}_{12}(k_{y,1}) - I^{r_m s_m}_{12}(k_{y,1})]\,dk_{y,1}, \quad m=s,a. \quad (76)$$

Substituting $C^t_{r_m}$ by the zeroth-order approximation (71) and evaluating the overlap integrals $K^{s_m s_m}_{22}$, $K^{r_m s_m}_{12}$, and $I^{r_m s_m}_{12}$ lead to

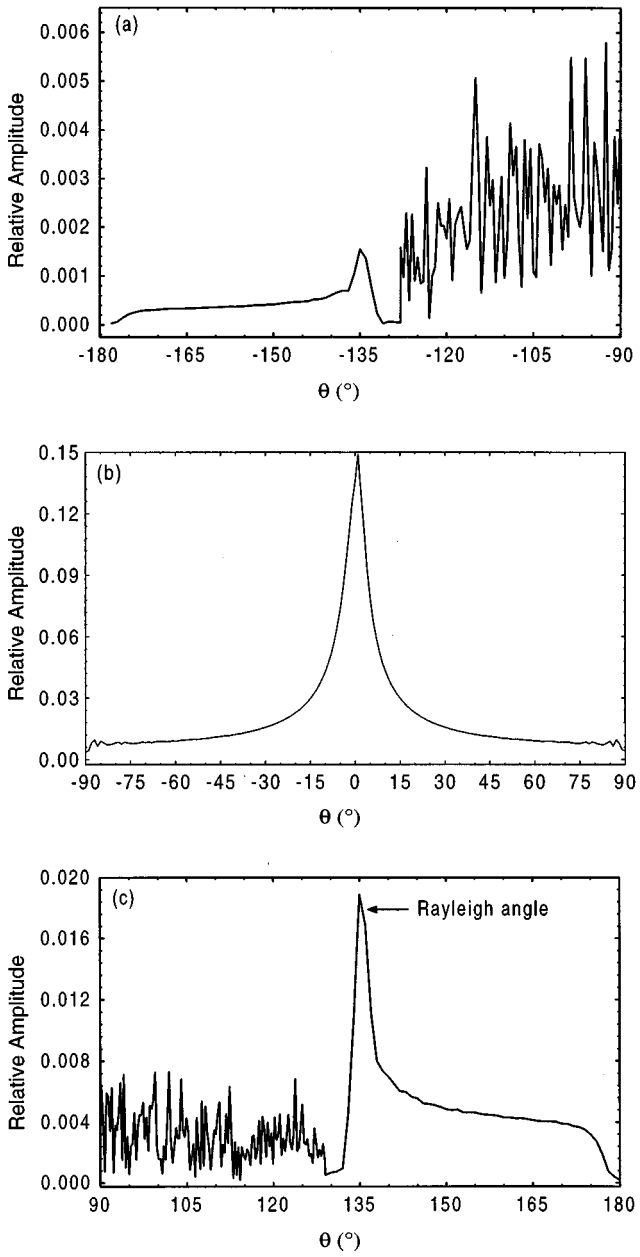

FIG. 8. Scattering of a 5-MHz Stoneley wave at the end of a water loaded brass plate of 1-cm thickness. Theoretically calculated relative amplitude of the (a) reflected bulk wave beneath the plate, (b) transmitted bulk wave in the water, (c) reflected bulk wave above the plate in the direction θ of the receiver ($r=15$ cm).

$$C^r_{s_m} = C^i_{s_m}\,\frac{4}{\pi}\left(\frac{\rho_1}{\rho}\right)^2\frac{1}{k^2}\,k^{s_m}_{y,2}\;k^{s_m}_{z,2} \times \int_0^{+\infty}\frac{1}{k_{z,1}}\,|M^{r_m s_m}_{12}(k_{y,1})|^2 dk_{y,1}, \quad m=s,a. \quad (77)$$

Substituting solutions (71), (75), and (77) for the unknown expansion coefficients $C^t_{r_m}$, $C^r_{r_m}$, and $C^r_{s_m}$ into the mode expansions (53)–(56), the displacement fields of all scattered and mode converted waves arising in the considered problem are known.

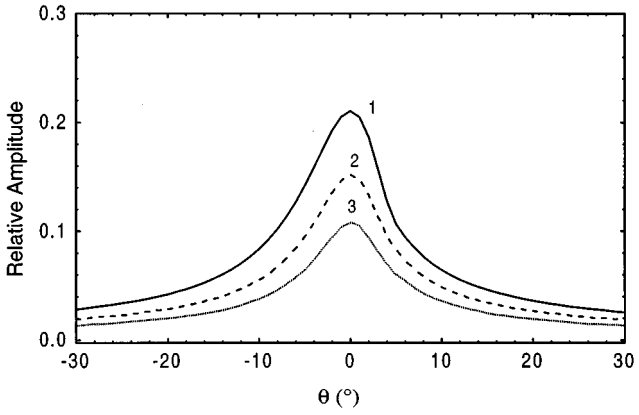

FIG. 9. Scattering of a 5-Mhz Stoneley wave at the end of a water loaded aluminum plate of 1-cm thickness. Relative amplitude of the transmitted bulk wave in the direction θ of the receiver for different distances r between edge and receiver: (1) $r=5$ cm, (2) $r=10$ cm, (3) $r=20$ cm.

IV. NUMERICAL RESULTS AND DISCUSSION

The behavior of the Stoneley wave when it reaches the extremity of a fluid loaded thick plate was studied experimentally by Tinel.[3] The superposition of two phenomena was established: the first one being the simple forward diffraction of the Stoneley wave in the liquid and the second one being its conversion into two leaky Rayleigh waves,

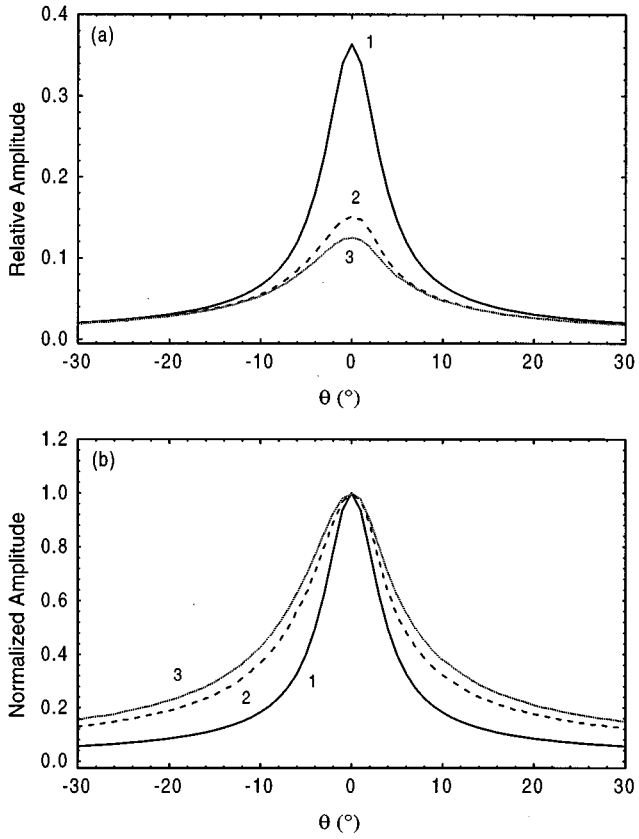

FIG. 10. Scattering of a 5-Mhz Stoneley wave at the end of a water loaded plate of 1-cm thickness. (a) Relative amplitude of the transmitted bulk wave in the direction θ of the receiver ($r=10$ cm) for different solid samples (1) steel, (2) aluminum, (3) Pyrex glass. (b) Normalized amplitude for the same solid samples as in (a).

namely the reflected and the transmitted Rayleigh wave. The reflected Rayleigh wave propagates along the same plane as the incident Stoneley wave, whereas the transmitted Rayleigh wave propagates along the vertical end face of the plate. The corresponding angles of observation (see Fig. 3) are $\theta=90°+\theta_R$ for the reflected and $\theta=-\theta_R$ for the transmitted Rayleigh wave, with θ_R the Rayleigh angle of the solid sample.

We performed numerical calculations for an aluminum and for a brass plate of 1-cm ($=2d$) thickness immersed in water. The values of the medium constants are given in Table I. The frequency of the incident Stoneley wave is 5 MHz. Figure 4(a) and (c) represents the amplitude of the total displacement field (relative to the amplitude of the incident Stoneley wave) beneath and above an aluminum plate in the direction θ of the receiver at a distance r of 15 cm. We remark that, theoretically, a Stoneley wave propagating along the upper side of a thick plate ($2dk \gg 1$) is described as the superposition of a symmetrical and antisymmetrical (Stoneley) eigenmode (see Fig. 2). Since for a plate with $2d=1$ cm, $k_{z,2}^{s_s} \approx k_{z,2}^{s_a}$, the amplitude of the incident Stoneley wave at ($y=0$, $z=d$) is given by

$$u_z^i = \sum_m C_{s_m}^i B_2^{s_m} k_{z,2}^{s_m} \approx 2 C_{s_s}^i B_2^{s_s} k_{z,2}^{s_s}.$$

To obtain the results in Fig. 4(a) and (c), we substituted the expansion coefficients represented by the complex one-dimensional integrals (75) into mode expansion (54), resulting in the evaluation of a complex two-dimensional integral. To emphasize the complexity of the integrals that have to be calculated in this problem, we represented in Fig. 5, as an example, the strongly oscillating character of the real and imaginary part of the symmetrical expansion coefficient $C_{r_s}^m$. We note that in this figure the first maximum occurs at the Rayleigh angle. The other peaks occur at the Lamb angles which, for a thick plate, are situated very close to each other.

Figure 4(b) shows the relative amplitude of the transmitted bulk wave in water. To obtain this result, we substituted expansion coefficient (71) in mode expansion (56). As expected, the maximum diffraction is obtained for $\theta=0°$. The secondary maximum at $\theta=120°$ corresponds to the reflected Rayleigh wave (the Rayleigh angle for aluminum is 30°). A good similarity (qualitatively and even quantitatively) exists between theory and experiment,[3] except that the transmitted Rayleigh wave (observed in the experiment as a minimum in the diffracted signal at $\theta=-30°$) has not shown up in Fig. 4(b). The reason for this is that for the calculation of the transmitted bulk wave we restricted ourselves to a zeroth-order approximation. Theoretically we found that, in order to obtain the mentioned minimum, a second-order approximation for the expansion coefficient $C_{r_m}^t$ is necessary. The obtained expression is a complex two-dimensional integral. Substituting that integral in mode expansion (56), we finally have to evaluate a cumbersome complex three-dimensional integral.

For thick plates we also developed another approach[14] whereby the liquid/plate/liquid structure is replaced by a liquid/solid structure (see Fig. 6). The incident Stoneley wave propagates along the $y=0$ interface. The excited leaky Rayleigh wave, propagating along the interface $z=0$, can now be described in structure 2 by evanescent radiation modes for a liquid/solid structure because of its exponentially decaying character in the $-z$ direction. In structure 1 (homogeneous liquid) the leaky Rayleigh wave is described by propagating radiation modes. The diffraction problem is now described by an infinite system of coupled complex integral equations in the unknown expansion coefficients for the scattered and mode converted waves. Taking into account only the coupling between a finite number of acoustic modes, the infinite system of equations can be limited and approximate expressions for the expansion coefficients $C_{r_m}^t (m = s,a)$ may be found. On the basis of this approach we obtained for an aluminum sample immersed in water the result that is shown in Fig. 7. We calculated the relative amplitude of the displacement field (in the direction of the receiver) for the transmitted bulk wave. The dashed line shows the correction to the result presented in Fig. 4(b). The dip near the Rayleigh angle did now clearly show up and the resulting graph is remarkably similar to the experimental one.[13]

In Fig. 8(a)–(c) numerical results are presented for a brass plate. A secondary maximum is now found at an angle $\theta=135°$ (the Rayleigh angle for brass is 45°), again corresponding to a mode converted reflected Rayleigh wave. The strong oscillating patterns in the Figs. 4(a), (c) and 8(a), (c) near the extremities of the plate (i.e., $\theta=90°$, $\theta=-90°$) can be attributed to interferences between re-emitted leaky Lamb waves.

All calculated relative amplitudes are highly dependent on the distance r between edge and receiver. This feature is illustrated in Fig. 9 for the purely forward diffraction in water. Figure 10 shows the relative amplitude of the transmitted bulk wave in water for different solid samples. The larger the Stoneley wave localization length in the liquid, the larger the relative amplitude [Fig. 10(a)] and the narrower the beam [Fig. 10(b)] emitted at the end of the solid (also in correspondence with the experimental observations of Tinel[13]).

V. CONCLUSION

Mode theory has been used to investigate the interaction of a Stoneley wave with the extremity of its solid support. Among the essential results, the Stoneley wave conversion into generalized Rayleigh waves on the two sides of the extremity must be noted. The conversion phenomenon can be very important in the field of NDE since the same conversion will occur when a Stoneley wave detects cracks, inclusions or when it reaches another support. In all cases, a generalized Rayleigh wave starts to exist at each irregularity and re-emits energy in a direction specific to the considered material.

ACKNOWLEDGMENT

The authors would like to thank the Research Council of the K. U. Leuven for the fellowship awarded to Professor Dr. G. N. Shkerdin, which enabled us to write this paper.

APPENDIX

$$M_{12}^{r_s s_s}(k_{y,1}) = \frac{\rho}{\rho_1}\frac{k_{y,2}^{s_s}\cos(k_{y,1}d) - k_{y,1}\sin(k_{y,1}d)}{k_{y,1}^2 + (k_{y,2}^{s_s})^2}$$
$$+ \frac{\rho}{\rho_1}\frac{2k_{y,2}^{s_s}k_{z,2}^{s_a}}{k_s^2}\left[\frac{k_{z,2}^{s_s} - k_s^2/2k_{z,2}^{s_s}}{k_{dy,2}^{s_s}}\frac{k_{dy,2}^{s_s}\cos(k_{y,1}d) + k_{y,1}\sin(k_{y,1}d)\coth(k_{dy,2}^{s_s}d)}{k_{y,1}^2 + (k_{dy,2}^{s_s})^2}\right.$$
$$\left. - \frac{k_{sy,2}^{s_s}}{k_{z,2}^{s_s}}\frac{k_{sy,2}^{s_s}\cos(k_{y,1}d) + k_{y,1}\sin(k_{y,1}d)\coth(k_{sy,2}^{s_s}d)}{k_{y,1}^2 + (k_{sy,2}^{s_s})^2}\right] - \frac{2k_{y,2}^{s_s}(2(k_{z,2}^{s_s})^2 - k_t^2)}{k_t^4}$$
$$\times k_{y,1}\left[\frac{k_{dy,2}^{s_s}\sin(k_{y,1}d)\coth(k_{dy,2}^{s_s}d) - k_{y,1}\cos(k_{y,1}d)}{k_{y,1}^2 + (k_{dy,2}^{s_s})^2} - \frac{k_{sy,2}^{s_s}\sin(k_{y,1}d)\coth(k_{sy,2}^{s_s}d) - k_{y,1}\cos(k_{y,1}d)}{k_{y,1}^2 + (k_{sy,2}^{s_s})^2}\right], \quad \text{(A1)}$$

$$M_{12}^{r_a s_a}(k_{y,1}) = \frac{\rho}{\rho_1}\frac{k_{y,1}\cos(k_{y,1}d) + k_{y,2}^{s_a}\sin(k_{y,1}d)}{k_{y,1}^2 + (k_{y,2}^{s_a})^2}$$
$$+ \frac{\rho}{\rho_1}\frac{2k_{y,2}^{s_a}k_{z,2}^{s_a}}{k_s^2}\left[\frac{k_{z,2}^{s_a} - k_s^2/2k_{z,2}^{s_a}}{k_{dy,2}^{s_a}}\frac{k_{dy,2}^{s_a}\sin(k_{y,1}d) - k_{y,1}\cos(k_{y,1}d)\tanh(k_{dy,2}^{s_a}d)}{k_{y,1}^2 + (k_{dy,2}^{s_a})^2}\right.$$
$$\left. - \frac{k_{sy,2}^{s_a}}{k_{z,2}^{s_a}}\frac{k_{sy,2}^{s_a}\sin(k_{y,1}d) - k_{y,1}\cos(k_{y,1}d)\tanh(k_{sy,2}^{s_a}d)}{k_{y,1}^2 + (k_{sy,2}^{s_a})^2}\right]$$
$$+ \frac{2k_{y,2}^{s_a}(2(k_{z,2}^{s_a})^2 - k_t^2)}{k_t^4}k_{y,1}\left[\frac{k_{dy,2}^{s_a}\cos(k_{y,1}d)\tanh(k_{dy,2}^{s_a}d) + k_{y,1}\sin(k_{y,1}d)}{k_{y,1}^2 + (k_{dy,2}^{s_a})^2}\right.$$
$$\left. - \frac{k_{sy,2}^{s_a}\cos(k_{y,1}d)\tanh(k_{sy,2}^{s_a}d) + k_{y,1}\sin(k_{y,1}d)}{k_{y,1}^2 + (k_{sy,2}^{s_a})^2}\right]. \quad \text{(A2)}$$

$$R_{12}^{r_a r_a}(k_{y,1};k_{y,2}) = F + \frac{1}{|\Delta_a|}\left\{\alpha_1\frac{1}{\sin^*(k_{dy,1}d)}(D_1 - D_2) + \alpha_2\frac{\cot^*(k_{dy,1}d)}{\cos^*(k_{sy,1}d)}(S_1 - S_2)\right.$$
$$\left. + \alpha_3\frac{\rho_1}{\rho}\cot^*(k_{dy,1}d)\left[\frac{1}{\cos^*(k_{dy,1}d)}(D_1 + D_2) - \frac{1}{\cos^*(k_{sy,1}d)}(S_1 + S_2)\right]\right\}, \quad \text{(A3)}$$

$$R_{12}^{r_s r_s}(k_{y,1};k_{y,2}) = G - \frac{1}{|\Delta_s|}\left\{\alpha_1\frac{1}{\cos^*(k_{dy,1}d)}(D_1 + D_2) + \alpha_2\frac{\tan^*(k_{dy,1}d)}{\sin^*(k_{sy,1}d)}(S_1 + S_2)\right.$$
$$\left. + \alpha_3\frac{\rho_1}{\rho}\tan^*(k_{dy,1}d)\left[\frac{1}{\sin^*(k_{dy,1}d)}(D_1 - D_2) - \frac{1}{\sin^*(k_{sy,1}d)}(S_1 - S_2)\right]\right\}, \quad \text{(A4)}$$

$$N_{12}^{r_a r_a}(k_{y,1};k_{y,2}) = F + \frac{1}{|\Delta_a|}\frac{\rho_1}{\rho}\left[\alpha_4\frac{1}{\sin^*(k_{dy,1}d)}(D_1 - D_2) + \alpha_5\frac{\cot^*(k_{dy,1}d)}{\cos^*(k_{sy,1}d)}(S_1 - S_2)\right], \quad \text{(A5)}$$

$$N_{12}^{r_s r_s}(k_{y,1};k_{y,2}) = G - \frac{1}{|\Delta_s|}\frac{\rho_1}{\rho}\left[\alpha_4\frac{1}{\cos^*(k_{dy,1}d)}(D_1 + D_2) + \alpha_5\frac{\tan^*(k_{dy,1}d)}{\sin^*(k_{sy,1}d)}(S_1 + S_2)\right], \quad \text{(A6)}$$

with

$$F = \pi\cos[k_{y,1}d + \varphi_a(k_{y,2})]\delta(k_{y,1} - k_{y,2}) - \sin[k_{y,1}d + \varphi_a(k_{y,2})]P\left(\frac{1}{k_{y,1} - k_{y,2}}\right) + \frac{\sin[k_{y,1}d - \varphi_a(k_{y,2})]}{k_{y,1} + k_{y,2}}, \quad \text{(A7)}$$

$$G = \pi\sin[k_{y,1}d + \varphi_s(k_{y,2})]\delta(k_{y,1} - k_{y,2}) + \cos[k_{y,1}d + \varphi_s(k_{y,2})]P\left(\frac{1}{k_{y,1} - k_{y,2}}\right) - \frac{\cos[k_{y,1}d - \varphi_s(k_{y,2})]}{k_{y,1} + k_{y,2}}, \quad \text{(A8)}$$

$$D_1=\frac{\sin^*[(k_{y,1}-k_{dy,1})d]}{k_{y,1}-k^*_{dy,1}}, \tag{A9}$$

$$D_2=\frac{\sin^*[(k_{y,1}+k_{dy,1})d]}{k_{y,1}+k^*_{dy,1}}, \tag{A10}$$

$$S_1=\frac{\sin^*[(k_{y,1}-k_{sy,1})d]}{k_{y,1}-k^*_{sy,1}}, \tag{A11}$$

$$S_2=\frac{\sin^*[(k_{y,1}+k_{sy,1})d]}{k_{y,1}+k^*_{sy,1}}, \tag{A12}$$

$$\alpha_1=\frac{2k^2_{z,2}}{k^2_t}-1, \tag{A13}$$

$$\alpha_2=\frac{2k^*_{dy,2}k^*_{sy,2}}{k^2_t}, \tag{A14}$$

$$\alpha_3=\frac{2k^*_{dy,2}k_{y,1}}{k^2_t}\,\alpha_1, \tag{A15}$$

$$\alpha_4=\frac{(k^2_t-2k^2_{dy,2})}{k^2_t}\,\alpha_1, \tag{A16}$$

$$\alpha_5=\frac{2k^2_{z,2}}{k^2_t}\,\alpha_2. \tag{A17}$$

[1] R. Stoneley, ''Elastic waves at the surface of separation of two solids,'' Proc. R. Soc. London, Ser. A **106**, 416–428 (1924).

[2] J. G. Scholte, ''On true and pseudo Rayleigh wave,'' Proc. Kon. Ned. Akad. van Wetensch. Amsterdam **52**, 652–653 (1949).

[3] H. L. Bertoni and T. Tamir, ''Unified theory of Rayleigh angle phenomena for acoustic beams at liquid/solid interfaces,'' J. Appl. Phys. **2**, 157 (1973).

[4] S. Devolder, M. Wevers, P. De Meester, and O. Leroy, ''Thin layer thickness measurements based on the acousto-optic technique,'' Appl. Phys. Lett. **68**, 1732–1734 (1996).

[5] F. Luppé and J. Doucet, ''Experimental study of the Stoneley wave at a plane liquid/solid interface,'' J. Acoust. Soc. Am. **83**, 1276–1279 (1988).

[6] J. R. Chamuel, ''Ultrasonic studies of transient seismo-acoustic waves in bounded solids and liquid/solid interfaces,'' Defense Technical Information Center Accession Report No. AD-A243441. Available from National Technical Information Center, U.S. Dept. of Commerce (1991).

[7] M. de Billy, ''Influence of the wetting and the angle of immersion on the generation of a Scholte wave: Experimental investigation,'' Phys. Lett. A **96**, 85–87 (1983).

[8] M. de Billy and G. Quentin, ''Experimental study of the Scholte wave propagation on a plane surface partially immersed in a liquid,'' J. Appl. Phys. **54**, 4314–4322 (1983).

[9] M. de Billy and G. Quentin, ''On the dispersion of Scholte wave propagating on a layered medium,'' J. Acoust. Soc. Am. **88**, 535–541 (1990).

[10] R. Briers, O. Leroy, G. N. Shkerdin, and Yu. V. Gulyaev, ''Mode theory as a framework for the investigation of the generation of a Stoneley wave at a liquid/solid interface,'' J. Acoust. Soc. Am. **95**, 1953–1966 (1994).

[11] R. Briers, O. Leroy, and G. N. Shkerdin, ''A fundamental study of the excitation of a Stoneley wave at a liquid/solid interface: Rayleigh angle and Gaussian beam incidence,'' J. Acoust. Soc. Am. **95**, 1967–1976 (1994).

[12] H. Uberall, ''Surface waves in acoustics,'' in *Physical Acoustics X*, edited by W. P. Mason and R. L. Thurston (Academic, New York, 1973).

[13] A. Tinel, ''Diffraction de l'onde de Scholte par un dièdre et par un réseau de stries,'' Ph.D. thesis, Université Le Havre, France, in French (1991).

[14] R. Briers, ''Contributions to the study of acoustic scattering and conversion phenomena in discontinuous structures by introducing a mode theory and by applying the inhomogeneous wave theory,'' Ph.D. thesis, Katholieke Universiteit Leuven, in English (1995).

Influence of an inclusion on the phase of a Stoneley wave

R. Briers,[a] O. Leroy, and G. N. Shkerdin[b]
Interdisciplinary Research Center, K. U. Leuven Campus Kortrijk, B-8500 Kortrijk, Belgium

(Received 29 April 1996; accepted for publication 20 November 1996)

The propagation of a Stoneley wave through an inclusion near a liquid/solid interface is investigated on the basis of mode theory [Briers *et al.*, J. Acoust. Soc. Am. **95**, 1953–1966, 1967–1976 (1994)]. An expression for the phase and amplitude changes of the Stoneley wave is derived and analyzed in the case of a thin ($kd \ll 1$) and of a thick ($kd \gg 1$) inclusion of arbitrary length (kd is the multiplication of the liquid wave number with the thickness of the inclusion). © *1997 Acoustical Society of America.* [S0001-4966(97)00303-2]

PACS numbers: 43.35.Cg [HEB]

INTRODUCTION

In geophysics the Stoneley wave (or Scholte wave) has already proved its importance to investigate thin sediment layers[1] or bottom geoacoustics.[2] Related problems were studied at ultrasonic frequencies. Chamuel[3] analyzed, for example, the effect of a liquid layer in a solid (due to the presence of a groove) on Stoneley wave propagation. The effect of a thin trapped gas layer underneath a floating plate on flexural waves in the plate was analysed as well.[4] Duclos *et al.*[5] studied the propagation of a Stoneley wave along a corrugated surface.

Most ultrasonic techniques used to evaluate materials are based on the measurements of the reflected or transmitted ultrasonic amplitude.[6–8] Recently a new ultrasonic technique[9] which focuses on the phase difference between the incident and the reflected bulk waves was elaborated on laboratory scale. This technique is based on light diffraction by ultrasound[10] and has the advantage of being very sensitive for thin layers.

Having in mind this sensitivity of phase changes to thin layer dimensions, we studied the Stoneley wave phase shift caused by an inclusion localized near a liquid/solid interface. Especially for a thin inclusion, when the amplitude of the incident Stoneley will not undergo changes, the phase shift can be important to characterize the inclusion.

In Sec. I we make use of an earlier developed mode theory[11,12] to derive an expression for the complex amplitude of a Stoneley wave transmitted through an inclusion of arbitrary thickness. The obtained expression is valid for liquid/solid structures whereby the Stoneley wave is mainly localized in the liquid. In Sec. II we consider more in detail the Stoneley wave phase shift in the case of a thin and of a thick inclusion layer. In Sec. III we analyze the dependence of the phase shift on the medium constants as well as on the inclusion dimensions.

I. EXPRESSION FOR THE AMPLITUDE AND THE PHASE OF A STONELEY WAVE TRANSMITTED THROUGH AN INCLUSION

The configuration of the two-dimensional scattering problem is shown in Fig. 1. A fluid loaded solid sample contains near the liquid/solid interface an inclusion of length L and thickness d. In fact, the configuration can be considered as formed by two identically liquid/solid structures (structures 1a and 1b) and a liquid/inclusion/solid structure (structure 2). When a Stoneley wave, propagating along the interface of structure 1a, is incident at the plane $z=0$, scattering and mode conversion phenomena take place. The waves generated in structure 2 cause the same phenomena at the plane $z=L$. In general, the total acoustic field in structure 1a is a superposition of the incident Stoneley wave ($\mathbf{u}_{1a}^{i}$), a reflected Stoneley and bulk wave, while the total acoustic field in structure 1b consists of a transmitted Stoneley ($\mathbf{u}_{1b}^{\mathrm{ston}}$) and bulk ($\mathbf{u}_{1b}^{t}$) wave. The total acoustic field in structure 2 is a superposition of a transmitted Stoneley ($\mathbf{u}_{2}^{\mathrm{ston}}$) and bulk wave ($\mathbf{u}_{2}^{t}$), and of a reflected Stoneley and bulk wave. To simplify the complicated system of reflected and transmissed waves at the planes $z=0$ and $z=L$ we neglect all reflected waves. The reason we may do so is connected with the fact that a Stoneley wave is mainly localized in the liquid where no reflection takes place.

The displacement fields of the scattered and mode converted waves can be expanded in terms of the complete and orthogonal set of radiation modes and eigenmodes specific for the structure to which the waves belong[11]

$$\mathbf{u}_{1a}^{i}(\mathbf{r}) = C_i^s \mathbf{u}_1^s(\mathbf{r}), \tag{1}$$

$$\mathbf{u}_{1b}^{\mathrm{ston}}(\mathbf{r}) = C_t^s \mathbf{u}_1^s(\mathbf{r}), \tag{2}$$

$$\mathbf{u}_{1b}^{t}(\mathbf{r}) = \int_0^{\xi} C_{1b}^{t}(k_{y,1}) \mathbf{u}_1^a(k_{y,1};\mathbf{r})\, dk_{y,1}, \tag{3}$$

$$\mathbf{u}_{2}^{\mathrm{ston}}(\mathbf{r}) = C_2^s \mathbf{u}_2^s(\mathbf{r}), \tag{4}$$

$$\mathbf{u}_{2}^{t}(\mathbf{r}) = \int_0^{\xi} C_2^t(k_{y,2}) \mathbf{u}_2^a(k_{y,2};\mathbf{r})\, dk_{y,2}. \tag{5}$$

Similar mode expansions are used for the corresponding components of the stress tensors. In mode expansions (1)–(5) the expansion coefficient C_i^s of the incident Stoneley

[a] Postdoctoral Fellow of the Flemish Institute for the Encouragement of the Scientific and Technological Research in Industry (I.W.T.).
[b] Permanent address: Institute of Radioengineering and Electronics, Russian Academy of Sciences, Moscow, Russia.

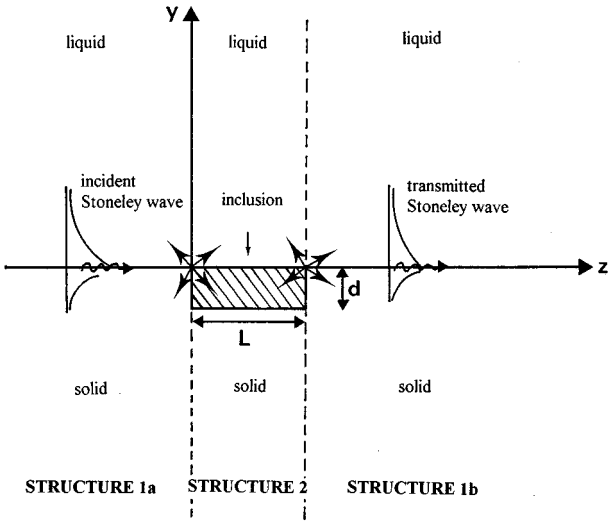

FIG. 1. Geometrical configuration of the two-dimensional scattering problem.

wave is a known quantity, while expansion coefficients C_{1b}^t, C_t^s, C_2^s, C_2^t of the transmitted Stoneley and bulk waves in structures 1b and 2 are the unknowns of the scattering problem and have to be found; **r** is a position vector with components (y,z) and

$$k_{y,i}=\sqrt{k^2-k_{z,i}^2}, \quad i=1,2 \tag{6}$$

with $k_{z,i}$ the z component of the wave vector of a radiation mode belonging to structure i $(i=1,2)$; k is the liquid wave number. The expressions for the displacement fields in the right hand members are summarized in the Appendix. Remember that the subscripts 1 and 2 are always used to make a distinction between quantities belonging to the structures 1 and 2. The upperbound of integration is given by

$$\xi=\sqrt{k^2-k_s^2} \tag{7}$$

with k_s the transverse wave number of the solid. It means that for the mode expansions of the bulk waves only radiation modes of the type a[11] are used, i.e., modes generated by plane waves incident from the liquid and for which $k_{z,i}>k_s$. These radiation modes are exponentially damped in the solid (we assume $k_d<k_s<k$, k_d the longitudinal wave number of the solid). It is justified to use only radiation modes of type a since these modes are mainly excited in the process of Stoneley wave scattering on division planes.[11] The assumption is also well consistent with the above used approximation to neglect waves reflected from the planes $z=0$ and $z=L$, because only for radiation modes of the type a this reflection is really small (for radiation modes of another type[11] the reflection can be important, but the interaction of those radiation modes with Stoneley waves is small).

By making use of the boundary conditions that have to be fulfilled along the planes $z=0$, $z=L$, i.e., continuity of the normal and tangential displacements and stresses, and with the help of the orthogonality relations that exist between all modes belonging to the same structure,[11] the following expressions for the unknown expansion coefficients C_t^s, C_2^s, C_2^t can be derived:

$$C_2^s=C_i^s\,\frac{I_{12}^{ss}+K_{12}^{ss}}{2I_{22}^{ss}}, \tag{8}$$

$$C_2^t(k_{y,2})=C_i^s\,\frac{I_{12}^{sa}(k_{y,2})+K_{12}^{sa}(k_{y,2})}{2\mathscr{T}_{22}^{aa}(k_{y,2})}, \tag{9}$$

$$C_t^s=C_2^s\,\frac{I_{21}^{ss}+K_{21}^{ss}}{2I_{11}^{ss}}\exp[i(k_{z,2}^s-k_{z,1}^s)L] + \int_0^{\xi} C_2^t(k_{y,2})\,\frac{I_{21}^{as}+K_{21}^{as}}{2I_{11}^{ss}}\exp[i(k_{z,2}-k_{z,1}^s)L]\,dk_{y,2}. \tag{10}$$

In Eqs. (8)–(10) the so-called overlap integrals $I_{ij}^{\gamma\beta}$ and $K_{ij}^{\gamma\beta}$ are defined as

$$I_{ij}^{\gamma\beta}=\int_{-\infty}^{+\infty}[T_{yz,i}^{\gamma}(k_{y,i})u_{y,j}^{\beta *}(k_{y,j}) - T_{zz,j}^{\beta *}(k_{y,j})u_{z,i}^{\gamma}(k_{y,i})]_{z=0}\,dy, \tag{11}$$

$$K_{ij}^{\gamma\beta}=\int_{-\infty}^{+\infty}[T_{zz,i}^{\gamma}(k_{y,i})u_{z,j}^{\beta *}(k_{y,j}) - T_{yz,j}^{\beta *}(k_{y,j})u_{y,i}^{\gamma}(k_{y,i})]_{z=0}\,dy. \tag{12}$$

Superscripts γ and β are used to indicate the type of mode, while subscripts i and j refer to the considered structure. For example, I_{12}^{sa} describes the interaction between a Stoneley eigenmode of structure 1 and a radiation mode of type a in structure 2. An asterisk denotes the complex conjugate and $k_{z,i}^s$ is the z component of the wave vector of a Stoneley wave propagating along the interface of the structure i. We also took into account that the overlap integrals $I_{22}^{aa}=K_{22}^{aa}=\mathscr{T}_{22}^{aa}(k_{y,2}-k_{y,2}')$ with δ the delta function of Dirac. Since we are only interested in the amplitude and phase of the transmitted Stoneley wave (C_t^s), the expression for the expansion coefficient of the transmitted bulk wave (C_{1b}^t) is not written down here.

Substituting Eqs. (8) and (9) in Eq. (10) and taking into account that $I_{ij}^{\gamma}=-(K_{ji}^{\beta\gamma})^*$ gives

$$\frac{C_t^s}{C_i^s}=-\frac{|I_{12}^{ss}+K_{12}^{ss}|^2}{4I_{11}^{ss}I_{22}^{ss}}\exp[i(k_{z,2}^s-k_{z,1}^s)L] - \frac{1}{4I_{11}^{ss}}\int_0^{\xi}\frac{|I_{12}^{sa}(k_{y,2})+K_{12}^{sa}(k_{y,2})|^2}{\mathscr{T}_{22}^{aa}(k_{y,2})} \times\exp[i(k_{z,2}-k_{z,1}^s)L]\,dk_{y,2}. \tag{13}$$

On the other hand, from the law of energy flux conservation it follows that

$$1=-\frac{|I_{12}^{ss}+K_{12}^{ss}|^2}{4I_{11}^{ss}I_{22}^{ss}} - \frac{1}{4I_{11}^{ss}}\int_0^{\xi}\frac{|I_{12}^{sa}(k_{y,2})+K_{12}^{sa}(k_{y,2})|^2}{\mathscr{T}_{22}^{aa}(k_{y,2})}\,dk_{y,2}. \tag{14}$$

Again it is important to remind that in order to derive Eqs. (13) and (14) we neglected reflected waves and took into

account only the contribution from radiation modes of type a. Subtracting Eqs. (13) and (14) gives

$$\frac{C_t^s}{C_i^s}=1-\frac{|I_{12}^{ss}+K_{12}^{ss}|^2}{4I_{11}^{ss}I_{22}^{ss}}\,(\exp[i(k_{z,2}^s-k_{z,1}^s)L]-1)$$
$$-\frac{1}{4I_{11}^{ss}}\int_0^{\xi}\frac{|I_{12}^{sa}(k_{y,2})+K_{12}^{sa}(k_{y,2})|^2}{\mathscr{T}_{22}^{aa}(k_{y,2})}$$
$$\times(\exp[i(k_{z,2}-k_{z,1}^s)L]-1)dk_{y,2}. \tag{15}$$

Note that, when no inclusion exists, Eq. (15) has the correct limit

$$\lim_{L\to 0}\frac{C_t^s}{C_i^s}=1. \tag{16}$$

The values of the overlap integrals $I_{ij}^{\gamma\beta}$, $K_{ij}^{\gamma\beta}$ as well as the value of the coefficient I_{22}^{aa} are summarized in the Appendix. To evaluate integrals I_{ij}^{ss} and K_{ij}^{ss} we neglected the small contributions from integration over the solid sample, since the energy of a Stoneley wave is mainly concentrated in the liquid. Substitution of the values for the overlap integrals $I_{ij}^{\gamma\beta}$, $K_{ij}^{\gamma\beta}$ in Eq. (15) leads to the following complex valued expansion coefficient of the Stoneley wave transmitted through the inclusion:

$$\frac{C_t^s}{C_i^s}=1+\frac{4k_{y,2}^sk_{y,1}^s}{(k_{y,2}^s+k_{y,1}^s)^2}\,(\exp[i(k_{z,2}^s-k_{z,1}^s)L]-1)$$
$$+\frac{\rho_1^2k_{y,1}^s}{\pi\rho^2k_{z,1}^s}\int_0^{\xi}\frac{(k_{z,2}\widetilde{I}+K_{z,1}^s\widetilde{K})^2}{k_{z,2}}$$
$$\times(\exp[i(k_{z,2}-k_{z,1}^s)L]-1)dk_{y,2} \tag{17}$$

with

$$(k_{y,i}^s)^2=(k_{z,i}^s)^2-k^2. \tag{18}$$

ρ and ρ_1 are, respectively, the density of the liquid and of the solid sample. The relative amplitude $|C_t^s/C_i^s|$ and the phase shift φ of a Stoneley wave transmitted through an inclusion are found by rewriting the complex quantity (17) under the form

$$\frac{C_t^s}{C_i^s}=\left|\frac{C_t^s}{C_i^s}\right|\exp(i\varphi). \tag{19}$$

The value of φ does not depend on the z coordinate in structure 1b and tends to zero when the medium constants of inclusion and solid sample are the same. For an inclusion of arbitrary thickness d the analytical expressions for the functions $\widetilde{I}$, $\widetilde{K}$ as well as the expression for the wave vector component $k_{z,2}^s$ of a Stoneley wave in a liquid/inclusion layer/solid structure are rather complicated. For this reason we will restrict our discussion of a Stoneley wave phase shift to two important cases, namely a thin or thick inclusion.

II. THE STONELEY WAVE PHASE SHIFT DUE TO A THIN OR THICK INCLUSION IN A SOLID SAMPLE

To define a thin or thick inclusion we compare the thickness d of the inclusion with the localization length d_l of the Stoneley wave in the solid sample. In general the value of d_l can be well estimated by $1/k$. Therefore, if $d\ll d_l$ or $kd\ll 1$ we will consider the inclusion as a thin one while $d\gg d_l$ or $kd\gg 1$ will define a thick inclusion.

Working out Eq. (15) in the special case of a thin inclusion we took into account only terms linear in the parameter d. In this approximation overlap integrals I_{12}^{sa}, K_{12}^{sa} (and thus the functions, $\widetilde{I}$ and K) are proportional to d (remark that if no inclusion is present, the Stoneley wave is orthogonal to all radiation modes so that the values of I_{12}^{sa} and K_{12}^{sa} are identically zero). Since the last term in Eq. (15) or Eq. (17) is proportional to d^2 it can be neglected in comparison with the other ones. So, in order to calculate the Stoneley wave phase shift caused by a thin inclusion the only problem is to find the value of $k_{z,2}^s$ for a Stoneley wave propagating along a liquid/inclusion/solid structure. Therefore, we have to derive the Stoneley wave dispersion equation for such a structure.

Representing the displacement field in the liquid ($y>0$) and in the solid ($y<-d$) under the form

$$\mathbf{u}_2^s(y>0)=\mathbf{A}\,\exp(-k_{y,2}^sy)\exp(ik_{z,2}^sz-i\omega t), \tag{20}$$

$$\mathbf{u}_2^s(y<-d)=[\mathbf{B}\,\exp(k_{dy,2}^sy)+\mathbf{C}\,\exp(k_{sy,2}^sy)]$$
$$\times\exp(ik_{z,2}^s-i\omega t) \tag{21}$$

with

$$(k_{sy,2}^s)^2=(k_{z,2}^s)^2-k_s^2;(k_{dy,2}^s)^2=(k_{z,2}^s)^2-k_d^2 \tag{22}$$

and writing the displacement field inside the inclusion layer as a superposition of two forward and two backward propagating transverse and longitudinal waves, seven unknown amplitudes have to be calculated. Expressing the seven boundary conditions along the liquid/inclusion ($y=0$) and the inclusion/solid ($y=-d$) interface results in a system of linear equations of which the characteristic equation gives the dispersion equation for a Stoneley wave in a liquid/inclusion layer/solid structure. For an inclusion of arbitrary thickness, this in principle quite simple procedure leads to a very cumbersome expression from which $k_{z,2}^s$ has to be solved as a function of the circular frequency ω.

However, in the case of a thin inclusion this expression can be strongly simplified since we may use the generalized boundary conditions for a Stoneley wave

$$u_{y,2}^s(y=0)-u_{y,2}^s(y=-d)$$
$$=d\left[\frac{k_{d1}^2}{\mu_2k_{s1}^2}\,T_{yy,2}^s(y=-d)-\left(1-2\frac{k_{d1}^2}{k_{s1}^2}\right)\right.$$
$$\left.\times ik_{z,2}^su_{z,2}^s(y=-d)\right], \tag{23}$$

$$T_{yy,2}^s(y=0)-T_{yy,2}^s(y=-d)=-d\mu_2\,k_{s1}^2u_{y,2}^s(y=-d), \tag{24}$$

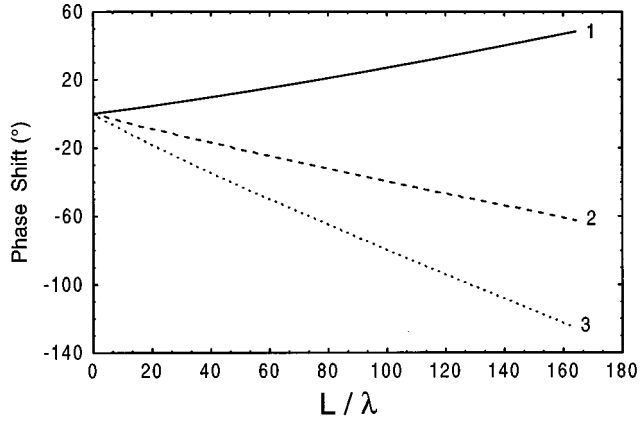

FIG. 2. The phase shift φ of a Stoneley wave propagating through a thick inclusion (i.e., $2\pi d \gg \lambda$) as a function of the length L of the inclusion. (1) A brass inclusion in a water loaded steel sample. (2) A steel inclusion in a water loaded brass sample. (3) A steel inclusion in a water loaded pyrex glass sample.

$$T^s_{yz,2}(y=-d) = d\,\frac{k^2_{s1}\mu_2}{k^2_{d1}}\left[(k^s_{dy,1})^2 + k^s_{z,2}\left(1-2\,\frac{k^2_{d1}}{k^2_{s1}}\right)^2\right] \times u^s_{z,2}(y=-d) + ik^s_{z,2}d \times\left(1-2\,\frac{k^2_{d1}}{k^2_{s1}}\right)T^s_{yy,2}(y=-d), \tag{25}$$

with T^s_{ij} the stress tensor components of the Stoneley wave; μ_2 is the Lamé constant of the inclusion; k_{s1}, k_{d1} are the wave numbers of transverse and longitudinal waves in the inclusion; $(k^s_{dy,l})^2 = (k^s_{z,2})^2 - k^2_{d1}$. Equations (22)–(25) are derived on the basis of the usual boundary conditions that have to be fulfilled along a liquid/layer and a layer/solid interface, taking into account only terms linear in the inclusion thickness d.

The solution $k^s_{y,2}$ of the dispersion equation for Stoneley wave propagating along a liquid/solid structure containing a thin inclusion can be written as

$$\frac{k^s_{y,2}}{k} = \frac{k^s_{y,1}}{k}\,(1+akd), \tag{26}$$

with

$$a = \frac{k^2_s}{k^s_{dy,1}k}\left(P_1 + \frac{k^s_{y,1}}{k_s}\,P_2\right), \tag{27}$$

$$P_1 = \frac{1}{k^4_s}\left[((k^s_{z,1})^2 - k^s_{dy,1}k^s_{sy,1})\left(2(k^s_{z,1})^2 - k^2_{s1} - \frac{2(k^s_{z,1})^2(2k^2_{d1}-k^2_{s1})}{k^2_{s1}}\right)\frac{\mu_2}{\mu_1} + 2(k^s_{z,1})^2\left(1-2\,\frac{k^2_{d1}}{k^2_{s1}}\right) \times (k^2_s - 2(k^2_{z,1})^2 + 2k^s_{dy,1}k^s_{sy,1}) - \frac{\rho_1}{\rho_2}\,\frac{k^2_{d1}}{k^2_s} \times (k^2_s - 2(k^s_{z,1})^2)^2 + 4\,\frac{\rho_1}{\rho_2}\,\frac{k^s_{dy,1}k^s_{sy,1}(k^s_{z,1})^2k^2_{d1}}{k^2_s}\right], \tag{28}$$

TABLE I. Values of the medium constants.

Medium	Longitudinal velocity v_d [m/s]	Transverse velocity v_s [m/s]	Density ρ (kg/m^3)
Steel	5720	3160	7800
Pyrex glass	5570	3440	2230
copper	4282	2244	8100
water	1460	-	1000

$$P_2 = \frac{1}{k^3_s}\left[-\frac{\rho_1}{\rho}\,k^s_{sy,1}\left(2(k^s_{z,1})^2 - k^2_{s1} - \frac{2(k^s_{z,1})^2(2k^2_{d1}-k^2_{s1})}{k^2_{s1}}\right)\frac{\mu_2}{\mu_1} + \frac{\rho_2}{\rho}\,k^2_s k^s_{dy,1}\right], \tag{29}$$

$$(k^s_{dy,1})^2 = (k^s_{z,1})^2 - k^2_d, (k^s_{sy,1})^2 = (k^s_{z,1})^2 - k^2_s. \tag{30}$$

In the limit when the medium constants of inclusion and solid sample are identical one finds

$$P_1 = \frac{k^s_{dy,1}(k^s_{dy,1}+k^s_{sy,1})}{k^2_s}, \quad P_2 = -\,\frac{k_s}{k^s_{y,1}}\,P_1, \quad a=0, \quad \text{and} \quad k^s_{y,2} = k^s_{y,1}. \tag{31}$$

The expressions for the displacement field of a Stoneley wave in structure 1 are given in the Appendix [see (A5)]. For structure 2, containing an inclusion, the expressions for the displacement components of a Stoneley wave in the liquid are the same as the ones for structure 1 with substitution of $k^s_{i,1}$ and B^s_1 by $k^s_{i,2}$ and B^s_2. As the expressions for the displacement components of a Stoneley wave in the solid are not needed here, we did not wrote them down.

Substitution of Eq. (26) in Eq. (17) and using the fact that $k^s_{y,i} \ll k$ leads to

$$\frac{C^s_t}{C^s_i} \simeq \exp[i(k^s_{z,2} - k^s_{z,1})L], \tag{32}$$

so that the phase shift φ is given by

$$\varphi = (k^s_{z,2} - k^s_{z,1})L = \frac{(k^s_{y,2})^2 - (k^s_{y,1})^2}{2k}\,L. \tag{33}$$

Finally, substituting the value of $k^s_{y,2}$ in Eq. (33) results in the following expression for the phase shift of a Stoneley wave caused by a thin ($kd \ll 1$) inclusion in a fluid loaded solid sample:

$$\varphi = (k^s_{y,1})^2 adL. \tag{34}$$

In the case of a thick inclusion ($kd \gg 1$) all terms of Eq. (17) have to be taken into account. Now the value of $k^s_{y,2}$ is the solution of the Stoneley wave dispersion equation (A8). Substitution of expressions (A16)–(A20) for $\tilde{I}$ and K as well as the values of $k^s_{y,1}$ and $k^s_{y,2}$ in Eq. (17) allows to calculate the change in amplitude and phase of a Stoneley wave propagating through a thick inclusion.

III. NUMERICAL RESULTS AND DISCUSSION

According to Eq. (17) two mechanisms contribute to a change in phase of the incident Stoneley wave while passing

TABLE II. Stoneley wave characteristics for different liquid/solid and liquid/inclusion/solid structures.

Liquid/solid structure	$k^s_{y,i}/k$	Liquid/inclusion/solid structure	a
water/steel	0.0237	water/brass/steel	0.35
water/brass	0.056	water/steel/brass	−0.438
water/Pyrex glass	0.0763	water/steel/Pyrex glass	−0.862

through an inclusion near a liquid/solid interface. The first mechanism is connected with the excitation of a Stoneley wave in the liquid/inclusion/solid structure and the second one with the excitation of bulk waves in the same liquid/inclusion/solid structure [described by the second respectively third term of Eq. (17)]. The incident Stoneley wave interacts with the waves generated in structure 2 which all have a phase velocity along the z axis that is different from the one of the incident Stoneley wave. As a result the phase of the transmitted Stoneley wave in structure 1b is turned out to be different from the phase of the incident Stoneley in structure 1a.

For small values of L such that $|(k^s_{z,2}-k^s_{z,1})L|\ll 1$ and $|(k_{z,2}-k^s_{z,1})L|\ll 1$, Eq. (17) becomes

$$\frac{C^s_t}{C^s_i}\simeq 1+\frac{4ik^s_{y,2}k^s_{y,1}(k^s_{z,2}-k^s_{z,1})L}{(k^s_{y,2}+k^s_{y,1})^2}+\frac{i\rho_1^2k^s_{y,1}L}{\pi\rho^2k^s_{z,1}}\int_0^{\xi}\frac{(k_{z,2}\tilde{I}+k^s_{z,1}\tilde{K})^2}{k_{z,2}}(k_{z,2}-k^s_{z,1})dk_{y,2}. \tag{35}$$

From this equation it can be easily seen that the excitation of bulk waves in structure 2 (the third term) always leads to a negative contribution to the Stoneley wave phase shift, since for radiation modes $k_{z,2}<k<k^s_{z,1}$ (we do not take into account the very small contributions to the Stoneley wave phase shift by local radiation modes[11]). On the other hand, the excitation of a Stoneley wave in structure 2 (the second term) can result in a negative or positive contribution to the phase shift depending on the sign of the difference $k^s_{z,2}-k^s_{z,1}$. In general, we may conclude that a greater Stoneley wave phase shift can be expected for configurations where both mechanisms lead to a negative contribution, i.e., when $k^s_{z,2}<k^s_{z,1}$ or $k^s_{y,2}<k^s_{y,1}$. This is for example illustrated in Fig. 2 where results for the Stoneley wave phase shift φ in the case of a thick inclusion ($kd\gg 1$) are presented for different liquid/inclusion/solid structures. These results were obtained on the basis of Eq. (17). The values of the medium constants are summarized in Table I. The value of $k^s_{y,i}$ ($i=1,2$) for different liquid/solid structures is given in Table II. It can also be seen from Fig. 2 that for a thick inclusion the phase shift is almost proportional to the frequency f.

Concerning the relative amplitude $|C^s_t/C^s_i|$ of the transmitted Stoneley wave in structure 1b, the greatest contribution is usually given by the second term in Eq. (17) although the third term has also to be taken into account. For large values of L the influence of the second term in Eq. (13) decreases as a result of bulk wave scattering in the structure 2 and the main contribution to the value of $|C^s_t/C^s_i|$ is given by the first term in Eq. (13). For large values of L the relative amplitude of the transmitted Stoneley wave is approximately given by

$$\left|\frac{C^s_t}{C^s_i}\right|\simeq\frac{4k^s_{y,2}k^s_{y,1}}{(k^s_{y,2}+k^s_{y,1})^2}. \tag{36}$$

The value of L for which the second term in Eq. (13) is negligible can be quite large. For example, for a brass inclusion in a steel sample the value of L is about 6 cm, but for a steel inclusion in a glass sample the value of L is about 0.8 cm. The dependence of the amplitude of the transmitted Stoneley wave on the inclusion length is shown in Fig. 3.

For a thin inclusion ($kd\ll 1$) the value of the Stoneley wave phase shift is given by Eq. (34). The phase shift strongly increases for structures with a greater value of $k^s_{y,1}$, or in other words, with a smaller value of Stoneley wave localization length d_l in the liquid ($d_l=1/k^s_{y,1}$). The value of φ also increases for structures with a greater value of the parameter $|a|$ [see Eq. (27)]. This value depends on the medium constants and grows with the value of the parameter $|\tilde{k}^s_{y,2}-k^s_{y,1}|/k$ whereby $\tilde{k}^s_{y,2}$ is the value of $k^s_{y,2}$ for a thick inclusion. For this reason we may expect rather large values

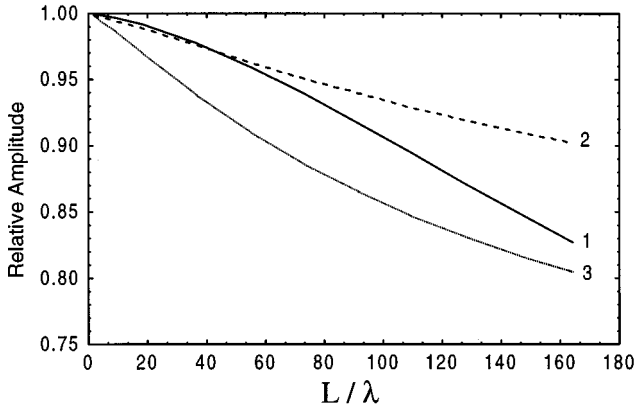

FIG. 3. The relative amplitude $|C^s_t/C^s_i|$ of a Stoneley wave propagating through a thick inclusion (i.e., $2\pi d\gg\lambda$) as a function of the length L of the inclusion for the same configurations as in Fig. 2.

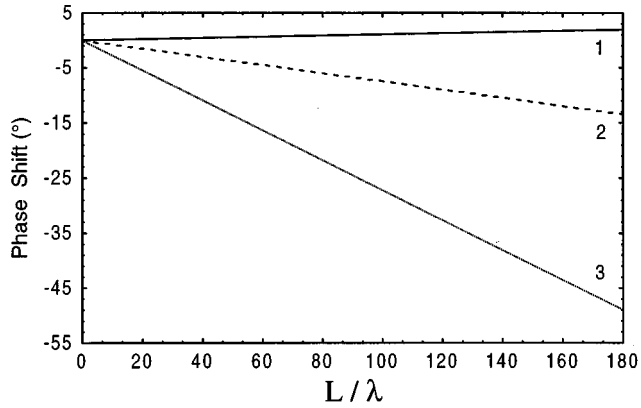

FIG. 4. The phase shift φ of a Stoneley wave propagating through a thin inclusion (i.e., $2\pi d\ll\lambda$) as a function of the length L of the inclusion for the same configurations as in Fig. 2.

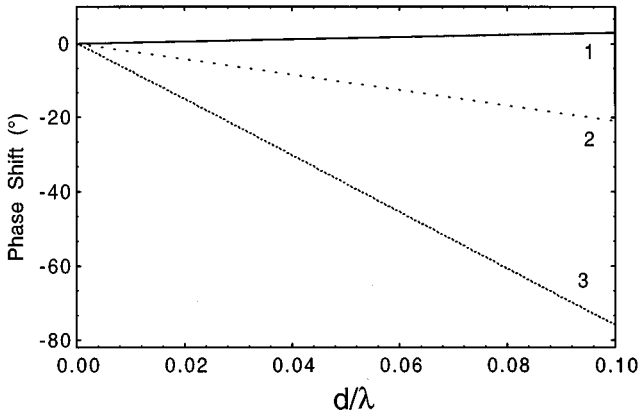

FIG. 5. The phase shift φ of a Stoneley wave propagating through a thin inclusion (i.e., $2\pi d \ll \lambda$) as a function of the thickness d of the inclusion ($L=2$ mm) for the same configurations as in Fig. 2.

of a Stoneley wave phase shift in configurations with greater values of the parameters $k^s_{y,1}/k$ and $|k^s_{y,2}-k^s_{y,1}|/k$ as illustrated in Figs. 4 and 5 (to obtain Fig. 4 we chose $kd=0.2$). Note that in the case of a thin inclusion the Stoneley wave phase shift now is proportional to f^2 [see Eq. (34)]. Especially for the detection of a thin inclusion the phase shift of a Stoneley wave is a very important quantity since the amplitude of the Stoneley wave is not sensitive to the presence of a thin inclusion [$|C^s_t|=|C^s_i|$; see Eq. (32)].

IV. CONCLUSION

The effect of the phase shift of a Stoneley wave due to an inclusion localized near the surface of a fluid loaded material has been shown. Mode theory was used to derive expressions which describe the amplitude and phase changes of a Stoneley wave transmitted through an inclusion of arbitrary thickness d and length L. These expressions have been analyzed in two particular cases, namely a thin ($kd \ll 1$) and thick ($kd \gg 1$) inclusion (k is the liquid wave number). We may conclude that the Stoneley wave phase shift strongly depends on the material constants (densities, transverse, and longitudinal velocities), on the dimensions of the inclusion and on the Stoneley wave frequency f in particular. For a thick inclusion the Stoneley wave phase shift is almost proportional to f and does not depend on the inclusion thickness d while for a thin inclusion the phase shift is proportional to dLf^2. Although the amplitude of a Stoneley wave is not sensitive to thin inclusions (opposite to thick inclusions) the phase changes of the Stoneley wave are considerable.

ACKNOWLEDGMENT

The authors would like to thank the Research Council of the K. U. Leuven for the fellowship awarded to Professor Dr. G. N. Shkerdin, which enabled us to write this paper.

APPENDIX

Radiation modes of the type a (in structure 1) are described by the displacement field:

in the liquid ($y>0$):

$$u_y = i\,\frac{k_{y,1}}{k^2}\sin(k_{y,1}y-\varphi_1),$$
$$u_z = \frac{k_{z,1}}{k^2}\cos(k_{y,1}y-\varphi_1); \tag{A1}$$

in the solid ($y<0$):

$$u_y = -i\,\frac{k_{y,1}}{k^2}\sin\varphi_1\left[\left(1-\frac{2k^2_{z,1}}{k^2_s}\right)\exp(k_{dy,1}y) + \frac{2k^2_{z,1}}{k^2_s}\exp(k_{sy,1}y)\right], \tag{A2}$$

$$u_z = \frac{k_{y,1}}{k^2}\sin\varphi_1\left[\frac{k_{z,1}}{k_{dy,1}}\left(1-\frac{2k^2_{z,1}}{k^2_s}\right)\exp(k_{dy,1}y) + \frac{2k_{z,1}k_{sy,1}}{k^2_s}\exp(k_{sy,1}y)\right], \tag{A3}$$

with

$$\varphi_1 = \arctan\frac{k_{dy,1}k^4_s}{4\dfrac{\rho_1}{\rho}\,k_{y,1}k^2_{z,1}\left[-k_{dy,1}k_{sy,1}+\left(k_{z,1}-\dfrac{k^2_s}{2k_{z,1}}\right)^2\right]}, \tag{A4}$$

and

$$k^2=k^2_{z,1}+k^2_{y,1},\quad k^2_d=k^2_{z,1}-k^2_{dy,1},\quad k^2_s=k^2_{z,1}-k^2_{sy,1}.$$

The displacement field for a Stoneley wave in structure 1 is given by:

in the liquid ($y>0$)

$$u^s_y = B^s_1 i k^s_{y,1}\exp(-k^s_{y,1}y),$$
$$u^s_z = B^s_1 k^s_{z,1}\exp(-k^s_{y,1}y); \tag{A5}$$

in the solid ($y<0$):

$$u^s_y = B^s_1 i k^s_{y,2}\left[\left(1-\frac{2(k^s_{z,1})^2}{k^2_s}\right)\exp(k^s_{dy,1}y) + \frac{2(k^s_{z,1})^2}{k^2_s}\exp(k^s_{sy,1}y)\right] \tag{A6}$$

$$u^s_z = -B^s_1 k^s_{y,1}\left[\frac{k^s_{z,1}}{k^s_{dy,1}}\left(1-\frac{2(k^s_{z,1})^2}{k^2_s}\right)\exp(k^s_{dy,1}y) + \frac{2k^s_{z,1}k^s_{sy,1}}{k^2_s}\exp(k^s_{sy,1}y)\right] \tag{A7}$$

with B^s_1 an arbitrary constant.

The dispersion equation for a Stoneley wave in structure 1 is given by

$$4\frac{\rho_1}{\rho}\,k^s_{y,1}(k^s_{z,1})^2\left[-k^s_{dy,1}k^s_{sy,1}+\left(k^s_{z,1}-\frac{k^2_s}{2k^s_{z,1}}\right)^2\right]+k^s_{dy,1}k^4_s=0. \tag{A8}$$

In the above expressions the factor $\exp[i(k_z z-\omega t)]$ was omitted.

For a thick inclusion ($kd \gg 1$) the displacement field and dispersion equation for a Stoneley wave in structure 2 are given by the same Eqs. (A5)–(A8) with substitution of the parameters for structure 2.

The values of the overlap integrals $I_{ij}^{\gamma\beta}$ and $K_{ij}^{\gamma\beta}$ in Eqs. (8)–(10) are given by

$$I_{22}^{aa} = I_2^a \delta(k_{y,2} - k'_{y,2}),$$

$$= i \frac{\pi}{2} \mu_1 \frac{\rho}{\rho_1} \frac{k_{z,2} k_s^2}{k^4} \delta(k_{y,2} - k'_{y,2}), \tag{A9}$$

$$I_{11}^{ss} \simeq \frac{i\lambda k^2 k_{z,1}^s}{2k_{y,1}^s} |B_1^s|^2, \tag{A10}$$

$$I_{22}^{ss} \simeq \frac{i\lambda k^2 k_{z,2}^s}{2k_{y,2}^s} |B_2^s|^2, \tag{A11}$$

$$I_{12}^{ss} \simeq \frac{i\lambda k^2 k_{z,1}^s}{k_{y,1}^s + k_{y,2}^s} B_1^s (B_2^s)^*, \tag{A12}$$

$$I_{12}^{sa} = \frac{i\mu_1 k_s^2 k_{z,1}^s}{k^2} B_1^s \overline{K}(k_{y,2}), \tag{A13}$$

$$K_{12}^{sa} = i\mu_1 \frac{k_s^2 k_{z,2}}{k^2} B_1^s \widetilde{I}(k_{y,2}), \tag{A14}$$

$$K_{12}^{ss} = \frac{k_{z,2}^s}{k_{z,1}^s} I_{12}^{ss}. \tag{A15}$$

For a thick inclusion the functions $\widetilde{K}$ and $\widetilde{I}$ in Eqs. (A13) and (A14) are defined as

$$\widetilde{K}(k_{y,2}) = \frac{\rho}{\rho_1} I(k_{y,2}) + \frac{2k_{y,1}^s k_{y,2}}{k_s^2} \sin \varphi_2 K_1, \tag{A16}$$

$$\widetilde{I}(k_{y,2}) = \frac{\rho}{\rho_1} I(k_{y,2}) + \frac{2k_{y,1}^s k_{y,2}}{k_s^2} \sin \varphi_2 I_1, \tag{A17}$$

with

$$I(k_{y,2}) = \frac{k_{y,1}^s \cos \varphi_2 + k_{y,2} \sin \varphi_2}{(k_{y,1}^s)^2 + (k_{y,2})^2}, \tag{A18}$$

$$K_1 = \left(\frac{2(k_{z,1}^s)^2}{k_s^2} - 1 \right) (k_{sy,1}^s - k_{dy,1}^s) \left(\frac{1 - 2(k_{z,2}^2/k_{s1}^2)}{(k_{dy,1}^s + k_{dy,2})(k_{sy,1}^s + k_{dy,2})} + \frac{2k_{z,2}^2}{k_{s1}^2 (k_{sy,2} + k_{dy,1}^s)(k_{sy,2} + k_{sy,1}^s)} \right)$$
$$+ \frac{\mu_2}{\mu_1} \left(\frac{2k_{z,2}^2}{k_{s1}^2} - 1 \right) \frac{k_{s1}^2 + 2k_{dy,2}^2}{2k_{dy,2} k_{dy,1}^s} \left(\frac{1 - 2(k_{z,1}^s)^2/k_s^2}{k_{dy,1}^s + k_{dy,2}} + \frac{2k_{dy,1}^s k_{sy,1}^s}{k_s^2 (k_{dy,2} + k_{sy,1}^s)} \right) - \frac{\mu_2}{\mu_1} \frac{2k_{z,2}^2 k_{sy,2}}{k_{dy,1}^s k_{s1}^2} \left(\frac{1 - 2(k_{z,1}^s)^2/k_s^2}{k_{dy,1}^s + k_{sy,2}} \right.$$
$$\left. + \frac{2k_{dy,1}^s k_{sy,1}^s}{k_s^2 (k_{sy,2} + k_{sy,1}^s)} \right), \tag{A19}$$

$$I_1 = \frac{\mu_2}{\mu_1} \left(\frac{2k_{z,2}^2}{k_{s1}^2} - 1 \right) (k_{sy,2} - k_{dy,2}) \left(\frac{1 - 2[(k_{z,1}^s)^2/k_s^2]}{(k_{dy,1}^s + k_{sy,2})(k_{dy,1}^s + k_{dy,2})} + \frac{2(k_{z,1}^s)^2}{k_s^2 (k_{sy,2} + k_{sy,1}^s)(k_{dy,2} + k_{sy,1}^s)} \right)$$
$$+ \left(\frac{2(k_{z,1}^s)^2}{k_s^2} - 1 \right) \frac{k_s^2 + 2(k_{dy,1}^s)^2}{2k_{dy,2} k_{dy,1}^s} \left(\frac{1 - 2k_{z,2}^2/k_{s1}^2}{k_{dy,1}^s + k_{dy,2}} + \frac{2k_{dy,2} k_{sy,2}}{k_{s1}^2 (k_{dy,1}^s + k_{sy,2})} \right) - \frac{2(k_{z,1}^s)^2 k_{sy,1}^s}{k_{dy,2} k_s^2} \left(\frac{1 - 2k_{z,2}^2/k_{s1}^2}{k_{sy,1}^s + k_{dy,2}} \right.$$
$$\left. + \frac{2k_{dy,2} k_{sy,2}}{k_{s1}^2 (k_{sy,1}^s + k_{sy,2})} \right), \tag{A20}$$

$$\varphi_2 = \arctan \frac{k_{dy,2} k_{s1}^4}{4(\rho_2/\rho) k_{y,2} k_{z,2}^2 [-k_{dy,2} k_{sy,2} + (k_{z,2} - k_{s1}^2/2k_{z,2})^2]}, \tag{A21}$$

and

$$k_{dy,2}^2 = k_{z,2}^2 - k_{d1}^2, \quad k_{sy,2}^2 = k_{z,2}^2 - k_{s1}^2.$$

[1] H. B. Ali and L. D. Bibee, ''The influence of a thin sediment layer on the dispersion of Scholte interface waves,'' Acoust. Lett. **17**, 13–18 (1993).

[2] H. B. Ali and L. D. Bibee, ''The influence of bottom geoacoustics on the dispersive behavior of Scholte interface waves,'' J. Acoust. Soc. Am. **92**, 2302(A) (1992).

[3] J. R. Chamuel, ''Backscattering of Scholte waves from a groove,'' IEEE Trans. Ultrason. Ferroelectr. Freq. Control **41**, (1994).

[4] J. R. Chamuel, ''Seismo-acoustic effect of trapped air pockets underneath a floating ice plate,'' J. Acoust. Soc. Am. **89**, 1963 (1991).

[5] H. Duflo, A. Tinel, and J. Duclos, ''Scholte wave propagation and diffraction on a fluid-solid periodic rough surface,'' Proc. IEEE Ultrasonics Symposium, Cannes 1994, Vol. 2, pp. 719–722.

[6] V. Dayal, ''An automated simultaneous measurement of thickness and wave velocity by ultrasound,'' Exp. Mech., 197–202 (1992).

[7] R. Dong and L. Adler, ''Measurements of reflection and transmission coefficients of Rayleigh waves from cracks,'' J. Acoust. Soc. Am. **76**, 1761–1763 (1994).

[8] M. Bashyam, ''Thickness compensation technique for ultrasonic evaluations of composite materials,'' Mater. Eval., 1360–1364 (1990).

[9] M. Wevers, S. Devolder, O. Leroy, and P. De Meester, ''Thin layer thickness measurements based on the acousto-optic technique,'' Appl. Phys. Lett. **68**, 1732–1734 (1996).
[10] E. Blomme and O. Leroy, ''Plane wave analysis of the near field of light diffracted by ultrasound,'' J. Acoust. Soc. Am. **91**, 1474–1483 (1992).
[11] R. Briers, O. Leroy, G. N. Shkerdin, and Yu. V. Gulyaev, ''Mode theory as a framework for the investigation of the generation of a Stoneley wave at a liquid–solid interface,'' J. Acoust. Soc. Am. **95**, 1953–1966 (1994).
[12] R. Briers, O. Leroy, and G. N. Shkerdin, ''A fundamental study of the excitation of a Stoneley wave at a liquid-solid interfaces: Rayleigh angle and Gaussian beam incidence,'' J. Acoust. Soc. Am. **95**, 1967–1976 (1994).

The generation of a Stoneley wave at the end of a fluid loaded plate by an incident bounded beam

R. Briers,[a] O. Leroy, and G. N. Shkerdin[b]
Interdisciplinary Research Center, K. U. Leuven Campus Kortrijk, B-8500 Kortrijk, Belgium

(Received 29 April 1996; accepted publication 20 November 1996)

This study shows, on the basis of a mode theory, that as a Gaussian ultrasonic beam strikes the edge of a thick plate immersed in a liquid, a Stoneley wave is generated along the liquid/solid interface. As expected, the largest amplitude for the excited Stoneley wave is obtained for normal incidence at the edge but a secondary maximum appears at Rayleigh angle incidence. In this way, it is proved theoretically that the conversion phenomenon of a Stoneley wave into a generalized Rayleigh wave at the extremity of a fluid loaded thick plate is reversible, as was observed experimentally by Tinel [Ph.D. thesis, Université Le Havre, France (1991)]. © *1997 Acoustical Society of America.* [S0001-4966(97)00403-7]

PACS numbers: 43.35.Cg [HEB]

INTRODUCTION

The Stoneley wave (also called the Scholte or Scholte–Stoneley wave) is trapped along a liquid/solid interface and does not experience radiation loss during its propagation. This makes of the Stoneley wave a useful tool for nondestructive probing of surfaces over large distances.

In the past several excitation techniques of a Stoneley wave have been studied. Chamuel[1–4] demonstrated experimentally the remote generation of a Stoneley wave from the conversion of underwater acoustic waves at abrupt liquid discontinuities and at steep topographic features, like the edge of a solid quarter, a down step, ridges, and grooves. It was shown that placing a point source at a liquid/solid interface is the most direct method of excitation. The two- and three-dimensional experimental results illustrate that any interface heterogeneity along a liquid/solid interface generates not only a Stoneley wave but also other wave types (compressional, shear, leaky Rayleigh,...).

de Billy[5] investigated the excitation of a Stoneley wave by conversion of a Rayleigh wave propagating at the air/solid interface of a partially immersed solid. Claeys *et al.*,[6] Mampaert *et al.*,[7] Jungman *et al.*,[8] and Jia *et al.*[9] used the conversion of an incident bulk wave on a periodically corrugated interface of a solid. Rasolofosaon[10] used a short pulse signal in the near field of a transducer. Duclos *et al.*,[11] Guzhev *et al.*,[12] and Nasr *et al.*[13] proposed the use of an interdigital transducer while Luppe *et al.*[14,15] introduced the liquid wedge method.

Concerning the liquid wedge method, it is important to distinguish between the different mechanisms described in literature. The first mechanism[14,15] is based on refraction and Snell's law (similar to the wedge method used for generating Rayleigh waves). According to this mechanism, no Stoneley wave would be generated if the acoustic bulk wave is incident from the low velocity liquid. The second mechanism[16–18] is based on scattering and mode conversion by the corner and does not depend on Snell's law at all. Experimentally one observes Stoneley waves generated when the acoustic volume wave is incident either from the low or high velocity liquid.[4]

We remark that not only in underwater acoustics but also in geophysics the Stoneley wave plays an important role (see for example the works of Stoll[19] and Stephen *et al.*[20]) in seafloor inspection and sediment characterization.

In this paper the generation of a Stoneley wave by conversion of a bulk wave incident at the extremity of a fluid loaded thick plate is analyzed. The first part of the paper shows how mode theory can model the scattering and conversion phenomena that arise. A general expression for the amplitude of the generated Stoneley wave is derived. In the second part, numerical calculations illustrate the theoretical results obtained from the mode theory.

I. GENERAL EXPRESSION FOR THE AMPLITUDE OF THE GENERATED STONELEY WAVE

A. The Gaussian beam is incident from the liquid structure

We apply the mode theory[17,18,21] to the configuration sketched in Fig. 1(a). This configuration is formed by a homogeneous liquid structure (structure 1) and a liquid/plate/liquid structure (structure 2). When a Gaussian beam, incident from the liquid of structure 1 at an angle θ_i ($-90° \leqslant \theta_i \leqslant 90°$), strikes the edge of the plate of thickness $2d$ scattering and mode conversion phenomena occur. All scattered and mode converted waves that are excited can be expanded in the complete and orthogonal set of acoustic modes which is specific for the structure to which they belong.[21]

In the homogeneous liquid structure ($z>0$) the total acoustic field ($\mathbf{u}_1^{\text{tot}}$) is a superposition of the incident and a reflected (scattered) bulk wave which can be expanded as

[a]Postdoctoral Fellow of the Flemish Institute for the Encouragement of the Scientific and Technological Research in Industry (I.W.T.).
[b]Permanent address: Institute of Radioengineering and Electronics, Russian Academy of Sciences, Moscow, Russia.

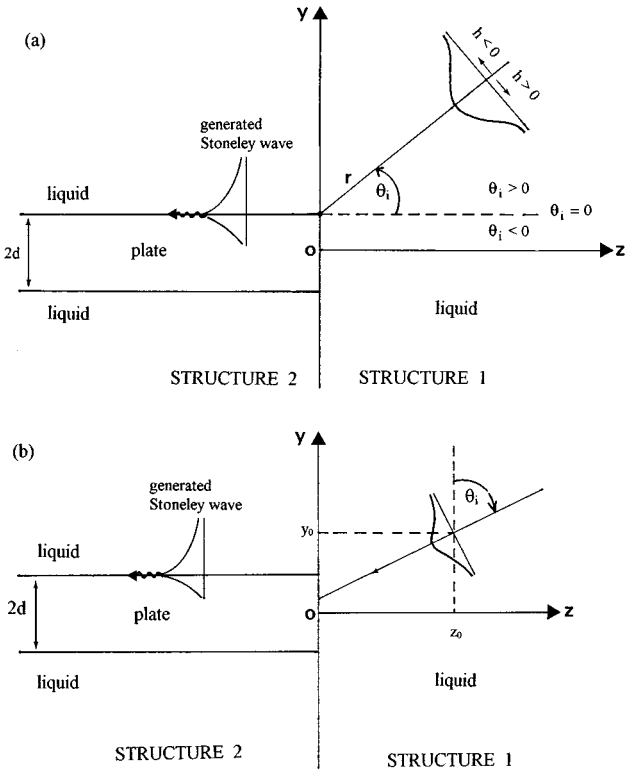

FIG. 1. Configuration for the conversion of a bulk wave into a Stoneley wave at the edge of a fluid loaded thick plate. (a) The central axis of the Gaussian beam is directed to the edge while varying the angle of incidence θ_i. (b) The central axis of the Gaussian beam is rotated over an angle θ_i around a fixed position (y_0, z_0).

$$\mathbf{u}_1^i(\mathbf{r}) = \int_0^{+\infty} \sum_m C_{r_m}^i(k_{y,1}) \mathbf{u}_1^{r_m}(k_{y,1};\mathbf{r}) dk_{y,1}$$

(incident bulk wave), (1)

$$\mathbf{u}_1^r(\mathbf{r}) = \int_0^{+\infty} \sum_m C_{r_m}^r(k_{y,1}) \mathbf{u}_1^{r_m}(k_{y,1};\mathbf{r}) dk_{y,1}$$

(reflected bulk wave), (2)

while in the liquid/plate/liquid structure ($z<0$) the most complete representation for the total acoustic field ($\mathbf{u}_2^{\text{tot}}$) is a superposition of a transmitted (scattered) bulk wave and a transmitted (mode converted) Stoneley wave

$$\mathbf{u}_2^t(\mathbf{r}) = \int_0^{+\infty} \sum_m C_{r_m}^t(k_{y,2}) \mathbf{u}_2^{r_m}(k_{y,2};\mathbf{r}) dk_{y,2}$$

(transmitted bulk wave), (3)

$$\mathbf{u}_2^{\text{ston}}(\mathbf{r}) = \sum_m C_{s_m}^t \mathbf{u}_2^{s_m}(\mathbf{r})$$

(transmitted Stoneley wave). (4)

Similar mode expansions have to be used for the stress tensor components, i.e.,

$$T_{kl,2}^t(\mathbf{r}) = \int_0^k \sum_m C_{r_m}^t(k_{y,2}) T_{kl,2}^{r_m}(k_{y,2};\mathbf{r}) dk_{y,2}, \quad (5)$$

$$T_{kl,2}^{\text{ston}}(\mathbf{r}) = \sum_m C_{s_m}^t T_{kl,2}^{s_m}(\mathbf{r}), \quad (6)$$

$$T_{kl,1}^i(\mathbf{r}) = \int_0^{+\infty} \sum_m C_{r_m}^i(k_{y,1}) T_{kl,1}^{r_m}(k_{y,1};\mathbf{r}) dk_{y,1}, \quad (7)$$

$$T_{kl,1}^r(\mathbf{r}) = \int_0^{+\infty} \sum_m C_{r_m}^r(k_{y,1}) T_{kl,1}^{r_m}(k_{y,1};\mathbf{r}) dk_{y,1}. \quad (8)$$

The subscripts 1 and 2 are always used to distinguish between quantities belonging to the structures 1 and 2. In the above mode expansions $\mathbf{r}$ is a position vector with components (y,z); $\mathbf{u}_i^{r_m}$ represents the displacement field of a symmetrical ($m=s$) or antisymmetrical ($m=a$) radiation mode in the structure i ($i=1,2$). Analogous, $\mathbf{u}_2^{s_m}$ is the displacement field of a symmetrical ($m=s$) or antisymmetrical ($m=a$) Stoneley eigenmode in the structure 2. The expressions of these displacement fields were derived in Ref. 22. In this reference a detailed description about the procedure to construct a complete and orthogonal set of radiation modes and eigenmodes for a liquid/plate/liquid structure and for a homogeneous liquid structure can be found as well. Note that the generated Stoneley wave is expanded in a symmetrical and antisymmetrical eigenmode of the liquid/plate/liquid structure. In the mode expansions each integral is taken over the continuous spectrum of radiation modes. The sum following the integral serves as a reminder that the contributions of the different types of radiation modes (symmetrical and antisymmetrical) must be added. To cross the continuous spectrum of radiation modes one lets vary the y component of the wave vector

$$k_{y,i} = (k^2 - k_{z,i}^2)^{1/2} \quad (9)$$

from zero up to infinity; k is the wave number of the liquid. The corresponding z component of the wave vector is then real or purely imaginary. In this way we include propagating radiation modes (k_z is real) as well as nonpropagating (or evanescent) radiation modes (k_z is purely imaginary). The expansion coefficient $C_{r_m}^i(k_{y,1})$ can be calculated from the given amplitude distribution of the incident bulk wave. The expansion coefficients $C_{r_m}^r(k_{y,1})$, $C_{r_m}^t(k_{y,2})$ of the scattered bulk waves and the expansion coefficient $C_{s_m}^t$ of the mode converted Stoneley wave are the unknowns of the problem and have to be found.

To find the expansion coefficient $C_{s_m}^t$, which is the only one of interest to us, we proceed as follows. The radiation modes and eigenmodes used in mode expansions (1)–(8) already satisfy to the boundary conditions along the interface $y=0$.[22] By making use of the boundary conditions that have to be satisfied along the plane $z=0$, i.e., continuity of the normal and tangential total displacements,

$$u_{z,1}^{\text{tot}} = u_{z,2}^{\text{tot}} \quad \forall y, \quad (10)$$

$$u_{y,1}^{\text{tot}} = u_{y,2}^{\text{tot}} \quad \forall y \in [-d,d], \quad (11)$$

and continuity of the normal and tangential total stresses,

$$T_{zz,1}^{\text{tot}} = T_{zz,2}^{\text{tot}} \quad \forall y, \quad (12)$$

$$T_{yz,1}^{\mathrm{tot}} = T_{yz,2}^{\mathrm{tot}} \quad \forall y, \tag{13}$$

we can derive integral equations in the unknown expansion coefficients. To this end, we multiply Eq. (10) by $(T_{zz,2}^{s_m})_{z=0}^{*}$ and Eq. (13) by $(u_{y,2}^{s_m})_{z=0}^{*}$, subtract the resulting equations and integrate over y from $-\infty$ to $+\infty$. $T_{zz,2}^{s_m}$ and $u_{y,2}^{s_m}$ are the components of a fixed symmetrical or antisymmetrical eigenmode in structure 2; an asterisk stands for complex conjugate. Taking into account that two modes of type α and β (α, $\beta = r_s, r_a, s_s, s_a$) and labeled by $k_z^{(1)}$ and $k_z^{(2)}$ satisfy the orthogonality condition[17]

$$\int_{-\infty}^{+\infty} [T_{yz}^{\alpha *}(k_z^{(1)}) u_y^{\beta}(k_z^{(2)}) - T_{zz}^{\beta}(k_z^{(2)}) u_z^{\alpha *}(k_z^{(1)})] dy$$

$$= N_1 \delta_{\alpha\beta} \delta(k_z^{(1)} - k_z^{*(2)}) + N_2 \delta_{\alpha\beta} \delta(k_z^{(1)} + k_z^{*(2)}), \tag{14}$$

with N_i ($i=1,2$) a normalization constant, one finds the integral equation

$$C_{s_m}^t I_{22}^{s_m s_m} = \int_0^k \sum_m [C_{r_m}^i(k_{y,1}) - C_{r_m}^r(k_{y,1})] I_{12}^{r_m s_m}(k_{y,1}) dk_{y,1}. \tag{15}$$

A second integral equation is obtained by repeating the previous procedure with the components $[T_{zz,2}^{r_m}(k'_{y,2})]_{z=0}^{*}$ and $[u_{y,2}^{r_m}(k'_{y,2})]_{z=0}$ of a fixed radiation mode (labeled by $k'_{y,2}$) of type r_m belonging to structure 2. This leads to the integral equation

$$C_{r_m}^t(k'_{y,2}) \mathscr{T}_{22}^{r_m r_m} = \int_0^k \sum_n [C_{r_n}^i(k_{y,1}) - C_{r_n}^r(k_{y,1})] I_{12}^{r_n r_m}(k_{y,1}, k'_{y,2}) dk_{y,1}, \tag{16}$$

with $I_{22}^{r_m r_m} = \mathscr{T}_{22}^{r_m r_m} \delta(k_{y,2} - k'_{y,2})$.

In Eqs. (15) and (16) the so-called overlap integral $I_{ij}^{\alpha\beta}$ is defined as

$$I_{ij}^{\alpha\beta} = \int_{-\infty}^{+\infty} [T_{yz,i}^{\alpha}(k_{y,i}) u_{y,j}^{\beta *}(k_{y,j}) - T_{zz,j}^{\beta *}(k_{y,j}) u_{z,i}^{\alpha}(K_{y,i})]_{z=0} \, dy \tag{17}$$

and describes the interaction that takes place in plane $z=0$ between a radiation mode (or eigenmode) of type α in structure i and a radiation mode of type β in structure j ($\alpha, \beta = r_s, r_a, s_s, s_a$; $i,j=1,2$). Next, we make use of the equality

$$[(T_{yz,2}^{r_m})^*(u_{y,1}^{\mathrm{tot}})]_{z=0} = [(T_{yz,2}^{r_m})^*(u_{y,2}^{\mathrm{tot}})]_{z=0}, \tag{18}$$

which holds for every value of y. For $-d \leqslant y \leqslant d$ this follows immediately from boundary condition (11) while for $y > d$ or $y < -d$, $u_{y,1}^{\mathrm{tot}}(z=0) \neq u_{y,2}^{\mathrm{tot}}(z=0)$, but for a perfect, elastic liquid $T_{yz,2}^{r_m} \equiv 0$. Multiplying Eq. (12) by $[u_{z,2}^{r_m}(k'_{y,2})]_{z=0}^{*}$, subtracting Eq. (18) of the resulting equation, and applying again the procedure mentioned above, gives the integral equation

$$C_{r_m}^t(k'_{y,2}) K_2^{r_m} = \int_{-\infty}^{\infty} \sum_n [C_{r_n}^i(k_{y,1}) + C_{r_n}^r(k_{y,1})] K_{12}^{r_n r_m}(k_{y,1}, k'_{y,2}) dk_{y,1}, \tag{19}$$

with $K_{22}^{r_m r_m} = \mathscr{K}_{22}^{r_m r_m} \delta(k_{y,2} - k'_{y,2})$ and $K_{ij}^{\alpha\beta}$ the overlap integral

$$K_{ij}^{\alpha\beta} = \int_{-\infty}^{+\infty} [T_{zz,i}^{\alpha}(k_{y,i}) u_{z,j}^{\beta *}(k_{y,j}) - T_{yz,j}^{\beta *}(k_{y,j}) u_{y,i}^{\alpha}(k_{y,i})]_{z=0} \, dy. \tag{20}$$

The derived integral equations can now be worked out more explicitly by evaluating the overlap integrals $I_{ij}^{\alpha\beta}$ and $K_{ij}^{\alpha\beta}$. First, we remark that overlap integrals between symmetrical and antisymmetrical modes are identically zero. Second, the main contributions to the overlap integrals $I_{ij}^{\alpha\alpha}$ and $K_{ij}^{\alpha\alpha}$ are given by the singular terms proportional to the delta function.[17] Finally, calculating the overlap integrals between a radiation mode and a Stoneley eigenmode, we neglect in a zeroth-order approximation by the contributions from the integration over the plate (the energy of a Stoneley wave is mainly localized in the liquid). As a result the system of Eqs. (15), (16), and (19) can be rewritten as

$$C_{s_m}^t I_{22}^{s_m s_m} = \int_0^k [C_{r_m}^i(k_{y,1}) - C_{r_m}^r(k_{y,1})] I_{12}^{r_m s_m} \, dk_{y,1}, \tag{21}$$

$$C_{r_m}^t \mathscr{T}_{22}^{r_m r_m} (C_{r_m}^i - C_{r_m}^r) \mathscr{T}_{12}^{r_m r_m}, \tag{22}$$

$$C_{r_m}^t \mathscr{K}_{22}^{r_m r_m} (C_{r_m}^i - C_{r_m}^r) \mathscr{K}_{12}^{r_m r_m}, \tag{23}$$

with

$$I_{12}^{r_m r_m} = \mathscr{T}_{12}^{r_m r_m} \delta(k_{y,2} - k'_{y,2}) \quad \text{and} \quad K_{12}^{r_m r_m} = \mathscr{K}_{12}^{r_m r_m} \delta(k_{y,2} - k'_{y,2}).$$

Subtracting Eqs. (22) and (23) and taking into account that within the used approximations $\mathscr{T}_{22}^{r_m r_m} = \mathscr{K}_{22}^{r_m r_m}$ and $\mathscr{T}_{12}^{r_m r_m} = \mathscr{K}_{12}^{r_m r_m}$, one obtains that $C_{r_m}^r = 0$. As a result it follows from Eq. (21) that, in a zeroth-order approximation, the expansion coefficient of the generated Stoneley wave is given by

$$C_{s_m}^t = \pm i 2 \frac{B_1^{r_m}}{B_2^{s_m}} \frac{k_{y,2}^{s_m}}{k_{z,2}^{s_m}} \int_0^k C_{r_m}^i(k_{y,1}) L_{12}^{r_m s_m}(k_{y,1}) k_{z,1} \, dk_{y,1}, \tag{24}$$

with

$$L_{12}^{r_a s_a}(k_{y,1}) = \frac{k_{y,2}^{s_a} \cos(k_{y,1} d) - k_{y,1} \sin(k_{y,1} d)}{k_{y,1}^2 + (k_{y,2}^{s_a})^2}, \tag{25}$$

$$L_{12}^{r_a s_a}(k_{y,1}) = \frac{k_{y,2}^{s_a} \sin(k_{y,1} d) + k_{y,1} \cos(k_{y,1} d)}{k_{y,1}^2 + (k_{y,2}^{s_a})^2}. \tag{26}$$

In Eqs. (24)–(26), $B_1^{r_m}$ and $B_2^{s_m}$ are arbitrary amplitudes; $k_{z,2}^{s_m}$ and $k_{y,2}^{s_m}$ are the wave vector components of a Stoneley eigenmode in the liquid/plate/liquid structure and can be found from the characteristic equation.[22] The minus sign must be used for the antisymmetrical expansion coefficient ($m=a$). In Eq. (24) the integrand contains the expansion

coefficient $C^i_{r_m}(k_{y,2})$ for the decomposition of a Gaussian beam in terms of radiation modes for a homogeneous liquid structure and can be calculated from the integral[17]

$$C^i_{r_m}(k_{y,1}) = -\frac{1}{\mathscr{T}^{r_m r_m}_{22}} \int_{-\infty}^{+\infty} [T^{r_m}_{zz,1}(k_{y,1};y,z=z_0)]^* \times u^i_{z,1}(y,z=z_0)\,dy, \tag{27}$$

with $u^i_{z,1}(y,z=z_0)$ the z component of the displacement field of the incident Gaussian beam in a plane $z=z_0$ ($z_0>0$). For the coordinate system as chosen in Fig. 1, one finds

$$C^i_{r_m}(k_{y,1}) = -a_m u_0 w k^2 (4\pi)^{-1/2} (k_{z,1})^{-1} \exp(-ik_{z,1}z_0) \times \left\{ \exp\left[-ik_{y,1}y_0 - \frac{w^2(k^i_y + k_{y,1})^2}{4\cos^2\theta_i} \right] \pm \exp\left[ik_{y,1}y_0 - \frac{w^2(k^i_y - k_{y,1})^2}{4\cos^2\theta_i} \right] \right\}. \tag{28}$$

In Eq. (28), $a_m = i$ (=the imaginary unit) for the symmetrical ($m=s$) expansion coefficient and $a_m = 1$ for the antisymmetrical ($m=a$) expansion coefficient. In the latter case one also has to use the minus sign instead of the plus sign; w is the half-beamwidth, u_0 is the maximum amplitude of the incident beam, (y_0, z_0) is the position of the center of the beam, and $k^i_y = k\cos\theta_i$.

B. The Gaussian beam is incident from the liquid/plate/liquid structure

The algorithm to calculate the expansion coefficient of the Stoneley wave generated by a Gaussian beam incident from the liquid above the thick plate ($90° \leqslant \theta_i \leqslant 180°$ [see Fig. 1(a)] is completely the same as the one that was used to model the conversion of a Stoneley wave at the end of a fluid loaded thick plate (see Sec. III of Ref. 22). The mode expansion for the incident acoustic wave [Eq. (53) in Ref. 22] has to be replaced by

$$\mathbf{u}^i_2(\mathbf{r}) = \int_0^{+\infty} \sum_m C^i_{r_m}(k_{y,2}) \mathbf{u}^{r_m}_2(k_{y,2};\mathbf{r})\,dk_{y,2}. \tag{29}$$

The total acoustic field in the liquid/plate/liquid structure is a superposition of the incident bulk wave ($C^i_{r_m}$), a reflected scattered bulk wave ($C^r_{r_m}$), and a reflected mode converted Stoneley wave ($C^r_{s_m}$), while in the homogeneous liquid structure only a transmitted scattered bulk wave ($C^t_{r_m}$) exists. Between brackets the corresponding expansion coefficients are written. Repeating the procedure in Sec. I A of this paper with the components of a fixed symmetrical or antisymmetrical radiation mode belonging to structure 1, gives the integral equation

$$C^t_{r_m}(k_{y,1}).\mathscr{K}^{r_m r_m}_{11}(k_{y,1}) = C^r_{s_m} K^{s_m r_m}_{21} + \int_0^k C^i_{r_m}(k_{y,2}) K^{r_m r_m}_{21}(k_{y,1};k_{y,2})\,dk_{y,2} + \int_0^{+\infty} C^r_{r_m}(k_{y,2}) K^{r_m r_m}_{21}(k_{y,1};k_{y,2})\,dk_{y,2}, \tag{30}$$

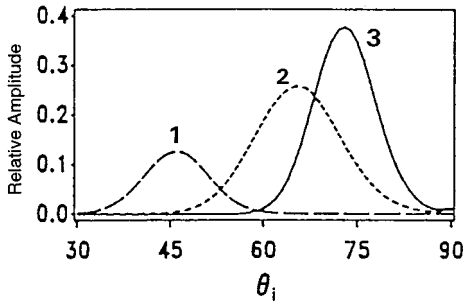

FIG. 2. Relative displacement amplitude of the Stoneley wave generated at the edge of a water loaded aluminum plate ($2d=1$ cm) by a 5-MHz Gaussian beam ($w=2$ mm). The beam is rotated around a fixed position (y_0, z_0) as sketched in Fig. 1(b): (1) $y_0=25$ mm, $z_0=20$ mm. (2) $y_0=15$ mm, $z_0=20$ mm. (3) $y_0=15$ mm, $z_0=30$ mm.

with $K^{r_m r_m}_{11} = \mathscr{K}^{r_m r_m}_{11}\delta(k_{y,1} - k'_{y,1})$. In a zeroth-order approximation for the expansion coefficient $C^t_{r_m}$ we neglect the reflected waves in structure 2 and put their expansion coefficients $C^r_{s_m}$ and $C^r_{r_m}$ equal to zero.

A first-order approximation for the expansion coefficient $C^r_{s_m}$ of the generated Stoneley wave is found by repeating the procedure in Sec. I A with the components of a symmetrical and antisymmetrical Stoneley eigenmode of structure 2. The resulting integral equations now takes the form

$$C^r_{s_m} = \frac{1}{K^{s_m s_m}_{22}} \int_0^{+\infty} C^t_{r_m}(k_{y,1}) K^{r_m s_m}_{12}(k_{y,1})\,dk_{y,1}. \tag{31}$$

Using in this expression the zeroth-order approximation for $C^t_{r_m}$ and evaluating the overlap integrals $K^{r_m r_m}_{21}$ and $K^{r_m s_m}_{12}$, we finally obtain for the amplitude of the generated Stoneley wave

$$C^r_{s_m}(k_{y,2}) = \pm i \frac{B^{r_m}_2}{B^{s_m}_2} \frac{2}{\pi} \frac{\rho_1}{\rho} k^{s_m}_{y,2} \int_0^k \left[\int_0^{+\infty} C^i_{r_m}(k_{y,2}) \frac{k_{z,2}}{k_{z,1}} \times (R^{r_m r_m}_{12})^* (M^{r_m s_m}_{12})\,dk_{y,2} \right] dk_{y,1}, \tag{32}$$

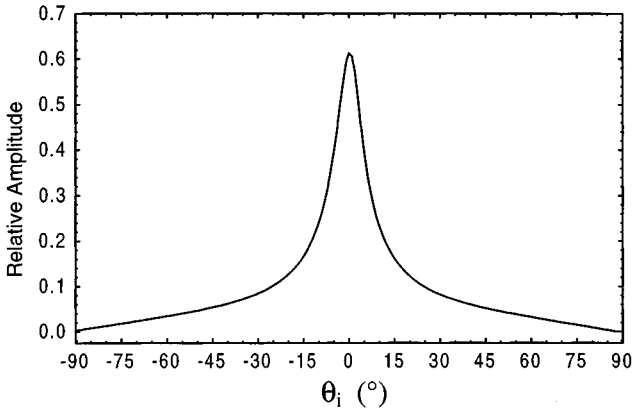

FIG. 3. Relative displacement amplitude of the Stoneley wave excited at the edge of a water loaded aluminum plate ($2d=1$ cm) by a 5-Mhz Gaussian beam ($w=2$ mm). The central axis of the beam is always directed to the edge of the plate while varying the angle of incidence θ_i ($-90° \leqslant \theta_i \leqslant 90°$) as sketched in Fig. 1(a). The distance r between source and edge is 15 cm.

ρ and ρ_1 are, respectively, the density of the liquid and of the plate, and $B_2^{r_m}$ and $B_2^{s_m}$ are arbitrary amplitudes. The minus sign must be used for the antisymmetrical expansion coefficient ($m=a$). The cumbersome analytical expressions for the functions $R_{12}^{r_m r_m}$ and $M_{12}^{r_m s_m}$ are given in the Appendix of Ref. 22. Both functions now take also into account the contributions to the overlap integrals $K_{21}^{r_m r_m}$ and $K_{12}^{r_m s_m}$ [see Eq. (20)] that arise from integration over the plate ($-d \leqslant y \leqslant d$).

The expansion coefficient $C_{r_m}^i(k_{y,2})$ in Eq. (32) for the decomposition of a Gaussian beam in terms of the radiation modes for a liquid/plate/liquid structure now takes the form

$$C_{r_m}^i(k_{y,2}) = u_0 w k^2 (4\pi)^{-1/2} (k_{z,2})^{-1} \exp(-ik_{z,2} z_0) \times \left\{ \exp\left[-i\varphi_m(k_{y,2}) + ik_{y,2}(y_0 - d) - \frac{w^2 (k_y^i - k_{y,1})^2}{4\cos^2\theta_i} \right] + \exp\left[i\varphi_m(k_{y,2}) - ik_{y,2}(y_0 - d) - \frac{w^2 (k_y^i - k_{y,1})^2}{4\cos^2\theta_i} \right] \right\}, \quad (33)$$

with $\varphi_m(k_{y,2})$ defined by Eqs. (25) and (32) in Ref. 22.

II. RESULTS FOR A WATER LOADED ALUMINUM PLATE

As an example we calculated the relative displacement amplitude $|(u_{z,2}^{\text{ston}}/u_0)(y=d, z=0)|$ of the Stoneley wave generated by a 5-MHz Gaussian ultrasonic beam incident at the end of an aluminum plate of thickness 1 cm ($=2d$) immersed in water. The values of the medium constants we used for the calculations are

Water:
longitudinal velocity: 1460 m/s
density: 1000 kg/m^3
Aluminum:
longitudinal velocity: 6350 m/s
transverse velocity: 3100 m/s
density: 2800 kg/m^3
The corresponding Rayleigh angle θ_R for aluminum is 30°.

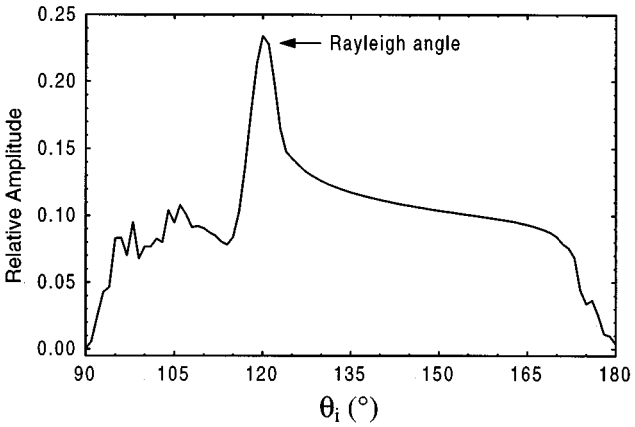

FIG. 4. The same as in Fig. 3 but the Gaussian beam is incident from above the plate [see Fig. 1(a), $90° \leqslant \theta_i \leqslant 180°$].

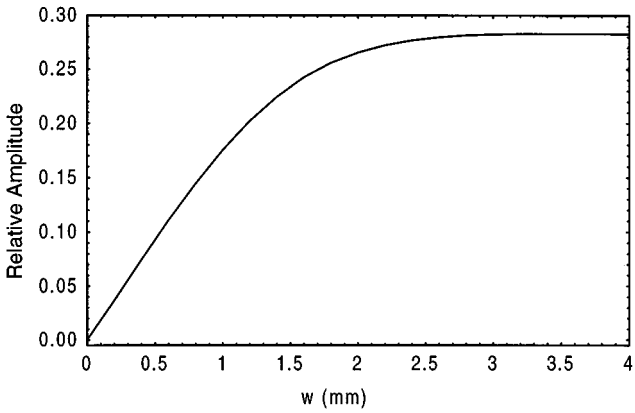

FIG. 5. Dependence of the relative displacement amplitude of the Stoneley wave excited at the edge of a water loaded aluminum plate ($2d=1$ cm) on the half-width w of the Gaussian beam at Rayleigh angle incidence ($f=5$ MHz, $r=15$ cm, $\theta_i=120°=90°+\theta_R$, θ_R the Rayleigh angle for aluminum).

The results shown in Figs. 2 and 3 correspond to the case when the Gaussian beam is incident from the homogeneous liquid (structure 1). They were obtained on the basis of Eq. (4) wherein the expansion coefficient (24) was substituted. To obtain Fig. 2, the central axis of the Gaussian beam with half-beamwidth $w=2$ mm was rotated around a fixed position (y_0, z_0) as sketched in Fig. 1(b). The angle of incidence θ_i is measured from the axis $z=z_0$. Just as for the liquid wedge, the maxima in Fig. 2 appear exactly at those angles of incidence for which the central axis is directed to the edge of the aluminum plate. These angles $\theta_{\max}$ immediately follow from the geometrical configuration: $\theta_{\max} = \arctan|(y_0 - d)/z_0|$. To obtain Fig. 3, the central axis of the Gaussian beam was always directed to the edge of the aluminum plate [see Fig. 1(a)], while changing the angle of incidence θ_i which now is measured from the axis $y=d$. As expected, the maximum relative displacement amplitude of the excited Stoneley wave is found for normal incidence ($\theta_i=0$) at the edge.

At this point it is more important to note that the conversion process of an incident Stoneley wave into a leaky

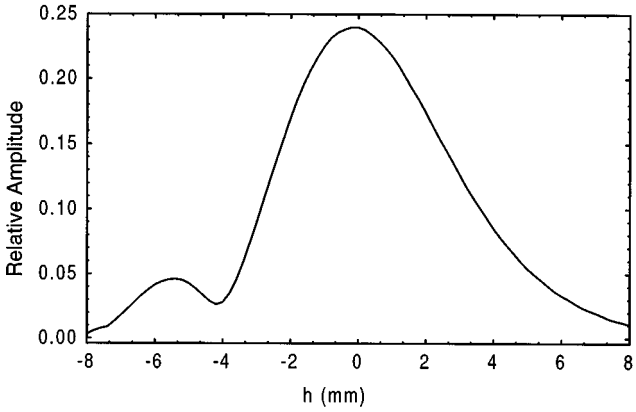

FIG. 6. Dependence of the relative displacement amplitude of the Stoneley wave excited at the edge of a water loaded aluminum plate ($2d=1$ cm) on the lateral shift h of the central axis of the Gaussian beam [see Fig. 1(a)]. The beam is incident at the Rayleigh angle ($f=5$ MHz, $w=2$ mm, $r=15$ cm, $\theta_i=120°=90°+\theta_R$, θ_R the Rayleigh angle for aluminum).

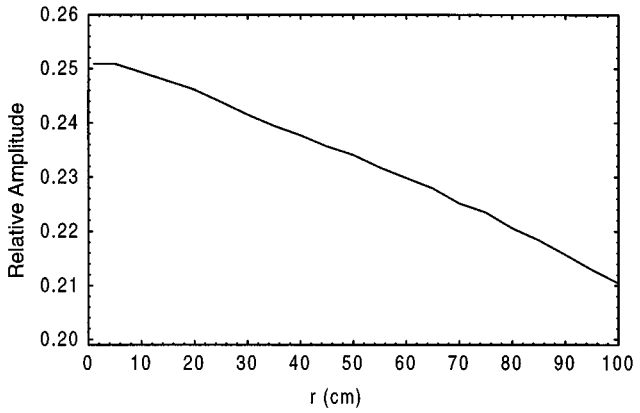

FIG. 7. Dependence of the relative displacement amplitude of the Stoneley wave excited at the edge of a water loaded aluminum plate ($2d=1$ cm) on the distance r between source and edge. The Gaussian beam is incident at the Rayleigh angle ($f=5$ MHz, $w=2$ mm, $\theta_i=120°=90°+\theta_R$, θ_R the Rayleigh angle for aluminum).

Raleigh wave at the end of a thick plate (as discussed in Ref. [22]) is reversible. Indeed, Fig. 4 shows the relative displacement amplitude of the Stoneley wave generated by a Gaussian beam ($w=2$ mm) incident from the liquid above the aluminum plate [see again Fig. 1(a) where now $90°\leqslant\theta_i\leqslant 180°$]. Therefore the expansion coefficient (32) was substituted in Eq. (4). A secondary maximum appears at an angle of incidence $\theta_i=90°+\theta_R$ ($=120°$), with θ_R the Rayleigh angle for aluminum. This phenomenom was observed experimentally by Tinel.[23] Figure 5 shows the dependence of the displacement amplitude of the excited Stoneley wave on the beamwidth of the bulk wave at Rayleigh angle incidence. For the aluminum sample, the strongest Stoneley wave excitation is realized using a Gaussian beam having at least a half-beamwidth of 3 mm. Figure 6 demonstrates the influence of a lateral shift h of the central axis of the bounded beam at Rayleigh angle incidence [see Fig. 1(a)]. As expected, the displacement amplitude of the generated Stoneley wave decreases when only that part of the incident Gaussian beam with a smaller amplitude can interact with the edge. Finally, in Fig. 7, the dependence of the Stoneley wave displacement amplitude on the distance r between the edge and source is illustrated. The amplitude starts to decrease when the distance r becomes greater than 4 cm. This is due to the fact that the incident beam is diverging. Indeed, the propagation length L after which a bounded beam starts to diverge is defined as $L=kw^2/2$ which is equal to 4 cm for the parameters used in this example.

III. CONCLUSION

We put in evidence theoretically the reversibility of the conversion process Stoneley wave-leaky Rayleigh wave that takes place at the end of a fluid-loaded plate. This is an alternative technique for Stoneley wave excitation. The theoretical results confirm the experimental observation of Tinel.[23]

The theoretical model presented here allows us to investigate the dependence of the amplitude of the excited Stoneley wave on the characteristics of the incident bulk wave such as angle of incidence, positioning of the central axis, beamwidth, distance between acoustic source and plate edge, etc.

ACKNOWLEDGMENT

The authors would like to thank the Research Council of the K. U. Leuven for the fellowship awarded to Professor Dr. G. N. Shkerdin, which enabled us to write this paper.

[1] J. R. Chamuel, ''Experimental observations on liquid/solid interface waves,'' J. Acoust. Soc. Am. **72**, S99 (1982).
[2] J. R. Chamuel and G. H. Brooke, ''Transient Scholte wave transmission along rough liquid/solid interfaces,'' J. Acoust. Soc. Am. **83**, 1336–1344 (1988).
[3] J. R. Chamuel, ''Scholte wave generation by vertically guided waves in steep topographic feature,'' J. Acoust. Soc. Am. **88**, S183 (1990).
[4] J. R. Chamuel, ''Ultrasonic studies of transient seismo-acoustic waves in bounded solids and liquid/solid interfaces,'' Sonoquest Report No. JRC-34-91, 23-36 (1991), available from National Technical Information Document No. AD-A243441.
[5] M. de Billy, ''Influence of the wetting and the angle of immersion on the generation of a Scholte wave: Experimental investigation,'' Phys. Lett. **96A**, 85–87 (1983).
[6] J. M. Claeys, O. Leroy, A. Jungman, and L. Adler, ''Diffraction of ultrasonic waves from periodically rough liquid/solid surfaces,'' J. Appl. Phys. **54**, 5657–5662 (1983).
[7] K. Mampaert and O. Leroy, ''Reflection and transmission of normally incident ultrasonic waves on periodic solid/liquid interfaces,'' J. Acoust. Soc. Am. **83**, 1390–1398 (1988).
[8] A. Jungman and G.Quentin, ''Génération d'une onde de Scholte sur une interface liquide/solide périodique,'' Proc. 4th Phase Congress **2c**, 107–111 (1984).
[9] X. Jia, A. Jungman, and G. Quentin, ''Generation and characterization of guided waves on a periodic corrugated plate,'' Ultrasonics International 1989, Madrid, Conference Proceedings (1989).
[10] P. Rasolofosoan, ''Propagation des ondes acoustiques dans les milieux poreux. Effets d'interface (théorie et expériences),'' Thèse de doctorat d'État, Université Paris 7, in French (1987).
[11] J. Duclos, P. Delestre, and M. Leduc, ''Propagation d'ondes de surface sur une structure couche mince piézoélectrique/substrat amorphe,'' Rev. Cethedec **71**, 184–195 (1982).
[12] S. N. Guzhev, V. M. Levin, R. G. Maev, and M. Kotelijanskii, ''Excitation of Stoneley surface acoustic waves at a solid/liquid interface using an interdigitated transducer,'' Sov. Phys. Tech. Phys. **29**, 817–818 (1984).
[13] S. Nasr, J. Duclos, and M. Leduc, ''PVDF transducers generating Scholte waves,'' Electron. Lett. **24**, 309–311 (1988).
[14] F. Luppé and J. Doucet, ''Experimental study of the Stoneley wave at a plane liquid/solid interface,'' J. Acoust. Soc. Am. **83**, 1276–1279 (1988).
[15] F. Luppé, J. Doucet, and M. de Billy, ''On the liquid-wedge technique to generate Scholte–Stoneley waves,'' J. Acoust. Soc. Am. **89**, 1972 (1991).
[16] J. R. Chamuel, ''On the validity of the liquid wedge technique for generating Scholte waves,'' J. Acoust. Soc. Am. **88**, S46 (1990).
[17] R. Briers, O. Leroy, G. N. Shkerdin, and Yu. V. Gulyaev, ''Mode theory as a framework for the investigation of the generation of a Stoneley wave at a liquid/solid interface,'' J. Acoust. Soc. Am. **95**, 1953–1966 (1994).
[18] R. Briers, O. Leroy, and G. N. Shkerdin, ''A fundamental study of the excitation of a Stoneley wave at a liquid/solid interface: Rayleigh angle and Gaussian beam incidence,'' J. Acoust. Soc. Am. **95**, 1967–1976 (1994).
[19] R. D. Stoll, ''Shear waves in marine sediments-Bridging the gap from theory to field application,'' in *Shear Waves in Marine Sediments*, edited by J. M. Hovem, M. D. Richardson, and R. D. Stoll (Kluwer Academic, Dordrecht, 1991), pp. 3–12.
[20] R. A. Stephen and S. T. Bolmer, ''Interface waves in seafloor propagation

and scattering problems,'' J. Acoust. Soc. Am. **99**, 2552 (1996).
[21] R. Briers, ''Contributions to the study of acoustic scattering and conversion phenomena in discontinuous structures by introducing a mode theory and by applying the inhomogeneous wave theory,'' Ph.D. thesis, Katholieke Universiteit Leuven, Belgium, in English (1995).
[22] R. Briers, O. Leroy, and G. N. Shkerdin, ''Conversion of a Stoneley wave at the extremity of a fluid loaded plate,'' J. Acoust. Soc. Am. **101**, 1347–1357 (1997).
[23] A. Tinel, ''Diffraction de l'onde de Scholte par un dièdre et par un réseau de stries'' Ph.D. thesis, Université Le Havre, France, in French (1991).

The use of large ultrasonic transducers to improve transmission coefficient measurements on viscoelastic anisotropic plates

Peter Cawley
Department of Mechanical Engineering, Imperial College, Exhibition Road, London SW7 2BX, England

Bernard Hosten
Laboratoire Méchanique Physique, Université Bordeaux I, C.N.R.S. (URA 867), 351 Cours de la Libération, 33405 Talence Cedex, France

(Received 3 November 1995; revised 22 July 1996; accepted 3 October 1996)

A study of the use of large transducers (80 mm×40 mm, 3.2 MHz center frequency) for the measurement of ultrasonic transmission coefficients is reported. Tests have been carried out on thick and thin glass plates and on a unidirectional carbon fiber composite plate. The material properties of the plates were obtained by comparing the transmission coefficient results at particular angles with the predictions of plane-wave theory for different material properties; the properties giving the best fit were then used to predict the transmission coefficients at other angles. The results of this preliminary study show that the use of large transducers makes it possible to obtain excellent agreement between measured transmission coefficients at all angles and those predicted using plane-wave theory. The large transducers give clearer definition of the transmission maxima than is obtained with smaller, conventional transducers, and also give good agreement with the predicted transmission coefficient amplitudes. This should improve the accuracy of inversion procedures for the determination of the real parts of the elastic constants from the frequencies of the transmission maxima, and the good amplitude agreement opens up the possibility of obtaining accurate estimates of the imaginary parts of the elastic constants. © *1997 Acoustical Society of America.* [S0001-4966(97)05603-8]

PACS numbers: 43.35.Cg, 43.35.Mr, 43.35.Yb [HEB]

INTRODUCTION

Ultrasonic transmission coefficient measurements are frequently used to measure the elastic constants of composite and other materials.[1–4] This technique has the advantage over the bulk-wave transit-time method[5–8] that there is no requirement to separate the signals corresponding to successive reverberations within the specimen, or to identify the wave arrivals corresponding to (quasi) longitudinal and (quasi) shear propagation. This means that the transmission coefficient method can be used on thinner specimens than the bulk-wave transit-time technique, and it is also more applicable to attenuative materials where lower frequencies may have to be used, making echo separation more difficult on a specimen of a given thickness.

However, there is an important disadvantage of the transmission coefficient method as it is usually applied. The elastic constants are obtained by fitting the experimental results to the predictions of plane-wave theory, but if conventional ultrasonic transducers of diameters typically 25 mm or less are employed then plane-wave theory does not provide an accurate model of the experiment, particularly at frequencies below 2 MHz. This reduces the quality of the fit between the experiments and the predictions. The errors in oblique incidence measurements are more severe than those at normal incidence since multiple reflections at oblique angles displace energy along the plate so it is not ''seen'' by a finite receiver. In reflection and transmission measurements in which a single echo or transmitted pulse is to be captured, this problem can be overcome by displacing the receiver so that it is centered on the signal of interest.[9,10] However, this is not possible when the full field is to be measured.

If the plate thickness is very small, the effect of beam spreading can be neglected,[1–4] but the sensitivity of the transmission coefficients to the elastic constants decreases as the plate thickness is reduced. For plate thicknesses of the order of a few mm, one solution to the problem of the poor fit between the experimental measurements and the predictions of plane-wave theory is to simulate a plane-wave transducer by taking measurements at different receiver positions and summing them.[11] A potentially better solution would be to use larger transducers which provide a good approximation to plane-wave characteristics. This paper describes an initial experimental study of this possibility.

I. EXPERIMENTS

Through transmission experiments were carried out using the setup shown schematically in Fig. 1. Before the test specimen was introduced, the transducer alignment was adjusted to maximize the amplitude of the through transmitted signal. The specimen was then placed in the goniometer and the orientations of the goniometer axes were adjusted to maximize the amplitude of the signal received by one of the transducers operating in pulse echo mode. This procedure ensured that the transducer axes were correctly aligned and that the faces of the specimen were normal to the beam path when the goniometer was set to 0°. Measurements could then be taken at different angles of goniometer rotation. It was also possible to displace the receiving transducer in the di-

 0001-4966/97/101(3)/1373/7/$10.00

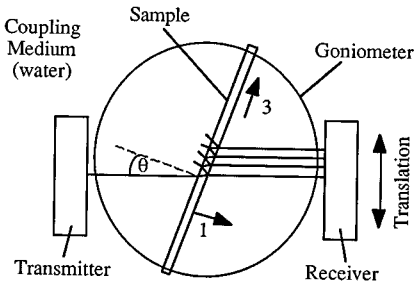

FIG. 1. Schematic diagram of experimental setup.

rection normal to the beam path in order to improve the detection of multiply reflected signals at oblique incidence.

The pulser-receiver used was a Panametrics 5052UA, the received signal being captured by a LeCroy 9410 digital oscilloscope. One hundred averages were carried out in the oscilloscope before the signal was transferred to an Apple Power Macintosh computer for subsequent processing. The transmission coefficients were obtained by dividing the spectrum of the received signal by the spectrum of the reference signal transmitted with no specimen in the goniometer.

The large transducers used were manufactured by Imasonic and had a center frequency of 3.2 MHz with 20-dB down points at 2 and 5 MHz. They had an 80 mm×40 mm rectangular section, the longer axis being aligned parallel to the plane of the wave propagation. This meant that the length of the transducer was 170 wavelengths in water (the coupling medium) at the center frequency and the product of the wave number and the length was the order of 1000, giving a good approximation to plane-wave conditions.

The results with the large transducers were compared with those obtained using standard Panametrics (V305) nominal 2.25 MHz, 19-mm-diam immersion transducers. These had a measured center frequency of 2.1 MHz with 20-dB down points at 1.2 and 3.4 MHz.

Tests were carried out on two glass plates and a unidirectional carbon fiber reinforced plastic (CFRP) plate. The first glass plate was 4.92 mm thick so the different received echoes could readily be separated with both types of transducer. It was therefore possible to use the bulk-wave transit-time method to measure its elastic constants. The second glass plate was 2.15 mm thick which was too thin for the echoes to be resolved using either type of transducer. This was therefore an example of the type of specimen on which the transmission coefficient method is advantageous. The CFRP plate was 4.15 mm thick and was designed to test the large transducers on a material which is highly anisotropic and is also much more attenuative than glass.

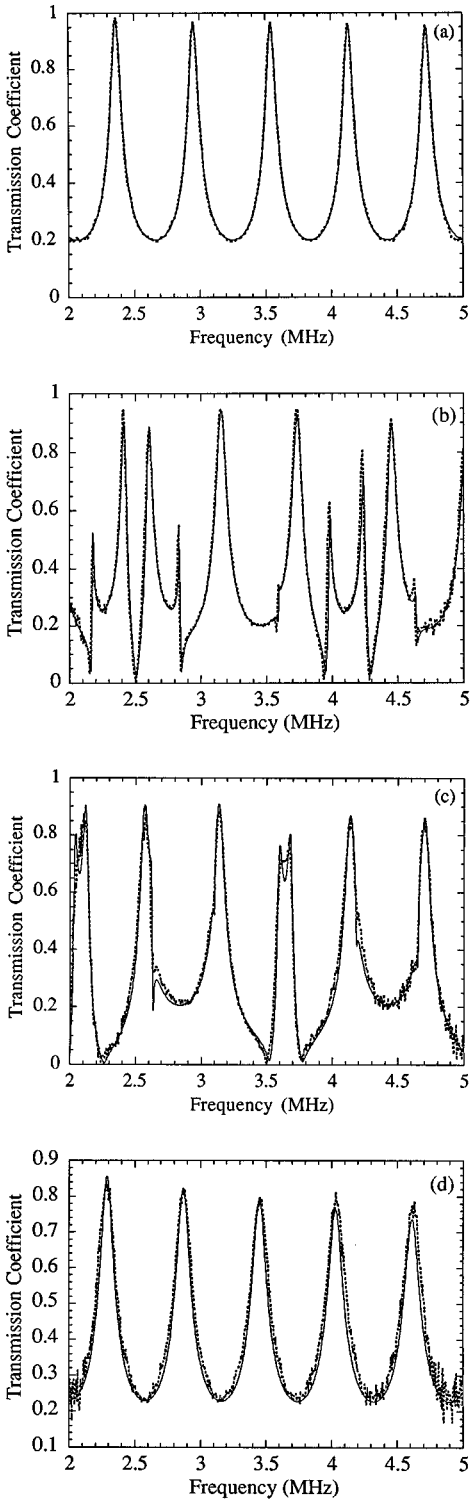

FIG. 2. Comparison of measurements on thick glass plate using large transducers with plane-wave predictions. (a) Normal incidence; (b) 5°; (c) 10°, (d) 20° (solid line: theory; dashed line: measurements).

II. RESULTS

A. Large transducers compared with plane-wave theory

Figure 2 shows comparisons between the measurements with the large transducers on the thicker glass plate at different angles of incidence and the predictions of plane-wave theory for a plate immersed in water. The predictions were done using the method of bulk heterogeneous wave propagation through the plate[11] with the material properties given in Table I.

The density of the glass was obtained by measuring the mass of the plate and its dimensions. It had originally been intended to use the bulk-wave transit-time method to obtain the elastic constants for the predictions. However, it was

TABLE I. Properties of glass plates used in predictions ($C_{ij}=C_{ij}'+iC_{ij}''$). Plates assumed to be isotropic.

	C_{11}' (GPa)	C_{11}'' (GPa)	Attenuation at 3 MHz (Nepers m^{-1})	C_{55}' (GPa)	C_{55}'' (GPa)	Attenuation at 3 MHz (Nepers m^{-1})	Density (kg/m^3)	Thickness (mm)
thick plate	84.9	0.07	1	30.0	0.075	7	2516	4.92
thin plate	87.3	0.07	1	29.8	0.085	7	2436	2.15

found that while this method gave precise estimates of the real parts of the elastic constants it was not practical to extend it to obtain the imaginary parts by measuring the reduction in amplitude of successive echoes. This was because the reduction due to material attenuation in the amplitude of a pulse during a single transit through the glass plate was very small, most of the observed amplitude reduction being due to reflection and mode conversion at the surfaces. Therefore the real and imaginary parts of C_{11} were obtained by fitting the predictions to the experimental transmission coefficient results at normal incidence [Fig. 2(a)], while the real and imaginary parts of C_{55} were obtained from a best fit to the results at 20° [Fig. 2(d)] which is beyond the critical angle so only shear waves are propagating in the glass and the predicted spectrum is only sensitive to the shear properties. In general, the estimation of material attenuation from transmission coefficient measurements is unreliable since beam spreading effects due to finite transducer size increase the apparent attenuation. Even with the large transducers there will be some bounded beam effects. However, these effects are most severe at low frequencies, so if this error was dominating the results, the apparent attenuation would decrease with frequency. The results of Fig. 2(a) and (d) clearly show that the attenuation increases with frequency (the amplitudes of the maxima reduce as the frequency increases) so the fitted attenuation values correspond to real effects, not just measurement artifacts. It is not claimed that the attenuation values obtained are very accurate; however, they are much better than can conceivably be obtained with the bulk-wave method in low attenuation materials.

The use of the measurements at normal incidence and at 20° to obtain the material properties means that good agreement between the measurements and predictions at these angles is unsurprising. (Good agreement is not assured since if the transducers used in the experiments do not provide a satisfactory approximation to plane-wave conditions, the form of the measured transmission coefficients may not correspond to plane-wave predictions with any properties; this point is discussed further in Sec. II B below.) However, if the measured results contained artifacts due to the experimental conditions not corresponding adequately to the assumptions of plane-wave theory, the predictions of the transmission coefficients at other angles made using best-fit properties at normal incidence and 20° would not give such good agreement with the experiments. It can be seen from Fig. 2(b) and (c) that the measured transmission coefficients at 5° and 10° are in excellent agreement with the predictions of plane-wave theory made using the material properties determined from the measurements at 0° and 20°. The transmission coefficients at the intermediate angles are dependent on both C_{11} and C_{55}, whereas the results at the angles used for the material property determination are each a function of only one of these constants. Similarly good results were obtained at other intermediate angles. This suggests that the large transducers are giving a good approximation to plane-wave conditions.

Figure 3 shows the corresponding results with the thinner glass plate, the elastic constants shown in Table I being obtained in the same way as on the thicker plate. The properties of the thinner plate were slightly different than those of the thicker one; this is not unexpected since they were obtained from different sources. Good agreement between the experiments at the intermediate angles not used in the material property determination and the predictions is again shown, though small discrepancies in the positions and amplitudes of some features can be seen. A small dip is predicted in the spectrum at about 3.6 MHz for an angle of incidence of 10° [Fig. 3(c)]. There is evidence of a shoulder on the experimental curve at this position, but the dip is not developed. This indicates that the angular bandwidth of the transducers is still too large for this feature to be resolved; it would become more apparent if even larger transducers were employed.

Figure 4 shows a selection of results from the unidirectional CFRP plate in the 1–3 (anisotropic) plane. In this case, the elastic constants were first estimated using the bulk-wave method. However, it is difficult to obtain accurate values of C_{33} in unidirectional composites with high modulus fibers using this technique. (In the notation used in this paper and in Refs. 5, 9, and 11, ''3'' is the fiber direction as shown in Fig. 1.) In this type of material, the quasilongitudinal (QL) and quasishear (QT) mode velocities are very similar when the angle of incidence approaches the critical angle for the generation of the QL mode, as shown in Fig. 5. The amplitudes of the two modes are also very similar in the region around 6°. This means that the two modes overlap in the time-domain signal and it is not possible to obtain accurate measurements of the transit time of either mode. Unfortunately, this is the region of greatest sensitivity to C_{33} so it is difficult to obtain reliable estimates of the real part of this elastic constant and it is almost impossible to estimate the imaginary part. Accordingly, the values obtained with this method were used as initial estimates for the constants which were then refined using a selection of the transmission coefficient results. C_{11} was obtained from the normal incidence results [Fig. 4(a)] and C_{33} and C_{55} were estimated using the results at 5° [Fig. 4(c)] and 20° [Fig. 4(f)] together. This fitting was done by eye; no attempt was made to automate the procedure.

As in Ref. 11, the theoretical predictions made to compare with the experimental measurements assumed that the imaginary parts of the elastic constants were frequency inde-

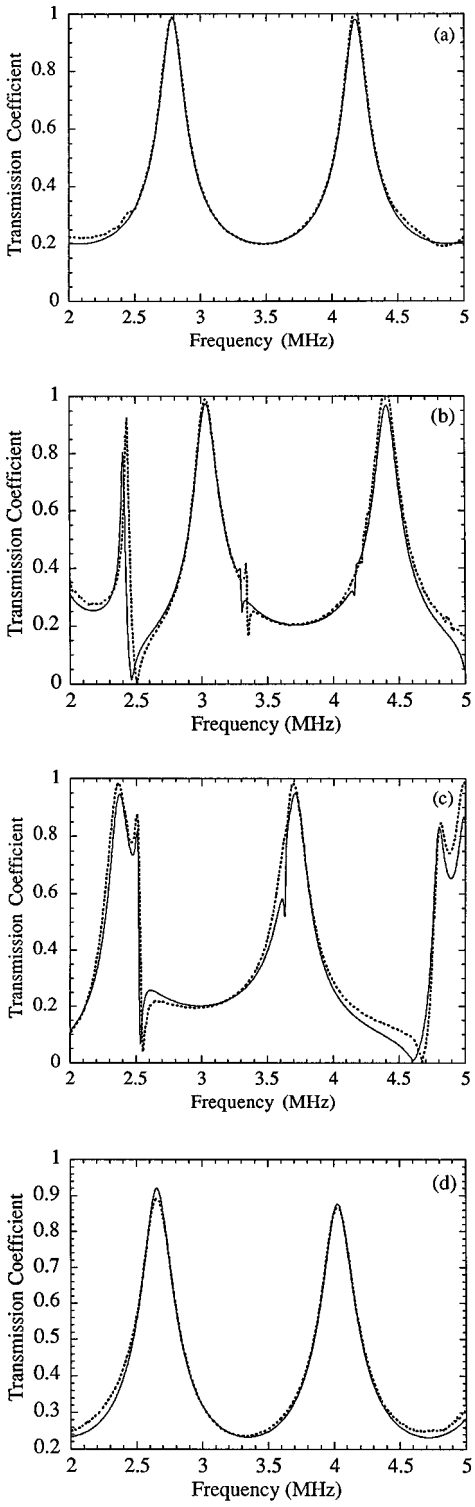

FIG. 3. Comparison of measurements on thin glass plate using large transducers with plane-wave predictions. (a) Normal incidence; (b) 5°; (c) 10°; (d) 20° (solid line: theory; dashed line: measurements).

pendent so the attenuation per unit propagation distance increases linearly with frequency. It is clear from the results at normal incidence [Fig. 4(a)] and beyond the longitudinal critical angle at 20° [Fig. 4(f)] that this simple model is not entirely appropriate for this material since it was not possible to obtain good amplitude fits at both the upper and lower ends of the frequency range. This indicates that a more complex model in which the imaginary parts of the elastic constants are functions of frequency will be required and this is currently being investigated. However, the simple model gives satisfactory results over a limited frequency range.

It was found that none of the transmission coefficients were very sensitive to C_{13}, indicating that this constant will only be obtained in a global optimization procedure in which C_{33}, C_{13}, and C_{55} are estimated together from measurements at multiple angles. The values of the real and imaginary parts of C_{13} used in the predictions were therefore those obtained from the bulk-wave measurements. The values of the elastic constants used are shown in Table II, together with the corresponding attenuations at a frequency of 3 MHz. The attenuations corresponding to C_{11} and C_{33} are of longitudinal waves traveling in the 1 and 3 directions, respectively, while that corresponding to C_{55} is of a shear wave polarized in the 1 direction and propagating in the 3 direction or polarized in the 3 direction and propagating in the 1 direction. These attenuations were calculated from the real and imaginary parts of the elastic constants using the standard analysis.[5,9] As expected, the attenuation rates are much higher than those shown in Table I for the glass plates. The longitudinal wave attenuation in the fiber direction is lower than that in the transverse direction, both longitudinal wave attenuations being lower than the shear wave attenuation.

Figure 4(b), (d), and (e) shows the comparison between the measurements at 4°, 6°, and 12°, respectively, and the predictions made using the material properties obtained in experiments at other angles. It can be seen that there is very encouraging agreement between the experiments and the predictions, particularly considering the inadequacy of the form of the attenuation model. The good prediction of the change in the form of the curves at around 6° as the longitudinal critical angle of about 7° is approached is especially encouraging. The form of the curves is strongly affected by the imaginary parts of the elastic constants.[11]

B. Comparison of results with large and small transducers

Having shown that good results could be obtained with the large transducers, it was then interesting to investigate the extent of the improvement obtained compared with tests using more conventional transducers. Figure 6 presents a set of comparisons on the thinner glass plate. At normal incidence [Fig. 6(a)], the agreement between the large and conventional transducer results is quite good except that the smaller transducers produce a spike at about 2.5 MHz. This is due to the excitation of a through thickness shear mode by mode conversion of the non-normal components of the bounded beam.[12] The occurrence of this spike could not be predicted by normal incidence plane-wave predictions with any material properties, and demonstrates that the smaller transducers do not provide as good an approximation to plane-wave conditions as the larger transducers. This feature would cause problems for any inversion scheme which attempted to use the whole data set.

At 10° [Fig. 6(b)] the smaller transducer does not give accurate amplitudes around the maxima, and does not satisfactorily resolve the two peaks between 2.3 and 2.5 MHz.

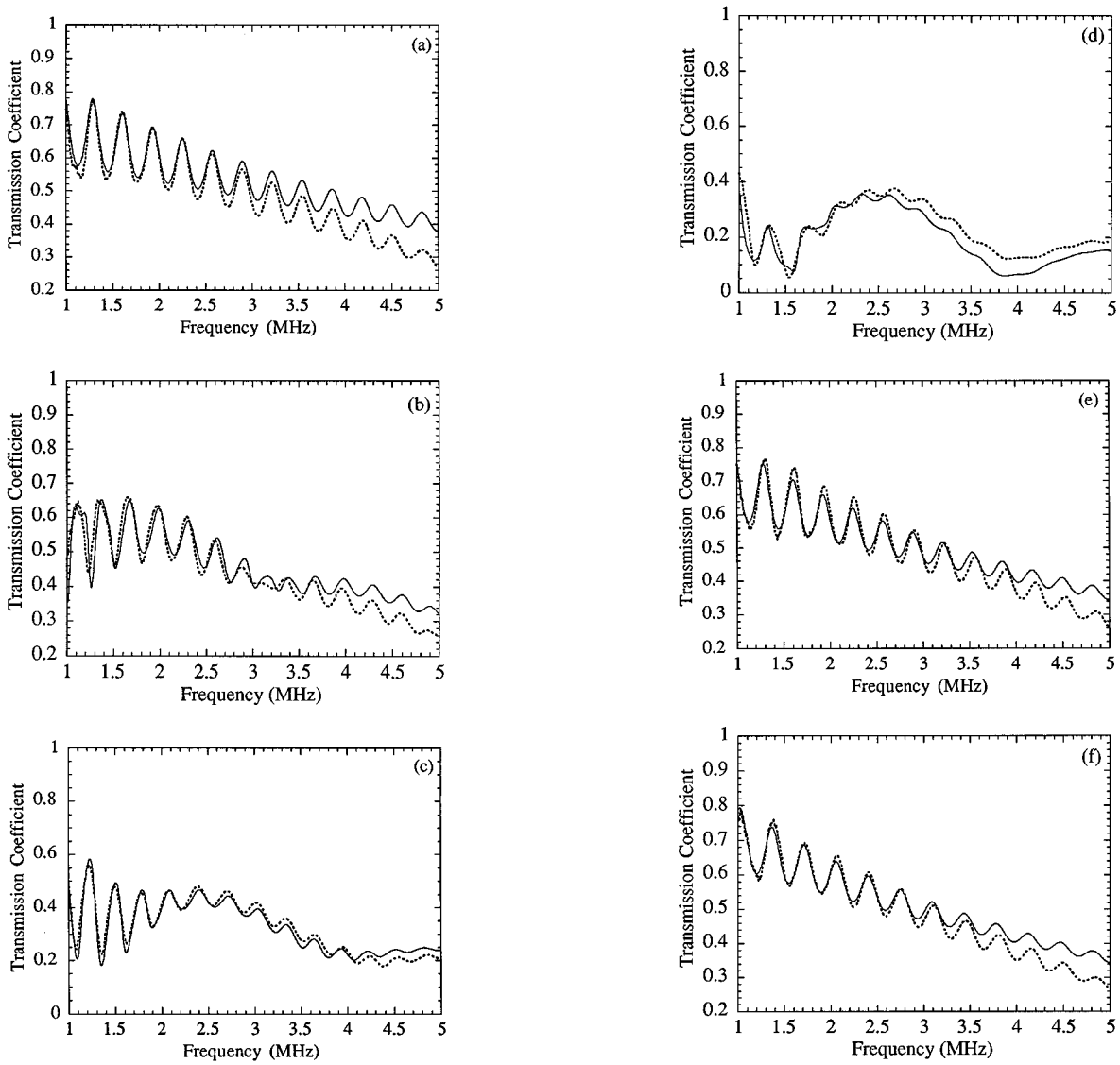

FIG. 4. Comparison of measurements on unidirectional CFRP plate using large transducers with plane-wave predictions. (a) Normal incidence; (b) 4°; (c) 5°; (d) 6°; (e) 12°; (f) 20° (solid line: theory; dashed line: measurements).

Figure 6(c) shows that at 20° the amplitude of the maximum is severely underestimated by the smaller transducer and there is a clear error in the frequency at which the maximum occurs. Figure 6(d) shows the corresponding result when the receiver was displaced in order to maximize the amplitude of the received signal. The amplitude of the peak has increased and its position has shifted from below to slightly above that given by the large transducers. In the tests with the large transducers, no significant difference in the transmission spectra was obtained with small receiver displacements. The amplitude errors mean that it will not be possible to obtain satisfactory attenuation values by comparing measurements made with conventional transducers and plane-wave predictions. The uncertainty in the frequencies of the maxima will

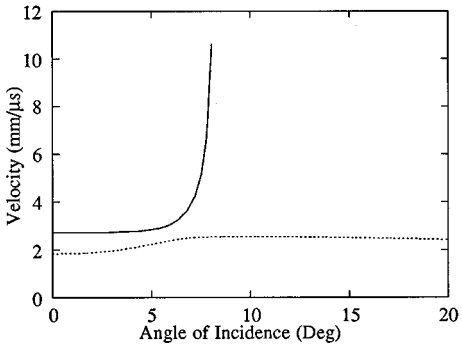

FIG. 5. Quasilongitudinal and quasishear mode velocities versus angle of incidence in typical CFRP material (solid line: QL; dashed line: QT).

TABLE II. Properties of unidirectional composite plate used in predictions. Thickness=4.15 mm; density=1542 kg/m^3. ''1'' direction is normal to plate; ''3'' direction is parallel to fibers.

Constant	Real part (GPa)	Imaginary part (GPa)	Attenuation at 3 MHz (Nepers m^{-1})
C_{11}	11.0	0.3	100
C_{33}	175	10	50
C_{55}	5.3	0.2	200
C_{13}	5.0	0.2	-

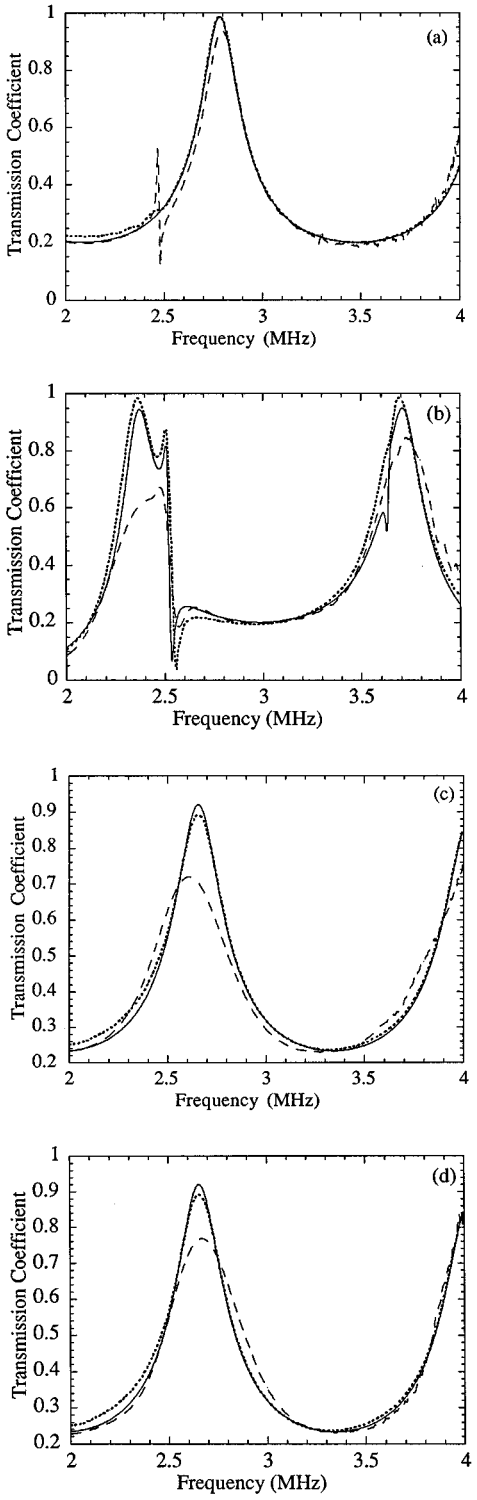

FIG. 6. Comparison of measurements on thin glass plate using large and small transducers. (a) Normal incidence; (b) 10°; (c) 20°; (d) 20° with receiver displaced by 4.8 mm to maximize received amplitude (solid line: theory; dashed line: large transducer measurements; – – – conventional transducer measurements).

also lead to errors in the estimates of the real parts of the elastic constants.

It should be stressed that the results presented in Fig. 6 are for a thin plate; the errors would be much more severe on thicker plates where the lateral displacement of the beam on

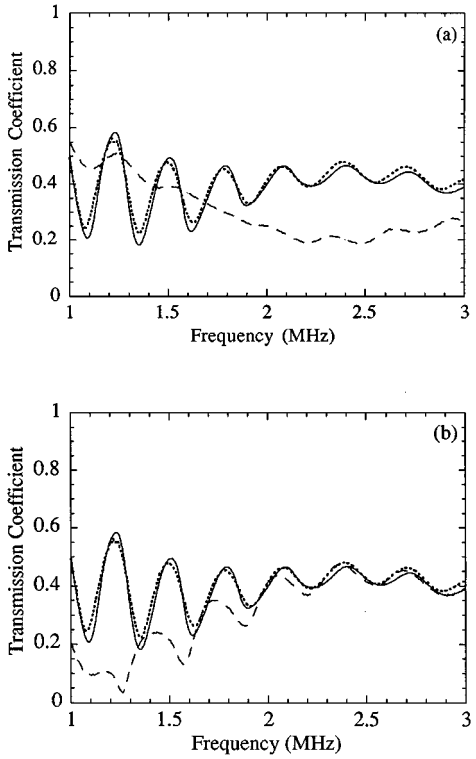

FIG. 7. Comparison of measurements on unidirectional CFRP plate using large and small transducers at 5°. (a) Transducers in line; (b) receiver displaced by 16 mm to maximize received amplitude (solid line: theory; dashed line: large transducer measurements; long dashed line: conventional transducer measurements).

successive reflections is larger. For example, Fig. 7(a) shows the results at 5° on the CFRP plate with no receiver displacement, while Fig. 7(b) shows the corresponding results when the receiver was displaced to maximize the signal amplitude. The results at the two receiver positions are very different, and neither bears much resemblance to the large transducer results and the predictions.

The large transducers are more expensive than conventional probes and require greater precision in alignment. It is therefore interesting to note that good agreement with plane-wave predictions can be obtained using one large and one small transducer. This is because if either the transmitter or receiver is a good approximation to a plane-wave transducer then the received signal will comprise a single plane-wave component. This effect was used[11] when a plane-wave receiver was simulated by taking measurements with a standard transducer at different receiver positions and summing them.

III. CONCLUSIONS

The results of this preliminary study show that the use of large transducers makes it possible to obtain excellent agreement between the form of the variation of the measured transmission coefficients with frequency and that predicted using plane-wave theory. The quantitative agreement between the measurements at angles not used in the determination of the material properties and the plane-wave predictions using these properties was also very encouraging. The large transducers give a clearer definition of the transmission

maxima than is obtained with smaller, conventional transducers, and also give good agreement with the predicted transmission coefficient amplitudes. This should improve the accuracy of inversion procedures for the determination of the real parts of the elastic constants from the frequencies of the transmission maxima, and the good amplitude agreement opens up the possibility of obtaining accurate estimates of the imaginary parts of the elastic constants.

Several groups[4,13] have developed algorithms to obtain the real parts of the elastic constants from measurements of the frequencies of the maxima (minima) in the transmission (reflection) spectra, and Kinra *et al.*[1–3] have developed methods using the whole of the measured spectra to obtain the real and imaginary parts of the elastic constants of isotropic materials. These algorithms could be applied directly to the results with the large transducers. The inverse problem to obtain the imaginary parts of the constants of anisotropic materials is much more difficult, particularly if the loss tangent varies with frequency. A suitable algorithm is now being developed using the full measured spectra and it is hoped to report its use in a future paper.

ACKNOWLEDGMENT

This work was carried out during a visit by Peter Cawley to Université de Bordeaux 1 funded by the university.

[1] V. K. Kinra and C. Zhu, ''Ultrasonic nondestructive evaluation of thin (sub-wavelength) coating,'' J. Acoust. Soc. Am. **93**, 2454–2467 (1993).
[2] V. K. Kinra and V. R. Iyer, ''Ultrasonic measurement of the thickness, phase velocity, density or attenuation of a thin viscoelastic plate. Part I: the forward problem,'' Ultrasonics **33**, 95–109 (1995).
[3] V. K. Kinra and V. R. Iyer, ''Ultrasonic measurement of the thickness, phase velocity, density or attenuation of a thin viscoelastic plate. Part II: the inverse problem,'' Ultrasonics **33**, 111–122 (1995).
[4] S. I. Rokhlin and W. Wang, ''Measurements of elastic constants of very thin anisotropic plates,'' J. Acoust. Soc. Am. **94**, 2721–2730 (1994).
[5] B. Hosten, ''Reflection and transmission of acoustic plane waves on an immersed orthotropic and viscoelastic solid layer,'' J. Acoust. Soc. Am. **89**, 2745–2752 (1991).
[6] Y. C. Chu and S. I. Rokhlin, ''Comparative analysis of through-transmission ultrasonic bulk wave methods for phase velocity measurements in anisotropic materials,'' J. Acoust. Soc. Am. **95**, 3204–3212 (1994).
[7] S. I. Rokhlin and W. Wang, ''Double through transmission bulk wave method for ultrasonic phase velocity measurement and determination of elastic constants of composite materials,'' J. Acoust. Soc. Am. **91**, 3303–3312 (1993).
[8] A. K. Mal, S. S. Lih, and Y. Bar-Cohen, ''Characterization of the elastic constants of unidirectional laminates using oblique incidence pulsed data,'' *Review of Progress in Quantitative NDE*, edited by D. O. Thompson and D. E. Chimenti (Plenum, New York, 1994), Vol. 13, pp. 1149–1156.
[9] B. Hosten, M. Deschamps, and B. R. Tittmann, ''Inhomogeneous wave generation and propagation in lossy anisotropic solids. Application to the viscoelastic characterization of composite materials,'' J. Acoust. Soc. Am. **82**, 1763–1770 (1987).
[10] T. P. Pialucha and P. Cawley, ''The reflection of ultrasound from interface layers in adhesive joints,'' *Review of Progress in Quantitative NDE*, edited by D. O. Thompson and D. E. Chimenti (Plenum, New York, 1991), Vol. 10B, pp. 1303–1309.
[11] B. Hosten and M. Castaings, ''Transfer matrix of multilayered absorbing and anisotropic media. Measurements and simulations of ultrasonic wave propagation through composite materials,'' J. Acoust. Soc. Am. **94**, 1488–1495 (1993).
[12] C. C. H. Guyott and P. Cawley, ''The measurement of through thickness plate vibration using a pulsed ultrasonic transducer,'' J. Acoust. Soc. Am. **83**, 623–631 (1988).
[13] M. R. Karim, A. K. Mal, and Y. Bar-Cohen, ''Inversion of leaky Lamb wave data by simplex algorithm,'' J. Acoust. Soc. Am. **88**, 482–491 (1990).

Acoustic *SH* phonons in a superlattice with (111) interfaces

Hatsuyoshi Kato
Tomakomai National College of Technology, 443, Nishikioka, Tomakomai, Hokkaido, 059-12 Japan

(Received 3 April 1996; accepted for publication 7 October 1996)

Transmission rates and dispersion relations of *SH* phonons in a (111) superlattice are calculated. Unlike the case of a (100) superlattice, phonon stop bands appear inside the folded Brillouin zone in general rather than at the center and edges. A superlattice structure factor is introduced appropriately for phonon reflection or Bragg conditions in the superlattice. More importantly, the transfer matrix contains information not only about the dispersion relation, but also about the condition for frequency bands or stop bands in the dispersion relation, and the extinction rule for the Bragg reflection. The locations of the stop bands inside of the folded zone are defined as a function of frequency and incidence angle of the phonons. © *1997 Acoustical Society of America.* [S0001-4966(97)05703-2]

PACS numbers: 43.35.Gk, 43.35.Cg [HEB]

INTRODUCTION

Since the first demonstration of phonon filtering by periodic semiconductor superlattices (SL's),[1] there have been extensive studies of the propagation of high-frequency acoustic phonons in multilayered structures composed of crystalline or amorphous thin films of nanometer thickness.[2–4] The basic transmission and reflection characteristics of phonons in periodic SLs can be understood in terms of the dispersion relations for phonons propagating within the structures. The artificially imposed periodicity of a SL induces the folding of the dispersion curves into a mini-Brillouin zone whose size is determined by the length of the SL period (unit cell). For a SL with interfaces of even-fold symmetry, frequency gaps appear at the zone center and zone boundary which are due to the intramode phonon Bragg reflections characteristic of a periodic structure.[1,5–7] These gaps mean that there are ranges of frequency over which no propagating modes exist in the superlattice. These frequency ranges act as phonon stop bands.

In the present paper we consider a SL with (111) interfaces and also oblique incidence of phonons. However, the phonons are limited to have wave vectors in the (110) plane and to be polarized in the [110] direction which is parallel to the (111) interfaces. Therefore, we consider the SH mode. This mode does not couple with the other modes and is pure-shear even if we consider the oblique incidence. In this case, the angles of incidence and reflection are not the same, unlike the case of interfaces with even-fold symmetries.

Figure 1 shows the structure of the periodic SL we consider. A unit cell consists of AlAs (with 150 monolayers) and GaAs (with 60 monolayers) as shown in Fig. 1(a). Each monolayer of constituent material has a thickness of 0.326 nm in the [111] direction, so the thickness of the assumed unit cell is $D=68.5$ nm. For simplicity, the substrate of the SL is assumed to be made of GaAs, while the detector layer is AlAs as shown in Fig. 1(b).

Figure 2(a) shows slowness curves of phonons in the (110) plane of GaAs. AlAs has similar slowness curves, but their sizes are smaller than those of GaAs. Figure 2(b) depicts slowness curves in the (110) plane; the left-hand side of the figure displays AlAs, while the right-hand side displays GaAs. The (111) interface is normal to the sheet. Thick lines in both Fig. 2(a) and (b) show slowness curves of pure-shear waves (*SH* phonons), whose polarization vector is perpendicular to the (110) plane.[8]

The pure-shear and quasi-shear waves generalize in three dimensions to slow-transverse (ST) and fast-transverse (FT) modes. The slowness surface of the ST mode lies entirely outside the FT mode, and these two surface touch conically along the [111] directions (and tangentially along the [100] directions). Consequently, the reflection shown in Fig. 2(b) corresponds to a mode conversion between ST and FT. In the present paper we deal only with wave vectors in the (110) plane, and only the *SH* portions of the slowness surface are considered. We do not consider in detail other mode conversions, which are physically allowed.

I. TRANSMISSION RATE

Figure 3 shows the coordinate system used for the calculation of the transmission rates and dispersion relations, where X, Y, and Z are the crystal axes of a cubic crystal and the axes x, y, and z are taken to be parallel to [112], [110], and [111], respectively. The coordinate system (x,y,z) is obtained from the system (X,Y,Z) by two consecutive orthogonal transformations. First (X,Y,Z) is rotated about the Z axis by 45°. The system is then rotated by $\arccos(1/\sqrt{3})$ radian about the y axis. After these transformations, the stiffness matrix of the cubic crystal in the coordinate system (x,y,z) becomes

$$[C]=\begin{bmatrix} C_{11} & C_{12} & C_{13} & 0 & C_{15} & 0 \\ C_{21} & C_{22} & C_{23} & 0 & C_{25} & 0 \\ C_{31} & C_{32} & C_{33} & 0 & C_{35} & 0 \\ 0 & 0 & 0 & C_{44} & 0 & C_{46} \\ C_{51} & C_{52} & C_{53} & 0 & C_{55} & 0 \\ 0 & 0 & 0 & C_{64} & 0 & C_{66} \end{bmatrix}. \tag{1}$$

Each element of this matrix can be expressed by the three independent stiffness coefficients, c_{11}, c_{12}, and c_{44} of the

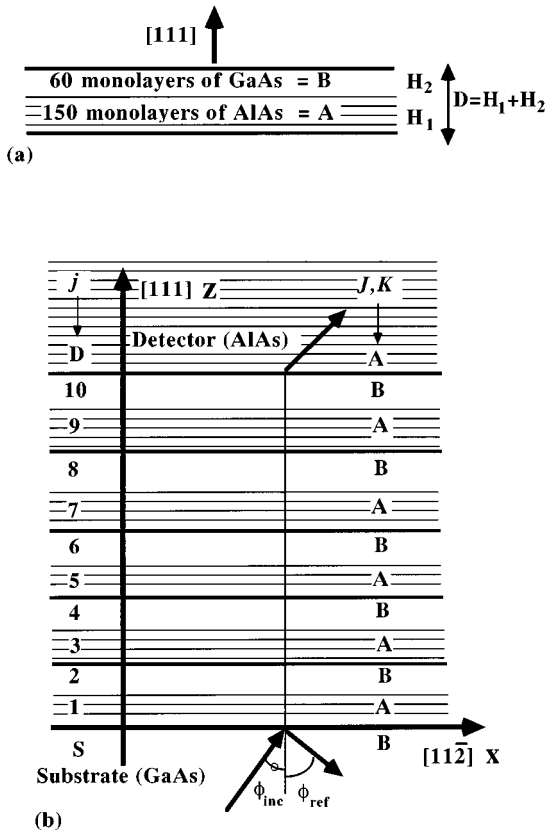

FIG. 1. Structure of the superlattice. (a) A unit cell consists of 60-monolayer GaAs and 150-monolayer AlAs, and their thicknesses are $H_2=60\times0.326$ nm, $H_1=150\times0.326$ nm, respectively. Total thickness becomes $D=H_1+H_2=68.5$ nm. (b) Substrate is made of GaAs. From the interface some part of incident phonons are reflected. Transmitted phonons appear in the detector layer, in which we assume that no reflections exist.

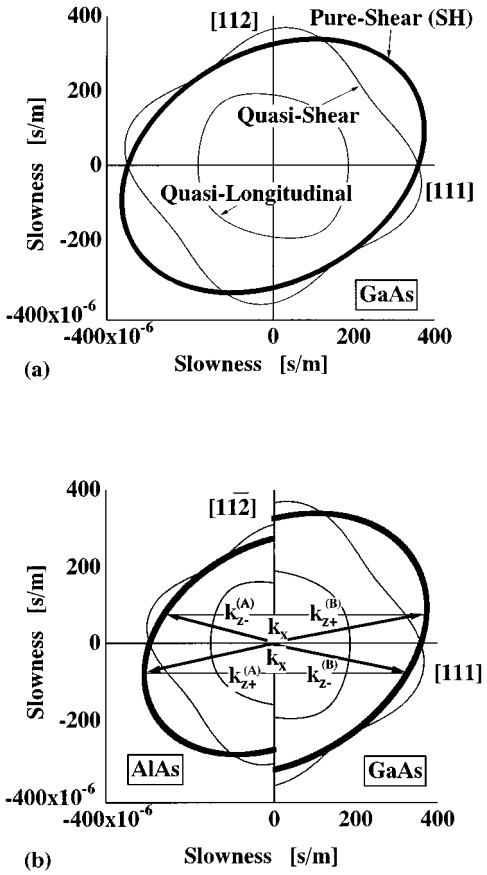

FIG. 2. Slowness curves on $(\bar{1}10)$ plane. (a) The slowness curves are shown for GaAs in bulk. The thick oval line represents pure-shear (SH) phonons. Other two curves are quasi-shear and quasi-longitudinal phonons. (b) Slowness curves of AlAs and GaAs are shown in the same figure separated by the (111) interface. If we consider incident wave propagating from GaAs to AlAs with a certain frequency, we can put a corresponding wave vector on the figure. Because of the translational symmetry, reflected and transmitted wave vectors are easily shown as in the figure.

cubic crystal. Explicit forms are given in the Appendix. Here, we only note that the above matrix $[C]$ is symmetric (i.e., $C_{ij}=C_{ji}$).

We take the displacement vector **u** of the medium as

$$\mathbf{u}=\begin{bmatrix}0\\ u_y\\ 0\end{bmatrix}, \tag{2}$$

$$u_y=|u_y|\exp(ik_x x+ik_z z-i\omega t), \tag{3}$$

i.e., the displacement is assumed to be a plane wave propagating on the $(\bar{1}10)$ plane and polarized to the $[11\bar{2}]$ direction. The equation of motion derived from Eq. (1) with Eq. (3) leads to

$$C_{66}k_x^2+C_{44}k_z^2+2C_{46}k_xk_z=\rho\omega^2. \tag{4}$$

From this equation we can obtain the slowness curves of SH phonons[9] (cf. Appendix A). Nonzero elements of the stress tensor derived from Eq. (2) and Eq. (3) are

$$\sigma_{yz}=i(C_{44}k_z+C_{46}k_x)u_y, \tag{5a}$$

$$\sigma_{xy}=i(C_{64}k_z+C_{66}k_x)u_y. \tag{5b}$$

The time-averaged acoustic energy flux associated with the lattice vibration of Eq. (2) is expressed as follows:

$$P_x=\tfrac{1}{2}(C_{64}k_z+C_{66}k_x)\omega|u_y|^2, \tag{6a}$$

$$P_y=0, \tag{6b}$$

$$P_z=\tfrac{1}{2}(C_{44}k_z+C_{46}k_x)\omega|u_y|^2. \tag{6c}$$

We apply the above results to the SL shown in Fig. 1. The displacement field in each layer can be written as

$$u_x^{(j)}=u_z^{(j)}=0, \tag{7a}$$

$$u_y^{(j)}=A^{(j)}\exp(ik_x x+ik_{z+}^{(j)}z_j-i\omega t)+B^{(j)}\times\exp(ik_x x-ik_{z-}^{(j)}z_j-i\omega t), \tag{7b}$$

where j specifies a layer (see Fig. 1), z_j is the z coordinate measured from the interface between the jth and $(j-1)$th layers. It should be noted that the z components of the wave vectors of incident waves and those of reflected waves are not the same due to three-fold symmetry of the (111) interface. The x components of the wave vectors are the same because of the translational symmetry in the x direction. Nonzero elements of the stress tensor are

$$\sigma_{yz}^{(j)}=i\alpha^{(j)}A^{(j)}\exp(ik_x x+ik_{z+}^{(j)}z_j-i\omega t)+i\beta^{(j)}B^{(j)}\exp(ik_x x-ik_{z-}^{(j)}z_j-i\omega t), \tag{8a}$$

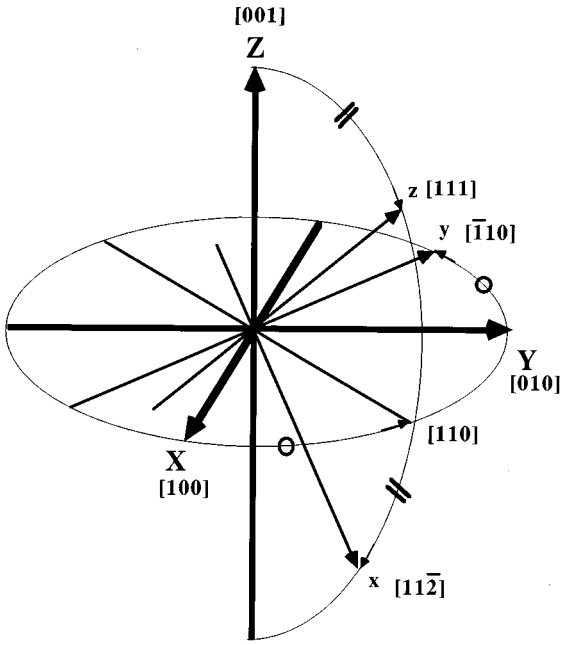

FIG. 3. Coordinate system for the stiffness matrix. X, Y, and Z axes are crystal axes of the cubic crystal. The axes x, y, and z are for Eq. (1), whose directions are [112], [110], and [111], respectively.

$$\sigma_{xy}^{(j)} = i\gamma^{(j)} A^{(j)} \exp(ik_x x + ik_{z+}^{(J)} z_j - i\omega t) + i\delta^{(j)} B^{(J)} \exp(ik_x x - ik_{z-}^{(j)} z_j - i\omega t), \tag{8b}$$

where

$$\alpha^{(j)} = C_{44}^{(j)} k_{z+}^{(j)} + C_{46}^{(j)} k_x, \tag{9a}$$

$$\beta^{(j)} = -C_{44}^{(j)} k_{z-}^{(j)} + C_{46}^{(j)} k_x, \tag{9b}$$

$$\gamma^{(j)} = C_{64}^{(j)} k_{z+}^{(j)} + C_{66}^{(j)} k_x, \tag{9c}$$

$$\delta^{(j)} = -C_{64}^{(j)} k_{z-}^{(j)} + C_{66}^{(j)} k_x. \tag{9d}$$

Using the boundary condition that the displacement and stress at each interface of the jth and $(j+1)$th layer must be the same, the following expression can be derived for the amplitudes in Eq. (7) and Eq. (8):

$$\begin{bmatrix} A^{(j+1)} \\ B^{(j+1)} \end{bmatrix} = [M^{j+1}(0)]^{-1} M^{(j)}(H_j) \begin{bmatrix} A^{(j)} \\ B^{(j)} \end{bmatrix}, \tag{10}$$

where

$$M^{(j)}(z_j) = \begin{bmatrix} \exp(ik_{z+}^{(j)} z_j) & \exp(-\overline{z}^{(j)}_{z-} z_j) \\ i\alpha^{(j)} \exp(ik_{z+}^{(j)} z_j) & i\beta^{(j)} \exp(-ik_{z-}^{(j)} z_j) \end{bmatrix}. \tag{11}$$

With repetition of the above calculation, we can get a relation between amplitudes in the substrate $(A^{(S)}, B^{(S)})$ and in the detector layer $(A^{(D)}, B^{(D)})$:

$$\begin{bmatrix} A^{(D)} \\ B^{(D)} \end{bmatrix} = [M^{(D)}(0)]^{-1} T^N M^{(S)}(0) \begin{bmatrix} A^{(S)} \\ B^{(S)} \end{bmatrix}, \tag{12}$$

where T is a transfer matrix and N is a number of the unit cells. In deriving Eq. (12), it should be noted that all layers with even numbers are of the same medium and so are the layers with odd numbers. The transfer matrix T is thus expressed as follows:

$$T = T^{(2)} T^{(1)}, \tag{13a}$$

where

$$T^{(j)} = M^{(j)}(H_j)[M^{(j)}(0)]^{-1}. \tag{13b}$$

The amplitude $B^{(D)}$ of the reflected phonons in the detector layer should vanish.[1] With this condition, the transmission rates of the SH phonons from the substrate to the detector layer are expressed as

$$\frac{P_z^{(D)}}{P_{z+}^{(S)}} = \frac{\alpha^{(D)}}{\alpha^{(S)}} |\tau|^2, \tag{14}$$

where $\alpha^{(D)}$ and $\alpha^{(S)}$ are defined by Eq. (9a) for the detector (D) and substrate (S) layers, and

$$\tau = \frac{A^{(D)}}{A^{(S)}}. \tag{15}$$

For simplicity, the detector and the substrate are assumed to be the same as A and B materials, respectively. The values of Eq. (15) are calculated from Eq. (12). In Eq. (14), $P_{z+}^{(S)}$ is an energy flux of the incident phonons in the substrate, and $P_z^{(D)}$ is of the transmitted phonons in the detector layer. Results of numerical calculation are shown in Fig. 4.

II. DISPERSION RELATION

With the use of the transfer matrix, we obtain the dispersion relation of the phonons in the (110) plane. For a periodic SL, it is convenient to redefine the transfer matrix as

$$T = T^{(B)} T^{(A)}, \tag{16}$$

where $T^{(A)}$ and $T^{(B)}$ denote the transfer matrices for odd and even layers, respectively. The superlattice wave number q is related to the two eigenvalues of the transfer matrix T. Thus, all we have to do is to solve the characteristic equation:

$$\det[T - \chi E] = 0, \tag{17}$$

where

$$\chi \equiv e^{iqD}, \tag{18}$$

and E is a 2×2 unit matrix. Results of numerical calculations are shown in Fig. 4 together with the transmission rates.

We should note here that the determinant of T is not unity:

$$\det[T] = \exp[i(k_{z+}^{(B)} - k_{z-}^{(B)}) H_B] \exp[i(k_{z+}^{(A)} - k_{z-}^{(A)}) H_A]. \tag{19}$$

Hence, $1/\chi$ is not an eigenvalue of Eq. (17) even if χ is an eigenvalue of T. [This is unlike the case of a SL with interfaces having even-fold symmetry like the (001) plane.] This stems from the fact that the angles of incidence and reflection are not the same, or $k_{z+}^{(J)} \neq k_{z-}^{(J)}$ $(J = A, B)$ for (111) interfaces.

III. STRUCTURE FACTOR

In order to calculate amplitude transmission coefficients, we express Eq. (12) as

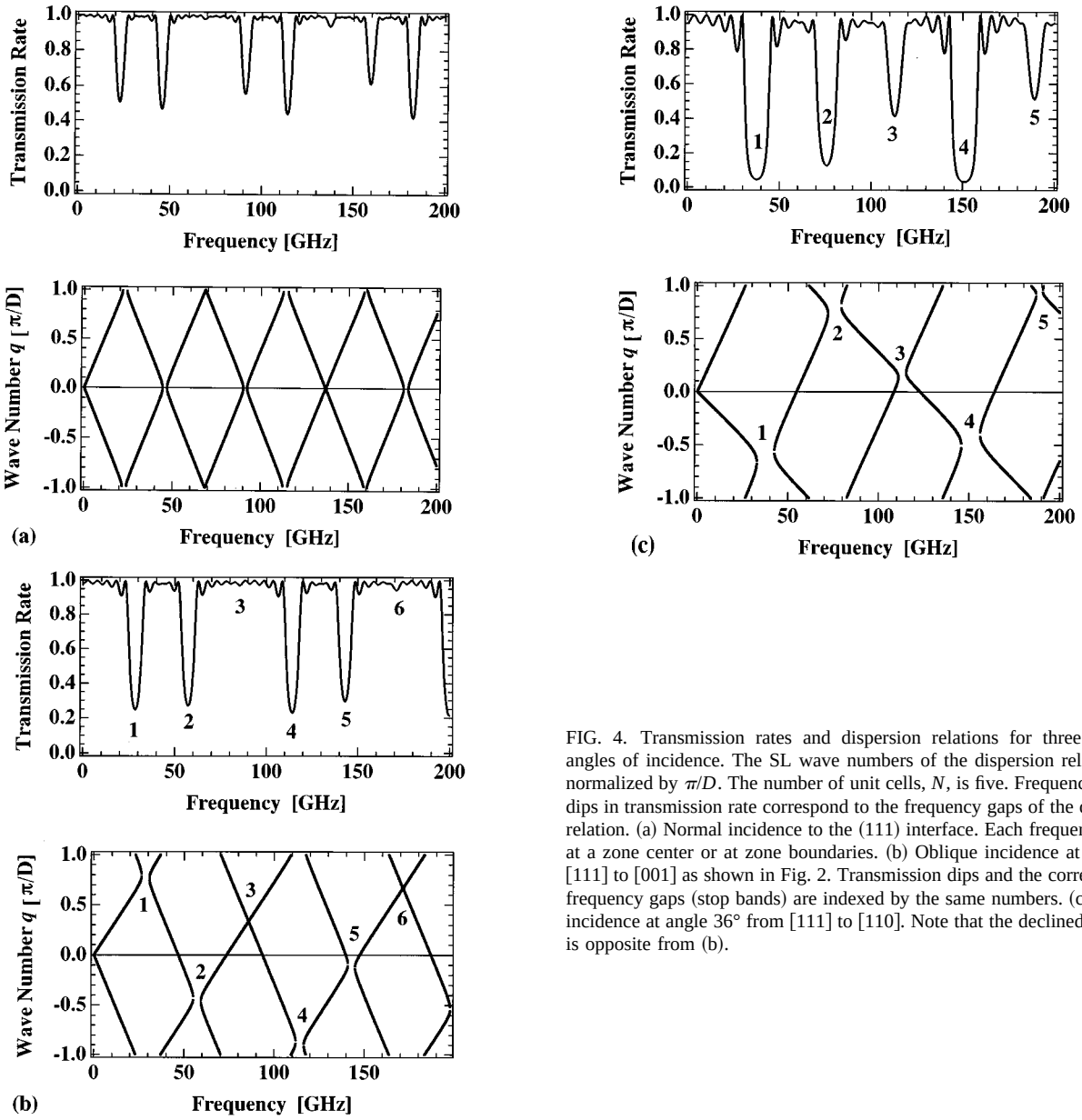

FIG. 4. Transmission rates and dispersion relations for three different angles of incidence. The SL wave numbers of the dispersion relations are normalized by π/D. The number of unit cells, N, is five. Frequencies of the dips in transmission rate correspond to the frequency gaps of the dispersion relation. (a) Normal incidence to the (111) interface. Each frequency gap is at a zone center or at zone boundaries. (b) Oblique incidence at 36° from [111] to [001] as shown in Fig. 2. Transmission dips and the corresponding frequency gaps (stop bands) are indexed by the same numbers. (c) Oblique incidence at angle 36° from [111] to [110]. Note that the declined direction is opposite from (b).

$$\begin{bmatrix} A^{(D)} \\ B^{(D)} \end{bmatrix} = f^{(BA)} F^N \begin{bmatrix} A^{(S)} \\ B^{(S)} \end{bmatrix}, \tag{20}$$

where

$$f^{(JK)} = [M^{(K)}(0)]^{-1} M^{(J)}(0), \tag{21}$$

$$F = \Phi^{(B)}(H_B) f^{(AB)} \Phi^{(A)}(H_A) f^{(BA)}, \tag{22}$$

$$\Phi^{(J)}(H_J) = \begin{bmatrix} \exp(ik_{z+}^{(J)} H_J) & 0 \\ 0 & \exp(-ik_{z-}^{(J)} H_J) \end{bmatrix}, \tag{23}$$

and $J,K = A$ or B. In these expressions, $f^{(JK)}$ can be interpreted as a matrix which expresses amplitude transmission and reflection coefficients, and $\Phi^{(J)}(H_J)$ expresses phase changes for the SH phonons which propagate through layer J.

To derive the superlattice structure factor for phonon reflection, we use a perturbation treatment. The structure factor S is obtained by neglecting multiple reflections from interfaces (see Fig. 5):

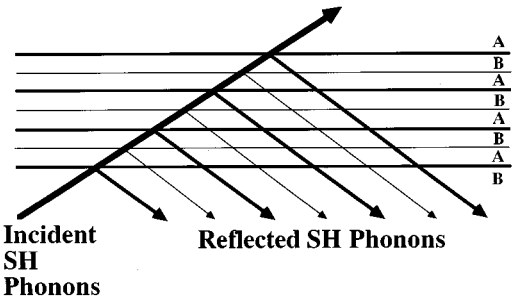

FIG. 5. Schematic of the reflection of phonons. Multiple reflections at interfaces are neglected.

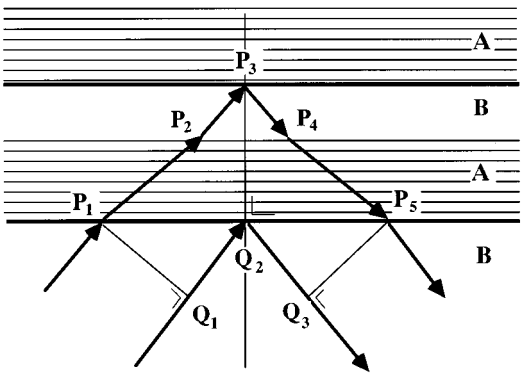

FIG. 6. If the phase difference between the paths $P_1-P_2-P_3-P_4-P_5$ and $Q_1-Q_2-Q_3$ is 2π times an integer, the reflection of the phonons is enhanced and this gives the Bragg condition for a SL as in Eq. (26).

$$S=r_{BA}+(r_{BA}+r_{AB}\exp(-i\theta_B))\exp[i(\theta_A+\theta_B)] \times\frac{1-\exp[iN(\theta_A+\theta_B)]}{1-\exp[i(\theta_A+\theta_B)]}, \tag{24}$$

where

$$\theta_J=k_{z+}^{(J)}H_J+k_{z-}^{(J)}H_J \quad (J=A \text{ or } B), \tag{25}$$

and r_{JK} is the amplitude reflection coefficient at an interface between media J and K (more precisely, for a phonon incident to the interface from layer J). The coefficient r_{JK} can be approximated by the element $[f^{(JK)}]_{21}$ of the matrix defined by Eq. (21). Thus, $|S|^2$ has a peak when the following condition is satisfied:

$$\theta_A+\theta_B=2\pi m, \tag{26a}$$

or

$$k_{z+}^{(A)}H_A+k_{z-}^{(A)}H_A+k_{z+}^{(B)}H_B+k_{z-}^{(B)}H_B=2\pi m, \tag{26b}$$

where m is an integer. This implies that the reflection from the interface is enhanced, and Eq. (26) is interpreted as the Bragg condition for SH phonons in the SL. Figure 6 shows this condition schematically. This reflection is suppressed when the following condition holds:

$$r_{BA}+r_{AB}\exp(-i\theta_B)=0. \tag{27}$$

This equation expresses the extinction rule caused by the structure of the unit cell.

IV. CHARACTERISTICS OF TRANSFER MATRIX

If e^{iq_1D} and e^{iq_2D} are two eigenvalues of the matrix T ($D=H_A+H_B$ is the thickness of a unit cell), we have

$$e^{iq_1D}e^{iq_2D}=\det[T]. \tag{28}$$

The determinant of the transfer matrix T is also expressed by Eq. (19). Thus, we obtain

$$q_1D+q_2D=(k_{z+}^{(B)}-k_{z-}^{(B)})H_B+(k_{z+}^{(A)}-k_{z-}^{(A)})H_A+2\pi m, \tag{29}$$

where m is an integer, and H_A and H_B are the layer thicknesses. (H_A and H_B are equivalent to H_1 and H_2, respectively. See Fig. 1.) The eigenvalues of the transfer matrix are complex in general (also q_1D and q_2D are complex). Because the right-hand side of Eq. (29) is real, the imaginary part of the left-hand side must vanish, i.e.,

$$\mathrm{Im}[q_1D+q_2D]=0. \tag{30}$$

If either q_1D or q_2D has an imaginary part, the other one must have an imaginary part with an opposite sign and the same magnitude. If one of them is real, so is the other. The wave numbers $k_{z\pm}^{(J)}$ in Eq. (29) depend linearly on phonon frequencies and are real numbers, as far as the total reflections at the interfaces do not occur. Also, their magnitudes are derived as a function of frequency ω and angle ϕ_{inc} of incidence phonons. Therefore, we define a real function L by

$$L(\omega,\phi_{\mathrm{inc}};m)=\tfrac{1}{2}[(k_{z+}^{(B)}-k_{z-}^{(B)})H_B+(k_{z+}^{(A)}-k_{z-}^{(A)})H_A]+\pi m =\tfrac{1}{2}(q_1D+q_2D), \tag{31}$$

or from Eq. (28)

$$L(\omega,\phi_{\mathrm{inc}};m)=\frac{1}{2i}\log(\det[T])+\pi m. \tag{32}$$

Hence, we explicitly write down the trace of the transfer matrix T:

$$\mathrm{Tr}[T]=\frac{1}{(\alpha^{(B)}-\beta^{(B)})(\alpha^{(A)}-\beta^{(A)})}[(\beta^{(B)}-\beta^{(A)})(\alpha^{(B)}-\alpha^{(A)})(e^{ik_{z+}^{(B)}H_B-ik_{z-}^{(A)}H_A}+e^{-ik_{z-}^{(B)}H_B+ik_{z+}^{(A)}H_A}) -(\beta^{(B)}-\alpha^{(A)})(\alpha^{(B)}-\beta^{(A)})(e^{ik_{z+}^{(B)}H_B+ik_{z+}^{(A)}H_A}+e^{-ik_{z-}^{(B)}H_B-ik_{z-}^{(A)}H_A})]. \tag{33}$$

Using eigenvalues introduced in Eq. (28), $\mathrm{Tr}[T]$ can also be expressed as follows:

$$e^{iq_1D}+e^{iq_2D}=\mathrm{Tr}[T]. \tag{34}$$

If the phonons are in the frequency band, q_1D and q_2D are real. Hence, Eq. (34) becomes

$$\left|\frac{1}{2}\mathrm{Tr}[T]\right|^2=\cos^2\frac{q_1D-q_2D}{2}. \tag{35}$$

Accordingly, SH phonons are inside a frequency band if

$$\left|\tfrac{1}{2}\mathrm{Tr}[T]\right|\leqslant 1 \tag{36}$$

is satisfied. On the other hands, If the condition

$$\left|\tfrac{1}{2}\mathrm{Tr}[T]\right|>1 \tag{37}$$

is satisfied, q_1D and q_2D must be complex. This condition means that the phonons are inside a stop band. Therefore, Eq. (37) is a more precise condition for the reflection of phonons than the Bragg condition given by Eq. (26).

Next, we derive the equation relating the wave number q and frequency ω for which the phonon stop bands are obtained. Let e^{iqD} be one of e^{iq_1D} or e^{iq_2D}, then

$$e^{iqD}=\tfrac{1}{2}\mathrm{Tr}[T]\pm\sqrt{(\tfrac{1}{2}\mathrm{Tr}[T])^2-\det[T]}. \tag{38}$$

If the Bragg condition, Eq. (26), is satisfied, the trace and determinant of T satisfy the following relation:

$$(\tfrac{1}{2}\mathrm{Tr}[T])^2=\det[T]R^2, \tag{39}$$

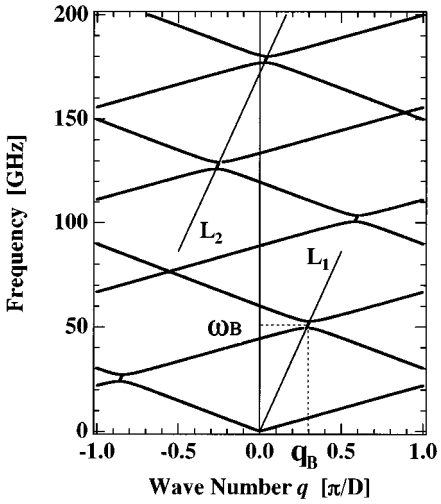

FIG. 7. Dispersion relation for *SH* phonons incident obliquely at 20° from [111] to [110]. For L_1 and L_2, see text. The Bragg reflection appears at (q_B,ω_B) satisfying Eq. (45).

where

$$R=1-\frac{2(\beta^{(B)}-\beta^{(A)})(\alpha^{(B)}-\alpha^{(A)})}{(\alpha^{(B)}-\beta^{(B)})(\alpha^{(A)}-\beta^{(A)})}\sin^2\frac{\psi}{2}, \tag{40}$$

$$\psi=(k_{z+}^{(B)}+k_{z-}^{(B)})H_B=-(k_{z+}^{(A)}+k_{z-}^{(A)})H_A+2\pi m. \tag{41}$$

Because $|\frac{1}{2}\mathrm{Tr}[T]|=1$,

$$|\tfrac{1}{2}\ \mathrm{Tr}[T]|=|R|. \tag{42}$$

We can notice here that R is real. Therefore, Eq. (38) becomes

$$qD=\arg\left(\frac{1}{2}\ \mathrm{Tr}[T]\right)+\frac{1}{i}\log|R|+\frac{1}{i}\log(1\pm\sqrt{1-1/R^2}), \tag{43}$$

where q is a superlattice wave number at the Bragg condition. When a frequency is inside a phonon stop band, Eq. (37) is satisfied, and Eqs. (37) and (40) lead to $|R|>1$ and $1/R^2<1$. Thus, both the second and third terms of Eq. (43) are purely imaginary. Therefore, the real part of qD becomes

$$\mathrm{Re}[qD]=\arg(\tfrac{1}{2}\ \mathrm{Tr}[T]). \tag{44}$$

This relation and Eq. (30) imply that stop band occurs at the wave number

$$q_BD=\mathrm{Re}[q_1D]=\mathrm{Re}[q_2D]=\frac{q_1D+q_2D}{2}$$
$$=L(\omega_B,\phi_{\mathrm{inc}},m), \tag{45}$$

where ω_B is a frequency at which the Bragg condition, Eq. (26b) is satisfied. This also means that the two branches of the dispersion relations intersect at $q=q_B$. Since L is linear in ω, the locations of the points (q_B,ω_B) in $q-\omega$ space satisfying Eq. (45) are found on a lines with a given slope. These lines (L_1 and L_2) are shown in Fig. 7.

When the Bragg condition is satisfied, Eq. (43) implies

$$\mathrm{Im}[qD]\to 0\ \ \text{as}\ \ |R|\to 1_{+0}. \tag{46}$$

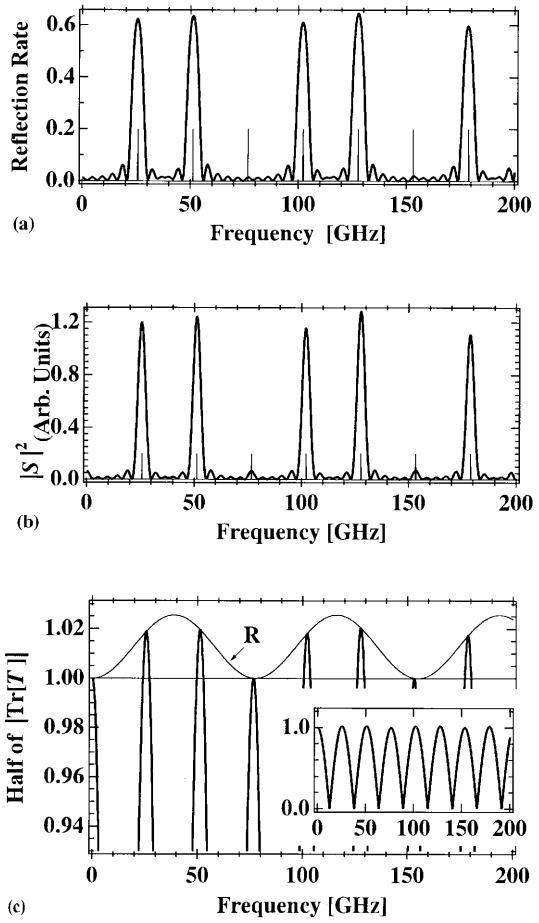

FIG. 8. (a) Reflection rate of obliquely incident *SH* phonons. Vertical lines show the frequencies that satisfy the Bragg condition. Parameters assumed are the same as Fig. 7. (b) The square of the magnitude of the structure factor. Vertical lines also indicate the frequencies satisfying the Bragg condition. (c) One-half of the trace of the transfer matrix. Inset shows the whole shape. If the Bragg condition is satisfied, this value becomes greater than unity. The extinction rule is satisfied, if this value becomes unity. R defined by Eq. (40) gives the envelope of the peaks.

Vanishing of the imaginary part of qD means that the Bragg reflection of phonons is suppressed. Hence, the extinction rule can be expressed more quantitatively than Eq. (27) in terms of the transfer matrix as follows:

$$|\tfrac{1}{2}\ \mathrm{Tr}[T]|=1. \tag{47}$$

In oblique incidence of *SH* phonons to the SL: (1) The stop bands in the dispersion relation appear, in general, inside the folded zone rather than the zone center and the zone edges as in Fig. 7. The position of the stop bands q_B is determined by Eq. (45) and directly proportional to the frequency ω_B that satisfies the Bragg condition. (2) The enhanced reflection of the phonons inside the stop band can be described by the trace of the transfer matrix as in Eq. (37). In addition, the condition for the frequency band is expressed by the trace of the transfer matrix as in Eq. (36). (3) The extinction rule for the Bragg reflection is also expressed using the transfer matrix via Eq. (47) as in Fig. 8.

V. CONCLUSION

As shown in Fig. 4, the dispersion relation has frequency gaps (stop bands) inside the folded zone. Inside these gaps, the transmission rates have sharp dips. Even if the declined angles are the same except their directions, the dips do not appear in the same frequencies in Fig. 4(b) and (c). These results stem from the three-fold symmetry of the interfaces (more precisely, the absence of mirror symmetry) and anisotropy of the media in the SL.

Figure 2 shows that two phonon modes, other than the *SH* phonon we have considered, exist. One is quasi-longitudinal and the other is the quasi-shear. We expect similar results should be obtained for these two modes.

The transfer matrix contains various kinds of information about the *SH* phonons in the SL, e.g., the dispersion relation, the reflection condition (more precise than the Bragg condition), the extinction rule for the Bragg reflection, and the location of the stop band in the dispersion relation. The transmission and reflection of the phonons have been observed experimentally. The observation of the shifts of the stop band from the zone center and zone edges for oblique incidence is an interesting challenge. Certain kinds of techniques (e.g., Raman scattering) should give possibilities to observe this phenomenon. For phonons normal to the interface, Raman scattering would show two Stokes lines from a stop band at zone center. For phonons oblique to the interface, the difference of frequency shifts between the two Stokes lines of the Raman scattering is expected to become large.[7,10–15]

The above results are obtained generally from the transfer matrix method. Therefore, they imply that there exist similar phenomena with the same origin in other types of SLs, e.g., a SL with (001) interfaces, and a SL with isotropic layers.

ACKNOWLEDGMENT

The author appreciates Professor S. Tamura in Hokkaido University for his instructive comments and discussions.

APPENDIX A: STIFFNESS AND SLOWNESS CURVES OF *SH* PHONONS

There are general expressions for slowness surfaces for cubic crystals.[16] These expressions have certain singularities not convenient to numerical calculations. We have used stiffness coefficients in the rotated coordinate system given in Eq. (1). Each element of Eq. (1) can be expressed in three independent elements of stiffness matrix for cubic crystals. For clarity, we express these three elements by a, b, and c instead of c_{11}, c_{12}, and c_{44} respectively in the usual crystal coordinate system. The elements of Eq. (1) then become as follows:

In the following formulae we put $Q=\arctan(1/\sqrt{2})$:

$$C_{11}=\frac{3a+5b+10c}{8}+\frac{a-b-2c}{8}\times(2+3\cos 2Q)\cos 2Q,$$

$$C_{12}=\frac{a-b-2c}{2}\sin^2 Q+b,$$

$$C_{13}=\tfrac{3}{8}(a-b-2c)\sin^2 2Q+b,\quad C_{14}=0,$$

$$C_{15}=-\frac{a-b-2c}{8}(1+3\cos 2Q)\sin 2Q,$$

$$C_{16}=0,\quad C_{21}=C_{12},$$

$$C_{22}=\frac{a+b+2c}{2},$$

$$C_{23}=\frac{a-b-2c}{2}\cos^2 Q+b,\quad C_{24}=0,$$

$$C_{25}=\frac{a-b-2c}{4}\sin 2Q,$$

$$C_{26}=0,\quad C_{31}=C_{13},\quad C_{32}=C_{23},$$

$$C_{33}=\frac{3a+5b+10c}{8}+\frac{a-b-2c}{8}\times(3\cos 2Q-2)\cos 2Q,$$

$$C_{34}=0,$$

$$C_{35}=\frac{a-b-2c}{8}(3\cos 2Q-1)\sin 2Q,$$

$$C_{36}=0,\quad C_{41}=C_{42}=C_{43}=0,$$

$$C_{44}=\frac{a-b-2c}{2}\cos^2 Q+c,$$

$$C_{45}=0,\quad C_{46}=\frac{a-b-2c}{4}\sin 2Q=C_{25},$$

$$C_{51}=C_{15},\quad C_{52}=C_{25},\quad C_{53}=C_{35},\quad C_{54}=0,$$

$$C_{55}=\tfrac{3}{8}(a-b-2c)\sin^2 2Q+c,$$

$$C_{56}=0,\quad C_{61}=C_{62}=C_{63}=0,$$

$$C_{64}=C_{46},\quad C_{65}=0,$$

$$C_{66}=\frac{a-b-2c}{2}\sin^2 Q+c.$$

If we rotate the z axis about the y axis by μ radians to [110] direction in Fig. 3, we can get stiffness from the above formulae by the substitution

$$Q\rightarrow Q-\mu.$$

The angular variable part of the above formulae can be rewritten only with $\cos 2Q$ and $\sin 2Q$. This implies the slowness curves have two-fold symmetry about the y axis. This is why the wave vectors of the phonons are placed in Fig. 2. Making use of the above expressions, we can consider various kinds of interfaces of a SL. Putting $\mu=-\arccos(1/\sqrt{3})$, we can get stiffness for a SL with the (001) interface. When we consider isotropic layers, then $a-b-2c=0$ and the stiffness coefficients do not depend on interfaces.

Equation (4) can be expressed more simply with the above stiffness, e.g.,

$$\frac{a-b-2c}{2}\cos^2(Q-\mu)+c=\rho\left(\frac{\omega}{k}\right)^2,$$

where k is the wave vector expressed as $k=\sqrt{k_x^2+k_z^2}$ (n.b., $k_y=0$), μ is the angle of the wave vector from the [111] direction whose positive value is taken to the [110] direction, and $Q=\arctan(1/\sqrt{2})$. We can notice this expression is very similar with C_{44} in the above expressions of stiffness because the *SH* phonon is pure shear and can be considered just like a transverse mode in isotropic medium even if the SL layers are anisotropic.

APPENDIX B: RYTOV'S DISPERSION RELATION

If the z components of incident and reflected phonons' wave vectors have the same value, i.e., $k_{z+}^{(J)}=k_{z-}^{(J)}\equiv k_z^{(J)}$, then Eq. (33) becomes

$$\tfrac{1}{2}\,\mathrm{Tr}[T]=\cos k_z^{(B)}H_B\cos k_z^{(A)}H_A + V\sin k_z^{(B)}H_B\sin k_z^{(A)}H_A,$$

where

$$V=\frac{(C_{46}^{(B)}-C_{46}^{(A)})^2}{2C_{44}^{(B)}C_{44}^{(A)}}\frac{k_x^2}{k_z^{(B)}k_z^{(A)}}-\frac{1}{2}\left(\frac{C_{44}^{(B)}k_z^{(B)}}{C_{44}^{(A)}k_z^{(A)}}+\frac{C_{44}^{(A)}k_z^{(A)}}{C_{44}^{(B)}k_z^{(B)}}\right).$$

Knowing that $\det[T]$ becomes unity [cf. Eq. (28)] and $\mathrm{Tr}[T]$ is real, the dispersion relation can be expressed with the above expression of $\mathrm{Tr}[T]$ as

$$\cos qD=\cos k_z^{(B)}H_B\cos k_z^{(A)}H_A + V\sin k_z^{(B)}H_B\sin k_z^{(A)}H_A.$$

This equation is a formula for the oblique *SH* phonon incidence. Its format is the same as in the case of the normal incidence of phonons without any interactions between their modes.[4,5,10–15] [n.b., For a SL with (001) interfaces, $C_{46}=0$; so the first term of expression V vanishes, as well as for a SL with isotropic layers.]

[1] V. Narayanamurti, H. L. Stormer, M. A. Chin, A. C. Gossard, and W. Wiegmann, Phys. Rev. Lett. **43**, 2012 (1979).
[2] O. Koblinger, J. Mebert, E. Dittrich, S. Dottinger, W. Eisenmenger, P. V. Santos, and L. Ley, Phys. Rev. B **35**, 9375 (1987).
[3] D. C. Hurley, S. Tamura, J. P. Wolfe, and H. Morkoc, Phys. Rev. Lett. **58**, 2446 (1987).
[4] S. Tamura, D. C. Hurley, and J. P. Wolfe, Phys. Rev. B **38**, 1427 (1988).
[5] S. M. Rytov, Akust. Zh. **2**, 71 (1956) [Sov. Phys. Acoust. **2**, 68 (1956)].
[6] A. S. Barker, Jr., J. L. Merz, and A. C. Gossard, Phys. Rev. B **17**, 3181 (1979).
[7] C. Colvard, R. Merlin, M. V. Klein, and A. C. Gossard, Phys. Rev. Lett. **45**, 298 (1980); C. Colvard, T. A. Gant, M. V. Klein, R. Merlin, R. Fischer, H. Morkoc, and A. C. Gossard, Phys. Rev. B **31**, 2080 (1985).
[8] Parameters for GaAs and AlAs used in the present paper are listed in a paper: S. Adachi, J. Appl. Phys. **58**(3), R1 (1985).
[9] B. A. Auld, *Acoustic Fields and Waves in Solids*, (Krieger, Malabar, FL, 1990), 2nd ed., Vols. I and II.
[10] T. J. Delph, G. Herrman, and R. K. Kaul, J. Appl. Mechan. **45**, 343 (1978).
[11] L. M. Brekhovskikh, *Waves in Layered Media* (Academic, New York, 1980), 2nd ed., p. 86.
[12] R. E. Camley, B. Djafari-Rouhani, L. Dobrzynski, and A. A. Maradudin, Phys. Rev. B **27**, 7318 (1983); B. Djafari-Rouhani, L. Dobrzynski, O. Hardouin Duparc, R. E. Camley, and A. A. Maradudin, Phys. Rev. B **28**, 1711 (1983).
[13] H. T. Grahn, H. J. Maris, J. Tauc, and B. Abeles, Phys. Rev. B **38**, 6066 (1988).
[14] A. Yamamoto, T. Mishina, Y. Masumoto, and M. Nakayama, Phys. Rev. Lett. **73**, 740 (1994).
[15] M. W. C. Dharma-wardana, D. J. Lockwood, J.-M. Baribeau, and D. C. Houghton, Phys. Rev. B **34**, 3034 (1986); D. J. Lockwood, M. W. C. Dharma-wardana, J.-M. Baribeau, and D. C. Houghton, Phys. Rev. B **35**, 2243 (1987).
[16] A. G. Every, Phys. Rev. Lett. **42**, 1065 (1979).

Measurements of scaling properties for acoustic propagation in a single pore

L. A. Wilen
Department of Physics and Astronomy, Ohio University, Athens, Ohio 45701

(Received 23 December 1995; accepted for publication 27 September 1996)

An experimental investigation of sound propagation in a single pore of circular cross section is described. By working at low frequencies and in various pressure ranges, viscous and thermal penetration depths which range from less than, to much greater than, the pore radius are achieved. The system is an experimental model for a pore in either sound absorbing material or the ''stack'' region of a thermoacoustic engine. The measured acoustic response compares favorably with theoretical predictions. Deviations are attributed to the cell geometry. In certain ranges of pressure and frequency, simple scaling properties may be utilized to determine the relative viscosity and thermal diffusivity of gases. Measurements of both quantities (relative to those of argon) for helium, neon, nitrogen, krypton, and water vapor (viscosity only) are presented and compared with known values. Practical applications of the experimental technique are discussed. © *1997 Acoustical Society of America.* [S0001-4966(97)05503-3]

PACS numbers: 43.35.Ud, 43.20.Mv, 43.20.Ye [HEB]

INTRODUCTION

Lately there has been renewed interest in thermoacoustic engines and refrigerators.[1] An important component of such devices is the ''stack'' region where heat flow is converted to acoustic power (for engines) or vice versa (for refrigerators). The stack usually consists of narrow parallel or circular channels. Kirchhoff originally worked out the propagation of sound in circular channels, and included the effects of thermal and viscous dissipation.[2] His work is summarized by Rayleigh,[3] who applies the results to sound absorption in porous media. A slab of porous medium is often modeled as an array of channels. An understanding of sound propagation in a single channel leads to an expression for absorption and transmission in the medium. More recently, studies have extended Kirchhoff's theory to pores of arbitrary cross section, both to better understand absorption in porous media and to model different possible ''stack'' structures in thermoacoustic devices.[4–6]

Experiments on sound propagation in small pores of uniform geometry are somewhat less common. Measurements of the efficiency of acoustic engines provide an indirect test of sound propagation in the stack according to the theory by Rott.[7,8] Such engines generally operate in a regime where the viscous and thermal penetration depths are comparable to the width of the pores in the stack. Recently, Arnott *et al.*[9] performed direct measurements of sound propagation in small rectangular tube arrays, finding good agreement with theory. Similar work was carried out by Stinson and Champoux[10,11] for circular, rectangular, and triangular arrays.

The present study is motivated by the continuing need to make direct experimental contact with the body of theory treating sound propagation in pores. A distinctive feature of the experiment is the ability to probe sound propagation in a *single pore*, in regimes where the penetration depths vary greatly relative to the pore radius.

A second motivation is the investigation of a potential new technique to determine the thermophysical properties of gases. Measurements of viscosity and thermal conductivity can be important for a variety of industrial applications. In particular, there has recently been an impetus to find alternatives to freon for use in conventional refrigeration.[12] It is therefore of interest to search for new measurement techniques which might potentially be more accurate, simpler or more versatile than those currently available.

Historically, acoustic methods have been successful in making precise measurements of gas properties. For example, acoustic resonance techniques are responsible for the best measurement to date of the gas constant.[13] They can also determine specific heats and virial coefficients for gases.[14] Because such techniques rely on an accurate measurement of the speed of sound, they are often designed to reduce the effects of viscous and thermal dissipation as much as possible. As such, they are not necessarily well suited to look at these properties.[15] In contrast, the acoustic technique described here probes sound propagation dominated by dissipation. There exist two pressure regimes where the measured acoustic response is determined by either viscous or thermal effects. When one or the other dominates, the responses for two gases are related in a way which allows their relative viscosity or thermal diffusivity to be simply determined.

The outline of this paper is as follows: A description of the experimental setup is followed by a presentation of experimental results. The next section contains a summary of the theory and a comparison of the experimental results with the theoretical model. Finally, measurements are used to determine the viscosity and thermal diffusivity of several gases and the results are compared with values found in the literature. The paper concludes with a discussion of additional applications of the apparatus.

I. EXPERIMENTAL SETUP

The experimental cell (Fig. 1) is a U-shaped cavity of cylindrical cross section constructed primarily of glass. The

 0001-4966/97/101(3)/1388/10/$10.00

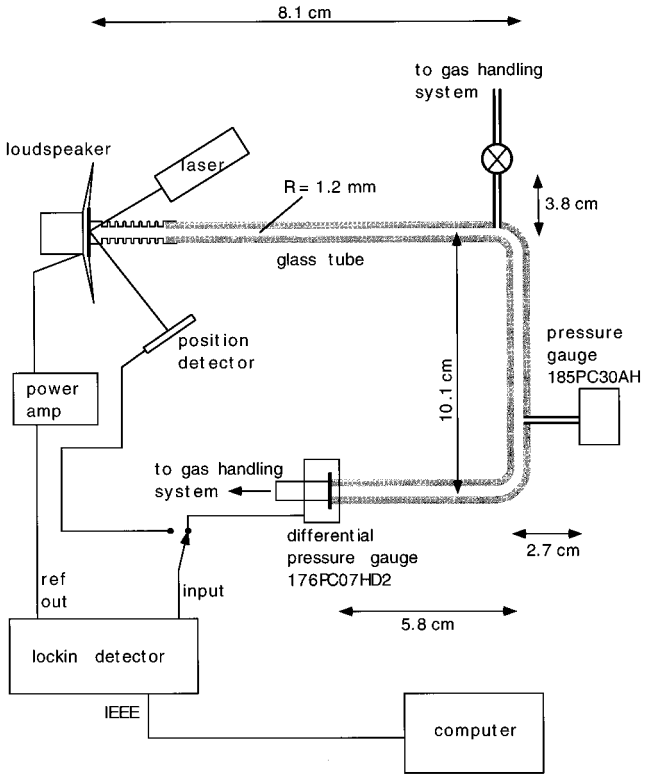

FIG. 1. Experimental setup.

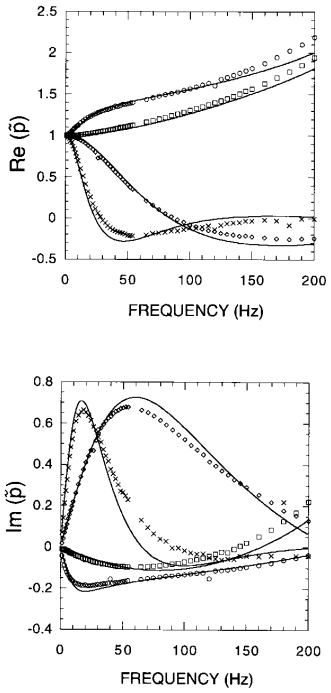

FIG. 2. Real and imaginary parts of the experimental pressure response $\tilde{p}$ for argon at equilibrium pressures of 765.6 Torr (circles), 100.1 Torr (squares), 3.7 Torr (diamonds), and 1.04 Torr (crosses). Also plotted are the real and imaginary parts of the theoretical pressure response for argon at the same pressures (solid lines). For the theoretical calculation, the radius R and length L of the tube were taken to be 1.2 mm and 29 cm, respectively.

cell may be evacuated through a valve and gas may be metered into the cell at pressures ranging from 0 to 780 Torr. The static gas pressure in the cell is measured by a silicon pressure gauge (Honeywell Microswitch model 185PC30AH) located along the tube. This gauge measures the pressure relative to atmospheric pressure and an additional gauge external to the cell measures atmospheric pressure, allowing the absolute equilibrium (or static) pressure P_0 in the cell to be determined with an estimated accuracy of 0.05 Torr.

A 2-in. tweeter drives a small electro-formed nickel bellows, thereby modulating the position of one end of the cavity. A differential silicon pressure sensor (Honeywell Microswitch model 176 PC07HD2) mounted at the opposite end of the cavity measures the resultant pressure oscillations. The reference side of the differential gauge is filled with gas to the same pressure as the cell and is then isolated.

An important feature of the apparatus is the ability to drive and detect small pressure oscillations down to very low frequencies. The differential pressure sensor has a flat frequency response in the range from 0 to 200 Hz. The reference frequency of a lock-in amplifier (buffered by a power amplifier) drives the loudspeaker, and the in- and out-of-phase pressure response is detected. In a typical run, the frequency is swept from 1 to 200 Hz. The position of the loudspeaker cone (which is not in phase with the lock-in reference due to the speaker's combined motional and electrical impedance) is calibrated by bouncing a helium–neon laser off of a small mirror on the cone and measuring the position of the reflected beam with an optical linear position detector (United Detector Technology model LSC-5D). This position detector senses the centroid of the laser spot and provides an analog signal proportional to the spot displacement as it scans across the active area. By moving the detector to different distances from the speaker cone, we can distinguish between translational motion of the cone in the direction of the pore and rocking motion of the cone.

Using this calibration technique, the amplitude and phase of the pressure response are measured relative to those of the displacement signal of the cone. In other words, the complex pressure response is divided by the complex displacement response for all measured frequencies. The response is further normalized by the signal amplitude at zero frequency. With these normalizations, the pressure response is always unity at zero frequency. For the remainder of the paper $\tilde{p}(\omega)$ will always refer to the pressure response normalized in this fashion.

Figure 2 shows a set of pressure response curves for argon gas measured at several different static pressures. To understand this behavior we apply an appropriate theoretical model for sound propagation in a tube under the conditions encountered in the experiment.

II. THEORY

Provided that the effects of viscosity and thermal conductivity are neglected, the propagation of sound in a gas can be expressed by a real wave vector k_0, given by $\omega/(\gamma P_0/\rho_0)^{1/2}$, where ρ_0 is the gas density, P_0 is the gas pressure, ω is the angular frequency of oscillation, and γ is the ratio of specific heats C_p/C_v at constant volume and pres-

sure. When dissipative effects are included, the wave vector is modified, and will generally be complex. Two principal length scales determine the importance of dissipative effects. These are the thermal and viscous penetration depths δ_κ and δ_ν, defined by:

$$\delta_k = \sqrt{\frac{2\kappa}{\omega\rho_0 C_p}}, \quad \delta_\nu = \sqrt{\frac{2\mu}{\omega\rho_0}}, \tag{1}$$

where C_p is the specific heat of the gas at constant pressure, κ is the thermal conductivity of the gas, and μ is the viscosity of the gas. The size of these scales relative to the experimental system dimensions determines the influence of thermal and viscous effects on sound propagation.

Kirchhoff[2] first worked out a general scheme to solve for the propagation of sound in a circular tube of radius R for arbitrary values of δ_ν and δ_κ by considering the Navier–Stokes equations and requiring the velocity and temperature oscillations to vanish at the cylinder wall. He obtained an analytic expression for the propagation vector in the limit that $\delta_\nu, \delta_\kappa \ll R$. Rayleigh[3] summarizes Kirchhoff's results, and also finds analytic results in the opposite limit, where $\delta_\nu, \delta_\kappa \gg R$.

In the first limit, the effect of viscosity and thermal conductivity are to produce a thin boundary layer near the wall, whose temperature and velocity oscillations are out of phase with those in the center of the tube. This causes a small shift in the propagation vector. Specifically, the wave vector k_0 for the case with no dissipation is modified to $k_0 + \delta k$ where $\delta k = k_0[(1+i)/2]\{[\delta_\nu + (\gamma-1)\delta_\kappa]/R\}$. The real part of δk produces a small shift in the speed of sound and the imaginary part causes attenuation.

In the second limit, when both δ_ν and δ_κ are larger than R, k is given by

$$k^2 = \frac{8i\mu\omega}{P_0 R^2}. \tag{2}$$

This propagation constant describes a highly damped wave. k is independent of γ because for $\delta_\kappa \gg R$, the pressure oscillations are strictly isothermal.

Various workers[17,4,5] have shown that simple solutions exist to the Navier–Stokes equations for arbitrary δ_κ and δ_ν, in the small k limit defined by $|k|R \ll 1$; a condition that is always satisfied in the present experiment. This condition, often referred to in the literature as the ''low reduced frequency limit,''[16] effectively means that any radial dependence to the pressure fluctuations may be neglected. Stinson[4] considers an ideal gas of viscosity μ and thermal conductivity κ and finds an expression for the wave vector k in the low reduced frequency limit:

$$k^2 = \omega^2 \rho(\omega) C(\omega), \tag{3}$$

where the *complex compressibility* function $C(\omega)$ is given by

$$C(\omega) = (1/\gamma P_0)[\gamma - (\gamma-1)F(\nu'/\gamma)], \tag{4}$$

and the *complex density* function $\rho(\omega)$ is given by

$$\rho(\omega) = \rho_0 / F(\nu). \tag{5}$$

The function F is defined according to

$$F[\eta] = 1 - 2\left(-\frac{i\omega}{\eta}\right)^{-1/2} \frac{J_1[R(-i\omega/\eta)^{1/2}]}{J_0[R(-i\omega/\eta)^{1/2}]R}. \tag{6}$$

Here, γ is the ratio C_p/C_v of specific heats, P_0 is the equilibrium pressure, ρ_0 is the equilibrium density, and ν and ν' are given by

$$\nu = \mu/\rho_0, \quad \nu' = \kappa/(\rho_0 C_v). \tag{7}$$

This solution for k reduces to Rayleigh's results in the two limiting cases described earlier. Stinson[4] has also generalized the theory to find the function $F[\eta]$ corresponding to other pore geometries.

The cell will be approximated by a closed tube of uniform radius R and length L. In Appendix A we describe how to generalize the results to more complicated geometries. By considering counter-propagating waves with zero particle velocity at the right and particle displacement $\xi(\omega)$ at the left, the acoustic pressure on the right is determined to be:[18]

$$\frac{p(\omega)}{P_0} = \frac{\xi(\omega)}{L} \frac{1}{P_0 C(\omega)} \frac{kL}{\sin kL}. \tag{8}$$

We normalize the response according to the prescription in Sec. I:

$$\tilde{p}(\omega) = \frac{p(\omega)}{\xi(\omega)} \frac{\xi(0)}{p(0)} = \frac{1}{P_0 C(\omega)} \frac{kL}{\sin kL}. \tag{9}$$

Note that the pressure response is a complex function of frequency. Figure 2 shows the real and imaginary part of $\tilde{p}$ plotted against frequency for various values of the static gas pressure. For these curves, the gas was taken to be argon. These theoretical results should be compared to the corresponding experimental curves. The qualitative agreement is evident. Quantitatively, the agreement is fairly good, and we attribute the discrepancy to the nonideal geometry of the experimental cavity compared to the ideal one used for the theoretical calculation. Since the original aim of this experiment was to develop an acoustic technique to study crystal growth, the design was not optimized for the present measurement. As shown in Fig. 1, the radius in the bellows section is different from that in the rest of the tube. There are also short side branches (each with different radii) going off to the second pressure gauge and the gas inlet.

In principle, it might be possible to determine absolute gas properties by a fit of the experimental data to the theory (see Appendix A). This is cumbersome in practice due to the nonideal nature of the experimental geometry.[19] Nevertheless, relative values of viscosity and thermal diffusivity may be determined by taking advantage of scaling relations between data for different gases.

III. SCALING BEHAVIOR

The functions $C(\omega)$ and $\rho(\omega)$ in Eqs. (3)–(9) contain the effects of the thermal conductivity and viscosity, respectively. It will be shown that it is possible to work at experimental conditions where one or the other of these effects is dominant. When working in either of these regimes, the behavior of different gases appears identical up to a scale factor in the frequency and amplitude axes. The scale factors simply determine the relative viscosity and thermal diffusivity of

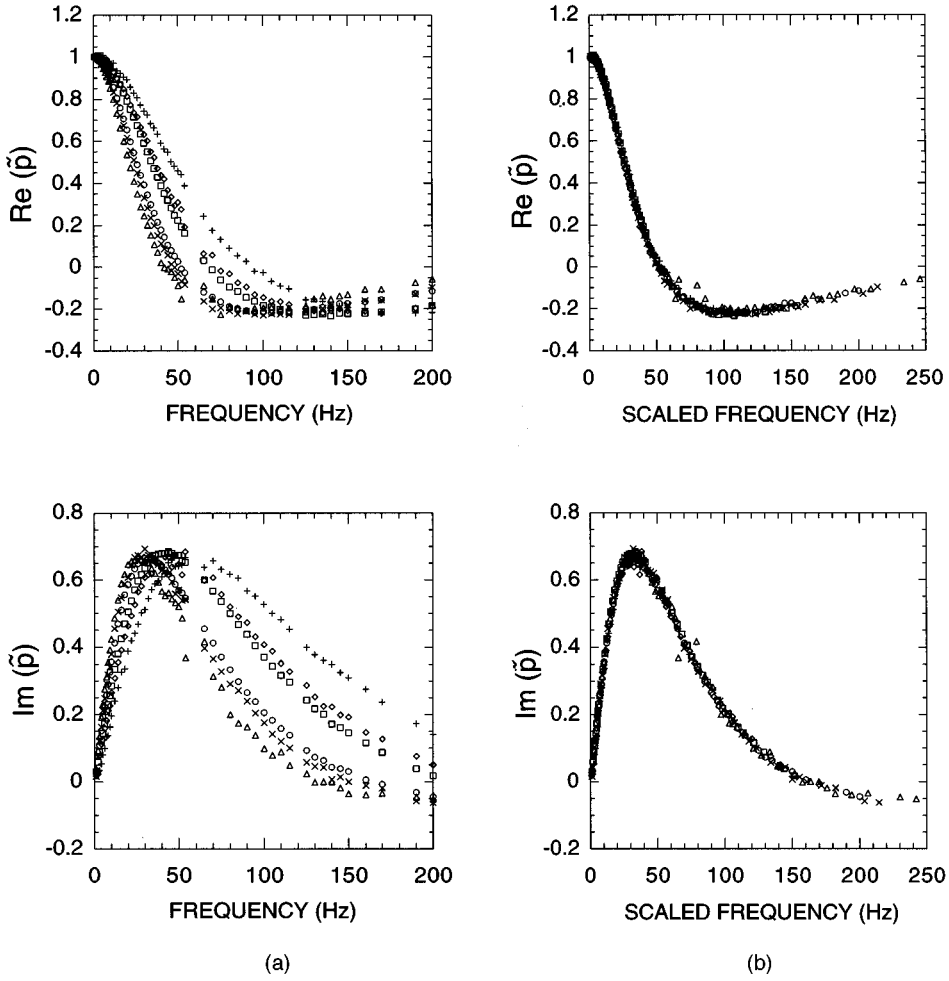

FIG. 3. Experimental pressure response $\tilde{p}$ for argon (P_0=2.06 Torr, circles), nitrogen (P_0=2.13 Torr, squares), helium (P_0=2.23 Torr, diamonds), krypton (P_0=2.17 Torr, crosses), water vapor (P_0=1.71 Torr, plusses), and neon (P_0=2.15 Torr, triangles). (a) Frequency axis unscaled. (b) Frequency axis scaled for each gas except argon. Scale factors are 0.76 (nitrogen), 0.71 (helium), 1.07 (krypton), 0.57 (water vapor), and 1.21 (neon).

any two gases. These ideas of scaling are essentially simple applications of the concept of similitude, which was recently applied to thermoacoustics by Olsen and Swift.[20]

A. Low-pressure regime

At low equilibrium pressures ($P_0 \approx 2$ Torr) and low frequencies (0→200 Hz), both δ_ν and δ_κ are larger than the tube radius. In this limit, $C(\omega) \approx (P_0)^{-1}$, and the pressure response is

$$\tilde{p}(\omega) = \frac{kL}{\sin kL}, \tag{10}$$

where the wave vector k is given by $k^2 = 8i\mu\omega/P_0R^2$.

Because the wave vector depends only on the combination $\mu\omega/P_0$, the measured frequency response for two gases of different viscosity, μ_a and μ_b, and different pressures, P_{0a} and P_{0b}, are related functionally by

$$\tilde{p}_a(\omega) = \tilde{p}_b\left(\omega \frac{\mu_a}{\mu_b}\frac{P_{0b}}{P_{0a}}\right). \tag{11}$$

The above equation shows that the pressure response for different gases should be similar up to a scale factor in the frequency axis. The scale factor gives the quantity μ_x/μ_{Ar} for each of the gases (the subscript x denotes the particular gas), according to:

$$\frac{\mu_x}{\mu_{\mathrm{Ar}}} = \beta_x \frac{P_{0x}}{P_{0\mathrm{Ar}}}. \tag{12}$$

Although Eq. (11) was derived from the theoretical result for the ideal geometry, it is not difficult to show that it also holds for the more complex geometry of the experiment. This calculation is deferred to Appendix A.

Figure 3 shows experimental results for argon, krypton, nitrogen, neon, helium, and water vapor all measured at approximately 2-Torr pressure. In part (b) of the figure, the frequency axis for argon was left unscaled, while that of each of the other gases was scaled by the value β_x to achieve the best fit.

Using the value of β_x for each of the gases produces fair agreement with literature values for the relative viscosity (see Table I). One source of systematic error is due to the effect of slip at the cavity walls. This effect is significant at low pressures where the mean-free path in the gas is appreciable relative to the cavity radius. At P_0=2 Torr, the mean-free paths for the gases used in the experiment range from

TABLE I. Literature values for the viscosity, relative viscosities calculated from literature values, experimental relative viscosities, and experimental relative viscosities after correcting for slip. The estimates for the experimental errors are based on (1) errors inherent in measuring the static pressure, (2) errors due to drifts in temperature, and (3) errors in the scale factors relating the response curves.

Gas	μ_x at 20 °C (literature[a])	μ_x/μ_{Ar}	μ_x/μ_{Ar} (exp;uncorrected)	μ_x/μ_{Ar} (exp;corrected)
Argon	221.7 μP	1	⋯	⋯
Nitrogen	174.8 μP	0.788	0.783±3%	0.779±3%
Helium	194.1 μP	0.876	0.763±3%	0.866±3%
Krypton	250.4 μP	1.129	1.129±3%	1.106±3%
Neon	311.1 μP	1.406	1.265±3%	1.360±3%
Water vapor	95.1 μP	0.429	0.472±3%	0.466±3%

[a]*Handbook of Chemistry and Physics*, edited by R. C. Wheast (CRC, Boca Raton, FL, 1981), pp. F-58–F-61.

0.017 mm for water vapor to 0.072 mm for helium, compared to a pore radius of 1.2 mm. Fortunately, a correction for slip can be determined experimentally in a straightforward way.

B. Correction for slip

Slip at the pore wall causes the measured viscosity to appear to be a function of the gas pressure[21,22] according to

$$\mu(P_0)=\frac{\mu(\infty)}{1+4\alpha L(P_0)/R}, \tag{13}$$

where the mean-free path L can itself be written as a function of the viscosity:

$$L(P_0)=\frac{\mu(\infty)}{P_0}\sqrt{\frac{\pi R_b T}{2M}}. \tag{14}$$

Here, $\mu(\infty)$ refers to the viscosity which is measured for equilibrium pressures high enough so that the effect of slip is negligible, R_b is Boltzmann's constant, T is the absolute temperature, and M is the molecular mass of the gas. The product αL is generally referred to in the literature as the coefficient of slip. α is a constant of order unity which depends upon properties of the gas/wall interaction and must be determined experimentally, as indicated below.

Equation (12) of the previous section should therefore be modified to read

$$\frac{\mu_x(P_{0x})}{\mu_{\mathrm{Ar}}(P_{0\mathrm{Ar}})}=\beta_x\frac{P_{0x}}{P_{0\mathrm{Ar}}}. \tag{15}$$

In other words, the scaling of the data yields the ratio of the *effective* viscosities of the gases which is a function of the pressure at which the data for each gas was taken. It is necessary to find the ratio $\mu(P_0)/\mu(\infty)$ for each gas in order to correct for the effect of slip. This can be done as follows:

The effective viscosity for a particular gas can be measured as a function of equilibrium pressure P_0' (relative to its effective viscosity at some given pressure P_0) with the same scaling technique as before (Fig. 4). The pressure response $\tilde{p}(\omega)$ is measured (for a single gas) at various pressures and the scale factors required to collapse the curves yield the ratio of viscosities according to:

$$\frac{\mu_x(P_0)}{\mu_x(P_0')}=\beta_x\frac{P_0}{P_0'}. \tag{16}$$

Combining Eqs. (13) and (14) yields a theoretical expression for the ratio of effective viscosities:

$$\frac{\mu_x(P_0)}{\mu_x(P_0')}=[1+4\alpha L(P_0)/R]^{-1}\{1+[4\alpha\mu(\infty)\times(\pi R_b T/2M)^{1/2}/R]P_0'^{-1}\}. \tag{17}$$

Thus, if one plots $\mu_x(P_0)/\mu_x(P_0')$ against $(P_0')^{-1}$, the result will be a straight line whose x-axis intercept is $[1+4\alpha L(P_0)/R]^{-1}$. This quantity is just the correction factor relating $\mu(P_0)$ to $\mu(\infty)$, according to Eq. (13).

This procedure was carried out for argon (Fig. 5) yielding a value of 0.916 for $\mu_{\mathrm{Ar}}(2.06)/\mu_{\mathrm{Ar}}(\infty)$. The correction factors for each of the other gases may in principle be found in a similar fashion. In practice, we had pressure dependence measurements for argon only, so the corrections for the other gases were calculated by assuming that α was the same for all the gases. Using the known value for the viscosity of argon, we found $\alpha=1.10$. Then we solved Eqs. (13) and (14) to find the ratio $\mu_x(P_{0x})/\mu_x(\infty)$ for a gas in terms of the measured value $\mu_x(P_{0x})$ and α:

$$\frac{\mu_x(P_{0x})}{\mu_x(\infty)}=1-4\alpha\frac{\mu_x(P_{0x})}{P_{0x}}\sqrt{\frac{\pi R_b T}{2M_x}}. \tag{18}$$

One must be careful about what is meant by the experimental value $\mu_x(P_{0x})$ in the above equation. The experiment measures only ratios of viscosities. $\mu_x(P_{0x})$ can be written as

$$\mu_x(P_{0x})=\frac{\mu_x(P_{0x})}{\mu_{\mathrm{Ar}}(P_{0\mathrm{Ar}})}\frac{\mu_{\mathrm{Ar}}(P_{0\mathrm{Ar}})}{\mu_{\mathrm{Ar}}(\infty)}\mu_{\mathrm{Ar}}(\infty), \tag{19}$$

which defines $\mu_x(P_{0x})$ completely in terms of experimentally measured ratios and the known value for the viscosity of argon. The corrected relative viscosities (Table I) agree with literature values for the relative viscosities to within a few percent for all the gases studied except water vapor. We speculate that this may be due to a significantly different value of α for water vapor as compared to the rest of the gases. This is not unreasonable since it is known that water adsorbs on glass at room temperature.

C. High-pressure regime

For higher pressures ($P_0\approx 765$ Torr) and at sufficiently low frequencies (0→20 Hz), the magnitude of the wave vec-

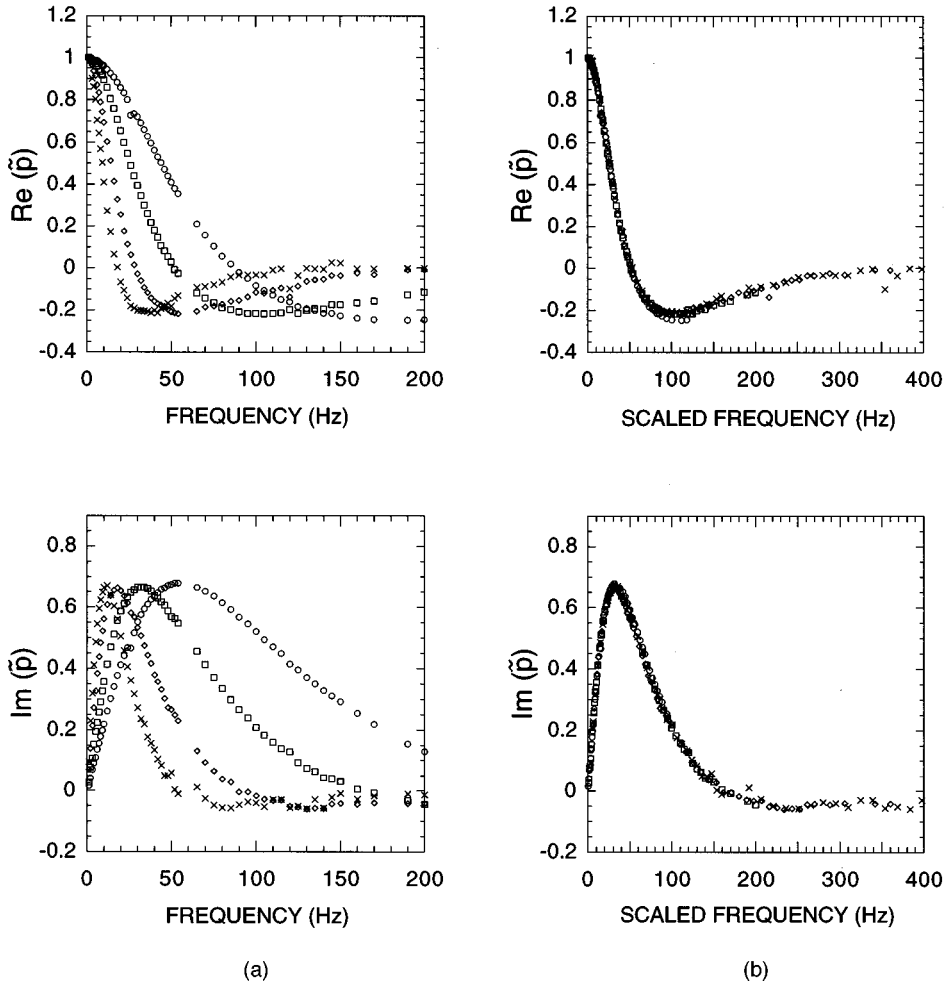

FIG. 4. Experimental pressure response $\tilde{p}$ for argon at equilibrium pressures of 3.70 Torr (circles), 2.06 Torr (squares), 1.08 Torr (diamonds), and 0.58 Torr (crosses). (a) Frequency axis unscaled. (b) Frequency axis scaled for all pressures except 2.06 Torr. Scale factors are 0.59 (3.70 Torr), 1.80 (1.08 Torr), and 2.95 (0.58 Torr).

tor is small, and it is a good approximation to assume that $|k|L \ll 1$. In this limit the pressure response is given by

$$\tilde{p}(\omega) = \frac{1}{P_0 C(\omega)}, \tag{20}$$

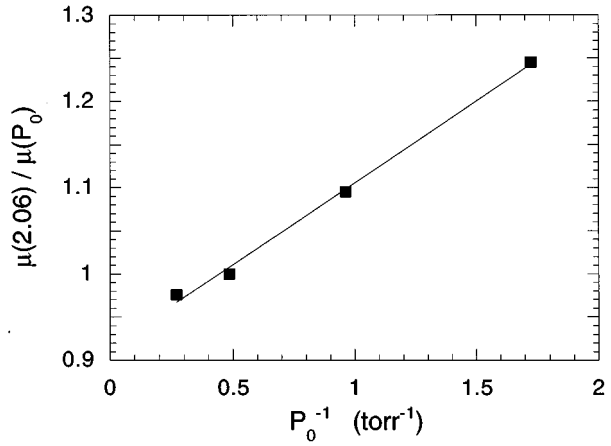

FIG. 5. A plot of the viscosity ratio $\mu_{\mathrm{Ar}}(2.06\ \mathrm{Torr})/\mu_{\mathrm{Ar}}(P_0)$ against the inverse equilibrium pressure $(P_0)^{-1}$. The line is a least squares fit to the data.

where $\tilde{p}(\omega)$ is independent of the viscosity but does depend upon the value of both γ and κ for each gas. Physically, Eq. (20) expresses the fact that the pressure can be considered uniform throughout the tube and heat is transferred between the solid and the gas. As the frequency is increased, δ_κ decreases from $\delta_\kappa > R$ to $\delta_\kappa < R$. The observed behavior is due to a crossover from isothermal to adiabatic pressure oscillations as the frequency is increased. The in-phase signal increases in amplitude while the quadrature phase shows a peak in response. This behavior was described qualitatively by Rayleigh.[23] Just as in the low pressure case one can find a scaling relationship between the data for different gases. Examination of Eqs. (4), (6), and (7) shows that the quantity $\gamma/(\gamma-1)[1-P_0 C(\omega)] = F(\nu'/\gamma)$ is a function of $\omega\rho_0 C_p/\kappa$ only. This implies the following scaling relation:

$$\tilde{p}\,'_a(\omega) = \tilde{p}\,'_b\left(\frac{\kappa_b}{\rho_{0b}C_{pb}}\,\frac{\rho_{0a}C_{pa}}{\kappa_a}\,\omega\right), \tag{21}$$

where we have defined

$$\tilde{p}\,' = \frac{\gamma}{(\gamma-1)}\,[1-\tilde{p}^{\,-1}]. \tag{22}$$

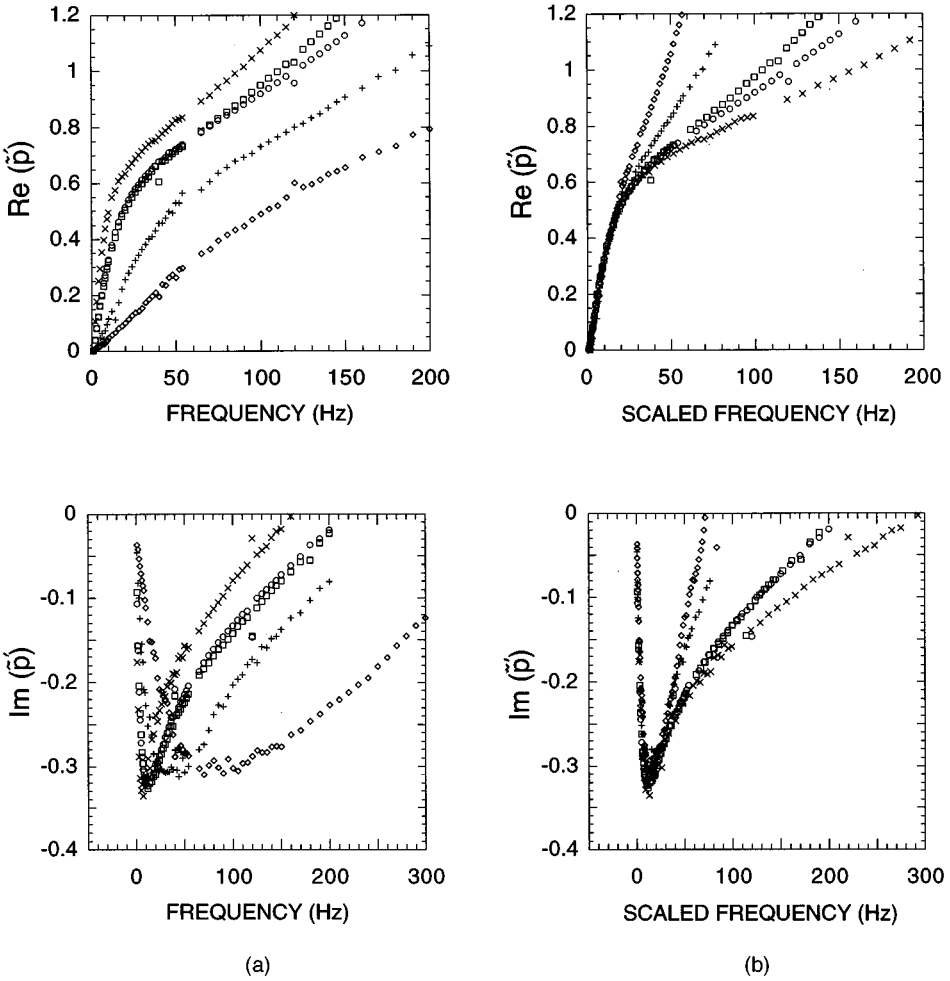

FIG. 6. Experimental pressure response $\tilde{p}\,'$ for argon (circles), nitrogen (squares), helium (diamonds), krypton (crosses), and neon (plusses). For all the gases, P_0=765 Torr (to within 0.5%). (a) Frequency axis unscaled. (b) Frequency axis scaled for all gases but argon. Scale factors are 0.95 (nitrogen) and 1.83 (krypton). For helium and neon, the scale factors found from the real and the imaginary response are different. These factors are 0.167 (helium, real), 0.117 (helium, imaginary), 0.383 (neon, real), and 0.333 (neon, imaginary).

Here, $\tilde{p}(\omega)$ was measured for each of the gases at a pressure of 765 Torr and $\tilde{p}\,'(\omega)$ was calculated from the data and plotted. The frequency axis of each curve was scaled so that at low frequencies, all the points lie on the curve measured for argon, which was left unscaled (Fig. 6). The scale factor β_x gives the thermal diffusivity $\nu'/\gamma=(\kappa/\rho_0 C_p)$ for each of the gases relative to that of argon, according to

$$\frac{(\nu'/\gamma)_x}{(\nu'/\gamma)_{\mathrm{Ar}}}=\frac{1}{\beta_x}. \tag{23}$$

As before, although this scaling property is obtained from the theory for the ideal cylindrical geometry, it can be shown to hold for the more complex geometry of the cell (see Appendix A). The results for the thermal diffusivity are shown in Table II.

In analogy to the effect of slip described in the previous section, there is a temperature jump at the pore wall associated with the finite mean-free path of the gas molecules. This effect will provide corrections to the thermal diffusivity of the order of L/R, which is too small to be observable with the present technique at pressures of $\approx$1 atm.

The measurements and analysis are straightforward for nitrogen and krypton, and the results agree with literature values of the (relative) thermal diffusivities to within a few percent. The analysis is somewhat more complicated for neon and helium. For these gases, the scaling of the data yielded slightly different results for the real and imaginary parts of the pressure response. Due to the relatively lower densities of these gases, it was necessary to extend the pressure measurements to higher frequencies than those needed

TABLE II. Literature and experimental values for the relative thermal diffusivities. The estimates for the experimental errors are based on (1) errors in the scale factors relating the response curves and (2) errors due to drifts in temperature.

Gas	$(\nu'/\gamma)_x/(\nu'/\gamma)_{\mathrm{Ar}}$ (literature[a])	$(\nu'/\gamma)_x/(\nu'/\gamma)_{\mathrm{Ar}}$ (exp.)
Nitrogen	1.04	1.05±4%
Krypton	0.543	0.546±4%
Helium	8.62	7.04
Neon	2.82	2.79

[a]*Handbook of Chemistry and Physics*, edited by R. C. Wheast (CRC, Boca Raton, FL, 1981), p. E-2.

for the other two gases. Consequently, these measurements were more susceptible to any high-frequency modes in the mechanical system (loudspeaker plus bellows). In fact, we isolated a particular mode which we believe accounted for the observed discrepancy. This was a rocking mode of the loudspeaker diaphragm which did not couple to the acoustic wave[24] but did influence our calibration signal for the loudspeaker cone displacement at the higher frequencies.

The influence of this mode was considerably smaller for neon than for helium, and in both cases the results in the table were determined by averaging the scale factors found from the real and imaginary parts of the pressure response. No further account of this effect will be given other than to say that it should be straightforward to eliminate it in future measurements.

IV. DISCUSSION

The measurements at high pressure and low frequency are particularly relevant to the stack behavior in thermoacoustic engines and refrigerators. In this regime, the modified pressure response $\tilde{p}'$ reduces to the function $F(\nu'/\gamma)$ defined in Eq. (6). This function is often denoted by $F(\lambda)$ in the thermoacoustic device literature and it has been calculated for pores of many different cross-sectional geometries.[25] Its importance is that it is directly related to the efficiency of heat transport in a thermoacoustic device. In particular, the peak value of the magnitude of the imaginary part of this function can be used as a figure of merit for a device with pores of specified cross section.[5] In addition, $F(\lambda)$ can be used to evaluate the dissipation of acoustic energy by viscosity. In contrast to studies which extract $F(\lambda)$ from a measurement of k (or equivalently via a resonance technique),[10,26–28] the present experiment probes $F(\lambda)$ directly for a circular pore.[29]

An important feature of the experiment is that the pore is large compared to typical pores in an acoustic engine. Nevertheless, by working at sufficiently low frequencies, penetration depths comparable to the pore radius are achieved, which is the experimentally relevant regime for thermoacoustic devices. A modification of the experimental geometry would allow measurements for pores of various different cross sections (see Appendix B). For example, we believe it would be possible to accurately measure $F(\lambda)$ for the ''pin array'' stack proposed by Swift and Keolian.[6] Such measurements would be a useful test of theory but could also be used to test complex geometries which might otherwise be hard to compute theoretically.

In addition to modeling stack structures, the experiment suggests some other useful practical applications. It has been demonstrated that the apparatus can be used to make relative measurements of both the viscosity and thermal diffusivity of gases. Absolute measurements are also possible with straightforward modifications to the design (see Appendix B). With such modifications, it should be possible to directly measure γ. Obviously, a single apparatus versatile enough to simply measure several different gas properties would be desirable.

Gas viscosity measurements are important in a variety of contexts. In addition to the industrial uses alluded to in the Introduction, there are also applications in astrophysics. Accurate measurements of the mean-free path (as calculated from the viscosity) of water vapor are extremely important for understanding physical processes in cometary atmospheres. These mean-free paths must be measured down to extremely low temperatures (and hence vapor pressures). The current technique has the potential to extend measurements of the viscosity down to as low as a couple tenths of a Torr, corresponding to temperatures of ≈ -30 °C. Such measurements would provide useful input for theories which attempt to extrapolate mean-free paths down to lower temperatures.[30]

Finally, the apparatus can be used to measure crystal growth. Preliminary experiments have shown that an ice crystal grown under pure vapor inside the cell causes a significant modification of the pressure response at low frequencies, in qualitative agreement with theoretical predictions. The particular form of the modified signal can be related to the rate of crystal growth.

V. CONCLUSIONS

We have described an experiment which probes sound propagation in a single channel. By exploiting the ideas of scaling, we have demonstrated how the apparatus is useful for measuring the thermophysical properties of gases and also for modeling stack structures in thermoacoustic devices. In the first case, scaling is used to relate the pressure response for gases of different viscosities or thermal diffusivities. In the second case, sound propagation in the large channel of the experiment can be related to propagation in much narrower pores by accessing the same range of penetration depths relative to the pore radius. Simple modifications of the apparatus may give rise to several useful applications.

Note added in proof: Since the original submission of this article, an accurate measurement of $F(\lambda)$ has been performed for a pin-array stack using a technique similar to that described herein. Details will be reported in J. Acoust. Soc. Am. by M. E. Hayden and G. W. Swift (private communication).

ACKNOWLEDGMENTS

This work was supported by NSF Grant No. DMR 94-00637 and ONR Grant No. N00014-90-J-1369. I gratefully acknowledge comments and criticism from Greg Dash, John Wettlaufer, Greg Swift, Mike Hayden, and Pat Arnott. I would also like to thank the reviewers for numerous helpful suggestions.

APPENDIX A: CALCULATION FOR NONIDEAL GEOMETRY

In this Appendix, it will be shown that the scaling relations which were derived using the results in Sec. III are valid for a cell with a more complicated geometry. To demonstrate this, it is adequate to show that the results hold for a

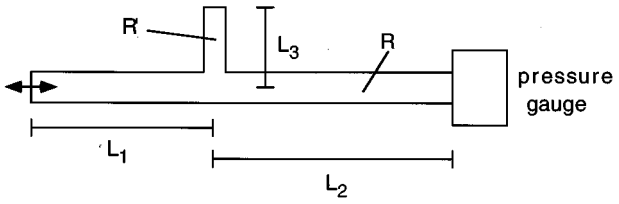

FIG. A1. Model experimental cell with extra side branch of length L_3 and radius R', adjoining main tube at a distance L_2 from the loudspeaker end.

cell which has a single extra side branch, as shown in Fig. A1. The side branch is assumed to have length L_3 and radius R'.

For such a cell, the particle displacement in each section can be written as follows:

$$-L_1<x<0, \quad \xi_1(x)=A_1\cos kx+B_1\sin kx, \tag{A1}$$

$$0<x<L_2, \quad \xi_2(x)=A_2\cos kx+B_2\sin kx, \tag{A2}$$

$$0<z<L_3, \quad \xi_3(z)=A_3\cos k'z+B_3\sin k'z. \tag{A3}$$

At $x=-L_1$, the displacement must match that of the loudspeaker, and at $x=L_2$ and $z=L_3$ the displacement must vanish, yielding three boundary conditions. Three additional equations arise from the boundary conditions at the junction between the side branch and the main tube ($x=0$, $z=0$). The total amount of gas must be conserved, and the pressure must be continuous at the junction.

The system of six equations in six unknowns can be solved to yield the A_i, B_i. Of principal interest is the solution for the normalized pressure measured at the gauge ($x=L_2$):

$$\tilde{p}(\omega)=\frac{1}{P_0C(\omega)}\left[\frac{k[L_1+L_2+(R'^2/R^2)L_3]}{\sin k(L_1+L_2)+[R'^2kC'(\omega)/R^2k'C(\omega)](\sin k'L_3\cos kL_2\cos kL_1/\cos k'L_3)}\right]. \tag{A4}$$

The functions k' and C' are defined by Eqs. (3)–(7) with R' replacing R. Note that the above expression reduces to Eq. (9) if either the radius or the length of the side branch is taken to vanish. We now examine this result in the low- and high-pressure regimes considered in Secs. III A and III C.

In the low-pressure regime, the penetration depths are larger than both R and R', implying that $C(\omega)\approx(P_0)^{-1}$ and $C'(\omega)\approx(P_0)^{-1}$. With these substitutions, Eq. (A4) becomes

$$\tilde{p}(\omega)=\left[\frac{k(L_1+L_2+(R'^2/R^2)L_3)}{\sin k(L_1+L_2)+(R'^2k/R^2k')(\sin k'L_3\cos kL_2\cos kL_1/\cos k'L_3)}\right], \tag{A5}$$

where $k^2=8i\mu\omega/P_0R^2$ and $k'^2=8i\mu\omega/P_0R'^2$. Therefore, as in the case for the simple geometry, $\tilde{p}$ is a function of $\mu\omega/P_0$, albeit a more complicated one.

In Sec. III C, it was found that for high pressures and low enough frequencies, $|k|L\ll 1$. The analogous conditions which hold for the more complex geometry are

$$k|L_1|\ll 1, \quad k|L_2|\ll 1, \quad k|L_3|\ll 1. \tag{A6}$$

Applying the conditions to Eq. (A4), one finds

$$\tilde{p}(\omega)=\frac{R^2(L_1+L_2)+R'^2L_3}{R^2(L_1+L_2)C(\omega)+R'^2L_3C'(\omega)}. \tag{A7}$$

Forming the quantity $\tilde{p}'=\gamma/\gamma-1[1-\tilde{p}^{-1}]$ yields

$$\tilde{p}'(\omega)=\frac{R^2(L_1+L_2)F(\nu'/\gamma)+R'^2L_3F(\nu'/\gamma)}{R^2(L_1+L_2)+R'^2L_3}. \tag{A8}$$

This is a function of $\omega\rho_0C_p/\kappa$ only, which demonstrates that the scaling property derived in Sec. III C is also valid for more complex cell geometries.

APPENDIX B: ABSOLUTE MEASUREMENTS

In this Appendix we describe a technique which can be used to measure the pressure response which would correspond to a pore of uniform (but arbitrary) cross section. For concreteness, we describe how the technique would work in the high-pressure, low-frequency limit.

The goal is to measure the complex compressibility $C(\omega)$ for a uniform pore of arbitrary cross-sectional geometry. Currently, the experiment measures an average of this function over circular regions of different radius. If $C(\omega)$ can be measured for a uniform circular pore, then a comparison with the theory (Sec. II) will give both the (absolute) thermal diffusivity and γ independently. Conversely, for a gas of known γ and thermal diffusivity, one can determine the function $C(\omega)$ [and hence $F(\lambda)$] corresponding to a pore of arbitrary geometry.

The basic idea is to measure the pressure response for two different lengths of the desired uniform pore inserted into the apparatus. Then, the part of the response due to everything but the uniform section can be subtracted out. The pressure response (in the high-pressure, low-frequency limit) can be written as

$$\tilde{p}=\frac{V+V'}{P_0[VC(\omega)+V'C'(\omega)]}, \tag{B1}$$

where V' is the volume of the inserted section and V is the volume of the rest of the apparatus. Similarly, $C'(\omega)$ is the complex compressibility corresponding to the inserted pore and $C(\omega)$ is the complex compressibility of the rest of the apparatus.

Taking V' equal to V_1 or V_2, depending on which section is inserted, one finds:

$$\tilde{p}_1 = \frac{V+V_1}{P_0(VC(\omega)+V_1C'(\omega))},$$
$$\tilde{p}_2 = \frac{V+V_2}{P_0(VC(\omega)+V_2C'(\omega))}. \quad \text{(B2)}$$

These can be solved to find $C'(\omega)$ in terms of the pressure responses and the volumes:

$$C'(\omega) = \frac{V+V_1}{V_1-V_2}(P_0\tilde{p}_1)^{-1} - \frac{V+V_2}{V_1-V_2}(P_0\tilde{p}_2)^{-1}. \quad \text{(B3)}$$

The volume ratios in the above equation can be found by realizing that the non-normalized pressure response $p(\omega=0)$ [as defined by Eq. (8)] is inversely proportional to the total volume of the system. Thus if we define $s \equiv p_2(0)/p_1(0)$, it is easily shown that:

$$\frac{V+V_1}{V_1-V_2} = \frac{s}{(s-1)}, \quad \frac{V+V_2}{V_1-V_2} = \frac{1}{(s-1)}. \quad \text{(B4)}$$

It is worth noting that, providing the shorter insert is several times longer than its pore width, this method will yield the response corresponding to an infinite pore (i.e., no edge effects).

[1] G. W. Swift, ''Thermoacoustic Engines and Refrigerators,'' Phys. Today **48**(7), 22–28 (1995).
[2] G. Kirchhoff, ''Ueber den Einflufs der Wärmeleitung in einem Gase auf die Schallbewegung,'' Ann. Phys. Chem. **134**, 177–193 (1868).
[3] J. W. Strutt (Lord Rayleigh), *Theory of Sound* (Dover, New York, 1945), 2nd ed., Vol. II, Sec. 348.
[4] M. Stinson, ''The propagation of plane sound waves in narrow and wide circular tubes, and the generalization to uniform tubes of arbitrary cross-sectional shape,'' J. Acoust. Soc. Am. **89**, 550–558 (1991).
[5] W. P. Arnott, H. E. Bass, and R. Raspet, ''General formulation of thermoacoustics for stacks having arbitrarily shaped pore cross sections,'' J. Acoust. Soc. Am. **90**, 3228–3237 (1991).
[6] G. W. Swift and R. M. Keolian, ''Thermoacoustics in pin-array stacks,'' J. Acoust. Soc. Am. **94**, 941–943 (1993).
[7] N. Rott, ''Damped and thermally driven acoustic oscillation in wide and narrow tubes,'' Z. Angew. Math. Phys. **20**, 230–243 (1969).
[8] G. W. Swift, ''Thermoacoustic engines,'' J. Acoust. Soc. Am. **84**, 1145–1180 (1988).
[9] W. P. Arnott, J. M. Sabatier, and R. Raspet, ''Sound propagation in capillary-tube-type porous media with small pores in the capillary walls,'' J. Acoust. Soc. Am. **90**, 3299–3306 (1991). See also H. S. Roh, W. P. Arnott, J. M. Sabatier, and R. Raspet, ''Measurement and calculation of acoustic propagation constants in arrays of small air-filled rectangular tubes,'' J. Acoust. Soc. Am. **89**, 2617–2624 (1991).
[10] M. R. Stinson and Y. Champoux, ''Propagation of sound and the assignment of shape factors in model porous materials having simple pore geometries,'' J. Acoust. Soc. Am. **91**, 685–695 (1992).
[11] Y. Champoux and M. R. Stinson, ''Measurement of the characteristic impedance and propagation constant of materials having high flow resistivity,'' J. Acoust. Soc. Am. **90**, 2182–2191 (1991).
[12] Montreal Protocol on Substances that Deplete the Ozone Layer: Final Act, United Nations Environmental Programme (UNEP), 16 Sept. 1987.
[13] M. R. Moldover, J. P. M. Trusler, T. J. Edwards, J. B. Mehl, and R. S. Davis, ''Measurement of the Universal Gas Constant *R* Using a Spherical Acoustical Resonator,'' Phys. Rev. Lett. **60**, 249–252 (1988).
[14] A. R. H. Goodwin and M. R. Moldover, ''Thermophysical properties of gaseous refrigerants from speed of sound measurements. I. Apparatus, model, and results for 1,1,1,2-tetraflouroethane R134a,'' J. Chem. Phys. **93**, 2741–2753 (1990).
[15] For an example of a resonance technique which is designed to be sensitive to dissipation, see K. A. Gillis, M. R. Moldover, and J. B. Mehl, ''Greenspan acoustic viscometer: Recent results,'' J. Acoust. Soc. Am. **97**, 3327(A) (1995).
[16] H. Tijdeman, ''On the propagation of sound waves in circular tubes,'' J. Sound Vib. **39**, 1–33 (1975).
[17] C. Zwikker and C. W. Kosten, *Sound Absorbing Materials* (Elsevier, Amsterdam, 1949), Chap. 2.
[18] In this model we have neglected the relatively small amount of thermal dissipation which occurs at the sensor and source.
[19] The theory can be worked out for a more complicated cell geometry (see Appendix A). It is simpler, however, to redesign the cell to more closely match the ideal geometry or to use a technique allowing one to measure the properties of a uniform pore (see Appendix B).
[20] J. R. Olsen and G. W. Swift, ''Similitude in thermoacoustics,'' J. Acoust. Soc. Am. **95**, 1405–1412 (1994).
[21] E. H. Kennard, *Kinetic Theory of Gases, with an Introduction to Statistical Mechanics* (McGraw-Hill, New York, 1938).
[22] J. H. Jeans, *An Introduction to the Kinetic Theory of Gases* (Cambridge U.P., Cambridge, England, 1940).
[23] See Ref. 3, section 247, p. 26.
[24] A pure rocking motion of the cone imparts no net cross-sectional averaged momentum to the gas.
[25] A related function, f_κ is also commonly used by Swift (Ref. 8). The two are related by $F^*(\lambda) = 1 - f_\kappa$.
[26] V. Tarnow, ''Measurement of sound propagation in glass wool,'' J. Acoust. Soc. Am. **97**, 2272–2281 (1995).
[27] J. D. Mcintosh, M. T. Zuroski, and R. F. Lambert, ''Standing wave apparatus for measuring fundamental properties of acoustic materials in air,'' J. Acoust. Soc. Am. **88**, 1929–1938 (1990).
[28] A. Cummings and I.-J. Chang, ''Acoustic propagation in porous media with internal mean flow,'' J. Sound Vib. **114**, 565–581 (1987).
[29] Strictly speaking, we measure $F(\lambda)$ directly over a restricted range of λ. This range can be extended by using a shorter cell. However, even with the present arrangement, the range of validity includes the peak in $|\mathrm{Im}\, F(\lambda)|$. It should also be noted that we are measuring an average of $F(\lambda)$ over the various circular pores making up the cell. In Appendix B we describe a technique to measure $F(\lambda)$ for a uniform pore of arbitrary cross section.
[30] J. F. Crifo, ''Inferences concerning water vapour viscosity and mean free path at low temperatures,'' Astron. Astrophys. **223**, 365–368 (1989).

Modeling of piezoelectric ceramic vibrators including thermal effects. Part III. Bond graph model for one-dimensional heat conduction

Won-kyu Moon and Ilene J. Busch-Vishniac
Department of Mechanical Engineering, The University of Texas at Austin, Austin, Texas 78712

(Received 29 December 1995; accepted for publication 26 September 1996)

A new bond graph model for conduction heat transfer is developed, and applied to thermal energy balance in the piezoelectric thickness vibrator. In formulation of the heat conduction model, the mechanical and electrical effects are included. Hence, it can be directly applied to the temperature-dependent thickness vibrator. For the purpose of evaluation of the new method, one-dimensional heat conduction excluding other variable effects is compared with the results of the analytic solutions in simple cases. The simulation illustrates the validity and the accuracy of the model. Although the model is applied to the one-dimensional case only, the method can be easily used for general heat conduction problems. © *1997 Acoustical Society of America.* [S0001-4966(97)02002-X]

PACS numbers: 43.38.Ar, 43.38.Fx [SLE]

INTRODUCTION

Every system is a thermodynamic system. Depending on the system characteristics, consideration of the thermal energy balance of a thermodynamic system can be separated from that of other kinds of energy balances such as energy balance from mechanical forces.[1] A piezoelectric ceramic body is a system in which the energy balance should consider various effects all together, since the temperature dependence of the elastic stiffness, dielectric impermeability, and piezoelectric coefficients makes it impossible to separate the thermal energy balance from mechanical and electrical energy balances.[2–4]

The partial differential equations describing a thermally coupled piezoelectric ceramic body have been considered by the authors.[4] Although the partial differential equations derived can predict the response of a piezoelectric ceramic body, their insolvability makes them nearly meaningless. For example, the equations for the thickness vibrator, one of the simplest cases, cannot be solved analytically except for a few cases with simple boundary conditions.[4] Numerical solution techniques must be used to predict the response of the body, which implies that one must rely on a purely mathematical method for partial differential equations in investigating the behavior of a physical system.[5] This procedure usually provides only limited physical insight. As indicated in a paper by the authors,[1] bond graphs can provide physical insight into one of the most popular numerical solution techniques, the finite element method.

Bond graphs, first invented by Paynter,[6] are extensively used for modeling various kinds of physical systems.[7–9] Since bond graphs are designed for reticulation of a network of discrete systems, reticulation of a continuous system is a challenge and many people using various techniques have attacked this problem.[1,10–14] As indicated in a paper by the authors,[1] bond graphs are useful especially for a system in which various effects are inherently coupled, such as the piezoelectric vibrator, and the method proposed by the authors has some advantages for modeling a continuous system with bond graphs. In a piezoelectric ceramic body, thermal state variables are coupled to other state variables and mechanical state variables are coupled to electrical ones. Bond graphs, hence, may be useful in constructing a complete model. A bond graph model for a temperature-independent piezoelectric thickness vibrator has been developed.[1] In this article, we take the first step in development of a temperature-dependent model by addressing the problem of heat conduction. In the final article in this series, the model developed here will be combined with the temperature independent model to produce a bond graph model of the thickness vibrator including thermal, electrical, and mechanical effects.

Ingrim *et al.* developed a bond graph model for heat conduction in a solid body using extended bond graph notation and reticulation techniques.[15] It is necessary, in the extended bond graphs for heat conduction, to find conjugate basis functions corresponding to a basis of the function space to which the solution of the problem belongs.[12,13] This usually makes solution of the problem difficult or complicated.[1,16,17]

Finite element formulations are based upon mathematical discretization of partial differential equations, while bond graph models are strictly based on energy balances. As a result, the models produced using the two approaches may not be the same. The bond graph modeling approach for a continuous system linking electrical and mechanical energy domains developed by the authors is equivalent to the finite element method[1] since the finite element method for mechanical systems can be explained by an energy based approach.[18,19] However, in the case of heat conduction, the standard finite element model relies on a mathematical approximation technique[18,19] that cannot be explained by a rigorous energy based approach. In particular, the functionals generated cannot be interpreted as energies. Hence, it is impossible to develop a finite element equivalent bond graph model of the thickness vibrator including thermal effects.

In this study, a bond graph model describing the thermal

energy balance in the thickness vibrator is considered to describe thermal state change, heat conduction, and internal heat generation. The formulation can be directly applied to the piezoelectric ceramic thickness vibrator. As a preparatory step to developing a complete model for the thickness vibrator including thermal effects, heat conduction without other state variable change is evaluated by comparing the simulation results to analytical solutions for simple conduction heat transfer cases.

I. BOND GRAPHS FOR THERMODYNAMIC SYSTEMS

The first law of thermodynamics can be considered as the energy balance principle including thermal energy, heat. Since bond graphs are also based on energy balance of a system, bond graphs are certainly able to describe thermal energy balance as well as mechanical and electrical energy balances. Bond graphs are graphical tools that represent the characteristics of a physical system with several simple elements in a graphical way.[8] The elements in the bond graphs are **C** elements (like mechanical springs), **R** elements (like mechanical dampers), **I** elements (like mechanical inertias), and transformer **T** and gyrator **G** elements. The elements are connected with bonds, which can be thought to be energy pipes, through the junction elements: **1** for common flow (velocity or current) and **0** for common effort (force or voltage). With these several simple elements, various physical systems can be understood, modeled, and represented.[1,7,8]

The number of energy ports associated with each energy storing or dissipating element (**R**, **C**, or **I**) is dictated by the number of independent variables needed to describe the energy interactions. This is a significant departure from electric circuit models, in which the elements that store or dissipate energy are restricted to a single port through which energy is exchanged with the environment. This difference is significant for the application to thermal systems, because one cannot create an accurate model of the irreversible conversion of energy from a form suitable for doing work into a form unsuitable for work using the traditional model of a one-port resistance leaking heat into the environment. Instead, one must model the heat flow using a two-port **R**, and this has become the standard treatment used in bond graph modeling.[6,8]

While bond graphs include the dynamics of a system, since thermodynamics deals with equilibrium states only, system dynamics are not included in thermodynamic laws. In application, however, the laws of equilibrium are used as if they were valid for any dynamic process and dynamic irreversible effects are treated separately in most cases. Since real processes are only approximately the reversible processes usually dealt with in thermodynamics, and, since even the second law of thermodynamics asserts only the direction of a possible process and not the possible dynamic path of the state in a state space, the laws of thermodynamics usually are not sufficient to describe the dynamic path of the states of a thermodynamic system. Information on the dynamics of related phenomena, such as heat transfer or diffusion, is necessary for a complete model. For example, consider a solid body. Information on the dynamics of heat transfer, such as the Fourier's law of heat conduction, is necessary in addition

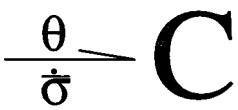

FIG. 1. The bond graph model for a discrete purely thermal system.

to the thermodynamic material properties of the solid body, in order to predict the entire dynamic path in the state space (as a function of time). The laws for the dynamics of transport phenomena, like conduction heat transfer, usually show resistancelike properties. In a continuous system, the effects of the transport phenomena are inherently fused into the effects of a change of the thermodynamic states. In developing a bond graph model, however, heat transfer effects as well as dynamic irreversibility effects, such as internal damping effects, are treated separately from changes of the thermodynamic states.

Before we begin developing a bond graph model for a continuous thermal system, it is helpful to consider a discrete thermal system. First, consider the definition of the effort and the flow variables corresponding to a thermal system. The natural choice for the thermal flow variable is found to be entropy[8] because the laws of thermodynamics and the macroscopic definition of entropy provide the following relation:[20,21]

$$\delta \mathcal{Q} = \theta \, \delta \overline{\sigma}, \tag{1}$$

where $\mathcal{Q}$, θ, and $\overline{\sigma}$ represent heat transferred into the system, temperature, and entropy of a system, respectively. In reality, Eq. (1) is valid only in a reversible process. Although every real process is inherently irreversible, by considering irreversible effects as a separate mechanism, Eq. (1) is rewritten in terms of time derivatives:

$$\dot{\mathcal{Q}} = \theta \dot{\overline{\sigma}}. \tag{2}$$

Equation (2) represents the thermal power flow, which is represented by the temperature times the time derivative of entropy of the system. Hence, θ and $\dot{\overline{\sigma}}$ are the effort and the flow variables of the system.[8] Since θ is a function of $\overline{\sigma}$ and not $\dot{\overline{\sigma}}$, and since $\overline{\sigma}$ is a displacementlike variable (because $\dot{\overline{\sigma}}$ is a flow variable), a thermal system is represented by a springlike **C** element in bond graphs as shown in Fig. 1.[8]

The above argument is almost impossible to apply to a continuous system because the total entropy of a continuous system cannot describe all its possible states. The entropy density may be more adequate to describe them. The entropy density, say σ, plays a similar role in a continuous thermal system to the strain in a continuous mechanical system. However, there is a difference. The strain is derived from the displacement field that is defined at each point in the system whereas the entropy density is defined as a volumetric derivative of the entropy and the entropy is thus a function of a spatial volume rather than a location.

If the entropy densities at some number of points are chosen as the thermal displacementlike state variables, as in Ref. 15, then the temperatures at those points cannot be the effort variables, because the units of temperature times time derivative of entropy density are power per unit volume and not power itself. This causes a serious problem when σ and θ

are uniformly distributed. In a uniformly distributed system, since the state variables do not change with the spatial location, the state variables at any location can represent the thermodynamic state of the entire system. Hence, a uniformly distributed system can be modeled as a discrete system, i.e., a system which exists at a point in space. In a discrete thermal system, temperature is the effort variable rather than a temperature per volume. Then, in order to be consistent, the flow variable must be the time rate of change of entropy at a point, and the displacement variable must be the entropy at that point. However, in a continuous system, the entropy at a point is always zero, so this choice to designate temperature as the effort variable results in a conflict between the continuous system and the discrete system model. To avoid this conflict, in the following section, a bond graph for a continuous thermal system is developed using entropy density as the flow variable and temperatures at some number of selected points in the system as the effort variables. In other words, the effort variable is defined only at specific locations, rather than at every location, and the product of the effort and flow variables is not power but power per volume. This permits the model to be easily interpreted and easily combined with bond graph models of other discrete thermal systems in modeling of a complicated network of systems.

II. A BOND GRAPH MODEL FOR HEAT BALANCE IN THE THICKNESS VIBRATOR

The first law of thermodynamics is the main physical principle which is used to develop a bond graph model for heat conduction. As shown in a previous paper by the authors,[4] the equations obtained by applying the first law to a piezoelectric body can be reduced to the thermal energy balance equations. The integral form of the thermal energy balance equation for a piezoelectric body is written as follows:[4]

$$\int\int\int_{\mathscr{V}_0} \theta\dot{\sigma}\, d\mathscr{V} = \int\int\int_{\mathscr{V}_0} \nabla\cdot(\kappa\nabla\theta)\, d\mathscr{V} - \int\int_{\partial\mathscr{V}_0} \vec{\mathbf{Q}}^{(e)}\cdot d\vec{\mathscr{A}} + \int\int\int_{\mathscr{V}_0} \dot{r}\, d\mathscr{V}, \tag{3}$$

where κ is the thermal conductivity, r is the heat generation rate per unit volume, $\vec{\mathbf{Q}}^{(e)}$ is the heat flux vector at the boundary of a body, $\mathscr{V}_0$ is the volume of a piezoelectric body, and $d\vec{\mathscr{A}}$ is the surface area differential vector. In order to reduce the problem into a one-dimensional case, as shown in Fig. 2, it is assumed that

$$v_1 = v_2 = 0, \tag{4}$$

$$D_1 = D_2 = 0, \tag{5}$$

$$v_3 = v_3(x_3,t), \tag{6}$$

$$D_3 = \frac{q(t)}{\mathscr{A}_0}, \tag{7}$$

and

$$\sigma = \sigma(x_3,t) \tag{8}$$

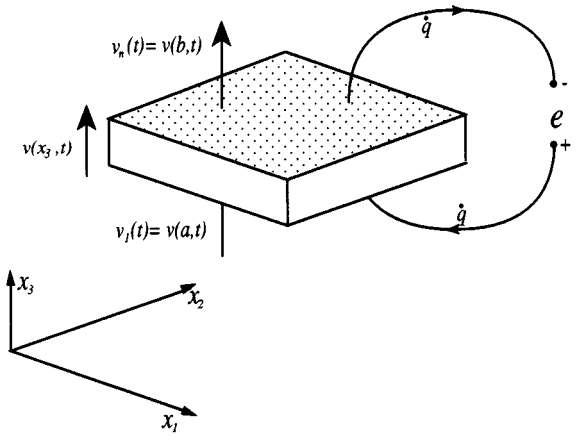

FIG. 2. The thickness vibrator (one-dimensional vibration drive).

or

$$\theta = \theta(x_3,t), \tag{9}$$

where x_i, v_i, D_i, q, t, and $\mathscr{A}_0$ are spatial coordinate, displacement, and electric flux density in the i direction, charge at the bottom conductor plate, time, and cross-sectional area, respectively.[4] Then, Eq. (3) is reduced to the following:

$$\mathscr{A}_0\int_a^b \theta\dot{\sigma}\, dx = \mathscr{A}_0\int_a^b \frac{\partial}{\partial x}\left(\kappa\frac{\partial\theta}{\partial x}\right)dx + \mathscr{A}_0\int_a^b \dot{r}\, dx - \mathscr{A}_0(Q^{(e)}|_{x=b} - Q^{(e)}|_{x=a}), \tag{10}$$

in which the 3 subscript has been suppressed and a and b are the locations of the bottom and top electrodes of the material. From this point, since we will deal with the thickness vibrator only, the subscripts to indicate direction are omitted. Equation (10) is the integral form of the thermal energy balance equation for the thickness vibrator. It is one of the fundamental equations for a bond graph model of the thickness vibrator including thermal effects. In this paper, only heat conduction is considered on the assumption that all the variables but the thermal variables are constant.

Entropy density is a convenient choice for an independent thermal state variable in developing a bond graph model, so we start with entropy density as an independent thermal state variable for describing material properties. However, temperature can be used as a state variable of the system in the state equations derived from the resulting bond graph model. Since a bond graph model should be finite dimensional, we assume that entropy density (Ref. 1), displacement, and charge can be expressed in the following forms:

$$\sigma(t,x) = \sum_{n=1}^{N} \sigma^{(n)}(t) f_n(x), \tag{11}$$

$$v(t,x) = \sum_{n=1}^{N} v^{(n)}(t) f_n(x), \tag{12}$$

$$q(t) = \mathscr{A}_0 D(t), \tag{13}$$

where

$$f_n(x)=\begin{cases}\dfrac{x-x^{(n-1)}}{x^{(n)}-x^{(n-1)}}, & \text{if } x^{(n-1)}\leqslant x\leqslant x^{(n)},\\ \dfrac{x-x^{(n+1)}}{x^{(n)}-x^{(n+1)}}, & \text{if } x^{(n)}\leqslant x\leqslant x^{(n+1)},\\ 0 \quad \text{otherwise,}\end{cases} \tag{14}$$

and $x^{(n)}$ denotes the nth node so that $a=x^{(1)}<x^{(2)}<\cdots<x^{(N)}=b$. The functions $f_n(x)$ are the global representations of the linear interpolation functions in the finite element method.[19] Note that

$$\sigma^{(n)}(t)=\sigma(t,x^{(n)}), \tag{15}$$

$$v^{(n)}(t)=v(t,x^{(n)}), \tag{16}$$

i.e., $\sigma^{(n)}(t)$ and $v^{(n)}(t)$ are entropy density and displacement at the nth nodes, respectively, and that N functions $f_n(x)$ for $n=1,2,\ldots,N$ are needed if N nodes are selected.

It is claimed that the $(2N+1)$ variables, $\sigma^{(n)}(t)$, $v^{(n)}(t)$, and $q(t)$, are a complete set of state variables for the thickness vibrator, as the dynamic equations can be written in terms of them. We define derivatives of $f_n(x)$ as follows:

$$f_n'(x)=\begin{cases}\dfrac{1}{x^{(n)}-x^{(n-1)}} & \text{if } x^{(n-1)}<x<x^{(n)},\\ \dfrac{1}{x^{(n)}-x^{(n+1)}} & \text{if } x^{(n)}<x<x^{(n+1)},\\ \dfrac{1}{(2-\delta_{1(n-1)})(x^{(n)}-x^{(n-1)})} & \text{if } x=x^{(n-1)},\\ \dfrac{1-\delta_{1n}}{(2-\delta_{Nn})(x^{(n)}-x^{(n-1)})}+\dfrac{1-\delta_{Nn}}{(2-\delta_{1n})(x^{(n)}-x^{(n+1)})} & \text{if } x=x^{(n)},\\ \dfrac{1}{(2-\delta_{N(n+1)})(x^{(n)}-x^{(n+1)})} & \text{if } x=x^{(n+1)},\\ 0 \quad \text{otherwise,}\end{cases} \tag{17}$$

$$f_n''(x)=\frac{\delta(x-x^{(n-1)})}{x^{(n)}-x^{(n-1)}}+\frac{\delta(x-x^{(n+1)})}{x^{(n)}-x^{(n+1)}}-\left(\frac{1}{x^{(n)}-x^{(n-1)}}+\frac{1}{x^{(n)}-x^{(n+1)}}\right)\delta(x-x^{(n)}), \tag{18}$$

where $\delta(\cdot)$ and δ_{ij} represent the Dirac delta function and the Kronecker delta, respectively. Figures 3 and 4 show the $f_n(x)$'s and $f_n'(x)$'s, respectively, for the case of four nodes $(N=4)$.

Since the strain in the x_3 direction, S_3, can be defined by

$$S_3=\frac{\partial v}{\partial x}=\sum_{n=1}^{N} v^{(n)}(t)f_n'(x),$$

the internal energy density u can be considered as follows:[3]

$$u=u(\{v^{(n)}(t)\},q(t),\{\sigma^{(n)}(t)\},\{f_n(x)\},\{f_n'(x)\}).$$

By integration over the whole domain, the internal energy of the thickness vibrator is obtained:

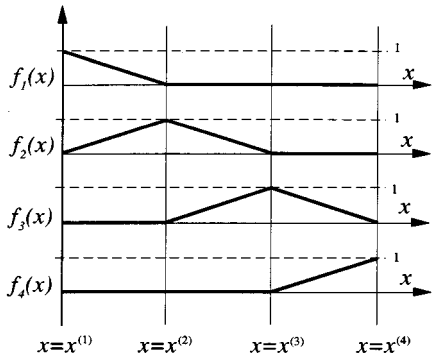

FIG. 3. $f_n(x)$ for $n=1,2,3,4$ $(N=4)$.

$$\mathscr{U}=\int\int\int_{\mathscr{V}} u\ d\mathscr{V}=\mathscr{A}_0\int_a^b u(\{v^{(n)}(t)\},q(t),\{\sigma^{(n)}(t)\},\{f_n(x)\},\{f_n'\})dx=\mathscr{U}(\{v^{(n)}(t)\},q(t),\{\sigma^{(n)}(t)\}). \tag{19}$$

Consider the time derivative of the internal energy

$$\frac{d\mathscr{U}}{dt}=\sum_{n=1}^{N}\frac{\partial\mathscr{U}}{\partial v^{(n)}}\dot{v}^{(n)}+\frac{\partial\mathscr{U}}{\partial q}\dot{q}+\sum_{n=1}^{N}\frac{\partial\mathscr{U}}{\partial\sigma^{(n)}}\dot{\sigma}^{(n)}. \tag{20}$$

The first and the second groups of terms on the right-hand side of Eq. (20) can be recognized as mechanical and electrical power flows. The physical meaning of the third group is of interest. Note that

$$\begin{aligned}\sum_{n=1}^{N}\frac{\partial\mathscr{U}}{\partial\sigma^{(n)}}\dot{\sigma}^{(n)}&=\sum_{n=1}^{N}\left[\frac{\partial}{\partial\sigma^{(n)}}\int\int\int_{\mathscr{V}} u\ d\mathscr{V}\right]\dot{\sigma}^{(n)}\\&=\int\int\int_{\mathscr{V}}\left(\sum_{n=1}^{N}\frac{\partial u}{\partial\sigma^{(n)}}\dot{\sigma}^{(n)}\right)d\mathscr{V}\\&=\int\int\int_{\mathscr{V}}\left(\sum_{n=1}^{N}\frac{\partial u}{\partial\sigma}\frac{\partial\sigma}{\partial\sigma^{(n)}}\dot{\sigma}^{(n)}\right)d\mathscr{V}\\&=\int\int\int_{\mathscr{V}}\frac{\partial u}{\partial\sigma}\left[\sum_{n=1}^{N}\dot{\sigma}^{(n)}f_n(x)\right]d\mathscr{V}\\&=\int\int\int_{\mathscr{V}}\left(\frac{\partial u}{\partial\sigma}\dot{\sigma}\right)d\mathscr{V}=\int\int\int_{\mathscr{V}}\theta\dot{\sigma}\ d\mathscr{V},\end{aligned} \tag{21}$$

where the Maxwell's relation $\theta=\partial u/\partial\sigma$ is used. Using this result with Eq. (20), Eq. (3) [or (10)] shows that the last term in Eq. (20) represents heat flowing into the thickness vibrator. However, the above does not provide information on how to draw a bond graph for a system because $\partial\mathscr{U}/\partial\sigma^{(n)}$ is not temperature, due to the fact that $\sigma^{(n)}$ is not entropy but entropy density at nth node. This means that $\partial\mathscr{U}/\partial\sigma^{(n)}$ has units of temperature times volume, and not temperature. In order to be consistent with bond graphs for discrete systems, temperature should be chosen as a thermal effort variable because temperature can be defined at each node whereas entropy cannot. In the following discussion, we propose a method to define the temperature at the nodes as the thermal effort variables and equivalent entropy change rates corre-

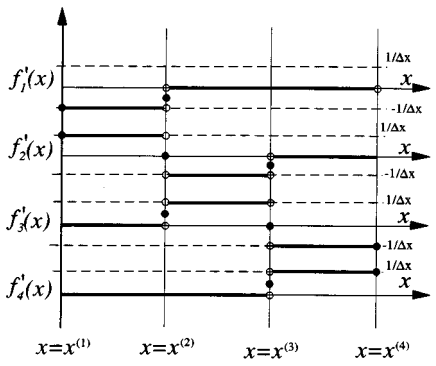

FIG. 4. $f_n'(x)$ for $n=1,2,3,4$ ($N=4$).

sponding to each nodal temperature as the thermal flow variables.

Before calculating the first term in Eq. (10), the thermodynamic state constitutive relations should be considered. The thermodynamic state constitutive relations can be given in the following two forms:

$$\theta=\theta(\sigma,S_3,D_3)=\theta\left(\sigma,\frac{\partial v}{\partial x},\frac{q}{\mathscr{A}_0}\right) \tag{22}$$

or

$$\sigma=\sigma(\theta,S_3,D_3)=\sigma\left(\theta,\frac{\partial v}{\partial x},\frac{q}{\mathscr{A}_0}\right), \tag{23}$$

depending on whether σ is the independent state variable [Eq. (22)] or θ is the independent state variable [Eq. (23)]. When Eq. (23) is used, in addition to selecting temperature as an independent thermal state variable, it is assumed, instead of Eq. (11), that

$$\theta=\sum_{n=1}^{N}\theta^{(n)}(t)f_n(x), \tag{24}$$

so that

$$\theta^{(n)}(t)=\theta(t,x^{(n)}). \tag{25}$$

In order to calculate the net heat flowing into the thickness vibrator [the first term in Eq. (10)], the independent thermal state variable and the constitutive relations should be previously determined. However, in many cases, the constitutive relation between temperature and entropy density is often so complicated that it is tedious to calculate the integrand in the first term in Eq. (10) by hand. Hence, we reject that procedure, and, instead, apply the constitutive relations at a finite number of points. Since Eqs. (11)–(13), and (19) each has at most only n, independent variables, a finite number of constitutive relations are sufficient for describing the whole system behavior. Hence, from the beginning, we set temperature and entropy density fields, at the same time, as in Eqs. (11) and (24) before fixing the form of the thermodynamic state constitutive relation. Then, using Eqs. (11)–(13) and (24), the net heat flow-in can be calculated.

$$\begin{aligned}
&\int\int\int_{\mathscr{V}}\theta\dot{\sigma}\,d\mathscr{V}\\
&=\mathscr{A}_0\int_a^b\left[\sum_{n=1}^{N}\sum_{m=1}^{N}\theta^{(n)}(t)\dot{\sigma}^{(m)}(t)f_m(x)f_n(x)\right]dx\\
&=\sum_{n=1}^{N}\theta^{(n)}(t)\left[\sum_{m=1}^{N}\dot{\sigma}^{(m)}(t)\left(\mathscr{A}_0\int_a^b f_m(x)f_n(x)dx\right)\right].
\end{aligned} \tag{26}$$

If $\theta^{(n)}$ is considered as an effort variable for heat flow, we can define a corresponding flow variable as follows:

$$\dot{\tilde{\sigma}}_n(t)=\sum_{m=1}^{N}\dot{\sigma}^{(m)}(t)\left(\mathscr{A}_0\int_a^b f_m(x)f_n(x)dx\right). \tag{27}$$

Note that $\dot{\tilde{\sigma}}_n$ has units of entropy per time while $\dot{\sigma}^{(m)}$ has units of entropy density per time. Hence, the $\dot{\tilde{\sigma}}_n$ can be thermal flow variables of a system, with the same physical meaning as entropy flows in discrete system bond graphs. Obviously, $\theta^{(n)}$ is the temperature at nth node, which also has identical physical meaning to thermal effort variable of a discrete system. In a discrete system, since temperature and entropy distributions are uniform throughout the entire system, it is sufficient to select temperature at one point as the thermal effort variable for the whole system. However, in the case of nonuniform temperature distribution, temperature at one point cannot represent the thermal characteristics of the entire system. Then, Eq. (25) can be used to define the thermal variables.

Consider the first term on the right-hand side of Eq. (10) which represents conduction heat transfer effects:

$$\begin{aligned}
\int\int\int_{\mathscr{V}}\nabla\cdot(\kappa\nabla\theta)d\mathscr{V}&=\int\int\int_{\mathscr{V}}\theta\,\frac{\nabla\cdot(\kappa\nabla\theta)}{\theta}\,d\mathscr{V}\\
&=\mathscr{A}_0\int_a^b\theta\,\frac{\dfrac{\partial}{\partial x}\left(\kappa\dfrac{\partial\theta}{\partial x}\right)}{\theta}\,dx.
\end{aligned} \tag{28}$$

Substituting Eq. (24) into (28) we get

$$\begin{aligned}
&\int\int_{\partial\mathscr{V}}\kappa\nabla\theta\cdot d\vec{\mathscr{A}}\\
&=\mathscr{A}_0\int_a^b\sum_{n=1}^{N}\theta^{(n)}(t)f_n(x)\,\frac{\kappa\Sigma_{m=1}^{N}\theta^{(m)}(t)f_m''(x)}{\Sigma_{k=1}^{N}\theta^{(k)}f_k(x)}\,dx\\
&=\sum_{n=1}^{N}\theta^{(n)}(t)\sum_{m=1}^{N}\mathscr{A}_0\theta^{(m)}(t)\int_a^b\frac{\kappa f_n(x)f_m''(x)}{\Sigma_{k=1}^{N}\theta^{(k)}(t)f_k(x)}\,dx\\
&=\sum_{n=1}^{N}\theta^{(n)}(t)\sum_{m=1}^{N}\mathscr{A}_0\theta^{(m)}(t)\left[\frac{\kappa f_n(x^{(m-1)})}{\theta^{(m-1)}(t)}\,\frac{1}{x^{(m)}-x^{(m-1)}}\right.\\
&\quad-\frac{\kappa f_n(x^{(m)})}{\theta^{(m)}(t)}\left(\frac{1}{x^{(m)}-x^{(m-1)}}+\frac{1}{x^{(m)}-x^{(m+1)}}\right)\\
&\quad\left.+\frac{\kappa f_n(x^{(m+1)})}{\theta^{(m+1)}(t)}\,\frac{1}{x^{(m)}-x^{(m+1)}}\right]
\end{aligned}$$

$$= \sum_{n=1}^{N} \theta^{(n)}(t) \left[\frac{\kappa \mathscr{A}_0}{\theta^{(n)}(t)} \left(-(1-\delta_{1n}) \frac{\theta^{(n)}(t) - \theta^{(n-1)}(t)}{x^{(n)} - x^{(n-1)}} + (1-\delta_{Nn}) \frac{\theta^{(n+1)}(t) - \theta^{(n)}(t)}{x^{(n+1)} - x^{(n)}} \right) \right], \tag{29}$$

where δ_{ij} is the Kronecker delta. Since we define the $\theta^{(n)}$'s as effort variables of the system, the terms in the bracket of Eq. (29) should represent the corresponding entropy flow into the system. Since the flow variables are dependent on the effort variables, the terms for each n can be represented by an **R** element in bond graphs. An **R** element in bond graphs is usually called a power dissipation element and without inclusion of thermal effects power always flows into an **R** element and never flows out. However, if thermal effects are included in bond graphs, no energy is stored in an **R** element. In this respect, an **R** element is identical to a transformer or a gyrator. However, inside an **R** element entropy is produced, whereas in a transformer or a gyrator there is no entropy production. (For further information on **R** elements see Ref. 8.)

The last term in the energy balance equation, Eq. (10), represents heat flow from outside of the body. It becomes a boundary condition of the differential form of the energy balance equation. It may be transformed into a product of temperature and entropy flow rate; i.e.,

$$\int \int_{\partial \mathscr{V}} \vec{\mathbf{Q}}^{(e)} \cdot d\vec{\mathscr{A}} = \mathscr{A}_0 \left(-\theta|_{x=a} \left. \frac{Q}{\theta} \right|_{x=a} + \theta|_{x=b} \left. \frac{Q}{\theta} \right|_{x=b} \right) = \mathscr{A}_0 \left(-\theta^{(1)} \frac{Q_1}{\theta^{(1)}} + \theta^{(N)} \frac{Q_N}{\theta^{(N)}} \right), \tag{30}$$

where $Q_1 = Q|_{x=a}$ and $Q_N = Q|_{x=b}$. Note that positive Q_1 or Q_N indicates the heat flux in the positive x-direction.

The remaining term in the energy balance equation can be rewritten as follows:

$$\mathscr{A}_0 \int_a^b \dot{r}\, dx = \sum_{n=1}^{N} \theta^{(n)}(t) \times \left[\mathscr{A}_0 \int_a^b \frac{\dot{r}(t,x) f_n(x)}{\sum_{k=1}^{N} \theta^{(k)}(t) f_k(x)}\, dx \right]. \tag{31}$$

Note that once again, the bracketed term can be interpreted as entropy generation due to heat source and be represented by using the source elements in bond graphs.[8]

Now we can draw the bond graph for one-dimensional heat conduction. Since the thickness vibrator includes mechanical and electrical effects, the mechanical and electrical behavior should also be considered in order to draw the complete bond graph. In this paper, only a bond graph for the conduction heat transfer in the thickness vibrator is considered by constraining constant the mechanical and the electrical variables. Figure 5 shows the bond graph for the conduction heat transfer with no heat source ($\dot{r} \equiv 0$). Here, the multiport capacitance represents the internal energy stored in the material, and the two-port resistances represent heat flow from one node to another. The zero-junctions define the temperature at each node in the material model, with the model

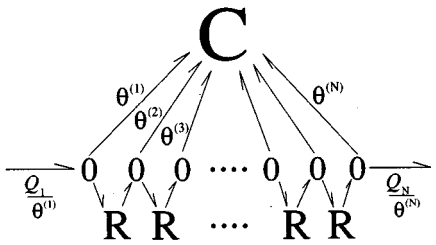

FIG. 5. Bond graph of a purely thermal continuous system with no internal heat source.

accuracy generally improving as the number of nodes increases. The entropy flow at the boundaries is shown as $Q_1/\theta^{(1)}$ and $Q_N/\theta^{(N)}$.

In order to derive the state equations for the thickness vibrator, we return to the energy balance equation Eq. (10). Using Eqs. (26), (29), (30), and (31),

$$\sum_{n=1}^{N} \theta^{(n)}(t) \left[\sum_{m=1}^{N} \dot{\sigma}^{(m)}(t) \left(\mathscr{A}_0 \int_a^b f_m(x) f_n(x)\, dx \right) \right] = \sum_{n=1}^{N} \theta^{(n)}(t) \left\{ \frac{\kappa \mathscr{A}_0}{\theta^{(n)}(t)} \left[-(1-\delta_{1n}) \frac{\theta^{(n)}(t) - \theta^{(n-1)}(t)}{x^{(n)} - x^{(n-1)}} + (1-\delta_{Nn}) \frac{\theta^{(n+1)}(t) - \theta^{(n)}(t)}{x^{(n+1)} - x^{(n)}} \right] \right\} - \mathscr{A}_0 \left(-\theta^{(1)} \frac{Q_1}{\theta^{(1)}} + \theta^{(N)} \frac{Q_N}{\theta^{(N)}} \right) + \sum_{n=1}^{N} \theta^{(n)}(t) \times \left[\mathscr{A}_0 \int_a^b \frac{\dot{r}(t,x) f_n(x)}{\sum_{k=1}^{N} \theta^{(k)}(t) f_k(x)}\, dx \right]. \tag{32}$$

The above equation can be rewritten as follows:

$$\sum_{n=1}^{N} \theta^{(n)}(t) \left\{ \sum_{m=1}^{N} \dot{\sigma}^{(m)}(t) \left(\mathscr{A}_0 \int_a^b f_m(x) f_n(x)\, dx \right) - \frac{\kappa \mathscr{A}_0}{\theta^{(n)}(t)} \left[-(1-\delta_{1n}) \frac{\theta^{(n)}(t) - \theta^{(n-1)}(t)}{x^{(n)} - x^{(n-1)}} + (1-\delta_{Nn}) \times \frac{\theta^{(n+1)}(t) - \theta^{(n)}(t)}{x^{(n+1)} - x^{(n)}} \right] + \mathscr{A}_0 \left(-\delta_{1n} \frac{Q_1}{\theta^{(1)}} + \delta_{Nn} \frac{Q_N}{\theta^{(N)}} \right) - \mathscr{A}_0 \int_a^b \frac{\dot{r}(t,x) f_n(x)}{\sum_{k=1}^{N} \theta^{(k)}(t) f_k(x)}\, dx \right\} = 0. \tag{33}$$

Since $\theta^{(n)}(t)$ can assume arbitrary values, we have

$$\sum_{m=1}^{N} \dot{\sigma}^{(m)}(t) \left(\mathscr{A}_0 \int_a^b f_m(x) f_n(x)\, dx \right) = \frac{\kappa \mathscr{A}_0}{\theta^{(n)}(t)} \left[-(1-\delta_{1n}) \frac{\theta^{(n)}(t) - \theta^{(n-1)}(t)}{x^{(n)} - x^{(n-1)}} + (1-\delta_{Nn}) \frac{\theta^{(n+1)}(t) - \theta^{(n)}(t)}{x^{(n+1)} - x^{(n)}} \right] - \mathscr{A}_0 \left(-\delta_{1n} \frac{Q_1}{\theta^{(1)}} + \delta_{Nn} \frac{Q_N}{\theta^{(N)}} \right) + \mathscr{A}_0 \int_a^b \frac{\dot{r}(t,x) f_n(x)}{\sum_{k=1}^{N} \theta^{(k)}(t) f_k(x)}\, dx, \tag{34}$$

where $n=1,2,\ldots,N$. The above equations are the state equations for the thermal variables of the thickness vibrator. Note that the left-hand side of Eq. (34) is $\dot{\bar{\sigma}}_n$, the time derivative of equivalent entropy variable for the system in the developed bond graph model.

One variable group of $\{\sigma^{(n)}(t)\}$ and $\{\theta^{(n)}(t)\}$ should be eliminated in Eq. (34) to solve the derived differential equations. The choice for elimination is dependent on the form of the given constitutive relations. For example, if the thermodynamic state constitutive relation is given in the form as Eq. (22), the $\theta^{(n)}(t)$s in Eq. (34) should be eliminated by use of the given relation, i.e.,

$$\theta^{(n)}(t)=\theta(\sigma^{(n)}(t),v_x^{(n)}(t),q/\mathscr{A}_0), \tag{35}$$

where

$$\begin{aligned} v_x^{(n)}(t)=\left.\frac{\partial v}{\partial x}\right|_{x=x^{(n)}} &= \sum_{n=1}^{N} v^{(n)}(t) f_n'(x) \\ &= \frac{1}{2}\left[(1-\delta_{1n}+\delta_{Nn})\,\frac{v^{(n)}(t)-v^{(n-1)}(t)}{x^{(n)}-x^{(n-1)}}\right. \\ &\quad \left.+(1+\delta_{1n}-\delta_{Nn})\,\frac{v^{(n+1)}(t)-v^{(n)}(t)}{x^{(n+1)}-x^{(n)}}\right]. \end{aligned} \tag{36}$$

If Eq. (23) is given, then the $\dot{\sigma}^{(m)}$s should be replaced by the following:

$$\dot{\sigma}^{(m)}=\left.\frac{\partial\sigma}{\partial\theta}\right|_m \dot{\theta}^{(m)}+\sum_{i=1}^{6}\left.\frac{\partial\sigma}{\partial S_i}\right|_m \dot{S}_i^{(m)}+\left.\frac{\partial\sigma}{\partial q}\right|_m \dot{q}, \tag{37}$$

where

$$\left.\frac{\partial\sigma}{\partial\theta}\right|_m=\left.\frac{\partial\sigma}{\partial\theta}\right|_{x=x^{(m)}}=\frac{\partial\sigma}{\partial\theta}\,(\theta^{(m)},v_x^{(m)},q), \tag{38}$$

$$\left.\frac{\partial\sigma}{\partial S_i}\right|_m=\left.\frac{\partial\sigma}{\partial S_i}\right|_{x=x^{(m)}}=\frac{\partial\sigma}{\partial S_i}\,(\theta^{(m)},v_x^{(m)},q), \tag{39}$$

$$\dot{S}_i^{(m)}=\frac{d}{dt}\,(v_x^{(m)}), \tag{40}$$

$$\left.\frac{\partial\sigma}{\partial q}\right|_m=\left.\frac{\partial\sigma}{\partial q}\right|_{x=x^{(m)}}=\frac{\partial\sigma}{\partial q}\,(\theta^{(m)},v_x^{(m)},q). \tag{41}$$

Substituting Eq. (37) into Eq. (34), the differential equations for $\theta^{(n)}(t)$ can be obtained.

III. ONE-DIMENSIONAL CONDUCTION HEAT TRANSFER

In this section we consider heat conduction excluding all other effects and compare the bond graph model predictions to the analytic solutions. The exclusively thermal system equations can be found by assuming that σ is a function of θ only or vice versa.[3,4] Hence, consider the thickness vibrator as a slab which has cross-sectional area $\mathscr{A}_0$, length l, and thermal conductivity κ as shown in Fig. 6. All the faces except cross-sectional faces are insulated, so that the conduction heat transfer is one-dimensional. For simplicity, heat capacity C_v is assumed to be constant. Then, the thermodynamic state constitutive relation is given by

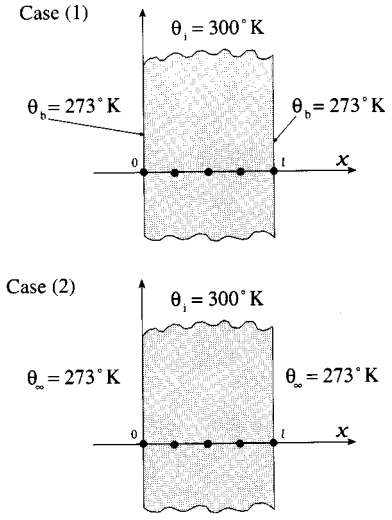

FIG. 6. One-dimensional conduction problem of a slab.

$$\sigma=\sigma(\theta),$$

so that the exact form of constitutive relation is easily calculated. Since $C_v=\theta\sigma'(\theta)$, we have

$$\sigma=\sigma_0+C_v\,\ln(\theta/\theta_0). \tag{42}$$

For this problem a five-node bond graph model is considered. Before developing a bond graph model, we choose five nodes as follows and shown in Fig. 6:

$$a=x^{(1)}=0,\quad x^{(2)}=\frac{l}{4},\quad x^{(3)}=\frac{l}{2},$$

$$x^{(4)}=\frac{3l}{4},\quad b=x^{(5)}=l.$$

Since

$$\left[\mathscr{A}_0\int_a^b f_m(x)f_n(x)dx\right]=\frac{\mathscr{A}_0 l}{24}\begin{bmatrix}2&1&0&0&0\\1&4&1&0&0\\0&1&4&1&0\\0&0&1&4&1\\0&0&0&1&2\end{bmatrix}, \tag{43}$$

$$\begin{aligned} &\frac{\kappa\mathscr{A}_0}{\theta^{(n)}}\left[-(1-\delta_{1n})\,\frac{\theta^{(n)}-\theta^{(n-1)}}{x^{(n)}-x^{(n-1)}}+(1-\delta_{Nn})\,\frac{\theta^{(n+1)}-\theta^{(n)}}{x^{(n+1)}-x^{(n)}}\right] \\ &\quad=\frac{4\kappa\mathscr{A}_0}{l\theta^{(n)}}\,[-(1-\delta_{1n})(\theta^{(n)}-\theta^{(n-1)})+(1-\delta_{Nn}) \\ &\qquad\times(\theta^{(n+1)}-\theta^{(n)})], \end{aligned} \tag{44}$$

and

$$\left.\frac{\partial\sigma}{\partial S_i}\right|_m=0, \tag{45}$$

$$\left.\frac{\partial \sigma}{\partial q}\right|_m = 0, \tag{46}$$

$$\left.\frac{\partial \sigma}{\partial \theta}\right|_m = \frac{C_v}{\theta^{(m)}}, \tag{47}$$

$$\dot{\sigma}^{(m)}(t) = \frac{C_v}{\theta^{(m)}}\,\dot{\theta}^{(m)}(t), \tag{48}$$

the state equations can be obtained directly from Eq. (34) as the following in matrix form:

$$\frac{\mathscr{A}_0 C_p l}{24}\begin{bmatrix} 2 & 1 & 0 & 0 & 0 \\ 1 & 4 & 1 & 0 & 0 \\ 0 & 1 & 4 & 1 & 0 \\ 0 & 0 & 1 & 4 & 1 \\ 0 & 0 & 0 & 1 & 2 \end{bmatrix}\begin{Bmatrix} \dot{\theta}^{(1)}/\theta^{(1)} \\ \dot{\theta}^{(2)}/\theta^{(2)} \\ \dot{\theta}^{(3)}/\theta^{(3)} \\ \dot{\theta}^{(4)}/\theta^{(4)} \\ \dot{\theta}^{(5)}/\theta^{(5)} \end{Bmatrix}$$

$$= \frac{4\kappa.\mathscr{A}_0}{l}\begin{Bmatrix} (\theta^{(2)}-\theta^{(1)})/\theta^{(1)} \\ (\theta^{(3)}-2\theta^{(2)}+\theta^{(1)})/\theta^{(2)} \\ (\theta^{(4)}-2\theta^{(3)}+\theta^{(2)})/\theta^{(3)} \\ (\theta^{(5)}-2\theta^{(4)}+\theta^{(3)})/\theta^{(4)} \\ -(\theta^{(5)}-\theta^{(4)})/\theta^{(5)} \end{Bmatrix}$$

$$+.\mathscr{A}_0\begin{Bmatrix} Q_1/\theta^{(1)} \\ 0 \\ 0 \\ 0 \\ -Q_N/\theta^{(N)} \end{Bmatrix}. \tag{49}$$

We consider two cases with different boundary conditions. The first case is heat conduction with a constant boundary temperature. The boundary and initial conditions are given as follows:

$$\theta = \theta_b \quad \text{at } x = 0, l, \tag{50}$$

$$\theta(0,x) = \theta_i, \quad 0 < x < l. \tag{51}$$

The analytic solution for this case is well known:[22]

$$\theta = \theta_b + (\theta_i - \theta_b)\,\frac{4}{\pi}\sum_{n=1}^{\infty}\frac{\exp(-\alpha_n \tau)\sin(\alpha_n \xi)}{2n-1}, \tag{52}$$

where

$$\alpha_n = (2n-1)\pi, \tag{53}$$

$$\tau = \frac{\kappa t}{C_p l^2}, \tag{54}$$

$$\xi = \frac{x}{l}, \tag{55}$$

and C_p is the constant pressure heat capacity per unit volume. The bond graph model predictions can be calculated

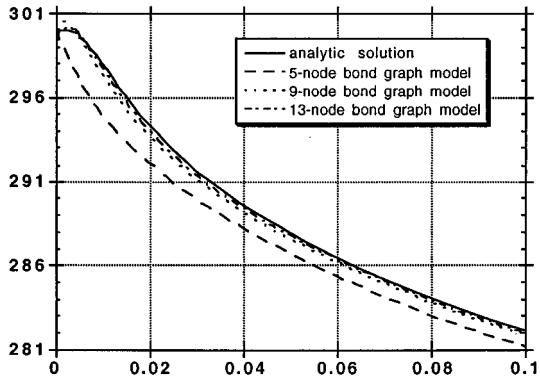

FIG. 7. The calculated temperatures at $x = l/4$ in the constant boundary temperature case.

easily by use of Eq. (49). Since $\theta^{(1)}$ and $\theta^{(N)}$ are constant, the first and the last equations in Eq. (49) become meaningless. Hence, we eliminate the first and the last equations to get

$$\begin{bmatrix} 4 & 1 & 0 \\ 1 & 4 & 1 \\ 0 & 1 & 4 \end{bmatrix}\begin{Bmatrix} \dot{\theta}^{(2)}/\theta^{(2)} \\ \dot{\theta}^{(3)}/\theta^{(3)} \\ \dot{\theta}^{(4)}/\theta^{(4)} \end{Bmatrix}$$

$$= \frac{96\kappa}{C_p l^2}\begin{Bmatrix} (\theta^{(3)}-2\theta^{(2)}+\theta_b)/\theta^{(2)} \\ (\theta^{(4)}-2\theta^{(3)}+\theta^{(2)})/\theta^{(3)} \\ (\theta_b-2\theta^{(4)}+\theta^{(3)})/\theta^{(4)} \end{Bmatrix}. \tag{56}$$

Figures 7 and 8 compare the results of Eq. (56) with the exact solution (52) when $\theta_i = 300$ K and $\theta_b = 273$ K, all other material properties being arbitrarily set to 1 ($l = \kappa = C_p = 1$). By increasing the number of nodes, the accuracy improves obviously as can be seen in the Figs. 7 and 8. Note that the temperature calculated by the bond graph model is always smaller than the analytic result except for a short beginning period.

The next case is heat conduction with convection boundaries and is shown in Fig. 6. Note that the problem has iden-

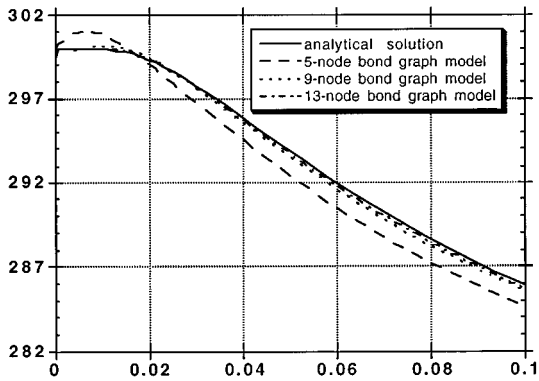

FIG. 8. The calculated temperatures at $x = l/2$ in the constant boundary temperature case.

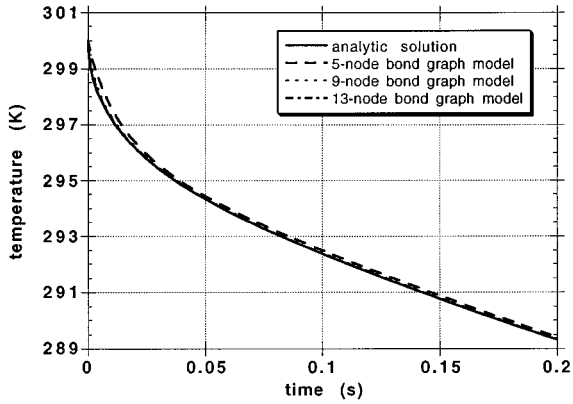

FIG. 9. The calculated temperatures at $x=0$ in the heat convection boundary case.

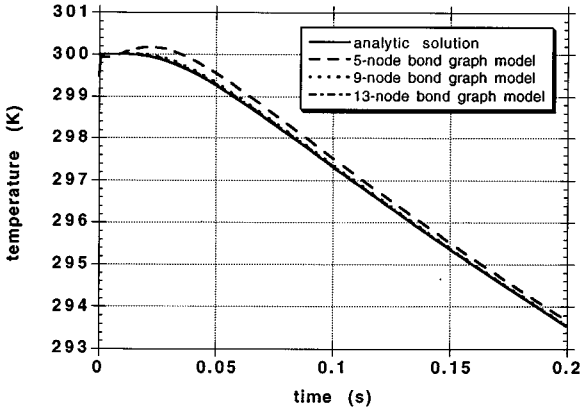

FIG. 11. The calculated temperatures at $x=l/2$ in the heat convection boundary case.

tical boundaries on the left and right. The boundary conditions can be expressed as follows:

$$Q_1 = h(\theta_\infty - \theta|_{x=0}) \quad \text{at } x=0,$$

$$Q_N = -h(\theta_\infty - \theta|_{x=l}) \quad \text{at } x=l,$$

where h is the convection coefficient. The initial condition is

$$\theta(0,x) = \theta_i, \quad 0 \leqslant x \leqslant l. \tag{57}$$

The analytic solution for this case can be found in Ref. 23:

$$\theta = \theta_\infty + (\theta_i - \theta_\infty) \sum_{n=1}^{\infty} A_n \exp(-4\alpha_n^2 \tau) \cos[\alpha_n (2\xi - 1)], \tag{58}$$

where

$$A_n = \frac{4 \sin \alpha_n}{2\alpha_n + \sin(2\alpha_n)}, \quad \tau = \frac{\kappa t}{C_p l^2}, \quad \xi = \frac{x}{l},$$

and α_n is the nth positive solution of the following equation:

$$\alpha_n \tan \alpha_n - \frac{hl}{2\kappa} = 0.$$

The bond graph model for this case again can be calculated from Eq. (49). The state equations are obtained by substituting the boundary conditions into Eq. (49). Numerical simulation results are shown in Figs. 9–11 with the exact solution values when $\theta_i = 300$ K and $\theta_\infty = 273$ K. Compared with the five-node bond graph model for the previous case, the result of this case is considerably better. Moreover, the bond graph simulation provides greater temperature values than those of the analytic solution, which is a contrast to the previous case. These differences come from the difference in boundary conditions. Since the constant temperature boundary makes an abrupt change in the distribution of temperature in space, it is more difficult to approximate the spatial distribution of the initial temperature with a piecewise linear function than the convection boundary case.

The effects of an abrupt change of condition in time at the beginning of the simulation can be seen in both cases. Although the temperature inside the body cannot be greater than 300 K, the simulation result shows that the values of temperature are greater than 300 K in the beginning period. This incorrect prediction continues during a short initial period only. However, in any period of simulation, accuracy of the simulation results improves considerably with the number of nodes as in the previous case. Figures 9–11 show the results for the convection boundary case calculated by 5-, 9-, and 13-node bond graph models at the three locations $x=0$, 1/4, 1/2, in which considerable accuracy increases are observed.

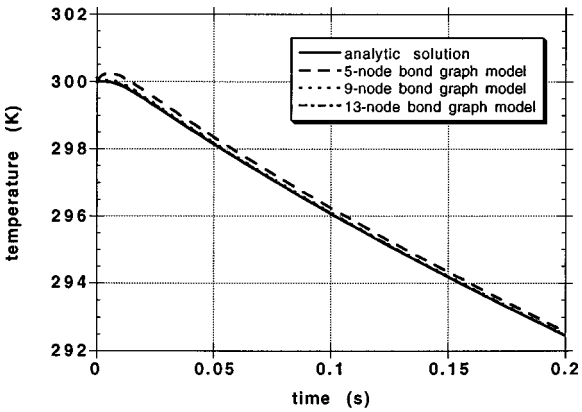

FIG. 10. The calculated temperatures at $x=l/4$ in the heat convection boundary case.

IV. CONCLUSIONS

The thermal energy balance in the piezoelectric thickness vibrator is considered in order to develop a complete bond graph model for the piezoelectric ceramic thickness vibrator including temperature dependence of the material coefficients. A bond graph model for one-dimensional heat conduction in the thickness vibrator is formulated. Although the formulation can be applied to the piezoelectric ceramic thickness vibrator in which thermal energy is coupled with mechanical and electrical energy, only conduction heat transfer without consideration of other variables is simulated to evaluate the accuracy and the validity of the method. Comparison of the bond graph simulation results with the analytical solutions of simple cases shows a good match. The approach developed in this paper is also applicable, as a bond

graph modeling method for a continuous thermal solid system, to a general three-dimensional heat conduction problem.

It remains to use the results obtained here in combination with mechanical and electrical effects to develop a bond graph model (and description) for a piezoelectric body. This is the subject of the final paper in this series.[24]

ACKNOWLEDGMENTS

The authors wish to thank Dr. Joseph Beaman for his discussions. This work was supported by a National Science Foundation Faculty Award for Women in Science and Engineering.

[1] W. Moon and I. J. Busch-Vishniac, ''Finite element equivalent bond graph modeling with application to the piezoelectric thickness vibrator,'' J. Acoust. Soc. Am. **93**, 3496–3506 (1993).
[2] W. P. Mason, *Physical Acoustics: Volume I* (Academic, New York, 1964).
[3] W. Moon and I. J. Busch-Vishniac, ''Modeling of piezoelectric ceramic vibrators including thermal effects: Part I. Thermodynamic property considerations,'' J. Acoust. Soc. Am. **98**, 403–412 (1995).
[4] W. Moon and I. J. Busch-Vishniac, ''Modeling of piezoelectric ceramic vibrators including thermal effects: Part II. Derivation of partial differential equations,'' J. Acoust. Soc. Am. **98**, 413–421 (1995).
[5] H. Allik and T. Hughes, ''Finite Element Methods for Piezoelectric Vibration,'' Int. J. Num. Meth. Eng. **2**, 151–157 (1970).
[6] H. M. Paynter, *Analysis and Design of Engineering Systems* (MIT, Cambridge, 1961).
[7] A. M. Bos and P. C. Breedveld, ''1985 Bond Graph Bibliography Update,'' J. Franklin Inst. **319(1/2)**, 269–286 (1985).
[8] D. C. Karnopp, D. L. Margolis, and R. C. Rosenberg, *System Dynamics: A Unified Approach* (Wiley, New York, 1990).
[9] E. P. Fahrenthold and J. D. Wargo, ''Vector Bond Graph Analysis of Mechanical Systems,'' ASME Trans. J. Dynam. Sys. Meas. Control **113**, 345–353 (1991).
[10] L. S. Bonderson, ''Vector Bond Graphs Applied to One-Dimensional Distributed Systems,'' ASME Trans. J. Dynam. Sys. Meas. Control **97**, 75–82 (1975).
[11] L. S. Bonderson, ''System Properties of One-Dimensional Distributed Systems,'' ASME Trans. J. Dynam. Sys. Meas. Control **99**, 85–90 (1977).
[12] M. E. Ingrim and G. Y. Masada, ''The Extended Bond Graph Notation,'' Trans. ASME J. Dynam. Sys. Meas. Control **113**, 113–117 (1991).
[13] M. E. Ingrim and G. Y. Masada, ''Extended Bond Graph Reticulation of the Mixed Boundary Value Problem in Finite Hyperelasticity,'' J. Franklin Inst. **328**, 753–764 (1991).
[14] E. P. Fahrenthold and A. Wu, ''Bond Graph Modeling of Continuous Solids in Finite Strain Elastic-Plastic Deformation,'' ASME Trans. J. Dynam. Sys. Meas. Control **110**, 284–287 (1988).
[15] M. E. Ingrim, G. Y. Masada, and J. J. Beaman, ''Bond Graph Representation of Thermomechanical Processes in One-Dimensional Thermoelastic Continua,'' in *Automated Modeling for Design*, ASME Winter Annual Meeting Symposium on Automated Modeling for Design, 27 Nov.–2 Dec. 1988 (ASME, New York, 1988), Vol. 8, pp. 1–8.
[16] J. T. Oden, *Applied Functional Analysis* (Prentice-Hall, Englewood Cliffs, NJ, 1979).
[17] J. T. Royden, *Real Analysis* (Prentice-Hall, Englewood Cliffs, NJ, 1979).
[18] K. Bathe, *Finite Element Procedures in Engineering Analysis* (Prentice-Hall, New Jersey, 1982).
[19] T. Hughes, *The Finite Element Method* (Prentice-Hall, Englewood Cliffs, NJ, 1987).
[20] H. B. Callen, *Thermodynamics: An Introduction to the Physical Theories of Equilibrium Thermostatics and Irreversible Thermodynamics* (Wiley, New York, 1960).
[21] G. J. Wylen and R. E. Sonntag, *Fundamentals of Classical Thermodynamics* (Wiley, New York, 1976), 2nd ed.
[22] J. P. Holman, *Heat Transfer* (McGraw-Hill, New York, 1986), 6th ed., pp. 131–133.
[23] F. P. Incropera and D. P. De Witt, *Fundamentals of Heat and Mass Transfer* (Wiley, New York, 1981), 2nd ed.
[24] W. Moon and I. J. Busch-Vishniac, ''Modeling of piezoelectric ceramic vibrators including thermal effects: Part IV. Development and experimental evaluation of a bond graph model of the thickness vibrator,'' J. Acoust. Soc. Am. **101**, 1408–1429 (1997).

Modeling of piezoelectric ceramic vibrators including thermal effects. Part IV. Development and experimental evaluation of a bond graph model of the thickness vibrator

Won-kyu Moon and Ilene J. Busch-Vishniac
Department of Mechanical Engineering, The University of Texas at Austin, Austin, Texas 78712

(Received 29 December 1995; accepted for publication 26 September 1996)

This article develops a model of the piezoelectric ceramic vibrator which includes thermal energy exchange on an equal footing with the electrical and mechanical energy. By use of an isentropically linear model for the material and the bond graph models for a piezoelectric thickness vibrator and heat conduction previously developed by the authors, a thermodynamically complete model is developed. For a simple case, the predicted results from the developed model are compared with the results from experiments. Predictions are found to compare very favorably with these measurements. © *1997 Acoustical Society of America.* [S0001-4966(97)02102-4]

PACS numbers: 43.38.Ar, 43.38.Fx [SLE]

INTRODUCTION

Prediction of the response of a system can be completed only if a solution technique for the state equations is known. Although it is desirable to construct a correct, detailed model, in many cases it is crucial to find a less-accurate but easily solvable model. In the process of modeling a piezoelectric vibrator including thermal effects, a set of partial differential equations is derived in Ref. 1 using the material property model proposed in Ref. 2. Although partial differential equations for piezoelectric ceramic vibrators can precisely describe the response of a piezoelectric body including thermal effects, their insolvability makes them nearly meaningless for practical uses such as design of transducers. For example, the equations for the thickness vibrator, one of the simplest cases, cannot be solved analytically except for a few, very simple, boundary conditions. Numerical solutions to the partial differential equations are available. However, numerical solutions do not provide a qualitative overview of system characteristics since they are restricted to one case per one calculation. As indicated in Ref. 3, bond graphs can provide some physical meaning to one of the most popular numerical solution techniques, the finite element method, as well as an overview of the system dynamics. Due to its graphical representability, a bond graph model for a system provides another advantage in integration of one system with another.[4]

In order to develop a model for the thickness vibrator including thermal effects, the results in the previous parts of this paper must be integrated. The isentropically linear material property model is used as a material property description because it is believed to be the closest to the conditions of the vibrator.[2] Then the bond graph models for electromechanical and for thermal energy balances presented in Refs. 1 and 3 are integrated into one complete model. The derived state equations can be simulated by numerical integration techniques in the time domain. However, numerical solutions to the state equations have limitations. First, since the rate of change of a thermal variable is so much slower than the electrical or mechanical variables, it is practically impossible to obtain useful numerical results which show the effects of changes in a thermal variable. Hence, before direct numerical integration techniques are applied, an approximation is necessary to investigate the effects of a thermal variable from the derived equations. Since the simplest model is a good choice for the beginning of a new approach, in any case, the two-node bond graph model is considered here. Since the two-node bond graph model can predict the response of the thickness vibrator with greater accuracy if a minor modification is made, a modified two-node bond graph model is presented and used in investigating the response of a real thickness vibrator which is influenced by a thermo-electro-mechanical coupling.

A dimensional analysis is useful in the approximation of differential equations because it provides necessary information for distinguishing dominant terms from trivial ones. We derive the dimensionless equations from the state equations of the modified two-node bond graph model to identify trivial terms in the derived dimensionless equations. Then, a typical case of the thickness vibrator is considered for experimental evaluation of the developed model because the corresponding mode shape of a real piezoelectric thin disc (or plate) is shown to be different from the mode shape assumed in the thickness vibrator model used here.[5,6] The response of the selected vibrator to a voltage excitation, which varies with temperature, is calculated by use of the developed model and measured in the experiments. In calculating the response, we use approximate equations which can describe the effects of thermal variations on the mechanical and electrical variables. The results from those approximate equations are compared with the data from experiments.

Thermal effects typically are not very important for a piezoelectric vibrator used as an acoustic sensor because the thermal variable is maintained almost constant by the environment. However, in the case of a high power drive of a piezoelectric actuator, since internal dissipation can cause the thermal variable of a piezoelectric body to vary, the mechanical and electrical responses can change as well. Then, this sophisticated model including thermal effects can permit *a priori* design for that kind of device, while considering

thermal effects, instead of *a posteriori* thermal compensation.

I. BOND GRAPH MODEL FOR THE PIEZOELECTRIC CERAMIC VIBRATOR

In this section, the methods for the bond graph formulation without thermal effects for a piezoelectric body are briefly presented. This brief review is a three-dimensional formulation of the finite element equivalent bond graph approach developed earlier.[3] This approach is integrated with the method for a bond graph model of a thermal system developed in Moon and Busch-Vishniac.[7]

There is a well-established unified approach for both mechanical and electrical responses of a system: Hamilton's principle (or least action principle). Hamilton's principle plays a key role in developing state equations from a bond graph model for the piezoelectric thickness vibrator in which thermal effects are not considered.[4,8] If thermal effects are neglected, the potential and the kinetic energy for a piezoelectric body are expressed as follows:

$$\Pi = \int\int\int_{\mathscr{V}} \pi(\mathbf{S}(t,\vec{\mathbf{x}}),\mathbf{D}(t,\vec{\mathbf{x}}))\,d\mathscr{V}, \tag{1}$$

$$\mathscr{T} = \int\int\int_{\mathscr{V}} \gamma\left(\frac{\partial\vec{\mathbf{v}}}{\partial t}\right) d\mathscr{V}, \tag{2}$$

where $\mathbf{S}$, $\mathbf{D}$, $\vec{\mathbf{v}}$, $\mathscr{V}$, t, Π, π, $\mathscr{T}$, and γ are strain, electric flux density, displacement vector, the volume of an arbitrary piezoelectric body, time, potential energy of the system, potential energy density, kinetic energy of the system, and kinetic energy density, respectively. The Lagrangian $\mathscr{L}$ of a system is defined as

$$\mathscr{L} = \mathscr{T} - \Pi. \tag{3}$$

The Hamilton's principle states that

$$\delta\int_{t_1}^{t_2} \mathscr{L}\,dt = 0, \tag{4}$$

where δ refers to the variation of a functional.

Now, as proposed in Ref. 3 assume that $\vec{\mathbf{K}}(\vec{\mathbf{x}},t)$, a vector potential function for electric flux density $\mathbf{D}$, and $\vec{\mathbf{v}}(\vec{\mathbf{x}},t)$ can be expressed as follows:[7]

$$\vec{\mathbf{v}}(\vec{\mathbf{x}},t) = \sum_{j=1}^{3}\left(\sum_{n=1}^{N} v_j^{(n)}(t) f_n(\vec{\mathbf{x}})\right)\hat{\imath}_j, \tag{5}$$

$$\vec{\mathbf{K}}(\vec{\mathbf{x}},t) = \sum_{j=1}^{3}\left(\sum_{n=1}^{N} K_j^{(n)}(t) f_n(\vec{\mathbf{x}})\right)\hat{\imath}_j, \tag{6}$$

where $f_n(\vec{\mathbf{x}})$s are appropriately defined basis functions. By use of the relations between $\mathbf{S}$, $\mathbf{D}$, $\vec{\mathbf{v}}$, and $\vec{\mathbf{K}}$, potential energy Π and kinetic energy $\mathscr{T}$ can be expressed as functions of $\{v_j^{(n)}\}$, $\{\dot{v}_j^{(n)}\}$, and $\{K_j^{(n)}\}$ after performing the volumetric integration in Eqs. (1) and (2):

$$\Pi = \Pi(\{v_j^{(n)}(t)\},\{K_j^{(n)}(t)\}), \tag{7}$$

$$\mathscr{T} = \mathscr{T}(\{\dot{v}_j^{(n)}(t)\}). \tag{8}$$

Hence, the Hamilton's principle is reduced to the following form:

$$\delta\int_{t_1}^{t_2} \mathscr{L}(\{\dot{v}_j^{(n)}(t)\},\{v_j^{(n)}\},\{K_j^{(n)}(t)\})dt = 0. \tag{9}$$

This is identical to the Hamilton principle for a discrete system, which produces Lagrange equations.

Since in the case of the thickness vibrator the vector potential can be reduced to a scalar quantity which is proportional to the charge in the conducting plate,[1] Eq. (9) becomes

$$\delta\int_{t_1}^{t_2} \mathscr{L}(\{\dot{v}_3^{(n)}\},\{v_3^{(n)}\},q)dt = 0. \tag{10}$$

Since the Hamilton principle does not have any thermodynamic constraints, it is reasonable to say that the Hamilton principle is valid for any kind of thermodynamic process if heat transfer is considered properly. It is well known that if a dynamic process is thermodynamically reversible and *isothermal* (or constant temperature), the Helmholtz free energy is identical to the potential energy (if potential energy due to gravity is neglected) since its derivatives with respect to displacement variables are generalized forces. Moreover, if a dynamic process is thermodynamically reversible and *isentropic* (or constant entropy), the internal energy is identical to the potential energy (again neglecting gravitational potential energy). Hence, in the case of a system with temperature-dependent mechanical and electrical characteristics such as piezoelectric ceramic vibrators, Lagrange equations can be applied in such a way that the independent thermal variable is constant no matter what it is, temperature or entropy. For example, if entropy is chosen as an independent thermal variable, Lagrange equations are applied to a dynamic process using internal energy as potential energy of the system.

II. A BOND GRAPH MODEL FOR THE THICKNESS VIBRATOR

It is more convenient to develop a bond graph model if entropy density is used as an independent thermodynamic state variable in the description of the thermodynamic property of a material.[5] As considered in the previous section, we can apply Lagrange equations to the piezoelectric thickness vibrator using the internal energy as the potential energy of the vibrator if entropy density is chosen as the independent thermal state variable. From this point, since we will deal with the thickness vibrator only, the subscripts used to indicate the direction are omitted. For example, v_3, x_3, and D_3 are replaced by v, x, and D, respectively.

Let θ and σ be temperature and entropy density per unit volume, respectively. In order to derive the bond graph model, the following are assumed:

$$v(t,x) = \sum_{n=1}^{N} v^{(n)}(t) f_n(x), \tag{11}$$

$$\sigma(t,x) = \sum_{n=1}^{N} \sigma^{(n)}(t) f_n(x), \tag{12}$$

$$q(t) = \mathscr{A}_0 D(t), \tag{13}$$

where

$$f_n(x)=\begin{cases}\dfrac{x-x^{(n-1)}}{x^{(n)}-x^{(n-1)}}, & \text{if } x^{(n-1)}\leqslant x\leqslant x^{(n)},\\ \dfrac{x-x^{(n+1)}}{x^{(n)}-x^{(n+1)}}, & \text{if } x^{(n)}\leqslant x\leqslant x^{(n+1)},\\ 0 \quad \text{otherwise,}\end{cases} \tag{14}$$

and $x^{(n)}$ denotes the nth node so that $a=x^{(1)}<x^{(2)}<\cdots<x^{(N)}=b$. Note that

$$\sigma^{(n)}(t)=\sigma(t,x^{(n)}), \tag{15}$$

$$v^{(n)}(t)=v(t,x^{(n)}), \tag{16}$$

i.e., $\sigma^{(n)}(t)$ and $v^{(n)}(t)$ are entropy density and displacement at the nth nodes, respectively. We define derivatives of $f_n(x)$ as follows:

$$f_n'(x)=\begin{cases}\dfrac{1}{x^{(n)}-x^{(n-1)}}, & \text{if } x^{(n-1)}<x<x^{(n)},\\ \dfrac{1}{x^{(n)}-x^{(n+1)}}, & \text{if } x^{(n)}<x<x^{(n+1)},\\ \dfrac{1}{(2-\delta_{1(n-1)})(x^{(n)}-x^{(n-1)})}, & \text{if } x=x^{(n-1)},\\ \dfrac{1-\delta_{1n}}{(2-\delta_{Nn})(x^{(n)}-x^{(n-1)})}+\dfrac{1-\delta_{Nn}}{(2-\delta_{1n})(x^{(n)}-x^{(n+1)})}, & \text{if } x=x^{(n)},\\ \dfrac{1}{(2-\delta_{N(n+1)})(x^{(n)}-x^{(n+1)})}, & \text{if } x=x^{(n+1)},\\ 0 \quad \text{otherwise,}\end{cases} \tag{17}$$

$$f_n''(x)=\frac{\delta(x-x^{(n-1)})}{x^{(n)}-x^{(n-1)}}+\frac{\delta(x-x^{(n+1)})}{x^{(n)}-x^{(n+1)}} -\left(\frac{1}{x^{(n)}-x^{(n-1)}}+\frac{1}{x^{(n)}-x^{(n+1)}}\right)\delta(x-x^{(n)}), \tag{18}$$

where $\delta(\cdot)$ and δ_{ij} represent the Dirac delta function and the Kronecker delta, respectively. Figures 1 and 2 show the $f_n(x)$'s, $f_n'(x)$'s, and $f_n''(x)$'s, respectively, if there are four nodes. The $f_n(x)$'s are the whole domain representations of linear shape functions in the finite element method.[9]

Since

$$S_3=\frac{\partial v}{\partial x}=\sum_{n=1}^{N} v^{(n)}(t)f_n'(x),$$

the internal energy density u can be considered as follows:

$$u=u(\mathbf{S},\mathbf{D},\sigma)=u(\{v^{(n)}(t)\},q(t),\{\sigma^{(n)}(t)\},\{f_n(x)\},\{f_n'(x)\}),$$

where the assumptions of the thickness vibrator are applied. By integration over the whole domain, the internal energy of the thickness vibrator is obtained:

$$\mathscr{U}=\int\int\int_{\mathscr{V}} u\, d\mathscr{V} =\mathscr{A}_0\int_a^b u(\{v^{(n)}(t)\},q(t),\{\sigma^{(n)}(t)\},\{f_n(x)\},\{f_n'(x)\})dx =\mathscr{U}(\{v^{(n)}(t)\},q(t),\{\sigma^{(n)}(t)\}). \tag{19}$$

The kinetic energy is

$$\mathscr{T}=\int\int\int_{\mathscr{V}}\rho\gamma\, d\mathscr{V}=\mathscr{A}_0\int_a^b \frac{1}{2}\rho\left(\frac{\partial v}{\partial t}\right)^2 dx =\mathscr{T}(\{\dot{v}^{(n)}(t)\},\{f_n(x)\}), \tag{20}$$

where ρ is the mass density of the material.

Now assume that thermodynamic state constitutive relations are known in the following form:

$$\theta=\theta(\sigma,S_3,D_3)=\theta\left(\sigma,\frac{\partial v}{\partial x},\frac{q}{\mathscr{A}_0}\right). \tag{21}$$

With Eqs. (11)–(13) and (19), Eq. (21) can be expressed as a function of $\{v^{(n)}(t)\}$, $q(t)$, $\{\sigma^{(n)}(t)\}$, $\{f_n(x)\}$, and $\{f_n'(x)\}$. Since Eqs. (11)–(13) and (19) are approximate expressions and we desire a finite number of discrete state variables to describe the whole system, it is sufficient to define only a finite number of temperature variables as presented in Ref. 7. First, set

$$\theta=\sum_{n=1}^{N}\theta^{(n)}(t)f_n(x) \tag{22}$$

so that

$$\theta^{(n)}(t)=\theta(t,x^{(n)}). \tag{23}$$

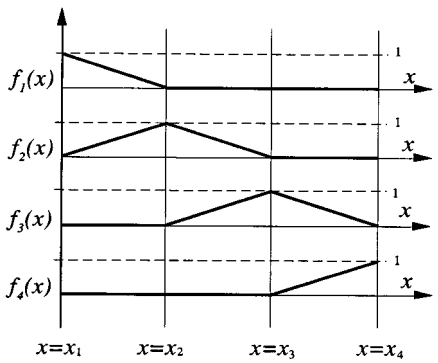

FIG. 1. $f_n(x)$ for $n=1,2,3,4$ ($N=4$).

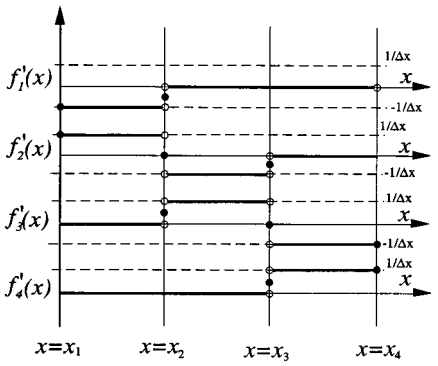

FIG. 2. $f_n'(x)$ for $n=1,2,3,4$ ($N=4$).

Then, applying thermodynamic state constitutive relations, Eq. (21), to the thermodynamic states at the nodes yields

$$\theta^{(n)}(t)=\theta(\sigma^{(n)}(t),v_x^{(n)}(t),q/\mathscr{A}_0), \tag{24}$$

where

$$\begin{aligned} v_x^{(n)}(t)=\left.\frac{\partial v}{\partial x}\right|_{x=x^{(n)}} &= \sum_{n=1}^{N} v^{(n)}(t) f_n'(x) \\ &= \frac{1}{2}\left[(1-\delta_{1n}+\delta_{Nn})\,\frac{v^{(n)}(t)-v^{(n-1)}(t)}{x^{(n)}-x^{(n-1)}}\right. \\ &\quad \left.+(1+\delta_{1n}-\delta_{Nn})\,\frac{v^{(n+1)}(t)-v^{(n)}(t)}{x^{(n+1)}-x^{(n)}}\right]. \end{aligned} \tag{25}$$

Now apply the Lagrange equations to the thickness vibrator. The Lagrangian has the following form:

$$\begin{aligned} \mathscr{L} &= \mathscr{L}(\{\dot v^{(n)}(t)\},\{v^{(n)}(t)\},q(t),\{\sigma^{(n)}(t)\}) \\ &= \mathscr{T}(\{\dot v^{(n)}(t)\})-\mathscr{U}(\{v^{(n)}(t)\},q(t),\{\sigma^{(n)}(t)\}). \end{aligned} \tag{26}$$

Lagrange's equations for an isentropic process give the following:

$$\frac{d}{dt}\left(\frac{\partial \mathscr{L}}{\partial \dot v^{(n)}}\right)-\frac{\partial \mathscr{L}}{\partial v^{(n)}}=F_n, \tag{27}$$

$$\frac{d}{dt}\left(\frac{\partial \mathscr{L}}{\partial \dot q}\right)-\frac{\partial \mathscr{L}}{\partial q}=\varepsilon, \tag{28}$$

where the F_ns are equivalent nodal forces due to nonconservative forces or loads, and ε is the voltage between the conductor plates.

As in usual energy approaches, we determine the F_n due to nonconservative forces, such as those associated with internal friction, by calculating the virtual work done, W. In the case of internal friction,

$$\begin{aligned} \delta W^{(I)}=\sum_{n=1}^{N} F_n \delta v^{(n)} &= \int\int\int_{\mathscr{V}}\left[\sum_{i=1}^{6}(-T_i^{(I)})\,\delta S_i\right] d\mathscr{V} \\ &= -\mathscr{A}_0\int_a^b T_3^{(I)}\delta S_3\,dx \\ &= \sum_{n=1}^{N}\left[-\mathscr{A}_0\int_a^b T_3^{(I)} f_n'(x)\,dx\right] dv^{(n)}, \end{aligned} \tag{29}$$

where the superscript (I) represents irreversibility and $T_i^{(I)}$ is stress due to irreversible effects. Here F_n is recognized from the above as

$$F_n=-\mathscr{A}_0\int_a^b T_3^{(I)} f_n'(x)\,dx. \tag{30}$$

The same procedure can be applied to calculation of the voltage drop due to internal loss in the body:

$$\begin{aligned} \delta W^{(I)}=\epsilon^{(I)}\delta q &= -\int\int\int_{\mathscr{V}}\left[\sum_{k=1}^{3} E_k^{(I)}\delta D_k\right] d\mathscr{V} \\ &= -\mathscr{A}_0\int_a^b E_3^{(I)}\delta D_3\,dx=-\int_a^b (E_3^{(I)}\,dx)\,\delta q. \end{aligned} \tag{31}$$

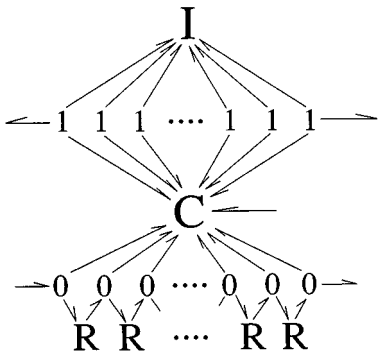

FIG. 3. Bond graph for the thickness vibrator including thermal effects.

Hence, $\epsilon^{(I)}=-\int_a^b E_3^{(I)}\,dx$.

By considering the time derivative of the internal energy

$$\frac{d\mathscr{U}}{dt}=\sum_{n=1}^{N}\frac{\partial \mathscr{U}}{\partial v^{(n)}}\,\dot v^{(n)}+\frac{\partial \mathscr{U}}{\partial q}\,\dot q+\sum_{n=1}^{N}\frac{\partial \mathscr{U}}{\partial \sigma^{(n)}}\,\dot\sigma^{(n)}, \tag{32}$$

a bond graph model of the thickness vibrator without internal dissipation can be drawn as shown in Fig. 3. The following state equations can be derived as given in Ref. 7:

$$\begin{aligned} &\sum_{m=1}^{N}\dot\sigma^{(m)}(t)\left(\mathscr{A}_0\int_a^b f_m(x)f_n(x)dx\right) \\ &=\frac{\kappa\mathscr{A}_0}{\theta^{(n)}(t)}\left[-(1-\delta_{1n})\,\frac{\theta^{(n)}(t)-\theta^{(n-1)}(t)}{x^{(n)}-x^{(n-1)}}\right. \\ &\quad\left.+(1-\delta_{Nn})\,\frac{\theta^{(n+1)}(t)-\theta^{(n)}(t)}{x^{(n+1)}-x^{(n)}}\right]-\mathscr{A}_0\left(-\delta_{1n}\,\frac{Q_1}{\theta^{(1)}}\right. \\ &\quad\left.+\delta_{Nn}\,\frac{Q_N}{\theta^{(N)}}\right)+\mathscr{A}_0\int_a^b\frac{\dot r(t,x)f_n(x)}{\sum_{k=1}^{N}\theta^{(k)}(t)f_k(x)}\,dx, \end{aligned} \tag{33}$$

where $n=1,2,\ldots,N$,

$$\dot r=\dot r_0+\sum_{i=1}^{6} T_i^{(I)}\dot S_i+\sum_{k=1}^{3} E_k^{(I)}\dot D_k, \tag{34}$$

and δ_{ij}, κ, $\dot r_0$, Q_1, and Q_N are the Kronecker delta, thermal conductivity, internal heat generation excluding mechanical or electrical dissipation, and boundary heat flux at nodes 1 and N, respectively.

A flow variable corresponding to a temperature at a node is defined as follows:

$$\dot{\bar\sigma}_n(t)=\sum_{m=1}^{N}\dot\sigma^{(m)}(t)\left(\mathscr{A}_0\int_a^b f_m(x)f_n(x)dx\right). \tag{35}$$

By solving Eq. (33) simultaneously with the Lagrange's equations, Eqs. (27) and (28), the responses of the thickness vibrator can be predicted.

In order to calculate responses of a real thickness vibrator, the thermodynamic property of a given material is needed. The available data on the thermodynamic property of PZT4 can be explained by two material property models. Since the isentropically linear model describes the known data better,[2] the state equations for the isentropically linear piezoelectric thickness vibrator are developed in the next section.

III. THE STATE EQUATIONS FOR ISENTROPICALLY LINEAR PIEZOELECTRIC THICKNESS VIBRATOR

Most of the available data about material constants of a piezoelectric ceramic are obtained through dynamic measurement procedures and are expressed in terms of temperature as a thermal-independent variable. The temperature data, however, may be the equilibrium temperature θ_0 rather than the instantaneous temperature θ. Hence, strain $\mathbf{S}$, electric flux density $\mathbf{D}$, and equilibrium temperature θ_0 may be the most convenient choice of all possible sets of independent thermodynamic state variables for a piezoelectric body. In bond graph formulations described in the previous section, the equilibrium temperature θ_0 can be substituted into Eq. (33) by use of the relations between entropy density σ and equilibrium temperature θ_0 at $\mathbf{S}=\mathbf{0}$ and $\mathbf{D}=\mathbf{0}$. Since $\theta_0=\theta_0(\sigma)$, the entropy density σ can be expressed as a function of θ_0 on the condition that the relation between θ_0 and σ be invertible. By use of a given thermodynamic relation the derived equations for thermal variables can be rewritten in terms of the equilibrium temperature.

The thermodynamic constitutive relations are the first thing necessary for derivation of the state equations for a thickness vibrator bond graph model. The internal energy density expression for piezoelectric ceramics is useful to obtain the constitutive relations. The following are true in the case of piezoelectric ceramic vibrators:[1]

$$\alpha_1(\sigma)=\alpha_2(\sigma), \tag{36}$$

$$\alpha_4(\sigma)=\alpha_5(\sigma)=\alpha_6(\sigma)=0, \tag{37}$$

$$\lambda_1(\sigma)=\lambda_2(\sigma)=0, \tag{38}$$

where α_i and λ_i are the thermal expansion and pyroelectric coefficients in the i direction, respectively. Substituting these into the internal energy expression derived in Ref. 2 and taking advantage of the one-dimensional condition of the thickness vibrator, the following expression for the internal energy may be derived:[1]

$$\begin{aligned} u=u_0(\sigma)&+\tfrac{1}{2}c_{33}^D(\sigma)[S_3-\alpha_3(\sigma)]^2-h_{33}(\sigma)[S_3\\ &-\alpha_3(\sigma)][D_3-\lambda_3(\sigma)]+\tfrac{1}{2}\beta_{33}^S(\sigma)[D_3-\lambda_3(\sigma)]^2\\ &+c_{12}^D(\sigma)[\alpha_1(\sigma)]^2-2c_{13}^D(\sigma)\alpha_1(\sigma)[S_3-\alpha_3(\sigma)]\\ &+2h_{31}(\sigma)\alpha_1(\sigma)[D_3-\lambda_3(\sigma)], \end{aligned} \tag{39}$$

where

$$u_0'(\sigma)=\theta_0, \tag{40}$$

and c_{33}^D, h_{33}, and β_{33}^S are the elastic stiffness, the piezoelectric constants, and the dielectric impermeability constants, respectively. As discussed previously,[1] we can neglect the last three terms in Eq. (39) because they come from the constraints on the sides of the thickness vibrator which are not representative of the real situation. Moreover, since the effects of thermal expansion and pyroelectricity are small,[2] and since a real thickness vibrator reacts statically free,[1] the internal energy expression can be simplified to

$$u=u_0(\sigma)+\tfrac{1}{2}c_{33}^D(\sigma)S_3^2-h_{33}(\sigma)S_3D_3+\tfrac{1}{2}\beta_{33}^S(\sigma)D_3^2. \tag{41}$$

From Eq. (41) we have the following constitutive relations:

$$T_3^{(R)}=c_{33}^D(\sigma)S_3-h_{33}(\sigma)D_3, \tag{42}$$

$$E_3^{(R)}=-h_{33}(\sigma)S_3+\beta_{33}^S(\sigma)D_3, \tag{43}$$

$$\theta=\theta_0(\sigma)+\theta_1(\sigma,\mathbf{S},\mathbf{D}), \tag{44}$$

where $T_3^{(R)}$ and $E_3^{(R)}$ are reversible stress and electric field intensity in the three-direction and

$$\theta_1(\sigma,\mathbf{S},\mathbf{D})=\tfrac{1}{2}c_{33}^{D\prime}(\sigma)(S_3)^2-h_{33}'(\sigma)S_3D_3+\tfrac{1}{2}\beta_{33}^{S\prime}(\sigma)(D_3)^2 \tag{45}$$

is the variation in temperature due to the mechanical and electrical coupling.

Equation (45) can be transformed into the following form provided that the relation between θ_0 and σ is invertible:[1,2]

$$\theta=\theta_0+\theta_1(\sigma(\theta_0),\mathbf{S},\mathbf{D}). \tag{46}$$

Since

$$\dot{\sigma}^{(m)}(t)=\left.\frac{d\sigma}{d\theta_0}\right|_m\dot{\theta}_0^{(m)}(t), \tag{47}$$

where

$$\left.\frac{d\sigma}{d\theta_0}\right|_m=\left.\frac{d\sigma}{d\theta_0}\right|_{\theta_0=\theta_0^{(m)}}, \tag{48}$$

Eq. (33) reduces to the following form:

$$\begin{aligned} &\sum_{m=1}^{N}\dot{\theta}_0^{(m)}(t)\left.\frac{d\sigma}{d\theta_0}\right|_m\left(\mathscr{A}_0\int_a^b f_m(x)f_n(x)dx\right)\\ &=\frac{\kappa\mathscr{A}_0}{\theta^{(n)}(t)}\left[-(1-\delta_{1n})\frac{\theta^{(n)}(t)-\theta^{(n-1)}(t)}{x^{(n)}-x^{(n-1)}}\right.\\ &\quad\left.+(1-\delta_{Nn})\frac{\theta^{(n+1)}(t)-\theta^{(n)}(t)}{x^{(n+1)}-x^{(n)}}\right]-\mathscr{A}_0\left(-\delta_{1n}\frac{Q_1}{\theta^{(1)}}\right.\\ &\quad\left.+\delta_{Nn}\frac{Q_N}{\theta^{(N)}}\right)+\mathscr{A}_0\int_a^b\frac{\dot{r}(t,x)f_n(x)}{\Sigma_{k=1}^N\theta^{(k)}(t)f_k(x)}\,dx, \end{aligned} \tag{49}$$

where

$$\theta^{(n)}=\theta_0^{(n)}+\theta_1(\theta_0^{(n)},v_x^{(n)},D),\quad n=1,2,\ldots,N, \tag{50}$$

$$\begin{aligned} \theta_1(\theta_0,\mathbf{S},\mathbf{D})=&\left(1\Big/\frac{d\sigma}{d\theta_0}\right)\left[\frac{1}{2}c_{33}^{D\prime}(\theta_0)(S_3)^2\right.\\ &\left.-h_{33}'(\theta_0)S_3D_3+\frac{1}{2}\beta_{33}^{S\prime}(\theta_0)(D_3)^2\right]. \end{aligned} \tag{51}$$

The heat generation in a piezoelectric body is due to energy dissipation from internal friction and electric field loss, unless some device is used to generate heat inside the vibrator. Then,

$$\dot{r}=T_3^{(I)}\dot{S}_3+E_3^{(I)}\dot{D}_3$$

$$=\psi\left(\frac{\partial v}{\partial x}\right)\left(\frac{\partial^2 v}{\partial t\,\partial x}\right)^2+\nu\left(\frac{q}{\mathscr{A}_0}\right)\frac{\dot{q}^2}{\mathscr{A}_0^2}$$

$$=\psi\left(\sum_{k=1}^{N} v^{(k)}(t)f_k'(x)\right)\left\{\sum_{m=1}^{N}\dot{v}^{(m)}(t)f_m'(x)\right\}$$

$$\times\left\{\sum_{n=1}^{N}\dot{v}^{(n)}(t)f_n'(x)\right\}+\nu\left(\frac{q}{\mathscr{A}_0}\right)\frac{\dot{q}^2}{\mathscr{A}_0^2}, \tag{52}$$

where ψ is the internal mechanical damping coefficient, ν is the dielectric loss coefficient of a piezoelectric material, and the irreversible effects are modeled as follows:

$$T_3^{(I)}=\psi\dot{S}_3, \tag{53}$$

$$E_3^{(I)}=\nu\dot{D}_3. \tag{54}$$

Since ψ is a function of strain $\partial v/\partial x$, it is dependent on the space variable x. Noting that $\partial v/\partial x$ is approximated as a series of step functions in the bond graph model, it is more convenient to set

$$\psi=\sum_{k=1}^{N-1}\psi^{(k)}g_k(x), \tag{55}$$

where

$$g_k(x)=\begin{cases}1, & \text{if } x^{(n)}<x<x^{(n+1)},\\ 0, & \text{otherwise.}\end{cases} \tag{56}$$

Using Eq. (55), the first term on the right-hand side of Eq. (52) can be calculated easily:

$$T_3^{(I)}\dot{S}_3=\psi^{(n)}\left[\frac{\dot{v}^{(n+1)}-\dot{v}^{(n)}}{x^{(n+1)}-x^{(n)}}\right]^2,\quad x^{(n)}\leqslant x<x^{(n+1)}, \tag{57}$$

where $n=1,2,\ldots,N-1$ and

$$\psi^{(n)}=\psi\left(\left.\frac{\partial v}{\partial x}\right|_{x=[x^{(n)}+x^{(n+1)}]/2}\right)=\psi\left(\frac{v^{(n+1)}-v^{(n)}}{x^{(n+1)}-x^{(n)}}\right),$$

$$n=1,2,\ldots,N-1. \tag{58}$$

The contribution of mechanical dissipation to the heat generation term in the energy balance equation (49) is calculated as follows:

$$\int_a^b\frac{T_3^{(I)}\dot{S}_3}{\Sigma_{k=1}^{N}\theta^{(k)}(t)f_k(x)}f_n(x)dx=(1-\delta_{1n})\int_{x^{(n-1)}}^{x^{(n)}}\frac{\psi^{(n-1)}\left(\frac{\dot{v}^{(n)}-\dot{v}^{(n-1)}}{x^{(n)}-x^{(n-1)}}\right)^2\frac{x-x^{(n-1)}}{x^{(n)}-x^{(n-1)}}}{\theta^{(n-1)}+(\theta^{(n)}-\theta^{(n-1)})\frac{x-x^{(n-1)}}{x^{(n)}-x^{(n-1)}}}dx$$

$$+(1-\delta_{Nn})\int_{x^{(n)}}^{x^{(n+1)}}\frac{\psi^{(n)}\left(\frac{\dot{v}^{(n+1)}-\dot{v}^{(n)}}{x^{(n+1)}-x^{(n)}}\right)^2\left\{1-\frac{x-x^{(n)}}{x^{(n+1)}-x^{(n)}}\right\}}{\theta^{(n)}+(\theta^{(n+1)}-\theta^{(n)})\frac{x-x^{(n)}}{x^{(n+1)}-x^{(n)}}}d\zeta$$

$$=\frac{1-\delta_{1n}}{x^{(n)}-x^{(n-1)}}\int_0^1\frac{\psi^{(n-1)}(\dot{v}^{(n)}-\dot{v}^{(n-1)})^2\zeta}{\theta^{(n-1)}+(\theta^{(n)}-\theta^{(n-1)})\zeta}dx$$

$$+\frac{1-\delta_{Nn}}{x^{(n+1)}-x^{(n)}}\int_0^1\frac{\psi^{(n)}(\dot{v}^{(n+1)}-\dot{v}^{(n)})^2(1-\zeta)}{\theta^{(n)}+(\theta^{(n+1)}-\theta^{(n)})\zeta}d\zeta$$

$$=\frac{(1-\delta_{1n})\psi^{(n-1)}}{x^{(n)}-x^{(n-1)}}\left(\frac{\dot{v}^{(n)}-\dot{v}^{(n-1)}}{\theta^{(n)}-\theta^{(n-1)}}\right)^2\left[\theta^{(n)}-\theta^{(n-1)}\left(1+\ln\frac{\theta^{(n)}}{\theta^{(n-1)}}\right)\right]$$

$$+\frac{(1-\delta_{Nn})\psi^{(n)}}{x^{(n+1)}-x^{(n)}}\left(\frac{\dot{v}^{(n+1)}-\dot{v}^{(n)}}{\theta^{(n+1)}-\theta^{(n)}}\right)^2\left[\theta^{(n)}-\theta^{(n+1)}\left(1-\ln\frac{\theta^{(n+1)}}{\theta^{(n)}}\right)\right]. \tag{59}$$

The entropy generation due to electrical dissipation is relatively simple to calculate:

$$\int_a^b \frac{E_3^{(I)}\dot{D}_3}{\theta} f_n(x)dx = \nu\left(\frac{q}{\mathscr{A}_0}\right)\frac{\dot{q}^2}{\mathscr{A}_0^2}\left[\int_{x^{(n-1)}}^{x^{(n)}} \frac{(x-x^{(n-1)})/(x^{(n)}-x^{(n-1)})}{\theta^{(n-1)}+(\theta^{(n)}-\theta^{(n-1)})[(x-x^{(n-1)})/(x^{(n)}-x^{(n-1)})]}\,dx\right.$$
$$\left.+\int_{x^{(n)}}^{x^{(n+1)}} \frac{1-(x-x^{(n)})/(x^{(n+1)}-x^{(n)})}{\theta^{(n)}+(\theta^{(n+1)}-\theta^{(n)})[(x-x^{(n)})/(x^{(n+1)}-x^{(n)})]}\,dx\right]$$
$$=\nu\left(\frac{q}{\mathscr{A}_0}\right)\frac{\dot{q}^2}{\mathscr{A}_0^2}\left[(1-\delta_{1n})\int_0^1 \frac{(x^{(n)}-x^{(n-1)})\zeta d\zeta}{\theta^{(n-1)}+(\theta^{(n)}-\theta^{(n-1)})\zeta}+(1-\delta_{Nn})\int_0^1 \frac{(x^{(n+1)}-x^{(n)})(1-\zeta)d\zeta}{\theta^{(n)}+(\theta^{(n+1)}-\theta^{(n)})\zeta}\right]$$
$$=\nu\left(\frac{q}{\mathscr{A}_0}\right)\frac{\dot{q}^2}{\mathscr{A}_0^2}\left\{(1-\delta_{1n})\frac{(x^{(n)}-x^{(n-1)})[\theta^{(n)}-\theta^{(n-1)}(1+\ln(\theta^{(n)}/\theta^{(n-1)}))]}{(\theta^{(n)}-\theta^{(n-1)})^2}\right.$$
$$\left.+(1-\delta_{Nn})\frac{(x^{(n+1)}-x^{(n)})[\theta^{(n)}-\theta^{(n+1)}(1-\ln(\theta^{(n+1)}/\theta^{(n)}))]}{(\theta^{(n+1)}-\theta^{(n)})^2}\right\}. \tag{60}$$

Substituting Eqs. (59) and (60) into Eq. (49) we obtain

$$\sum_{m=1}^{N}\dot{\theta}_0^{(m)}(t)\left.\frac{d\sigma}{d\theta_0}\right|_m\left(\int_a^b f_m(x)f_n(x)dx\right)$$
$$=\frac{\kappa}{\theta^{(n)}(t)}\left[-(1-\delta_{1n})\frac{\theta^{(n)}(t)-\theta^{(n-1)}(t)}{x^{(n)}-x^{(n-1)}}+(1-\delta_{Nn})\frac{\theta^{(n+1)}(t)-\theta^{(n)}(t)}{x^{(n+1)}-x^{(n)}}\right]+\delta_{1n}\frac{Q_1}{\theta^{(1)}}-\delta_{Nn}\frac{Q_N}{\theta^{(N)}}$$
$$+(1-\delta_{1n})\left[\frac{\psi^{(n-1)}(\dot{v}^{(n)}-\dot{v}^{(n-1)})^2}{x^{(n)}-x^{(n-1)}}+\nu\frac{\dot{q}^2}{\mathscr{A}_0^2}(x^{(n)}-x^{(n-1)})\right]\frac{\theta^{(n)}-\theta^{(n-1)}(1+\ln(\theta^{(n)}/\theta^{(n-1)}))}{(\theta^{(n)}-\theta^{(n-1)})^2}$$
$$+(1-\delta_{Nn})\left[\frac{\psi^{(n)}(\dot{v}^{(n+1)}-\dot{v}^{(n)})^2}{x^{(n+1)}-x^{(n)}}+\nu\frac{\dot{q}^2}{\mathscr{A}_0^2}(x^{(n+1)}-x^{(n)})\right]\frac{\theta^{(n)}-\theta^{(n+1)}(1-\ln(\theta^{(n+1)}/\theta^{(n)}))}{(\theta^{(n+1)}-\theta^{(n)})^2}, \tag{61}$$

where

$$\nu=\nu\left(\frac{q}{\mathscr{A}_0}\right),$$
$$\psi^{(n)}=\psi\left(\frac{v^{(n+1)}-v^{(n)}}{x^{(n+1)}-x^{(n)}}\right),\quad n=1,2,\ldots,N-1,$$
$$\theta^{(n)}=\theta_0^{(n)}+\theta_1(\sigma(\theta_0^{(n)}),v_x^{(n)},D),\quad n=1,2,\ldots,N,$$

and $\theta_1(\theta_0^{(n)},v_x^{(n)},q/\mathscr{A}_0)$ is given in Eq. (51).

Now we build a complete set of Lagrange equations for the isentropically linear piezoelectric thickness vibrator. The first requirement is to calculate the potential energy of the system. Since entropy density is chosen as an independent thermodynamic variable, internal energy density may be used for calculating the potential energy of the system. Equation (41) can be used for the internal energy density expression of the piezoelectric ceramic thickness vibrator in derivation of the bond graph model. As discussed before, σ is represented as a function of the equilibrium temperature θ_0 provided that the relation between σ and θ_0 is invertible. Therefore, Eq. (41) can be transformed into the following form:

$$u=u_0(\theta_0)+\tfrac{1}{2}c_{33}^D(\theta_0)(S_3)^2-h_{33}(\theta_0)S_3D_3+\tfrac{1}{2}\beta_{33}^S(\theta_0)(D_3)^2. \tag{62}$$

Since c_{33}^D, h_{33}, and β_{33}^S are functions of θ_0 which is approximated in the bond graph model, it is more convenient to set

$$c_{33}^D(\theta_0)=\sum_{k=1}^{N}c_{33}^{(k)}f_k(x), \tag{63}$$

$$h_{33}(\theta_0)=\sum_{k=1}^{N}h_{33}^{(k)}f_k(x), \tag{64}$$

$$\beta_{33}^D(\theta_0)=\sum_{k=1}^{N}\beta_{33}^{(k)}f_k(x), \tag{65}$$

where

$$c_{33}^{(k)}=c_{33}^D(\theta_0^{(k)}), \tag{66}$$
$$h_{33}^{(k)}=h_{33}(\theta_0^{(k)}), \tag{67}$$
$$\beta_{33}^{(k)}=\beta_{33}^S(\theta_0^{(k)}). \tag{68}$$

The potential energy

$$\Pi=\mathscr{U}=\mathscr{A}_0\int_a^b u(\sigma(\theta_0),\mathbf{S},\mathbf{D})dx$$
$$=\mathscr{A}_0\int_a^b u_0(\theta_0)dx+\frac{1}{2}\sum_{m=1}^{N}\sum_{n=1}^{N}v^{(m)}(t)v^{(n)}(t)$$
$$\times\left\{\mathscr{A}_0\int_a^b\left[\sum_{k=1}^{N}c_{33}^{(k)}f_k(x)\right]f_m'(x)f_n'(x)dx\right\}$$
$$-\sum_{n=1}^{N}v^{(n)}(t)q(t)\left\{\int_a^b\left[\sum_{k=1}^{N}h_{33}^{(k)}f_k(x)\right]f_n'(x)dx\right\}$$
$$+\frac{[q(t)]^2}{\mathscr{A}_0}\int_a^b\left[\sum_{k=1}^{N}\beta_{33}^{(k)}f_k\right]dx. \tag{69}$$

Let

$$k_{mn}=\mathscr{A}_0\int_a^b\left[\sum_{k=1}^{N} c_{33}^{(k)}f_k(x)\right]f_m'(x)f_n'(x)dx$$

$$=\frac{\mathscr{A}_0}{2}\left[(1-\delta_{1n})(\delta_{mn}-\delta_{m(n-1)})\frac{c_{33}^{(n)}+c_{33}^{(n-1)}}{x^{(n)}-x^{(n-1)}}\right.$$

$$\left.+(1-\delta_{Nn})(\delta_{mn}-\delta_{m(n+1)})\frac{c_{33}^{(n+1)}+c_{33}^{(n)}}{x^{(n+1)}-x^{(n)}}\right], \tag{70}$$

$$H_n=\int_a^b\left[\sum_{k=1}^{N} h_{33}^{(k)}f_k(x)\right]f_n'(x)dx$$

$$=\tfrac{1}{2}[(1-\delta_{1n})(h_{33}^{(n-1)}+h_{33}^{(n)})-(1-\delta_{Nn})(h_{33}^{(n)}+h_{33}^{(n+1)})], \tag{71}$$

$$\frac{1}{\mathscr{C}}=\frac{1}{\mathscr{A}_0}\int_a^b\left[\sum_{k=1}^{N}\beta_{33}^{(k)}f_k\right]dx$$

$$=\frac{1}{2\mathscr{A}_0}\sum_{n=1}^{N-1}(x^{(n+1)}-x^{(n)})(\beta_{33}^{(n+1)}+\beta_{33}^{(n)}). \tag{72}$$

Then,

$$\mathscr{U}=\mathscr{A}_0\int_a^b u_0(\theta_0)dx+\frac{1}{2}\sum_{m=1}^{N}\sum_{n=1}^{N}k_{mn}v^{(m)}v^{(n)}$$

$$-\sum_{n=1}^{N}H_nv^{(n)}q+\frac{q^2}{2\mathscr{C}}. \tag{73}$$

It is noticed that in Eq. (73) the first term represents the thermal energy while the second, the third, and the fourth are contributions from mechanical, piezoelectric, and electrical effects, respectively.

The kinetic energy is

$$\mathscr{T}=\frac{1}{2}\sum_{m=1}^{N}\sum_{n=1}^{N}M_{mn}\dot{v}^{(m)}\dot{v}^{(n)}, \tag{74}$$

where

$$M_{mn}=\mathscr{A}_0\int_a^b\rho f_m(x)f_n(x)dx$$

$$=\tfrac{1}{6}\rho\mathscr{A}_0[(1-\delta_{1n})(2\delta_{mn}+\delta_{m(n-1)})(x^{(n)}-x^{(n-1)})$$

$$+(1-\delta_{Nn})(2\delta_{mn}+\delta_{m(n+1)})(x^{(n+1)}-x^{(n)})]. \tag{75}$$

Calculation of nonconservative forces $F_m^{(I)}$ and $\epsilon^{(I)}$ due to dissipation gives

$$F_m^{(I)}=-\mathscr{A}_0\int_a^b T_3^{(I)}f_m'(x)dx=-\sum_{n=1}^{N}B_{mn}\dot{v}^{(m)}, \tag{76}$$

$$\epsilon^{(I)}=-\int_a^b E_3^{(I)}dx=-\frac{b-a}{\mathscr{A}_0}\,\nu\left(\frac{q}{\mathscr{A}_0}\right)\dot{q}, \tag{77}$$

where

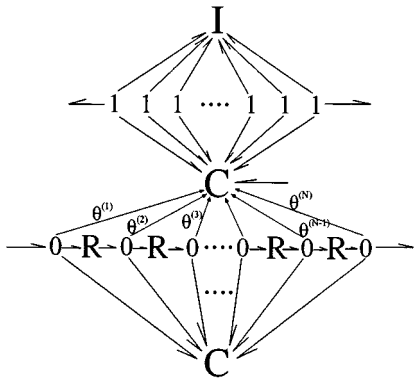

FIG. 4. Bond graph for an approximate model of the thickness vibrator with temperature modulation.

$$B_{mn}=(1-\delta_{1n})(\delta_{mn}-\delta_{m(n-1)})\frac{\mathscr{A}_0\psi^{(n-1)}}{x^{(n)}-x^{(n-1)}}$$

$$+(1-\delta_{Nn})(\delta_{mn}-\delta_{m(n+1)})\frac{\mathscr{A}_0\psi^{(n)}}{x^{(n+1)}-x^{(n)}}. \tag{78}$$

Application of Lagrange's equation provides the following state equations:

$$\sum_{n=1}^{N}M_{mn}\ddot{v}^{(n)}+\sum_{n=1}^{N}k_{mn}v^{(n)}-H_mq=F_m, \tag{79}$$

$$-\sum_{n=1}^{N}H_nv^{(n)}+\frac{q}{\mathscr{C}}=\epsilon, \tag{80}$$

where

$$F_m=F_m^{(I)}+\delta_{1m}F_1^{(e)}+\delta_{Nm}F_N^{(e)}, \quad \epsilon=\epsilon^{(I)}+\epsilon^{(e)},$$

and $\epsilon^{(e)}$, $F_1^{(e)}$, and $F_N^{(e)}$ are the applied external voltage, and the boundary external force at nodes 1 and N, respectively.

Equations (61), (79), and (80) are a complete set of state equations. As presented in Ref. 1 an approximate model can be obtained by replacing $\theta^{(n)}$ in Eq. (61) with $\theta_0^{(n)}$ under appropriate assumptions. In this mathematical approximation, thermodynamic coupling between the thermal and other state variables is ignored. In terms of bond graphs, the approximate model can be represented using a temperature-modulated multiport **C** element instead of a **C** element with thermal power bonds. The distinction between thermal power bonds and thermal modulation relates to energetic content. A thermal power bond shows the flow of thermal power, while thermal modulation indicates that something about the constitutive relations of the element depend on information about the thermal state, although thermal power is not flowing. Figure 4 shows the bond graph for a temperature modulated system without internal dissipation. It is interesting to note that Fig. 4 is not a *proper* bond graph model because it has been shown that a modulated energy storage element results in violation of the energy conservation principle.[4,8] In other words, the bond graph model resulting from mathematical approximation to the complete state

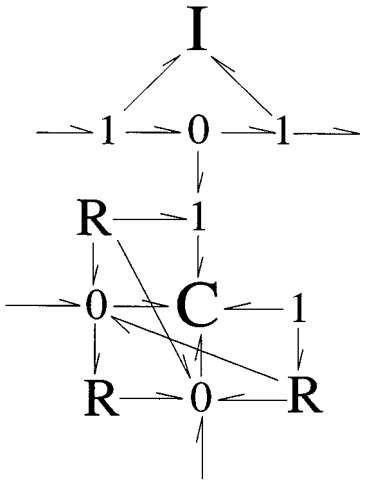

FIG. 5. Two-node bond graph model of a thickness vibrator.

equations is not realizable physically. Nonetheless, the approximate model is more convenient and numerically accurate enough for calculations.

IV. TWO-NODE BOND GRAPH MODEL FOR THE THICKNESS VIBRATOR

The simplest bond graph model from the above approach is one with two nodes. The corresponding bond graph model is shown in Fig. 5. Using Eqs. (61), (79), and (80), the following state equations for the two-node bond graph model can be easily derived:

$$\frac{\mathscr{A}_0 l}{6}\begin{bmatrix} 2\left.\frac{d\sigma}{d\theta_0}\right|^{(1)} & \left.\frac{d\sigma}{d\theta_0}\right|^{(1)} \\ \left.\frac{d\sigma}{d\theta_0}\right|^{(2)} & 2\left.\frac{d\sigma}{d\theta_0}\right|^{(2)} \end{bmatrix}\begin{Bmatrix}\dot\theta_0^{(1)}\\ \dot\theta_0^{(2)}\end{Bmatrix}$$

$$=\frac{\kappa\mathscr{A}_0}{l}\begin{Bmatrix}(\theta^{(2)}-\theta^{(1)})/\theta^{(1)}\\ -(\theta^{(2)}-\theta^{(1)})/\theta^{(2)}\end{Bmatrix}+\mathscr{A}_0\begin{Bmatrix}Q_1/\theta^{(1)}\\ -Q_2/\theta^{(2)}\end{Bmatrix}$$

$$+\mathscr{A}_0\frac{(\psi^{(1)}/l)(\dot v^{(2)}-\dot v^{(1)})^2+(\nu l/\mathscr{A}_0^2)\dot q^2}{(\theta^{(2)}-\theta^{(1)})^2}$$

$$\times\begin{Bmatrix}\theta^{(1)}-\theta^{(2)}\left(1-\ln\frac{\theta^{(2)}}{\theta^{(1)}}\right)\\ \theta^{(2)}-\theta^{(1)}\left(1+\ln\frac{\theta^{(2)}}{\theta^{(1)}}\right)\end{Bmatrix}, \tag{81}$$

$$\frac{\rho l\mathscr{A}_0}{6}\begin{bmatrix}2&1\\1&2\end{bmatrix}\begin{Bmatrix}\ddot v^{(1)}\\ \ddot v^{(2)}\end{Bmatrix}$$

$$=-\frac{\psi^{(1)}\mathscr{A}_0}{l}\begin{bmatrix}1&-1\\-1&1\end{bmatrix}\begin{Bmatrix}\dot v^{(1)}\\ \dot v^{(2)}\end{Bmatrix}-\frac{(c_{33}^{(1)}+c_{33}^{(2)})\mathscr{A}_0}{2l}$$

$$\times\begin{bmatrix}1&-1\\-1&1\end{bmatrix}\begin{Bmatrix}v^{(1)}\\ v^{(2)}\end{Bmatrix}+\frac{h_{33}^{(1)}+h_{33}^{(2)}}{2}\begin{Bmatrix}-1\\1\end{Bmatrix}q+\begin{Bmatrix}F_1^{(e)}\\ F_2^{(2)}\end{Bmatrix}, \tag{82}$$

$$\frac{\nu l}{\mathscr{A}_0}\dot q=\frac{h_{33}^{(1)}+h_{33}^{(2)}}{2}(v^{(2)}-v^{(1)})-\frac{(\beta_{33}^{(1)}+\beta_{33}^{(2)})}{2\mathscr{A}_0}q+\epsilon^{(e)}. \tag{83}$$

The two-node bond graph model presented above includes a rigid body motion (translation) as one mode of vibration. Since a translation mode is not of interest in most cases, we consider a special case when the boundary condition is both mechanically and thermally symmetric. This boundary condition implies

$$-F_1^{(e)}=F_2^{(e)}=F_0, \tag{84}$$

$$\theta_0^{(1)}=\theta_0^{(2)}=\theta_0, \tag{85}$$

$$\theta^{(1)}=\theta^{(2)}=\theta, \tag{86}$$

$$Q_1=-Q_2=Q_0, \tag{87}$$

$$c_{33}^{(1)}=c_{33}^{(2)}, \tag{88}$$

$$h_{33}^{(1)}=h_{33}^{(2)}, \tag{89}$$

$$\beta_{33}^{(1)}=\beta_{33}^{(2)}, \tag{90}$$

where

$$\theta=\theta_0+\left(1\Big/\frac{d\sigma}{d\theta_0}\right)\left[\frac{1}{2}c_{33}^{D\prime}(\theta_0)\frac{(v^{(2)}-v^{(1)})^2}{l^2}\right.$$

$$\left.-h_{33}'(\theta_0)\frac{v^{(2)}-v^{(1)}}{l}+\frac{1}{2}\beta_{33}^{S\prime}(\theta_0)\frac{q^2}{\mathscr{A}_0}\right]. \tag{91}$$

By use of the L'Hospital theorem the following can be easily shown:

$$\lim_{\theta^{(2)}\to\theta^{(1)}}\frac{\theta^{(1)}-\theta^{(2)}[1-\ln(\theta^{(2)}/\theta^{(1)})]}{(\theta^{(2)}-\theta^{(1)})^2}=\frac{1}{2\theta^{(1)}} \tag{92}$$

$$=\frac{1}{2\theta}, \tag{93}$$

$$\lim_{\theta^{(1)}\to\theta^{(2)}}\frac{\theta^{(2)}-\theta^{(1)}[1+\ln(\theta^{(2)}/\theta^{(1)})]}{(\theta^{(2)}-\theta^{(1)})^2}=\frac{1}{2\theta^{(2)}} \tag{94}$$

$$=\frac{1}{2\theta}. \tag{95}$$

Then, Eq. (81) reduces to

$$l\frac{d\sigma}{d\theta_0}\dot\theta_0=\frac{1}{\theta}\left[2Q_0+\frac{\psi^{(1)}}{l}(\dot v^{(2)}-\dot v^{(1)})^2+\frac{\nu l}{\mathscr{A}_0^2}\dot q^2\right], \tag{96}$$

where $l=b-a$.

Now the state equations for mechanical variables can be separated into two parts: one for rigid translation and the other for deformation. From modal analysis of Eq. (82) the following two equations can be calculated:

$$\ddot\xi_1=\frac{F_1^{(e)}+F_2^{(e)}}{\rho\mathscr{A}_0 l}=0, \tag{97}$$

$$\ddot\xi_2+\frac{12\psi^{(1)}}{\rho l^2}\dot\xi_2+\frac{12c_{33}^D(\theta_0)}{\rho l^2}\xi_2=\frac{2\sqrt{3}[h_{33}(\theta_0)q+F_0]}{\rho\mathscr{A}_0 l}, \tag{98}$$

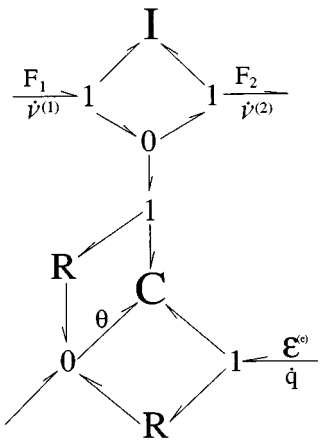

FIG. 6. Two-node bond graph model of a thickness vibrator with symmetrical boundaries.

where

$$\xi_1=\frac{v^{(1)}+v^{(2)}}{2}, \tag{99}$$

$$\xi_2=\frac{v^{(2)}-v^{(1)}}{2\sqrt{3}}. \tag{100}$$

Clearly, Eq. (97) describes the rigid translation, and Eq. (98) the deformation of the piezoelectric body. The equation for electrical variables, Eq. (83), is rewritten in terms of ξ_2:

$$\epsilon^{(e)}-\frac{\nu l}{\mathscr{A}_0}\,\dot{q}=-2\sqrt{3}h_{33}(\theta_0)\xi_2+\frac{\beta_{33}^S(\theta_0)l}{\mathscr{A}_0}\,q. \tag{101}$$

Using ξ_2, Eq. (96) can be rewritten as follows:

$$\theta\,\frac{d\sigma}{d\theta_0}\,\dot{\theta}_0=\frac{2Q_0}{l}+\frac{12\psi^{(1)}}{l^2}\,(\xi_2)^2+\frac{\nu}{\mathscr{A}_0^2}\,\dot{q}^2. \tag{102}$$

The bond graph for the two-node bond graph with symmetric boundaries is shown is Fig. 6. The mechanical and the electrical internal dissipation are represented by the R-element in that bond graph.

V. MODIFIED TWO-NODE BOND GRAPH MODEL

The response of the thickness vibrator including thermal effects can be predicted using Eqs. (61), (79), and (80) after the number of nodes is determined depending on the frequency range of interest and the necessary accuracy. Since the thermal effects on the stiffness, piezoelectric, and electric coefficients in Eqs. (79) and (80) yield nonlinear equations, without appropriate approximation, the only known solution techniques for those equations are numerical. It is practically impossible to simulate these equations for a sufficient period of time to observe thermal effects upon the mechanical or electrical responses because the change rate of the thermal variable is very much slower than that of the mechanical variable. Further, the simulations become significantly more cumbersome and time consuming as the number of nodes in the model increases. Thus there is a strong motivation to use as simple a model (fewest nodes) as possible. However, this desire must be balanced against the quest for accurate modeling. We choose to balance these conflicting needs by using a very simple two-node model, and modifying it to improve its accuracy for dynamic prediction. The two-node model is justified for most cases since the temperature distribution is almost uniform throughout the thickness direction if the thickness vibrator is small, and the frequency of interest is below the first antiresonance frequency. Note that in this and subsequent uses of the terms resonance and antiresonance, we refer to the entire system rather than the purely mechanical or electrical resonance and antiresonance.

It has been observed previously[3] that the antiresonance frequency from the two-node bond graph model derived in the previous section is about 10% greater than the first antiresonance frequency of the continuum model for the thickness vibrator. The accuracy of the antiresonance frequency of the two-node bond graph model can be improved by modifying the mass matrix [the first term in Eq. (82)]. Since the stiffness matrix [the third term in Eq. (82)] and the piezoelectric matrix [the fourth term Eq. (82)] are directly related to the static response, only the mass matrix can be modified without changing the static response of the model. Although the exact value of the antiresonance frequency can be calculated from the equations with the modified mass matrix, the value of the resonance frequency calculated from the model derived by modifying the mass matrix is about 3% different from that from the continuum model in the case of a PZT4 thin disc. By introducing a scaling factor for the piezoelectric coefficient, α_f, and adjusting it to fit the analytical resonance frequency, the dynamic accuracy can be improved but at the expense of accuracy in the static response. However, such an approach degrades the static response by less then 3%. Hence, the modification of the piezoelectric constant may be useful when a thickness vibrator is operated at resonance frequency. The following are the state equations for the mechanical and electrical variables which are modified from Eqs. (82) and (83) for a resonator so that they provide exact values of the first resonance and antiresonance frequencies:

$$\begin{aligned}\frac{\rho l\mathscr{A}_0}{4\pi^2}&\begin{bmatrix}\pi^2+4\pi^2-4\\ \pi^2-4\pi^2+4\end{bmatrix}\begin{Bmatrix}\ddot{v}^{(1)}\\ \ddot{v}^{(2)}\end{Bmatrix}\\ &=-\frac{\psi^{(1)}\mathscr{A}_0}{l}\begin{bmatrix}1&-1\\ -1&1\end{bmatrix}\begin{Bmatrix}\dot{v}^{(1)}\\ \dot{v}^{(2)}\end{Bmatrix}-\frac{(c_{33}^{(1)}+c_{33}^{(2)})\mathscr{A}_0}{2l}\\ &\quad\times\begin{bmatrix}1&-1\\ -1&1\end{bmatrix}\begin{Bmatrix}v^{(1)}\\ v^{(2)}\end{Bmatrix}+\alpha_f\,\frac{h_{33}^{(1)}+h_{33}^{(2)}}{2}\\ &\quad\times\begin{Bmatrix}-1\\ 1\end{Bmatrix}q+\begin{Bmatrix}F_1^{(e)}\\ F_2^{(2)}\end{Bmatrix},\end{aligned} \tag{103}$$

$$\frac{\nu l}{\mathscr{A}_0}\,\dot{q}=\alpha_f\,\frac{h_{33}^{(1)}+h_{33}^{(2)}}{2}\,(v^{(2)}-v^{(1)})-\frac{(\beta_{33}^{(1)}+\beta_{33}^{(2)})}{2\mathscr{A}_0}\,q+\epsilon^{(e)}, \tag{104}$$

where π is the circular constant and

$$(\alpha_f)^2=\frac{1}{k_t^2}-\frac{4\mu}{\pi^2k_t^2}, \tag{105}$$

$$k_t^2=\frac{(h_{33})^2}{c_{33}^D\beta_{33}^S}, \tag{106}$$

and μ is the solution of the following:

$$\frac{\mu}{\tan\mu}=k_t^2. \tag{107}$$

Considering the case where the boundary condition is both mechanically and thermally symmetric, as in the previous section, the following can be derived from Eqs. (103) and (104):

$$\ddot{\xi}_1=\frac{F_1^{(e)}+F_2^{(e)}}{\rho\mathscr{A}_0 l}=0, \tag{108}$$

$$\ddot{\xi}_2+\frac{\pi^2\psi^{(1)}}{\rho l^2}\dot{\xi}_2+\frac{\pi^2 c_{33}^D(\theta_0)}{\rho l^2}\xi_2=\frac{\pi[\alpha_f h_{33}(\theta_0)q+F_0]}{\rho\mathscr{A}_0 l}, \tag{109}$$

$$\epsilon^{(e)}-\frac{\nu l}{\mathscr{A}_0}\dot{q}=-\pi\alpha_f h_{33}(\theta_0)\xi_2+\frac{\beta_{33}^S(\theta_0)l}{\mathscr{A}_0}q, \tag{110}$$

$$\theta\frac{d\sigma}{d\theta_0}\dot{\theta}_0=\frac{2Q_0}{l}+\frac{\pi^2\psi^{(1)}}{l^2}(\xi_2)^2+\frac{\nu}{\mathscr{A}_0^2}\dot{q}^2, \tag{111}$$

where

$$\xi_1=\frac{v^{(1)}+v^{(2)}}{2}, \tag{112}$$

$$\xi_2=\frac{v^{(2)}-v^{(1)}}{\pi}. \tag{113}$$

Equation (96) can be used as the state equation for the thermal variable for this modified two-node bond graph model. Although various kinds of boundary conditions can be applied to Eq. (103), symmetrical boundaries are assumed from this point and this case is used as an example.

VI. DERIVATION OF DIMENSIONLESS EQUATIONS

The two-node bond graph models are useful for quantitative as well as qualitative analysis of the thickness vibrator. The closed form solution of them, however, cannot be found easily because of coupling between the thermal, mechanical, and electrical variables. Dimensional analyses may help to derive approximate equations for which a closed form solution can be obtained.

A dimensional analysis begins with definitions of scaling constants of each dimension. In order to make Eqs. (96), (109), and (110) nondimensional, we need to define scaling constants for displacement, voltage, charge, equilibrium temperature, entropy density, and time. In the following notation, $\hat{(\cdot)}$ is used for the scaling constant of variable $(\cdot)$ and $\tilde{(\cdot)}$ for the dimensionless parameter corresponding to the variable $(\cdot)$. For example, $\hat{v}$ and $\tilde{\xi}_2$ are the scaling factor for displacement and the dimensionless parameter corresponding to ξ_2, respectively. One exception to this rule for notation is the dimensionless time parameter which will be represented by τ. Now define scaling constants as follows:

$$\hat{v}=\frac{\hat{\epsilon}^{(e)}}{2\zeta_a\alpha_f\pi\hat{h}_{33}}, \tag{114}$$

$$\hat{q}=\frac{\mathscr{A}_0\hat{\epsilon}^{(e)}}{2\zeta_a\hat{\beta}_{33}^S l}, \tag{115}$$

$$\hat{\theta}_0=\theta_{0m}-\theta_\infty, \tag{116}$$

$$\hat{t}=\frac{1}{\pi}\sqrt{\frac{\rho l^2}{\hat{c}_{33}^D}}, \tag{117}$$

$$\hat{F}_0=\frac{\rho\mathscr{A}_0 l\hat{v}}{\hat{t}^2}, \tag{118}$$

$$\hat{c}_{33}^D=c_{33}^D|_{\theta_0=\theta_\infty}, \tag{119}$$

$$\hat{h}_{33}=h_{33}|_{\theta_0=\theta_\infty}, \tag{120}$$

$$\hat{\beta}_{33}^S=\beta_{33}^S|_{\theta_0=\theta_\infty}, \tag{121}$$

$$\hat{\sigma}=\rho c_{p0}, \tag{122}$$

where θ_∞, θ_{0m}, and c_{p0} are the ambient equilibrium temperature, the maximum equilibrium temperature, and the heat capacity per unit mass, respectively. The damping effect scale factor, ζ_a, is defined such that at a given frequency

$$\sup|\tilde{\xi}_2|=\mathscr{O}(1), \tag{123}$$

$$\sup|\tilde{q}|=\mathscr{O}(1), \tag{124}$$

where ''sup'' stands for the supremum, or maximum, value. By use of the above constants the dimensionless parameters can be defined as follows:

$$\tilde{\xi}_2=\frac{\xi_2}{\hat{v}},\quad \tau=\frac{t}{\hat{t}},\quad \tilde{\theta}_0=\frac{\theta_0-\theta_\infty}{\hat{\theta}_0},\quad \tilde{\theta}=\frac{\theta-\theta_\infty}{\hat{\theta}_0},$$

$$\tilde{q}=\frac{q}{\hat{q}},\quad \tilde{\epsilon}^{(e)}=\frac{\epsilon^{(e)}}{\hat{\epsilon}^{(e)}},\quad \tilde{f}_0=\frac{F_0}{\hat{F}_0},\quad \tilde{c}_{33}^D=\frac{c_{33}^D}{\hat{c}_{33}^D},$$

$$\tilde{h}_{33}=\frac{h_{33}}{\hat{h}_{33}},\quad \tilde{\beta}_{33}^S=\frac{\beta_{33}^S}{\hat{\beta}_{33}^S},\quad \hat{k}_t=k_t|_{\theta_0=\theta_\infty},$$

$$\zeta_{am}=\frac{\psi^{(1)}}{2\hat{t}\hat{c}_{33}^D},\quad \zeta_{ae}=\frac{\nu_{33}}{2\hat{t}\hat{\beta}_{33}^S},\quad \zeta_{ac}=\frac{\pi}{4}\frac{Z_{\text{rad}}}{\sqrt{\rho\hat{c}_{33}^D}},$$

where α_f is calculated using $\hat{k}_t$ with Eqs. (105) and (107), and Z_{rad} is the equivalent acoustic wave radiation impedance per unit area of a disc. Applying the scale factors and dimensionless parameters to Eqs. (109)–(111), the following dimensionless equations can be derived:

$$\frac{d^2\tilde{\xi}_2}{d\tau^2}+2(\zeta_{am}+\zeta_{ac})\frac{d\tilde{\xi}_2}{d\tau}+\tilde{c}_{33}^D\tilde{\xi}_2=\alpha_f^2\hat{k}_t^2\tilde{h}_{33}\tilde{q}, \tag{125}$$

$$2\zeta_{ae}\frac{d\tilde{q}}{d\tau}+\tilde{\beta}_{33}^S\tilde{q}-\tilde{h}_{33}\tilde{\xi}_2=2\zeta_a\tilde{\epsilon}^{(e)}, \tag{126}$$

$$\left(\tilde{\theta}\frac{d\tilde{\sigma}}{d\tilde{\theta}_0}\right)\frac{d\tilde{\theta}_0}{d\tau}=\frac{2Q_0\hat{t}}{\rho c_{p0}l}+\frac{\hat{v}^2}{c_{p0}l\hat{t}^2}\left[2\zeta_{am}\left(\frac{d\tilde{\xi}_2}{d\tau}\right)^2+2\zeta_{ae}\alpha_f^2\hat{k}_t^2\left(\frac{d\tilde{q}}{d\tau}\right)^2\right]. \tag{127}$$

Since the derived dimensionless equations are coupled, they should be solved simultaneously. Hence, it is almost impossible to obtain exact solutions for them by analytical methods. Numerical simulation techniques can be used to determine responses of a piezoelectric vibrator. However, since in many cases the time rate of change of a thermal variable is very much slower than that of mechanical and electrical variables, it is often impossible to simulate responses of the vibrator for a long enough period for thermal variable changes to affect the other variables significantly. In these cases additional approximations are necessary.

Now assume that the dimensionless parameters are order of 1; i.e.,

$$\tilde{\xi}_2=\mathcal{O}(1), \tag{128}$$

$$\tilde{q}=\mathcal{O}(1), \tag{129}$$

$$\tilde{\theta}_0=\mathcal{O}(1), \tag{130}$$

$$\frac{d\tilde{\xi}_2}{d\tau}=\mathcal{O}(1), \tag{131}$$

$$\frac{d\tilde{q}}{d\tau}=\mathcal{O}(1). \tag{132}$$

From Eq. (127) it can be easily seen that

$$\sup\left|\frac{d\tilde{\theta}_0}{d\tau}\right|\ll 1 \tag{133}$$

if

$$\left|\frac{2\zeta_{\max}\hat{v}^2}{\hat{t}^2c_{p0}\hat{\theta}_0}\right|,\left|\frac{2Q_0\hat{t}}{\rho c_{p0}l}\right|\ll\left|\tilde{\theta}\frac{d\tilde{\theta}_0}{d\tau}\right|, \tag{134}$$

where

$$\zeta_{\max}=\max\{\zeta_{am},\zeta_{ae}\}. \tag{135}$$

While ρ, c_{p0}, l, and h_c are determined if the system is fixed, Q_0, $\hat{\theta}_0$, $\hat{v}$, and $\hat{t}$ are dependent on an input magnitude. If $\hat{\theta}_0$ is determined so that the mechanical and electrical material property constants vary considerably with that amount of temperature change, it cannot be affected by an input. The magnitude of time scale factor $\hat{t}$ is also defined so that the derivatives of $\tilde{\xi}_2$ and $\tilde{q}$ with respect to τ are $\mathcal{O}(1)$ in the case of an electrical or mechanical input. Only the magnitude of $\hat{v}$ is dependent on that of an electrical or a mechanical input. Since Q_0 can be controlled independently, the magnitudes of Q_0 and $\hat{v}$ can change the magnitude of $d\tilde{\theta}_0/d\tau$. However, since Q_0 can vary within a relatively small range, in most cases Eq. (133) holds. There are other terms that are much less than 1 in Eqs. (125)–(127): the terms with damping factors (ζ_{am}, ζ_{ae}, ζ_{ac}). If

$$\left|\frac{\hat{v}^2}{\hat{t}^2c_{p0}\hat{\theta}_0}\right|\ll 1, \tag{136}$$

$$\left|\frac{2Q_0\hat{t}}{\rho c_{p0}l}\right|\ll\mathcal{O}\left(\left|\frac{2\zeta_{\max}\hat{v}^2}{\hat{t}^2c_{p0}\hat{\theta}_0}\right|\right), \tag{137}$$

then we can neglect the terms with the time derivative of temperature in calculating mechanical and electrical responses of a vibrator. This approximation makes it possible to obtain a closed-form solution for some specific cases. In the next section we consider a voltage drive of a thickness vibrator for which numerical calculations and experiments are performed.

VII. A VOLTAGE DRIVE OF A THICKNESS VIBRATOR

In many cases a piezoelectric vibrator is excited by a voltage input because a voltage source is easy to make. Thermal variables can be controlled by the environment if the internal dissipation due to changes of mechanical and electrical variables is relatively small. Since in many cases the temperature of the environment does not change considerably, thermal effects are not important. However, in the case of a high power drive of a piezoelectric vibrator, the internal dissipation can be large enough to change the temperature of the vibrator so that changes in mechanical and electrical property constants affect the response of the vibrator considerably. In that case the model derived here may be useful to predict the response precisely.

In driving a piezoelectric vibrator electrically, the resonance frequency of the vibrator is a convenient input frequency for a high-power mechanical output. Consider a voltage drive at the fundamental resonance frequency of a PZT4 lead zirconate-titanate thickness vibrator with a symmetrical boundary condition. Let the normalized voltage input be described by

$$\tilde{\epsilon}^{(e)}=\sin(r\tau), \tag{138}$$

where r is a normalized angular frequency; i.e.,

$$r=\omega\hat{t}. \tag{139}$$

For simplicity, assume ρc_{p0} is constant. Since in Ref. 1 it is shown that

$$\rho c_{p0}=\theta_0\frac{d\sigma}{d\theta_0}\approx\theta\frac{d\sigma}{d\theta_0}, \tag{140}$$

we assume

$$\tilde{\theta}\frac{d\tilde{\sigma}}{d\tilde{\theta}_0}=1. \tag{141}$$

As in the previous section, assume Eqs. (134), (136), and (137) hold. Then the following equation can be derived by ignoring the terms with time derivatives of temperature $\tilde{\theta}_0$ in Eqs. (125) and (126):

$$2\zeta_{ae}\frac{d^3\tilde{\xi}_2}{d\tau^3}+[\tilde{\beta}^S_{33}+4\zeta_{ae}(\zeta_{am}+\zeta_{ac})]\frac{d^2\tilde{\xi}_2}{d\tau^2}+2[\tilde{\beta}^S_{33}(\zeta_{am}+\zeta_{ac})+\tilde{c}^D_{33}\zeta_{ae}]\frac{d\tilde{\xi}_2}{d\tau}+(\tilde{\beta}^S_{33}\tilde{c}^D_{33}-\alpha_f^2\hat{k}_t^2\tilde{h}^2_{33})\tilde{\xi}_2=2\zeta_a\alpha_f^2\hat{k}_t^2\tilde{h}_{33}\tilde{\epsilon}^{(e)}. \tag{142}$$

The displacement can be calculated by solving Eq. (142) as a linear ordinary differential equation with constant coefficients. Since the rate of change of the coefficient is assumed to be very small, the obtained solution should be a good approximation to the exact solution of Eq. (142), in which the coefficients of the differential equation vary slowly with time. The charge can be calculated using Eq. (126) in the same manner. Velocity and current are easily found by differentiating the displacement and the charge expressions.

Now consider the thermal variable response. Since transient effects are damped out very quickly relative to the rate of thermal variable change, only the steady state responses are important in the interaction between thermal and other variables. Using Eqs. (127) and (142), the following are obtained:

$$\tilde{\xi}_2=|X|\sin(r\tau+\phi_\xi), \tag{143}$$

$$\tilde{q}=|Q|\sin(r\tau+\phi_q), \tag{144}$$

where

$$X=\frac{2\zeta_a\alpha_f^2\hat{k}_t^2\tilde{h}_{33}}{R_r+jR_i}, \tag{145}$$

$$Q=\frac{2\zeta_a[\tilde{c}^D_{33}-r^2+j2r(\zeta_{am}+\zeta_{ac})]}{R_r+jR_i}, \tag{146}$$

$$\phi_\xi=\arg X=-\arctan\left(\frac{R_i}{R_r}\right), \tag{147}$$

$$\phi_q=\arg Q=\arctan\left[\frac{2r(\zeta_{am}+\zeta_{ac})}{\tilde{c}^D_{33}-r^2}\right]+\phi_\xi, \tag{148}$$

$$R_r=\tilde{\beta}^S_{33}\tilde{c}^D_{33}-\alpha_f^2\hat{k}_t^2\tilde{h}^2_{33}-r^2[\tilde{\beta}^S_{33}+4\zeta_{ae}(\zeta_{am}+\zeta_{ac})], \tag{149}$$

$$R_i=2r[\tilde{\beta}^S_{33}(\zeta_{am}+\zeta_{ac})+(\tilde{c}^D_{33}-r^2)\zeta_{ae}]. \tag{150}$$

Substituting Eqs. (143) and (144) into Eq. (127), the following are obtained:

$$\left(\tilde{\theta}\frac{d\tilde{\sigma}}{d\tilde{\theta}_0}\right)\frac{d\tilde{\theta}_0}{d\tau}=-\frac{2Q_0\hat{t}}{\rho c_{p0}l}+\frac{\hat{v}^2}{c_{p0}l\hat{t}^2}r^2(\zeta_{am}|X|^2+\zeta_{ae}|Q|^2)+\frac{\hat{v}^2}{c_{p0}l\hat{t}^2}r^2[\zeta_{am}|X|^2\cos(2r\tau+2\phi_\xi)+\zeta_{ae}|Q|^2\cos(2r\tau+2\phi_q)]. \tag{151}$$

Since the last group of terms in Eq. (151) is oscillatory, they do not contribute to the long term average value of $\tilde{\theta}_0$. Their effects become negligible as $\tilde{\theta}_0$ increases due to the second group of terms on the right-hand side of Eq. (151). By neglecting the last group of terms and substituting Eq. (141) into Eq. (151), we have

$$\frac{d\tilde{\theta}_0}{d\tau}=-\frac{2Q_0\hat{t}}{\rho c_{p0}l}+\frac{\hat{v}^2}{c_{p0}l\hat{t}^2}r^2(\zeta_{am}|X|^2+\zeta_{ae}|Q|^2). \tag{152}$$

The time history of the temperature can be calculated using Eq. (152) in the case of a harmonic voltage drive. Since amplitudes and phase lags of displacement, velocity, charge, and current from the voltage input are described as functions of temperature $\tilde{\theta}_0$ in Eqs. (145), (146), (149), and (150), their time histories also can be obtained by using Eq. (152).

The modified two-node bond graph model derived here cannot predict the difference between the surface and the internal temperatures. If the thickness of a disc is small enough, there is only a slight difference between them. In most cases, the thickness of a thickness vibrator is very small because the ratio of the depth to the width of cross section is small. However, in other cases, the temperature difference can be sufficiently large that it may cause the model to be significantly inaccurate. For evaluating the temperature distribution inside a thickness vibrator the Biot number is a good guide.[10] In our model, the radial variance in temperature cannot be considered because of the basic assumption of uni-dimensionality of the model, although the temperature distribution is not uniform in the radial direction. Only a thickness direction conduction effect may be considered. Hence, the Biot number of the thickness vibrator is expressed as follows:

$$\mathrm{Bi}=\frac{h_c l}{\kappa}. \tag{153}$$

VIII. SIMULATION AND EXPERIMENT

The following PZT4 lead zirconate-titanate disk was used as a thickness vibrator for numerical calculation and experimental measurement of thermal variable effects upon mechanical and electrical responses:

$$\mathscr{A}_0=2.822\times10^{-3}\ \mathrm{m}^2, \tag{154}$$

$$l=5.004\times10^{-3}\ \mathrm{m}, \tag{155}$$

$$\rho=7500\ \mathrm{kg/m}^3, \tag{156}$$

$$\hat{c}^D_{33}=1.59\times10^{11}\ \mathrm{N/m}^2, \tag{157}$$

$$\hat{h}_{33}=2.68\times10^9\ \mathrm{V/m}, \tag{158}$$

$$\hat{\beta}^S_{33}=1.779\times10^8\ \mathrm{m/F}, \tag{159}$$

$$c_{p0}=420\ \mathrm{J/(kg\ ^\circ C)}. \tag{160}$$

From the above data, other scale constants can be easily calculated:

$$\hat{t}=3.459\times10^{-7}\ \mathrm{s}, \tag{161}$$

$$\hat{k}_t^2=0.2539. \tag{162}$$

Since a voltage input at the fundamental resonance frequency of the disc is applied in the simulation and experiment, we set

$$\alpha_f=0.9240. \tag{163}$$

Since the published data show that the material constants for PZT4 vary less than 10% from the nominal values with a 100 °C change of temperature, $\hat{\theta}_0$ is set to be 50 °C. Since the ambient temperature is 24 °C for the experiments done, let $\theta_\infty = 297$ K. Although the ambient medium may be water or a fluid whose characteristic acoustic impedance is close to that of water, if a piezoelectric vibrator is used as a sonar projector, let the ambient fluid be air for experimental convenience. In calculating the equivalent damping factor due to the acoustic wave in air, the formula for radiation impedance of a baffled circular piston can be used.[11] In our case, since the wave number times the cross-sectional area ($k\mathscr{A}_0$) is very large ($k\mathscr{A}_0 = 7405$), the radiation impedance is the characteristic impedance of air times the disc cross-sectional area. Hence,

$$\zeta_{ac} = 9.438 \times 10^{-6}.$$

Since a natural convection boundary is assumed in our example,

$$Q_0 = -h_c \tilde{\theta}_0. \tag{164}$$

The convection coefficient is calculated by applying the natural convection coefficient of a vertical plane to a circular shaped one:

$$h_c = 10.05 \ \text{W/(m}^2 \ \text{K)}. \tag{165}$$

The most important data for numerical simulation of a circular disk piezoelectric vibrator are the numerical values of the equivalent damping factor due to internal mechanical and electrical dissipation (ζ_{am}, ζ_{ae}) and the functional dependence of material constants ($c_{33}^D, h_{33}, \beta_{33}^S$) on temperature. The equivalent damping factors can be calculated from the available data for quality factors. The mechanical quality factor is known to vary with the amplitude of dynamic stress. For small stress amplitude the mechanical quality factor is known to be 500, and for large amplitude (about 2000 psi) it is 110. However, the internal damping effect is known to vary considerably from one specimen to another even if they are made by an identical manufacturing process. Hence, two extreme values are used for simulation: 8.85×10^{-4} and 4.023×10^{-3}. Since the ratios of ζ_{ac} to the smallest values of $\zeta_{\mathbf{am}}$ and ζ_{ae} are less than 1.1%, the effect of acoustic power consumption is negligibly smaller than that of power consumption due to mechanical or electrical internal dissipation. This is because the ambient medium is air. In the case of water, the acoustic power consumption can be larger than that due to internal dissipation.

Although accurate information about the functional dependence of the material constants ($c_{33}^D, h_{33}, \beta_{33}^S$) on temperature is most important, this data is not available. Since the functional dependence of g_{31} and ϵ_{33}^T are found in publications,[12] the values of the needed constants are calculated at several values of temperature by using the g_{31} and ϵ_{33}^T data and the theory of ferroelectrics. In ferroelectric theory, the temperature dependence of material constants is due to the variance of the spontaneous polarization in a piezoelectric ceramic vibrator, and the piezoelectric constants g_{31} and h_{33} are almost linearly dependent on the spontaneous polarization.[12] Hence, the relationship between the normalized values of g_{31} and θ_0 can be used for calculating that between h_{33} and θ_0. Even though a functional dependence of ϵ_{33}^T on the spontaneous polarization may be of different form from that of $1/\beta_{33}^S$, they both are dependent on the spontaneous polarization only, so the functional form of the normalized values of ϵ_{33}^T are used for calculating the needed data on β_{33}^S. Since temperature dependence of the material property is assumed to depend only on the variance of the spontaneous polarization with temperature, the stiffness coefficient c_{33}^D is assumed to be constant. Table I shows the numerical values of c_{33}^D, h_{33}, β_{33}^S which are used for the simulation.

TABLE I. Temperature dependence of material constants of PZT4.

θ_0 (K)	$c_{33}^D \times 10^{-10}$ N/m^2	$h_{33} \times 10^{-8}$ N/C	$\beta_{33}^S \times 10^{-8}$ m/F
273	15.9	28.14	1.791
293	15.9	27.08	1.781
297	15.9	26.80	1.779
313	15.9	26.28	1.773
333	15.9	25.39	1.721
353	15.9	24.30	1.688
373	15.9	23.53	1.626

Before proceeding to the simulation, we determine an appropriate value for the damping effect scale factor ζ_a at resonance frequency. Since the amplitudes of variables such as displacement can be different from one frequency to another, ζ_a can be determined only after the frequency of an input voltage is given. Substituting the fundamental resonance frequency $r = \sqrt{1-\alpha_f^2 \hat{k}_t^2}$ into Eqs. (145) and (146), the amplitudes of the displacement and the charge can be written as follows:

$$|X| = \frac{1}{\sqrt{1+4\zeta_{ae}^2 \left(\dfrac{\zeta_{am}+\zeta_{ac}}{\zeta_{am}+\zeta_{ac}+\alpha_f^2 \hat{k}_t^2 \zeta_{ae}} \right)^2 (1-\alpha_f^2 \hat{k}_t^2)}}, \tag{166}$$

$$|Q| = \frac{\sqrt{1+4(1-\alpha_f^2 \hat{k}_t^2)(\zeta_{am}+\zeta_{ac})^2/(\alpha_f^4 \hat{k}_t^4)}}{\sqrt{1+4\zeta_{ae}^2 \left(\dfrac{\zeta_{am}+\zeta_{ac}}{\zeta_{am}+\zeta_{ac}+\alpha_f^2 \hat{k}_t^2 \zeta_{ae}} \right)^2 (1-\alpha_f^2 \hat{k}_t^2)}}, \tag{167}$$

if we set

$$\zeta_a = (\zeta_{am}+\zeta_{ac}+\alpha_f^2 \hat{k}_t^2 \zeta_{ae}) \frac{\sqrt{1-\alpha_f^2 \hat{k}_t^2}}{\alpha_f^2 \hat{k}_t^2}. \tag{168}$$

From Eqs. (166) and (167) it can be easily seen that $|X| \approx 1$ and $|Q| \approx 1$ if ζ_{am}, ζ_{ac}, and ζ_{ae} are sufficiently small.

It is important to examine the validity of our assumptions: Eqs. (134), (136), and (137). When the data of the given vibrator are used, the following can be easily obtained:

$$\left| \frac{\hat{v}^2}{\hat{t}^2 c_{p0} \hat{\theta}_0} \right| = 6.040 \times 10^{-6} \ll 1, \tag{169}$$

$$\left| \frac{2\zeta_{\max} \hat{v}^2}{\hat{t}^2 c_{p0} \hat{\theta}_0} \right| = 6.002 \times 10^{-9}, \tag{170}$$

$$\left|\frac{2Q_0\hat{t}}{\rho c_{p0} l}\right| = 4.411\times 10^{-10}\tilde{\theta}_0 \leqslant \mathcal{O}(6.002\times 10^{-9}), \qquad (171)$$

where we set $\hat{\epsilon}^{(e)}=10.00$, which is the value of voltage amplitude used in the experiments. These calculations suggest that the terms with time derivatives of the temperature can be safely neglected.

Experiments were carried out and compared with simulation results. The PZT4 disc with both ends exposed to air was used. The disc is supported as shown in Fig. 7. Since vibrations at the surface and the inside of the vibrator can cause difficulty in using a thermocouple for monitoring the surface temperature, an IR (infrared) camera was used to measure the surface temperature of the disc. The value of the Biot number of the disc (4.203×10^{-2}) supports the assumption that the surface temperature is close to the internal temperature. While a voltage source was applied to the disc, the voltage between the conductor plates and the current flowing into the plates were measured. Figure 8 shows the experimental setup. The voltage input is 10 V at about 408 kHz. While 407.1 kHz is obtained for a resonance frequency from the model, the phase lag between the voltage input and the current is measured to be zero at about 408 kHz.

Five sets of measured data are presented here. In the first two, the waveform data were collected every 5 s during 95 s. The third to fifth sets have a sampling interval of 10 s during a total measuring period of 190 s. The measured excitation frequencies are listed in Table II. The number of waveforms and the size of waveform data are restricted by the memory and data transfer rate between the oscilloscope used for measuring the waveform and the PC for collecting data to a maximum of 20 waveform data per measurement set. However, the data clearly show drifting of the phase lag and temperature. Figures 9 and 10 show the waveforms of voltage and current at the beginning and the end of the third set of measurements. While driving frequency is not changed, the change of phase lag between the two signals can be easily noticed.

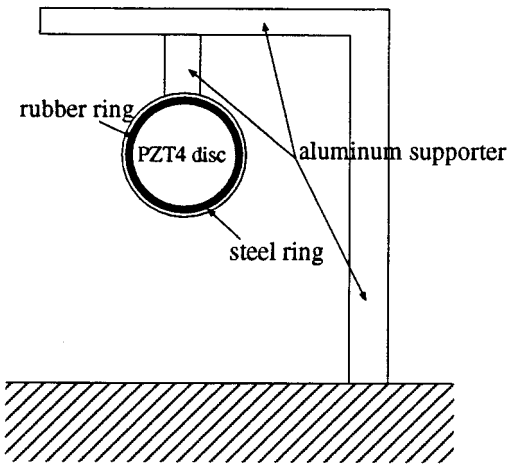

FIG. 7. Supporter of the PZT-4 disc.

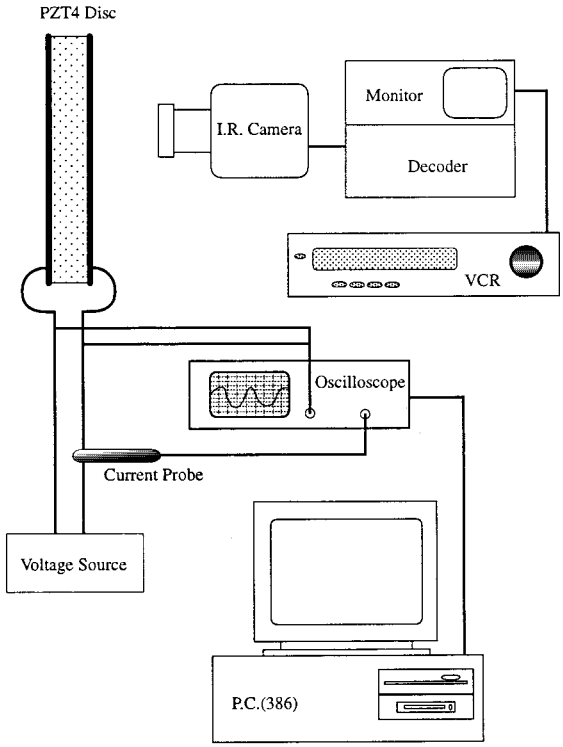

FIG. 8. Experimental diagram.

IX. RESULTS AND DISCUSSIONS

The limitation in the modified two-node bond graph model should be pointed out before comparing the results from simulations and experiments. While the two-node model assumes a constant strain field in the thickness direction as well as other directions, the real strain field is expected to be more similar to a sine function than to constant because the air is more nearly a free boundary. This will cause errors in the temperature prediction in addition to those due to computing the average temperature rather than that at the surface. The temperature at the surface is increased by conduction heat transfer from internal points, where most of the energy is dissipated. This may cause a delay in the increase of the surface temperature and a larger difference between the surface and center temperatures. These effects can be observed by comparing short period numerical simulations of the bond graph model with eleven nodes and the modified two-node bond graph model. The results are shown in Figs. 11–13. As shown in those figures, the displacement and the charge calculated by those two models are almost identical. However, the temperature predicted from the two-node model lies between the internal and the surface temperatures calculated from the 11-node model. Since the figures show the initial transient responses of the variables, before conduction heat transfer affects temperature at the surface, the rate of increase of internal temperature is larger than that of the surface. Furthermore, since in the two-node

TABLE II. The frequencies of voltage input in experiments.

Experiment No.	1.1	1.2	2.1	2.2	2.3
Frequency (kHz)	408.3	408.3	408.0	408.1	407.8

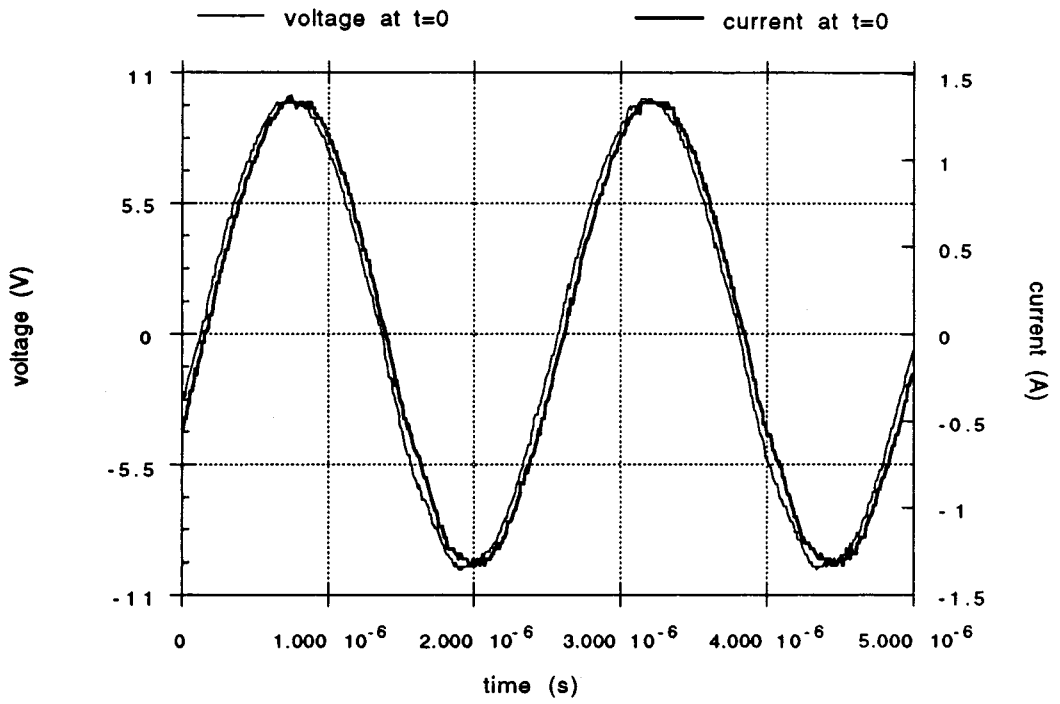

FIG. 9. Measured voltage and current waveforms at $t=0$ s.

model heat is generated by dissipation uniformly throughout the vibrator, the temperature from the two-node model follows the trend of the internal temperature.

Now let us investigate the results from the simple two-node model and from the measurements. Figures 14 and 15 show the time histories of amplitude of the current and shift of phase difference between the voltage and the current. The calculated values of current amplitude are considerably larger than the measured values at early times. Although the external load of the vibrator is virtually zero because acoustic wave radiation is negligibly small in this case, it is difficult to estimate the dynamic stress amplitude and determine an appropriate value of mechanical damping factor ζ_{am}. Instead of assuming that the damping effects change with stress amplitude, the strain amplitude is used for determination of the damping factor value in our model [see Eq. (53)]. The calculated values for strain amplitude are 7.73×10^{-5} if $\zeta_{am}=8.85\times10^{-4}$ and 2.24×10^{-5} for $\zeta_{am}=4.023\times10^{-3}$.

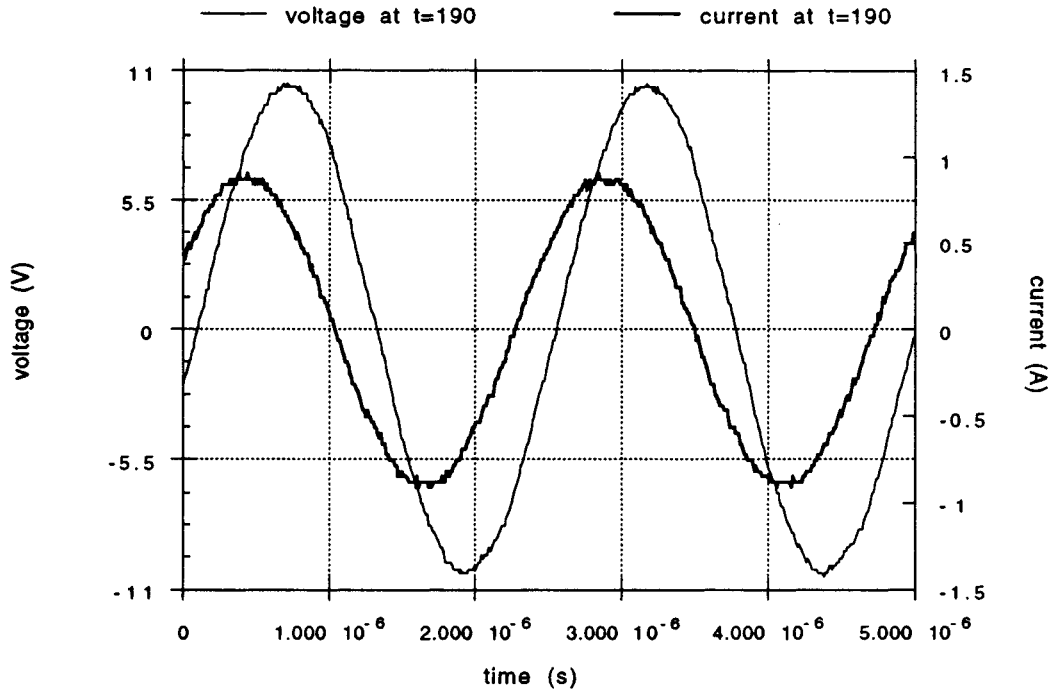

FIG. 10. Measured voltage and current waveforms at $t=190$ s.

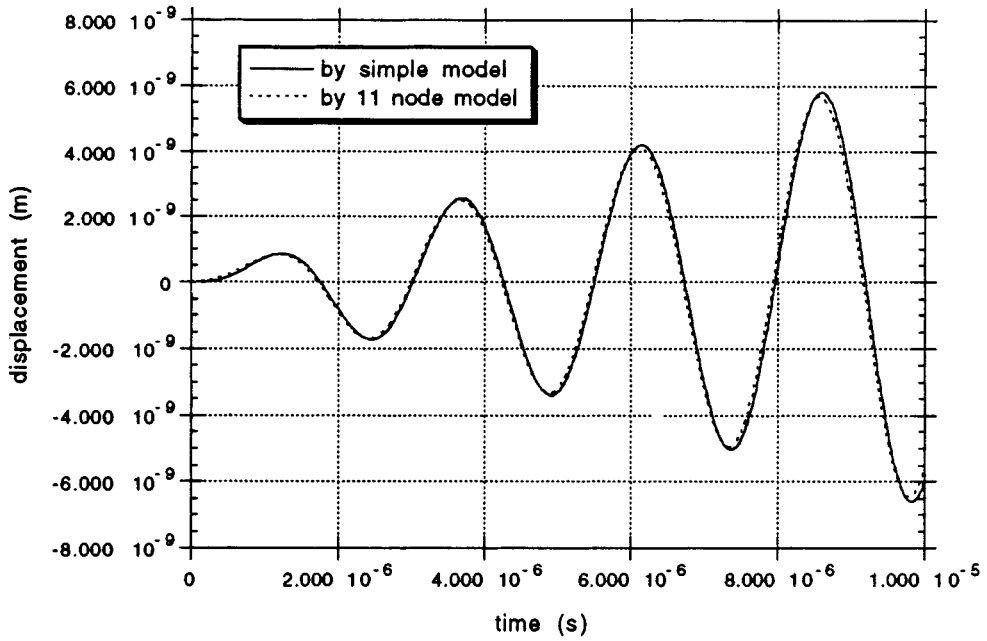

FIG. 11. Displacement transient time histories calculated using 11-node and modified two-node bond graph models.

These values for strain amplitudes suggest that ζ_{am} is larger than 8.85×10^{-4} but smaller than 4.023×10^{-3}. However, the measured current amplitudes are even less than the calculated amplitude with $\zeta_{am}=4.023\times10^{-3}$. In Fig. 14 the calculated current amplitude is about 1.6 times the measured one at the initial time even though the trends of their time histories are similar. The normalized current amplitude plot shown in Fig. 16 does not show considerable improvement in the trends of the time histories. The difference is thought to come mainly from the fact that a real PZT4 disc cannot be an ideal thickness vibrator. Shaw and Ikegami show that the real mode shape of a disc is different from the mode shape assumed in the thickness vibrator, even though the detected mode has the same value of resonance frequency as the thickness vibrator model.[5,6] The difference between the assumed and the real mode shapes is also observed from numerical calculations of the three-dimensional model of a thin disc.[11,12] Since the effective area of a conductor plate is smaller than that of a disc in the real mode shape, the current amplitude measured should be smaller than the calculated one. This argument can be tested by measuring the surface temperature distribution with an IR camera. The surface temperature of a small spot (about a fifth of the diameter of the whole disc) at the center is measured to be higher than for

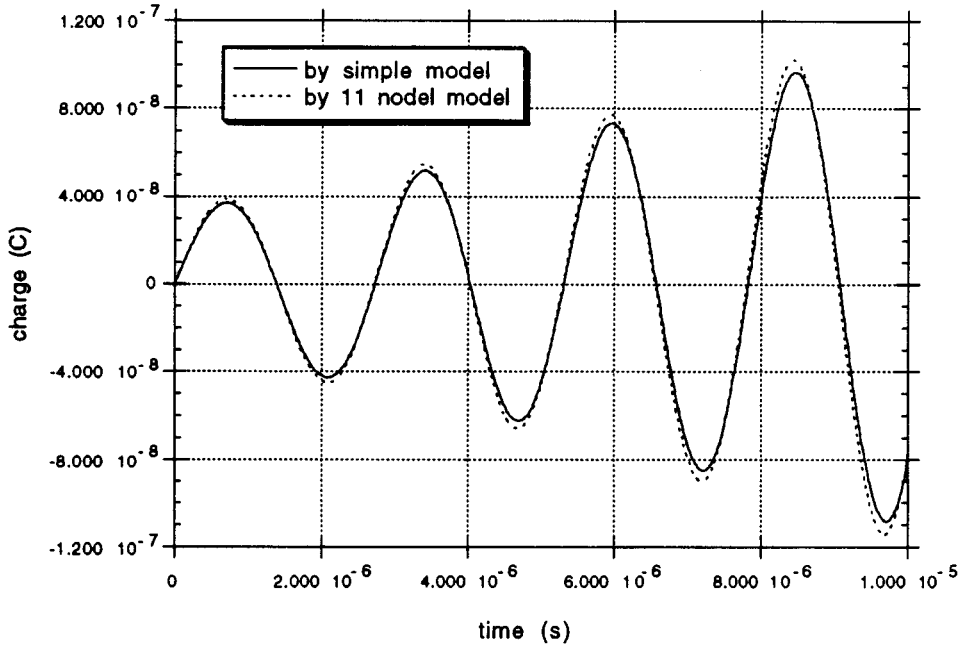

FIG. 12. Charge transient time histories calculated using 11-node and modified two-node bond graph models.

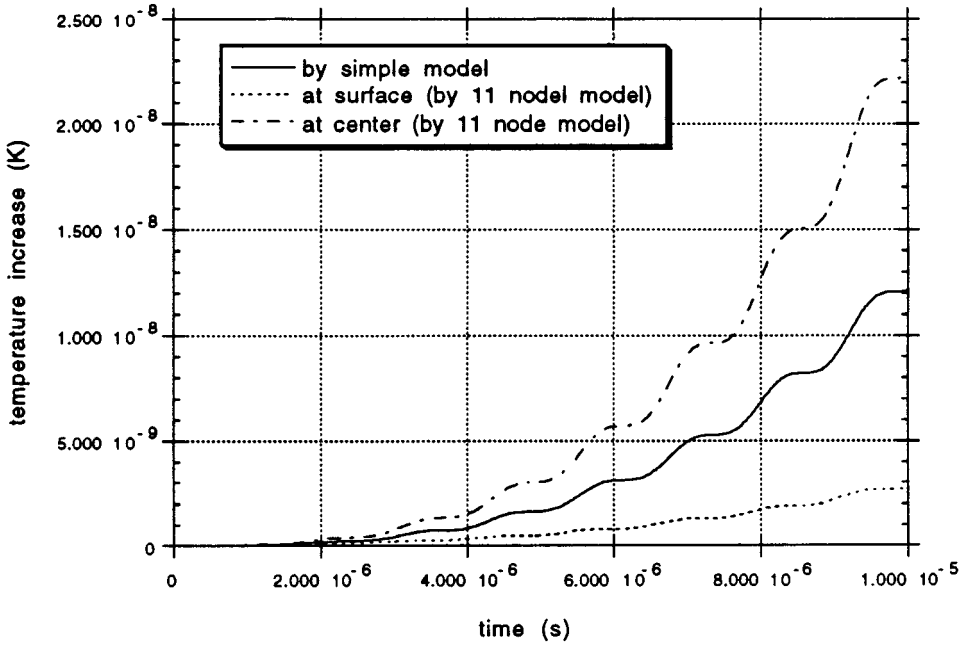

FIG. 13. Equilibrium temperature increase transient time histories calculated using 11-node and modified two-node bond graph models.

the remaining area from the start of voltage application. This suggests that the amplitude of the displacement is not uniform in the radial direction because the temperature increase is caused only by internal dissipation. The surface temperature increase measured at the center is smaller than the calculated one as shown in Fig. 17.

The time history of the shifts of phase difference between the voltage and the current match better than temperature and current amplitude (Fig. 15) but still show relatively big differences. These differences in phase shifts are mainly due to those in temperatures. Since the effective area of a thickness vibrator is smaller than the disc area, the total dissipated energy in the disc is considerably less than that calculated by the model. Since heat is diffused over the disc from the center due to conduction, even the center surface temperature is considerably smaller than expected.

The calculations provide better results if the phase and the amplitude of current are compared at a given temperature. In Fig. 18, the phase is plotted as a function of temperature increase. The calculation results with $\zeta_{am}=4.023\times10^{-3}$

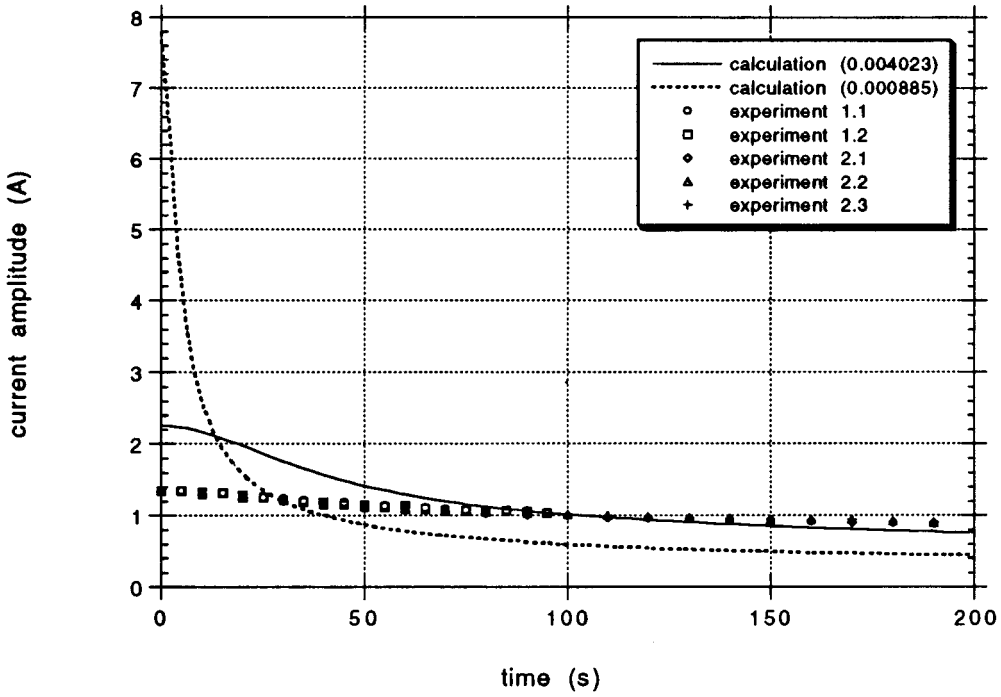

FIG. 14. Current amplitude time history.

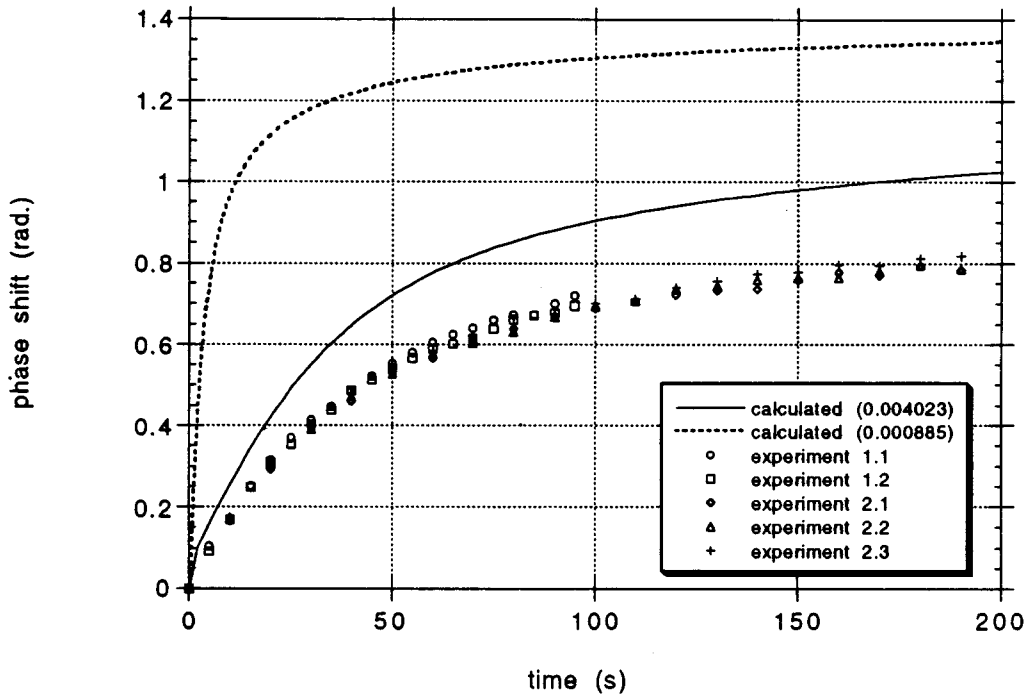

FIG. 15. The time history of shift of phase difference between voltage and current.

are close to the measured values. This suggests that the strain amplitude is larger than expected because the equivalent strain calculated from the stress of 2000 psi is larger than the calculated strain with $\zeta_{am}=4.023\times10^{-3}$. This is due to the smaller effective area for a thickness mode.

In the case of current amplitude, Fig. 19 shows less improvement in accuracy than the time history plot. As can be seen in Fig. 20, the decrease of normalized current amplitude is measured to be less than calculated, which implies that the temperature increase has less influence than expected on the current amplitude. It is not believed to be a general trend because there is another resonance at 400 kHz near the thickness mode one (408 kHz). Since another resonance with weaker coupling factor can be placed near the fundamental thickness mode resonance frequency with a proper aspect ratio as shown by Ikegami,[6] it may be due to the aspect ratio of the disc used for our experiments.

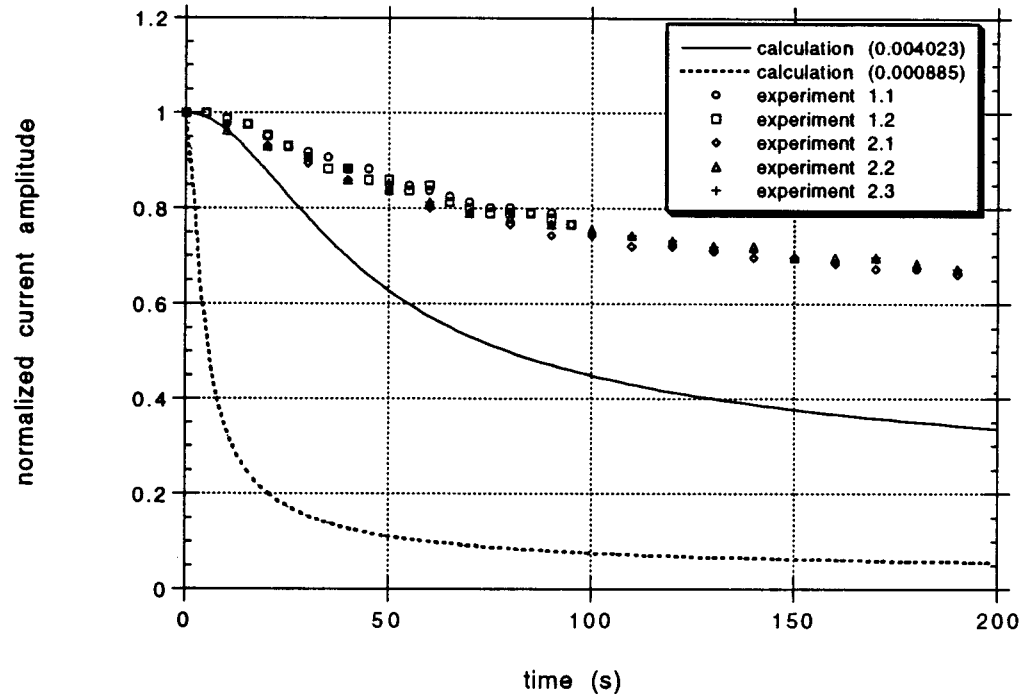

FIG. 16. Normalized current amplitude time history.

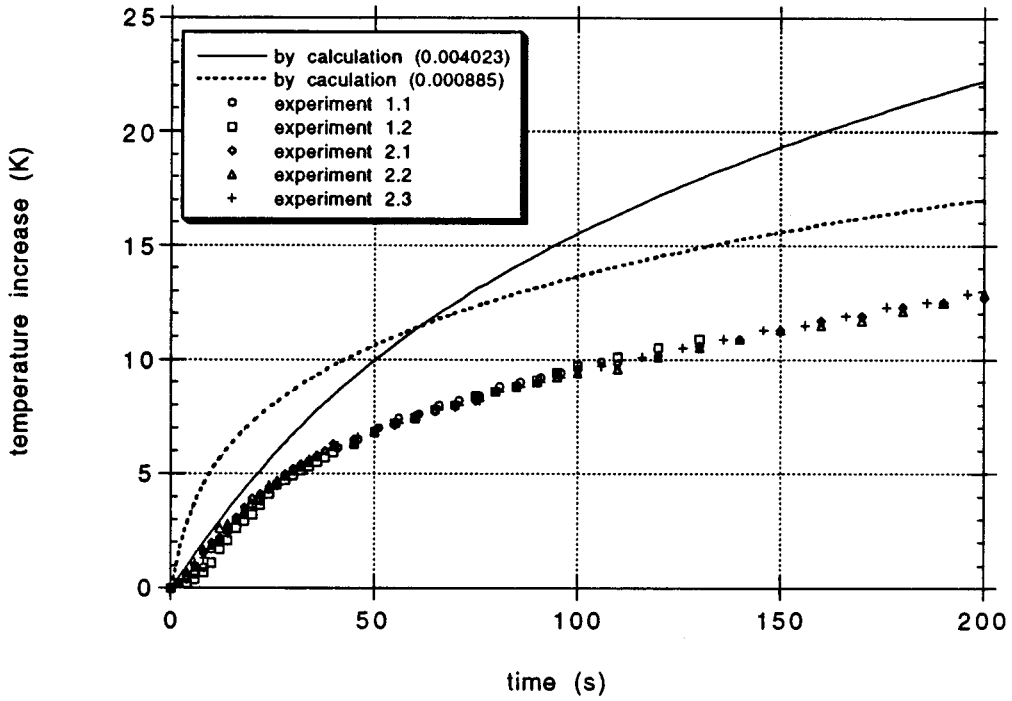

FIG. 17. Equivalent temperature increase time histories.

X. CONCLUSIONS

The effects of temperature variations in the dynamic response of a thickness vibrator have been investigated comparing calculations and experiment results. Bond graphs have been successfully used under the isentropically linear material property assumption to model the thermo-electro-mechanical coupling. Since the resulting state equations are nonlinear and have both rapidly varying and slowly changing variables, the simulation of a complicated detailed model cannot be done for a sufficiently long period that the effects of the slowly varying variables can be detected. Instead, a modified version of the simplest form of the developed bond graph model was successfully used to predict the effects of temperature by use of approximations. The calculations predict correct trends and accurate shifts of phase differences between voltage and current even though the data used for

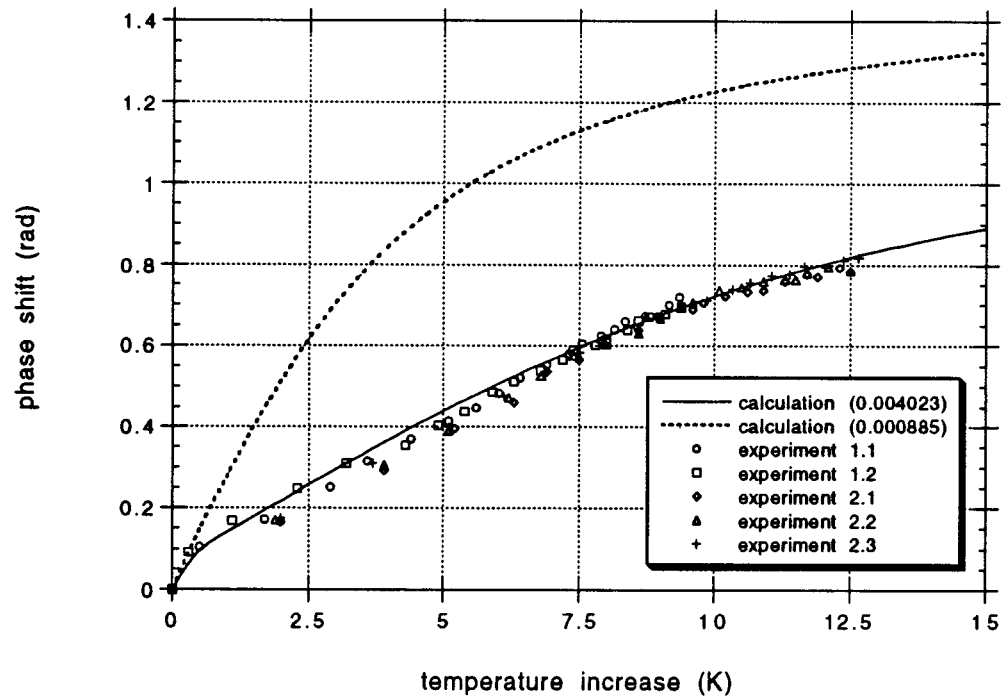

FIG. 18. The shift of phase difference between voltage and current versus temperature increase.

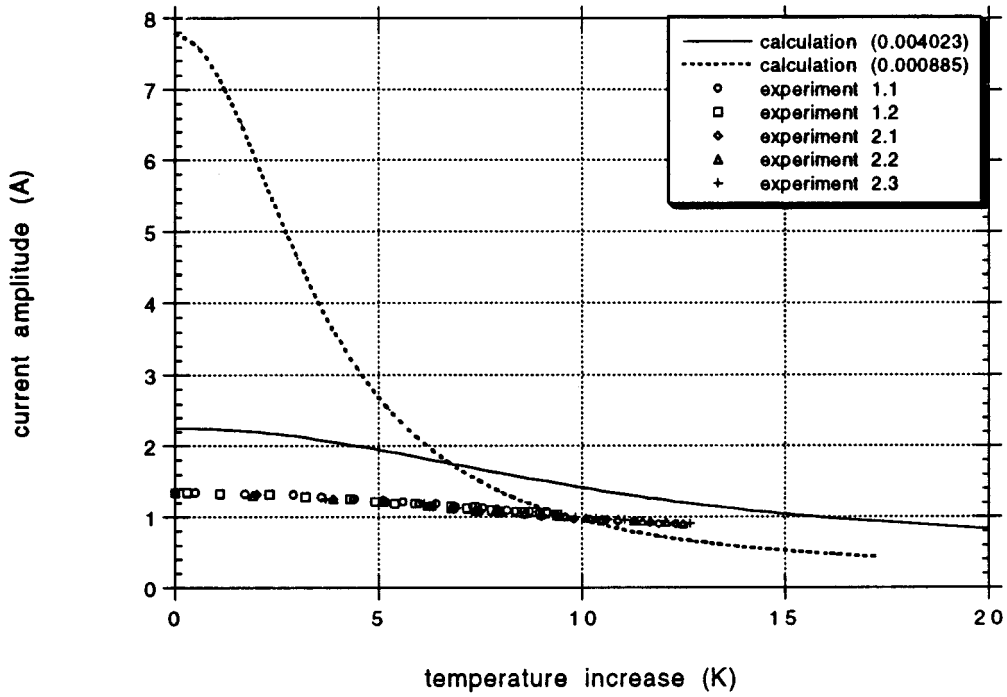

FIG. 19. The current amplitude versus temperature increase.

the functional dependence of material parameters on temperature are relatively inaccurate. The approximation approach to obtain the solution of the modified two-node model can be applied to the bond graph model with many nodes; however, as the results of the experiment suggest, the model with many nodes is not believed to provide considerable improvement because the difference between the results from calculation and experiment comes from the variations in the radial direction and not in the thickness direction.

While this work is restricted to the piezoelectric thickness mode vibrator, this approach is applicable to other modes such as the longitudinal expander mode. Furthermore, a general three-dimensional model can be developed using the approach described here. In order to improve the accuracy of prediction of the model a full set of the material property constants should be measured as functions of temperature in addition to development of a three-dimensional model.

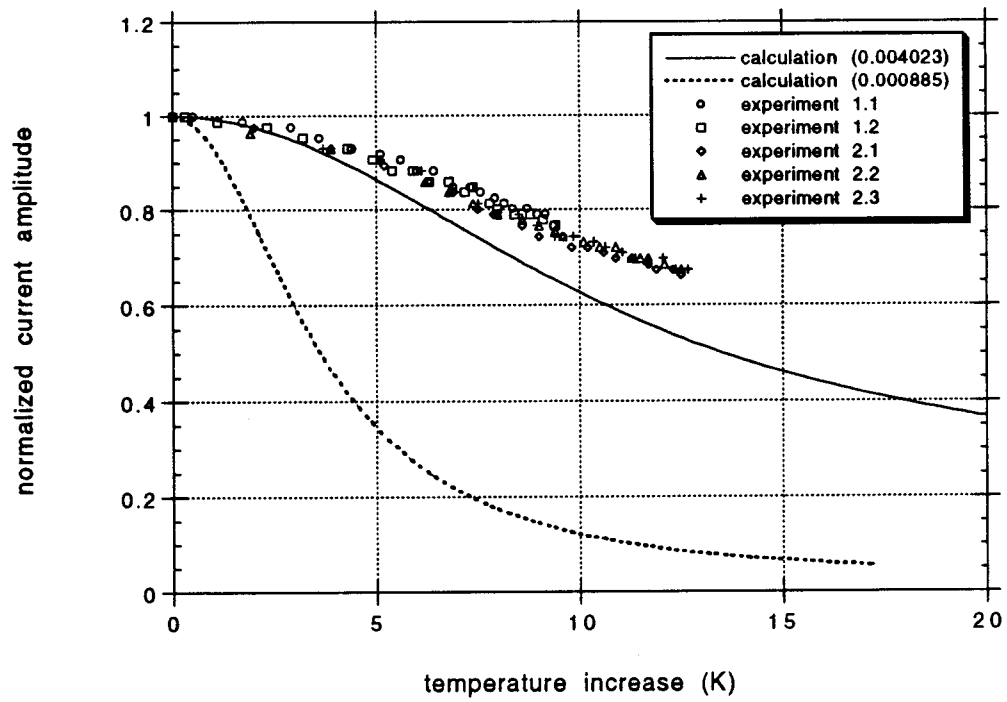

FIG. 20. The normalized current amplitude versus temperature increase.

This work to include the thermal energy on an equal footing with the mechanical and electrical energy in a model for the piezoelectric thickness vibrator was made possible to a large extent by the choice to use a bond graph approach. Bond graph models, because they do not assume linear constitutive relations and because they are well suited for multiple energy domains, are ideal for the piezoelectric problem which necessarily links thermal, mechanical, and electrical energy domains. Previous attempts to model piezoelectric behavior have focused on only two energy domains, and added the third in an *ad hoc* manner if at all. In the first paper of this series, a thermodynamic material property model of piezoelectric ceramics for the data in the publications is proposed and the effects of the thermo-electro-mechanical coupling are evaluated. The change of the instantaneous temperature due to the mechanical and electrical state variables is shown to be so small that it may be logically ignored. In the second part, the partial differential equations for the piezoelectric body including thermal effects are derived. From those partial differential equations, proper conditions for the thickness vibrator including thermal variables are proposed and the partial differential equations for the thickness vibrator are derived. In the third paper, a bond graph model for one-dimensional thermal conduction is developed. Finally, this last paper combines results of previous parts to construct a complete, quasi-dynamic model of the piezoelectric thickness vibrator in which thermal, mechanical, and electrical energy domains are treated evenly.

ACKNOWLEDGMENTS

The authors wish to thank Dr. Eric Fahrenthold, Dr. Elmer Hixson, and Dr. David Blackstock for their helpful discussions. This work was supported by a National Science Foundation Faculty Award for Women in Science and Engineering.

[1] W. Moon and I. J. Busch-Vishniac, ''Modeling of piezoelectric ceramic vibrators including thermal effects: Part II. Derivation of partial differential equations,'' J. Acoust. Soc. Am. **98**, 413–421 (1995).
[2] W. Moon and I. J. Busch-Vishniac, ''Modeling of piezoelectric ceramic vibrators including thermal effects: Part I. Thermodynamic property considerations,'' J. Acoust. Soc. Am. **98**, 403–412 (1995).
[3] W. Moon and I. J. Busch-Vishniac, ''Finite element equivalent bond graph modeling with application to the piezoelectric thickness vibrator,'' J. Acoust. Soc. Am. **93**, 3496–3506 (1993).
[4] D. C. Karnopp, D. L. Margolis, and R. C. Rosenberg, *System Dynamics: A Unified Approach* (Wiley, New York, 1990).
[5] E. A. G. Shaw, ''On the resonant vibrations of thick barium titanate disks,'' J. Acoust. Soc. Am. **28**, 38–50 (1956).
[6] S. Ikegami, I. Ueda, and S. Kobayashi, ''Frequency spectra of resonant vibration in disk plate of $PbTiO_3$ piezoelectric ceramics,'' J. Acoust. Soc. Am. **55**, 339–344 (1974).
[7] W. Moon and I. J. Busch-Vishniac, ''Modeling of piezoelectric ceramic vibrators including thermal effects: Part III. Bond graph model for one dimensional heat conduction,'' J. Acoust. Soc. Am. **101**, 1398–1407 (1997).
[8] J. J. Beaman and H. M. Paynter, *Modeling of Physical Systems* (Class Note, The University of Texas at Austin, 1989), 2nd ed.
[9] T. Hughes, *The Finite Element Method* (Prentice-Hall, Englewood Cliffs, NJ, 1987).
[10] F. P. Incropera and D. P. De Witt, *Fundamentals of Heat and Mass Transfer* (Wiley, New York, 1981), 2nd ed.
[11] A. D. Pierce, *Acoustics: An Introduction to Its Physical Principles and Applications* (McGraw-Hill, New York, 1981).
[12] W. P. Mason, *Physical Acoustics: Volume I* (Academic, New York, 1964).
[13] E. P. Eer Nisse, ''Variational Method for Electroelastic Vibration Analysis,'' IEEE Trans. Sonics Ultrason. **SU-14**(4), 153–160 (1967).
[14] H. A. Kunkel, S. Locke, and B. Pikeroen, ''Finite-Element Analysis of Vibrational Modes in Piezoelectric Ceramic Disks,'' IEEE Trans. Ultrason. Ferroelectr. Freq. Control **37(4)**, 316–328 (1990).

Applications of matched-field processing to structural vibration problems

G. Turek and W. A. Kuperman
Marine Physical Laboratory of the Scripps Institution of Oceanography, University of California, San Diego, La Jolla, California 92093-0701

(Received 15 March 1996; accepted for publication 23 October 1996)

Matched-field processing (MFP) is a generalized procedure of array processing used in ocean acoustics to localize sources. It is based on comparing data with solutions to the wave equation using an assortment of linear and nonlinear methods. The applicability of MFP techniques to localize sources of vibration in structures is explored through simulations, starting with the relatively simple problem of localizing a point force on a simply supported laterally vibrating beam. The Bartlett, minimum variance (as well as the eigenvector versions of these two), and a matched modal processor are used. In all cases localization was achieved. Additional complications such as spring constraints were added in order to determine whether the MFP methods can still localize sources of vibrations without full detailed modeling of additional structural complexity. An application to nondestructive testing is also presented. © *1997 Acoustical Society of America.* [S0001-4966(97)03103-2]

PACS numbers: 43.40.At, 43.40.Cw, 43.40.Le, 43.40.Yq [CBB]

INTRODUCTION

We explore, through numerical simulation, the applicability of matched-field processing (MFP) techniques to localize sources of vibration in structures and perform nondestructive testing. MFP is a generalized procedure of array processing used in ocean acoustics to either localize sources[1,2] or do inversions i.e., matched-field tomography.[3] MFP formulations involve correlations between the solutions (or ''replicas'') of the wave equation for a given acoustic model of the ocean, and the data measured at an array of sensors. The correlations are made using an assortment of linear and nonlinear methods. The MFP method can be thought of as an inverse method using forward solutions.

In ocean acoustics, the ocean can be treated as a waveguide whose boundaries are the ocean surface and a solid basement that typically may have a sediment above it. The index of refraction of the waveguide is determined by the geophysical properties of the ocean environment such as sound speed, density in the water column and ocean bottom, as well as the geometrical shape of the waveguide boundaries. A source is located in the waveguide in range and depth by comparing the data received on an array of acoustic sensors with model solutions generated from the Green's function of the waveguide. Limiting factors in this process is an inexact knowledge of the ocean environment which prevents the construction of highly accurate Green's functions and ocean ambient noise.

An application of simple sonar procedure has already been applied to an acoustic emission problem[4] in which correlation techniques were applied to localizing a source of vibration on a plate. Localizing a source without using direct solutions has also been studied.[5] Nondestructive testing has received much attention in recent years.[6,7] Most recently, neural network methods in which a processor is ''trained'' to interpret accelerometer inputs have been developed to detect and localize defects.[8] The work discussed in this paper utilizes a model of the structure for enhanced resolution and may have potential for being incorporated in neural network and other sophisticated processor implementations.

We initially consider the relatively simple problem of localizing a harmonic point force on a simply supported laterally vibrating beam using an array of sensors, typically accelerometers. The Bartlett, minimum variance (MV), and a matched modal processor are used. The eigenvector versions of the first two are also introduced. In all cases localization is achieved. Additional complications such as spring constraints are added in order to determine whether the MFP methods can still localize sources of vibrations without full detailed modeling of the additional structural complexity. For a highly complex structure (i.e., springs of high stiffness) these methods do not work with replicas that do not correspond to the full structural complexity. Multiple constraint methods, tolerant to solution mismatch are introduced to deal with complicated structures which can be approximately modeled with statistical techniques.[9] It is also demonstrated that MFP techniques methods might also be used as means of nondestructive testing in order to locate defects.

We start by reviewing the forward solution of the equation of the simple vibrating beam in Sec. II. Basic MFP concepts, algorithms, and numerical results are discussed in Sec. III. Section IV discusses a more complicated beam problem from the point of investigating the degradation of the processors when the replica fields are not the exact solutions of the exact equation of motion. A more tolerant processor based on a statistical approach is then introduced. Finally, an example of how the method can be used for nondestructive testing applications is presented in Sec. V.

I. GENERAL SOLUTION FOR LATERAL FORCED VIBRATIONS OF AN EULER BEAM

We consider the (time harmonic) lateral vibrations of a beam such as that depicted in Fig. 1, as described by Euler's

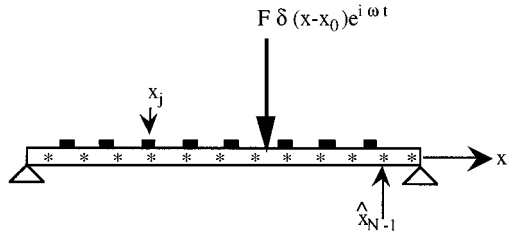

FIG. 1. Simply supported beam excited by harmonic point force at $x=x_0$. x indicates position of jth motion sensor along the beam, $\hat{x}_n$ $(n=1,\ldots,N)$ is the ''look'' direction (scanning position).

beam equation[10,11] which neglects the effect of rotatory inertia and shear deformation. This assumption is valid if the ratio between the length of the beam and its height is relatively large (length/height$\gg$10). Euler's equation is

$$EI\,\frac{d^4u(x,t)}{dx^4}-\rho\,\frac{d^2u(x,t)}{dt^2}=F(x,t), \tag{1}$$

where $u(x)$ is the lateral displacement along the beam, EI is the flexural rigidity of the beam [E=Young's modulus (Pa), I=second moment of the cross section (m^4)], ρ the mass per unit length (kg/m), ω the angular frequency (rad/s), and F is the loading force (N). Throughout our analysis we will keep E, I, and ρ constant.

The response of the system to excitation can be obtained by the mode summation method.[10] Given the normal modes φ_n and natural frequencies ω_n of the beam, its deflection at any point x can be represented by

$$u(x,t)=\sum_{n=0}^{\infty} q_n(t)\varphi_n(x). \tag{2}$$

The normal modes satisfy the orthogonality condition

$$\int_0^L \varphi_m(x)\varphi_n(x)dx=\delta_{nm}, \tag{3}$$

and q_n are the generalized coordinates which satisfy the equation

$$\ddot{q}_m(t)+\omega_m^2 q_m(t)=\frac{1}{M_m}\left[\int_0^L F(x,t)\varphi_m(x)dx\right], \tag{4}$$

$F(x,t)$ is the exciting force per unit length, and M_m is the generalized mass

$$M_m=\int_0^L \rho(x)\varphi_n(x)\varphi_m(x)dx. \tag{5}$$

If we assume that both the generalized coordinates and the force are harmonic in time

$$q_m(t)=\overline{q_m}e^{-i\omega t} \quad \text{and} \quad F(x,t)=f(x)e^{-i\omega t}, \tag{6}$$

we can then write (for constant mass)

$$\overline{q_m}=\frac{1}{M_m(\omega_m^2-\omega^2)}\left[\int_0^L f(x)\varphi_m(x)dx\right]. \tag{7}$$

If $f(x)$ is a point force expressed as $F\delta(x-x_0)$, Eq. (7) reduces to

$$\overline{q_m}=\frac{1}{M_m(\omega_m^2-\omega^2)}\,[F\varphi_m(x_0)]. \tag{8}$$

Equation (8) can be written as the matrix equation

$$\begin{bmatrix} \rho(\omega_1^2-\omega^2) & 0 & 0 \\ 0 & \ddots & 0 \\ 0 & 0 & \rho(\omega_m^2-\omega^2) \end{bmatrix} \begin{Bmatrix} \overline{q_1} \\ \vdots \\ \overline{q_m} \end{Bmatrix} = \begin{Bmatrix} F\varphi_1(x_0) \\ \vdots \\ F\varphi_m(x_0) \end{Bmatrix}, \tag{9}$$

which can be further written as

$$\mathbf{Z_0}(\omega)\overline{\mathbf{q}}=\mathbf{f}, \tag{10}$$

where $\mathbf{Z_0}(\omega)$ is the generalized impedance matrix.

We choose to work with a simply supported beam with boundary conditions $u=0$ and $E(d^2u/dx^2)=0$ at $x=0$ and $x=L$, whose normalized natural modes of vibration are then given by

$$\varphi_n(x)=\sqrt{2/L}\,\sin(\beta_n x), \tag{11}$$

and the natural frequencies of vibration are given by

$$\omega_n=\left(\frac{n\pi}{L}\right)^2\sqrt{\frac{EI}{\rho}}. \tag{12}$$

The spatial solution for a such a beam (Fig. 1) is

$$u(x)=\sum_{n=0}^{\infty}\frac{2F}{L\rho}\,\frac{\sin(\beta_n x_0)}{(\omega_n^2-\omega^2)}\,\sin(\beta_n x). \tag{13}$$

II. CONVENTIONAL MFP ALGORITHMS

MFP is an array processing technique to locate the position of the source excitation by comparing forward solutions of the wave equation with data measured on an array of motion sensors (see Fig. 1). Various processors (beamformers) can be used for this procedure.

A. The Bartlett processor[12]

The Bartlett beamformer is the most basic of all beamformers: given N ''sensors'' located at $x_1,x_2,\ldots,x_N$ along the length of the beam, we construct a data vector

$$\mathbf{d}^T=[d(x_1)\quad d(x_2)\quad \cdots\quad d(x_N)], \tag{14}$$

where the superscript ''T'' denotes the transpose and $d(x_i)$, $i=1,\ldots,N$ are the data relayed by each sensor, (for example, the displacement as measured by accelerometers positioned along the beam). For the purpose of simulation the data are obtained from Eq. (14). We then form an average of the projection of the data vector on the normalized ''replica'' vector $\mathbf{w}(\hat{x})$

$$\mathbf{w}(\hat{x})=\frac{\mathbf{u}(\hat{x})}{|\mathbf{u}(\hat{x})|}, \tag{15}$$

constructed by computing the solution of the problem at each sensor location while scanning for all possible force locations

$$B_{\mathrm{Bart}}(\hat{x}) = \frac{1}{N} \sum_{i=1}^{N} |\mathbf{w}^T(\hat{x})\mathbf{d}(x)|^2. \tag{16}$$

This can be expressed in a quadratic form in terms of the cross spectral density matrix (CSDM) $\mathbf{K}=\mathbf{d}\mathbf{d}^T$,

$$B_{\mathrm{Bart}}(\hat{x}) = \mathbf{w}^T(\hat{x})\mathbf{K}(x)\mathbf{w}(\hat{x}). \tag{17}$$

It is typically the CSDM estimated from a particular FFT frequency bin of the data that is used in the MFP:[1]

$$\mathbf{K} = \frac{1}{L} \sum_{n=1}^{L} \mathbf{d}_n(f)\mathbf{d}_n^T(f), \tag{18}$$

where L is the number of ''snapshots,'' and f the frequency. Typically, the number of snapshots should exceed the number of sensors[1] (especially for the processors described below).

B. The minimum variance (MV) processor[12]

The minimum variance (MV) processor optimizes the match to a signal by trying to reject signals and correlated noise from other directions or in this case, scanning positions $\hat{x}$. We seek a weight replica vector $\mathbf{w}_{\mathrm{MV}}^T$ which, when applied to the CSDM matrix, minimizes the output of the beamformer (16) except in the ''look'' direction, the scanning position $\hat{x}$. This vector is chosen to minimize the functional

$$F = \mathbf{w}_{\mathrm{MV}}^T K \mathbf{w}_M + \gamma(\mathbf{w}_{\mathrm{MV}}^T \mathbf{w} - 1). \tag{19}$$

Following the method of Lagrange multipliers, we take the gradient with respect to $\mathbf{w}_{\mathrm{MV}}$ and set it equal to zero

$$\mathbf{w}_{MV} = -\frac{\gamma}{2}(\mathbf{K}^{-1}\mathbf{w}) \Rightarrow \mathbf{w}_{\mathrm{MV}}^T = -\frac{\gamma}{2}(\mathbf{K}^{-1}\mathbf{w})^T. \tag{20}$$

The constraint condition of unity in the look direction gives

$$\frac{\partial F}{\partial \gamma} = \mathbf{w}_{\mathrm{MV}}^T \mathbf{w} - 1 = 0. \tag{21}$$

Equations (18) and (19) taken together give (after some manipulation) an expression for the Lagrange multiplier

$$\gamma = -2(\mathbf{w}^T\mathbf{K}^{-1}\mathbf{w})^{-1}. \tag{22}$$

This leads to an expression for the weight vector

$$\mathbf{w}_{\mathrm{MV}} = -\frac{\mathbf{K}^{-1}\mathbf{w}}{\mathbf{w}^T\mathbf{K}^{-1}\mathbf{w}}, \tag{23}$$

which, substituted into the quadratic form (16) gives

$$B_{\mathrm{MV}}(\hat{x}) = [\mathbf{w}^T(\hat{x})\mathbf{K}^{-1}(x)\mathbf{w}(\hat{x})]^{-1}. \tag{24}$$

The MV processor is often very useful when only a ''sparse'' array of sensors is available but the replicas can be accurately computed.

C. Eigenvector beamformers[12]

The CSDM $\mathbf{K}$ can be expressed in terms of its eigenvectors and eigenvalues as

$$\mathbf{K} = \sum_{n=1}^{N} \lambda_{\mathbf{n}} \mathbf{v}_n \mathbf{v}_n^T, \tag{25}$$

where $\lambda_1 \geqslant \lambda_2 \geqslant \cdots \geqslant \lambda_N$. When noise is uncorrelated from sensor to sensor (''white'' noise, i.e., $n_{ij}=0$ for $i \neq j$) the eigenvector corresponding to the largest eigenvalues span the subspace containing the uncorrelated signal vectors $\mathbf{S}_i$, $i=1,\ldots,M$, and the remaining $(N\text{-}M)$ eigenvectors span the subspace orthogonal to this signal subspace. The inverse of the correlation matrix $\mathbf{K}^{-1}$ has the same eigenvectors as $\mathbf{K}$ and is given by

$$\mathbf{K}^{-1} = \sum_{n=1}^{N} \frac{1}{\lambda_n} \mathbf{v}_n \mathbf{v}_n^T. \tag{26}$$

If the eigenvector expansion of $\mathbf{K}^{-1}$ is truncated to include only those terms not corresponding to signal propagation directions:

$$[\mathbf{K}_N]^{-1} = \sum_{n=N-M}^{N} \frac{1}{\lambda_n} \mathbf{v}_n \mathbf{v}_n^T, \tag{27}$$

it will be orthogonal to the signal space and B_{MV} as evaluated in Sec. II B will have an extremely sharp peak in the signal direction (this is essentially the ''MUSIC'' algorithm[13]). It also follows that the eigenvector expansion of $\mathbf{K}$ can be truncated to include only $N\text{-}M$ terms corresponding to the signal propagation direction. Thus, both the Bartlett and the minimum variance beamformers can be subsequently calculated from $\mathbf{K}$ and $[\mathbf{K}_N]^{-1}$ obtained in this manner, using Eqs. (17) and (24), respectively.

D. Modal beamformer[14]

The ''data'' at each ''sensor'' are expressed as a summation of normal modes

$$d(x_i) = \sum_{m=1}^{M} A_m \varphi_m(x_i), \tag{28}$$

where $i=1,\ldots,N$ is the number of sensors and $m=1,\ldots,M$ is the number of modes. This ''spatial'' data set is then transformed to a new data set consisting of the modal amplitudes by utilizing the orthogonality of the normal modes. We rewrite (28) in matrix form

$$\mathbf{d} = \mathbf{E}\mathbf{a}, \tag{29}$$

where $\mathbf{u}$ and $\mathbf{a}$ are vectors of dimension $[N\times 1]$ and $[M\times 1]$, respectively, and $\mathbf{E}$ is an $[N\times M]$ matrix whose individual components are given by

$$E_{ij} = \varphi_j(x_i). \tag{30}$$

The mode amplitude vector can be obtained for example, from

$$\mathbf{a} = (\mathbf{E}^T\mathbf{E})^{-1}\mathbf{E}^T\mathbf{d}. \tag{31}$$

This is the least-mean-square method which finds the best fit to data on N sensors by a finite number of M modes ($M < N$), suppressing the noise in the $N\text{-}M$ space. The matched-mode processor can then be expressed as

$$B_{\mathrm{Modal}}(\hat{x}) = \left| \sum_{m=1}^{M} b_m^* a_m \right|^2, \tag{32}$$

where b_m is the mth replica-mode amplitude, obtainable from Eq. (14).

E. Multiple constraint matched-field processors[15,16]

If there is some uncertainty in the precise replica field, the multiple constraint matched-field processor (MC) may be useful. In constructing the minimum variance processor (MV) we sought a weight replica vector $\mathbf{w}_{\mathrm{MV}}$ which, when applied to the CSDM matrix, minimizes the output of the beamformer (17) except in the ''look'' direction, which is defined as the solution to a wave equation for a particular structure. The MC approach seeks a weight replica vector $\mathbf{w}_{\mathrm{MC}}$ which, when applied to the CSDM matrix, minimizes the output of the beamformer (17) within a ''spot'' in the vicinity of the replica source location and/or a ''spot'' in the parameter space. The size of the ''spot'' is dictated by a number of constraints which can be expressed in the form:

$$\mathbf{w}_{\mathrm{MC}}\mathbf{w}_m = c_m, \tag{33}$$

where $\mathbf{w}_{\mathrm{MC}}$ is the weight vector and $\mathbf{w}_m$ is the replica vector for the mth constraint. The weight vector is chosen to minimize the functional[15]

$$F = \mathbf{w}_{\mathrm{MC}}^T \mathbf{K} \mathbf{w}_{\mathrm{MC}} + \sum_{m=1}^{M} \gamma_m (\mathbf{w}_{\mathrm{MC}}^T \mathbf{w} - c_m). \tag{34}$$

Following the method of Lagrange multipliers, we take the gradient with respect to $\mathbf{w}_{\mathrm{MC}}$ and set it equal to zero. We introduce the replica matrix $\mathbf{W}=[\mathbf{w}_1, \mathbf{w}_2, 1...,\mathbf{w}_M]$ and the Lagrange multiplier vector $\Gamma^T=[\gamma_1, \gamma_2, ..., \gamma_M]$ so that the minimization condition can be written as

$$\frac{\partial F}{\partial \mathbf{w}_{\mathrm{MC}}} = 2\mathbf{K}\mathbf{w}_{\mathrm{MC}} + \mathbf{E}\boldsymbol{\Gamma} = 0. \tag{35}$$

This equation is solved for the weight vector $\mathbf{w}_{\mathrm{MC}}$ in terms of the Lagrangian multiplier vector Γ which is determined by imposing the constraint equations (33). This leads to the following expression for the Lagrangian multiplier vector:

$$\boldsymbol{\Gamma} = -2[\mathbf{W}^T\mathbf{K}^{-1}\mathbf{W}]^{-1}\mathbf{c}^T, \tag{36}$$

where $\mathbf{c}=[c_1, c_2, \ldots, c_M]$ is the constraint column vector. Finally

$$\mathbf{w}_{\mathrm{MC}} = \mathbf{K}^{-1}\mathbf{W}[\mathbf{W}^T\mathbf{K}^{-1}\mathbf{W}]^{-1}\mathbf{c}^T, \tag{37}$$

which, substituted into the quadratic form (16) gives

$$B_{\mathrm{MC}}(\hat{x}) = \mathbf{c}^T[\mathbf{W}^T\mathbf{K}^{-1}\mathbf{W}]^{-1}\mathbf{c}, \tag{38}$$

For a structure too complicated to model deterministically,[9] we can use an ensemble of replicas derived from a statistical description of the structure.[16] In this method we construct the matrix $\mathbf{W}$ consisting of a set of $m=1,\ldots,M$ realizations of the replica vector $\mathbf{r}$ corresponding to M perturbations of the exact solution.

$$\mathbf{W} = [\mathbf{r}_1, \mathbf{r}_2, \ldots, \mathbf{r}_M]. \tag{39}$$

A set of constraint equations for this method can be expressed as

$$\mathbf{W}^T\mathbf{w} = \mathbf{c}, \tag{40}$$

where the elements of $\mathbf{c}$ specify the desired response at each constraint point. Using the singular value decomposition of $\mathbf{W}$

$$\mathbf{W} \cong \mathbf{H}\Lambda\Gamma^T, \tag{41}$$

where $\mathbf{H}$ is a $L\times J$ matrix whose columns are the left singular vectors of $\mathbf{W}$ corresponding to the largest singular values, Λ is a $J\times J$ diagonal matrix of the largest singular values of $\mathbf{W}$, and Γ is a $M\times J$ matrix whose columns are the largest right singular vectors, the perturbation constraints (40) can be rewritten as

$$\mathbf{H}^T\mathbf{w} = \Lambda^{-1}\Gamma^T\mathbf{c}. \tag{42}$$

Using Eq. (37), the beamformer weight vector for this statistical multiple constraint beamformer is then given by

$$\mathbf{w}_{\mathrm{MCS}} = \mathbf{K}^{-1}\mathbf{H}(\mathbf{H}^T\mathbf{K}^{-1}\mathbf{H})^{-1}\Lambda^{-1}\Gamma^T\mathbf{c}. \tag{43}$$

We choose the desired response $\mathbf{c}$ to be

$$\mathbf{c} = \mathbf{P}^T\mathbf{h}_1, \tag{44}$$

where $\mathbf{h}_1$ is that weight vector that maximizes the average gain achieved against spatially uncorrelated noise over all signal perturbations, and corresponds to the first column, denoted $\mathbf{h}_1$, of the matrix $\mathbf{H}$. Substituting (44) into (42) and using (41) we obtain the eigenvector constraint equation

$$\mathbf{H}^T\mathbf{w} = \mathbf{H}^T\mathbf{h}_1 = \mathbf{e}_1, \tag{45}$$

where $\mathbf{e}_1=[1,0,...,0]^T$. Finally, using (48), the weight vector (46) can be rewritten as

$$\mathbf{w}_{\mathrm{MCS}} = \mathbf{K}^{-1}\mathbf{H}(\mathbf{H}^T\mathbf{K}^{-1}\mathbf{H})^{-1}\mathbf{e}_1, \tag{46}$$

so that the output beamformer is

$$B_{\mathrm{MCS}}(\hat{x}) = \mathbf{e}_1^T[\mathbf{H}^T\mathbf{K}^{-1}\mathbf{H}]^{-1}\mathbf{e}_1. \tag{47}$$

F. Numerical results: Forced vibrations of simply supported beam

We apply, through numerical simulation, MFP techniques used in ocean acoustics to localize the source of vibrations in the beam described in Sec. II. For all cases, the values used for all calculations are as follows: $L=20$ m, $m_0=451.44$ kg/m, $E=109.0\times10^9$ Pa, $I=8450\times10^{-6}$ m^4, $F=75\,000$ N, exciting frequency $f=1000$ Hz. The material constants are that for rolled steel.[10,17] The number of ''sensors'' is 17 and for some processors, we use as few as 5 sensors. This choice is dictated by the fact that at 1000 Hz, the dominant mode is the 12th mode. The scanning step size is 0.1 m. In order for the CSDM matrix to be invertible, ''white noise'' was added by setting all diagonal elements of $\mathbf{K}$ equal to $K_{ii}=K_{ii}+0.1K_{11}$.

Figure 2 shows results when the Bartlett and the MV beamformers are employed to locate an exciting force located at $x=6$ m. The processor's output is expressed in terms of decibels (dB$=10.0\ \log|B|$ *re*: 1 m^2). For this simple forced vibration case the exact known solution has been used for both the data and the replica vectors, while scanning along the beam for the force position. The MV has high resolution while suppressing side lobes. However the MV is high resolution in all parameters and degrades rapidly if the

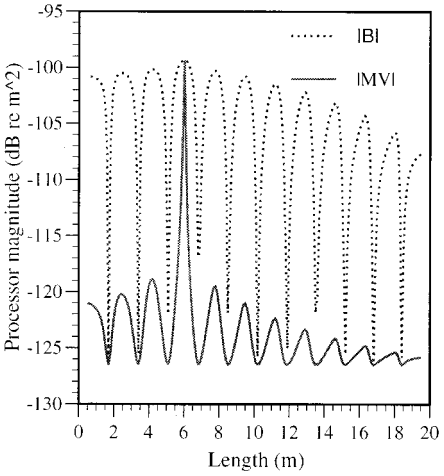

FIG. 2. Bartlett and MV beamformers (17 sensors) for a 20-m-long simply supported beam excited by a point force located at $x=6$ m.

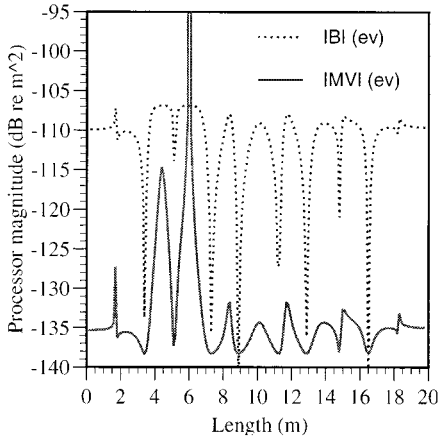

FIG. 4. Bartlett and MV eigenvectors beamformers (five sensors) for a 20-m-long simply supported beam excited by a point force located at $x=6$ m.

replica solutions are not exact. Figure 3 depicts the results for five sensors: the MV still ''locates'' the source for this ''sparse'' array, but the number of sensors are insufficient for the Bartlett to successfully locate the source.

Figure 4 shows results for the same settings as Fig. 3 for the eigenvector version of the Bartlett and MV processors. The CSDM decomposition yields, in this case, one eigenvalue belonging to the signal space and (for the case of five sensors) four eigenvalues belonging to noise space. The peak of the eigenvector MV processor is truncated to maintain the same scale as Fig. 3 but actually the magnitude of the eigenvector MV tends to infinity at the source location for this ideal example.

Figure 5 is a modal beamformer for 17 modes. Although in this case the modal beamformer does not illustrate any significant improvements on the results obtained from the previous beamformers, it is however introduced here, as it is often a more advantageous method in the case of correlated noise and low signal-to-noise ratios with correlated noise. There also may be some computational advantages.

III. MFP FOR COMPLEX STRUCTURES

In this section we consider vibrations of a beam in the presence of one (or more) springs (or lumped masses). An example of such a system is depicted in Fig. 6. We refer to such a system as a constrained structure.[10] The detailed solutions for such cases are summarized in the Appendix. We are interested in exploring what the effect of adding constraints (whose location and nature are potentially unknown) to the system, when trying to localize the exciting force by the MFP techniques described above. The analysis and equations are motivated by Ref. 4.

A. Lateral forced vibrations of constrained beam

Consider a simply supported beam constrained by a single spring. The solution is given by Eq. (A3) and in matrix form by Eq. (A4), which we rewrite as

$$[\mathbf{Z}_0(\omega)+\mathbf{Z}_\mathbf{L}(\omega)]\overline{\mathbf{q}}=\mathbf{f}, \tag{48}$$

where $\mathbf{Z_0}(\omega)$ is a diagonal matrix corresponding to the impedance matrix of the problem without any springs present, and $\mathbf{Z_L}(\omega)$ is a symmetric matrix containing the contribution(s) of the spring(s). We are interested in finding out how ''small'' $\mathbf{Z_L}$ has to be in order to be considered a perturba-

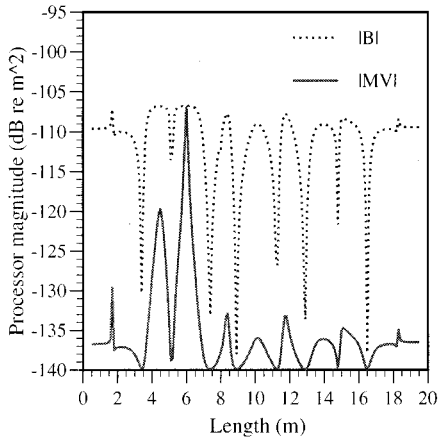

FIG. 3. Bartlett and MV beamformers (five sensors) for a 20-m-long simply supported beam excited by a point force located at $x=6$ m.

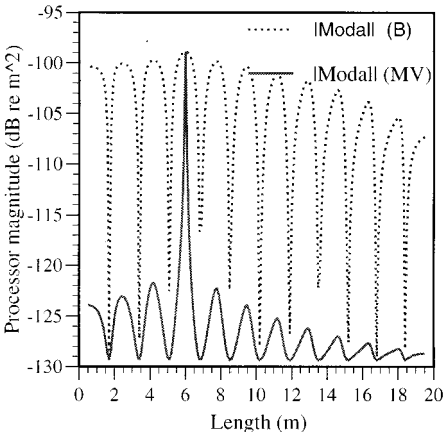

FIG. 5. Modal beamformer for a 20-m-long simply supported beam excited by a point force located at $x=6$ m.

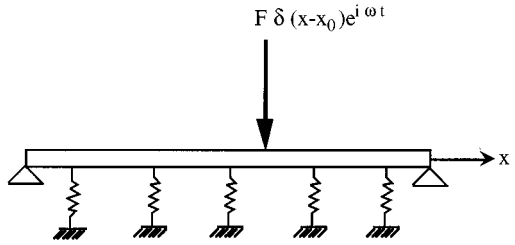

FIG. 6. Simply supported constrained beam excited by harmonic point force at $x=x_0$.

tion on $\mathbf{Z}_0$, i.e., by how much does $\mathbf{Z_0}^{-1}$ differs from $[\mathbf{Z_0}+\mathbf{Z_L}]^{-1}$. Equation (48) can be further simplified to

$$\mathbf{Z}_0[\mathbf{I}-\mathbf{T}]\overline{\mathbf{q}}=\mathbf{f}, \tag{49}$$

where $\mathbf{T} = \mathbf{Z_0}^{-1}\mathbf{Z_L}$. If $\mathbf{Z_0}^{-1}$ and $[\mathbf{Z_0}+\mathbf{Z_L}]^{-1}$ are nonsingular we can the write the solution of this problem as

$$\overline{\mathbf{q}}=[\mathbf{I}-\mathbf{T}]^{-1}\mathbf{Z_0}^{-1}\mathbf{f}. \tag{50}$$

Since $\mathbf{Z_0}$ is nonsingular, we are left with exploring the conditions for which $[\mathbf{I}-\mathbf{T}]^{-1}$ exists. $[\mathbf{I}-\mathbf{T}]$ is nonsingular[18] as long as $\|\mathbf{T}\|<1$, where $\|\mathbf{T}\|$ signifies a consistent matrix norm on $\mathfrak{R}^{n\times n}$ satisfying $\|\mathbf{I}\|=1$. For this particular case we choose to work with the ∞ norm defined as

$$\|\mathbf{T}\|_\infty=\max\left(\sum_{j=1}^{N}|\mathbf{T}_{ij}|:i=1,2,\ldots,N\right), \tag{51}$$

where N denotes the number of columns in the matrix (in our case this is the number of modes in the solution). When only one spring is present the elements of matrix $\mathbf{T}$ are of the form

$$T_{ij}=\frac{-k\varphi_i(a)\varphi_j(a)}{\rho(\omega_i^2-\omega^2)}. \tag{52}$$

Now $\varphi_i(x) = \sqrt{2/L}\,\sin(\beta_n x)$ so $|\varphi_i\varphi_j|\leqslant 2/L$. Consequently for each coefficient we have

$$\|T_{ij}\|\leqslant\left|\frac{2k}{\rho L(\omega_i^2-\omega^2)}\right|, \tag{53}$$

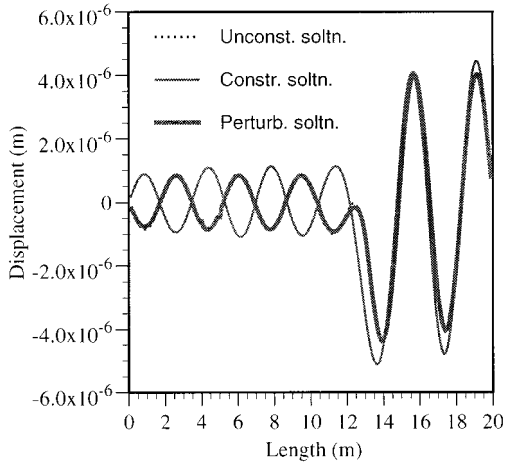

FIG. 7. Displacements along a 20-m beam constrained by six springs (each with spring constant $k=3.4e9$ N/m) and excited by a point force at $x=13$. Inequality (56) has been satisfied.

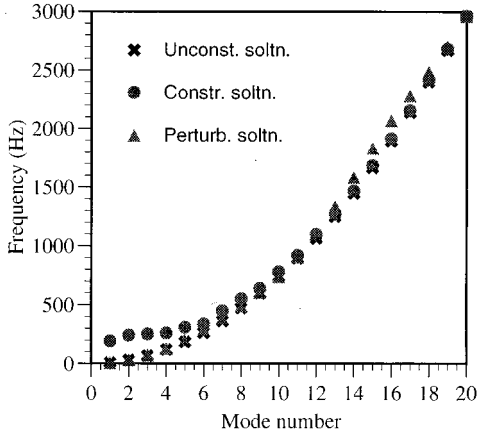

FIG. 8. Frequencies of vibration for the first 20 modes for a 20-m beam constrained by six springs (each with spring constant $k=3.4e9$ N/m) and excited by a point force at $x=13$. Inequality (56) has been satisfied.

so that

$$\sum_{j=1}^{N}|T_{ij}|\leqslant\left|\frac{2Nk}{\rho L(\omega_i^2-\omega^2)}\right|, \quad i=1,2,\ldots,N. \tag{54}$$

Finally, this quantity is maximized at resonance when $\omega_i=\omega_r$ (where ω_r is the resonant frequency of the unconstrained system).

In conclusion, we have

$$\|T\|_\infty\lessdot| \text{ when } k\leqslant\left|\frac{(\omega_r^2-\omega^2)\rho L}{2N}\right|. \tag{55}$$

If there are J equal springs the estimate for k becomes

$$k\leqslant\left|\frac{(\omega_r^2-\omega^2)\rho L}{2NJ}\right|. \tag{56}$$

The condition that $\|\mathbf{T}\|<1$ allows us to rewrite (50) in terms of the perturbation expansion:

$$\overline{\mathbf{q}}=[\mathbf{Z_0}^{-1}+\mathbf{T}\mathbf{Z_0}^{-1}+\cdots]\mathbf{f}. \tag{57}$$

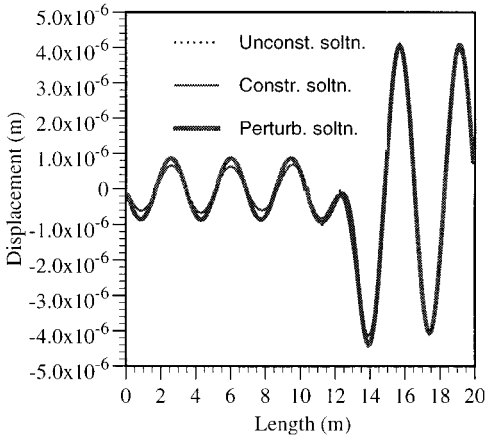

FIG. 9. Displacements along a 20-m beam constrained by six springs (each with spring constant $k=3.4e8$ N/m) and excited by a point force at $x=13$. Inequality (56) has been satisfied.

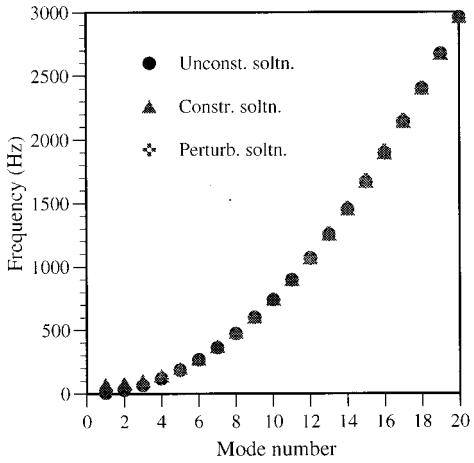

FIG. 10. Frequencies of vibration for the first 20 modes for a 20-m beam constrained by 6 springs (each with spring constant $k=3.4e9$ N/m) and excited by a point force at $x=13$. Inequality (56) has been satisfied.

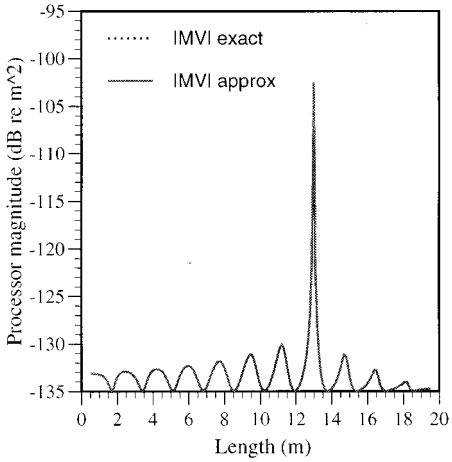

FIG. 12. MV beamformer for a 20-m beam constrained by six springs (each with spring constant $k=3.4e8$ N/m) and excited by a point force at $x=13$. Inequality (56) has been satisfied. For the approximate case, solution of unconstrained beam has been used for replica vector.

B. Numerical results

We consider a beam constrained by six springs located at $x=2$, 4, 7, 11, 14, and 17 m and excited by a point force located at $x=13$ m. We first compare the behavior of three different solutions [unconstrained (simple beam), constrained (exact), and perturbed solution] for the displacement when k is that given by estimate (56) (with $N=12$ and $M=6$) which in this case yields $k=3.4e9$ N/m.

When the spring stiffness is set at this value, the displacements predicted by each solution are fairly close in magnitude, however the phase of the constrained solution is different from the approximations' (Fig. 7). The frequencies of the solutions are also fairly close to each other although those for the exact solution begin to exhibit a deviation from the approximations' (Fig. 8). So, in fact, this estimate must be considered as a upper limit for the validity of the perturbation approximation.

For a value of k ten times smaller than the estimate given by (56), the unconstrained (simple beam), constrained and perturbed solutions are fairly close together (Fig. 9) and so are the frequencies (Fig. 10) except for the first four.

We first investigate the efficiency of two of the simplest processors. Bartlett and minimum variance (MV). Figures 11 and 12 show results when these beamformers are employed to locate the exciting force, located at $x=13$ m. Each figure shows two cases. In one case the exact known solution has been used for both the data and the replica vectors, while in another case the replica vector is derived from the solution to an unconstrained beam. In this regime, the resonant frequency of the system has not changed too drastically: the resonant frequency of the constrained system is $\omega_{12}=1066$ Hz, to be compared to $\omega_{12}=1070$ Hz of the unconstrained system (the 12th mode is the dominant mode for both constrained and unconstrained systems).

Next we increase the value of k hundred-fold to $k=3.4e10$ N/m. Figure 13 shows the behavior of three different solutions for the displacement in this regime. The unconstrained (simple beam) and the perturbed solutions do not adequately describe the displacement as correctly depicted by the constrained solution. The frequencies of the con-

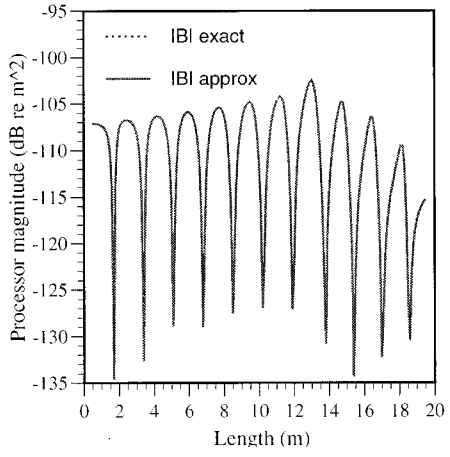

FIG. 11. Bartlett beamformer for a 20-m beam constrained by six springs (each with spring constant $k=3.4e8$ N/m) and excited by a point force at $x=13$. Inequality (56) has been satisfied. For the approximate case, solution of unconstrained beam has been used for replica vector.

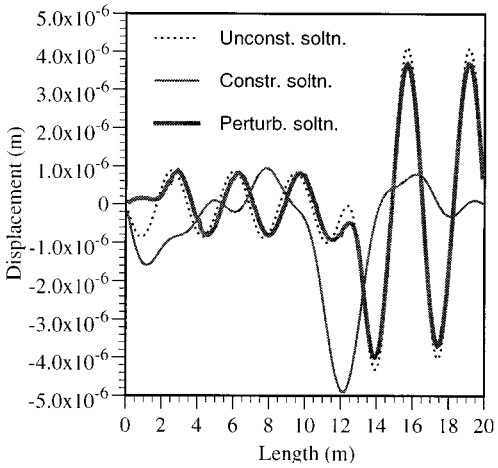

FIG. 13. Displacements along a 20-m beam constrained by six springs (each with spring constant $k=3.4e10$ N/m) and excited by a point force at $x=13$. Inequality (56) has not been satisfied.

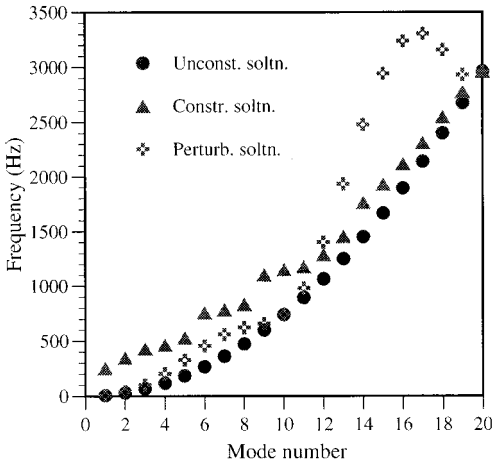

FIG. 14. Frequencies of vibration for the first 20 modes for a 20-m beam constrained by six springs (each with spring constant $k=3.4e10$ N/m) and excited by a point force at $x=13$. Inequality (56) has not been satisfied.

strained system do not match those of the simple beam until mode 20. The resonant frequency of the system is now $\omega_9=1104$ Hz, which is to be compared to $\omega_{12}=1070$ Hz of the unconstrained system (the 9th mode is the dominant mode for the constrained system) (Fig. 14).

For the large spring constant case, Figs. 15 and 16 show that the beamformers with the approximate solution do not work.

Finally we consider the MCS processor. This processor ''scans'' through perturbations of the exact solution consisting of random spring locations and random spring stiffness. Results vary but are promising. Two cases are illustrated in Figs. 17–19. When the system is weakly constrained, the MCS processor has no problem localizing the source by scanning through random spring locations and random stiffnesses. The accuracy of the solution varies with the choice of stiffness scanning range, but given a wide enough stiffness range to scan over ($3.4e7<k<8.3e8$), the MCS solution matches that obtained with the Bartlett processor.

When the system is highly constrained ($k=3.4e10$), the choice of range of spring stiffness for the solutions to scan

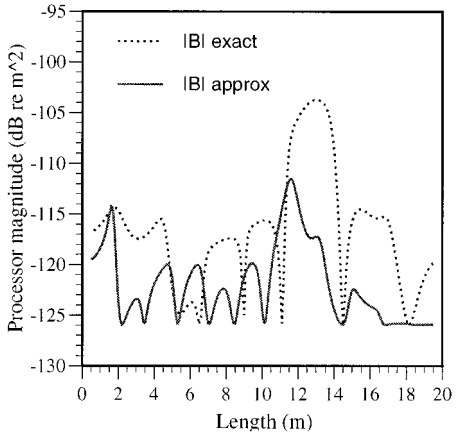

FIG. 15. Bartlett beamformer for a 20-m beam constrained by six springs (each with spring constant $k=3.4e10$ N/m) and excited by a point force at $x=13$. Inequality (56) has not been satisfied. For the approximate case, solution of unconstrained beam has been used for replica vector.

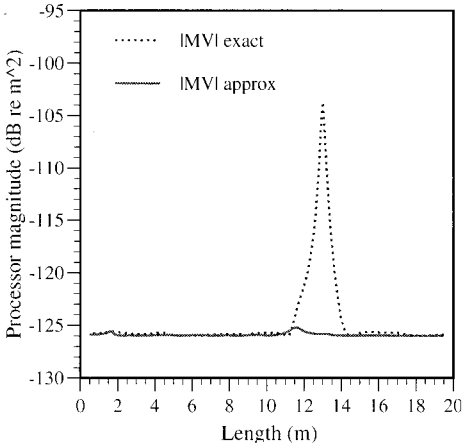

FIG. 16. MV beamformer for a 20-m beam constrained by six springs (each with spring constant $k=3.4e10$ N/m) and excited by a point force at $x=13$. Inequality (56) has been satisfied. Solution of unconstrained beam has been used for replica vector.

through must be more restricted than the above example for localization to be achieved (Fig. 18). Localization is also achieved when the solution involves two random parameters (stiffnesses and location) (Fig. 19). Note that in the latter two cases, the Minimum Variance processor without accurate replicas completely fails.

IV. APPLICATIONS: NONDESTRUCTIVE TESTING

A motivation for this work has been to use MFP methods as a means of nondestructive testing. For example, we would like to be able, by analyzing the vibrations of a given structure, to localize sources of changes in the known vibratory signature of such structure.

Consider a 20-m beam constrained by six springs (located at $x=2,4,7,11,14,17$). Now assume one of the springs has weakened. Figure 20 shows the displacement for such a beam due to a 75 000-N force located at $x=13$ m, both for

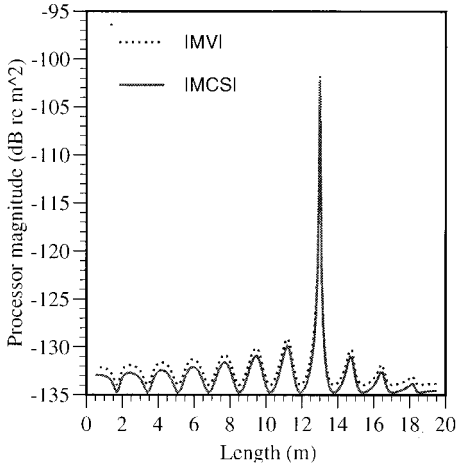

FIG. 17. MCS beamformer for a 20-m beam constrained by six springs (each with spring constant $k=3.4e8$ N/m) and excited by a point force at $x=13$. Inequality (56) has been satisfied. Replicas are exact solution with random spring locations and stiffness ($3.4e7<k<8.3e8$, 20 solutions, 17 eigenvalues).

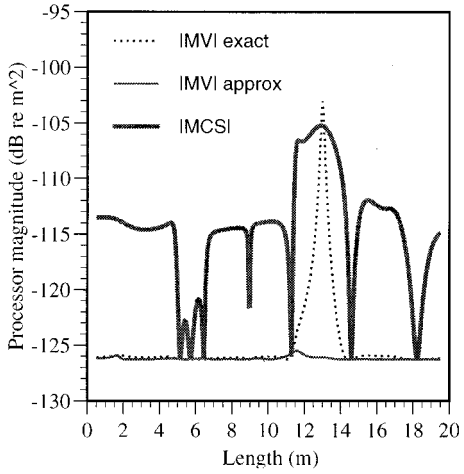

FIG. 18. MCS beamformer for a 20-m beam constrained by six springs (each with spring constant $k=3.4e10$ N/m) and excited by a point force at $x=13$. Inequality (56) has not been satisfied. Replicas are exact solution with random spring stiffness ($3.0e10<k<3.6e10$, 20 solutions, 14 principal values).

the case of no weakened springs ($k=8.07e9$ N/m), and one weakened spring ($k=8.07e6$ N/m) located at $x=7$.

The magnitude of the minimum variance processor (MV) at the force location will be at a maximum when the correct replica (i.e., the assumed solution contains a weakened spring at the correct location) is utilized. This result can be seen in Fig. 21.

The MV processor's high resolution also works to our advantage in another way since it can locate the weakened spring with quite a small number of sensors (Fig. 22), which in real life would translate to cost effectiveness. The method also works well in localizing more than one weakened spring, as it can be seen in Fig. 23.

V. CONCLUSION

We have applied matched-field methods from ocean acoustics to study a structural vibration problem. Four dis-

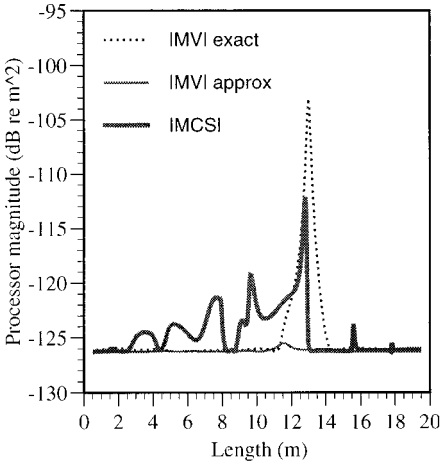

FIG. 19. MV-MC beamformer for a 20-m beam constrained by six springs (each with spring constant $k=3.4e10$ N/m) and excited by a point force at $x=13$. Inequality (56) has not been satisfied. Replicas are exact solution with random spring locations and stiffnesses ($3.0e10<k<3.6e10$, 20 solutions, 14 principal values).

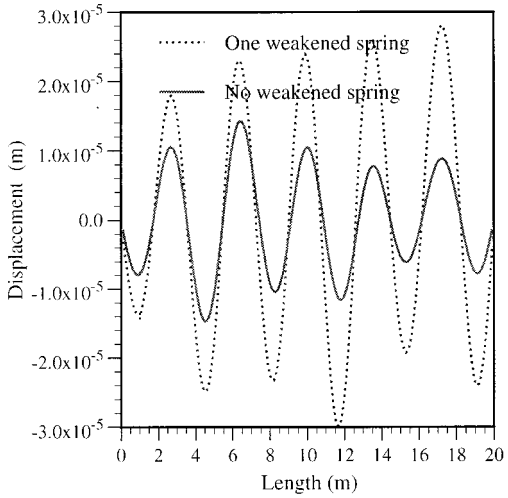

FIG. 20. Displacement of a 20-m beam constrained by six springs and excited by a point force at $x=13$.

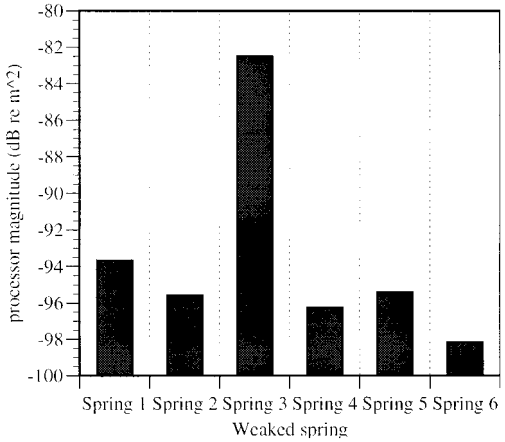

FIG. 21. Magnitude of MV processor (20 sensors) at exciting force location for a beam constrained by six springs. The third spring has been weakened by a factor of 1000.

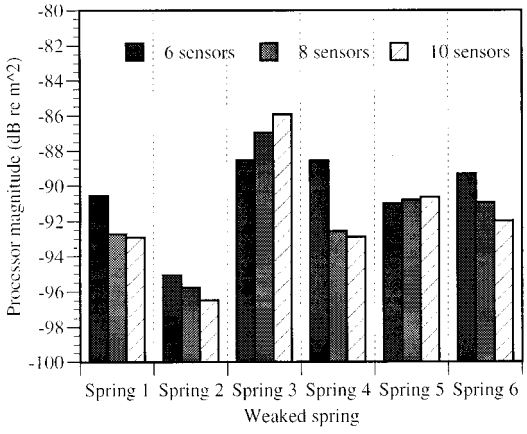

FIG. 22. Magnitude of MV processor (for six, eight, and ten sensors) at exciting force location for a beam constrained by six springs. The third spring has been weakened by a factor of 1000.

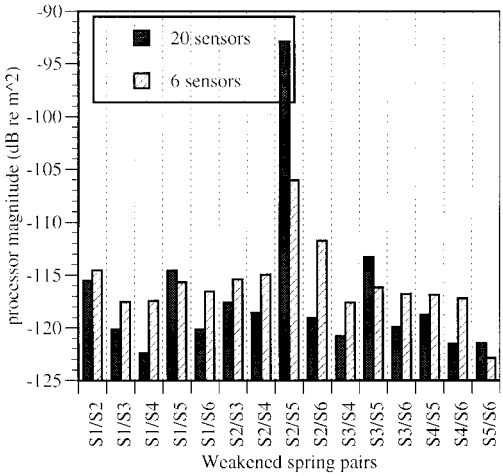

FIG. 23. Magnitude of MV processor (20 and 6 sensors) at exciting force location for a beam constrained by six springs. The second and fifth springs has been weakened by a factor of 1000.

tinct MFP techniques used in ocean acoustics have been applied to the problem of localizing the source of lateral vibrations of a simply supported beam. All methods were successful in locating the source when the exact solution was used for the replicas. In the case of a constrained system, i.e., a more complex system, a limiting value of the stiffness of the constraints was calculated beyond which beamformers will fail unless the exact solution to the full problem is known. A more ''tolerant'' beamformer which can perform adequately with incomplete replica information (MCS) was also demonstrated to partially address this circumstance. Finally, we successfully applied the method to the problem of localizing a weakened spring in the case of a constrained system. This is especially interesting in view of applying MFP methods to nondestructive testing.

In conclusion, although we have selected a simple test example, it appears that matched-field processing may be a promising technique to apply to an assortment of structural vibration problems. An important next step would be applying the MFP method to realistic problems with noise for which data are available or can be obtained, and to also apply broad band processing which has been used in ocean MFP.[1]

ACKNOWLEDGMENTS

We would like to thank Dr. David Feit for discussions on structural vibrations issues. This work was supported by ONR Contract No. N00014-90-J-1275 and NSWC Contract No. N00167-95-M-6298.

APPENDIX

In case of a linear spring (Fig. 6), the force exerted on the beam is equal to

$$F(a,t) = -ky(a,t) = -k\sum_{m=0}^{\infty} q_m(t)\varphi_m(a). \tag{A1}$$

It follows that for a point force excited beam constrained by a spring the equation of motion is

$$\ddot{q}_n(t) + \omega_n^2 q_n(t) = \frac{1}{M_n}\left[-k\varphi_n(a)\sum_{m=0}^{\infty} q_m(t)\varphi_m(a) + F\varphi_n(x_0)e^{i\omega t}\right]. \tag{A2}$$

Assuming harmonic time dependence for the generalized coordinates the solution to the nth equation is then

$$\overline{q_n} = \frac{1}{\rho(\omega_n^2-\omega^2)}\left[-k\varphi_n(a)\sum_{m=0}^{\infty}\overline{q_m}\varphi_m(a) + F\varphi_n(x_0)\right], \tag{A3}$$

which, written in matrix form becomes

$$\begin{bmatrix} \rho(\omega_1^2-\omega^2)+k\varphi_1^2(a) & k\varphi_1(a)\varphi_2(a) & \cdots & k\varphi_1(a)\varphi_m(a) \\ k\varphi_2(a)\varphi_1(a) & \ddots & \cdots & \vdots \\ \vdots & \vdots & \ddots & \vdots \\ k\varphi_m(a)\varphi_1(a) & \cdots & \cdots & \rho(\omega_m^2-\omega^2)+k\varphi_m^2(a) \end{bmatrix} \begin{Bmatrix} \overline{q_1} \\ \vdots \\ \vdots \\ \overline{q_m} \end{Bmatrix} - \begin{Bmatrix} F\varphi_1(x_0) \\ \vdots \\ \vdots \\ F\varphi_m(x_0) \end{Bmatrix}. \tag{A4}$$

The determinant formed by the coefficients of the $\overline{q_m}$, with F set equal to 0, will lead to the natural frequencies of the constrained system. The effect of spring(s) is to increase the natural frequencies of the system.

If the beam is loaded with a lumped mass m_0, the force exerted on the beam is equal to

$$F(b,t) = -m_0\ddot{y}(b,t) = -m_0\sum_{m=0}^{\infty}\ddot{q}_m(t)\varphi_m(b). \tag{A5}$$

It follows that for a point force excited beam loaded with a lumped mass the equation of motion is

$$\ddot{q}_n(t) + \omega_n^2 q_n(t) = \frac{1}{M_n}\left[-m_0\varphi_n(b)\sum_{m=0}^{\infty}\ddot{q}_m(t)\varphi_m(b) + F\varphi_n(x_0)e^{i\omega t}\right]. \tag{A6}$$

Assuming harmonic time dependence for the generalized coordinates the solution to the nth equation is then

$$\overline{q_n}=\frac{1}{\rho(\omega_n^2-\omega^2)}\left[\omega^2 m_0\varphi_n(b)\sum_{m=0}^{\infty}\overline{q_m}\varphi_m(b)+F\varphi_n(x_0)\right]. \tag{A7}$$

The determinant formed by the coefficients of the $\overline{q_m}$, with F set equal to 0, will lead to the natural frequencies of the constrained system. The effect of addition of lumped masses is to decrease the natural frequencies of the system.

[1] A. B. Baggeroer, W. A. Kuperman, and P. N. Mikhalevsky, ''An overview of matched field methods in ocean acoustics,'' IEEE J. Oceanic Eng. **18**, 401–424 (1993).

[2] D. H. Johnson, ''The application of spectral estimation methods to bearing estimation problems,'' Proc. IEEE **70**, 1018–1028 (1982).

[3] A. Tolstoy, *Matched Field Processing for Underwater Acoustics* (World Scientific, Singapore, 1993).

[4] S. M. Ziola and M. R. Gorman, ''Source location in thin plates using cross correlation,'' J. Acoust. Soc. Am. **90**, 2551–2556 (1991).

[5] C. Pezerat and J. L. Guyader, ''Two inverse methods for localization of external sources exciting a beam,'' Acta Acust. **3**, 1–10 (1995).

[6] D. Bray and D. McBride, *Nondestructive Testing Techniques* (Wiley, New York, 1992).

[7] D. E. Bray and R K. Stanley, *Nondestructive Evaluation, A Tool in Design, Manufacturing and Service* (McGraw-Hill, New York, 1989).

[8] P. M. Akerberg, B. H. Jansen, and R. D. Finch, ''Neural net-based monitoring of steel beams,'' J. Acoust. Soc. Am. **98**, 1505–1509 (1995).

[9] C. Soize, ''A model and numerical method in the medium frequency range for vibroacoustic predictions using the theory of structural fuzzy,'' J. Acoust. Soc. Am. **94**, 849–865 (1993).

[10] W. T. Thomson, *Theory of Vibration with Applications* (Prentice-Hall, Englewood Cliffs, NJ, 1981), 2nd ed.

[11] M. C. Junger and D. Feit, *Sound, Structures, and their Interaction* (MIT Cambridge, MA, 1986).

[12] F. B. Jensen, W. A. Kuperman, M. B. Porter, and H. Schmidt, *Computational Ocean Acoustics* (AIP Press, New York, 1994).

[13] R. O. Schmidt, ''Multiple emitter location and signal parameter estimation,'' IEEE Trans. Antennas Propag. **AP34**, 276 (1986).

[14] T. C. Yang, ''A method of range and depth estimation by modal decomposition,'' J. Acoust. Soc. Am. **82**, 1736–1745 (1987).

[15] H. Schmidt, A. B. Baggeroer, W. A. Kuperman, and E. K. Scheer, ''Environmentally tolerant beam-forming for high-resolution matched field processing: deterministic mismatch,'' J. Acoust. Soc. Am. **88**, 1851–1862 (1990).

[16] J. L. Krolik, ''Matched field minimum variance beamforming in a random ocean channel,'' J. Acoust. Soc. Am. **92**, 1408–1419 (1992).

[17] F. P. Beer and J. E. R. Johnston, *Mechanics of Materials* (McGraw-Hill, New York, 1981).

[18] G. W. Stewart, *Introduction to Matrix Computations* (Academic, New York, 1973).

Mean and mean-square responses of a prototypical master/fuzzy structure

R. L. Weaver
Department of Theoretical and Applied Mechanics, University of Illinois, Urbana, Illinois 61801

(Received 29 April 1996; accepted for publication 22 October 1996)

Analytical estimates are made for mean and mean-square transient responses of a single degree of freedom master oscillator attached to an undamped N degree of freedom random substructure. The ensemble averaged response is found to be, asymptotically for a large number of substructural degrees of freedom, in accord with the predictions of the Pierce–Sparrow–Russell theory. In particular the mean response of the master oscillator manifests an apparent damping. Corrections to this behavior are also predicted, but are found to lie well below the root-mean-square level of the fluctuations. The corrections are therefore, for practical purposes, unimportant. The ensemble average of the square of the response is also investigated and found to take a value at later times that is in accord with simple equipartition arguments advanced in an earlier paper. The power spectral density of the late time behavior is shown to be proportional to the square of the power spectrum of the early time response, and thus to be a narrower-band process than that of the early time behavior. Numerical simulations are presented which agree with the analytical predictions at moderate times, but also show an enhanced backscatter that develops over longer time scales. © *1997 Acoustical Society of America.* [S0001-4966(97)02903-2]

PACS numbers: 43.40.At, 43.40.Qi [CBB]

INTRODUCTION

In recent years the structural acoustics community has considered a proposal by Soize[1,2] that the effect of complex uncertain substructures, when attached to a simple master structure, may be represented by means of the impedance presented to the master structure. In the parlance of the field the substructure is termed a ''fuzzy substructure.'' The idea has been amplified in recent work by Pierce *et al.*[3,4] and by Strasberg and Feit.[5] Ruckman,[6] and Ruckman and Feit[7] have provided reviews and tutorials. In all this work the impedance presented to the master structure has been found to have a dissipative real part that corresponds to an effective damping, and a reactive imaginary part which is of somewhat less interest. In the limit that the substructure has many many degrees of freedom, it was found that the resulting effective impedance is smooth and independent of the details of the substructure. The derivations require certain assumptions, amongst which, as emphasized by Strasberg and Feit,[5] is the assumption that there is sufficient damping in the substructure. In this case their conclusion is clearly sound: the master oscillator manifests an apparent damping that is independent of the precise degree and mechanism of damping in the substructure. If however, the substructure has insufficient damping to justify the approximations, the conclusion is more problematic.

Recently Weaver[8] considered the system of Fig. 1 as a simple prototype of an undamped master/fuzzy structure. Weaver argued, and showed numerically, that the above conclusion is correct even if the substructure lacks damping, *if* one confines attention to early times. His numerical solutions showed, furthermore, that at later times the master structure oscillates in a random fashion with a mean-square amplitude that appears to be in accord with an SEA-like equipartition argument.

It is the intention of this paper to explore these questions analytically. An analytic theory for the system of Fig. 1 is presented that supports the observations made in Ref. 8. In the following sections a procedure (related to certain methods in quantum field theory used in recent years for studying the electronics of disordered structures) is introduced for calculating response moments. Mean and mean-square responses are then evaluated. Mean responses are calculated to be different from, but practically indistinguishable from, the responses predicted by others.[3–5] The mean-square calculations show that variances are small at early times: i.e., that mean responses are, at those times, good estimates of actual responses. The more careful analysis therefore proves that the simple theory[3–5] is valid for these early times. This is in accord with the observations and arguments made earlier.[8] The mean-square amplitude is calculated at later times also and found to be in accord with the equipartition argument advanced previously.[8] In the last section the results are successfully compared to numerical simulations. At extremely late times, however, an enhanced backscatter is observed that was not predicted.

I. THEORY: PRELIMINARIES

Much of the preliminary theory for the system of Fig. 1 is given in Ref. 8. That derivation is not repeated here. Nevertheless there are some issues that require emphasis. Among these is a matter related to the existence of the Fourier transform as a distribution. The Fourier transform is defined here with a negative sign in the exponent,

$$\tilde{y}(\omega) \equiv \int_{-\infty}^{\infty} y(t) \exp\{-i\omega t\} dt, \tag{1}$$

 0001-4966/97/101(3)/1441/9/$10.00

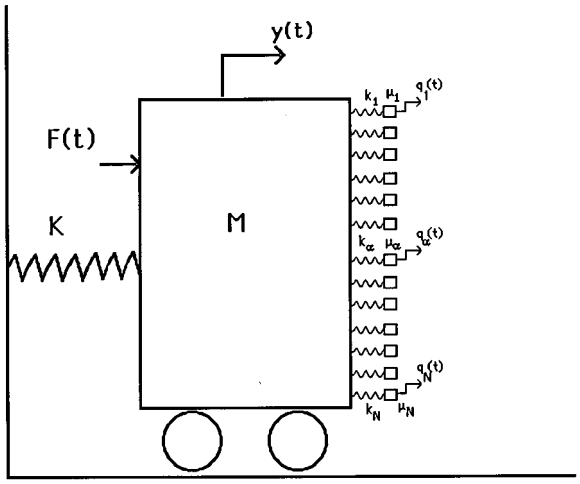

FIG. 1. A master structure consisting of the mass M and stiffness K described by the coordinate $y(t)$ is attached to a many degree of freedom fuzzy substructure consisting of masses μ_α and stiffnesses k_α described by coordinates $q_\alpha(t)$ and having isolated natural frequencies $\omega_\alpha=\sqrt{k_\alpha/\mu_\alpha}$.

in such a way that causality (the vanishing of forces and responses for negative values of time) assures that the Fourier transforms are analytic functions in the lower half-complex ω plane. Thus, a nominally real frequency ω needs to be understood as having an infinitesimal negative imaginary part, $\omega\rightarrow\omega-\imath\varepsilon$. For real ω the Fourier transform is defined only in the limit as ε vanishes. In that limit the Fourier transform is a distribution, not a function. ε may ultimately be made to vanish, but only after other manipulations are completed. The term in ε may be thought of as representing a small amount of damping. The analysis presented in this paper is, however, for the case of ε infinitesimal. Rather than representing a damping, ε should therefore be thought of as merely a device, from the theory of distributions and Fourier transforms, that assures causality; its presence assures that one is solving a problem with quiescent initial conditions.

After Fourier transforming and eliminating the degrees of freedom, q_α, of the substructure, a single equation is derived for the response G of the master to a unit impulsive excitation applied to the master:

$$(K-M\omega^2)\tilde{G}(\omega)-\tilde{V}(\omega)\tilde{G}(\omega)=1. \tag{2}$$

The ''scattering potential'' V presented to the master by the substructure is given by

$$\tilde{V}(\omega)\equiv\sum_\alpha \tilde{v}_\alpha(\omega)\equiv\omega^2\sum_\alpha \frac{\mu_\alpha}{[1-(\omega-i\epsilon)^2/\omega_\alpha^2]}, \tag{3}$$

where the ω_α^2 are defined as the ratios of the stiffnesses and masses of the individual oscillators in the substructure; $\omega_\alpha^2=k_\alpha/\mu_\alpha$. It can be seen that the term in ϵ allows resolution of the singularities.

If the number of degrees of freedom, N, of the fuzzy is large, but in such a fashion that the individual masses μ_α of the fuzzy are small, the sum, (3) it has been presumed,[3–5] can be replaced with an integral and V found to be a smooth complex function of frequency. The replacing of the sum by an integral is, however, a questionable step. Indeed, for $N<\infty$, V, Eq. (3), is a highly discontinuous function of ω. Were it a smooth function of ω, the replacement of the sum with an integral would be less problematic. As emphasized by Strasberg and Feit[5] the introduction of damping sufficient to provide for modal overlap in the substructure would make it smooth. Weaver[8] emphasized that, *if* interest is confined to early times, then introduction of damping does not change responses. He concluded that the simple theory[3–5] for effective damping applies at early times even in undamped systems.

If, however, interest is also directed towards later times, and in undamped systems with finite N, there is at present no theory for the response. Such a theory is presented here.

II. MEAN RESPONSES

For purposes of definiteness a particular distribution for the masses and stiffnesses within the substructure is considered here. All stiffnesses k_α are chosen equal, at a value of order $1/N$; $k_\alpha=k=\kappa K/N$, with κ of order unity and dimensionless. Values of κ that are somewhat less than unity are probably the most relevant in practice, as one usually wishes to consider a master structure that is only moderately perturbed by the substructure. Such values of κ will assure that the loss tangent associated with the effective damping is less than unity. The masses μ_α are taken from the associated substructure frequencies $\omega_\alpha(\mu_\alpha=k_\alpha/\omega_\alpha^2)$ and these frequencies are chosen from a distribution

$$\begin{aligned} &p(\omega_1,\omega_2,\omega_3,\ldots,\omega_N)=\prod_\alpha p(\omega_\alpha);\\ &p(\omega_\alpha)=\frac{\omega_0/\pi}{\omega_0^2+\omega_\alpha^2}\quad(-\infty<\omega_\alpha<\infty). \end{aligned} \tag{4}$$

This corresponds to a smoothed modal density within the substructure of

$$\rho(\omega)=\frac{2N}{\pi}\frac{\omega_0}{\omega_0^2+\omega^2}\quad(0<\omega<\infty), \tag{5}$$

with a characteristic frequency ω_0 and a smoothed spectral mass density

$$m(\omega)=\kappa\frac{K\omega_0}{\pi\omega^2}\frac{2}{\omega_0^2+\omega^2}\quad(0<\omega<\infty). \tag{6}$$

The distribution has been chosen so as to allow easy analytic evaluation of certain integrals. It is not expected that the choice will affect the conclusions of this paper. This distribution also has the peculiar property of corresponding to a finite total stiffness κK, but a total mass with infinite expectation: $\langle\Sigma\mu_\alpha\rangle=\infty$. It could be modified so as to have a finite value for both quantities, at a cost of a slight additional complexity.

Ensemble average of a quantity $f(\omega_1,\omega_2,\ldots,\omega_N)$ is indicated by brackets $\langle f\rangle$, and is evaluated by the multiple integral:

$$\langle f\rangle=\prod_\alpha\int_{-\infty}^{\infty}p(\omega_\alpha)d\omega_a\quad f(\omega_1,\omega_2,\ldots,\omega_N). \tag{7}$$

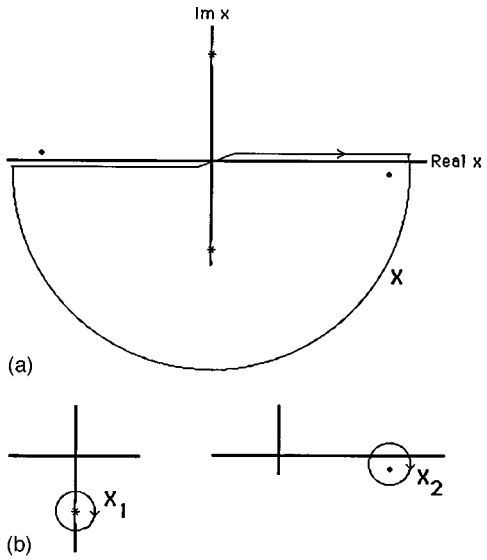

FIG. 2. (a) The contour for the evaluation of the integral of Eqs. (10) and (17). (b) The contours for the evaluation of the contributions of each singularity.

The mean impulse response is given, in the frequency domain, by the average of the solution of Eq. (2):

$$\langle \widetilde{G}(\omega)\rangle = \left\langle \frac{1}{-M\omega^2+K-\widetilde{V}(\omega)} \right\rangle . \tag{8}$$

The Pierce–Sparrow–Russell (PSR)[3,4] expression for the response is given by replacing V with its average:

$$\widetilde{G}^{\,\mathrm{PSR}}(\omega) \equiv \frac{1}{-M\omega^2+K-\langle \widetilde{V}(\omega)\rangle} . \tag{9}$$

That (8) and (9) are not equal in general follows from the observation that the average of an inverse is not in general the inverse of the average. Here, $\langle V\rangle = \langle \Sigma v\rangle$ is

$$\begin{aligned} \langle \widetilde{V}(\omega)\rangle &= \sum_{\alpha=1}^{N} \int_{-\infty}^{\infty} d\omega_\alpha \, p(\omega_\alpha) \, \frac{k_\alpha \omega^2}{\omega_\alpha^2-\omega^2} \\ &= \kappa\omega^2 K \int_{-\infty}^{\infty} dx \, \frac{p(x)}{[x^2-(\omega-i\epsilon)^2]} \\ &= \kappa\omega^2 K \int_{-\infty}^{\infty} dx \, \frac{\omega_0/\pi}{x^2+\omega_0^2} \, \frac{1}{x^2-(\omega-i\epsilon)^2} . \end{aligned} \tag{10}$$

This integral may be done by analytic continuation and evaluation of residues. There are simple poles in the lower half x plane, at $x=\omega-i\epsilon$ and at $x=-i\omega_0$. (See Fig. 2.) The term in ϵ has allowed unambiguous identification of the position of the poles near $x=\pm\omega$. The result is

$$\langle \widetilde{V}(\omega)\rangle = -\kappa\omega^2 K \left[\frac{1}{\omega^2+\omega_0^2} + i \, \frac{\omega_0/\omega}{\omega^2+\omega_0^2} \right] . \tag{11}$$

Thus the PSR impulse response function is given by

$$\begin{aligned} \widetilde{G}^{\,\mathrm{PSR}}(\omega) &= 1/[K-M\omega^2+i\kappa\omega\omega_0 K/(\omega^2+\omega_0^2) \\ &\quad +\kappa\omega^2 K/(\omega^2+\omega_0^2)] \equiv \frac{1}{KA(\omega)} , \end{aligned} \tag{12}$$

which serves also to define the quantity $A(\omega)$.

For values of κ that are small enough that the substructure only slightly modifies the behavior of the master, G^{PSR} may be approximated by its behavior in the vicinity of the dominating poles near $\omega = \sqrt{K/M}$:

$$\widetilde{G}^{\,\mathrm{PSR}}(\omega) \approx \frac{1}{K} \left(1 - \frac{\omega^2}{\omega_{\mathrm{PSR}}^2} + i \, \mathrm{sgn}(\omega) \, \alpha_{\mathrm{PSR}} \, \frac{2M}{K} \right)^{-1} , \tag{13}$$

where

$$\begin{aligned} \omega_{\mathrm{PSR}} &\equiv \sqrt{\frac{K}{M+\kappa K/(K/M+\omega_0^2)}} \approx \sqrt{\frac{K}{M}} \equiv \omega_b , \\ \alpha_{\mathrm{PSR}} &\equiv \frac{\kappa\omega_0\omega_{\mathrm{PSR}}^2}{2(\omega_{\mathrm{PSR}}^2+\omega_0^2)} = \frac{c_{\mathrm{eff}}(\omega_{\mathrm{PSR}})}{2M} \, \frac{\omega_{\mathrm{PSR}}^2}{K/M} \approx \frac{c_{\mathrm{eff}}(\omega_{\mathrm{PSR}})}{2M} \end{aligned} \tag{14}$$

corresponding to a damped simple harmonic oscillator with a frequency ω_{PSR} and a decay rate $\sim\exp(-\alpha_{\mathrm{PSR}}t)$. It has been, and will continue to be, occasionally convenient to disregard the small difference (at moderate values of κ) between ω_{PSR} and $\sqrt{K/M}$.

Notwithstanding the attractiveness and simplicity of the Pierce *et al.*[3,4] and Strasberg and Feit[5] arguments, it may also be desirable to attempt a derivation which does not depend on a limit of infinite N or on an assumption of sufficient damping in the substructure. An appeal to well developed formal methods for mean solutions of stochastic differential equations is therefore indicated. There is a substantial literature treating responses of disordered linear systems. Among the more popular methods are those sometimes termed multiple scattering methods in which the response (2) is expanded in a Born–Neumann series of powers of the perturbing potential V.[9] The infinite series so obtained is averaged and the result resummed. This author is not comfortable with the notion of a power series in an unbounded quantity. He nevertheless found that the multiple scattering method did yield reasonable answers for mean responses $\langle G\rangle$. The author was, however, unable to apply the methods successfully for the case of $\langle G^2\rangle$. In lieu of the multiple scattering method therefore a different procedure is followed here. The method is related to certain path integral procedures used in quantum field theory in recent years for studying the electronics of disordered structures (see, e.g., Ref. 10).

The exact, nonstochastic, response is given formally by Eq. (2); which is difficult to average as it stands. The exact response is also given by the following expression:

$$\begin{aligned} K\widetilde{G}(\omega) = -i \int_0^{\infty} dy \, \exp\Bigg\{ iy \left(1 - \frac{(\omega-i\epsilon)^2}{\omega_b^2} \right) \\ - iy \sum_{\alpha} \frac{v_\alpha}{K} \Bigg\} , \end{aligned} \tag{15}$$

where the quantity ω_b is the frequency of the bare master; $\omega_b^2 = K/M$. The integral converges by virtue of the positive

quantity ϵ.[11] Equation (15) is a formal identity which may be established simply by doing the integration with respect to y. The variable y has little physical significance. The virtue of this representation for G is that it may be averaged. We exchange the order of integrations and obtain

$$K\langle\widetilde{G}(\omega)\rangle=-i\int_0^\infty dy\ \exp\left\{iy\left(1-\frac{\omega_{-i\epsilon}^2}{\omega_b^2}\right)\right\}\times\prod_{\alpha=1}^{N}\int_{-\infty}^{\infty}d\omega_\alpha\, p(\omega_\alpha)\exp\left\{-\frac{iyv_\alpha}{K}\right\}$$
$$=-i\int_0^\infty dy\ \exp\{iy(1-(\omega-i\epsilon)^2/\omega_b^2)\}X^N, \quad (16)$$

where

$$X\equiv\langle\exp\{-iyv_\alpha/K\}\rangle=\int_{-\infty}^{\infty}dx\ \frac{\omega_0}{\pi}\frac{1}{x^2+\omega_0^2}\times\exp\left\{-iy\ \frac{\kappa}{N}\frac{(\omega-i\epsilon)^2}{x^2-(\omega-i\epsilon)^2}\right\}. \quad (17)$$

Here, X may be evaluated exactly by analytic continuation. As illustrated in Fig. 2, there are nonanalyticities at $x=\pm i\omega_0$ and at $x=\pm(\omega-i\epsilon)$. In the lower half x plane there is a simple pole at $x=-i\omega_0$, and an essential singularity at $x=\omega-i\epsilon$. The term in ϵ has allowed unambiguous identification of the position of that singularity. We write X as the sum of the contributions from each singularity in the lower half-plane: $X=X_1+X_2$. The contribution from the simple pole is

$$X_1=\exp\left\{iy\ \frac{\kappa}{N}\frac{\omega^2}{\omega^2+\omega_0^2}\right\} \quad (18)$$

and the contribution from the essential singularity is

$$X_2=-\frac{\kappa y\omega\omega_0}{N(\omega^2+\omega_0^2)}. \quad (19)$$

It is the Nth power of X which is needed, so, as $X^N=\exp\{N\ln X\}$, we construct an asymptotic estimate for $\ln X$:

$$\ln X=\frac{\kappa\xi}{N}\left(i-\frac{\omega_0}{\omega}\right)+\frac{\kappa^2\xi^2}{2N^2}\left(\frac{2i\omega_0}{\omega}-\frac{\omega_0^2}{\omega^2}\right)+\cdots, \quad (20)$$

where the quantity ξ is defined by

$$\xi=y\omega^2/(\omega^2+\omega_0^2). \quad (21)$$

This allows an asymptotic estimate for X^N:

$$X^N=\exp\{N\ \ln\ X\}\approx\exp\left\{\kappa\xi\left(i-\frac{\omega_0}{\omega}\right)\right\}\times\exp\left\{\frac{\kappa^2\xi^2}{2N}\left(\frac{2i\omega_0}{\omega}-\frac{\omega_0^2}{\omega^2}\right)+\cdots\right\} \quad (22)$$

and, by means of Eq. (16), a corresponding estimate for $\langle G\rangle$.

If the second factor is ignored as being, for large N, essentially unity, it is found that

$$K\langle\widetilde{G}\rangle=-i\int_0^\infty dy\ \exp\left\{iy\left(1-\frac{(\omega-i\epsilon)^2}{\omega_b^2}\right)+\frac{iy\kappa\omega^2}{(\omega^2+\omega_0^2)}-\frac{y\kappa\omega\omega_0}{(\omega^2+\omega_0^2)}\right\}$$
$$\equiv-i\int_0^\infty dy\ \exp\{iyA(\omega)\}$$
$$=1/A(\omega), \quad (23)$$

or

$$\langle\widetilde{G}\rangle=\widetilde{G}^{\ \mathrm{PSR}}. \quad (24)$$

The mean impulse response is, to leading order at large N, equal to the PSR impulse response. This is one of the chief results of this section.

The next correction may be obtained by retaining the second factor in Eq. (22);

$$K\langle\widetilde{G}(\omega)\rangle=-i\int_0^\infty dy\ \exp\{iyA(\omega)\}\exp\{-y^2B(\omega)/N\}, \quad (25)$$

where

$$B(\omega)=\frac{\kappa^2\omega^4}{2(\omega^2+\omega_0^2)^2}\left[\frac{\omega_0^2}{\omega^2}-\frac{2i\omega_0}{\omega}\right]. \quad (26)$$

The second factor has a significant effect on the integrand only for y greater than or of the order of $(N/|B|)^{1/2}$. For such large values of y, however, the first factor has a magnitude of the order of $\exp\{-(2N)^{1/2}\}\ll 1$. One concludes that these large values of y are unimportant in the evaluation of the integration (25); the second factor may be ignored.

At late times, however, the inverse Fourier transform reconstruction of $\langle G(t)\rangle$ can be very sensitive to slight errors in $\langle\widetilde{G}(\omega)\rangle$. Some indication of the form taken by $\langle G(t)\rangle$ at finite N and late time may be found by assuming that $\omega=\omega_b$ is the important part of the inverse Fourier transform, thus

$$K\langle\widetilde{G}(\omega)\rangle=-i\int_0^\infty dy\ \exp\{2iy(\omega_b-\omega)/\omega_b+iy\kappa\omega_b^2/(\omega_b^2+\omega_0^2)-\kappa\omega_b\omega_0/(\omega_b^2+\omega_0^2)-B(\omega_b)y^2/N\}+\text{c.c.}. \quad (27)$$

The inverse Fourier transform to the time domain is then obtained, from inspection, after making the change of variables $y=\omega_b t/2$:

$$K\langle G(t)\rangle=\frac{\omega_b}{2i}\exp\left\{i\left(\omega_b+\frac{\kappa\omega_b^3}{2(\omega_b^2+\omega_0^2)}\right)t-\frac{\kappa\omega_0\omega_b^2}{(\omega_b^2+\omega_0^2)}\ t\right\}\exp\{-t^2\omega_b^2B(\omega_b)/4N\}+\text{c.c.}, \quad (28)$$

where c.c. indicates a complex conjugate. The effect of the correction is to multiply the simply damped PSR oscillation

by a very slowly decaying Gaussian function of time. The Gaussian correction is important only for times of the order or greater than $(2/\omega_b)(N/B(\omega_b))^{1/2}$. At these times G^{PSR} has decayed by a factor of $\exp\{-(2N)^{1/2}\}$ and is very small anyway. As will be seen in the next section, the fluctuating part $\langle G^2(t)\rangle^{1/2}$ dominates the low amplitude of the mean response $\langle G(t)\rangle$ at these late times. These Gaussian corrections to the PSR response are therefore arguably irrelevant and would in any case be very hard to detect.

III. MEAN-SQUARE RESPONSES

It is also useful to consider the square of the response

$$E(t)=G^2(t), \tag{29}$$

which is called E in deference to its interpretation as, after multiplying by K, the strain energy in the master spring. Its Fourier transform is

$$\begin{aligned}\widetilde{E}(\Omega)&\equiv\int_0^\infty G^2(t)\exp\{-i(\Omega-i\delta)t\}dt\\&=\int_{-\infty}^\infty G^2(t)\exp\{-i(\Omega-i\delta)t\}dt\\&=\frac{1}{4\pi^2}\int_{-\infty}^\infty\exp\{-i\Omega t-\delta t\}\int_{-\infty}^\infty\widetilde{G}(\omega)e^{i\omega t}\,d\omega\\&\quad\times\int_{-\infty}^\infty\widetilde{G}^*(\omega')e^{-i\omega' t}\,d\omega'\,dt\\&=\frac{1}{2\pi}\int_{-\infty}^\infty\left[\widetilde{G}\left(\omega+\frac{\Omega-i\delta}{2}-i\epsilon\right)\right.\\&\quad\left.\times\widetilde{G}^*\left(\omega-\frac{\Omega-i\delta}{2}+i\epsilon\right)\right]d\omega.\end{aligned} \tag{30}$$

A small positive quantity δ that assures the analyticity of the transform has been introduced above. It will now be suppressed until it is needed. We also define a smoothed and averaged $E(t)$

$$E'(t)\equiv\frac{1}{2\pi}\int_{-\infty}^\infty\widetilde{E}(\Omega)\exp\{i\Omega t\}W(\Omega)d\Omega, \tag{31}$$

where the filter function W is constructed to cut off rapid temporal fluctuations of $E(t)$ in a smooth fashion (this will aid in the evaluation of integrals later)

$$W(\Omega)\equiv\frac{\Omega_0^2}{\Omega_0^2+\Omega^2}, \tag{32}$$

and Ω_0^{-1} is some characteristic time scale, long compared to $1/\omega_b$, over which one is willing to smooth. With these definitions one finds that

$$\begin{aligned}\langle E'(t)\rangle&=\frac{1}{4\pi^2K^2}\int_{-\infty}^\infty\int_{-\infty}^\infty d\omega\,H(\omega,\Omega)\\&\quad\times\exp(i\Omega t)W(\Omega)d\Omega,\end{aligned} \tag{33}$$

where the key quantity of interest H has been defined by

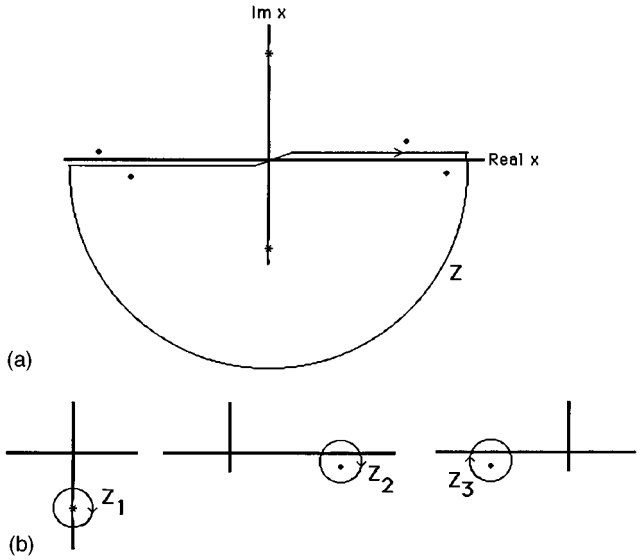

FIG. 3. (a) The contour for the evaluation of the integral of Eq. (36). (b) The contours for the evaluation of each contribution to Z.

$$H(\omega,\Omega)\equiv\left\langle K^2\widetilde{G}\left(\omega+\frac{\Omega}{2}-i\epsilon\right)\widetilde{G}^*\left(\omega-\frac{\Omega}{2}+i\epsilon\right)\right\rangle, \tag{34}$$

and it is understood that the ''outer frequency'' Ω is much less than the ''inner'' or carrier frequency ω. It is for H that we now construct a field theoretic description.

As before G may be represented by expression (15). We append a similar representation for G^* and take an average:

$$\begin{aligned}H=&\int_0^\infty\int_0^\infty dy\,dy'\,\exp\left\{iy\left[1-\left(\omega+\frac{\Omega}{2}-i\epsilon\right)^2\Big/\,\omega_b^2\right]\right.\\&\left.-iy'\left[1-\left(\omega-\frac{\Omega}{2}+i\epsilon\right)^2\Big/\,\omega_b^2\right]\right\}\\&\times\prod_{\alpha=1}^N\int_{-\infty}^\infty d\omega_\alpha p(\omega_\alpha)\exp\{-iyv_\alpha/K+iy'v_\alpha^*/K\},\end{aligned} \tag{35}$$

where v and v^* are defined by Eq. (3) but now with the implicit understanding of the respective substitutions $\omega\to\omega+\Omega/2-\iota\epsilon$ and $\omega\to\omega-\Omega/2+\iota\epsilon$.

The latter part of (35) consists of N identical factors of Z, where Z is

$$\begin{aligned}Z\equiv&\frac{\omega_0}{\pi}\int_{-\infty}^\infty dx\,\frac{1}{x^2+\omega_0^2}\\&\times\exp\left\{-iy\,\frac{\kappa}{N}\,\frac{\omega^2}{x^2-(\omega+\Omega/2-\iota\epsilon)^2}\right.\\&\left.+iy'\,\frac{\kappa}{N}\,\frac{\omega^2}{x^2-(\omega-\Omega/2+\iota\epsilon)^2}\right\}.\end{aligned} \tag{36}$$

As illustrated in Fig. 3, this integrand, when analytically extended, has simple poles at $x=\pm i\omega_0$ and essential singularities at $x=\pm(\omega+\Omega/2-\iota\epsilon)$ and $x=\pm(\omega-\Omega/2+\iota\epsilon)$. We close the contour in the lower half-plane, as in Fig. 3(a), and represent Z exactly as the sum of three contributions, one from

the contour around each singularity in the lower half-plane. $Z=Z_1+Z_2+Z_3$. Z_1 is the contribution from the simple pole at $x=-i\omega_0$:

$$Z_1=\exp\left\{ i\,\frac{\kappa}{N}\,\omega^2\left[\frac{y}{\omega_0^2+(\omega+\Omega/2)^2}-\frac{y'}{\omega_0^2+(\omega-\Omega/2)^2}\right]\right\}, \tag{37}$$

$$Z_1\approx\exp\left\{ i\,\frac{\kappa}{N}\,\omega^2\,\frac{y-y'}{\omega_0^2+\omega^2}\right\}.$$

Z_2 is the contribution from the singularity at $x=\omega+\Omega/2-\iota\epsilon$:

$$Z_2=-\frac{\omega\omega_0}{(\omega^2+\omega_0^2)}\,\frac{\kappa}{N}\,y\,\exp\left\{ iy'\,\frac{\kappa}{N}\,\frac{\omega}{2\Omega}\right\}. \tag{38}$$

Similarly,

$$Z_3=-\frac{\omega\omega_0}{(\omega^2+\omega_0^2)}\,\frac{\kappa}{N}\,y'\,\exp\left\{ iy\,\frac{\kappa}{N}\,\frac{\omega}{2\Omega}\right\}. \tag{39}$$

To leading order $\ln Z$ is then given by

$$\ln Z=\frac{1}{N}\left\{\frac{i\kappa\omega^2}{\omega^2+\omega_0^2}\,(y-y')-\frac{\kappa\omega\omega_0}{\omega^2+\omega_0^2}\times[ye^{iy'\kappa\omega/2N\Omega}+y'e^{iy\kappa\omega/2N\Omega}]\right\}+\cdots, \tag{40}$$

so Z^N is given, to leading order, by

$$Z^N=\exp\left\{\frac{i\kappa\omega^2}{\omega^2+\omega_0^2}\,(y-y')-\frac{\kappa\omega\omega_0}{\omega^2+\omega_0^2}\times[ye^{iy'\kappa\omega/2N\Omega}+y'e^{iy\kappa\omega/2N\Omega}]\right\}, \tag{41}$$

and H is, to this leading order,

$$H=\int_0^\infty\int_0^\infty dy\;dy'\times\exp\left\{ iy\left(1-\frac{(\omega+\Omega/2-i\epsilon)^2}{\omega_b^2}+\kappa\,\frac{\omega^2}{\omega^2+\omega_0^2}\right)-iy'\left(1-\frac{(\omega-\Omega/2+i\epsilon)^2}{\omega_b^2}+\kappa\,\frac{\omega^2}{\omega^2+\omega_0^2}\right)\right\}\times\exp\left\{-\frac{\kappa\omega\omega_0}{\omega^2+\omega_0^2}\,[ye^{iy'\kappa\omega/2N\Omega}+y'e^{iy\kappa\omega/2N\Omega}]\right\}. \tag{42}$$

If the product $N\Omega$ were treated as asymptotically large (while N is large, Ω is arbitrarily small, depending on the time scale one wishes to probe, so the treating of $N\Omega$ as large implies that Ω is in some sense not small, or that interest is in early times), then the integrals over y and y' would decouple:

$$H_{\Omega\gg\kappa\omega/N}=\int_0^\infty dy\,\exp\left\{ iy\left(1-\frac{\omega^2}{\omega_b^2}+\kappa\,\frac{\omega^2}{\omega^2+\omega_0^2}+i\,\frac{\kappa\omega\omega_0}{\omega^2+\omega_0^2}\right)\right\}\times\int_0^\infty dy\,\exp\left\{-iy'\left(1-\frac{\omega^2}{\omega_b^2}+\kappa\,\frac{\omega^2}{\omega^2+\omega_0^2}-i\,\frac{\kappa\omega\omega_0}{\omega^2+\omega_0^2}\right)\right\}=1/|A(\omega)|^2. \tag{43}$$

One concludes that at early times the mean-square response is the square of the mean. In accord with previous arguments,[8] fluctuations vanish at early times.

The chief interest is, however, with later times, for which the approximation $N\Omega$ large is not justified. In order to most easily evaluate $E'(t)$ at late times we define an intermediate quantity

$$\mathscr{E}(\omega,t)=\int_{-\infty}^\infty H(\omega,\Omega)W(\Omega)\exp(i\Omega t)\,d\Omega \tag{44}$$

and note

$$E'(t)=\frac{1}{4\pi^2K^2}\int_{-\infty}^\infty d\omega\,\mathscr{E}(\omega,t). \tag{45}$$

By exchanging the order of the Ω and y and y' integrations one constructs an expression for $\mathscr{E}(\omega,t)$

$$\mathscr{E}(\omega,t)\equiv\int_0^\infty\int_0^\infty dy\;dy'\,\exp\left\{ i(y-y')\times\left(1-\frac{\omega^2}{\omega_b^2}+\kappa\,\frac{\omega^2}{\omega^2+\omega_0^2}\right)\right\}e(y,y',t), \tag{46}$$

where

$$e(y,y',t)\equiv\int_{-\infty}^\infty\frac{\Omega_0^2}{\Omega_0^2+\Omega^2}\,\exp\{i\Omega t-i\Omega(y+y')\omega/\omega_b^2\}\times\exp\{-Dye^{iFy'/N\Omega}-Dy'e^{iFy/N\Omega}\}d\Omega, \tag{47}$$

and where D and F are defined by

$$D=\frac{\kappa\omega\omega_0}{\omega^2+\omega_0^2};\quad F=\frac{\kappa\omega}{2}. \tag{48}$$

We also recall that by Ω is meant $\Omega-i\delta$. Thus when the integral (47) over Ω is performed by evaluating residues, we must recognize that there are simple poles at $\Omega=\pm i\Omega_0$ and that there is an essential singularity at $\Omega=i\delta\sim0$.

The contour must be closed in the lower half Ω plane if $t<(y+y')\omega/\omega_b^2$. In this case one has only contributions from the pole at $\Omega=-\iota\Omega_0$. But for the late times of chief interest, the integral over y and y' will then be confined to only the largest values of $y+y'$, and the corresponding contribution to $\mathscr{E}$ unimportant compared to the contribution from smaller values of $y+y'$.

Thus, in the large t limit, the integral over Ω must be closed in the upper half-plane. There are contributions from the simple pole at $i\Omega_0$ and from the essential singularity at $\Omega=\iota\delta$:

$$e=e_1+e_2, \tag{49}$$

where e_1 is the contribution from the simple pole:

$$e_1=\pi\Omega_0\,\exp\{-\Omega_0(t-(y+y')\omega/\omega_b^2)\}$$
$$\times\exp\{-Dye^{Fy'/N\Omega_0}-Dy'e^{Fy/N\Omega_0}\}. \tag{50}$$

It is exponentially unimportant at large times. Thus e is dominated by e_2, the contribution from the essential singularity at $\Omega=\iota\delta$:

$$e\approx e_2=4\pi\,\frac{DFyy'}{N}\,\exp\{-D(y+y')\}. \tag{51}$$

If this expression is substituted into (46), one obtains, for late time,

$$\mathscr{E}(\omega,\infty)\equiv\frac{2\pi}{N}\int_0^\infty\int_0^\infty dy\;dy'yy'\,\frac{\kappa^2\omega^2\omega_0}{\omega^2+\omega_0^2}$$
$$\exp\left\{i(y-y')\left(1-\frac{\omega^2}{\omega_b^2}+\kappa\,\frac{\omega^2}{\omega^2+\omega_0^2}\right)\right\}$$
$$\exp\left\{-(y+y')\,\frac{\kappa\omega\omega_0}{\omega^2+\omega_0^2}\right\}$$
$$=\frac{2\pi}{N}\,\frac{\kappa^2\omega^2\omega_0}{\omega^2+\omega_0^2}\int_0^\infty\int_0^\infty dy\;dy'yy'$$
$$\times\exp\{iyA(\omega)-iy'A^*(\omega)\}$$
$$=\frac{2\pi}{N}\,\frac{\kappa^2\omega^2\omega_0}{\omega^2+\omega_0^2}\,\frac{1}{|A(\omega)|^4}. \tag{52}$$

This is presumably the power spectral density of the response at late times. It is noteworthy that it is centered at the same place ($\omega_{\rm PSR}$) as is the mean response $\approx\widetilde{G}^{\rm PSR}$. It is also noteworthy that it is proportional to the fourth power of $\langle\widetilde{G}(\omega)\rangle$, and so is a more strongly peaked function of frequency. In other words, the random process which is $G(t)$ at late times is narrower band than is the mean impulse response $\langle G(t)\rangle$.

The late time mean-square level is given by an integral (45) of the above expression. If that integral is approximated by the dominant contribution from the vicinity of the double poles in $|A|^{-4}$ near $\omega=\pm\omega_{\rm PSR}$, then

$$E'(\infty)\approx\frac{1}{2\pi K^2N}\,\frac{\kappa^2\omega_{\rm PSR}^2\omega_0}{\omega_{\rm PSR}^2+\omega_0^2}$$
$$\times\int_{-\infty}^{\infty}d\omega\left|1-\frac{\omega^2}{(\omega_{\rm PSR}+i\alpha_{\rm PSR})^2}\right|^{-4}$$
$$=\frac{1}{2\pi K^2N}\,\frac{\kappa^2\omega_{\rm PSR}^2\omega_0}{\omega_{\rm PSR}^2+\omega_0^2}*\int_{-\infty}^{\infty}d\omega$$
$$\times\left[1-\frac{\omega}{\omega_{\rm PSR}+i\alpha_{\rm PSR}}\right]^{-2}\left[1+\frac{\omega}{\omega_{\rm PSR}+i\alpha_{\rm PSR}}\right]^{-2}$$
$$\times\left[1-\frac{\omega}{\omega_{\rm PSR}-i\alpha_{\rm PSR}}\right]^{-2}\left[1+\frac{\omega}{\omega_{\rm PSR}-i\alpha_{\rm PSR}}\right]^{-2}. \tag{53}$$

On closing the contour in the upper half-plane, it is found that the first and fourth of the above factors contribute residues from the double poles at $\omega=\omega_{\rm PSR}+i\alpha_{\rm PSR}$ and $\omega=-\omega_{\rm PSR}+i\alpha_{\rm PSR}$, respectively. In the convenient limit in which we assume that $\alpha_{\rm PSR}\ll\omega_{\rm PSR}$, each double pole gives a contribution of $(\pi/32)\;{\omega_{\rm PSR}}^4{\alpha_{\rm PSR}}^{-3}$ (plus neglected terms of order α^{-2}.) One concludes

$$E'(\infty)=\frac{1}{32K^2N}\,\frac{\kappa^2\omega_{\rm PSR}^6\omega_0}{\omega_{\rm PSR}^2+\omega_0^2}\,\alpha_{\rm PSR}^{-3}$$
$$=\frac{1}{8K^2N}\,\omega_{\rm PSR}^2\,\frac{\omega_{\rm PSR}^2+\omega_0^2}{\omega_0}\,\alpha_{\rm PSR}^{-1}$$
$$=\frac{1}{4\pi}\,\frac{\omega_{\rm PSR}^2}{K^2}\,\frac{1}{\alpha_{\rm PSR}\rho(\omega_{\rm PSR})}. \tag{54}$$

This is the main result of this section. It may be interpreted as consistent with an SEA-like equipartition argument. The amount of energy originally deposited by the unit impulse is $1/2M$. The mean amount of strain energy stored in the spring K at late times is $KE(\infty)/2$, also equal to the mean amount of kinetic energy in the master oscillator at late times. The ratio of the mean amount of total energy at late times to that originally deposited is thus

$$\frac{\text{Energy in late time fluctuations}}{\text{Energy originally deposited}}$$
$$=2MKE(\infty)=\frac{1}{2\pi}\,\frac{M}{K}\,\frac{\omega_{\rm PSR}^2}{\alpha_{\rm PSR}\rho(\omega_{\rm PSR})}$$
$$\approx\frac{1}{2\pi\alpha_{\rm PSR}\rho(\omega_{\rm PSR})}. \tag{55}$$

It is seen that the master oscillator has, at late times, a share of the originally deposited energy, as if it were shared equally amongst the substructural modes within a band of width $2\pi\;\alpha_{\rm PSR}$. This was anticipated in an argument advanced earlier[8] based on equipartition notions from statistical energy analysis.

The present analysis has supported the inferences made in the earlier work.[8] It is concluded that the Master oscillator, and in particular the decay of its amplitude, is well described by the PSR theory. But that applicability is found to be confined to early times, before the coherent oscillations have decayed to the point at which they are comparable to the rising fluctuations. The energy in the coherent response, proportional to $|\langle G(t)\rangle|^2$, decays with time like $\exp(-2\alpha_{\rm PSR}t)$. It becomes comparable to the energy in the late time fluctuations at time $T=-\ln\{2\pi\alpha\rho\}/2\alpha_{\rm PSR}$. This time T may be identified as the limit of the validity of the PSR theory for undamped systems.

IV. NUMERICAL SIMULATIONS

In order to corroborate these results a numerical integration of the transient dynamics was undertaken. Many (400) equivalent samples were integrated. Ensemble averages of the solutions and square roots of ensemble averages of their squares are plotted below. The statistics used in the earlier[8] numerical investigation were retained; the masses of the oscillators in the substructure were fixed, and their frequencies ω_α were taken from an exponential distribution: $p(\omega_\alpha)=\exp(-\omega_\alpha)$. Here, M and K were chosen to be unity. In Fig. 4 the absolute value of the mean response, and the root-mean-square response, are plotted versus time for the

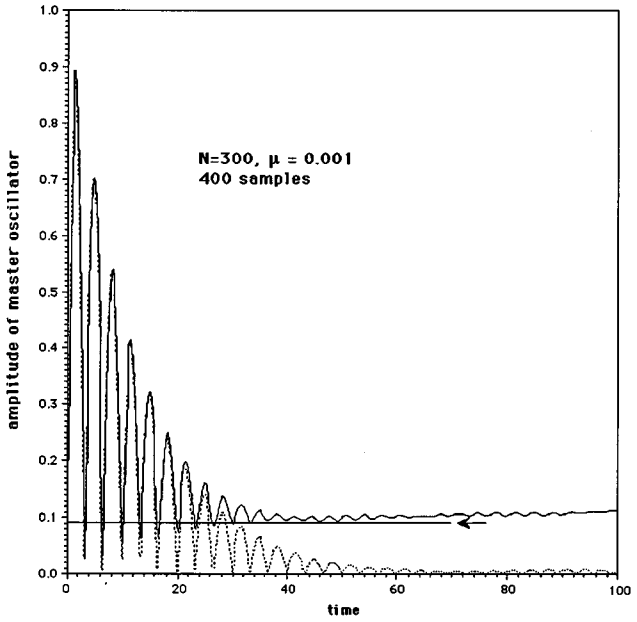

FIG. 4. Plots of numerically calculated absolute value of the mean (dotted line), and root-mean square (solid line), response of the master/fuzzy system of Ref. 8. The horizontal line and arrow is the prediction of Eq. (54).

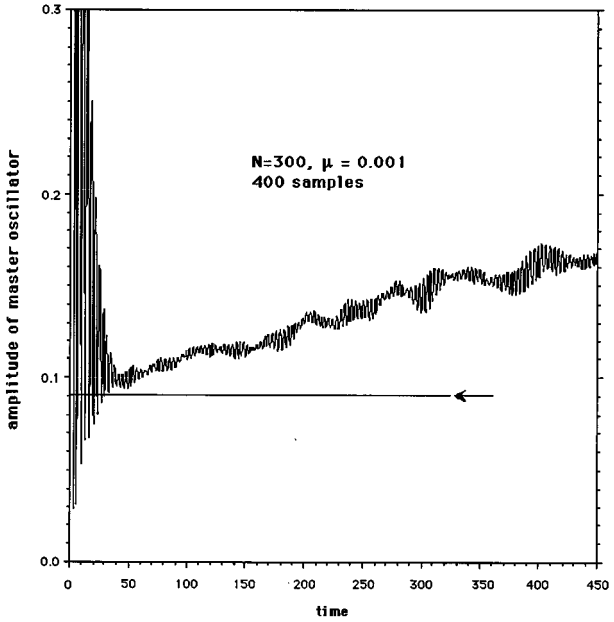

FIG. 5. The root-mean-square response of the system of Fig. 4 is studied over longer times. The discrepancy between theory and simulation is seen to grow.

case of $N=300$ substructural degrees of freedom, each with a small mass $\mu=0.001$. As predicted in the discussion following Eq. (43), there is little difference at early times, reflecting the small variance and weak fluctuations. At late times, however, the mean response has decayed to a level which is essentially zero. It is nonzero presumably only because of the finite number of samples, 400, averaged over. In contrast, the root mean-square response achieves an approximately constant value slightly higher than that predicted by the square root of Eq. (54) and indicated in the plot by the horizontal line and arrow. The agreement with theory is fairly good. The small difference is, though, intriguing. One is at first tempted to ascribe the slight difference to having had only a finite number of samples to average over, and to speculate that the difference would vanish as this number was increased. Alternatively one might ascribe the discrepancy to the neglect, here, of the slight difference between ω_{PSR} and $\sqrt{K/M}$, or to neglect of corrections of order α/ω. Such speculations are not confirmed by further study. Indeed, if the system studied in Fig. 4 is studied over longer times (Fig. 5) one sees that the difference grows with time.

The discrepancy does not grow indefinitely. Figure 6 shows the case of $N=200$, $\mu=0.0015$, again with 400 samples taken from the ensemble. These parameters correspond to the same value of effective damping, but to a smaller modal density ρ, so the predicted root-mean-square level is greater. It is seen in Fig. 6 that the actual root-mean-square level saturates at a value roughly 50% higher than predicted. (There are some residual fluctuations so this number is only approximate.) The saturation takes place on a time scale comparable to a time that would be required to resolve the modes, $\pi\rho=231$. These features, the final 50% discrepancy, and the time scale being of order $\pi\rho$, were observed over a range of system parameters with independent variations of N and μ. It is hypothesized here that these values are general.

This behavior is strongly reminiscent of the enhanced backscatter effect described recently in a room-acoustics context.[12] It was shown there that reverberant structural acoustic systems will show an enhancement of their energy densities at the position of the transient source, and that this enhancement grows in time by 50%, over a time scale of the order of $\pi\rho$. That the analytical calculation presented above has failed to predict the enhancement is not surprising; as

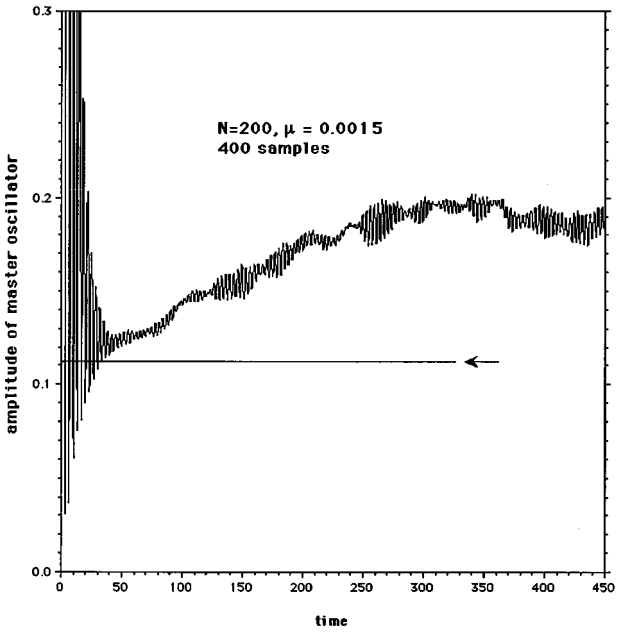

FIG. 6. A different system is studied, in which it can be seen that the discrepancy between theory and measurement ceases its growth, and does so at a time of order $\pi\rho$.

shown in Ref. 12 the effect depends on eigenfrequency correlations and can only be derived by means of random matrix theory or related methods. The present analytical derivation has, however, correctly described the level of backscatter at times short compared to $\pi\rho$.

V. CONCLUSIONS

An analytical theory has been presented for the calculation of mean and mean-square responses of an undamped master/fuzzy system. Ensemble average responses are found to agree, to high practical accuracy, with the simple predictions of Pierce *et al.* Calculated mean-square responses indicate that variances are small at early times and that therefore the mean response $\langle G \rangle$, which is very nearly equal to G^{PSR}, is a good representation of an actual response, at least for these early times. At later times, however, when the mean response has decayed to a level comparable to that of the late time random process, mean responses do not accurately describe actual responses. The period over which the simple theory is a good description depends on what that late time random process level is, but is typically only a couple of effective decay times. The analytic theory for the level of the late time random process is found to agree with SEA-like arguments. It also agrees with numerical simulations, but only for finite times. It disagrees on very late times scales comparable to the modal density. It is as yet unclear what analytical methods might be used to predict these very late time enhancements. It also remains to apply these methods to the cases of multidegree of freedom master structures, to nonlocal substructures, to coupled substructures, and to continuous systems.

ACKNOWLEDGMENTS

The author thanks the Institute for Theoretical Physics at UC—Santa Barbara for support while these calculations were done, and in particular Drs. Harsh Mathur and Yan Fyodorov for discussions. This work was supported by the office of Naval Research, Contract No. N00014-94-0855 and by the National Science Foundation through Grant No. NSF PHY94-07194.

[1] C. Soize, ''Probabilistic structural modeling in linear dynamic analysis of complex mechanical systems I. Theoretical elements,'' La Recherche Aerospatiale (English edition) **5**, 23–48 (1986).

[2] C. Soize, ''A model and numerical method in the medium frequency range for vibroacoustic predictions using the theory of structural fuzzy,'' J. Acoust. Soc. Am. **94**, 849–865 (1993).

[3] A. D. Pierce, V. W. Sparrow, and D. A. Russell, ''Fundamental structural-acoustic idealizations for structures with fuzzy internals,'' J. Vibration Acoust. **117**, 339–348 (1995).

[4] D. A. Russell, ''The theory of fuzzy structures and its application to waves in plates and shells,'' Ph. D. dissertation, The Pennsylvania State University, Graduate Program in Acoustics, State College, PA, 1995.

[5] M. Strasberg and D. Feit, ''Vibration damping of large structures induced by attached small resonant structures,'' J. Acoust. Soc. Am. **99**, 335–344 (1996).

[6] C. Ruckman, ''A review of publications related to fuzzy structures analysis'' (private communication) .

[7] C. E. Ruckman and D. Feit, ''A Tutorial on Soize's method for stochastic modeling in structural acoustics (Fuzzy Structures Analysis),'' *Proceedings of the ASME 15th Biennial Conference on Mechanical Vibration and Noise* (American Society of Mechanical Engineers, Boston, MA, 1995), pp. 241–246.

[8] R. Weaver, ''The effect of an undamped finite degree of freedom ''fuzzy'' substructure: numerical solutions and theoretical discussion,'' submitted to J. Acoust. Soc. Am. (January 1996).

[9] U. Frisch, ''Wave Propagation in Random Media,'' in *Probabalistic Methods in Applied Mathematics*, edited by T. Bharucha-Reid (Academic, New York, 1968), pp. 75–197.

[10] A. J. McKane and M. Stone, ''Localization as an alternative to Goldstone's Theorem,'' Ann. Phys. **131**, 36–55 (1981).

[11] The integral converges for positive ω. Responses may be constructed at real negative ω by means of the identity $G(-\omega) = G^*(\omega)$.

[12] R. Weaver and J. Burkhardt, ''Weak localization and enhanced backscatter in reverberation rooms and quantum dots,'' J. Acoust. Soc. Am. **96**, 3186–3190 (1995).

Reciprocity calibration of acoustic emission transducers in Rayleigh-wave and longitudinal-wave sound fields

Hajime Hatano
Department of Applied Electronics, Science University of Tokyo, Yamazaki, Noda, 278 Japan

Tetsuo Watanabe[a)]
Nippon Steel Corporation, Chiyoda-ku, Tokyo, 100-71 Japan

(Received 26 January 1996; revised 28 August 1996; accepted 15 October 1996)

A new system was developed for the reciprocity calibration of acoustic emission transducers in Rayleigh-wave and longitudinal-wave sound fields. In order to reduce interference from spurious waves due to reflections and mode conversions, a large cylindrical block of forged steel was prepared for the transfer medium, and direct and spurious waves were discriminated between on the basis of their arrival times. Frequency characteristics of velocity sensitivity to both the Rayleigh wave and longitudinal wave were determined in the range of 50 kHz–1 MHz by means of electrical measurements without the use of mechanical sound sources or reference transducers. © *1997 Acoustical Society of America.* [S0001-4966(97)02003-1]

PACS numbers: 43.40.Le, 43.35.Zc [PJR]

INTRODUCTION

Calibration of acoustic emission transducers is of significant importance in acoustic emission measurements.[1] As for the acoustic emission test equipment, electronic instruments such as amplifiers and filters can be calibrated easily by electrical means. Without calibrating transducers, overall characteristics of the test equipment cannot be determined. This means not just the quantitative evaluation, but even the mutual comparison of data obtained by different laboratories is difficult, unless an appropriate method of transducer calibration is established.[2]

For characterizing acoustic emission transducers, a number of methods utilizing various mechanical sound sources, for instance, a falling steel ball, a breaking pencil lead, a sand blast, and an electric spark, appeared in the literature.[1] Breckenridge developed the seismic surface pulse method wherein the breaking of a glass capillary is employed for the sound source and the capacitive transducer for the reference.[3–5]

Reciprocity calibration of acoustic emission transducers in a Rayleigh-wave sound field was formerly proposed by one of the authors.[6] However, since a steel plate was employed for the transfer medium, it was difficult to carry out the longitudinal-wave calibration, as well as to avoid the influence of reflections at the top and bottom of the plate. A new system for reciprocity calibration was developed in the hope of overcoming these problems. In order to reduce interference from spurious waves due to reflections and mode conversions, a large forged-steel block was prepared for the transfer medium, and direct and spurious waves were discriminated between on the basis of their arrival times. Frequency characteristics of velocity sensitivity to both the Rayleigh wave and longitudinal wave were determined in the range of 50 kHz–1 MHz.

[a)]Current address: 3-7-3, Hiyoshidai, Takatsuki, 569 Japan.

I. METHOD

A. Reciprocity calibration

In the reciprocity calibration, three reversible acoustic emission transducers 1, 2, and 3 are prepared, and three independent transmission/reception pairs are configurated through a transfer medium (see Fig. 1).[7–10] Voltages of transmission and reception signals, E_{Sij} and E_{0ij}, respectively, are measured on each pair, where the subscript ij corresponds to transducer i for transmission and j for reception. If the reciprocity parameter H, which is independent of transducer design, is given, absolute sensitivity is determined by purely electrical measurements without the use of mechanical sound sources or reference transducers. For instance, sensitivity of transducer 1 is given by

$$M_{01}=\left(\frac{1}{H}\frac{Z_1Z_3}{Z_2}\frac{E_{012}E_{S23}E_{031}}{E_{S12}E_{023}E_{S31}}\right)^{1/2}, \tag{1}$$

where Z_i is electrical impedance of transducer i.

Once reciprocity calibration has been carried out, sensitivity of an optional transducer, which is not necessarily reversible, can be determined by a relatively simple procedure by using the calibrated transducer as a reference for sound transmission or reception.[6]

B. Wave mode

In a bounded elastic medium, it is possible to propagate various wave modes, while acoustic emission transducers generally assume different sensitivities to different wave modes. For estimating actual characteristics of transducers, it is necessary in the calibration to use the wave mode identical to that of the acoustic emission waves detected in the actual objects.[6] Recently, application fields of acoustic emission measurements have expanded to include various bulky objects, for instance, thick-walled vessels and huge concrete structures. For such applications, sensitivity to longitudinal waves is of primary importance. In addition, longitudinal-

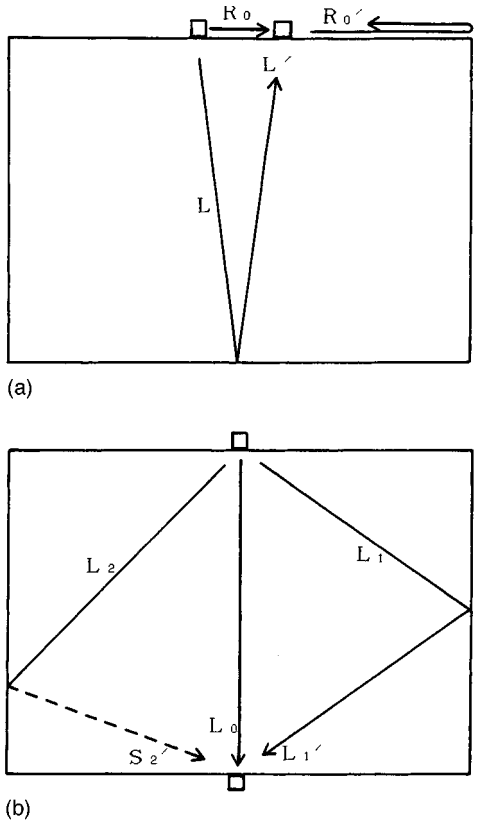

FIG. 1. Schematic illustration of transducer arrangements on a cylindrical medium and assumed paths of elastic waves. (a) Rayleigh-wave calibration. (b) Longitudinal-wave calibration.

wave sensitivity represents the fundamental characteristics of acoustic emission transducers, since these transducers usually employ thickness-mode piezoelectric elements, while Rayleigh-wave sensitivity is subject to the aperture effect of the transducer. In the new calibration system a longitudinal-wave sound field as well as a Rayleigh-wave sound field was employed.

C. Free-field sensitivity

For the calibration of acoustic emission transducers free-field velocity sensitivity M_0 was defined as

$$M_0 = E_0 / w_0, \tag{2}$$

where E_0 is the output open-circuit voltage and w_0 is the vertical component of displacement velocity of incident elastic wave at the point where the transducer is to be placed.[6]

In the conventional calibration of microphones and hydrophones, which are immersed in a fluid medium, sound pressure is taken as the measure of intensity of incident waves.[7,8] On the other hand, acoustic emission transducers are placed on the free surfaces of a solid medium, where it is difficult to measure the sound pressure since specific acoustic impedance of the ambient atmosphere is negligible compared to that of the solid. Consequently, sensitivity of acoustic emission transducers should be defined in terms of displacement of incident elastic waves, for instance, amplitude, velocity or acceleration instead of sound pressure.[6]

TABLE I. Constants in the reciprocity parameter for Rayleigh-wave calibration.

σ	X	Y
0.00	0.2844	1.1441
0.25	0.1835	1.0877
0.26	0.1800	1.0857
0.27	0.1765	1.0838
0.28	0.1731	1.0820
0.29	0.1697	1.0801
0.30	0.1664	1.0783
0.31	0.1631	1.0765
0.32	0.1598	1.0747
0.33	0.1566	1.0730
0.34	0.1535	1.0712
0.35	0.1504	1.0695

D. Reciprocity parameter

The reciprocity parameter for Rayleigh-wave calibration H_R was formerly derived from Lamb's theory as follows:

$$H_R = 2\pi f \frac{1+\sigma}{E} kX \left(\frac{2}{\pi k D_R} \right)^{1/2}, \tag{3}$$

where

$$k = 2\pi f Y \left(\frac{2(1+\sigma)\rho}{E} \right)^{1/2},$$

and D_R is the distance between the transmission and reception transducers, f is the frequency, and E, σ, and ρ are Young's modulus, Poisson's ratio, and density of the transfer medium, respectively.[6] Here, X and Y are constants obtained from the numerical solutions to Lamb's equation as a function of Poisson's ratio.[11] Table I shows corrected values of the constants X and Y, whereas some typing errors were found in the previous paper.

For longitudinal-wave calibration, the reciprocity parameter H_L was derived in the Appendix as

$$H_L = 2 f \frac{(1+\sigma)(1-2\sigma)}{E(1-\sigma) D_L}, \tag{4}$$

where D_L is the distance between the transmission and reception transducers in the longitudinal-wave calibration.

E. Transducer arrangement

In both the Rayleigh-wave and longitudinal-wave calibrations, a cylindrical solid block is commonly used for the transfer medium. Figure 1 shows schematically the transducer arrangements on the medium, and assumed propagation paths of various elastic waves. Figure 1(a) shows the setup for the Rayleigh-wave calibration. Both the transmission and reception transducers are placed on the top plane of the cylindrical medium with a distance D_R apart from each other, and the direct Rayleigh-wave R_0 is employed for the calibration. The longitudinal-wave L' reflected at the bottom of the cylinder, and the Rayleigh-wave R_0' reflected at the edge of the top plane, are assumed to be possible spurious waves, which reach the reception transducer subsequent to the direct Rayleigh-wave R_0. Figure 1(b) shows the setup for the longitudinal-wave calibration. The transmission trans-

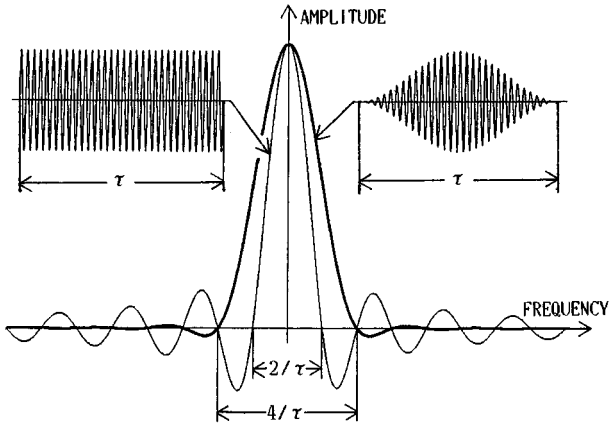

FIG. 2. Tone burst signals and their frequency spectra.

ducer is placed on the top plane of the cylindrical medium, and the reception transducer on the bottom plane where their axes coincide with each other. The direct longitudinal-wave L_0 is most significant for the calibration here. The longitudinal-wave L_1' reflected at the side of the cylinder, and the shear wave S_2' converted from the longitudinal-wave L_2 are supposed to be possible spurious waves.

F. Calibration signal

A tone burst signal, in place of a continuous wave, was employed for the calibration signal in order to discriminate between the direct wave and the subsequent spurious waves on the basis of their arrival times. Figure 2 shows schematically two representative waveforms of tone burst signals with duration τ and their frequency spectra. Because of comparatively small ripples in the skirt regions of the spectrum, the squared-sine envelope was adopted. Bandwidth of the spectrum, which determines the frequency resolution of calibration, decreases with increasing duration τ. However, maximum duration of the tone burst is limited by the minimum difference of the arrival times. Namely, half of the duration of the squared-sine envelope should not exceed the time difference in order to measure the amplitude of the direct wave signal from the peak value without the interference from the subsequent spurious waves.

G. Transfer medium

As a larger dimension of the transfer medium causes a greater difference in the arrival times, a large solid block was prepared for the new calibration system. Figure 3 shows the cylindrical medium of forged steel ($E=2.1\times10^{11}$ N/m^2, $\sigma=0.28$, $\rho=7.7\times10^3$ kg/m^3) with a diameter of 1.1 m, height of 0.76 m, and weight of about 6 tons. Ultrasonic testing was conducted at 2 MHz throughout the block and no detectable flaws were recorded. In addition, ultrasonic attenuation was measured at each point on the rectangular lattice with a separation of 0.15 m on the top plane. The averaged value of B_3/B_1 ratio, where B_1 and B_3 are amplitudes of the first and third bottom echo signals, respectively, was determined to be about 32.1%. This suggests that mechanical losses of the medium should be small enough for reciprocity calibration, since the theoretical value of B_3/B_1 is 33.3% for purely geometrical attenuation. The transfer medium was designed so that the difference of arrival times of the direct and spurious

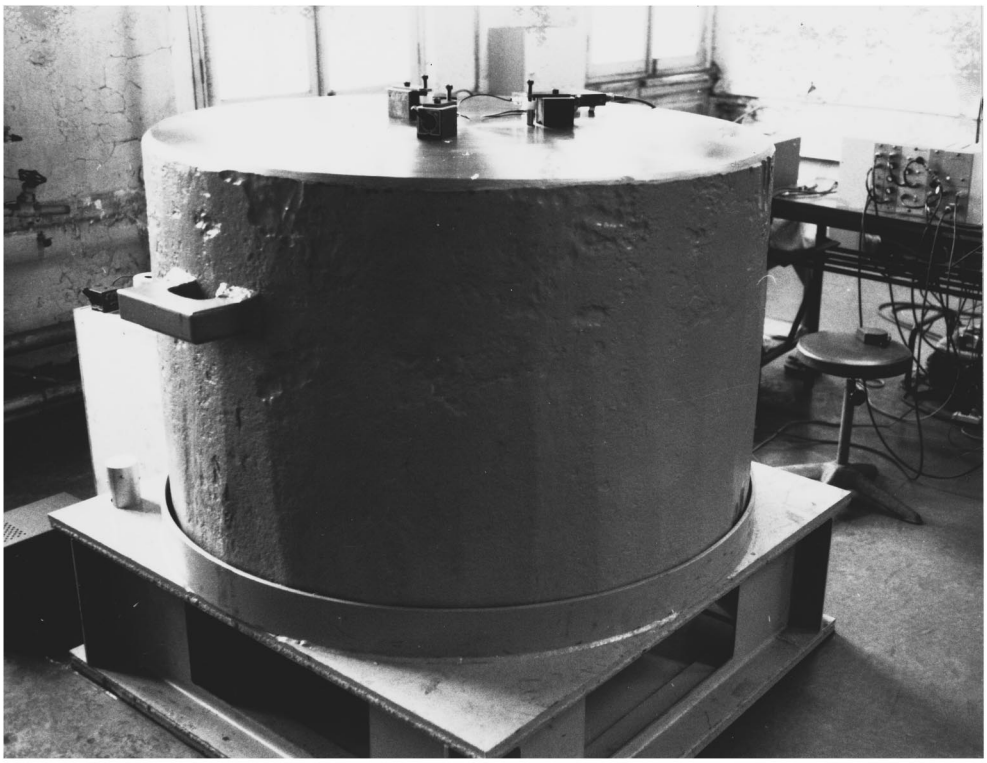

FIG. 3. Forged-steel transfer medium (diameter: 1.1 m, height: 0.76 m).

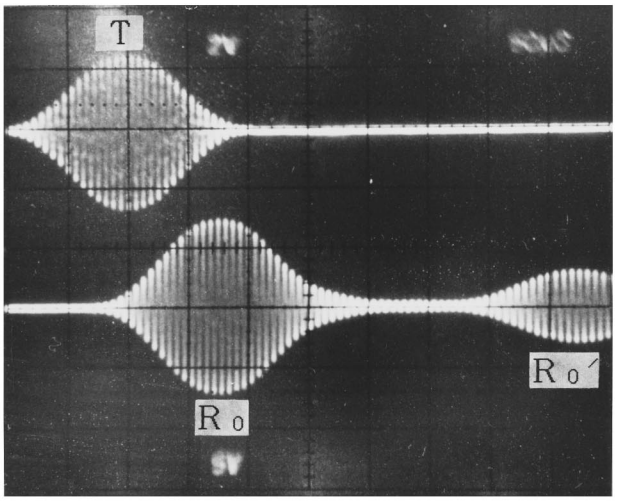

(a)

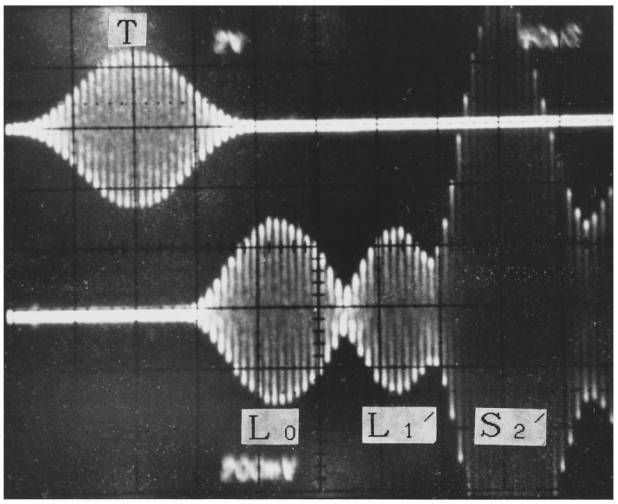

(b)

FIG. 4. Waveforms of transmission and reception signals (horizontal: 50 μs/div). (a) Rayleigh-wave calibration. (b) Longitudinal-wave calibration.

waves was longer than 0.1 ms for any case in either the Rayleigh-wave or longitudinal-wave calibration. Duration of the tone burst signal τ was set to 0.2 ms.

II. RESULTS

A. Wave propagation in transfer medium

Prior to accomplishing the reciprocity calibration, propagation of elastic waves in the transfer medium was studied using acoustic emission transducers (0.14Z10), which employ a 10-mm-diam cylindrical piezoelectric element with a nominal thickness resonance of 140 kHz.

Figure 4(a) shows waveforms of transmission and reception signals recorded in the Rayleigh-wave calibration at 160 kHz. It is shown that the direct Rayleigh-wave R_0 reached the reception transducer, at 0.2 m apart from the transmission transducer, with a propagation time of about 70 μs. With a further delay of about 320 μs, spurious Rayleigh-wave R_0' arrived. Although it had been supposed that the spurious longitudinal-wave L' would follow the direct wave R_0 with a delay of about 190 μs, the spurious wave was not recorded, presumably because its magnitude was too small at that frequency compared with the Rayleigh waves.

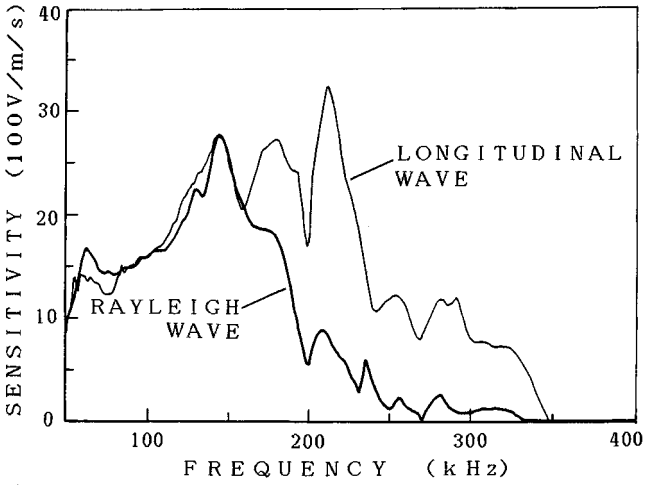

FIG. 5. Rayleigh-wave and longitudinal-wave sensitivities of an acoustic emission transducer (0.14Z10).

Figure 4(b) shows waveforms recorded in the longitudinal-wave calibration at 160 kHz. The direct longitudinal-wave L_0 reached the reception transducer, placed on the bottom plane of the cylindrical medium, with a propagation time of about 130 μs. The spurious longitudinal-wave L_1' and shear-wave S_2' followed the direct wave L_0 with delays of about 100 and 190 μs, respectively.

B. Calibration result

In the reciprocity calibration, voltages of transmission and reception signals, and impedances of transducers were measured at each frequency with an interval of 4 kHz in the range of 50 kHz–1 MHz. Frequency characteristics of velocity sensitivity was determined using a computer.[12]

Figure 5 shows the calibration results for one of the same acoustic emission transducers (0.14Z10) used in the study of the wave propagations described above. In the figure, the bold line represents the Rayleigh-wave sensitivity and the thin line the longitudinal-wave sensitivity. Below about 150 kHz the two sensitivities were consistent. On the other hand, beyond that frequency, the Rayleigh-wave sensitivity rapidly decreased in comparison with the longitudinal-wave sensitivity due to the aperture effect of the transducer.

Figure 6 shows the results of Rayleigh-wave calibrations of the same transducer (1Z8) previously calibrated using a steel-plate transfer medium, which employs an 8-mm-diam piezoelectric disk with a nominal thickness resonance of 1 MHz.[6] The thin line represents the sensitivity replotted from the data in the former paper, and the bold line is the result obtained by the new calibration system. The newly obtained sensitivity decreased nearly to zero beyond about 400 kHz, although the previous data exhibited some sensitivity in this frequency range. The difference between the transfer mediums is hypothesized to be caused by the reflections and mode conversions of elastic waves in the steel-plate medium employed in the previous calibration.

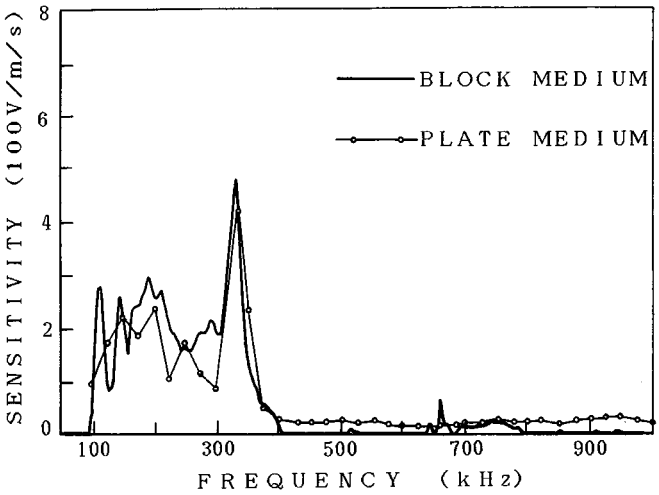

FIG. 6. Rayleigh-wave sensitivity of an acoustic emission transducer (1Z8) in relation to the shape of the transfer medium.

C. Correlation with surface pulse method

For the seismic surface pulse method, theoretical dynamic displacements of the surface were calculated on the basis of Lamb's theory.[3] On the other hand, the reciprocity parameter for the Rayleigh-wave calibration was derived from Lamb's theory as well. There is a common theoretical basis in the two calibration methods. Round robin experiments on the Rayleigh wave calibration were carried out in a collaborative effort between the USA and Japan, and good correlation was found between the two calibration results.[12]

III. CONCLUSIONS

A new system was developed for the reciprocity calibration of acoustic emission transducers using a large forged-steel transfer medium. In order to discriminate between the direct and spurious waves on the basis of their arrival times, a tone burst signal was employed for the calibration signal. It was shown that frequency characteristics of velocity sensitivity to both the Rayleigh wave and longitudinal wave were determined without interference from the spurious waves. An outstanding advantage of the reciprocity calibration is that absolute sensitivity can be determined by means of purely electrical measurements without the use of mechanical sound sources or reference transducers. Reciprocity calibration of impulse response of acoustic emission transducers, which is essential for estimating actual waveforms of acoustic emission waves, will be a significant area to investigate in the next stage of the research.

ACKNOWLEDGMENTS

The authors wish to thank S. Hashirizaki for his efforts to develop the calibration system. They further acknowledge D. A. Watson for reading the manuscript.

APPENDIX

The reciprocity parameter for the longitudinal-wave calibration H_L, which is independent of transducer design,[7] is derived for an idealized disk-type transducer with a diameter d, cross-sectional area S, and force factor A.

Free-field current sensitivity M_S is given by

$$M_S=\frac{I_0}{w_{L0}}=\frac{I_0}{w_L}\frac{w_L}{w_{L0}}=A\frac{Z_r}{Z_t+Z_r}, \tag{A1}$$

where I_0 is the output short-circuit current, w_{L0} is the vertical component of longitudinal-wave displacement velocity at the transducer when its aperture is free, w_L is that of actual displacement velocity, Z_t is the mechanical impedance of the transducer, and Z_r is the radiation impedance.

When the transducer is used for transmission, the vertical displacement velocity of the transducer v is given by

$$v=F_0\frac{1}{Z_t+Z_r}, \tag{A2}$$

where F_0 is the driving force of the transducer when its aperture is clamped. The vertical component of longitudinal-wave displacement velocity at an axial point on the opposite free surface of the transfer medium, w_{LD} is given by

$$w_{LD}=2\frac{vS}{2\pi}\frac{2\pi/\lambda}{D_L}=2F_0\frac{1}{Z_t+Z_r}\frac{S}{\lambda D_L}, \tag{A3}$$

where $D_L\gg d\gg\lambda$, and λ and c are the wavelength and velocity of the longitudinal wave in the transfer medium, respectively. Transmission voltage response is given by

$$S_S=\frac{w_{LD}}{E_S}=\frac{2F_0}{E_S}\frac{1}{Z_t+Z_r}\frac{S}{\lambda D_L}$$

$$=2A\frac{1}{Z_t+Z_r}\frac{S}{\lambda D_L}, \tag{A4}$$

where E_S is the input terminal voltage.

Consequently, the reciprocity parameter for the longitudinal-wave calibration H_L is obtained as follows:

$$H_L=\frac{S_S}{M_S}=\frac{2}{Z_r}\frac{S}{\lambda D_L}=\frac{2f}{\rho c^2 D_L}$$

$$=2f\frac{(1+\sigma)(1-2\sigma)}{E(1-\sigma)D_L}. \tag{A5}$$

[1] N. N. Hsu, J. A. Simmons, and S. C. Hardy, ''An approach to acoustic emission signal analysis—Theory and experiment,'' Mater. Eval. **35**, 100–106 (1977).
[2] H. Hatano, ''Quantitative measurements of acoustic emission related to its microscopic mechanisms,'' J. Acoust. Soc. Am. **57**, 639–645 (1975).
[3] F. R. Breckenridge and M. Greenspan, ''Surface-wave displacement: Absolute measurements using a capacitive transducer,'' J. Acoust. Soc. Am. **69**, 1177–1185 (1981).
[4] F. R. Breckenridge, ''Acoustic emission transducer calibration by means of the seismic surface pulse,'' J. Acoust. Emiss. **1**, 87–94 (1982).
[5] ''Standard method for primary calibration of acoustic emission sensors,'' ASTM Designation: E1106-86, American Society for Testing and Materials (1986).
[6] H. Hatano and E. Mori, ''Acoustic-emission transducer and its absolute calibration,'' J. Acoust. Soc. Am. **59**, 344–349 (1976).
[7] W. R. MacLean, ''Absolute measurement of sound without a primary standard,'' J. Acoust. Soc. Am. **12**, 140–146 (1940).

[8] R. K. Cook, ''Absolute pressure calibration of microphones,'' J. Acoust. Soc. Am. **12**, 415–420 (1941).
[9] L. L. Foldy and H. Primakoff, ''A general theory of passive linear electroacoustic transducers and the electroacoustic reciprocity theorem I, II,'' J. Acoust. Soc. Am. **17**, 109–120 (1945); **19**, 50–58 (1947).
[10] N. N. Hsu and F. R. Breckenridge, ''Characterization and calibration of acoustic emission sensors,'' Mater. Eval. **39**, 60–68 (1979).
[11] H. Lamb, ''On the propagation of tremors over the surface of an elastic solid,'' Philos. Trans. R. Soc. London, Ser. A **203**, 1–42 (1904).
[12] F. R. Breckenridge, T. Watanabe, and H. Hatano, ''Calibration of acoustic emission transducers: Comparison of two methods,'' Prog. Acoust. Emiss. **1**, 448–458 (1982).

The simulation of structural response to sonic booms using structural acoustic techniques

Joel Garrelick and Kyle Martini
Cambridge Acoustical Associates, Inc., 200 Boston Avenue, Suite 2500, Medford, Massachusetts 02155-4243

Micah Downing
USAF AL/OEBN, 2610 Seventh Street, Wright Patterson AFB, Ohio 435433-7901

Ron Brown
Wyle Laboratories, 128 Maryland Street, El Segundo, California 90245-4000

(Received 5 February 1996; revised 8 October 1996; accepted 15 October 1996)

Structural damage from sonic booms is one of the potential environmental impacts of supersonic flight. This paper illustrates how structural acoustic techniques may be used to assess the potential for such damage in the absence of actual flyovers. Procedures are described whereby transfer functions relating structural response to sonic boom signature may be obtained with a stationary acoustic source and appropriate data processing. Further, by invoking structural acoustic reciprocity, these transfer functions may also be acquired by measuring the radiated sound from a structure that is mechanically driven. The approach is based on the fundamental assumption of linearity, both with regard to the (acoustic) propagation of the boom in the vicinity of the structure and to the structure's response. Practical issues revolve around acoustic far field, source strength, and directivity requirements. The technique was evaluated on a specially fabricated test structure at Edwards AFB, CA. Blank shots from a cannon served as the acoustic source and taps from an instrumented hammer generated the mechanical drive. Simulated response functions were constructed. Results of comparisons with corresponding measurements recorded during dedicated supersonic flyovers with F-15 aircraft are presented for a number of sensor placements. Using the prediction of peak structural response as a metric, it was found that the direct and reciprocal simulation techniques produced ensemble-averaged mean percent errors of -4% and -26%, respectively. The corresponding standard deviations of these errors were 18% and 16%. Also, it was concluded that these uncertainties are consistent with that connected to the representation of the sonic boom itself.
 [S0001-4966(97)02403-X]

PACS numbers: 43.40.Qi, 43.28.Mw, 43.30.Lz [PJR]

INTRODUCTION

The potential impact of supersonic operations includes damage to structures from the sonic boom overpressure. The harm is typically cosmetic, window breakage, plaster cracking, etc.[1] For a particular damage assessment one may, of course, actually subject a vulnerable structure to the supersonic operations envisioned. This is costly at a minimum and in the case of irreplaceable, e.g., historic structures, quite risky. The alternative is simulation-based predictions. In this context, this paper discusses the use of structural acoustic methods. Specifically, these methods are employed to construct transfer functions that allow one to predict the response of a structure to any specified boom signature. Predicted levels may then be compared with failure values which must be obtained independently. This study builds on previous works that exploited similar techniques to obtain structural impedance data for diagnosing potential boom induced damage[1] and to simulate damage from subsonic operations.[2]

Under the fundamental assumption of linearity, both with regard to the (acoustic) propagation of the sonic boom in the vicinity of the structure and to the structure's response, the problem may be posed as one of structural acoustics. In the vicinity of the structure, the sonic boom (shortened to ''boom'' in the remainder of the paper) is represented by an acoustic plane wave (Fig. 1). Its spectrum is that of the boom signature, for example, the classic N wave. It impinges on the ground topography and structure with a unit propagation vector having an elevation angle measured from the vertical of $\beta_i = \sin^{-1}(1/M)$, where the local Mach number $M = U/c$ with U the effective flight speed and c the local air sound speed.[3] The flight heading determines an azimuthal angle, ϕ_i, not shown in Fig. 1.

The response of a structure to any given boom signature may now be formulated in terms of an impulse response function in the time domain, or transfer function in the frequency domain. Specifically, the response of a structure at location $\overline{x}$, say acceleration $a_b(t;\overline{x})$, may be expressed as the inverse transform of the product of the frequency-transformed boom signature and impulse response function, or spectral transfer function. In equation form

$$a_b(t;\overline{x}) = \pi^{-1}\ \mathrm{Re}\left\{\int_0^\infty \tilde{a}_b(\omega;\overline{x})\exp(-i\omega t)\ d\omega\right\} \qquad (1)$$

with

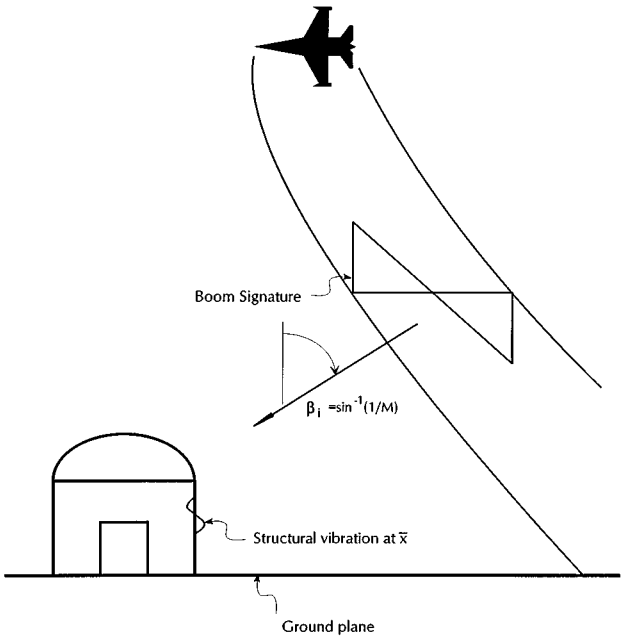

FIG. 1. Sonic boom from supersonic flyover incident on structure.

$$\tilde{a}_b(\omega;\overline{x}) = \tilde{G}(\omega;\overline{x,r_i})\tilde{p}_b(\omega;\overline{x,r_i}), \tag{2}$$

where $\tilde{a}_b(\omega;\overline{x})$=boom-induced response spectrum, Fourier transform of response time history; $\tilde{p}_b(\omega;\overline{x,r_i})$=boom pressure spectrum incident along $\overline{r_i}$, Fourier transform of boom signature $p_b(t;\overline{x,r_i})$; and $G(\omega;\overline{x,r_i})$=transfer function; Fourier transform of impulse response function.

I. STRUCTURAL ACOUSTIC SIMULATION

With our plane acoustic wave representation of the boom, the transfer function $\tilde{G}(\omega;\overline{x,r_i})$, or equivalently its transform, may be obtained with a stationary acoustic source. Consider a simple acoustic source placed along $\overline{r_i}$ at a range (R) sufficiently long to produce a plane wave at and near $\overline{x}$ [Fig. 2(a)]. The spectral transfer function now becomes

$$\tilde{G}(\omega;\overline{x,r_i}) = \tilde{a}_d(\omega;\overline{x})/\tilde{p}_d(\omega;R\overline{r_i}-\overline{x}) \tag{3}$$

with $\tilde{a}_d(\omega;\overline{x})$=response spectrum at $\overline{x}$ due to acoustic source at $R\overline{r_i}$, $\tilde{p}_d(\omega;R\overline{r_i}-\overline{x})$=free-field pressure spectrum at $\overline{x}$ due to acoustic source at $R\overline{r_i}$, and

$$\tilde{p}_d(\omega;R\overline{r_i}-\overline{x}) = (\rho\ddot{Q}_d/4\pi|R\overline{r_i}-\overline{x}|)\exp(ik|R\overline{r_i}-\overline{x}|), \tag{4}$$

where $k(=\omega/c)$ is the acoustic wave number and $\ddot{Q}_d$ is the acoustic source strength (volume acceleration).[4] We refer to the above development as our ''direct'' structural acoustic boom representation, thus the subscript ''d.''

Within the realm of structural acoustics, certain ''reciprocal'' relationships hold and may be exploited to develop an alternate method for obtaining $\tilde{G}(\omega;\overline{x,r_i})$. First, for purposes of discussion, we confine our attention to the acceleration response of our structure at $\overline{x}$, $\tilde{a}_d(\omega;\overline{x})$. Consider the problem of a force applied to our structure at $\overline{x}$ and oriented along

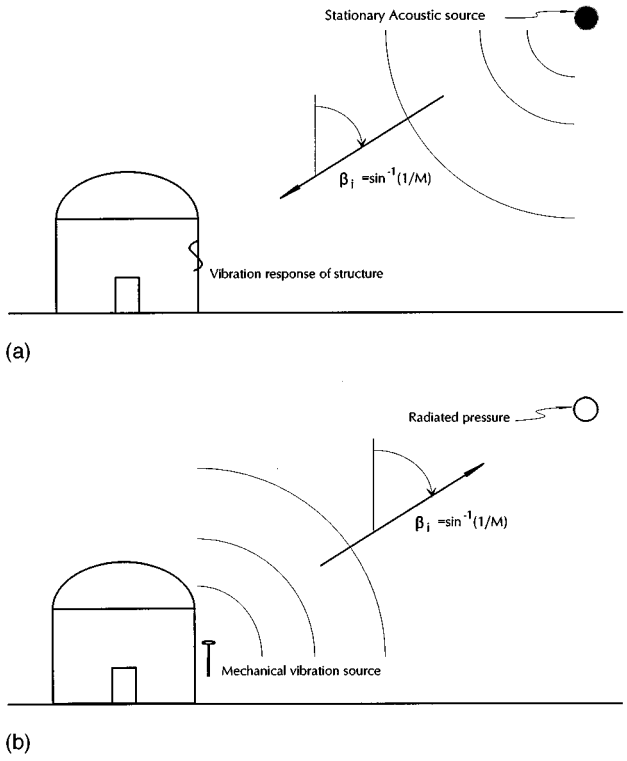

FIG. 2. (a) Direct structural-acoustic simulation of boom-induced impulse response function. (b) Reciprocal structural-acoustic simulation of boom-induced impulse response function.

$\tilde{a}_d$. The structure vibrates in response and radiates sound [Fig. 2(b)]. This situation is ''reciprocal'' to our direct problem in that the following relation holds:[5]

$$\tilde{p}_r(\omega;R\overline{r_i})/\tilde{F}(\omega;\overline{x}) = \tilde{a}_d(\omega;\overline{x})/\ddot{Q}(\omega;R\overline{r}), \tag{5}$$

and therefore

$$\tilde{G}(\omega;\overline{x,r_i}) = [4\pi|R\overline{r_i}-\overline{x}|\exp(-ik|R\overline{r_i}-\overline{x}|)/\rho]\tilde{p}_r(\omega;R\overline{r_i})/F(\omega;\overline{x}), \tag{6}$$

where $\tilde{F}(\omega;\overline{x})$=Fourier spectrum of applied force at $\overline{x}$ oriented with $\tilde{a}_d(\omega;\overline{x})$, and $\tilde{p}_r(\omega;\overline{x,R\overline{r_i}})$=Fourier spectrum of pressure radiated to $R\overline{r_i}$.

Equation (6) is valid for all ω and consequently it may be used to obtain the corresponding displacement and velocity response. Also, it completely defines the corresponding impulse response functions in the time domain.

To this point our discussion has been in terms of translational response functions. However, reciprocity is not so limited, at least in theory. Through linear superposition, Eq. (6) may serve as an influence function for obtaining other responses. Rotations, for example, may be obtained reciprocally with two adjacent, out of phase, forces effectively producing a moment drive on the structure. Letting $\tilde{F}(\omega;\overline{x}) \Rightarrow \tilde{F}_1(\omega;\overline{x_1}) + \tilde{F}_2(\omega;\overline{x_2})$ in Eq. (5) with $\tilde{F}_2(\omega;\overline{x_2}) = -\tilde{F}_1(\omega;\overline{x_1})$,

$$\tilde{p}_r(\omega;R\overline{r_i})/\tilde{F}_1(\omega;\overline{x_1}) = [\tilde{a}_d(\omega;\overline{x_1}) - \tilde{a}_d(\omega;\overline{x_2})]/\ddot{Q}(\omega;R\overline{r}). \tag{7}$$

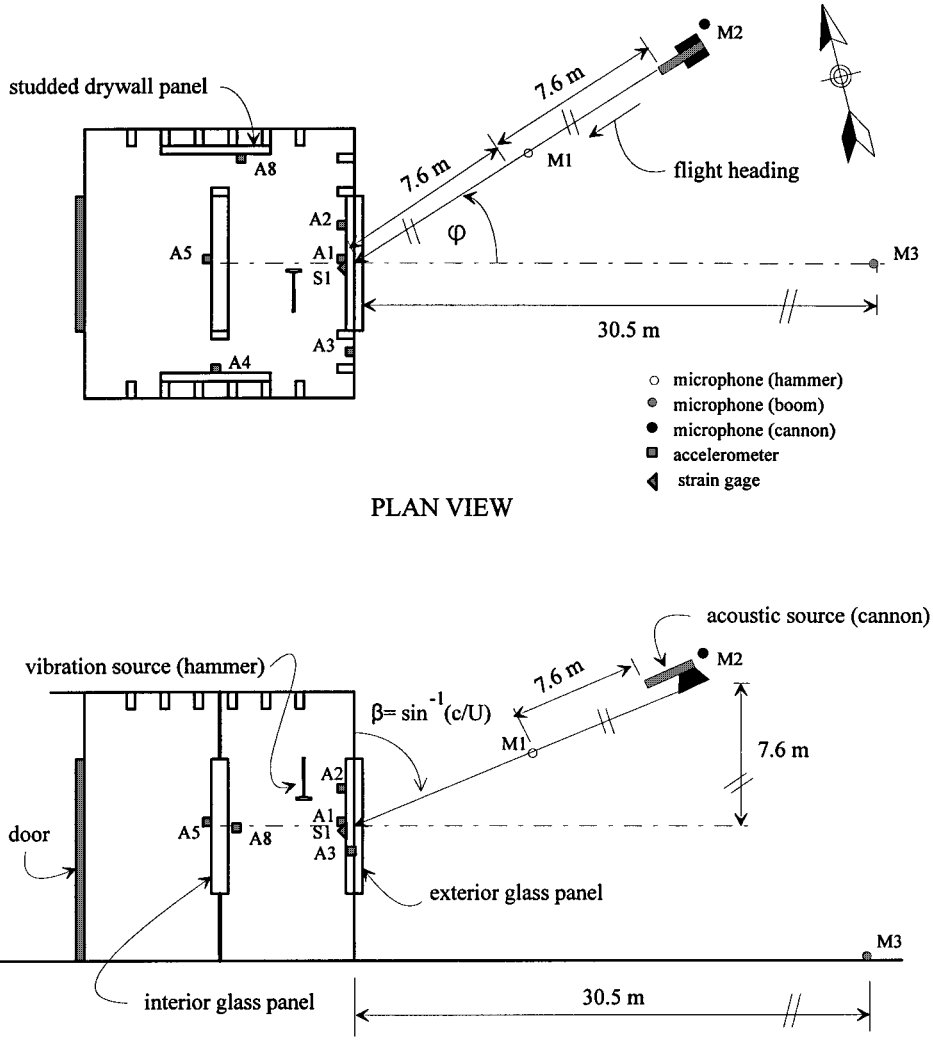

FIG. 3. Sketch of test structure and source/sensor geometry.

Taking $\overline{x_2}=\overline{x_1}+\overline{\epsilon}$ with $\overline{\epsilon}$ a differential distance, and expressing $\tilde{a}_d(\omega;\overline{x_2})$ as a Taylor series expansion about $\tilde{a}_d(\omega;\overline{x_1})$, we obtain

$$\tilde{p}_r(\omega;R\overline{r_i})/\tilde{M}(\omega;\overline{x_1})=\tilde{a}'_d(\omega;\overline{x_1})/\ddot{Q}(\omega;R\overline{r}), \tag{8}$$

where the dipole, or moment, drive $\tilde{M}(\omega;\overline{x_1})=\tilde{F}(\omega;\overline{x_1})|\overline{\epsilon}|$ and the $'$ notation indicates the spatial derivative along $\overline{\epsilon}$, that is, $\tilde{a}'_d(\omega;\overline{x_1})$ is the slope or rotation of $\tilde{a}_d(\omega;\overline{x_1})$ along $\overline{\epsilon}$. In a like manner and practical issues aside, higher-order spatial derivatives may be simulated with forces of higher-order pole, e.g., quadrupole, etc. By supplementing the process with a model of the structure to relate displacements to stress/strain, one may reciprocally determine these response functions as well.

II. IMPLEMENTATION ISSUES

In this section we outline a few of the implementation issues one confronts with the structural acoustic simulations explored in this study.

A. Direct simulation

1. Plane wave incidence

With a direct simulation, structures and ground areas that influence the response must be in the far field of the acoustic source. Otherwise near-field effects introduce errors owing to both phase and level differences with the planar wavefront of the boom. This imposes a minimum stand-off distance ($R_{\min}$) for the source, such that $kR_{\min}>1$ for frequencies of interest.

2. Replication of sonic boom incidence

Having achieved an effective plane wave for our simulation, it must be incident from the appropriate direction. Matching the required elevation angle is of particular concern for high Mach numbers where the associated source height may not be practical.

3. Source level requirements

The requirement on our acoustic source levels is that over the frequency band of concern, they provide adequate signal-to-noise (S/N) for the structural response sensor suite.

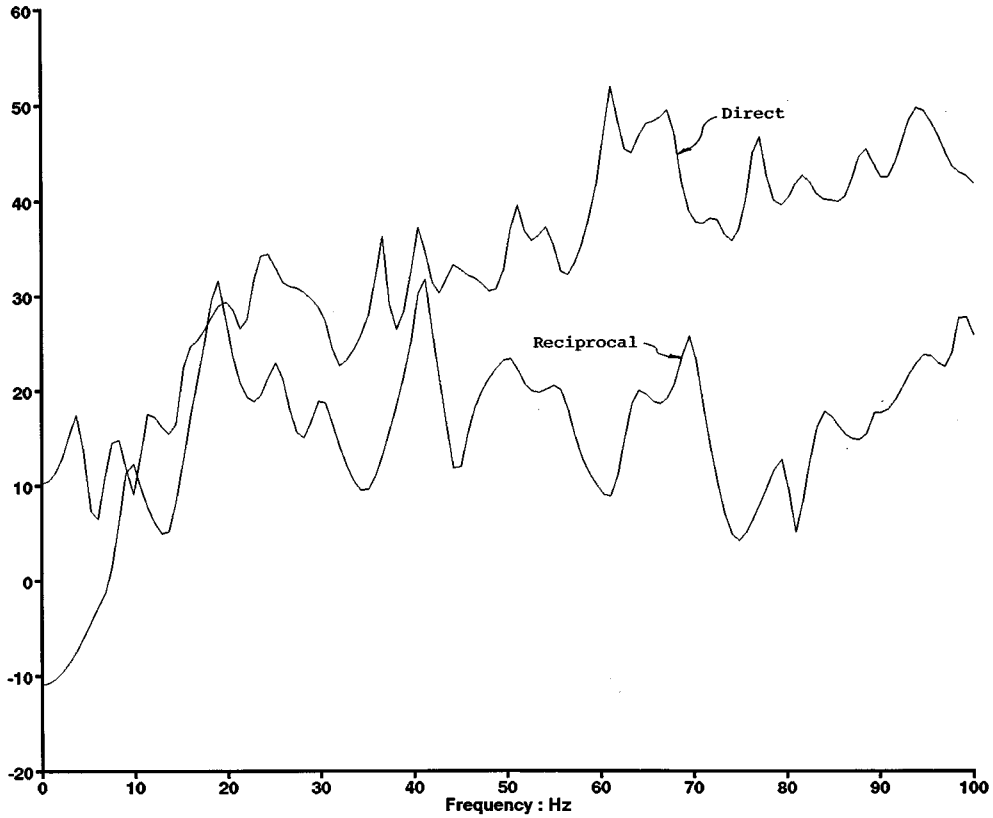

FIG. 4. Typical signal-to-noise measurements for direct and reciprocal tests.

There is no other requirement with regard to the spectrum, again under the assumption of system linearity. For a given source, this criterion tends to lead one to shorter ranges and potential conflict with the above plane wave requirement.

4. Source directivity requirements

For a direct simulation there is actually no separate requirement on the directivity of the acoustic source. By separate is meant independent achievement of effective plane wave incidence over the required solid angle.

B. Reciprocal simulation

For our reciprocal test, there are no separate plane wave requirements to be imposed on the radiated field. A plane wave is not required to satisfy reciprocity but rather to simulate a boom (see Sec. II A 1). The reciprocal equivalent of source directivity is the receiving directivity of the microphone that monitors the radiated sound. Source strength requirements are governed by the ratio of radiated-to-ambient airborne noise.

III. MEASUREMENTS

A. Overview

In this section we present measurements on a specially fabricated test structure that are part of a larger test program to validate the structural acoustic techniques described above. The tests were performed on the grounds of Phillips Laboratory at Edwards AFB, CA, by the team of Cambridge Acoustical Associates and Wyle Laboratories under the supervision of the Armstrong Laboratory of WPAFB. The responses of various components of this structure to dedicated booms and booms of opportunity were recorded and compared with predictions based on our simulations. We focused on a subset of these measurements, principally the accelera-

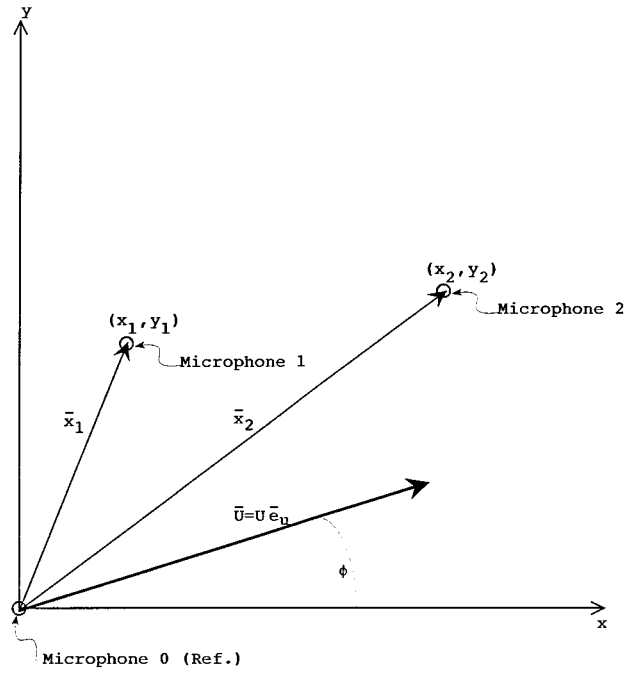

FIG. 5. Triangulation geometry for determining effective flight azimuth and speed.

TABLE I. Gross boom characteristics for six dedicated F-15 flyovers.

Boom number	5	6	7	8	9	10	Average
Peak pressure[a] Pa (psf)	137 (2.87)	78 (1.62)	148 (3.10)	87 (1.81)	104 (2.18)	121 (2.53)	112 (2.35)
Duration (s)	0.146	0.160	0.143	0.153	0.156	0.150	0.151
Rise time[b] (ms)	6.8	11.6	1.7	14.9	4.9	1.1	6.8
Local Mach No. ($M=U/c$)	1.08	1.07	1.12	1.09	1.08	1.04	1.08
Elevation angle (β_i)	67.5	68.5	66.4	67.0	68.0	73.8	68.1
Azimuthal angle (ϕ_i)	40.2	36.2	36.7	35.6	37.7	40.1	37.8

[a]Measured at M3 and assumed to be twice the free-field peak pressure.
[b]Defined as the time interval between 10% and 90% of the initial peak pressure.

tion of a glass panel embedded in an exterior wall subjected to six booms from dedicated flyovers, three nominally identical passes by each of two F-15 aircraft flying at approximately 9100 m (30 000 ft). All six booms occurred over a time interval of less than 30 min. Additional comparisons are presented for other accelerometers mounted on the walls of the structure and, in response to a boom of opportunity, a strain gage mounted on the panel. For our direct simulations, blank cannon shots served as an acoustic source and an instrumented hammer was the source of vibrations for our reciprocal tests.

B. Test structure and sensor suite

The test structure was a wood shed of standard studded plywood construction with overall dimensions 2.4 m×2.7 m×3 m (8 ft×9 ft×10 ft). It is sketched in Fig. 3. The interior was unfinished with the exception of 2.4 m×1.2 m (8 ft×4 ft) sheetrock partitions in the middle of two opposite walls. There was one exterior window, or test panel, an interior test panel supported by a wood frame, and an exterior door. The peculiarities in construction, e.g., the partial sheetrock coverage of the walls or the open construction of the interior panel, were for convenience. All exterior joints/seams were caulked and the door and window gasketed. This minimized the diffracted airborne pressure on the interior surfaces of the structure which tend to oppose the external pressure and reduce their response. The lateral dimensions of the test panels were 0.9 m×1.2 m (3 ft×4 ft) and, for the measurements described here, they were made of 6.3×10^{-3}-m (1/4 in.)-thick plate glass. All natural frequencies of the test structure and panels were above 15 Hz.

Figure 3 also shows the subset of sensors on the structure that will be considered. They consist of accelerometers placed on, and oriented normal to, the interior and exterior test panels, the north and south walls on sheetrock and the east wall directly on the plywood. In addition, a single (horizontal) axis strain gauge is located at the center of the exterior window. These placements were held constant for all three types of excitation: the flyovers, the direct simulation with a cannon, and the reciprocal simulation with the hammer. In contrast for various practical considerations, the microphones were moved depending on the excitation, as indicated in the figure.

C. Instrumentation and processing

A variety of microphones, accelerometers, strain gauges, and a force gauge were employed to measure source levels and monitor the response of the structure. During flyovers and cannon shots, Endevco type 2242C and 2213 accelerometers with Endevco type 2735 charge amplifiers and Measurement Group type EA-06-10CBE-120 and EA-06-250YA-120 strain gauges coupled with type 2310 bridge amplifiers measured the structural response. The accelerometers exhibit a flat response down to 4 Hz and may detect signals above 0.002 g. The high pressure levels created by the booms and cannon shots were measured using PCB type 106B50 pressure transducers. Their response is flat down to 0.5 Hz with a dynamic level range from 85–170 dB *re*: 20 μ Pa. For the direct simulations, a yachting cannon loaded with blank 10-gauge shotgun shells served as the acoustic source.

The mechanical source required with our reciprocal tests was a PCB model 086C03 calibrated impulse force hammer.

TABLE II. Normalized response statistics over ensemble of six booms.

	Peak acceleration (g)			Peak acceleration/peak boom pressure[a] (g/Pa)		
Sensor	Mean	Standard deviation	Standard deviation as % of mean	Mean	Standard deviation	Standard deviation as % of mean
A1	2.78	0.67	24	0.025	0.0036	14
A2	1.86	0.44	24	0.016	0.0015	9
A3	1.95	0.38	19	0.018	0.0025	14
A5	0.86	0.23	27	0.008	0.0008	11
A8	0.90	0.26	29	0.008	0.0016	21

[a]As measured on the ground and taken to be twice the free-field peak pressure.

TABLE III. Comparison of measured and simulated peak structural responses: Direct.

Sensor	Boom no.	Correlation coefficient	Peak acceleration: Measured (g)	Peak acceleration: Simulated (g)	Difference (%)
A1	5	0.48	2.64	3.35	27
Exterior glass panel	6	0.59	1.71	2.33	37
(center)	7	0.39	3.60	3.90	8
	8	0.53	2.22	2.12	−5
	9	0.54	3.11	3.34	8
	10	0.62	3.42	3.91	14
	Six boom average	0.52	2.78	3.16	15
A2	5	0.53	1.95	1.90	−2
Exterior glass panel	6	0.63	1.24	1.35	9
(off-center)	7	0.64	2.48	2.25	−9
	8	0.40	1.34	1.23	−8
	9	0.57	1.92	1.85	−4
	10	0.69	2.21	2.06	−7
	Six boom average	0.58	1.86	1.77	−4
A3	5	0.50	1.80	1.78	−1
East wall on plywood	6	0.41	1.45	1.43	−2
	7	0.39	2.35	2.68	14
	8	0.36	1.64	1.35	−18
	9	0.44	1.96	2.12	8
	10	0.41	2.52	2.09	−17
	Six boom average	0.42	1.95	1.91	−3
A5	5	0.40	0.88	0.52	−41
Interior glass panel	6	0.44	0.56	0.40	−28
(center)	7	0.54	1.30	1.00	−23
	8	0.52	0.68	0.64	−5
	9	0.49	0.91	0.58	−36
	10	0.61	0.86	0.80	−7
	Six boom average	0.50	0.86	0.66	−23

Sensor	Boom no.	Correlation coefficient	Peak strain (stress): Measured ϵE, 10^6 Pa (psi)	Peak strain (stress): Simulated ϵE, 10^6 Pa (psi)	Difference (%)
S1: Exterior glass panel (Horiz.)	13	0.86	4.40(638)	5.48(795)	25
S2: Exterior glass panel (vert.)		0.87	2.95(428)	4.85(703)	64
S3: Exterior glass panel (diag.)		0.85	2.95(428)	3.85(558)	30

A B&K-type 2230 condenser microphone measured the acoustic response. Its response is flat down to 2.6 Hz and it has a dynamic range from 15–146 dB *re*: 20 μ Pa. The sensor data were stored on a 16-channel Sony PC216A digital tape recorder. This recorder has a 2.5-kHz low-pass filter. Individual gain controls were used to maximize dynamic range. The digital data were played back (D-A) and down loaded to a Dolch personal computer using a Data Translation model DT2821-F-16SE A-D board. Each channel of data was down loaded at 12 500 samples per second. The processing of the data on the PC was performed using the signal analysis software package SIGNAL created by Engineering Design (Belmont, MA). A rectangular window, 16 384 points, and 1.31 s of data were used to create each transform with a frequency resolution of 0.76 Hz and a bandwidth of 5000 Hz.

Ensemble averaging was used to reduce the random error in the measured transfer functions. For the direct simulations, transfer functions were averaged over a minimum of three cannon shots and they were constructed from an average of ten or more hammer blows for the reciprocal tests. With the prevailing wind conditions and the strength of the simulation sources, transfer functions were limited by noise below approximately 6.5 Hz (Fig. 4). Consequently, computed transfer functions were high-pass filtered at 6.5 Hz with only minor repercussions, at least with respect to response peaks. Finally, structural response predictions with a focus on response peaks were obtained by multiplying simulated transfer functions by the boom spectra and performing an inverse transform of the product.

D. Measurements with flyovers

Measurements with the supersonic flyovers consisted of signals from the test structure sensors and three microphones making up a triangulation system. The local sound speed was measured using the cannon and two of the triangulation microphones. As described below, the system was used to com-

TABLE IV. Comparison of measured and simulated peak structural responses: Reciprocal.

Sensor	Boom no.	Correlation coefficient	Peak acceleration		
			Measured (g)	Simulated (g)	Difference (%)
A1	5	0.51	2.64	2.59	−2
Exterior glass panel	6	0.59	1.71	1.84	8
(center)	7	0.54	3.60	2.62	−27
	8	0.41	2.22	1.33	−40
	9	0.57	3.11	2.55	−18
	10	0.60	3.42	2.32	−32
	Six boom average	0.54	2.78	2.21	−19
A2	5	0.45	1.95	1.42	−27
Exterior glass panel	6	0.53	1.24	1.13	−8
(off-center)	7	0.45	2.48	2.18	−12
	8	0.34	1.34	1.16	−14
	9	0.52	1.92	1.77	−8
	10	0.56	2.21	1.95	−12
	Six boom average	0.48	1.86	1.60	−14
A3	5	0.38	1.80	1.08	−40
East wall on plywood	6	0.41	1.45	0.87	−40
	7	0.35	2.35	1.75	−25
	8	0.25	1.64	0.73	−55
	9	0.30	1.96	1.14	−42
	10	0.26	2.52	1.57	−38
	Six boom average	0.33	1.95	1.19	−40
A5	5	0.49	0.88	0.46	−47
Interior glass-panel	6	0.52	0.56	0.36	−36
(on-center)	7	0.64	1.30	0.79	−39
	8	0.55	0.68	0.50	−26
	9	0.65	0.91	0.53	−41
	10	0.55	0.86	0.67	22
	Six boom average	0.57	0.86	0.55	−35
A8	5	0.77	0.82	0.69	−16
North wall on sheetrock	6	0.70	0.64	0.50	−22
	7	0.60	1.07	1.01	−6
	8	0.44	0.63	0.47	−24
	9	0.71	0.88	0.73	−17
	10	0.56	1.39	0.77	−44
	Six boom average	0.63	0.90	0.70	−22

pute the effective local Mach number and azimuthal flight heading for each event, information required for the simulations.

Consider the geometry sketched in Fig. 5. A boom propagates over the ground at speed U, velocity $\underline{U}$, with the unit propagation vector in the xy (ground) plane, $\overline{e_u}=\underline{U}/U=\cos\phi i+\sin\phi j$. One (reference) microphone is placed at the origin and the other two at coordinates (x_1, y_1) and (x_2, y_2). The time delays of the signal arriving at microphones 1 and 2 relative to the reference point are given by

$$t_1=\overline{x_1}\cdot\overline{e}/U=(x_1\cos\phi+y_1\sin\phi)/U \tag{9a}$$

and

$$t_2=x_2\cdot\overline{e}/U=(x_2\cos\phi+y_2\sin\phi)/U. \tag{9b}$$

Solving Eqs. (9) and U and ϕ yields

$$U=(x_1\cos\phi+y_1\sin\phi)/t_1=(x_2\cos\phi+y_2\sin\phi)/t_2 \tag{10a}$$

and

$$\phi=\tan^{-1}[(x_1/x_2-r_t)/(r_t y_2/x_2-y_1/x_2)] \tag{10b}$$

with $r_t=t_1/t_2$.

Steady state supersonic passes were flown over the test area to produce carpet booms at the site. The supersonic passes were performed by F-15E aircraft flying at a nominal flight altitude of 9100 m (30 000 ft) and flight Mach No. of 1.25. These conditions were expected to produce a 100-Pa N-shaped wave with a 150-ms duration at the site. The actual flight profile was coordinated with the test site so that the incident boom would be downtrack of the focus and postfocus regions.[3] Six passes were flown that varied about the nominal conditions from flight Mach Nos. from 1.23 to 1.31 and flight altitudes from 9100–10 100 m (30 000–33 000 ft). The passes began at 1200 local time when the atmospheric turbulence was starting to increase. The pressure–time histories for these six booms are shown in Fig. 6. Variations in the incident booms are accounted for by turbulence, profile variations, and unsteadiness in the flight path for each pass.

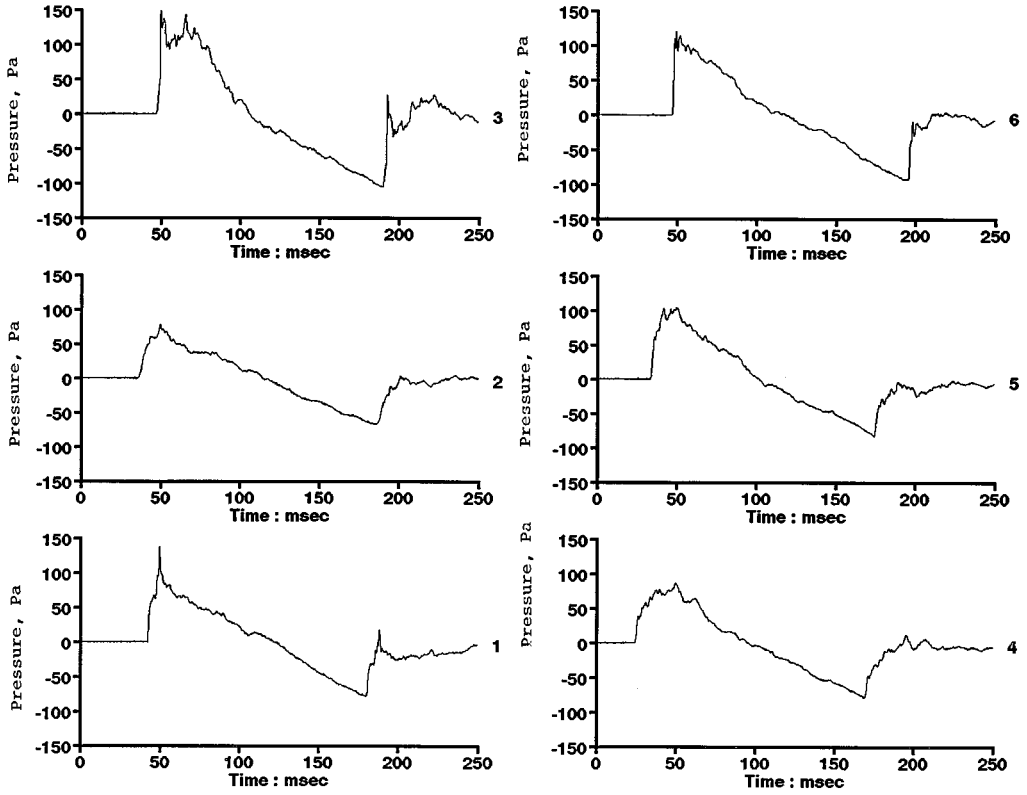

FIG. 6. Six boom signatures from F-15E dedicated flyovers.

Overall characteristics for all six flights are summarized on Table I.

In Table II for a subset of the accelerometer placements, we show the peak response measured and normalized to the peak boom pressure. The flight-to-flight variations shown in Tables I and II will provide the context for evaluating the accuracy of the simulations that follow.

E. Simulations: Direct

For all of the direct simulations the cannon was placed at the azimuthal angle $\phi_i \sim 35°$ and at an elevation angle of $\beta_i \sim 64°$. The latter corresponds to a cannon positioned roughly 7.62 m above the panel center (9.14 m from the ground) at a standoff distance of 15.24 m (Fig. 7). The source level was measured at M1.

The short pulse length of the cannon shots, which is the order of 10 ms, in stark contrast to the much longer boom duration, is shown in Fig. 8. The effects of this disparity on their respective spectra are indicated in Fig. 9 for a typical boom and shot. The reader is reminded, however, that there is no requirement for these spectra to correspond since our interest is a transfer function only. Rather, we require only that our acoustic source provide adequate signal level. The simulated response is calculated from Eqs. (1) and (2) using the direct transfer function described in Eq. (3).

We compare the simulated response of one of the sensors to that measured during a single flyover in Fig. 10. The sensor is an accelerometer affixed to the external glass panel.

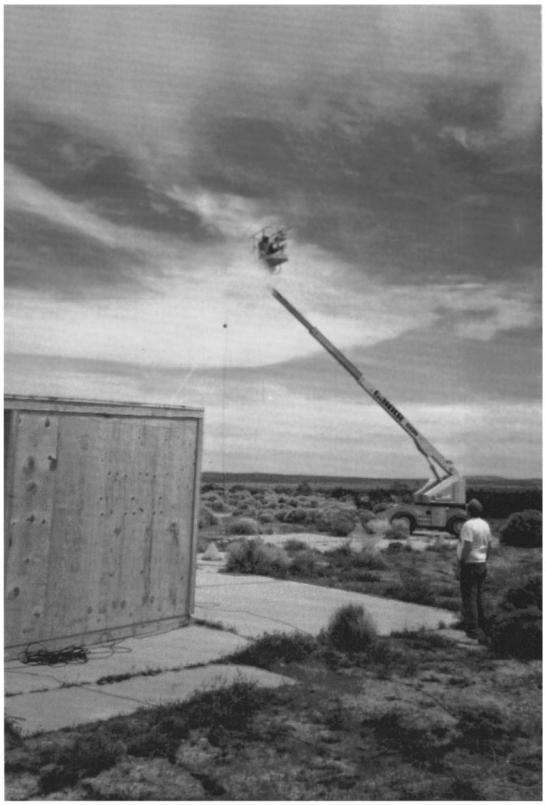

FIG. 7. Positioning of elevated acoustic source (cannon) and receiver (microphone) for structural-acoustic simulations.

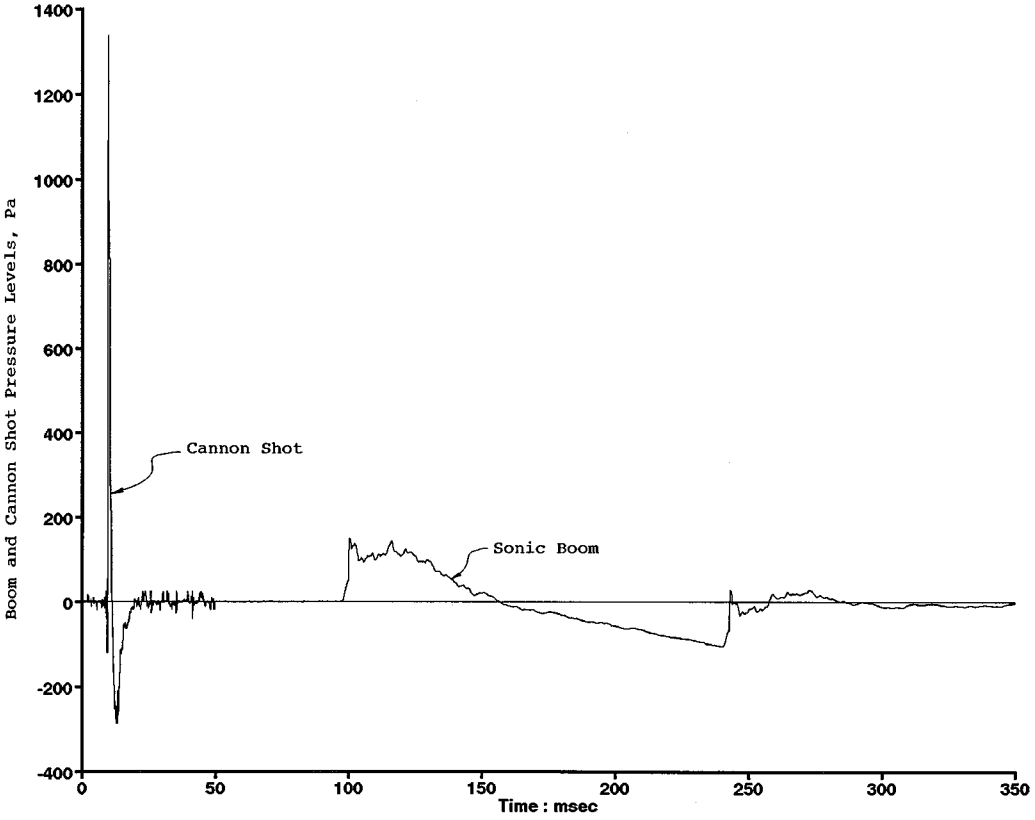

FIG. 8. Comparison of typical boom and cannon shot time signatures.

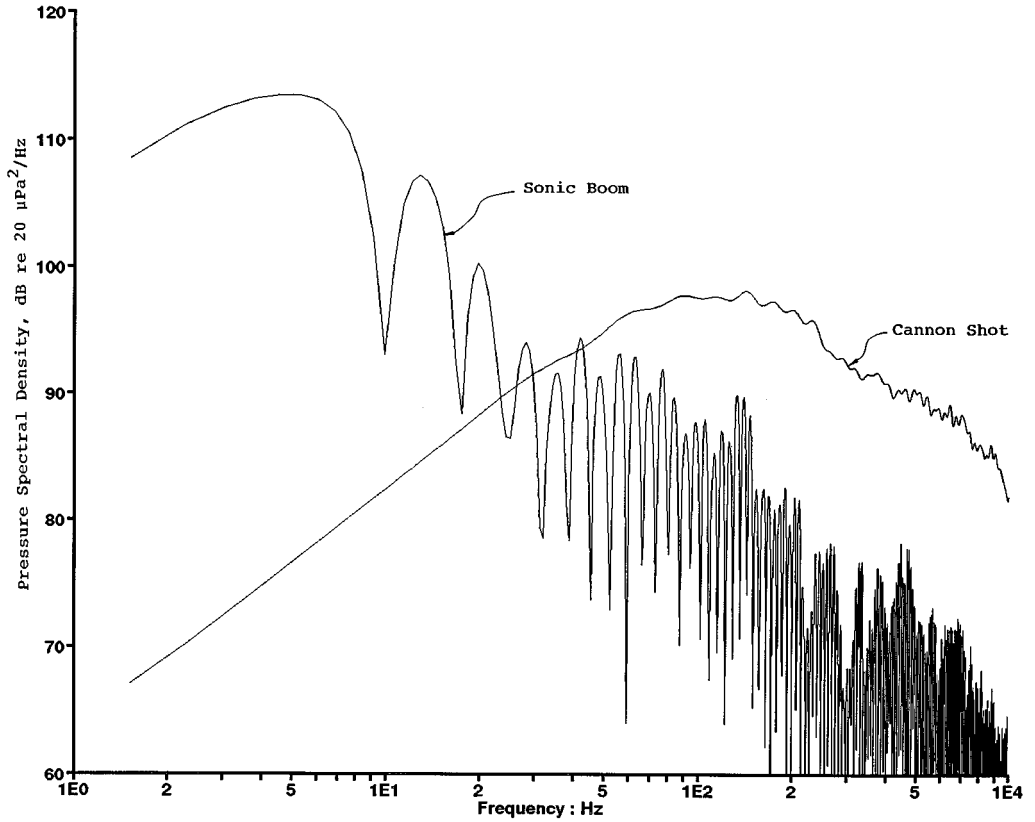

FIG. 9. Comparison of typical boom and cannon shot spectra.

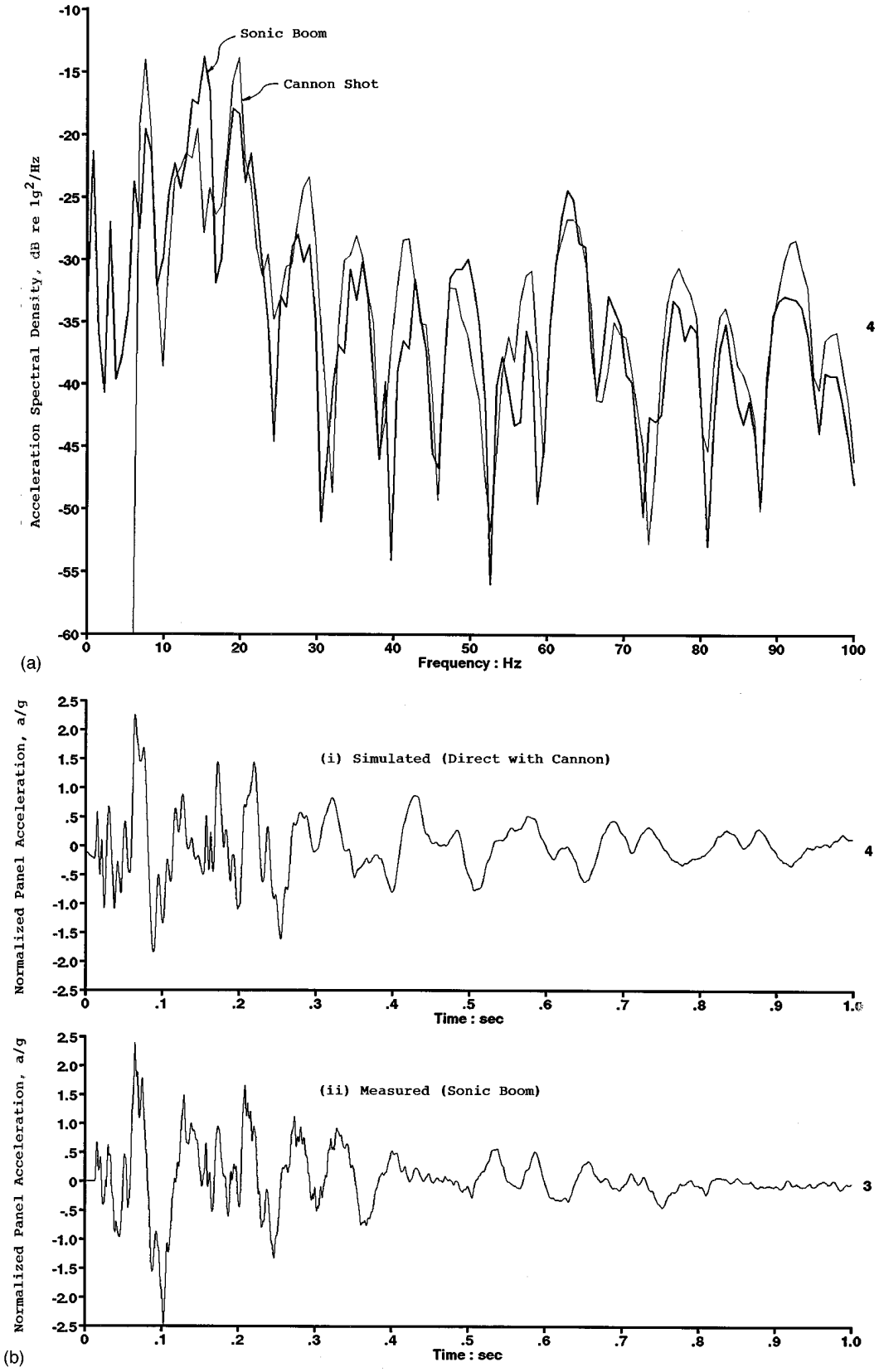

FIG. 10. (a) Comparison of measured and simulated acceleration response spectra of exterior glass panel (A2) to a single flyover: direct simulation. (b) Comparison of measured and simulated acceleration response time histories of exterior glass panel (A2) to a single flyover: direct simulation.

In Fig. 10(a) the comparison is shown in the frequency domain. The time histories are presented in Fig. 10(b). This comparison along with those for a number of other accelerometers mounted elsewhere are summarized in Table III. Specifically, the correlation coefficient between the simulated and measured signals is listed and the measured and simulated response peaks are compared.

In Table III a total of 24 comparisons of peak accelera-

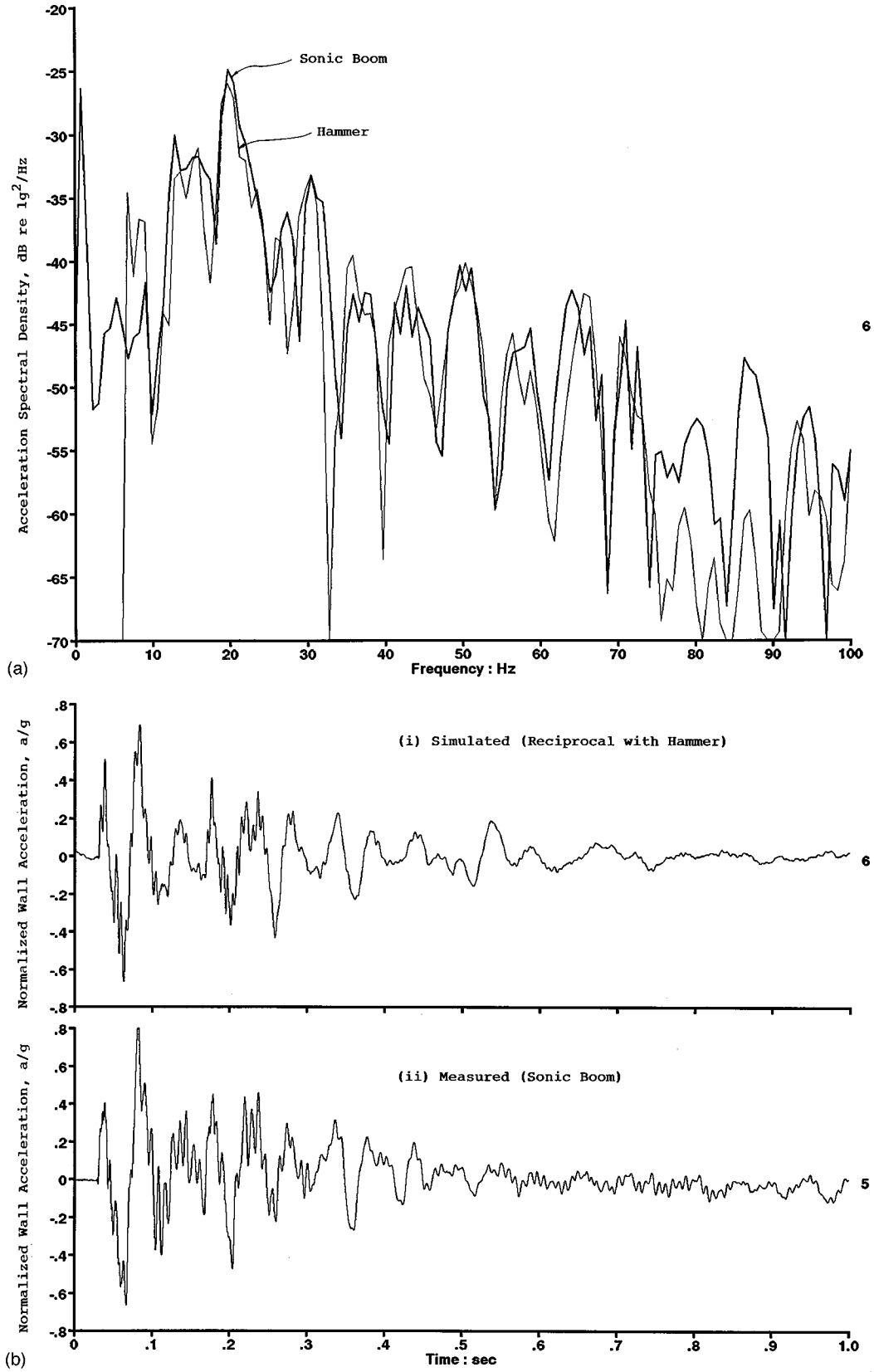

FIG. 11. (a) Comparison of measured and simulated acceleration response spectra of sheetrock wall (A8) to a single flyover: reciprocal simulation. (b) Comparison of measured and simulated acceleration response time histories of sheetrock wall (A8) to a single flyover: reciprocal simulation.

tion are shown (six booms, four sensors). Over this ensemble, the maximum discrepancies are −46% and +35% with a mean percent error of −4% and a standard deviation of 18%. In addition, strain gauge measurements are listed for one boom of opportunity.

It is interesting to observe that our accuracy in simulating the peak responses does not track very well with the corresponding correlation coefficients. In other words, the factors that are responsible for decorrelating the simulated and measured time histories and, consequently the modest

coefficients, appear to have a more limited influence on the peaks. This would occur, for example, if the decorrelation was associated with relatively high-frequency ''rattling,'' while the peak responses were dominated by the lower frequency, low-order, natural modes of the structure.

F. Simulations: Reciprocal

For our reciprocal simulations, the structure was struck by the instrumented hammer at the approximate accelerometer locations and the radiated pressure was recorded by microphone M2, positioned at $\phi \sim 35°$, $\beta \sim 64°$. The simulated response was computed using Eqs. (1), (2), and (6). A comparison with measurements in both the frequency and time domains for sensor A8 on the interior dry wall panel is shown in Fig. 11(a) and (b), respectively. Also, results are summarized in Table IV similar to the presentation given above for our direct simulations in Table III.

Over an ensemble of 30 peak acceleration comparisons (six booms, five sensors), the mean percent error is -26% and the standard deviation is 16%. The maximum measured discrepancies were -55% and $+8\%$. The larger difference in the mean than was observed with the direct tests might indicate a systematic bias in these predictions, for example, arising from an inaccurate calibration. However, no such error could be identified.

IV. CONCLUSIONS

To assess the variations shown in Tables III and IV, they must be placed in the overall simulation context and be compared with other uncertainties such as that associated with boom characterization. For example, for all practical purposes, our dedicated flights occurred under nominally identical conditions within 30 min of each other. The statistics over this ensemble for the measured peak boom pressure and accelerations are given in Tables I and II. Over the ensemble of six nominally identical flights, the standard deviation of the peak boom pressure is 23% of the mean. For the peak responses, the equivalent values range from 19%–29%, or 9%–21% when normalized, depending on the sensor. We conclude that the uncertainty introduced by these methods is consistent with that for boom representation. Therefore structural acoustic techniques, both direct and reciprocal, should provide a precision that is comparable to alternate simulation approaches.

ACKNOWLEDGMENT

The authors wish to thank John Perkins of Wyle Laboratories, Inc., for his untiring help with the tests, the Armstrong Laboratory of Wright–Patterson AFB, OH, for their support of the project, and the reviewer for his thoughtful comments.

[1] A comprehensive review as of 1990 may be found in Louis C. Sutherland, R. Brown, and D. Goerner, ''Evaluation of Potential Damage to Unconventional Structures by Sonic Booms,'' Report No. HSD-TR-90-021, U.S. Air Force, Human Systems Division, Noise & Sonic Boom Impact Technology Program, Wright–Patterson AFB, OH, May 1990.

[2] J. C. Battis, ''Effects of Low Flying Aircraft on Archaeological Structures,'' AFGL-TR-88-0263, Earth Sciences Division, Air Force Geophysics Laboratory, Hanscom AFB, MA, 26 September 1988.

[3] D. J. Maglieri and K. J. Plotkin, *Sonic Boom, Aeroacoustics of Flight Vehicles, Theory and Practice*, edited by H. Hubbard (American Institute of Physics, Woodbury, NY, 1995), Chap. 10.

[4] A. D. Pierce, *Acoustics* (Acoustical Society of America, New York, 1989), p. 160.

[5] T. ten Wolde, ''On the Validity and Application of Reciprocity in Acoustical, Mechano-Acoustical and Other Dynamical Systems,'' Acustica **28**, 23–32 (1973). Also, Y. I. Belousov and A. V. Rimskii-Korsakov, ''The Reciprocity Principle in Acoustics and Its Application to the Calculation of Sound Fields of Bodies,'' Sov. Phys. Acoust. **21**(2), 103–109 (1975).

A boundary integral approach for acoustic radiation of axisymmetric bodies with arbitrary boundary conditions valid for all wave numbers

Weiping Wang, Noureddine Atalla, and Jean Nicolas
Group of Acoustics and Vibration, Department of Mechanical Engineering, Université de Sherbrooke, Sherbrooke, Québec J1K 2R1, Canada

(Received 18 January 1996; accepted for publication 17 August 1996)

A boundary integral method for solving the exterior acoustic radiation problem of axisymmetric bodies with arbitrary boundary conditions is developed. The new formulation derives from the method proposed by Burton and Miller [Proc. R. Soc. London Ser. A **323**, 201–210 (1971)], which uses a linear combination of the Helmholtz integral equation and its normal derivative to ensure the uniqueness of the numerical solution at all frequencies. It is shown that the use of tangential operators enables one to easily compute the hypersingular integral without much extra effort. By taking advantage of the properties of axisymmetric geometry, and using the expansion of the boundary conditions and the surface distribution functions in Fourier series with respect to the angle of revolution, the surface integral is reduced to a line integral along the generator of the body, and Fourier integrals of the Green's function and its derivatives over the circumferential angle. The Fourier integrals with singular kernels are evaluated using recurrence formulas in terms of the complete elliptic integrals. A new approach is then proposed to evaluate the Burton and Miller formulation at a corner by using the left-hand and right-hand limits of normal derivatives. Doing so, isoparametric elements throughout the surface of the body are able to be used. In order to demonstrate the validity and accuracy of the method, numerical results with quadratic isoparametric curvilinear elements are presented for radiation problems of a pulsating sphere, an oscillating sphere, and a finite cylinder with various boundary conditions. [S0001-4966(97)05712-3]

PACS numbers: 43.40.Rj [CBB]

INTRODUCTION

Boundary integral methods based on the Helmholtz integral equation for the analysis of exterior acoustic radiation and scattering problems have been developed extensively over the past three decades. A great deal of work has been performed to address the two major difficulties in the application of boundary integral methods on acoustic problems: the evaluation of singular and hypersingular integrals, and the uniqueness of solutions.

The boundary integral method applied to exterior domain fails to provide a unique solution at certain frequencies associated with the resonances of the interior region. These resonances do not correspond to a physical situation when solving an exterior problem and yield meaningless peaks in the radiated noise spectrum. A number of different methods have been developed to eliminate the nonuniqueness problem, and summaries of these developments were presented by Schenck,[1] Meyer *et al.*,[2] and Chien.[3] Up to date, the combined Helmholtz integral equation formulation (CHIEF) proposed by Schenck[1] and the composite Helmholtz integral equation by Burton and Miller[4] are the most popular techniques. Schenck showed that the surface Helmholtz integral equation augmented with the Helmholtz integral equations evaluated at selected interior points, can give unique solutions at all frequencies. However, the method fails if the interior points are located on a nodal surface of the interior domain. The method proposed by Burton and Miller[4] is based on a linear combination of the Helmholtz equation and its normal derivative. Even if both the Helmholtz integral equation and its normal derivative suffer from the nonuniqueness problem, it has been proven that the combination of the two integral equations leads to a unique solution for a complex combination coefficient. Although this method appears to be robust for numerical implementation, it suffers from the main drawback of hypersingular integrals.

Several regularization schemes have been devised to lower the order of kernel singularity before numerical treatment. Burton and Miller,[4] and Panich[5] introduced double-surface integrals throughout the integrals to reduce the order of the singularity, such that only a C° Holder continuity of the density function is sufficient for the existence of such integrals. Although such a technique gives rise to numerically tractable kernels, it is inefficient from a computational viewpoint. The integral-by-parts approach[4,2,6] has been the most largely pursued, where one of the normal derivative of Green's function is, in fact, transferred to tangential derivatives of the density function. This regularization process lowers the integrand singularity to at most $1/R^2$ so that the integral of the limit exists. Meyer *et al.*[2,6] made implicit use of the tangential operators, and derived the following regularization

$$\int_S p(Q)\,\frac{\partial^2 G}{\partial n_p\,\partial n_Q}\,dS(Q)$$

$$= \int_S [p(Q)-p(P)]\,\frac{\partial^2 G}{\partial n_p\,\partial n_Q}\,dS(Q) - p(P)\int_S (\mathbf{n}_p\cdot\mathbf{n}_q) \times (ik)^2 G(P,Q)\,dS(Q). \quad (1)$$

In their studies, the resulting integral was discretized into a number of flat elements, and the acoustic potential was assumed as constant over each element, such that the first integrand in the right-hand side of the equation is never singular. It should be noted here that the kernel singularity would pose a problem if higher-order elements were to be implemented. Terai[7] managed to evaluate the hypersingular kernels in closed form, thus obviating the need to handle such singular integrals numerically. But such an approach was again limited in its application to constant flat elements, where the source point was taken to be at the centroid of the element. Chien *et al.*[3] proposed a regularization by using certain known identities associated with the interior Laplace problems. Krishnasamy *et al.*[8] presented another approach which converses the hypersingular integrands into a sum of a solid angle, line integrals, and surface integrals with a less singular integrands by use of Stokes' theorem. Since such a formulation involves derivatives of the density function explicitly, maintaining the continuity of such derivatives at the collocation point in the numerical implementation is essential for the solution to converge in a stable manner for a finer boundary element mesh. It is also interesting to note, however, the work of Guiggiani *et al.*,[9] which operates in the local coordinates of parent elements, and allows the hypersingular integrals to be directly transformed into a sum of double and one-dimensional regular integrals.

The solution of radiation and scattering problems involving axisymmetric bodies have been proposed by a number of researchers. Copley[10,11] devised the method of interior Helmholtz integral equation to solve acoustic problems for axisymmetric radiators, where the surface pressure is determined by constraining the source point to lie in the interior region of the body. Difficulties arise in the method when interior source points coincide with nodes of standing wave associated with the interior Dirichlet problem. Patel[12] presented a formulation for axisymmetric bodies and arbitrary boundary conditions, in which the arbitrary pressure and velocity distributions were expressed in Fourier series along the angle of revolution, all integrals are evaluated using Gaussian quadrature. Seybert *et al.*[13] proposed an approach where the surface Helmholtz integral is reduced to a line integral and an integral over the angle revolution. The latter integral is evaluated partly analytically in terms of elliptic integrals and partly numerically using Gaussian quadrature. This method was further extended by Juhl[14,15] and Soenarko[16] to analysis of nonaxisymmetric radiation and scattering problems of axisymmetric bodies. However, their formulations break down when the wave number is at or near an interior Dirichlet eigenvalue.

Since the boundary integral equations for axisymmetric bodies are derived from the general three-dimensional one, they also suffer the main drawback of nonuniqueness of solutions. However, published studies on the acoustic radiation of axisymmetric bodies have so far largely ignored the nonuniqueness problem. The few exceptions may be the researches done by Meyer *et al.*,[6] and Grannell *et al.*[17] Meyer *et al.*[6] extended their formulation of Burton and Miller's method in general three dimensions[2] to axisymmetric bodies. In their studies, however, the resulting integral was discretized into a number of flat elements, and the acoustic potential was assumed as constant over each element, such that the first integrand in Eq. (1) is never singular. It should be noted here that the kernel singularity would pose a problem if higher-order elements were to be implemented. Grannell *et al.*[17] proposed the *p*-version boundary element implementation of Burton and Miller's method for axisymmetric bodies. However, their formulation was inefficient from a computational viewpoint, as they used the double surface integrals throughout the integral equation to reduce the order of singularity. Moreover their formulation was limited to axisymmetric boundary conditions only.

The aim of this work is to implement numerically the composite Helmholtz integral equation proposed by Burton and Miller for radiation problems of axisymmetric bodies with arbitrary boundary conditions. This paper is organized as follows. In Sec. I, the composite Helmholtz integral equation is introduced, and its application on nonaxisymmetric radiation problems is formulated. We demonstrate that the use of tangential operators regularizing the hypersingular kernel in the normal gradient equation enables to easily compute all integrals in the equation without much extra effort compared with the surface Helmholtz integral equation, since the resulting equation has the same order of singularity as the surface Helmholtz integral equation. The velocity and the pressure functions are then expressed in Fourier series with respect to the angle of revolution, such that the surface integrals are reduced to line integrals along the generator of the body. In Sec. II, we present new recurrence formulas to precisely evaluate all singular integrals of the Green's function and its derivatives over the circumferential angle in terms of the complete elliptic integrals. In Sec. III, for the first time, we propose that the composite Helmholtz integral equation can be directly evaluated at a corner or edge as its left-hand and right-hand limits. Doing so, one can discretize the generator of a body using isoparametric elements, and avoid the necessity of modifying the BEM mesh if using double nodes with a small gap, or of employing special interpolation functions if using traditional discontinuous elements, where the node at a corner is placed inside the element. In Sec. IV, we provide the results of several examples for spherical and cylindrical geometries. Comparisons with exact solutions and other published results are made to demonstrate the accuracy and efficiency of the proposed formulation.

I. THEORETICAL DEVELOPMENT

The most robust formulation to overcome the nonuniqueness difficulty is proposed by Burton and Miller.[4] The

formulation uses a composite boundary integral equation which is a linear combination of the Helmholtz integral equation and its normal gradient as follows:

$$c(P)\left[p(P)+\alpha\frac{\partial p(P)}{\partial n_p}\right] = \int_S\left[p(Q)\frac{\partial G(P,Q)}{\partial n_q}-\frac{\partial p(Q)}{\partial n_q}G(P,Q)\right]dS(Q) + \alpha\int_S\left[p(Q)\frac{\partial^2 G(P,Q)}{\partial n_p\,\partial n_q}-\frac{\partial p(Q)}{\partial n_q}\frac{\partial G(P,Q)}{\partial n_q}\right]dS(Q), \tag{2}$$

where P and Q are points on the surface, n is outwards normal direction at a point on the surface, p is the surface pressure, and α is a complex constant. The quantity $c(P)$ is a geometric constant given by

$$c(P)=1+\int_S\frac{\partial}{\partial n_q}\left[\frac{1}{4\pi R}\right]dS(Q) \tag{3}$$

and $G(P,Q)$ is the three-dimensional free-space Green's function defined as

$$G(P,Q)=\frac{e^{-ikR}}{4\pi R},\quad R=|\mathbf{r}_p-\mathbf{r}_q|. \tag{4}$$

It has been demonstrated that although the Helmholtz integral equation, and its normal derivative equation fail to yield unique solution at the characteristic frequencies of the interior Dirichlet and Neumman problems, respectively, Eq. (2) has a unique solution at all wave numbers.[2,4] The composite integral equation (2), however, contains the term

$$\int_S p\frac{\partial^2 G}{\partial n_p\,\partial n_q}\,dS(Q) \tag{5}$$

which is hypersingular as the field point Q approaches the source point P. As Martin and Rizzo[19] have shown, such an integral can be interpreted as the Hadamard finite parts of hypersingular integrals, and the actual behavior of the pressure function $p(Q)$ should be C^1 holder continuous. Moreover, as pointed out by Krishnasamy *et al.*,[8] this smoothness condition is required by the nature of the hypersingular kernel and hence needs to be satisfied no matter what regularization method is used. Burton and Miller[4] suggested to regularize the hypersingular kernel by using the equation derived by Maue[20] and later by Mitzner,[21]

$$\int_S p\frac{\partial^2 G}{\partial n_p\,\partial n_q}\,dS(Q)=\int_S\{k^2(\mathbf{n}_p\cdot\mathbf{n}_q)pG + [\mathbf{n}_p\times\boldsymbol{\nabla}_p G]\cdot[\mathbf{n}_q\times\boldsymbol{\nabla}_q p]\}dS(Q), \tag{6}$$

which lowers the integrand singularity to at most $1/R^2$ so that the integral of the limit exists. Wu *et al.*[22] implemented Eq. (6) using discontinuous quadratic elements where collocation points are placed inside each element to ensure the continuity of tangential derivatives of acoustic pressure and the uniqueness of normal direction. Their numerical results indicated that the accuracy obtained by the use of Eq. (6) is satisfactory, although it is computationally inefficient—because the number of collocation points is always greater than the number of geometric nodes which results in an overdetermined system of higher order. Unfortunately, most researchers have been deterred from implementing the above regularization, because it requires the continuity of the derivatives of the pressure function, and the vector operators appear to give rise to the computation complexity. However, it will be proved that the cross-product vector items in Eq. (6), which stand for tangential derivatives, can be efficiently evaluated over an axisymmetric surface by using the following procedure.

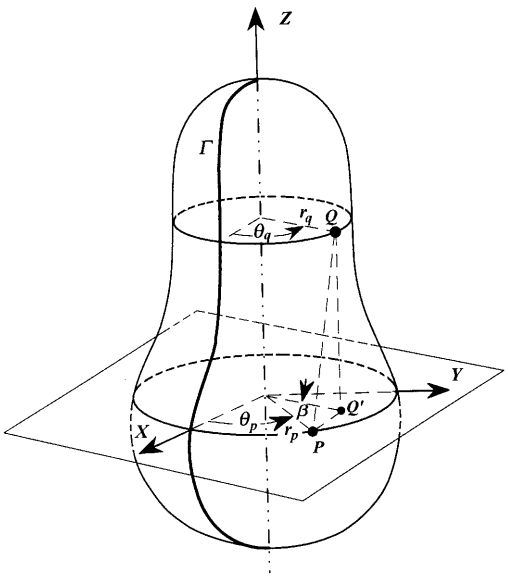

FIG. 1. Geometry of a cylindrical surface.

For axisymmetric bodies, the geometrical distance, R, between the points Q and P can be expressed in terms of the cylindrical coordinates, shown in Fig. 1, as follows:

$$R^2(P,Q)=r_p^2+r_q^2-2r_p r_q\cos(\theta_q-\theta_p)+(z_q-z_p)^2. \tag{7}$$

For simplicity, let

$$\beta=\theta_q-\theta_p$$
$$\rho=\sqrt{(r_p+r_q)^2+(z_p-z_q)^2}, \tag{8}$$
$$\lambda=2\sqrt{r_p r_q}/\rho$$

then the geometric distance $R(P,Q)$ in Eq. (7) can be expressed as follow:

$$R=\rho\sqrt{1-\lambda^2\cos^2\frac{\beta}{2}}. \tag{9}$$

It is clear from the definition that $\lambda\to 1$, and $\rho\to 2r$, where $r=r_p=r_q$, as $P\to Q$.

For structures with the axisymmetric surface, the normal vector, $\mathbf{n}$, lies in the r-z plane, i.e.,

$$\mathbf{n}=n_r\mathbf{e}_r+n_z\mathbf{e}_z, \tag{10}$$

and the vector operators in Eq. (6) can be written in the form

$$\mathbf{n}_p\cdot\mathbf{n}_q=n_{rp}n_{rq}\cos\beta+n_{zp}n_{zq}, \tag{11}$$

$$[\mathbf{n}_p\cdot\boldsymbol{\nabla}_p]\cdot[\mathbf{n}_q\cdot\boldsymbol{\nabla}_q]$$
$$=(n_{rp}n_{rq}+n_{zp}n_{zq}\cos\beta)\frac{1}{r_pr_q}\frac{\partial}{\partial\theta_p}\frac{\partial}{\partial\theta_q}+\sin\beta\left(\frac{n_{zq}}{r_q}\frac{\partial}{\partial t_p}\frac{\partial}{\partial\theta_q}-\frac{n_{zp}}{r_p}\frac{\partial}{\partial\theta_p}\frac{\partial}{\partial t_q}\right)+\cos\beta\frac{\partial}{\partial t_p}\frac{\partial}{\partial t_q},\tag{12}$$

where $\partial/\partial t$ is the tangential derivative along the generator, and lies in the r-z plane, i.e.,

$$\frac{\partial}{\partial t}=-n_z\frac{\partial}{\partial r}+n_r\frac{\partial}{\partial z}.\tag{13}$$

For radiation problems of axisymmetric bodies, it is convenient to expand the surface pressure and normal velocity functions in Fourier series in the angle of revolution:

$$p(r,\theta,z)=\sum_{m=-\infty}^{\infty}p_m(r,z)e^{im\theta}$$
$$v(r,\theta,z)=\sum_{m=-\infty}^{\infty}v_m(r,z)e^{im\theta},\tag{14}$$

where v_m are the Fourier coefficients obtained from the prescribed boundary conditions, and p_m are the unknown coefficients.

Substituting Eqs. (6), (11), (12), (14) into Eq. (2), we have

$$c(P)\sum_m\left[p_m(P)+\alpha\frac{\partial p_m(P)}{\partial n_p}\right]e^{im\theta_p}$$
$$=\sum_m\int_S\left[p_m(Q)\frac{\partial G}{\partial n_q}-\frac{\partial p_m(Q)}{\partial n_q}G\right]e^{im(\beta+\theta_p)}\,dS(Q)+\alpha\sum_m\int_S\Bigg\{k^2(n_{rp}n_{rq}\cos\beta+n_{zp}n_{zq})p_m(Q)G(P,Q)$$
$$+(n_{rp}n_{rq}+n_{zp}n_{zq}\cos\beta)\frac{im}{r_pr_q}\frac{\partial G}{\partial\theta_p}p_m(Q)+\sin\beta\left(\frac{imn_{zq}}{r_q}\frac{\partial G}{\partial t_p}p_m(Q)-\frac{n_{zp}}{r_p}\frac{\partial G}{\partial\theta_p}\frac{\partial p_m(Q)}{\partial t_q}\right)$$
$$+\cos\beta\frac{\partial G}{\partial t_p}\frac{\partial p_m(Q)}{\partial t_q}-\frac{\partial p_m(Q)}{\partial n_q}\frac{\partial G}{\partial n_p}\Bigg\}e^{im(\beta+\theta_p)}\,dS(Q).\tag{15}$$

It is seen from Eqs. (8), (9) that $\partial G/\partial\theta_p$ is independent of θ_p, and furthermore, there is that

$$\frac{\partial G}{\partial\theta_p}=-\frac{\partial G}{\partial\beta}.\tag{16}$$

Now, applying the linear independent property of the series, $e^{im\theta_p}$, we obtain

$$c(P)\left[p_m(P)+\alpha\frac{\partial p_m(P)}{\partial n_p}\right]$$
$$=\int_S\left[p_m(Q)\frac{\partial G}{\partial n_q}-\frac{\partial p_m(Q)}{\partial n_q}G\right]e^{im\beta}dS(Q)+\alpha\int_S\Bigg\{k^2(n_{rp}n_{rq}\cos\beta+n_{zp}n_{zq})p_m(Q)G(P,Q)$$
$$-(n_{rp}n_{rq}+n_{zp}n_{zq}\cos\beta)\frac{im}{r_pr_q}\frac{\partial G}{\partial\beta}p_m(Q)+\sin\beta\left(\frac{imn_{zq}}{r_q}\frac{\partial G}{\partial t_p}p_m(Q)+\frac{n_{zp}}{r_p}\frac{\partial G}{\partial\beta}\frac{\partial p_m(Q)}{\partial t_q}\right)$$
$$+\cos\beta\frac{\partial G}{\partial t_p}\frac{\partial p_m(Q)}{\partial t_q}-\frac{\partial p_m(Q)}{\partial n_q}\frac{\partial G}{\partial n_p}\Bigg\}e^{im\beta}dS(Q).\tag{17}$$

Considering the axisymmetric body in Fig. 1, noting $dS=r_qd\beta d\Gamma$, and carrying out the integration over β first, we have

$$c(P)\left[p_m(P)+\alpha\frac{\partial p_m(P)}{\partial n_p}\right]$$
$$=\int_\Gamma h_{mq}p_m(Q)r_qd\Gamma+\alpha\int_\Gamma\Bigg\{k^2\left(n_{rp}n_{rq}\frac{g_{m+1}+g_{m-1}}{2}+n_{zp}n_{zq}g_m\right)+\frac{m(j_{m+1}-j_{m-1})n_{zq}}{2r_q}$$
$$-\left[n_{rp}n_{rq}mg_m+n_{zp}n_{zq}\left(\frac{m+1}{2}g_{m+1}+\frac{m-1}{2}g_{m-1}\right)\right]\frac{m}{r_pr_q}\Bigg\}p_m(Q)r_qd\Gamma$$
$$+\alpha\int_\Gamma\left(\frac{j_{m+1}+j_{m-1}}{2}-\frac{n_{zp}}{2r_p}[(m+1)g_{m+1}-(m-1)g_{m-1}]\right)\frac{\partial p_m(Q)}{\partial t_q}r_qd\Gamma-\int_\Gamma(g_m+\alpha h_{mp})\frac{\partial p_m(Q)}{\partial n_q}r_qd\Gamma,\tag{18}$$

where g_m, h_m, and j_m are the Fourier transformation of Green's function, $G(P,Q)$, and its normal and tangent derivatives, respectively, as follows:

$$g_m = \int_0^{2\pi} G(P,Q) e^{im\beta}\, d\beta, \tag{19}$$

$$h_m = \int_0^{2\pi} \frac{\partial G(P,Q)}{\partial n}\, e^{im\beta}\, d\beta = \frac{\partial g_m}{\partial n}, \tag{20}$$

$$j_m = \int_0^{2\pi} \frac{\partial G(P,Q)}{\partial t}\, e^{im\beta}\, d\beta = \frac{\partial g_m}{\partial t}. \tag{21}$$

Equation (18) shows that the composite Helmholtz integral equation, Eq. (2), is now reduced to a line integral along the generator which can be numerically evaluated by using Gaussian quadratic formula. It should also be noted that the coefficients of Eq. (18) are the same for the circumferential modes m or $-m$, thus the calculation time can be significantly reduced.

II. EVALUATION OF SINGULAR INTEGRALS

The Fourier integral of the free-space Green's function in Eq. (19) can be expressed as the sum of a regular integral that is frequency dependent, and an irregular integral that is frequency independent, such as

$$g_m = g_m^k + g_m^0 = \int_0^{2\pi} \frac{e^{-ikR}-1}{4\pi R}\, e^{im\beta}\, d\beta + \int_0^{2\pi} \frac{1}{4\pi R}\, e^{im\beta}\, d\beta. \tag{22}$$

In this way, any additional effort required to evaluate singular integrals will be expended only once for a given problem, regardless of the number of frequencies for which a solution is sought.

The regular integral, g_m^k, is numerically evaluated with the Gaussian quadratic formula, and the singular integral, g_m^0, can be efficiently calculated by using the following recurrence formulation.

Substituting the geometric distance $R(P,Q)$ in Eq. (9) into Eq. (22), we obtain the following recurrence equations

$$g_m^0 = \begin{cases} \dfrac{1}{\pi\rho} F\left(\lambda, \dfrac{\pi}{2}\right), & m=0, \\ \left(\dfrac{2}{\lambda^2}-1\right) g_{m-1}^0 + \dfrac{4m-6}{\lambda^2} I_{m-1}, & m \geqslant 1, \end{cases} \tag{23}$$

where $F(\lambda,\pi/2)$ is the Legendre's complete elliptic integral of the first kind, and I_m is a regular integral, defined by

$$F\left(\lambda, \frac{\pi}{2}\right) = \int_0^{\pi/2} \frac{1}{\sqrt{1-\lambda^2 \cos^2 \phi}}\, d\phi, \tag{24}$$

$$I_m = \frac{1}{\pi\rho} \int_0^{\pi/2} \cos 2m\phi \sqrt{1-\lambda^2 \cos^2 \phi}\, d\phi, \tag{25}$$

and $\phi=\beta/2$ is the half-angle between the points P and Q.

Using the similar procedure, the Fourier transformation of the derivative of the free-space Green's function in Eqs. (20) and (21) are expressed as the sum of a regular integral and an irregular integral,

$$h_m = h_m^k + h_m^0 = \frac{\partial}{\partial n} \int_0^{2\pi} \frac{e^{-ikR}-1}{4\pi R}\, e^{im\beta}\, d\beta + \frac{\partial}{\partial n} \int_0^{2\pi} \frac{1}{4\pi R}\, e^{im\beta}\, d\beta, \tag{26}$$

$$j_m = j_m^k + j_m^0 = \frac{\partial}{\partial t} \int_0^{2\pi} \frac{e^{-ikR}-1}{4\pi R}\, e^{im\beta}\, d\beta + \frac{\partial}{\partial t} \int_0^{2\pi} \frac{1}{4\pi R}\, e^{im\beta}\, d\beta. \tag{27}$$

Again, the integrands of the first part in the above two equations are nonsingular, therefore, they can be numerically evaluated. Although the integrands of the second item are singular, a recurrence formula similar to Eq. (25) can be derived as follows:

$$h_0^0 = \frac{1}{\pi\rho^2}\left[\rho \frac{\partial F}{\partial \lambda}\frac{\partial \lambda}{\partial n} - F\frac{\partial \rho}{\partial n}\right] \tag{28}$$

$$h_m^0 = \left(\frac{2}{\lambda^2}-1\right) h_{m-1}^0 - \frac{4m-6}{\rho\lambda^2}\frac{\partial \rho}{\partial n} I_{m-1} - \frac{1}{\lambda^3}\left[(4m+6) \times g_{m-1}^0 + (4m-6) I_{m-1}\right] \frac{\partial \lambda}{\partial n}, \quad m \geqslant 1, \tag{29}$$

$$j_0^0 = \frac{1}{\pi\rho^2}\left[\rho \frac{\partial F}{\partial \lambda}\frac{\partial \lambda}{\partial t} - F\frac{\partial \rho}{\partial t}\right] \tag{30}$$

$$j_m^0 = \left(\frac{2}{\lambda^2}-1\right) j_{m-1}^0 - \frac{4m-6}{\rho\lambda^2}\frac{\partial \rho}{\partial t} I_{m-1} - \frac{1}{\lambda^3}\left[(4m+6) \times g_{m-1}^0 + (4m-6) I_{m-1}\right] \frac{\partial \lambda}{\partial t}, \quad m \geqslant 1, \tag{31}$$

where

$$\frac{\partial F}{\partial \lambda} = \frac{\pi\rho I_0 - (1-\lambda^2)F}{\lambda(1-\lambda^2)}. \tag{32}$$

III. COMPUTATIONAL IMPLEMENTATION

Equation (18) can be evaluated numerically for a body of arbitrary shape by discretizing the generator Γ of the body into a series of curvilinear isoparametric elements. Then the coordinates (r,z) of points located within the lth element are expressed in terms of nodal coordinates (r_a, z_a) and the associated shape function $N_a(\eta)$ as follows:

$$r = \sum_{a=1}^{M} N_a(\eta) r_a, \qquad z = \sum_{a=1}^{M} N_a(\eta) z_a, \tag{33}$$

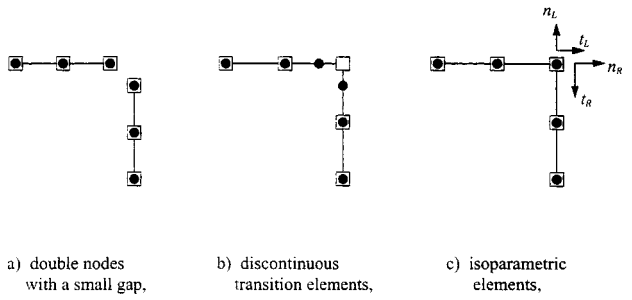

FIG. 2. Discontinuous and transition elements at corners. □ geometric node, ● field node.

where M is the number of nodes of the element, and the shape functions, $N_a(\eta)$, are the same as used in finite element analysis, and can be easily found elsewhere (see Ref. 13). The above equations map each element on the generator onto a straight line—the parent element, as shown in Fig. 2. The computer program developed allows for use of linear ($M=2$) and quadratic elements ($M=3$).

Similarly, the surface pressure p and the normal velocity v for a circumferential mode m are also approximated over each element in the similar form:

$$p_m(\eta)=\sum_{a=1}^{M}\phi_a(\eta)p_{ma}$$
$$v_m(\eta)=\sum_{a=1}^{M}\phi_a(\eta)v_{ma}, \tag{34}$$

where p_{ma} and v_{ma} are the values of p_m and v_m respectively, at the node a of the element, and ϕ_a are the interpolation function associated with the node a. For isoparametric elements, the interpolation functions ϕ_a are the same as the shape functions N_a in Eq. (33).

It is a common belief that the Burton and Miller formulation is valid at smooth collocation or source points only.[3] This is because the normal derivative of the Helmholtz integral equation cannot be defined at a corner or an edge, since the normal vector itself is discontinuous at such a point. There is no problem applying the constant elements in this case, since all source points are located in the centers of elements. If higher-order elements are to be used, the simple way to solve the problem is by duplicating the corner node with a small gap between [see Fig. 2(a)]. Then one has to modify the mesh and wonder how large the gap should be to guarantee the convergence of solutions.

An alternative way to satisfy those continuity conditions is the use of nonconforming (often so called discontinuous) elements in which the collocation points are placed inside the element rather than on its border,[23] as seen in Fig. 2(b). However, if doing so, special interpolation functions have to be used for these elements, because of the different locations of geometric and field nodes.[23] The lack of numerical studies on how the edge distance of a discontinuous element affects the accuracy and convergence of a solution should also be noted. Rêgo Silva[23] proposed to take the edge distance as 1/4 and 1/6 of the element length for linear and quadratic elements, respectively, but gave no details of the reason.

On the treatment of corners in the application of the Helmholtz integral equation, the work directed by Gray and Lutz[24] is notable. In their studies, a corner is discretized using multiple nodes, and for each extra node at the corner, the necessary additional equation is obtained by using the interior or exterior limit of differentiating the Helmholtz integral equation. Although this method is only applicable to the use of Helmholtz integral equation, their study indicates that employing multiple normal derivatives of Helmholtz integral equation at the corner node is perfectly acceptable.

In the following studies, it is assumed that the normal vector at a corner is bounded, and its left-hand and right-hand limits exist as the source point approaches the corner from the left and right sides, even though the normal vector itself is discontinuous at a corner [see Fig. 2(c)]. In the application of Burton and Miller formulation, the explicit presence of the surface normal derivatives at the field point in Eq. (18) enables us to discretize a corner as double nodes and to evaluate the equation directly by taking its left-hand and right-hand limits at the corner without the need to add additional equations. It also enables us to discretize the surface of a structure by the use of isoparametric elements shown in Fig. 2(c). As the surface pressure is a continuous function, there should be no need to use two pressure variables at the corner. Since Eq. (18) is evaluated twice at each of the corners as the field point P approaches the corner from left and right sides, using one variable at a corner would result in a set of the overdetermined linear equations, which is undesired from the viewpoint of computational efficiency. To circumvent the difficulty, one can assume two independent pressure variables at each of the corners since discontinuities of pressure function between elements do not invalidate the convergence of the boundary element method.[23] By doing so, we can now write Eq. (18) for each of the nodes in the boundary element mesh of a generator, and generate a set of simultaneous linear algebraic equations which can be solved by using the Gaussian elimination algorithm. The results of the next section demonstrate the robustness of this approach.

IV. NUMERICAL EXAMPLES

As a preliminary check on the accuracy of our numerical implementation of the solution method above, the first case is a pulsating sphere of radius a, vibrating with a uniform radial velocity v_0. The analytical solution of acoustic pressure at the position (r,θ,z) radiated by the sphere is given by[25]

$$\frac{p(\rho)}{z_0 v_0}=\frac{a}{\rho}\frac{ika}{1+ika}e^{-ik(\rho-a)}, \tag{35}$$

where $\rho=\sqrt{r^2+z^2}$ is the distance from the center of the sphere, and z_0 is the characteristic impedance of the fluid surrounding the sphere.

The generator of the sphere is modeled by six isoparametric quadratic elements with a total of 13 nodes, shown in Fig. 3, where the field nodes are the same as the geometric nodes. All numerical computations of integrals along the

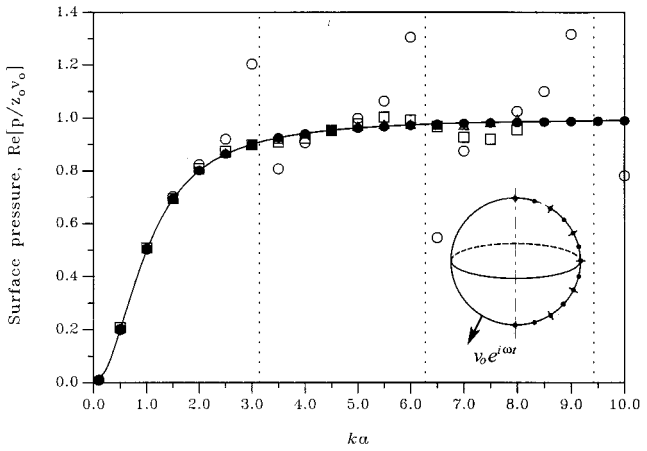

FIG. 3. Real part of surface pressure of a pulsating sphere. ——— exact solution. ○ HIE solution,[13–16] □ Meyer's method,[2,3] △ Chien's method,[3] ● current method.

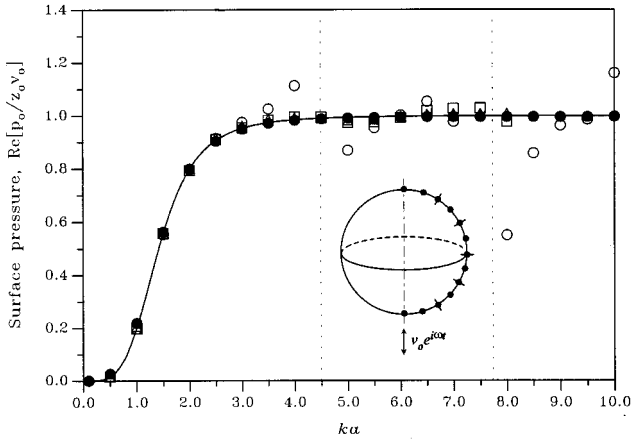

FIG. 5. Real part of surface pressure of an oscillating sphere. ——— exact solution, ○ HIE solution,[13–16] □ Meyer's method,[2,3] △ Chien's method,[3] ● current method.

generator were carried out using four-point Gaussian quadrature. The real and imaginary parts of nondimensionalized surface acoustic pressure are plotted against the nondimensional wave number ka from 0.1 to 10 in Figs. 3 and 4, respectively. In order to demonstrate the accuracy and efficiency of the present method, the exact solutions and the results obtained by Chien *et al.*[3] using Meyer's and Chien's methods with 40 three-dimensional quadratic elements and a total of 122 nodes were included for comparison. The results obtained using the surface Helmholtz integral equation developed by Seybert *et al.* in Refs. 13–16 with six quadratic elements was also included to show the nonuniqueness problem.

As seen in the figures the agreement between the proposed method and the exact solution is excellent for all wave numbers considered, while the Helmholtz integral equation fails to provide reliable solutions at the wave numbers near the interior Dirichlet frequencies, $ka=\pi$, 2π, and 3π. Inspection of the figures reveals that both the real part and imaginary part of the surface pressure obtained by the method presented in this paper are, in general, significantly more accurate than Meyer's three-dimensional formulation.[2,3] The difference between the present method and Chien's formulation is negligible, while the former exhibits better accuracy at wave numbers higher than 4.0. Moreover, it should be noted here that the present method is computationally more efficient and economical to use, considering that the use of only six quadratic curvilinear elements with 13 degrees of freedom has achieved accuracy better than the use of 40 3-D quadratic elements with 122 degrees of freedom.

Our next example is the radiation problem of an oscillating sphere of radius a with a normal velocity $v_0 \cos\phi$, where ϕ is the angle made by the radial direction and the velocity. The analytical solution of acoustic pressure radiated by the sphere is given by[25]

$$\frac{p(\rho,\phi)}{z_0 v_0} = \cos\phi \left(\frac{a}{\rho}\right)^2 \frac{ika(1+ik\rho)}{2(1+ika)-(ka)^2}\, e^{-ik(\rho-a)}, \tag{36}$$

where $\rho=\sqrt{r^2+z^2}$ is the radial distance from the center of

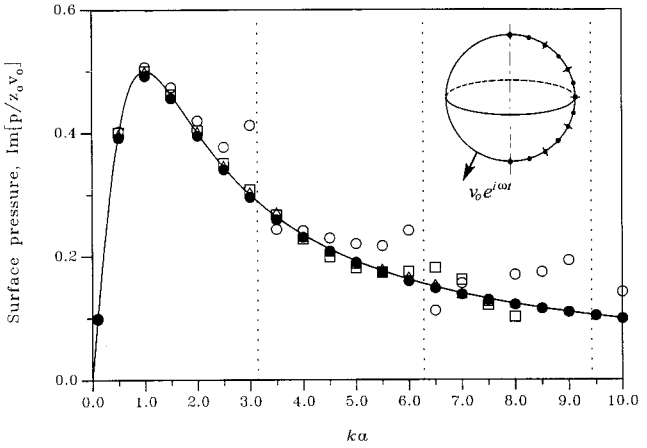

FIG. 4. Imaginary part of surface pressure of a pulsating sphere. ——— exact solution, ○ HIE solution,[13–16] □ Meyer's method,[2,3] △ Chien's method,[3] ● current method.

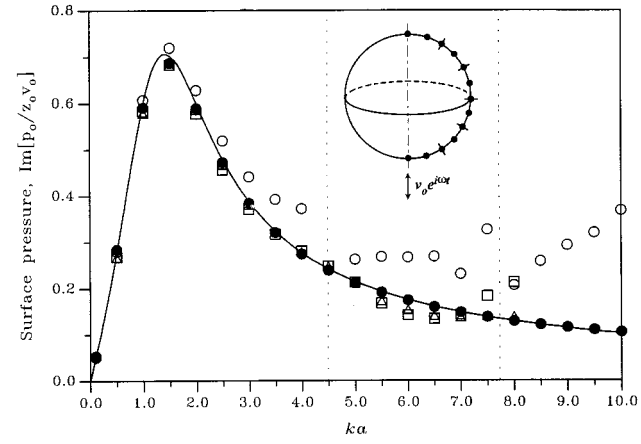

FIG. 6. Imaginary part of surface pressure of an oscillating sphere. ——— exact solution, ○ HIE solution,[13–16] □ Meyer's method,[2,3] △ Chien's method,[3] ● current method.

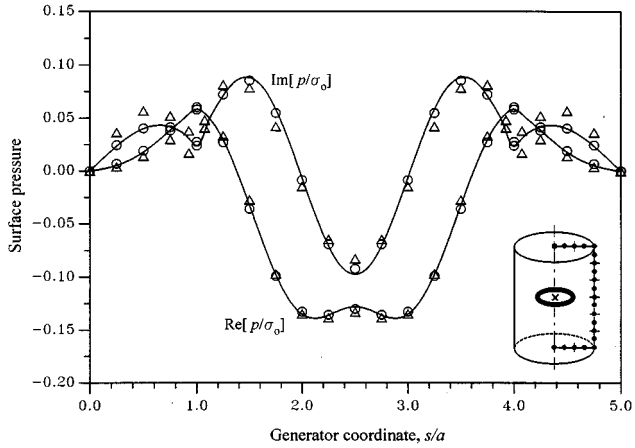

FIG. 7. Surface pressure of a finite cylinder for $m=1$ and $ka=3.9722$. ——— exact solution, △ with mixed elements, ○ with isoparametric elements.

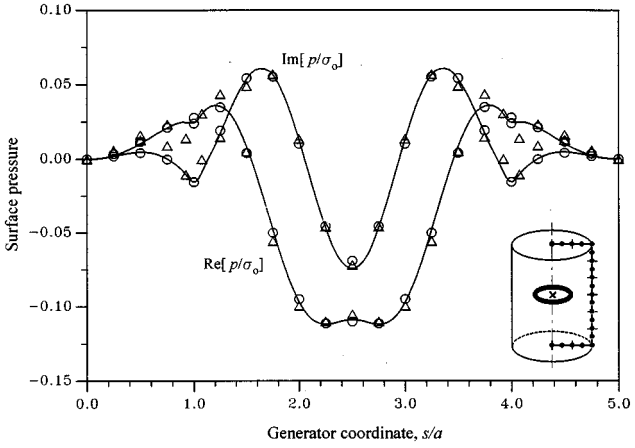

FIG. 8. Surface pressure of a finite cylinder for $m=2$ and $ka=5.2413$. ——— exact solution, △ with mixed elements, ○ with isoparametric elements.

the sphere, and z_0 is the characteristic impedance of the fluid surrounding the sphere.

Again, the generator of the sphere is modeled by six isoparametric quadratic elements (of C° continuity) with a total of 13 nodes, shown in Fig. 5. The surface pressure at $\phi=0$ obtained by the present method is compared with the exact solutions, and with those obtained by Chien *et al.* using Meyer's method[2] and Chien's method[3] with 40 three-dimensional quadratic elements and 122 degrees of freedom. Once again, the results obtained using the surface Helmholtz integral equation in Refs. 13–16 were also included to demonstrate the nonuniqueness problem.

As seen in Figs. 5 and 6, the Helmholtz integral equation failed to provide reliable solutions at the wave numbers near the interior Dirichlet frequencies, $ka=4.49$ and 7.73. The real and imaginary parts of the surface pressure obtained by the method presented in this paper are again more accurate than Meyer's 3-D methods[2,3] for the whole range of wave numbers concerned, and also substantially better than those obtained by Chien's formulation at wave numbers higher than 4.0.

Let us now consider the radiation problem of a finite circular cylinder of radius a and length $3a$. This case is significant because the generator contains two corners, where the normal vectors are discontinuous, and sufficient to demonstrate the versatility of the present formulation. The solution of this problem for the exterior region is a very difficult analytical task. Thus it is of interest to investigate use of the following substitute scheme for this problem. First, the normal velocity over the surface of a cylinder is assumed to equal to that produced by a ring source located inside the cylinder as if no object is present and the total space is filled with the same fluid. Then the pressure field radiated by the cylinder is calculated using the present formulation, and compared to the exact solution of the ring source. This allows to evaluate the accuracy and efficiency of our formulation.

To simulate various boundary conditions, the strength of the ring source of radius b is assumed in the form:

$$\sigma(\theta)=\sigma_0 \cos m\theta, \tag{37}$$

where σ_0 is the magnitude of the strength of the ring sources.

The pressure and normal velocity generated by the ring source are then given by

$$p(r,\theta,z)=\int_0^{2\pi}\sigma_0 \cos m\theta_q \frac{e^{-ikR}}{4\pi R} b\, d\theta_q, \tag{38}$$

$$v(r,\theta,z)=\frac{i}{z_0 k}\frac{\partial}{\partial n_p}\int_0^{2\pi}\sigma_0 \cos m\theta_q \frac{e^{-ikR}}{4\pi R} b\, d\theta_q. \tag{39}$$

The generator is modelled as ten isoparametric quadratic elements with a total of 21 nodes, which results in 23 deg of freedom (note double pressure variables at corners). Again numerical evaluations are carried out using four-point Gaussian quadrature for each element along the generator.

In Figs. 7, 8, and 9 is presented a comparison of the normalized pressure along the generator obtained by using the isoparametric elements and by using mixed elements (with six isoparametric and four discontinuous transition el-

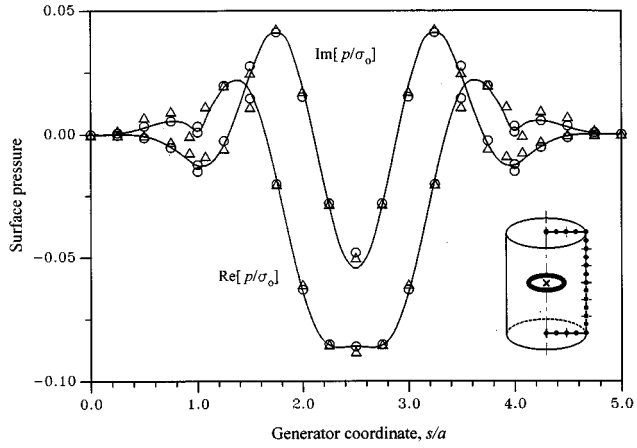

FIG. 9. Surface pressure of a finite cylinder for $m=3$ and $ka=6.4655$. ——— exact solution. △ with mixed elements, ○ with isoparametric elements.

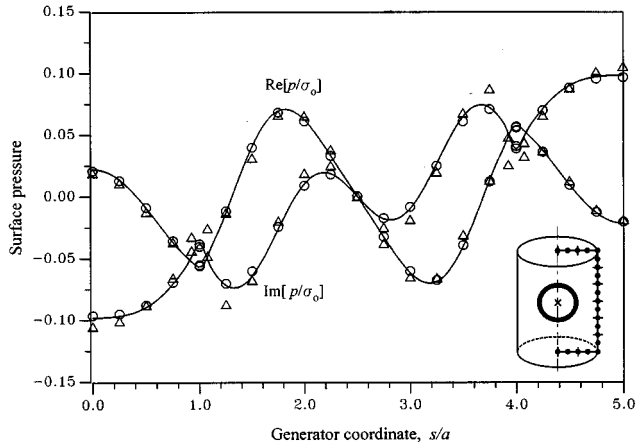

FIG. 10. Surface pressure of a finite cylinder for $ka=4$, as the ring source lies in the generator's plane. ——— exact solution, △ with mixed elements, ○ with isoparametric elements.

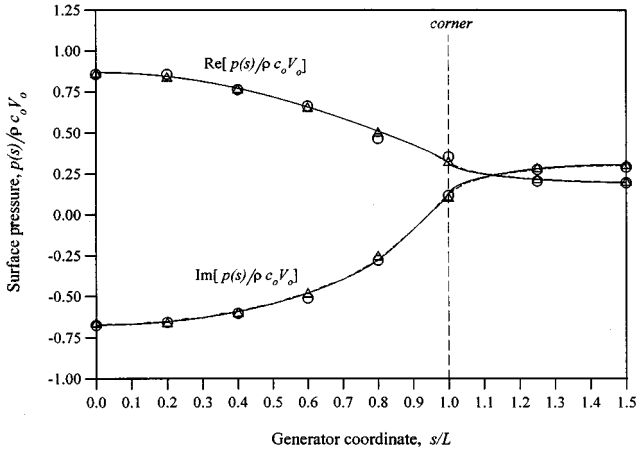

FIG. 11. Surface pressure for a finite cylinder of half-length L and radius a with $a/L=0.5$ at wave number $kL=2$. ——— 60 elements, ... 30 elements, --- 15 elements, ○ Copley's method,[10] △ Fenlon's method.[26]

ements at the corners, where the node at a corner is shifted 1/6 of the element length inside the element, as proposed by Rêgo Silva,[23]) at $ka=3.9722$ for $m=1$, $ka=5.2413$ for $m=2$, and $ka=6.4655$ for $m=3$, respectively. The direct evaluation of Eq. (38) is taken as the exact solution, and also included for comparison. It should be pointed out that the Helmholtz integral equation employed in Refs. 14–16 fails to provide a unique solution at these wave numbers, because they are actually the first eigenvalues of the associated interior Dirichlet problems for circumferential modes $m=1$, 2, and 3, respectively.

As seen in the figures, the agreement of the isoparametric element solutions is good when compared with the exact solutions, while the mixed element solutions showed poorer accuracy, especially at the corners ($s/a=1.0$ and 4.0) and on the ends of the cylinder. It is interesting to note that the accuracy at the corners obtained with the isoparametric elements is quite impressive, considering the relatively crude element mesh with respect to the wave number. Our detailed studies also suggested that the accuracy obtained with the mixed elements can be improved when a smaller edge distance is used for the transition elements, and converged to those obtained with isoparametric elements. As one may notice, the largest errors in the results obtained with the isoparametric elements are found at the middle node ($s/a=2.5$) of the cylinder, which is most close to the ring source. The results at this point can be improved with a finer discretization.

In order to simulate arbitrary boundary conditions or to provoke all items in the Fourier series of the normal velocity on the cylinder surface, the ring source of strength, $\sigma(\theta)=\sigma_0 \cos\theta$, is placed in the plane of the generator, shown in Fig. 10. Figure 10 presents the real and imaginary parts of the pressure along the generator at $ka=4.0$ obtained by retaining the first seven items (i.e., $|m|\leqslant 6$) in the Fourier series. Since the wave number is close to the first eigenvalue ($ka=3.9722$) of the associated interior Dirichlet problem for $m=1$, the Helmholtz integral equation employed in Refs. 14–16 fails to provide a unique solution. As can be seen in the figure, the isoparametric element solution is again of high accuracy in both the real and imaginary parts of the pressure, even at the corners. And the accuracy in pressure obtained with the isoparametric elements is also evidently much better than that with the mixed elements.

Finally, the radiation problem of a finite circular cylinder of radius a and length $2L$ with $a=0.5L$ studied by Copley,[10] using the method of subsectional bases, and by Fenlon,[26] using the method of weighted residuals, will be examined here. The end caps of the cylinder were considered to be clamped (with zero velocity) and the velocity profile over the cylindrical surface was taken as unity in the range $[-0.8a<z<0.8a]$. Beyond this range, the velocity profile tapers off linearly to the value zero at the end edges. Because of the symmetry of the problem, only the half-generator is needed to be modeled. The exact solution of this problem is a very difficult analytical task. Thus it is of interest to examine the convergence of numerical solutions as the element mesh is refined, and to compare with the previously reported results.

In Figs. 11, 12, and 13, the normalized pressure along

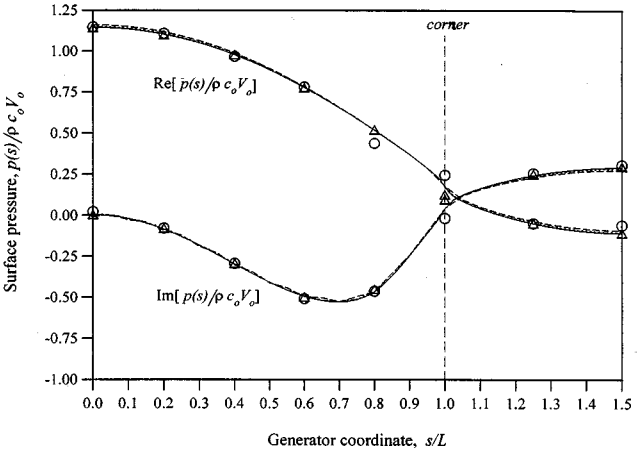

FIG. 12. Surface pressure for a finite cylinder of half-length L and radius a with $a/L=0.5$ at wave number $kL=4$. ——— 60 elements, ... 30 elements, --- 15 elements, ○ Copley's method,[10] △ Fenlon's method.[26]

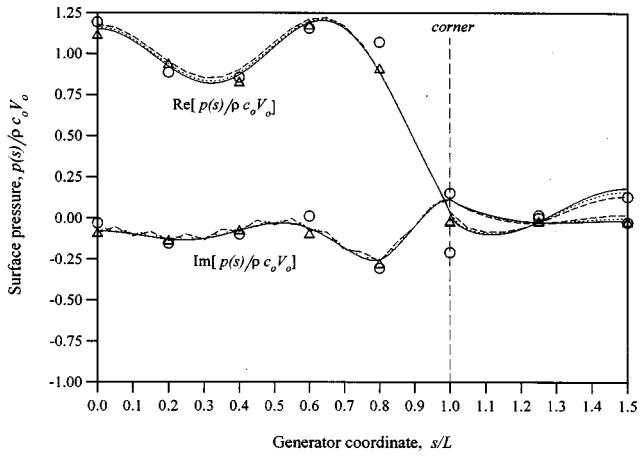

FIG. 13. Surface pressure for a finite cylinder of half-length L and radius a with $a/L=0.5$ at wave number $kL=10$. ——— 60 elements, ... 30 elements, --- 15 elements, ○ Copley's method,[10] △ Fenlon's method.[26]

the generator obtained by using the presented method with 15, 30, and 60 isoparametric quadratic elements are compared for $kL=2$, 4, and 10, respectively. Results obtained by Fenlon,[26] using the weighted-residuals method, and with those obtained by Copley,[10] using the method of subsectional bases, are also included for comparison.

As seen in Figs. 11 and 12, the relative coarse mesh of 15 elements is entirely adequate for the lower wave numbers $ka=2$ and 4. However, reference to Fig. 13 indicates the refined mesh of 30 elements must be used before adequate convergence of numerical solution is achieved at $kL=10$. Reference to Figs. 11–13 reveals that, in general, our solutions are in good agreement with those computed by Fenlon and Copley at most points in the range. The disagreement is most pronounced near the corner and on the end cap, especially, at $kL=10$. The surface pressure on the end cap at $kL=10$ obtained by the present method have the same format of distribution as that obtained by Copley, but is quite different with that obtained by Fenlon. To further verify our results, Fig. 14 shows the comparison of the results obtained by the present method using 60 line quadratic elements with those obtained using the variational method[27] with 1416 eight-node quadrature elements of a total of 4666 nodes for the full cylinder. The results obtained by Fenlon[26] are also included for comparison. As seen in Fig. 14, results computed by the 3-D variational methods are in excellent agreement with those obtained by the present method at all points, but again, are quite different from Fenlon's results, of which the correctness seems questionable at this wave number, especially, for points near the corner and on the end cap.

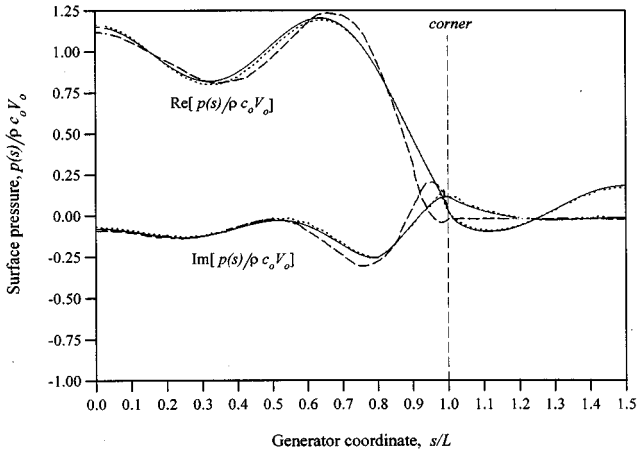

FIG. 14. Surface pressure for a finite cylinder of half-length L and radius a with $a/L=0.5$ at wave number $kL=10$. ——— the present method, ... variational method[27] --- Fenlon's method.[26]

V. CONCLUSIONS

A unique boundary integral method has been developed to analyze the exterior acoustic radiation problem of axisymmetric bodies with arbitrary boundary conditions. The new formulation derives from the Burton and Miller's method to ensure the uniqueness of the numerical solution at all frequencies. Unlike most current methods and formulations it is straightforward to implement using isoparametric elements regardless of how complicated the surface geometry or the boundary conditions may be.

The pulsating and oscillating sphere problems were chosen to illustrate the superior accuracy and efficiency of the proposed formulation compared with other published three-dimensional formulations. We demonstrated that the use of only six quadratic line elements has achieved the accuracy higher than the use of 40 3-D quadratic elements in both cases. The problems of a finite cylinder have also been presented to show the usefulness of the formulation for bodies with corners and arbitrary boundary conditions. The results obtained by using isoparametric elements are seen to exhibit better accuracy than those obtained by using mixed elements, and reveal that corners can be handled as easily and accurately as other points. The examples presented in the paper were only for bodies of simple geometries; however, the generality of formulations and the results obtained from these examples indicate that more practical problems can be treated with good accuracy by the present formulations.

ACKNOWLEDGMENTS

This work has been made possible with the combined financial support of NSERC (National Science and Engineering Research Council of Canada), and IRSST (Institut de Recherche en Santé et en Sécurité du Travail du Québec).

[1] H. A. Schenck, ''Improved integral formulation for acoustic radiation problems,'' J. Acoust. Soc. Am **44** 41–58 (1968).
[2] W. L. Meyer, W. A. Bell, and B. T. Zinn, ''Boundary Integral Solutions of Three Dimensional Acoustic Radiation Problems,'' J. Sound Vib. **59**(2), 245–262 (1978).
[3] C. C. Chien, H. Rajiyah, and S. N. Atluri, ''An effective method for solving the hypersingular integral equations in 3-D acoustics,'' J. Acoust. Soc. Am. **88**, 918–937 (1990).
[4] A. J. Burton and G. F. Miller, ''The application of the integral equation method to the numerical solution of some exterior boundary values problems,'' Proc. R. Soc. London Ser. A **323**, 201–210 (1971).
[5] O. I. Panich, ''On the question of the solvability of the exterior boundary problem for the wave equation and Maxwell equation,'' Usp. Mat. Nauk **20**(1), 221–226 (1965).
[6] W. L. Meyer, W. A. Bell, M. P. Stallybrass, and B. T. Zinn, ''Prediction

of the sound field radiated from axisymmetric surfaces,'' J. Acoust. Soc. Am. **65**, 631–638 (1979).
[7] T. Terai, ''On calculation of sound fields around three-dimensional objects by integral equation methods,'' J. Sound Vib. **69**, 71–100 (1980).
[8] G. Krishnasamy, L. W. Schmerr, T. J. Rudolphi, and F. J. Rizzo, ''Hypersingular boundary integral equations: some applications in acoustic and elastic wave scattering,'' ASME J. Appl. Mech. **57**, 404–414 (1990).
[9] M. Guiggiani, G. Krishnasamy, T. J. Rudolphi, and F. J. Rizzo, ''A general algorithm for the numerical solution of hypersingular boundary integral equations,'' ASME J. Appl. Mech. **59**, 604–614 (1992).
[10] L. G. Copley, ''Integral equation method for radiation from vibrating bodies,'' J. Acoust. Soc. Am. **41**, 807–816 (1967).
[11] L. G. Copley, ''Fundamental results concerning integral representations in acoustic radiation,'' J. Acoust. Soc. Am. **44**, 41–88 (1968).
[12] J. S. Patel, ''Radiation and scattering from arbitrary elastic structure using consistent fluid structure formulation,'' Comput. Struct. **9**, 287–291 (1978).
[13] A. F. Seybert, B. Soenarko, F. J. Rizzo, and D. J. Shippy, ''A special integral equation formulation for acoustic radiation and scattering for axisymmetric bodies and boundary conditions,'' J. Acoust. Soc. Am. **80**, 1241–1247 (1986).
[14] P. Juhl, ''Axisymmetric integral formulation for nonaxisymmetric conditions,'' Report No. 47, The acoustic laboratory, Technical University of Denmark, ISSN 0105-3027 (1991).
[15] P. Juhl, ''An axisymmetric integral equation formulation for free space non-axisymmetric radiation and scattering of a known incident wave,'' J. Sound Vib. **163**(3), 397–406 (1993).
[16] B. Soenarko, ''A boundary element formulation for radiation of acoustic waves for axisymmetric bodies with arbitrary boundary conditions,'' J. Acoust. Soc. Am. **93**, 631–639 (1993).
[17] J. J. Grannell, J. J. Shirron, and L. S. Couchman, ''A hierarchic *p*-version boundary element method for axisymmetric acoustic scattering and radiation,'' J. Acoust. Soc. Am. **95**, 2320–2329 (1994).
[18] I. C. Mathews, ''Numerical techniques for three-dimensional steady state fluid–structure interaction,'' J. Acoust. Soc. Am. **79**, 1317–1325 (1986).
[19] P. A. Martin and F. J. Rizzo, ''On boundary integral equations for crack problems,'' Proc. Roy. Soc. London Ser. A **421**, 341–355 (1989).
[20] A. W. Maue, ''Zur formulierung eines allgemeimen beugungsproblems durch eine integral-gleichung,'' Z. Phys. **126**, 601–618 (1949).
[21] K. M. Mitzner, ''Acoustic scattering from an interface between media of greatly different density,'' J. Math. Phys. **7**, 2053–2060 (1966).
[22] T. W. Wu, A. F. Seybert, and G. C. Wan, ''On the numerical implementation of a Cauchy principal value integral to insure a unique solution for acoustic radiation and scattering,'' J. Acoust. Soc. Am. **90**(1), 554–560 (1991).
[23] J. J. do Rêgo Silva, ''Acoustic and elastic wave scattering using boundary elements,'' Computational Mechanics Publications (1994).
[24] Gray, L. J. and E. Lutz, ''On the treatment of corners in the boundary element method,'' J. Comput. Appl. Math. **32**, 369–386 (1990).
[25] A. D. Pierce, *Acoustics: An Introduction to Its Physical Principles and Applications* (The Acoustical Society of America, Woodbury, NY, 1991).
[26] H. F. Fenlon, ''Calculation of the acoustic radiation field at the surface of a finite cylinder by the method of weighted residuals,'' Proc. IEEE **57**, 291–306 (1969).
[27] W. Wang and N. Atalla, ''A new algorithm for acoustic radiation of vibrating structures using variational boundary element methods,'' internal report, GAUS, Université de Sherbrooke (1995).

Power transmission from a vibrating body to a circular cylindrical shell through passive and active isolators

Carl Q. Howard, Colin H. Hansen, and Jiaqiang Pan
Department of Mechanical Engineering, University of Adelaide, Adelaide, South Australia 5005, Australia

(Received 29 July 1992; revised 12 March 1996; accepted 6 November 1996)

The transmission of harmonic vibratory power from a vibrating rigid body into a thin supporting cylindrical shell through multiple passive and active isolators is investigated theoretically. The model allows for the transmission of vertical and horizontal harmonic forces and moments about all three coordinate axes. Results show that over a frequency range from 0 to 200 Hz, the real power transmission into the supporting shell can be reduced substantially by employing in parallel with existing passive isolators, active isolators adjusted to provide appropriate control force amplitudes and phases. © *1997 Acoustical Society of America.* [S0001-4966(97)04003-4]

PACS numbers: 43.40.Vn [PJR]

LIST OF SYMBOLS

$\alpha_{m,n}$	relation between axial and radial modal amplitudes
$[\alpha]$	quadratic equation matrix coefficient
$\beta_{m,n}$	relation between circumferential and radial modal amplitudes
$[\beta]$	quadratic equation matrix coefficient
$\alpha_{m,n}$	modal amplitude constants
$\beta_{m,n}$	modal amplitude constants
$[\Gamma_J]$	transpose of the cylinder modal vector matrix at the Jth mount
∇	gradient operator
δ	Dirac delta function
ε	differential displacement
ε_f	transmissibility
η_k	modal loss factor of cylindrical shell
$\eta_{J,i}$	damping loss factor of Jth isolator in the ith direction
θ	circumferential cylinder coordinate
κ	shell thickness parameter
λ	modified axial mode number
ν	Poisson ratio
ξ_s	displacement in axial direction
ξ_θ	displacement in circumferential direction
ρ	density of the shell material
σ	general 3D coordinate
σ_J	location of the Jth mount on cylindrical shell
σ_J^t	top location of the Jth isolator on the rigid body
ψ_k	mode shape function in radial direction of cylinder
ψ_{ks}	mode shape function in axial direction of cylinder
$\psi_{k\theta}$	mode shape function in circumferential direction of cylinder
ω	circular frequency
ω_k	resonance frequency of cylinder with shear diaphragm end conditions
Ω_k	kth component of uncoupled shell characteristic matrix
χ	identifying number of the axis which the control actuator provides the restoring force
$a_{m,n}$	modal amplitude in axial direction
$[a]$	quadratic equation matrix coefficient
$[\hat{a}]$	modified quadratic equation matrix coefficient to exclude redundant equations
$[A]$	matrix of the equations of motion for the cylinder and rigid body
$b_{m,n}$	modal amplitude in circumferential direction
$[b_1]$	quadratic equation vector coefficient
$[\hat{b}_1]$	modified quadratic equation vector coefficient to exclude redundant equations
$[b_2]$	quadratic equation vector coefficient
$[\hat{b}_2]$	modified quadratic equation vector coefficient to exclude redundant equations
$[B]$	inverted matrix of the equations of motion for the cylinder and rigid body
c_k	modal amplitude in radial direction
$c_{m,n}$	modal amplitude in radial direction
$[c]$	quadratic equation coefficient
$[c^s]$	vector of modal amplitudes
$C_{i,k}$	i,k element of matrix representing the influence of the lower mounts on the cylindrical shell
d_n	nth principal subdeterminant
$[D_0]$	displacement vector of rigid body
$[D_J^t]$	displacement of top of the Jth isolator
$[D_J^b]$	displacement of the Jth support point in Cartesian coordinates
e	exponential function
E	Young's modulus
F	force
$[G_a]$	matrices used in the construction of the quadratic equation
h	thickness of cylindrical shell
$[H_a]$	matrices used in the construction of the quadratic equation
I_{xx}	moments of inertia about the xx axis
$\mathrm{Im}\{R\}$	imaginary part of R
j	complex number
$k_{J,i}$	stiffness of the Jth isolator in the ith direction
$[K]$	stiffness matrix of all isolators
$[K_J]$	stiffness matrix of the Jth isolator
L_0	axial length of cylinder
L_1	number of isolators
$L(x)$	quadratic function

 0001-4966/97/101(3)/1479/13/$10.00

m axial mode number
m_0 mass of the rigid body
m_s mass of the cylindrical shell
m_J^b mass of the Jth lower mount
M moment
M_c mobility of cylindrical shell
M_i mobility of passive vibration isolator
M_r mobility of rigid body
n circumferential mode number
p force and moment loading from isolators on cylindrical shell
P number of modes used in the analysis
P_1 time averaged power transmission from the vibrating rigid body
$P_{2,J}$ power transmission into the Jth passive isolator
P_2 total power transmission into all passive isolators
P_3 total power transmission into the cylindrical shell
$P_{3,0}$ power transmission into cylindrical shell using passive control
ΔP difference of power transmitted into cylindrical shell using passive and active vibration control
q_1 inertial load of lower mounts on cylindrical shell
q_2 force and moment loading from isolators on cylindrical shell
$[q^c]$ vector of the real and imaginary parts of the combined control force vector of all actuators
$[Q_0]$ harmonic driving force vector
$[Q^c]$ combined control force vector of all actuators
$[Q_J^c]$ control force vector of the Jth actuator
$[Q_J^b]$ force at bottom of Jth isolator
$[Q_J^t]$ force at top of Jth isolator
$[Q_J]$ force at bottom of Jth isolator, expressed in cylindrical coordinates
r radial coordinate
R radius of the midsurface of the cylindrical shell
$[R_J^t]$ force location matrix on the rigid body for the Jth isolator
$[R_J^b]$ modal vector matrix for the Jth isolator
$\mathrm{Re}\{R\}$ real part of R
s nondimensional axial cylinder coordinate
t time
$[T_J]$ Cartesian to cylindrical coordinate transformation matrix
w displacement in radial direction
$[W_J]$ displacement vector of the Jth support point in cylindrical coordinates
$[Z_0]$ impedance matrix of rigid body
$[Z_s]$ uncoupled shell characteristic matrix

INTRODUCTION

When considering the possibility of including a feedforward, adaptive isolation system in parallel with existing passive equipment isolators for minimizing harmonic vibratory power transmission from vibrating equipment to a cylindrical support structure, it is useful to have an analytical model to estimate potential performance benefits. The purpose of the work described here is to develop such a model which allows the calculation of the harmonic vibratory power transmission from an arbitrarily vibrating rigid body through flexible isolators to a flexible cylinder. The model allows the inclusion of active force elements acting in parallel with passive isolators to form part of an active control system, and takes into account existing forces acting in an arbitrary direction and existing moments acting about any axis.

A review of previous work[1,2] considers the general topic of active vibration isolation. To the author's knowledge, no previous work has been done concerning the active isolation of a rigid body from a flexible cylinder at the time this paper was submitted. As explained in those earlier papers, the cost function chosen to be minimized in that work and also here is the total vibratory power transmission into the flexible support structure (support cylinder in this case).

As in the earlier work, the active isolators consist of a passive element incorporating both stiffness and damping, in parallel with an active element which applies control forces to both the rigid body and the flexible cylinder simultaneously; that is, the actuator pushes on the rigid body and reacts against the flexible cylinder.

I. THEORETICAL MODEL

A. Vibration source and elastic isolators

Figure 1 shows the arrangement of the modeled system, which consists of a three-dimensional rigid body connected to a simply supported, thin, closed circular cylindrical shell through L_1 elastic isolators. A vibratory source of frequency ω acting on the rigid body can be described by a harmonic external force vector $[Q_0]e^{j\omega t}$ acting on the center of gravity of the body as follows:

$$[Q_0]=[F_x \quad F_y \quad F_z \quad M_x \quad M_y \quad M_z]^T, \tag{1}$$

where the symbols F and M are, respectively, the force and moment components of the 6-D force vector.

The top location of the Jth isolator on the rigid body is denoted σ_J^t and its bottom location on the inside surface of the cylinder at $r=R-h/2$ is denoted σ_J, where $J=1,\ldots,L_1$, R is the radius of the midsurface of the cylinder and h is the thickness of the cylinder shell. The origin of the coordinate system (X,Y,Z) of the rigid body is located at its center of gravity and the orientation of its X axis is parallel to the central axis of the cylinder. The motion of the rigid body can be described by its translational displacements x_0, y_0, z_0 and angular displacements θ_{0x}, θ_{0y}, θ_{0z}, respectively, around the X, Y and Z axes. The displacements can be expressed by using a 6-D displacement vector $[D_0]$ as follows:

$$[D_0]=[x_0 \quad y_0 \quad z_0 \quad \theta_{0x} \quad \theta_{0y} \quad \theta_{0z}]^T. \tag{2}$$

Similarly, the 6-D displacement vectors at the top and bottom ends of the isolators are described as $[D_J^t]$ and $[D_J^b]$, respectively. The elements of displacement vectors $[D_J^b]$ are given in the Cartesian coordinate system on the Jth support point and for the same point, the displacement vector given

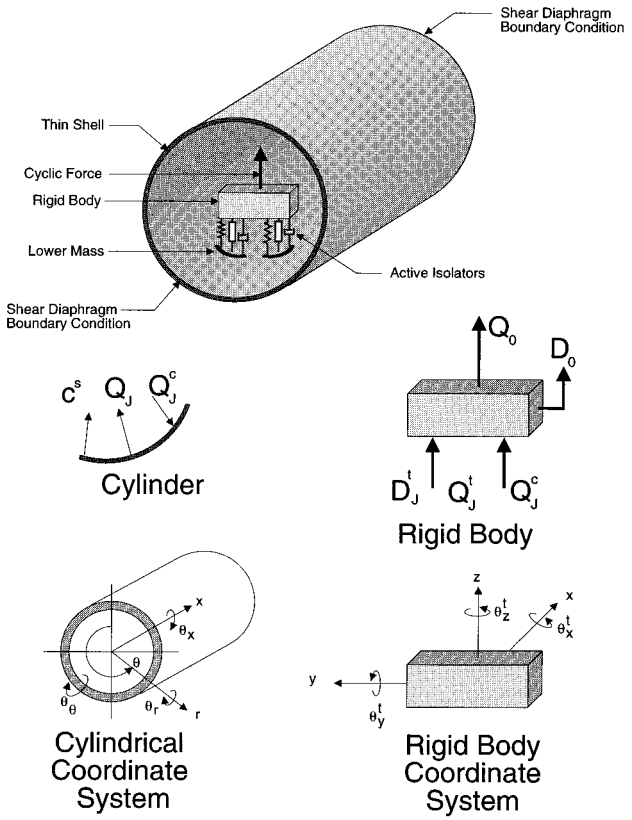

FIG. 1. Cylinder model and coordinate systems for cylinder and rigid body.

in the cylindrical coordinate system is expressed as $[W_J]$, as shown in Fig. 1.

The elastic forces F and moments M acting on each isolator from the rigid body and the supporting shell are proportional to the relative displacement between the top and bottom surfaces of the isolator. Therefore, the relationship between the 6-D elastic force vectors $[Q_J^t]$ acting on the top of the isolators and the 6-D displacement vectors $[D_J^t]$ and $[D_J^b]$ is

$$[Q_J^t]=[K_J]([D_J^b]-[D_J^t]), \tag{3}$$

where $[K_J]$ is the stiffness matrix of the Jth isolator. The matrix is a complex diagonal matrix, nonzero diagonal elements of which can be expressed as $k_{J,i}(1+j\,\eta_{J,i})$ $(i=1,...,6)$, where $\eta_{J,i}$ are the damping loss factors of the Jth isolator and $j=\sqrt{-1}$.

Thus the equation of motion of the rigid body can be written as follows:

$$[Z_0][D_0]=[Q_0]+\sum_{J=1}^{L_1}[R_J^t][Q_J^t], \tag{4}$$

where

$$[Z_0]=-\omega^2\begin{bmatrix} m_0 & 0 & & & & \\ & m_0 & & 0 & & \\ 0 & & m_0 & & & \\ & & & I_{xx} & I_{xy} & I_{xz} \\ & 0 & & I_{yx} & I_{yy} & I_{yz} \\ & & & I_{zx} & I_{zy} & I_{zz} \end{bmatrix}, \tag{5}$$

m_0 is the mass of the rigid body and I_{xx}, I_{xy},..., I_{zz}, $(I_{xy}=I_{yx}, I_{yz}=I_{zy}, I_{zx}=I_{xz})$ are its moments of inertia and $[R_J^t]$ is a (6×6) force location matrix (on the rigid body) for the Jth elastic force vector defined as follows:

$$[R_J^t]=\begin{bmatrix} 1 & 0 & 0 & 0 & 0 & 0 \\ 0 & 1 & 0 & 0 & 0 & 0 \\ 0 & 0 & 1 & 0 & 0 & 0 \\ 0 & -z_{0J} & y_{0J} & 1 & 0 & 0 \\ z_{0J} & 0 & -x_{0J} & 0 & 1 & 0 \\ -y_{0J} & x_{0J} & 0 & 0 & 0 & 1 \end{bmatrix}, \tag{6}$$

where (x_{0J},y_{0J},z_{0J}) are the Cartesian coordinates of the top end of the Jth isolator. It can be shown that for small displacements of the rigid body, the following relationship holds:

$$[D_J^t]=[R_J^t]^T[D_0]. \tag{7}$$

B. Supporting thin cylinder

The supporting cylinder is driven by L_1 force vectors, defined as $[Q_J^b]=[F_{xJ}^b \;\; F_{yJ}^b \;\; F_{zJ}^b \;\; M_{xJ}^b \;\; M_{yJ}^b \;\; M_{zJ}^b]^T$ in the Cartesian coordinate system or $[Q_J]=[F_{xJ} \;\; F_{\theta J} \;\; F_{rJ} \;\; M_{xJ} \;\; M_{\theta J} \;\; M_{rJ}]^T$ in the cylindrical coordinate system, as shown in Fig. 1, where $J=1,\ldots,L_1$. The force vectors acting on the top of each isolator are related to those acting on the bottom as follows:

$$[Q_J^b]=-[Q_J^t], \tag{8}$$

and the forces expressed in the cylindrical coordinate system are related to those expressed in the Cartesian coordinate system as follows:

$$[Q_J]=[T_J][Q_J^b], \tag{9}$$

where $[T_J]$ is a coordinate transformation matrix between the Cartesian and cylindrical coordinates of the support point σ_J and is defined as follows:

$$[T_J]=\begin{bmatrix} [T_{0J}] & 0 \\ 0 & [T_{0J}] \end{bmatrix}, \tag{10}$$

where [0] is a three-order zero matrix and

$$[T_{0J}]=\begin{bmatrix} 1 & 0 & 0 \\ 0 & \cos\theta_J & -\sin\theta_J \\ 0 & \sin\theta_J & \cos\theta_J \end{bmatrix}. \tag{11}$$

It can be shown that $[T_J]^{-1}=[T_J]^T$.

The force and moment components in $[Q_J^b]$ or $[Q_J]$ are also assumed to be concentrated point actions at support

points σ_J on the thin shell, so that Dirac delta functions and their partial derivatives can be used to describe the external force distribution on the cylinder.

The motion of the cylindrical shell can be described by the Donnell–Mushtari theory[3] which uses eighth-order differential equations. These equations can be simplified if the radius R of the cylindrical shell is significantly large compared to the shell thickness h. In this case the vibration of the cylinder is primarily radial, with the axial x and tangential θ displacements being small enough to allow the corresponding inertia terms in the axial and tangential directions in the equation of motion of the cylindrical shell to be neglected. Forces acting in the axial x and tangential θ directions excite vibration in these directions, which in turn couples with the radial vibration to produce vibration in the radial w direction but at a much smaller amplitude. However, the radial vibration amplitude produced in this way is considered small compared to the radial vibration produced directly by moments and radial forces. This assumption, which results in the right hand side of Eqs. (12) and (13) being zero, is important as it simplifies the analysis enormously. The limitations of this assumption are the subject of ongoing work. Note that the axial and tangential forces produced on the inside surface of the cylinder produce moments about the midsurface of the shell, which results in direct excitation of radial motion. This is taken into account in the following analysis.

The Donnell–Mushtari equations of motion for a cylindrical shell may be written as

$$\frac{\partial^2 \xi_s}{\partial s^2}+\frac{(1-\nu)}{2}\frac{\partial^2 \xi_s}{\partial \theta^2}+\frac{(1+\nu)}{2}\frac{\partial^2 \xi_\theta}{\partial s\,\partial \theta}+\nu\frac{\partial w}{\partial s}=0, \tag{12}$$

$$\frac{(1+\nu)}{2}\frac{\partial^2 \xi_s}{\partial s\,\partial \theta}+\frac{(1-\nu)}{2}\frac{\partial^2 \xi_\theta}{\partial s^2}+\frac{\partial^2 \xi_\theta}{\partial \theta^2}+\frac{\partial w}{\partial \theta}=0, \tag{13}$$

$$\nu\frac{\partial \xi_s}{\partial s}+\frac{\partial \xi_\theta}{\partial \theta}+w+\kappa\nabla^4 w+\frac{\rho(1-\nu^2)R^2}{E}\frac{\partial^2 w}{\partial t^2}$$
$$=\frac{(1-\nu^2)}{Eh}[q_1(x,\theta)+q_2(x,\theta)]e^{j\omega t}, \tag{14}$$

where $s=x/R$ is the nondimensionalized length, the gradient operator is defined as

$$\nabla^4=\nabla^2\nabla^2=\left\{\frac{\partial^2}{\partial s^2}+\frac{\partial^2}{\partial \theta^2}\right\}^2, \tag{15}$$

$\xi_s(s,\theta;t)$, $\xi_\theta(s,\theta;t)$, and w are the orthogonal components of the displacement in the axial x, circumferential θ, and radial w directions, and the force distribution functions q_1, q_2 in the right side of Eq. (14) are:

$$q_1=\sum_{J=1}^{L_1} m_J^b\omega^2 w(\sigma_J)\,\delta(\sigma-\sigma_J), \tag{16}$$

$$q_2=p(s,\theta), \tag{17}$$

where ρ, E, ν are, respectively, the density, Young's modulus, and Poisson's ratio of the shell material, R and h are, respectively, the radius and thickness of the cylinder, m_J^b is a concentrated mass modeling the base at the bottom of the Jth mount, κ is a dimensionless shell thickness parameter defined as

$$\kappa=\frac{h^2}{12R^2}, \tag{18}$$

and $p(s,\theta)$ can be expressed as follows (see the Appendix):

$$p(s,\theta)=\sum_{J=1}^{L_1}\left[-\frac{h}{2}\frac{\partial\delta(\sigma-\sigma_J)}{\partial x},-\frac{h}{2R}\frac{\partial\delta(\sigma-\sigma_J)}{\partial\theta},\right.$$
$$\left.\delta(\sigma-\sigma_J),-\frac{1}{R}\frac{\partial\delta(\sigma-\sigma_J)}{\partial\theta},\frac{\partial\delta(\sigma-\sigma_J)}{\partial x},0\right][Q_J] \tag{19a}$$

$$=\sum_{J=1}^{L_1}\left[-\frac{h}{2}\frac{\partial\delta(\sigma-\sigma_J)}{R\partial s},-\frac{h}{2R}\frac{\partial\delta(\sigma-\sigma_J)}{\partial\theta},\right.$$
$$\left.\delta(\sigma-\sigma_J),-\frac{1}{R}\frac{\partial\delta(\sigma-\sigma_J)}{\partial\theta},\frac{\partial\delta(\sigma-\sigma_J)}{R\partial s},0\right][Q_J]. \tag{19b}$$

For a simply supported circular cylindrical shell, the following harmonic solutions can be employed:

$$\xi_s(s,\theta;t)=\xi_s(s,\theta)e^{j\omega t}, \tag{20a}$$

$$\xi_\theta(s,\theta;t)=\xi_\theta(s,\theta)e^{j\omega t}, \tag{20b}$$

$$w(s,\theta;t)=w(s,\theta)e^{j\omega t}, \tag{20c}$$

and

$$\xi_s(s,\theta)=\sum_{m,n=1}^{\infty} a_{m,n}\cos\lambda s\,\sin n\theta, \tag{21a}$$

$$\xi_\theta(s,\theta)=\sum_{m,n=1}^{\infty} b_{m,n}\sin\lambda s\,\cos n\theta, \tag{21b}$$

$$w(s,\theta)=\sum_{m,n=1}^{\infty} c_{m,n}\sin\lambda s\,\sin n\theta, \tag{21c}$$

where $a_{m,n}$, $b_{m,n}$, and $c_{m,n}$ are modal amplitude constants for mode (m,n), L_0 is the length of the cylinder, and $\lambda=m\pi R/L_0$. Substituting Eq. (20) into Eqs. (12) and (13) gives

$$a_{m,n}=\lambda\alpha_{m,n}c_{m,n}=\frac{\lambda(\nu\lambda^2-n^2)}{(\lambda^2+n^2)^2}c_{m,n}, \tag{22}$$

$$b_{m,n}=n\beta_{m,n}c_{m,n}=\frac{n\{(2+\nu)\lambda^2+n^2\}}{(\lambda^2+n^2)^2}c_{m,n}, \tag{23}$$

where $m,n=1,2,...$

$$\alpha_{m,n}=\frac{(\nu\lambda^2-n^2)}{(\lambda^2+n^2)^2}, \tag{24}$$

$$\beta_{m,n}=\frac{(2+\nu)\lambda^2+n^2}{(\lambda^2+n^2)^2}. \tag{25}$$

For convenience, the modes will be identified by a single index k, rather than the double index (m,n) and arranged in ascending order of resonance frequency. Thus, $c_{m,n}$ will be represented as c_k from now on. Substituting Eqs. (16), (17),

and (21) into Eq. (14), multiplying each side by $\psi_k(\sigma_J)$ and integrating over the cylinder length L_0 (orthogonal property of the mode shape functions) and using the results

$$\int_0^{L_0/R} \sin \lambda_1 s \sin \lambda_2 s ds = \frac{L_0}{2R}$$

if $\lambda_1 = \lambda_2$ and 0 if $\lambda_1 \neq \lambda_2$ and

$$\int_0^{2\pi} \sin n_1\theta \sin n_2\theta d\theta = \pi$$

if $n_1 = n_2$ and 0 if $n_1 \neq n_2$, gives the following equation for the radial modal amplitude coefficients c_k, $(k=1,2,...)$ for all shell modes:

$$\left(\frac{R^2\rho(1-\nu^2)}{E}\right)\left(\frac{\pi L_0}{2R}\right)(\omega_k^2 + j\eta_k\omega_k^2 - \omega^2)c_k = \frac{(1-\nu^2)}{Eh}\sum_{J=1}^{L_1}\left\{\left[\frac{h}{2R}\psi_{ks}(\sigma_J), \frac{h}{2R}\psi_{k\theta}(\sigma_J), \psi_k(\sigma_J), \frac{1}{R}\psi_{k\theta}(\sigma_J), -\frac{1}{R}\psi_{ks}(\sigma_J), 0\right][Q_J] + \sum_{i=1}^{\infty} C_{ik}c_i\right\}, \quad (26)$$

where the shell modal damping has been included by way of the modal loss factor η_k, c_i and c_k are the coefficients for the ith shell mode and kth shell mode, respectively, ω_k are the shell mode resonance angular frequencies arranged in ascending order, and C_{ik} is the concentrated mass contribution given by

$$C_{ik} = \sum_{J=1}^{L_1} m_J^b \omega^2 \psi_i(\sigma_J)\psi_k(\sigma_J). \quad (27)$$

The quantities $\psi_k(\sigma_J), \psi_{ks}(\sigma_J), \psi_{k\theta}(\sigma_J)$, are three dimensionless functions evaluated at the point $\sigma_J(s_J, \theta_J)$ on the shell and defined as follows:

$$\psi_k(\sigma_J) = \sin \lambda s_J \sin n\theta_J, \quad (28a)$$

$$\psi_{ks}(\sigma_J) = \lambda \cos \lambda s_J \sin n\theta_J, \quad (28b)$$

$$\psi_{k\theta}(\sigma_J) = n \sin \lambda s_J \cos n\theta_J, \quad (28c)$$

where n is the modal order of the kth mode in the circumferential direction.

Substituting Eqs. (20), (22), and (23) into Eq. (14), and setting the right hand side of the expression to zero, an expression for the shell mode resonance angular frequencies ω_k, $(k=1,2,...)$ can be derived as:

$$\omega_k^2 = \left[\frac{(1-\nu^2)\lambda^4}{(\lambda^2+n^2)^2} + \kappa(\lambda^2+n^2)^2\right]\frac{E}{\rho(1-\nu^2)R^2}. \quad (29)$$

This theory is less accurate for small circumferential mode numbers. For a comparison of the error in the estimation of the resonance frequencies with other shell theories, see Leissa.[3]

When only the first P modes are taken into account, Eq. (26) can be written in the following matrix form:

$$[Z_s][c^s] = \sum_{J=1}^{L_1} [R_J^b][Q_J], \quad (30)$$

where $[Z_S]$ is the uncoupled shell characteristic matrix, including the influence of the concentrated masses of the isolating mounts:

$$[Z_s] = \begin{bmatrix} \Omega_1 - C_{1,1} & -C_{1,2} & -C_{1,3} & \cdots & -C_{1,P} \\ -C_{2,1} & \Omega_2 - C_{2,2} & -C_{2,3} & \cdots & -C_{2,P} \\ \vdots & \vdots & \vdots & \vdots & \vdots \\ \vdots & \vdots & \vdots & \vdots & \vdots \\ -C_{P,1} & -C_{P,2} & -C_{P,3} & \cdots & \Omega_P - C_{P,P} \end{bmatrix}, \quad (31)$$

where $C_{ik} = C_{ki}$ and Ω_k $(k=1,\ldots,P)$ is defined as

$$\Omega_k = \frac{m_s}{4}(\omega_k^2 + j\eta_k\omega_k^2 - \omega^2), \quad (32)$$

where $m_s = 2\pi R\rho h L_0$ is the mass of the cylindrical shell, and $[c^S] = [c_1, c_2, \ldots, c_P]^T$.

The quantity $[R_J^b]$ in Eq. (30) is a force location matrix corresponding to force vector $[Q_J]$ acting on the Jth support point on the cylindrical shell:

$$[R_J^b] = \begin{bmatrix} \frac{h}{2R}\psi_{1s}(\sigma_J) & \frac{h}{2R}\psi_{1\theta}(\sigma_J) & \psi_1(\sigma_J) & \frac{1}{R}\psi_{1\theta}(\sigma_J) & -\frac{1}{R}\psi_{1s}(\sigma_J) & 0 \\ \frac{h}{2R}\psi_{2s}(\sigma_J) & \frac{h}{2R}\psi_{2\theta}(\sigma_J) & \psi_2(\sigma_J) & \frac{1}{R}\psi_{2\theta}(\sigma_J) & -\frac{1}{R}\psi_{2s}(\sigma_J) & 0 \\ \vdots & \vdots & \vdots & \vdots & \vdots & \vdots \\ \frac{h}{2R}\psi_{Ps}(\sigma_J) & \frac{h}{2R}\psi_{P\theta}(\sigma_J) & \psi_P(\sigma_J) & \frac{1}{R}\psi_{P\theta}(\sigma_J) & -\frac{1}{R}\psi_{Ps}(\sigma_J) & 0 \end{bmatrix}. \quad (33)$$

In the cylindrical coordinate system, the rotational displacements of a point on the shell can be calculated by using the following equation:

$$\theta_x = \frac{1}{R}\frac{\partial w}{\partial \theta}, \quad \theta_\theta = -\frac{\partial w}{\partial s}. \quad (34a,b)$$

Note that θ_r is zero (essentially rotation in the curved plane of the cylinder surface). Thus, using Eqs. (20), (22), (23), and (33), the following matrix expression can be obtained:

$$[W_J]=[\xi_s \quad \xi_\theta \quad w \quad \theta_x \quad \theta_\theta \quad \theta_r]^T=[\Gamma_J][c^s] \quad (J=1,\ldots,L_1), \tag{35}$$

where $[W_J]$ is the 6D displacement vector of the Jth support point σ_J in the cylindrical coordinate system, and the matrix $[\Gamma_J]$ is given as follows:

$$[\Gamma_J]=[R_J^b]^T$$

$$=\begin{bmatrix} \frac{h}{2R}\psi_{1s}(\sigma_J) & \frac{h}{2R}\psi_{2s}(\sigma_J) & \cdots & \frac{h}{2R}\psi_{Ps}(\sigma_J) \\ \frac{h}{2R}\psi_{1\theta}(\sigma_J) & \frac{h}{2R}\psi_{2\theta}(\sigma_J) & \cdots & \frac{h}{2R}\psi_{P\theta}(\sigma_J) \\ \psi_1(\sigma_J) & \psi_2(\sigma_J) & \cdots & \psi_P(\sigma_J) \\ \frac{1}{R}\psi_{1\theta}(\sigma_J) & \frac{1}{R}\psi_{2\theta}(\sigma_J) & \cdots & \frac{1}{R}\psi_{P\theta}(\sigma_J) \\ -\frac{1}{R}\psi_{1s}(\sigma_J) & -\frac{1}{R}\psi_{2s}(\sigma_J) & \cdots & -\frac{1}{R}\psi_{Ps}(\sigma_J) \\ 0 & 0 & \cdots & 0 \end{bmatrix}. \tag{36}$$

C. System equation of motion

The displacement vector $[D_J^b]$ of the shell support point σ_J in the Cartesian coordinate system can be expressed in terms of $[W_J]$ in the cylindrical coordinate system by using the following relationship:

$$[W_J]=[T_J][D_J^b]. \tag{37}$$

Synthesizing Eqs. (3), (4), (7), (8), (9), (30), (35), and (37) gives the following equation of motion for the coupled system:

$$\begin{bmatrix} A_{11} & A_{12} \\ A_{21} & A_{22} \end{bmatrix}\begin{bmatrix} D_0 \\ c^s \end{bmatrix}=\begin{bmatrix} Q_0 \\ 0 \end{bmatrix}, \tag{38}$$

where the element matrices $A_{11},\ldots,A_{22}$ are given by the following expressions:

$$A_{11}=[Z_0]+\sum_{J=1}^{L_1}[R_J^t][K_J][R_J^t]^T, \tag{39a}$$

$$A_{12}=-\sum_{J=1}^{L_1}[R_J^t][K_J][T_J]^T[\Gamma_J], \tag{39b}$$

$$A_{21}=-\sum_{J=1}^{L_1}[R_J^b][T_J][K_J][R_J^t]^T, \tag{39c}$$

$$A_{22}=[Z_s]+\sum_{J=1}^{L_1}[R_J^b][T_J][K_J][T_J]^T[\Gamma_J]. \tag{39d}$$

The resonance frequencies and mode shapes of the coupled system can be obtained by solving the eigenvalue problem of the coefficient matrix $[A]$ when $[Q_0]=0$:

$$[A]=\begin{bmatrix} A_{11} & A_{12} \\ A_{21} & A_{22} \end{bmatrix}. \tag{40}$$

D. Active isolator

The passive isolators can be made active by using force actuators connected in parallel with each of them, as shown in Fig. 1. When used with a suitable feedforward control system, these actuators exert control forces on the rigid body and the shell support points simultaneously, to minimize the chosen cost function. In this case, the right-hand side of Eq. (38) is replaced by a combined force vector, and the equation becomes

$$\begin{bmatrix} A_{11} & A_{12} \\ A_{21} & A_{22} \end{bmatrix}\begin{bmatrix} D_0 \\ c^s \end{bmatrix}=\begin{bmatrix} Q_0+\sum_{J=1}^{L_1}[R_J^t][Q_J^c] \\ -\sum_{J=1}^{L_1}[R_J^b][T_J][Q_J^c] \end{bmatrix}, \tag{41}$$

where $[Q_J^c]$ is the control force vector acting on the rigid body from the Jth actuator connected in parallel with the Jth mount attaching the rigid body to the flexible shell, and is defined for the Jth actuator in terms of forces and moments in the Cartesian coordinate system as: $[Q_J^c]=[F_x^c \quad F_y^c \quad F_z^c \quad M_x^c \quad M_y^c \quad M_z^c]_J^T$. A positive control force is defined here as one which acts on the rigid body in the direction of positive rigid body displacement and on the cylinder in the direction of negative cylinder displacement.

E. Power transmission into the support cylinder

The time averaged power transmission P_1 from the vibrating source into the rigid body is given by

$$P_1=\tfrac{1}{2}\mathrm{Re}\{j\omega[Q_0]^T[D_0]\}. \tag{42}$$

The power transmission P_{2J} into each passive isolator from the rigid body is

$$P_{2J}=-\tfrac{1}{2}\mathrm{Re}\{j\omega([Q_J^t]^H+[Q_J^c]^H)[D_J^t]\} \quad J=1,\ldots,L_1, \tag{43}$$

where superscript H represents the transpose and conjugate of a matrix. In cases where the matrix is real, H can be replaced with symbol T representing the transpose of the matrix. The total time averaged power transmission into all L_1 passive isolators from the rigid body is

$$P_2=\sum_{J=1}^{L_1}P_{2J}=-\frac{1}{2}\mathrm{Re}\left\{j\omega\sum_{J=1}^{L_1}[Q_J^t]^H[D_J^t]\right\}. \tag{44}$$

The total power transmission P_3 into the cylinder through the isolating mounts can be calculated as follows:

$$P_3=-\frac{1}{2}\mathrm{Re}\left\{j\omega\sum_{J=1}^{L_1}([Q_J]-[T_J][Q_J^c])^H[W_J]\right\}, \tag{45a}$$

$$=\frac{1}{2}\mathrm{Re}\left\{j\omega\sum_{J=1}^{L_1}[W_J]^H([Q_J]-[T_J][Q_J^c])\right\}, \tag{45b}$$

$$= -\frac{\omega}{2}\,\mathrm{Im}\left\{\sum_{J=1}^{L_1}[W_J]^H([Q_J]-[T_J][Q_J^c])\right\}. \tag{45c}$$

This is the quantity which may be used as the active control cost function to be minimized. It can be seen that the output power transmission P_3 depends on system parameters and control forces. For a given system, it is possible to express the output power by using an explicit quadratic function. Here a two-isolator system is taken as an example. For the case of $L_1=2$,

$$\sum_{J=1}^{L_1}[W_J]^H([Q_J]-[T_J][Q_J^c])$$

in Eq. (45c) can be expressed as follows:

$$\sum_{J=1}^{2}[W_J]^H([Q_J]-[T_J][Q_J^c])$$

$$=[Q^c]^H[a][Q^c]+[Q^c]^H[b_1]+[b_2][Q^c]+c, \tag{46}$$

where

$$[a]=[G_1][K][G_2]-[G_1], \tag{47}$$

$$[b_1]=[G_1][K][G_3], \tag{48}$$

$$[b_2]=[G_4][K][G_2]-[G_4], \tag{49}$$

$$[c]=[G_4][K][G_3], \tag{50}$$

and

$$[G_1]=\begin{bmatrix} H_1^H\Gamma_1^TT_1 & H_1^H\Gamma_2^TT_2 \\ H_2^H\Gamma_1^TT_1 & H_2^H\Gamma_2^TT_2\end{bmatrix}, \tag{51}$$

$$[G_2]=\begin{bmatrix} [R_1^t]^TH_3-T_1^T\Gamma_1H_1 & [R_1^t]^TH_4-T_1^T\Gamma_1H_2 \\ [R_2^t]^TH_3-T_2^T\Gamma_2H_1 & [R_2^t]^TH_4-T_2^T\Gamma_2H_2\end{bmatrix}, \tag{52}$$

$$[G_3]=\begin{bmatrix} [R_1^t]^TB_{11}-T_1^T\Gamma_1B_{21} \\ [R_2^t]^TB_{11}-T_2^T\Gamma_2B_{21}\end{bmatrix}[Q_0], \tag{53}$$

$$[G_4]=[Q_0]^T[B_{21}^H\Gamma_1^TT_1 \quad B_{21}^H\Gamma_2^TT_2], \tag{54}$$

$$[K]=\begin{bmatrix} K_1 & 0 \\ 0 & K_2\end{bmatrix}, \tag{55}$$

where the matrices H_1,H_2,H_3,H_4 are

$$[H_1]=[B_{21}][R_1^t]-[B_{22}][R_1^b][T_1], \tag{56}$$

$$[H_2]=[B_{21}][R_2^t]-[B_{22}][R_2^b][T_2], \tag{57}$$

$$[H_3]=[B_{11}][R_1^t]-[B_{12}][R_1^b][T_1], \tag{58}$$

$$[H_4]=[B_{11}][R_2^t]-[B_{12}][R_2^b][T_2], \tag{59}$$

and the matrices $[B_{11}]$, $[B_{12}]$, $[B_{21}]$, $[B_{22}]$ in the above expressions are the submatrix elements of the inverse of system matrix $[A]$, as follows:

$$\begin{bmatrix} B_{11} & B_{12} \\ B_{21} & B_{22}\end{bmatrix}=\begin{bmatrix} A_{11} & A_{12} \\ A_{21} & A_{22}\end{bmatrix}^{-1}, \tag{60}$$

$$[B_{11}]=\{[A_{11}]-[A_{12}][A_{22}]^{-1}[A_{21}]\}^{-1}, \tag{61}$$

$$[B_{22}]=\{[A_{22}]-[A_{21}][A_{11}]^{-1}[A_{12}]\}^{-1}, \tag{62}$$

$$[B_{12}]=-[A_{11}]^{-1}[A_{12}]\{[A_{22}]-[A_{21}][A_{11}]^{-1}[A_{12}]\}^{-1}, \tag{63}$$

$$[B_{21}]=-[A_{22}]^{-1}[A_{21}]\{[A_{11}]-[A_{12}][A_{22}]^{-1}[A_{21}]\}^{-1}. \tag{64}$$

The control force vector $[Q^c]$ of dimension (12×1) in Eq. (46) is a combined vector of control forces $[Q_1^c]$ and $[Q_2^c]$ as follows:

$$[Q^c]=\begin{bmatrix} Q_1^c \\ Q_2^c\end{bmatrix}. \tag{65}$$

By evaluating Eq. (46) and grouping the imaginary terms, the output power P_3 can be expressed as the following real quadratic function:

$$P_3=-\frac{\omega}{2}\left\{[q^c]^T\begin{bmatrix} a^{(i)} & a^{(r)} \\ -a^{(r)} & a^{(i)}\end{bmatrix}[q^c]+[q^c]^T\begin{bmatrix} b_1^{(i)} \\ -b_1^{(r)}\end{bmatrix}\right.$$

$$\left.+[b_2^{(i)} \quad b_2^{(r)}][q^c]+c^{(i)}\right\}, \tag{66}$$

or in terms of the following equivalent expression, with a symmetrical coefficient matrix for the quadratic term:

$$P_3=-\frac{\omega}{2}\{[q^c]^T[\alpha][q^c]+[q^c]^T[\beta]+[\beta]^T[q^c]+c^{(i)}\}, \tag{67}$$

where

$$[\alpha]=[\alpha]^T=\frac{1}{2}\begin{bmatrix} [a^{(i)}]+[a^{(i)}]^T & [a^{(r)}]-[a^{(r)}]^T \\ -[a^{(r)}]+[a^{(r)}]^T & [a^{(i)}]+[a^{(i)}]^T\end{bmatrix}, \tag{68}$$

$$[\beta]=\frac{1}{2}\begin{bmatrix} [b_2^{(i)}]^T+[b_1^{(i)}] \\ [b_2^{(r)}]^T-[b_1^{(r)}]\end{bmatrix}, \tag{69}$$

and the real matrices $[a^{(r)}]$, $[a^i]$, $[b_1^{(r)}]$,... represent, respectively, the real and imaginary parts of the complex matrices $[a]$, $[b_1]$ $[b_2]$, and c. Clearly, the real output power for the uncontrolled case where $[q^c]=0$ is given by $P_{3,0}=\frac{1}{2}\omega c^i$. The real control ''force'' vector $[q^c]$ of 24 elements consists of real $[Q^{cr}]$ and imaginary $[Q^{ci}]$ parts of the control force vector $[Q^c]$; thus,

$$[q^c]=\begin{bmatrix} Q^{cr} \\ Q^{ci}\end{bmatrix}. \tag{70}$$

A reduction in output power as a result of the action of the control forces will occur when the relationship $\Delta P=P_{3,0}-P_3>0$ is satisfied. In other words, control force vectors satisfying the following inequality can result in a reduction of the output power:

$$[q^c]^T[\alpha][q^c]+[q^c]^T[\beta]+[\beta]^T[q^c]<0. \tag{71}$$

It is well known[4] that the function

$$L([q^c])=[q^c]^T[\alpha][q^c]+[q^c]^T[\beta]+[\beta]^T[q^c] \tag{72}$$

has a minimum given by

$$L_{\min}=-[\beta]^T[\alpha]^{-1}[\beta] \tag{73}$$

corresponding to an optimum control force vector given by

$$[q^c_{\text{opt}}] = -[a]^{-1}[\beta] \tag{74}$$

when the following sufficient conditions (i.e., $[\alpha]$ is positive definite matrix) are satisfied:

$$d_n > 0 \quad (n = 1,2,\ldots,24), \tag{75}$$

where d_n is the nth principal subdeterminant of the coefficient matrix $[\alpha]$ of the quadratic term in the function $L([q^c])$.

Therefore, the maximum power reduction into the support shell, if a maximum exists, is

$$(\Delta P)_{\text{opt}} = (\omega/2)[\beta]^T[\alpha]^{-1}[\beta]. \tag{76}$$

From the control force vector $[q^c_{\text{opt}}]$, which results in the maximum power reduction, the amplitudes and phases of a set of optimal active control forces $[Q^c_1]_{\text{opt}}$ and $[Q^c_2]_{\text{opt}}$ can be obtained.

F. Zero power transmission into support cylinder

It is theoretically possible to reduce the power which is transmitted through the multiple isolators into the support structure to zero. Assume that each control actuator provides restoring forces and moments equal and opposite to the force applied by the isolator to the cylindrical shell given by

$$[Q^c_J] = [K_J]\{[D^t_J] - [D^b_J]\}. \tag{77}$$

Substituting this relationship into Eq. (41) yields

$$\begin{bmatrix} Z_0 & 0 \\ 0 & Z_S \end{bmatrix} = \begin{bmatrix} Q_0 \\ 0 \end{bmatrix}. \tag{78}$$

Equation (78) shows that the cylindrical shell dynamics have been uncoupled from the dynamics of the rigid body. The matrices $[Z_0]$ and $[Z_s]$ are invertible, hence the matrix $[A]$ is invertible. Solving for the rigid body and shell displacements gives

$$[D_0] = [Z_0]^{-1}[Q_0], \tag{79}$$

$$[c^S] = [Z_S]^{-1}[0] = [0]. \tag{80}$$

TABLE I. System parameters used in the numerical simulation.

L_0	1.4 m	I_{xx}	1.971 kg m^2
R	0.7 m	I_{yy}	0.102 kg m^2
h	0.003 m	I_{zz}	1.942 kg m^2
ρ	7800 kg m^{-3}	x_{01}	0 m
E	2.16×10^{11} N m^{-2}	y_{01}	0 m
ν	0.3	z_{01}	0 m
m_0	32.7 kg	x_{02}	0 m
m^b_1	3.56 kg	y_{02}	0 m
m^b_2	3.56 kg	z_{02}	0 m
η_{1-128}	0.1	θ_1	154°
$\eta_{J,1-6}$	0.47	θ_2	206°

This means the cylindrical shell remains stationary and the power transmitted into the cylinder must equal zero.

Power will only be transmitted into the cylinder if the control actuator is unable to provide an equal and opposite restoring force. This may occur in practice if the control actuator can only provide a (linear) restoring force when a (rotational) moment is applied, or if the control signal to the control actuator is not a sufficiently accurate representation of the actual required control signal.

G. Control actuator with restoring force in a single axis

A typical active vibration isolator comprising of a single spring and a force actuator colinear with the spring, can only provide effective vibration control in one axis. To calculate the power transmission into the support cylinder for this situation, the matrices in Eq. (41) have to be reduced in size to prevent poorly conditioned matrices which cannot be inverted. Consider an active isolator which can provide a restoring force in the Z direction, colinear with the passive vibration isolators. In this case the control force vector will be

$$[Q^c_J] = [0 \quad 0 \quad F^c_z \quad 0 \quad 0 \quad 0]^T_J. \tag{81}$$

If this were substituted into Eq. (66), this would result in an equation which is unsuitable for matrix inversion operations. The matrices $[a]$, $[b_1]$, $[b_2]$ can be simplified to accommodate the matrix inversion operations by substituting $[\hat{a}] = [a]$, $[\hat{b}_1] = [b_1]$, $[\hat{b}_2] = [b_2]$ as follows;

$$[\hat{a}] = \begin{bmatrix} a_{6\times0+\chi,6\times0+\chi} & a_{6\times0+\chi,6\times1+\chi} & \cdots & a_{6\times0+\chi,6\times(L_1-1)+\chi} \\ \vdots & \vdots & \ddots & \vdots \\ a_{6\times(L_1-1)+\chi,6\times0+\chi} & a_{6\times(L_1-1)+\chi,6\times1+\chi} & \cdots & a_{6\times(L_1-1)+\chi,6\times(L_1-1)+\chi} \end{bmatrix}, \tag{82}$$

$$[\hat{b}_1] = \begin{bmatrix} b_{1_{6\times0+\chi,1}} \\ b_{1_{6\times1+\chi,1}} \\ \vdots \\ b_{1_{6\times(L_1-1)+\chi,1}} \end{bmatrix}, \tag{83}$$

$$[\hat{b}_2] = [b_{2_{1,6\times0+\chi}} \quad b_{2_{1,6\times1+\chi}} \quad \cdots \quad b_{2_{1,6\times(L_1-1)+\chi}}], \tag{84}$$

where χ is the number of the axis along or around which the control actuator provides the linear or rotational restoring

TABLE II. Stiffness coefficients of isolators.

E_0		2.25×10^7 N m^{-2}
μ		0.44
a		0.045 m
b		0.051 m
L		0.206 m
k_{J1}	$\frac{3\pi E_0(b^4-a^4)}{4L^3}$	1.34×10^4 N m^{-1}
k_{J2}	$\frac{3\pi E_0(b^4-a^4)}{4L^3}$	1.34×10^4 N m^{-1}
k_{J3}	$\frac{\pi E_0(b^2-a^2)}{L}$	1.85×10^5 N m^{-1}
k_{J4}	$\frac{\pi E_0(b^4-a^4)}{4L}$	216 N m rad^{-1}
k_{J5}	$\frac{\pi E_0(b^4-a^4)}{4L}$	216 N m rad^{-1}
k_{J6}	$\frac{\pi E_0(b^4-a^4)}{4(1+\mu)L}$	150 N m rad^{-1}

force or moment, respectively. For example, if the control actuator acts in the Z direction, then $\chi=3$.

II. NUMERICAL RESULTS

A two isolator system, having the properties listed in Tables I and Tables II, was used as an example for numerical calculations. Both isolators are aligned in the Z direction ($\chi=3$). For the numerical analysis undertaken here, a frequency range of 0–200 Hz was considered, which is well below the ring frequency (1052 Hz). This frequency range was used as active vibration isolation offers advantages over passive isolation only at low frequencies. At higher frequencies, the active control system does not offer significantly greater vibration isolation compared to passive isolation. This analytical model was programmed using MATLAB version 4.0 (copyright MathWorks, Inc.) operating on a personal computer.

The complete circumferential modal solution of the theoretical model comprises sine (odd) and cosine (even) responses. The numerical results for the forced response are calculated by using the sine function (odd) with the Z axis in the vertical plane as shown in Fig. 1 and then summed with the even response by recalculating the solution with the coordinate system rotated 90° in the positive θ direction. Figure 2 illustrates the power transmission into the cylindrical support structure by the odd and even circumferential modal response, for a 1-N force in the Y direction, using passive vibration isolation. For this arrangement of isolators, further matrix reduction is required when calculating the odd modes for all loads $[Q_0]$ as the $[\alpha]$ matrix is singular. It is necessary to assume that the load in each isolator is half the total load, calculate the required control force for a single isolator, then reconstruct the matrices for the two isolators to calculate the transmitted power. All further numerical results are calculated using the summation of the odd and even circumferential modal response.

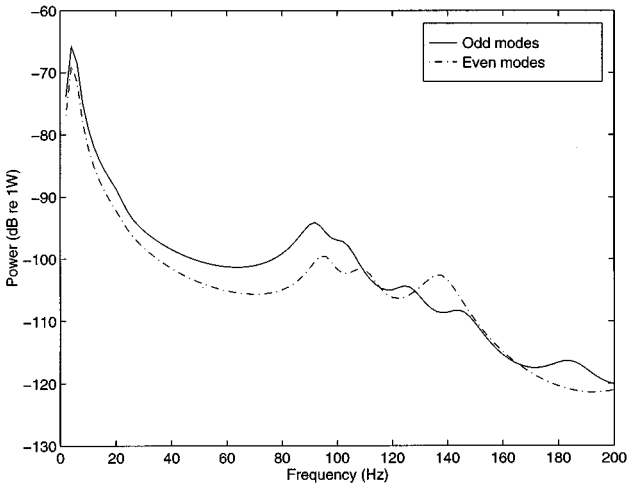

FIG. 2. Comparison of the relative importance of odd and even modes in calculating the power transmission into cylinder (dB) for the passive isolation case, $F_y=1$ N.

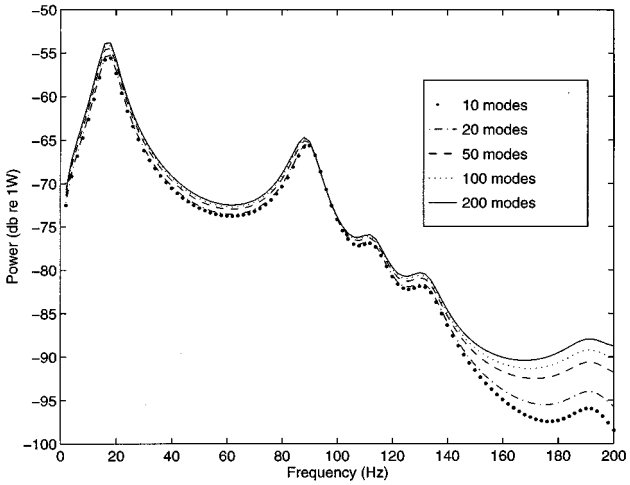

FIG. 3. Effect of varying the number of modes used in calculating the power transmission into cylinder (dB) for the passive isolator case, $F_z=1$ N.

For practical reasons the number of system vibration modes included in the analysis must be limited with a corresponding reduction in accuracy of the response calculations. Figure 3 illustrates the effect of varying the number of modes used in the numerical simulation P, on the calculation of the power transmission into the support cylinder P_3, for a 1-N force in the Z direction, using passive vibration isolation. All further numerical results are calculated using 100 modes. The resonance frequency of the cylindrical shell for the 100th mode is $\omega_{100}=706$ Hz, where the axial and circumferential modal indices are $m=7$ and $n=11$, respectively. In the 0–200 Hz frequency range, there are 10 resonant modes ($\omega_{10}=197$ Hz). Figure 3 shows that the performance of the passive isolators increases with frequency. This result can be explained by considering the mobilities of the rigid body M_r, cylindrical structure M_c and passive vibration isolator M_i. The transmissibility of the isolator ϵ_f is defined as[5]

$$\epsilon_f=\left|\frac{M_r+M_c}{M_i+M_r+M_c}\right|. \tag{85}$$

As the frequency increases, the mobility of the isolator increases at a greater rate than the mobility of the rigid body

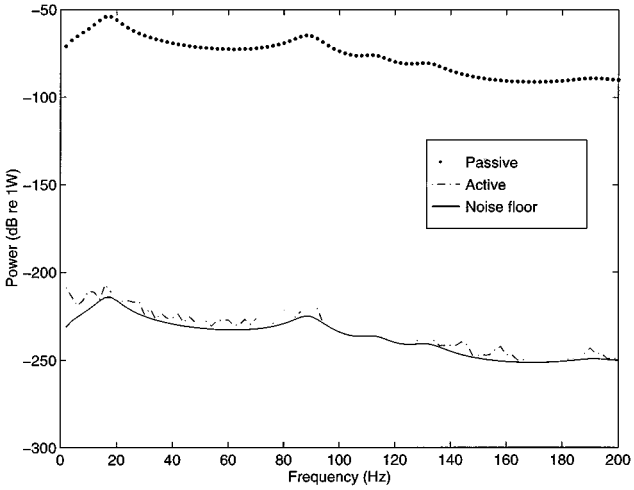

FIG. 4. Power transmission into cylinder (dB) for the passive isolator and single axis active isolator, $F_z=1$ N.

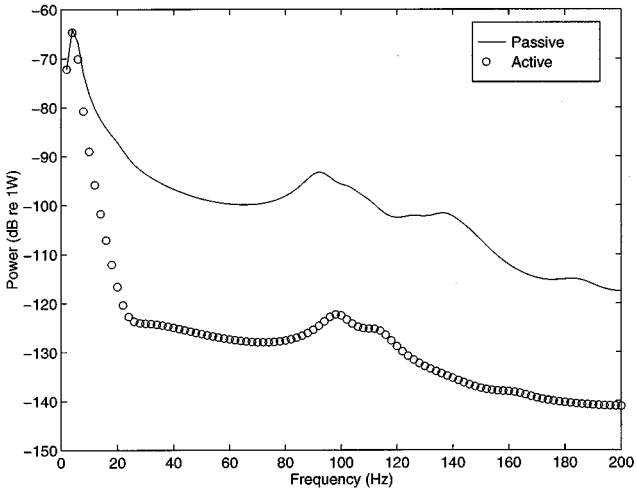

FIG. 6. Power transmission into cylinder (dB) for the passive isolator and single axis active isolator, $F_y=1$ N.

and cylindrical structure. Hence, from Eq. (85), the transmissibility decreases with frequency. The effect of active control is to increases the mobility of the isolators.

Figure 4 illustrates the power transmission into the support cylinder, under passive and active vibration control, for the case of a 1-N force in the Z direction. In this case it is possible to reduce the power transmitted into the support cylinder to zero using active vibration control. The graph shows a curve which is equivalent to the ''noise floor'' of the calculations in MATLAB, which is 1×10^{-16} of the transmitted power for the passive vibration isolation case. Only the even modes contribute to the vibration response. The calculated transmitted power for the odd modes is of the order -360 dB. Intuitively, this seems reasonable as each isolator is compressed equally in the Z direction, causing a symmetric response about the ZX plane, which couples into the even modal response.

Figure 5 illustrates power transmission into the support cylinder, under passive and active vibration control, for the case of a 1-N force in the X direction. Again, only the even modes contribute to the vibration response, and the calculated transmitted power for the odd modes is of the order -360 dB. Intuitively, this again seems reasonable as each isolator is rotated equally about the Y axis, causing a symmetric response about the ZX plane, which only couples into the even modal response. The active control case is identical to the passive control case. The control actuator in the Z axis cannot counteract the resulting driving force in the X direction and moment about the Y axis.

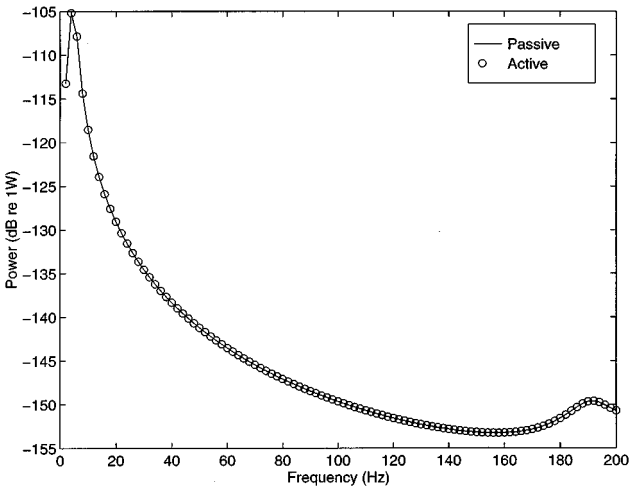

FIG. 5. Power transmission into cylinder (dB) for the passive isolator and single axis active isolator, $F_x=1$ N.

Figure 6 illustrates power transmission into the support cylinder, under passive and active vibration control, for the case of a 1-N force in the Y direction. Both even and odd modes contribute to the vibration response and transmitted power as shown in Fig. 2 for the transmitted power for the even and odd modes. Each isolator is rotated equally about an axis parallel to the X axis, causing a symmetric response about the ZX plane, which couples into the even modal response, and displaced in opposite directions along the Z axis, causing an antisymmetric response about the ZX plane, which couples into the odd modal response. The active control case provides around 25-dB vibration attenuation. When a force is applied to the rigid body in the Y direction, the rigid body moves in the Y direction and rotates about the X axis. This rotation about the X axis causes one isolator to extend and the other compress in the Z direction. The active isolators aligned in the Z direction can attenuate the linear force in the Z direction, but not the resulting moment about the X axis or force along the Y axis.

Figure 7 illustrates power transmission into the support cylinder, under passive and active vibration control, for the case of a 1-N m moment about the X axis. Both even and odd modes contribute to the vibration response. Intuitively, this seems reasonable as each isolator will be rotated equally about an axis parallel to the X axis, causing a symmetric response about the ZX plane, which couples into the even modal response, and displaced in opposite directions along the Z axis, causing an antisymmetric response about the ZX plane, which couples into the odd modal response. The active control case provides around 25-dB vibration attenuation. When a moment is applied to the rigid body about the X

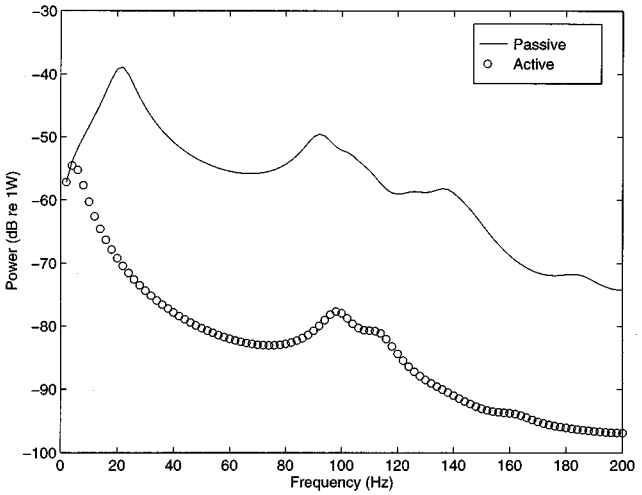

FIG. 7. Power transmission into cylinder (dB) for the passive isolator and single axis active isolator, $M_x=1$ N m.

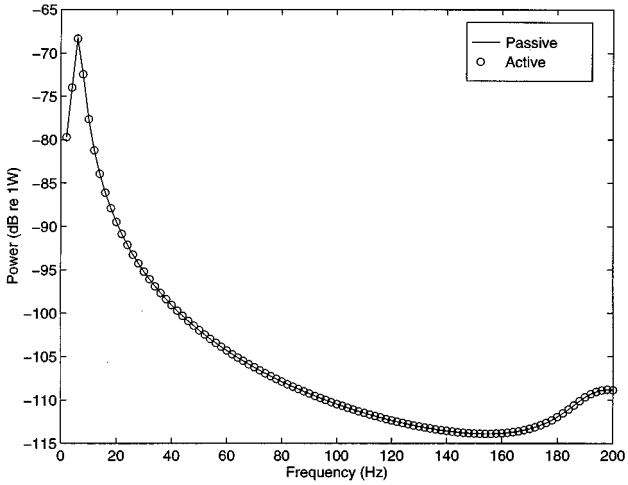

FIG. 9. Power transmission into cylinder (dB) for the passive isolator and single axis active isolator, $M_z=1$ N m.

axis, the rigid body rotates about the X axis, which causes one isolator to extend and the other compress. The active isolators aligned in the Z direction can attenuate the linear force in the Z direction, but not the resulting moment about the X axis.

Figure 8 illustrates power transmission into the support cylinder, under passive and active vibration control, for the case of a 1-N m moment about the Y axis. Only the even modes contribute to the vibration response. The calculated transmitted power for the odd modes is of the order -360 dB. Intuitively, this seems reasonable as each isolator will be rotated equally about the Y axis, causing a symmetric response about the ZX plane, which couples into the even modal response. The active control case is identical to the passive control case. When a moment is applied to the rigid body about the Y axis, the rigid body rotates about the Y axis, which causes both isolators to rotate equally. The active isolators aligned in the Z direction cannot attenuate the moment along the Y axis.

Figure 9 illustrates power transmission into the support cylinder, under passive and active vibration control, for the case of a 1-N m moment about the Z axis. Both even and odd modes contribute to the vibration response. Intuitively, this seems reasonable as each isolator will be rotated equally about an axis parallel to the Z axis, causing a symmetric response about the ZX plane, which couples into the even modal response, and displaced in opposite directions along the X axis, causing an asymmetric response about the ZX plane, which couples into the odd modal response. The active control case is identical to the passive control case. When a moment is applied to the rigid body about the Z axis, the rigid body rotates about the Z axis, which causes each isolator to displace equally in opposite directions along the X axes. The active isolators aligned in the Z direction cannot attenuate the moment along the Z axis or the forces along the X axis.

In a physical active vibration control installation, it is likely that the control system will have modeling errors, which in turn leads to suboptimal vibration control. Possible

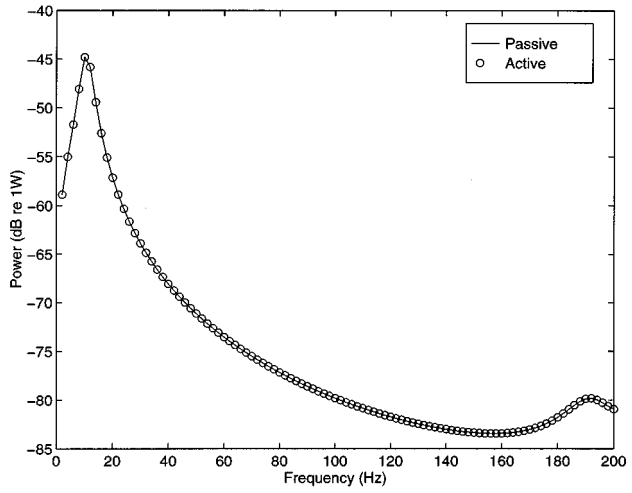

FIG. 8. Power transmission into cylinder (dB) for the passive isolator and single axis active isolator, $M_y=1$ N m.

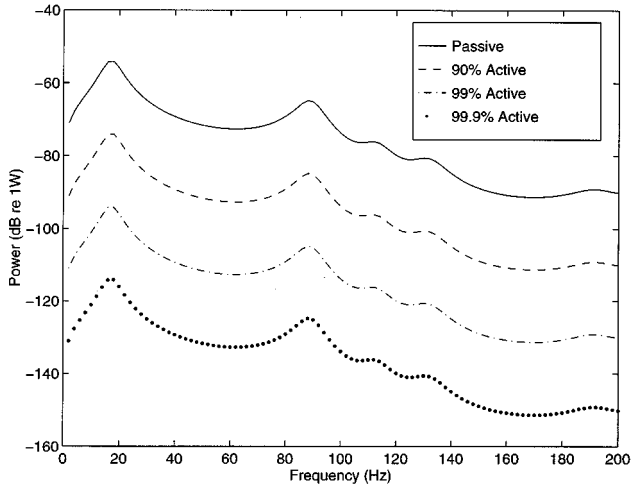

FIG. 10. Effect of inaccuracies in the control force amplitude on the power transmission into cylinder (dB) for the passive isolator and single axis active isolator, $F_z=1$ N.

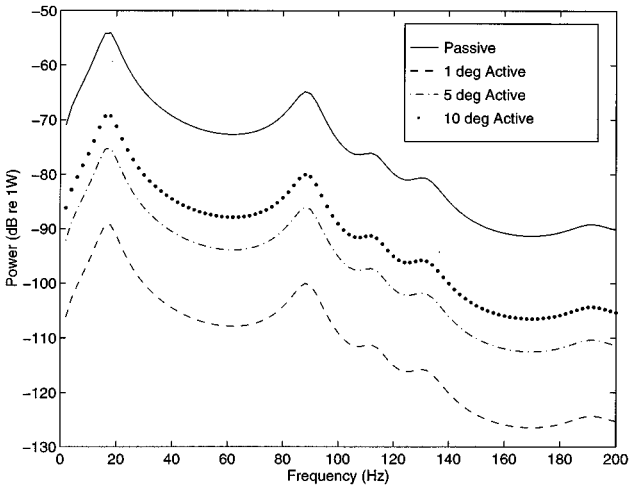

FIG. 11. Effect of inaccuracies in the control force phase on the power transmission into cylinder (dB) for the passive isolator and single axis active isolator, $F_z=1$ N.

errors include inaccurate measurements of vibration amplitude and phase, errors in modeling the cancellation path transfer function or errors attributable to the dynamic range of the controller. Figure 10 illustrates the power transmission into the support cylinder, under passive and active vibration control, for the case of a 1-N force in the Z direction, when the control actuator provides a restoring force with the correct phase but inaccurate force amplitude. Figure 11 illustrates a similar case for which the control actuator provides a restoring force with the correct force amplitude but inaccurate phase. These results may be compared with those shown in Fig. 4, which represents the case of the control actuator providing the theoretically optimal restoring force, producing zero power transmission into the support cylinder.

III. CONCLUSIONS

An analytical model to calculate the maximum achievable reduction of vibratory power transmission from a rigid body through elastic isolators to a cylindrical shell has been developed. The model allowed the maximum achievable performance of a feedforward active control system to be calculated for single axis vibration isolators.

It was found that when the driving force is aligned with the vibration isolators, it is theoretically possible to reduce the vibratory power transmission into the support cylinder to zero. When the driving force is not aligned with the axes of the vibration isolators, active control provides limited vibration attenuation. Numerical results indicate that slight errors in the phase or magnitude of the control force cause a substantial decrease in the achievable attenuation of vibration transmission.

ACKNOWLEDGMENTS

Financial support for this work from the Australian Defence Science and Technology Organisation, Material Research Laboratories and the Sir Ross and Sir Keith Smith Fund is gratefully acknowledged.

APPENDIX

(1) A point force F_z acting in the Z direction on point $\sigma_J(x_J,y_J)$ on a support structure is equivalent to a distributed load $F_z\delta(x-x_J,y-y_J)$.

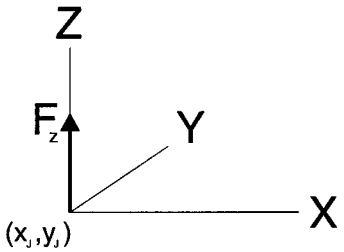

(2) A point moment around the Y axis, M_y, is statically equivalent to a pair of point forces in the Z direction, $(M_y/2\epsilon)\,\delta(x-x_J+\epsilon,y-y_J)$ and $(M_y/2\epsilon)\,\delta(x-x_J-\epsilon, y-y_J)$ when $\epsilon\to 0$, they correspond to a distributed load:

$$\lim_{\epsilon\to 0}\frac{M_y}{2\epsilon}\,\delta(x-x_J+\epsilon,y-y_J)-\frac{M_y}{2\epsilon}\,\delta(x-x_J-\epsilon,y-y_J)$$

$$\to M_y\,\frac{\partial\delta(x-x_J,y-y_J)}{\partial x},$$

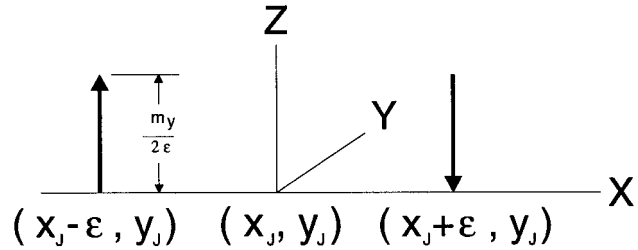

(3) Similarly, a point moment around the X axis, M_x, is statically equivalent to a distributed load in the Z direction:

$$-M_x\,\frac{\partial\delta(x-x_J,y-y_J)}{\partial y}.$$

(4) Integral of Dirac functions

$$\int_\sigma \Gamma_k(\sigma)\,\delta(\sigma-\sigma_J)\,d\sigma=\Gamma_k(\sigma_J).$$

(5) Integral of the partial derivatives of Dirac functions

$$\int_\sigma \Gamma_k(\sigma)\,\frac{\partial\delta(\sigma-\sigma_J)}{\partial x}\,d\sigma$$

$$=\lim_{\epsilon\to 0}\int_\sigma\frac{1}{2\epsilon}\,\Gamma_k(\sigma)\{\delta(x-x_J+\epsilon,y-y_J)$$

$$-\delta(x-x_J-\epsilon,y-y_J)\}d\sigma,$$

$$=\lim_{\epsilon\to 0}\frac{1}{2\epsilon}\{\Gamma_k(x_J-\epsilon,y_J)-\Gamma_k(x_J+\epsilon,y_J)\},$$

$$=-\frac{\partial\Gamma_k(\sigma_J)}{\partial x},$$

$$=-\Gamma_{kx}(\sigma_J).$$

[1] J-Q. Pan, C. H. Hansen, and J. Pan, ''Active isolation of a vibration source from a thin beam using a single active mount,'' Proceedings of Internoise '91, 683–686 (1991).
[2] J. Pan, J-Q. Pan, and C. H. Hansen, ''Total power flow from a vibrating rigid body to a thin panel through multiple elastic mounts,'' J. Acoust. Soc. Am. **92**, 895–907 (1992).
[3] A. W. Leissa, ''Vibration of shells,'' NASA SP-288 (1973).
[4] P. A. Nelson, A. R. D. Curtis, S. J. Elliott, and A. J. Bullmore, ''The active minimisation of harmonic enclosed sound fields. Part I. Theory,'' J. Sound Vib. **117**, 1–13 (1987).
[5] L. L. Beranek, *Noise and Vibration Control—Revised edition*, (Institute of Noise Control Engineering, Washington, DC, 1988).

Actively created quiet zones by multiple control sources in free space

Jingnan Guo, Jie Pan, and Chaoying Bao
Department of Mechanical and Materials Engineering, University of Western Australia, Nedlands, WA 6907, Australia

(Received 22 December 1995; revised 14 October 1996; accepted 28 October 1996)

Local attenuation of sound pressure, which creates a zone of quiet, seems to be the only option if primary and secondary sources are well separated. Two major indexes of local control, the size of the quiet zone and the total sound power output, are mainly determined by the arrangement of primary sources, secondary sources, and error sensors. It has been found that the size of the quiet zone created by the control system with multiple secondary sources and error sensors is not simply the summation of quiet zones created by each individual control source. The interactions of the control sources, which are determined by the configuration of the system, play a very important role in the system performance. In this paper, a typical control arrangement with multiple secondary sources and multiple error sensors equally spaced in two parallel lines is examined. Results from computer simulation and experiments in an anechoic chamber show that there exists a range of optimal spacing for the secondary sources and error sensors. The control system will create the largest quiet zone and suffer the least increase of total sound power output in the optimal configuration. © *1997 Acoustical Society of America.* [S0001-4966(97)03303-1]

PACS numbers: 43.50.Ki [GAD]

INTRODUCTION

Previous work on active noise control in free space has shown that the performance of the control system is largely dependent on the distance between primary sources and secondary sources. The most desirable noise control result would be the attenuation of sound pressure in all directions in space. Unfortunately, such global control can only be achieved when primary sources and control sources are closely located.[1–5] Nelson and Elliott have thoroughly examined the active noise control system with a pair of point sources on the basis of sound energy analysis.[3] They developed a set of matrix equations for a number of noise and control point sources located in a free space and presented a great detail on the global control of sound field.[4,5] Their work indicated that for a global control of noise, substantial reductions in total power output can be achieved only if the secondary sources are less than one half-wavelength away from the primary sources at the frequency of interest. In practical applications, the condition of short separation between primary and secondary sources may not always be satisfied. For these cases, to cancel sound pressure in some areas and achieve quiet zones seems to be the only choice for the active noise control in free space. This control strategy is called local control or zone of quiet control.

The authors have investigated the quiet zone created by a control system with a single primary/secondary source in free space.[6] They have found that the arrangement of the primary/secondary source and the error microphone is critical to the effectiveness of the noise control. The size of the quiet zone and the total power output of the system were the two indexes used to examine the performance of the control system. Both of them are mainly determined by the relative positions of the sources and sensors of the control system. For local control, the total sound power output of the control system always increases after control.[6] When multiple secondary sources are used for control of local sound pressure at multiple error sensor locations, only suitably arranged positions of the sources and sensors will allow less increase in total power output and larger size of quiet zones than those of a single control source system.

The objective of this paper is to examine the ability of a control system with multiple secondary sources and error sensors in creating quiet zones. A typical control system with multiple secondary sources and error sensors will be focused on the following discussion, in which both secondary sources and error sensors are equally placed in two parallel lines. This kind of arrangement of control system has been used for the active noise barriers.[7] For the analyses presented here, a feedforward control mechanism has been assumed, with a reference signal correlated to the output of the primary source. The control sources are modeled as constant volume velocity sources, the outputs of which are linearly related to their inputs.

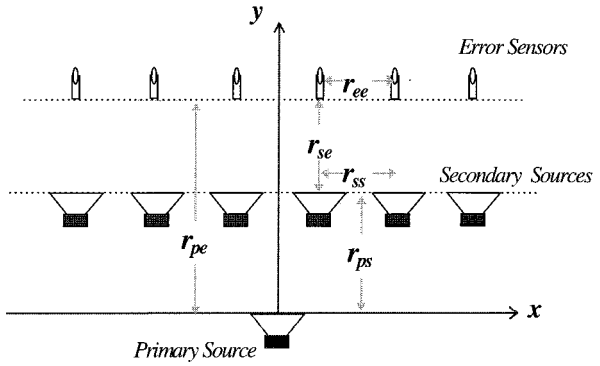

FIG. 1. A typical arrangement of a control system with multiple secondary sources.

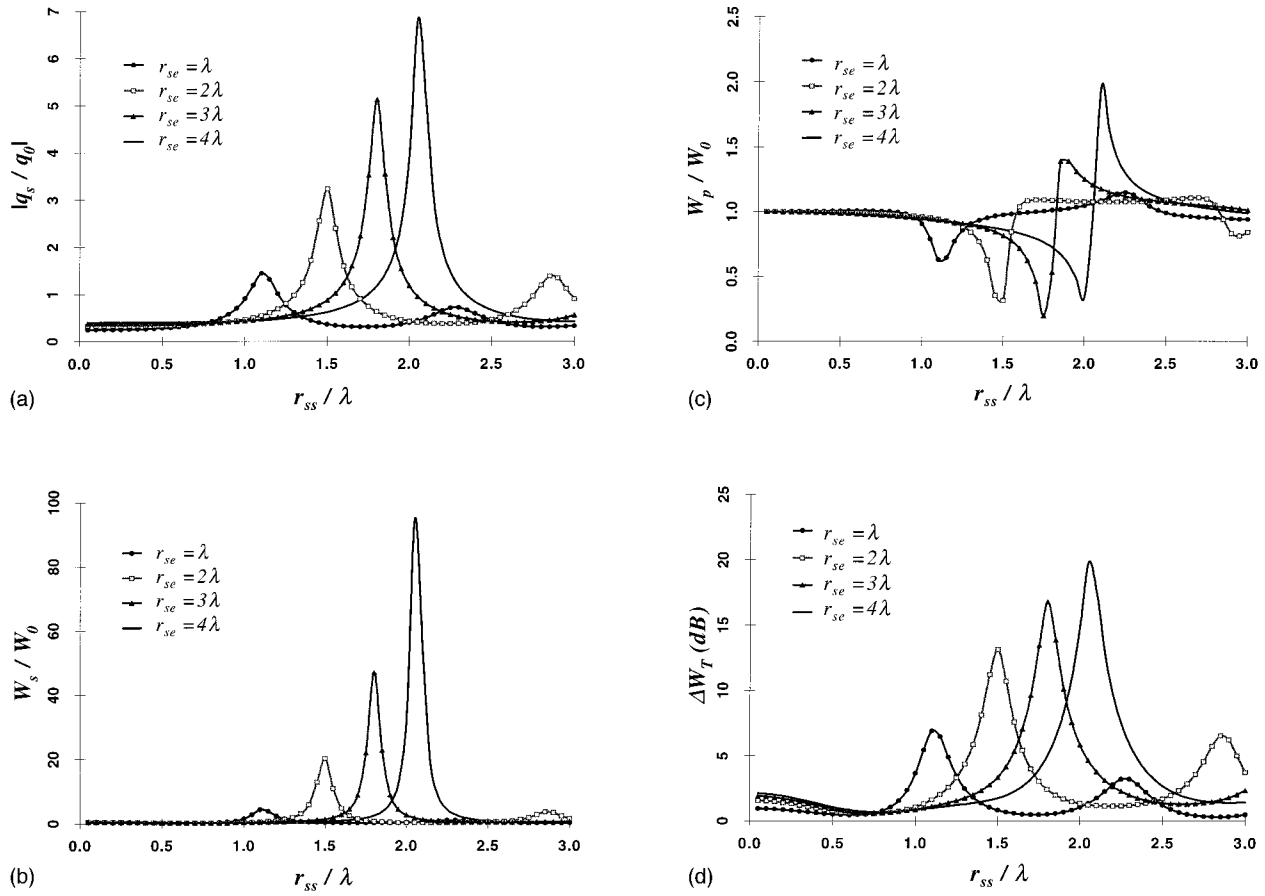

FIG. 2. Acoustic power outputs of a control system with two secondary sources and two error sensors, in the configurations of $r_{ps}=\lambda$ and $r_{se}=\lambda$, 2λ, 3λ, and 4λ, respectively. Figures shown are (a) secondary source strength ratio $|q_s/q_0|$ (b) secondary power output ratio W_s/W_0, and (c) primary power output ratio W_p/W_0, and (d) the total power output increase ΔW_T in dB.

I. GENERAL THEORY AND SYSTEM DESCRIPTION

The objectives of local control of a sound-pressure field are (1) to create large quiet zones at required positions (where error sensors are located) and (2) to minimize the increase of sound pressure at other locations (or to minimize the increase in total power flow from all sources). The quiet zone is defined as the area where the primary sound-pressure level is attenuated by more than 10 dB.[8,9] If there are M primary sources and N secondary control sources distributed in the free field, and the corresponding source strengths are, respectively,

$$\mathbf{q}_p=[q_{p1},\ q_{p2},\ \ldots,\ q_{pM}]^T, \tag{1}$$

$$\mathbf{q}_s=[q_{s1},\ q_{s2},\ \ldots,\ q_{sN}]^T, \tag{2}$$

where T denotes the transpose; the sound pressure at an observation position in the space can be expressed as

$$P=P_p+P_s=\mathbf{Z}_p\mathbf{q}_p+\mathbf{Z}_s\mathbf{q}_s, \tag{3}$$

where P_p and P_s are the complex sound pressures at the particular field point position due to primary sources and secondary sources, respectively. $\mathbf{Z}_p$ and $\mathbf{Z}_s$ are row vectors of acoustic transfer impedance from primary sources and from secondary sources to the observation position, respectively.

If L error microphones (error sensors) are used, the complex pressures at the L error microphones are $\mathbf{P}=\mathbf{Z}_{pe}\mathbf{q}_p+\mathbf{Z}_{se}\mathbf{q}_s$. The sum of the squared sound pressures at microphone positions is selected as the cost function, J, for local control:

$$J=\mathbf{P}^H\mathbf{P}=(\mathbf{Z}_{pe}\mathbf{q}_p+\mathbf{Z}_{se}\mathbf{q}_s)^H(\mathbf{Z}_{pe}\mathbf{q}_p+\mathbf{Z}_{se}\mathbf{q}_s), \tag{4}$$

where $\mathbf{Z}_{pe}$ is an $L\times M$ matrix of acoustic transfer impedance from the primary sources to the error sensors, $\mathbf{Z}_{se}$ an $L\times N$ matrix of acoustic transfer impedance from the secondary sources to the error sensors, and the superscript H denotes the Hermitian transposed. The strengths of the secondary source array are adjusted to minimize the cost function. This yields[8]

$$\mathbf{q}_{s0}=-(\mathbf{Z}_{se}^H\mathbf{Z}_{se})^{-1}\mathbf{Z}_{se}^H\mathbf{Z}_{pe}\mathbf{q}_p. \tag{5}$$

If $L=N$, and with properly arranged secondary source and error sensor locations, $\mathbf{Z}_{se}$ can be nonsingular. For this case, the optimal secondary source strengths are simplified as[10]

$$\mathbf{q}_{s0}=-\mathbf{Z}_{se}^{-1}\mathbf{Z}_{pe}\mathbf{q}_p. \tag{6}$$

This enables the sound pressures to be zero at all error sensors. Thus, the quiet zones around these L positions can always be guaranteed. It has been found that the condition of $L=N$ may give rise to large area of quiet zone in a diffuse sound field.[11,12] As can be seen later, it is also the case in a

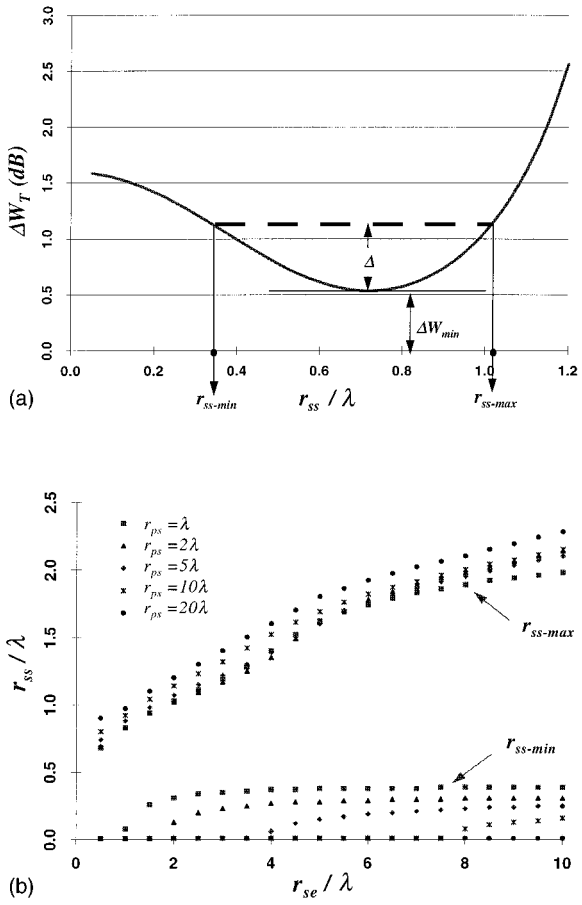

FIG. 3. The definition of upper and lower limits of the range of low total power output (a), and the computed results of both upper and lower limits for the control system with two control sources and two error sensors (b).

free field. Therefore, in the following analyses, the number of error sensors is chosen to be the same as that of secondary sources, i.e., $L=N$. Then the sound pressure at any position of the space after control becomes

$$P=\mathbf{Z}_p\mathbf{q}_p-\mathbf{Z}_s\mathbf{Z}_{se}^{-1}\mathbf{Z}_{pe}\mathbf{q}_p. \tag{7}$$

On the other hand, the acoustic power outputs of primary sources and secondary sources are given by[4,13]

$$W_p=\tfrac{1}{2}[\mathbf{q}_p^H\ \mathrm{Re}(\mathbf{Z}_{pp})\mathbf{q}_p+\mathbf{q}_p^H\ \mathrm{Re}(\mathbf{Z}_{ps}^T)\mathbf{q}_s], \tag{8}$$

$$W_s=\tfrac{1}{2}[\mathbf{q}_s^H\ \mathrm{Re}(\mathbf{Z}_{ss})\mathbf{q}_s+\mathbf{q}_s^H\ \mathrm{Re}(\mathbf{Z}_{ps})\mathbf{q}_p]. \tag{9}$$

The total radiated acoustic power of the system, which is the summation of power outputs of primary sources and secondary sources, can be written as

$$W_T=\tfrac{1}{2}\,[\mathbf{q}_p^H\ \mathrm{Re}(\mathbf{Z}_{pp})\mathbf{q}_p+\mathbf{q}_s^H\ \mathrm{Re}(\mathbf{Z}_{ss})\mathbf{q}_s+\mathbf{q}_p^H\ \mathrm{Re}(\mathbf{Z}_{ps}^T)\mathbf{q}_s+\mathbf{q}_s^H\ \mathrm{Re}(\mathbf{Z}_{ps})\mathbf{q}_p], \tag{10}$$

where $\mathbf{Z}_{pp}$ is an $M\times M$ transfer impedance matrix among the primary sources, $\mathbf{Z}_{ss}$ an $N\times N$ transfer impedance matrix among the secondary sources, and $\mathbf{Z}_{ps}$ the $M\times N$ transfer impedance matrix between the primary and secondary sources. The principle of acoustic reciprocity applies in this discussion, i.e., $\mathbf{Z}_{sp}=\mathbf{Z}_{ps}^T$.

Equations (7) and (10) show that both the sound pressure and the total sound power output are determined by the transfer impedances among primary sources, secondary sources, and error sensors. Those impedances depend on the positions of sources and error sensors. The aim of the following analysis is to find out how the configurations of sound sources and error sensors affect the total power output and the size of quiet zone.

Figure 1 is a typical configuration of a control system with multiple secondary sources, where the equally spaced secondary sources and error sensors are placed in two parallel lines. A monopole primary source is located in the central axis of the arrays of secondary sources and error sensors. The distance between the primary source and the secondary source array in the y direction is r_{ps}, and that between the secondary source array to the error sensor of array is r_{se}. The secondary sources and the error sensors are separated, respectively, by r_{ss} and r_{ee}, with $r_{ss}=r_{ee}$ in this discussion. Similar to systems with single primary/secondary sources, r_{ps} and r_{se} are important design variables that determine the performance of control systems with multiple secondary sources. Moreover, for a multiple secondary sources control system, r_{ss} plays much more important role in the system performance. The performance of the multiple secondary sources control system is to be examined in two aspects: the total sound power output and the size of the quiet zone.

II. TOTAL SOUND POWER OUTPUT

As stated previously, a local control system deals with the case when primary sources and secondary sources are at least a half-wavelength apart. This usually results in an increase of the total sound power output after control. The optimization of a local control system is to find out a configuration with least increase of total sound power output and largest quiet zone. The total power output of control system with different number of control sources and error sensors has been computed. Without losing the generality, the results of control systems with (1) two secondary sources and two error sensors and (2) multiple ($N>2$) secondary sources and error sensors are presented and discussed as follows.

A. Two secondary sources and two error sensors

Two secondary sources and two error sensors are symmetrically located at both sides of the axis of the primary source (shown in Fig. 1), $r_{ps'}$ and $r_{pe'}$ away from the primary source respectively. Both secondary sources and error sensors are spaced by $r_{ss}=r_{ee}$. The distance from one secondary source to its adjacent error sensor is r_{se}, and that to the other error sensor is $r_{se'}$.

The impedance vector from the primary source to two error sensors is

$$Z_{pe}=iZ_0\begin{bmatrix}e^{-ikr_{pe'}}/kr_{pe'}\\ e^{-ikr_{pe'}}/kr_{pe'}\end{bmatrix}, \tag{11}$$

and the impedance matrix from two secondary sources to two error sensors

$$\mathbf{Z}_{se}=iZ_0\begin{bmatrix}e^{-ikr_{se}}/kr_{se} & e^{-ikr_{se'}}/kr_{se'}\\ e^{-ikr_{se'}}/kr_{se'} & e^{-ikr_{se}}/kr_{se}\end{bmatrix}, \tag{12}$$

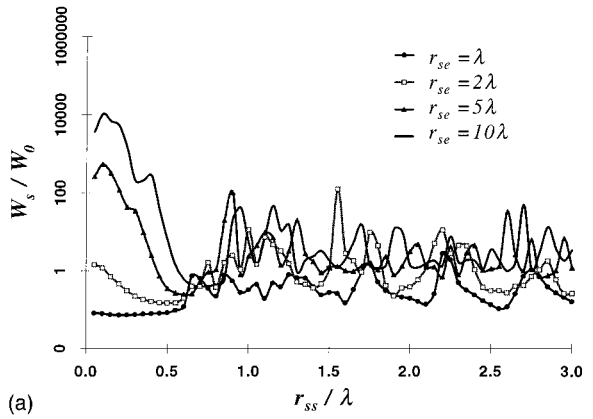

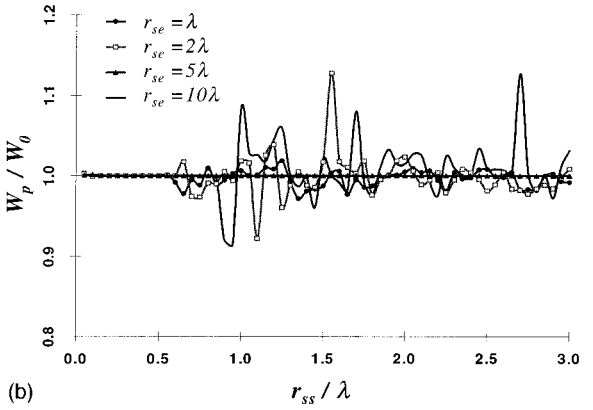

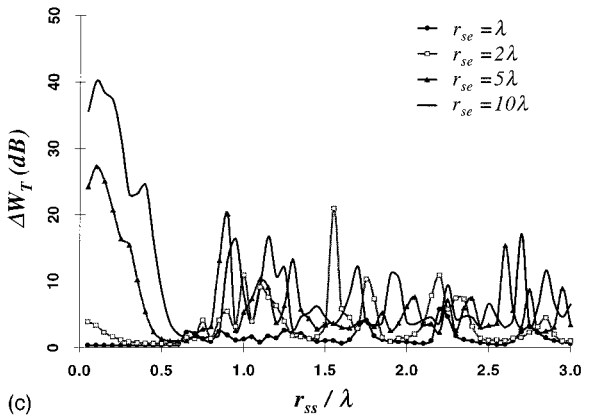

FIG. 4. Acoustic power outputs of a specific control system with 21 secondary sources and 21 error sensors, when $r_{ps}=5\lambda$, and $r_{se}=\lambda$, 2λ, 5λ, and 10λ, respectively. Figures shown are (a) secondary power output ratio W_s/W_0, (b) primary power output ratio W_p/W_0, and (c) total power output increase ΔW_T in dB.

where k is the wave number, $Z_0=\omega^2\rho_0/4\pi c_0$, $r_{se'}=\sqrt{r_{se}^2+r_{ss}^2}$, $r_{pe'}=\sqrt{r_{pe}^2+r_{ee}^2/4}$, and $r_{ps'}=\sqrt{r_{ps}^2+r_{ss}^2/4}$. If $\mathbf{Z}_{se}$ is a nonsingular matrix ($r_{se'}\neq r_{se}$ or $r_{ss}\neq 0$ for the arrangement shown in Fig. 1), according to Eq. (6), the optimal source strengths of the two secondary sources can be given by

$$q_{s1}=q_{s2}=Aq_p, \tag{13}$$

where A is the source strength ratio between the secondary source and the primary source, and can be expressed by

$$A=-\frac{e^{-ikr_{pe'}}(e^{ikr_{se}}/r_{se}+e^{ikr_{se'}}/r_{se'})}{r_{pe'}[1/r_{se}^2+1/r_{se'}^2+2\cos k(r_{se'}-r_{se})/r_{se}r_{se'}]}. \tag{14}$$

Other impedances vectors and matrices in Eq. (10) are described as the follows:

$$Z_{sp}=Z_{ps}=iZ_0\begin{bmatrix}e^{-ikr_{ps'}}/kr_{ps'}\\ e^{-ikr_{ps'}}/kr_{ps'}\end{bmatrix}, \tag{15}$$

$$\mathrm{Re}(Z_{pp})=Z_0, \tag{16}$$

and

$$\mathrm{Re}(\mathbf{Z}_{ss})=Z_0\begin{bmatrix}1 & \mathrm{sinc}(kr_{ss})\\ \mathrm{sinc}(kr_{ss}) & 1\end{bmatrix}. \tag{17}$$

The acoustic power outputs of primary source and secondary sources after control are, respectively,

$$W_p=W_0[1+2\,\mathrm{Re}(iAe^{-ikr_{ps'}}/kr_{ps'})], \tag{18}$$

$$W_s=2W_0[(1+\mathrm{sinc}(kr_{ss}))|A|^2+\mathrm{Re}(iA^*e^{-ikr_{ps'}}/kr_{ps'})], \tag{19}$$

where $W_0=Z_0|q_p|^2/2$ is the sound power output of the primary source before control. The total sound power output of the system with two secondary sources becomes

$$W_T=W_0[1+2(1+\mathrm{sinc}(kr_{ss}))|A|^2+4\,\mathrm{sinc}(kr_{ps'})\mathrm{Re}(A)]. \tag{20}$$

Equations (18)–(20) indicate that the total power output of the control system, as well as the power output of the secondary sources and that of the primary source after control, are largely dependent on the strength of the secondary sources.

Equation (14) shows that if $r_{se}\ll r_{ss}$, which corresponds to the error sensors at the positions around the near field of control sources, the source strength ratio $|A|$ approaches the ratio $r_{se}/r_{pe'}$, which is exactly the strength ratio for the control system with single control source.[6] This configuration also implies the condition of $r_{se}\ll r_{pe'}$. Under this condition, although the secondary source strength is very small and thus is the increase of total sound power output, only very small quiet zones can be created by the control system. We are more concerned with those configurations of the control system which can create large area of quiet zones. To satisfy this requirement, the error sensors should not be in the near field of the control sources, and r_{se} should be greater than or comparable to r_{ss}. It can be shown from Eq. (14) that in this

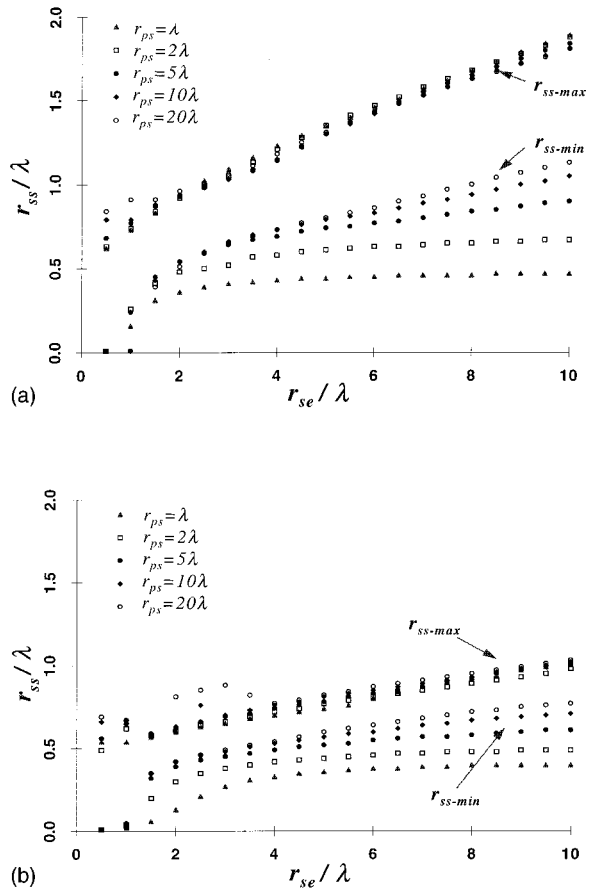

FIG. 5. The upper and lower limits of the range of low total power output increase for the control systems with 5 control sources and error sensors (a), and with 12 control sources and error sensors (b).

case, although the overall value of source strength ratio is still determined by the ratio $r_{se}/r_{pe'}$, the secondary strength has the maximum values if $k(r_{se'}-r_{se})=(2n-1)\pi$ $(n=1,2,...)$, or

$$r_{ss}=((2n-1)\lambda/2)\sqrt{1+4r_{se}/(2n-1)\lambda}. \tag{21}$$

Consequently, the total power output will also reach to the maximum. The physical explanations of this are as follows:

It can be shown that under condition (21), the sound pressures radiated by the two secondary sources are exactly out of phase at each of the two error sensors. The self-cancellations of the secondary pressures at the error sensors means that the strengths of the secondary sources have to be very large in order to cancel the primary pressures.

Equations (14) and (20) also indicate that when $r_{ss}\rightarrow 0$, the control system reduces to that with one secondary source and one error sensor, in which the strength and power output of the secondary source are always less than those of primary source, and the total power output increase has the maximum value of 3 dB (for large r_{se} and small r_{ps}).[6]

Figure 2 plots the secondary source strength ratio $(|q_s/q_p|)$, the secondary power output ratio (W_s/W_0), the primary power output ratio (W_p/W_0), and the total power output increase $[\Delta W=10\log(W_T/W_0)$ in dB] against r_{ss}. In the figure, the distance between primary source and secondary source array is fixed as $r_{ps}=\lambda$, and the distance between secondary source array and error sensor array is selected as $r_{se}=\lambda$, 2λ, 3λ, and 4λ, respectively.

The strength of each secondary source can be very large for some configurations, as shown in Fig. 2(a). For the discussed configuration, the strength of each secondary source can be about seven times bigger than that of primary source at a peak position. Figure 2(a) does show that the overall level of each secondary source strength is directly proportional to the ratio of $r_{se}/(r_{ps}+r_{se})$.

The secondary power output ratio W_s/W_0 shows a similar trend. In the positions of the secondary strength peaks, the secondary power output can be more than 100 times larger than that of the uncontrolled primary source. Figure 2(b) also shows that there is no negative secondary power output in these configurations, which indicates that the control mechanism of local control is not energy absorption, but the sound energy redistribution. The secondary sources function somewhat like a noise barrier, which reflects the incoming sound pressure and creates quiet zones behind it. This kind of ''noise barrier'' bears the cost of a sound-pressure increase elsewhere. Figure 2(c) illustrates that although the presence of control sources does reduce the primary power output for certain configurations, the reduction is much less than the secondary power output. The total power output always increases and the increase is contributed mostly by the secondary power output, as shown in Fig. 2(d). Figure 2(d) also indicates that the overall total power output increase is directly proportional to the distance ratio of $r_{se}/(r_{ps}+r_{se})$.

The total power output increase in Fig. 2(d) as a function of r_{ss} indicates that there exists a range of r_{ss} around $r_{ss}=\lambda/2$ for small total power output increase. In this range, the total power output increase is much less than that at the ''peaks'' of Fig. 2(d) and also less than that of the single secondary source control system $(r_{ss}\rightarrow 0)$ in most cases. As the purpose of local control is to create the largest area of quiet zone with the least total power output increase, it is reasonable to believe that the optimal configuration will be within this range. The width and the position of that range can be specified by the upper limit $r_{ss-\max}$ and the lower limit $r_{ss-\min}$ of r_{ss} as shown in Fig. 3(a). In Fig. 3(a), $r_{ss-\max}$ and $r_{ss-\min}$ correspond to the total power output increase from its minimum dB value by $\Delta=r_{se}/(r_{se}+r_{ps})$ in dB. The reason we chose the relative level derivation for the minimum power output range is that the flatness of ΔW_T in dB in the range is proportional to $r_{se}/(r_{se}+r_{ps})$. Therefore, the maximum derivation level for this range is 1 dB (when $r_{se}\gg r_{ps}$). The calculated results of numerous configurations are shown in Fig. 3(b). It is obvious that the upper limits are mainly determined by the distance between the secondary source array and error sensor array r_{se}, which can be approximately fitted as

$$r_{ss-\max}\cong\frac{\lambda}{2}\sqrt{1+\frac{2r_{se}}{\lambda}}. \tag{22}$$

The minimum possible value of the upper limit is $\lambda/2$, and $r_{ss-\max}$ can increase to a very large value with the increase of r_{se}. The lower limit, on the other hand, is inversely pro-

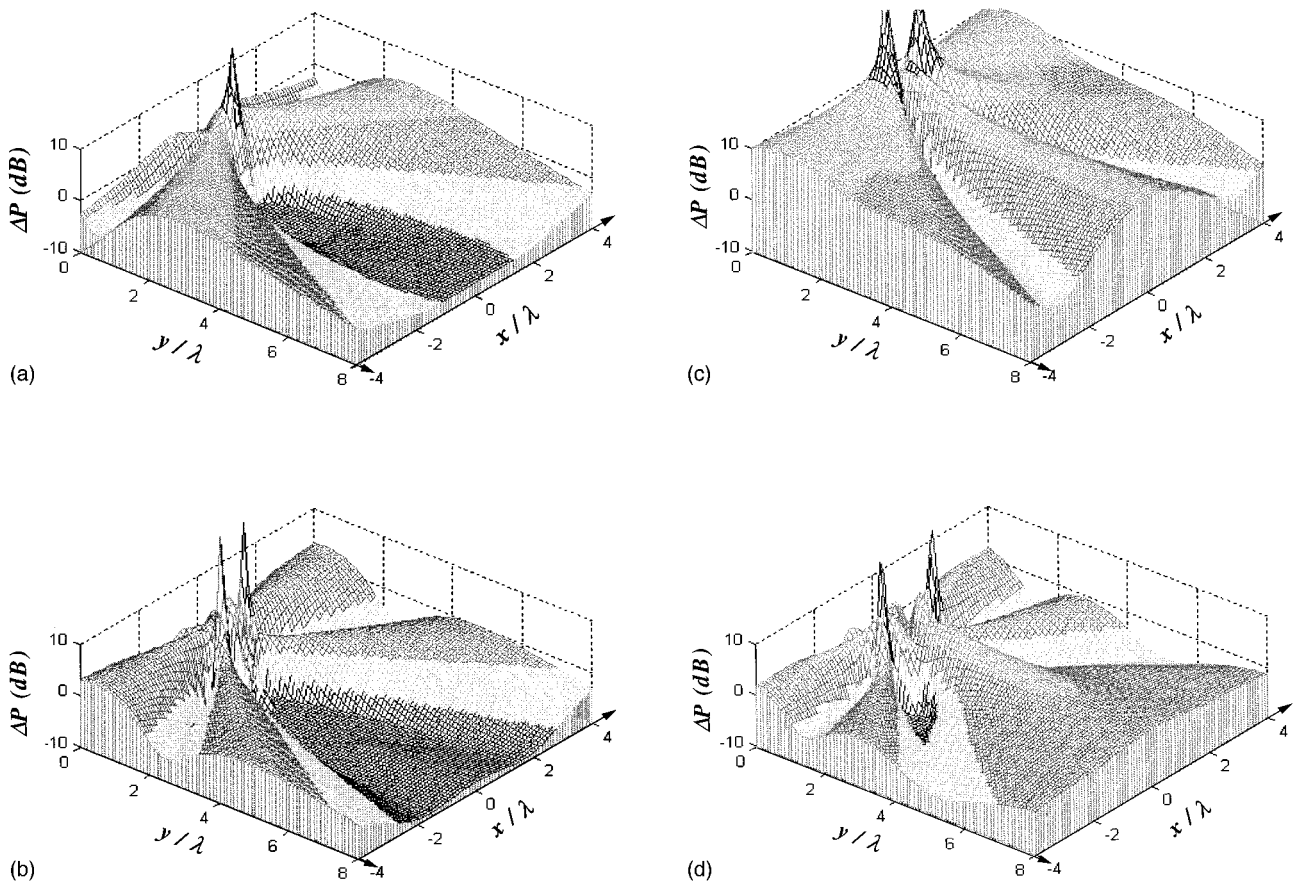

FIG. 6. Sound-pressure attenuation of a control system with two secondary sources and two error sensors when $r_{ps}=\lambda$, $r_{se}=\lambda$ and (a) $r_{ss}=0.1\lambda$, (b) $r_{ss}=0.739\lambda$, (c) $r_{ss}=1.12\lambda$, (d) $r_{ss}=1.71\lambda$.

portional to r_{ps} and becomes zero when $r_{se}/r_{ps}\leqslant 0.8$. It can be roughly fitted as

$$r_{ss-\min}=0 \quad r_{se}/r_{ps}\leqslant 0.8$$
$$r_{ss-\min}\cong 0.42\lambda\exp\left[-\left(\frac{2r_{ps}}{25\lambda}+\frac{\lambda}{2(r_{se}-0.8r_{ps})}\right)\right] \quad \frac{r_{se}}{r_{ps}}>0.8. \tag{23}$$

Clearly $r_{ss-\min}$ is always less than $\lambda/2$.

B. Multiple ($N>2$) secondary sources and error sensors

When the numbers of secondary sources and error sensors are greater than two, the strengths of secondary sources, the secondary power output, and the total power output do not have simple forms as in the case of two control sources. The $r_{ss-\max}$ and $r_{ss-\min}$ for this case can be obtained by numerically solving Eqs. (6)–(8) and curve fitting the results.

The authors have computed and examined the outputs of various configurations for multiple control sources, ranging from $L=N=3$ to $L=N=21$. They all exhibit a similar pattern. Figure 4 shows one of those computation results with $L=N=21$. Some similar conclusions to the case of two control sources and two error sensors can be made from the results: (1) the power output of the secondary sources is always positive, and can be very large (some 10 000 times larger than that of the uncontrolled primary source!) for some configurations; (2) the change of the primary power output is much less than that of the secondary power output; (3) the increase of the total power output is mainly determined by the secondary power output. Unlike the case of two control sources, the secondary power output and the total power output increase for multiple control sources can be very large for small r_{ss}. That means the control system with more than two control sources will not reduce to a single secondary source system in the sense of total power output increase when r_{ss} closes to zero.

From the computations, there always exists a range of low-power output increase for each configuration. The width and the position of this range can also be expressed by the upper and lower limits calculated using the same method and deviation described in Fig. 3(a). The upper limits and the lower limits of various control systems with control sources ranging from 3 to 21 have been computed, and two examples of $N=5$ and $N=12$ are shown in Fig. 5. It is clear that $r_{ss-\max}$ and $r_{ss-\min}$ for the multiple source control system depend not only on r_{se} and r_{ps}, but also on the number of secondary sources N. It has been found that the upper limit of the range can be fitted as

$$_{ss-\max}\cong\frac{\lambda}{2}\sqrt{1+\frac{4r_{se}}{N\lambda}}$$
$$r_{ss-\max}\cong\frac{\lambda}{2}\sqrt{1+\frac{N+1}{N-1}\frac{4r_{se}}{N\lambda}}$$
$$\begin{cases}N=2n & (n=1,2,3,\ldots,10)\\ N=2n+1 & (n=1,2,3,\ldots,10).\end{cases} \tag{24}$$

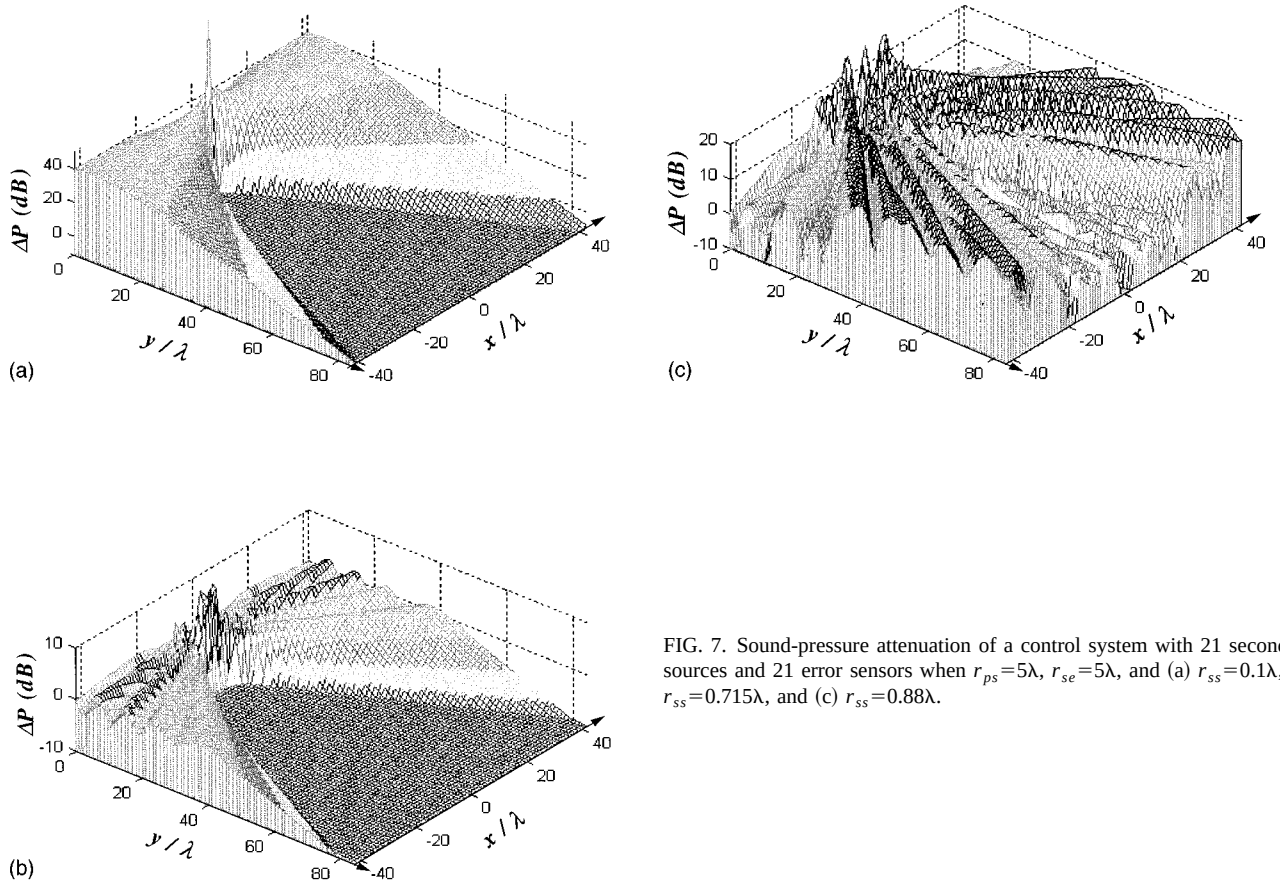

FIG. 7. Sound-pressure attenuation of a control system with 21 secondary sources and 21 error sensors when $r_{ps}=5\lambda$, $r_{se}=5\lambda$, and (a) $r_{ss}=0.1\lambda$, (b) $r_{ss}=0.715\lambda$, and (c) $r_{ss}=0.88\lambda$.

Equations (24) also indicate that $r_{ss-\max}$ is dependent upon if the number of secondary sources (as well as that of error microphones) is even or odd. However, the difference of $r_{ss-\max}$ for odd or even N diminishes with large N. It can be noted that the upper limit of Eq. (24) also covers the case of $N=2$ and has the minimum value of $\lambda/2$, and is directly proportional to r_{se} and inversely proportional to N.

Comparing Fig. 5 with Fig. 3(b) shows that for given r_{se}, $r_{ss-\min}$ value increases as r_{ps} decreases for $L=N=2$, while the $r_{ss-\min}$ value increases as r_{ps} increases for $L=N>2$. The observation of Fig. 5 shows that $r_{ss-\min}=0$ for $r_{se}\leqslant\lambda$. When $r_{se}>\lambda$, the lower limit becomes nonzero, and the curve fitting of the lower limit data gives rise to

$$r_{ss-\min}\cong\frac{5\lambda}{2}\exp\left[-\left(\frac{3(\lambda+0.04r_{ps})}{2r_{se}-\lambda}+\frac{20\lambda}{15\lambda+r_{ps}}\right)\right]$$

$$r_{ss-\min}\cong\frac{3\lambda(N+1)}{N}\exp\left[-\left(\frac{\lambda+2r_{ps}}{2(2r_{se}-\lambda)}+\frac{12\lambda}{5\lambda+r_{ps}}\right)\right]$$

$$\begin{cases}N=2n\ \ (n=2,3,\ldots,10)\\ N=2n+1\ \ (n=1,2,3,\ldots,10).\end{cases}\tag{25}$$

The number of control sources does not affect the lower limit much, but whether N is even or odd does. The lower limit can be larger than $\lambda/2$ for far field control (large r_{se} and r_{ps}). The range for small power output becomes narrow with large number of control sources N and large distance between primary and secondary sources r_{ps}. It will be shown that the ''optimal spacing'' of the secondary sources (as well as the error sensors) is just in the range between $r_{ss-\min}$ and $r_{ss-\max}$.

III. ZONE OF QUIET

The purpose of following discussions is to illustrate that the configurations of $r_{ss-\min}\leqslant r_{ss}\leqslant r_{ss-\max}$, which correspond to a small total power output increase, will also produce large area of quiet zone. Without losing generality, the numerical simulations of the control system with 2 secondary sources and 21 secondary sources are used as examples. The changes of the sound pressure before and after control will be observed in the $x-y$ plane containing the secondary source array, the error sensor array and the primary source, and will be expressed by $\Delta P=20\log|P_{\text{after}}/P_{\text{before}}|$ in dB.

A. Two secondary sources and two error sensors

For the control system demonstrated below, one primary source is located at the origin of the coordinate (0,0), two secondary sources at the positions $(-r_{ss}/2,\ \lambda)$ and $(r_{ss}/2,\ \lambda)$, and two error sensors at $(-r_{ss}/2,\ 2\lambda)$ and $(r_{ss}/2,\ 2\lambda)$. The performance of the control system in creating quiet zones is examined with four configurations: (a) very small r_{ss} ($r_{ss}=0.1\lambda<r_{ss-\min}$); (b) r_{ss} in the small power output range, i.e., $r_{ss}=0.739\lambda$; (c) $r_{ss}>r_{ss-\max}$ and at the position of first peak ($r_{ss}=1.12\lambda$) of total power output, where the total power output suffers about 7-dB increase as shown in Fig. 2(d); and (d) $r_{ss}=1.71\lambda$, the configuration with small power output increase but $r_{ss}>r_{ss-\max}$.

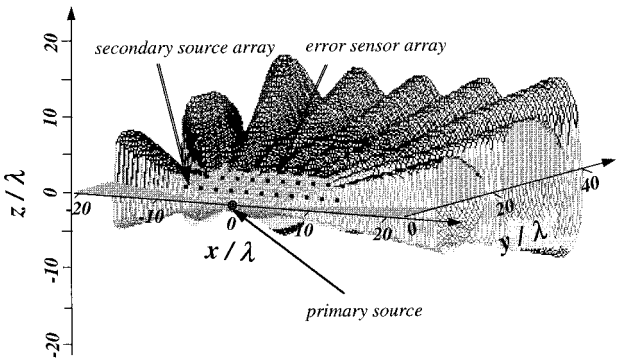

FIG. 8. Profile of the quiet zone created by the control system with 21 secondary sources and 21 error sensors, when $r_{ss}=r_{ee}=\lambda/2$, $r_{ps}=\lambda$, and $r_{se}=\lambda$.

The quiet zones created by the control systems with these four configurations are plotted in Fig. 6. Figure 6(a) and (b) shows that although both configurations can create a large area of quiet zone in the spaces behind the control sources and enclosing the error sensors, the latter can create a larger zone of quiet. When the system is working in the configuration with maximum total power output increase, although it can still create two separate quiet zones around the two error sensors, these two quiet zones are very narrow as shown in Fig. 6(c). The sound-pressure level in other locations, however, suffers great increase up to more than 10 dB. In Fig. 6(d), although the total power has a small increase [less than 1 dB, see Fig. 2(d) at $r_{ss}=1.71\lambda$], there is also no large quiet zone but only two small separated quiet zones around error sensors. This indicates that the small power output increase is not necessarily accompanied by a large quiet zone. One has to look at both aspects (small increase in total power output and large area of quiet zone) in selecting optimal configurations.

B. Twenty-one secondary sources and twenty-one error sensors

The configuration chosen as an example to demonstrate the ability in creating quiet zones of control systems with more secondary sources and error sensors is $N=L=21$, $r_{ps}=5\lambda$, and $r_{se}=5\lambda$. As shown in Fig. 1, the primary source is at the position (0,0), the 21 secondary sources are at $(5\lambda, (i-11)r_{ss})$ $(i=1,2,...,21)$, and the 21 error sensors are at $(10\lambda, (i-11)r_{ss})$ $(i=1,2,...,21)$. The performance of the system in creating quiet zones is examined in three typical spacings of secondary sources and error sensors: (a) very small r_{ss}, with $r_{ss}=\lambda/10<r_{ss-\min}$, where according to Fig. 4(c), the total power output endures more than 20-dB increase; (b) $r_{ss}=r_{ss-\max}$, which can be calculated through Eq. (24) as $r_{ss}=0.715\lambda$, and (c) $r_{ss}=0.88\lambda>r_{ss-\max}$. The sound pressure changes before and after control with these three spacings are shown in Fig. 7. It can be seen that although configuration (a) can create a large quiet zone behind the secondary sources and enclosing error sensors, the sound pressure in the areas outside the quiet zone suffers up to 40-dB increase. The quiet zone created by the configuration (b) is the largest [Fig. 7(b)], with no significant increase of sound-pressure level outside the quiet zone. When r_{ss} increases to $0.88\lambda>r_{ss-\max}$, there is hardly any evident quiet zone and most of the areas suffer large increase of sound-pressure level, as shown in Fig. 7(c).

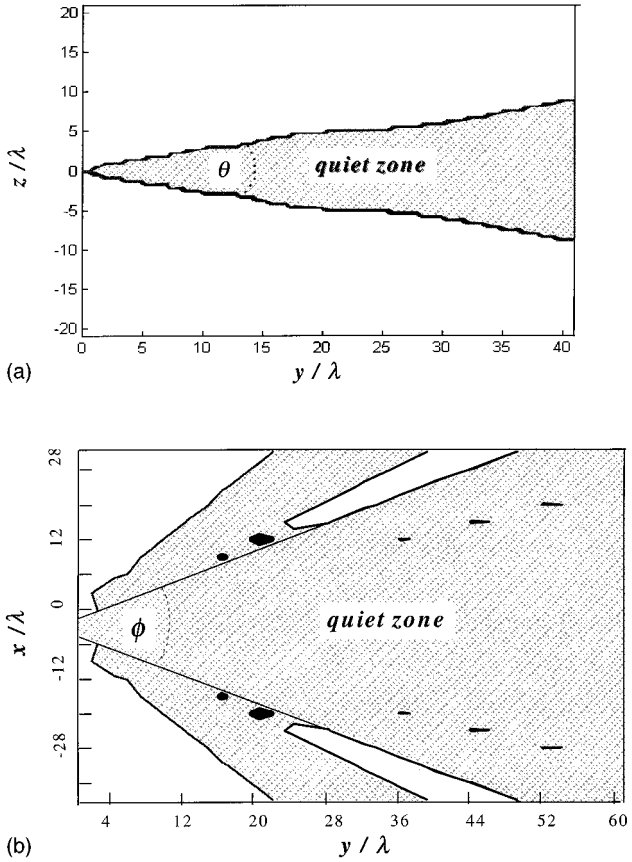

FIG. 9. (a) Size of quiet zone in a $y-z$ plane ($x=0$) and (b) in an $x-y$ plane ($z=0$).

From the above demonstration, it is clear that the optimal configuration is indeed corresponding to that for the small total power output increase range as defined in Sec. II. This configuration creates the largest quiet zone and has the least sound-pressure level increase in the areas outside the quiet zone. Although the large quiet zone can also be obtained by the arrangement of r_{ss} less than the lower limit $r_{ss-\min}$, it is at the cost of big increase of sound pressure in other places. For $r_{ss}>r_{ss-\max}$, the control system will not be able to create a large quiet zone at all.

C. Profiles of quiet zones

So far, the quiet zones created by multiple control source systems are shown only on a plane containing the secondary source array and the error sensor array ($x-y$ plane). As the quiet zones are three-dimensional areas in space, it is also necessary to show the size of quiet zone in the other directions. For the control system with equally spaced secondary sources and error sensors arranged in two parallel lines as shown in Fig. 1, it can be shown that the quiet zone has the shape of a wedge.

The profile of the quiet zone created by a control system with 21 secondary sources and 21 error sensors is shown in

Fig. 8, where the primary source is located at $(-\lambda,0,0)$, the 21 secondary sources and the 21 error sensors at $(0,(i-11)r_{ss},0)$, and $(\lambda,(i-11)r_{ee},0)$ $(i=1,2,...,21)$, respectively, and the separation between the adjacent control sources is within the optimal range, i.e., $r_{ss-\min} < r_{ss} = r_{ee} = \lambda/2 < r_{ss-\max}$. The shape, although with some fluctuations, resembles a wedge with its edge on the position of the secondary source array. The size of the quiet zone can be seen in detail in Fig. 9. The cross sections of the quiet zone in a $y-z$ plane [Fig. 9(a)] and in an $x-y$ plane [Fig. 9(b)] show that both the height of the quiet zone in z direction and the width of the quiet zone in x direction increase as the observation position is away from the secondary sources in the positive y direction. These increases are along the angles θ and ϕ, respectively. In this specific configuration, $\theta \approx 30°$ and $\phi \approx 80°$. Further research shows that these two angles, consistent with the solid angle of quiet zone in a single secondary source control system,[6] are directly proportional to r_{ps} and inversely proportional to r_{se}. The width angle ϕ is also directly proportional to the number of control sources and of error sensors N. Similar to the case of a control system with single control source, it has been found that the length of the quiet zone in the y direction is also directly proportional to the distance ratio of r_{se}/r_{ps}, and becomes much longer for the case of multiple control sources.

The general observation described above is also true to other multiple sources and sensors systems (e.g., $N=L=3,4,\ldots,20$). In summary, the size of the quiet zone created by multiple control sources and error sensors in free space can be very large, if the arrangement of the system is selected within $r_{ss-\min} \leqslant r_{ss} = r_{ee} = \lambda/2 \leqslant r_{ss-\max}$.

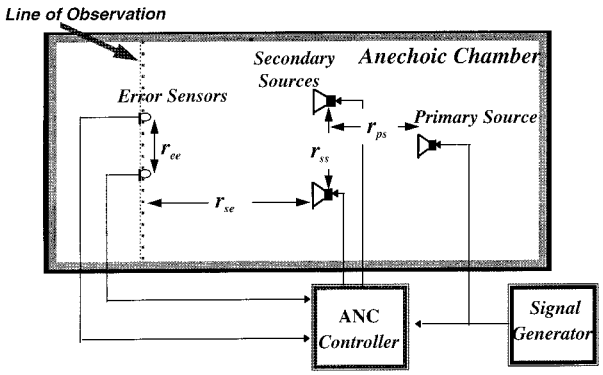

FIG. 10. Experimental setup in an anechoic chamber.

IV. EXPERIMENTS

Experiments were carried out in an anechoic chamber to verify the simulation results, more specifically, to demonstrate the quiet zones created by the MIMO control system in free space and to verify the result of optimal spacing for secondary sources and error sensors.

As shown in Fig. 10, the system has one primary source, two secondary sources, and two error sensors. The whole system is set in a plane of about 1.5 m in height. A multichannel adaptive ANC controller is used for the minimiza-

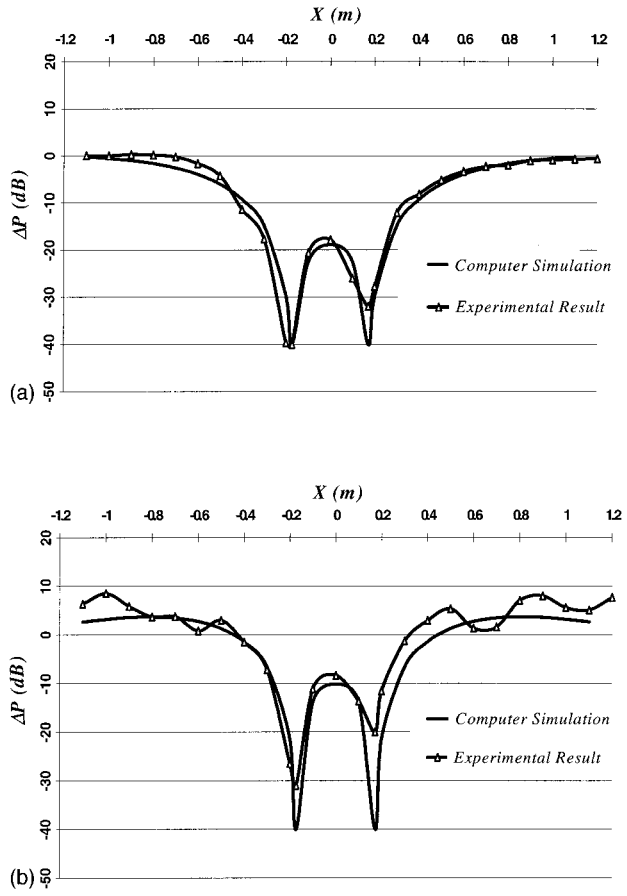

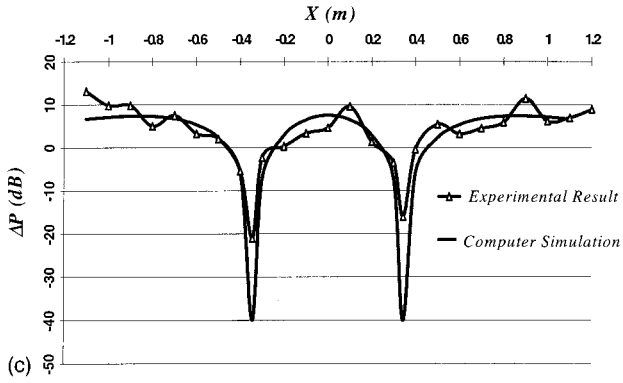

FIG. 11. Measured and calculated sound-pressure attenuation along the observation line when (a) $r_{ss}=r_{ee}=\lambda/2$, (b) $r_{ss}=\lambda$, $r_{ee}=\lambda/2$, and (c) $r_{ss}=r_{ee}=\lambda$.

tion of the error signals.[14] The signal from the signal generator drives the primary source, and is also used by the ANC controller as the reference signal. The frequency of the primary noise is 500 Hz. The sound pressure is measured in a line containing the two error sensors (line of observation). Altogether 24 measuring microphones are equally located in this line with the separation of 10 cm. The distance between the primary source and the secondary source array is one wavelength ($r_{ps}=\lambda$), and the distance between the second source array to the error sensor array is also one wavelength ($r_{se}=\lambda$).

The comparison of the measured and computed sound pressure attenuation along the measuring line for three different configurations, (a) $r_{ss}=r_{ee}=\lambda/2$, (b) $r_{ee}=\lambda/2$, $r_{ss}=\lambda$, and (c) $r_{ss}=r_{ee}=\lambda$, is given in Fig. 11. It shows that the results from the computer simulation and from the experiment agree well. For the case of ''optimal spacing'' of the two secondary sources and the two error sensors [Fig. 11(a)], there does exist a large quiet zone around the error microphones, and the sound-pressure levels outside the quiet zone are virtually unchanged. When the distance between the two secondary sources increases to one wavelength while the two error microphones are still spaced by half-wavelength [Fig. 11(b)], although a quiet zone still exists, it is smaller than configuration (a). The sound-pressure level outside quiet zone also increases (as high as 10 dB in the measuring line). This indicates that to obtain a large zone of quiet without having large increase of total power output, both the secondary source array and the error microphone array should satisfy $r_{ss-\min}<r_{ss}=r_{ee}=\lambda/2<r_{ss-\max}$.

If both the distances between the secondary sources and between the error sensors increase to one wavelength, there is no significant sound-pressure attenuation along the measuring line except in two very narrow areas around the two error sensors [Fig. 11(c)]. The sound-pressure level along the measuring line suffers big increase up to more than 10 dB. This clearly demonstrates that if the spacing of control sources and error sensors is larger than the upper limit, there will be no desired quiet zone but a great increase of sound-pressure level elsewhere.

V. CONCLUSIONS

When the local control strategy is used to create quiet zones in free space, the total sound power output of the system will always increase, and therefore the sound-pressure level in the areas outside the quiet zones will rise. The optimal configurations of the control system are those that have the largest size of quiet zone and the least increase of total power output.

For the multiple secondary sources control system, the quiet zone created by the system is not simply the summation of the quiet zones created by each single control source, but largely dependant on source interaction. For a typical arrangement where all secondary sources and error sensors are equally distributed in two parallel lines, the destructive interaction among the control sources may occur for some configurations. These configurations may require large strength of the control sources to minimize sound pressure at the sensors, and result in a great increase of total sound power output. As a result, the control system may not be able to create large area of quiet zones but cause a sound-pressure increase in most of the space. There exists a range of optimal configuration for the multiple secondary sources control system, which can create the largest quiet zone and suffer the least total power output increase. This range of optimal configuration is described by Eqs. (23)–(25). When the frequency or the frequency range of interest is given, the optimal configurations or the range of optimal spacing can be obtained using these equations. Also for a given configuration of a multiple secondary sources control system, the frequency range suitable for that control system can be also determined. The upper limit of that frequency range can be calculated by solving Eq. (24), and the lower limit by solving Eq. (25) or Eq. (23), depending on whether the number of control sources is larger or equal to two. If the frequency of interest is higher than the upper limit, the control system can not create large area of quiet zones. For the frequency lower than the lower limit, though the large area of quiet zone can still be gained, the total sound power output, as well as the sound pressure in the space outside the quiet zone, may suffer a great increase.

Large areas of quiet zone created by the optimally arranged multiple control sources were observed. They resemble a wedge with its edge around the position of secondary source array. The size of the quiet zone is directly proportional to the distance ratio of error sensor array to secondary source array and primary source to secondary source array, and to the number of the control sources and error sensors.

[1] J. Tichy, ''Current and future issues of active noise control,'' J. Acoust. Soc. Jpn. (E) **12**, 6, 255–262 (1991).
[2] P. A. Nelson and S. J. Elliott, *Active Control of Sound* (Academic, San Diego, CA, 1992).
[3] P. A. Nelson and S. J. Elliott, ''The minimum power output of a pair of free field monopole sources,'' J. Sound Vib. **105**, 173–178 (1986).
[4] P. A. Nelson, A. R. D. Curtis, S. J. Elliott, and A. J. Bullmore, ''The minimum power output of free field point sources and the active control of sound,'' J. Sound Vib. **116**, 397–414 (1987).
[5] S. J. Elliott, P. Joseph, P. A. Nelson, and M. E. Johnson, ''Power output minimization and power absorption in the active control of sound,'' J. Acoust. Soc. Am. **90**, 2501–2512 (1991).
[6] J. Guo and J. Pan, ''Analysis of active noise control in a free field,'' Proceedings of Active 95, Newport Beach, California, 649–660 (1995).
[7] A. Omoto and K. Fujiwara, ''A study of an actively controlled noise barrier,'' J. Acoust. Soc. Am. **94**, 2173–2180 (1993).
[8] A. David and S. J. Elliott, ''Numerical studies of actively generated quiet zones,'' Appl. Acoust. **41**, 63–79 (1994).
[9] P. Joseph, S. J. Elloitt, and P. A. Nelson, ''Near field zones of quiet,'' J. Sound Vib. **172**, 605–627 (1994).
[10] S. Barnett, *Matrices in Control Theory: With applications and linear programming* (Van Nostrand Reinhold, London, 1971).
[11] S. J. Elliott andJ. Garcia-Bonito, ''Active cancellation of pressure and pressure gradient in a diffuse sound field,'' J. Sound Vib. **186**(4), 696–704 (1995).
[12] J. Garcia-Bonito and S. J. Elliott, ''Alternative strategies for actively generating quiet zones,'' ISVR Technical Memorandum 745 (1994).
[13] A. D. Pierce, *Acoustics: An Introduction to Its Physical Principles and Applications* (Acoustical Society of America, Woodbury, New York, 1989).
[14] C. Bao, ''Adaptive algorithms for active noise control and their applications,'' Ph.D. thesis, Katholieke Universiteit Leuven, 1994.

Time-domain analysis and synthesis of active noise control systems in ducts

Zhen Wu,[a] Vijay K. Varadan,[b] and Vasundara V. Varadan
Department of Engineering Science and Mechanics, Research Center for the Engineering of Electronic and Acoustic Materials, The Pennsylvania State University, 149 Hammond Building, University Park, Pennsylvania 16802

(Received 23 November 1994; revised 12 March 1996; accepted 19 July 1996)

This paper presents time-domain analysis and synthesis of active low-frequency noise control systems in rigid-walled ducts. In contrast to frequency-domain analysis, time-domain modeling provides a direct physical insight of the noise cancellation mechanism, where noise signals are assumed to be arbitrary real functions of time instead of harmonics. The time-domain analysis is based on a state-space model which is derived from the governing wave equation using combined numerical (finite difference) and analytical techniques. Optimal feedback control laws are synthesized for a variety of active noise control systems with different sensor and source arrangements. The responses of closed-loop systems are simulated, and the results are compatible with those of transfer function synthesis. In addition, the active control systems so designed have the potential of providing global, broadband, and optimal noise reductions without running into the annoying feedback problems in most feedforward control systems. © *1997 Acoustical Society of America.* [S0001-4966(97)01412-4]

PACS numbers: 43.50.Ki, 43.55.Rg [GAD]

INTRODUCTION

Active noise control has received growing attention in recent years, since it provides an efficient solution to the attenuation of low-frequency sound, for which the passive method, i.e., use of absorbent materials, has not been very successful. A large portion of the active noise control work has been directed toward one-dimensional studies, partly because the problem is relatively simple compared to 2-D and 3-D cases, and partly because of its wide industrial applications such as noise control in air conditioning ducts (Eriksson and Allie, 1988), engine exhaust silencing (Active Noise and Vibration Technologies, 1989), etc.

Active absorption of unwanted sound energy is accomplished by one or several appropriately driven secondary sources, such that a destructive interference occurs with the primary sound field. A typical active control system consists of at least one sensor, actuator (secondary source), and analog or digital controller. A high performance control system should be able to provide an optimal noise reduction globally and over a broad frequency range based on limited sensing and actuating power. In many cases, the controller design plays an important role in achieving optimal noise reduction.

To design an effective active control system, an appropriate model of the system dynamics is required, since system modeling is the basis of control law synthesis. Classical system models describe the dynamics of the acoustic systems via transfer functions, where noise signals are assumed to be time harmonics $e^{i\omega t}$ (Munjal and Eriksson, 1988, 1989; Nelson and Elliott, 1991; Snyder and Hansen, 1989; Curtis *et al.*, 1987; Tichy *et al.*, 1984; Trinder and Nelson, 1983). In general, the aim of all the classical approaches is to achieve a proper magnitude and phase response of the control system by manipulating its transfer function. On the other hand, a state-space model describes the system dynamics in terms of a minimal set of internal system parameters, i.e., states in the time domain. Based on the state-space model, a number of powerful control analysis and synthesis tools is provided by which an optimal control algorithm can be synthesized. For example, the linear quadratic feedback control law allows minimal state errors (maximal noise reduction level) to be achieved while using minimal control effort (secondary source strength). The state-space model is also capable of analyzing a multi-input/multi-output system, which is necessary for global noise cancellation. Therefore, by describing an acoustic system in a state-space form, one can take advantage of modern control design tools in designing active control systems for broadband global noise attenuation.

In recent years, an adaptive feedforward control technique based on a so-called filtered-X algorithm has been successful in active noise control (Orduña-Bustamante and Nelson, 1992; Hall *et al.*, 1990). Although it is a time-domain procedure, it is basically a signal processing technique which does not involve the physics of acoustics (Widrow and Stearns, 1985). Therefore, it works adequately for control of local sound pressure with a single-channel scheme, but for global sound control with multi-channels, it is not as successful. Overall, previous studies on active noise control have not taken advantage of modern control theories which are well known for control of dynamic systems.

The state-space control approach has been widely applied in the field of active vibration control also where the dynamics of a finite structure can be easily modeled in state-

[a]Current address: Automated Analysis Corp., 2805 S. Industrial, Suite 100, Ann Arbor, MI 48104.
[b]Corresponding author: Professor V. K. Varadan. Phone: (814)863-4210, Fax: (814)865-3052.

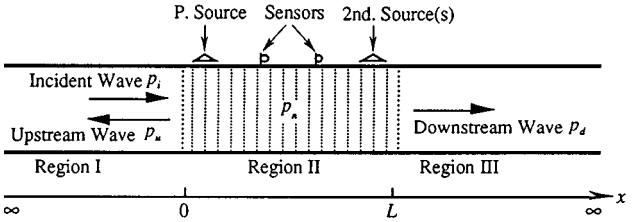

FIG. 1. One-dimensional active noise control system.

space form using standard discretization techniques (Meirovitch and Baruh, 1981). However, for the control of acoustic systems, this approach is rather new. Hull and his co-authors (1990a, 1991) have developed a state-space model for an acoustic duct of a finite length with dissipative end conditions, and achieved global noise reductions using the pole-placement technique. The approach uses a modal decomposition based on the eigenvalues and eigenfunctions of the system, and selects the modal pressures as the state variables. Dohner and Shoureshi (1989) developed a state-space model for a three-dimensional active noise control system also using the modal approach. A single-input, single-output feedback controller was designed and implemented using optimal control or linear quadratic Gaussian (LQG) theory. Although modal decomposition leads to an elegant diagonal system matrix, the state variables are not physical system parameters and therefore cannot be measured directly. In our previous work, a simple system model has been developed for an infinite one-dimensional noise control system using combined numerical (finite difference) and analytical methods (Wu *et al.*, 1993a). In addition, an optimal controller was designed for a broadband active underwater echo cancellation system (Wu *et al.*, 1993b). In this work, a more comprehensive and versatile model including passive damping is developed for low-frequency active noise control systems in ducts.

This paper presents a systematic analysis and synthesis of a variety of active noise control systems in ducts by means of state-space modeling and optimal feedback control techniques. First, a generic state-space model is developed based on the governing 1-D wave equation to describe the dynamics of wave propagation in a rigid walled duct at its fundamental mode. Second, a feedback controller including a state estimator is designed using the optimal control theory. The goal is to enable the active control system to effectively attenuate broadband noise globally.

I. STATE-SPACE MODELING

In order to apply the optimal control theory, a state-space model of duct acoustics must be established first. Considering an infinitely long, rigid walled duct, sound propagation in it can be assumed one dimensional if the sound frequency is below the cut-on frequency of higher duct modes. Figure 1 shows a conceptual drawing of the one-dimensional active noise control system. The acoustic system under consideration is comprised of three regions, i.e., one finite region II ($x \in [0,L]$) and two semi-infinite regions I and III ($x \in (-\infty,0]$ and $x \in [L,\infty)$, respectively). In region II, a number of sources can be arbitrarily planned as the primary and secondary sources, and a number of sensors may also be arranged. Here, the proposed model is intended to be generic; i.e., it may fit in a variety of noise control systems in ducts by customizing the boundary conditions at locations $x=0$ and $x=L$. For example, if perfect reflection boundaries are assigned to the two ends, the system becomes a finite duct studied by many researchers. If the boundaries of total transmission are assigned to the two ends, the system becomes an infinite duct system. Meanwhile, boundaries with intermediary reflection and transmission resemble dissipation or radiation end conditions. The disturbance input of the system can be either an incident plane wave with arbitrary waveform p_i or a primary source Q_p. The system outputs can be an upstream pressure p_u, a downstream pressure p_d, and/or sound pressure at other locations of interest. A number of sensors and actuators (secondary sources) can be located anywhere inside the region $[0,L]$. Both the sensors and actuators are assumed to be transparent to sound; i.e., their existence does not affect wave propagation characteristics. The object is to model the dynamics of the acoustic system and to describe the system outputs (p_u, p_d, etc.) in terms of the system input (p_i or Q_p) in the time domain. The model will also comprehend passive viscous damping which usually appears in actual noise control systems.

Assuming that low-frequency noise propagates in a rigid-walled duct at its fundamental mode, the acoustics of the duct can be characterized by a one-dimensional wave equation. The governing equation for one-dimensional wave propagation in a stationary fluid medium containing sources is as follows (Kinsler *et al.*, 1982):

$$\frac{\partial^2 p(x,t)}{\partial x^2} + \tau \frac{\partial^3 p(x,t)}{\partial x^2\, \partial t} - \frac{1}{c^2} \frac{\partial^2 p(x,t)}{\partial t^2} = -\sum_{j=1}^{m} \frac{dq_j(t)}{dt}\, \delta(x-x_j), \tag{1}$$

where $p(x,t)$ is the acoustic pressure as a function of the spatial coordinate x and time t, and c is the speed of sound. The source term at the right-hand side of Eq. (1) represents plane monopole sources with mass inject rates per unit volume q_j (kg m^{-3} s). To account for the passive damping that many systems may actually have, an equivalent viscous damping term is included in Eq. (1) characterized by a relaxation constant τ.

To convert the wave equation, which is a second-order partial differential equation, into the state equation, which contains a set of first-order ordinary differential equations, the spatial derivative in Eq. (1) must be rewritten in a numerical form. However, most numerical techniques can only be applied to a finite region with defined boundaries. Therefore, sound pressure in region II is presented in a numerical form, while sound pressures in regions I and III are presented analytical forms. Here, the finite difference method is used in order to preserve the state variables as real sound pressures, which is measurable experimentally.

In region II, the sound field is represented by discrete acoustic pressures at $N+1$ locations, p_n $(n=0,1,2,L,N)$ with a spacing $h=L/N$. Using standard finite difference, the spatial derivative of p is approximated to be

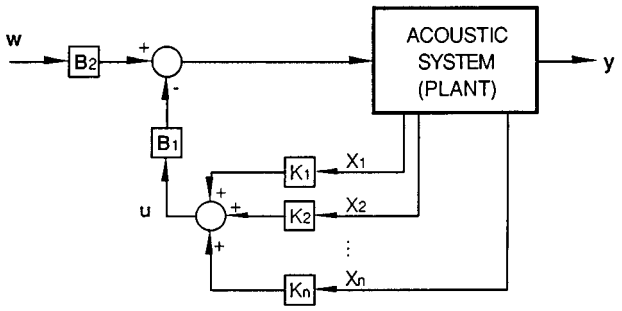

FIG. 2. Block diagram of full state-feedback control system.

$$\frac{\partial^2 p}{\partial x^2} \approx \frac{p_{n+1}-2p_n+p_{n-1}}{h^2}. \tag{2}$$

Thus, Eq. (1) becomes

$$\ddot{p}_n = \frac{c_{\mathrm{II}}^2}{h^2}(p_{n+1}-2p_n+p_{n-1}) + \tau \frac{c_{\mathrm{II}}^2}{h^2}(\dot{p}_{n+1}-2\dot{p}_n+\dot{p}_{n-1}) \tag{3}$$

for those locations other than the actuator location, and

$$\ddot{p}_n = \frac{c_{\mathrm{II}}^2}{h^2}(p_{n+1}-2p_n+p_{n-1}) + \tau \frac{c_{\mathrm{II}}^2}{h^2} \times (\dot{p}_{n+1}-2\dot{p}_n+\dot{p}_{n-1}) + c_{\mathrm{II}}^2 \rho_{\mathrm{II}} \frac{\dot{Q}_j}{Sh} \tag{4}$$

for the locations of the primary and secondary sources, where c_{II} and ρ_{II} are the sound speed and mass density in region II, respectively. Q_j is the volume velocity strength of a monopole source, and S is the cross-sectional area of the duct. The dots above variables denote time derivatives.

In regions I and III, the acoustic pressure corresponding to the incident, upstream, and downstream waves are represented in analytical forms as solutions of the homogenous and nondamping version of Eq. (1) (Kinsler *et al.*, 1982):

$$p_i = f_i(t - x/c_{\mathrm{I}}), \tag{5a}$$

$$p_u = f_u(t + x/c_{\mathrm{I}}), \tag{5b}$$

$$p_d = f_d(t - x/c_{\mathrm{III}}), \tag{5c}$$

where f_i, f_u, and f_d are arbitrary real functions, and c_{I} and c_{III} are the speeds of sound in regions I and III, respectively. The minus signs in Eqs. (5a) and (5c) indicate that the incident and downstream waves are propagating along the positive x axis, while the plus sign in Eq. (5b) shows that the upstream wave is propagating along the negative x axis. By knowing the waveform at one location, one can predict the sound pressure at another location or time instant through these relations.

The discrete and analytical sound pressures are then related by enforcing the boundary conditions of pressure and velocity continuity at the boundaries $x=0$ and $x=L$ as

$$p_0 = p_i(0,t) + p_u(0,t), \tag{6a}$$

$$\frac{1}{\rho_{\mathrm{II}}}\frac{p_1-p_0}{h} = \frac{1}{\rho_1}\left[\frac{\partial p_i(x,t)}{\partial x} + \frac{\partial p_u(x,t)}{\partial x}\right]_{x=0} \tag{6b}$$

and

$$p_N = p_d(L,t) \tag{7a}$$

$$\frac{1}{\rho_{\mathrm{II}}}\frac{p_N-p_{N-1}}{h} = \frac{1}{\rho_{\mathrm{III}}}\left.\frac{\partial p_d(x,t)}{\partial x}\right|_{x=L}, \tag{7b}$$

where ρ_{I} and ρ_{III} are the mass densities of regions I and III, respectively. Considering Eq. (5), the spatial derivatives of p_i, p_u, and p_d in Eqs. (6b) and (7b) can be expressed in terms of time derivatives as follows:

$$\left.\frac{\partial p_i(x,t)}{\partial x}\right|_{x=0} = -\frac{1}{c_{\mathrm{I}}}\left.\frac{\partial p_i(x,t)}{\partial t}\right|_{x=0} = 0 - \frac{1}{c_{\mathrm{I}}}\dot{p}_i(0),$$

$$\left.\frac{\partial p_u(x,t)}{\partial x}\right|_{x=0} = \frac{1}{c_{\mathrm{I}}}\left.\frac{\partial p_u(x,t)}{\partial t}\right|_{x=0} = \frac{1}{c_{\mathrm{I}}}\dot{p}_u(0), \tag{8}$$

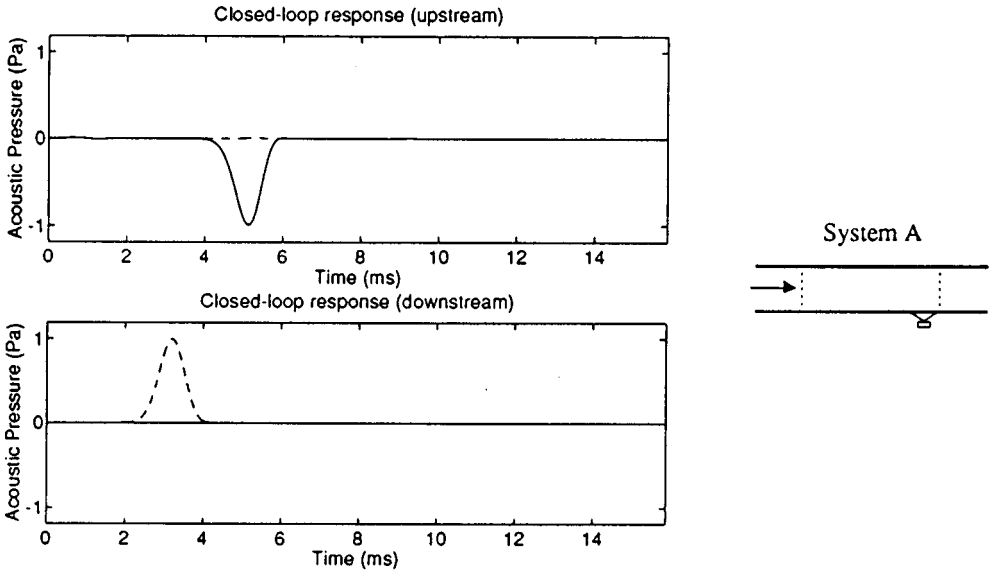

FIG. 3. Closed-loop response of system A with full state-feedback controller: Solid line—closed-loop response; dashed line—open-loop response.

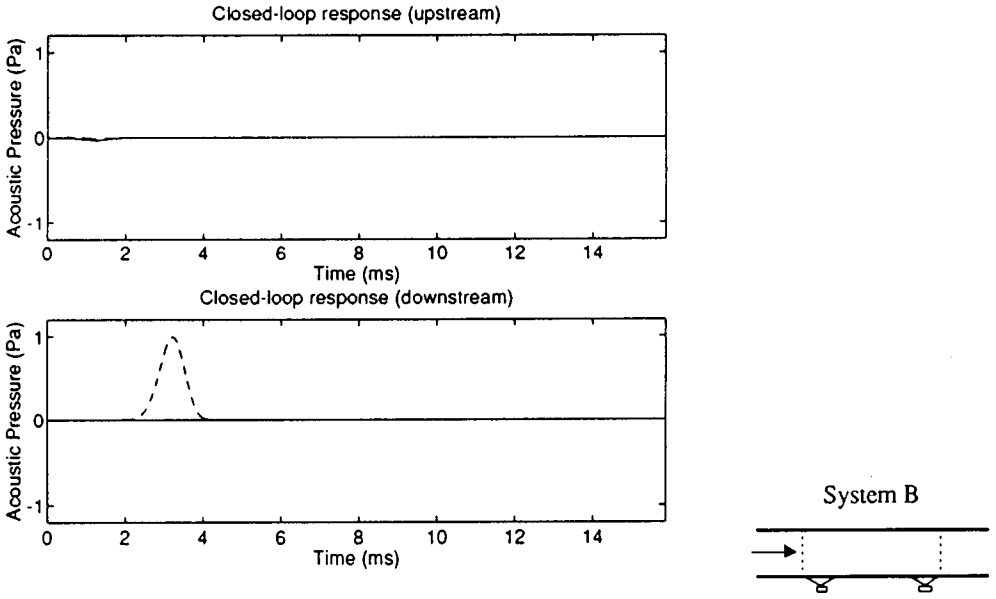

FIG. 4. Closed-loop response of system B with full state-feedback controller: Solid line—closed-loop response; dashed line—open-loop response.

$$\left.\frac{\partial p_d(x,t)}{\partial x}\right|_{x=L} = -\frac{1}{c_{\mathrm{I}}}\left.\frac{\partial p_d(x,t)}{\partial t}\right|_{x=L} = -\frac{1}{c_{\mathrm{III}}}\dot{p}_d(L).$$

If $Z_{\mathrm{I}}=\rho_{\mathrm{I}}c_{\mathrm{I}}$, $Z_{\mathrm{II}}=\rho_{\mathrm{II}}c_{\mathrm{II}}$ and $Z_{\mathrm{III}}=\rho_{\mathrm{III}}c_{\mathrm{III}}$ are defined as the acoustic impedances of regions I, II, and III, respectively, Eqs. (6b) and (7b) can be rewritten as

$$\frac{c_{\mathrm{II}}}{h}(p_1-p_0)=\frac{Z_{\mathrm{II}}}{Z_{\mathrm{I}}}[-\dot{p}_i(0)+\dot{p}_u(0)] \tag{9}$$

and

$$\frac{c_{\mathrm{II}}}{h}(p_N-p_{N-1})=-\frac{Z_{\mathrm{II}}}{Z_{\mathrm{III}}}\dot{p}_d(L). \tag{10}$$

From Eqs. (3), (4), (6), and (7), the state model can be derived by choosing the following as the state variables: discrete sound pressures $p_1,\ p_2,\ L,\ p_{N-1}$ in the finite region and their first time derivatives $\dot{p}_1,\ \dot{p}_2,\ L,\ \dot{p}_{N-1}$; the downstream pressure at $x=L$, $p_d(L)$; and the upstream pressure at $x=0$, $p_u(0)$. The total number of state variables is $2N$. The state-space model has the following form:

$$\dot{\mathbf{x}}(t)=\mathbf{A}\mathbf{x}(t)+\mathbf{B}_1\mathbf{u}(t)+\mathbf{B}_2\mathbf{w}(t), \tag{11a}$$

$$\mathbf{y}(t)=\mathbf{C}\mathbf{x}(t), \tag{11b}$$

where $\mathbf{x}(t)$ is the state vector containing the discretized acoustic pressures in region $[0,L]$ and the up- and downstream pressures; $\mathbf{u}(t)$ is the control input vector containing the secondary sources strength; $\mathbf{w}(t)$ is the disturbance vector containing the incident pressure or the primary source's strength; and $\mathbf{y}(t)$ is the output vector containing noise level upstream, downstream, and/or other locations of interest. System matrix $\mathbf{A}$ has a dimension of $2N\times 2N$, and input

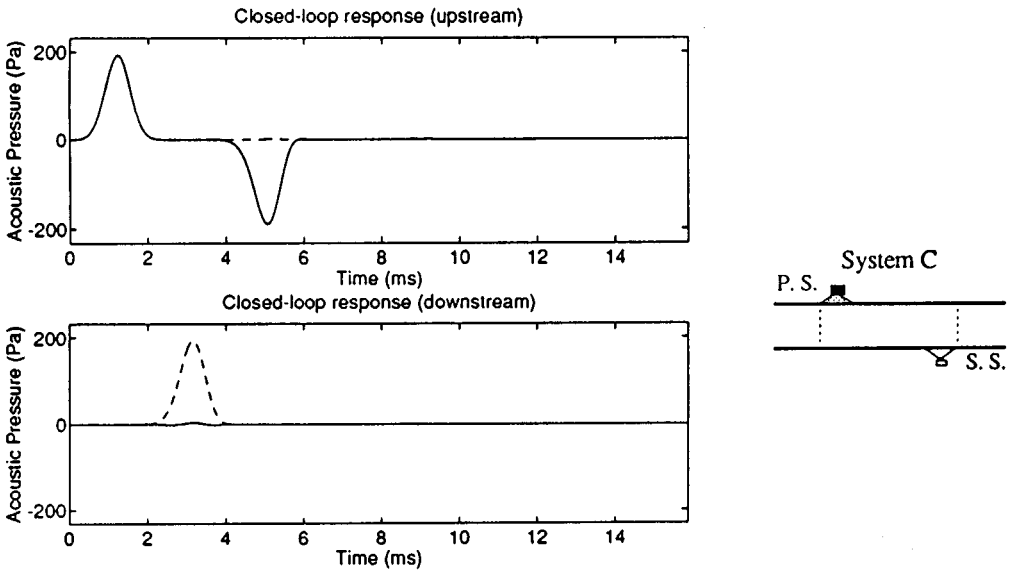

FIG. 5. Closed-loop response of system C with full state-feedback controller: Solid line—closed-loop response; dashed line—open-loop response.

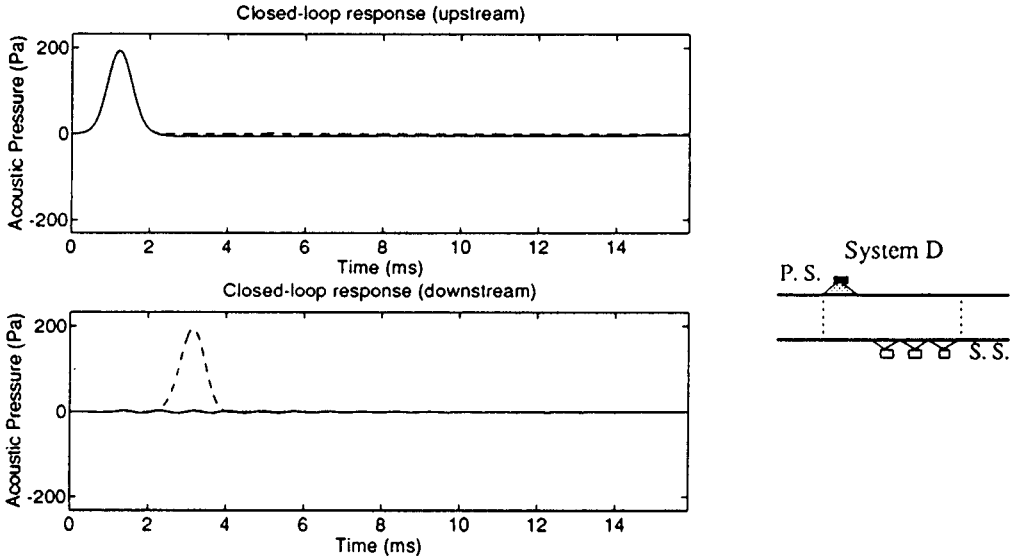

FIG. 6. Closed-loop response of system D with full state-feedback controller: Solid line—closed-loop response; dashed line—open-loop response.

matrices $\mathbf{B}_1$ and $\mathbf{B}_2$ and output matrix $\mathbf{C}$ have proper dimensions.

The state equation can be solved for the system's time response subject to a given initial condition $\mathbf{x}_0$ at time t_0 (assumed to be zero in this case) and inputs [for example, $w(t)$] (DeCarlo, 1989):

$$\mathbf{x}(t)=\Phi(t,t_0)\mathbf{x}_0+\int_{t_0}^{t}\Phi(t,t')\mathbf{B}_2(t')\mathbf{w}(t')dt', \tag{12}$$

where

$$\mathbf{\Phi}(t,t_0)=\exp[\mathbf{A}\cdot(t-t_0)] \tag{13}$$

is the state transition matrix. The simulated time response will describe the noise propagation and cancellation mechanisms in one-dimensional space in the time domain, which should be equivalent to the frequency-domain description. In this paper, MATLAB *Control System Toolbox* routines (The MathWork, Inc., MA) were employed to perform the model simulation and the control law synthesis later on.

In order to fully describe this distributed parameter system, the order of the system model or the size of the system matrix must be infinite. However, a finite-order system model should have good accuracy when the low-frequency components are dominant in the input signal spectrum. A higher-order model provides better accuracy, but it requires large computational power which is limited in real-time implementation. Therefore, one must compromise between the model order and accuracy. It has been found that model errors can be reduced by using unevenly spaced grids with finer spacing near interfaces for the same model order. For more detailed model derivation, verification, and discussion about accuracy and convergence, readers can refer to Wu *et al.* (1993a).

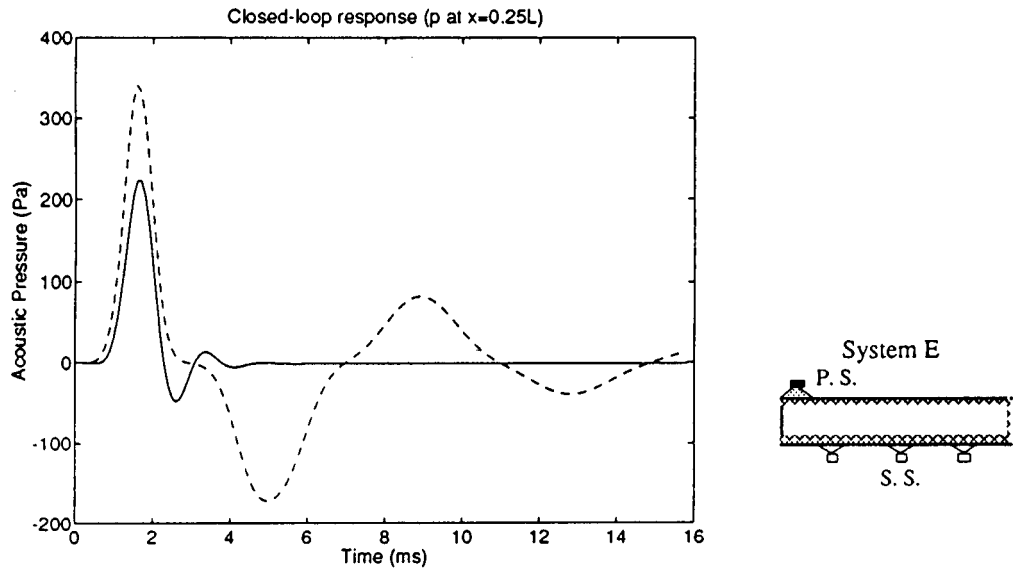

FIG. 7. Closed-loop time response of system E with full state-feedback controller (acoustic pressure at $x=0.25L$): Solid line—closed-loop response; dashed line—open-loop response.

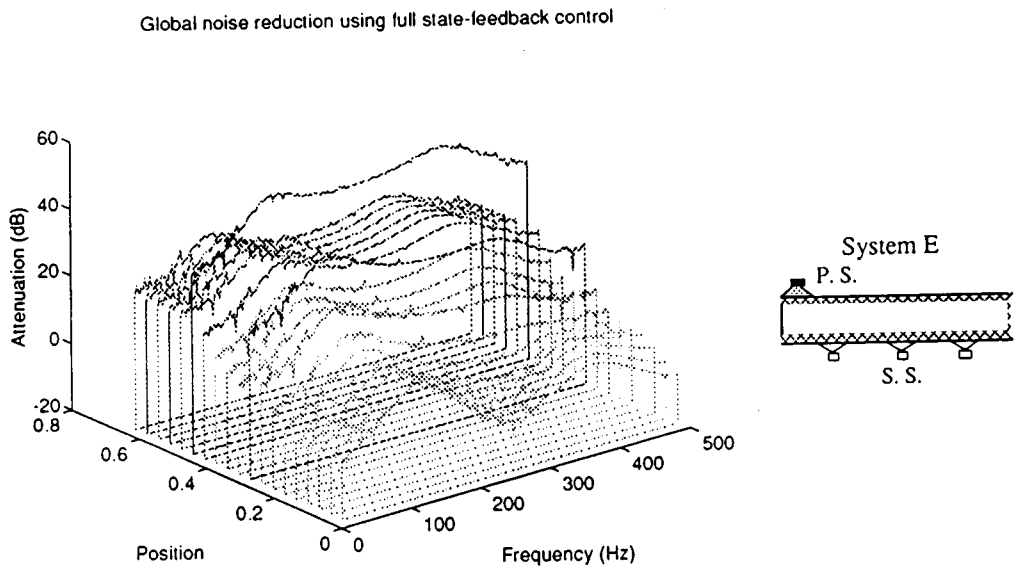

FIG. 8. Noise reduction spectra of system E with full state-feedback controller.

II. CONTROL SYSTEM ANALYSIS AND SYNTHESIS

In this section, based on the state-space model, a feedback control algorithm is synthesized using LQG optimal control theory.

A. Full state-feedback controller design

One commonly used controller structure is the so-called full state feedback. As seen in the block diagram of the full state feedback shown Fig. 2, the control inputs are the weighted sum of state variables:

$$\mathbf{u}(t) = -\mathbf{K}\mathbf{x}(t), \tag{14}$$

where $\mathbf{K}$ is the feedback gain matrix which is usually constant but can be time varying.

To determine the feedback gain $\mathbf{K}$, the LQG optimal control theory is applied. It solves for the optimal feedback gain under the criteria of minimizing a quadratic performance index:

$$J = \int_0^\infty (\mathbf{x}^T\mathbf{G}\mathbf{x} + \mathbf{u}^T\mathbf{H}\mathbf{u})dt, \tag{15}$$

where $\mathbf{G}$ and $\mathbf{H}$ are diagonal weighting matrices of appropriate dimensions. Each diagonal element in the weighting matrices determines the relative importance of the corresponding states. By appropriately selecting the weighting matrices, maximum noise reduction in a desired pattern can be achieved while compromising for the required actuating energy. After the performance index is defined, the feedback gain $\mathbf{K}$ can be computed by solving the associated matrix Reccati equation:

$$0 = \mathbf{S}\mathbf{A} + \mathbf{A}^T\mathbf{S} - \mathbf{S}\mathbf{B}\mathbf{R}^{-1}\mathbf{B}^T\mathbf{S} + \mathbf{Q}, \tag{16}$$

where $\mathbf{K} = \mathbf{R}^{-1}\mathbf{B}^T\mathbf{S}$. Here, a MATLAB routine *lqr* is used to compute the optimal $\mathbf{K}$ (controllability of the system has been check before running *lqr*).

A variety of active noise control systems with different arrangements in ducts were studied. Following the discussions by Nelson and Elliot (1991), as well as by Munjal and Eriksson (1988, 1989) on some existing control system configurations, analysis and syntheses of these systems from the time-domain perceptive were conducted instead of the frequency-domain approach. Figures 3–7 compare the simulated closed- and open-loop responses of five typical control schemes using the full state-feedback control algorithm, where equivalent or better control results are shown compared to those from the frequency-domain approach. In the numerical simulation, a model with uneven grids and the following model parameters is used: $\rho_{II} = 1.129$ kg/m^3; $c_{II} = 340$ m/s; $L = 0.68$ m; $N = 20$. The disturbance input is either a broadband pulse of Gaussian shape or a low-frequency random noise-sequence.

Systems A and B have an infinite long duct with a plane wave incident from upstream. In system A, only one control source is used to cancel downstream noise. By selecting the weighting matrix $\mathbf{Q}$ in favor of downstream pressure in Eq. (14), an optimal feedback gain can be computed. The resulting closed-loop response in Fig. 3 shows a total cancellation of downstream pressure. However, an upstream wave is also produced in the meantime. This phenomenon coincides with what was predicted by the frequency-domain analysis. Because an acoustic zero is actually produced at the location of secondary source, a total reflection occurs (Snyder and

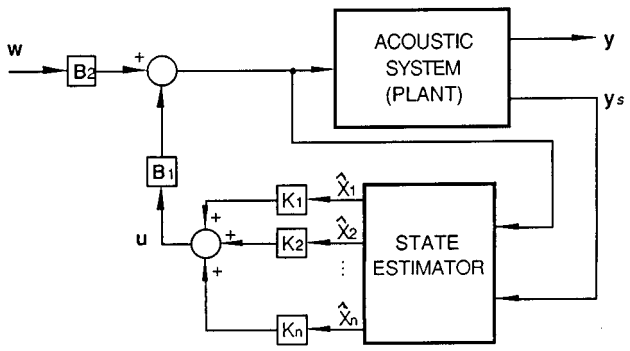

FIG. 9. Block diagram of feedback control system including a state estimator.

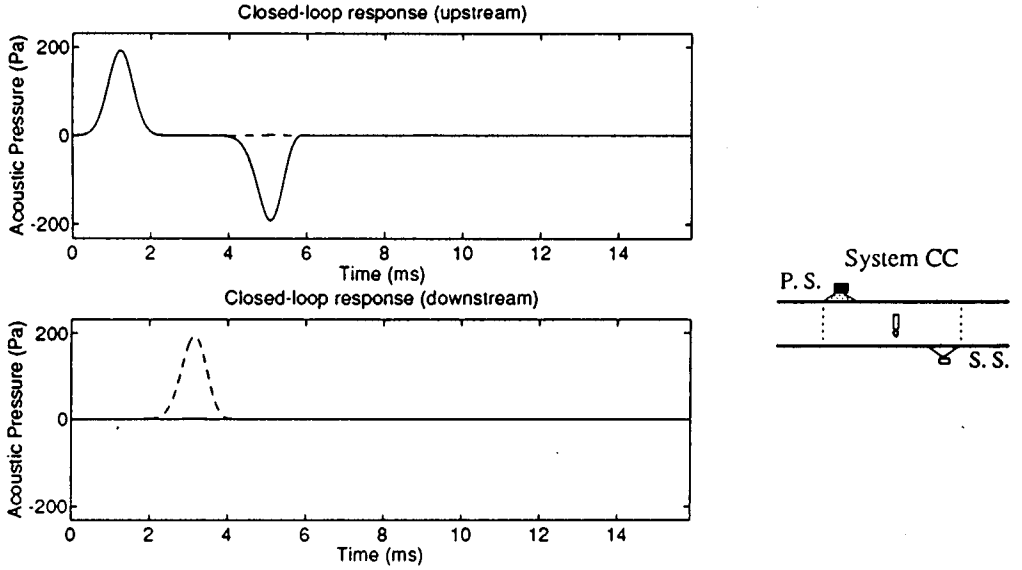

FIG. 10. Closed-loop response of system CC with state estimator and feedback controller: Solid line—closed-loop response; dashed line—open-loop response.

Hansen, 1989). In system B, two control sources are employed to cancel downstream noise without producing an upstream wave. This can be achieved by selecting the weighting matrix **Q** in favor of both upstream and downstream pressures. The closed-loop response is shown in Fig. 4. The frequency-domain synthesis can only achieve this for certain frequencies at which standing waves are generated between the two secondary sources, but not for a broad frequency band.

Systems C and D have an infinite long duct with a primary source. In system C, only one secondary source is used to cancel downstream noise. If the weighting matrix is selected in the same manner as for system A, the control system can completely cancel the downstream pressure and meanwhile produces an upstream wave as shown in Fig. 5. This is also expected from the frequency-domain analysis (Nelson and Elliot, 1991). In system D, three control sources are employed to cancel downstream noise without producing an upstream wave. This can be achieved by selecting the weighting matrix **Q** in favor of both the pressure at a location right next to the primary source and the downstream pressure. The closed-loop response is shown in Fig. 6. This is equivalent to the outcome of frequency-domain study, where a unidirectional source is formed to cancel the downstream pressure.

One of the unique features of the state-space, time-domain control approach is that the requirement of global noise reduction can be directly cast in the optimal formulation, whereas traditional frequency-domain control and single-channel adaptive control can only provide local reduction which would likely increase noise level at another location. System E represents a duct with a totally reflective boundary at one end and a partially reflective boundary at the other end, which is similar to the system model considered

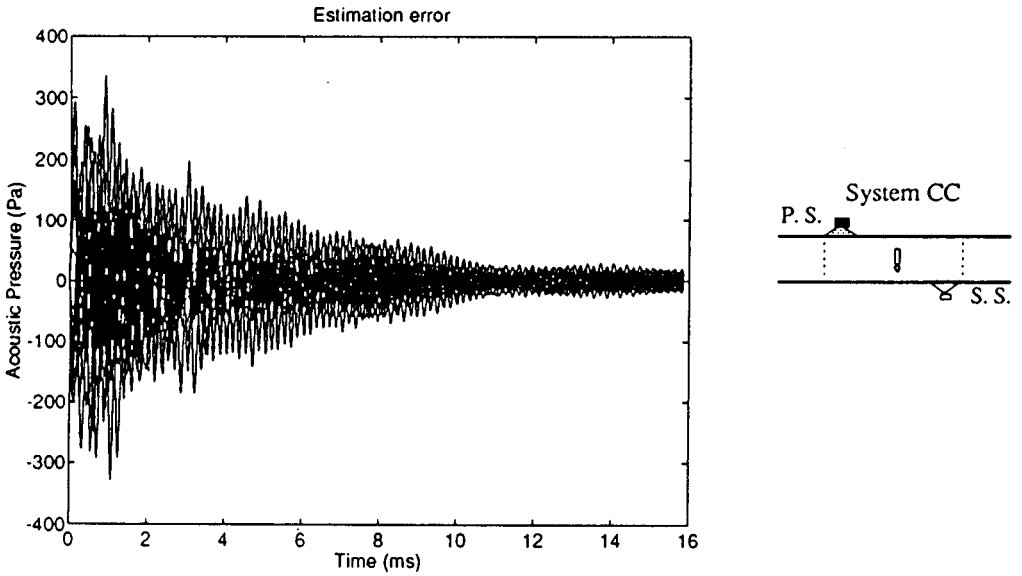

FIG. 11. State estimation errors of system CC.

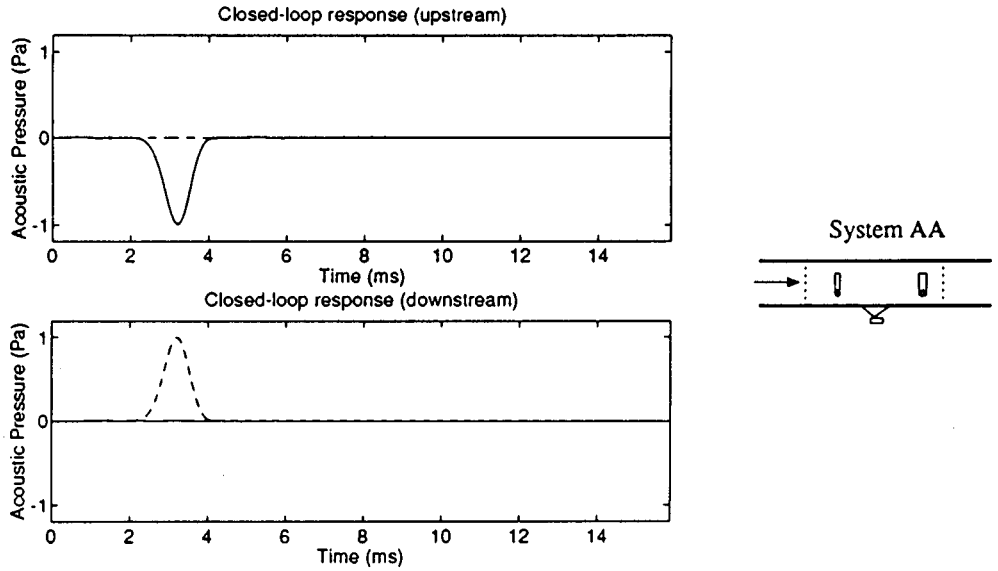

FIG. 12. Closed-loop response of system AA with state estimator and feedback controller: Solid line—closed-loop response; dashed line—open-loop response.

by Hull *et al.* (1991). In addition, passive absorption is also taken into account by setting an equivalent τ value. Three secondary sources are spaced evenly in the duct in order to globally reduce the noise level from a primary source located at the totally reflective end. The positions of the secondary sources can be optimized if the cancellation of certain resonant modes is desired, in which case the weighting matrix is selected to match the mode shapes. Figure 7 shows the time response of the closed-loop system subject to a pulse input, where the sound pressure at $x=0.25L$ is seen to be heavily damped and the resonances are significantly suppressed. Figure 8 shows the 3-D plot of noise attenuation spectra at every discrete location in the duct, which is calculated by comparing the FFT of open- and closed-loop responses subject to a low-pass filtered ($<$500 Hz) random noise input. As seen in Fig. 8, positive noise reduction levels appear at every position and frequency up to 500 Hz. Therefore, this design would lead to a global and broadband noise reduction.

B. Controller design including state estimator

A full state feedback requires the knowledge of all state variables, which means a large number of sensors is needed. However, a fewer number of sensors, one or two for instance, is preferred in a practical control system. Thus a state estimator or observer is designed instead to estimate the state variables from a subset of state measurements. The observer is a dynamic model that runs in parallel with the actual acoustic system. Its input is the input into the actual system plus an error feedback designed to drive the model states, called state estimates, to values approaching the actual system states. The outputs of the observer are the estimation of

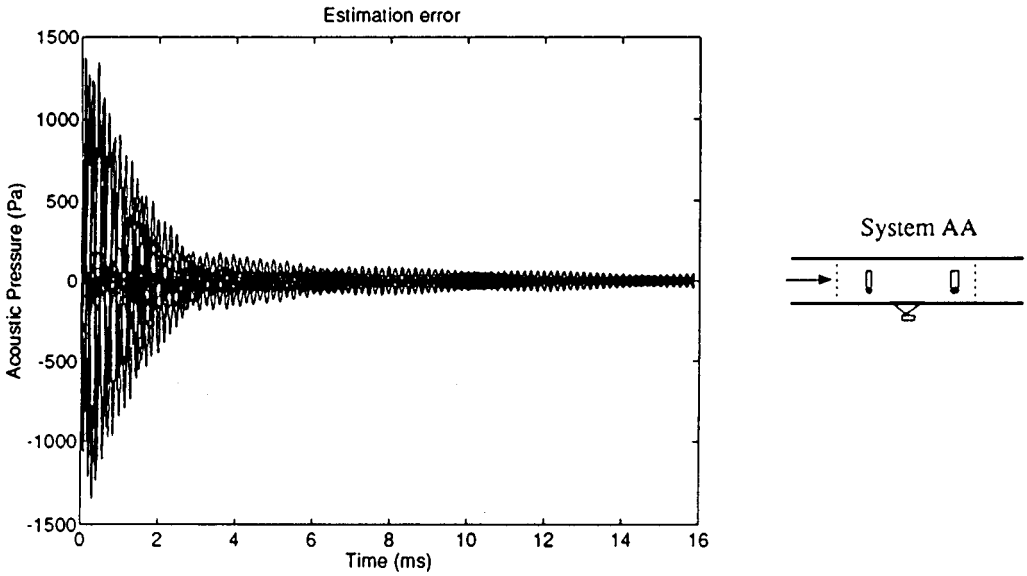

FIG. 13. State estimation errors of system AA.

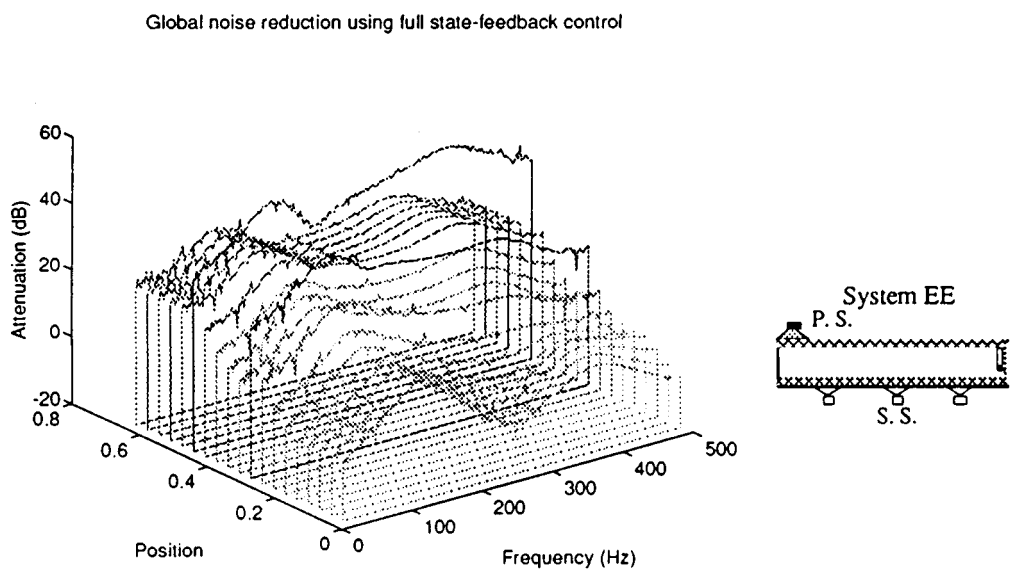

FIG. 14. Noise reduction spectra of system EE with state estimator and feedback controller.

the actual state variables, and then feedback control is computed from the estimated states rather than the actual states. Figure 9 shows a block diagram of the feedback control system including a state estimator.

The estimated state vector $\hat{\mathbf{x}}$ is computed using the model equation

$$\dot{\hat{\mathbf{x}}} = \mathbf{A}\hat{\mathbf{x}} + \mathbf{B}_1\mathbf{u} + \mathbf{B}_2\mathbf{w} + \mathbf{L}(\mathbf{y}_s - \mathbf{C}_s\hat{\mathbf{x}}), \tag{17}$$

where $\mathbf{y}_s = \mathbf{C}_s\mathbf{x}$ is the sensor output vector and $\mathbf{L}$ is the observer gain matrix. The observer gain $\mathbf{L}$ is determined in a similar manner as the feedback gain $\mathbf{K}$, so that the observer produces optimal estimations of actual state variables. A MATLAB routine *lqe* is used to compute the optimal $\mathbf{L}$ (observability of the system has been check before running *lqe*). The estimation error $\mathbf{e} = \mathbf{x} - \hat{\mathbf{x}}$ satisfies the following equation which can be derived from Eqs. (9) and (17):

$$\dot{\mathbf{e}} = (\mathbf{A} - \mathbf{L}\mathbf{C}_s)\mathbf{e}. \tag{18}$$

The final control system includes the state estimator and feedback controller. Here, the control signal has the form

$$\mathbf{u}(t) = -\mathbf{K}\hat{\mathbf{x}}(t). \tag{19}$$

Combining Eqs. (9) and (19), the closed-loop system becomes

$$\dot{\mathbf{x}} = (\mathbf{A} - \mathbf{B}_1\mathbf{K})\mathbf{x} + \mathbf{B}_1\mathbf{K}\mathbf{e} + \mathbf{B}_2\mathbf{w}. \tag{20}$$

The closed-loop response and the estimation errors are coupled, and they can be simulated simultaneously by forming a combined state equation as follows:

$$\begin{pmatrix} \dot{\mathbf{x}} \\ \dot{\mathbf{e}} \end{pmatrix} = \begin{bmatrix} \mathbf{A} - \mathbf{B}_1\mathbf{K} & \mathbf{B}_1\mathbf{K} \\ \mathbf{0} & \mathbf{A} - \mathbf{L}\mathbf{C}_s \end{bmatrix} \begin{pmatrix} \mathbf{x} \\ \mathbf{e} \end{pmatrix} + \begin{bmatrix} \mathbf{B}_2 \\ \mathbf{0} \end{bmatrix} \mathbf{w}. \tag{21}$$

Some of the active noise control systems previously described were redesigned to include state estimators. System CC is based on system C with one microphone placed upstream from the secondary source. The closed-loop response along with the estimation errors of system CC are shown in Figs. 10 and 11, respectively. It is noticed that the estimation errors decay from their initial values (assumed to be small random numbers) to zeros in a very short time period. The closed-loop results are almost as good as that of full state feedback in this simulation. For practical implementation of the control system with the state estimator, the closed-loop results may be inferior to that of full state feedback due to the computing speed limitation of a real-time controller.

In some situations, disturbance input may not be available to the observer, so a modified observer design is used by assuming the disturbance input to be random noise. System AA has two microphones, one upstream and one downstream of the secondary source, which is similar to the adaptive feedforward control system. Figures 12 and 13 show the closed-loop response and the estimation errors of system AA, respectively. The control system is able to cancel the downstream pressure with decaying estimation errors.

Finally, the global noise control system is redesigned using a microphone placed at the dissipative end. The actual pressure in the duct is estimated by an observer using signals from the sensor and the primary source. Figure 14 shows the final noise reduction levels at every discrete point in the duct of system EE, which is almost identical to the results of full state feedback.

III. CONCLUSION

The system dynamics of one-dimensional noise propagation in ducts can be described by a state-space model, which contains state variables corresponding to physical quantities of the system. In developing the state-space model, the finite difference technique is used in combination with the analytical solutions. This allows for modeling of long (infinite) ducts by discretizing only in a small finite region where sensors and secondary sources are located. Based on the state-space models, feedback control laws for a variety of typical noise control systems are synthesized using the LQG optimal control theory which leads to a broadband and global noise reduction. The noise cancellation mecha-

nism is described with a clear physical insight by the simulated time responses of the systems. Furthermore, the feedback control system is shown to be more feasible by including state estimators and eliminating the requirement of a large number of sensors.

Some comments on selecting the weighting matrix in the LQG design are in order. The choice of weighting matrix depends on the control objective for different control systems. In this paper, all the weight matrices are diagonal matrix. If local cancellation is desired, one can choose a higher positive value for the term corresponding to the state variable representing sound pressure at a particular location. If global noise reduction is desired, all terms in the weighting matrix should be equal. Usually, higher positive values in the weighting matrix lead to higher noise reduction. However, in real implementation, one must be careful of system instability caused by high feedback gain.

ACKNOWLEDGMENTS

The authors wish to thank Dr. Xiaoqi Bao of the Research Center for the Engineering of Electronic and Acoustic Materials and Dr. Kwang Y. Lee of the Electrical Engineering Department at Penn State for their helpful suggestions and comments regarding this work. This research was supported in part by the industrial consortium of the Research Center for the Engineering of Electronic and Acoustic Materials.

Active Noise and Vibration Technologies (**1989**). *Electronic Muffler Systems*, Technical Brochure (Active Noise and Vibration Technologies, Tempe, AZ).

Curtis, A. R. D., Nelson, P. A., Elliott, S. J., and Bullmore, A. J. (**1987**). ''Active suppression of acoustic resonance,'' J. Acoust. Soc. Am. **81**, 624–631.

DeCarlo, R. A. (**1989**). *Linear Systems—A State Variable Approach With Numerical Implementation* (Prentice-Hall, Englewood Cliffs, NJ).

Dohner, J. L., and Shoureshi, R. (**1989**). ''Modal Control of Acoustic Plants,'' J. Vib. Acoust. Stress Reliability Design **111**, 326–330.

Eriksson, L. J., and Allie, M. C. (**1988**). ''A Practical System for Active Attenuation in Ducts,'' J. Sound Vib. **22**, 797–802.

Hall, R. H., Ferren, W. B., and Bernhard, R. J. (**1990**). ''Active control of radiated sound from ducts,'' in *Active Control of Noise and Vibration* (ASME, New York), pp. 143–152.

Hull, A. J., Radcliffe, C. J., Miklavcic, M., and MacCluer, C. R. (**1990a**). ''State space representation of the nonself-adjoint acoustic duct system,'' J. Vib. Acoust. **112**, 483–488.

Hull, A. J., Radcliffe, C. J., and MacCluer, C. R. (**1990b**). ''State estimation of the nonself-adjoint acoustic duct system,'' *ASME Winter Annual Meeting*, Dallas, TX (ASME, New York), pp. 43–48.

Hull. A. J., Radcliffe, C. J., and Southward, S. C. (**1991**). ''Global active noise control of a one-dimensional acoustic duct using a feedback controller,'' *ASME Winter Annual Meeting* (ASME, New York), No. 91-WA-DSC-10.

Kinsler, L. E., Frey, A. R., Coppens, A. B., and Sanders, J. V. (**1982**). *Fundamentals of Acoustics* (Wiley, New York).

Meirovitch, L., and Baruh, H. (**1981**). ''Optimal control of damped flexible gyroscopic system,'' J. Guidance Control. **4**(2), 157–163.

Munjal, M. L., and Eriksson, L. J. (**1988**). ''An analytical, one-dimensional, standing-wave model of a linear active noise control system in a duct,'' J. Acoust. Soc. Am. **84**, 1086–1093.

Munjal, M. L., and Eriksson, L. J. (**1989**). ''Analysis of a linear one-dimensional active noise control system by means of block diagrams and transfer functions,'' J. Sound Vib. **129**, 443–455.

Nelson, P. A., and Elliott, S. J. (**1991**). *Active Control of Sound* (Academic, London), Chap. 5.

Orduña-Bustamante, F., and Nelson, P. A. (**1992**). ''An adaptive controller for the active absorption of sound,'' J. Acoust. Soc. Am. **91**, 2740–2747.

Snyder, S. D., and Hansen, C. H. (**1989**). ''Active Noise Control in Ducts: Some Physical Insights,'' J. Acoust. Soc. Am. **86**, 184–194.

Stevens, J. C., and Ahuja, K. K. (**1991**). ''Recent advances in active noise control,'' AIAA J. **29**, 1058–1067.

Trinder, M. C. J., and Nelson, P. A. (**1983**). ''Active noise control in finite length ducts,'' J. Sound Vib. **89**, 95–105.

Tichy, J., Warnaka, G. E., and Poole, L. A. (**1984**). ''A study of active control of noise in ducts,'' J. Vib. Acoust. Stress Reliability Design **106**, 399–404.

Varadan, V. K., Hong, S-Y., and Varadan, V. V. (**1990**). ''Piezoelectric sensors and actuators for active vibration damping using digital control,'' *Proceedings of the IEEE Ultrasonics Symposium* (IEEE, New York), pp. 1211–1214.

Warnaka, G. (**1982**). ''Active attenuation of noise—the state of the art,'' Noise Control Eng. **18**(3), 100–110.

Widrow, B., and Stearns, S. D. (**1985**). *Adaptive Signal Processing* (Prentice-Hall, Englewood Cliffs, NJ).

Wu, Z., Varadan, V. K., Varadan, V. V., and Lee, K. Y. (**1995a**). ''A state-space model for one-dimensional active noise control systems,'' J. Sound Vib. **117**, 220.

Wu, Z., Varadan, V. K., Varadan, V. V., and Lee, K. Y. (**1995b**). ''Active absorption of acoustic wave using state-space model and optimal control theory,'' J. Acoust. Soc. Am. **97**, 1078–1087.

A new hybrid passive/active noise absorption system

Samson Beyene and Ricardo A. Burdisso
Vibration and Acoustics Laboratories, Mechanical Engineering Department, Virginia Polytechnic Institute and State University, Blacksburg, Virginia 24061-0238

(Received 14 August 1995; revised 6 May 1996; accepted 15 October 1996)

A new hybrid passive/active system is developed for sound absorption over a wide frequency range. The system is comprised of a layer of absorbing material positioned at a distance from an active wall, leaving an air space. The motion of the active wall is based on a new control approach which consists of the minimization of the reflected wave within the airspace which modifies the layer's back surface impedance so as to match the characteristic impedance of air. This technique is referred here as inducing an *impedance-matching* condition. Both numerical and experimental results of such a system are presented for normally incident planar waves. The hybrid passive/active system results in a high absorption coefficient of .8–1.0 over the frequency range 100–2000 Hz and is insensitive to system parameters such as air space depth and absorbing layer thickness. © *1997 Acoustical Society of America.* [S0001-4966(97)02303-5]

PACS numbers: 43.55.Ev, 43.50.Ki [PJR]

INTRODUCTION

In general, passive noise control methods that employ the use of sound-absorbing materials are practical and most effective at mid to high frequencies. On the other hand, active noise control techniques are more efficient at low frequencies. The complementary strengths and weaknesses of passive and active noise control methods have motivated many researchers to develop a system that integrates both methods. One of the first published works on a noise absorption system that comprises both active and passive control methods is that of Guicking and Lorenz.[1] The passive component was comprised of a porous plate located in an impedance tube a small distance from the open end of the tube which was terminated by a control speaker. The signal from a microphone in front of the porous plate was sent to the control speaker after it was passed through a suitable amplification scheme. A second microphone controlled the complex amplification factor such that the sound pressure at that location was minimized so as to produce a pressure-release condition just behind the plate. Almost total absorption of the acoustic energy was reported over the frequency range 100–600 Hz.

Thenail *et al.*[2] investigated an active system that included a fiberglass absorbing layer backed by an air cavity terminated with an active surface. Their work was intended to show that a pressure-release condition on the back surface of the fiberglass leads to improvement in absorption. They investigated two different control approaches. In the first control approach, an error microphone was located on the back surface of the fiberglass layer, and the pressure at that location was minimized. The result of this study showed an improvement of absorption that declines with an increase in frequency. The result reported was for the frequency range of 200–800 Hz. The second control approach investigated was identical to Guicking and Lorenz's work,[1] where the porous plate was replaced with the fiberglass layer. Their results show almost total absorption for the frequency range of 500–1400 Hz. In both control approaches, the authors used an optimum fiberglass layer thickness of 2 cm. Both the numerical and experimental results demonstrated that the system was sensitive to fiberglass thickness and porosity.

Fuller *et al.*[3] presented an experimental study done on the potential of an ''adaptive foam'' for radiation and reflection control. Their adaptive foam included a polyvinylidene fluoride film (PVDF) imbedded in polyurethane foam in a sine wave shape. In the reflection control experiment, the adaptive foam was rigidly backed and positioned at the open end of an impedance tube. The incident and reflected waves in front of the adaptive foam were separated using a set of identical microphones and a wave deconvolution circuit, and the reflected wave signal was minimized. The experiment performed was for a frequency range of 100–1000 Hz. At frequencies above 600 Hz, attenuation of the reflected wave of up to 40 dB was reported. Without active control, the passive attenuation of the adaptive foam was reported to be low.

A hybrid passive/active system for sound absorption which is again based on the concept of mounting a layer of sound-absorbing material at a distance from a wall is proposed here. Unlike in previous work where the wall is driven so as to produce a pressure-release condition at the back surface of the layer,[1,2] in this new approach the impedance at the back surface of the layer is modified to match the characteristic impedance of air. This condition is referred here as *impedance matching* to differentiate it from the pressure-release (or zero impedance) condition. In practice, the impedance-matching condition is simply achieved by minimizing the reflected wave in the airspace behind the absorbing layer. The effectiveness of this approach is demonstrated both numerically and experimentally for normal incident waves and single frequency excitations.

I. CONTROL APPROACH

A simple one-dimensional (1-D) numerical model is developed to simulate the proposed hybrid passive/active system. This system was modeled as a two-layer media where

 0001-4966/97/101(3)/1512/4/$10.00

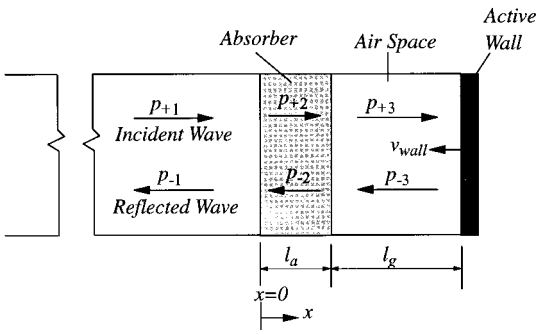

FIG. 1. Passive/active sound absorption system.

the first medium is a layer of a sound-absorbing material and the second is a cavity of air, backed by an active wall as shown in Fig. 1. The fluid in front of the absorbing layer is also assumed to be air. The incident and reflected waves in each of the three regions are represented in their exponential form as

$$p_{+n}(x,t)=A_n e^{-\Gamma x}e^{i\omega t}, \quad p_{-n}(x,t)=B_n e^{\Gamma x}e^{i\omega t}, \qquad n=1,2,3, \tag{1}$$

where the coefficients A_n and B_n are the amplitude of the incident and reflected waves, respectively; $\omega=2\pi f$ is the angular frequency; Γ is the propagation constant; and $i=\sqrt{-1}$. Due to the dissipative nature of the absorbing material ($n=1$), the propagation constant Γ is complex and can be expressed as $\Gamma_a=\xi_a+ik_a$, where the real part ξ_a is the attenuation constant and the imaginary part k_a is the phase constant. In the airspace and in front of the absorber, the propagation constant is purely imaginary and equal to the acoustic wave number given as $ik=i\omega/c$, where c is the speed of sound in air.

The particle velocity for the above waves can be written in terms of the plane wave impedance of the medium as

$$v_{\pm 2}(x,t)=\pm\frac{p_{\pm 1}(x,t)}{Z_a}, \quad v_{\pm n}(x,t)=\pm\frac{p_{\pm n}(x,t)}{\rho c}, \qquad n=1,3, \tag{2}$$

where Z_a is the complex impedance of the absorbing material and ρc is the characteristic impedance of air.

The conditions of continuity of pressure and particle velocity are now imposed at the front and back surfaces, e.g., $x=0$ and $x=l_a$, of the absorbing layer as well as the matching of the fluid particle and active wall velocities at $x=l_a+l_g$. These conditions lead to the linear system of equations[3]

$$\begin{bmatrix} -1 & 1 & 1 & 0 & 0 \\ \hat{Z}_a & 1 & -1 & 0 & 0 \\ 0 & E^{-1} & E & -D^{-1} & -D \\ 0 & E^{-1} & -E & -D^{-1}\hat{Z}_a & D\hat{Z}_a \\ 0 & 0 & 0 & G^{-1} & -G \end{bmatrix} \begin{Bmatrix} B_1 \\ A_2 \\ B_2 \\ A_3 \\ B_3 \end{Bmatrix} = \begin{Bmatrix} 1 \\ \hat{Z}_a \\ 0 \\ 0 \\ 0 \end{Bmatrix} A_1 + \begin{Bmatrix} 0 \\ 0 \\ 0 \\ 0 \\ \rho c \end{Bmatrix} v_{\text{wall}}, \tag{3}$$

where $E=\exp(\Gamma_a l_a)$, $D=\exp(ikl_a)$, $G=\exp(ik(l_a+l_g))$, and $\hat{Z}_a=Z_a/\rho c$.

The optimum control input $(v_{\text{wall}})_{\text{opt}}$ should be determined to minimize the total reflected wave, B_1, in front of the absorbing layer. One approach is the use of a wave sensor that directly measures the total reflected wave, B_1. This sensing approach was implemented previously in the work by Fuller *et al.*[4] and Guicking and Karcher[5] in purely active systems. However, it presents a design drawback since the error transducer is located in the acoustic field to be minimized, i.e., zone of quiet. This is impractical in many applications, a fact clearly recognized by Guicking and Karcher.[5] Here, we seek a sensing strategy where, first, the error transducer is positioned in the airspace (so it does not interfere with the system, i.e., the error sensor is not in the zone of quiet) and, second, by canceling the measured acoustic response in the airspace, minimization of the total reflected wave in front of the system is obtained. To this end, it is important to review the behavior of a layer of absorbing material for normal incident waves.

The input impedance, Z_I, of a layer of absorbing material can be computed from the impedance at the back surface of the absorbing layer (Z_2), the acoustical properties of the material (Γ_a and Z_a), and the layer thickness (l_a) as[6]

$$Z_I=Z_a\frac{Z_2\cosh(\Gamma l_a)+Z_a\sinh(\Gamma l_a)}{Z_a\cosh(\Gamma l_a)+Z_2\sinh(\Gamma l_a)}. \tag{4}$$

The impedance at the back surface of the absorbing layer can be computed from the relative values of the incident and reflected sound waves in the airspace as

$$Z_2=\rho c\frac{A_3e^{-ikl_a}+B_3e^{ikl_a}}{A_3e^{-ikl_a}-B_3e^{ikl_a}}. \tag{5}$$

Replacing the last equation in the linear system of Eq. (3) into (5) leads to

$$Z_2=\rho c\frac{\rho c\,v_{\text{wall}}+B_3e^{ikl_a}2\cos(kl_g)}{\rho c\,v_{\text{wall}}+B_3e^{ikl_a}2\sin(kl_g)}, \tag{6}$$

where it is clear that the impedance at the back surface of the absorbing layer is a function of the active wall velocity, i.e., explicitly through the first terms in the numerator and denominator and implicitly through the wave amplitude B_3. Setting v_{wall} to zero in Eq. (6) yields the well-known impedance $Z_2=-i\tan(kl_g)$ due to a rigid wall at a distance l_g from the absorber layer.[6]

Equation (6) clearly indicates that the active control system, i.e., motion of the wall, can be interpreted as an active modification of the layer back surface impedance and consequently of the input impedance Z_I as well. In this context, the control approach of minimizing the pressure at the back surface of the layer (referred as pressure release condition) is equivalent to imposing a zero impedance condition, $Z_2=0$.

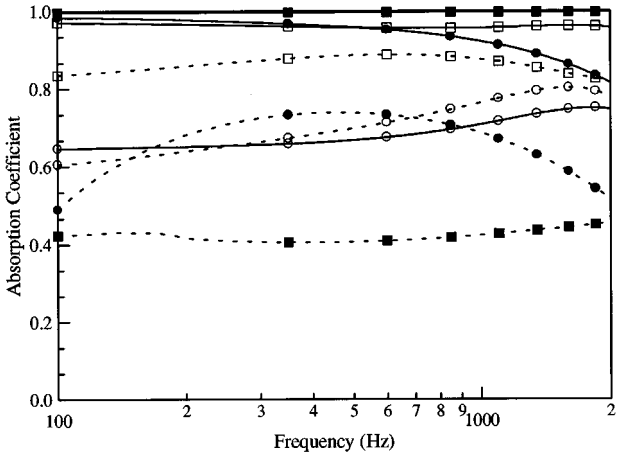

FIG. 2. Absorption coefficient of absorbing layer with (———) impedance-matching and (---) pressure-release conditions at the layer's back surface: ■ fiberglass, □ foam, ● sponge rubber, and ○ Kevlar.

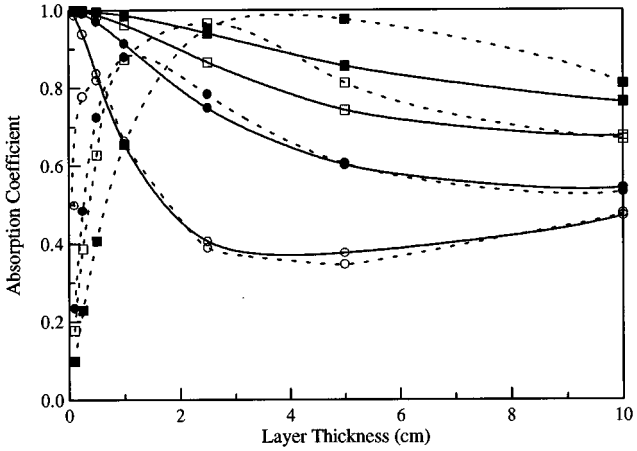

FIG. 3. Absorption coefficient at 300 Hz as a function of the absorbing layer thickness, l_a, for (———) impedance-matching and (---) pressure-release conditions: ■ fiberglass, □ foam, ● sponge rubber, and ○ Kevlar.

The optimum impedance, Z_2, that would lead to perfect absorption can easily be obtained by setting the input impedance equal to the characteristic impedance of air, i.e., $Z_I = \rho c$ in Eq. (4), and solving for Z_2. This optimum impedance is a complex function of the acoustical properties and thickness of the absorbing layer and may be difficult to implement in practice. However, further inspection of Eq. (4) reveals that as the arguments of the hyperbolic functions decrease ($\Gamma l_a \rightarrow 0$), the $\cosh(\Gamma l_a)$ and $\sinh(\Gamma l_a)$ function will approach unity and zero, respectively. This implies that the optimum back impedance should approach the characteristic impedance of air, i.e., $Z_2 = \rho c$, in spite of the value of the characteristic impedance of the absorbing material, Z_a. The decrease in the argument Γl_a will take place when (a) the thickness of the absorbing layer is reduced and/or (b) when the propagation characteristic is reduced which occurs in most acoustic-absorbing materials as the frequency is decreased. Thus, an impedance equal to the characteristic impedance of air at the back surface of the absorbing layer is the optimum value for a thin layer and low frequencies. An impedance of $Z_2 = \rho c$ is referred to here as *impedance-matching* condition.

To further validate the above conclusions, the input absorption coefficient for various absorbing materials is computed assuming both impedance-matching and pressure-release conditions at the back of the absorbing layer. The absorbing materials selected for this analysis are fiberglass,[6] open cell foam,[7] Kevlar,[7] and sponge rubber,[8] all of which have markedly different acoustic characteristics. Figure 2 shows the absorption coefficient as a function of the frequency for a layer thickness of 0.5 cm. The results show that the impedance-matching condition leads to better absorption characteristics than the pressure-release condition at all frequencies except for Kevlar, where the absorption coefficient is essentially the same for both conditions. Figure 3 shows the absorption coefficient as a function of the absorbing layer thickness, l_a, for the various materials at a frequency of 300 Hz. The results indicate that there is an optimum thickness, which differs for the different materials, to obtain high absorption when a pressure-release condition is induced. Thus, the performance of the sound-absorbing system with an actively induced pressure-release condition at the back of the absorbing layer is very sensitive to the thickness of the absorbing layer. This fact was also observed by Thenail *et al.*[2] On the other hand, for the impedance-matching condition, absorption decreases slowly as the thickness, l_a, is increased, i.e., the system is insensitive to the absorbing layer thickness. Figure 3 also shows that the impedance-matching condition outperforms the pressure-release condition in most situations, in particular for thin layers.

Based on the previous analysis, a new active system for sound absorption is proposed which consists of introducing an impedance-matching condition at the absorbing layer back surface. This impedance-matching condition is easily achieved by the sensing and minimization of the reflected wave within the airspace. The minimization of the reflected wave in the airspace causes the acoustic impedance along the airspace (and at the back of the absorbing layer) to be equal to the characteristic impedance of air. In practice, the reflected wave in the airspace can be sensed by using a two-microphone system.[3,5]

II. NUMERICAL AND EXPERIMENTAL RESULTS

The numerical model described above is used to investigate the performance of the proposed passive/active sound absorption system. The system investigated is comprised of a 5-cm partially reticulated polyurethane foam layer and an airspace depth of 10 cm. The density of air ρ and the speed of sound c in air are assumed to be 1.21 $N.s^2/m^4$ and 343 m/s, respectively. The complex propagation constant, Γ_a, and characteristic impedance, Z_a, of the foam were empirically determined.[4]

The absorption coefficient of the passive system as a function of the frequency is shown in Fig. 4. The optimum active wall velocity is computed from Eq. (3) to minimize B_l and is used to predict the absorption coefficient for the passive/active system also shown in Fig. 4. As the figure shows, the minimization of the reflected wave in the airspace successfully resulted in a high absorption coefficient over the whole frequency range of interest. Although the absorption

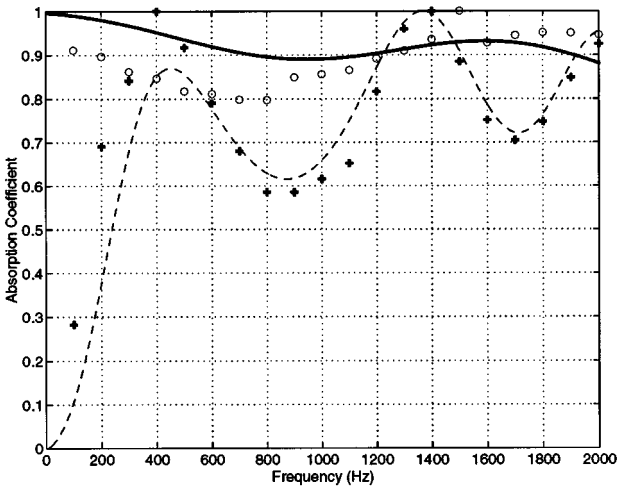

FIG. 4. Absorption coefficient of passive/active system: analytical, --- before and — after control; experimental, +++ before and ○○○ after control.

peaks at 1350 and 2000 Hz achieved by the passive system were slightly reduced with the introduction of the active component, overall, a consistent high absorption coefficient of 0.89–1.0 was achieved throughout the frequency range of interest. Moreover, the best performance of this hybrid system occurs at frequencies below the first peak of the passive system, i.e., $f<450$ Hz, where improvement is most desirable.

An experimental validation of the proposed passive/active system was also performed. Due to the one-dimensional nature of the model, the experiments performed were carried out in a standard impedance tube with a 10-cm diameter and lower and upper frequency limits of 90 and 2000 Hz, respectively. The disturbance source is located at one end of the impedance tube and the other end of the tube is terminated with a control speaker. The sound-absorbing layer, a 5-cm-thick partially reticulated foam, is placed at 10 cm from the control speaker, creating an airspace between the foam and the control speaker. The absorption coefficient of the system was measured using the standing wave technique (SWR).[9] A wave deconvolution circuit first described by Fahy[10] was used to sense the reflected wave in the airspace. This circuit gives a real time domain estimate of the incident and reflected components of a sound field from the outputs of two closely spaced identical microphones. The two microphones used in this experiment were located in the airspace with a 5-cm spacing between them with the closest microphone to the sound-absorbing layer at 1.25 cm. The signals detected by these microphones were fed into the wave deconvolution circuit where the incident and reflected waves in the airspace were then separated and the reflected wave signal processed by a single-channel-filtered X-LMS controller as the error signal.[11] The reference signal was simply tapped from the disturbance. The required control signal to minimize the reflected wave was then generated by the controller and sent to the control speaker. The sampling rate for each experiment was four times the operating frequency.

The experimental results for both before and after control cases are also presented in Fig. 4. As shown in the figure, a high absorption coefficient of 0.8–1.0 is achieved experimentally over the frequency range 100–2000 Hz. At the lower frequencies, the experimentally obtained absorption coefficient tends to be lower than the numerical result. The maximum deviation between the experimental and numerical results is an absorption coefficient difference of 0.1. This deviation occurs at the lower frequencies due to a phase mismatch between the two particular microphones used. In spite of this problem, the absorption coefficient at 100 Hz is increased from 0.28 to 0.91. Overall, a good agreement between the numerical and the experimental results is observed which validates the proposed approach.

III. CONCLUSIONS

A new passive/active sound absorption system is proposed which consists of a layer of sound-absorbing material and an airspace terminated by an active wall. The motion of the wall is used to modify the layer's back impedance so as to match the characteristic impedance of air. This is accomplished by sensing and minimizing the reflected wave in the airspace. The numerical results show high absorption (0.8–1.0) over a wide frequency range of 100–2000 Hz. The proposed system is insensitive to the absorbing layer thickness and airspace depth. An experimental study is also carried out in an standing wave tube. The very good agreement found between the numerical and experimental results validates the new proposed system.

[1] D. Guicking and E. Lorenz, ''An Active Sound Absorber with Porous Plate,'' J. Vib. Acoust. Stress Reliab. Design **106**, 389–392 (1984).
[2] D. Thenail, M. Galland, M. Sunyach, and M. Sunhack, ''Active Enhancement of the Absorbent Properties of a Porous Material,'' Smart Mater. Struct. **3**, 18–25 (1994).
[3] C. R. Fuller, M. J. Bronzel, C. H. Gentry, and D. E. Whittington, ''Control of Sound Radiation/Reflection with Adaptive Foams,'' in Proceedings of *Noise-Con 1994* Fort Lauderdale, Florida 1–4 May, pp. 429–436.
[4] S. Beyene, ''Feasibility study of a Hybrid Passive/Active Noise Absorption System,'' Master's thesis, Virginia Polytechnic Institute and State University 1995.
[5] D. Guicking and K. Karcher, ''Active Impedance Control for One-Dimensional Sound,'' J. Vib. Acoust. Stress Reliabil. Design **106**, 393–396 (1984).
[6] L. Beranek and I. L. Vèr, *Noise and Vibration Control Engineering: Principles and Applications* (Wiley, New York, 1992).
[7] C. D. Smith and T. L. Parrot, ''Comparison of three methods for measuring acoustic properties of bulk materials,'' J. Acoust. Soc. Am. **74**, 1577–1582 (1983).
[8] M. Mongy, ''Acoustical Properties of Porous Materials,'' Acustica **28**, 243–247 (1973).
[9] ''Standard Test Method for Impedance and Absorption of Acoustical Materials by the Impedance Tube Method,'' ASTM C384, Philadelphia, USA (1990).
[10] F. J. Fahy, ''A Technique for Measuring Sound Intensity with a Sound Level Meter,'' Noise Control Eng. J. **9**.(3), 155–162 (1977).
[11] B. Widrow and S. D. Stearns, *Adaptive Signal Processing* (Prentice-Hall, Englewood Cliffs, NJ, 1985).

Classification by multiple-resolution statistical analysis with application to automated recognition of marine mammal sounds

Thomas J. Hayward
Naval Research Laboratory, Washington, DC 20375-5350

(Received 30 September 1995; accepted for publication 30 September 1996)

A multiple-resolution statistical pattern recognition technique for classification by supervised learning is developed and then applied to automated recognition of marine mammal sounds. The data to be classified may be either unprocessed or transformed, e.g., time series or time-frequency distributions of acoustic transients. Training data consist of samples previously grouped by a human expert into labeled sets; these sets are presumed to be associated with different ''classes.'' The labeled sets are then characterized by occupancy statistics associated with a multiple-resolution, binary partition of the (unreduced) sample space. Classification of a new sample is performed by calculating *a posteriori* probabilities of membership of the new sample in each class, computed by Bayesian inference from the occupancy statistics of the associated labeled set. These *a posteriori* probabilities are calculated by a recursive algorithm that progresses from coarse to fine resolution in the sample space. The algorithm is implemented in a simple, highly efficient computer program. Automated classification of both time series and time-frequency distributions of marine-mammal vocalizations is demonstrated using a small number of labeled samples (approximately ten samples per class). [S0001-4966(97)05303-4]

PACS numbers: 43.60.Lq, 43.30.Sf, 43.80.Ka [JLK]

INTRODUCTION

The variability of received waveforms of acoustic transients in the ocean results from both the variability of the source waveforms and the variability of the propagation characteristics of the ocean medium between the source and the receiver. Acoustic transients of biological origin, including those associated with marine mammal vocalizations, are grouped by experts into distinct types, or ''classes.'' Within a class, the source waveforms may vary among different individuals producing the sounds and among different instances of sound production by the same individual. Similarly, the acoustic transfer function of the ocean medium from a marine-mammal source to an underwater receiver may vary as a result of both medium fluctuations and changes in source position associated with movements of the animal. These observations suggest that characterization of classes of underwater biological sounds might best be approached by obtaining an adequate statistical sampling of the variations of both source waveforms and propagation effects. Propagation modeling could provide additional characterization or prediction of the variability of the acoustic transfer function in a given ocean environment. Assuming this variability is smaller in magnitude than the differences between distinct classes of source waveforms, it should not prevent classification of the sounds based on the received waveforms.

Many approaches to pattern classification include, as an initial step in the processing, some mapping from the original space of observations (the sample space) to a lower-dimensional *feature space*.[1] This step involves human or automated selection of the features of the received signals that are to be used as the basis for classification. In the case of underwater acoustic transients, the acoustic medium may distort features through multipath propagation effects. One approach to minimizing performance degradation due to such effects is to select features that are found, based on extensive experience, to be robust with respect to medium distortions.[2] An alternative is to employ statistical characterizations of the distributions of training data in the unreduced sample space. Robust features will then be manifested by clustering of these distributions. With a suitable statistical formulation of the classification problem, this statistical characterization can then provide a basis for classification of new samples. A potential advantage of such an approach is that the statistical characterization of a class can be explicitly modified to include acoustic propagation effects for a prospective new site of acoustic reception.

In this work, we develop a statistical approach to classification of data and apply it to automated recognition of some marine mammal sounds. The classification of a new sample is based on the grouping of previous samples into sets by a human expert, who has identified the members of each set as belonging to the same ''class'' of sounds. In the pattern recognition literature, this procedure is referred to as *supervised learning*,[1,3] and the samples grouped by the expert are referred to as *labeled samples*;[3] the groups are referred to as *training sets*.[1]

In an idealized form, the statistical approach presented here consists of evaluating, for a new sample S to be classified, the quantities $p_k(S)$, where p_k is the probability density associated with the kth class. Since, in practice, the probability densities p_k are unknown, we apply Bayesian inference to compute, in lieu of $p_k(S)$, *a posteriori* probabilities of membership of S in each class. This computation is based on a multiple-resolution partitioning process, which is defined in two stages. The first stage partitions the *data space*, which, in the case of a sample defined by a function (e.g., a time series or a time-frequency distribution of an acoustic tran-

sient) is the Cartesian product of the domain and range of the function. This partition in turn defines a second multiple-resolution partition, this time of the *sample space* (the space of all possible samples, or subsets of the data space). The training data for each class are characterized by integer-valued occupancy statistics associated with this second partition. The *a posteriori* probabilities of membership in each class are then used as a basis for a classification decision. Since the computation operates in the unreduced sample space, there is no requirement for prior selection of a feature set.

Section I describes the statistical formulation of the classification problem, the characterization of the training data, and the classification algorithm. Details of the algorithm and its computer implementation are provided in the Appendixes. Section II provides examples of application of the algorithm to automated recognition of marine mammal sounds. Section III concludes with a discussion of the results.

I. DESCRIPTION OF THE CLASSIFICATION ALGORITHM

Section I A provides some background on statistical pattern recognition by supervised learning. For completeness, Appendix A contains some needed material that was not found in standard references. Section I B provides a general preview of the statistical approach used in this paper. Sections I C–I F and Appendixes B and C provide details of the statistical characterization of the training data and a description of the classification algorithm.

A. Background on statistical pattern recognition

Suppose that the expert has grouped the training samples into K sets $\mathscr{T}_1, \mathscr{T}_2, \ldots, \mathscr{T}_K$, with $\mathscr{T}_k$ denoting the set of N_k samples

$$\mathscr{T}_k = \{S_1^{(k)}, S_2^{(k)}, \ldots, S_{N_k}^{(k)}\}, \quad k = 1,2,\ldots,K. \tag{1}$$

We are then given a new sample S to be classified as belonging to one of K ''classes'' presumed to be associated with these sets. A formal definition of a sample will be given in Sec. I C. For now we will think of a sample simply as a point (element) of a space (set) Σ of possible samples; this space will be defined formally in Sec. I D. [In the applications described in this paper, a sample consists of either a time series or a time-frequency distribution of a received acoustic transient.] The assumption that the members of $\mathscr{T}_k$ belong to the same class is formalized by the statement that $\mathscr{T}_k$ consists of N_k observed values of independent random variables $\boldsymbol{S}_1^{(k)}, \boldsymbol{S}_2^{(k)}, \ldots, \boldsymbol{S}_{N_k}^{(k)}$ having the same probability density p_k defined on Σ. The new sample S is assumed to be a sample from a random variable $\boldsymbol{S}$ that is independent of the training samples and has probability density p, which may or may not be one of the densities p_k.

Bayesian approaches to statistical pattern recognition by supervised learning[4] are based on the computation of *a posteriori* probabilities of membership of the new sample in each class. These *a posteriori* probabilities are derived by Bayes' formula from the training data, assumed *a priori* probability densities on parameters of the densities p_k, and *a priori* probabilities of occurrence of samples from each class. Let $\mathscr{C}_k$ denote the class membership alternative $p = p_k$, and let $P(\mathscr{C}_k)$ denote the *a priori* probability that an observed sample belongs to the kth class. We wish to compute the *a posteriori* probability of $\mathscr{C}_k$ given the training data

$$\mathscr{T} = (\mathscr{T}_1, \mathscr{T}_2, \ldots, \mathscr{T}_K)$$

and given the new sample S, i.e., to compute

$$P(\mathscr{C}_k | S, \mathscr{T}). \tag{2}$$

We assume that the class membership alternatives $\mathscr{C}_k$ are mutually exclusive and exhaustive. Appendix A shows that, under some mild additional assumptions concerning the training data, we have the following variant of Bayes' formula:

$$P(\mathscr{C}_k | S, \mathscr{T}) = \frac{P(S | \mathscr{T}_k, \mathscr{C}_k) P(\mathscr{C}_k)}{\sum_{j=1}^{K} P(S | \mathscr{T}_j, \mathscr{C}_j) P(\mathscr{C}_j)}. \tag{3}$$

This equation relates the *a posteriori* probabilities $P(\mathscr{C}_k | S, \mathscr{T}_k)$ of membership of S in each class to the *a priori* probabilities $P(\mathscr{C}_k)$ of occurrence of samples from each class. If we do not assume that $\mathscr{C}_1, \mathscr{C}_2, \ldots, \mathscr{C}_K$ are exhaustive, then we instead have

$$P(\mathscr{C}_k | S, \mathscr{T}) = \alpha P(S | \mathscr{T}_k, \mathscr{C}_k) P(\mathscr{C}_k), \tag{4}$$

where α is an unknown positive constant (see Appendix A). In that case, the quantities $P(\mathscr{C}_k | S, \mathscr{T})$ may still be interpreted as relative *a posteriori* probabilities. In either case, in order to compute the K values $P(\mathscr{C}_k | S, \mathscr{T})$ from the *a priori* probabilities $P(\mathscr{C}_k)$, it suffices, by Eq. (3) or (4), to compute the K probabilities

$$P(S | \mathscr{T}_k, \mathscr{C}_k) = \frac{P(S, \mathscr{T}_k | \mathscr{C}_k)}{P(\mathscr{T}_k | \mathscr{C}_k)}, \quad k = 1,2,\ldots,K. \tag{5}$$

B. General description of the statistical approach

Computation of the numerator and denominator on the right-hand side of Eq. (5) would be straightforward if the probability densities p_k associated with each class were known. In practice, however, these densities are not known. Moreover, the dimension of the space Σ of possible samples is likely to be much larger than the number of available training samples. This fact presents a significant obstacle to direct estimation of p_k. For example, a transient signal of duration $T = 1$ s, analyzed in a bandwidth of $W = 1000$ Hz, has up to $TW = 1000$ independent degrees of freedom; thus Σ (considered as a vector space) has dimension 1000. If the available labeled samples are few in number, they clearly may not support high-resolution estimates of p_k.

However, if we partition Σ into two disjoint subsets $\Sigma^{(0)}$ and $\Sigma^{(1)}$, we can count the number of labeled samples in each training set $\mathscr{T}_k$ that belong to the same set in this partition as does the new sample S. These integer-valued occupancy statistics provide a basis for Bayesian inference leading to *a posteriori* probabilities of the observed event $S \in \Sigma^{(0)}$ (or $S \in \Sigma^{(1)}$) given membership in each class. Since these *a posteriori* probabilities are based on a partition of Σ into only two subsets, they may not provide sufficient statistical evidence to classify S. However, if we increase the

number of subsets in the partition to four (that is, refine the partition) we may be able to update the *a posteriori* probabilities. At the same time, there are likely to be fewer samples in each training set $\mathscr{T}_k$ that belong to the same set in the partition as does the new sample S. If we continue refining the partition, we may eventually arrive at a partition that is no longer supported by the available data. That is, the set in the refined partition to which S belongs may contain no data from any of the training sets. Nevertheless, the *a posteriori* probabilities computed up to that point will be available as a basis for a classification decision.

Classification techniques based on partitioning processes have been used previously in hierarchical pattern recognition.[5–7] For computational tractability, the partitioning process is usually applied to a reduced feature space. In this work, we construct a multiple-resolution, binary partition of the unreduced sample space, based on a similar partition of the data space. This construction avoids the need for prior reduction to a feature space. The classification algorithm progresses from coarse to fine resolution. Thus, computational savings may be realized when samples can be classified on the basis of large-scale features, thereby avoiding the need for fine-scale feature comparisons. If classification requires discrimination of fine-scale features, such discrimination can be achieved as the algorithm progresses to higher resolution.

The multiple-resolution partitioning process will be specified in Sec. I D after formal definition of a sample in Sec. I C.

C. Definition of a sample

We now give a definition of a sample of data to be classified. This definition is general enough to provide for classification of samples consisting of time series or any of the standard transforms of time series (e.g., Fourier transforms, time-frequency distributions, wavelet transforms, etc.). We define a *sample* S to be a subset of the Cartesian product X of D bounded real-number intervals; i.e.,

$$S \subseteq X = X_1 \times X_2 \times \cdots \times X_D, \tag{6}$$

where each set X_d denotes a finite interval of real numbers

$$X_d = [x_{\min}^{(d)}, x_{\max}^{(d)}).$$

We will refer to the set X as the *data space*. Thus S is a set of points (D-tuples), each having the form

$$\mathbf{x} = (x_1, x_2, \ldots, x_D), \tag{7}$$

with $x_d \in X_d$. [Complex data can be treated as real data by separation into real and imaginary parts.] For example, if $D=2$, with $X_1 = [t_{\min}, t_{\max})$ interpreted as a time interval, and X_2 is the interval of real numbers $[x_{\min}, x_{\max})$, then a sample could consist of a real-valued time series $x(t)$ defined on $[t_{\min}, t_{\max})$ and taking values in $[x_{\min}, x_{\max})$. Note that in this case a sample S is a function mapping X_1 into X_2. This functional relationship is a special case of a set of the type in Eq. (6), since the function x is, by definition, the set of ordered pairs

$$\{(t, x(t)) | t \in [t_{\min}, t_{\max})\}.$$

To simplify notation, we map each of the intervals $X_1, X_2, \ldots, X_D$ linearly onto the unit interval $[0,1)$ and identify each coordinate $x_d \in X_d$ with its image under this map. In practice, we will deal only with discrete data; for example, a time series will consist of a discrete set

$$\{(t_i, x(t_i)) | i = 1, \ldots, N\},$$

where $0 \leqslant t_1 \leqslant \cdots \leqslant t_N < 1$ and $0 \leqslant x(t_1) \leqslant \cdots \leqslant x(t_N) < 1$.

D. Multiple-resolution partition of the sample space

Suppose now that we are given a sample S of the form in Eq. (6) to be classified. As indicated in Sec. I B, the classification will be based on Bayesian inference applied to a sequence of partitions of the sample space Σ. [Σ is the set of all possible samples of the form in Eq. (6), i.e., the set of all subsets of X. In the mathematical literature, this set is commonly denoted by 2^X.] This sequence of partitions is in turn based on a sequence of partitions of the data space X. This first sequence of partitions is constructed recursively as follows: The entire data space X is defined to be the one (and only) cell of the first partition in the sequence. Inductively, the next partition is obtained by bisecting each cell of the current partition along a hyperplane perpendicular to a coordinate axis; these axes are selected by cyclic progression through the set of coordinates. Details of this partitioning process are provided in Appendix B. The process terminates when the resolution limit of the available data is reached; a lower resolution may also be chosen to improve computational speed if it is found adequate to discriminate amongst the classes.

Associated with the partition of the data space X is a multiple-resolution description of each sample. The essential nature of this description is illustrated in Fig. 1 for the case where the sample is a time series. [Transformed data will more frequently be used as input to the classification algorithm.] At each resolution level, a given sample S is represented by identifying those cells of the partition that contain one or more points of S. These cells are indicated by shading in Fig. 1. For the Lth partition, a simple indexing scheme enumerates the 2^L cells

$$\{\mathscr{D}_{b_1 b_2 \cdots b_L} | b_i \in \{0,1\}, \quad i = 1,2, \ldots, L\}.$$

For each cell, an *indicator number* $n_{b_1 b_2 \cdots b_L}(S)$ is set to the value 1 or 0 according to whether the cell $\mathscr{D}_{b_1 b_2 \cdots b_L}$ does or does not contain at least one point of S. [For $L=0$, we define $n(S)=0$ if $S=\varnothing$ and $n(S)=1$ if $S \neq \varnothing$.] These indicator numbers are conveniently represented by a tree structure [see Fig. 2]; the Lth level of the tree contains the 2^L indicator numbers

$$\{n_{b_1 b_2 \cdots b_L}(S) | b_i \in \{0,1\}, \quad i = 1,2, \ldots, L\}. \tag{8}$$

[We denote the level corresponding to the maximum resolution by $L_{\max}$.] This tree representation will be convenient for describing the classification algorithm. Details of this representation are provided in Appendix B.

To establish notation needed for the partition of the sample space and for the statistical description of the training sets, we prescribe an ordering of the subscripts of the indi-

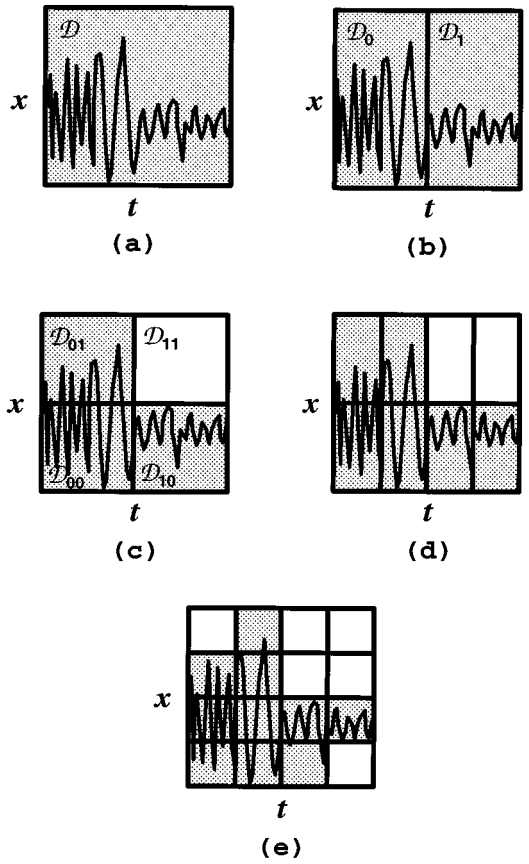

FIG. 1. Multiple-resolution representation of a time series, showing resolution cells and indicator numbers as the partitioning stage L varies. Cells for which the indicator number is equal to 1 are shaded. (a) $L=0$; (b) $L=1$; (c) $L=2$; (d)$L=3$; (e) $L=4$.

cator numbers $n_{b_1 b_2 \cdots b_L}(S)$. This ordering is shown by arrows in Fig. 3, and is defined explicitly in Appendix B. Let β_λ denote the λth subscript in this ordering.

With the prescribed ordering, the tree of indicator numbers forms a binary sequence of length $\Lambda = 2^{L_{\max}+1}-1$ given by

$$\mathbf{n}(S) = (n_{\beta_1}(S), n_{\beta_2}(S), \ldots, n_{\beta_\Lambda}(S)). \tag{9}$$

Thus, the indicator numbers define a mapping

$$\mathbf{n}: \Sigma = 2^X \rightarrow \{0,1\}^\Lambda = \Gamma \tag{10}$$

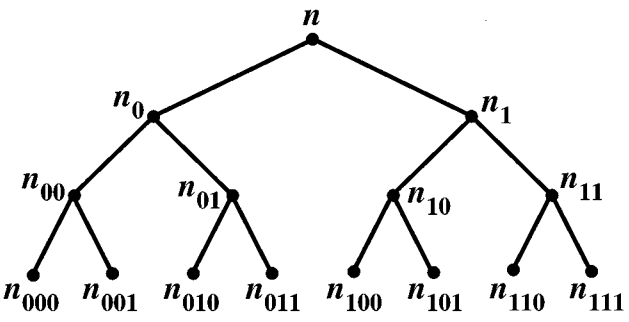

FIG. 2. Tree representation of the indicator numbers $n_{b_1 b_2 \cdots b_L}$, $L=0,1,2,3$.

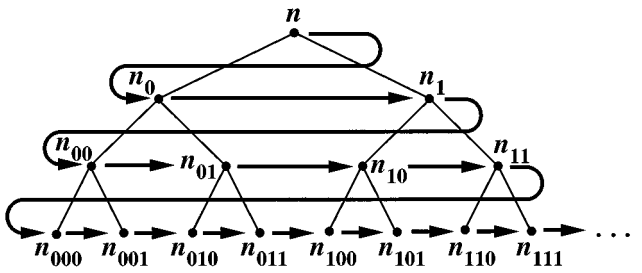

FIG. 3. Ordering of the indicator numbers (indicated by arrows).

from the set Σ of all subsets of X (the sample space) into the set Γ of binary sequences of length Λ. [For a fixed maximum resolution $L_{\max}$, this mapping is not one-to-one; however, if two samples S_1 and S_2 are distinct within this maximum resolution, we clearly have $\mathbf{n}(S_1) \neq \mathbf{n}(S_2)$.]

We now use the multiple-resolution description of samples to define successive partitions of the sample space $\Sigma = 2^X$. This partitioning is based on the values (0 or 1) of the indicator numbers, taken in the prescribed order. At the first stage, we divide Σ into 2 disjoint sets Σ_0 and Σ_1, defined by

$$\Sigma_{b_1} = \{T \in \Sigma \,|\, n_{\beta_1}(T) = b_1\}, \quad b_1 = 0,1. \tag{11}$$

Continuing this process, at the λth stage we partition Σ into the 2^λ sets

$$\Sigma_{b_1 b_2 \cdots b_\lambda} = \{T \in \Sigma \,|\, n_{\beta_\mu}(T) = b_\mu, 1 \leqslant \mu \leqslant \lambda\}, \tag{12}$$

where $b_\mu \in \{0,1\}, \mu = 1,2,\ldots,\lambda$. [Some of these sets will be empty, while others will be equal to each other, because of constraints discussed in Appendix B and expressed explicitly by Eq. (B10). For example, referring to Eq. (B10), we find $\Sigma_{01} = \Sigma_{100} = \varnothing$; similarly, $\Sigma_{00} = \Sigma_0$ and $\Sigma_{101} = \Sigma_{10}$.]

E. Statistical characterization of the training sets

The training data $\mathcal{T}$ can be statistically characterized by counting the number of elements of each training set $\mathcal{T}_k$ that belong to each set $\Sigma_{b_1 b_2 \cdots b_\lambda}$; denote this number by $\nu^{(k)}_{(b_1 b_2 \cdots b_\lambda)}$. These numbers, which constitute histograms of the training data in the sample space, can be stored in computer memory. Figure 4(a) shows, schematically, the 4 nonempty sets $\Sigma_{b_1 b_2 \cdots b_\lambda}$ for $\lambda = 3$, and hypothetical training samples for 3 classes. Figure 4(b) shows the corresponding histogram.

Note that the computer storage requirements for these histograms expand rapidly with increasing resolution, since the number of cells grows as an exponential function of λ. However, as Sec. I F will show, *a posteriori* probabilities of class membership can be obtained if the values of $\nu^{(k)}_{(b_1 b_2 \cdots b_\lambda)}$ are known only for those indices $b_1 b_2 \cdots b_\lambda$ for which $S \in \Sigma_{b_1 b_2 \cdots b_\lambda}$. These values can readily be computed from the indicator numbers of S and those of the training samples; storage of the indicator numbers requires much less computer memory than would storage of the histograms.

For a new sample S, define

$$\Sigma^{(0)} = \Sigma^{(0)}(S) = \Sigma, \tag{13}$$

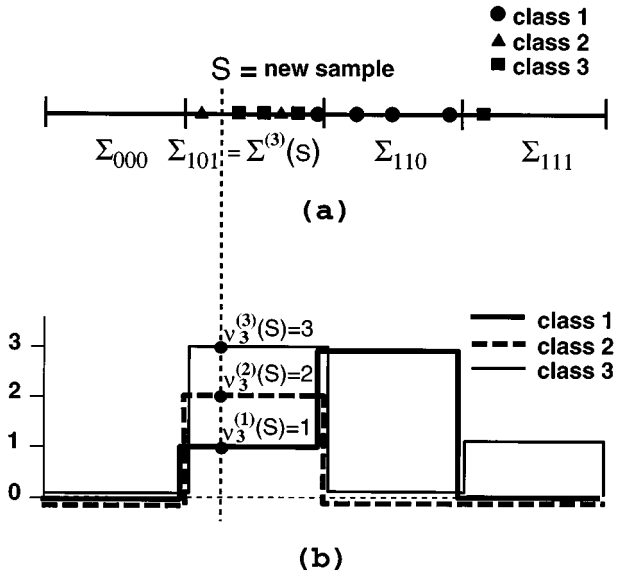

FIG. 4. Schematic illustration of (a) training sets for three classes, and partition of the sample space Σ for $\lambda=3$; (b) histograms associated with this partition, and occupancy statistics $\nu_\lambda^{(k)}$.

and for $1\leqslant\lambda\leqslant\Lambda$, let $\Sigma^{(\lambda)}=\Sigma^{(\lambda)}(S)$ denote the particular one of the sets $\Sigma_{b_1 b_2 \cdots b_\lambda}$ to which S belongs. Equivalently, $\Sigma^{(\lambda)}(S)$ is the set of all $T\in\Sigma$ whose indicator numbers agree with those of S up to the λth index in the prescribed ordering; i.e.,

$$\Sigma^{(\lambda)}=\Sigma^{(\lambda)}(S)=\{T\in\Sigma|n_{\beta_\mu}(T)=n_{\beta_\mu}(S),\ \mu=1,2,\ldots,\lambda\}. \tag{14}$$

Let $\nu_\lambda^{(k)}$ denote the number of samples in the training set $\mathscr{T}_k$ that belong to $\Sigma^{(\lambda)}$; i.e.,

$$\nu_\lambda^{(k)}=\nu_\lambda^{(k)}(S)=\text{card}\{T\in\mathscr{T}_k|T\in\Sigma^{(\lambda)}\}. \tag{15}$$

Since $\mathscr{T}_k$ is a random sample from the probability density p_k, each number $\nu_\lambda^{(k)}$ can be interpreted as an observed value of an integer-valued random variable, which we will denote by $\boldsymbol{\nu}_\lambda^{(k)}$. Since

$$\Sigma=\Sigma^{(0)}\supseteq\Sigma^{(1)}\supseteq\Sigma^{(2)}\supseteq\cdots\supseteq\Sigma^{(\Lambda)}, \tag{16}$$

we have

$$N_k=\nu_0^{(k)}\geqslant\nu_1^{(k)}\geqslant\nu_2^{(k)}\geqslant\cdots\geqslant\nu_\Lambda^{(k)}. \tag{17}$$

[Note that, because of the conditions in Eq. (B11), successive sets in Eq. (16) may be equal.] The numbers $\nu_\lambda^{(k)}$ specify the number of samples in each training set that have indicator numbers the first λ of which agree with those of the new sample S. [Figure 4(b) illustrates these values for $\lambda=3$.] These numbers provide a statistical basis for comparison of S with each training set $\mathscr{T}_k$ and thence for classification of S.

F. Classification of a new sample

We now apply the statistical characterization of training data described in Sec. I E to classification of a new sample S. In lieu of $P(S|\mathscr{T}_k,\mathscr{C}_k)$ appearing in Eq. (5), we compute the conditional probabilities $P_\Lambda^{(k)}$, $1\leqslant\lambda\leqslant\Lambda$, given by

$$P_\lambda^{(k)}=\Pr\{\boldsymbol{S}\in\Sigma^{(\lambda)}|\boldsymbol{\nu}_\lambda^{(k)}=\nu_\lambda^{(k)},\ \boldsymbol{\nu}_{\lambda-1}^{(k)}=\nu_{\lambda-1}^{(k)},\ldots,\boldsymbol{\nu}_1^{(k)}=\nu_1^{(k)},\mathscr{C}_k\}. \tag{18}$$

That is, we replace S in Eq. (5) by the observed event $\{\boldsymbol{S}\in\Sigma^{(\Lambda)}\}$ and replace $\mathscr{T}_k$ by the integer-valued occupancy statistics

$$\boldsymbol{\nu}_\lambda^{(k)}=\nu_\lambda^{(k)},\quad 1\leqslant\lambda\leqslant\Lambda,$$

derived from the multiple-resolution partition and the training set $\mathscr{T}_k$. $P_\lambda^{(k)}$ is computed as an *a posteriori* probability derived from prior densities of the (unknown) parameters $\theta_\lambda^{(k)}$ defined by

$$\theta_\lambda^{(k)}=\Pr\{\boldsymbol{S}\in\Sigma^{(\lambda)}|\boldsymbol{S}\in\Sigma^{(\lambda-1)},\mathscr{C}_k\},\quad \lambda=1,2,\ldots,\Lambda. \tag{19}$$

The prior densities of $\theta_\lambda^{(k)}$ are assumed to be uniform on the interval $[0,1]$ except in cases where the value of n_{β_λ} is determined from previous values by the conditions in Eq. (B11); in those cases we have $\Sigma^{(\lambda)}=\Sigma^{(\lambda-1)}$ and therefore $\theta_\lambda^{(k)}=1$. Appendix C shows that, with the exceptions just mentioned,

$$P_\lambda^{(k)}=\frac{\nu_\lambda^{(k)}+1}{\nu_{\lambda-1}^{(k)}+2}P_{\lambda-1}^{(k)}. \tag{20}$$

In the excepted cases, we clearly have

$$P_\lambda^{(k)}=P_{\lambda-1}^{(k)}. \tag{21}$$

By Eq. (13), $P_0^{(k)}=1$; thus, $P_1^{(k)}$, $P_2^{(k)}$, ..., $P_\Lambda^{(k)}$ can be computed recursively from the values $\nu_\lambda^{(k)}$ using Eqs. (20) and (21). Equation (20) is Laplace's Succession Rule,[8] which has appeared in work on hierarchical pattern recognition techniques.[5] Here it is applied to the statistics $\nu_\lambda^{(k)}$ associated with the chain of subsets of Σ displayed in Eq. (16); this chain of subsets is in turn derived from the multiple-resolution description specified in Secs. I D and I E. Note that in Eq. (20), when $\nu_{\lambda-1}^{(k)}=0$ [and therefore $\nu_\lambda^{(k)}=0$], we have $P_\lambda^{(k)}=\frac{1}{2}P_{\lambda-1}^{(k)}$, as expected in view of the uniform prior density of $\theta_\lambda^{(k)}$.

The recursive computation defined by Eq. (20) is efficiently implemented as follows. During the training phase, binary digits are extracted from each data point $\mathbf{x}=(x_1,x_2,\ldots,x_D)$ of each training sample, in the sequence described by Eq. (B1). The corresponding indicator numbers are set to 1 and stored in a compact form in data files. When a new sample S is to be classified, the indicator numbers of S are first computed. For the kth class, the numbers $\nu_\lambda^{(k)}=\nu_\lambda^{(k)}(S),1\leqslant\lambda\leqslant\Lambda$, are then computed as running sums by comparison of the indicator numbers of S with those of each training sample in turn. Then the recursion given by Eq. (20) [or Eq. (21), where applicable] is applied.

Note that at each step of the recursion that is governed by Eq. (20) rather than by Eq. (21), the value of $P_\lambda^{(k)}$ diminishes by a factor of as much as 1/2, while the ratio of the values of $P_\lambda^{(k)}$ for two different class indices k changes by a factor that lies between 1/2 and 1. This change in relative *a posteriori* probabilities reflects the contribution of the single

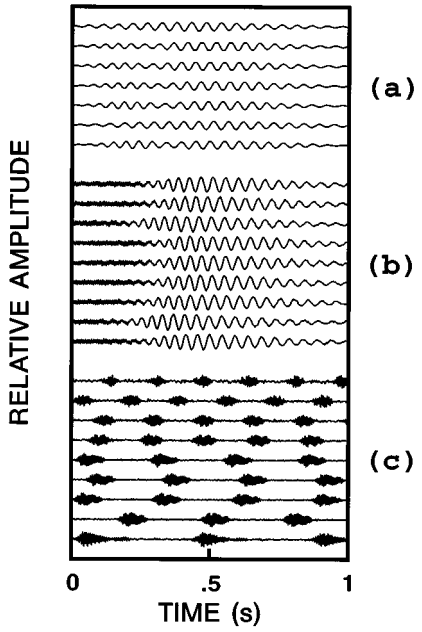

FIG. 5. Time-series training data for the first example, representing three vocalization types: (a) *Balaenoptera physalus* pulse; (b) *Balaenoptera physalus* pulse with falsetto; (c) *Balaenoptera acutorostrata* (?) pulses.

binary value n_{β_λ}. In this sense, the algorithm defines a procedure for updating the *a posteriori* probabilities one data bit at a time.

From the discussion in Sec. I D and Appendix B, there are as many as $2^{L_{\max}}$ steps governed by Eq. (20); thus, the ratio of two values of $P_\Lambda^{(k)}$ could be as high as $2^{2^{L_{\max}}}$. For this reason, it is desirable, in fixed word-length computations, to implement Eqs. (20) and (21) as a recursion for $L_\lambda^{(k)}=\log(P_\Lambda^{(k)})$, given by

$$L_0^{(k)}=0;\quad L_\lambda^{(k)}=\begin{cases} L_{\lambda-1}^{(k)}+\log(\nu_\lambda^{(k)}+1)-\log(\nu_{\lambda-1}^{(k)}+2), \\ \quad \text{if Eq. (20) applies,} \\ L_{\lambda-1}^{(k)}, \quad \text{if Eq. (21) applies;} \end{cases} \tag{22}$$

exponentiation then yields the values $e^{L_\Lambda^{(k)}}=P_\Lambda^{(k)}$. By analogy with Eq. (3), we then obtain *a posteriori* probabilities of membership of S in the K classes. More explicitly, letting

$$\boldsymbol{\nu}^{(k)}=(\boldsymbol{\nu}_\Lambda^{(k)},\boldsymbol{\nu}_{\Lambda-1}^{(k)},\ldots,\boldsymbol{\nu}_1^{(k)}), \tag{23}$$

we have

TABLE I. Class symbols, species and transient types, and number of training samples for the first example. [a]Species identification for this sound has not been definitively confirmed.

Class symbol	Genus and species, transient type	Number of training samples
(a)	*Balaenoptera physalus* pulse	7
(b)	*Balaenoptera physalus* pulse with falsetto	9
(c)	*Balaenoptera acutorostrata*[a] pulses	9

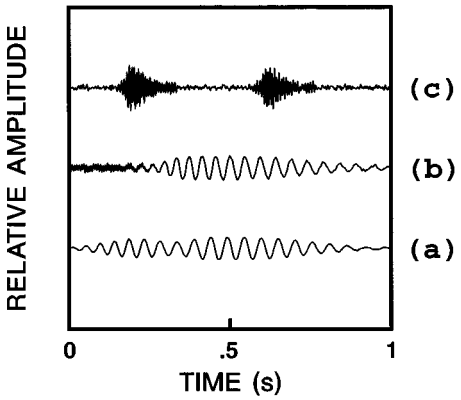

FIG. 6. Three new samples presented for classification in the first example: (a) *Balaenoptera physalus* pulse; (b) *Balaenoptera physalus* pulse with falsetto; (c) *Balaenoptera acutorostrata* (?) pulses.

$$\begin{aligned} P(\mathscr{C}_k|S\in\Sigma^{(\Lambda)},\boldsymbol{\nu}^{(k)}) &= \frac{\Pr\{S\in\Sigma^{(\Lambda)}|\boldsymbol{\nu}^{(k)},\mathscr{C}_k\}P(\mathscr{C}_k)}{\sum_{j=1}^K \Pr\{S\in\Sigma^{(\Lambda)}|\boldsymbol{\nu}^{(j)},\mathscr{C}_j\}P(\mathscr{C}_j)} \\ &= \frac{P_\Lambda^{(k)}P(\mathscr{C}_k)}{\sum_{j=1}^K P_\Lambda^{(j)}P(\mathscr{C}_j)}. \end{aligned} \tag{24}$$

These *a posteriori* probabilities provide a statistical basis for classification of a new sample S, based on a maximum-*a posteriori* decision rule.

Section II gives some examples of application of this computation to classification of marine mammal sounds.

II. APPLICATION TO AUTOMATED CLASSIFICATION OF MARINE MAMMAL SOUNDS

A. Classification of time series

As a first example, we take as training data 25 time series representing three classes of low-frequency baleen whale sounds. Each training set consists of seven or nine time series of 1 s duration (see Fig. 5). These data were recorded on a low-frequency, bottom-mounted hydrophone array located in deep water in the North Atlantic Ocean near Bermuda. The first training set consists of seven samples of the well-known ''20-Hz'' narrow-band pulse[9] of the finback whale, *Balaenoptera physalus* [see Fig. 5(a)]. The second training set contains nine samples of a variant of this sound in which the 20-Hz pulse is preceded by a brief ''falsetto'' tonal of approximately 130 Hz center frequency [see Fig. 5(b)]. The third training set consists of nine samples of pulse trains having center frequencies of approximately 140 Hz and repetition rates varying from approximately 2 to 6 s^{-1}

TABLE II. *A posteriori* probabilities for the first example, with classification of time series data.

Class	*A posteriori* probability (a)	(b)	(c)
(a)	1.0^-	8.7×10^{-10}	8.7×10^{-10}
(b)	1.7×10^{-9}	1.0^-	2.4×10^{-35}
(c)	1.2×10^{-6}	0.006	0.994

TABLE III. Confusion matrix for the first example, with classification of time series data.

Class	(a)	(b)	(c)
(a)	0.5	0.5	0.0
(b)	0.1	0.9	0.0
(c)	0.0	0.1	0.9

[see Fig. 5(c)]. The source of these sounds is identified by some experts as the minke whale, *Balaenoptera acutorostrata*; however, this identification has not been definitively confirmed. Table I associates symbols with a brief description of each class of sounds.

The sample transients were approximately aligned by eye and appear to have random phase shifts within each class. The samples were energy-normalized and then processed as described in Sec. I, with a maximum precision of 5 bits in each of the two coordinates (time and amplitude). Thus $L_{\max}=2\times5=10$ and $\Lambda=2^{11}-1=2047$. A new sample not in the training data was then selected for each of the three classes (Fig. 6). Table II shows the values of the *a posteriori* probabilities $P(\mathscr{C}_k|S\in\Sigma^{(\Lambda)},\boldsymbol{\nu}^{(k)})$, calculated from assumed equal *a priori* probabilities [$P(\mathscr{C}_k)=1/3$ for each class] and Eqs. (22) and (24). The results show correct classification of all three sounds, with large ratios of the *a posteriori* probabilities. The computation time on a Silicon Graphics 4D-35 workstation was 10 s for the training phase, in which the 25 training samples were converted to indicator numbers, which were then stored in a disk file. Computation time for classification of all three new samples was 2 s.

To compute rates of correct classification associated with this example, the training data were first combined with the three new samples. For each of the 28 samples in the combined set, the training set consisted of the other 27 samples. The classification of each selected sample was then performed as just described. Table III shows the *confusion matrix* for this data set. In this matrix, the correct classes are

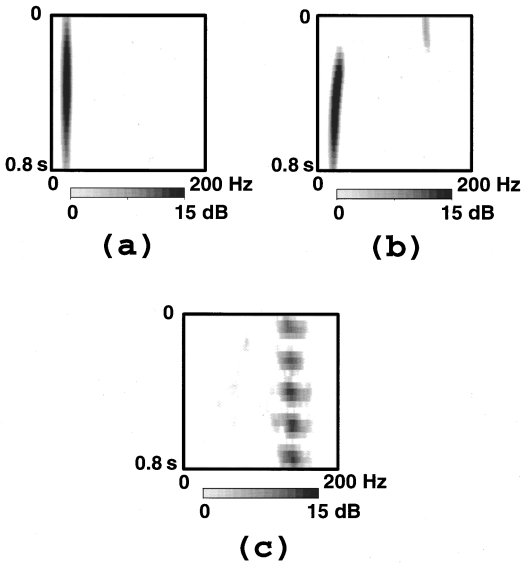

FIG. 7. Representative spectrograms for the three classes in the first example: (a) *Balaenoptera physalus* pulse; (b) *Balaenoptera physalus* pulse with falsetto; (c) *Balaenoptera acutorostrata* (?) pulses.

TABLE IV. *A posteriori* probabilities for the first example, with classification of spectrogram data.

	A posteriori probability		
Class	(a)	(b)	(c)
(a)	1.0^{-}	8.0×10^{-27}	3.9×10^{-38}
(b)	5.5×10^{-32}	1.0^{-}	5.8×10^{-42}
(c)	5.0×10^{-34}	4.8×10^{-34}	1.0^{-}

associated with the rows, and the fractions of classifications resulting from a maximum-*a posteriori* decision rule are shown in the columns. As one might expect, the results show the most difficulty in discriminating classes (a) and (b).

Section II B will show that classification performance for this example can be improved by classifying time-frequency distributions instead of the unprocessed time series.

B. Classification of spectrogram data

The time series for the first example were spectrum analyzed in a frequency band of 0–200 Hz. Conventional (windowed-FFT) spectrograms were constructed from overlapping time segments of duration 0.2 s, with an offset of approximately 0.03 s between segments. Figure 7 shows representative spectrograms for each of the three classes.

Table IV shows the values of the *a posteriori* probabilities $P(\mathscr{C}_k|S\in\Sigma^{(\Lambda)},\boldsymbol{\nu}^{(k)})$, computed from spectrogram data for the same three samples as in Table II. These three classifications are again correct. Table V shows the confusion matrix for this data set. For the spectrogram data, all 28 samples were correctly classified.

In the preceding example, the three types of transients have a relatively simple spectral structure, and the time-frequency distributions for classes (a) and (b) show relatively little variability. We will next give an example of classification of signals with more complex and variable spectral structures. Conventional spectrogram data are again used as input to the classification algorithm.

The data consist of 64 spectrograms representing 6 classes of low-frequency baleen whale sounds [see Table VI]. The species are the bowhead whale (*Balaena mysticetus*), finback whale (*Balaenoptera physalus*), gray whale (*Eschrichtius robustus*), southern right whale (*Eubalaena australis*), northern right whale (*Eubalaena glacialis*), and humpback whale (*Megaptera novaeangliae*). The time series were obtained from the SOUND database of marine mammal vocalizations.[10] Spectrograms covering the frequency band 0–1 kHz were calculated for each sample and normalized to unit average power. [Some of the samples have measurable

TABLE V. Confusion matrix for the first example, with classification of spectrogram data.

Class	(a)	(b)	(c)
(a)	1.0	0.0	0.0
(b)	0.0	1.0	0.0
(c)	0.0	0.0	1.0

TABLE VI. Class symbols, species, and number of samples for the second example.

Class symbol	Genus and species	Number of samples
(a)	Balaena mysticetus	16
(b)	Balaenoptera physalus	5
(c)	Eschrichtius robustus	13
(d)	Eubalaena australis	9
(e)	Eubalaena glacialis	12
(f)	Megaptera novaeangliae	9

energy outside of the frequency band processed.] Figure 8 shows a representative spectrogram for each training set.

For each of the 64 samples, the training data consisted of the other 63 samples. The classification of each sample was performed as described in Section I. The samples (spectrogram data) were analyzed to a precision of 4 bits in each of three coordinates (time, frequency, and power in decibels). Thus $L_{\max}=3\times4=12$ and $\Lambda=2^{13}-1=8191$. The results are summarized by the confusion matrix in Table VII. The rates of correct classification vary from 56% to 89% for the six classes, with an overall rate of 75% correct classifications. These rates are lower than in the first example, reflecting both the greater variability of the signals in the second example and the need for larger training sets for more complex and variable signals. Nevertheless, the results appear promising in view of the relatively small training sets used.

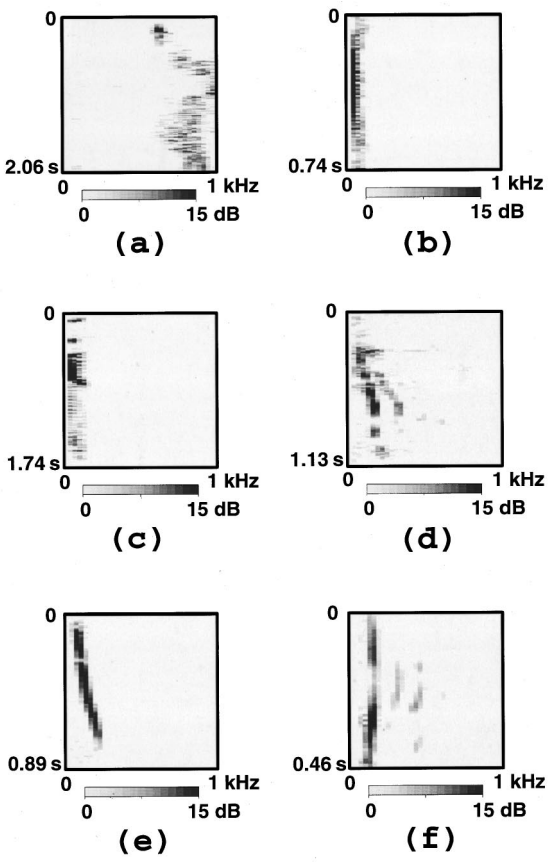

FIG. 8. Representative spectrograms for the six training sets in the second example: (a) *Balaena mysticetus*; (b) *Balaenoptera physalus*; (c) *Eschrichtius robustus*; (d) *Eubalaena australis*; (e) *Eubalaena glacialis*; (f) *Megaptera novaeangliae*.

TABLE VII. Confusion matrix for the second example.

Class	(a)	(b)	(c)	(d)	(e)	(f)
(a)	0.75	0.00	0.13	0.06	0.00	0.06
(b)	0.00	0.80	0.00	0.00	0.20	0.00
(c)	0.00	0.00	0.85	0.00	0.15	0.00
(d)	0.00	0.00	0.00	0.89	0.00	0.11
(e)	0.00	0.08	0.17	0.00	0.67	0.08
(f)	0.00	0.00	0.11	0.11	0.22	0.56

Computation time was 1.0 s per sample for the training phase and 2.0 s per sample for the classification.

III. CONCLUSION AND DISCUSSION

A multiple-resolution statistical pattern recognition technique for classification by supervised learning has been developed and implemented in an efficient computer algorithm. Because the classification is based on statistical characterization of training data in the unreduced sample space rather than a reduced feature space, this technique is especially suitable for applications where features may be significantly distorted. This applies, for example, to classification of underwater acoustic transients received in strongly dispersive propagation environments. The algorithm makes use of an efficient binary partitioning of the unreduced sample space. The binary partition is especially well suited to implementation on a digital computer employing binary representation of data. This has led to very fast computations for both training and classification.

Classification of marine mammal sounds has been demonstrated using small training sets (on the order of 10 samples per class). Because of the small sample size, these results should be considered an initial demonstration of a new classification technique rather than an extensive performance analysis. More extensive testing and adaptation of this technique will be pursued in future work. [Other approaches have been more extensively tested at this writing. For example, Refs. 2 and 11 provide results of extensive performance analyses for classification of marine mammal sounds using, respectively, hierarchical classification techniques applied to statistics of spectrogram data and artificial neural networks.]

As illustrated by the improved performance achieved by classifying spectrogram data instead of time series, signal processing and filtering are desirable in order to diminish the effects of additive noise. For this reason, the fact that the classification technique presented here can be applied to any signal processor output is advantageous. Small residual noise should not be a problem, since it merely becomes another factor affecting the statistical distributions on which the classification is based. Higher noise levels at the signal processor output may require modifications or extensions of the algorithm.

ACKNOWLEDGMENT

The author thanks Clyde Nishimura and William Watkins for providing the time series data used in the examples. This work was supported by the Office of Naval Research and the Naval Research Laboratory.

APPENDIX A

To show that Eq. (3) holds, assume that $\mathscr{C}_1, \mathscr{C}_2, \ldots, \mathscr{C}_K$ are mutually exclusive and exhaustive. We also assume that the prior density $P(\mathscr{C}_k)$ does not depend on the training data, i.e., that

$$P(\mathscr{C}_k|\mathscr{T}) = P(\mathscr{C}_k), \tag{A1}$$

and that the conditional probability of the sample S given $\mathscr{C}_k$ and given the training data $\mathscr{T}$ does not depend on the training sets $\mathscr{T}_m$, $m \neq k$, i.e.,

$$P(S|\mathscr{T}, \mathscr{C}_k) = P(S|\mathscr{T}_k, \mathscr{C}_k). \tag{A2}$$

We start with

$$P(\mathscr{C}_k|S,\mathscr{T}) = \frac{P(\mathscr{C}_k, S, \mathscr{T})}{P(S,\mathscr{T})}. \tag{A3}$$

By Eqs. (A1) and (A2), the numerator in Eq. (A3) can be written as

$$\begin{aligned} P(\mathscr{C}_k, S, \mathscr{T}) &= P(S|\mathscr{T}, \mathscr{C}_k) P(\mathscr{C}_k) P(\mathscr{T}) \\ &= P(S|\mathscr{T}_k, \mathscr{C}_k) P(\mathscr{C}_k) P(\mathscr{T}). \end{aligned} \tag{A4}$$

Since $\mathscr{C}_1, \mathscr{C}_2, \ldots, \mathscr{C}_K$ are mutually exclusive and exhaustive, the denominator in Eq. (A3) can be expressed as

$$\begin{aligned} P(S,\mathscr{T}) &= \sum_j P(S,\mathscr{T},\mathscr{C}_j) \\ &= \sum_j P(S|\mathscr{T},\mathscr{C}_j) P(\mathscr{C}_j) P(\mathscr{T}) \\ &= \sum_j P(S|\mathscr{T}_j,\mathscr{C}_j) P(\mathscr{C}_j) P(\mathscr{T}). \end{aligned} \tag{A5}$$

Substituting the final expressions in Eqs. (A4) and (A5) for the numerator and denominator in Eq. (A3) yields Eq. (3).

If $\mathscr{C}_1, \mathscr{C}_2, \ldots, \mathscr{C}_K$ are mutually exclusive but not assumed to be exhaustive, let $\mathscr{C}'$ denote the complementary set. Then Eq. (A5) is replaced by

$$\begin{aligned} P(S,\mathscr{T}) &= \sum_j P(S,\mathscr{T},\mathscr{C}_j) + P(S,\mathscr{T},\mathscr{C}') \\ &= \sum_j P(S|\mathscr{T}_j,\mathscr{C}_j) P(\mathscr{C}_j) P(\mathscr{T}) \\ &\quad + P(S|\mathscr{T},\mathscr{C}') P(\mathscr{C}') P(\mathscr{T}). \end{aligned} \tag{A6}$$

In general $P(S|\mathscr{T},\mathscr{C}')$ cannot be determined; thus neither can $P(S,\mathscr{T})$. Denoting the unknown value of $P(S,\mathscr{T})$ by $\alpha^{-1}P(\mathscr{T})$ and substituting it for the denominator in Eq. (A3), while applying Eq. (A4) to the numerator, yields Eq. (4).

APPENDIX B

This Appendix provides details of the multiple-resolution description of a sample S consisting of a set of points (D-tuples) of the form in Eq. (7). Each coordinate $x_d \in [0,1)$ can be represented to a binary precision of q bits by the binary expression

$$.x_d^{(1)} x_d^{(2)} x_d^{(3)} \cdots x_d^{(q)},$$

representing the sum

$$\sum_{i=1}^{q} x_d^{(i)} \cdot 2^{-i},$$

where $x_d^{(i)} \in \{0,1\}$. For an integer $q>0$ and for $1 \leqslant d \leqslant D$, we may represent a point $\mathbf{x} \in S$ to a binary precision of q bits in coordinates 1 through d and to a binary precision of $q-1$ bits in coordinates $d+1$ through D via the mapping

$$\begin{aligned} \tau_L : \mathbf{x} \mapsto (&x_1^{(1)}, x_2^{(1)}, \ldots, x_D^{(1)}, x_1^{(2)}, x_2^{(2)}, \ldots, \\ &x_D^{(2)}, \ldots, x_1^{(q-1)}, x_2^{(q-1)}, \ldots, x_D^{(q-1)}, x_1^{(q)}, \\ &x_2^{(q)}, \ldots, x_d^{(q)}) \in \{0,1\}^L, \end{aligned} \tag{B1}$$

where $L=(q-1)D+d$ is the total number of coordinates (bits) in the representation. The bits are arranged in nonincreasing order of significance and are selected in a cyclic fashion from the binary expansions of the D coordinates $x_1, x_2, \ldots, x_D$. For a fixed L, the representation in Eq. (B1) identifies the point $\mathbf{x}$ as belonging to one of the 2^L disjoint cells $\mathscr{D}_{b_1 b_2 \cdots b_L} \subseteq X$ specified by

$$\begin{aligned} \mathscr{D}_{b_1 b_2 \cdots b_L} &= \tau_L^{-1}(b_1, b_2, \ldots, b_L) \\ &= \{\mathbf{x} | \tau_L(\mathbf{x}) = (b_1, b_2, \ldots, b_L)\}, \end{aligned} \tag{B2}$$

where $b_l \in \{0,1\}, l=1,\ldots,L$. These cells form a partition of the space X. The locus of points in a sample $S \subseteq X$ can then be specified to a precision of q bits in coordinates 1 through d and to a precision of $q-1$ bits in coordinates $d+1$ through D by the 2^L numbers

$$n_{b_1 b_2 \cdots b_L}(S) = \begin{cases} 1, & \text{if } \tau_L(\mathbf{x}) = (b_1, b_2, \cdots, b_L), \\ & \text{for some } \mathbf{x} \in S, \\ 0, & \text{otherwise.} \end{cases} \tag{B3}$$

The number $n_{b_1 b_2 \cdots b_L}(S)$ is equal to 1 if one or more points of S belong to the cell $\mathscr{D}_{b_1 b_2 \cdots b_L}$, and is equal to 0 otherwise. [For $L=0$ we define $n(S)=0$ if $S=\varnothing$ and $n(S)=1$ if $S \neq \varnothing$.] We refer to the numbers $n_{b_1 b_2 \cdots b_L}(S)$ as the *indicator numbers* of the sample S.

As L increases, the numbers $n_{b_1 b_2 \cdots b_L}$ provide an increasingly resolved binary image of the locus of points in S [see Fig. 1]. In practice, we eventually reach the resolution limit of the available measurements of $x \in S$. Without loss of generality, we assume that in each component space X_d the data are specified up to a binary precision of $q_{\max}$ bits. [If the precision is $q<q_{\max}$ bits in some component, we can add $q-q_{\max}$ trailing 0's to the binary representation in that component.] Then the numbers

$$\{n_{b_1 b_2 \cdots b_L}(S) | 0 \leqslant L \leqslant L_{\max} = q_{\max} D,$$

$$b_l \in \{0,1\}, l = 1, \ldots, L\} \tag{B4}$$

completely specify a sample S up to the maximum resolution of $q_{\max}$ bits in each coordinate.

Figure 3 shows the ordering of the subscripts of the indicator numbers. This ordering, denoted by ''$<$,'' is completely specified by the two rules

$$\begin{aligned} &b_1 b_2 \cdots b_L < b_1' b_2' \cdots b_{L'}', \quad \text{if } L < L'; \\ &b_1 b_2 \cdots b_L < b_1' b_2' \cdots b_L', \text{ if } . b_1 b_2 \cdots b_L < . b_1' b_2' \cdots b_L'. \end{aligned} \tag{B5}$$

For notational convenience, we will denote by β_λ the λth subscript in this ordering; thus

$$\begin{aligned} &\beta_1 = \langle \text{null index} \rangle, \quad \beta_2 = 0, \quad \beta_3 = 1, \\ &\beta_4 = 00, \quad \beta_5 = 01, \quad \beta_6 = 10, \quad \beta_7 = 11, \cdots. \end{aligned} \tag{B6}$$

With the prescribed ordering, the indicator numbers form a binary sequence $\mathbf{n}(S)$ of length $\Lambda = 2^{L_{\max}+1} - 1$. Thus the indicator numbers define a mapping

$$\mathbf{n}: \Sigma = 2^X \rightarrow \{0,1\}^\Lambda = \Gamma \tag{B7}$$

from the set Σ of all subsets of X (i.e., the sample space) to the set Γ of binary sequences of length Λ. Note that the image $\underline{\Gamma}$ of Σ under the map $\mathbf{n}$ does not include all of Γ. In fact, the indicator numbers in the entire tree are completely determined by those at the bottom ($L_{\max}$-th) level; this follows from the fact that, by definition in Eq. (B3), the indicator number at a given node of the tree is equal to the logical OR of the indicator numbers at the two ''child'' nodes, i.e.,

$$n_{b_1 b_2 \cdots b_L} = n_{b_1 b_2 \cdots b_L 0} \vee n_{b_1 b_2 \cdots b_L 1}, \tag{B8}$$

$L = 0,1, \ldots, L_{\max} - 1$. Thus the image of Σ under $\mathbf{n}$ is in one-to-one correspondence with the set of binary sequences of length $2^{L_{\max}}$:

$$\overline{\Gamma} \leftrightarrow \{0,1\}^{2^{L_{\max}}}. \tag{B9}$$

Despite this fact, the entire vector (or tree) of indicator numbers is needed for classification, since most cells at the highest resolution will not be occupied by any training data.

Equation (B8) implies the conditions

$$\begin{aligned} &n_{b_1 b_2 \cdots b_L} = 0 \;\Rightarrow\; n_{b_1 b_2 \cdots b_L 0} = n_{b_1 b_2 \cdots b_L 1} = 0; \\ &n_{b_1 b_2 \cdots b_L} = 1, \; n_{b_1 b_2 \cdots b_L 0} = 0 \;\Rightarrow\; n_{b_1 b_2 \cdots b_L 1} = 1. \end{aligned} \tag{B10}$$

In the ordering of indices prescribed by Eq. (B6), these conditions are expressed by

$$\begin{aligned} &n_{\beta_\lambda} = 0 \;\Rightarrow\; n_{\beta_{2\lambda}} = n_{\beta_{2\lambda+1}} = 0; \\ &n_{\beta_\lambda} = 1, \; n_{\beta_{2\lambda}} = 0 \;\Rightarrow\; n_{\beta_{2\lambda+1}} = 1. \end{aligned} \tag{B11}$$

These alternative conditions are used in the computer implementation of the classification algorithm.

APPENDIX C

We show that the recursion given by Eq. (20) [or by Eq. (21) for the case $\Sigma^{(\lambda)} = \Sigma^{(\lambda-1)}$] is valid for the conditional probabilities $P_\lambda^{(k)}$ defined by Eq. (18). Let $\theta_\lambda^{(k)}$ denote the (unknown) conditional probability defined by Eq. (19). As described in the text, the prior density $\pi_\lambda^{(k)}(\theta)$ of $\theta_\lambda^{(k)}$ is assumed to be concentrated at 1 if $n_{\beta_\lambda}(S)$ is determined from previous values by Eq. (B11); otherwise it is assumed to be uniform on the interval $[0,1]$. In the former case, Eq. (21) follows immediately from Eq. (19). We will show next that Eq. (20) holds for the other cases. By analogy with Eq. (5), we have

$$P_\lambda^{(k)} = \frac{Q_\lambda^{(k)}}{R_\lambda^{(k)}}, \tag{C1}$$

where

$$\begin{aligned} Q_\lambda^{(k)} = \Pr\{ &\boldsymbol{S} \in \Sigma^{(\lambda)}, \boldsymbol{\nu}_\lambda^{(k)} = \nu_\lambda^{(k)}, \boldsymbol{\nu}_{\lambda-1}^{(k)} = \nu_{\lambda-1}^{(k)}, \ldots, \\ &\nu_1^{(k)} = \nu_1^{(k)} | \mathscr{C}_k \} \end{aligned} \tag{C2}$$

and

$$R_\lambda^{(k)} = \Pr\{ \boldsymbol{\nu}_\lambda^{(k)} = \nu_\lambda^{(k)}, \boldsymbol{\nu}_{\lambda-1}^{(k)} = \nu_{\lambda-1}^{(k)}, \ldots, \boldsymbol{\nu}_1^{(k)} = \nu_1^{(k)} | \mathscr{C}_k \}. \tag{C3}$$

Let

$$\begin{aligned} q_\lambda^{(k)}(\theta) = \Pr\{ &\boldsymbol{S} \in \Sigma^{(\lambda)}, \boldsymbol{\nu}_\lambda^{(k)} = \nu_\lambda^{(k)} | \boldsymbol{S} \in \Sigma^{(\lambda-1)}, \\ &\boldsymbol{\nu}_{\lambda-1}^{(k)} = \nu_{\lambda-1}^{(k)}, \ldots, \boldsymbol{\nu}_1^{(k)} = \nu_1^{(k)}, \mathscr{C}_k, \theta_\lambda^{(k)} = \theta \}, \end{aligned} \tag{C4}$$

and let

$$q_\lambda^{(k)} = \int q_\lambda^{(k)}(\theta) \pi_\lambda^{(k)}(\theta) d\theta. \tag{C5}$$

From Eqs. (16), (C2), and (C4) we have

$$Q_\lambda^{(k)} = q_\lambda^{(k)} Q_{\lambda-1}^{(k)}, \lambda = 1, \ldots, \Lambda; \tag{C6}$$

by induction we have

$$Q_\lambda^{(k)} = q_1^{(k)} q_2^{(k)} \cdots q_\lambda^{(k)}. \tag{C7}$$

Similarly, let

$$\begin{aligned} r_\lambda^{(k)}(\theta) = \Pr\{ &\boldsymbol{\nu}_\lambda^{(k)} = \nu_\lambda^{(k)} | \boldsymbol{\nu}_{\lambda-1}^{(k)} = \nu_{\lambda-1}^{(k)}, \ldots, \boldsymbol{\nu}_1^{(k)} = \nu_1^{(k)}, \\ &\mathscr{C}_k, \theta_\lambda^{(k)} = \theta \} \end{aligned} \tag{C8}$$

and let

$$r_\lambda^{(k)} = \int r_\lambda^{(k)}(\theta) \pi_\lambda^{(k)}(\theta) d\theta. \tag{C9}$$

Then by Eqs. (C3) and (C8) and induction on λ, we have

$$R_\lambda^{(k)} = r_1^{(k)} r_2^{(k)} \cdots r_\lambda^{(k)}. \tag{C10}$$

Equations (C1), (C7), and (C10) give the recursion

$$P_\lambda^{(k)} = \frac{q_\lambda^{(k)}}{r_\lambda^{(k)}} P_{\lambda-1}^{(k)}. \tag{C11}$$

Now $\nu_{\lambda-1}^{(k)}$ samples in the training set $\{S_1^{(k)}, S_2^{(k)}, \ldots, S_{N_k}^{(k)}\}$ belong to $\Sigma^{(\lambda-1)}$; of those, $\nu_\lambda^{(k)}$ belong to $\Sigma^{(\lambda)}$. Thus, from Eq. (19) and the assumed independence of $\boldsymbol{S}$, $\boldsymbol{S}_1^{(k)}$,

$\boldsymbol{S}_2^{(k)}, \ldots, \boldsymbol{S}_{N_k}^{(k)}$, we see that $q_\lambda^{(k)}(\theta)$ and $r_\lambda^{(k)}(\theta)$ can be computed via a binomial density with parameter $\theta_\lambda^{(k)}=\theta$. Equations (C4), (C5), (C8), and (C9) and the fact that $\pi_\lambda^{(k)}(\theta)=1$ on the interval $[0,1]$ then give

$$q_\lambda^{(k)}=\int_0^1 \binom{\nu_{\lambda-1}^{(k)}}{\nu_\lambda^{(k)}} \theta^{\nu_\lambda^{(k)}+1}(1-\theta)^{\nu_{\lambda-1}^{(k)}-\nu_\lambda^{(k)}} d\theta,$$
$$r_\lambda^{(k)}=\int_0^1 \binom{\nu_{\lambda-1}^{(k)}}{\nu_\lambda^{(k)}} \theta^{\nu_\lambda^{(k)}}(1-\theta)^{\nu_{\lambda-1}^{(k)}-\nu_\lambda^{(k)}} d\theta. \tag{C12}$$

It is readily shown by induction on $\nu_\lambda^{(k)}$ that

$$q_\lambda^{(k)}=\frac{1}{\nu_{\lambda-1}^{(k)}+2}\cdot\frac{\binom{\nu_{\lambda-1}^{(k)}}{\nu_\lambda^{(k)}}}{\binom{\nu_{\lambda-1}^{(k)}+1}{\nu_\lambda^{(k)}+1}}, \quad r_\lambda^{(k)}=\frac{1}{\nu_{\lambda-1}^{(k)}+1}. \tag{C13}$$

Substituting these expressions into Eq. (C11) and simplifying yields Eq. (20).

[1] R. J. Schalkoff, *Pattern Recognition: Statistical, Structural, and Neural Approaches* (Wiley, New York, 1992).

[2] K. Fristrup and W. Watkins, ''Marine animal sound classification,'' Woods Hole Oceanographic Institution, Technical Report WHOI-94-13, 1994.

[3] W. S. Meisel, *Computer-Oriented Approaches to Pattern Recognition* (Academic, New York, 1972).

[4] See Ref. 1, Chap. 3.

[5] R. G. Casey and G. Nagy, ''Decision tree design using a probabilistic model,'' IEEE Trans. Inf. Theory **30**(1), 93 (1984).

[6] I. K. Sethi and G. P. R. Sarvarayudu, ''Hierarchical classifier design using mutual information,'' IEEE Trans. Pattern Anal. Mach. Intel. **PAMI-4**(4), 441 (1982).

[7] E. G. Henrichon, Jr. and K.-S. Fu, ''A nonparametric partitioning procedure for pattern classification, IEEE Trans. Comput. **C-18**(7), 614 (1969).

[8] P. S. de Laplace, *Essai Philosophique Sur les Probabilitiés* (1820), reprinted as *Philosophical Essay on Probability* (Dover, New York, 1951).

[9] W. Watkins, P. Tyack, and K. E. Moore, ''The 20-Hz signals of finback whales (*Balaenoptera physalus*),'' J. Acoust. Soc. Am. **82**, 1901–1912 (1987).

[10] W. A. Watkins, K. Fristrup, M. A. Daher, and T. Howald, ''SOUND Database of Marine Animal Vocalizations; Structure and Operations,'' Woods Hole Oceanographic Institution, Technical Report WHOI-92-31, 1992.

[11] J. R. Potter, D. K. Mellinger, and C. W. Clark, ''Marine mammal call discrimination using artificial neural networks,'' J. Acoust. Soc. Am. **96**, 1255–1262 (1994).

Frequency dependence of acoustic distortion products in a locally active model of the cochlea[a)]

Luc J. Kanis and Egbert de Boer[b)]
Room D2-226, Academic Medical Center, Meibergdreef 9, 1105 AZ, Amsterdam, The Netherlands

(Received 25 March 1996; revised 19 August 1996; accepted 22 October 1996)

In two-tone experiments it has been shown that acoustic distortion products are ''tuned'' as a function of primary frequency ratio, that is, at a certain frequency ratio a maximum in emission occurs. Several authors maintain that this ''tuning'' is caused by band-pass filtering of the distortion products as they are coupled back to the basilar membrane. In this paper one possible other cause for this type of tuning is brought to light. It is shown that the same kind of ''tuning'' is present in a locally active cochlea model without such a filtering of distortion products. In this view ''tuning'' becomes evident because, when the frequency ratio is near unity, the primary components tend to suppress one another, and suppress the DP, too. © *1997 Acoustical Society of America.* [S0001-4966(97)01203-4]

PACS numbers: 43.64.Bt, 43.64.Kc, 43.64.Jb [RDF]

INTRODUCTION

In 1986 Matthews and Molnar showed that in the nonlinear cochlea model they used, acoustic distortion products (DPs) were (bandpass) ''tuned'' as a function of primary frequency ratio. Similar tuning has been observed in experiments where maximal otoacoustic emissions occur at a frequency ratio of about 1.2 (Kim, 1980; Wilson, 1980; Fahey and Allen, 1986; Lonsbury-Martin *et al.*, 1987; Harris *et al.*, 1988; Brown and Gaskill, 1990a, 1990b; Gaskill and Brown, 1990; Whitehead *et al.*, 1992).

In recent papers several authors maintain that the DP ''tuning'' is the result of an additional filtering mechanism inside the cochlea (Brown and Gaskill, 1990a; Brown and Williams, 1993; Allen and Fahey, 1993). Defining the first filter as the one caused by the resonance mechanism of the BM, the second filter would reside in the micromechanics of the organ of Corti. It is clear why the DP emission decreases when the primary frequency ratio is increased above approximately 1.2. A ''second filter'' would be necessary to explain why the DP emission also decreases when the primary frequency ratio is lowered from about 1.2 to 1.0.

It should be noted that the ''second filter'' hypothesis is in contradiction with the findings of Matthews and Molnar because in their model ''tuning'' was observed while *no* filtering of the DPs was built in. We show in this paper that the same kind of ''tuning'' is present in a more realistic nonlinear model with local activity in which there is *no* filtering of DPs *after* generation. In other words, we show that one cannot conclude from the available experimental emission data that a DP filtering mechanism is necessarily present in the real cochlea. We also show that the DP ''tuning'' disappears at levels where the cochlea model operates more in the linear regime, i.e., at input levels of 20 dB SPL and lower. If in experiments DP ''tuning'' at correspondingly low levels would be shown, this would be strong evidence that the second filter exists. In any event, the ''tuning'' seen at higher levels should not solely result from the second filter.

I. MODEL AND METHOD

In macromechanical models of the cochlea the cochlear partition can be described by an impedance consisting of a mass, a resistance, and a stiffness part. A micromechanical model of the partition may be described by three impedances, for instance Z_{BM}, Z_{RL}, and Z_{OC}; the first one describing the mechanics of the basilar membrane (BM), and the other two describing the mechanics of the reticular lamina (RL) and the organ of Corti (OC). The situation at one location x is shown schematically in Fig. 1, where $-2p$ denotes the pressure difference across the cochlear partition and v_{BM}, v_{RL}, and v_{OC} stand for BM velocity, RL velocity and velocity of the OC, respectively. Thus, in the case of Fig. 1, the total impedance of the cochlear partition consists of the BM impedance and a parallel combination formed by the impedances of the RL and the OC. In a different model of the same class the parallel combination might be formed by the impedance of the tectorial membrane (TM) and the impedance that describes the stereociliar coupling with the TM.

In a locally active cochlea model the outer hair cells (OHCs) amplify the traveling wave in the peak region by generating an extra pressure difference across the cochlear partition. Since the OHCs are embedded in the organ of Corti, the pressure source is to be added in series with the impedance of the organ of Corti (at the location of the open circle in Fig. 1), so that the OHC pressures are *filtered* as they are coupled back to the BM (details are given in Kanis, 1995, chapter 6). Several recently published locally active cochlea models are of this class (Geisler, 1991; Geisler *et al.*, 1993; Neely, 1993; Neely and Stover, 1993). The model by Neely and Kim (1986) is simpler: the effective action of the OHCs has been put directly across the cochlear partition (at the location of the filled circle in Fig. 1). In their model there is *no* filtering of the OHC-generated pressures.

[a)]Preliminary results were presented during the *1995 Midwinter Meeting* of the Association for Research in Otolaryngology, St. Petersburg, FL.
[b)]Electronic mail: e.deboer@amc.uva.nl

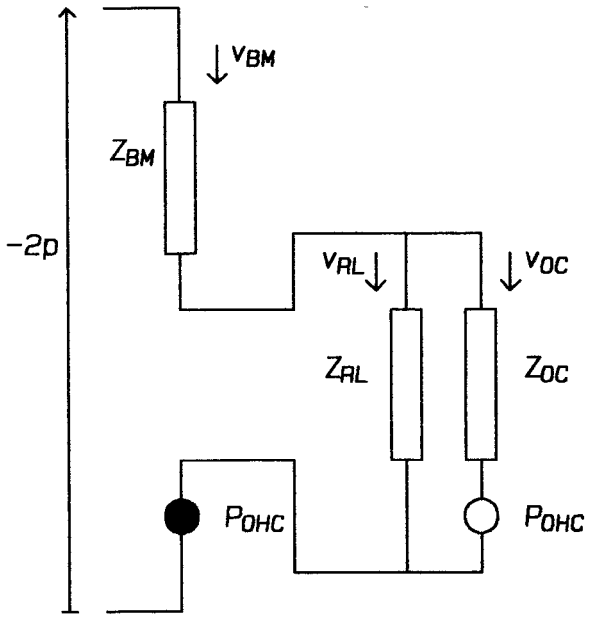

FIG. 1. Electrical circuit for a cochlear section. The velocity of the BM is denoted by v_{BM}, the velocity of the reticular lamina (RL) by v_{RL}, and the velocity associated with compression and expansion of the organ of Corti by v_{OC}. The impedance Z_{BM} is the BM impedance, the impedance Z_{RL} describes how the cilia are attached to the modiolus via the tectorial membrane, and Z_{OC} represents the internal mechanics of the organ of Corti. The pressure p_{OHC} is the pressure generated by the outer hair cells, and $-2p$ is the pressure difference over the cochlear partition.

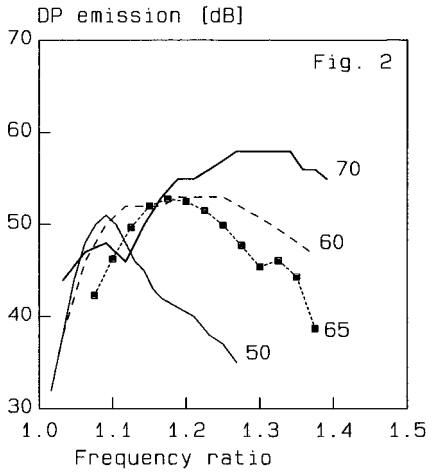

FIG. 2. DP emissions as a function of primary frequency ratio displayed for three different primary input levels (50 dB SPL: thin solid line; 60 dB SPL: dashed line; 70 dB SPL: thick solid line). We have monitored the pressure at the location of the stapes with a reference level of 1×10^{-5} N m^{-2}. The experimental curve with the squares is taken from Gaskill and Brown (1990, Fig. 2d, dashed line). The reference level of the experimental curve is 3.16×10^{-8} N m^{-2}.

To sharpen our arguments we will use in this paper a (long-wave) model of the cochlea that is similar to that of Neely and Kim. For details of the model and the method that we used to solve for the response (called the *quasilinear* solution method) we refer to Kanis and de Boer (1993). It is to be remembered that the only nonlinear elements in the model are the OHCs, and that OHC transduction is assumed to be instantaneous.

When two primary components are present in the input stimulus, two peaks will occur in the velocity response of the cochlear partition. In a nonlinear model they will give rise to various DP components in the locally generated OHC pressure. In our model the locally generated DP pressure is applied to the BM directly without being filtered. In what follows DP will denote only the component with frequency $2f_1-f_2$. This DP pressure (at one location) is shown in Fig. 1 by the filled circle. From the assembly of such DP pressure sources along the x axis, a traveling wave is set up which during its travel towards the place of resonance will be amplified by the OHCs. As a result, the total input to the OHCs consists of the two primary components and the DP components. The DP pressure component with radian frequency ω_{DP} generated by the OHCs will be called $P_{\mathrm{OHC}}(x;\omega_{\mathrm{DP}})$.

In this paper the response of the nonlinear model is solved in the frequency domain by considering only the relevant Fourier components in the pressures generated by the OHCs. Thus, we first compute the responses to the two primaries as described in Kanis and de Boer (1994), then we proceed with the computation of the DP responses without bothering about the primaries; this is done in a number of iteration steps. The whole procedure is justified because the influence of higher-order components on primary components is negligible (see Kanis and de Boer, 1993, Appendix B). With the two primary responses we compute $P^{(1)}_{\mathrm{OHC}}\times(x;\omega_{\mathrm{DP}})$, an initial guess to the ultimate pressure distribution $P_{\mathrm{OHC}}(x;\omega_{\mathrm{DP}})$, and $Z^{(1)}_{\mathrm{OHC}}(x;\omega_{\mathrm{DP}})$, an inital guess to the quasilinear OHC transfer impedance at the DP frequency $Z^{ql}_{\mathrm{OHC}}(x;\omega_{\mathrm{DP}})$. These two functions lead to a first estimate $v^{(1)}_{\mathrm{BM}}(x;\omega_{\mathrm{DP}})$ of the DP component of the velocity response $v_{\mathrm{BM}}(x;\omega_{\mathrm{DP}})$ [see Kanis and de Boer, 1993, Eq. (B7)]. In the second iteration step we compute $P^{(2)}_{\mathrm{OHC}}(x;\omega_{\mathrm{DP}})$ which is the pressure generated by a local OHC if both primaries *and* the estimate $v^{(1)}_{\mathrm{BM}}(x;\omega_{\mathrm{DP}})$ are used as input. In fact, $P^{(2)}_{\mathrm{OHC}}\times(x;\omega_{\mathrm{DP}})$ includes amplification effects at the DP frequency, and provides a better approximation to the ultimate pressure distribution $P_{\mathrm{OHC}}(x;\omega_{\mathrm{DP}})$. The estimate for the effective OHC impedance function in the kth iteration step is

$$Z^{(k)}_{\mathrm{OHC}}(x;\omega_{\mathrm{DP}})=\frac{P^{(k)}_{\mathrm{OHC}}(x;\omega_{\mathrm{DP}})-P^{(1)}_{\mathrm{OHC}}(x;\omega_{\mathrm{DP}})}{v^{(k-1)}_{\mathrm{BM}}(x;\omega_{\mathrm{DP}})}. \tag{1}$$

In theory the iteration sequence can be carried on indefinitely. In practice two iteration steps suffice to get a good estimate of $P_{\mathrm{OHC}}(x;\omega_{\mathrm{DP}})$, $Z^{ql}_{\mathrm{OHC}}(x;\omega_{\mathrm{DP}})$, and $v_{\mathrm{BM}}(x;\omega_{\mathrm{DP}})$, i.e., an estimate that differs by less than 1 dB from the result after 20 more iterations. It should be noted that in all iteration steps we use $P^{(1)}_{\mathrm{OHC}}(x;\omega_{\mathrm{DP}})$ as the ''distributed excitation'' to the cochlea. Details of the computational method are given by Kanis and de Boer (1993, 1994, Appendix A).

II. RESULTS

To monitor the emission of the DP, we have considered the DP pressure at the location of the stapes. In Fig. 2, two tones with frequencies and f_1 and f_2 ($f_2>f_1$) and equal amplitudes have been used as primary tones. The amplitude of the $2f_1-f_2$ DP emission computed with the model is shown

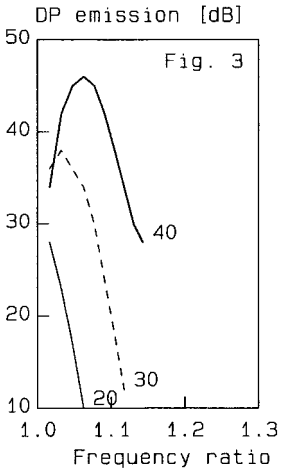

FIG. 3. DP emissions as a function of primary frequency ratio. Same as Fig. 2 but for lower input levels (20 dB SPL: thin solid line; 30 dB SPL: dashed line; 40 dB SPL: thick solid line). We see that the DP ''tuning'' disappears completely at the level of 20 dB SPL.

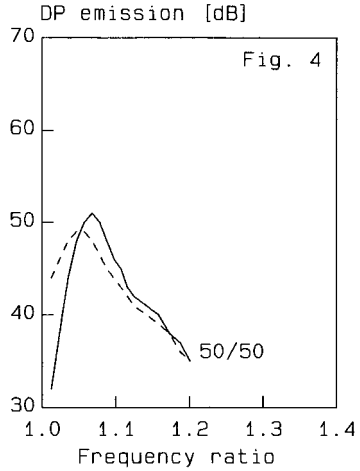

FIG. 4. Effect of removal of nonlinearity on DP emissions. The solid curve has been obtained as a function of primary frequency ratio and is the same as the 50 dB SPL curve from Fig. 2. The dashed curve has been obtained with the same parameters but the suppressive effect of the primaries on the amplification of the DP has artificially been removed. We see that although the ''tuning'' of the dashed curve is much less than for the solid curve, it has not fully disappeared.

as a function of primary frequency ratio (f_2/f_1) with the DP frequency held constant at 6 kHz. The curves were obtained for input levels of 50, 60 and 70 dB SPL. In this figure we see that ''tuning'' of the DP is clearly present. Keeping the lower primary frequency f_1 or the higher frequency f_2 constant (instead of the DP frequency) does not change the nature of this result. One experimental curve by Gaskill and Brown (1990, Fig. 2d, dashed line, shown here as squares) is added for comparison.[1]

Since in the model the DPs are not filtered after generation, the ''tuning'' shown by Fig. 2 cannot be produced by a second filter. One possible explanation is that the ''tuning'' near $f_2/f_1=1$ is a principal byproduct of nonlinear ''overloading'' in the system. To check whether this is true, we computed the DP emission at lower levels than in Fig. 2. The result is shown in Fig. 3 for which we have used primary levels of 20, 30, and 40 dB SPL. We see that, at the lowest level, the emission increases monotonically as the frequency ratio decreases to 1.0, or, in other words, DP ''tuning'' disappears completely at that level. Therefore, in our model DP ''tuning'' is a direct result of overloading.

To examine whether suppression of the active mechanism at the DP frequency by the primary components might be the cause of the DP ''tuning'' we have artificially removed this suppression; that is, we have taken the impedance $Z_{\mathrm{OHC}}^{(k)}(x;\omega_{\mathrm{DP}})$ of Eq. (1) as fully active [see Eq. (9) in Kanis and de Boer (1993)]. (Note that such an action is only possible with the quasilinear method and not with time-domain methods.) We have plotted the resulting DP emission as a function of primary frequency ratio in Fig. 4. The solid line is the 50 dB SPL curve from Fig. 2, and the dashed line the corresponding unsuppressed curve. We observe that the ''tuning'' has not fully disappeared. This indicates that suppression of the DP by the primary components is a partial, but not the full explanation of the ''tuning''. The ''tuning'' is also caused by complex interaction of waves originating from many different locations.

Several authors have stated that for DPs of different order the DP emission curves (as a function of DP frequency) peak at the same primary frequency ratio (e.g., Allen and Fahey, 1993). This is not universally true, however, as can be seen from Fig. 4 from Brown and Gaskill (1990a). In that figure the primary frequency ratio at which a DP response curve peak shifts to a lower value for higher order of the DP. In our modeling we found the same property.

III. DISCUSSION

In our model filtering is involved in the *input* path to the OHCs. However, such a filtering cannot produce the observed type of ''tuning'' of the DPs. This is seen as follows. Consider one OHC, its input (stereociliary displacement) being a filtered version of the BM response. The nonlinear effects in that OHC will be largest when the overlap between the input signals produced by the two primary tones is largest. Irrespective of how the BM response is filtered before it arrives at the OHC, the overlap between these two excitations is largest when the two frequencies are equal (i.e., for $f_2/f_1=1$), and this is true for all OHCs.

In this paper we have demonstrated that in order to explain the ''tuning'' of DP emissions one does not absolutely need a filtering mechanism in the *output* path of OHCs (as hypothesized by Brown and Gaskill, 1990a; Brown and Williams, 1993; Allen and Fahey, 1993; Neely and Stover, 1993). We have replicated ''tuning'' of acoustic DPs in a cochlea model in which OHC-generated pressures are *not* filtered as they are coupled back to the BM. In our model, DP ''tuning'' results from *overloading* of the active process. Therefore, our model does not show DP ''tuning'' at low levels. Because entirely comparable stimulus conditions have not yet been exploited in experiments, we have to await future experiments to decide whether DP ''tuning'' exists at low levels. In any event, the ''tuning'' seen at higher levels should not solely result from the second filter.

In the cochlea model by Neely and Stover (1993) the evidence about DP ''tuning'' at low input levels is meager (Neely, personal communication). In their model DP components in the OHC pressures are filtered before they are coupled back to the BM. However, this DP filtering cannot give rise to DP ''tuning'' because the maximum of the filter $F(x;\omega)$ in Eq. (A6) lies at the same location as the peak of the velocity response (at least for low levels). Therefore, the DP filtering cannot give rise to DP ''tuning'' in their model. The situation is different for the locally active model by Geisler (1991). In that model the filter peak lies at a more basal location than the DP's resonance place. Thus, in Geisler's model DP ''tuning'' at low levels would be possible.

With a future experiment performed at low levels it might be possible to discriminate between a class of models in which DP filtering is reflected in the acoustic distortion data and a class of models in which that is not the case. It is a fact that the OHCs are embedded in the organ of Corti, and it is therefore likely that the DPs are filtered before they are coupled back on the BM. The question is what the nature of this filter is. If a future experiment shows DP ''tuning'' at sufficiently low levels (equal primary levels of 20 dB SPL), the class of models to which Neely and Stover's model belongs is not of the right type. Such a finding would be in favor of models like that of Geisler (1991) in which a filter is present.

APPENDIX: FILTERING OF THE OHC PRESSURE

In the frequency domain one longitudinal section of the cochlear models by Neely and Stover (1993) and Geisler *et al.* (1993) can be represented by a similar network as the one shown in Fig. 1 with the active pressure source at the location of the open circle. We will show in this appendix that in that case the pressure generated by the OHCs is filtered as it is coupled back to the BM.

The network is described by three equations:

$$Z_{\mathrm{BM}}(x;\omega)v_{\mathrm{BM}}(x;\omega)+Z_{\mathrm{RL}}(x;\omega)v_{\mathrm{RL}}(x;\omega) = -2p(x;\omega), \tag{A1}$$

$$v_{\mathrm{OC}}(x;\omega)=v_{\mathrm{BM}}(x;\omega)-v_{\mathrm{RL}}(x;\omega), \tag{A2}$$

and

$$Z_{\mathrm{OC}}(x;\omega)v_{\mathrm{OC}}(x;\omega)-Z_{\mathrm{RL}}(x;\omega)v_{\mathrm{RL}}(x;\omega) = P_{\mathrm{OHC}}(x;\omega). \tag{A3}$$

Here all variables and impedances are complex functions of location x and radian frequency ω; $Z_{\mathrm{RL}}(x;\omega)$ is the impedance with which the reticular lamina (RL) are attached to the modiolus via the tectorial membrane, $Z_{\mathrm{OC}}(x;\omega)$ the impedance of the organ of Corti, and $Z_{\mathrm{BM}}(x;\omega)$ the BM impedance. Furthermore, $v_{\mathrm{BM}}(x;\omega)$ and $v_{\mathrm{RL}}(x;\omega)$ are the BM velocity and the velocity of the RL, respectively. The difference between these two velocities is $v_{\mathrm{OC}}(x;\omega)$, the measure of amplitude changes of the organ of Corti.

For the distortion products the pressure $P_{\mathrm{OHC}}(x;\omega_{\mathrm{DP}})$, generated by the OHCs, consists of a term $P^{(1)}_{\mathrm{OHC}}(x;\omega_{\mathrm{DP}})$ that is produced by the primaries, and a term that is produced by the DP itself:

$$P_{\mathrm{OHC}}(x;\omega_{\mathrm{DP}})=P^{(1)}_{\mathrm{OHC}}(x;\omega_{\mathrm{DP}})+Z_0^{ql}(x;\omega_{\mathrm{DP}})v_{\mathrm{RL}}(x;\omega_{\mathrm{DP}}) \tag{A4}$$

with $Z_0^{ql}(x;\omega_{\mathrm{DP}})$ the (quasilinear) transduction impedance of the OHCs at the frequency of the DP. The impedance $Z_0^{ql}(x;\omega_{\mathrm{DP}})$ is influenced by the primaries and by self-suppression. Solving Eq. (A1) for $v_{\mathrm{RL}}(x;\omega_{\mathrm{DP}})$ leads to

$$[Z_{\mathrm{BM}}(x;\omega_{\mathrm{DP}})+Z_{\mathrm{OC}}(x;\omega_{\mathrm{DP}})F(x;\omega_{\mathrm{DP}})]v_{\mathrm{BM}}(x;\omega_{\mathrm{DP}}) = -2p(x;\omega_{\mathrm{DP}})+F(x;\omega_{\mathrm{DP}})P^{(1)}_{\mathrm{OHC}}(x;\omega_{\mathrm{DP}}), \tag{A5}$$

where $F(x;\omega)$ is given by

$$F(x;\omega)=\frac{Z_{\mathrm{RL}}(x;\omega)}{Z_{\mathrm{OC}}(x;\omega)+Z_{\mathrm{RL}}(x;\omega)+Z_0^{ql}(x;\omega)}. \tag{A6}$$

On the right-hand side of Eq. (A5), $F(x;\omega)$ is to be interpreted as *the* filtering of the DPs before they are added to the pressure difference over the BM. Whether, at very low input levels, ''tuning'' is detected in the DP emissions or not depends on where the maximum of the filter $F(x;\omega)$ lies. If it lies at the same location as the velocity peak of the DP, there will be no tuning of the DP emissions.

[1]With the time-domain model described in Kanis and de Boer (1996) DP ''tuning'' becomes somewhat less than in Fig. 2 due to differences between the quasilinear and the time-domain method at some combinations of input parameters. The main conclusions of this paper, however, remain the same.

Allen, J. B., and Fahey, P. F. (**1993**). ''A second cochlear-frequency map that correlates distortion products and neural tuning measurements,'' J. Acoust. Soc. Am. **94,** 809–816.

Brown, A. M., and Gaskill, S. A. (**1990a**). ''Can basilar membrane tuning be inferred from distortion measurement?,'' in *Mechanics and Biophysics of Hearing*, edited by P. Dallos, C. D. Geisler, J. W. Matthews, M. A. Ruggero, and C. R. Steele (Springer-Verlag, Berlin), pp. 164–169.

Brown, A. M., and Gaskill, S. A. (**1990b**). ''Measurement of acoustic distortion reveals underlying similarities between human and rodent mechanical responses,'' J. Acoust. Soc. Am. **88,** 840–849.

Brown, A. M., and Williams, M. W. (**1993**). ''A second filter in the cochlea,'' in *Biophysics of Hair Cell Sensory Systems*, edited by H. Duifhuis, J. W. Horst, P. van Dijk, and S. M. van Netten (World Scientific, Singapore), pp. 72–77.

Fahey, P. F., and Allen, J. B. (**1986**). ''Characterisation of cubic intermodulation distortion products in the cat external auditory meatus,'' in *Peripheral Auditory Mechanisms*, edited by J. B. Allen, J. L. Hall, A. Hubbard, S. T. Neely, and A. Tubis (Springer-Verlag, Berlin), pp. 314–321.

Gaskill, S. A., and Brown, A. M. (**1990**). ''The behaviour of the acoustic distortion product, $2f1$-$f2$, from the human ear and its relation to auditory sensitivity,'' J. Acoust. Soc. Am. **88,** 821–839.

Geisler, C. D. (**1991**). ''A model for cochlear vibrations based on feedback from motile outer hair cells,'' Hear. Res. **54**, 105–117.

Geisler, C. D., Bendre, A., and Liotopoulos, F. K. (**1993**). ''Time-domain modeling of a nonlinear, active model of the cochlea,'' in *Biophysics of Hair-cell Systems*, edited by H. Duifhuis, J. W. Horst, P. van Dijk, and S. M. van Netten (World Scientific, Singapore), pp. 330–337.

Harris, F. P., Lonsbury-Martin, B. L., Stagner, B. B., Coats, A. C., and Martin, G. K. (**1988**). ''Acoustic distortion products in humans: Systematic changes in amplitude as a function of $f2/f1$ ratio,'' J. Acoust. Soc. Am. **85,** 220–229.

Kanis, L. J. (**1995**). ''Cochlear nonlinearity: A computational model of the cochlea solved in the frequency domain,'' doctoral dissertation, University of Amsterdam (available from the author).

Kanis, L. J., and de Boer, E. (**1993**). ''Self-suppression in a locally active nonlinear model of the cochlea: A quasilinear approach,'' J. Acoust. Soc. Am. **94,** 3199–3206.

Kanis, L. J., and de Boer, E. (**1994**). ''Two-tone suppression in a locally active nonlinear model of the cochlea,'' J. Acoust. Soc. Am. **96,** 2156–2165.

Kanis, L. J., and de Boer, E. (**1996**). ''Comparing frequency-domain with time-domain solutions for a locally active nonlinear model of the cochlea,'' J. Acoust. Soc. Am. **100**, 2543–2546.

Kim, D. O. (**1980**). ''Cochlear mechanics: Implications of electrophysiological and acoustical observations,'' Hear. Res. **2**, 297–317.

Lonsbury-Martin, B. L., Martin, G. K., Probst, R., and Coats, A. C. (**1987**). ''Acoustic distortion products in rabbit ear canal. I. Basic features and physiological vulnerability,'' Hear. Res. **28**, 173—189.

Matthews, J. W. , and Molanar, C. E. (**1986**). ''Modeling intracochlear and ear canal distortion product $(2f_1 - f_2)$,'' in *Peripheral Auditory Mechanisms*, edited by J. B. Allen, J. L. Hall, A. Hubbard, S. T. Neely, and A. Tubis (Springer-Verlag, Berlin), pp. 258–265.

Neely, S. T. (**1993**). ''A model of cochlear mechanics with outer hair cell motility,'' J. Acoust. Soc. Am. **94,** 137–146.

Neely, S. T., and Kim, D. O. (**1986**). ''A model for active elements in cochlear biomechanics,'' J. Acoust. Soc. Am. **79,** 1472–1480.

Neely, S. T., and Stover, L. J. (**1993**). ''Otoacoustic emissions from a nonlinear, active model of cochlear mechanics,'' in *Biophysics of Hair Cell Sensory Systems*, edited by H. Duifhuis, J. W. Horst, P. van Dijk, and S. M. van Netten (World Scientific, Singapore), pp. 64–70.

Whitehead, M. L., Lonsbury-Martin, B. L., and Martin, G. K. (**1992**). ''Evidence for two discrete sources of $2f1\text{-}f2$ distortion-product otoacoustic emission in rabbit: I. Differential dependence on stimulus parameters,'' J. Acoust. Soc. Am. **91,** 1587–1607.

Wilson, J. P. (**1980**). ''The combination tone, $2f1\text{-}f2$, in psychophysics and ear canal recording,'' in *Psychophysical, Physiological and Behavioural Studies in Hearing*, edited by G. van den Brink and F. A. Bilsen (Delft U.P., Delft), pp. 43–50.

The middle ear of a lion: Comparison of structure and function to domestic cat

Gregory T. Huang, John J. Rosowski, Deborah T. Flandermeyer, Thomas J. Lynch III,[a] and William T. Peake

Eaton–Peabody Laboratory of Auditory Physiology, Massachusetts Eye and Ear Infirmary, Boston, Massachusetts 02114 and Research Laboratory of Electronics, Massachusetts Institute of Technology, Cambridge, Massachusetts 02139

(Received 21 June 1996; accepted for publication 5 November 1996)

Acoustic and anatomical measurements were made on the middle ear of a deceased lion and compared with measurements from the domestic cat. The acoustic input impedance and sound-transmission ratios measured in the two species have similar features but differ quantitatively. Three-dimensional anatomical reconstructions show that the middle-ear structures of the lion and cat are similarly arranged but have large differences in absolute and relative size. In all felids, a bony septum divides the middle-ear air space into two cavities that are coupled through a small opening. A six-element analog-circuit model based on this distinctive structure captures the main features of both sets of middle-ear frequency responses, except at high frequencies. The element values are consistent with the structural dimensions of the cavities. The results suggest that quantitative measures of middle-ear cavity structure could allow prediction of frequency-dependent features of acoustic sensitivity for the entire cat family. [S0001-4966(97)04303-8]

PACS numbers: 43.64.Ha, 43.64.Tk, 43.80.Lb [RDF]

INTRODUCTION

A goal of auditory physiology is to relate the middle ear's structure to its signal-processing function. Here, we focus on the cat family (*Felidae*) as a group that is qualitatively similar in structure and spans a large size range. The middle ear of one species, domestic cat (*Felis silvestris catus*—Wozencraft, 1993), has been studied extensively (e.g., Møller, 1965; Guinan and Peake, 1967; Dallos, 1970; Nedzelnitsky, 1980; Lynch *et al.*, 1982; Rosowski *et al.*, 1986; Funnell *et al.*, 1987, 1992; Decraemer *et al.*, 1989, 1990, 1991; Puria, 1991; Lynch *et al.*, 1994). In this paper, we report acoustic and anatomical measurements made on the ear of a much larger species, a lion (*Panthera leo*), and compare them to the measurements from domestic cat.

In Fig. 1, middle-ear configuration and size can be compared between lion and domestic cat. Although the sizes differ—the linear dimensions of the lion's ear are roughly twice those of the cat's ear—the middle ears have common structural features. In all felids, a bony septum divides the middle-ear air space into two distinct regions (the tympanic cavity and the bullar cavity) that are connected through a narrow opening (the foramen) between the septum and the petrous bone. A bony septum is present in nearly all species of the superfamily *Feloidia*, composed of the cat, hyena, civet, and mongoose families (Wozencraft, 1989, p. 508). A quantitative model, previously formulated for cat, relates this distinctive cavity structure to measures of function such as middle-ear acoustic impedances (Peake and Guinan, 1967; Lynch, 1981; Peake *et al.*, 1992).

The middle-ear input impedance Z_{TM}, the ratio of the sound pressure in the ear canal just lateral to the tympanic membrane (P_{TM}) to the volume velocity of the tympanic membrane (U_{TM}), affects the sound pressure in the ear canal and the transfer of acoustic power into the ear (Rosowski *et al.*, 1986; Voss and Allen, 1994; Stinson and Khanna, 1994). For ears from diverse mammalian taxa (e.g., guinea pig, cat, and human), Z_{TM} has been interpreted as the sum of two components: (1) Z_{TOC}, the impedance of the tympanic membrane, ossicles, and cochlea, and (2) Z_{CAV}, the impedance of the middle-ear cavities (Onchi, 1961; Zwislocki, 1962; Mundie, 1963; Møller, 1965). This ''series-network'' model [Fig. 2(A)] represents some features of the middle ear's acoustic function; for instance, the fraction of the ear-canal sound pressure that drives the ossicular chain, $(P_{TM} - P_{TC})/P_{TM}$, is equal to $Z_{TOC}/(Z_{TOC} + Z_{CAV})$.

For domestic cat, an analog network for the middle-ear cavities (Z_{CAV}) consists of four lumped elements that are associated with specific structures [Fig. 2(B)]. Measurements of cavity impedance for stimulus frequencies between 0.01 and 10 kHz are consistent with this model (Lynch, 1981; Peake *et al.*, 1992). Our hypothesis is that the circuit topology applies to all species of felids, as their middle ears are similar in structure. In this paper, we test the model over a large size range with measurements made on the ears of a lion and a cat.

The goals of the paper are: (1) to show that qualitatively similar middle-ear structure is associated with qualitatively similar acoustic measurements in a lion and a cat; (2) to represent the acoustic measurements made in both specimens with a lumped-network model; and (3) to relate the model's element values to ear dimensions where possible. The results are a first step toward relating middle-ear size and structure to acoustic function across the cat family.

[a]Current address: BBN Systems and Technologies, 150 Cambridge Park Drive, Cambridge, MA 02140.

I. METHODS

A. Experimental specimens

The lion (''Reggie'') was a large male that died at the Franklin Park Zoo in Boston, MA on 4 September 1992. We acquired the frozen head (skull length 375 mm)[1] on 17 May 1994 and kept it frozen until a few days before the initial acoustic measurements on 3 August 1994. All lion measurements reported, acoustic and anatomical, were made on this head.

The data for domestic cat are from two average-sized specimens. Acoustic and anatomical measurements similar to those made on lion were made on one anesthetized cat (''53L,'' with skull length 86.8 mm) by Lynch (1981). All acoustic data reported here and the structure-based values for cat (in Table II) are from this animal. More detailed anatomical measurements were available from histological sections of the temporal bone of another cat (''H,'' whose middle-ear cavities are reconstructed in Fig. 6). The data in Table I include measurements from both of these animals, as well as the means and standard deviations of measurements on other specimens.

B. Anatomical techniques

1. Lion

Measurements of ear dimensions were made (1) from serial computerized tomography (CT) scans of the frozen head made before the acoustic measurements, (2) from the head during the acoustic measurements, and (3) from the cleaned skull after completion of the acoustic measurements.

The CT scans were performed on 20 June 1994 with the Siemens Somatome Plus scanner at the Massachusetts Eye and Ear Infirmary. The frozen head was placed on the stepping table of the scanner such that each scan produced a coronal section. The resolution of the scans within each section was about 0.2 mm. A sequence of scans, generated with the table advanced 1 mm between scans, indicated large, well-aerated middle-ear cavities on both sides of the head. Ice was discernible in the cochleas and the epitympanic portions of the tympanic cavities on both sides.

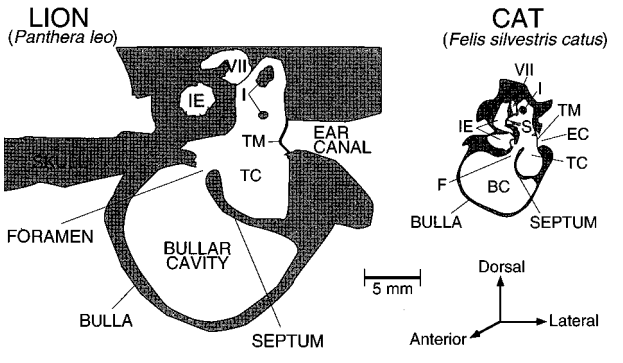

FIG. 1. Coronal sections through the middle ear of a lion and a domestic cat. The lion section was traced from a CT scan. For the cat, a histological section was used. Dark shading is bone, medium shading is fluid or soft tissue, and white is air-filled space. Abbreviations: TM—tympanic membrane; TC—tympanic cavity; I—incus; S—stapes; VII—7th nerve; F—foramen between the tympanic and bullar cavities; IE—inner ear. These sections were chosen to include both the foramen and the TM; in both specimens, the posterior regions of the TM and bony ear canal appear, so that their dorsoventral extent is smaller than it is at more anterior locations. (The 3-D orientation of the TM is not captured here; e.g., see Stinson and Khanna, 1989.)

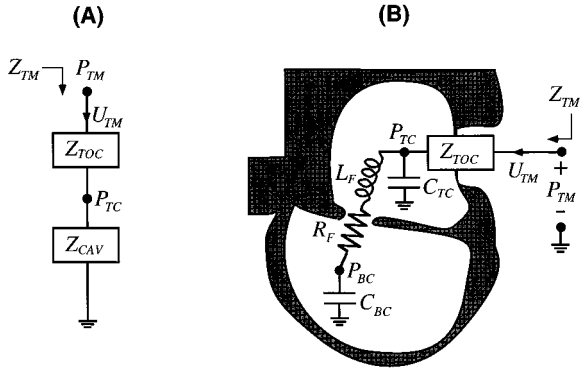

FIG. 2. (A) Series-network model for a mammalian middle ear. Acoustic variables are analogous to electric variables: Z_{TOC} is the impedance of the TM, ossicles, and cochlea; Z_{CAV} is the impedance of the cavity air spaces. Sound pressures are analogous to node voltages: P_{TM} is the sound pressure in the ear canal just lateral to the TM; P_{TC} is the sound pressure in the tympanic cavity. U_{TM} is the volume velocity of the TM (analogous to current). (B) Analog-circuit model for a felid middle ear. The superposed schematized middle-ear section shows the structural basis for the model. Z_{CAV} is made up of four lumped elements— C_{TC} (acoustic compliance of the tympanic cavity), C_{BC} (acoustic compliance of the bullar cavity), L_F (acoustic mass of the foramen), and R_F (acoustic resistance of the foramen). P_{BC} is the sound pressure in the bullar cavity.

Each scan was stored, and 53 photographic ''blow-ups'' of the left middle ear were generated. From these photographs, outlines were traced of the structures of interest (Fig. 1)—the ear canal, the tympanic membrane (TM), the ossicles, the tympanic cavity, the bullar cavity, the foramen, and the inner-ear fluid spaces—to describe the configuration of each middle-ear region within each scan. Three ''registration'' (reference) points with fixed positions on the scans were marked on each tracing.

The middle-ear air space was classified into three regions: (1) The tympanic cavity was defined as the region dorsal, anterior, and lateral to the septum, bounded by the septum, the TM, the ectotympanic bone, and the petrous bone. (2) The bullar cavity was defined as the region ventral, posterior, and medial to the septum, bounded by the septum, the petrous bone, and the endotympanic bone. (3) The foramen, defined only in sections in which the cavities were connected through a space between the dorsal edge of the septum and the petrous bone, consisted of one region, narrow in its latero-medial extent and extending from the round window anteriorly. For scans in which the septum was orthogonal to the plane of section (e.g., Fig. 1), the foramen boundaries were unambiguous. In other scans, however, the foramen boundary was somewhat arbitrary. This uncertainty has little effect on the computed volumes of the two cavities (as the foramen is relatively small) but can play a role in comparisons between lion and cat of the foramen's dimensions and its acoustic function.

The tracings and registration points were digitized manually using a data tablet. Standard computerized planimetry equations were used to determine the area of each region in each section. The volumes of the different middle-ear re-

TABLE I. Comparison of ear-canal and middle-ear dimensions in lion and cat. Unattributed entries come from this report. The unlabeled lion entries were computed from CT-scan sections of the left ear as described in the text (Sec. I B); lion volume measurements labeled V are the results of space-filling measurements made on the right ear (the ear used in acoustic measurements). Most of the anatomical data for cat are from *in vivo* measurements made in 12 ears used in physiological measurements (Lynch, 1981; Lynch *et al.*, 1994). This database yields an estimate of the anatomical variance within *catus*; each entry represents either an estimate from an individual ear (H or 53L), a mean, or a mean plus and minus a standard deviation. The lion/cat ratios use mean data wherever possible; for instance, the volume ratios use the mean of the two estimates of the lion volumes to define the numerator. The ''effective'' foramen dimensions represent estimates of the length and radius of the narrowest part of the foramen. The foramen dimensions for 53L were measured in its dried skull.

Ear dimensions	Lion	Cat	Lion/Cat
Bony ear canal length (mm)	10.9	3.8±1.2 (Lynch, 1981; $n = 12$) 3.7 (53L)	2.9
Bony ear canal radius (mm)	3.3	2.3±0.2 (Lynch, 1981; $n = 12$) 2.3 (53L)	1.4
Bullar cavity volume (cm^3)	16.7 15.0 (V)	0.68±0.13 (Lynch, 1981, and H; $n = 13$) 0.66 (H) 0.78 (53L)	23.3
Tympanic cavity volume (cm^3)	3.3 2.8 (V)	0.22±0.05 (Lynch, 1981, and H; $n = 13$) 0.24 (H) 0.25 (53L)	13.9
Foramen volume (cm^3)	0.1	0.017 (H)	5.9
Total middle-ear volume (cm^3)	20.1 17.9 (V)	0.89±0.16 (Lynch, 1981, and H; $n = 13$) 0.92 (H) 1.03 (53L)	21.3
Effective foramen length (mm)	1.5	3.8 (H) 2 (53L)	0.52
Effective foramen radius (mm)	3.7	1.25 (H) 1.5 (53L)	2.7
Footplate area (mm^2)	5.3 3.76 (Hemilä *et al.*, 1995)	1.25 (Lynch *et al.*, 1982)	3.6
Tympanic ring area (mm^2)	120	40.3 (Wever and Lawrence, 1954; $n = 16$)	3.0

gions were then calculated as the sum of volumes of the 1-mm-thick sections with areas equal to the region areas. We estimate that this ''stacked coin'' approximation is accurate within 10%. To aid in visualizing the spatial arrangement of the cavities and the foramen, reconstructions of the middle ear were made with MacReco® software from the digitized contours (Fig. 6).

Although the TM was not clearly resolved in all of the CT scans, we estimated the area of the bony ring that supports the TM from lines drawn between the medial edges of the ear canal. The scans showed a clear bony rim at the anteroventral edge of the tympanic ring; the posterodorsal edge of the ring was less clearly defined. Estimates of the ear-canal diameter and the lengths of the ossicles were made directly from the drawings of the scans.

After completion of the physiological measurements, the skull was cleaned at the Harvard University Museum of Comparative Zoology. Measurements were then made of middle-ear cavity volumes with wax used to close off the foramina that enter the middle-ear cavities and the foramen between the cavities plugged with masking tape. To measure the bullar-cavity volume, the air space was filled with plasticine; the plasticine was then removed and submerged in water in a graduated cylinder and the displaced volume measured. With the plasticine in the bullar cavity, the tympanic cavity volume was measured by water-filling from a calibrated syringe. These measurements were each made twice with repeatability within 5%.

2. Cat

The spatial arrangement of the foramen and the tympanic and bullar cavities was investigated by three-dimensional reconstruction of the air spaces from histological sections of one middle ear. After an experiment, the cat (H) was perfused with formalin saline. The ears were removed and embedded in celloidin (Schuknecht, 1974, p. 6). Registration holes were drilled into the celloidin block parallel to the long axis of the bulla. Twenty-micron sections were cut orthogonal to the long axis. Every tenth section was then stained

with hematoxylin and eosin and mounted on a slide. The sections were projected, and tracings were drawn of the TM, ossicles, inner ear, and middle-ear air spaces. The tracings were then digitized, analyzed, and reconstructed using the techniques described above for the lion.

Water-filling volumetric measurements of the middle-ear cavities of 12 anesthetized cats were performed by Lynch (1981) during measurements of input impedance and cavity sound pressures. A hole 3–4 mm in diameter was opened in the posterior wall of the auditory bulla just medial to the foramen, and the foramen was plugged with silicone grease. The head was oriented such that the hole was the highest point on the bulla, and a calibrated syringe was used to fill the bullar cavity with water. Care was taken to avoid entrapment of air bubbles in the cavity. The bullar cavity was then drained and dried using low-pressure suction. The volume of the tympanic cavity was estimated by filling the cavity with water via a small hole in the anterior-cavity wall (used to insert a microphone into the cavity) with the foramen plugged. The filling procedure was carefully monitored through the nearly transparent TM. After filling, the foramen was opened and the cavity dried before repeating the procedure. Measurements were generally performed three times; the results are in Table I. Anatomical data in Table I are also given for the individual (53L) in which a set of acoustic measurements similar to those for lion were made.

C. Acoustic measurements in lion

While the lion head thawed, it was skinned and muscles were removed to expose the auditory bullae.[2] A small hole (diameter approximately 1 mm) was drilled through the posteroventral portion of the bulla to prevent the buildup of static pressure. The pinna and cartilaginous ear canal on the right side were resected near the lateral end of the bony external ear canal. A washer was cemented to the entrance of the canal to enable reproducible coupling of the sound source (Rosowski *et al.*, 1990). Care was taken to seal the source tightly into the ear canal with acoustic putty.

The sound system consisted of an earphone (Beyerdynamic DT48, Germany) and a hearing-aid microphone (Knowles Electronics EK-3027, Elk Grove, IL) with a probe tube. This system, used to stimulate the ear acoustically and to measure the acoustic impedance in the ear canal, is similar to the ''large'' high-frequency sound source described by Ravicz *et al.* (1992), but the coupling tube is larger (inner diameter 4 mm) to couple to the lion's ear canal. Sound pressures in the middle-ear cavities were measured with a separate microphone (Knowles EK-3027) attached to a probe tube (of length 20 mm and inner diameter 1 mm). The bullar-cavity sound pressure was measured with the microphone's probe tube inserted to a depth of 8.5 mm through a hole drilled in the bulla.[3] Sound-pressure measurements were made also with this microphone sealed into the tympanic cavity through a small hole drilled in the septum.

Relative calibrations of the cavity microphone and the ear-canal microphone were performed before, during, and after experimental sessions. The impedance-measurement system was sealed in a short open-ended cylinder, and the cavity probe was introduced into the cylinder via the other end. The two probe tips were brought within 2 mm of one another, and the cylinder was sealed with plasticine. The earphone then generated a sound pressure of approximately 100 dB SPL, and the two microphone responses were compared. The ratio of the magnitudes of the output voltages was roughly 3 dB for frequencies below 1 kHz and as large as 12 dB at higher frequencies. The ratios of the sound pressures in the middle-ear cavities to the sound pressure in the ear canal (Secs. II B, C) were scaled by this factor to account for differences between the microphones.

Stimuli were generated and electric responses measured by an Ariel DSP-16+ board and SYSID (Ariel) software (e.g., Voss and Allen, 1994). Broadband chirps were digitally generated and played out via a digital-to-analog convertor at 50 000 samples per second. The analog signal was attenuated and fed into a power amplifier that drove the earphone. The sound pressures generated in the lion's ear canal were 60–100 dB SPL, which was in the linear range of the earphone and the microphone. Simultaneous measurements were made of the amplified microphone voltages via two analog-to-digital convertors. The analog input and output signals were low-pass filtered to prevent aliasing. The DSP-16+ board averaged the responses to multiple stimuli. The PC processor then computed a scaled transfer function (relating the output and input voltages) containing 1024 frequency components with a spacing of 24.4 Hz.

D. Measurement of acoustic impedance

The acoustic source was characterized by a Norton equivalent circuit consisting of a volume velocity source U_S in parallel with a source impedance Z_S (Rabinowitz, 1981; Rosowski *et al.*, 1984; Ravicz *et al.*, 1992; Lynch *et al.*, 1994). The source parameters were inferred from sound-pressure measurements in two reference loads: an open tube of inner diameter 4.1 mm and length 10 m (assumed to be functionally infinite), and a small cylindrical cavity of inner diameter 4 mm and length 0.139 mm.

For an unknown acoustic load, the pressure P_L produced by the source in the load was measured and the impedance Z_L calculated as

$$Z_L = \frac{1}{(U_S/P_L) - (1/Z_S)}. \tag{1}$$

The measurement system was tested on acoustic loads of theoretically known impedance. A representative comparison of measurement and theory is shown in Fig. 3 for a rigid, closed cylindrical cavity. The theoretical impedance was calculated with a lossy transmission line model (Egolf, 1977; White *et al.*, 1980; Keefe, 1984; Allen, 1986; Zuercher *et al.*, 1988). Impedance measurements of this cavity on different days varied less than 10% in magnitude and 0.03 periods in angle.

For frequencies above 0.1 kHz, the measured impedance in Fig. 3 captures the low-frequency magnitude and slope, as well as the frequencies and shapes of the first three pairs of resonances and antiresonances.[4] In the frequency range 0.1–16 kHz, the measured impedance is within 20% of the theoretical curve in magnitude and 0.04 periods in angle ex-

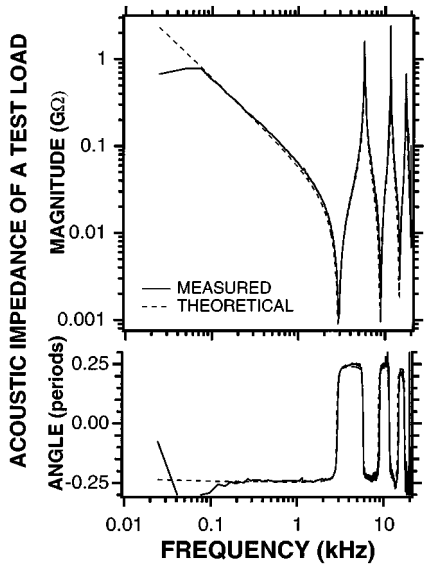

FIG. 3. Test of the impedance-measurement system. The test load is a closed cylindrical tube of inner diameter 3.9 mm and length 29.44 mm; the low-frequency compliancelike impedance is similar to that of the lion's middle ear. Phase angles are plotted in periods (1 period$=2\pi$ radians).

cept near the frequencies of the extrema, where errors are larger. Near these frequencies, inaccuracies in the theoretical impedance (produced by small errors in length, for instance) can result in large differences between the theoretical and measured impedances.

For frequencies below 0.1 kHz (Fig. 3), the load-impedance magnitude is greater than the source-impedance magnitude. With these impedances in parallel, the measured sound pressure becomes insensitive to changes in the load impedance, and small errors in P_L, Z_S, or U_S result in large errors in the estimated Z_L (Lynch *et al.*, 1994). At high frequencies, measurement accuracy is limited by the earphone-output level and the microphone sensitivity, which makes the microphone output noisy above 16 kHz. Hence, we restrict our report of input-impedance measurements in the lion to frequencies between 0.1 and 16 kHz. For this frequency range, the general size of errors illustrated in Fig. 3 is applicable to measurements made on the lion's ear, as the impedances measured in the specimen are within the range of impedances measured with the test load.

E. Correction for the ear-canal space

The desired measurements were the sound pressure P_{TM} and the acoustic impedance Z_{TM} in the ear canal just lateral to the TM. However, because some stiff cartilaginous ear canal remained in the lion, the microphone probe tip was a few centimeters lateral to the TM. To correct for the difference in location, a lossless cylindrical-tube model of the residual ear canal was employed (Møller, 1965; Rabinowitz, 1981; Lynch *et al.*, 1994), so that:

$$Z_{\mathrm{TM}}=Z_0\frac{Z_{\mathrm{MEAS}}-jZ_0\tan(kl)}{Z_0-jZ_{\mathrm{MEAS}}\tan(kl)} \tag{2}$$

and

$$P_{\mathrm{TM}}=\frac{P_{\mathrm{MEAS}}\ Z_{\mathrm{TM}}}{Z_{\mathrm{TM}}\cos(kl)+jZ_0\sin(kl)}, \tag{3}$$

where Z_{MEAS} and P_{MEAS} are the impedance and sound pressure measured at the probe tip; $Z_0=\rho_0 c/(\pi a^2)$ is the characteristic impedance of the tube, l is the length of the tube, a is the radius of the tube, $k=2\pi f/c$ is the wave number, ρ_0 is the density of air, c is the sound-propagation velocity in air, f is the frequency, and $j=\sqrt{-1}$.

The dimensions of the model tube were determined from a combination of acoustic and anatomical measurements. The tube length, $l=25$ mm, was chosen to match the frequencies of sharp maxima and minima in the impedance magnitude measured with the tympanic cavity filled with saline and sealed with acoustic putty (rigidifying the TM as much as possible). A ''residual'' ear-canal volume measurement from saline filling (0.41 cm^3) was then used to determine the model tube's radius $a=2.3$ mm. These dimensions are consistent with estimates of the length and diameter of the remaining ear canal made from the CT scans and the head.

The effects of the ear-canal correction on the measured impedance are shown in Fig. 4. The most dramatic effect is near the frequency (3.4 kHz) at which the model-tube length is equal to a quarter wavelength. There, the residual ear canal acts as a quarter-wave transformer, converting a pressure maximum at the TM to a pressure minimum at the microphone's location.[5] That is, the impedance-magnitude minimum at 2.7 kHz measured at the ear-canal entrance is the transformation of an impedance-magnitude local *maximum* at the TM (an antiresonance due to the middle-ear cavities, not the ear canal).

The presence and frequency of the inferred-impedance maximum at the TM are not particularly sensitive to the ear-canal model parameters. Variations of 20% in the tube length result in shifts of less than 10% in both the frequency and the magnitude of the impedance maximum at 2.7 kHz. Variations of 10% in the tube radius result in shifts of less than 40% in the magnitude of the impedance peak and no shift in the corresponding frequency.

Because of the irregular geometry of the ear-canal space, the correction is less accurate at high frequencies; here, we quantify the error. For frequencies up to 4 kHz, the impedance measurement made with the TM stiffened could be fit to within 2 dB in magnitude and 0.05 periods in angle by the model tube with a resistive termination (0.14 GΩ). For higher frequencies, there was less quantitative agreement but some qualitative agreement, e.g., maxima and minima at roughly the correct frequencies.

For frequencies below 0.8 kHz, the impedance at the TM shows the expected increase that results from removal of the residual ear-canal compliance; the ratio of the corrected-to-measured impedance magnitudes is fairly constant, and the angles differ by less than 0.02 periods (Fig. 4). The measured equivalent air volume (at low frequencies) is 1.6 cm^3, whereas the (corrected) equivalent air volume at the TM is approximately 1.2 cm^3.[6] The volume of the ear canal accounts for the difference. All measurements in the lion

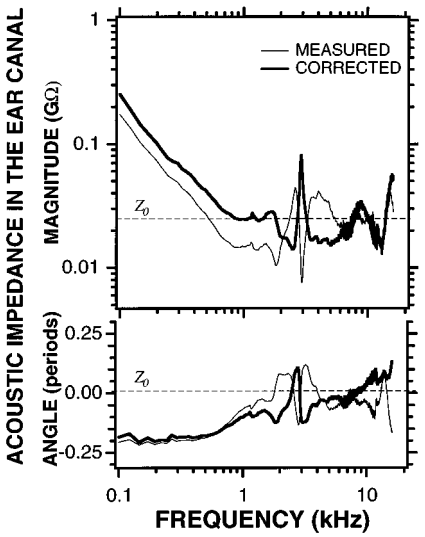

FIG. 4. The effect of the ear-canal coupling space on the middle-ear input impedance of the lion. The ''measured'' impedance (thin line) was obtained with the probe located a few centimeters lateral to the TM. The ''corrected'' impedance at the TM (thick line) was calculated by approximating the residual ear-canal space by a lossless uniform tube of length 25 mm and radius 2.3 mm. Below 0.8 kHz, the tube acts as a compliance in parallel with Z_{TM}. Near the tube's quarter-wave frequency, the measured minimum in impedance magnitude (at 2.7 kHz) is transformed into a maximum at the TM. The dashed line is the characteristic impedance Z_0 of the tube.

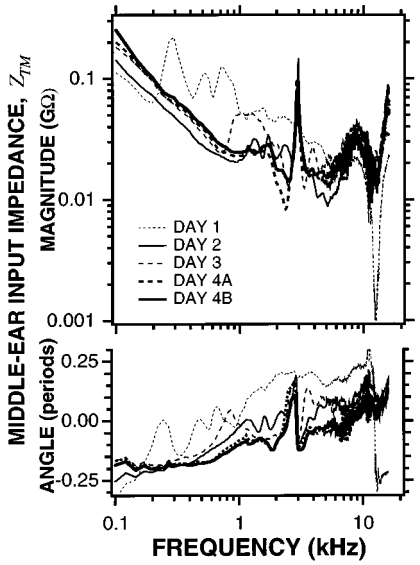

FIG. 5. Lion middle-ear input impedances (Z_{TM}) measured on four different days (spanning nine days). Impedances measured on days 2–4 are approximately compliant at low frequencies, roughly resistive at high frequencies, and contain sharp local changes at 2.7 kHz. Curves 4A and 4B were measured $5\frac{1}{2}$ h apart, before and after the middle-ear cavities were manipulated (Fig. 8).

reported below are corrected for the ear-canal space using the values $l=25$ mm and $a=2.3$ mm.

F. Stability of impedance measurements

Acoustic input-impedance measurements made on the lion's ear on four separate days (spanning a period of nine days) are shown in Fig. 5. On each day the source was recalibrated and tested on known acoustic loads. For frequencies below 0.7 kHz, the impedances on days 2–4 are compliance dominated with equivalent volumes in the range 1.1–1.6 cm^3 and angles close to -0.2 periods. In the frequency ranges 1.0–1.8 kHz and 3.6–5.0 kHz, the impedances are more nearly resistive, in that the magnitudes level off near 0.02 GΩ and the angles are between -0.1 and 0.1 periods. The impedances have a pronounced local maximum in magnitude and an angle shift of roughly 0.25 periods at 2.7 kHz ($\pm 5\%$), which is consistent with an antiresonance. Above 5 kHz, all curves have similar variations with frequency.

The impedance measured on day 1 is significantly different from the rest. It is not clearly compliance dominated at low frequencies; below 0.2 kHz, the slope of the magnitude is compliancelike, but the angle varies with frequency. In the range 0.2–2.0 kHz, the impedance is two to three times higher in magnitude than the other measurements and fluctuates about 0.1 GΩ, while the angle varies by as much as 0.25 periods. The local maximum in impedance magnitude near 2.7 kHz observed on all subsequent days is not present, whereas an impedance-magnitude minimum at 13 kHz is much more dramatic than in later measurements. The aberrant data from day 1 could result from incomplete thawing in the specimen; for frequencies between 0.2 and 2 kHz, the increased impedance magnitude is consistent with a partially frozen (and hence stiffer) TM and ligaments.

Over subsequent days, the data are clearly more stable. The acoustic measurements in Sec. II were made on day 4, during the $5\frac{1}{2}$ h separating measurements 4A and 4B in Fig. 5. In that interval, middle-ear structures were manipulated (see Sec. II C). The intact configuration was then approximated by clearing the foramen of visible obstructions, sealing the bulla hole with plasticine, and sealing the small septum holes (for microphone and vent insertion) with petrolatum. The impedance measured in this reconstituted ''intact'' configuration (curve 4B) is similar to the earlier intact measurements.

II. RESULTS

A. Structural comparison of lion and cat middle ears

The configurations of the middle-ear cavities of lion and cat are compared in Fig. 6. The tympanic cavity is generally dorsal and lateral to the anterior portion of the bullar cavity [Fig. 6(A) and (B)]. The ventral protrusion of the bullar cavity, a prominent feature of the felid skull (Jayne, 1898), is seen in both species. The foramen connecting the tympanic and bullar cavities is posterior and ventral to the tympanic cavity and generally dorsal to the bullar cavity. The linear dimensions of the lion's cavities are between two and three times those of the cat's cavities.

The total middle-ear air volume of the lion is about 20 times that of cat (Table I). Much of the interspecies difference in total volume is due to the bullar cavity in lion; the tympanic-cavity volume in lion is only about 14 times larger than in cat. In both species, the bullar air volume is much larger than the tympanic air volume; the ratio of bullar- to tympanic-cavity volumes is 5.2 in lion and 3.1 in cat.

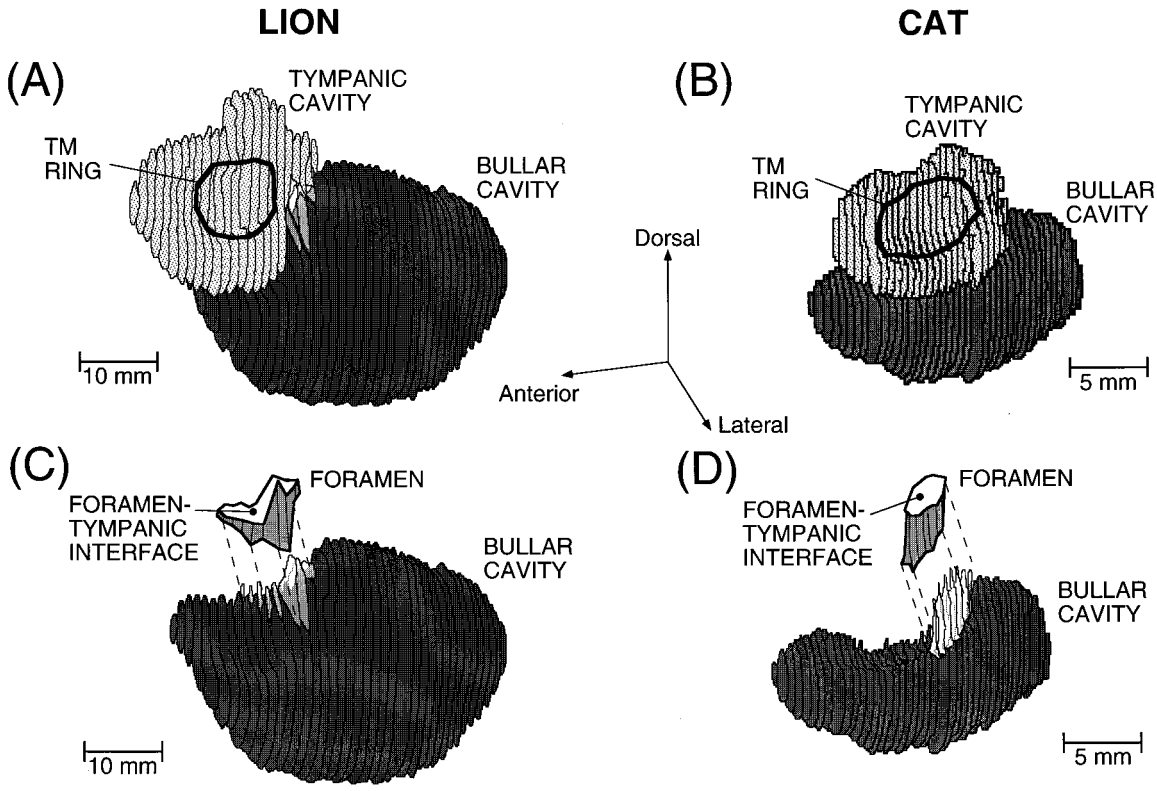

FIG. 6. Reconstruction of the middle-ear air spaces of left ears of a lion and a cat. The lion reconstruction is based on serial CT scans done at 1-mm spacing; the cat's air spaces are reconstructed from serial histological sections that are 400-μm apart. Note the difference in scale: The cat reconstructions are magnified by a factor of 2 relative to the lion reconstructions. (A) and (B) show the arrangement of the tympanic (lighter shading) and bullar (darker shading) air spaces as seen from a point anterior and lateral to the ear. The tympanic ring is shown in each ear. Most of the foramen that connects the two cavities is hidden behind the tympanic cavity. A small section of the lion's foramen (with transparent shading that alters the color of the bullar cavity seen through it) is visible posterior to the tympanic cavity in (A). (C) and (D) show the connection of the foramen to the bullar cavity, with the tympanic cavity ''removed.'' Two views of each foramen are shown. The lower view shows sections through the foramen adjacent to the bullar cavity. The foramen sections are outlined in black and colored with a ''transparent'' white that allows the colors behind each section to show through. The upper (''exploded'') view is a volume representation of the displaced foramen, showing the size and shape of the foramen–tympanic interface.

Two views of the foramen between the tympanic and bullar cavities are shown in Fig. 6(C) and (D) (with the tympanic cavity ''removed''): The lower view shows the sections of each foramen attached to the bullar-cavity sections. The upper (displaced) view is a volumetric reconstruction that identifies the foramen-tympanic interface. The foramen's shape differs between the two species, appearing relatively longer (from tympanic cavity to bullar cavity) and narrower in the cat. Estimation of the foramen's dimensions is complicated by its irregular shape; for acoustic-modeling purposes, the foramen is approximated by a short uniform tube of much smaller volume than the cavity volumes. Estimates of the dimensions of the narrowest portion of the foramen (assumed to play a significant role in determining its acoustic properties) were made from the scan tracings and termed ''effective'' dimensions (Table I). While the measurements suggest that the effective radius of the lion's foramen is 2.7 times that of cat, the foramen's effective length is the one measure in which the lion's ear is *smaller* than the cat's ear.

Table I compares the dimensions of other middle-ear structures. The bony ear-canal dimensions of lion are 1.4–2.9 times larger than those in cat, with the largest difference in the length of the canal. The bony ear-canal volumes estimated from these dimensions are 0.063 cm^3 and 0.34 cm^3 for cat and lion, respectively. While this volume yields a good approximation of the coupling volume between the sound source and the TM in cat (Lynch *et al.*, 1994), it underestimates the coupling space in the lion. The underestimation results because a very-stiff-walled terminal portion of the lion's cartilaginous ear canal (roughly of length 10 mm and inner diameter 4 mm) remained in place during the acoustic measurements. Thus, the total ear-canal coupling space in the lion is about 20 mm in length with a volume of 0.47 cm^3, which compares well with our acoustic measurements of ear-canal length (25 mm) and the water-filling measurement of ear-canal volume (0.41 cm^3) (see Sec. I E).

The tympanic rings are outlined on the surface of the tympanic cavities [Fig. 6(A) and (B)] both to aid in orienting the reconstructions spatially and to allow comparison of the relative size of the rings. Estimates of the areas of the lion's tympanic ring and stapes footplate (from the CT sections) can be compared with the respective areas in cat from the literature (Table I): These areas in lion are a factor of 3 larger than those in cat. This area scale factor is significantly smaller than the value (7.4) that would be inferred from the factor-of-20 difference in middle-ear air volumes. Thus, it is

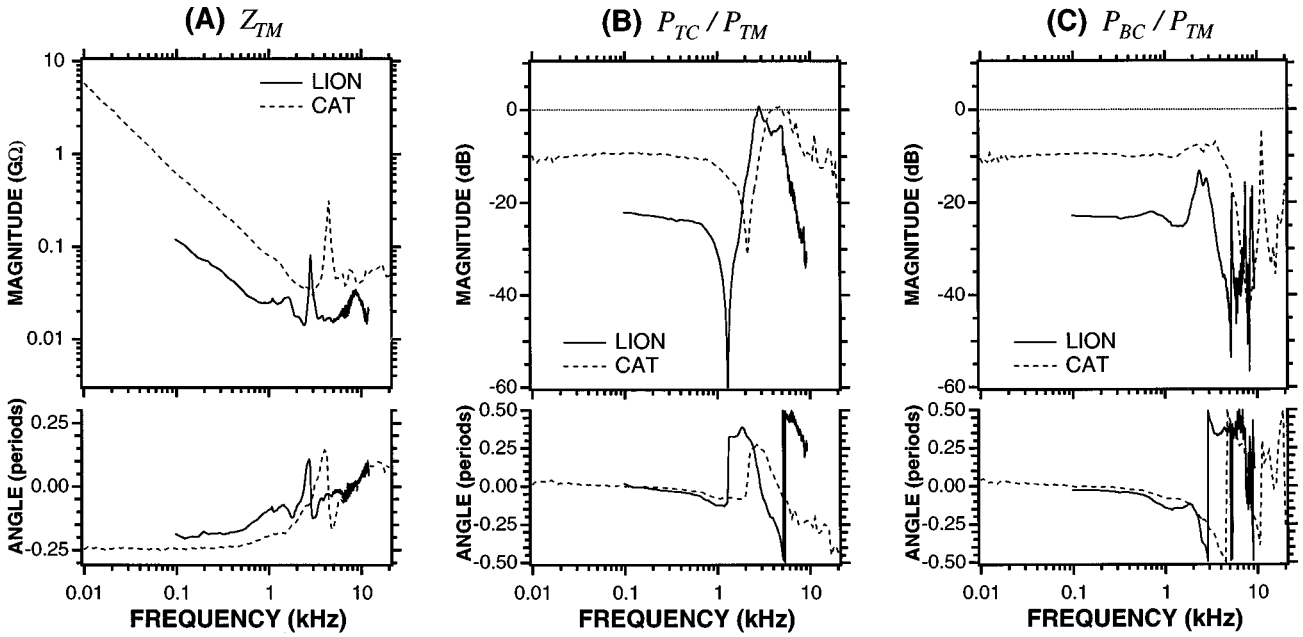

FIG. 7. Comparison of acoustic measurements made in a lion and a cat with the middle ears intact: (A) the middle-ear input impedance (Z_{TM}), (B) the ratio of sound pressure in the tympanic cavity to sound pressure at the TM (P_{TC}/P_{TM}), and (C) the ratio of sound pressure in the bullar cavity to sound pressure at the TM (P_{BC}/P_{TM}). The horizontal dotted line in the pressure-ratio plots is 0 dB. The ''intact'' condition was approximated by sealing the holes in the cavity walls around the microphone probe. Measurements in the cat (53L from Lynch, 1981) extend over a larger frequency range (0.01–20 kHz).

clear that felid middle-ear structures do not all scale similarly with size.[7] However, the ratio of the tympanic-ring area to the footplate area is similar in the two species—26 in the lion and 32 in the cat—which is consistent with observations that this ratio is near 20 in many mammals (Rosowski, 1994).[8]

The overall conclusion from the anatomical measurements is that the middle-ear structures of lion and cat are similar in spatial arrangement but have notable differences in both absolute and relative sizes.

B. Acoustic measurements with intact middle-ear cavities

In Fig. 7, acoustic measurements for lion and cat are shown together for comparison. Three sets of data are plotted: (A) middle-ear input impedance (Z_{TM}), (B) the ratio of sound pressure in the tympanic cavity to sound pressure at the TM (P_{TC}/P_{TM}), and (C) the ratio of sound pressure in the bullar cavity to sound pressure at the TM (P_{BC}/P_{TM}).

In each of the three panels, the measurements show clear qualitative similarities between lion and cat. Z_{TM} is compliance dominated at low frequencies and roughly resistive at higher frequencies, with a prominent local maximum in magnitude at an intermediate frequency. $|P_{TC}/P_{TM}|$ is roughly constant at low frequencies, has a prominent minimum that does not correspond to any similar feature in Z_{TM}, and has a maximum (of 0 dB) at a higher frequency corresponding to the local maximum in $|Z_{TM}|$. $|P_{BC}/P_{TM}|$ is essentially equal to $|P_{TC}/P_{TM}|$ at low frequencies and has a maximum at the frequency of the local maximum in $|Z_{TM}|$, a steep rolloff above this frequency, and large fluctuations at higher frequencies.

The acoustic measurements also show notable quantitative differences between lion and cat. In the compliancelike low-frequency region, $|Z_{TM}|$ in cat is nearly four times greater than in lion (equivalent air volumes of 0.3 cm^3 and 1.1 cm^3, respectively), while in the resistancelike high-frequency range it is roughly twice as large. At low frequencies, the pressure-ratio magnitudes $|P_{TC}/P_{TM}|$ and $|P_{BC}/P_{TM}|$ are also greater in cat than in lion. In addition, the transition in the impedance between compliant and resistive behavior occurs at a lower frequency in lion, as does the sharp local maximum in $|Z_{TM}|$. Similarly, the extrema in $|P_{TC}/P_{TM}|$ and $|P_{BC}/P_{TM}|$ occur at lower frequencies in lion than in cat. The general trend is that the frequency dependence of the lion data is qualitatively similar to that of the cat data but is shifted to lower frequencies.

Interpretation of the input-impedance and sound-pressure measurements is organized conceptually by the model of Fig. 2, which predicts that P_{TC}/P_{TM} is equal to $Z_{CAV}/(Z_{TOC}+Z_{CAV})$, or Z_{CAV}/Z_{TM}. In lion, P_{TC}/P_{TM} is small and roughly constant (at about -23 dB with an angle near 0 periods) for frequencies below 0.7 kHz, where Z_{TM} is compliant (Fig. 7). The zero angle and constant magnitude of the pressure ratio imply that Z_{CAV} is also compliant in this region, with $Z_{TM} \approx 14 Z_{CAV}$. The low-frequency P_{TC}/P_{TM} is much greater in cat (approximately constant at -10 dB with an angle near 0 periods), which implies that for low frequencies $Z_{TM} \approx 3 Z_{CAV}$. Thus for low frequencies Z_{CAV} has little influence on Z_{TM} in lion but is a significant part of Z_{TM} in cat. For high frequencies, $|P_{TC}/P_{TM}|$ decreases rapidly, which indicates that $|Z_{CAV}| \ll |Z_{TOC}|$; this result is consistent with the tympanic-cavity compliance C_{TC} approaching a short circuit at high frequencies.

The minima of $|P_{TC}/P_{TM}|$ in Fig. 7 (at 1.25 kHz in lion and 2.1 kHz in cat) are consistent with a series (Helmholtz) resonance between the bullar-cavity compliance C_{BC} and the

foramen mass L_F (see Fig. 2). At these resonant frequencies, $|Z_{CAV}|$ and $|P_{TC}/P_{TM}|$ are minimized, and $Z_{TM} \approx Z_{TOC}$. The sharp local maxima of $|Z_{TM}|$ in Fig. 7 (at 2.7 kHz in lion and 4.4 kHz in cat) are consistent with a parallel antiresonance between the series combination of the bullar- and tympanic-cavity compliances and the mass of the foramen (see Fig. 2). At these antiresonant frequencies, $|Z_{CAV}| \gg |Z_{TOC}|$, and hence $|Z_{TM}|$ is maximized locally and $|P_{TC}/P_{TM}| \approx 1$ (0 dB).

In both lion and cat, $P_{BC}/P_{TM} \approx P_{TC}/P_{TM}$ at low frequencies (Fig. 7), which is consistent with the circuit model (Fig. 2), in which the foramen is effectively a short circuit for these low frequencies. Furthermore, in each specimen: (1) $|P_{BC}/P_{TM}|$ is approximately constant (not minimized) at the frequency of the deep minimum of $|P_{TC}/P_{TM}|$; (2) $|P_{BC}/P_{TM}|$ is maximized (locally, in cat) at the frequency of the parallel antiresonance exhibited by P_{TC}/P_{TM} and Z_{TM} with $\max\{|P_{BC}/P_{TM}|\} < \max\{|P_{TC}/P_{TM}|\}$; the pressure drop across the foramen in the model accounts for the inequality; (3) $|P_{BC}/P_{TM}|$ falls off rapidly for frequencies above its maximum, as the cavity compliance approach short-circuit behavior and most of the decreasing pressure $|P_{TC}|$ is across the foramen.

At high frequencies, for both lion (above 4 kHz) and cat (above 7 kHz), P_{BC} shows large-magnitude fluctuations that are not accounted for in the lumped-circuit model. These features are most likely the result of wave effects in the bullar cavity, as the largest linear dimensions of the bullar cavities are comparable to a wavelength at these frequencies. Lynch (1981) measured large spatial variations in bullar-cavity pressure and impedance at high frequencies, consistent with the notion of standing waves in the cavity. High frequency extrema are also present in P_{TC} for both lion and cat but are less pronounced in the reported frequency range.

In summary: The lumped-circuit model of Fig. 2 is consistent with the qualitatively similar acoustic measurements made in the lion and cat and relates the salient features of the data (e.g., the extrema and the low-frequency behavior) to the middle-ear structures. Quantitative model comparisons are presented in Sec. III C.

C. Acoustic measurements after structural manipulations

1. Lion–cat comparisons

To test the structure–function associations implied by the network model (Fig. 2), acoustic measurements were made after experimental modifications of the middle-ear cavities. Middle-ear input impedance (Z_{TM}) and the sound-pressure ratio P_{TC}/P_{TM} for lion and cat are shown in Fig. 8 for three conditions of the cavities: intact (data from Sec. II B), bulla opened, and foramen plugged.

Qualitatively similar effects are seen in the two species. For low frequencies, opening the bulla decreases $|Z_{TM}|$ somewhat and $|P_{TC}/P_{TM}|$ dramatically. Plugging the foramen (1) increases $|Z_{TM}|$ and $|P_{TC}/P_{TM}|$ at low frequencies and (2) removes the local maxima in $|Z_{TM}|$ and $|P_{TC}/P_{TM}|$ and the deep minimum in $|P_{TC}/P_{TM}|$. Qualitative differences include: (1) the effects of cavity manipulations on the low-frequency impedance are greater in cat than in lion; and (2) opening the bulla affects the local maximum in $|Z_{TM}|$ differently in lion (reduction in magnitude) than in cat (shift in frequency).

2. Lion

The bulla-opened condition was achieved by widening the bulla-vent hole (drilled to equalize static pressure) to a diameter of approximately 18 mm (14.8 mm by 20.8 mm). The foramen-plugged configuration was achieved by inserting strips of vaseline-coated gauze into the foramen with the tympanic cavity vented.

In the bulla-opened configuration, Z_{TM} differs little from the intact case at most frequencies (Fig. 8). For low frequencies, the impedance is compliancelike with a slightly smaller magnitude (by 10%); the compliance corresponds to an equivalent volume of 1.2 cm^3. The local magnitude maximum at 2.7 kHz is much less pronounced but occurs at the same frequency as in the intact case.[9] For higher frequencies, Z_{TM} is approximately unchanged. The bulla-opened P_{TC}/P_{TM} has a magnitude slope of about 40 dB/decade and an angle near 0.45 periods below 0.6 kHz. The great reduction of pressure at low frequencies is consistent with the bullar cavity being opened to the atmosphere; in terms of the network model, the reduced cavity impedance $|Z_{CAV}|$ acts to decrease both $|P_{TC}/P_{TM}|$ and $|Z_{TM}|$. For higher frequencies, $|P_{TC}/P_{TM}|$ shows nonmonotonic behavior, including a maximum (of approximately 0 dB) at 3 kHz. The maximum occurs at the same frequency as the local maximum in $|Z_{TM}|$, as in the intact case. The deep minimum at 1.25 kHz present in the intact case is absent, which supports the interpretation of this feature as a Helmholtz resonance involving the bullar cavity's compliance and the foramen's acoustic mass.

The foramen-plugged Z_{TM} has features that are qualitatively similar to the data from the other structural conditions, with two clear differences: (1) For frequencies below 0.7 kHz, the foramen-plugged Z_{TM} is approximately compliant but is 20%–30% greater in magnitude (equivalent volume 0.9 cm^3) than in the other cases. This result is consistent with the stiffer net air volume that results from the ''removal'' of the bullar-cavity volume. (2) For frequencies above 1 kHz, the foramen-plugged Z_{TM} is within 20% of the other cases in magnitude and 0.08 periods in angle, *except* near 2.7 kHz where there is no comparable local maximum. The absence of the peak supports the interpretation of this feature as a parallel antiresonance involving the acoustic mass of the foramen (and the series combination of the compliances of the bullar and tympanic cavities).

With the foramen plugged, P_{TC}/P_{TM} is greater in magnitude than in the other two cases and roughly constant (-10 dB with an angle near 0 periods), for frequencies below 1 kHz. This increase in the low-frequency pressure ratio is consistent with a higher cavity impedance (due to the blocking of the bullar cavity branch), which leads to a higher input-impedance magnitude $|Z_{TM}|$. The absence of the deep minimum at 1.25 kHz in both the bulla-opened *and* foramen-plugged cases strongly supports the interpretation of this feature as resulting from a resonance involving the bullar cavity's compliance in series with the foramen's acoustic mass.

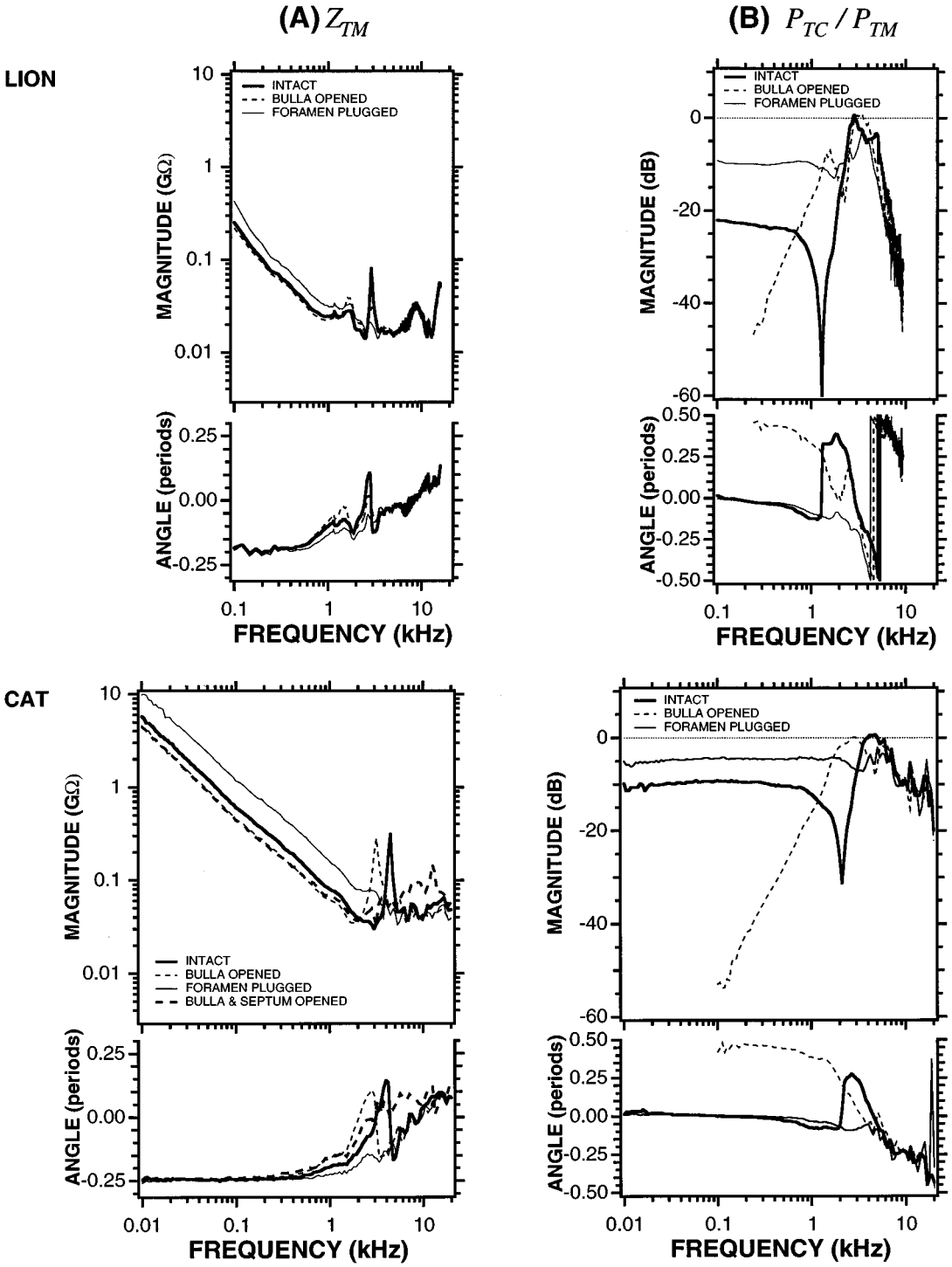

FIG. 8. Effects of structural manipulations on (A) the input impedance Z_{TM} and (B) the sound-pressure ratio P_{TC}/P_{TM}, in lion and cat. The conditions of the middle ear are: intact, bulla opened, and foramen plugged. In cat, Z_{TM} is shown also for the case of widely opened bulla and septum. The frequency scales are identical for lion and cat, except the cat data extend over a larger frequency range (0.01–20 kHz).

3. Cat

The bulla-opened configuration was achieved by enlarging the vent hole drilled in the bulla wall (to equalize static pressure) to a diameter of roughly 5 mm (5.5 mm by 4 mm). The foramen-plugged configuration was achieved by blocking the foramen with silicone grease. The bulla- and septum-opened condition (not done in the lion) consisted of the removal of the bony septum, the chorda tympani nerve, the styloid projection, and the ventral wall of the tympanic cavity.

For low frequencies, opening the bulla in cat decreases the input impedance Z_{TM}, as in lion (Fig. 8); in cat the change is greater (a 30% decrease). In cat, the opened bulla also leads to a shift of 30% in the frequency of the local maximum in $|Z_{TM}|$ (down to 3.1 kHz), while the magnitude

of the local maximum decreases by only 10%. This result contrasts with the bulla-opened effect in lion, in which the local maximum of $|Z_{TM}|$ does not shift in frequency but decreases greatly in *magnitude*. Here, the geometry of the bulla holes can influence the acoustic behavior (see Secs. III D, E).

With the bulla opened, P_{TC}/P_{TM} is greatly reduced in magnitude at low frequencies (as in lion), with a slope of roughly 35 dB/decade and an angle near 0.45 periods. $|P_{TC}/P_{TM}|$ has a maximum (approximately 0 dB) at 3.1 kHz, which is also the frequency of the local maximum in the bulla-opened $|Z_{TM}|$. The deep minimum present in the intact case (at 2.1 kHz) is absent, which is consistent with the lion results and further supports the notion of a Helmholtz resonance involving the bullar-cavity compliance.

The foramen-plugged condition results in a low-frequency increase in $|Z_{TM}|$ of a factor of 2 (to an equivalent volume of 0.15 cm^3), which is similar to the effect in lion but greater (Fig. 8). However, plugging the foramen in cat also raises $|P_{TC}/P_{TM}|$ for low frequencies by 5 dB (to -5 dB), which is smaller than the 13-dB increase (to -10 dB) observed in lion. In terms of the network model (Fig. 2), these results are evidence that at low frequencies: (1) Z_{TOC} is the dominant component of Z_{TM} in lion but not in cat; and (2) C_{BC} is a greater fraction of the total cavity compliance in lion than in cat. Furthermore, in cat (as in lion) both the sharp local maximum in $|Z_{TM}|$ and the deep minimum in $|P_{TC}/P_{TM}|$ are absent in the foramen-plugged condition. These extrema are clearly dependent on the open foramen's acoustic mass as described by the circuit model.

Opening the bulla *and* septum widely in cat leads to little change in the low-frequency $|Z_{TM}|$ compared with the bulla-opened case (Fig. 8, lower left panel). At higher frequencies, however, this manipulation has larger effects: The local maximum of $|Z_{TM}|$ is removed, and near 10 kHz $|Z_{TM}|$ is larger by 20%–40%. In terms of the network model (Fig. 2), this measurement gives an estimate of Z_{TOC}, as the cavities are widely opened and hence $Z_{CAV} \approx 0$. This plot suggests that Z_{TOC} could be well-approximated by a series resistance-compliance network (see Sec. III B).

4. Summary

The acoustic measurements on lion and cat have two distinctive frequency-dependent features whose representation in the model (Fig. 2) is supported qualitatively by the results of the structural manipulations: (1) a series resonance between the acoustic mass of the foramen constriction and the acoustic compliance of the bullar cavity, and (2) a higher-frequency parallel antiresonance between the acoustic mass of the foramen constriction and the acoustic compliances of the tympanic and bullar cavities. The effects of the manipulations on the low-frequency behavior of Z_{TM} and P_{TC}/P_{TM} are qualitatively consistent with the model.

III. DISCUSSION

A. Applicability of post-mortem measurements to a live ear

Acoustic measurements from temporal-bone preparations can closely approximate *in vivo* middle-ear behavior. Measurements in human ears (Rosowski *et al.*, 1990) suggest that post-mortem middle-ear input impedance is similar to measurements made *in vivo* provided that the ear is kept moist and the middle-ear cavity is vented to prevent static-pressure changes. Also, measurements of umbo motion made in live patients and in fresh post-mortem human ears have been shown to be similar (Goode *et al.*, 1993). Additional experiments should be performed to determine more precisely any live–dead differences and their dependence on the experimental conditions.

The use of frozen material introduces a potential complication: Freezing could produce cracks in the inner ear and lead to a loss of inner-ear fluid. However, two lines of reasoning suggest that the lion's inner ear was indeed fluid filled during the acoustic measurements: (1) The CT scans performed on the frozen head before its preparation for acoustic measurements showed fluid in the inner ear. (2) Draining the cochlea in domestic cat results in a readily discernible sharp decrease in the magnitude of the middle-ear input impedance near 1 kHz (Møller, 1965; Lynch, 1981; Allen, 1986), which was not observed in any of the lion measurements.

The available evidence, although consistent with a fluid-filled cochlea, is circumstantial. We cannot rule out the possibility that freezing and thawing the lion's head had an effect on the acoustic measurements. Clearly, the issue of *in vivo* preparation versus thawed material needs to be more fully addressed in future work. Also, the lion data in this paper are from one zoo specimen and are not necessarily representative of the species. Nevertheless, they are the only acoustic measurements on a lion ear reported to date.

B. Analog-circuit model of the felid middle ear

The acoustic and anatomical data from lion and cat provide a quantitative test of the generalized felid middle-ear circuit model (Fig. 2). Here, we define network representations of (1) Z_{CAV}, the impedance of the cavities, and (2) Z_{TOC}, the impedance of the TM, ossicles, and cochlea. To review, the cavity model Z_{CAV} consists of four acoustic elements associated with the cavity structures [Figs. 2(B) and 9(A)]: C_{TC} (compliance of the tympanic cavity), C_{BC} (compliance of the bullar cavity), L_F (mass of the foramen), and R_F (resistance of the foramen). The values of these elements can be related to ear dimensions (Sec. III E). Input-impedance measurements made on cats with the bulla and septum widely opened (e.g., Fig. 8, lower left panel) such that $Z_{CAV} \approx 0$ (and $Z_{TM} \approx Z_{TOC}$) suggest that Z_{TOC} is well-approximated by the series combination of a resistance R_{TOC} and a compliance C_{TOC} [Fig. 9(A)]; R_{TOC} is associated primarily with the resistance of the cochlea, and C_{TOC} represents the equivalent compliance of the TM and ossicular chain (Møller, 1965; Lynch, 1981; Allen, 1986). Impedance measurements made on the lion with a hole in the septum (not reported here) are consistent with this representation.[10] We have not, however, found a clear dependence of R_{TOC} and C_{TOC} on ear dimensions.

Our hypothesis is that the acoustic measurements in the lion and cat can be represented quantitatively by the same six-element circuit model [Fig. 9(A)], with two different sets of element values that are related to structure. The first stage

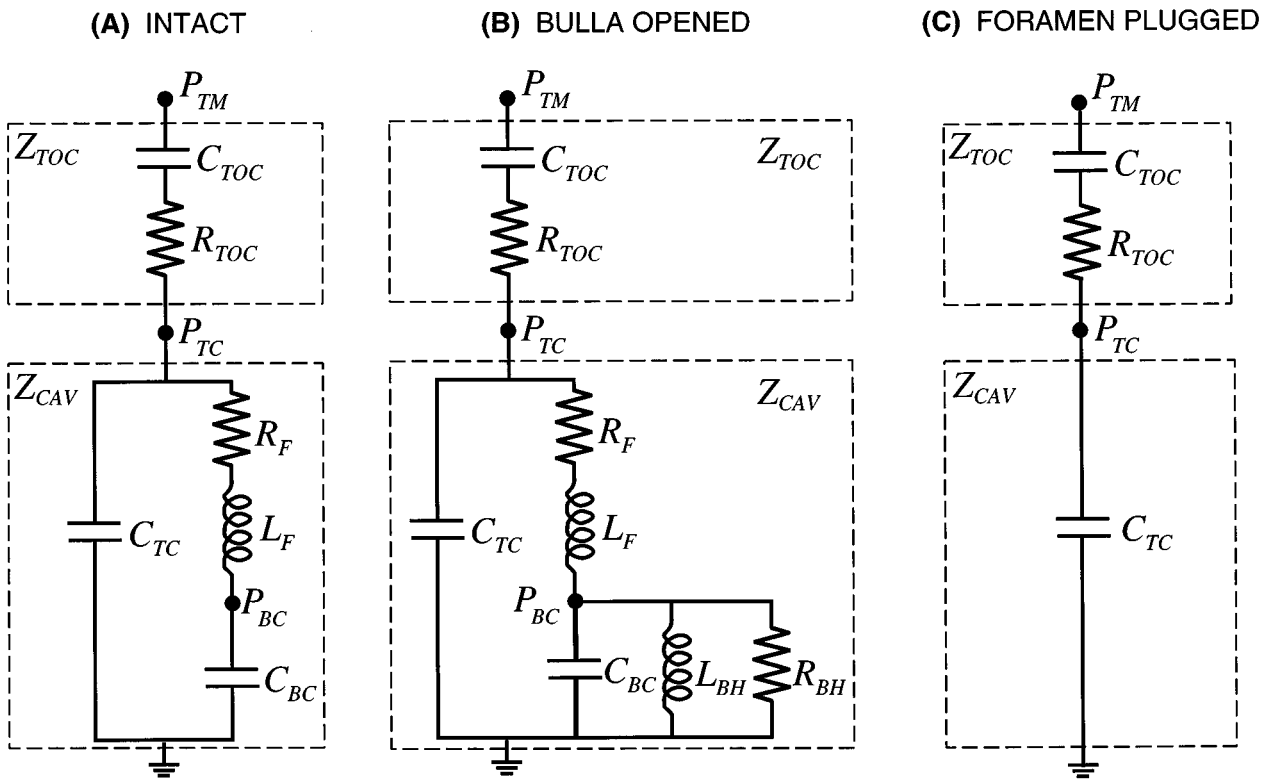

FIG. 9. Analog circuits for the felid middle ear in (A) intact, (B) bulla-opened, and (C) foramen-plugged conditions. The input impedance Z_{TM} is the series combination of Z_{TOC} and Z_{CAV}. Z_{TOC} consists of R_{TOC} (primarily contributed by the cochlea) in series with C_{TOC} (compliance of the TM and ossicular chain). (A) The element values C_{TC}, C_{BC}, R_F, and L_F are chosen to fit impedance measurements and can be related to structural dimensions. (B) R_{BH} and L_{BH} are added to account for the radiation impedance associated with the bulla hole. (C) The foramen is replaced by an open circuit; the cavity model reduces to the compliance C_{TC}.

of testing this hypothesis was to choose model parameters that best matched the acoustic measurements made in the two species (Fig. 7) and to compare the model predictions to these measurements (Sec. III C). The second stage was to test whether the effects of structural manipulations (Fig. 8) could be represented by modifications of the model's topology (Sec. III D). The third and last stage was to compare the acoustically determined element values of the model with the anatomical measurements (Sec. III E), thereby relating the model to structure.

C. Comparison of model predictions to acoustic measurements

The model's element values were chosen to match salient features of acoustic measurements made on the lion and the cat (Fig. 7). First, C_{TOC} and R_{TOC} were chosen to fit the low-frequency compliance and the high-frequency resistance of opened-septum Z_{TM} measurements (discussed above). Given C_{TOC}, the compliances C_{TC} and C_{BC} were chosen to fit (1) the low-frequency compliance of the intact Z_{TM} measurements (or equivalently, the low-frequency pressure ratio $P_{\mathrm{TC}}/P_{\mathrm{TM}}$) and (2) the ratio of the frequencies of the intact $|Z_{\mathrm{TM}}|$ local maximum ($f_{z\ \max}$) and the pressure-ratio minimum ($f_{p\ \min}$).

The first constraint is expressed as

$$Z_{\mathrm{TM}}\big|_{f=0.22\ \mathrm{kHz}} \approx \frac{1}{j2\pi f}\,\frac{(C_{\mathrm{TOC}}+C_{\mathrm{TC}}+C_{\mathrm{BC}})}{C_{\mathrm{TOC}}(C_{\mathrm{TC}}+C_{\mathrm{BC}})}\bigg|_{f=0.22\ \mathrm{kHz}}, \tag{4a}$$

or equivalently,

$$\frac{P_{\mathrm{TC}}}{P_{\mathrm{TM}}}\bigg|_{f=0.22\ \mathrm{kHz}} \approx \frac{C_{\mathrm{TOC}}}{C_{\mathrm{TOC}}+C_{\mathrm{TC}}+C_{\mathrm{BC}}}, \tag{4b}$$

where the quantities on the left sides were measured. Constraints (4a) and (4b) are equivalent and provide one equation for the compliances C_{TC} and C_{BC} in terms of C_{TOC} and measured quantities (and a check for consistency between impedance and sound-pressure measurements).

The second constraint involves the resonant frequencies of the cavity network. The circuit model predicts a maximum in $|Z_{\mathrm{TM}}|$ at

$$f_{z\ \max} = \frac{1}{2\pi}\,\frac{1}{\sqrt{L_F C_{\mathrm{TC}} C_{\mathrm{BC}}/(C_{\mathrm{TC}}+C_{\mathrm{BC}})}} \tag{5}$$

caused by a parallel resonance between the mass L_F and the compliances C_{TC} and C_{BC}, and a minimum in $|Z_{\mathrm{CAV}}|$ (not in $|Z_{\mathrm{TM}}|$) and hence in $|P_{\mathrm{TC}}/P_{\mathrm{TM}}|$ at

$$f_{p\ \min} = \frac{1}{2\pi}\,\frac{1}{\sqrt{L_F C_{\mathrm{BC}}}} \tag{6}$$

TABLE II. Comparison of circuit-model element values to structure-based element values in the lion and cat (53L). The ''model'' values were used to calculate the predictions in Figs. 10–12. The structure-based compliances (i.e., air volumes) are from CT-scan reconstructions (lion) and water-filling measurements (cat). The structure-based foramen element values, L_F and R_F, were calculated from effective foramen dimensions (Table I). The structure-based radiation-impedance elements, L_{BH} and R_{BH}, were calculated from bulla-hole dimensions. Compliances are given as equivalent volumes of air. % diff.=(|model−structure|)/(model)×100%.

	C_{TOC} (cm^3)	R_{TOC} (MΩ)	C_{TC} (cm^3)	C_{BC} (cm^3)	L_F (H)	R_F (Ω) [a]	L_{BH} (H)	R_{BH} (MΩ)
Lion								
Model	1.33	15	3.51	14.4	148	$900\sqrt{f}$	100	1.8
Structure	-	-	3.30	16.4	211	$904\sqrt{f}$	25.6	2.4
% diff.	-	-	6.0%	14%	43%	0.44%	74%	33%
Cat								
Model	0.441	30	0.253	0.801	950	$20\,000\sqrt{f}$	230	35
Structure	-	-	0.247	0.780	760	$7800\sqrt{f}$	92.1	31
% diff.	-	-	2.4%	2.6%	20%	61%	60%	11%

[a] f in Hz.

caused by a series resonance between L_F and C_{BC}. Dividing (5) by (6) gives an expression for the second constraint:

$$f_{z\,max}/f_{p\,min}=\sqrt{1+(C_{BC}/C_{TC})}, \tag{7}$$

where the frequency values on the left side were obtained from measurements (Fig. 7). Equations (4) and (7) were then solved for C_{TC} and C_{BC}.

With the compliances determined, the foramen mass L_F was chosen to fit the measured frequencies of the local maximum of $|Z_{TM}|$ and the minimum of $|P_{TC}/P_{TM}|$ from (5) and (6). Lastly, a frequency-dependent resistance R_F (Beranek, 1986, pp. 137–138) was chosen to fit the magnitude and bandwidth of the measured extrema. The model's element values are given in Table II.

As illustrated in Fig. 10, the six-element circuit model captures the main features of the three sets of acoustic measurements made with intact middle-ear cavities, except at high frequencies. The model impedances Z_{TM}: (1) are compliance dominated at low frequencies; (2) are roughly resistive at higher frequencies; and (3) have a sharp local magnitude maximum at an intermediate frequency. The model sound-pressure ratios P_{TC}/P_{TM}: (1) are constant at low frequencies; (2) have a sharp minimum; and (3) have a maximum of approximately 0 dB in magnitude at the frequency of the local maximum of $|Z_{TM}|$. The model sound-pressure ratios P_{BC}/P_{TM}: (1) are constant and approximately equal to P_{TC}/P_{TM} at low frequencies; (2) have a maximum at the frequency of the local maximum of $|Z_{TM}|$; and (3) show a steep rolloff in magnitude at high frequencies. The differences between the lion and cat acoustic measurements are accounted for quantitatively by changes in the circuit model's element values. For each specimen, three frequency responses can be summarized by six element values.

For high frequencies, the model becomes inaccurate. The errors could result from a number of factors, including wave effects related to the middle-ear dimensions, and the simple representation of the TM-ossicular chain. Also, the ear-canal correction leads to errors in the data for frequencies above 4 kHz (Sec. I E). The model fits (Fig. 10) show that above 4 kHz, (1) some acoustic behavior is captured qualitatively in both species, and (2) the error for cat is generally smaller than the error for lion, for a given frequency. The latter point is consistent with the fact that the ear dimensions in cat are smaller fractions of a wavelength than in lion.

D. Model representations of structural manipulations

1. Bulla opened

The circuit model was tested quantitatively against the acoustic measurements made with the bulla opened. If the bulla were *widely* opened, one might expect that replacing the bullar-cavity compliance C_{BC} with an electrical short circuit would give predictions consistent with measurements. However, because of the small size of the hole in the bulla (in both specimens), it was necessary to account for its acoustic-radiation impedance [Fig. 9(B)]. For simplicity, the bulla hole's radiation impedance (placed in parallel with C_{BC}) was approximated by a resistance R_{BH} in parallel with a mass L_{BH} (e.g., Beranek, 1986, p. 125). From the ''bulla-opened'' curves in Fig. 8, R_{BH} and L_{BH} (given in Table II) were chosen to match (1) the magnitude and frequency of the local maximum of $|Z_{TM}|$ near 3 kHz and (2) the low-frequency magnitude and slope of $|P_{TC}/P_{TM}|$. The other six elements were not changed from their intact-state values.

Figure 11 shows generally good agreement between the bulla-opened model [Fig. 9(B)] and the acoustic measurements made in the bulla-opened condition on lion and cat. For both specimens, predictions based on replacing the bullar-cavity compliance with a short circuit do *not* agree with the measurements as closely. For instance, the ''short-circuit'' model predicts shifts (from the intact case) in the frequency of the local maximum of $|Z_{TM}|$ of 11% in lion and 15% in cat, whereas the data show no shift in lion and a 30% shift in cat. For lion, the radiation-impedance model underpredicts (by a factor of 2) the maximum value of $|P_{TC}/P_{TM}|$ and does not capture its high-frequency slope; the accuracy of the lumped model is limited at higher frequencies by the size of the lion's bullar cavity.

In summary, the model, with the addition of a two-element radiation impedance to represent the effect of sound

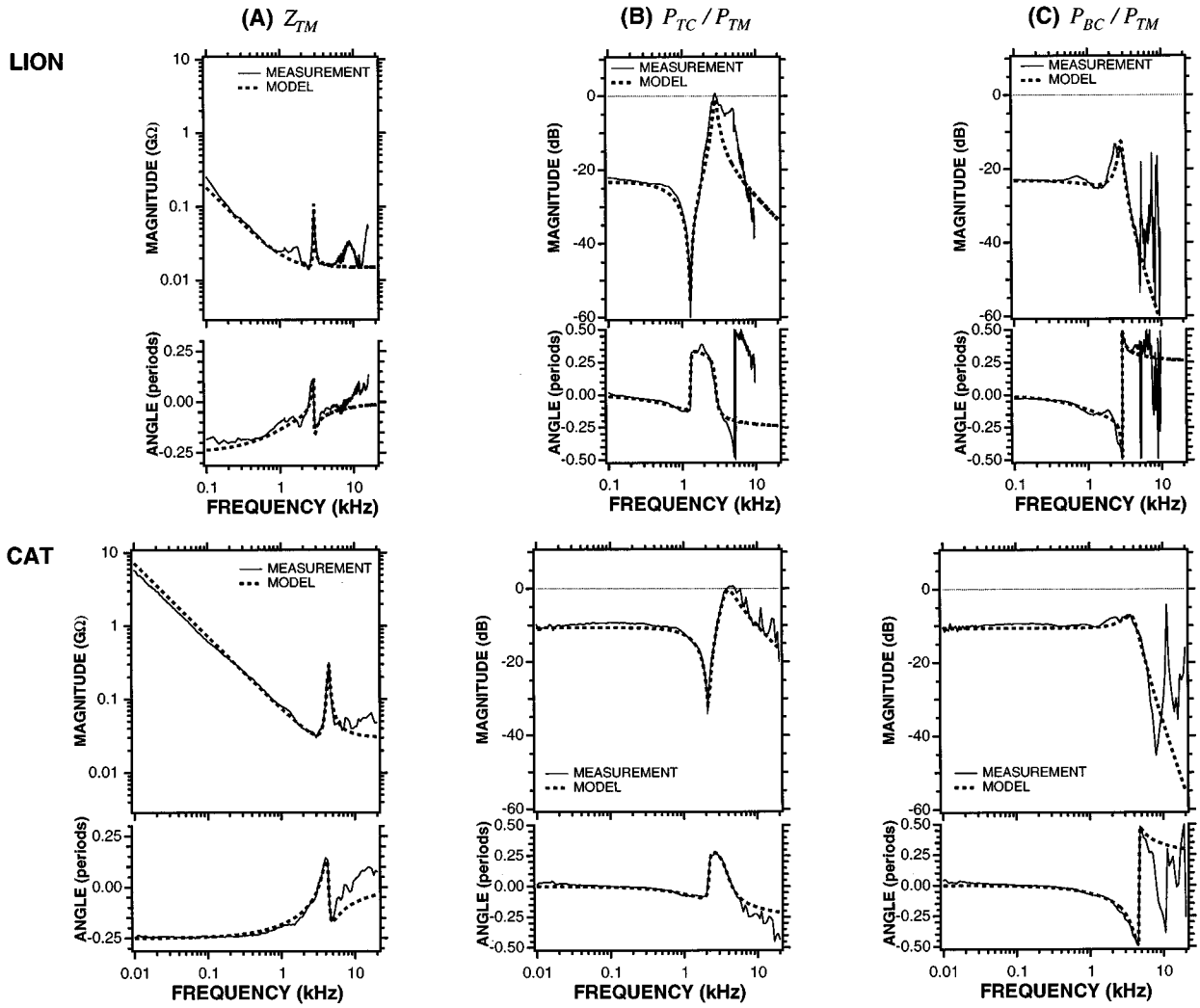

FIG. 10. Comparison of measured input impedance (Z_{TM}) and sound-pressure ratios (P_{TC}/P_{TM} and P_{BC}/P_{TM}) to circuit-model predictions in a lion and a cat with middle ears intact. The element values used in the model are from Table II.

leaving the ear through the bulla hole, provides a good representation of the bulla-opened measurements except at high frequencies.

2. Foramen plugged

The circuit model was also tested quantitatively against the acoustic measurements made with the foramen plugged. The blocking of the foramen is represented in the model by the removal of the bullar-cavity branch [Fig. 9(C)]; the cavity model reduces to one compliance, C_{TC}. No new elements are introduced.

Figure 12 demonstrates that this change in the model removes the extrema in the input impedance and the sound-pressure ratio (attributed to a resonance and an antiresonance, both involving the foramen's acoustic mass). These effects are consistent with the measurements. For low frequencies, the model generally predicts the values of Z_{TM} and P_{TC}/P_{TM} to within 3 dB in magnitude and 0.05 periods in angle. Thus, with no new parameters, the model can represent another set of measurements. However, the lumped model cannot account for the maximum of $|P_{TC}/P_{TM}|$ at 3–4 kHz observed in lion (or its high-frequency slope); an explanation is that the dimensions of the lion's tympanic cavity are roughly a quarter wavelength at these frequencies, and therefore wave effects become significant.

E. Comparison of circuit-model parameters to structural dimensions

The next step is to relate the model's element values to measures of structural features. As a basis for comparison, we define ''structure-based'' values for the four cavity elements in the intact-state model [Fig. 9(A)] and for the two radiation-impedance elements in the bulla-opened analog circuit [Fig. 9(B)]. The structure-based parameters are derived from measurements in Table I, as described below. We do not attempt to define values for R_{TOC} and C_{TOC} based on structural dimensions.

Structure-based values for the cavity compliances C_{TC} and C_{BC} are from CT-scan volumetric calculations for lion and from water-filling volumetric measurements for cat (Table I).[11] Structure-based values for R_F and L_F are calculated from the approximation of the foramen as a tube of length l_F and radius a_F: For frequencies f (Hz) for which

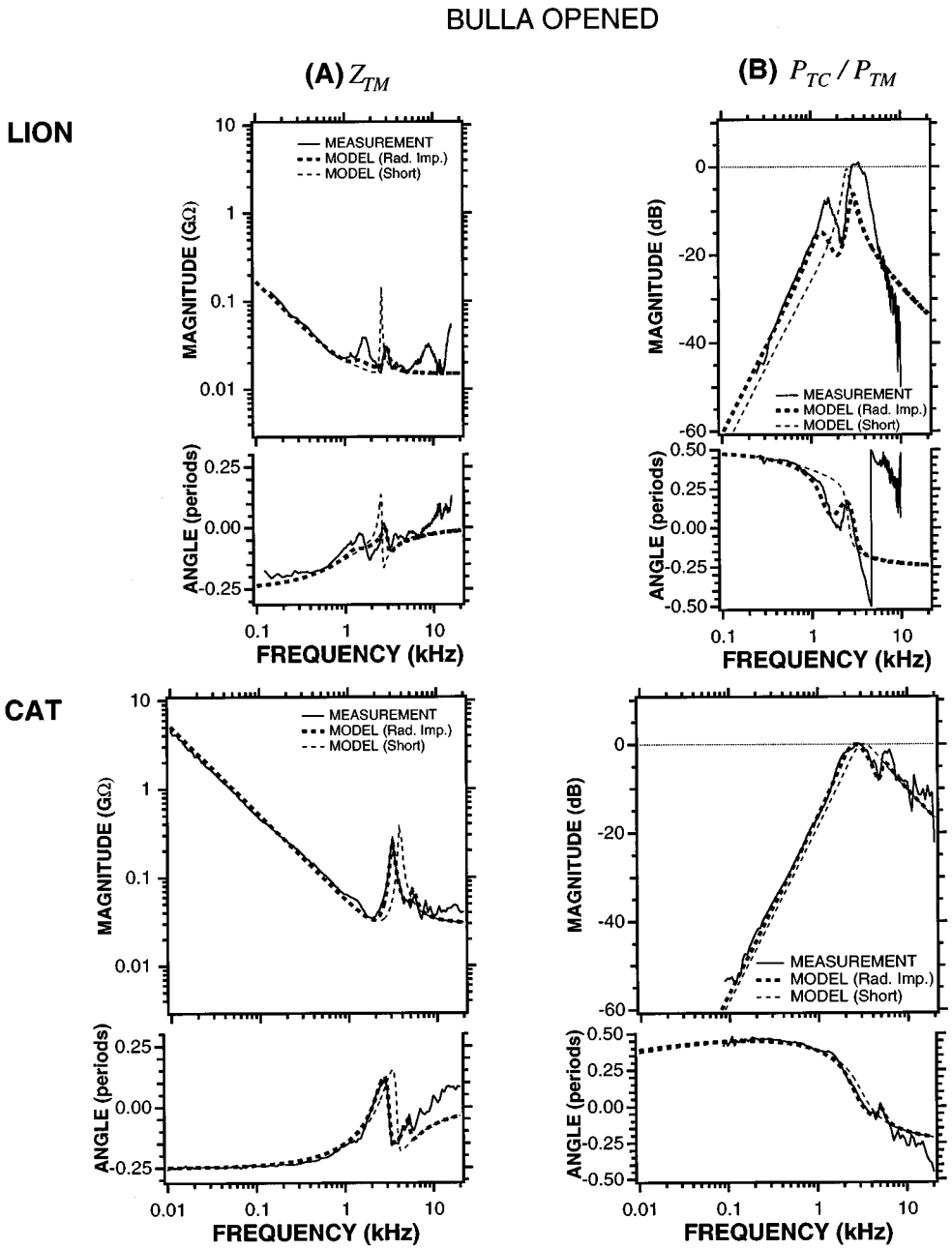

FIG. 11. Comparison of measured (A) input impedance Z_{TM} and (B) sound-pressure ratio P_{TC}/P_{TM} to circuit-model predictions in a lion and a cat with the bulla opened. The ''model (radiation impedance)'' curves (thick dashed lines) were calculated from the circuit of Fig. 9(B) with element values from Table II. The ''model (short)'' curves (thin dashed lines) were calculated from a simpler circuit in which the compliance C_{BC} was replaced by a short circuit.

$a_F(\mathrm{m}) > 0.01/\sqrt{f}$ and $a_F < 10/f$, the acoustic impedance of the tube can be approximated by the series combination of a resistance R_F and a mass L_F, where

$$R_F = \frac{\rho_0 \sqrt{4\pi f \mu}}{\pi a_F^2}\left(\frac{l_F}{a_F} + 2\right) \tag{8}$$

and

$$L_F = \frac{\rho_0 (l_F + 2l_F')}{\pi a_F^2} \tag{9}$$

(Beranek, 1986, pp. 137–138); μ is the kinematic coefficient of viscosity, and $l_F' = 0.85 a_F$ is the end correction. Given the effective foramen dimensions (Table I), this lumped approximation is accurate for frequencies below about 3 kHz for the lion and 7 kHz for the cat.[12]

Lastly, structure-based values for R_{BH} and L_{BH} are calculated from the approximation of the bulla hole as the open end of a tube of radius a_h: At frequencies for which $ka_h < 0.5$, the radiation impedance of the hole can be approximated by the parallel combination of a resistance R_{BH} and a mass L_{BH}, where

$$R_{BH} = \frac{0.479 \rho_0 c}{a_h^2} \tag{10}$$

and

$$L_{BH} = \frac{0.1952 \rho_0}{a_h} \tag{11}$$

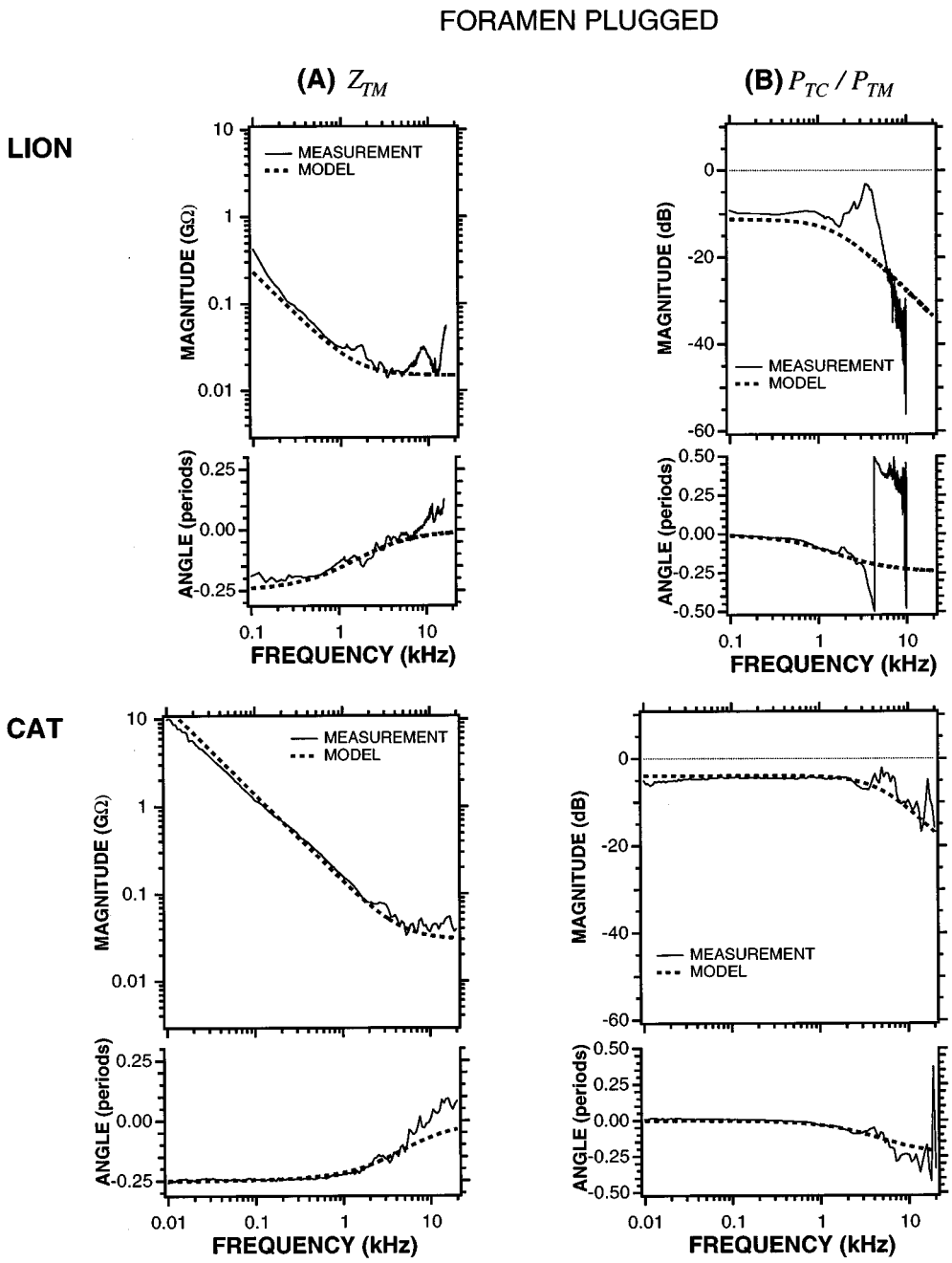

FIG. 12. Comparison of measured (A) input impedance Z_{TM} and (B) sound-pressure ratio P_{TC}/P_{TM} to circuit-model predictions in a lion and a cat with the foramen plugged. The ''model'' curves (dashed lines) were calculated from the circuit of Fig. 9(C) with element values from Table II.

(Beranek, 1986, p. 125); a_h is set equal to the radius of the hole in the bulla (9 mm in the lion and 2.5 mm in the cat). Given the bulla-hole dimensions, the approximation is accurate for frequencies below about 3 kHz for the lion and 10 kHz for the cat. The form of the radiation impedance was chosen for simplicity; clearly there exist better approximations to the geometry of the bullar cavity and the hole (e.g., a piston in a sphere—see Morse and Ingard, 1968, pp. 343–346).

A comparison between the model's parameters and the structure-based parameters is shown in Table II. The structure-based cavity-compliance values agree with those used in the circuit model to within the volumetric measurement error. The less precise agreement for the foramen and bulla-hole parameters might be expected, as the structure-based values are dependent on simple approximations of irregular structural features. To an extent, the differences between these ''model'' and ''structure'' parameters reflect the limits of the structural approximations. Overall, the acoustically determined parameters of the cavity model are consistent with those predicted from anatomy.

F. Model conclusions

The felid middle-ear model represents quantitatively the acoustic data from a lion and a domestic cat. The model relates salient features of the measurements to structural measures and can account for the effects of structural ma-

nipulations. The lumped-element representation gives rise to errors above 4 kHz, partly because structural dimensions are on the order of a wavelength. The quantitative relation between model parameters and structure could be further tested, particularly to clarify the effects of the irregular geometry of the foramen. Nevertheless, the model provides a useful approach for representing the acoustic behavior of middle ears with qualitatively similar structure and should be further tested on other felid species of intermediate and smaller size.

IV. SUMMARY

Acoustic and anatomical measurements in the middle ear of a lion were compared to similar measurements in domestic cats. Measurements of acoustic impedance in the ear canal and sound pressures in the tympanic and bullar cavities show qualitatively similar frequency dependence in lion and cat, but the lion's impedance and sound pressures are generally smaller and the salient features occur at lower frequencies. The predictions of a six-element lumped-circuit model are consistent with the main features of both sets of measurements, with errors occurring at high frequencies. The acoustic effects of the middle-ear size differences are represented by changes in the model's element values that are consistent with structural dimensions. The results in this paper suggest that the relationship between middle-ear structural size and acoustic behavior could be described rather simply for the entire cat family and perhaps extended to other carnivores.

ACKNOWLEDGMENTS

We thank The Franklin Park Zoo (A. Bullied) for access to the lion head; the Mammal Department of the Harvard Museum of Comparative Zoology (J. Chupasko and M. Rutzmoser) for help with cleaning the skulls and access to the collection; D. Ketten and the New England Aquarium for help with storage; D. D. Jones of the Otopathology Laboratory of the Massachusetts Eye and Ear Infirmary for the histological preparation; B. Kiang and H. Peake for entering histological sections into the computer; S. Puria, M. Ravicz, and S. Voss of EPL for helpful discussions; and W. R. J. Funnell and an anonymous JASA reviewer for valuable comments on the manuscript. Portions of this work were presented at the 18th Midwinter Meeting of the Association for Research in Otolaryngology (Rosowski *et al.*, 1995) and at the 131st Meeting of the Acoustical Society of America (Huang *et al.*, 1996). This work was supported by NIDCD (Grant No. R01-DC-00194).

[1]Skull length was measured as the distance from the upper incisors to the posterior edge of the occipital condyles.

[2]''Bulla'' refers to the bony prominence that encloses each middle-ear air space, on the postero-ventral aspect of the skull; see Fig. 1.

[3]Variations of ± 3 mm in the depth of the probe produced differences in sound pressure of less than 2 dB over the reported frequency range.

[4]Resonances are characterized by sharp minima in impedance magnitude with rapid changes in angle from near -0.25 periods to 0.25 periods, whereas antiresonances are characterized by sharp maxima in impedance magnitude with rapid angle changes from near 0.25 periods to -0.25 periods.

[5]Equivalently, near 3.4 kHz, the measured impedance normalized by the characteristic impedance of the canal (0.025 GΩ) is the reciprocal of the normalized impedance at the TM.

[6]Equivalent air volume V_{eq} is related to compliance C by $V_{eq}=(\rho_0 c^2)C$.

[7]If all linear dimensions of the middle ears of the two species scaled similarly, we would expect areas to increase as the 2/3 power of the volume increase, with $20^{2/3} \approx 7.4$.

[8]Figure 6.15B in Rosowski (1994) shows that, for 63 terrestrial mammals, about 80% of the variation of footplate area with tympanic-ring area is explained by a regression line corresponding to a ratio of about 20. Figure 1 in Funnell and Laszlo (1982) points out that the spread of the ratio is at least from 7 to 53.

[9]Over several repetitions of bulla-opened measurements, this impedance-magnitude maximum varied 40% in magnitude, but only 10% in the frequency of the peak.

[10]In the lion, however, the septum was not as ''widely'' opened; the impedance is more frequency-dependent at high frequencies.

[11]For the lion, the value of C_{BC} based on structure is reduced by 0.3 cm^3 to account for the volume occupied by the microphone's probe tube (to the tympanic cavity) during acoustic measurements.

[12]Structure-based values of R_F and L_F calculated for cat H (whose middle ear is reconstructed in Fig. 6) are within 40% of the values calculated for cat 53L (given in Table II).

Allen, J. B. (**1986**). ''Measurements of eardrum acoustic impedance,'' in *Peripheral Auditory Mechanisms*, edited by J. L. Hall, J. B. Allen, A. Hubbard, S. T. Neely, and A. Tubis (Springer-Verlag, New York), pp. 44–51.

Beranek, L. L. (**1986**). *Acoustics* (American Institute of Physics, New York), pp. 137–138.

Dallos, P. (**1970**). ''Low frequency auditory characteristics: Species dependence,'' J. Acoust. Soc. Am. **48,** 489–499.

Decraemer, W. F., Khanna, S. M., and Funnell, W. R. J. (**1989**). ''Interferometric measurement of the amplitude and phase of tympanic membrane vibrations in cat,'' Hearing Res. **38**, 1–18.

Decraemer, W. F., Khanna, S. M., and Funnell, W. R. J. (**1990**). ''Heterodyne interferometer measurements of the frequency response of the manubrium tip in cat,'' Hearing Res. **47**, 205–218.

Decraemer, W. F., Khanna, S. M., and Funnell, W. R. J. (**1991**). ''Malleus vibration mode changes with frequency,'' Hearing Res. **54**, 305–318.

Egolf, D. P. (**1977**). ''Mathematical modeling of a probe-tube microphone,'' J. Acoust. Soc. Am. **61,** 200–205.

Funnell, W. R. J., Decraemer, W. F., and Khanna, S. M. (**1987**). ''On the damped frequency response of a finite-element model of the cat eardrum,'' J. Acoust. Soc. Am. **81,** 1851–1859.

Funnell, W. R. J., Khanna, S. M., and Decraemer, W. F. (**1992**). ''On the degree of rigidity of the manubrium in a finite-element model of the cat eardrum,'' J. Acoust. Soc. Am. **91,** 2082–2090.

Funnell, W. R. J., and Laszlo, C. A. (**1982**). ''A critical review of experimental observations on ear-drum structure and function,'' J. Oto-Rhino-Laryngol. **44**, 181–205.

Goode, R. L., Ball, G., and Nishihara, S. (**1993**). ''Measurement of umbo vibration in human subjects—Method and possible clinical applications,'' Am. J. Otolaryngol. **14**, 247–251.

Guinan, J. J., Jr., and Peake, W. T. (**1967**). ''Middle-ear characteristics of anesthetized cats,'' J. Acoust. Soc. Am. **41,** 1237–1261.

Hemilä, S., Nummela, S., and Reuter, T. (**1995**). ''What middle ear parameters tell about impedance matching and high frequency hearing,'' Hearing Res. **85**, 31–44.

Huang, G. T., Rosowski, J. J., Flandermeyer, D. T., and Peake, W. T. (**1996**). ''Middle ear of a lion: Comparison of structure and function to domestic cat,'' J. Acoust. Soc. Am. **99,** 2562.

Jayne, H. (**1898**). *Mammalian Anatomy, A Preparation for Human and Comparative Anatomy*, Part I, The Skeleton of the Cat (Lippincott, London).

Keefe, D. (**1984**). ''Acoustical wave propagation in cylindrical ducts: Transmission line parameter approximations for isothermal and nonisothermal boundary conditions,'' J. Acoust. Soc. Am. **75,** 58–62.

Lynch, T. J., III (**1981**). ''Signal processing by the cat middle ear: Admittance and transmission, measurements and models,'' Ph.D. dissertation, Massachusetts Institute of Technology.

Lynch, T. J., III, Nedzelnitsky, V., and Peake, W. T. (**1982**). ''Input impedance of the cochlea in cat,'' J. Acoust. Soc. Am. **72,** 108–130.

Lynch, T. J., III, Peake, W. T., and Rosowski, J. J. (**1994**). ''Measurements

of the acoustic input-impedance of cat ears: 10 Hz to 20 kHz,'' J. Acoust. Soc. Am. **96**(4), 2184–2209.
Møller, A. R. (**1965**). ''An experimental study of the acoustic impedance of the middle ear and its transmission properties,'' Acta Oto-Laryngol. **60**, 129–149.
Morse, P. M., and Ingard, K. U. (**1968**). *Theoretical Acoustics* (McGraw-Hill, New York), pp. 343–346.
Mundie, J. R. (**1963**). ''The impedance of the ear—A variable quantity,'' in U.S. Army Medical Research Lab, Report 576, edited by J. L. Fletcher, pp. 65–85.
Nedzelnitsky, V. (**1980**). ''Sound pressures in the basal turn of the cat cochlea,'' J. Acoust. Soc. Am. **68,** 1676–1689.
Onchi, Y. (**1961**). ''Mechanism of the middle ear,'' J. Acoust. Soc. Am. **33,** 794–805.
Peake, W. T., and Guinan, J. J., Jr. (**1967**). ''Circuit model for the cat's middle ear,'' MIT Quarterly Prog. Report of the Research Laboratory of Electronics **84**, 320–326.
Peake, W. T., Rosowski, J. J., and Lynch, T. J., III (**1992**). ''Middle-ear transmission: Acoustic vs. ossicular coupling in cat and human,'' Hearing Res. **57**, 245–268.
Puria, S. (**1991**). ''A theory of cochlear input impedance and middle ear parameter estimation,'' Ph.D. dissertation, City University of New York.
Rabinowitz, W. (**1981**). ''Measurement of the acoustic input immittance of the human ear,'' J. Acoust. Soc. Am. **70,** 1025–1035.
Ravicz, M. E., Rosowski, J. J., and Voigt, H. (**1992**). ''Sound-power collection by the auditory periphery of the Mongolian gerbil *Meriones unguiculatus*: I. Middle-ear input impedance,'' J. Acoust. Soc. Am. **92,** 157–177.
Rosowski, J. J. (**1994**). ''Outer and middle ears,'' in *Springer Handbook of Auditory Research, Volume 4: Comparative Hearing: Mammals*, edited by R. R. Fay and A. N. Popper (Springer-Verlag, New York), pp. 172–247.
Rosowski, J. J. Carney, L. H., Lynch, T. J., III, and Peake, W. T. (**1986**). ''The effectiveness of the external and middle ears in coupling acoustic power into the cochlea,'' in *Peripheral Auditory Mechanisms*, edited by J. B. Allen, J. L. Hall, A. Hubbard, S. T. Neely, and A. Tubis (Springer-Verlag, New York), pp. 3–12.
Rosowski, J. J., Davis, P. J., Merchant, S. N., Donahue, K. M., and Coltrera, M. D. (**1990**). ''Cadaver middle ears as models for living ears: Comparisons of middle-ear input immittance,''Ann. Otol. Rhinol. Laryngol. 99, 403–412.
Rosowski, J. J., Peake, W. T., Huang, G. T., and Flandermeyer, D. T. (**1995**). ''Middle-ear structure and function in the family Felidae,'' Abstracts of the 18th Midwinter Meeting of the Association for Research in Otolaryngology.
Rosowski, J. J., Peake, W. T., and Lynch, III, T. J. (**1984**). ''Acoustic input-admittance of the alligator-lizard ear: Nonlinear features,'' Hearing Res. **16**, 205–223.
Schuknecht, H. F. (**1974**). *Pathology of the ear* (Harvard U.P., Cambridge, MA), Chap. 1, ''Histological Method,'' pp. 1–20.
Stinson, M. R., and Khanna, S. M. (**1989**). ''Sound propagation in the ear canal and coupling to the eardrum, with measurements on model systems,'' J. Acoust. Soc. Am. **85,** 2481–2491.
Stinson, M. R., and Khanna, S. M. (**1994**). ''Spatial distribution of sound pressure and energy flow in the ear canals of cats,'' J. Acoust. Soc. Am. **96,** 170–180.
Voss, S. E., and Allen, J. B. (**1994**). ''Measurement of acoustic impedance and reflectance in the human ear canal,'' J. Acoust. Soc. Am. **95,** 372–384.
Wever, E. G., and Lawrence, M. (**1954**). *Physiological Acoustics* (Princeton U.P., Princeton, NJ), p. 416.
White, R. E. C., Studebaker, G. A., Levitt, H., and Mook, D. (**1980**). ''The application of modeling techniques to the study of hearing aid acoustic systems,'' in *Acoustical Factors Affecting Hearing Aid Performance*, edited by G. E. Studebaker and I. Hochberg (University Park, Baltimore, MD), pp. 267–296.
Wozencraft, W. C. (**1989**). ''The Phylogeny of the Recent Carnivora,'' in *Carnivore Behavior, Ecology, and Evolution*, edited by J. L. Gittleman (Cornell U.P., Ithaca, NY), pp. 495–535.
Wozencraft, W. C. (**1993**). ''Order Carnivora,'' in *Mammal Species of the World, A Taxonomic and Geographic Reference*, 2nd ed., edited by D. E. Wilson and D. M. Reeder (Smithsonian Institution, Washington, DC).
Zuercher, J. C., Carlson, E. V., and Killion, M. C. (**1988**). ''Small acoustic tubes: New approximations including isothermal and viscous effects,'' J. Acoust. Soc. Am. **83,** 1653–1660.
Zwislocki, J. (**1962**). ''Analysis of the middle-ear function. Part I. Input impedance,'' J. Acoust. Soc. Am. **34,** 1514–1523.

The effect of sound intensity on f_1-sweep and f_2-sweep distortion product otoacoustic emissions phase delay estimates in human adults

Denise M. Bowman, David K. Brown, and Jos J. Eggermont
Department of Psychology, The University of Calgary, Calgary, Alberta T2N 1N4, Canada

Barry P. Kimberley
Department of Surgery, The University of Calgary, Calgary, Alberta T2N 1N4, Canada

(Received 12 January 1996; revised 30 May 1996; accepted 7 August 1996)

Phase measurements of distortion product otoacoustic emissions (DPOAE) provide an estimate of round-trip travel times in the cochlea. This study examined differences in f_1- and f_2-sweep round-trip delays estimated from DPOAE phase responses in 20 normal-hearing adult human subjects as a function of f_2 frequency and sound intensity. Eight different f_2 frequencies ranging from 1.1–13 kHz were presented. For both the f_1- and the f_2-sweep stimulation conditions the f_2/f_1 ratios were between 1.1 and 1.3. Primary intensity levels for f_2 were varied in 5-dB steps from 30–50 dB SPL (where f_1 was 15 dB$>f_2$). Delays in the f_2-sweep condition were equal to or longer than travel times in the f_1-sweep condition. Round-trip delays showed a significant intensity dependence in both the f_1- and f_2-sweep conditions ($p \leqslant 0.01$). In both conditions, the delay increased as stimulus intensity decreased. Delay estimates in the f_2-sweep condition were more strongly intensity dependent than estimates in the f_1-sweep condition at f_2 frequencies above 1.6 kHz. The mean difference in f_2- and f_1-sweep delays at low intensities ranged from 15.9 periods at the 9.2 kHz f_2 place, to 2.5 periods at the 1.6 kHz f_2 place. The intensity dependence of round-trip delay estimates in both conditions may be attributed to intensity-dependent changes in the cochlear filter response time related to the sharpness of tuning of DPOAE responses. The steeper intensity dependence and longer delays observed in the f_2-sweep condition may similarly be attributed to a greater proportion of the f_2-sweep response being composed of the filter response time. [S0001-4966(97)01103-X]

PACS numbers: 43.64.Jb, 43.64.Nf [RDF]

INTRODUCTION

Kemp (1978) was the first to demonstrate that the cochlea does not only receive sound, but also produces recordable acoustic energy or otoacoustic emissions (OAEs). Studies examining the effect of suppression tones, hearing loss, noise exposure, and a variety of pharmacological agents on OAEs indicate that emissions arise from sharply tuned elements and are dependent upon the physiological and structural integrity of the cochlea (see Probst, 1990, for review).

The OAEs can be recorded in response to a variety of acoustic stimuli and spontaneously. Distortion product otoacoustic emissions (DPOAEs) are recorded in the ear canal when the acoustic stimulus consists of two continuous pure tones (or primaries) of different frequency presented simultaneously, and energy is emitted at a number of frequencies not present in the acoustic stimulus (distortion products). Distortion is generated as a result of the nonlinear interaction of the primary tones, where the traveling waves of the lower frequency tone (f_1) and higher frequency tone (f_2) overlap along the basilar membrane. Both the low-frequency and the high-frequency primaries stimulate the f_2 place in the cochlea, and lead to the generation of distortion in the region of f_2 (e.g., Brown and Kemp, 1984; Furst and Lapid, 1988). The frequency of the distortion is dependent upon the frequencies of both primary tones (e.g., Brown *et al.*, 1992). In humans, and most animal species, the intermodulation distortion product at the frequency $2f_1-f_2$ (where $f_1<f_2$) is the most prominent, and consequently the most studied form of DPOAE (Probst, 1990).

A number of psychophysical and physiological studies have shown that distortion due to a cubic nonlinearity can only be heard or measured as a DPOAE over a small range of primary tone frequency separations (e.g., Goldstein, 1967; Wilson, 1980; Gaskill and Brown, 1990). The distortion provides an indication of the degree to which the vibration of a particular region of the cochlea (associated with a certain characteristic frequency) can be influenced by tones at other frequencies (Brown *et al.*, 1992). Therefore, DPOAEs can be utilized to investigate mechanical tuning in the cochlea.

A. Mechanisms of DPOAE generation

In order for an OAE to be recorded in the ear canal, vibratory energy must be retrogradely conducted from the cochlea, through the ossicular chain to the tympanic membrane where it is transduced into an acoustic signal (Probst, 1990). There are several different mechanisms that could underlie the generation of retrograde traveling waves within the cochlea (e.g., Kemp, 1986). Retrograde transmission could be passive (Allen and Neely, 1992), or could be combined with active feedback at the point of reflection (De Boer, 1991). The amount of energy return inferred by measurements of OAE amplitude and incidence in normal hearing

human and nonhuman primates suggests the involvement of an active mechanism in the generation of OAEs (Probst, 1990). Dallos (1992) also asserts that the response properties of the live cochlea can best be accounted for by models that assume there is a local energy supply available in the cochlea which provides a force that selectively boosts basilar membrane motion in a periodic manner. Several studies which have examined the response of haircells to physiological and acoustic stimulation *in vitro* suggest that outer haircells (OHCs) may generate a motile response capable of providing a form of mechanical feedback in the cochlea (Flock *et al.*, 1986; Ashmore, 1987; Canlon *et al.*, 1988; Dallos and Corey, 1991; Ashmore, 1993; Dallos *et al.*, 1993; Mammano *et al.*, 1995).

B. DPOAE phase as an estimate of round-trip travel time in the human cochlea

While the effects of varying different stimulus parameters on DPOAE amplitude have been closely examined, only a few studies have examined DPOAE phase measurements, even though it has been demonstrated that phase measurements provide an effective measure of mechanical transmission in the live cochlea (Kemp and Brown, 1983; Fahey and Allen, 1986; Kimberley *et al.*, 1993; Brown *et al.*, 1994; O'Mahoney and Kemp, 1995). Kimberley *et al.* (1993) and Brown *et al.* (1994, 1995) have shown that the slope of DPOAE phase responses can be utilized to estimate round-trip delays in the adult and neonatal cochlea. The phase of the $2f_1-f_2$ DPOAE depends upon the phase of the two primaries and for a cubic nonlinearity is defined as

$$\phi dp = 2\phi f_1 - \phi f_2 .$$

A number of different models of mechanical transmission have been proposed to account for the time delay between the presentation of the acoustic stimulus and the occurrence of the emission, or the round-trip delay. The cochlear-echo model proposes that the anterograde traveling wave delay to the site of maximal displacement along the basilar membrane is equal to the retrograde traveling-wave delay from the site of origin to the external ear canal (Neely *et al.*, 1988). In this model, the travel time is composed of the delay to the site of maximum displacement along the basilar membrane, and does not explicitly include the resonance or filter response time at the site of maximal displacement (Ruggero, 1980). In contrast, Sutton and Wilson (1983) suggest that the round-trip travel time can be entirely attributed to the anterograde traveling wave delay ($\approx$3 periods) and a filter buildup time for emission generation ($\approx$5 or more periods). However, the round-trip travel times observed in a number of DPOAE studies were found to be substantially longer than delays predicted by the Sutton and Wilson model (e.g., Brown *et al.*, 1994). Hall (1974) posits that the round-trip delay is composed of both an anterograde and retrograde traveling wave of equal delay (transport time), and a filter buildup time. This model proposes that the round-trip travel time is composed of an intensity-independent transport time determined by passive membrane properties such as stiffness and mass loading, and an intensity-dependent filter buildup time at the site of distortion generation (Ruggero, 1992a; Ruggero *et al.*, 1992). Rutten (1980) has shown that the round-trip travel times of human transient OAEs are best approximated by such a three stage ''echo-latency'' model composed of a forward-going traveling wave delay, a cochlear filter response time, and a retrograde traveling-wave delay.

C. Round-trip travel time estimates from f_1-sweep DPOAEs

Several studies have employed DPOAE phase measurements to determine the latency of DPOAEs when the f_2 primary is fixed and f_1 is varied—an f_1-sweep stimulation paradigm (Wilson, 1980; Kemp and Brown, 1983; Kemp, 1986; Kimberley *et al.*, 1993). Wilson (1980) and Kemp and Brown (1983) noted a relationship between DPOAE latency and f_2/f_1. In particular, Wilson noted a latency of a half-cycle for ratios of 1.3, and 2.5 cycles for ratios of 1.1. Kemp (1986) noted that group delay increased with decreasing ratios and that DPOAE latency decreased with increasing primary intensity levels with slow frequency shifts of the primaries at a constant ratio of 1.3.

Kimberley *et al.* (1993) and Brown *et al.* (1994) have shown that round-trip travel time estimates obtained from DPOAE phase responses in human adults and neonates were influenced by both f_2 frequency and the sound intensity level of the primaries in normal hearing human ears (Kimberley *et al.*, 1993; Brown *et al.*, 1994, 1995). Kimberley *et al.* (1993) found that round-trip travel times in adults ranged from about 2.0 ms at the 10 kHz place (20 periods) to 7.0 ms at the 0.78 kHz place (5.5 periods), when DPOAE generation is assumed to be at the f_2 place. All of these studies indicated that there was a linear decrease in round-trip travel time for increasing primary intensity level. Brown *et al.* (1995) suggested that the intensity dependence of round-trip travel times may be attributed to intensity-related changes in the sharpness of tuning of cochlear responses, where sharply tuned responses at low sound intensities have longer filter response times than broadly tuned responses at high intensities (Ruggero, 1992a). Alternatively, the same study suggested that the intensity dependence of travel times could be due to shifts in the region of overlap between the two primary tones. Stover *et al.* (1996) have recently posited that the intensity dependence of f_1-sweep DPOAE latency may be attributed to multiple DPOAE sources in the human cochlea. In particular, it was suggested that long latency responses to low-intensity primaries may be principally generated at the $2f_1-f_2$ place where as shorter latency responses to higher intensity primaries may be primarily generated at the f_2 place.

D. Round-trip travel time estimates from f_2-sweep DPOAEs

The vast majority of studies which use DPOAE phase responses to estimate round-trip travel times also employ an experimental protocol where the f_2 primary is fixed, and the f_1 primary is swept across a range of frequencies—an f_1-sweep stimulation paradigm (Probst, 1990). Consequently, the effect of fixing the f_1 primary and varying the f_2

primary on DPOAE phase is not well understood (an f_2-sweep stimulation paradigm). Kemp and Brown (1983) found that when f_1 was fixed and f_2 was swept, DPOAE phase was reversed when compared to fixed f_2 responses in normal hearing human ears. Generally, travel time estimates are substantially longer in an f_2-sweep paradigm than in an f_1-sweep paradigm. O'Mahoney and Kemp (1995) found that f_1-sweep-derived delay measurements were 21.5% smaller than f_2-sweep-derived delay measurements in six normal hearing subjects when averaged across a frequency range of 1–6 kHz. In both-sweep conditions DPOAE latency (ms) decreased as f_2 frequency increased. Latency differences in the f_1- and f_2-sweep conditions were attributed to an underestimation of travel times in the f_1-sweep condition. In particular, it was suggested that f_1-sweep data do not include components of transmission time corresponding to the peak of the traveling wave delay. Whitehead *et al.* (1994) demonstrated that f_2-sweep latency was approximately six periods longer than f_1-sweep latency when the mean f_2=1.098 kHz, and four periods longer when the mean f_2=4.404 kHz at an intensity of 75 dB SPL. Furthermore, differences in f_1- and f_2-sweep latency were greater at low intensities than at high intensities. In this study it was suggested that the difference in f_1- and f_2-sweep latencies may be attributed to an overestimation of DPOAE latency in the f_2-sweep condition. O'Mahoney and Kemp (1995) have proposed that f_2-sweep latency may overestimate traveling-wave delay if the launch site of the DPOAE is fixed to the f_2 envelope and the f_2 source is moving. The predicted f_2-sweep latency in their model was twice the f_1-sweep latency.

E. DPOAE phase in f_1- and f_2-sweep stimulation paradigms

For a cubic nonlinearity the phase of the DPOAE is defined as

$$\phi dp = 2\phi f_1 - \phi f_2 .$$

One would expect in an f_2-sweep condition (fixed f_1), where $\Delta\phi dp = \Delta\phi f_2$, that the phase shift of the DPOAE would only be half of that observed in an f_1-sweep condition (fixed f_2), where $\Delta\phi dp = \Delta 2\phi f_1$. The group delay estimated from the slope of the DPOAE phase response is defined as $\Delta(dp\text{-phase})/\Delta\text{frequency}$. An f_1-sweep stimulation paradigm (where $\Delta\phi dp = \Delta 2\phi f_1$) should give rise to a steeper DPOAE phase response slope and consequently a longer delay than an f_2-sweep stimulation paradigm (where $\Delta\phi dp = \Delta\phi f_2$).

In order to determine why differences in f_1- and f_2-sweep travel time estimates occur, one must examine the phase of the changing primary in both stimulation conditions. Figure 1 shows a schematic representation of the movement patterns of the cochlear partition for the two primaries. In an f_1-sweep paradigm, the f_2 primary is held constant and therefore does not contribute to the delay estimate derived from the phase response [Fig. 1(a)]. Consequently, the phase of the DPOAE reflects the phase of f_1 at the f_2 place—the site of DPOAE generation. The phase response does not include the entire filter buildup time at the site of DPOAE generation, and subsequently only undergoes fewer cycles of delay. In a f_2-sweep paradigm, the f_1 primary is held constant and does not contribute to the phase response [Fig. 1(b)]. The phase of the DPOAE in this case reflects the phase of f_2 at the site of DPOAE generation and includes the delay associated with the filter buildup time. Therefore, round-trip delays estimated from DPOAE phase responses in an f_2-sweep paradigm will be greater than delay estimates in an f_1-sweep paradigm at the same f_2 place because the f_2-sweep response includes the filter buildup time at the f_2 place. Furthermore, f_2-sweep round-trip delays should show a stronger dependence on filter response properties than f_1-sweep delays if they are composed of a greater proportion of the filter build-up time. By assuming that round-trip delay is composed of an anterograde and retrograde traveling-wave delay, and a filter buildup time at the f_2 place (Hall, 1974), a large portion of the delay associated with the filter response at the f_2 place can be isolated by subtracting f_1-sweep delay estimates from f_2-sweep delay estimates when f_2 and intensity are the same in both sweep conditions [Fig. 1(a) and (b)].

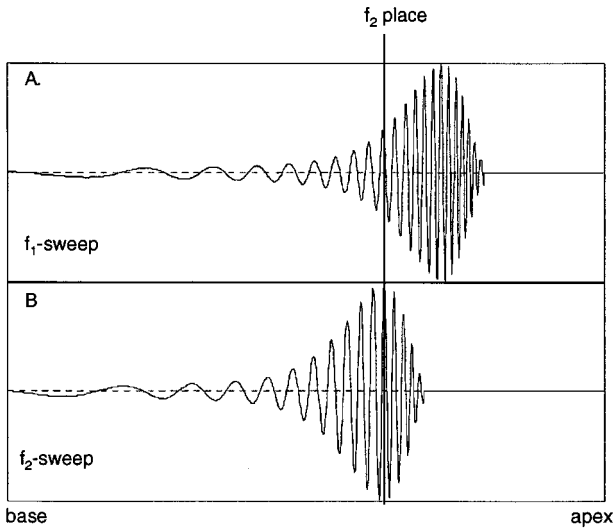

FIG. 1. A schematic representation of DPOAE phase in a f_1-sweep (a) and f_2-sweep stimulation paradigm (b). (a) In the f_1-sweep paradigm the phase response represents the change in phase of the f_1 primary at the f_2 place (dashed line). Note that the phase response does not include the entire filter buildup component of the f_1 response. (b) In the f_2-sweep stimulation paradigm the phase response represents the change in phase of f_2 at the f_2 place and includes the filter buildup component of the f_2 response.

The present study will investigate the effect of intensity on f_1- and f_2-sweep round-trip delays estimated from DPOAE phase responses in normal hearing human subjects. The f_1-sweep delays will be compared to f_2-sweep delays for each subject. The expectation is that both f_1- and f_2-sweep round-trip delays should be dependent upon f_2 frequency and stimulus intensity. Round-trip delays derived from f_1-sweep data should be shorter than f_2-sweep delays. If longer delays in the f_2-sweep condition can be attributed to a greater proportion of the response being composed of a filter buildup time at the site of emission generation, then f_2-sweep delays should show a stronger dependence on intensity, and, similarly, differences in the f_1- and f_2-sweep

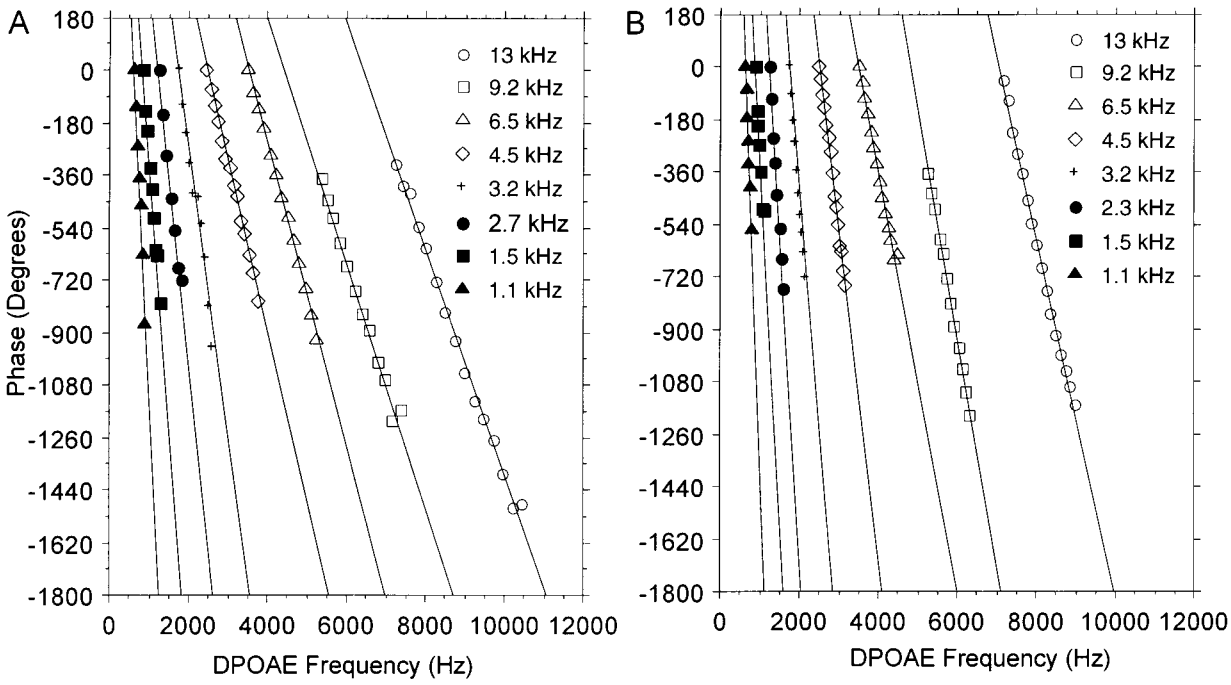

FIG. 2. The unwrapped DPOAE phase responses of one male ear in the f_1-sweep (a) and f_2-sweep stimulation conditions (b) at eight f_2 frequencies. Slopes were determined by fitting a linear least squares regression line to the data. Note that slopes were steeper in the f_2-sweep condition (b) than in the f_1-sweep condition (a) at each f_2 frequency. The round-trip delays calculated from these DPOAE phase responses are shown in Table I.

delay measures should be dependent upon both f_2 frequency and stimulus intensity.

I. METHODS

A. Subjects

The DPOAE phase responses were measured in 20 human ears (10 female ears; 10 male ears). Subjects had audiometric thresholds $\leqslant$15 dB HL in the standard audiometric frequency range of 0.25–8.0 kHz and an age range 18–35 years, as hearing loss and aging reduce or abolish DPOAE responses (see Probst, 1990, for review).

B. Recording and stimulation procedure

Subjects were seated in a reclining chair in a sound-treated booth. The DPOAEs were measured from the subject's external ear canal with an ER 10C probe system and a modified version of the CUBDISFI software (J. Allen, Bell Labs). The probe apparatus consisted of two miniature speakers (stimulus delivery) and a low noise recording microphone connected to a disposable soft foam ear tip.

The phase of the stimulus was measured prior to DPOAE recording by a calibration chirp with constant amplitude up to 20 kHz. Phase shifts measured by the calibration procedure were subtracted from later recordings. Thus, the zero phase reference utilized in this study was a tone in the ear canal in the region of the microphone.

The modified CUBDISF1 program measured DPOAE amplitude as a function of f_2/f_1 ratio. The DPOAE amplitude was measured for ratios ranging from 1.3–1.1 in steps of 48.8 Hz. The DPOAE frequencies were the same for both the f_1- and f_2-sweep conditions. In the f_1-sweep condition DPOAEs were measured at eight different f_2 frequencies ranging from 1.1–13 kHz. In the f_2-sweep condition the geometric mean of f_2 was kept within 10% of the fixed f_2 value in the f_1-sweep condition. In order to investigate the effect of intensity level on DPOAE phase response, primary intensity levels were varied in 5dB steps from 30–50 dB SPL (f_2 intensity) in both the f_1- and f_2-sweep conditions (where f_1 is 15 dB$>f_2$). Only DPOAEs that were 6 dB above the noise floor of the recording were considered for further analyses.

C. Data analysis

The DPOAE phase response was calculated from the discrete fast Fourier transform (DFFT) of the DPOAE by applying a four-quadrant arctangent function to the ratio of imaginary and real DFFT components produced by the CUBDISF1 program. The phase data obtained through this procedure were unwrapped by subtracting 360° at points where phase discontinuities exceeded 180°. The unwrapped DPOAE phase response was plotted as the change in DPOAE phase as a function of DPOAE frequency in both the f_1- and f_2-sweep conditions [Fig. 2(a) and (b)].

The DPOAE phase responses were assumed to be associated with an f_2 generation site, thus either the fixed f_2 value or the geometric mean of the f_2-sweep was used as the frequency reference point in all subsequent analyses. The slope of the unwrapped DPOAE phase response at each f_2 frequency was calculated using simple linear regression to obtain a least squares fit [Fig. 2(a) and (b); Table I]. The slope of the unwrapped DPOAE phase response was defined as

$$\Delta\, dp\phi/\Delta\, dp \quad \text{frequency (degrees/kHz).}$$

TABLE I. Delay calculation from DPOAE phase responses.

f_2 frequency (kHz)	Slope (degrees/kHz)	Delay (ms)	Delay (periods)
f_1 sweep			
13	−0.426	1.183	15.369
9.2	−0.497	1.381	12.673
6.5	−0.523	1.453	9.399
4.5	−0.586	1.628	7.431
3.2	−1.003	2.786	8.979
2.3	−1.226	3.517	7.985
1.6	−1.799	4.997	7.930
1.1	−2.809	7.803	8.572
f_2 sweep			
13	−0.639	1.775	21.321
9.2	−0.785	2.181	18.473
6.5	−0.868	2.411	14.392
4.5	−1.133	3.147	13.216
3.2	−1.619	4.497	13.285
2.3	−2.221	6.619	12.652
1.6	−2.382	6.617	9.646
1.1	−3.657	10.158	10.168

The round-trip delay was obtained by converting the slope of each unwrapped phase response to either the number of periods of delay or the delay time in milliseconds:

$$\text{delay (ms)} = \#\ \text{cycles/kHz},$$

$$\text{delay (periods of } f_2) = \text{delay (ms)} * f_2(\text{kHz}).$$

Round-trip delays obtained in the f_1-sweep condition were compared to round-trip delays in the f_2-sweep condition with simple linear regression using STATVIEW II software for the Macintosh at all frequencies and intensities. Round-trip delay differences in the two conditions were further examined by subtracting the f_1-sweep delays from f_2-sweep delays for each subject. The effect of intensity and f_2 frequency on the delay difference was also examined with linear regression.

II. RESULTS

Figure 3 illustrates group [Fig. 3(a)–(d)] and individual round-trip delays [Fig. 3(e)–(h)] plotted as a function of f_2 intensity at four different f_2 frequencies. Round-trip traveling-wave delays obtained from a group of 20 ears showed a significant intensity dependence in both the f_2- (filled circles) and f_1-sweep (open squares) conditions ($p \leqslant 0.01$). In both stimulation paradigms, the travel time increased as stimulus intensity decreased. Travel times obtained from one male ear are similarly intensity dependent [Fig. 3(e)–(h)]. The slope of the regression line in the f_2-sweep condition was significantly steeper than the slope in the f_1-sweep condition for frequencies above 1.6 kHz for the grouped data ($p \leqslant 0.01$). Thus, f_2-sweep round-trip delays were more strongly intensity dependent than f_1-sweep delays at high frequencies [Fig. 3(a)–(c)]. Differences between the slopes at each f_2 frequency within the same stimulation condition were not significant at frequencies greater than 1.6 kHz.

Figure 4 shows the effect of intensity on delay differences between the f_1- and f_2-sweep stimulation conditions at each f_2 frequency. Differences were obtained by subtracting f_1-sweep delays from f_2-sweep delays for each subject at all intensities and frequencies. The differences between the f_1- and f_2-sweep delays were significantly dependent on intensity at f_2 frequencies above 1.6 kHz (Fig. 4). At high frequencies, delay differences decreased as intensity increased [Fig. 4(a)–(c), (e)–(g)]. At frequencies below 1.6 kHz, the travel time difference remained constant for all intensities [Fig. 4(d) and (h)].

Figure 5 depicts the mean delay difference for f_2- and f_1-sweep responses at low (30–35 dB), medium (40 dB), and high intensities (45–50 dB) as a function of f_2 frequency. Mean delay differences were greatest at high f_2 frequencies and low intensities. At low intensities (filled circles), delay differences ranged from 15.9 periods at the 9.2 kHz f_2 place to 3.4 periods at the 1.1 kHz f_2 place. At high intensities (open triangles), the greatest difference occurred at the 9.2 kHz place (10.6 periods), and the smallest difference at the 1.6 kHz place (2.5 periods). Table II summarizes the results of a comparison of mean differences in round-trip delays in the f_2- and f_1-sweep conditions at low, medium, and high intensities. Differences in f_2- and f_1-sweep delays decreased as primary intensity increased. Travel time differences at low intensities were significantly longer than travel time differences at high intensities for frequencies above 1.6 kHz. Significant travel time differences were also observed between medium and low intensities as well as high and medium intensities at frequencies above 1.6 kHz.

III. DISCUSSION

The aim of the present study was to investigate the effect of intensity on f_1- and f_2-sweep round-trip phase delays estimated from DPOAE phase responses in normal hearing human subjects. Travel times in the f_2-sweep condition were equal to or longer than delays in the f_1-sweep condition (Fig. 3). Round-trip delays had a significant intensity dependence in both the f_1- and f_2-sweep conditions ($p \leqslant 0.01$). The delay increased as stimulus intensity decreased in both stimulation paradigms. Delay estimates in the f_2-sweep condition were more strongly intensity dependent than estimates in the f_1-sweep condition at f_2 frequencies above 1.6 kHz [Fig. 3(a)–(d)]. Delay differences in the two conditions were significantly dependent on intensity at f_2 frequencies above 1.6 kHz (Fig. 4). Delay differences decreased as intensity increased for f_2 frequencies above 1.6 kHz. At f_2 frequencies below 1.6 kHz, the delay difference was not influenced by intensity.

A. Comparing f_1- and f_2-sweep DPOAEs

Several studies have indicated that f_1-sweep estimates of round-trip travel time are considerably shorter than f_2-sweep estimates (O'Mahoney and Kemp, 1995; Whitehead *et al.*, 1994). O'Mahoney and Kemp (1995) found that f_1-sweep delays were 21.5% smaller than f_2-sweep delays in normal hearing human subjects when averaged across a frequency range of 1–6 kHz. The findings of the present study similarly indicate that f_1-sweep delays are consistently shorter than f_2-sweep delays when measured in the same ear. However, the difference in delays estimated in the two stimulation con-

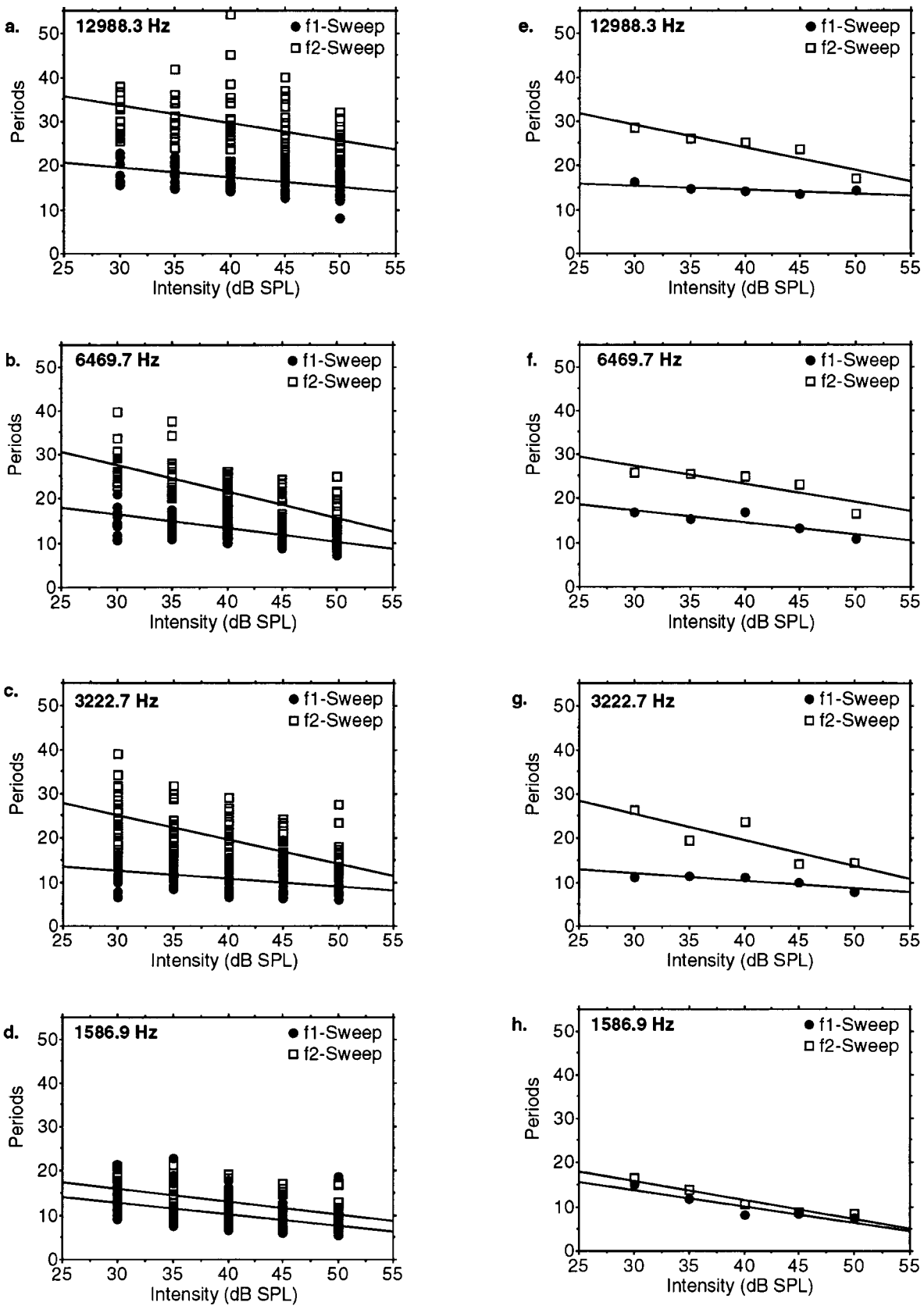

FIG. 3. The effect of intensity on f_1-(open squares) and f_2-sweep (filled circles) DPOAE round-trip delay estimates as a function of f_2 frequency for 20 ears [(a)–(d)] and one male ear [(e)–(h)]. Both the f_1- and the f_2-sweep delays were dependent on stimulus intensity [$p \leqslant 0.01$, (a)–(d)]. Delay decreased as intensity increased. DPOAE round-trip delays obtained from one male ear showed a similar intensity dependence [(e)–(h)]. Note that the regression slopes in the f_2-sweep condition were significantly steeper than the slopes in the f_2-sweep condition at f_2 frequencies above 1.6 kHz, indicating that f_2-sweep delays were more strongly influenced by stimulus intensity than f_1-sweep delays in this f_2 frequency range [(a)–(c)]. Slope differences within the f_2-sweep condition were not significant at f_2 frequencies above 1.6 kHz.

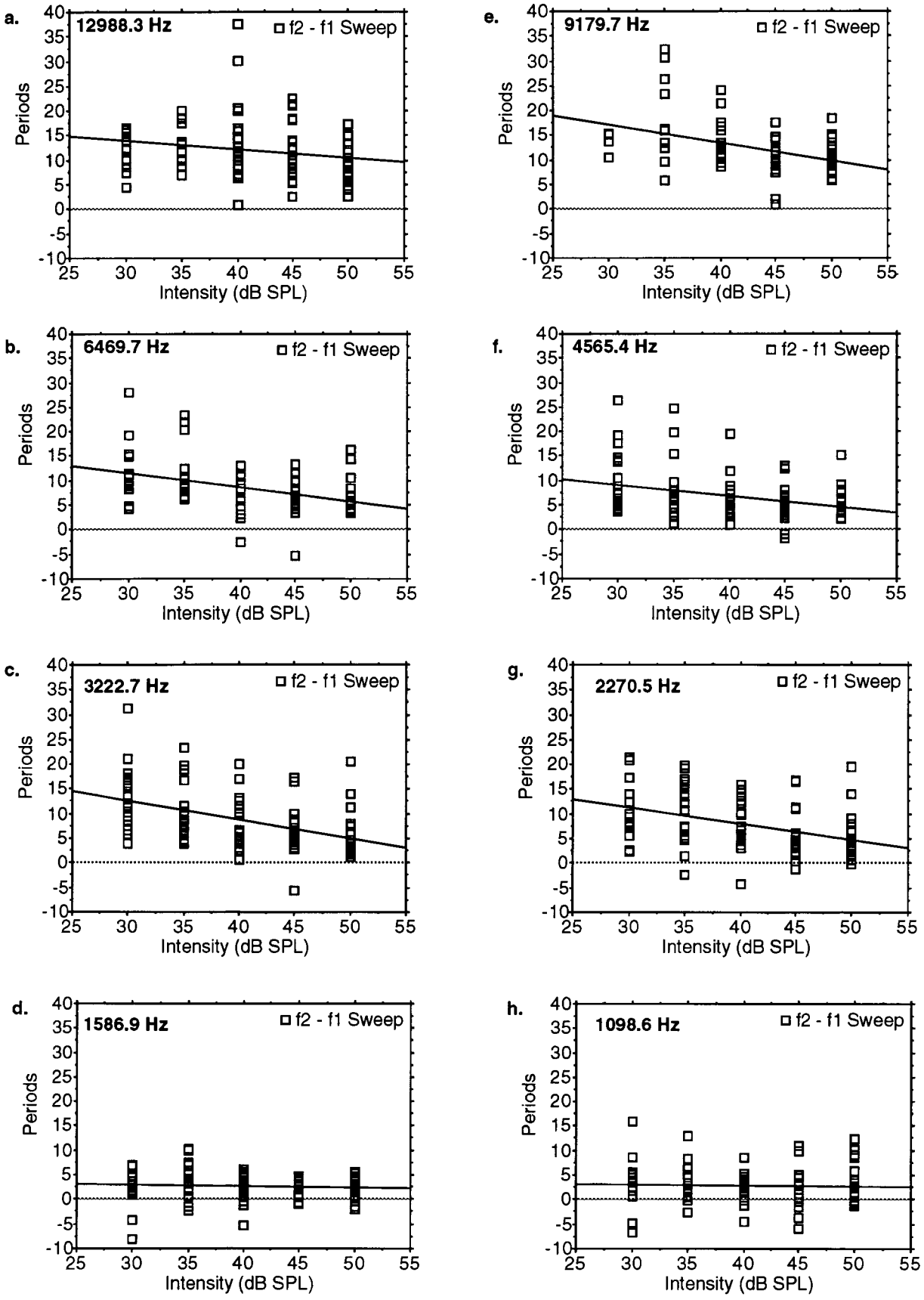

FIG. 4. The effect of intensity on delay differences between the f_1- and f_2-sweep DPOAE round-trip delay estimates as a function of f_2 frequency. Delay differences were calculated by subtracting f_1-sweep delays from f_2-sweep delays for each ear. Delay differences were significantly dependent on intensity at f_2 frequencies above 1.6 kHz [$p \leqslant 0.05$, (a)–(c), (e)–(g)]. Differences increased as intensity decreased. Delay differences remained constant for all intensities at f_2 frequencies below 1.6 kHz.

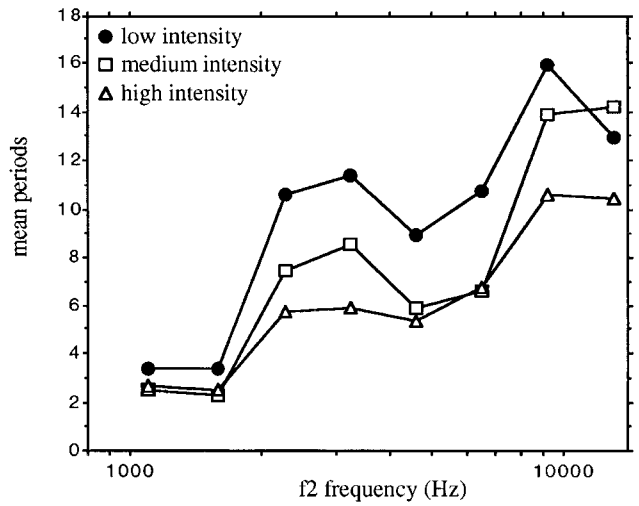

FIG. 5. Mean differences in delay between the f_1- and f_2-sweep conditions plotted as a function of f_2 frequency at three intensities: low intensities (30–35 dB SPL) shown with filled circles; medium intensities (40 dB SPL) shown with open squares; and high intensities (45–50 dB SPL) shown with open triangles. Differences in mean delay were intensity dependent at f_2 frequencies above 1.6 kHz. The range of observed delay differences was similar at f_2 above 1.6 kHz. Delay differences were smallest at high intensities. At f_2 frequencies below 1.6 kHz, mean delay difference was constant at all intensities. Table II summarizes the results of dependent *t* tests comparing these mean delay differences as a function of f_2 frequency and intensity.

ditions changed as a function of f_2 frequency and stimulus intensity. In particular it was noted that delay differences were greater at f_2 frequencies above 1.6 kHz than at lower frequencies. Whitehead *et al.* (1994) demonstrated that f_2-sweep latency was approximately six periods longer than f_1-sweep latency when the mean f_2=1.098 kHz, and four periods longer when the mean f_2=4.404 kHz at an intensity of 75 dB SPL in one human ear. In this study the mean f_2-sweep delay was 2.7 periods longer than the f_1-sweep delay when f_2=1.1 kHz and 5.3 periods longer when f_2=4.5 kHz at high intensities (f_2 intensity 45–50 dB SPL) in 20 human ears. The disparity between our findings and those of Whitehead *et al.* (1994) at low frequencies may be attributed to the difference in the number of subjects in the two studies. In the present study, delay differences of up to 12 periods were observed in a few ears at f_2 frequencies of less than 1.6 kHz; however, most subjects had small delay differences at low f_2 values [Fig. 4(d) and (h)]. Small delay differences were also occasionally observed at the 4.5 kHz f_2 place in the present study [Fig. 4(f)]. Therefore, the range of delay differences observed in the present study could encompass the values obtained from a single ear reported in the Whitehead *et al.* (1994) study.

TABLE II. Mean difference in round-trip delays f_2-sweep and f_1-sweep DPOAES at low, medium, and high intensities as a function of f_2 frequency.

f_2 frequency (Hz)	Intensity low–medium	medium–high	low–high
12 988.3	N.S.	3.76[a]	2.48[a]
9179.7	N.S.	3.35[b]	5.35[a]
6469.7	4.16[b]	N.S.	4.04[b]
4565.4	3.06[b]	N.S.	3.62[b]
3222.7	2.86[a]	2.62[b]	5.48[b]
2270.5	3.12[a]	N.S.	4.83[b]
1586.9	N.S.	N.S.	N.S.
1098.6	N.S.	N.S.	N.S.

[a] $p \leq 0.05$.
[b] $p \leq 0.01$.

B. Intensity dependence of f_1- and f_2-sweep DPOAE estimates of round-trip delay

In the present study, round-trip delays were intensity dependent in both the f_1- and f_2-sweep conditions (Fig. 3). Delay increased as stimulus intensity decreased in both stimulation paradigms. This finding is consistent with those of Kimberley *et al.* (1994) and Brown *et al.* (1995), where a linear decrease in round-trip travel time for increasing primary intensity level was observed in human ears when a f_1-sweep stimulation paradigm was employed. Brown *et al.* (1995) suggest that the intensity dependence of round-trip travel times may be attributed to intensity-related changes in the sharpness of tuning of cochlear responses, where sharply tuned responses at low sound intensities have longer filter response times than broadly tuned responses at high intensities (i.e., Ruggero, 1992a,b). Thus, according to Brown *et al.* (1995) round-trip travel times estimated from DPOAE phase responses in an f_1-sweep paradigm must incorporate at least part of the filter buildup time at the site of emission generation. Hall (1974) posited that the round-trip traveling-wave delay in the cochlea is composed of both an anterograde and retrograde traveling wave of equal delay, and a filter buildup time. According to this model, round-trip travel time estimates would be composed of an intensity-independent transport time to and from the site of distortion generation, and an intensity-dependent filter buildup time at the site of distortion generation (Ruggero, 1992a).

The findings of the present study demonstrated that delay estimates in the f_2-sweep condition were more strongly intensity dependent than estimates in the f_1-sweep condition at f_2 frequencies above 1.6 kHz [Fig. 3(a)–(d)]. Round-trip delay differences between the two stimulation conditions increased as stimulus intensity decreased (Fig. 4). The longer delays observed in the f_2-sweep condition cannot be attributed to an increase in the transport time to and from the site of emission generation because differences in primary frequencies utilized in the f_2- and f_1-sweep conditions were relatively small. The geometric mean of the f_2-sweep was kept within 10% of the fixed f_2 value in the f_1-sweep condition. Consequently, DPOAEs were generated in the same f_2 filter region of the cochlea for both conditions. The region of primary overlap on the basilar membrane was the same in both sweep conditions because the primaries were swept through the same f_2/f_1 ratios. Moreover, the intensity dependence of the delay difference between the two conditions cannot be attributed to an intensity-dependent shift in the origin of the DPOAE from the f_2 place to the DPOAE site at low intensities as suggested by Stover *et al.* (1996) because the DPOAE frequency was the same in both stimulation conditions. Consequently, the delay components associated with different generation sites will not be present in the delay difference which is calculated by subtracting f_1-sweep de-

lays from f_2-sweep delays at each frequency and intensity. Therefore, it is most likely that differences in f_2- and f_1-sweep round-trip delays arise from the filter response component of the round-trip traveling-wave delay in the cochlea. The filter buildup time at the site of emission generation would add several periods of delay to the round-trip delay estimate in the f_2-sweep condition (Fig. 1). The filter buildup time, and consequently round-trip delay, would increase as stimulus intensity decreased (Ruggero, 1992a). Thus, the stronger intensity dependence of delays observed in the f_2-sweep condition supports the view that f_2-sweep DPOAE responses are composed of a greater proportion of the filter buildup time or resonance at the site of maximal displacement than f_1-sweep responses (e.g., O'Mahoney and Kemp, 1995). Differences between f_1- and f_2-sweep delay estimates were also highly intensity dependent at frequencies above 1.6 kHz (Fig. 4). This finding also suggests that the difference between f_1- and f_2-sweep delay measures represent the intensity-dependent filter response component of the round-trip travel time and not the intensity independent transport time to and from the site of emission generation. Delay differences between the f_2- and f_1-sweep conditions cannot be attributed to an overestimation of traveling-wave delay in the f_2-sweep condition due to a moving f_2 source because f_2-sweep delays are not twice as long as f_1-sweep delays, as would be predicted by a ''wave-fixed'' model (O'Mahoney and Kemp, 1995). Moreover, f_2-sweep delays have a better correspondence with electrophysiological measures of traveling-wave delay than f_1-sweep travel time estimates and do not substantially overestimate travel time when compared to electrophysiological measures (e.g., O'Mahoney and Kemp, 1995). In contrast, traveling-wave delays estimated from f_1-sweep DPOAEs are shorter than electrophysiological measures of traveling-wave delay in the human cochlea (O'Mahoney and Kemp, 1995; Kimberley *et al.*, 1993; Eggermont, 1979).

In the present study, mean travel time differences were greatest at high f_2 frequencies and low intensities (Figs. 4 and 5). Differences at f_2 frequencies below 1.6 kHz remained constant for all intensities. The differential effect of intensity on low-frequency and high-frequency f_2-sweep responses may be attributed to frequency-related changes in the sharpness of tuning of cochlear responses, where responses at f_2 frequencies above 1.6 kHz are more sharply tuned than low-frequency responses. Ruggero (1992a) demonstrated that filter buildup time at the basilar membrane response maxima reflect filter tuning properties. Sharply tuned responses at low sound intensities had longer filter buildup delays than broadly tuned responses at high intensities. Electrophysiological studies of single auditory nerve fiber responses also indicate that the CF normalized tuning curve bandwidth decreases as CF increases (see Ruggero 1992b, for review). Fagelson and Champlin (1996) suggest that the mechanisms underlying the generation of the nonlinear component of cochlear responses to acoustic stimuli are not uniformly distributed along the length of the cochlea and that the processes associated with the sharp tuning and sensitivity of the peripheral auditory system were more strongly associated with high frequency sites of DPOAE generation than low-frequency sites. The similar intensity dependence observed in both the f_1- and f_2-sweep conditions at low f_2 frequencies in the present study may therefore reflect frequency-dependent filter response properties, where both the f_1- and f_2-sweep responses are composed of a similar broadly tuned filter response at low f_2 frequencies.

There is some variability associated with mean delay differences in the f_1- and f_2-sweep conditions at f_2 frequencies above 1.6 kHz (Fig. 5). The slope relating round-trip delay differences to intensity are not significantly different at f_2 frequencies above 1.6 kHz, indicating that differences in the 2.3–13 kHz frequency range have a similar intensity dependence (Fig. 4). Mean differences at f_2 frequencies above 1.6 kHz are consistently 3.0–4.0 periods greater at low intensities than at high intensities (Table II). Mean delay differences in f_1- and f_2-sweep responses increase slightly as a function of frequency at most f_2 frequencies above 2.0 kHz. The similar intensity dependence of delay differences at high and middle frequencies suggest that filter response properties are similar for responses in the mid-frequency and high-frequency f_2 regions in the cochlea (Fig. 4). However, a reduction in the mean delay difference is observed in the 4.5–7.0 kHz f_2 region (Fig. 5). The reduction in the mean delay difference in this frequency range may be explained by differences in the sound pressure levels at the ear drum for these mid-frequency primaries, rather than a difference in filter response properties for mid- and high-f_2 frequency regions. Siegel (1994) has shown that large errors in estimating the sound pressure level at the ear drum can occur when pressure level is monitored 15–20 mm from the ear drum at quarter wavelength resonance frequencies. In this study, measurements of sound pressure level were made by a probe placed in the external ear canal, not at the ear drum. Therefore, sound pressure level may have been under estimated by as much as 20 dB SPL in the 4.5–7-kHz range (Siegel, 1994). Sound pressure level may also have been underestimated in the 13.0-kHz region which corresponds roughly to the three-quarter wavelength resonance of the ear canal (Siegel, 1994). The errors associated with sound pressure level estimation may lead to systematic errors in the estimation of DPOAE phase measurements of round-trip travel time (Dreisbach and Siegel, 1996). Systematic errors in the estimation of sound pressure level for primaries corresponding to quarter wavelength frequencies could have lead to an intensity-dependent reduction in round-trip delay, and may explain the smaller mean delay differences observed in the 4.5–6.5-kHz and 13.0-kHz f_2 frequency ranges.

IV. SUMMARY AND CONCLUSIONS

This study has shown that round-trip delays estimated from DPOAE phase responses in an f_2-sweep stimulation paradigm are consistently longer than f_1-sweep delay estimates in the human cochlea. Round-trip delays were influenced by intensity in both the f_1- and f_2-sweep conditions. In both conditions, the delay increased as stimulus intensity decreased. Delay estimates in the f_2-sweep condition were more strongly intensity dependent than estimates in the f_1-sweep condition at f_2 frequencies above 1.6 kHz. Differences between the f_1- and f_2-sweep delays were also inten-

sity dependent at f_2 frequencies above 1.6 kHz. At high f_2 frequencies, delay differences decreased as intensity increased. The intensity dependence of round-trip delay estimates in both conditions may be attributed to intensity-dependent changes in the cochlear filter response time related to the sharpness of tuning of DPOAE responses. The steeper intensity dependence and longer delays observed in the f_2-sweep condition suggest that DPOAE responses are composed of a greater proportion of the filter buildup time or resonance at the site of maximal displacement than f_1-sweep responses.

ACKNOWLEDGMENTS

This research was supported by the Alberta Heritage Foundation for Medical Research (DMB, DKB, JJE, BPK), the Campbell McLaurin Foundation (BPK), and the Natural Sciences and Engineering Research Council of Canada (DMB, JJE). The authors would like to thank Istvan Hernadi, Danny Ramotowski, and Geoff Smith for their technical assistance.

Allen, J. B., and Neely, S. T. (**1992**). ''Micromechanical models of the cochlea,'' Phys. Today **45(7),** 40–47.

Ashmore, J. F. (**1987**). ''A fast motile event in outer hair cells isolated from guinea pig cochlea,'' J. Physiol. (London) **388,** 323–347.

Ashmore, J. F. (**1993**). ''The ear's fast cellular motor,'' Curr. Biol. **3**, 38–40.

Brown, A. M., and Kemp, D. T. (**1984**). ''Suppressibility of the 2 $f1$-$f2$ stimulated acoustic emissions in gerbil and man,'' Hear. Res. **13,** 29–37.

Brown, A. M., Gaskill, S. A., and Williams, D. M. (**1992**). ''Mechanical filtering of sound in the inner ear,'' Proc. R. Soc. London, Ser. B **250,** 29–34.

Brown, D., Kimberley, B., and Eggermont, J. (**1994**). ''Cochlear traveling-wave delays estimated by distortion-product emissions in normal hearing adults and term-born neonates,'' J. Otolaryngol. **23**, 234–238.

Brown, D. K., Kimberley, B., and Eggermont, J. J. (**1995**). ''The effect of intensity on DPE round trip travel time in adult humans,'' Abstracts of the Eighteenth Midwinter Research Meeting of the Association for Research in Otolaryngology, Vol. 481, p. 121.

Canlon, B., Brundin, L., and Flock, A. (**1988**). ''Acoustic stimulation causes tonotopic alterations in the length of outer hair cells from the guinea pig hearing organ,'' Phys. Rev. A **85,** 7033–7035.

Dallos, P. (**1992**). ''The active cochlea,'' J. Neurosci. **12,** 4575–4585.

Dallos, P., and Corey, M. E. (**1991**). ''The role of outer hair cell motility in cochlear tuning,'' Curr. Opin. Neurobiol. **1**, 215–220.

Dallos, P., Hallworth, R., and Evans, B. N. (**1993**). ''Theory of electrically driven shape changes of cochlear outer haircells,'' J. Neurophysiol. **70,** 299–323.

De Boer, E. (**1991**). ''Auditory physics. Physical principles in hearing theory. III.,'' Phys. Rep. **203,** 125–231.

Dreisbach, L. E., and Siegel, J. H. (**1996**). ''Further characterization of ultra-high frequency distortion-product otoacoustic emissions (DPOAEs),'' Abstracts of the Nineteenth Midwinter Research Meeting of the Association for Research in Otolaryngology, #717, p. 180.

Eggermont, J. J. (**1979**). ''Narrow-band AP latencies in normal and recruiting human ears,'' J. Acoust. Soc. Am. **65,** 463–470.

Fagelson, M. A., and Champlin, C. A. (**1996**). ''Distortion-product otoacoustic emissions and auditory filter shape,'' Abstracts of the Nineteenth Midwinter Research Meeting of the Association for Research in Otolaryngology, #716, p. 179.

Fahey, P., and Allen, J. (**1986**). ''Characterization of cubic intermodulation distortion products in the cat external auditory meatus,'' in *Peripheral Auditory Mechanisms*, edited by J. Allen, J. L. Hall, A. Hubbard, S. T. Nelly, and A. Tubis (Springer-Verlag, New York), pp. 314–321.

Flock, Å., Flock, B., and Ulfendahl, M. (**1986**). ''Mechanisms of movement in outer hair cells and a possible structural basis,'' Arch. Otorhinolaryngol. **243**, 83–90.

Furst, M., and Lapid, M. (**1988**). ''A cochlear model for otoacoustic emissions,'' J. Acoust. Soc. Am. **84,** 222–229.

Gaskill, S. M., and Brown, A. M. (**1990**). ''The behavior of the acoustic distortion product, $2f_1 - f_2$, from the human ear and its relation to auditory sensitivity,'' J. Acoust. Soc. Am. **88,** 821–839.

Goldstein, J. L. (**1967**). ''Auditory nonlinearity,'' J. Acoust. Soc. Am. **41,** 676–689.

Hall, J. (**1974**). ''Two-tone distortion products in a nonlinear model of the basilar membrane,'' J. Acoust. Soc. Am. **62,** 1818–1828.

Kemp, D. T. (**1978**). ''Stimulated acoustic emissions from within the human auditory system,'' J. Acoust. Soc. Am. **64,** 1386–1391.

Kemp, D. T. (**1986**). ''Otoacoustic emissions, travelling waves and cochlear mechanisms,'' Hear. Res. **22,** 95–100.

Kemp, D., and Brown, A. **(1983)**. ''An integrated view of cochlear mechanical nonlinearities observable from the ear canal,'' in *Mechanics of Hearing*, edited by E. DeBoer and M. Viergever (Martinus Nijhoff, Delft), pp. 75–82.

Kimberley, B. P., Brown, D. K., and Eggermont, J. J. (**1993**). ''Measuring human cochlear traveling wave delay using distortion product emission phase responses,'' J. Acoust. Soc. Am. **94**, 1343–1350.

Mammano, F., Kros, C. J., and Ashmore, J. F. **(1995)**. ''Measuring outer hair cell motility in the intact adult organ of Corti,'' in Abstracts of the Eighteenth Midwinter Research Meeting of the Association for Research in Otolaryngol, Vol. 621, p. 156.

Neely, S. T., Norton, S. J., Gorga, M. P., and Jesteadt, W. (**1988**). ''Latency of auditory brainstem responses and otoacoustic emissions using tone-burst stimuli,'' J. Acoust. Soc. Am. **83,** 652–656.

O'Mahoney, C. F., and Kemp, D. T. (**1995**). ''Distortion product otoacoustic emission delay measurement in human ears,'' J. Acoust. Soc. Am. **97,** 3721–3735.

Probst, R. **(1990)**. ''Otoacoustic emissions: an overview,'' New Aspects of Cochlear Mechanics and Inner Ear Pathophysiology, Adv. Otorhinolaryngol. **44**, 1–91.

Ruggero, M. A. (**1980**). ''Systematic errors in indirect estimates of basilar membrane travel times,'' J. Acoust. Soc. Am. **67,** 707–710.

Ruggero, M. A. **(1992a)**. ''Response to sound of the basilar membrane of the mammalian cochlea,'' Curr. Opin. Neurobiol. **2**, 449–456.

Ruggero, M. A. **(1992b)**. ''Physiology and coding of sound in the auditory nerve,'' in *The Mammalian Auditory Pathway: Neurophysiology*, edited by R. Fay and A. Popper (Springer-Verlag, New York), pp. 34–93.

Ruggero, M. A., Rich, N. A., and Recio, A. (**1992**). ''Basilar membrane responses to clicks,'' Adv. Biosci. **83,** 85–91.

Rutten, W. L. C. (**1980**). ''Latencies of stimulated acoustic emissions in normal human ears,'' in *Psychophysical, Physiological and Behavioral Studies in Hearing*, edited by G. van den Brink and F. A. Bilsen (Delft U.P., Delft), pp. 43–50.

Siegel, J. H. (**1994**). ''Ear-canal standing waves and high-frequency sound calibration using otoacoustic emission probes,'' J. Acoust. Soc. Am. **95,** 2589–2597.

Stover, L. J., Neely, S. T., and Gorga, M. P. (**1996**). ''Latency and multiple sources of distortionproduct otoacoustic emissions,'' J. Acoust. Soc. Am. **99,** 1016–1024.

Sutton, G. J., and Wilson, J. P. **(1983)**. ''Modelling cochlear echoes: the influence of irregularities in frequency mapping on summed cochlear activity,'' in *Mechanics of Hearing*, edited by E. DeBoer and M. Viergever (Martinus Nijhoff, Delft), pp. 83–90.

Whitehead, M. L., Stagner, B. B., Lonsbury-Martin, B. L., and Martin, G. K. **(1994)**. ''Comparison of the onset latency and group latency of distortion-product otoacoustic emissions in human ears,'' in Abstracts of the Seventeenth Midwinter Research Meeting of the Association for Research in Otolaryngology, Vol. 182, p. 46.

Wilson J. P. (**1980**). ''The combination tone, $2f_1 - f_2$, in psychophysics and ear canal recording,'' in *Psychophysical, Physiological and Behavioral Studies in Hearing*, edited by G. Van den Brink and F. A. Bilsen (Delft U.P., Delft), pp. 43–50.

Activity of primary auditory neurons in the cochlear ganglion of the emu *Dromaius novaehollandiae*: Spontaneous discharge, frequency tuning, and phase locking

Geoffrey A. Manley and Christine Köppl
Institut für Zoologie, Technische Universität München, Lichtenbergstrasse 4, 85747 Garching, Germany and Department of Physiology, University of Western Australia, Nedlands, 6009, Australia

Graeme K. Yates
Department of Physiology, University of Western Australia, Nedlands 6009, Australia

(Received 3 June 1996; accepted for publication 30 September 1996)

The spontaneous and pure-tone sound-driven activity of primary auditory units was recorded in the cochlear ganglion of emu chicks aged between post-hatching days 1 and 14. Spontaneous activity tended to increase both with the chick's age and as a function of the unit's characteristic frequency (CF). The CF of 887 units ranged from 0.04 to 4 kHz, the thresholds down to 0 dB SPL. Although the CF range did not change, the thresholds improved with age during the first two weeks after hatching, by up to 18 dB at the highest frequencies. The threshold spread between units of similar CF in single animals was up to 60 dB. Rate-threshold tuning-curve symmetry varied with CF. In low-frequency units, the slope of the low-frequency tuning-curve flank was on average steeper than the high-frequency flank, whereas for high-frequency units, the reverse was true. Units of CF $>$ 0.5 kHz generally showed low-frequency ''tails'' similar to those seen in mammalian primary auditory fibers. The mean tuning-curve frequency selectivity increased with CF. For units of CF $>$ 0.2 kHz, thresholds were moderately correlated with tuning-curve frequency selectivity. Significant phase locking was observed up to about 4 kHz, the corner frequency of phase locking being at 1.15 kHz.
 [S0001-4966(97)04402-0]

PACS numbers: 43.64.Pg, 43.64.Ri, 43.64.Tk, 43.80.Lb [RDF]

INTRODUCTION

The structure of the auditory sensory epithelium in modern terrestrial vertebrates is very diverse. Our present understanding of the evolution of the vertebrates indicates that the separate ancestors of mammals and birds diverged from the stem reptiles about 300 million years ago (Carroll, 1988; Feduccia, 1980), at which time the ancestors of the birds and mammals almost certainly possessed primitive hearing organs without the specialized hair-cell populations of modern representatives. One of the most interesting developments during the evolution of the hearing organ of amniotic vertebrates is the tendency towards the independent development of anatomical and physiological specialization of hair-cell populations across the width of the epithelium (Manley, 1990; Manley *et al.*, 1988, 1989). One approach to understanding the significance of this development is to study the hearing process in those animals other than man and mammals that have also developed specialized hair-cell populations arranged across the width of the sensory epithelium, i.e., archosaurs such as birds.

Hair-cell populations in vertebrate hearing organs are distinguished on the basis of cell structure, position, and innervation pattern. Avian basilar papillae differ from mammalian organs of Corti in that they are generally much shorter; they have nonetheless a comparably large number of hair cells. Unlike in the mammalian hearing organ, the hair cells of the avian papilla are not so clearly divided into two populations, but instead show a continuum of structure from the tall hair cells (THC) on the neural (inner) side to the short hair cells (SHC) on the abneural side of the papilla (Fischer, 1994; Takasaka and Smith, 1971; Tanaka and Smith, 1978; Smith, 1981, 1985). The tall hair cells differ from the short hair cells in their columnar shape and their innervation pattern. They are found predominantly supported by the neural limbus, i.e., except at the apex of the papilla, they are not sitting on the basilar membrane. In contrast, the short hair cells are wider than they are tall and occupy most of the space over the free basilar membrane. More recently, Fischer (1994) proposed restricting the definition of short hair cells to those that lack an afferent innervation. In some species, such cells occupy much of the basal-abneural region of the papilla, but the actual distribution of hair-cell types is species specific (Fischer, 1992; Fischer *et al.*, 1992; Gleich and Manley, 1988; Manley and Gleich, 1991; Köppl, 1993). Considering the independent evolutionary origin of these two vertebrate classes from different groups of reptilian ancestors, it is remarkable to find such indications of clear functional parallels between birds and mammals, that suggests a similar kind of division of labor (Manley *et al.*, 1988, 1989).

As yet, the underlying hair-cell specializations and the selection pressures leading to differentiation of form in both birds and mammals are not well understood, although they are presumably highly important in understanding the hearing process (Manley, 1995). Interesting parallels exist between the tall and short hair cells of birds and the inner and outer hair cells of mammals, respectively (for references see Manley, 1990; Manley *et al.*, 1988, 1989). First, the relative position of the cell groups with respect to each other is

the same, the hair cells lying on the neural side of the papilla being regarded as the less specialized. Second, the THC and IHC receive a much stronger afferent innervation than the SHC and OHC and the efferent innervation of both OHC and SHC is by much larger terminals than that to THC or that contacting the afferent fibers of IHC. Thirdly, the ontogenetic development of the afferent and efferent innervation follows very similar patterns in birds and mammals. Finally, both SHC and OHC are the most sensitive populations to noise damage.

While there are both quantitative and qualitative differences in the activity patterns of primary auditory neurons of birds and mammals, the available physiological data suggest that in both cases there is only one physiologically definable population of afferent fibers (e.g., Manley *et al.*, 1985). In mammals, this paradox was explained by the finding that all acoustically-active afferent fibers innervate only one population of hair cells, the IHC (see, e.g., Robertson, 1984). More recent evidence indicates that the OHC actually amplify basilar-membrane displacement and thus increase the sensitivity of the hearing organ (e.g., Dallos, 1992). Is a division of labor of the kind seen in mammals typical of auditory papillae which show more than one type of hair cell across their width? In such papillae, one hair-cell population may be specialized as reverse transducers or have a different function concerned with the efferent control of the hearing organ. Data from the chicken, starling, pigeon, and the barn owl indicate that, as in mammals, acoustically-active primary auditory afferents innervate hair cells either only (basal region) or predominantly (apical region) on the neural half of the auditory papilla (Gleich, 1989; Köppl *et al.*, 1993; Manley *et al.*, 1989; Smolders *et al.*, 1995).

The extant avian fauna consists of about 6000 species in 150 families, from which approximately 5000 belong to the family of the passerines or song birds. As the avian skeleton is seldom fossilized, the fossils do not provide a great deal of information with regard to the ancestry of the various avian families and the relationships between them (Feduccia, 1980). Among the birds, the ratites or flightless birds are highly interesting. The evidence indicates that the ratites are more closely related to each other than to any other birds and that earlier attempts to show that the ratites have a polyphyletic origin can no longer be sustained (Cracraft, 1974, 1981; Hennig, 1983; Sibley and Ahlquist, 1981). The body structure of ratites shows a number of primitive and/or neotenic features and thus the structure of the inner ear can be expected to be relatively unspecialized.

We have studied the auditory physiology of the inner ear of the emu *Dromaius novaehollandiae* as a representative of this important group. In addition, we are carrying out an anatomical study of the papilla. The present paper describes some aspects of the activity patterns of the auditory-nerve fibers of this species. Two additional papers describe the frequency map of the emu (Köppl and Manley, 1997) and the rate-level functions of the nerve fibers (Yates *et al.*, in preparation). Our recent investigations demonstrate that there are anatomical features of the hearing organ of different families of birds that can be correlated with their evolutionary status. The inner ear of the emu is more primitive than any bird so far investigated, and an unusually large percentage of the hair cells belong to the tall type (Fischer, 1994). The primary afferent fibers are large and the great majority of hair cells are innervated by afferents. The primary question addressed in this paper is: Do the physiological responses from the cochlear ganglion of the emu reflect the relatively primitive structure of its auditory organ?

I. METHODS

A. Subjects and surgical procedures

Young emus (*Dromaius novaehollandiae*) were obtained on the day of hatching from the breeding program of the Department of Agriculture of Western Australia. They were kept at the animal house of the University of Western Australia until the day of the experiment, with food and water available *ad libidum*. During the first few days after hatching, the animals ate little, but consumed the substantial yolk still available. This resulted in a weight loss from an average near 425 g at hatching to about 350 g after 5 days. After the fifth day, they ate more and steadily gained weight at the rate of about 10 g per day.

Experiments were carried out on 19 emus ranging in age from 1 to 14 days posthatch (P1 to P14). The actual age distribution was as follows: P1 (1 animal), P2 (1), P3 (1), P4 (3), P6 (2), P7 (4), P10 (3), P11 (1), P13 (1), and P14 (2). Neither Ketamine/Xylazine nor diazepam (''Valium'') or Stresnil (Azeperone 5 mg/kg, which is effective in adult emus) proved useful as anesthetic agents. Anesthesia was initiated by intramuscular injections of 30 mg/kg pentobarbital (''Nembutal'') and 100–170 mg/kg chloral hydrate (''Chlorthesin''). Supporting doses of 20–28 mg/kg pentobarbital and 60–120 mg/kg chloral hydrate were necessary at roughly hourly intervals to maintain anesthesia. The doses used to maintain anesthesia changed significantly with age. For both Nembutal and Chlorthesin, the mean doses necessary increased about 40% from age P1 (18 mg/kg Nembutal, 65 mg/kg Chlorthesin) to age P10 (26 mg/kg Nembutal and 105 mg/kg Chlorthesin), after which age the doses stabilized. The electrocardiogram and muscle-potential recording from intramuscular needle electrodes were used to monitor the animal's state. The emus rarely showed cessation of their breathing reflex. Since pentobarbital is known to depress respiration, however, they were intubated and artificially respirated with (mostly humidified) carbogen. The ventilation rate (about 40 breaths/min) and volume were adjusted to the individual's rhythm.

The animal was placed in a custom-built body mould with an integrated heating platform that was feedback-controlled via a calibrated temperature sensor inserted approximately 3 cm into the cloaca. Abdominal temperature was thus maintained at 38.7 ± 0.7 °C. This value corresponded to sample measurements taken from two awake emu chicks in their normal, heated enclosure. During the experiments, a desk lamp near the animal's head helped minimize any potential temperature difference between head and abdomen, since it has been shown in the pigeon that a temperature difference of 1 °C shifts the tuning frequency of primary auditory neurons by 0.07 octaves (Schermuly and Klinke,

1985). Measurements of the air temperature in the small skull cavity just dorsal to the opening in the recessus scala tympani of the cochlea with a calibrated minisensor in five cases gave a mean value of 35.5 °C. Since this cavity was open to the room air, this suggests that the temperature of the inner ear itself, which would likely be higher, was very close to the abdominal temperature.

The cochlear ganglion was exposed by opening the recessus of scala tympani via the dorsolateral approach originally developed in the starling (Manley *et al.*, 1985). This is a rapid technique, although the bone and other connective tissues were more vascularized in the younger individuals, which could lead to more bleeding. In addition, a capillary vessel suspended in the scala tympani, and that was sometimes branched, needed to be avoided during electrode placement. Using appropriate head angles, access to the entire visible length of the ganglion was possible in most preparations.

B. Stimulation and recording procedure

Short, cone-shaped ear bars with abbreviated, smoothed tips were inserted into both external ear canals to hold the head in a fixed position without damage to the eardrum, which lies relatively superficial. On the right side (the recording side), a Koss walkman earphone and a probe tube connected to a Bruel & Kjaer 0.5-in. microphone were sealed into the ear bar which thus served as a closed sound-delivery and sound-calibration system. Stimuli were generated alternatively by a custom-built, white-noise source or a computer-controlled HP 3325A sine-wave synthesizer. Stimuli were shaped by a custom-built ramp gate and attenuated by a custom-built, programmable attenuator that was linear over the range of intensities used in this study. The signals were then impedance matched and fed to the earphone.

Glass microelectrodes filled with 3M KCl (impedances 40–90 MΩ) or with 5%–10% horseradish peroxidase in Tris/KCl solution (0.05 M/0.15 M) were advanced into the ganglion using a custom-built motor drive while presenting white-noise bursts as a search stimulus. The HRP electrodes were beveled before use to reduce their impedance to below 200 MΩ (for details see Köppl and Manley, 1997). Custom hardware and software was used to control the frequency synthesizer, attenuator, and tone gate by a PC, as well as to record the spike responses digitized through a custom-built window discriminator. Only clearly single-unit responses with a uniform spike amplitude over a given time period were recorded and analyzed.

For a detailed analysis of spontaneous discharge activity, up to 6000 inter-spike intervals were recorded with a resolution of 0.1 ms. From these, time-interval histograms with varying bin widths could be derived. Interval histograms from recordings of at least 1000 spontaneous spikes were subjected to a fast Fourier transform (FFT) analysis to check for preferred inter-spike intervals. If both the FFT amplitude spectrum and the interval histogram showed subjectively clear peaks, a unit was classified as showing preferred intervals, the inverse of the frequency of maximal FFT amplitude defining the basic interval. In a subset of 36 units, the basic interval was also determined graphically, as described in Manley *et al.* (1985).

C. Derivation of tuning curves

Two programs were used for deriving frequency-threshold tuning curves. One of these, that we shall refer to as ''FTC,'' used a threshold hunting routine that was described in detail by Winter *et al.* (1990). After initially collecting 5 s of spontaneous activity, tones of selected frequencies were automatically presented at different sound pressures and with a duration of 50 ms and a repetition rate of 10/s. The rise/fall times of the sinusoidal signals were adjusted for the frequencies being used to avoid producing onset and offset clicks. Above a frequency of 500 Hz, however, rise/fall times were kept constant at 5 ms. The program adjusted the sound pressure until a response (of selectable statistical certainty) was detected, whereupon the next frequency was tested. The number of spikes occurring during the stimulus was compared with the number of spikes occurring in an equivalent period immediately following stimulus offset. The threshold criterion represented an increase in spike rate of about 20/s. The statistical criterion used by the program was chosen to enable collection of a 20-point tuning curve in about 2 min (see Winter *et al.*, 1990). The actual elapsed time depended on the spontaneous rate of the unit. The second program, that we refer to as ''Raster,'' presented stimuli pseudo-randomly within a predefined matrix of frequencies and sound-pressure levels centered at the unit's CF (tone duration 50 ms, rise/fall 5 or 10 ms, repetition rate 3 or, mostly, 5/s, 5-dB steps). The matrix was generally repeated three times and the discharge rate for each combination of frequency and sound pressure averaged. This response matrix was then analyzed using a program that interpolated isorate contours, choosing a rate of 20 spikes/s above spontaneous as the criterion for tuning curves. Frequency step sizes for both FTC and Raster measurements were adjusted according to the frequency range and were generally between 0.1 and 0.2 octaves for CFs below 1 kHz and between 0.05 and 0.1 octaves for CFs above 1 kHz.

For 120 units, tuning curve data were recorded with both the FTC and the raster program. Wilcoxon tests for paired samples were used in these cases to test for differences between the two methods in the standard tuning curve parameters: CF (characteristic frequency = frequency with the most sensitive threshold), threshold at CF, $Q_{10\ \mathrm{dB}}$, $Q_{40\ \mathrm{dB}}$ (the cell's characteristic frequency divided by the frequency bandwidth of the tuning curve 10 dB or 40 dB, respectively, above the best threshold) and the slopes of the low-frequency and high-frequency flanks of the tuning curves (measured by linear interpolation between 3 and 23 dB above CF threshold). Of these, only the high-frequency slopes proved to be significantly ($p = 0.0002$), but only slightly, different (median value from the FTC procedure 92 dB/octave, from the Raster procedure 72 dB/octave). Tuning curve data were therefore pooled between the two methods, giving preference to the FTC data in cells where both were available.

Phase locking in responses to pure tones was examined using peri-stimulus-time histograms (PSTH). Depending on

the frequency under study, the data were collected using bin resolutions from 50 to 1000 μs (high to low frequencies, respectively, with a minimum of 4 bins/cycle) and using gated tones of 50 to 200 ms duration, repeated up to 50 times at rates of 5/s or 2/s. In general, several frequencies within the tuning curve's range were presented. The onset phase of the tonal stimuli was held constant for all presentations. The quality of phase locking was derived by calculating vector strength (Goldberg and Brown, 1969). Rayleigh's test was then used to assess the statistical significance of phase locking, taking into account the vector strength and number of spikes collected. PSTH with less than 90 spikes were discarded, for all others, phase locking was accepted if $p < 0.01$.

Precautions were taken to eliminate data collected when the animals' condition was no longer optimal. In all animals, the sequence of CFs, thresholds, and spontaneous rates over time was closely examined and compared with the records on anesthetic doses, EKG, temperature, and respiration. Wherever a consistent rise in thresholds and/or drop of spontaneous rates occurred that was not correlated with significant changes in CF but was associated with changes in the EKG, the data from that point in time on were discarded (later data from four animals). Data from another 4 animals were discarded entirely because of very early problems with the surgery and/or physiology (evident as obvious changes in the EKG).

These experiments were carried out under a license from the Western Australian Department of Conservation and Land Management (SF001293) and the Animal Experimentation Ethics Committee of the University of Western Australia (64/93/93 and 180/94/94). They also followed the Australian NH&MRC guidelines.

II. RESULTS

In this study, we describe data from 19 emus ranging in age from 1 to 14 days posthatch (P1 to P14) and weighing between 295 and 555 g. Since none of the experimental animals was adult, the quantitative data on each aspect of the physiology of the auditory nerve were initially subjected to an analysis designed to reveal possible trends in response activity with developmental age. These are discussed in the relevant sections below.

We encountered nonauditory units in the ganglion that had either regular or irregular spontaneous discharge patterns, corresponding to previous experience with this approach in birds (e.g., Manley *et al.*, 1985, 1991a,b). These units neither increased their discharge rate to the loudest stimuli tested (approximately 100 dB SPL), nor did they exhibit phase locking to continuous tones, as judged audiovisually. Responses to loud, low-frequency tones were recorded for a few of these units and never showed any significant phase locking. We thus assumed that these fibers were afferents emanating from the lagenar macula (Manley *et al.*, 1991a) and did not study them further.

A. Spontaneous activity

The analysis of the rates of spontaneous activity excluded all those units that showed an audible rhythmical activity (e.g., heart rate). Spontaneous activity was irregular. The spontaneous rates of 836 units analyzed, as measured by the FTC program over a 5-s period, ranged from 0 to 105.2 spikes/s over all age groups, with a mean of 25.7 ($\pm$17.4) spikes/s. Rates averaged in a smaller number of fibers over at least 1000 spontaneous spikes ranged from 2.3 to 96 spikes/s. There was no significant difference between rates measured by the two methods, when compared for the same units (Wilcoxon test, $n=221$, $p=0.04$).

The different ages of the emu chicks used in this study made it necessary to test for maturational changes in the spontaneous activity. To minimize the effects of individual variation on statistical procedures used to test for such effects, the animals were pooled into four age groups: P1 to P4 (total of 6 emus); P6 and P7 (6 emus); P10 and P11 days (4 emus); P13 and P14 (3 emus). First, spontaneous discharge rates were compared across the age groups by a Kruskal-Wallis one-way analysis of variance with subsequent pairwise Mann-Whitney U tests. Significantly higher spontaneous rates were found in animals aged P13 and P14 compared to all younger ages ($p \leqslant 0.0001$), as well as in P10 to P11 animals compared to all younger ages ($p \leqslant 0.005$); the two youngest age groups did not differ with respect to spontaneous rates. The mean rates ($\pm$ standard deviation) were 13.4 $\pm$12.6 spikes/s for P1 to P7 animals, 19.8$\pm$18.9 spikes/s for P10/11 and 29.4$\pm$21.0 spikes/s for P13/14. Thus, spontaneous discharge rates seemed to increase in our sample after the first week of life. Examining the distributions of spontaneous rates across the age groups, it was obvious that this was largely due to a decrease of very low or nonspontaneously active units, i.e., the shape of the distribution changed [Fig. 1(A)]. Across all age groups, however, the rate distribution was unimodal. In addition, there was a tendency for the spontaneous rates to rise with the CF of the unit [Fig. 1(B) and (C)].

In a sample of 210 fibers with CFs from 0.04 to 3.8 kHz (excluding units with audible rhythmic activity), 60 showed preferred intervals. The highest CF at which this phenomenon was detected was 1.5 kHz. The basic interval determined from the time-interval histograms differed slightly, but significantly between the two methods used (Wilcoxon test, $p = 0.003$), the interval values given by the FFT analysis being longer than the ones read off graphically according to Manley *et al.* (1985). We assume this is due to the inclusion (FFT method) or exclusion (graphical method), respectively, of the first peak in the time-interval histogram, which could be influenced by the refractory time of the fiber. The product of CF and the basic interval was used as an indicator for the similarity of both parameters, perfect correspondence of the basic interval to the CF period giving a value of 1. These products ranged from 0.67 to 2.64 for the data derived from an FFT analysis, with an average of 1.23 and a median of 1.06. With the graphic method, product values ranged from 0.41 to 1.81, with an average of 1.04 and a median of 1.02. The basic interval thus reflected the CF closely in both cases.

There is evidence that some of the preferred intervals observed were the result of inadvertent ambient noise. For one, the recordings were obtained in two experimental series

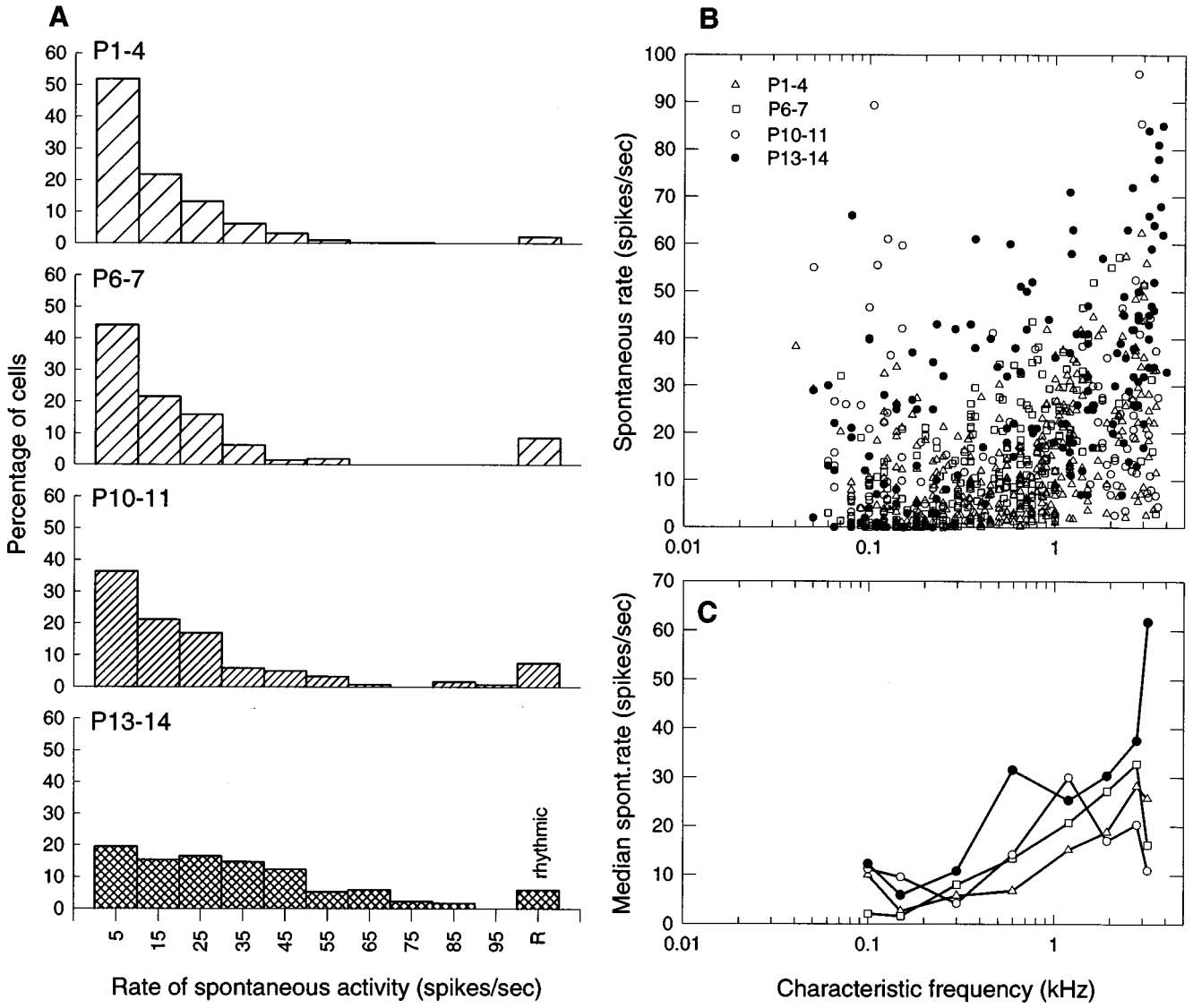

FIG. 1. (A) Histogram of the distribution of spontaneous activity rates in emus of the four age groups groups P1–P4; P6,7; P10,11; P13,14. Fibers showing an audibly rhythmical discharge are shown separately in the last bin. (B) Spontaneous activity rate as a function of the CF of auditory-nerve fibers in the emu. Four different symbols as shown have been used for the animals' age groups P1–P4; P6,7; P10,11; P13,14. (C) Median spontaneous rates for the four age groups of emu chicks, in each case for the following 8 frequency bins (of mostly one octave): all CFs below 0.1 kHz; CFs from 0.101–0.2 kHz; 0.201–0.4 kHz; 0.401–0.8 kHz; 0.801–1.6 kHz; 1.601–2.26 kHz; 2.261–3.2 kHz, and finally all CFs above 3.201 kHz. The symbols used for the age groups are as in (B).

using different acoustically-shielded chambers, and the proportion of units with a CF below 1.5 kHz showing preferred intervals was much higher in one series (48%) than in the other (20%). Also, there was a clear tendency for many (but not all) units showing preferred intervals to be among the most sensitive ones. Since the origin of the preferred intervals observed was thus ambiguous, we have not analyzed the data further in this respect.

B. Frequency range and thresholds

Characteristic frequencies (CF) were measured in 887 cochlear ganglion units and ranged from 0.04 to 4.0 kHz. There appeared to be no maturational changes with respect to the hearing range, CFs as low as 0.1 kHz and as high as 3.5 kHz were recorded at age P2. The emu hatchling thus perceives the full range of frequencies found in a two-week old animal.

To examine for maturational changes in the auditory-nerve responses with respect to response threshold, the obvious effects of frequency on this parameter were minimized by dividing the data into the following 8 frequency bins (of mostly one octave): all CFs below 0.1 kHz; CFs from 0.101–0.2 kHz; 0.201–0.4 kHz; 0.401–0.8 kHz; 0.801–1.6 kHz; 1.601–2.26 kHz; 2.261–3.2 kHz, and finally all CFs above 3.201 kHz. Kruskal–Wallis one-way analyses of variance, with subsequent pairwise Mann-Whitey U tests, were then performed, comparing thresholds at CF of the four age groups (P1–4, P6/7, P10/11, P13/14) in each frequency bin.

Except where there was an occasional paucity of data in certain frequency bins at certain ages, the following pattern

was revealed by statistically significant differences ($p < 0.05$): Threshold was unchanged across age for frequencies up to 0.2 kHz. Above 0.2 kHz, thresholds showed a consistent improvement in P13 to P14 animals compared with younger ages. Between 0.2 and 2.26 kHz, the P13 to P14 animals proved, on average, to be 10–15 dB more sensitive than animals aged up to P11. Above a CF of 2.26 kHz, P13/14 animals were, on average, 8 dB more sensitive than P10 and P11, which were in turn about 10 dB more sensitive than animals aged up to P7 [Fig. 2(B)]. We conclude that thresholds were mature at the low frequencies (up to about 0.2 kHz), but improved between 10 and 18 dB at the higher frequencies within the first two weeks of life.

The units' thresholds ranged widely [Fig. 2(A)], even within a given ear. When comparing the threshold ranges of all units recorded, threshold differences of up to 40 dB between units of the same CF were quite common, but differences even greater than 50 or 60 dB were occasionally encountered. The spread of CF thresholds at a given frequency was greater for younger animals, and, at least in older animals, was reduced to 20 to 30 dB at CF above 1 kHz. By joining the most sensitive units from all animals and continuing the flanks of the tuning curves having the highest and lowest CFs, an audiogram for the young emu (for stimulation in our closed acoustic system) was obtained [Fig. 2(A)].

The data collected using the Raster program from cells having moderate to high spontaneous rates were also carefully examined for the presence of single-tone suppression. In no case was there any clear evidence of suppressive areas outside the excitatory tuning curve. Two-tone suppression was not examined.

C. Frequency selectivity and the slopes of tuning-curve flanks

An examination of possible maturational changes in the auditory-nerve responses with respect to frequency tuning and tuning curve slopes showed that, after hatching, these parameters did not change in any frequency range. As described above for the thresholds, $Q_{10\ dB}$-, $Q_{40\ dB}$-, and the slope-steepness values of the low-frequency and high-frequency tuning-curve flanks were compared between the four age groups in 8 frequency bins. None of these parameters showed any consistent change with age (Figs. 3, 5, and 6). Data from different ages will therefore not be distinguished in the following. In general, the tuning selectivity as measured in terms of the $Q_{10\ dB}$ and the $Q_{40\ dB}$ values [Fig. 3(A) and (B), respectively] tended to increase towards higher CFs. The scatter of data values was, however, much greater at higher CFs.

The threshold frequency-tuning curves were V-shaped, but varied in shape between low- and high-CF units [Fig. 4(A)]. Low-CF units tended to be more symmetrical in shape, whereas high-CF units tended to be asymmetrical, being steeper on the high-frequency flank [Fig. 4(B)]. Overall, the slope of the high-frequency tuning-curve flank was substantially steeper than the slope of the low-frequency flank (Fig. 5). The ratio of the flank slopes is plotted as a function of CF in Fig. 6. The average slope ratio (high-frequency flank to low-frequency flank) was 1.66 ($n = 751$).

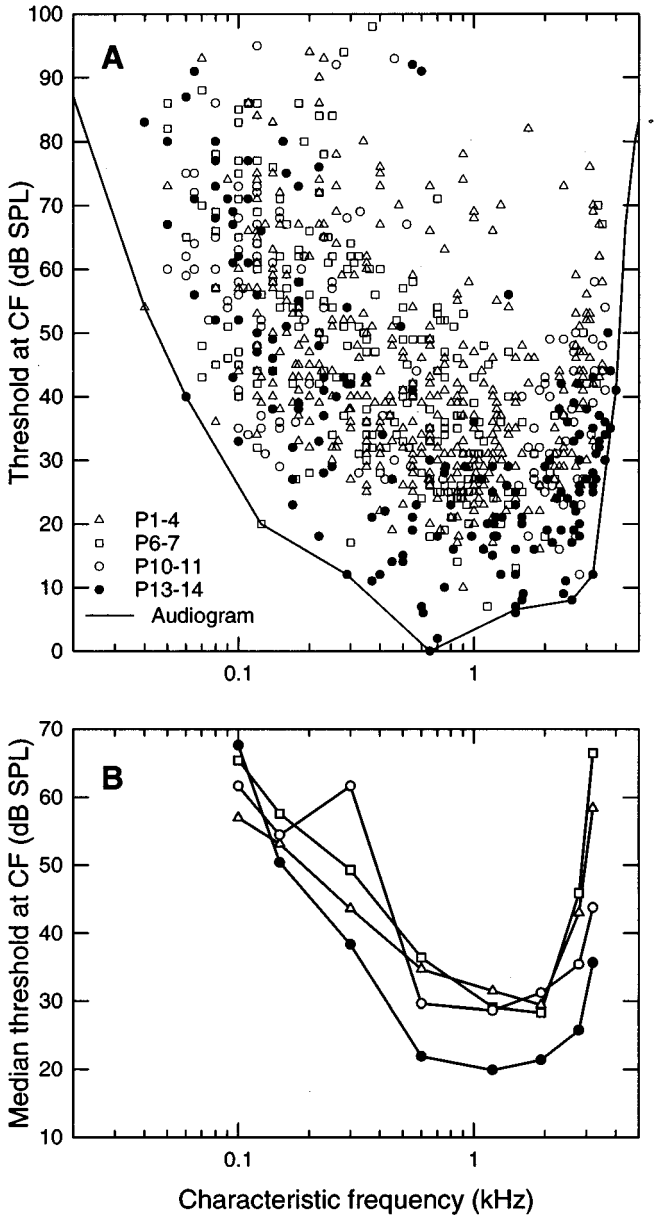

FIG. 2. (A) Scattergram of the rate thresholds of emu auditory-nerve fibers as a function of their CF. The four age groups P1–P4; P6,7; P10,11; P13,14 are coded using different symbols as shown. The number of data points for the different ages is as follows: P1–4, 382; P6,7, 214; P10, 11, 117; P13, 14, 170. The continuous line is an emu ''audiogram'' constructed using the most sensitive fibers, and extending the lower and upper frequency range according to the tuning curve flanks of the highest and lowest-CF fibers. The latter procedure assumes that at the extreme frequencies, the animal has no more sensitive units; the flanks, must, thus be regarded as upper bounds of the threshold curves. (B) Median thresholds for the four age groups of emu chicks and using the same frequency bins as in Fig. 1(C). The symbols used for the age groups are as in (A).

On average, however, this slope ratio becomes greater towards higher CFs (Fig. 6). Whereas below CF 0.1 kHz the ratio was 0.65, it rose to 2.54 above CF 3.2 kHz.

Tuning curves of units with CFs above about 0.5 kHz tended to have low-frequency ''tails'' resembling those reported from mammalian eighth-nerve units [Fig. 4(B)].

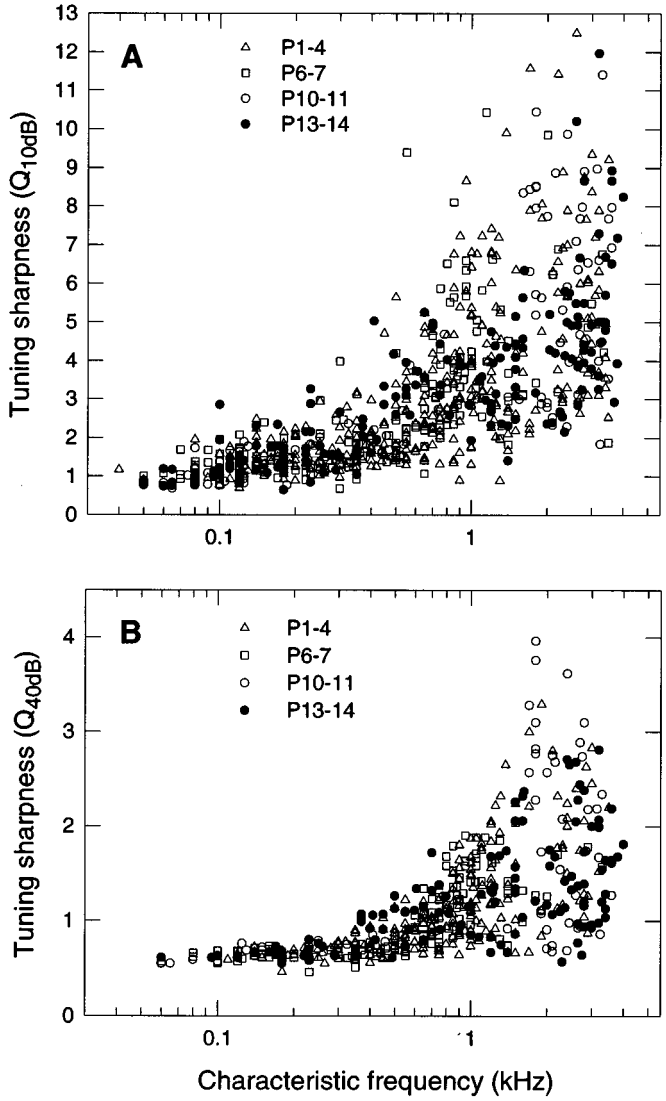

FIG. 3. (A) Sharpness coefficients of frequency tuning of auditory-nerve fibers of the emu expressed as $Q_{10\ dB}$. The four age groups P1–P4; P6,7; P10,11; P13,14 are represented by different symbols. The number of data points in each age group was 369, 202, 112, and 159, respectively. (B) Sharpness coefficients of frequency tuning of auditory-nerve fibers of the emu expressed as $Q_{40\ dB}$. The four age groups P1–P4; P6,7; P10,11; P13,14 are represented by different symbols as in Fig. 4. The number of data points in each age group was 216, 126, 57, and 119, respectively.

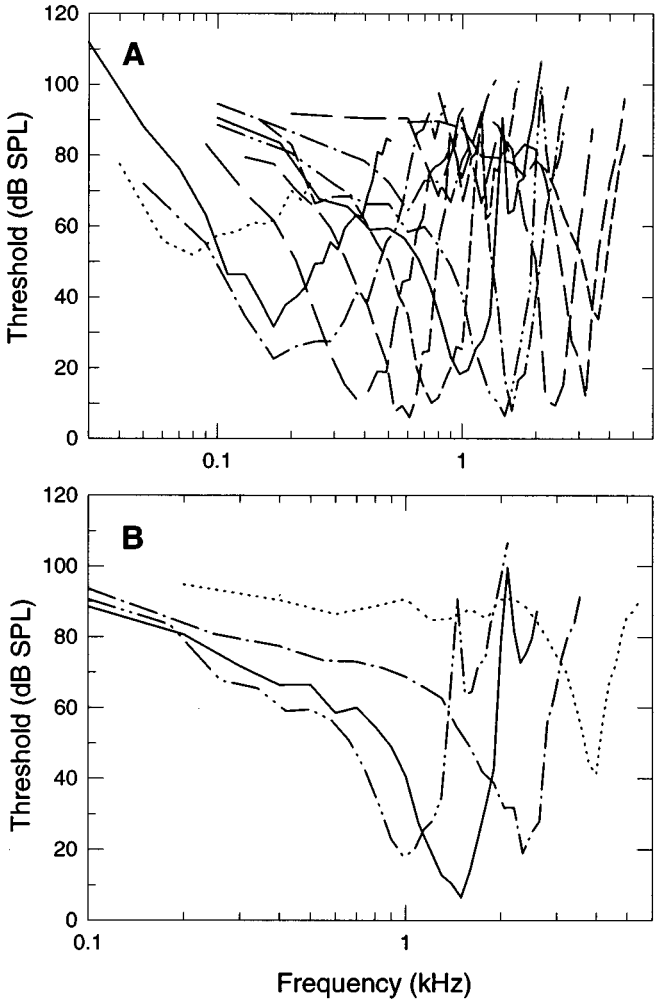

FIG. 4. Representative rate-threshold frequency tuning curves of (A) 12 single auditory-nerve fibers in the emu. The data are from two animals, one of which was especially studied at frequencies below 1 kHz, the other above 1 kHz. The change of symmetry between the lowest-CF units, which have steeper low-frequency flanks, to the highest-CF units, which have steeper high-frequency flanks, can be seen. In (B), 4 rate-threshold frequency tuning curves from single fibers of CF 1 kHz or higher are shown, to show the low-frequency ''tails.'' The two fibers with the lowest CF in (B) also show secondary sensitivity notches on their high-frequency flanks.

Whereas units with a CF of 1 kHz showed a break in the slope of the low-frequency tuning-curve flank near 50–60-dB sound-pressure level (SPL), the low-frequency flanks of the highest-frequency units did not make the transition to the tail region until levels of 75 to 90 dB SPL were reached. The latter units then showed extremely low slopes extending to frequencies of 200 Hz at levels of below 100 dB SPL [Fig. 4(B)]. Cells of intermediate CF often showed small secondary sensitivity minima in their tail regions and also on their high-frequency flanks. There was no obvious difference between very young and older individuals with respect to the development of the tail region or tuning-curve shape in general.

D. Correlation between spontaneous rate, threshold, and $Q_{10\ dB}$

To examine for relationships between spontaneous discharge rate, response threshold, and tuning, the data were divided into the 8 frequency bins described above (Sec. II B) to minimize the influence of frequency. For each frequency bin, the spontaneous discharge rate was plotted as a function of the threshold at CF and of $Q_{10\ dB}$, and threshold was examined as a function of $Q_{10\ dB}$. All three pairs of parameters were also tested for Spearman rank correlation. Since spontaneous discharge rates and thresholds differed significantly between ages (see above) this analysis was carried out separately for three age groups of emus (up to P7, P10/11, and P13/14). Units with a rhythmic spontaneous discharge (e.g., correlated with the heart beat) were always excluded from the analysis.

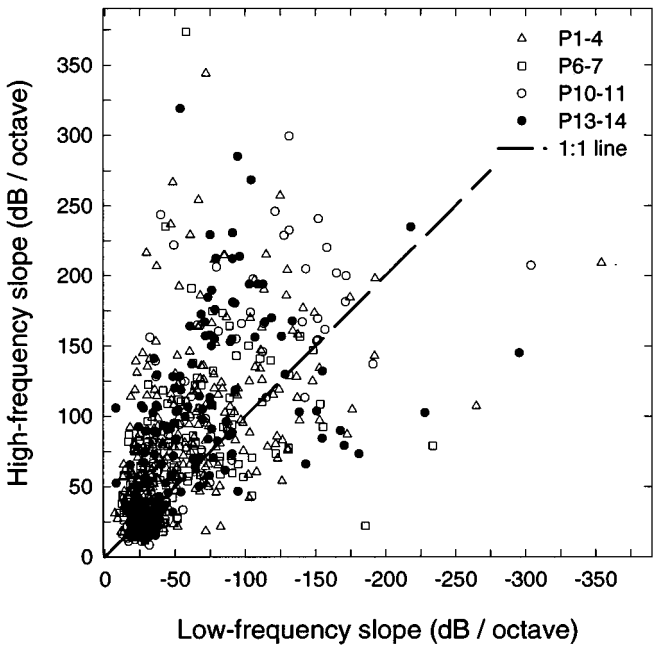

FIG. 5. Slopes of low- and high-frequency tuning-curve flanks in the emu. In each case, the slope of the high-frequency flank is plotted as a function of the slope of the low-frequency flank. The number of data points in each age group was P1,4, 333; P6,7, 183; P10,11, 95; P13,14, 140.

The following patterns were observed: (a) The most consistent relationship was seen between threshold and $Q_{10\ \mathrm{dB}}$, in the data from P1 to P7 animals. For CFs between 0.2 and 3.2 kHz, those two parameters were moderately correlated in this age group ($r=-0.28$ to -0.86; $p\leqslant 0.003$). In older animals, the correlation was less consistent across frequency bins, possibly due to fewer available data points.

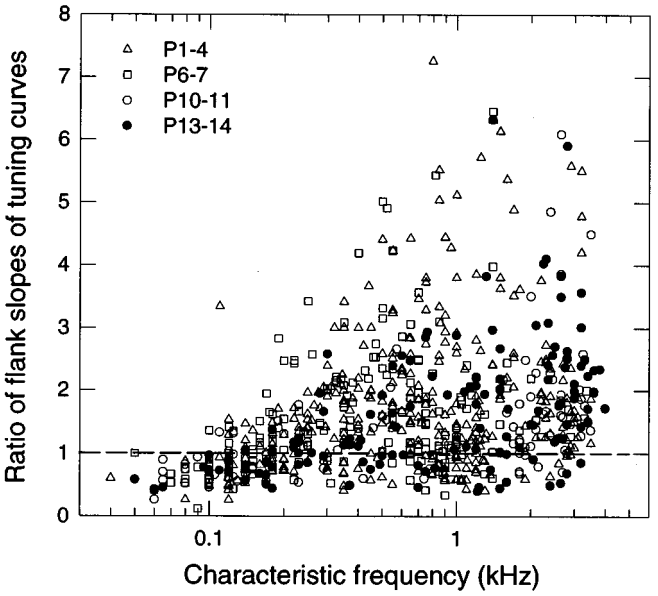

FIG. 6. The ratio of the high- to low-frequency flank slopes of rate-threshold frequency tuning curves as a function of the CF of nerve fibers in the emu. The number of data points in each age group was P1–4, 333; P6,7, 183; P10,11, 95; P13,14, 140.

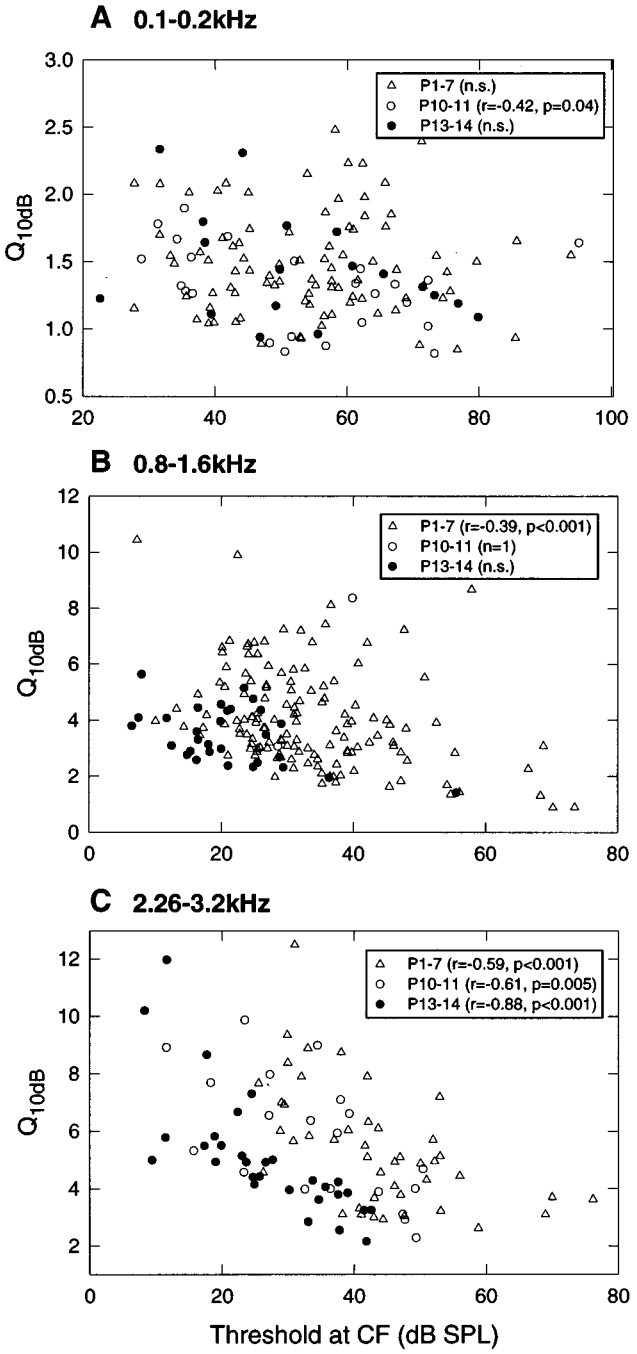

FIG. 7. The tuning sharpness coefficient $Q_{10\ \mathrm{dB}}$ as a function of threshold at CF for three different frequency ranges (A)–(C). The 3 figures only show data from restricted frequency ranges to minimize the influence of CF. In each figure, data from three different age groups (P1–7, P10,11, P13,14) are represented by different symbols and the correlation parameters for each group are given in the legend (n.s. = not significant). Note that consistently high correlations are seen for both parameters at high frequencies (C), but no or only weak correlations at the lowest frequencies (A).

Examples for the relation between threshold and $Q_{10\ \mathrm{dB}}$ in three frequency ranges are shown in Fig. 7(A)–(C). (b) A correlation between spontaneous rate and threshold was not consistently present across age or frequency. Only at CFs between 2.26 and 3.2 kHz were these two parameters moderately correlated in all age groups ($r=-0.43$ to -0.55; $p=0.012$ to 0.002). Taking the log of spontaneous rate,

which has been shown to strongly correlate with threshold in mammals (Winter *et al.*, 1990), also did not reveal a more consistent or stronger correlation in the emu. (c) Spontaneous rate and $Q_{10\ dB}$ showed no consistent pattern of correlation at all.

We conclude from these data that lower response thresholds are often found associated with higher frequency selectivity. This correlation appeared to become stronger at higher frequencies (Fig. 7). Spontaneous rates seem not to be consistently correlated with sensitivity or frequency selectivity.

E. Phase locking

Our primary interests with respect to phase locking were the maximal vector strengths across frequency of which units were capable. Statistically significant vector-strength values (as described in Sec. I) were therefore further reduced to values obtained with stimulation at least 10 dB above threshold at the respective frequency. This criterion corresponded to the level at which most units which were stimulated with a series of different sound pressure levels at the same frequency reached saturation of vector strength. Data were thus selected from 73 cells from ten animals, whereby many of these cells were tested at several frequencies, giving 714 measurements in total. The units' CFs covered the entire range, and examples for data from a low- and high-frequency cell are shown in Fig. 8. Phase locking measured as the vector strength was strong over a wide frequency range (Fig. 9), with almost perfect phase locking between 0.05 and 0.8 kHz. The upper limit of statistically-significant phase locking was 4–4.5 kHz. The corner frequency (where vector strength reached $1/\sqrt{2}$ of its maximal value; Weiss and Rose, 1988) was 1.15 kHz, the frequency of half-maximal vector strength 1.9 kHz.

III. DISCUSSION

Data from single auditory-nerve fibers in birds are available for the pigeon (Gross and Anderson, 1976; Gummer, 1991; Hill *et al.*, 1989a,b; Klinke *et al.*, 1994; Richter *et al.*, 1996; Sachs *et al.*, 1974, 1978, 1980; Schermuly and Klinke, 1990a,b; Smolders *et al.*, 1995; Temchin, 1980, 1988) for the starling (Gleich, 1989, 1994; Gleich and Klump, 1995; Gleich and Narins, 1988; Klump and Gleich, 1991; Manley, 1979; Manley and Gleich, 1984; Manley *et al.*, 1985), for the redwing blackbird (Sachs *et al.*, 1980) and for the chicken (Chen *et al.*, 1994; Jones and Jones, 1995a,b; Manley *et al.*, 1987, 1991b).

The large sample of this study, in which data are reported from nearly 900 auditory-nerve units, provides a good foundation for comparisons to data derived from other avian species but also to other nonmammals and to mammals. The CFs reported here also cover a larger proportion of the total hearing range than has been reported for other bird species, due to the large recessus of scala tympani and thus the unusually good accessibility of the whole of the cochlear ganglion. In other species, for example the chicken, the starling, and the pigeon, the approach through scala tympani does not give access to the entire range of CFs (Manley *et al.*, 1985, 1991b; Richter *et al.*, 1995).

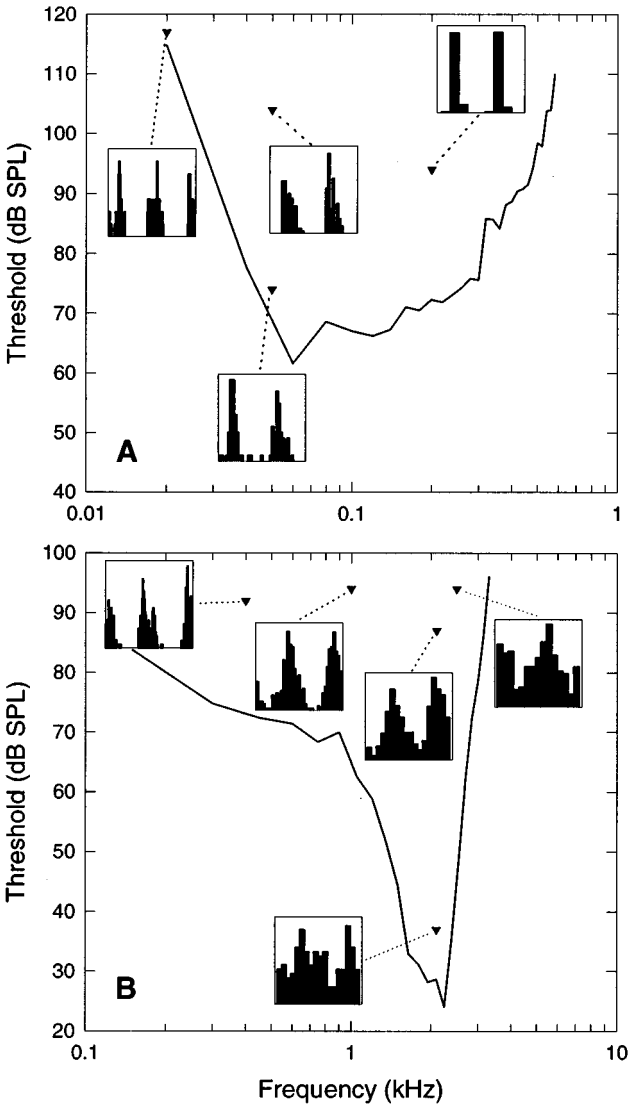

FIG. 8. Two examples (A) and (B) of auditory-nerve fibers tested for phase locking across their frequency-response range. Each figure shows the fiber's tuning curve as a continuous line. The insets are phase histograms, each covering a time frame of 2 cycles on their abscissa and displaying the response to stimulation at the frequency-level combinations indicated by the associated filled, inverted triangles. The time resolution for data display is the same for all histograms.

A. Spontaneous activity

The spontaneous activity patterns observed in time-interval histograms for the emu were unremarkable and resemble those previously described for other avian species (for references see Manley, 1990). The distribution of spontaneous rates in birds is consistently unimodal, whereas it is bimodal in mammals (Sachs *et al.*, 1980; Manley *et al.*, 1985). Great variation is, however, seen in the absolute spontaneous rates reported for different bird species and in different studies. The spontaneous rates reported by Manley *et al.* (1991b) for P2 and P21 chickens (somewhat over 20 spikes/s) are the lowest ever reported for birds. Salvi *et al.* (1992) reported a mean rate of 86 spikes/sec in adult chickens. In some other avian species, the mean spontaneous activity rates of primary fibers lie above those typically re-

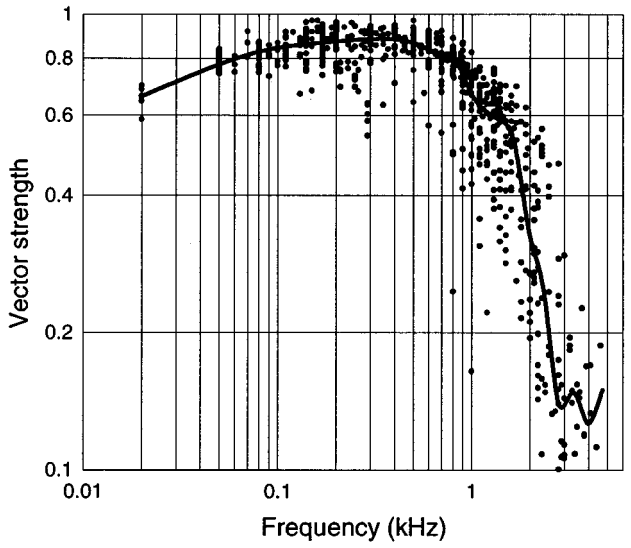

FIG. 9. Vector strength of phase locking as a function of stimulus frequency. The symbols show data points from 73 cells (average 10 frequency points per cell) that represent statistically-significant phase locking and that were obtained at levels at least 10 dB above the respective threshold. The solid line joins the median values calculated in octave bins up to 0.32 kHz, in half-octave bins to 0.64 kHz, and in quarter-octave bins above that.

corded for mammalian auditory fibers. In the starling the mean rate of all fibers was 48 spikes/s (Manley *et al.*, 1985). For pigeon auditory-nerve fiber spontaneous rates, very different rates have also been reported. Whereas Sachs *et al.* (1980) report a rate of 90 spikes/s for both the pigeon and the redwing blackbird, and Temchin (1988) gives an average rate of 78 spikes/s for spontaneous activity in 26 pigeon units, Hill *et al.* (1989a) found an average rate of only 34 spikes/s and Smolders *et al.* (1995) report a mean value of 91 spikes/s. Thus, even within one species, differences of two or three times exist that appear to be the result of technical procedures during the experiments, probably primarily temperature and anesthetic differences. In a study of primary afferents of the *vestibular* system in anesthetized and unanesthetized pigeons, Anastasio *et al.* (1985) found the spontaneous activity rates to be about 80% higher in the unanesthetized state. Kettembeil *et al.* (1995) found that different anesthetic agents were capable of strongly reducing the size of the compound action potential in starlings and chickens. Different anesthetics and changing levels of anesthesia may thus produce different degrees of depression of the activity of avian nerve fibers.

This apparent vulnerability of spontaneous rates also has to be kept in mind when comparing data from different ages in the same species. It is thus unclear whether the differences seen between young and adult chickens in the studies of Manley *et al.* (1991b) and Salvi *et al.* (1992), respectively, represent a maturational increase in spontaneous rates with age. We report here a roughly twofold increase of overall spontaneous activity within the first two weeks after hatching in the emu. Experimental artefacts were minimized by using the same general protocol across ages, but taking care to adjust the anesthetic regime to each individual. These results thus strongly indicate a true maturational change in the fibers' spontaneous activity. Spontaneous rates in the emu may still not have reached their adult values in the oldest emu chicks used (P13/14), since the rate distribution, although mono-modal, was skewed towards low values compared with the distributions published for other bird species (Sachs *et al.*, 1974; Manley *et al.*, 1985, 1991b; Hill *et al.*, 1989a; Gummer, 1991; Salvi *et al.*, 1992; Smolders *et al.*, 1995). An increase in spontaneous rates has also recently been reported for the pigeon, where the rates in immature animals were about half of those of adults (Richter *et al.*, 1996).

Many, especially very low-frequency, fibers showed preferred intervals in their spontaneous activity. In the red-eared turtle, such preferred intervals were shown to reflect spontaneous hair-cell membrane potential oscillations associated with an electrical tuning mechanism (Crawford and Fettiplace, 1980). However, care has to be taken to exclude ambient noise unintentionally phase-locking the fibers to their CF around threshold levels and thus producing a similar pattern. There was clear evidence in our data for noise-driven activity, and, although preferred intervals were not only seen in the most sensitive fibers, this makes it impossible to separate a noise-driven effect from any true preferred intervals. In this respect, the emu resembles the pigeon (Klinke *et al.*, 1994). Interestingly, evidence for single-tone, or primary, suppression, which has previously been reported from the starling (Manley *et al.*, 1985), chicken (Manley *et al.*, 1991b) and pigeon (Gross and Anderson, 1976; Gummer, 1991; Temchin, 1988) and has been associated with the presence of preferred intervals in the pigeon (Temchin, 1988), was not observed in the emu.

B. Frequency range and thresholds

Thresholds were obviously not mature in the emu at hatching, and the same was true of the chicken. Manley *et al.* (1991b) reported a difference in the mean thresholds of fibers of CF above 1.5 kHz from P2 and P15 chickens, such that the older animals were significantly more sensitive by 10–15 dB. This is probably partly attributable to a gradual change in middle-ear admittance up to 10 weeks post-hatching (Saunders *et al.*, 1986). In the pigeon also, rate thresholds were reported to be poorer in immature animals (Richter *et al.*, 1996). Similarly in the emu, units with CF above 0.2 kHz showed a consistent improvement in threshold with age, improving by up to 18 dB at the higher frequencies within the first two weeks of life. As there is no information available on the hearing of adult emus, it is possible that the thresholds reported here are still not mature. However, the sensitivity of young emus is already comparable to adults of most other bird species studied (see below), making significant further improvements unlikely. Since the eardrum is much larger in adult emus than in our chicks, any improvement in thresholds is likely to be at low frequencies. It should perhaps be noted that whereas a middle-ear change could be responsible for an improvement in threshold, it cannot explain the change in spontaneous rates. Thus, other developmental changes are occurring simultaneously with the improvement in thresholds.

Characteristic frequencies (CF) were measured in 887 cochlear ganglion units and ranged from 0.04 to 4.0 kHz, a

range that corresponds well to the typical hearing range of larger birds (Dooling, 1980, 1992; Manley, 1990). In comparison to other birds, the emu has a relatively low-frequency audiogram. At 0.5 kHz, the young emu's sensitivity is near 0 dB SPL, and thus, 20 dB more sensitive than the pigeon, chicken, and parakeet, 30 dB more than the redwing blackbird, and 50 dB more than the canary (for references see Manley, 1990). The low-frequency sensitivity estimated from the emu neural data below 1 kHz is very similar to human thresholds over this range (Yeowart and Evans, 1974). The only bird more sensitive over the very lowest part of this range is the pigeon, which, due to its specialization for infrasound hearing (Kreithen and Quine, 1979; Schermuly and Klinke, 1990a,b) exceeds the emu's sensitivity at frequencies below about 0.08 kHz. However, without behavioral data from the emu, this comparison is not reliable. It should, however, be noted in this context that very low-frequency units in the emu did not behave like the infrasound units described by Schermuly and Klinke (1990a,b) in the pigeon and by Warchol and Dallos (1989) in the chicken. Emu units had normal rate-threshold responses and did not show exceptionally high spontaneous discharge rates. They also did not appear to phase lock far below rate threshold, although, due to the generally low spontaneous rates, this was not routinely checked. It thus appears as if either the population of infrasound cells present in the specialized areas of the pigeon and chicken are not present in the emu or, very unlikely, we missed this group of units completely. A third possibility is that infrasound responses may not be mature in the emu chicks recorded. Indeed, there was evidence that spontaneous rates were increasing with age. Preliminary anatomical information on the emu auditory papilla, however, does not indicate the presence of any specialized hair-cell areas (Fischer and Gleich, personal communication and unpublished data).

As seen in other birds (Gleich, 1989; Gummer, 1991; Manley *et al.*, 1985, 1989, 1991b; Sachs *et al.*, 1974), the spread of thresholds in primary auditory neurons is quite large. Even in the older animals (P10 to P14), threshold ranges of 50 dB or more below 1 kHz and about 30 dB above 1 kHz were found. In young chickens (Manley *et al.*, 1991b) thresholds at CF ranged from below 20 to over 100 dB SPL, but in individual animals, the range of thresholds was maximally 59 dB. In adult chickens, thresholds across the whole CF range were between 0 and 80 dB SPL, and at some individual frequencies, the threshold range exceeded 60 dB (Salvi *et al.*, 1992). In starlings, a difference of 59 dB between the ''best'' and ''worst'' thresholds were found at single frequencies (Manley *et al.*, 1985). There thus seems to be no doubt that a threshold range of up to about 60 dB is typical for avian species studied to date, at least for the lower frequencies.

The sensitivity of emu chick units correlated moderately with frequency selectivity, such that the most sensitive units showed the highest $Q_{10\ \mathrm{dB}}$. In the chicken, Manley *et al.* (1991b) and Salvi *et al.* (1992) found a correlation between threshold and spontaneous activity of eighth-nerve fibers, but do not describe any analyses for correlations between threshold and selectivity. In the pigeon, Smolders *et al.* (1995) reported that the spontaneous rate is (negatively) correlated with the CF threshold and weakly correlated with the sharpness of tuning. Also in the pigeon, among a group of 36 stained primary afferents, fibers that innervated hair cells in a position about 20% from the papilla's neural edge were both the most sensitive and had the highest frequency selectivity. A similar relationship between tuning sharpness and threshold is also present in physiological data for the emu (present data), for the starling (Gleich, personal communication), pigeon (Smolders *et al.*, 1995), and for *Caiman* (Klinke and Pause, 1980). In the starling, however, Gleich (1989) found no evidence for such a relationship in the small group of fibers that had been stained and traced to the papilla in a specific frequency range. He did, however, find a strong correlation between position of the innervated hair cells across the papilla and their threshold.

Thus a consistent picture emerges that birds typically have a large threshold spread that, where studied, is mostly correlated with the spontaneous activity, with the $Q_{10\ \mathrm{dB}}$ value, and with the position of hair cell across the width of the papilla. These correlations are weaker or stronger depending on the frequency range and the species. In mammals, differences in these response parameters are also present, but there, they correlate with the *position of the synapse* made by the different afferent fiber types on individual inner hair cells (Liberman and Oliver, 1984). Thus mammals achieve in single hair cells at least partly what birds achieve through cells distributed across the hearing epithelium.

C. Frequency selectivity and tuning-curve shape

In common with all other vertebrate auditory fibers, single units of the avian auditory nerve are highly frequency selective. The tuning curves are, if anything, more sharply tuned than those of mammals in the equivalent frequency range (Manley *et al.*, 1985; Sachs *et al.*, 1980; Salvi *et al.*, 1992) when measured as the sharpness of the tip region ($Q_{10\ \mathrm{dB}}$) and at higher sound-pressure levels ($Q_{40\ \mathrm{dB}}$). In the emu chicks, tuning-curve sharpness did not show a consistent change with age. Similarly in the chicken (Manley *et al.*, 1991) and the pigeon (Richter *et al.*, 1996), there is no significant change in $Q_{10\ \mathrm{dB}}$ with age. As suggested by Jones and Jones (1995a), tuning selectivity matures very early in birds.

Avian tuning curves described to date, however, do not show the consistent asymmetry of mammalian tuning curves, where the high-frequency flank is steeper than the low-frequency flank. The slopes of the low- and the high-frequency flank in birds tend to differ for each fiber, although both tend to increase with CF. In starlings and chickens, fibers with a steeper low-frequency flank are reported to be almost as numerous as those with a steeper high-frequency flank (Manley *et al.*, 1985, 1991b; Salvi *et al.*, 1992). In young chickens, 36 of tuning curves were steeper on the low-frequency flank, but most fibers of CF$>$1.5 kHz had tuning curves with steeper high-frequency flanks (Manley *et al.*, 1991b). This same trend was seen in the starling (Manley *et al.*, 1985), where twice as many fibers below CF 1 kHz showed steeper low-frequency slope, above 1 kHz the oppo-

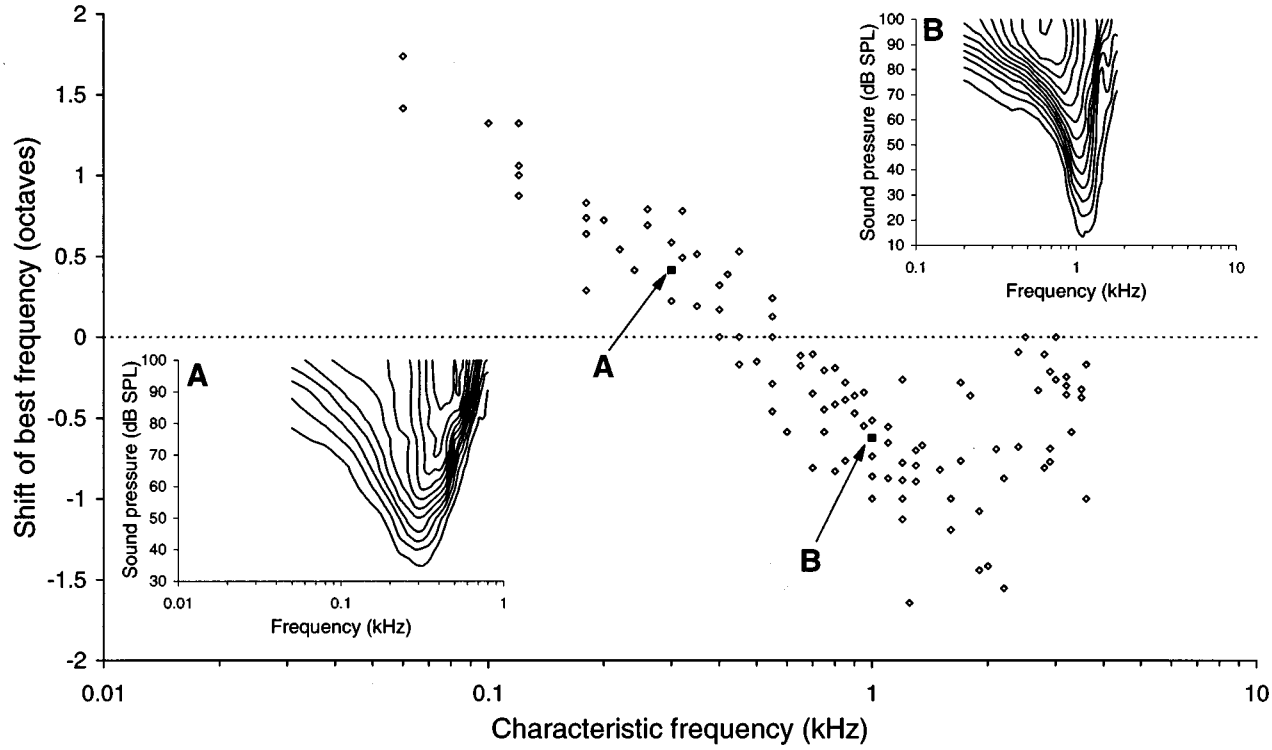

FIG. 10. The shift of the best (most sensitive) frequency between threshold-rate curves on the one hand and iso-rate curves calculated for very high discharge rates on the other hand as a function of the CF of the fiber (putative effect of phase locking). The dashed line shows the no-shift situation, i.e., where the best frequency is independent of the rate criterion; this is approximated by fibers of CF 0.4 to 0.5 kHz. Insets (A) and (B): Two examples of families of iso-rate curves for single fibers. The individual data points are indicated by arrows on the main graph. (A) is a low-CF fiber which shifts up with increasing rate criterion, and (B) is a higher-frequency fiber which shifts down.

site was true. In the emu, the relative steepness of the high-frequency flank sets in at lower frequencies than in the other species. Thus the pattern of tuning-curve symmetry in the emu more strongly resembles that of mammals than does that of any other bird.

The ''tail'' seen in higher-frequency units of the young emus has, in this rather obvious form, never before been reported from avian species. In young chickens, about a quarter of tuning curves over the whole CF showed a break to lower slopes on the low-frequency flank (Manley *et al.*, 1991b). These slope breaks were, however, not as consistently found and not as prominent as the low-frequency ''tails'' of the emu units and of higher-frequency mammalian nerve fibers. It might be speculated that the tuning-curve shape seen in the emu is in fact the form typical for the ancestors of birds and mammals, and that the more symmetrical shape only developed in more advanced avian groups such as the song birds. The Caiman, however, also shows no tuning-curve tails, but this species has perhaps an even greater specialization of hair-cell populations than in birds (Manley, 1990).

In similar data collected from the auditory nerve of the Tokay gecko, Sams-Dodd and Capranica (1994) found a shift of the iso-rate contours with stimulus level. They also measured the iso-synchronization contours in the phase-locked responses of the fibers, and established that the shift in best frequency with level that they had observed in fibers of CF$<$1.2 kHz (a shift toward 600 Hz in their data) was correlated with an increase in synchronization coefficient toward these same frequencies. Sams-Dodd and Capranica (1994) thus noted that each unit encodes stimulus frequency in a unique combination of firing rate and phase-locking coefficient. In order to compare the present data to those of Sams-Dodd and Capranica, we interpolated emu tuning curves from the response matrix using different iso-rate response criteria. The shape of tuning curves often changed, in that the best frequency of low-CF cells tended to shift up when using higher rate criteria, and the best frequency of high-CF cells shifted down (Fig. 10).

In Fig. 10, which shows the shift of best frequency with level for 125 fibers between threshold and the highest sound-pressure levels used (usually about 100 dB SPL), it can be seen that the shift for all fibers converged (i.e., showed zero shift) at 400 to 500 Hz, indicating that at high levels, this is the frequency at which the highest discharge rates are found (Fig. 10). It is probable that frequencies near 400–500 Hz represent the highest frequencies at which auditory-nerve fibers can reliably phase-lock to a high proportion of stimulus cycles (see Fig. 9).

It may thus be that similar conclusions to those of Sams-Dodd and Capranica can be drawn for the emu data, at least for cells of CF$<$2.0 kHz. Phase locking may have a strong influence on the shape of higher-criterion iso-rate curves up to a CF of about 1 kHz. Cells of CF $>$2.0 kHz, however, still tended to shift their CF down with level (Fig. 10, on average by 0.47 octaves), in a similar manner to the tuning curves of mammals (e.g., Geisler *et al.*, 1974). In the shifts of high-CF cells, phase locking will play an ever decreasing role, and

any shift above CF 2.0 kHz (cf. Fig. 9) is likely to be due to a different phenomenon.

D. Phase locking

The phase-locking capabilities of the emu units compare favorably with those previously reported from birds and from mammals. In general, birds such as the starling (Gleich and Narins, 1988) and the pigeon (Hill *et al.*, 1989b) show very little phase locking above 3-4 kHz; here, the emu is no exception. The barn owl is exceptional, and phase locks to stimuli up to 9 kHz, with a corner frequency of 3.56 kHz (Köppl, 1995; Sullivan and Konishi, 1984). At the other extreme, Schermuly and Klinke (1990a) describe cells in the pigeon eighth nerve that phase locked strongly to a broad range of infrasound frequencies, but for which a rate-threshold CF below 90 dB SPL could not be determined. Such cells were not found in the emu.

ACKNOWLEDGMENTS

We would like to thank all members of the Auditory Laboratory at the Dept. of Physiology, University of Western Australia, for their hospitality and cooperation which made the experimental work for this study possible. We are also very grateful to the West Australian Department of Agriculture, that reliably provided us with hatchling emus from their experimental farming program. Supported by the Deutsche Forschungsgemeinschaft within the program of the SFB 204 ''Gehör,'' a grant from the Australian NH&MRC and a Visiting International Exchange Fellowship from the Australian ARC.

Anastasio, T. J., Correia, M. J., and Perachio, A. A. (**1985**). ''Spontaneous and driven responses of semicircular canal primary afferents in the unanaesthetized pigeon,'' J. Neurophysiol. **54,** 335–347.

Carroll, R. L. (**1988**). *Vertebrate Palaeontology and Evolution* (Freeman, New York).

Chen, L., Salvi, R., and Shero, M. (**1994**). ''Cochlear frequency-place map in adult chickens: Intracellular biocytin labeling,'' Hear. Res. **81**, 130–136.

Cracraft, J. (**1974**). ''Phylogeny and evolution of the ratite birds,'' Ibis **116**, 494–521.

Cracraft, J. (**1981**). ''Towards a phylogenetic classification of recent birds of the world (class Aves),'' Auk **98**, 681–714.

Crawford, A. C., and Fettiplace, R. (**1980**). ''The frequency selectivity of auditory nerve fibres and hair cells in the cochlea of the turtle,'' J. Physiol. (London) **306,** 79–125.

Dallos, P. (**1992**). ''The active cochlea,'' J. Neurosci. **12,** 4575–4585.

Dooling, R. J. (**1980**). ''Behavior and psychophysics of hearing in birds,'' in *Comparative Studies of Hearing in Vertebrates*, edited by A. N. Popper and R. R. Fay (Springer-Verlag, New York), pp. 261–288.

Dooling, R. J. (**1992**). ''Hearing in birds,'' in *The Evolutionary Biology of Hearing*, edited by D. B. Webster, R. R. Fay, and A. N. Popper (Springer-Verlag, New York), pp. 545–559.

Feduccia, A. (**1980**). *The Age of Birds* (Harvard U.P., Cambridge, MA).

Fischer, F. P. (**1992**). ''Quantitative analysis of the innervation of the chicken basilar papilla,'' Hear. Res. **61**, 167–178.

Fischer, F. P. (**1994**). ''General pattern and morphological specializations of the avian cochlea,'' Scan. Electr. Micros. **8,** 351–364.

Fischer, F. P., and Gleich, O. (**1996**). Personal communication.

Fischer, F. P., Miltz, C., Singer, I., and Manley, G. A. (**1992**). ''The ultrastructure and innervation of hair cells of the starling's cochlea,'' J. Morphol. **213**, 225–240.

Geisler, C. D., Rhode, W. S., and Kennedy, D. T. (**1974**). ''Responses to tonal stimuli of single auditory nerve fibers and their relationship to basilar membrane motion in the squirrel monkey,'' J. Neurophysiol. **37,** 1156–1172.

Gleich, O. (**1989**). ''Auditory primary afferents in the starling: correlation of function and morphology,'' Hear. Res. **37**, 255–267.

Gleich, O. (**1994**). ''Excitation patterns in the starling cochlea: A population study of primary auditory afferents,'' J. Acoust. Soc. Am. **95,** 401–409.

Gleich, O. (**1996**). Personal communication.

Gleich, O., and Klump, G. M. (**1995**). ''Temporal modulation transfer functions in the European Starling (*Sturnus vulgaris*): II. Responses of auditory-nerve fibres,'' Hear. Res. **82,** 81–92.

Gleich, O., and Manley, G. A. (**1988**). ''Quantitative morphological analysis of the sensory epithelium of the starling and pigeon basilar papilla,'' Hear. Res. **34,** 69–85.

Gleich, O., and Narins, P. M. (**1988**). ''The phase response of primary auditory afferents in a songbird (*Sturnus vulgaris L.*),'' Hear. Res. **32,** 81–91.

Goldberg, J. M., and Brown, P. B. (**1969**). ''Response of binaural neurons of dog superior olivary complex to dichotic tonal stimuli: Some physiological mechanisms of sound localization,'' J. Neurophysiol. **32,** 613–636.

Gross, N. B., and Anderson, D. J. (**1976**). ''Single unit responses recorded from the first order neuron of the pigeon auditory system,'' Brain Res. **101,** 209–222.

Gummer, A. W. (**1991**). ''First order temperal properties of spontaneous and tone-evoked activity of auditory afferent neurones in the cochlear ganglion of the pigeon,'' Hear. Res. **55,** 143–166.

Hennig, W. (**1983**) *Stammesgeschichte der Chordaten* (Verlag Paul Parey, Hamburg).

Hill, K. G., Mo, J., and Stange, G. (**1989a**). ''Excitation and suppression of primary auditory fibres in the pigeon,'' Hear. Res. **39**, 37–48.

Hill, K. G., Stange, G., and Mo, J. (**1989b**). ''Temporal synchronization in the primary auditory response in the pigeon,'' Hear. Res. **39**, 63–74.

Jones, S. M., and Jones, T. A. (**1995a**). ''Neural tuning characteristics of auditory primary afferents in the chicken embryo,'' Hear. Res. **82**, 139–148.

Jones, S. M., and Jones, T. A. (**1995b**). ''The tonotopic map of the embryonic chick cochlea,'' Hear. Res, **82**, 149–157.

Kettembeil, S., Manley, G. A., and Siegl, E. (**1995**). ''Distortion-product otoacoustic emissions and their anaesthesia sensitivity in the European Starling and the chicken,'' Hear. Res. **86**, 47–62.

Klinke, R., and Pause, M. (**1980**). ''Discharge properties of primary auditory fibres in *Caiman crocodilus*: Comparisons and contrasts to the mammalian auditory nerve,'' Exp. Brain Res. **38**, 137–150.

Klinke, R., Müller, M., Richter, C.-P., and Smolders, J. (**1994**). ''Preferred intervals in birds and mammals: A filter response to noise?,'' Hear. Res. **74**, 238–246.

Klump, G. M., and Gleich, O. (**1991**). ''Gap detection in the European starling (Sturnus vulgaris). III: Processing in the peripheral auditory system,'' J. Comp. Physiol. A **168**, 469–476.

Köppl, C. (**1993**). ''Hair-cell specializations and the auditory fovea in the barn owl cochlea,'' in *Biophysics of Hair-cell Sensory Systems*, edited by H. Duifhuis, J. W. Horst, P. van Dijk, and S. van Netten (World Scientific, London), pp. 216–222.

Köppl, C. (**1995**). ''Phase locking at high frequencies in the barn owl's auditory nerve,'' Midwinter Mtg. Assoc. Res. Otolaryngol. Abstract No. 382.

Köppl, C., and Manley, G. (**1997**). ''Frequency representation in the emu basilar papilla,'' J. Acoust. Soc. Am. **101**, 1574–1584.

Köppl, C., Gleich, O., and Manley, G. A. (**1993**). ''An auditory fovea in the barn owl cochlea,'' J. Comp. Physiol. **171**, 695–704.

Kreithen, M. L., and Quine, D. B. (**1979**). ''Infrasound detection by the homing pigeon: a behavioural audiogram,'' J. Comp. Physiol. **129**, 1–4.

Liberman, M. C., and Oliver, M. E. (**1984**). ''Morphometry of intracellularly labeled neurons of the auditory nerve: Correlations with functional properties,'' J. Comp. Neurol. **223,** 163–176.

Manley, G. A. (**1979**). ''Preferred intervals in the spontaneous activity of primary auditory neurones,'' Naturwissenschaften **66,** 582.

Manley, G. A. (**1990**). *Peripheral Hearing Mechanisms in Reptiles and Birds* (Springer-Verlag, Berlin).

Manley, G. A. (**1995**). ''The avian hearing organ: a status report,'' in *Advances in Hearing Research*, edited by G. A. Manley, G. M. Klump, C. Köppl, H. Fastl, and H. Oeckinghaus (World Scientific, Singapore), pp. 219–229.

Manley, G. A., and Gleich, O. (**1984**). ''Avian primary auditory neurones: the relationship between characteristic frequency and preferred intervals,'' Naturwissenschaften **71,** 592–594.
Manley, G. A., and Gleich, O. (**1991**). ''Evolution and specialization of function in the avian auditory periphery,'' in *The Evolutionary Biology of Hearing*, edited by R. R. Fay, A. N. Popper, and D. B. Webster (Springer-Verlag, Heidelberg), pp. 561–580.
Manley, G. A., Gleich, O., Leppelsack, H.-J., and Oeckinghaus, H. (**1985**). ''Activity patterns of cochlear ganglion neurones in the starling,'' J. Comp. Physiol. A **157**, 161–181.
Manley, G. A., Brix, J., and Kaiser, A. (**1987**). ''Developmental stability of the tonotopic organization of the chick's basilar papilla,'' Science **237,** 655–656.
Manley, G. A, Gleich, O., Brix, J., and Kaiser, A. (**1988**). ''Functional parallels between hair-cell populations of birds and mammals,'' in *Basic Issues in Hearing*, edited by H. Duifhuis, J. W. Horst., and H. P. Wit (Academic, London), pp. 64–71.
Manley, G. A., Gleich, O., Kaiser, A., and Brix, J. (**1989**). ''Functional differentiation of sensory cells in the avian auditory periphery,'' J. Comp. Physiol. A **164**, 289–296.
Manley, G. A., Haeseler, C., and Brix, J. (**1991a**). ''Innervation patterns and spontaneous activity of afferent fibres to the lagenar macula and apical basilar papilla of the chicken's cochlea,'' Hear. Res. **56**, 211–226.
Manley, G. A., Kaiser, A., Brix, J., and Gleich, O. (**1991b**). ''Activity patterns of primary auditory-nerve fibres in chickens: development of fundamental properties,'' Hear. Res. **57,** 1–15.
Richter, C.-P., Heynert, S., and Klinke, R. (**1995**). ''Rate-intensity functions of pigeon auditory-nerve afferents,'' Hear. Res. **83**, 19–25.
Richter, C.-P., Sauer, G., Hoidis, S., and Klinke, R. (**1996**). ''Development of activity patterns in auditory-nerve fibres of pigeons,'' Hear. Res. **95**, 77–86.
Robertson, D. (**1984**). ''Horseradish peroxidase injection of physiologically characterized afferent and efferent neurones in the guinea pig spiral ganglion,'' Hear. Res. **15**, 113–121.
Sachs, M. B., Lewis, R. H., and Young, E. D. (**1974**). ''Discharge patterns of single fibers in the pigeon auditory nerve,'' Brain Res. **70**, 431–447.
Sachs, M. B., Sinnott, J. M., and Heinz, R. D. (**1978**). ''Behavioral and physiological studies of hearing in birds,'' Fed. Proc. **37**, 2329–2335.
Sachs, M. B., Woolf, N. K., and Sinnott, J. M. (**1980**). ''Response properties of avian auditory-nerve fibres and medullary neurons,'' Acta XVII Congressus Intern. Ornith., pp. 710–713.
Salvi, R. J., Saunders, S. S., Powers, N. L., and Boettcher. F. A. (**1992**). ''Discharge patterns of cochlear ganglion neurons in the chicken,'' J. Comp. Physiol. A. **170**, 227–241.
Sams-Dodd, F., and Capranica, R. R. (**1994**). ''Representation of acoustic signals in the eighth nerve of the Tokay gecko: I. Pure tones,'' Hear. Res. **76**, 16–30.
Saunders, J. C., Relkin, E. M., Rosowski, J. J., and Bahl, C. (**1986**). ''Changes in middle-ear input admittance during postnatal development in chickens,'' Hear. Res. **24**, 227–235.
Schermuly, L., and Klinke, R. (**1985**). ''Change of characteristic frequencies of pigeon primary auditory afferents with temperature,'' J. Comp. Physiol. A **156**, 209–211.
Schermuly, L., and Klinke, R. (**1990a**). ''Infrasound sensitive neurones in the pigeon cochlear ganglion,'' J. Comp. Physiol. A **166**, 355–363.
Schermuly, L., and Klinke, R. (**1990b**). ''Origin of infrasound sensitive neurones in the papilla basilaris of the pigeon: a HRP study,'' Hear. Res. **48**, 69–78.
Sibley, C. G., and Ahlquist, J. E. (**1981**). ''The phylogeny and relationships of the ratite birds as indicated by DNA-DNA hybridization,'' in *Evolution Today*, Proceedings of the 2nd International Congress of Systematic and Evolutionary Biology, edited by G. Scudder and J. Reveal (Carnegie, Pittsburgh), pp. 305–335.
Smith, C. A. (**1981**). ''Recent advances in structural correlates of auditory receptors,'' Prog. Sens. Physiol. **2**, 135–187.
Smith, C. A. (**1985**). ''Inner ear'' in *Form and Function in Birds*, edited by A. S. King and J. McLeland (Academic, London), Vol. 3, pp. 273–310.
Smolders, J. W. T., Ding-Pfennigdorff, D., and Klinke, R. (**1995**). ''A functional map of the pigeon basilar papilla: correlation of the properties of single auditory nerve fibres and their peripheral origin,'' Hear. Res. **92**, 151–169.
Spoendlin, H. H. (**1969**). ''Innervation patterns in the organ of Corti,'' Acta Otolaryngol. (Stockholm) **67**, 239–254.
Sullivan, W. E., and Konishi, M. (**1984**). ''Segregation of stimulus phase and intensity coding in the cochlear nucleus of the barn owl,'' J. Neurosci. **4,** 1787–1799.
Takasaka, T., and Smith, C. A. (**1971**). ''The structure and innervation of the pigeon's basilar papilla,'' J. Ultrastruct. Res. **35**, 20–65.
Tanaka, K., and Smith, C. A. (**1978**). ''Structure of the chicken's inner ear,'' Am. J. Anat. **153**, 251–271.
Temchin, A. N. (**1980**). ''Multimodality of the interspike distribution of spontaneous activity in pigeon's auditory nerve fibers,'' Dokl. Akad. Nauk SSSR **253,** 743–747.
Temchin, A. N. (**1988**). ''Discharge patterns of single fibres in the pigeon's auditory nerve,'' J. Comp. Physiol. A. **163**, 99–115.
Warchol, M. E., and Dallos, P. (**1989**). ''Neural response to very low-frequency sound in the avian cochlear nucleus,'' J. Comp Physiol. A **166**, 83–95.
Weiss, T. F., and Rose, C. (**1988**). ''A comparison of synchronization filters in different auditory receptor organs,'' Hear. Res. **33**, 175–180.
Winter, I. M., Robertson, D., and Yates, G. M. (**1990**). ''Diversity of characteristic frequency rate-intensity functions in guinea-pig auditory nerve fibres,'' Hear. Res. **45**, 191–202.
Yeowart, N. S., and Evans, M. J. (**1974**). ''Thresholds of audibility for very low-frequency pure tones,'' J. Acoust. Soc. Am. **55,** 814–818.

Frequency representation in the emu basilar papilla

Christine Köppl and Geoffrey A. Manley
Institut für Zoologie der Technischen Universität München, Lichtenbergstrasse 4, 85747 Garching, Germany and Department of Physiology, University of Western Australia, Nedlands 6009, W.A., Australia

(Received 3 June 1996; accepted for publication 30 September 1996)

The frequency representation on the basilar papilla of the emu was investigated by recording from single auditory afferents and labeling them iontophoretically with horseradish peroxidase. Successfully labeled fibers covered a range of characteristic frequencies from 0.05 to 3.3 kHz, which corresponded to nearly 90% of the total papillar length. The termination sites of labeled fibers within the basilar papilla correlated with their characteristic frequency, the lowest frequencies being represented apically, the highest basally. The best mathematical description of the frequency distribution was given by an exponential regression, with a uniform mapping constant of 0.8 mm/octave. This function deviates from the more commonly observed pattern of increasing space constant towards higher frequencies. Most labeled fibers innervated only one hair cell; those contacting 4 or more hair cells were all of low characteristic frequency ($\leqslant$0.11 kHz). All labeled fibers terminated within the neural 56% of the basilar papilla's width. This innervation pattern is consistent with that observed in other bird species. There was no conclusive evidence for a change of sensitivity and/or frequency selectivity with innervational position across the papilla's width. [S0001-4966(97)04502-5]

PACS numbers: 43.64.Pg, 43.64.Nf [RDF]

INTRODUCTION

In recent years, the bird inner ear has become an increasingly popular system to study the mechanisms of sound transduction and neural coding in a cochlea with specialized hair-cell populations. Many similarities, as well as important differences, exist between the avian and mammalian cochleae (e.g., Manley *et al.*, 1989; Klinke and Smolders, 1993). Through comparative studies, these can lead to a better understanding of both systems. Like mammals, birds show a differentiation of their hair cells into two types, tall hair cells and short hair cells. Although tall and short hair cells are morphologically not sharply distinguished, but grade into each other, their extreme forms are characterized by an innervation pattern very similar to that typical for mammals: Tall hair cells are contacted by several afferent as well as small efferent terminals, whereas, according to the revised cell-type definition of Fischer (1994a), short hair cells receive no afferent but large efferent terminals. The proportion of tall to short hair cells varies along the length of the papilla, with a majority of tall hair cells at low frequencies gradually changing into a majority of short hair cells at high frequencies (e.g., Manley, 1990; Fischer, 1994a). The function of the tall hair cells currently appears to be analogous to that of mammalian inner hair cells, that is, to act as a relay to the brain, transducing and transmitting to the afferent fibers the stimulus impinging on them. The function of the short hair cells is much less clear, as is the significance of a gradual transition between the two hair-cell types.

One approach to tackle the problem of possible interaction between those hair-cell types and the relationship between structure and function is to compare species with different degrees of differentiation. Among the birds, the ratites or flightless birds promise to be highly interesting. Flightless birds are more closely related to each other than to any other birds and their body structure shows a number of primitive and/or neotenic features (Cracraft, 1974, 1981; Sibley and Ahlquist, 1981). It is reasonable to expect that the inner ear is also relatively unspecialized. We have thus begun morphological and physiological studies in a flightless bird, the Australian emu, to establish whether this species may be useful as a model of the primitive bird basilar papilla. Preliminary anatomical data showed an interesting mix of features with a great number of tightly-packed morphologically tall hair cells, a primitive feature, on the one hand, and a fairly advanced innervation pattern on the other (Fischer, 1994a and unpublished observations).

The present study aims to provide a frequency map for the emu basilar papilla, an essential prerequisite for any correlation of structure and function. The basic tonotopic organization of the avian basilar papilla is already well-known and conforms to the general vertebrate pattern of increasing frequency towards the basal end. Details of the map's shape, however, vary between species (Gleich, 1989; Manley *et al.*, 1987; Chen *et al.*, 1994; Jones and Jones, 1995; Köppl *et al.*, 1993; Klinke and Smolders, 1993; Smolders *et al.*, 1995). In addition, a very exciting issue has been raised by the demonstration of functional gradients in sensitivity and/or frequency selectivity across the width of the basilar papilla in the starling and pigeon (Gleich, 1989; Smolders *et al.*, 1995). We were therefore also interested to see whether such gradients are present in the emu.

I. METHODS

A. Subjects and experimental setup

Young emus (*Dromaius novaehollandiae*) were obtained on the day of hatching from the breeding program of the Department of Agriculture of Western Australia. They were kept at the animal house of the University of Western Aus-

tralia until the day of the experiment, with food and water available *ad libidum*. Experiments were carried out on 19 emus ranging in age from 1 to 11 days posthatch (P1 to P11). Experimental procedures and animal care were according to the guidelines of the Australian NH&MRC and approved by the Animal Experimentation Ethics Committee of the University of Western Australia (64/93/93 and 180/94/94).

Most animals were also used in a parallel study of discharge patterns in the auditory nerve. Details of the routine anaesthesia, animal homeostasis, acoustic stimulation, and recording procedures which are not unique to the data reported here can therefore be found in Manley *et al.* (1997) and will only be summarized briefly.

Emus were anaesthetized with a combination of pentobarbital and chloral hydrate (initial doses 30 mg/kg and 100–170 mg/kg, respectively). They were artificially respirated with carbogen and their rectal temperature was held at 38.7 $\pm$0.7 °C. Acoustic stimuli were generated by a frequency synthesizer, attenuated, gated, and delivered through a closed, individually calibrated sound system. The cochlear ganglion was exposed by adapting the dorsolateral approach through the recessus scala tympani originally developed in the starling (Manley *et al.*, 1985). A computer-controlled threshold-hunting routine that was described in detail by Winter *et al.* (1990), was used to obtain single-unit frequency tuning curves.

B. Single-unit recording and iontophoresis

Glass microelectrodes were pulled to the same specifications as electrodes normally used for single-unit recordings in the cochlear ganglion (40–90 MΩ when filled with 3M KCl). They were usually prefilled with a solution containing 0.15 M KCl and 0.05 M Tris buffer, which was aspirated from the electrode shaft after 1 to several hours and superfused with the same solution that in addition contained 5% or 10% horseradish peroxidase (HRP). Some electrodes were filled directly with 5% HRP; these were always found to contain small air bubbles in the tip region, but were also used. Electrodes were then stored in a moist box in a refrigerator for 2 to 6 days. On the day of the experiment, their tips were beveled by dipping them into a smoothly-stirred suspension of 0.05 μm particles of Al_2O_3 (approximately 20 vol.% in 0.9% NaCl) and monitoring their impedance until it had decreased from several hundred MΩ to 120–200 MΩ.

While advancing the electrode within the cochlear ganglion, the electrode's dc-potential was continuously monitored to detect sudden changes associated with the appearance of spikes, indicating cell-membrane penetration. Selected units which gave stable spike recordings (although the dc potential was rarely stable) and from which at least one complete tuning curve had been obtained were injected with HRP. A positive direct current of 0.5 to 10 nA that was generated by the internal current source of a WPI model M-707A microprobe system was passed for 1–30 min. The current applied was monitored continuously and adjusted to avoid electrode blockage. Tone bursts at the characteristic frequency (CF) of the cell that produced a clearly discernable discharge were given throughout the current application and the current was usually turned down at intervals of one minute to check if the unit was still present. Mostly, contact with the unit was lost gradually, as evident in a decreasing spike size. The current was usually stopped at the latest when spikes were no longer discernible.

C. Histology

One to ten hours after current application, the animal was given an anaesthetic overdose and perfused transcardially with about 100 ml of warm 0.9% NaCl containing 1000 units of heparin. This was followed by 500–1000 ml of 1% (in some cases 2%) paraformaldehyde and 2.5% glutaraldehyde in 0.1 M phosphate buffer (*p*H 7.4), taking 30–40 min, and immediately followed by 500 ml of phosphate buffer rinse. After storing the head in buffer in the refrigerator overnight, the relevant ear was dissected out and processed as a wholemount to visualize the HRP label. Following three rinses in 0.1 M Tris buffer (*p*H 7.6), one hour in 0.5% $CoCl_2$ and 1% DMSO in Tris buffer, two rinses each in Tris buffer and in 0.1 M phosphate buffer (*p*H 7.4), the ear was preincubated in 0.05% DAB and 1% DMSO in phosphate buffer for 20 min before adding approximately 0.01% H_2O_2 and incubating for a further 25–35 min. The ear was then rinsed in phosphate buffer, dehydrated in a graded series of ethanol and embedded in Araldite via propylenoxide as the intermedium.

D. Microscopic analysis

The Araldite block was temporarily mounted and coverslipped with immersion oil and examined under $\times$100 magnification. A camera-lucida drawing of the papillar outline and any labeled fibers was carried out at this stage. Very smooth and transparent surfaces were then cut on the block with glass knives to improve vision and permit exact measurement of papillar length in the wholemount, using the technique described in Köppl *et al.* (1993) for the barn-owl cochlea. In the emu, 2 to 3 surfaces at different angles and always oriented as closely as possible parallel to the papilla, proved sufficient to approximate its curvature. Measurements of the papillar length (along the midline of the epithelium) and the termination points of labeled fibers along and across the papilla were then taken, again under immersion oil, using $\times$100 to $\times$400 magnification. In cases of labeled fibers branching within the epithelium, the midpoint of the terminal field was taken.

Areas of the papilla containing labeled fiber terminals classified as single or pseudo-single (see Results) were subsequently cross-sectioned at 5 or 10 μm, mounted, and coverslipped. From these sections, an estimate of the number of hair cells contacted, as well as their rank across the papillar width (counting every hair cell, including those only partially contained within the section) was derived.

II. RESULTS

A. Evaluation of stains

We made a total of 41 HRP injections in 19 ears. Up to four injections (mostly two) were made in a single cochlea, provided unit CFs were separated by at least one octave.

Each cochlear wholemount was carefully examined before and after surface polishing with ×200 magnification and a camera-lucida drawing was made. Labeled neurons were divided into groups of neurons lying spatially close together, using their termination sites along the papilla, the course of the fibers, and the location of the cell bodies within the ganglion. In cases of multiple HRP injections, those groups could (by comparison with single stains in other ears) usually be assigned with confidence to specific CFs according to their termination sites along the papilla. In cases with fewer labeled groups than there were HRP injections made (five ears), it was always obvious from the position of label which injections were represented. There was, however, no consistent relationship between the strength or duration of injected current and labeling success. Cases showing several labeled neurons that did not show any grouping were excluded from further analysis as ambiguous. In three ears, more labeled neuron groups were identified than HRP injections made. One of these showed no clear difference in labeling intensity between the neurons and was excluded as ambiguous. In the remaining two, one fiber group was labeled much more faintly than the others and its fibers ran to the macular lagena and, in one case, to the very apical end of the papilla. These faint stains were rejected as inadvertent, an interpretation also consistent with the experimental protocol, that noted many brief recordings of nonauditory and very low CF neurons with relatively low-impedance HRP-filled electrodes in these cases.

According to this interpretation, 15 of the 41 HRP injections made did not yield any label. Twelve injections resulted in a single labeled neuron in the papilla, four in a single darkly labeled neuron plus one or two much more faintly labeled ones (these cases we call pseudo-single). A further two injections yielded only a single labeled cell body each, with no labeled fibers. Three injections gave two equally intensely stained neurons (these we call dual) and the remaining five cases resulted in ambiguous labeling.

B. Distribution of frequencies along the basilar papilla

The termination points of labeled auditory-nerve fibers along the basilar papilla, as determined in the wholemounts, were clearly correlated with their characteristic frequency (CF). Fibers of low CF innervated hair cells near the apical end of the papilla and fibers of increasingly higher CF terminated at increasing distance from the apex. In order to pool data from different individuals, the termination points were normalized to each basilar papilla's total length. The average value for the papillar length was 5.15 mm (in the fixed, plastic-embedded state), individual values ranged from 4.85 to 5.42 mm. There was no evidence for maturational growth of the basilar papilla within the first 11 days posthatch, i.e., the age range of animals used in this study (Fig. 1). The length of an adult basilar papilla is around 5.5 mm (unpublished observations).

To arrive at a quantitative description of the frequency distribution, several different functions were fitted according to the least-squares method. In addition to the measurements from single-fiber stains, data points were also accepted from the darkest labeled fiber in each pseudo-single case, as well as average values from the dual-stain cases. Since Köppl *et al.* (1993) had shown in the barn owl that a reliable estimate of the papillar termination point may be obtained from the location of the ganglion cell body, the two cases having only labeled cell bodies were also included. This gave a total of 21 data points covering a frequency range from 0.05 to 3.3 kHz and close to 90% of the total papillar length (Fig. 2).

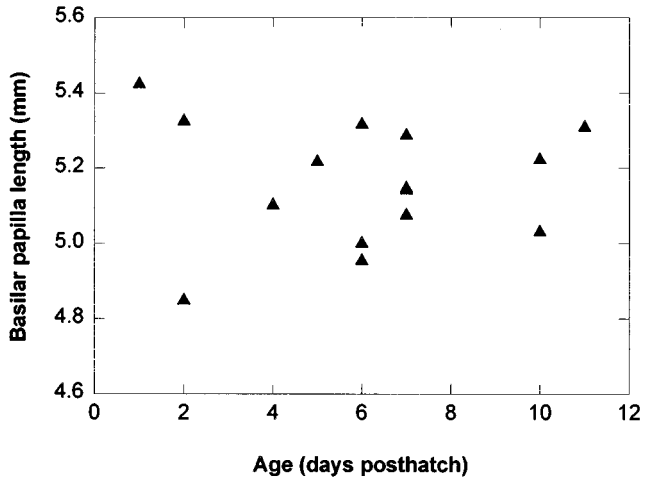

FIG. 1. Basilar papilla length as a function of posthatching age. There is no significant correlation between the two parameters, i.e., no change over the first 11 days.

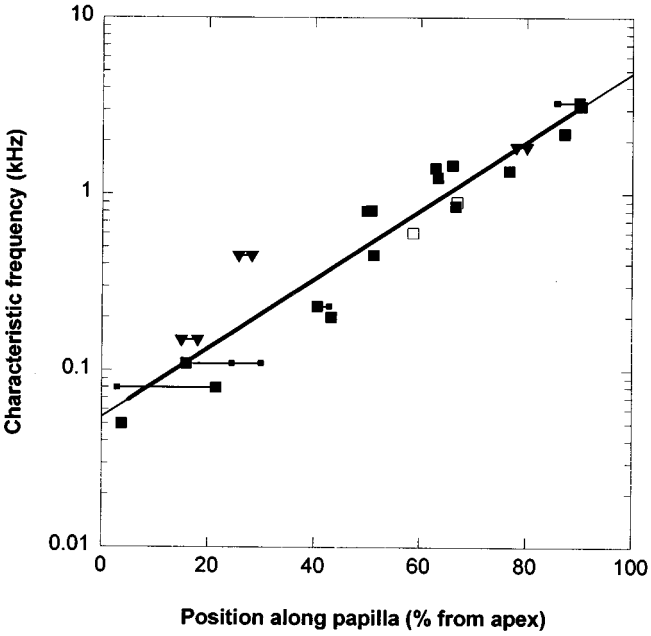

FIG. 2. Frequency map of the emu basilar papilla. The characteristic frequency determined immediately before iontophoresis is shown as a function of the normalized position of innervation of the labeled fiber(s) along the papilla. Large filled squares represent single-fiber labels, open squares represent single ganglion cell bodies; large filled squares joined to small squares represent pseudo-single cases, the large square denotes the darkly-stained fiber; pairs of triangles represent the dual-label cases (for classification see text). The thick solid line is an exponential fit to the data, extended thinly at both ends to show its intersects, i.e., frequency predictions, at both ends of the papilla.

Linear, logarithmic, exponential, and power functions, as well as a modified exponential function suggested by Greenwood (1990) were applied. The goodness-of-fit to the data for each function was judged according to standard statistical criteria, i.e., the value of the correlation coefficient, the statistical significance, and the distribution of residuals. Although all functions gave a significant correlation, the exponential one showed the highest correlation coefficient ($r = 0.95$, $p < 0.0001$) and, most importantly, was the only one with a random scatter of residuals, indicating an adequate fit throughout the range of values of the independent variable (position). Thus, the exponential function

$$f = 54.4\, e^{0.0449\, x},$$

where f = frequency in Hz and x = position in % from apical end, was chosen to represent the data (Fig. 2). The basilar papilla of the emu thus appears to have frequencies mapped uniformly along a logarithmic scale, with a mapping constant of 0.8 mm/octave (assuming an average papillar length of 5.15 mm). The extreme frequencies predicted by the exponential function are 0.054 kHz apically and 4.83 kHz basally.

C. Number of hair cells contacted by individual fibers

Most of the labeled fibers could be followed beyond their point of entry into the basilar papilla and into the hair-cell area. From cross sections, an estimate of the number of innervated hair cells could be derived, counting every hair cell that was touched. Only single-fiber stains and the darkest labeled fiber from each pseudo-single case were analyzed.

Most of the fibers (8 out of 13) contacted only one hair cell. These included all higher-frequency fibers with a CF above 0.8 kHz and one low-frequency fiber with CF 0.23 kHz. Two examples are shown in Figs. 3 and 4. Of the remaining five fibers, four with CFs between 0.08 and 0.8 kHz innervated from 2 to 8 hair cells (example in Fig. 5); one very low-frequency fiber (CF 0.05 kHz) contacted up to 19 hair cells. In this latter case, the estimate was difficult, because the stain extended over several 5-μm sections and errors due to counting the same hair cell twice cannot be excluded. Fibers contacting only 1 to 2 hair cells all innervated the neural area, up to hair cells of rank 14 (counting from the neural edge of the papilla). In contrast, for the few fibers contacting four or more hair cells, all these hair cells were of rank 16 or higher. Taken together, the labeled fibers of our sample thus showed a tendency such that lower frequency fibers contacted both hair cells at increasingly abneural positions across the width of the basilar papilla and more hair cells.

Despite a sometimes substantial number of hair cells contacted, none of the labeled fibers branched extensively. Instead, they appeared to make multiple contacts either en passant or through short branches no longer than one or two hair cells (Fig. 5). As a result, none of the fibers showed a large area of input, the maximal extension in the baso-apical dimension being about 25 μm or 0.5%, in the neural-abneural dimension ten hair cells, corresponding to 25% of all cells in the transect.

D. Position of stained fibers across the basilar papilla

The termination points of labeled fibers never reached more than 56%, or about halfway across the distance towards the abneural edge. Only in two cases with ambiguous labeling, where many more fibers were stained than injections had been made, were a few fibers observed that reached close to the abneural edge. These stains were in the apical third of the basilar papilla, conforming to the trend already described above.

Since gradients in tuning sharpness and/or neural thresholds across the basilar papilla have been reported for other birds (Gleich, 1989; Smolders *et al.*, 1995), we examined our data closely for similar correlations. Only single-fiber stains and the darkest labeled fiber from each pseudo-single case were included. In cases with more than one hair cell contacted by a fiber, the average rank of those hair cells was used to indicate its innervation point across the papilla.

The emu chicks in our sample ranged from 1 to 11 days posthatch (P1–11). Thresholds are not yet mature at those ages; however, this is probably due to the middle ear rather than to an incomplete development of the basilar papilla (Manley *et al.*, 1997). To be able to pool data across the ages used in the present study, thresholds of animals up to P7 were thus first normalized to the audiogram at P10/11, by subtracting 10 dB at CFs above 2.3 kHz (Manley *et al.*, 1997). Data were then pooled for CFs between 0.8 and 1.5 kHz, a region where the audiogram varies only within 5 dB (Manley *et al.*, 1997). There was no relationship apparent between neural thresholds and rank of the innervated hair cell across the basilar papilla [Fig. 6(A)]. Although the thresholds of all fibers labeled in this frequency range had been fairly sensitive (up to 25 dB SPL), the hair cells contacted by them ranked anywhere between number 5 and 22 from the neural edge, or between 21% and 69% of all hair cells counted from the neural to the abneural edge (see examples in Figs. 3 and 4). Thresholds were then, in addition, corrected for the emu audiogram (Manley *et al.*, 1997) and pooled across all frequencies [Fig. 6(B)]. There was still no statistically-significant correlation, even if the one outlying threshold value (near 80 dB) was omitted.

We also examined for trends in the tuning selectivity, measured as $Q_{10\ \mathrm{dB}}$. Since the $Q_{10\ \mathrm{dB}}$ is mature at all frequencies at hatching (Manley *et al.*, in press), no correction for age was applied in this case. The data were split into three frequency ranges (0.05–0.23 kHz, 0.8–1.45 kHz, and 2.2–3.15 kHz), within which the average $Q_{10\ \mathrm{dB}}$ varies by no more than 0.5 units (Manley *et al.*, 1997). There appeared to be a trend of falling $Q_{10\ \mathrm{dB}}$ with increasing distance from the neural edge in the upper frequency ranges [Fig. 7(B) and (C)], however, the small number of points precludes a definite statement. No change was obvious for the very low frequencies [Fig. 7(A)].

III. DISCUSSION

The data reported in this paper were obtained by an established technique, i.e., filling single physiologically characterized neurons with HRP. Our overall success rate of ob-

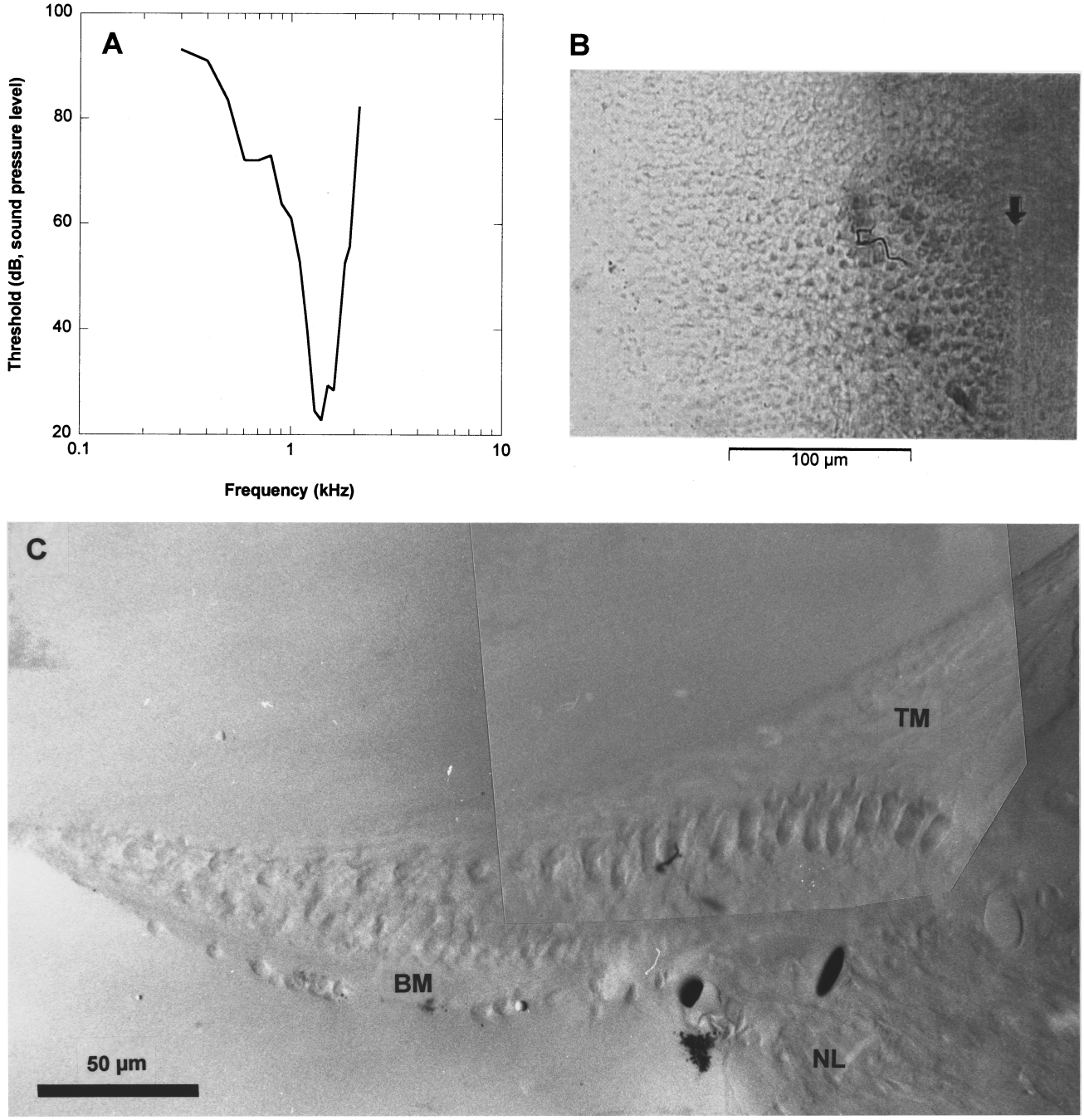

FIG. 3. Example of an HRP-labeled fiber in a 7-day old emu. (A) Frequency-threshold curve of the unit before current application. The CF was 1.4 kHz, threshold at CF 23 dB SPL. (B) Surface view of the papillar wholemount in the immediate area of the labeled fiber. An arrow points out the neural edge of the epithelium, abneural is to the left. The darkly labeled fiber comes into focus a short distance from the neural edge and terminates in a semicircle. (C) A cross section of the same preparation, showing the full width of the basilar papilla. Neural is to the right, TM = tectorial membrane, BM = basilar membrane, NL = neural limbus. The labeled fiber is seen to terminate on the 12th hair cell (of 28) from the neural edge.

taining any label at all, 64% or 26 labels of 41 attempts, was very good compared to similar studies of the peripheral auditory system in a variety of species (Liberman, 1982a; Manley *et al.*, 1987; Schermuly and Klinke, 1990b; Chen *et al.*, 1994; Jones and Jones, 1995; Smolders *et al.*, 1995). However, the success rate in achieving unambiguous single-cell labeling (29% or 12 out of 41) was on the low side, we believe for two main reasons. First, the surface polishing technique used provides an excellent view of the cochlear wholemounts, especially for the detection of faintly labeled fibers. In several cases, what seemed to be single-cell labels in the first check of the plastic-embedded wholemount turned out, after polishing to obtain a clearer view, to be accompanied by other labeled neurons, meaning that these cases could not be classified as a single-cell label. Second, we had to reject several cases as ambiguous because two or more HRP injections had been attempted in one ear and the resulting stains in those cases could not be assigned with complete confidence.

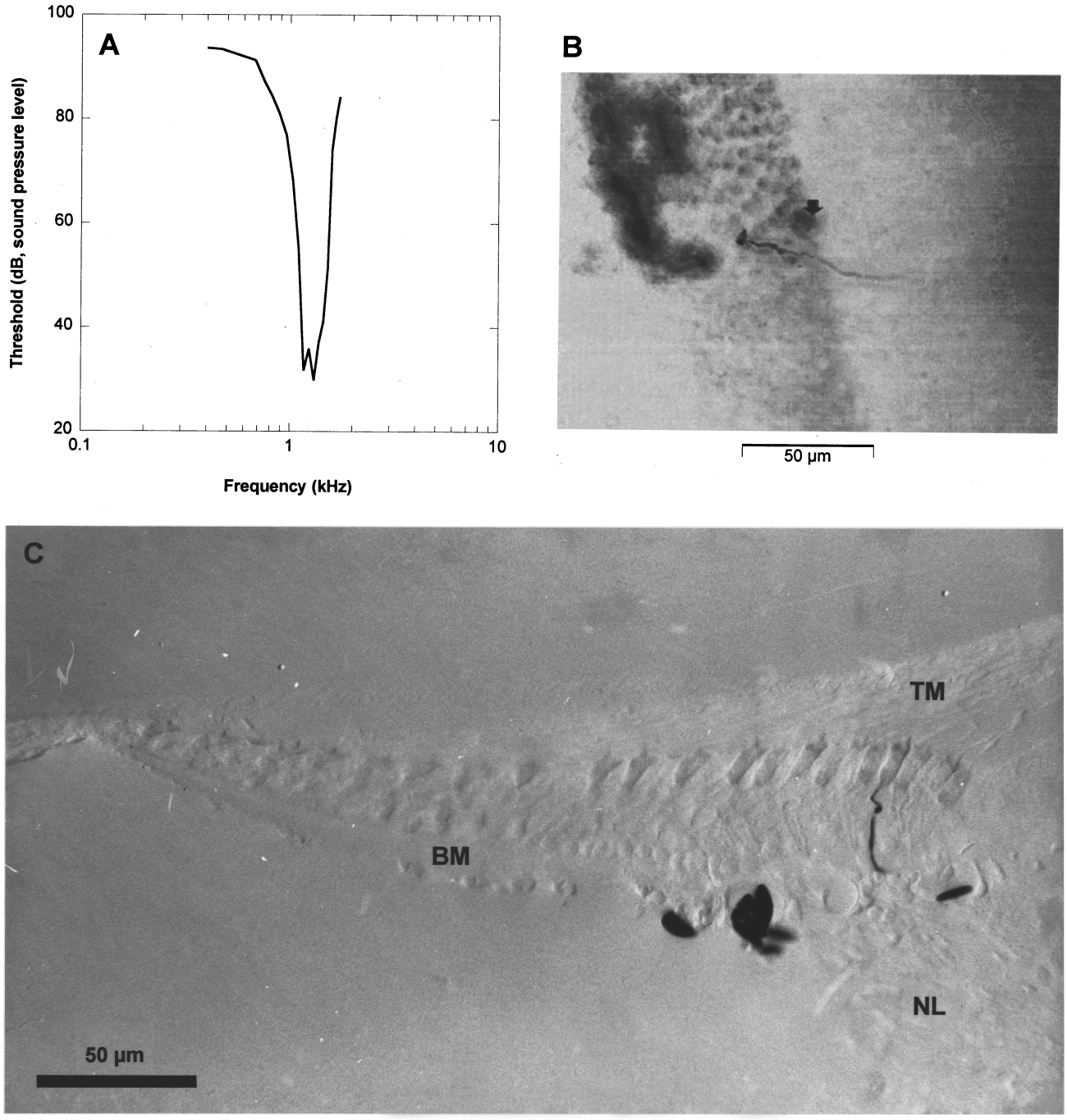

FIG. 4. Example of an HRP-labeled fiber in a 4-day-old emu. (A) Frequency-threshold curve of the unit before current application. The CF was 1.24 kHz, threshold at CF 30 dB SPL. (B) Surface view of the papillar wholemount in the immediate area of the labeled fiber. An arrow points out the neural edge of the epithelium, abneural is to the left and out of focus. The labeled fiber comes into focus just outside the basilar papilla and terminates close to the neural edge. (C) A cross section of the same preparation, showing the full width of the basilar papilla. Neural is to the right, TM = tectorial membrane, BM = basilar membrane, NL = neural limbus. The labeled fiber is seen to terminate on the 5th hair cell (of 25) from the neural edge.

A. Peripheral frequency maps

The frequency map derived from our data was an exponential function, i.e., a logarithmic spacing of CFs along the basilar papilla of the emu, with a uniform mapping constant of 0.8 mm/octave. The exponential function fit the data, which covered almost 90% of the total papillar length, very well. In addition, it predicted lower and upper frequency limits (0.054 and 4.83 kHz) that correspond closely to the CF range found in a large sample of auditory-nerve units: 0.04 to 4.0 kHz (Manley *et al.*, 1997).

The exponential frequency map of the emu is somewhat unusual. Most frequency maps in birds and mammals show a more compressed representation of low frequencies compared to higher ones (Liberman, 1982a; Manley *et al.*, 1987; Gleich, 1989; Müller, 1991; Müller *et al.*, 1991, 1993; Chen *et al.*, 1994). Greenwood (1990) proposed a modified exponential function that describes this general kind of frequency representation with a gradually increasing space constant towards higher frequencies. However, since different hypotheses exist as to the mechanisms underlying this kind of fre-

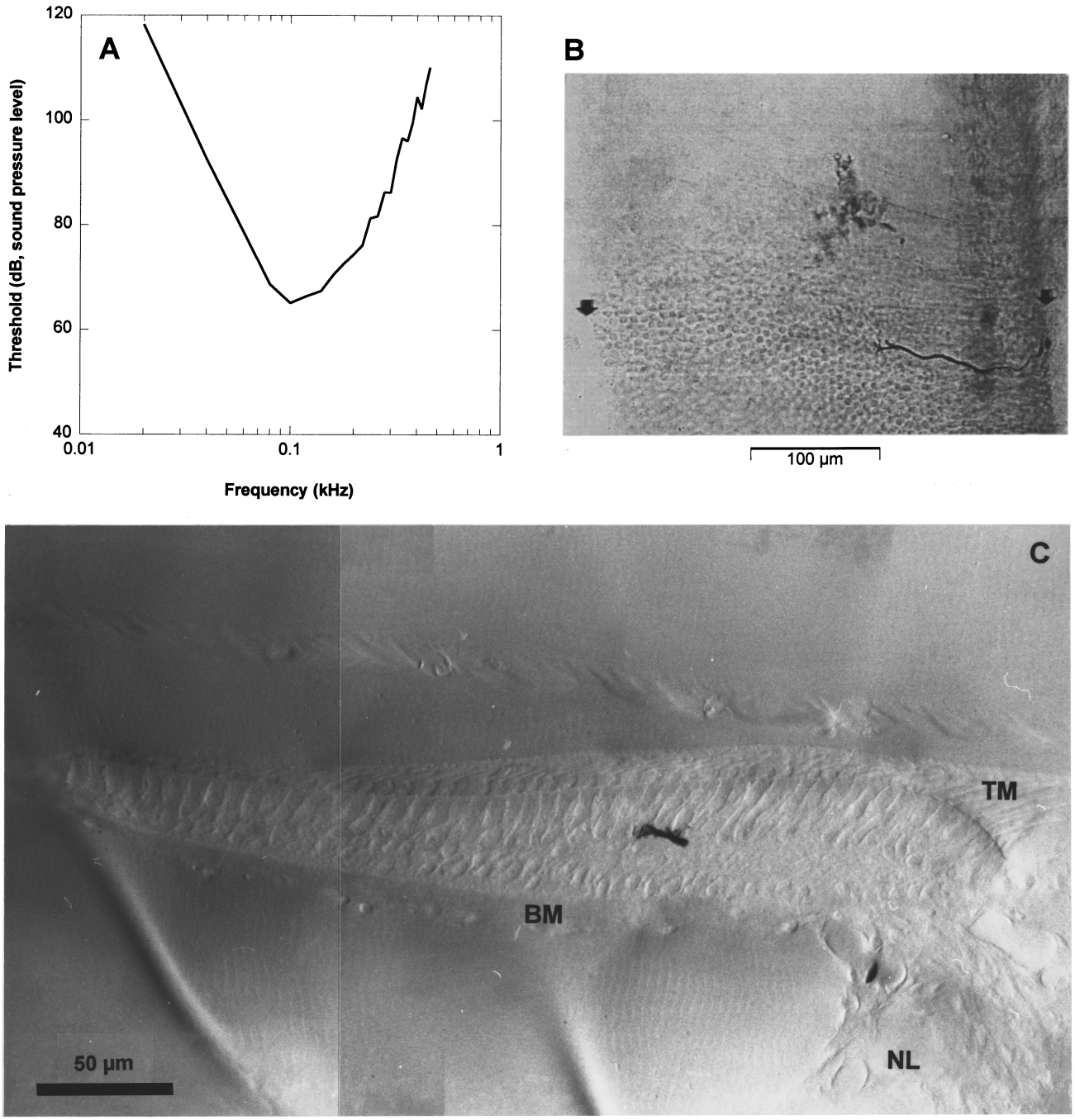

FIG. 5. Example of a low-frequency HRP-labeled fiber in a 7-day-old emu. (A) Frequency-threshold curve of the unit before current application. The CF was 0.11 kHz, threshold at CF 64 dB SPL. (B) Surface view of the papillar wholemount in the immediate area of the labeled fiber. Arrows point out the edges of the epithelium, neural is to the right, abneural to the left. The labeled fiber comes into focus at the neural edge and travels some distance across the papilla before terminating in several short branches. (C) A cross section of the same preparation, showing the full width of the basilar papilla. Neural is to the right, TM = tectorial membrane, BM = basilar membrane, NL = neural limbus. In this section, the labeled fiber is seen to contact 3 hair cells (ranks 17–19 from the neural edge, of 47); in neighboring sections, contacts with 5 more hair cells were observed.

quency distribution and the mechanisms may also be different in different taxa (e.g., Manley *et al.*, 1988; Greenwood, 1990), the significance of a particular shape of frequency map is still unclear.

A number of exceptions to the above rule have already been found, which are correlated with known enhanced behavioral importance of particular frequency ranges. Certain bat species, for example, show a highly expanded cochlear representation of the frequencies most prominent in their echolocation calls (Kössl and Vater, 1985; Vater *et al.*, 1985). An expanded representation of lower-frequency bands is seen in the Mexican free-tailed bat (Vater and Siefer, 1995) and the African mole rat (Müller *et al.*, 1992). Among birds, both the chicken and starling show frequency maps conforming to the unspecialized vertebrate pattern (Manley *et al.*, 1987; Gleich, 1989; Chen *et al.*, 1994). The barn owl has been identified as a clear specialist with an expanded representation of its upper hearing range (5–10 kHz) that is

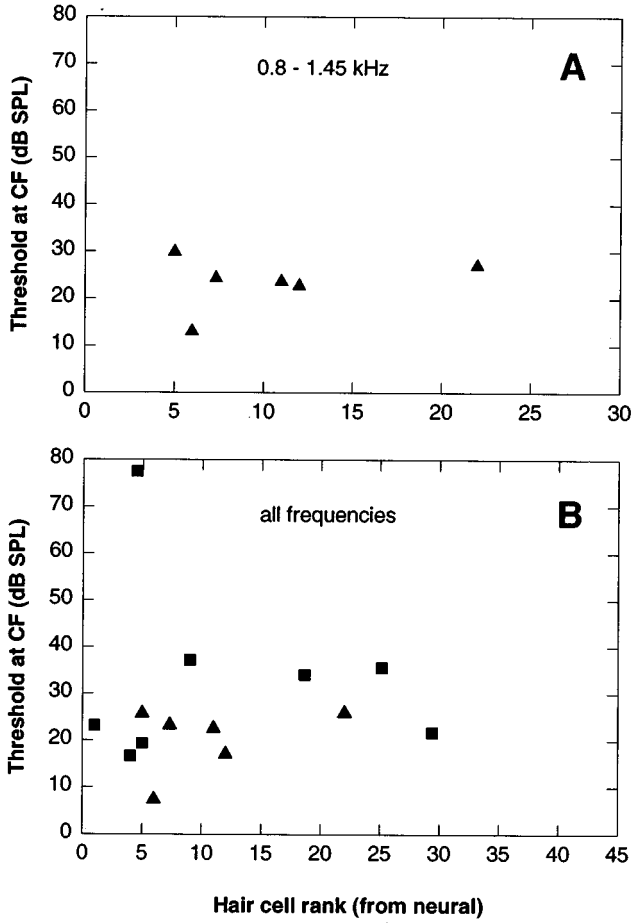

FIG. 6. Threshold at CF as a function of rank of the contacted hair cell(s), counted from the neural edge. (A) Only data from fibers with a CF between 0.8 and 1.45 kHz are shown. This minimizes threshold variations due to changing overall sensitivity across frequencies. (B) All data pooled across frequencies. Thresholds are corrected for both age and audiogram (see text). Triangles represent the same data points as shown in (A) (with additional correction for the audiogram), squares are all other CFs.

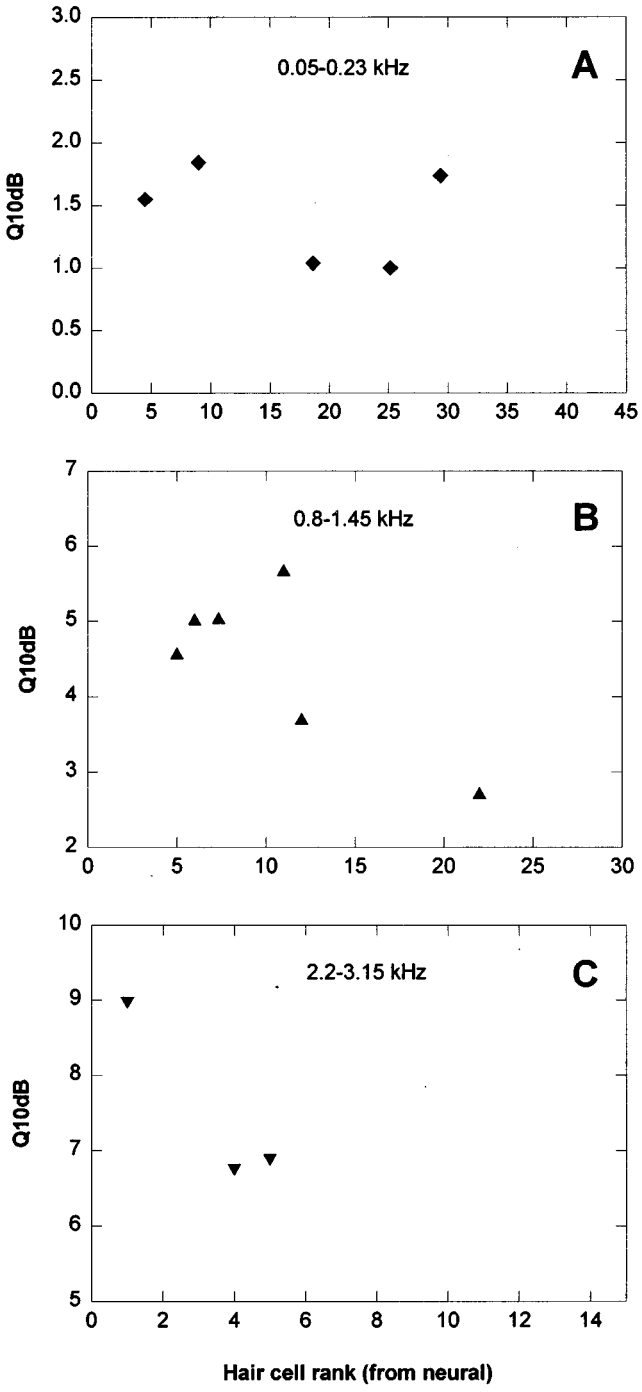

FIG. 7. Frequency selectivity (expressed as $Q_{10\ dB}$) as a function of rank of the contacted hair cell(s), counted from the neural edge. Data are shown separately for three frequency ranges to minimize $Q_{10\ dB}$ variations due to an overall trend of increasing $Q_{10\ dB}$ with frequency. (A) 0.05–0.23 kHz. (B) 0.8–1.45 kHz. (C) 2.2–3.15 kHz. Note the different scales of all three panels.

crucial to this nocturnal hunter for acoustic prey localization (Köppl *et al.*, 1993).

For the pigeon, an even, exponential spacing of frequencies, like in the emu and with a similar space constant (0.63 mm/octave), was found (Smolders *et al.*, 1995). Thus, these two species do not show any spatial expansion of a particular frequency band like the species mentioned above. Since emu and pigeon are among the phylogenetically most primitive of the bird species studied (Manley and Gleich, 1992), the question arises whether their exponential representation is to be interpreted as a low-frequency specialization or, in fact, as the basic bird pattern. Comparing their papillar space constants with the values of the chicken and starling in their upper and lower frequency ranges, about 0.5 mm/octave and 0.1 mm/octave, respectively (Gleich, 1989; Manley *et al.*, 1987), suggests that the chicken and starling have relatively compressed their low-frequency representation (rather than expanded their high-frequency representation).

In the pigeon, an unusual sensitivity to infrasound (below 20 Hz) has been described (Kreithen and Quine, 1979; Schermuly and Klinke, 1990a), that originates in the basilar papilla (Schermuly and Klinke, 1990b). However, the infrasound representation co-exists, on the abneural part of the apical basilar papilla, with the ''normal'' low frequencies represented along the same portion of basilar papilla (Schermuly and Klinke, 1990b; Smolders *et al.*, 1995). This is also consistent with an unusual widening of the pigeon basilar papilla towards its apical end (Gleich and Manley, 1988).

The infrasound representation therefore appears to be a true specialization in the pigeon, and unrelated to the spatial representation of conventional low audio frequencies. In the emu, no evidence for an infrasound sensitivity was found (Manley *et al.*, 1997) and the papilla is not especially wide apically (unpublished observations).

The fact that the two most primitive species, the emu and the pigeon, have a straight, exponential frequency map can be interpreted as indicating that this is the primitive condition. It is known, however, that the dominant frequencies in the vocalizations of adult emus are below 0.5 kHz (Marchant and Higgins, 1990). It cannot be excluded that the relatively generous low-frequency representation on the emu basilar papilla may be an adaptation to the behavioral importance of those frequencies. It thus seems impossible at present to distinguish between the primitive pattern in peripheral frequency representation in birds and possible changes in the map due to low-frequency specialization.

B. Innervation pattern of afferent fibers

Auditory afferent fibers in birds mostly contact only one hair cell (Gleich, 1989; Manley *et al.*, 1989; Fischer, 1992; Fischer *et al.*, 1992; Köppl *et al.*, 1993; Chen *et al.*, 1994; Smolders *et al.*, 1995). If two or more hair cells are innervated, these are predominantly situated apically (Gleich, 1989; Schermuly and Klinke, 1990b; Fischer, 1992, 1994b; Köppl *et al.*, 1993; Smolders *et al.*, 1995). Our results on the emu also conformed to this general pattern. They further indicated a greater tendency for fibers contacting several hair cells to innervate further away from the neural edge of the papilla. The same tendency was observed in the starling (Gleich, 1989) and the pigeon (Schermuly and Klinke, 1990b; Smolders *et al.*, 1995), using similar methods. Ultrastructurally, nonexclusive innervation was also regularly seen at the neural edge (Fischer, 1992, 1994b; Fischer *et al.*, 1992).

In the bird basilar papilla, a significant number of hair cells does not receive afferent innervation at all. This is most clearly seen in ultrastructural studies (Fischer, 1992, 1994a, b; Fischer *et al.*, 1992) and is corroborated by the uniform failure to label afferent fibers in these areas (Gleich, 1989; Manley *et al.*, 1989; Köppl *et al.*, 1993; Chen *et al.*, 1994; Smolders *et al.*, 1995). The extent of the area bare of afferents is species-specific, but generally begins at the abneural edge some 1 or 2 mm from the apical end of the papilla and broadens towards the basal end (Fischer, 1994a). This pattern is reminiscent, but not coincident, with the distribution of tall and short hair cells described previously in many studies. It has to be kept in mind, however, that the morphological tall-short hair cell distinction has always been an arbitrary one, since they are not sharply distinguished, but grade into each other in every respect (Takasaka and Smith, 1971; Fischer *et al.*, 1992; Fischer, 1994a). Fischer (1994a) therefore suggested using the presence or absence of afferent innervation as a new and potentially more functional definition for tall and short hair cells. The emu probably best illustrates the need for a more functional definition. Both our sample of labeled afferent fibers and preliminary ultrastructural data show the typical lack of afferent innervation in the basal-abneural region, while the conventional arbitrary criterion of hair-cell length and width suggests a virtually complete absence of short hair cells in the emu papilla (Fischer, 1994a and unpublished observations).

C. Functional gradients across the papillar width

The avian basilar papilla has many hair cells across its width, from at least 5 basally up to 50 at the apical end (see reviews by Manley, 1990; Manley and Gleich, 1992). Depending on the baso-apical position, a varying proportion of these hair cells are afferently innervated (from about the neural half basally to all apically; Fischer, 1994a).

In the starling, Gleich (1989) showed for the first time that such afferent fibers from the same longitudinal position, but contacting hair cells at different distances from the neural edge, differ in their physiological properties. He found a significant linear threshold gradient, such that fibers contacting hair cells near the neural edge were the most sensitive. In the CF range between 0.6 and 1.8 kHz, where the audiogram of the starling is nearly flat and thus does not contribute to threshold variation, the slope of this gradient indicated a remarkable loss of sensitivity of about 6 dB/hair cell moving away from the neural edge. Subsequently, a threshold gradient was also reported across the width of the pigeon basilar papilla (Smolders *et al.*, 1995). However, there was considerable scatter in the pigeon data (which were pooled across frequencies after correction for the audiogram), such that very insensitive as well as sensitive fibers were found to innervate hair cells over most of the neural half of the basilar papilla. This resembles our data on the emu, which showed a great spread of the innervation points of afferent fibers of comparable low threshold across the width of the papilla. In the pigeon, a moving average through the large sample of labeled fibers indicated a nonlinear threshold change despite the scatter, with a threshold minimum at about 20% of the distance from the neural edge. The threshold variation was mirrored by a similar $Q_{10\ \mathrm{dB}}$ variation with maximal values at the place of minimal threshold (Smolders *et al.*, 1995).

It appears that gradients in sensitivity and frequency selectivity of afferent fibers innervating hair cells at different positions across the basilar papilla are probably typical for birds, although their shape may differ across species. The failure to conclusively show such gradients in the emu may be due to our relatively small sample size. Another confounding influence, however, may be frequency. Whereas both in the starling and the pigeon, the sample of labeled fibers was markedly skewed toward low frequencies (Gleich, 1989; Smolders *et al.*, 1995), our sample in the emu was more homogenous across frequencies. It is still unknown whether functional variation across the papilla's width is similar or, indeed, even typical across all frequencies. It is important to point out in this regard that in both emu and chicken, a narrowing of the threshold range at frequencies above about 2 kHz, is obvious (Chen *et al.*, 1996; Manley *et al.*, 1997).

The mechanisms underlying functional gradients across the papilla's width are equally unclear. An obvious influence on the sensitivity might be expected from the gradual change of hair-cell bundle orientation from both edges toward the

middle of the papilla (review in Manley, 1990). Assuming a strictly radial mechanical motion, hair cells with increasingly rotated bundles would be stimulated at increasingly unsuitable angles. As discussed by Gleich (1989), this effect could account for a threshold variation of 20–30 dB in the starling, too little by far to explain the observed threshold gradient in that species. In the pigeon, such a numerical comparison has not yet been made. However, the relative positions of the reported threshold minima in starling and pigeon correlate with differences in the hair-cell orientation patterns between the two species (Gleich and Manley, 1988). If hair-cell orientation is involved in generating differential sensitivity across the basilar papilla, a diminishing effect would be predicted towards higher frequencies, since the greatest variation in hair-cell orientation typically occurs within the apical half of the papilla (review in Manley, 1990).

Smolders *et al.* (1995) suggested that sensitivity correlates with the position of the hair cell relative to the transition from neural limbus to free-basilar membrane, the most sensitive point being about halfway between the neural edge of the papilla and the neural edge of the free-basilar membrane. This hypothesis would predict that the sensitivity gradient across the width of the papilla looks different for different frequencies, since the proportions of the basilar papilla situated on the neural limbus and the free-basilar membrane, respectively, change along its length, i.e., along the tonotopic axis (Takasaka and Smith, 1971; Fischer, 1994a,b).

Synaptic efficacy or afferent metabolic rate, which is most probably underlying differential sensitivity in mammalian auditory afferents (Liberman, 1982b), is unlikely to play a role in birds. In this case, a correlation of spontaneous rate and threshold would be expected, which was found neither in the starling (Gleich, 1989) nor in the emu (Manley *et al.*, 1997). For the pigeon, only a weak correlation between those parameters has been reported (Smolders *et al.*, 1995).

ACKNOWLEDGMENTS

We thank all members of the Auditory Lab at the Department of Physiology, University of Western Australia for their hospitality and cooperation, which made the experimental work for this study possible. Special thanks are due to Dr. Graeme Yates, who gathered all the necessary permits and experimental equipment as well as to Dr. Don Robertson and Alan Light, who were always helpful with histology. We are also very grateful to the West Australian Department of Agriculture, that reliably provided us with hatchling emus from their experimental farming program. Supported by the Deutsche Forschungsgemeinschaft within the programme of the SFB 204 ''Gehör,'' a grant from the Australian NH &MRC, and a Visiting International Exchange Fellowship from the Australian ARC (DEET).

Chen, L., Salvi, R., and Shero, M. (**1994**). ''Cochlear frequency-place map in adult chickens: Intracellular biocytin labeling,'' Hear. Res. **81**, 130–136.

Chen, L., Salvi, R., Trautwein, P. G., and Powers, N. (**1996**). ''Two-tone rate suppression boundaries of cochlear ganglion neurons in normal chickens,'' J. Acoust. Soc. Am. **100,** 442–450.

Cracraft, J. (**1974**). ''Phylogeny and evolution of the ratite birds,'' Ibis **116**, 494–521.

Cracraft, J. (**1981**). ''Towards a phylogenetic classification of recent birds of the world (class Aves),'' Auk **98**, 681–714.

Fischer, F. P. (**1992**). ''Quantitative analysis of the innervation of the chicken basilar papilla,'' Hear. Res. **61**, 167–178.

Fischer, F. P. (**1994a**). ''General pattern and morphological specializations of the avian cochlea,'' Scanning Microsc. **8**, 351–364.

Fischer, F. P. (**1994b**). ''Quantitative TEM analysis of the barn owl basilar papilla,'' Hear. Res. **73**, 1–15.

Fischer, F. P., Singer, I., Miltz, C., and Manley, G. A. (**1992**). ''Morphological gradients in the starling basilar papilla,'' J. Morphol. **213**, 225–240.

Gleich, O. (**1989**). ''Auditory primary afferents in the starling: Correlation of function and morphology,'' Hear. Res. **37**, 255–268.

Gleich, O., and Manley, G. A. (**1988**). ''Quantitative morphological analysis of the sensory epithelium of the starling and pigeon basilar papilla,'' Hear. Res. **34**, 69–85.

Greenwood, D. D. (**1990**). ''A cochlear frequency-position function for several species—29 years later,'' J. Acoust. Soc. Am. **87,** 2592–2605.

Jones, S. M., and Jones, T. A. (**1995**). ''The tonotopic map in the embryonic chicken cochlea,'' Hear. Res. **82**, 149–157.

Klinke, R., and Smolders, J. W. T. (**1993**). ''Performance of the avian inner ear,'' Progress Brain Res. **97**, 31–43.

Köppl, C., Gleich, O., and Manley, G. A. (**1993**). ''An auditory fovea in the barn owl cochlea,'' J. Comp. Physiol. A **171**, 695–704.

Kössl, M., and Vater, M. (**1985**). ''The cochlear frequency map of the mustache bat, *Pteronotus parnellii*,'' J. Comp. Physiol. A **157**, 687–697.

Kreithen, M. L., and Quine, D. B. (**1979**). ''Infrasound detection by the homing pigeon: a behavioral audiogram,'' J. Comp. Physiol. **129**, 1–4.

Liberman, M. C. (**1982a**). ''The cochlear frequency map for the cat: Labeling auditory nerve fibers of known characteristic frequency,'' J. Acoust. Soc. Am. **72,** 1441–1449.

Liberman, M. C. (**1982b**). ''Single-neuron labeling in the cat auditory nerve,'' Science **216,** 1239–1240.

Manley, G. A. (**1990**). *Peripheral Hearing Mechanisms in Reptiles and Birds* (Springer-Verlag, Berlin, 1990), 1st ed., p. 288.

Manley, G. A., and Gleich, O. (**1992**). ''Evolution and specialization of function in the avian auditory periphery,'' in *The Evolutionary Biology of Hearing*, edited by D. B. Webster, R. R. Fay, and A. N. Popper (Springer-Verlag, New York), 1st ed., pp. 561–580.

Manley, G. A., Gleich, O., Leppelsack, H.-J., and Oeckinghaus, H. (**1985**). ''Activity patterns of cochlear ganglion neurones in the starling,'' J. Comp. Physiol. A **157**, 161–181.

Manley, G. A., Brix, J. and Kaiser, A. (**1987**). ''Developmental stability of the tonotopic organization of the chick's basilar papilla,'' Science **237,** 655–656.

Manley, G. A., Brix, J., Gleich, O., Kaiser, A., Köppl, C., and Yates, G. K. (**1988**). ''New aspects of comparative peripheral auditory physiology,'' in *Auditory Pathway—Structure and Function*, edited by J. Syka and R. B. Masterton (Plenum, London), pp. 3–12.

Manley, G. A., Gleich, O., Kaiser, A., and Brix, J. (**1989**). ''Functional differentiation of sensory cells in the avian auditory periphery,'' J. Comp. Physiol. A **164**, 289–296.

Manley, G. A., Köppl, C., and Yates, G. K. (**1997**). ''Activity of primary auditory neurones in the cochlear ganglion of the emu *Dromaius novaehollandiae*: Spontaneous discharge, frequency tuning, and phase locking,'' J. Acoust. Soc. Am. **101**, 1560–1573.

Marchant, S., and Higgins, P. J. (**1990**). *Handbook of Australian, New Zealand & Antarctic Birds* (Oxford U.P., Melbourne, 1990), pp. 47–58 (*Dromaius novaehollandiae*).

Müller, M. (**1991**). ''Frequency representation in the rat cochlea,'' Hear. Res. **51**, 247–254.

Müller, M., Ott, H., and Bruns, V. (**1991**). ''Frequency representation and spiral ganglion cell density in the cochlea of the gerbil *Pachyuromys duprasi*,'' Hear. Res. **56**, 191–196.

Müller, M., Laube, B., Burda, H., and Bruns, V. (**1992**). ''Structure and function of the cochlea in the African mole rat (*Cryptomys hottentotus*): Evidence for a low frequency acoustic fovea,'' J. Comp. Physiol. A **171**, 469–476.

Müller, M., Wess, F.-P., and Bruns, V. (**1993**). ''Cochlear place-frequency map in the marsupial *Monodelphis domestica*,'' Hear. Res. **67**, 198–202.

Schermuly, L., and Klinke, R. (**1990a**). ''Infrasound sensitive neurones in the pigeon cochlear ganglion,'' J. Comp. Physiol. A **166**, 355–363.

Schermuly, L., and Klinke, R. (**1990b**). ''Origin of infrasound sensitive neurones in the papilla basilaris of the pigeon: An HRP study,'' Hear. Res. **48**, 69–78.

Sibley, C. G., and Ahlquist, J. E. (**1981**). ''The phylogeny and relationships of ratite birds as indicated by DNA-DNA hybridization,'' in *Evolution Today (Proceedings of the 2nd International Congress of Systematic and Evolutionary Biology)*, edited by G. Scudder and J. Reveal (Carnegie U.P., Pittsburgh), pp. 305–335.

Smolders, J. W. T., Ding-Pfennigdorff, D., and Klinke, R. (**1995**). ''A functional map of the pigeon basilar papilla: correlation of the properties of single auditory nerve fibres and their peripheral origin,'' Hear. Res. **92**, 151–169.

Takasaka, T., and Smith, C. A. (**1971**). ''The structure and innervation of the pigeon's basilar papilla,'' J. Ultrastructure **35**, 20–65.

Vater, M., Feng, A. S., and Betz, M. (**1985**). ''An HRP-study of the frequency-place map of the horseshoe bat cochlea: Morphological correlates of the sharp tuning to a narrow frequency band,'' J. Comp. Physiol. A **157**, 671–686.

Vater, M., and Siefer, W. (**1995**). ''The cochlea of *Tadarida brasiliensis*: specialized functional organization in a generalized bat,'' Hear. Res. **91**, 178–195.

Winter, I. M., Robertson, D., and Yates, G. K. (**1990**). ''Diversity of characteristic frequency rate-intensity funcions in guinea pig auditory nerve fibers,'' Hear. Res. **45**, 191–202.

The effects of decreased audibility produced by high-pass noise masking on cortical event-related potentials to speech sounds /ba/ and /da/[a)]

Brett A. Martin
Department of Otolaryngology, Albert Einstein College of Medicine, 1410 Pelham Parkway, Bronx, New York 10461 and Doctoral Program in Speech and Hearing Sciences, CUNY Graduate Center, 33 West 42nd Street, New York, New York 10036

Alain Sigal
Department of Otolaryngology, Albert Einstein College of Medicine, 1410 Pelham Parkway, Bronx, New York 10461

Diane Kurtzberg
Departments of Neuroscience and Neurology, Albert Einstein College of Medicine, 1410 Pelham Parkway, Bronx, New York 10461

David R. Stapells[b)]
Departments of Otolaryngology and Neuroscience, Albert Einstein College of Medicine, 1410 Pelham Parkway, Bronx, New York 10461

(Received 5 July 1995; accepted for publication 30 September 1996)

This study investigated the effects of decreased audibility produced by high-pass noise masking on cortical event-related potentials (ERPs) N1, N2, and P3 to the speech sounds /ba/ and /da/ presented at 65 and 80 dB SPL. Normal-hearing subjects pressed a button in response to the deviant sound in an oddball paradigm. Broadband masking noise was presented at an intensity sufficient to completely mask the response to the 65-dB SPL speech sounds, and subsequently high-pass filtered at 4000, 2000, 1000, 500, and 250 Hz. With high-pass masking noise, pure-tone behavioral thresholds increased by an average of 38 dB at the high-pass cutoff and by 50 dB one octave above the cutoff frequency. Results show that as the cutoff frequency of the high-pass masker was lowered, ERP latencies to speech sounds increased and amplitudes decreased. The cutoff frequency where these changes first occurred and the rate of the change differed for N1 compared to N2, P3, and the behavioral measures. N1 showed gradual changes as the masker cutoff frequency was lowered. N2, P3, and behavioral measures showed marked changes below a masker cutoff of 2000 Hz. These results indicate that the decreased audibility resulting from the noise masking affects the various ERP components in a differential manner. N1 is related to the presence of audible stimulus energy, being present whether audible stimuli are discriminable or not. In contrast, N2 and P3 were absent when the stimuli were audible but not discriminable (i.e., when the second formant transitions were masked), reflecting stimulus discrimination. These data have implications regarding the effects of decreased audibility on cortical processing of speech sounds and for the study of cortical ERPs in populations with hearing impairment. © *1997 Acoustical Society of America.* [S0001-4966(97)04302-6]

PACS numbers: 43.64.Qh, 43.64.Ri, 43.64.Sj [RDF]

INTRODUCTION

Both obligatory (N1) and discriminative (N2 and P3) cortical event-related potentials (ERPs) have been elicited using speech stimuli (e.g., Dorman, 1974; Galambos *et al.*, 1975; Hink *et al.*, 1978; Kraus *et al.*, 1992; Kurtzberg *et al.*, 1984; Novak *et al.*, 1989; Sams *et al.*, 1985; Wood, 1975; Wood *et al.*, 1971). Much of the literature in the area of ERPs and speech perception has focused on hemispheric dominance and lateralization issues (for review, see Molfese *et al.*, 1983; Molfese and Betz, 1988), on categorical perception (e.g., Aaltonen *et al.*, 1987; Maiste *et al.*, 1995; Molfese, 1978; Sams *et al.*, 1985; Sharma *et al.*, 1993a), or on acoustic versus phonetic processing (e.g., Dorman, 1974; Sharma *et al.*, 1993b; Wood, 1975). Studies of the effects of hearing impairment on ERPs elicited by speech stimuli, however, are few (Polen, 1984; Wall *et al.*, 1991), and the effects of various hearing impairments have not been studied systematically. A few studies of hearing-impaired listeners have demonstrated changes in ERPs to speech stimuli with hearing aids (Kurtzberg, 1989) or cochlear implants (Kaga *et al.*, 1991; Kraus *et al.*, 1993), but these studies generally exam-

[a)]Portions of this research were presented at the 13th Biennial Symposium of the International Electric Response Audiometry Study Group, Park City, UT, 8 September 1993, and at the 17th Midwinter Research Meeting of the Association for Research in Otolaryngology, St. Petersburg Beach, FL, 7 February 1994.

[b)]Author to whom correspondence should be addressed. Present address: School of Audiology and Speech Sciences, The University of British Columbia, 5804 Fairview Ave., Vancouver, BC V6T 1Z3, Canada. Electronic mail: stapells@audiospeech.ubc.ca

ined small numbers of subjects. Data in our laboratories from children with hearing loss showed large variability in the audiometric configurations associated with a present cortical response to speech sounds (Stapells *et al.*, in preparation).

Recordings of cortical ERPs, as well as concomitant behavioral measures, provide a view of the timing, strength, and location of early versus later cortical processes associated with auditory perceptions. As such, they may prove of use for the understanding of the effects of hearing loss. The cortical ERPs may also be useful in clinical audiological assessment. Cortical ERPs may be useful in demonstrating suprathreshold discrimination (such as speech, frequency, and temporal discrimination) in difficult-to-test populations such as infants. In addition to measures of speech discrimination ability, the potentials might be used to measure the benefit from hearing aids, cochlear implants, or other habilitation strategies. In order to use the cortical ERPs clinically, however, it is important to better understand the effects of hearing loss on N1, N2, and P3 to speech sounds, using well-controlled groups of subjects, in order to carefully examine the effects of different degrees and configurations of hearing loss.

The effects of decreased audibility on behavioral measures of speech perception performance are reasonably well known (for reviews, see Boothroyd, 1978; Walden, 1984). The perception of place of articulation contrasts tends to be particularly susceptible to the effects of hearing loss (e.g., Boothroyd, 1984; Dubno *et al.*, 1982; Dubno *et al.*, 1989; Gordon, 1987; Walden, 1984). Typical methods used to examine the effect of decreased audibility on speech perception performance are to use normal-hearing listeners and to progressively filter or mask specific spectral regions and then examine patterns of performance (e.g., Dubno *et al.*, 1989; Fabry and Van Tasell, 1986; Humes *et al.*, 1987; Miller and Nicely, 1955; Sher and Owens, 1974; Walden *et al.*, 1981; Wang *et al.*, 1978). Another method is to use hearing-impaired listeners with various audiometric configurations and to compare performance across groups (e.g., Bilger and Wang, 1976; Dubno *et al.*, 1982; Reed, 1975; Walden and Montgomery, 1975). The effects of sensorineural impairment, however, are not limited solely to audibility (e.g., Fabry and Van Tasell, 1986; Festen and Plomp, 1983; Scharf, 1978; Thibodeau, 1991). For example, processing of frequency, intensity, and temporal information may be affected. Therefore, studies using listeners with sensorineural hearing loss may show increased variability due to these additional effects of sensorineural hearing loss that are difficult to control.

In order to study the effects of controlled threshold elevations in specific spectral regions, with less of the variability present in sensorineural populations, we used high-pass noise-masked normal listeners. High-pass noise masking results in decreased audibility for frequencies above the noise masker cutoff. The data obtained from studies of noise-masked normal listeners may be useful in determining the optimal ERP parameters to apply to hearing-impaired listeners and may aid in the interpretation of their data. Filtered noise masking was selected because it is a more appropriate way to ''simulate'' sensorineural hearing loss than is use of filtered signals. Threshold elevations produced by masking are predominantly cochlear in origin (e.g., Fletcher, 1953; Humes *et al.*, 1987). Additionally, noise masking results in loudness recruitment that is similar to that seen with sensorineural hearing loss (e.g., Humes *et al.*, 1987; Humes and Roberts, 1990; Needleman and Crandell, 1995; Stevens, 1966). Noise masking, however, does not perfectly simulate all aspects of sensorineural hearing loss. Use of noise masking nevertheless provides a way to isolate the effects of decreased audibility in order to begin to understand some of the changes seen in speech-sound processing with sensorineural hearing loss.

The purpose of this study was to investigate the effects of decreased audibility produced by high-pass noise masking on the cortical obligatory N1, and the discriminative N2 and P3 ERPs to the speech sounds /ba/ and /da/, and their relationship to behavioral measures of discrimination.

I. METHOD

A. Subjects

Ten normal-hearing adults (five males and five females), aged 18–37 years (mean=27 years) with no history of neurological disorder, participated. All subjects had hearing sensitivity of 20 dB HL (ANSI, 1989) or better than 250–4000 Hz bilaterally. Additionally, immittance testing was performed prior to each session in order to rule out changing middle ear function. All subjects had normal tympanograms and present ipsilateral acoustic reflexes at 1000 Hz in the test ear.

B. Stimuli

The stimuli /ba/ and /da/ were selected for this study as they differ in place of articulation and thus in the frequency domain. The /ba/ and /da/ stimuli were created by digitizing natural tokens produced by a male talker. The tokens were then processed using linear prediction coefficient (LPC) analysis, and synthesized stimuli were regenerated using the LPC polynomial roots. The stimuli were digitized using a 30 000-Hz sampling rate (Neuroscan STIM; 12 bits; 10 000-Hz low-pass antialiasing filter, 12 dB/oct), edited to 150-ms duration by eliminating the final portion of the steady-state vowel and windowing the offset of the vowel, and calibrated in peak-to-peak equivalent SPL (dB ppe SPL). The acoustic waveforms of the speech stimuli, the wideband spectrograms, and a schematic of the spectrograms showing the frequencies of the first three formants and the formant transitions are displayed in Fig. 1. The stimuli differed primarily in second and third formant transition frequencies. The frequencies of the steady-state portion of the vowels were: $F0=108$ Hz, $F1=674$ Hz, $F2=1140$ Hz, and $F3=2350$ Hz. The transitions for /ba/ began at 328 Hz for $F1$, 1071 Hz for $F2$, and 2298 Hz for $F3$; the transitions for /da/ began at 362 Hz for $F1$, 1832 Hz for $F2$, and 2540 Hz for $F3$. Thus the largest differences between the stimuli are in the 1000–2000-Hz range. The stimuli were delivered at a D/A rate of 30 000 Hz (10 000-Hz anti-imaging filter, 12 dB/oct), and presented to the right ear of the subjects at 65 and 80 dB ppe SPL using 200 stimuli per run. Each condition was replicated

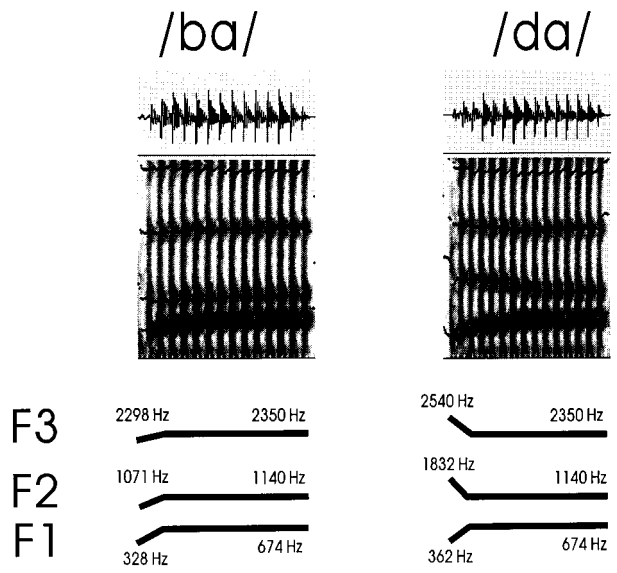

FIG. 1. The acoustic waveforms, wideband spectrograms, and a schematic of the spectrograms showing the frequencies of the first three formants and the formant transitions (obtained from LPC formant analyses) are displayed for the /ba/ and /da/ stimuli.

yielding a total of 400 stimuli. Stimuli were presented in an oddball paradigm (e.g., ba, ba, ba, ba, **da**, ba, etc.) whereby stimuli presented as standards (e.g., ba) had 0.80 probability and stimuli presented as deviants (e.g., da) had 0.20 probability of occurrence. The onset-to-onset interstimulus interval was 1100 ms. Both speech sounds were presented as standards and deviants in separate runs. Stimulus presentation order within a run was pseudo-randomized, with the provision that there were not more than two successive deviant stimuli and the first stimulus could not be a deviant. The 65-dB ppe SPL intensity was selected because of its similarity to conversational speech levels. The 80-dB ppe SPL intensity was selected because it is a higher intensity and therefore mimics, in part, the effects of amplification. Inclusion of this intensity allows for examination of whether noise-masked stimuli that were inaudible at 65 dB ppe SPL become audible at 80 dB and whether stimuli not discriminable at the lower intensity become discriminable. Additionally, this is the same intensity we previously employed in a study with hearing-impaired infants (Stapells *et al.*, in preparation), and we hoped to explain some of the results of that study.

C. Maskers

The speech stimuli were presented in quiet, and in conditions where they were mixed with ipsilateral masking noise. The masking noise (Nicolet white noise generator, model NIC-1007a) was fed to a filter (Wavetek, model 852) with both channels set to high pass and connected in series (96-dB/oct slope). After passing through the filter, the noise was attenuated (Med Associates, model ANL 918) and the output of this attenuator/mixer was fed to another attenuator/mixer where the noise masker was mixed with the stimulus (either the speech sounds for the ERP experiment or the pure tones for the masked behavioral audiograms), and then fed to a passive attenuator and an EAR-3A insert earphone. The level of the broadband noise (BBN) required to fully mask the behavioral perception of the 65-dB ppe SPL speech sounds was determined by increasing the masking level in 10-dB steps until the speech sounds were not audible. The masking level was then decreased by 10 dB and a bracketing approach was initiated using a 1-dB step size. Masked threshold was defined as the level at which the speech sounds were inaudible 50% of the time. The masking noise was then increased 7 dB above this level to ensure adequate masking of the speech sounds. These broadband masking levels ranged from 78.8–84.8 dB SPL for the ten subjects, with a mean level of 81.7 dB SPL. Without changing noise level, the noise was subsequently high-pass filtered using filter settings of 4000, 2000, 1000, 500, and 250 Hz. The same noise intensity (in dB SPL) was used for both the 65- and 80-dB ppe SPL speech stimuli. The 80-dB ppe SPL stimuli, therefore, were not completely masked and they remained audible, even in broadband noise, but not discriminable under some conditions.

D. EEG recordings

Seven EEG channels were recorded from electrodes placed at Fz, Cz, Pz, M1, M2, C3M (midway between C3 and M1), and C4M (midway between C4 and M2), all referenced to an electrode at the tip of the nose (Vaughan and Ritter, 1970). An eighth channel to monitor vertical eye movements and eyeblinks (EOG) was recorded from electrodes on the right supraorbital ridge of the frontal bone and on the zygomatic bone under the right eye. An electrode placed on the neck served as ground. Electrode impedances were maintained below 5000 Ohms, with differences between electrode pairs not exceeding 2000 Ohms. The seven EEG channels were amplified (gain=10 000), filtered (0.1–100 Hz, 6-dB/oct slope), and digitized (568 Hz per channel, 512 points) using a 900-ms analysis time (including a 100-ms prestimulus baseline, against which amplitude measures were made). The EOG channel was filtered and digitized as above, but amplifier gain was set to 5000. The ERP waveforms were saved for offline baseline correction, digital filtering (30-Hz low-pass filter, 12 dB/oct), artifact rejection ($\pm 100\ \mu$V in any of the EEG/EOG channels), and averaging. The ERPs were averaged separately for each stimulus. Two replications of each condition were obtained for each intensity to assess response reliability.

E. Behavioral measures

Behavioral pure-tone audiograms obtained in quiet and in the presence of the noise maskers were obtained for all of the subjects from 250–4000 Hz using a Beltone 10D audiometer. Testing was performed in a double-walled sound-attenuating booth.

Measures of reaction time (RT) and percent correct discrimination were obtained simultaneously with the ERP measures using button-press responses to the deviant stimuli. Measures of median reaction time, and number of hit, false alarm, correct rejection, and miss trials were obtained, and criterion-free measures of sensitivity (d') were calculated.

F. Calibration

The calibrations of the speech sounds, broadband noise, pure-tone stimuli (for the masked and nonmasked audiograms), and EEG amplifiers were checked daily. The speech sounds were calibrated in dB ppe SPL (relative to a 1000-Hz tone, using the vowel portion of the syllables) and the noise and tones in dB SPL using a Brüel and Kjaer sound level meter (model 2209) and Brüel and Kjaer coupler (model 4152) with a 2-cc adaptor (model DB0138). Amplifier channels were calibrated by sending a 50-μV square wave generated by the Grass amplifier through the amplifier channels and into the Neuroscan ''SCAN.'' All channels were within ± 2.5 μV of 50 μV.

G. Procedure

The experiment consisted of 65- and 80-dB ppe SPL stimulus intensity conditions which were run on separate days. The sessions took place in a double-walled sound-attenuated booth. Subjects were instructed to fixate on a small dot placed 1.5 m in front of them at eye level, to minimize eyeblinks, and to press a button as soon as they heard the deviant stimulus. They were advised to place equal weight on the speed and accuracy of their button presses. Subjects were trained on the button-press task using two runs of 100 stimuli in the quiet condition. Subjects were required to have at least 90% accuracy over both training runs for inclusion in the study. No subjects were excluded from the study based on this requirement.

Responses to the speech sounds were obtained in quiet, in broadband noise, and in 250-, 500-, 1000-, 2000-, and 4000-Hz high-pass noise. The quiet condition was always tested first to ensure that a response was present. This was followed by a broadband noise condition to ensure that the masking level was adequate to eliminate responses to the 65-dB ppe SPL stimuli. The remaining conditions were randomized, and the quiet condition was repeated at the end of the experiment.

H. Data analysis

After offline processing (baseline correction, artifact rejection, and digital filtering), the single-trial responses were averaged so that responses to stimuli presented as standards and deviants were grouped separately. On average, across all subjects and all conditions, 10% of the responses to standard and deviant stimuli were removed by the artifact rejection procedure. Replications were averaged together for each condition. Difference waveforms for each condition, used to measure N2, were obtained by subtracting averaged responses to the stimuli presented as standards from the averaged responses to the stimuli presented as deviants.

Latency windows to aid in response measurement for data from individual subjects were developed using the data from the grand mean waveforms (ten subjects). The onset of the response windows was developed using the grand mean data from the quiet conditions minus approximately 10% of the peak duration to accommodate individual subjects whose responses were earlier than the grand mean. Additionally, the noise-masked data from individual subjects were inspected to ensure that the windows were adequate. The offset of response windows was developed using the grand mean responses from the most difficult conditions where responses were present in the grand mean data (250-Hz high-pass conditions for both stimulus intensities and the BBN condition for the 80-dB ppe SPL stimulus intensity) as well as inspection of the data from individual subjects. Response windows were 80–200 ms for N1, 200–420 ms for N2, and 285–800 ms for P3. N1 was measured in the waveforms to the stimuli presented as standards at Cz; P3 was measured in the waveforms to the stimuli presented as deviants at Pz; and N2 was measured in the difference waveforms at Cz, within the appropriate response window. These measurement locations were chosen because largest amplitudes were seen at these sites in the grand mean waveforms. Measurements were made on the average of the two replicated waveforms for each condition. Amplitude measures were determined at the point of largest amplitude within the response window. Latency measures were taken at the center of the peak within the window. In cases where a wave was multi-peaked, both amplitude and latency measures were taken at the point of largest amplitude within the response window. In cases of double peaks of equal amplitude, amplitude was measured at either peak, and latency was measured at the midpoint of the waveform. For P3, measures were obtained after digital low-pass filtering at 5 Hz (12 dB/oct) in the frequency domain to smooth the waveform (Picton, 1992).

Determination of response presence/absence required the agreement of two experienced judges. The presence of N1 was determined using the waveforms to the stimuli presented as standards. N1 was required to be larger in amplitude at fronto-central electrode sites than at parietal electrode sites. Inversion at the mastoid electrode sites confirmed response presence, but lack of inversion was not used to indicate response absence. The presence of N2 was determined using the difference waveforms. N2 was required to be larger in amplitude at fronto-central electrode sites. When questionable, the waveforms to the stimuli presented as standards and deviants were compared at Cz, and larger negativity in the waveforms to the deviant stimuli than to the standard stimuli in the N2 latency window was required for N2 presence. The presence of P3 was determined using the waveforms to the stimuli presented as deviants. P3 was required to be larger at Pz than at frontocentral electrode sites. When questionable, the waveforms to the stimuli presented as standards and deviants were compared, and larger positivity in the waveforms to the deviant stimuli than to the standard stimuli in the P3 latency window was required for P3 presence. When judgments were considered questionable using the above rules, the replicability of the waveforms was examined. If the wave was replicable, then it was judged as present. When a wave was judged to be absent, measures for it were given an amplitude of 0 μV.[1]

Three-way repeated measures analyses of variance (ANOVA) as a function of speech stimulus, stimulus intensity, and noise condition were carried out on the amplitude and latency data. Main effects and interactions from the ANOVA were considered significant if $p<0.01$. Greenhouse–Geisser epsilon correction factors were applied

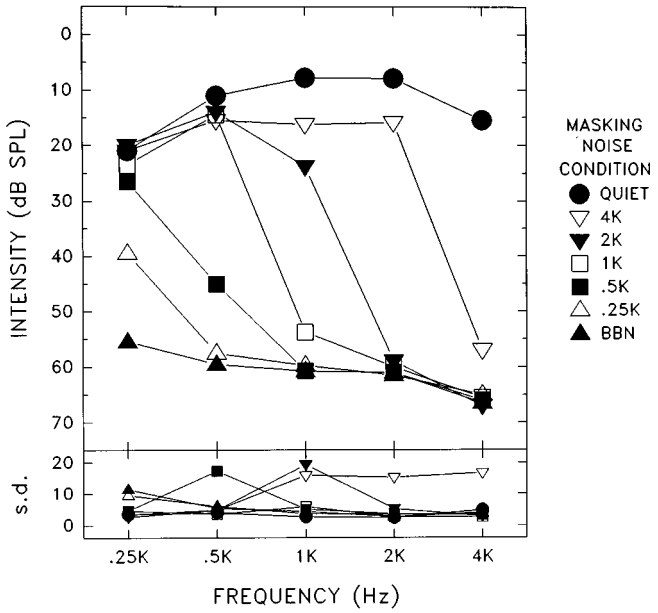

FIG. 2. Mean (top) and standard deviation (bottom) behavioral pure-tone masked and nonmasked audiograms across the ten subjects are displayed in dB SPL as a function of pure-tone frequency. Audiograms are shown for the quiet (nonmasked) condition, 4000- to 250-Hz high-pass noise masked conditions, and the broadband noise (BBN) masked condition.

to the degrees of freedom where appropriate (Greenhouse and Geisser, 1959). For latency measures, the repeated measures ANOVAs were performed in a manner to maximize the number of conditions in the analysis. This required that some subjects be eliminated in order to avoid missing data. Conditions were eliminated, however, if fewer than seven subjects remained. Tukey Honestly Significant Difference (HSD) *post hoc* measures were performed only when significant main effects or interactions were obtained (Tukey, 1953). The *post hoc* results were considered significant when $p<0.10$. This level of significance was selected so that significant main effects and interactions indicated by the ANOVAs (using the more strict $p<0.01$ criteria) were likely to be delineated by the *post hoc* analyses. Pearson product-moment correlation coefficients were calculated between the behavioral measures of discrimination and reaction time and N1, N2, and P3 latency and amplitude. Results of correlational analyses were considered to be significant when $p<0.01$.

II. RESULTS

A. Masked audiograms

Behavioral masked and nonmasked pure-tone audiograms are displayed in Fig. 2. Shown are the mean threshold data in dB SPL for the ten subjects, and corresponding standard deviations. The masking noise produced moderate threshold elevations at and above the filter cutoff. Across all cutoff frequencies, the high-pass noise increased thresholds by an average of 38 dB at the high-pass cutoff, and by 50 dB one octave above the cutoff frequency. Thresholds for frequencies below the cutoff frequency remained essentially unchanged. The increased masking above the cutoff is likely due both to the characteristics of the filter and to the presence

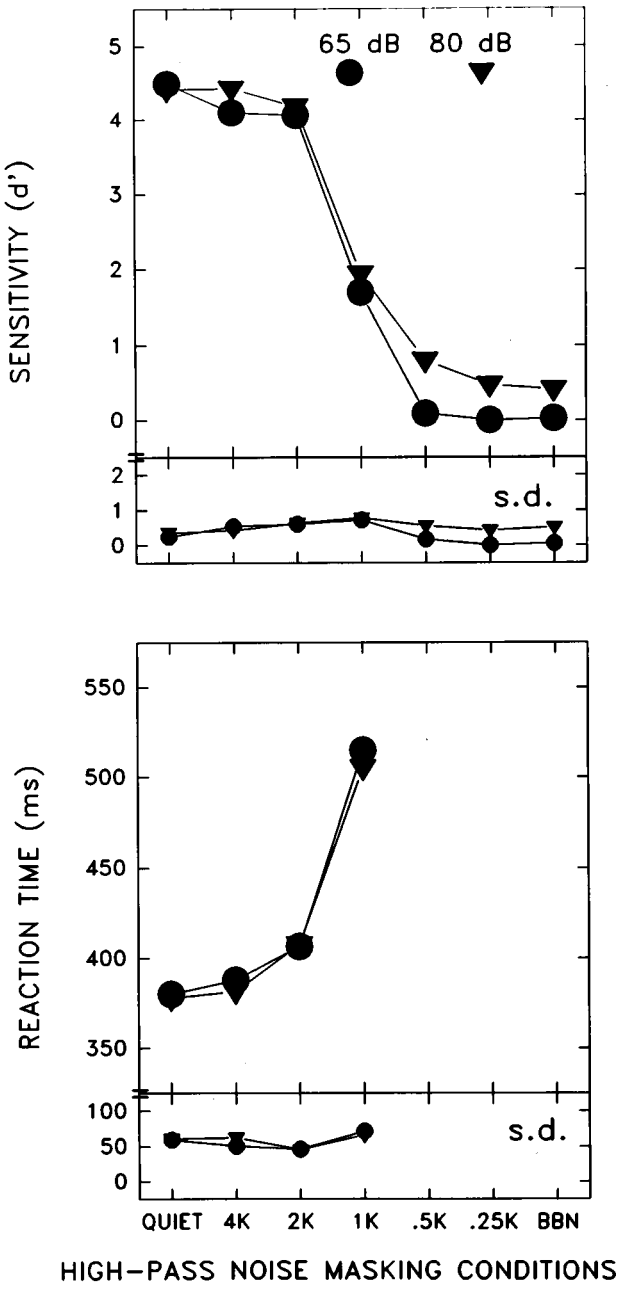

FIG. 3. The top graph displays d' measures of the discriminability of the stimuli as a function of noise masking condition, along with corresponding standard deviations. The lower graph displays reaction times as a function of noise masking condition. Corresponding standard deviations are also shown. Circles indicate the data for the 65-dB ppe SPL speech stimuli, and triangles indicate the data for the 80-dB ppe SPL stimuli. Data are pooled across /ba/ and /da/.

of upward spread of masking. As noise from lower frequencies is added, additional masking of the high frequencies occurs.

B. Sensitivity (d')

Figure 3 shows the behavioral results calculated from button-press responses to the deviant stimuli that were obtained during the ERP recordings. The top graph displays d' measures, which reflect the discriminability of the stimuli, as

a function of noise condition. Results for the two speech stimuli are collapsed as there was no significant difference in discriminability between the two speech stimuli [$F(1,9) = 1.82$; $p = 0.210$]. Results for the two quiet conditions are averaged in this and all other graphs; as there were no clear and significant differences between the quiet condition tested at the start of the experiment and the quiet condition tested at the end of the experiment. Discriminability decreased as the high-pass noise cutoff decreased [$F(7,30) = 28.96$; $p < 0.001$]. *Post hoc* testing indicated that discriminability does not change significantly until the noise cutoff frequency is lowered to 1000 Hz and below. After this point, discriminability drops off sharply to near-zero levels. The 80-dB ppe SPL stimuli were not discriminated once the high-pass cutoff frequency extends down to 500 Hz and below, even though they were audible. Although across all conditions the d' scores are significantly larger in response to the 80-dB ppe SPL stimuli than to the 65-dB ppe SPL stimuli [$F(1,9) = 14.40$; $p = 0.004$], this significant effect is probably the result of the trend for a larger effect of the masking on the responses to the 65-dB compared to the 80-dB speech sounds. This trend, however, was not quite sufficient to result in a significant intensity×condition interaction [$F(7,23)$; $p = 0.014$]. Further evidence for this lack of difference for intensity is that mean d' values in the quiet conditions are 4.40 for 65 dB and 4.41 for 80 dB.

C. Reaction time

The lower portion of Fig. 3 shows the reaction time (RT) measures to the deviant stimuli. For both behavioral and ERP measures of latency, only conditions with at least seven subjects showing responses are plotted. Results were collapsed across speech sounds because there is no significant difference in reaction time between the two speech stimuli [$F(1,6) = 2.07$; $p = 0.200$]. No significant stimulus intensity effect is present [$F(1,6) = 0.47$; $p = 0.520$]. Decreasing the high-pass cutoff frequency resulted in significantly increased RTs [$F(4,12) = 32.38$; $p < 0.001$]. The RT results are similar to d' results in that *post hoc* testing indicates that no significant change in RT occurred until the 1000-Hz high-pass noise condition.

D. Event-related potentials

The grand mean waveforms from all ten subjects to /ba/ presented at 80 dB ppe SPL in the quiet condition are displayed in Fig. 4. Responses recorded at midline electrode sites Fz, Cz, and Pz and in the EOG channel are shown. The difference waveforms were obtained by subtracting the responses to the stimuli presented as standards from the responses to the same stimuli presented as deviants. N1 was measured at Cz in the waveforms to the stimuli presented as standards. It is typically largest at fronto-central electrode sites (Vaughan and Ritter, 1970). N2 was measured at Cz in the difference waveforms (Novak *et al.*, 1990), and P3 was measured in the waveforms to the stimuli presented as deviants at Pz (Vaughan and Ritter, 1970). As can be seen in Fig. 4, these electrode sites are where the responses in this study were largest in the grand mean waveforms. The EOG channel was monitored to reject trials contaminated by eye movements and blinks to ensure that deflections contaminated by eye movements would not be considered responses.

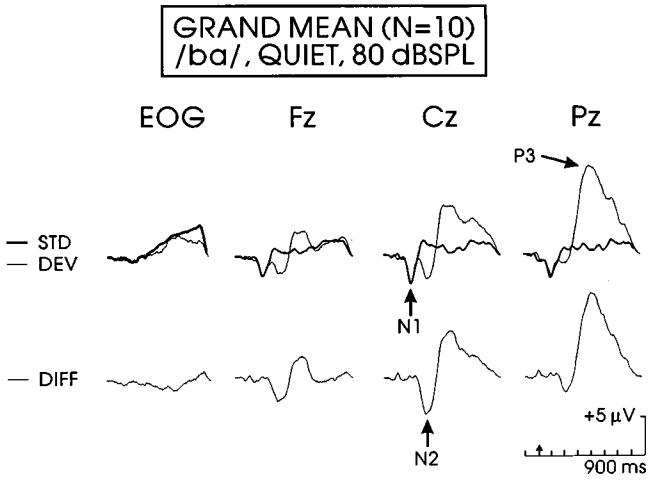

FIG. 4. The grand mean waveforms to /ba/, presented at 80 dB ppe SPL in the quiet condition, are displayed at Fz, Cz, Pz and in the EOG channel. The top row of waveforms is the responses to the stimuli presented as standards, (thick line) and as deviants (thin line). The bottom row of waveforms is the difference responses calculated by subtracting the responses to stimuli presented as standards from the responses to stimuli presented as deviants. The N1, N2, and P3 waves are labeled. In this and in subsequent waveform figures, positivity at the vertex is represented as an upward deflection.

The grand mean waveforms recorded in all the quiet and masking conditions to the /ba/ and /da/ stimuli at 65 and 80 dB ppe SPL are shown in Fig. 5. Responses to the standards are displayed for Cz; responses to the deviants are displayed for Pz. There are essentially no differences between the responses to the two speech sounds. In quiet, and in the 4000- and 2000-Hz high-pass noise conditions, a clear P3 is present in the grand mean waveforms to the deviant stimuli. In contrast, P3 is not present in the broadband noise condition. In the 1000- to 250-Hz high-pass noise conditions, P3 decreases in amplitude and increases in latency until it disappears with further masking into the lower frequencies. Results for P3 for the two intensities are fairly similar. In contrast to P3, N1 shows a different pattern as a function of noise condition and stimulus intensity. In general, as high-pass noise cutoff decreases, N1 amplitude decreases and latency increases. For the 80-dB ppe SPL stimuli, N1 is clearly present in the grand mean waveforms for all noise conditions, including broadband noise. For the 65-dB ppe SPL stimuli, N1 remains present for high-pass noise cutoffs through approximately 500 Hz. As would be expected, N1 to the 65-dB ppe SPL speech sounds is completely masked by the broadband noise.

The grand mean difference waveforms for /ba/ and /da/ presented at 65 and 80 dB ppe SPL are displayed in Fig. 6. There are no clear differences in the responses to the different stimuli or intensities. N2 is present in the difference waves for the quiet condition and in the waveforms for the 4000- and 2000-Hz high-pass noise conditions. N2 is not clearly present in the 500-Hz high-pass noise through broadband noise conditions. N2 amplitude decreases with high-pass noise masking, with the greatest change occurring when

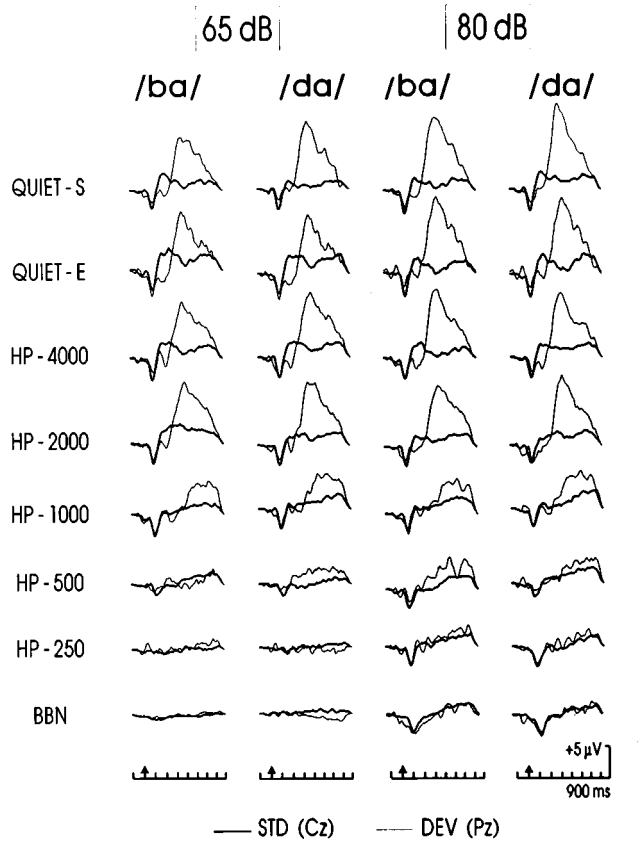

FIG. 5. The grand mean waveforms recorded in all of the noise conditions to the /ba/ and /da/ stimuli at 65 and 80 dB ppe SPL are displayed. QUIET-S indicates responses in the quiet condition at the start of the experiment; and QUIET-E denotes responses in the quiet condition at the end of the experiment. The high-pass noise conditions are denoted by the letters HP followed by the noise cutoff frequency. Responses to stimuli presented as standards are displayed for Cz (thick line); responses to stimuli presented as deviants are displayed for Pz (thin line). The arrow indicates stimulus onset.

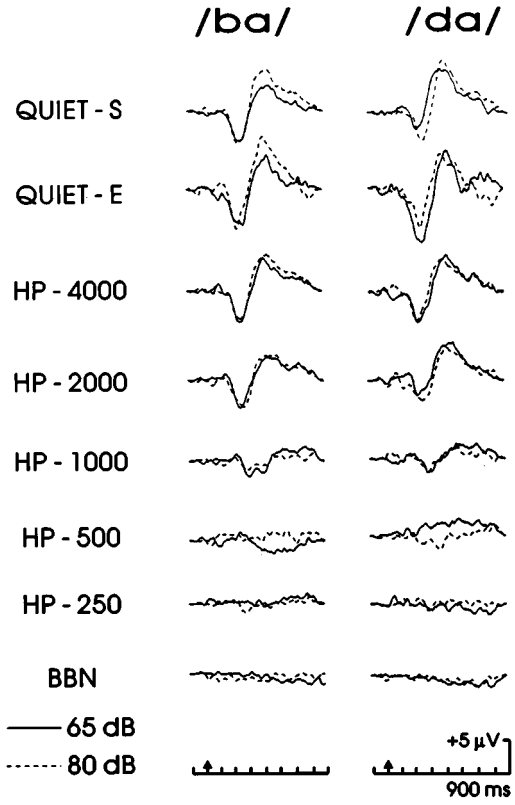

FIG. 6. The grand mean difference waveforms for /ba/ and /da/ presented at 65 and 80 dB ppe SPL are displayed for Cz. QUIET-S denotes responses in the quiet condition recorded at the start of the experiment; QUIET-E indicates responses in the quiet condition recorded at the end of the experiment. The high-pass noise conditions are indicated by the letters HP followed by the noise cutoff frequency. The arrow indicates stimulus onset.

the cutoff is below 2000 Hz. Latencies first increase at approximately the 2000-Hz high-pass noise condition.

E. N1

Figure 7 displays the effects of the noise conditions on N1 amplitudes and latencies. The data in these and all other graphs are collapsed across the /ba/ and /da/ speech stimuli because, in most cases, the effects of noise masking were the same for both stimuli. For N1 to the 80-dB ppe SPL stimuli, amplitudes decrease gradually from -3.99 μV for the quiet conditions down to -2.36 μV for the broadband noise condition. For N1 to the 65-dB ppe SPL stimuli, amplitudes decrease slightly through the 2000-Hz high-pass cutoff frequency and drop off steeply thereafter. N1 amplitudes in response to the 65- and 80-dB ppe SPL stimuli were similar in the quiet through approximately 2000-Hz noise conditions. As the high-pass cutoff frequency was further lowered, the noise resulted in a greater decrease in amplitude for the responses to 65-dB stimuli than for the 80-dB ppe SPL stimuli, resulting in a significant intensity×condition interaction [$F(7,21)=6.41$; $p<0.001$]. *Post hoc* analyses reveal that, for the 65-dB ppe SPL speech sounds, N1 amplitudes for the 250-Hz and BBN conditions are significantly smaller than for the quiet through 1000-Hz conditions. Additionally, N1 amplitudes for the 250-Hz and BBN conditions for the 65-dB ppe SPL stimuli are significantly smaller than the quiet through 250-Hz conditions for the 80-dB ppe SPL stimuli.

Progressively lowering the cutoff frequency of the high-pass noise results in progressively increased N1 latencies [$F(5,16)=31.50$; $p<0.001$]. This effect was gradual for both stimulus intensities. *Post hoc* analysis indicated that the main effect of noise condition was due to the longer latency of N1 in the 500-Hz high-pass noise condition compared to the quiet through 1000-Hz high-pass noise conditions. The latency of N1 was longer for the 65-dB ppe SPL speech sounds than for the 80-dB ppe SPL speech sounds [$F(1,8)=13.72$; $p=0.006$], even in the quiet condition. The specific speech stimulus also affected latency: N1 latencies to /ba/ were longer than to /da/ [$F(1,8)=36.69$; $p<0.001$], even in the quiet condition (116 vs 110 ms).

F. N2

The effects of the noise conditions on N2 amplitudes and latencies are displayed in Fig. 8. Progressively lowering the high-pass cutoff frequency resulted in decreased N2 amplitudes [$F(7,13)=20.18$; $p<0.001$]. *Post hoc* testing indicates that responses in the quiet conditions have significantly larger amplitudes than the 500-Hz high-pass through BBN

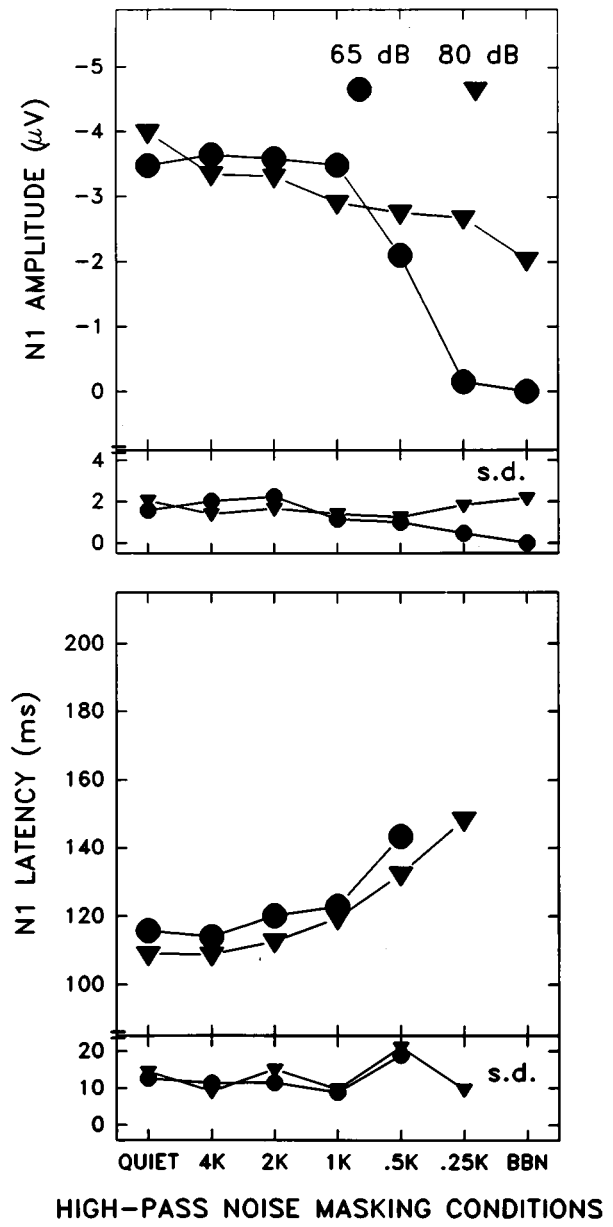

FIG. 7. The top graph displays the effects of the high-pass noise masking on mean N1 amplitudes. The lower graph displays the effects of the high-pass noise masking on mean N1 latencies. Corresponding standard deviations are also displayed. Circles indicate results for the 65-dB ppe SPL speech sounds; triangles indicate results for the 80-dB ppe SPL speech sounds.

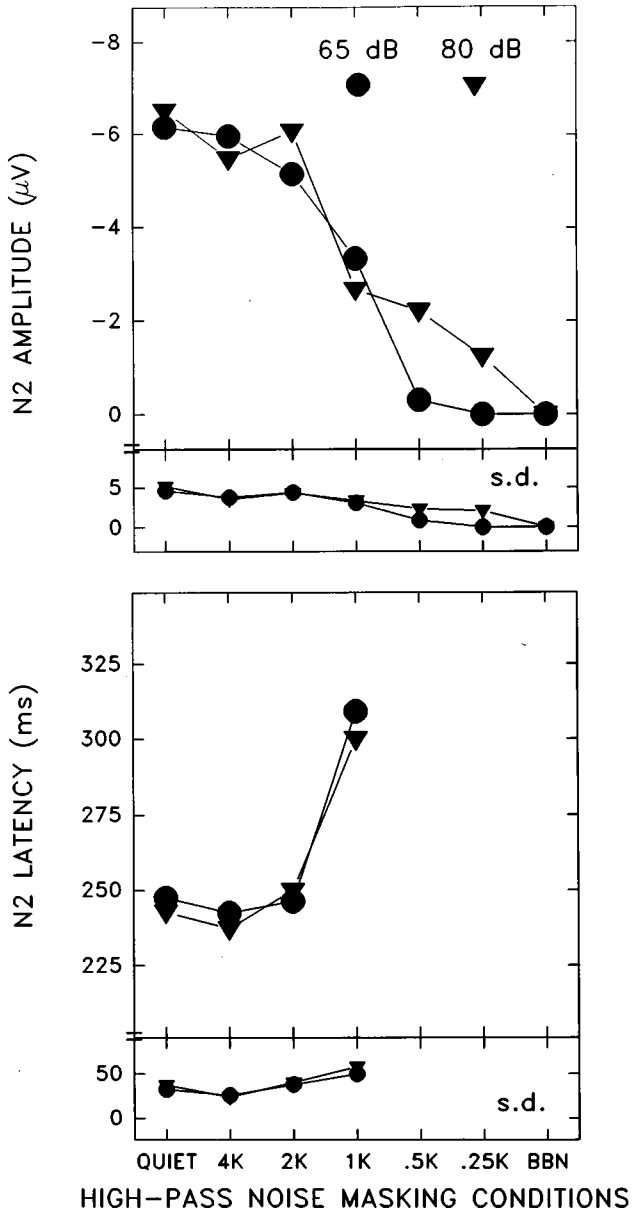

FIG. 8. The top graph displays the effects of the high-pass noise masking on mean N2 amplitudes. The lower graph displays the effects of the high-pass noise masking on mean N2 latencies. Corresponding standard deviations are also displayed. Circles indicate results for the 65-dB ppe SPL speech sounds; triangles indicate results for the 80-dB ppe SPL speech sounds.

conditions. No significant stimulus [$F(1,9)=2.41$; $p=0.155$] or intensity [$F(1,9)=1.72$; $p=0.222$] effects are present. N2 latencies increase as the high-pass noise cutoff frequency decreases [$F(4,15)=16.77$; $p<0.001$]. *Post hoc* testing reveals longer latencies for the 1000-Hz high-pass conditions than for the quiet and 4000-Hz high-pass conditions. No significant stimulus [$F(1,7)=2.98$; $p=0.128$] or intensity [$F(1,7)=0.85$; $p=0.387$] effects are present for N2 latencies.

G. P3

The effects of noise condition on P3 amplitudes and latencies are displayed in Fig. 9. Lowering the high-pass noise cutoff below 2000 Hz results in decreased P3 amplitudes. This is reflected statistically in a significant main effect of noise condition on P3 amplitude [$F(7,26)=49.07$; $p<0.001$]. *Post hoc* testing shows that this effect is due to smaller amplitudes for the 500-Hz high-pass noise through BBN conditions compared to the quiet through 2000-Hz high-pass noise conditions. P3 amplitudes are larger to the 80-dB ppe SPL stimuli than to the 65-dB ppe SPL stimuli [$F(1,9)=14.87$; $p<0.001$], though there was a trend toward a greater effect of the noise conditions on the lower intensity stimuli when the noise extended below 1000 Hz. This intensity by condition interaction, however, did not reach significance [$F(7,27)=2.27$; $p=0.040$].

High-pass noise cutoff frequency also affects P3 latencies [$F(4,18)=45.04$; $p<0.001$]. *Post hoc* testing reveals that

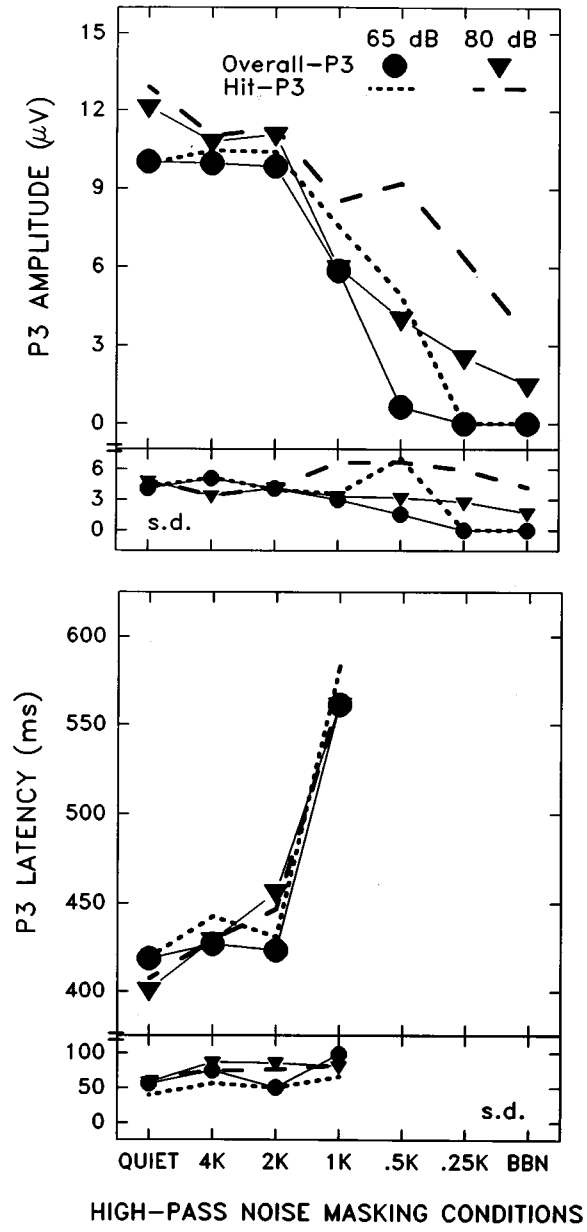

FIG. 9. The top graph displays the effects of the high-pass noise masking on mean P3 amplitudes. The lower graph displays the effects of the high-pass noise masking on mean P3 latencies. Corresponding standard deviations are also displayed. Circles indicate results for the 65-dB ppe SPL speech sounds and triangles indicate results for the 80-dB ppe SPL speech sounds for overall-P3; the dotted lines indicate results for the 65-dB ppe SPL speech sounds and the dashed lines indicate results for the 80-dB ppe SPL speech sounds for P3 associated with correct button-press responses (hit-P3).

this is due to longer latencies in the 1000-Hz high-pass noise condition than for the quiet through 2000-Hz high-pass noise conditions. No stimulus [$F(1,8)=1.59$; $p=0.243$] or intensity [$F(1,8)=0.02$; $p=0.882$] effects are significant.

Responses associated with the subjects' correct discriminations (''hits'') were also analyzed. The overall pattern of these ''hit-P3'' results is similar to those for the ''overall-P3'' for latencies and amplitudes (see Fig. 9), except that the amplitudes of the P3 responses associated with hits are larger than for the overall-P3 responses [$F(1,9)=14.87$; $p=0.004$]. There were no interactions involving ''hit-P3'' and ''overall-P3.''

TABLE I. Results of correlational analyses between behavioral [sensitivity (d') and reaction time (RT)] and ERP measures [N1, N2, and P3]. Shown are Pearson product-moment correlation coefficients.

		Amplitude			Latency		
		N1	N2	P3	N1	N2	P3
d'	r	0.50[a]	0.63[a]	0.78[a]	−0.67[a]	−0.55[a]	−0.78[a]
	N	320	320	320	269	221	240
RT	r	−0.34[a]	−0.32[a]	−0.25[a]	0.22	0.41[a]	0.56[a]
	N	205	205	205	202	197	203

[a] $p<0.01$.

The relationships between behavioral measures of discrimination and ERP measures were investigated using Pearson product–moment correlations (see Table I). There is a progression in the correlations between N1, N2, and P3 amplitudes and behavioral d', such that P3 has a strong relationship to d', N2 has a moderate relationship, and N1 shows the weakest relationship. The effect of noise condition on d' was similar to that for N2 and particularly P3, with d' scores dropping as the high-pass noise cutoff lowers, most notably below the 2000-Hz cutoff. N2 and P3 amplitudes showed similar changes. In contrast to the correlations with d', N1, N2, and P3 amplitudes are weakly correlated to behavioral reaction time measures. RT increases gradually in the quiet through 2000-Hz high-pass conditions and more rapidly as the high-pass noise extends into lower frequencies. This is clearly different from the gradual decrease in amplitude that N1 shows as the high-pass noise cutoff frequency is lowered.

There is a progression in the correlations between N1, N2, and P3 latencies and behavioral reaction time measures, such that P3 latency has a moderate relationship, N2 latency has a moderate though weaker relationship, whereas N1 latency shows no significant ($p>0.01$) relationship to behavioral reaction times. N1 latency increased only slowly as the high-pass noise cutoff was lowered. N2 and P3 latencies increased rapidly as the noise cutoff was lowered below 2000 Hz. The correlations between ERP latencies and d' are significant, with N1 and N2 latencies showing a moderate relationship to d', and P3 latencies showing a stronger relationship (Table I).

III. DISCUSSION

The high-pass noise maskers resulted in decreased audibility in specific spectral regions. The resulting masked audiograms are similar to those seen with steep high-frequency hearing losses. As the noise cutoff frequency was lowered, the portion of the audiogram showing decreased audibility extended from encompassing only the high-frequency regions (in the 4000- and 2000-Hz high-pass conditions) to encompassing both high and mid frequencies (in the 500- and 1000-Hz high-pass conditions) and, in the broadband noise conditions, high, mid, and low frequencies. This decreased audibility results in decreased ERP amplitudes and increased ERP latencies. Additionally, the threshold elevations produced by the high-pass noise masking resulted in

lower behavioral d' values and increased reaction times. For the stimuli used in this study (/ba/ and /da/), the effects of the high-pass noise masking are greatest when the 1000–2000-Hz spectral region is masked. This is the frequency region where the primary acoustic cues differentiating /da/ from /ba/ occur. As lower frequency regions were masked, ERP amplitudes decreased and latencies increased even further. Behavioral measures indicated the subjects' inability to discriminate the stimuli when these lower frequency regions were masked.

A. Behavioral measures

The moderate threshold elevations produced by high-pass noise masking result in decreased ability to behaviorally discriminate the speech sounds /ba/ and /da/. This is reflected in the decreased d' values and increased reaction times when the noise cutoff frequency is lowered below 2000 Hz and frequency regions containing the second and third formant transitions for the speech sounds are masked. At least for the speech contrast used in this study, the most important frequency region for discrimination was approximately 1000–2000 Hz. The addition of spectral information above 2000 Hz had little effect on discrimination performance.

To our knowledge, the effects of high-pass noise maskers on reaction time, which indicates temporal characteristics of discrimination, have not been investigated previously. Reaction time may provide a metric of processing difficulty or ease of listening (e.g., Downs, 1982; Downs and Crum, 1978). In the present study, reaction-time changes occurred when the noise cutoff frequency was lowered below 2000 Hz, indicating the listening task was more difficult when the spectral regions containing the second formant were masked.

Previous studies have demonstrated that reaction times to speech sounds are increased when speech is presented in broadband noise, speech-weighted noise, or in multi-talker babble (e.g., Downs and Crum, 1978; Gatehouse and Gordon, 1990; Hecker *et al.*, 1966; Whiting *et al.*, submitted). The increase in reaction times seen with high-pass noise masking are consistent with these findings, with the present study adding a frequency-specific effect. In contrast to studies showing that reaction time may be a more sensitive measure of processing difficulty than percent correct (Gatehouse and Gordon, 1990; Hecker, Stevens and Williams, 1966; Whiting *et al.*, submitted), the present study shows that reaction times and recognition scores (as reflected by d') for consonant–vowel syllables are similarly affected by the high-pass noise conditions. The previous studies, however, did not use high-pass noise masking. The results of the present study also differ with results of previous studies which indicated reaction times decrease when speech intensity is increased or when speech is amplified using a hearing aid (e.g., Downs, 1982; Wright *et al.*, 1981). The lack of an effect of intensity on RT in this study may be due to a ceiling effect resulting from our use of relatively high stimulus intensities (65 and 80 dB ppe SPL).

Speech recognition performance has often been examined in normal listeners using noise masking (e.g., Bell *et al.*, 1989; Fabry and Van Tasell, 1986; Humes *et al.*, 1987) or filtering (e.g., Bell *et al.*, 1989; Dubno *et al.*, 1989; Fabry and Van Tasell, 1986; French and Steinberg, 1947; Kryter, 1960; Miller and Nicely, 1955; Owens *et al.*, 1972; Pollack, 1948; Sher and Owens, 1974; Walden *et al.*, 1981; Wang *et al.*, 1978) of stimuli to control for audibility in specific spectral regions. The majority of these studies differ in design from the present study. For example, most used open-set recognition designs and examined performance on multiple phonemes. However, there are results directly related to those of the present study. For example, the effect of low-pass filtering of stimuli on the recognition of /b/ and /d/ can be extracted from the tables presented by Miller and Nicely (1955). At a signal-to-noise ratio of +12 dB, recognition performance decreased gradually as high frequencies were removed by low-pass filtering. Their subjects' performance, however, was superior to those of the present study in conditions where frequencies above 1200 Hz were removed (Miller and Nicely, 1955). The differences in the results of that study and the present study may be due to the use of low-pass filtering of stimuli instead of high-pass noise masking, to different filter slopes, or to inclusion of other consonant–vowel stimuli. Miller and Nicely (1955) used a filter with a slope of 24 dB/oct, whereas in the present study the filter slope was 96 dB/oct. Dubno *et al.* (1989) used a filter with a slope of more than 100 dB/oct, and the recognition data for their subjects are more in line with those of the present study. When performance for /b/ and /d/ at 73 dB SPL are averaged and examined as a function of low-pass filtering of the speech stimuli (see their Fig. 2), their subjects' recognition performance dropped significantly when frequencies above 1500 Hz were removed (Dubno *et al.*, 1989). This is consistent with the findings of the present study showing d' scores dropping when audibility above 1000 Hz is decreased by noise masking (Fig. 3).

In the present study, subjects reported that they perceived the stimuli as /ba/ and /da/ until the noise masking included approximately the 1000-Hz region. At this point, the perception of /da/ tended to move toward /ja/. This may be due to partial masking of the second formant transition which may have interfered with the perception of the duration and frequency of the second formant transition. As the masking cutoff frequency was further lowered, the subjects were unable to discriminate the stimuli, and, if the stimuli were audible, tended to report hearing only /a/ for both /da/ and /ba/.

B. ERP measures

Decreased audibility of the speech sounds produced by high-pass noise-masking results in increased latencies and decreased amplitudes of the ERP peaks. No studies examining the effect of high-pass noise masking on cortical N1, N2, or P3 ERPs to auditory stimuli have previously been published. One earlier study (Polich *et al.*, 1985) examined the effects of 60-dB nHL white noise masking on P3 latency to 60-dB nHL tones (approximately 70-dB SPL, *re:* ANSI, 1989) during an auditory frequency discrimination task. Results showed that the white noise increased P3 latencies by approximately 10 ms (Polich *et al.*, 1985). In the present

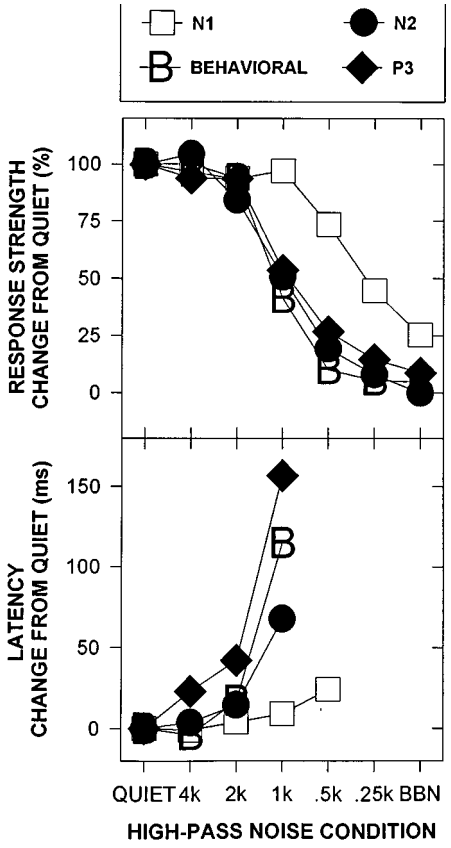

FIG. 10. Normalized behavioral and ERP results. The top graph shows response strength (ERP amplitude and d', expressed as percent of results for QUIET condition). The bottom graph depicts latency change (ERP latency and reaction time, expressed as shift in ms from QUIET condition). Squares indicate results for N1; circles indicate results for N2; diamonds indicate results for P3; ''*B*'' indicate behavioral (d' and RT) results. Results are pooled across speech stimulus (/ba/ and /da/) and stimulus intensity (65 and 85 dB ppe SPL).

study, the use of 81.7-dB SPL (on average) broadband noise essentially eliminated P3 responses to the speech sounds.

The masking noise had a differential effect on the N1, N2, and P3 waves. The later the wave, the greater the effect of high-pass noise masking. Examination of changes in amplitude over conditions where a response was present for all of the waves (4000- to 1000-Hz high-pass noise conditions, averaged across stimulus and intensity) indicates that N1 amplitude decreased by 0.63 μV, N2 amplitude decreased by 2.2 μV, and P3 amplitude decreased by 5.13 μV, suggesting a larger effect of the masking noise at higher levels in the auditory system. Similarly, the noise masking resulted in latency shifts (4000- to 1000-Hz high-pass noise conditions, averaged across stimulus and intensity) of 9 ms for N1, 68 ms for N2, 115 ms for RT, and 157 ms for P3.

The effects of the high-pass noise masking on the different measures are best compared by normalizing the results as a function of change from the QUIET condition, as shown in Fig. 10. Changes in responses strength (d' and amplitude: percent of QUIET) for N2, P3, and behavioral d' showed a similar pattern, with large changes beginning with the 1000-Hz high-pass noise condition. N1 showed a different pattern, with more gradual changes in amplitude across high-pass noise condition, with the N1 function shifted approximately 1 oct below those for the other measures. N1 response strength was greater than the other measures for the 1000-Hz high-pass noise through broadband noise conditions. In the 1000-Hz high-pass noise condition, N1 amplitude was 88% of QUIET, N2 was 58%, and P3 was 54% (Fig. 10, top). In other words, the masking noise had a larger effect at higher levels in the auditory system. This same pattern is seen with latency shift (Fig. 10, bottom).

The latency shifts shown in Fig. 10 are plotted in terms of milliseconds from the QUIET condition. An alternative procedure would be to normalize each measure's latency shifts to a percentage of that measure's baseline (QUIET) latency (e.g., N1 latency in QUIET=112 ms; therefore a 9-ms shift is equivalent to an 8% shift). Considered this way, the pattern of results remain the same: N1, N2, RT, and P3 showed 8%, 26%, 30%, and 37% shifts in latency, respectively. Progressively higher-level processing of these stimuli, as indicated by these ERP and behavioral measures, is increasingly disrupted by the noise masking.

Previous ERP studies have shown that when the deviant stimulus is made more difficult to discriminate, ERP latencies increase and ERP amplitudes decrease (for reviews, see Duncan-Johnson and Donchin, 1982; Picton, 1992). Studies of the effects of visual masking on cortical ERPs to visual stimuli indicate that increased latencies and decreased amplitudes occur when the visual stimuli are degraded (e.g., Magliero *et al.*, 1984; Ritter *et al.*, 1982). The increased latencies and decreased amplitudes seen with visual masking are consistent with the auditory masking effects of the present study, and the degree of change seen with visual ''masking'' is more in line with the findings of the present study than are the small latency increases with white noise masking reported by Polich and colleagues (Polich *et al.*, 1985). The present study adds a frequency-specific effect, particularly in the 1000- to 2000-Hz region, related to the specific speech contrasts. These decreases in amplitudes and increases in latencies resulting from noise masking probably reflect the effects of increased task difficulty (Backs, 1987; Duncan-Johnson and Donchin, 1982). The high-pass noise makes the determination of whether a particular stimulus is deviant more difficult, resulting in increased latencies and decreased amplitudes. These changes reflect increased processing time, increased response variability, and generally less-effective cortical processing.

N1 latency was longer for /ba/ than for /da/, even in the quiet conditions (116 vs 110 ms). Although statistically significant, this finding was unexpected because the stimuli were equal in intensity, time of onset, and duration. Maiste (1989), using the same stimuli, also reported slightly longer N1 latencies for /ba/ than for /da/ (121 vs 118 ms). This may be a ramification of traveling wave delays at the cochlear level for /ba/ relative to /da/ that are manifested to an even greater degree at the cortical level (Békésy, 1960; Hind, 1953). That is, these delays could be due the presence of the lower frequency onset of the $F2$ transition for /ba/ compared to /da/ (see Fig. 1). Another possibility may be a different cortical representation of the two speech sounds due, in part, to their differing frequency composition (e.g., Mendelson

and Cynader, 1985; Phillips and Irvine, 1981; Ponton *et al.*, 1993; Sams and Näätänen, 1991; Steinschneider *et al.*, 1990).

Stimulus intensity affected some, but not all, of the ERPs. N1 amplitudes were slightly larger and latencies were significantly shorter in response to the 80-dB ppe SPL stimuli than to the 65-dB ppe SPL stimuli. This is consistent with studies showing that N1 increases in amplitude and decreases in latency with increases in intensity (e.g., Adler and Adler, 1989; Arlinger, 1976; Davis and Zerlin, 1966; Keidel and Spreng, 1965). N2 showed no effect of stimulus intensity (65 vs 80 dB). Overall-P3 amplitude and hit-P3 amplitude were larger for the 80-dB stimuli than for the 65-dB stimuli, even in the quiet condition (Polich, 1989). There was a trend ($0.01<p<0.05$) for the effect of intensity on P3 to be larger when the high-pass noise extended below 1000 Hz. Behavioral measures, however, did not show differences between responses in quiet to the 65- vs 80-dB stimuli.

C. Relationship between behavioral and ERP measures of discrimination

Behavioral measures of sensitivity (d') were correlated both to ERP amplitudes and to ERP latencies. There was a progression in the relationship of d' to ERP amplitudes, such that there was a weak relationship with N1 amplitudes, a moderate relationship with N2 amplitudes, and a strong relationship with P3 amplitudes. The d' measure was also strongly, though negatively, correlated with N1, N2, and P3 latencies. Similar to d', there was a progression in the relationship of reaction time with ERP latencies. The correlation between RT and ERP latencies was weak for N1, moderate for N2, and strongest for P3. The correlations between behavioral reaction time and ERP amplitudes, however, were low.

The presence of N1 appears to reflect only the presence of audible stimulus energy because it was present even when behavioral measures indicated the subjects' inability to discriminate the speech stimuli. Thus, N1 does not provide information on the discrimination of speech stimuli. For example, N1 was present in the broadband masking condition for the 80-dB ppe SPL stimulus intensity; P3, however, was not present in this condition for most subjects, and behavioral measures indicated their inability to discriminate the speech sounds. In contrast to N1, N2 and P3 are highly correlated with behavioral measures of discrimination, and thus reflect conscious discrimination of the speech sounds. It should be noted that N2 in an attend condition (such as the present study) is comprised of both N2b and the mismatch negativity. Thus, the N2 changes may be due to changes with either (or both) of these components (for review, see Näätänen, 1990).

As discussed above, the relationship between behavioral indices of discrimination and ERP waves N2 and P3 was relatively strong. As d' decreased, amplitudes decrease. Additionally, as reaction time increased, latencies increased. Specifically, when behavioral performance was good (e.g., quiet through 2000-Hz conditions), N2 and P3 amplitudes were large and latencies were relatively short. When behavioral performance was poor (e.g., 500-Hz through BBN conditions), N2 and P3 amplitudes were low, and if present, latencies were long.

Because of the strong relationship seen in the present study between behavioral and N2 and P3 electrophysiological measures of discrimination, P3 and perhaps N2 might be used as measures of auditory discrimination in patients with hearing loss. P3 recordings typically require subject participation such as button-press responses to deviant stimuli. Behavioral measures of percent correct discrimination and reaction time are therefore available, and it might be argued that ERP measures are unnecessary. An advantage of ERP recordings over behavioral indices alone, however, is that ERPs provide measures of the sequence, timing, and strength of different levels of auditory processing within the brain. The power of including these ERP measures is their ''ability to augment, rather than to substitute for, the more traditional [behavioral] approaches'' (Donchin and Coles, 1988).

D. Implications

Decreased audibility in specific spectral regions resulted in longer ERP latencies and behavioral reaction times, and smaller ERP amplitudes and behavioral d' scores, at least in response to /ba/ and /da/ stimuli. Thus, the decreased audibility resulting from the masking noise altered brain processes associated with the processing of speech sounds. The time required to process the speech sounds was lengthened, and the strength (amplitude) of the responses to the speech sounds was reduced. Moreover, N1, N2, and P3 were differentially affected by the maskers. Recordings of these waves permit evaluation of processing within different levels of the auditory system. The increase in latency (ms/oct) and decrease in amplitude (μV/oct) resulting from the noise maskers are smallest for N1, larger for N2, and largest for P3. Further studies might determine how stimulus evaluation, as evaluated by these ERP measures, is altered with peripheral compared to central auditory pathologies.

Although the use of noise-masked normal listeners is a reasonable way to examine the effects of decreased audibility, similar to those of listeners with sensorineural loss but in a controlled manner (e.g., Humes *et al.*, 1987), decreased audibility resulting from masking noise is not completely equivalent to sensorineural hearing loss. Listeners with sensorineural hearing loss have problems in addition to elevated thresholds in specific spectral regions (e.g., Fabry and Van Tasell, 1986; Festen and Plomp, 1983; Scharf, 1978; Thibodeau, 1991). Nevertheless, studies of speech perception in individuals with sensorineural hearing loss indicate that the primary problem is audibility of the spectral information important for speech perception (e.g., Boothroyd, 1984; Dubno *et al.*, 1989; Erber, 1972, 1974; Humes *et al.*, 1988; Smith, 1975; Yoshioka and Thornton, 1980; Zurek and Delhorne, 1987). The present study clearly demonstrates that when required spectral information is missing (i.e., masked), the ability (as reflected by both behavioral and ERP measures) to differentiate /ba/ and /da/ deteriorates. When spectral energy is above the masked threshold, the ability to differentiate /ba/ and /da/ returns.

The present study provides new information concerning the changes in neural processing (and in behavior) that occur when audibility is reduced. Studies of individuals with sensorineural hearing loss showing thresholds similar to those produced by the high-pass noise masking conditions in the present study are now needed in order to examine whether the ERP changes with audibility loss seen in this study are similarly present in hearing-impaired listeners. Results from studies in our laboratory currently in progress suggest such ERP changes will be observed. Should this remain the case, then the observation that the problem faced by hearing-impaired listeners is primarily related to loss of audibility will be supported. If different changes are seen, then the additional deficits associated with sensorineural hearing loss are of critical importance for speech perception, and need to be examined much more closely. The present study provides some of the results, both behavioral and physiological, necessary for these comparisons.

The ERP changes seen in this study suggest that stimulus evaluation time, as reflected by P3 latency (for reviews, see Duncan-Johnson and Donchin, 1982; Picton, 1992), is increased when audibility is reduced. This slowing could conceivably result in speech perception difficulties, and may provide a partial explanation of the general belief by aural rehabilitation clinicians that slowing the rate of speech helps hearing-impaired listeners to better understand a message. Further studies of hearing-impaired listeners may validate this hypothesis.

The 80-dB ppe SPL stimuli were audible in all of the high-pass noise masking conditions, but not discriminable for all conditions. The results obtained with these stimuli may have implications regarding the effects of amplification for individuals with hearing loss. The discriminability (d') of /ba/ versus /da/ was better for 80- compared to 65-dB stimuli in the presence of masking, particularly when the masking noise extended into low frequencies. Discriminability in these conditions was quite poor, however, even for responses to 80-dB stimuli. N1 and P3 amplitudes and N1 latencies also showed changes related to stimulus intensity. Specifically, amplitudes were larger and latencies were shorter to the 80- compared to 65-dB ppe SPL stimuli, especially when the noise masking extended into low frequencies. It is conceivable that increasing speech sound discriminability through use of amplification results in stronger and faster brain processing, as indicated by larger ERP amplitudes (N1, P3) and shorter latencies (N1). This implication may be limited, however, to increasing the intensity of the signal, rather than changing the signal-to-noise ratio. Interpretation of the results is constrained by the relatively poor behavioral d' scores when the noise masking extended into low frequencies. It also should be noted that the noise masking in the present study was used to change audibility for specific frequency regions. It did not systematically assess the effects of background noise (Whiting *et al.*, submitted), and thus is not applicable to the results of listeners with sensorineural hearing loss in background noise.

The ERP amplitude and latency changes seen with decreased audibility should be considered when studying populations where hearing impairment is likely, such as the aged. Depending on the degree and configuration of hearing loss, hearing-impaired populations may have responses to speech sounds that are smaller and/or later than those seen in normal listeners. It may be necessary to use more sweeps in order to improve the signal-to-noise ratio of the recordings, and longer sweep times and larger display gains in order to detect responses.

The presence of ERPs provides evidence of brain responsivity to (N1, N2, and P3) and discrimination of (N2 and P3) speech sounds. It might, therefore, be beneficial to use them with populations where behavioral measures of speech detection and discrimination are difficult to obtain, such as infants. Unfortunately, it is difficult to record P3 in infants and other patients who are difficult to test. Similar work using high-pass noise masking is underway in our laboratory on the mismatch negativity (for review, see Näätänen, 1990), an automatic discriminative response which has been recorded in infants (Alho *et al.*, 1990; Kurtzberg *et al.*, 1995). Unlike P3, the presence of the MMN does not require active participation/attention by the listener and may therefore permit evaluation of auditory processing in normal or impaired infant populations.

ACKNOWLEDGMENTS

This work was supported by USPHS–NIDCD Clinical Center Grant P50 DC00223, and by NICHD Mental Retardation Research Center Grant HD01799. Brett Martin was partially supported by a CUNY Graduate Student Research Assistantship. Alain Sigal was supported by a MICEFA summer exchange fellowship; he is currently at the University of Paris West School of Medicine. We thank Dr. T. W. Picton for the stimuli that were used for this study.

[1]Out of 960 possible amplitude measures, a total of 230 no-response results required 0-μV insertions. Seventy-nine percent of these no-response results occurred in the BBN condition and the 250-Hz high-pass noise condition. The lowest amplitude values recorded for ''response-present'' waveforms for each wave were assessed to determine whether these values were close to 0 μV. The smallest recorded values for N1, N2, and P3 were -0.06, -0.19, and $+0.06$ μV, respectively, which are very close to 0 μV, particularly when one considers the relatively large amplitudes of these waves. Thus the 0-μV value inserted for the waves judged as ''no response'' was a reasonable estimate. It is possible that the insertion of 0 μV for those waves judged as ''no response'' violated the assumptions of normal distributions and heterogeneity of variances, although the ANOVA is quite robust to such violations (Glass and Hopkins, 1996). We therefore reanalyzed the amplitude results two ways. First, we recalculated the ANOVAs for each wave, leaving out those conditions with no-response results. The pattern of results for high-pass CONDITION remained the same. (The exception to this was that no CONDITION effect was found for the amplitude of N1, due to this analysis including only the QUIET through 500-Hz high-pass noise conditions. The 250-Hz high-pass noise condition, however, was where the first large drop in N1 amplitude occurred.) Second, we also reanalyzed the data by replacing the inserted zero values with an estimate of the waveforms' residual noise. The estimate of the residual noise was obtained from a subset of subjects ($N=4$), for whom single-trial waveform data remained available, using the Fsp procedure (Elberling and Don, 1984). The residual noise was calculated over the 0- to 800-ms window. The resulting mean residual noise level was 0.49 μV. The amplitude ANOVAs were rerun with this noise estimate. Results of these analyses were consistent with those obtained with the 0 μV inserted to indicate no response. Thus, both sets of reanalyses indicate the results of the original analyses are valid.

Aaltonen, O., Niemi, P., Nyrke, T., and Tuhkanen, M. (**1987**). ''Event-

related brain potentials and the perception of a phonetic continuum,'' Biol. Psychol. **24**, 197–207.
Adler, G., and Adler, J. (**1989**). ''Influence of stimulus intensity on AEP components in the 80- to 200-millisecond latency range,'' Audiology **28**, 316–324.
Alho, K. Sainio, K., Sajaniemi, N., Reinikainen, K., and Näätänen, R. (**1990**). ''Event-related brain potential of human newborns to pitch change of an acoustic stimulus,'' Electroencephalogr. Clin. Neurophysiol. **77**, 151–155.
American National Standards Institute (ANSI) (**1989**). *American National Standard Specification for Audiometers (ANSI S3.6-1989)* (American National Standards Institute, New York).
Arlinger, S. D. (**1976**). ''N1 latencies of the slow auditory evoked potential,'' Audiology **15**, 370–375.
Backs, R. W. (**1987**). ''Stimulus intensity and task complexity effects on late components of the event-related potential,'' in *Current Trends in Event-Related Potential Research* (EEG Suppl. 40), edited by R. Johnson, J. W. Rohrbaugh, and R. Parasuraman (Elsevier Science, New York), pp. 163–169.
Békésy, G. von (**1960**). *Experiments in Hearing* (McGraw–Hill, New York).
Bell, R. S., Dirks, D. D., and Carterette, E. C. (**1989**). ''Interactive factors in consonant confusion patterns,'' J. Acoust. Soc. Am. **85,** 339–346.
Bilger, R. C., and Wang, M. D. (**1976**). ''Consonant confusions in patients with sensorineural hearing loss,'' J. Speech Hear. Res. **19**, 718–748.
Boothroyd, A. (**1978**). ''Speech perception and sensorineural hearing loss,'' in *Auditory Management of Hearing-Impaired Children*, edited by M. Ross and T. G. Giolas (University Park, University Park, MD), pp. 117–144.
Boothroyd, A. (**1984**). ''Auditory perception of speech contrasts by subjects with sensorineural hearing loss,'' J. Speech Hear. Res. **27**, 134–144.
Davis, H., and Zerlin, S. (**1966**). ''Acoustic relations of the human vertex potential,'' J. Acoust. Soc. Am. **39,** 109–116.
Donchin, E., and Coles, M. G. H. (**1988**). ''Postcommentary to 'Is the P300 component a manifestation of context updating?','' Behav. Brain Sci. **11,** 406–425.
Dorman, M. (**1974**). ''Auditory evoked potential correlates of speech sound discrimination,'' Percept. Psychophys. **15,** 215–220.
Downs, D. W. (**1982**). ''Effects of hearing aid use on speech discrimination and listening effort,'' J. Speech Hear. Disord. **47**, 189–193.
Downs, D. W., and Crum, M. A. (**1978**). ''Processing demands during auditory learning under degraded listening conditions,'' J. Speech Hear. Res. **21**, 702–714.
Dubno, J. R., Dirks, D. D., and Ellison, D. E. (**1989**). ''Stop-consonant recognition for normal-hearing listeners and listeners with high-frequency hearing loss. I: The contribution of selected frequency regions,'' J. Acoust. Soc. Am. **85,** 347–354.
Dubno, J. R., Dirks, D. D., and Langhofer, L. R. (**1982**). ''Evaluation of hearing-impaired listeners using a nonsense-syllable test. II. Syllable recognition and consonant confusion patterns,'' J. Speech Hear. Res. **25,** 141–148.
Dubno, J. R., Dirks, D. D., and Schaefer, A. B. (**1989**). ''Stop-consonant recognition for normal-hearing listeners and listeners with high-frequency hearing loss. II: Articulation index predictions,'' J. Acoust. Soc. Am. **85**, 355–364.
Duncan-Johnson, C. C., and Donchin, E. (**1982**). ''The P300 component of the event-related brain potential as an index of information processing,'' Biol. Psychol. **14**, 1–52.
Elberling, C., and Don, M. (**1984**). ''Quality estimation of averaged auditory brain stem responses,'' Scand. Audiol. **13**, 187–197.
Erber, N. P. (**1972**). ''Auditory, visual, and auditory-visual recognition of consonants by children with normal and impaired hearing,'' J. Speech Hear. Res. **15**, 413–422.
Erber, N. P. (**1974**). ''Pure-tone thresholds and work-recognition abilities of hearing-impaired children,'' J. Speech. Hear. Res. **17**, 194–202.
Fabry, D. A., and Van Tasell, D. J. (**1986**). ''Masked and filtered simulation of hearing loss: Effects on consonant recognition,'' J. Speech Hear. Res. **29**, 170–178.
Festen, J. M., and Plomp, R. (**1983**). ''Relations between auditory functions in impaired hearing,'' J. Acoust. Soc. Am. **73,** 652–662.
Fletcher, H. (**1953**). *Speech and Hearing in Communication* (Van Nostrand, New York).
French, N. R., and Steinberg, J. C. (**1947**). ''Factors governing the intelligibility of speech sounds,'' J. Acoust. Soc. Am. **19,** 90–119.
Galambos, R., Benson, P., Smith, T. S., Schulman-Galambos, C., and Osier, D. (**1975**). ''On hemispheric differences in evoked potentials to speech stimuli,'' Electroencephalogr. Clini. Neurophysiol. **39**, 279–283.
Gatehouse, S., and Gordon, J. (**1990**). ''Response times to speech stimuli as measures of benefit from amplification,'' Br. J. Audiol. **24**, 63–68.
Glass, G. V., and Hopkins, K. D. (**1996**). *Statistical Methods in Education and Psychology* (Allyn and Bacon, Boston), 3rd ed., pp. 402–405.
Gordon, T. G. (**1987**). ''Communication skills of mainstreamed hearing-impaired children,'' in *Development of Language and Communication Skills in Hearing-Impaired Children* (ASHA Monograph 26), edited by H. Levitt, N. S. McGarr, and D. Geffner (American Speech-Language-Hearing Association, Maryland), pp. 108–122.
Greenhouse, S. W., and Geisser, S. (**1959**). ''On methods in the analysis of profile data,'' Psychometrika **24**, 95–112.
Hecker, M. H. L., Stevens, K. N., and Williams, C. E. (**1966**). ''Measurements of reaction time in intelligibility tests,'' J. Acoust. Soc. Am. **39,** 1188–1189.
Hind, J. E. (**1953**). ''An electrophysiological determination of tonotopic organization in auditory cortex of cat,'' J. Neurophysiol. **16,** 473–489.
Hink, R. F., Hillyard, S. A., and Benson, P. J. (**1978**). ''Event-related brain potentials and selective attention to acoustic and phonetic cues,'' Biol. Psychol. **6**, 1–16.
Humes, L. E., and Roberts, L. (**1990**). ''Speech-recognition difficulties of the hearing-impaired elderly: The contributions of audibility,'' J. Speech Hear. Res. **33**, 726–735.
Humes, L. E., Espinoza-Varas, B., and Watson, C. S. (**1988**). ''Modeling sensorineural loss. I. Model and retrospective evaluation,'' J. Acoust. Soc. Am. **83,** 188–202.
Humes, L. E., Dirks, D. D., Bell, T. S., and Kincaid, G. E. (**1987**). ''Recognition of nonsense syllables by hearing-impaired listeners and by noise-masked normal hearers,'' J. Acoust. Soc. Am. **81,** 765–773.
Kaga, K., Kodera, K., Hirota, E., and Tsuzuka, T. (**1991**). ''P300 response to tones and speech sounds after cochlear implant: A case report,'' Laryngoscope **101**, 905–907.
Keidel, W. D., and Spreng, M. (**1965**). ''Neurophysiological evidence for the Stevens power function in man,'' J. Acoust. Soc. Am. **38,** 191–195.
Kraus, N., McGee, T., Sharma, A., Carrell, T., and Nicol, T. (**1992**). ''Mismatch negativity event-related potential elicited by speech stimuli,'' Ear Hear. **13**, 158–164.
Kraus, N., Micco, A. G., Koch, D. B., McGee, T., Carrell, T., Sharma, A., Wiet, R. J., and Weingarten, C. Z. (**1993**). ''The mismatch negativity cortical evoked potential elicited by speech in cochlear-implant users,'' Hear. Res. **65**, 118–124.
Kryter, K. D. (**1960**). ''Speech bandwidth compression through spectrum selection,'' J. Acoust. Soc. Am. **32,** 547–556.
Kurtzberg, D. (**1989**). ''Cortical event-related potential assessment of auditory system function,'' Sem. Hear. **10**, 252–261.
Kurtzberg, D., Hilpert, P. L., Kreuzer, J. A., and Vaughan, H. G. (**1984**). ''Differential maturation of cortical auditory evoked potentials to speech sounds in normal fullterm and very low-birthweight infants,'' Develop. Med. Child Neurol. **26**, 466–475.
Kurtzberg, D., Vaughan, H. G., Kreuzer, J. A., and Fliegler, K. Z. (**1995**). ''Developmental studies and clinical application of mismatch negativity: Problems and prospects,'' Ear Hear. **16**, 104–116.
Magliero, A., Bashore, T. R., Coles, M. G. H., and Donchin, E. (**1984**). ''On the dependence of P300 latency on stimulus evaluation processes,'' Psychophysiology **21**, 171–186.
Maiste, A. (**1989**). ''Human auditory event-related potentials to frequency changes in speech and non-speech sounds,'' Unpublished doctoral dissertation, University of Ottawa, Ottawa, Ontario.
Maiste, A. C., Wiens, A. S., Hunt, M. J., Scherg, M., and Picton, T. W. (**1995**). ''Event-related potentials and the categorical perception of speech sounds,'' Ear Hear. **16**, 68–90.
Mendelson, J. R., and Cynader, M. S. (**1985**). ''Sensitivity of cat primary auditory cortex (AI) to the direction and rate of frequency modulation,'' Brain Res. **327**, 331–335.
Miller, G. A., and Nicely, P. E. (**1955**). ''An analysis of perceptual confusions among some English consonants,'' J. Acoust. Soc. Am. **27,** 338–352.
Molfese, D. L. (**1978**). ''Neuroelectrical correlates of categorical speech perception in adults,'' Brain Lang. **5**, 25–35.
Molfese, D. L., and Betz, J. C. (**1988**). ''Electrophysiological indices of the early development of lateralization for language and cognition, and their implications for predicting later development,'' in *Brain Lateralization in*

Children: Developmental Implications, edited by D. L. Molfese and S. J. Segalowitz (Guilford, New York), pp. 171–190.
Molfese, V. J., Molfese, D. L., and Parsons, C. (**1983**). ''Hemisphere processing of phonological information,'' in *Language Functions and Brain Organization*, edited by S. J. Segalowitz (Academic, New York), pp. 29–49.
Näätänen, R. (**1990**). ''The role of attention in auditory information processing as revealed by event-related potentials and other brain measures of cognitive function,'' Behav. Brain Sci. **13,** 201–288.
Needleman, A. R., and Crandell, C. C. (**1995**). ''Speech recognition in noise by hearing-impaired and noise-masked normal-hearing listeners,'' J. Am. Acad. Audiol. **6**, 414–424.
Novak, G. P., Kurtzberg, D., Kreuzer, J. A., and Vaughan, H. G. (**1989**). ''Cortical responses to speech sounds and their formants in normal infants: Maturational sequence and spatiotemporal analysis,'' Electroencephalogr. Clin. Neurophysiol. **73**, 295–305.
Novak, G. P., Ritter, W., Vaughan, H. G., and Wiznitzer, M. L. (**1990**). ''Differentiation of negative event-related potentials in an auditory discrimination task,'' Electroencephalogr. Clin. Neurophysiol. **75**, 255–275.
Owens, E., Benedict, M., and Schubert, E. D. (**1972**). ''Consonant phonemic errors associated with pure-tone configurations and certain kinds of hearing impairment,'' J. Speech Hear. Res. **15**, 308–322.
Phillips, D. P., and Irvine, D. R. F. (**1981**). ''Responses of single neurons in physiologically defined primary auditory cortex (AI) of the cat: Frequency tuning and responses to intensity,'' J. Neurophysiol. **45,** 48–58.
Picton, T. W. (**1992**). ''The P300 wave of the human event-related potential,'' J. Clin. Neurophysiol. **9**, 456–479.
Polen, S. B. (**1984**). ''Auditory event-related potentials,'' Sem. Hear. **5**, 127–141.
Polich, J. (**1989**). ''Frequency, intensity and duration as determinants of P300 from auditory stimuli,'' J. Clin. Neurophysiol. **6**, 277–286.
Polich, J., Howard, L., and Starr, A. (**1985**). ''Stimulus frequency and masking as determinants of P300 latency in event-related potentials from auditory stimuli,'' Biol. Psychol. **21**, 309–318.
Pollack, I. (**1948**). ''Effects of high pass and low pass filtering on the intelligibility of speech in noise,'' J. Acoust. Soc. Am. **20,** 259–266.
Ponton, C. W., Don, M. Waring, M. D., Eggermont, J. J., and Masuda, A. (**1993**). ''Spatio-temporal source modeling of evoked potentials to acoustic and cochlear implant stimulation,'' Electroencephalogr. Clin. Neurophysiol. **88**, 478–493.
Reed, C. (**1975**). ''Identification and discrimination of vowel-consonant syllables in listeners with sensorineural hearing loss,'' J. Speech Hear. Res. **18**, 773–794.
Ritter, W., Simson, R., Vaughan, H. G., and Macht, M. (**1982**). ''Manipulation of event-related potential manifestations of information processing stages,'' Science **218,** 909–911.
Sams, M., and Näätänen, R. (**1991**). ''Neuromagnetic responses of the human auditory cortex to short frequency glides,'' Neurosci. Lett. **121**, 43–46.
Sams, M., Aulanko, R., Aaltonen, O., and Näätänen, R. (**1985**). ''Event-related potentials to infrequent changes in phonetic features of synthetic CV stimuli,'' J. Cognit. Neurosci. **2**, 344–357.
Sams, M., Paavilainen, P., Alho, K., and Näätänen, R. (**1985**). ''Auditory frequency discrimination and event-related potentials,'' Electroencephalogr. Clin. Neurophysiol. **62**, 437–448.
Scharf, B. (**1978**). ''Comparison of normal and impaired hearing II. Frequency analysis, speech perception,'' Scand. Audiol. Suppl. **6**, 81–106.
Sharma, A., Kraus, N., McGee, T., Carrell, T., and Nicol, T. (**1993a**). ''Acoustic versus phonetic representation of speech as reflected by the mismatch negativity event-related potential,'' Electroencephalogr. Clin. Neurophysiol. **88**, 64–71.
Sharma, A., Kraus, N., McGee, T., Carrell, T., and Nicol, T. (**1993b**). ''Processing of pitch vs. phonetic aspects of speech as reflected by the mismatch negativity evoked potential [abstract],'' Abstracts of the *Thirteenth Biennial Symposium of the International Electric Response Audiometry Study Group*, Park City, Utah, p. 50.
Sher, A. E., and Owens, E. (**1974**). ''Consonant confusions associated with hearing loss above 2000 Hz,'' J. Speech Hear. Res. **17**, 669–681.
Smith, C. R. (**1975**). ''Residual hearing and speech production in deaf children,'' J. Speech Hear. Res. **18**, 795–811.
Stapells, D. R., Kurtzberg, D., Martin, B., Gravel, J., and Kreuzer, J. (**in preparation**). ''Effects of hearing loss and amplification on cortical auditory evoked potentials to speech sounds.''
Steinschneider, M., Arezzo, J. C., and Vaughan, H. G. (**1990**). ''Tonotopic features of speech-evoked activity in primate auditory cortex,'' Brain Res. **519**, 158–168.
Stevens, S. S. (**1966**). ''Power-group transformations under glare, masking, and recruitment,'' J. Acoust. Soc. Am. **39,** 725–735.
Thibodeau, L. M. (**1991**). ''Exploration of factors beyond audibility that may influence speech recognition,'' Ear Hear. **12**, 109s–115s.
Tukey, J. W. (**1953**). ''The problem of multiple comparisons,'' unpublished manuscript, Princeton University.
Vaughan, H. G., Jr., and Ritter, W. (**1970**). ''The sources of auditory evoked responses recorded from the human scalp,'' Electroencephalogr. Clin. Neurophysiol. **28**, 360–367.
Walden, B. E. (**1984**). ''Speech perception of the hearing-impaired,'' in *Hearing Disorders in Adults*, edited by J. Jerger (College-Hill, San Diego, CA), pp. 263–309.
Walden, B. E., and Montgomery, A. A. (**1975**). ''Dimensions of consonant perception in normal and hearing-impaired listeners,'' J. Speech Hear. Res. **18**, 444–455.
Walden, B. E., Schwartz, D. M., Montgomery, A. A., and Prosek, R. A. (**1981**). ''A comparison of the effects of hearing impairment and acoustic filtering on consonant recognition,'' J. Speech Hear. Res. **46**, 32–43.
Wall, L., Dalebout, S. D., Davidson, S. A., and Fox, R. A. (**1991**). ''Effect of hearing impairment on event-related potentials for tone and speech distinctions,'' Folia Phoniatr. **43**, 265–274.
Wang, M. D., Reed, C. M., and Bilger, R. C. (**1978**). ''A comparison of the effects of filtering and sensorineural hearing loss on patterns of consonant confusions,'' J. Speech Hear. Res. **21**, 5–36.
Whiting, K., Martin, B. A., and Stapells, D. R. (**submitted**). ''The effects of broadband noise masking on cortical event-related potentials to speech sounds /ba/ and /da/.''
Wood, C. C. (**1975**). ''Auditory and phonetic levels of processing in speech perception: Neurophysiological and information-processing analyses,'' J. Exp. Psychol. Hum. Percept. Perform. **104,** 3–20.
Wood, C. C., Goff, W. R., and Day, R. S. (**1971**). ''Auditory evoked potentials during speech perception,'' Science **173,** 1248–1251.
Wright, R., Spanner, M., and Martin, M. (**1981**). ''Pilot experiments with a reaction time audiometer,'' Br. J. Audiol. **15**, 275–281.
Yoshioka, P., and Thornton, A. R. (**1980**). ''Predicting speech discrimination from the audiometric thresholds,'' J. Speech Hear. Res. **23**, 814–827.
Zurek, P. M., and Delhorne, L. A. (**1987**). ''Speech reception in noise by hearing-impaired listeners,'' J. Acoust. Soc. Am. Suppl. 1 **79,** S23.

Masking by modulated and unmodulated noise: Effects of bandwidth, modulation rate, signal frequency, and masker level[a)]

Sid P. Bacon,[b)] Jungmee Lee, Daniel N. Peterson, and Dawne Rainey
Psychoacoustics Laboratory, Department of Speech and Hearing Science, P.O. Box 871908, Arizona State University, Tempe, Arizona 85287-1908

(Received 16 May 1996; revised 9 September 1996; accepted 21 October 1996)

The threshold for a sinusoidal signal masked by a band of noise is often times lower when the masking noise is modulated than when it is unmodulated. The difference in masked thresholds is referred to as the modulated–unmodulated difference, or MUD. These present experiments examined the effects of masker bandwidth, masker rate, and masker level on the MUD at several different signal frequencies. The MUD generally increased with increasing masker bandwidth; for masker bandwidths wider than a critical band (or an equivalent rectangular bandwidth—ERB), the results may be influenced by across-channel processes underlying comodulation masking release. The MUD for an ERB masker (MUD_{ERB}) was influenced less by masker rate than was the MUD for a broadband (BB) masker (MUD_{BB}). The MUD_{ERB} and especially the MUD_{BB} increased significantly with increasing masker level when the modulated masker was modulated at a depth (m) of 1.0, but not when it was modulated at a depth of 0.75. These results have significant implications for extending the MUD paradigm to hearing-impaired subjects. Finally, the MUD_{ERB} and the MUD_{BB} increased with increasing signal frequency. This effect for the ERB masker is largely (if not completely) due to the wider absolute bandwidths at higher frequencies. The effect with the BB masker may be influenced by differences in the magnitude of suppression across frequency. [S0001-4966(97)02703-3]

PACS numbers: 43.66.Ba, 43.66.Dc, 43.66.Mk [WJ]

INTRODUCTION

Sounds such as speech and music consist of more or less rapid changes in frequency and intensity. Indeed, a considerable amount of acoustic information is carried by the dynamic aspects of these and other sounds. It is apparent, therefore, that the auditory system must be able to follow or resolve these changes. In other words, the system must have good temporal resolution in order to extract the information carried by the dynamic nature of sound.

Temporal resolution has been measured in a variety of ways, including gap detection (Plomp, 1964) and modulation detection (Viemeister, 1979). In the 1970s, Zwicker examined temporal resolution by measuring the threshold for a brief signal as a function of the signal's temporal position within a time-varying masker (e.g., Zwicker, 1976a, b). The resulting patterns were referred to as masking period patterns. Zwicker and Schorn (1982) suggested that temporal resolution could be described by considering just the difference between the maximum and minimum thresholds in those patterns, eliminating the need to measure a large number of thresholds. Moreover, they showed that the difference between the maximum and minimum thresholds could be estimated from the difference between the threshold for a long-duration signal in the presence of an unmodulated masker and that obtained in the presence of a modulated masker. They argued that these long signals would be easier for untrained subjects, and thus that this approach would be particularly useful for evaluating temporal resolution in hearing-impaired subjects.

One might argue, following Zwicker and Schorn (1982), that the larger the difference between the threshold in the presence of the modulated masker and that in the presence of the unmodulated masker [i.e., the larger the modulated–unmodulated difference, or MUD (Carlyon *et al.*,1989)], the better the temporal resolution. However, when using this paradigm to obtain estimates of temporal resolution, it is important to distinguish between processing that occurs solely within a single auditory channel and that which occurs across two or more channels. In particular, as shown by Hall *et al.* (1984; also see Hall and Haggard, 1983), and many others since, the threshold for a signal in a modulated masker can be lowered by the presence of comodulated masker energy outside the auditory filter centered at the signal frequency. This phenomenon, referred to as comodulation masking release (CMR), is thought to reflect across-channel processing. This processing could be influenced by factors other than temporal resolution, such as frequency resolution (e.g., Hall *et al.*, 1988), and in general it may represent a different type of processing than that observed within channel. Because Zwicker and Schorn (1982) used octave-band maskers, their estimates of temporal resolution may have been influenced by both within- and across-channel processing.

[a)]Portions of this research were presented at the 131st meeting of the Acoustical Society of America [S. P. Bacon, J. Lee, D. N. Peterson, and D. Rainey, ''Detection of tones in modulated noise: Effects of masker level and masker depth,'' J. Acoust. Soc. Am. **99**, 2566(A) (1996)].

[b)]Corresponding author: Voice: 602/965-8227; Fax: 602/965-0965; E-mail: spb@asu.edu

The MUD paradigm may reveal important insights into the processing of temporally complex sounds. One of our long-range goals is to use the MUD paradigm to assess auditory processing in subjects with sensorineural hearing loss. Prior to embarking upon those studies, however, we wished to examine the effects of various stimulus parameters on the MUD in normal-hearing subjects. Of particular interest were the effects of signal frequency, masker modulation rate, and masker level.

Although the literature is somewhat inconclusive regarding the general effect of frequency on temporal resolution, most recent evidence suggests that temporal resolution is independent of spectral location once the confounding influence of stimulus bandwidth is taken into account (see review by Viemeister and Plack, 1993). The effect of signal frequency on the size of the MUD is thus far unclear. Zwicker and Schorn (1982) found no effect of signal frequency for frequencies of 500, 1500, and 4000 Hz using a relatively broad (octave-band) masker, whereas Hall and Grose (1989) observed a slightly larger MUD at 2000 Hz than at 500 Hz using masker bandwidths ranging from 0.1 to 1.6 times the signal frequency.

With regard to the effect of masker modulation rate, the general finding is that the MUD decreases with increases in rate, as would be expected based on the auditory system's limited temporal resolution. This has been observed consistently with both broadband maskers (Weber, 1977; Hall and Haggard, 1983; Carlyon *et al.*, 1989; Schooneveldt and Moore, 1989; Peters and Hall, 1994) and narrow-band maskers (Carlyon *et al.*, 1989; Schooneveldt and Moore, 1989; Peters and Hall, 1994). However, in some cases there has been little or no MUD with narrow-band maskers (Hall and Haggard, 1983; Hall and Grose, 1989). Consequently, the effects of rate on CMR (defined as the MUD for a broadband masker minus the MUD for a narrow-band masker) have been mixed. Hall and Haggard (1983), for example, found that CMR declined with increasing rate, whereas Carlyon *et al.* found that CMR did not vary systematically with masker rate (also see Schooneveldt and Moore, 1989). More recently, Peters and Hall (1994) found that CMR remained roughly constant up to a masker rate of 30 Hz, but then declined with further increases in rate.

Most studies of the effects of masker level on the MUD have used relatively broadband maskers. Using maskers wider than a critical band, Weber (1977), Zwicker and Schorn (1982), and Moore and Shailer (1991) all found that the MUD increased with increasing masker level. To gain a complete understanding of the effects of masker level on the processing underlying the MUD, however, it is necessary to extend those studies to evaluate the effects of level with narrow-band maskers. The results will be of theoretical interest, and of interest in terms of extending the MUD paradigm to the testing of hearing-impaired subjects.

In summary, the effects of signal frequency, masker rate, and masker level on the MUD for narrow-band and broadband maskers are at least somewhat unclear. The intent of the present study was to examine these stimulus parameters in some detail and consequently lay the groundwork for future work in subjects with sensorineural hearing impairment. An important aspect of the present study is that we attempted to separate the processing which occurs strictly within channel from that which occurs across channel. To that end, the first experiment examined the effects of masker bandwidth for bandwidths ranging from less than a critical band to those considerably wider than a critical band, in order to determine how the MUD is influenced by masker bandwidth and to determine the bandwidths to be used in the remaining two experiments to reveal within- and across-channel processing. The second and third experiments examined masker rate and masker level for narrow-band and broadband maskers, and all three experiments employed more than one signal frequency in order to examine the effects of signal frequency on the MUD.

I. GENERAL METHODS

A. Apparatus and stimuli

The sinusoidal signals were digitally generated and produced (TDT DA1) at a 20 000-Hz sampling rate; they were low-pass filtered at 8000 Hz (Kemo VBF 25.01, 135 dB/oct). The noise masker was created by multiplying a sinusoid (HP 8904A synthesizer) whose frequency was equal to the signal frequency by a low-pass filtered (Kemo VBF 25.01) random noise (GenRad 1381). The multiplied noise had a bandwidth that was twice the cutoff frequency of the low-pass filter, and an attenuation rate (measured with an HP 3561A signal analyzer) that ranged from about 200 dB/oct to about 1500 dB/oct, depending on the center frequency of the noise.

The duration of the signal and masker was 500 ms, including the 20-ms $\cos^2$ rise/fall times. The analog noise was gated via a digital gating function (TDT DA1) that was low-pass filtered (Kemo VBF 25.01) prior to multiplication (Analog Devices 435K). This gating function determined whether the masker was unmodulated or sinusoidally amplitude modulated.[1]

The levels of the signal and masker were adjusted via a programmable attenuator (Wilsonics PATT). Signal level was varied adaptively whereas masker level was fixed throughout a block of trials. The signal and masker were added together prior to being transduced by a TDH-49P headphone mounted in an MX/51 cushion.

B. Procedure

Thresholds were measured using an adaptive, two-interval, forced-choice procedure using a 3-down, 1-up decision rule that tracked 79.4% correct detection (Levitt, 1971). Each run consisted of a block of 60 trials. The initial step size of 4 dB was reduced to 2 dB after the first two reversals. The first two (or three, if the total number of reversals was odd) reversal points were discarded, and the threshold estimate for a given block was based on the average of the signal level at the remaining reversal points. On the rare occasions when there were fewer than six reversals in the mean or when the standard deviation of the given threshold estimate was greater than 5 dB, the run was discarded. Final threshold values for a particular condition are based on the average of

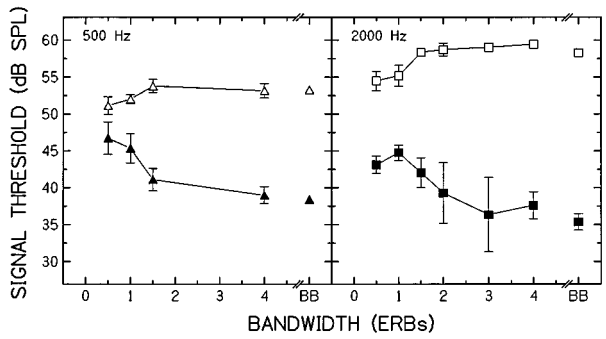

FIG. 1. Average signal threshold as a function of masker bandwidth for the four listeners in Crew A. Signal frequency was 500 Hz (left panel) or 2000 Hz (right panel). The masker was unmodulated (unfilled symbols) or sinusoidally amplitude modulated (SAM) at a rate of 8 Hz and a depth (m) of 1.0 (filled symbols). Error bars indicate plus and minus one standard error.

at least three runs. If the standard deviation of that average was greater than 3 dB, an additional estimate was obtained and all four estimates were averaged.

C. Subjects

Two different crews participated approximately nine months apart from one another; the conditions were not necessarily the same for both crews, as detailed below. All subjects had audiometric thresholds within 15 dB of ANSI (1989) standards. They received 2 h of practice prior to data collection. Crew A consisted of four subjects ranging in age from 21 to 33 years; one of those subjects was author DNP. Crew B consisted of three subjects ranging in age from 23 to 25 years; author DR was one of those subjects. Except for the two authors who served as subjects, all subjects were paid an hourly wage for their participation.

II. EXPERIMENT 1: EFFECTS OF MASKER BANDWIDTH

A. Conditions

The spectrum level of the masker was 40 dB SPL. The masker was unmodulated ($m=0.0$) or sinusoidally amplitude modulated at a rate of 8 Hz and a depth (m) of 1.0 for Crew A, and at a depth of 0.75 or 1.0 for Crew B. The frequency of the signal was 500 or 2000 Hz for Crew A, and 250, 2000, or 4000 Hz for Crew B. The bandwidth of the masker was expressed in terms of the number of equivalent rectangular bandwidths (ERBs; see Glasberg and Moore, 1990); it ranged from 0.5 to 4.0 ERBs. A broadband (BB) condition (10 kHz) was also employed. The values (in Hz) used for a single ERB at the given signal frequencies were as follows: 60 at 250 Hz; 80 at 500 Hz; 240 at 2000 Hz; and 460 at 4000 Hz.

B. Results and discussion

The results were similar across the four subjects comprising Crew A, and thus only their group mean data are shown in Fig. 1, where signal threshold is plotted as a function of masker bandwidth for both the 500-Hz (left panel) and 2000-Hz (right panel) signal. For the unmodulated masker (unfilled symbols), threshold initially increased as

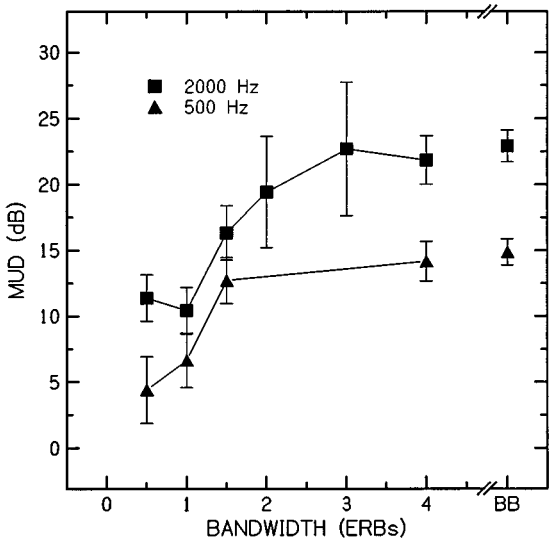

FIG. 2. MUD values from the data in Fig. 1. Error bars indicate plus and minus one standard error, calculated as: $s.e.^2_{MUD}=s.e.^2_{unmod}+s.e.^2_{mod}$ (Carlyon *et al.*, 1989).

the bandwidth increased, but it then reached an asymptote at a bandwidth of 1.5 ERBs. This, of course, is a replication of the classical bandwidening experiment of Fletcher (1940), and it suggests that the critical band for these subjects is somewhere between 1.0 and 1.5 ERBs. For the modulated masker (filled symbols), threshold decreased slightly or remained constant as the bandwidth increased from 0.5 to 1.0 ERB, but then it decreased as the bandwidth of the masker increased beyond 1.0 ERB. The threshold reached or nearly reached an asymptote at a bandwidth of about 1.5 ERBs for the 500-Hz signal and 3.0 ERBs for the 2000-Hz signal. These results are similar to those published previously (e.g., Hall and Haggard, 1983; Hall *et al.*, 1984; Schooneveldt and Moore, 1989). One difference between these results and those of Hall *et al.*, however, is that here the thresholds in the presence of the modulated masker are clearly lower than those in the presence of the unmodulated masker at all bandwidths, not just those wider than a critical band. It may be that this difference reflects the fact that we used a sinusoidally amplitude-modulated (SAM) masker modulated at a relatively low rate (8 Hz), whereas Hall *et al.* used a noise-modulated masker with a relatively wide modulator bandwidth (50 Hz). Seemingly inconsistent with this possibility, however, are results from Schooneveldt and Moore (1989), which showed a MUD at narrow masker bandwidths for modulator bandwidths from 12.5 to 50 Hz.

At any given bandwidth, the difference between the filled and unfilled symbols defines the MUD. These values are shown in Fig. 2. The pattern of results was similar for the two signal frequencies, although one obvious difference is that the MUD is larger at 2000 Hz (squares) than at 500 Hz (triangles) for all masker bandwidths, particularly for the wider bandwidths.

The results for the three subjects comprising listening Crew B were similar to one another, and thus only their mean results are shown in Fig. 3. First consider the results for masker modulation depths of 0.0 and 1.0. The pattern of

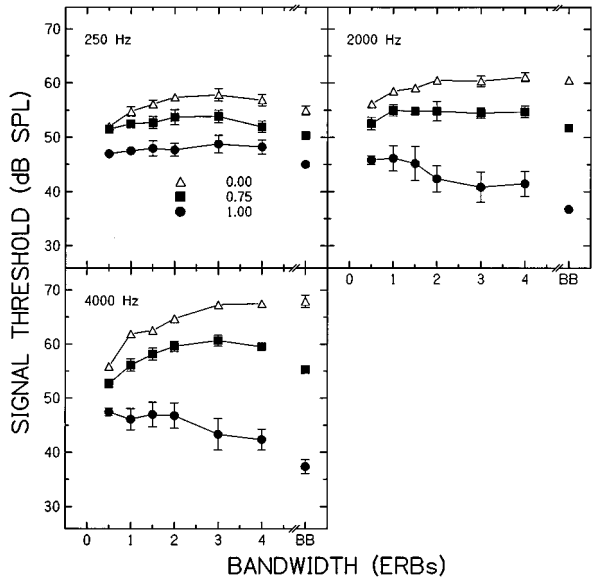

FIG. 3. Average signal threshold as a function of masker bandwidth for the three listeners in Crew B. Signal frequency was 250 Hz (upper left panel), 2000 Hz (upper right panel), or 4000 Hz (bottom left panel). The masker was unmodulated (unfilled triangles) or SAM at a rate of 8 Hz and a depth of 0.75 (filled squares) or 1.0 (filled circles). Error bars indicate plus and minus one standard error.

results at 2000 and 4000 Hz is similar to that seen in Fig. 1: Thresholds in the presence of the unmodulated masker (triangles) increase as bandwidth increases to about 1.5–2.0 ERBs, whereas those in the presence of the modulated masker (circles) decrease as bandwidth increases to about 3.0 ERBs. The pattern was somewhat different at 250 Hz, where the threshold in the presence of the modulated masker ($m=1.0$; circles) did not decline much, if at all, but remained essentially constant as masker bandwidth increased. At all bandwidths, these thresholds were lower than those in the presence of the unmodulated masker (triangles).

Now consider the results obtained when the masker was modulated at a depth of 0.75 (squares). These thresholds were intermediate to those obtained at masker depths of 0.0 and 1.0, suggesting a monotonic relation between masker depth and signal threshold. Surprisingly, the pattern of results was more similar to that observed with an unmodulated masker (triangles) than to that observed with a masker modulated at a depth of 1.0 (circles).

Figure 4 shows the results in terms of the MUD. One

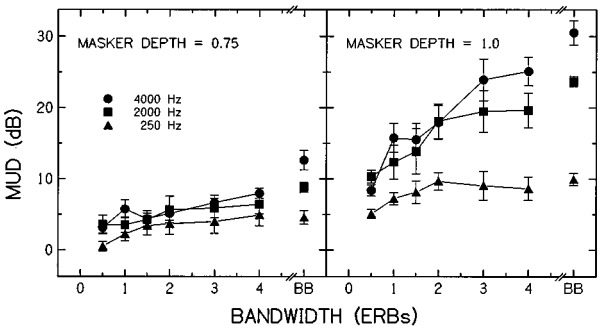

FIG. 4. MUD values from the data in Fig. 3. Error bars indicate plus and minus one standard error (see caption for Fig. 2).

finding is that the MUD was considerably (as much as two to three times) larger for a masker depth of 1.0 (right panel) than for a depth of 0.75 (left panel). For both depths, the MUD increased with increasing bandwidth, and reached or nearly reached an asymptote at a bandwidth of about 2.0–3.0 ERBs (there was, however, a tendency for the MUD at 2000 and 4000 Hz to increase somewhat when the masker was increased from 4.0 ERBs to BB). Another finding is that the MUD increased with increasing signal frequency (also see Fig. 2), particularly for a masker depth of 1.0. This effect of signal frequency is larger at wider bandwidths, where there is a clear monotonic effect of signal frequency. At narrow relative bandwidths, the MUD is larger at 2000 and 4000 Hz than it is at 250 Hz, but there is little difference in the size of the MUD at the two highest frequencies.

Some previous evidence suggesting that temporal resolution is superior at higher frequencies has been confounded by changes in stimulus bandwidth (e.g., Viemeister, 1979; Fitzgibbons and Wightman, 1982). The frequency effect observed here with BB maskers cannot be accounted for by differences in stimulus bandwidth. The same is not necessarily true, however, for the frequency effect observed with the narrower maskers. Because bandwidths were relative to an ERB at the signal frequency, a given relative bandwidth will be wider (in Hz) at the higher signal frequencies, raising the possibility that the larger MUD at higher signal frequencies is simply due to a wider absolute masker bandwidth. To address this issue, author DNP and a newly recruited subject with normal hearing (and considerable listening experience with this psychoacoustic task) were tested at signal frequencies of 500 and 2000 Hz using fixed absolute masker bandwidths. Their results were similar, and thus their average results are shown in Table I.

For the 500-Hz signal, all bandwidths were wider than an ERB (80 Hz), whereas for the 2000-Hz signal, the first two bandwidths were less than an ERB (240 Hz). The effect of signal frequency on the MUD was quite small—within measurement error—for bandwidths of 100 and 200 Hz, but for wider bandwidths the difference in the size of the MUD was about 8–10 dB. This suggests that the signal frequency effect observed in Figs. 2 and 4 at narrow relative bandwidths (1.0 ERB or less) does not, at least for the most part, reflect differences in temporal processing per se, but instead reflects differences in masker bandwidth. Consistent with this are results from a study in progress from our laboratory, which showed no consistent effect of signal frequency (from 250 to 4000 Hz) on the MUD for a group of three subjects when the masker bandwidth was fixed at 100 Hz. This interpretation, however, must be made with some caution: The comparison at the two narrowest bandwidths (Table I) may actually underestimate the ''true'' signal frequency effect for narrow bandwidths, because the MUD for the 500-Hz signal may represent the combination of a within- and an across-channel effect, whereas that for the 2000-Hz signal will only represent a within-channel effect. It is unlikely, however, that the MUD for the 500-Hz signal at a bandwidth of 100 Hz reflects any substantial across-channel processing because these subjects' thresholds at that bandwidth were

TABLE I. Signal thresholds in the presence of an unmodulated and modulated masker, and the resulting MUD, for various absolute masker bandwidths. The standard errors are given in parentheses (refer to the caption for Fig. 2 to see how the standard error for the MUD values was determined). For the BB condition, the bandwidth was 10 000 Hz (10-kHz low-pass masker). The results are the average of two subjects, author DNP from listening Crew A and one additional subject with considerable experience with these listening tasks. The signal frequency was 500 or 2000 Hz.

BW (Hz)	100	200	400	800	BB
unmod	50.8 (0.1)	52.1 (0.1)	52.2 (0.1)	52.6 (0.2)	51.9 (0.6)
500 Hz mod	39.3 (1.2)	38.2 (0.2)	35.8 (0.4)	36.8 (0.1)	37.7 (1.5)
MUD	11.5 (1.2)	13.9 (0.2)	16.4 (0.4)	15.8 (0.2)	14.2 (1.6)
unmod	51.5 (2.2)	55.0 (0.4)	57.4 (1.3)	58.5 (1.0)	58.4 (0.4)
2000 Hz mod	38.9 (0.9)	39.7 (0.7)	37.8 (2.1)	34.7 (1.5)	34.5 (0.7)
MUD	12.6 (2.4)	15.3 (0.8)	19.6 (2.5)	23.8 (1.8)	23.9 (0.8)

nearly identical to their thresholds obtained with a 1.0-ERB (80-Hz) masker (data not shown).

According to Carlyon *et al.* (1989), it is possible to estimate the amount of CMR by subtracting the MUD obtained with a relatively narrow masker from that obtained with a relatively broad masker. This has been done for the results from experiment 1, and the estimates of CMR are given in Table II. The magnitude of CMR increases monotonically with increasing signal frequency for both modulation depths, although the effect of signal frequency is much larger at the larger modulation depth. These results contrast with those of Schooneveldt and Moore (1987), who found no consistent change in CMR as a function of signal frequency from 250 to 4000 Hz. This difference may be due to the differences in stimuli between the two studies: Whereas we used a SAM masker of varying bandwidth, Schooneveldt and Moore used a 25-Hz-wide on-frequency masking band coupled with a 25-Hz-wide flanking band to obtain their estimates of CMR.

III. EXPERIMENT 2: EFFECTS OF MASKER RATE

A. Conditions

The purpose of experiment 2 was to evaluate the effects of masker modulation rate on the MUD for both a narrow and a broad bandwidth masker. The bandwidth of the masker was 1.0 ERB or BB (10 kHz). We assume that the results with the ERB masker will reveal processing that occurs solely within a single channel, whereas those with the BB masker will reveal a combined within- and across-channel processing. The spectrum level of the masker was 40 dB SPL. The masker was unmodulated ($m=0.0$) or SAM ($m=1.0$). The modulation rate ranged from 2 to 200 Hz, with the restriction that the highest modulation rate tested was always less than one-half the bandwidth of the masker (prior to modulation). The frequency of the signal was 500 or 2000 Hz. Listening Crew A participated.

TABLE II. Estimates of CMR based on the MUD values shown in Figs. 2 and 4. The magnitude of CMR is given by MUD_{BB}-MUD_{ERB}, where MUD_{BB} is the MUD obtained with the BB masker and MUD_{ERB} is the MUD obtained with the ERB masker. The results from listening Crew A are the average of four subjects, whereas those from Crew B are the average of three subjects. The signal frequency was 250, 500, 2000, or 4000 Hz, and the depth of the modulated masker was 0.75 or 1.0.

	250 Hz	500 Hz	2000 Hz	4000 Hz
Crew A, $m=1.0$	⋯	8.3	12.5	⋯
Crew B, $m=1.0$	2.7	⋯	11.4	14.7
Crew B, $m=0.75$	2.4	⋯	5.3	6.9

B. Results and discussion

The results were similar across the four subjects, and thus only their averaged results are shown in Fig. 5. For the BB masker (right panel), the function relating the MUD to masker modulation rate was generally low pass. The MUD tended to decrease as the modulation rate increased, as observed previously by others (Carlyon *et al.*, 1989; Peters and Hall, 1994). The peak in the function at 4 Hz is probably an artifact: The size of the MUD at 2 Hz, where there is only one cycle of modulation in the observation interval, is probably too low, because there is no dip in the envelope of the masker in the modulated condition (given stimulus gating and the fact that the envelope starts at its minimum) to allow optimum signal detection. Across the range of rates, the MUD was about 9 dB larger for the 2000-Hz signal, and thus these results extend the signal frequency effect observed in experiment 1 to both lower and higher modulation rates. Related to this is the finding that the highest modulation rate where a positive MUD exists was higher at 2000 than at 500 Hz.

For the ERB masker (left panel), the functions were relatively flat, except for the decrease in MUD when going

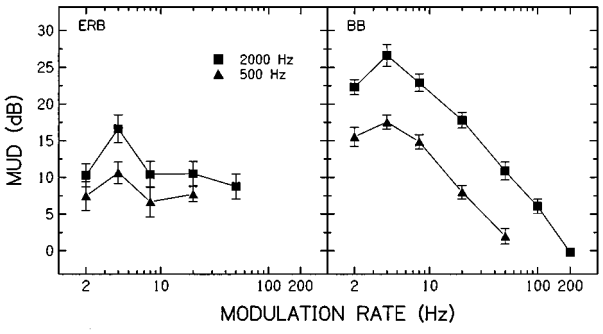

FIG. 5. MUD values as a function of masker modulation rate averaged across the four listeners in Crew A. Signal frequency was 500 Hz (filled triangles) or 2000 Hz (filled squares). The masker was one ERB wide (left panel) or BB (right panel). Error bars indicate plus and minus one standard error (see caption for Fig. 2).

TABLE III. Estimates of CMR based on the MUD values shown in Fig. 5. The magnitude of CMR is given by MUD_{BB}-MUD_{ERB}. The results are from experiment 2 (average of the four subjects in listening Crew A) at signal frequencies of 500 and 2000 Hz.

	500 Hz					2000 Hz				
Rate (Hz)	2	4	8	20	50	2	4	8	20	50
	8.0	7.0	8.3	0.3	···	12.0	10.0	12.5	7.3	2.1

from a rate of 4 to 8 Hz (again, the value at 2 Hz should be interpreted cautiously). This suggests that the within-channel processing is influenced less by changes in masker modulation rate than is the combined within- and across-channel processing, at least over the range of rates tested here.[2] An estimate of the across-channel processing alone can be acquired by subtracting the MUD obtained with an ERB masker (MUD_{ERB}) from that obtained with a broadband masker (MUD_{BB}). This difference is an estimate of CMR (Carlyon *et al.*, 1989), and is shown in Table III. At both signal frequencies, the amount of CMR was roughly constant for masker rates from 2 to 8 Hz, but then it declined at higher rates. The magnitude of CMR was larger at 2000 Hz than it was at 500 Hz for all masker rates, thus extending the effect of signal frequency on CMR observed in experiment 1 (Table II) to lower and higher rates. A similar effect of signal frequency on CMR was observed by Hall and Grose (1989), although only for their 40-Hz rate and not their 15-Hz rate.

Two (related) aspects of the data from this experiment differ from previous results. First, the results with the ERB masker differ from those in Peters and Hall (1994). They found that MUD_{ERB} decreased as the masker modulation rate increased from 10 to 50 Hz. The difference between our results and their results may be related to the type of modulator used. We used sinusoidal modulation, whereas Peters and Hall used square-wave modulation. Consistent with this possibility is the fact that Carlyon *et al.* (1989) found that the effect of rate was much more pronounced for a square-wave modulator than for a sinusoidal modulator (their Fig. 1). The reason for this difference is unclear, although it may be that the square-wave modulator—which generally produces larger MUD values, at least at lower rates—is simply more sensitive to changes in rate, perhaps as a result of its more clearly defined dip. The second aspect of our data that differs from previous data is that the amount of CMR ($MUD_{BB} - MUD_{ERB}$) was relatively constant up to a masker rate of 8 Hz, but then decreased with further increases in rate (Table III). Hall and Haggard (1983), using balanced modulation (they multiplied their noise carrier by a sinusoid that was not dc shifted), found that CMR decreased with increasing rate from 4 to 64 Hz. Peters and Hall (1994), using square-wave modulation, found that CMR remained constant up to a masker rate of 30 Hz, but that it declined at higher rates. Finally, Carlyon *et al.* (1989) reported no systematic effect of masker rate on CMR for either sinusoidal or square-wave modulation. Further research will be necessary to gain a better understanding of why the results regarding the effects of modulation rate on CMR have differed across these studies.

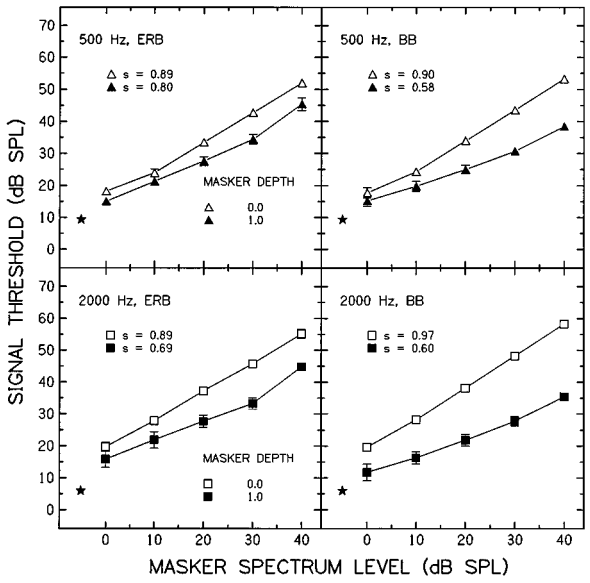

FIG. 6. Average signal threshold as a function of masker spectrum level for the four listeners in Crew A. Signal frequency was 500 Hz (top panels) or 2000 Hz (bottom panels). Masker bandwidth was one ERB (left panels) or BB (right panels). The masker was unmodulated (unfilled symbols) or SAM at a rate of 8 Hz and a depth of 1.0 (filled symbols). Each growth-of-masking function was fitted with a straight line using linear regression analysis; the slope of each function is given in the appropriate panel. Absolute thresholds are given in the lower left of each panel (filled stars). Error bars indicate plus and minus one standard error.

IV. EXPERIMENT 3: EFFECTS OF MASKER LEVEL

A. Conditions

The purpose of this experiment was to measure the MUD as a function of masker level for an ERB and BB masker. The spectrum level of the masker ranged from 0 to 40 dB SPL in 10-dB steps. The masker was unmodulated ($m=0.0$) or SAM at a depth of 1.0 for listening Crew A and at a depth of 0.75 or 1.00 for Crew B. The modulation rate was 8 Hz. The frequency of the signal was 500 or 2000 Hz for Crew A and 2000 or 4000 Hz for Crew B.

B. Results and discussion

The results were similar within a listening crew, and thus only group mean data are shown. Figure 6 shows the results in terms of signal threshold for Crew A. The average quiet thresholds are shown in the lower left of each panel (filled stars). The unfilled symbols show the growth-of-masking functions for the unmodulated masker, and the filled symbols show those for the modulated masker. The slopes of those functions, based on a linear regression analysis, are shown in the corresponding panels. For any given masker bandwidth and signal frequency (i.e., within a given panel), but especially for the BB masker, the growth-of-masking functions were steeper for the unmodulated masker, and thus the difference between the two functions (defining the MUD) generally increased with increases in masker level. This is seen more clearly in Fig. 7. For both the 500-Hz (left panel) and 2000-Hz (right panel) signal frequency, the MUD increased monotonically with level for the BB masker, with no clear evidence of an asymptote. For the ERB masker, how-

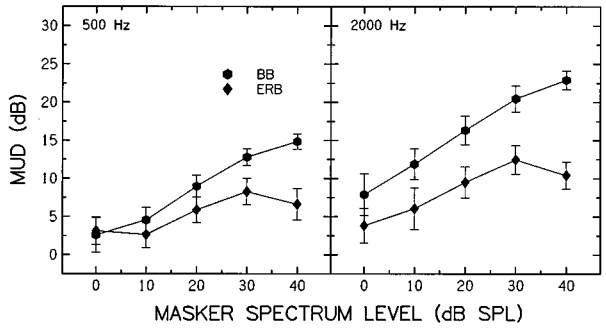

FIG. 7. MUD values from the data in Fig. 6. Error bars indicate plus and minus one standard error (see caption for Fig. 2).

ever, the MUD reached an asymptote—or even declined—at the highest levels. This is due to the especially large increase in threshold in the presence of the modulated masker when going from a masker level of 30 to 40 dB SPL (Fig. 6).

Figures 8 and 9 show the average results for Crew B. The results for the modulation depths of 0.0 and 1.0 were similar to those for Crew A at those same depths, even to the extent that the MUD reached an asymptote for the ERB masker at high levels (Fig. 9). In addition, Crew B was tested at a modulation depth of 0.75. The masking functions at this depth were intermediate to those of the other two depths, but the slopes were more similar to those obtained at a masker depth of 0.0 (triangles) than at 1.0 (circles). Consequently, the MUD at this lower depth (bottom panels in Fig. 9) was less dependent upon masker level than it was for the depth of 1.0 (upper panels in Fig. 9).

Similar effects of masker level have been observed previously with broadband maskers, modulated either by a sinusoid (Weber, 1977), a square wave (Zwicker and Schorn, 1982), or a low-pass noise (Moore and Shailer, 1991). Only Moore and Shailer, however, have examined the effects of level with narrow-band maskers, and our results differ from theirs. They observed only a small MUD that was more or less constant with masker level over a range of spectrum levels from 10 to 50 dB SPL. It is possible that this difference in findings can be explained by the different modulators; an effect of level, at least with narrow-band maskers, may require a clearly defined and rather substantial dip. The smaller effect of level (for both bandwidth maskers) observed in Fig. 9 for a masker depth of 0.75 compared to 1.0 is certainly consistent with this possibility.

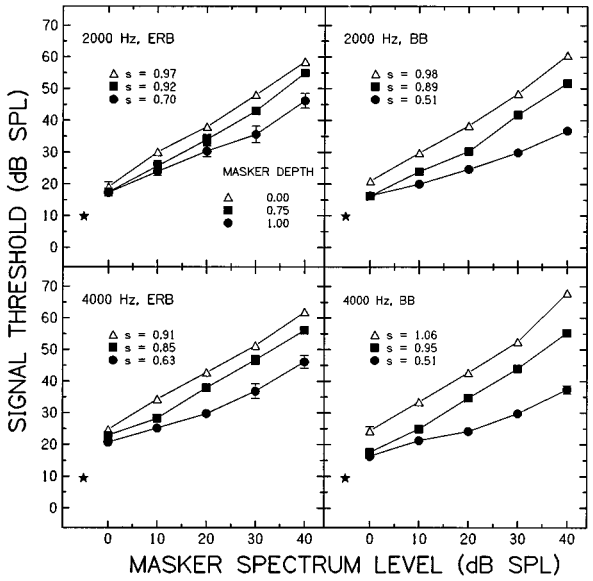

FIG. 8. Average signal threshold as a function of masker spectrum level for the three listeners in Crew B. Signal frequency was 2000 Hz (top panels) or 4000 Hz (bottom panels). Masker bandwidth was one ERB (left panels) or BB (right panels). The masker was unmodulated (unfilled triangles) or SAM at a rate of 8 Hz and a depth of 0.75 (filled squares) or 1.0 (filled circles). Each growth-of-masking function was fitted with a straight line using linear regression analysis; the slope of each function is given in the appropriate panel. Absolute thresholds are given in the lower left of each panel (filled stars). Error bars indicate plus and minus one standard error.

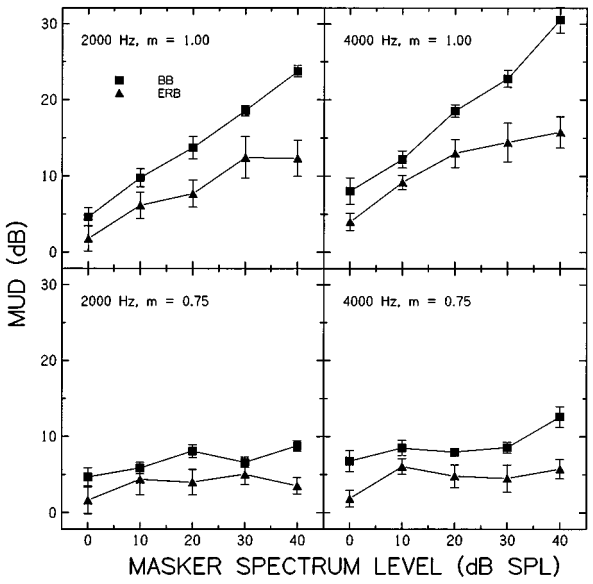

FIG. 9. MUD values from the data in Fig. 8. Error bars indicate plus and minus one standard error (see caption for Fig. 2).

Table IV shows the estimates of CMR for both listening crews. The magnitude of CMR increased with increases in masker level, at least when the modulated masker was modulated at a depth of 1.0. Moore and Shailer (1991) observed a similar effect with their noise-modulated noise. When the modulated masker was modulated at a depth of 0.75, however, the effect of masker level was somewhat inconsistent, although at both signal frequencies the largest CMR occurred at the highest masker level.

V. GENERAL DISCUSSION

Although the MUD paradigm was introduced by Zwicker and Schorn (1982) as a convenient way to measure temporal resolution, it is clear that the bandwidth of the masker may influence the type of processing involved. This, of course, does not minimize the importance of the MUD paradigm for studying auditory processing. Indeed, the processing revealed in this paradigm may be quite fundamental, and may be especially important for the processing of sound in temporally complex environments. It does, however, indicate that masker bandwidth is an important consideration. When the masker is no wider than a critical band, the MUD

TABLE IV. The effect of masker level on the estimate of CMR (MUD_{BB}-MUD_{ERB}) based on the MUD values shown in Fig. 7 (average of four subjects in listening Crew A) and Fig. 9 (average of three subjects in listening Crew B). Crew A was tested at signal frequencies of 500 and 2000 Hz; the modulated masker had a depth of 1.0. Crew B was tested at signal frequencies of 2000 and 4000 Hz; the modulated masker had a depth of 1.0 or 0.75.

	Crew A									
	500 Hz					2000 Hz				
	$m=1.0$									
Level (dB SPL)	0	10	20	30	40	0	10	20	30	40
	−0.5	1.8	3.1	4.5	8.3	4.1	5.8	6.8	8.0	12.5
	Crew B									
	2000 Hz					4000 Hz				
	$m=1.0$									
Level (dB SPL)	0	10	20	30	40	0	10	20	30	40
	2.8	3.6	6.0	6.2	11.4	4.0	3.0	5.5	8.4	14.7
	$m=0.75$									
	3.1	1.5	4.1	1.6	5.3	4.9	2.4	3.2	4.1	6.9

presumably represents solely a within-channel type of processing. When the masker is broader than a critical band, however, across-channel processing like that revealed in CMR may contribute substantially to the MUD.

The general purpose of the present study was to lay the groundwork for future work in subjects with sensorineural hearing loss by examining the effects of masker rate, masker level, and signal frequency in normal-hearing subjects. As discussed above (Sec. III B), the results from studies examining the effects of masker rate using BB maskers have been fairly consistent, whereas the results from those using narrow-band maskers have been rather mixed. We suggested that differences in the modulators that have been used may contribute to the differences in results, although additional research is needed to address this possibility. The remainder of this section will focus on the effects of masker level and signal frequency.

A. Effects of masker level

The slopes of the masking functions (Figs. 6 and 8) when the masker was unmodulated were generally close to unity, as expected (Hawkins and Stevens, 1950), whereas the slopes when the masker was modulated at a depth of 1.0 were generally much less than that. Consequently, the size of the MUD increased with increasing masker level (Figs. 7 and 9). The differences in these slopes can be understood by assuming that thresholds in the presence of a masker modulated at a depth of 1.0 are governed by forward masking, where the growth of masking is much less than unity (e.g., Widin and Viemeister, 1979; Jesteadt *et al.*, 1982; Moore and Glasberg, 1983). In other words, the shallow growth-of-masking functions are consistent with the possibility that subjects listen for the signal in the dip of the masker envelope (e.g., Buus, 1985), and that the masking in that case is determined primarily by the preceding masker peak. That the masking functions had a slope close to unity when the masker was modulated at a depth of 0.75 (Fig. 8) suggests that the thresholds in the presence of that masker were governed more by simultaneous masking than by forward masking. We address this issue in more detail in a companion paper (Bacon and Lee, in press).

The results in Table III indicate that the amount of CMR increased with increases in masker level, at least when the modulated masker was modulated at a depth of 1.0. Because CMR is given by $MUD_{BB}-MUD_{ERB}$, this means that the MUD_{BB} increased more with level than did the MUD_{ERB} (Figs. 7 and 9). This occurred primarily because the slope of the masking function for the modulated masker was generally less with a BB masker than with an ERB masker (Figs. 6 and 8). One explanation for this is that thresholds in the presence of the modulated BB—but not ERB—masker are influenced by suppression. Because suppression tends to increase with increases in level (Houtgast, 1974), the difference between the threshold in the presence of the BB masker and that in the presence of the ERB masker (and hence the difference between MUD_{BB} and MUD_{ERB}) will increase with level. Moore and Shailer (1991) offered a similar explanation for the increase in CMR with level that they observed using multiple, narrow bands of noise. The lack of a consistent effect of level on CMR when the masker was modulated at a depth of 0.75 (Table III) may reflect the fact that the thresholds in the presence of a masker modulated at that depth are influenced significantly by simultaneous masking, as suggested above.

The MUD_{ERB} reached an asymptote at the highest masker levels, whereas the MUD_{BB} continued to increase even at the highest levels tested (Figs. 7 and 9—modulation depth of 1.0). It is possible to understand these effects in terms of forward masking as well. Within this context, we consider two different explanations. The first relates to the possible combination of forward and simultaneous masking.

When the masker is modulated at a depth of 1.0, the level of the masker in the dip is about 35 dB lower than the level of the unmodulated masker (as measured with a 20-ms Hanning window centered in the dip). Thus, at low masker levels, the masker energy in the dip will be below threshold, and thus signal threshold in the presence of the modulated masker will be influenced only by forward masking. The amount of masking in the presence of the modulated masker ($m=1.0$) will therefore increase gradually with increases in masker level, and thus the MUD will increase with increases in level. At higher masker levels, the masker energy in the dip will no longer be below threshold, and thus it will contribute to the masking. At this point, masking will be influenced by both simultaneous and forward masking, and thus the growth of masking will increase (Jesteadt *et al.*, submitted). For the signal frequencies tested here, simultaneous masking should begin to occur when the spectrum level in the dip reaches a value of about -10 to -5 dB (Hawkins and Stevens, 1950); this will occur at a masker spectrum level between 25 and 30 dB, which is the point where the MUD_{ERB} levels off. It is interesting that the MUD_{BB} did not reach an asymptote at high levels, as the same argument should seemingly apply to that masker as well. It is possible, however, that the threshold in the presence of the modulated BB masker was influenced by suppression, which would reduce the effective level of the masker. Thus, throughout the range of levels tested here, the masker level in the dip may have been too low to produce any simultaneous masking.

The second explanation for the finding that the MUD asymptotes at the highest masker levels for the ERB masker, suggested by Plack (1996), is related to the possible influence of basilar membrane nonlinearity on forward masking. In particular, he suggested, following Plack and Oxenham (1996), that the gradual, nonlinear growth of masking in the presence of the *modulated* masker results from the masker being in a compressive region of basilar membrane response while the (lower level) signal is in a linear region. He further proposed that the increased growth of masking observed when the modulated ERB masker is increased in level from 30 to 40 dB is the result of the signal also being in a compressive region. Following this argument, the MUD_{ERB} asymptotes at high masker levels because the signal and masker are both compressed at the level of the basilar membrane. The MUD_{BB} presumably did not asymptote because the signal level remained relatively low (possibly as a result of suppression of the masker's response) and hence in a linear region.

Regardless of the explanation for the asymptote in the MUD_{ERB} at high masker levels, the effects of masker level observed here have significant implications for testing hearing-impaired subjects, even if level effects are not observed in these subjects (which could be the case if the level effects are related to normal basilar membrane responses). In particular, they suggest that comparisons between normal-hearing and hearing-impaired subjects will be complicated by the effects of level when the modulated masker is modulated at a depth of 1.0, but considerably less so when the masker is modulated at a depth of 0.75. Unfortunately, the size of the MUD is reduced significantly at this lower modulation depth, which may make it more difficult to observe subtle changes in the magnitude of the MUD as a consequence of hearing loss. Whether a slightly greater depth would yield considerably larger values of MUD and still be more or less level invariant is unknown, although we plan to pursue that possibility.

B. Effects of signal frequency

All three experiments revealed a clear effect of signal frequency on the size of the MUD. In particular, the MUD increased with increasing signal frequency for both the ERB and BB maskers (Figs. 2, 4, 5, 7, and 9). The effect of signal frequency was larger for the BB masker than for the ERB masker, suggesting that there is both a within-channel and an across-channel effect of frequency. We argued earlier, however, that the within-channel effect was probably largely (if not completely) influenced by stimulus bandwidth (see Sec. II B and Table I). That is, the larger MUD_{ERB} at higher frequencies was primarily the result of the ERB masker being wider (in Hz) at higher than at lower frequencies. It is now worth considering precisely how stimulus bandwidth might influence the size of the MUD as a function of signal frequency. We consider two explanations that are not necessarily mutually exclusive.

First, the unmodulated masker will contain inherent fluctuations that depend upon the masker bandwidth (Rice, 1954). These fluctuations will be slower and thus more prominent perceptually at low signal frequencies, where the ERB masker is relatively narrow. At these frequencies, thresholds in the presence of the unmodulated masker may be relatively low because subjects are detecting the signal in the dips of the inherent fluctuations. If so, then the MUD values will be smaller than the ''true'' MUD values at that signal frequency. At higher signal frequencies, where the ERB masker is relatively wide, the fluctuations will be more rapid and will be effectively smoothed by the auditory system (Viemeister, 1979). Thus, at these higher frequencies, the inherent fluctuations in the unmodulated masker probably will not influence threshold or the size of the MUD. It follows that the inherent fluctuations in the unmodulated masker will presumably only affect relatively low signal frequencies. This perhaps explains why the signal frequency effect with ERB maskers exists when comparing 250 Hz to 2000 or 4000 Hz (Fig. 4) or 500 Hz to 2000 Hz (Fig. 2), but not when comparing 2000 Hz to 4000 Hz (Fig. 4).

The second way that stimulus bandwidth could influence the size of the MUD_{ERB} as a function of frequency results from the fact that the overall level of the ERB-wide noise increased with increasing frequency (because the spectrum level of the masker was fixed). Given the change in overall masker level, one would expect thresholds—at least in the presence of the unmodulated masker—to be higher at higher frequencies (Hawkins and Stevens, 1950). This would tend to result in larger MUD values at higher frequencies.

Both of the above explanations suggest that the effect of signal frequency on the MUD_{ERB} is a result of changes in threshold in the presence of the unmodulated masker. The data certainly support this, as is illustrated in Fig. 10. In this figure, we have replotted some of the data from Figs. 1 and 3

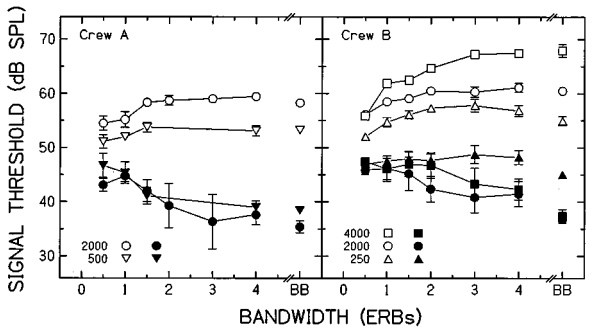

FIG. 10. Average signal threshold as a function of masker bandwidth for the four listeners in Crew A (left panel) and the three listeners in Crew B (right panel). These results are replotted from Figs. 1 and 3, respectively. The masker was unmodulated (unfilled symbols) or SAM at a rate of 8 Hz and a depth of 1.0 (filled symbols). Error bars indicate plus and minus one standard error.

in the left and right panels, respectively. The thresholds in the presence of the unmodulated masker (unfilled symbols) increase with increasing signal frequency, whereas for bandwidths less than about 2.0 ERBs, the thresholds in the presence of the modulated masker (filled symbols) overlap at the different signal frequencies (the lack of an overlap at wider bandwidths is discussed below). The increase in threshold is roughly equal to the increase in overall level, consistent with the second explanation proposed above.

The signal frequency effect with a BB masker cannot be explained by differences in masker bandwidth, as the same BB masker was used for all signal frequencies. However, it might be explained by the masker bandwidth that exists after being processed by an auditory filter. In particular, the bandwidth of the noise at the output of the auditory filter centered at (or near) the signal frequency will increase with increasing signal frequency (in the same way that the ERB-wide masker increases in bandwidth as a function of frequency). Thus, the two explanations proposed above might also be applicable to the BB masker case. However, they cannot account for the entire effect, because they predict that the magnitude of the signal frequency effect with BB maskers will be the same as that with ERB maskers, which was not observed.[3] Indeed, as noted above, the effect of signal frequency with BB maskers was considerably larger than that with ERB maskers, suggesting the presence of an across-channel component effect that is sensitive to frequency.

It may be possible to account for this across-channel component by appealing to processes that are typically revealed in forward masking. As discussed above, thresholds in the presence of the masker modulated at a depth of 1.0 may be governed largely by forward masking. As we discuss in more detail elsewhere (Bacon and Lee, in press), the across-channel component may be influenced by suppression. Suppression could influence threshold when the modulated masker is BB. To account for the signal frequency effect, the amount of suppression would have to increase with increasing signal frequency (the greater the suppression, the lower the threshold in the presence of the modulated masker, and hence the greater the MUD). Only a few studies have examined psychophysical suppression as a function of frequency (Shannon, 1976; Thibodeau and Fagelson, 1993). Shannon's (1976) results suggest that suppression magnitude may be smaller at a signal frequency of 500 Hz than at higher frequencies, and Thibodeau and Fagelson (1993) found more suppression at a signal frequency of 2000 Hz than at 500 Hz. Moreover, more recent data from our laboratory (Bacon and Lee, 1995, in press; Lee and Bacon, in preparation) suggest that suppression may increase with increasing signal frequency, at least from 250 Hz to about 1000 or 2000 Hz. These latter results are consistent with the results in the right panel of Fig. 10, which show that, *at wide bandwidths*, thresholds in the presence of a modulated masker at 2000 and 4000 Hz (filled circles and squares) are similar to one another but are lower than those at 250 Hz (filled triangles). An increase in suppression with increasing frequency could also explain the finding that CMR increased as signal frequency increased from 250 to 4000 Hz (Tables II and III), given that CMR is supposed to represent an across-channel process.

The influence of suppression can exist only when the threshold in the presence of the modulated masker is governed by forward masking. The considerably smaller signal frequency effect that exists when the modulated masker is modulated at a depth of 0.75 is consistent with the suggestion above that thresholds in the presence of this modulated masker are not influenced as much by forward masking, but instead are governed largely by simultaneous masking in the dips.

VI. FINAL COMMENT

The results from the present experiments suggest that the processing underlying the masking produced by a SAM noise may depend strongly on the modulation depth of that noise. At large depths, thresholds may be influenced primarily by forward masking, whereas at smaller depths, thresholds are likely to be influenced more by simultaneous masking. This difference will, of course, exist for both narrowband and broadband maskers. This means that the across-channel processing—representing what is now commonly referred to as CMR—will differ depending upon modulation depth. For example, it seems likely that forward masking will play a significant role when the masker is modulated by a sine or a square wave (at large depths), but it may play a much more limited role (if any) when other modulators (such as low-pass noise) are used. Its role may also be rather small when the modulations are simply those that are inherent to a relatively narrow band of noise. The implication of this is that researchers who wish to understand the across-channel processing underlying CMR should consider carefully the type of maskers that are being used and compared. Forward masking and processes revealed in forward masking, such as suppression, may dominate in some circumstances, but may play little or no role in others.

ACKNOWLEDGMENTS

This research was supported by a grant from NIDCD (DC01376), and is based in part on a master's thesis submitted by the third author to the Graduate College at Arizona

State University. We thank Chris Plack and an anonymous reviewer for their helpful comments on a previous version of this manuscript.

[1]Because the maskers were modulated after bandlimiting, their bandwidths were somewhat wider when they were modulated than when they were unmodulated. For most conditions in the present study, the modulation rate was 8 Hz or less, and thus the differences in bandwidth were relatively small, and probably did not influence significantly the results presented here.

[2]Although the bandwidth of the ERB masker varies somewhat with modulation rate (see footnote 1), this is unlikely to explain the finding that the results with the ERB masker were influenced less by masker rate than were those for the BB masker (where the slight increase in bandwidth with increase in modulation rate would almost certainly be insignificant). This is because the effect of increasing the bandwidth of a modulated masker is to, if anything, *decrease* the threshold (see Fig. 1).

[3]Another problem with these explanations for the signal frequency effect with BB maskers is that they do not account for the fact that the effect is much smaller for a masker depth of 0.75 than it is for a depth of 1.0 (Fig. 4), given that they implicate processing in the presence of the unmodulated masker as the source of the frequency effect.

ANSI (**1989**). ANSI S3.6-1989, ''Specifications for audiometers'' (American National Standards Institute, New York).

Bacon, S. P., and Lee, J. (**1995**). ''Temporal resolution and CMR can depend upon frequency,'' J. Acoust. Soc. Am. **97,** 3273(A).

Bacon, S. P., and Lee, J. (**in press**). ''The modulated-unmodulated difference: Effects of signal frequency and masker modulation depth,'' J. Acoust. Soc. Am.

Buus, S. (**1985**). ''Release from masking caused by envelope fluctuations,'' J. Acoust. Soc. Am. **78,** 1958–1965.

Carlyon, R. P., Buus, S., and Florentine, M. (**1989**). ''Comodulation masking release for three types of modulator as a function of modulation rate,'' Hear. Res. **42**, 37–46.

Fitzgibbons, P. J., and Wightman, F. L. (**1982**). ''Gap detection in normal and hearing-impaired listeners,'' J. Acoust. Soc. Am. **72,** 761–765.

Fletcher, H. (**1940**). ''Auditory patterns,'' Rev. Mod. Phys. **12,** 47–65.

Glasberg, B. R., and Moore, B. C. J. (**1990**). ''Derivation of auditory filter shapes from notched-noise data,'' Hearing Res. **47**, 103–138.

Hall, J. W., Davis, A. C., Haggard, M. P., and Pillsbury, H. C. (**1988**). ''Spectro-temporal analysis in normal-hearing and cochlear-impaired listeners,'' J. Acoust. Soc. Am. **84,** 1325–1331.

Hall, J. W., and Grose, J. H. (**1989**). ''Spectrotemporal analysis and cochlear hearing impairment: Effects of frequency selectivity, temporal resolution, signal frequency, and rate of modulation,'' J. Acoust. Soc. Am. **85,** 2550–2562.

Hall, J. W., and Haggard, M. P. (**1983**). ''Co-modulation—a principle for auditory pattern analysis in speech,'' Proc. 11th I.C.A. **4**, 69–71.

Hall, J. W., Haggard, M. P., and Fernandes, M. A. (**1984**). ''Detection in noise by spectro-temporal pattern analysis,'' J. Acoust. Soc. Am. **76,** 50–56.

Hawkins, J. E., Jr., and Stevens, S. S. (**1950**). ''The masking of pure tones and of speech by white noise,'' J. Acoust. Soc. Am. **22,** 6–13.

Houtgast, T. (**1974**). ''Lateral suppression in hearing,'' Doctoral thesis, Academische Pers B.V.

Jesteadt, W., Bacon, S. P., and Lehman, J. R. (**1982**). ''Forward masking as a function of frequency, masker level, and signal delay,'' J. Acoust. Soc. Am. **71,** 950–962.

Jesteadt, W., Wilke, S., and Bacon, S. P. (**submitted**). ''Combinations of forward and simultaneous masking,'' J. Acoust. Soc. Am.

Lee, J., and Bacon, S. P. (**in preparation**). ''Measures of psychophysical suppression as a function of frequency,'' J. Acoust. Soc. Am.

Levitt, H. (**1971**). ''Transformed up-down methods in psychoacoustics,'' J. Acoust. Soc. Am. **49,** 467–477.

Moore, B. C. J., and Glasberg, B. R. (**1983**). ''Growth of forward masking for sinusoidal and noise maskers as a function of signal delay; implications for suppression in noise,'' J. Acoust. Soc. Am. **73,** 1249–1259.

Moore, B. C. J., and Shailer, M. J. (**1991**). ''Comodulation masking release as a function of level,'' J. Acoust. Soc. Am. **90,** 829–835.

Peters, R. W., and Hall, J. W. (**1994**). ''Comodulation masking release for elderly listeners with relatively normal audiograms,'' J. Acoust. Soc. Am. **96,** 2674–2682.

Plack, C. J. (**1996**). Personal communication.

Plack, C. J., and Oxenham, A. J. (**1996**). ''Basilar membrane nonlinearity and the growth of forward masking,'' J. Acoust. Soc. Am. **99,** 2543(A).

Plomp, R. (**1964**). ''Rate of decay of auditory sensation,'' J. Acoust. Soc. Am. **36,** 277–282.

Rice, S. O. (**1954**). ''Mathematical analysis of random noise,'' in *Selected Papers on Noise and Stochastic Processes*, edited by N. Wax (Dover, New York), pp. 133–294.

Schooneveldt, G. P., and Moore, B. C. J. (**1987**). ''Comodulation masking release (CMR): Effects of signal frequency, flanking-band frequency, masker bandwidth, flanking-band level, and monotic versus dichotic presentation of the flanking band,'' J. Acoust. Soc. Am. **82,** 1944–1956.

Schooneveldt, G. P., and Moore, B. C. J. (**1989**). ''Comodulation masking release (CMR) as a function of masker bandwidth, modulator bandwidth, and signal duration,'' J. Acoust. Soc. Am. **85,** 273–281.

Shannon, R. V. (**1976**). ''Two-tone unmasking and suppression in a forward-masking situation,'' J. Acoust. Soc. Am. **59,** 1460–1470.

Thibodeau, L. M., and Fagelson, M. A. (**1993**). ''Comparison of suppression across frequencies,'' J. Acoust. Soc. Am. **93,** 2314(A).

Viemeister, N. F. (**1979**). ''Temporal modulation transfer functions based upon modulation thresholds,'' J. Acoust. Soc. Am. **66,** 1364–1380.

Viemeister, N. F., and Plack, C. J. (**1993**). ''Time analysis,'' in *Human Psychophysics*, edited by W. A. Yost, A. N. Popper, and R. R. Fay (Springer-Verlag, New York).

Weber, D. L. (**1977**). ''Spectral and temporal integration in auditory detection as a function of masker intensity,'' Doctoral thesis, Harvard University, Cambridge, MA.

Widin, G. P., and Viemeister, N. F. (**1979**). ''Intensive and temporal effects in pure-tone forward masking,'' J. Acoust. Soc. Am. **66,** 388–395.

Zwicker, E. (**1976a**). ''Psychoacoustic equivalent of period histograms,'' J. Acoust. Soc. Am. **59,** 166–175.

Zwicker, E. (**1976b**). ''Masking-period patterns of harmonic complex tones,'' J. Acoust. Soc. Am. **60,** 429–439.

Zwicker, E., and Schorn, K. (**1982**). ''Temporal resolution in hard-of-hearing patients,'' Audiology **21**, 474–492.

A model of auditory streaming

Susan L. McCabe and Michael J. Denham
Neurodynamics Research Group, School of Computing, University of Plymouth, Drake Circus, Plymouth PL4 8AA, United Kingdom

(Received 11 August 1995; revised 6 August 1996; accepted 21 October 1996)

An essential feature of intelligent sensory processing is the ability to focus on the part of the signal of interest against a background of distracting signals, and to be able to direct this focus at will. In this paper the problem of auditory streaming is considered and a model of the early stages of the process is proposed. The behavior of the model is shown to be in agreement with a number of well-known psychophysical results, including the relationship between presentation rate, frequency separation and streaming, the temporal development of streaming, and the effect of background organization on streaming. The principal contribution of this model is that it demonstrates how streaming might result from interactions between the tonotopic patterns of activity of incoming signals and traces of previous activity which feed back and influence the way in which subsequent signals are processed. The significance of these results for auditory scene analysis is considered and a framework for the integration of simultaneous and sequential grouping cues in the perception of auditory objects is proposed. © *1997 Acoustical Society of America.* [S0001-4966(97)02603-9]

PACS numbers: 43.66.Ba, 43.66.Mk [LLF]

INTRODUCTION

The appropriate segmentation and grouping of incoming sensory signals is important in enabling an organism to interact effectively with its environment (Llinas and Pare, 1991). Perception may be seen as essentially a creative act in which an organism creates its interpretation of sensory stimuli within the context of its current state of alertness, attention, and previous experience (Luria, 1980). The creative aspects of perception are exemplified in the auditory system where peripheral processing decomposes acoustic stimuli. Since the frequency spectra of complex sounds generally overlap, this poses a complicated problem for the auditory system: which parts of the signal belong together, and which of the subgroups should be associated with each other from one moment to the next given the extra complication of possible discontinuities and occlusion of sound signals?

It has been argued that the basic aim of the process of segregation, or ''streaming,'' of auditory signals is to associate those sounds emitted from the same source while excluding others, thereby enabling an organism to recognize significant patterns and relationships within a signal, without being confused by accidental coincidences between unrelated signals (Bregman, 1990). Sequential associations between sounds appear to underlie the perception of coherent patterns over extended time frames; the emergence of temporal patterns, including rhythm, melody, and speech, generally occurs within and not across streams.

Over the years there have been many investigations into the phenomena of streaming. Focusing on simple stimuli consisting of alternating pure tones, the influence of frequency separation and tone presentation rate on stream formation was explored, among others, by van Noorden (1975), who identified two thresholds which he called the temporal coherence and fission boundaries. The temporal coherence boundary indicates the frequency separation above which streaming always occurs and decreases with increasing tone presentation rate. The fission boundary, the frequency interval below which integration always occurs, is approximately rate invariant and is always less than the temporal coherence boundary. In other experiments, generally using more complex stimuli, further grouping cues have been identified, including timbre, sound source location, common onset, and harmonicity (Bregman, 1978, 1990; Darwin *et al.*, 1995; Hukin and Darwin, 1995; Darwin, 1981; Moore *et al.*, 1985; Warren, 1982). Teasing out the relative influence of these cues can be difficult and it is important to distinguish between simultaneous grouping cues, such as those just mentioned, and the sequential grouping cues of frequency and temporal proximity, which have been shown to be capable of overriding the formation of groups which might be formed on the basis of common pitch or location, for example (Bregman, 1990; Darwin *et al.*, 1995).

Understanding the way in which streams are formed is an important step in developing a more comprehensive theory of auditory perception. An influential conceptual model of streaming based primarily on Gestalt principles such as common fate, proximity, similarity, and good continuation is described by Bregman (1990). In this model, streaming is seen as a multistage process, in which an initial, preattentive process partitions the sensory input over short time spans, causing successive sounds to be associated depending on the relationship between frequency proximity and presentation rate. It is suggested that further refinement of these sound streams involves the use of attention and memory in the processing of single streams over longer time spans. However, it is not clear how other apparently low level grouping cues such as pitch, timbre, or location interact and contribute to stream formation, nor is the physiological basis for streaming explored in any depth.

More recently attempts have been made to develop computational models of streaming. These models generally use as input a spatiotemporal representation of incoming stimuli

which corresponds to that resulting from auditory peripheral processing; spectral groups and streams are then formed in response to various cues depending on the model. For example, common pitch is used as the primary grouping cue in the models described by Cooke (1992), Brown (1992), and Brown and Cooke (1994). Pitch groups are subsequently tracked by means of pitch trajectories in order to form sequential associations.

The earliest computational model to offer an explanation of streaming in terms of peripheral auditory processes, in contrast to higher level cognitive explanations, is that developed by Beauvois and Meddis (1991). In their model an attempt is made to explicitly identify the basis of primitive streaming in terms of peripheral auditory physiology. Incoming signals are processed by a composite cochlear model. Competitive interactions between the resulting activity in each frequency channel determine the dominant channel and this information is used to gate the output from the model. The judgment of streaming is based on which tones in the input sequence form part of the output sequence. The model is restricted to two channels and the processing of pure tones and does not address the problem of grouping the components of complex sounds. However, it does demonstrate a sensitivity to frequency difference and tone presentation rate and the gradual buildup of streaming similar to that of human subjects.

The coherence of activity within networks of coupled oscillators may be interpreted to indicate both simultaneous and sequential groupings and has been used to model the streaming of complex stimuli (Wang, 1994; Brown and Cooke, 1995). In these multichannel models, sounds belonging to the same stream are distinguished by synchronous activity and components arising from a common source are grouped primarily on the basis of common onset. The relationship between frequency proximity and stream formation is modelled by the degree of coupling between oscillators; this arises either as a result of the distance between nodes in a frequency/time map in Wang's model or from the relative firing rates of different frequency channels in Brown's. Although both models claim a firm basis in auditory physiology, Wang identifies his model with thalamo-cortical processing while Brown's model appears to be located more peripherally. Both models reproduce a number of two-tone streaming experiments with some degree of success, but in neither case have the interactions with other grouping cues been considered.

The model of streaming described here focuses primarily on the formation of sequential associations and suggests a spectral account of streaming rather than one which depends on temporal fine structure. Beauvois' work was used as a starting point and extended to include multichannel processing. Streaming in our model also arises from competitive interactions between frequency channels, but instead of simply halving activity levels in channels other than the dominant one, we use inhibitory feedback signals which result in graded inhibition related to the frequency proximity between input signals. Since previous activity tends to suppress differences in subsequent incoming stimuli, this may be seen as amounting to an implementation of Bregman's ''old+new'' heuristic (Bregman, 1990), which suggests that the auditory system extracts from incoming signals those parts which resemble signals recently received and processes the residual signal separately. In our model, the inclusion of an additional background stream allows the model to output both the dominant stream and the residual activity. As will be demonstrated in Sec. II, it can account for the relationship between streaming and frequency difference and time interval (Beauvois and Meddis, 1991; van Noorden, 1975), the temporal development and variability of streaming perceptions (Anstis and Saida, 1985), and the influence of background organization on foreground perceptions (Bregman and Rudnicky, 1975).

I. A MODEL OF AUDITORY SCENE SEGMENTATION

We have used physiological characteristics of the auditory system and the perceptual model of streaming proposed by Bregman to guide the development of a model of primitive streaming capable of replicating a number of psychophysical experiments. It should be stressed that the model we have developed is one which aims to capture the functionality of auditory processes involved in stream formation, rather than one which makes claim to precise physiological basis. We have, however, attempted to ensure that the model is consistent with auditory processing and think that the insights provided by the model will support the development of a more accurate physiological model in the future.

As input to the model we assume the existence of a tonotopic map in which frequency is represented as a distributed pattern of activity. Although we do not intend to imply that fine temporal detail has no role in the processing of other grouping cues, such as periodicity or direction, it seems that the dependency of streaming on frequency interval can be explained in spectral terms; consequently temporal fine structure is not modeled in these inputs.

The input pattern of activation across the tonotopic axis is represented by a Gaussian function,

$$i(x,t)=a(t)e^{c_1(f_c(x)-f_s)}, \tag{1}$$

where $i(x,t)$ is the probability of activity, $f_c(x)$ the characteristic frequency at position x, f_s is the stimulus frequency, and c_1 is a constant which determines the spread of activation. The relationship between frequency and position is determined by equal spacing within the ERB scale (Glasberg and Moore, 1990).

The time course of the input signal is given by

$$a(t)=c_2+c_3(t-t_0)^{c_4}e^{c_5(t-t_0)}, \tag{2}$$

where t_0 is the starting time of the signal and c_i are constants which determine the temporal envelope of the signal. These constants, shown in Table I, have been chosen so that the spatiotemporal characteristics of the input match the spread of activation and temporal course of activity resulting from summing the output of a composite cochlear model (Patterson *et al.*, 1988; Meddis, 1990) in response to a 50-dB signal in 5-ms chunks; a characteristic primarylike pattern.

Interactions between the excitatory tonotopic patterns of activity reflecting stimulus input and the inhibitory signals resulting from previous activity determine the behavior of

TABLE I. Settings used for the model parameters.

Parameter	Effect	Value
c_1	adjusts the width of the input activation	0.0002
c_2	alters the asymptotic value of $a(t)$	0.4
c_3	alters the maximum value of $a(t)$	2.3
c_4	alters the rise of time of $a(t)$	0.23
c_5	alters the adaptation rate of $a(t)$	-30
V_+, V_-	weights determining the relative influence of the excitatory and inhibitory inputs	40, 3.4
τ_+, τ_-	time constants used to adjust the speed of decay of the excitatory and inhibitory inputs	0.05,0.6
n	width of neighborhood on feedback connections	2
N	number of frequency channels	100

the streaming model. The model consists of two interacting arrays of neurons, the foreground array, F, and background array, B; as shown in Fig. 1. The output from F indicates the activity in the foreground stream, and the output from B reflects any other activity. However, it should be pointed out that the terms foreground and background are used primarily for convenience, analogous to the use of the terms in visual perception. The connectivity of the arrays in entirely symmetrical and which output is actually considered to be foreground and which background may vary, reminiscent of the visual vase-faces illusion (Bregman, 1990).

Interactions between the two arrays eventually ensure that those signals appearing in the output from F, i.e., in the foreground stream, do not appear in the output from B, the background, and vice versa. In models where competitive interactions within a single network are used to model the streaming process, such as that of Beauvois and Meddis (1991), it is difficult to see how the organization of background sounds can be used to improve foreground perceptions as noted by Bregman and Rudnicky (1975) and Dowling *et al.* (1987), since the strengthening of one stream generally serves to weaken others. Here, strengthening of the organization of the background sounds results in the spectral sharpening of the foreground stream due to the enhanced inhibition produced by a more coherent background.

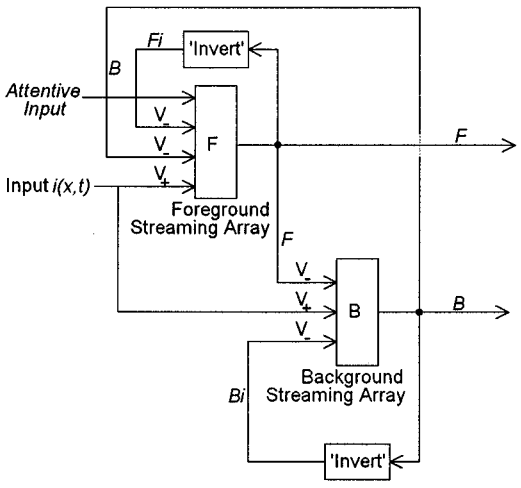

FIG. 1. Model diagram showing the connectivity of the streaming arrays.

In this model stream formation is an automatic, data-driven process, determined by interactions between incoming signals and short term traces of previous activity. The attentive input shown in the diagram is not generally used, but is intended to offer a way in which higher level cognitive processes might influence primitive streaming; the attentive input may be used to speed up or strengthen streaming, or to influence the stream to which a signal is allocated.

Neurons within each of the arrays F and B do not interact directly and with the exception of the calculation of a mean level of activity, processing is restricted to within channel computations. We use a simple leaky integrator neuron model with output representing the probability of firing, as in Beauvois and Meddis (1991).

The inputs to each neuron in the foreground array, F, are

$$\nu_1(x,t) = \left(1 - \frac{dt}{\tau_+}\right)\nu_1(x,t-dt) + V_+\phi(i(x,t))dt, \quad (3)$$

$$\nu_2(x,t) = \left(1 - \frac{dt}{\tau_-}\right)\nu_2(x,t-dt) + V_-\phi(Fi(x,t-dt))dt, \quad (4)$$

$$\nu_3(x,t) = \left(1 - \frac{dt}{\tau_-}\right)\nu_3(x,t-dt) + V_-\phi(B(x,t-dt))dt, \quad (5)$$

where x is the position across the array, t is the time, and dt is the sampling interval. Here, τ_+ and τ_- are the filter time constants which determine the rate of decay of excitatory and inhibitory activity, respectively, V_+ and V_- are the weights on the excitatory and inhibitory inputs, and $\phi(y)$ is a probabilistic function, used to approximate the stochastic properties of nerve cell firing, which returns a value of *1* with uniform probability y, else *0*.

The output activity pattern in the foreground net and its ''inverse'' are then defined by

$$F(x,t) = \sigma[\nu_1(x,t) - \eta(\nu_2(x,t),n) - \eta(\nu_3(x,t),n)], \quad (6)$$

$$Fi(x,t) = \max\left\{\left[\frac{1}{N}\sum_{i=1}^{N} F(x_i, t-dt)\right] - F(x,t-dt), 0\right\}, \quad (7)$$

where $F(x,t)$ is the activity in the foreground array, σ is the sigmoid function, $\eta(\nu(x,t),n)$ is the mean of the activity within neighborhood n of position x at time t, and N is the number of frequency channels. $Fi(x,t)$, which we refer to as the inverse of the activity in F, is the amount by which F at each position across the array falls below the mean level of activity, restricted to positive values. This produces an inhibitory pattern of activity which is strongest where F is least active and weak or zero where F is currently most active. The inputs and resulting outputs from the background, B, are calculated in a similar way, according to the connectivity indicated in Fig. 1.

The behavior of the model can be described as follows. The activity across the tonotopic axis in response to the acoustic stimulus forms an excitatory input, $i(x,t)$, to both the foreground and background streaming arrays, F and B. In addition, F receives inhibitory inputs reflecting the back-

ground activity, $B(x,t)$, which serves to suppress responses in F where B is currently active, and the inverse of the foreground activity, $Fi(x,t)$, which has the effect of suppressing the response to those frequencies where F previously responded least. Similarly, B receives inhibitory inputs reflecting the foreground activity, $F(x,t)$, and the inverse of the background activity, $Bi(x,t)$. The interplay between the excitatory and inhibitory activities causes the model to gradually focus each of the streams and exclude extraneous stimuli. The result of using patterns of inhibitory input to the networks which reflect the distributed patterns of activity in the input signal is that a relationship between frequency difference and streaming arises from the graded inhibition produced by these patterns. The effect of tone presentation rate on streaming is determined by the time constants in the model which can be tuned to alter the rate of decay of activity. The experimental results described in Sec. II below show how these relationships in the model match the characteristics of those observed in psychophysical experiments.

To enable comparisons with the results of psychophysical experiments, we relate the judgment of coherence or streaming made by the model to the correlation between the output patterns of activity with the input to the streaming model. The degree to which the output activity resembles that in the input indicates the degree to which a tone is present in F or B. By comparing the correlation to successive tones in the sequence we obtain a measure of coherence. If the strength of response to each tone is similar, then the signals are considered to be coherent; conversely, if the response to one set of tones is much stronger than to the other, then streaming is judged to have occurred.

The correlation between F and the input to the streaming model ranges between 0, uncorrelated, and 1, correlated, and is given by

$$\mathrm{Corr}(F,i)=\frac{2*\Sigma_{x=1}^{N}F(x,t)*i(x,t)}{\Sigma_{x=1}^{N}F(x,t)^2+i(x,t)^2}, \tag{8}$$

where $F(x,t)$ is the probability of activity in F and $i(x,t)$ is the probability of activity in the input at position x at time t.

The degree of coherence may then be found as a function of the difference between the correlation to successive tones:

$$\mathrm{Coh}_n=1-\frac{|\mathrm{corr}(F_n,i_n)-\mathrm{corr}(F_{n-1},i_{n-1})|}{\mathrm{corr}(F_n,i_n)+\mathrm{corr}(F_{n-1},i_{n-1})}, \tag{9}$$

where n is the tone index. Coh_n ranges between 0, when either $\mathrm{corr}(F_n,i_n)$ or $\mathrm{corr}(F_{n-1},i_{n-1})$ vanishes and the difference between correlations is maximum, indicating maximum streaming effect, and 1, when the correlations are equal and maximum coherence is obtained. Values between these limits are interpreted as the *degree of coherence* and are used in Sec. II as a means of comparison between the model response and the probability of human subjects making a judgment of coherence in the various experiments aimed at investigating primitive streaming. An equivalent measurement of coherence can be found by considering the correlation between activity in B and the input. The degree of coherence measures found on the basis of activity in F and B are generally very similar and in the results which follow we plot a composite measure found by averaging the two.

II. RESULTS

In this section, the behavior of the model is compared with psychophysical results from a range of experiments. The model is shown to be capable of replicating many of the characteristics of streaming perception exhibited by human subjects.

Investigations exploring the effects of frequency interval and tone presentation rate on streaming are described by Beauvois and Meddis (1991). Subjects were required to listen to an alternating sequence of tones, ABABAB... for 15 s, and then to judge whether at the end of the sequence they perceived an oscillating, trill-like, temporally coherent sequence, or two separate streams, one of interrupted high tones, the other of interrupted low tones. The experiments were repeated for a range of frequency intervals and tone presentation rates and their results show clearly an increasing tendency towards stream segmentation both with increasing frequency difference and increasing tone presentation rate. In order to replicate this experiment, the model parameters were set as shown in Table I and the characteristic frequencies of the channels were set to range from 100–2000 Hz. The model managed to substantially reproduce Beauvois' results. In Fig. 2, a clear decrease in coherence, or increase in streaming, with increasing difference in frequency between tones A and B is evident for all tone presentation rates. Similarly, the increase in streaming with decreasing tone presentation rates is also evident.

In investigating the temporal development of stream segmentation, Anstis and Saida (1985) required subjects to indicate continually whether they were perceiving a coherent or streaming signal. The stimulus was similar to that in the experiment described above but the alternating tones were produced by means of a frequency modulated signal, in one case square wave modulation and in the other sine wave modulation was used. The same values of the model parameters were retained, and the response of the model to the stimulus ABAB..., with A=800 Hz and B=1200 Hz recorded. In Fig. 3 the model and experimental results are shown for square-wave and for sinusoidally modulated stimuli. As can be seen, the model reproduces the principal features found in the experiment, i.e., the probability of hearing a single, fused, stream declines during each run; the more rapid the tone presentation rate, the quicker stream segmentation occurs; and square-wave modulation increases streaming as compared to sinusoidal modulation. The variability evident in the model response results from the interpretation of the activity patterns in each of the input arrays as probabilities of firing. However, the model clearly does not reproduce the wide variability evidenced in the experimental results.

Bregman and Rudnicky (1975) describe an experiment aimed at determining whether the organization of the background sounds affects the foreground, and whether, in effect, more than one stream may be formed. Subjects were required

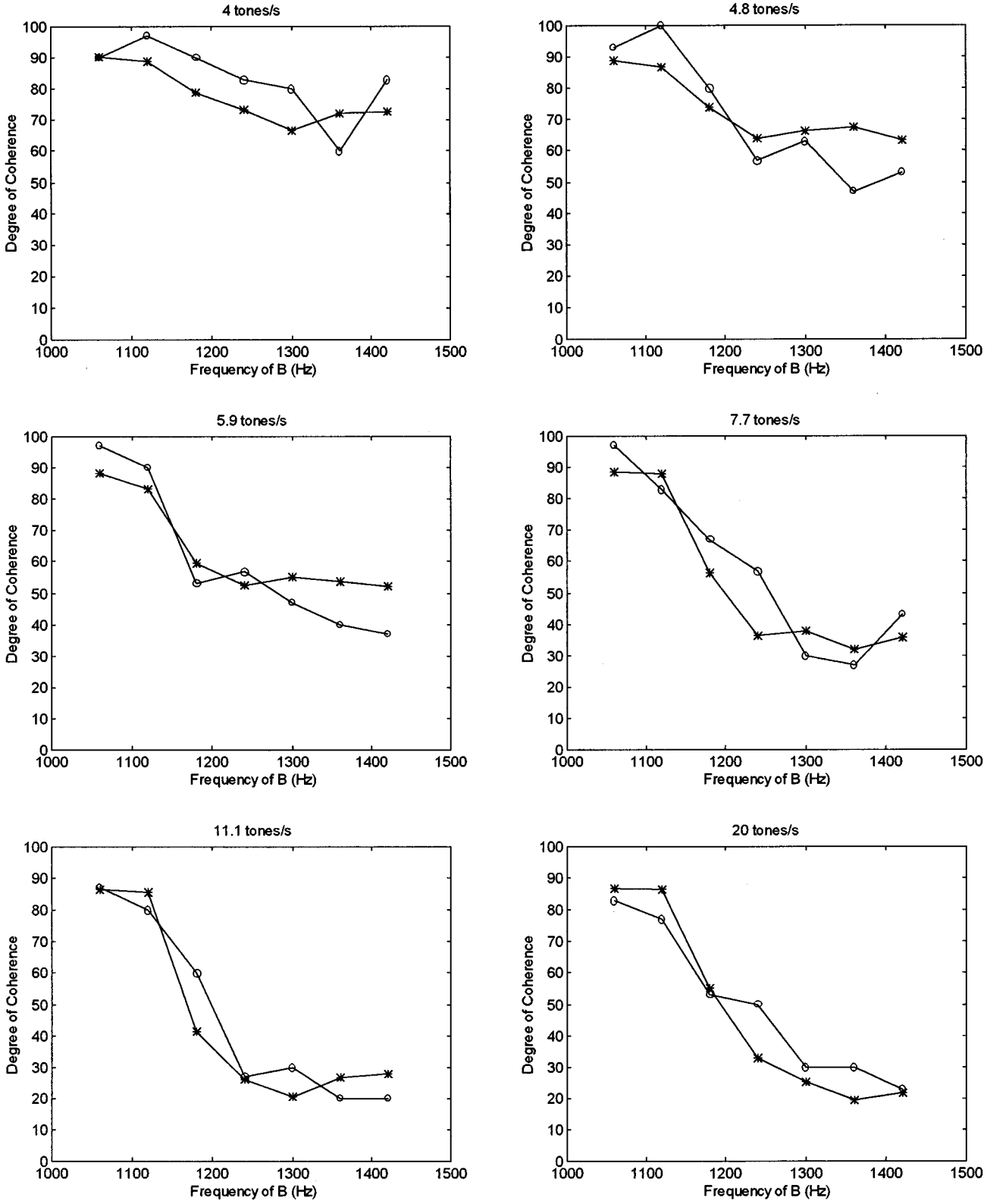

FIG. 2. Plots showing average model, ''*,'' and experimental (Beauvois and Meddis, 1991), ''○,'' results in response to the stimulus ABAB... for each tone presentation rate. The frequency of the A tones was held at 1000 Hz, and the B tones were set to the values 1060, 1120, 1180, 1240, 1300, 1360, and 1420 Hz for each presentation rate. Model results are the mean of 25 runs; parameters used are shown in Table I.

to judge whether tone A was higher or lower than B. This judgment was an easy one to make when the two tones were presented in isolation, but performance degraded significantly when distractor tones, X, were included before and after the AB pair. However, it was found that if a series of captor tones, C, with frequency close to X were added, then the judgment became easier, and the degree of improvement was inversely related to the difference in frequency between

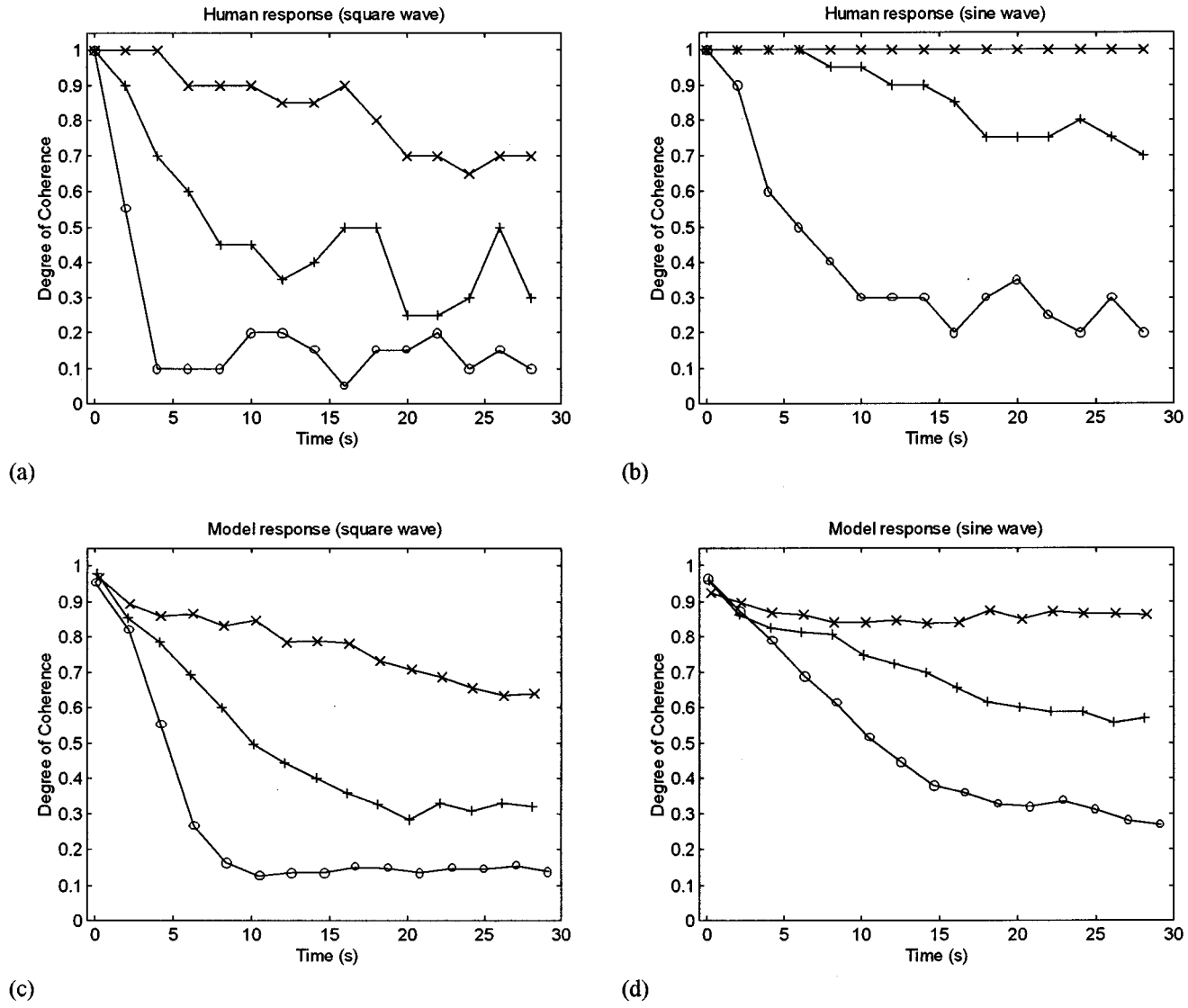

FIG. 3. The probability of perceptual coherence as a function of time in response to two alternating tones, with presentation rates indicated. (a) and (b) Mean human response (Anstis and Saida, 1985). (c) and (d) Mean model response to square- and sine-wave-modulated stimuli. Symbols: ''×''—4, ''+''—8, ''○''—16 tones per second. Plots show mean responses over 25 runs; parameters used are shown in Table I.

X and C. In the experiment, subjects received an initial priming AB stimulus, followed by a set of nine tones: CCCXABXCC, and the frequency of the captor tones was manipulated to investigate how the proximity of captor to distractor tones affected the required AB order judgment.

In order to model this experiment and the effect of attentional priming we use an additional excitatory input focused on the region of the map corresponding to the A and B tones. We have no evidence for such a signal but use a weak pattern of excitation with Gaussian distribution centered halfway between A and B. Characteristic frequencies were adjusted to range from 100–3000 Hz, but the remainder of the model parameters were set as shown in Table I. We assume, as argued by Bregman and Rudnicky (1975), that the subjects' performance in this task is related to the degree to which they are able to segment the sound space and stream the AB pair separately. The model's performance may then be related to the difference between the coherence of the foreground response and the AB pair, as compared to the coherence of the foreground response and the distractor

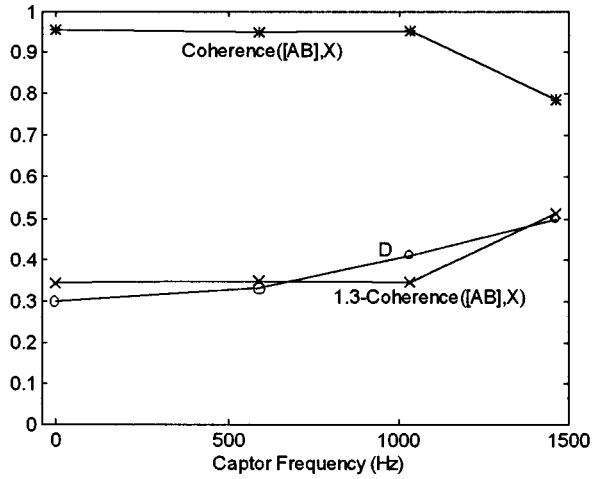

FIG. 4. Responses to the stimulus CCCXABXCC. Symbols: ''*'' indicates the mean degree of coherence to signals XABX; ''○,'' Bregman's D parameter, a measure of the degree to which AB/BA can be discriminated (Bregman and Rudnicky, 1975); ''×,'' a function of the model's judgment of coherence, related to the degree of streaming between X and AB.

tones. The results plotted in Fig. 4 can be seen to exhibit a sensitivity to the distractor/captor frequency difference similar to that of human subjects, and it appears that the decreasing coherence between the AB pair and the X tones and the formation of a coherent background stream can help the model to distinguish the AB group more clearly.

III. DISCUSSION

The model of streaming which we have presented here is essentially a very simple one, which can nevertheless replicate human perception in a number of psychophysical experiments exploring the formation of sequential associations. Embodied in the model is the idea that the characteristics of the incoming sensory signals result in activity which modifies the way in which subsequent signals are processed. The inhibitory feedback signals effectively comprise a short term memory of previous activity which influences the allocation of later inputs to streams. The distributed nature of this inhibition both in time and frequency allows the model to form sequential associations between incoming signals and ones which have occurred recently. For example, when presented with stimuli such as those used in the crossing scales experiment (van Noorden, 1975), illustrated in Fig. 5, the model tends to stream the higher and lower notes separately, resulting in streams containing the bouncing patterns generally perceived by people rather than the alternative crossing patterns which would be perceived if streams were formed on the basis of trajectory.

Processing in much of the auditory system seems to be restricted to processing within frequency channels. In this model, it is shown how local interactions, restricted almost entirely to within-channel activity, can form a global computation of stream formation. The graded inhibition intrinsic in the model results directly from incoming excitation rather than from extensive lateral connections between channels. Summerfield *et al.* (1984) describe an experiment in which people presented with a broad-band noise signal with spectral gaps where the formants of a vowel are usually found, i.e., a signal which is the noise complement of a vowel, will subsequently perceive a vowel after-effect if the signal is followed by broadband noise. As shown in Fig. 6, the vowel components similarly appear in the output in one of the streams when the model is presented with such a stimulus, a consequence of local disinhibition. Because of the slow decay in inhibition, the model also shows a similar insensitivity to the insertion of silent intervals between the vowel complement and broadband noise to that found in Summerfield's experiments. We suggest that similar differences in inhibitory feedback may underlie the phenomenon of mismatch negativity found in ECG recordings in response to auditory oddball stimuli (Naatenen, 1995).

The default condition of the model is to process all sounds equally, i.e., coherence, but as successive signals are received, the feedback of inhibitory activity begins to cause some signals to be preferentially processed. We see this as supporting the view that streaming results from an accumulation of evidence (Bregman, 1990), rather than the breakdown of some integration mechanism (van Noorden, 1975; Jones, 1976; Anstis and Saida, 1985). The explicit inclusion

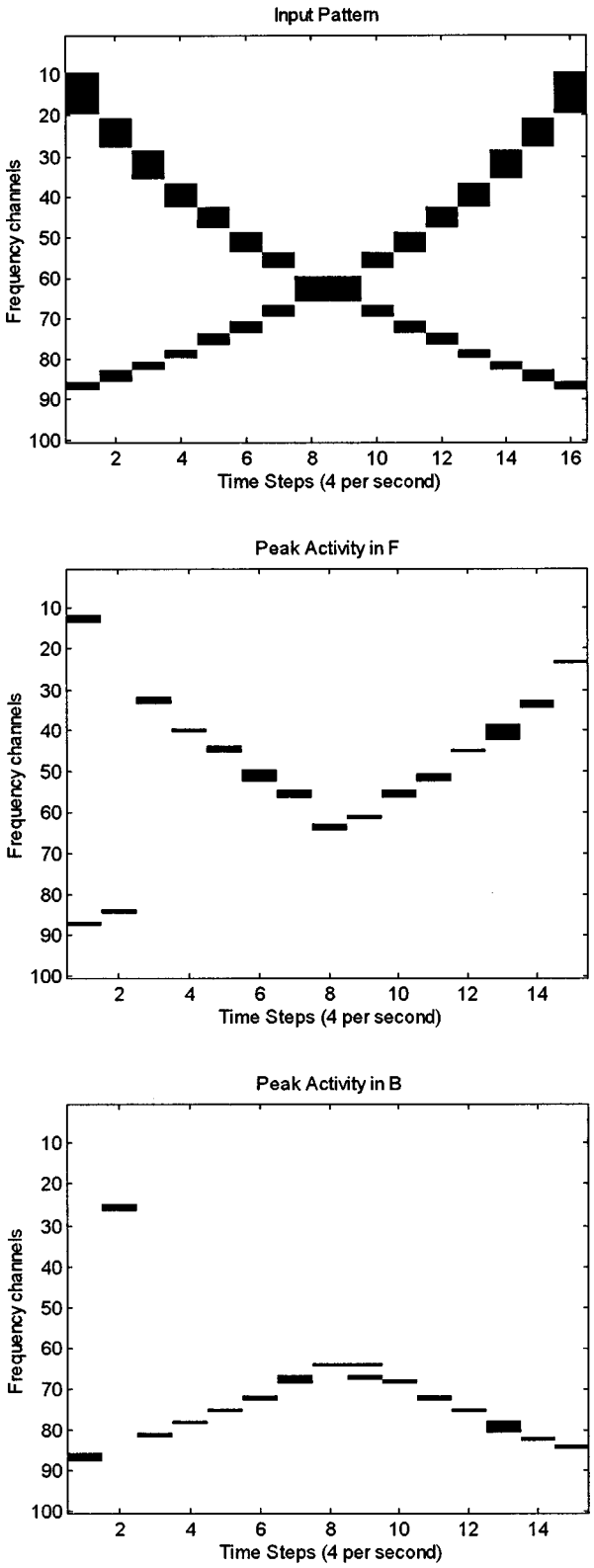

FIG. 5. Model response to a crossing scales input pattern, illustrating the tendency of the model to stream the higher and lower notes separately, resulting in streams containing the bouncing patterns generally perceived by people rather than the alternative crossing pattern which would be perceived if streams were formed on the basis of trajectory. Plots indicate where the level of activity exceeds some threshold.

in the model of foreground and background pathways does not arise from any direct physiological evidence, although multiple tonotopic maps are found without the auditory system so this is not implausible. However, it does give the

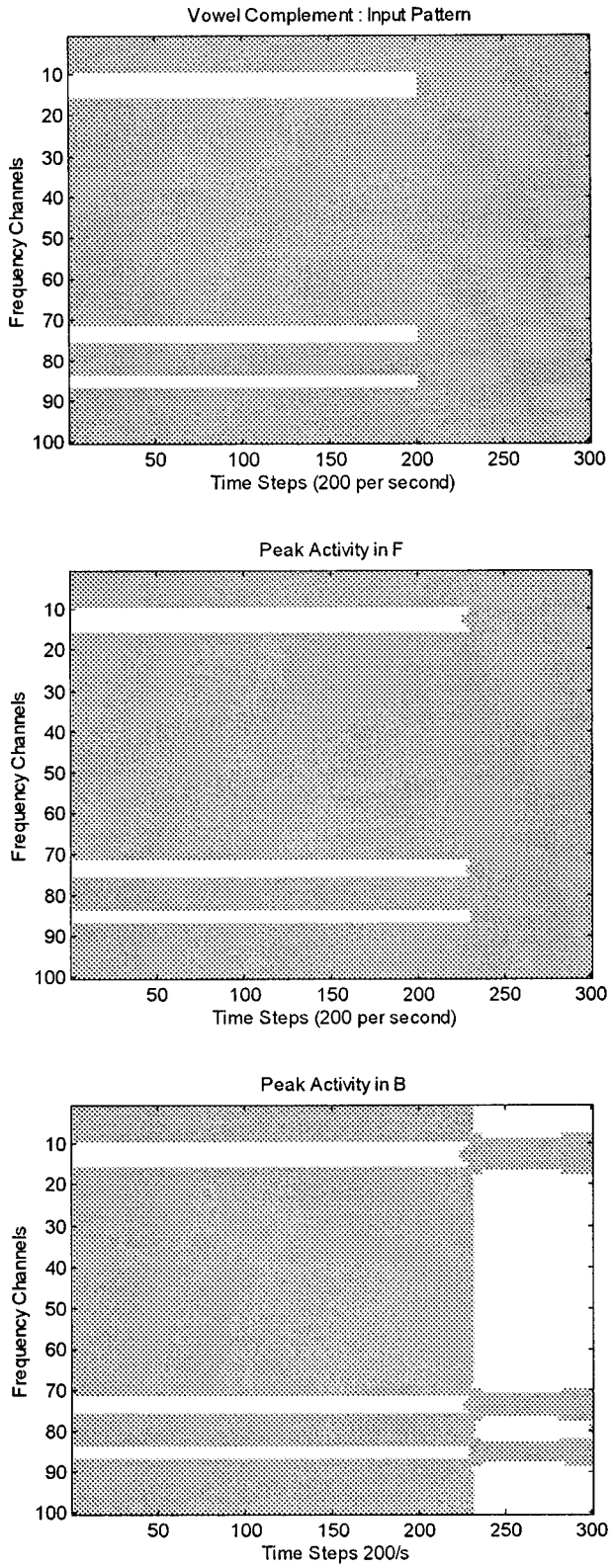

FIG. 6. Model response to a broadband noise signal with spectral gaps, showing the appearance of a complementary pattern when this signal is followed by a uniform broadband noise.

system the ability to switch attention from one stream to another. If only the dominant stream were retained, this would not be possible.

The behavior of the model may be tuned by means of four parameters, the excitatory and inhibitory weights and time constants. As can be seen in Table I, the model relies on relatively weak inhibition. The excitatory weights are an order of magnitude larger than the inhibitory weights. For simplicity all weights in the same class are equal and, since primitive streaming is thought to be an automatic process, no provision for adapting the weights is included. Increasing the weights tends to cause more rapid streaming and decreasing them ultimately eliminates streaming; the model is particularly sensitive to the inhibitory weight. The time constants determine the rate of decay of excitatory and inhibitory activity and were chosen to give a good match to Beauvois' experimental data, resulting in an excitatory time constant approximately ten times shorter than the inhibitory one.

Although we have not attempted to model the details of the auditory system, the model is broadly consistent with auditory physiology. The primary auditory pathway is fast, excitatory, and tonotopically organized and there is evidence for longer lasting inhibitory activity (Creutzfeldt *et al.*, 1980). However, in adjusting the model to produce behavior consistent with human perception, it became apparent that the resulting time constants of 50 and 600 ms were more consistent with the temporal processing of auditory signals within cortical rather than peripheral areas (Greenberg, 1996), in contradiction with Beauvois' argument for a more peripheral basis for streaming (Beavois and Meddis, 1991).

IV. IMPLICATIONS FOR AUDITORY SCENE ANALYSIS

An underlying assumption in Beauvois' model was that activity in those frequency channels present in a stream is higher than that in other channels. Our model is similarly based on this assumption; consequently if we consider those parts of the spectrum in which activity exceeds some suitable threshold we can determine which frequency components are in the same stream, an aspect used in producing Figs. 5–7. Another effect of the time constants discussed above is that the model tends to groups those parts of the frequency spectrum with concurrent low frequency modulation and this grouping is evident in the peaks of activity in the output from F or B. In addition, as previously pointed out, the model may also be seen to encapsulate Bregman's ''old+new'' heuristic. This gives rise in the model to an interplay between streaming on the basis of frequency proximity and grouping on the basis of concurrent low-frequency modulation, a phenomenon similarly noted by Bregman (1990). We illustrate this behavior in Fig. 7 in an experiment where the stimulus consists of alternating pure tones and complex sounds. If the pure tone corresponds to one of the components in the complex, then the model tends to stream the common component separately from the complex, leaving the residual components in the other stream. However, if the pure tone does not match any of the complex components, then grouping on the basis of concurrent low-frequency modulation prevails and the pure tone and complex tones may eventually fall into separate streams.

We would argue that the simultaneous grouping of disparate parts of the frequency spectrum results primarily from primitive streaming along the lines we have described, i.e., greater intensity and concurrent low-frequency modulation, and not from other cues such as common pitch or direction.

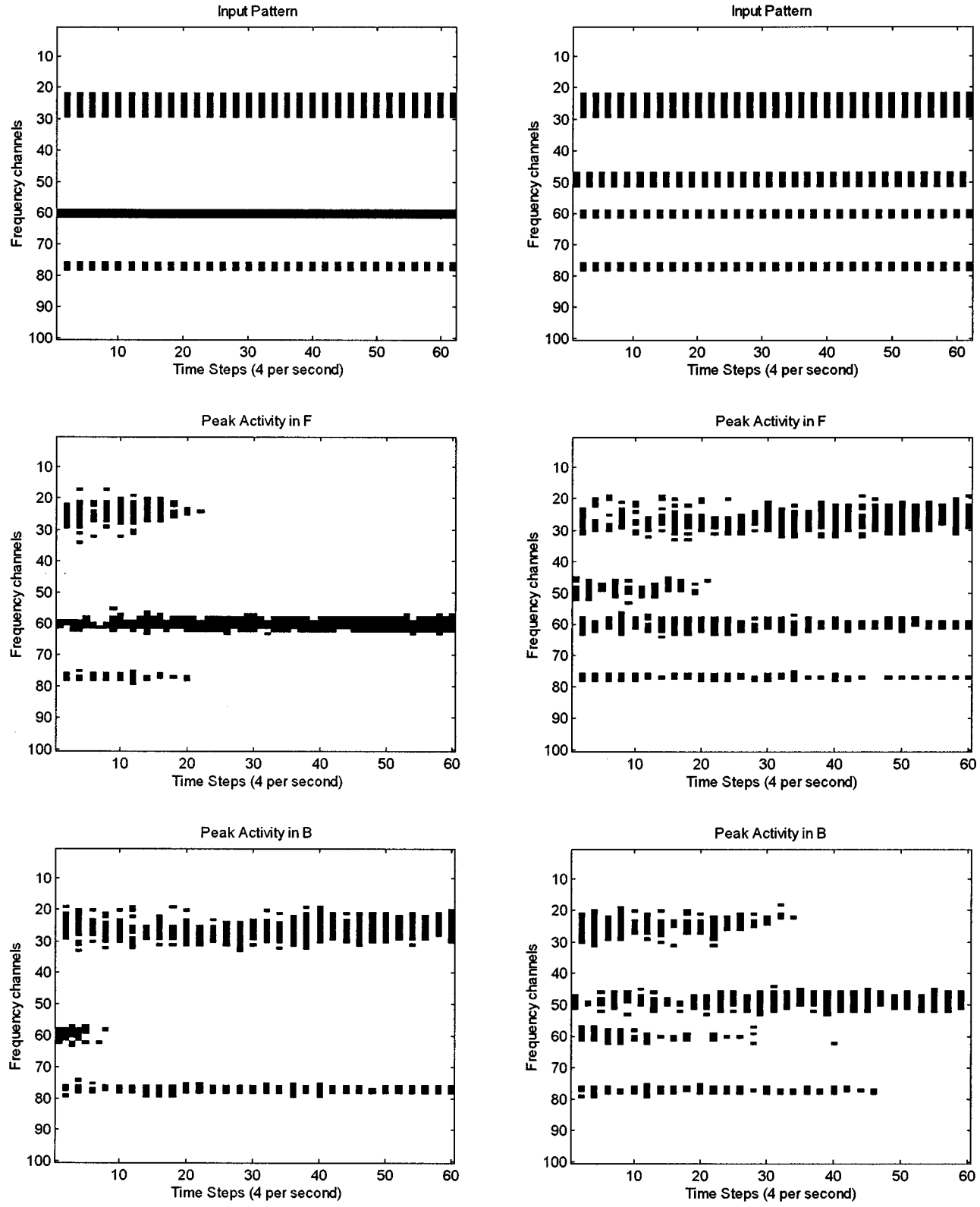

FIG. 7. A demonstration of the ''old+new'' heuristic (Bregman, 1990) using alternating pure tone and complex stimuli. Plots in column 1 show the model's response when the pure tone corresponds to the second component in the complex tone. Plots in column 2 show the model's response when the pure tone differs from the second component in the complex tone. In the first case, the central component and pure tone fall into one stream and the residual complex tone falls into the other stream; in the second case the complex tone is streamed separately from the pure tone and the streams take much longer to form.

We suggest that the within-channel computations of periodicity and direction which take place subcortically are not used as grouping cues and that the pitch and direction of a complex sound may actually be computed at the cortical level across those channels which are contained in a stream, in effect a weighted summary autocorrelation similar to that proposed by Meddis and Hewitt (1991). This would help to explain why primitive streaming has been found in numerous

cases to override the grouping which would otherwise have resulted from the use of common periodicity or direction. For example, in the crossing scales experiment of Fig. 5, even presenting one ear with the descending scale and the other ear with the ascending scale fails to produce the perception of crossing scales (Deutsch, 1975). Darwin *et al.* (1995) have also shown that primitive streaming can effectively remove a harmonic from a complex sound and in the case of a mistuned harmonic, the presence or absence of the harmonic affects the pitch percept.

The model of streaming presented here resembles the first stage in Bregman's concept of a two-stage process; the first, data driven and automatic, the latter, affected by attention and higher cognitive processes (Bregman, 1990). The model offers a way to incorporate attentional effects and could be extended to include the preferential processing of recognized sounds or sounds of interest. Although aspects of auditory streaming have been found to be quite automatic, it would be wrong to ignore the influence of higher level attentive or memory-based processes on the processing of incoming signals and we would argue that the formation of auditory expectations may be an intrinsic aspect of auditory processing.

While there have been experiments suggesting that at least three streams may be formed and separately manipulated (Warren, 1982), it seems that this depends on the use of binaural stimuli and we think that there may be another explanation for this phenomenon. Suga (1996) has reported finding combination sensitive neurons in the thalamus of the bat which only respond to particular sequences of sounds. These neurons effectively recognize components common in bat calls. It seems reasonable to suppose that such neurons may also be found in the human thalamus, and there is some evidence for phoneme discrimination in the thalamus (Kraus *et al.*, 1994). If the signals to each ear are carefully manipulated as they were in Warren's experiment, components of phonemes could be timed to activate these neurons whether they were presented to the same or different ears. The recognition of such phonemes may not therefore necessarily be a result of primitive streaming, although the concatenation of phonemes into syllables may be determined by streaming. The question of how many streams there actually are remains an open one, but while there is no reason in principle why the model cannot be extended to include more streams, the evidence for more than two streams is not very strong. Perhaps primitive streaming only segregates sounds into two streams within which memory and attentional processes act in order to build perceptions of discrete sounds.

V. CONCLUSION

An important aspect of intelligent sensory processing is the ability to focus on signals of interest against a background of distracting signals, thereby enabling the perception of significant temporal patterns. An artificial sensory system which could form sequential associations between the sounds emitted by a particular source and stream those signals separately from other background sounds could act as a useful preprocessor for other systems, such as automatic speech recognizers, which require the dynamic extraction and temporal linking of subsets of the overall signal in order to perform robust and sensible pattern recognition. The model we have described may form an important step in this process. In addition, the opportunity to influence the streaming process by means of an attentive input may allow higher level processes to focus on the target of interest.

ACKNOWLEDGMENTS

We would like to thank Dr. Guido Bugmann and two anonymous reviewers for their helpful comments on earlier drafts of this paper. We would also like to thank Ray Meddis, Steve Greenberg, Neil Todd, and others at the recent ESCA workshop for comments and discussions which helped clarify some of the ideas expressed in this paper.

Anstis, S., and Saida, S. (**1985**). ''Adaptation to auditory streaming of frequency-modulated tones,'' J. Exp. Psychol. **11**(3), 257–271.

Beauvois, M. W., and Meddis, R. (**1991**). ''A computer model of auditory stream segregation,'' J. Exp. Psychol. **43**(3), 517–541.

Bregman, A. S. (**1978**). ''Auditory streaming and the building of timbre,'' Can. J. Psychol. **32**(1), 19–31.

Bregman, A. S. (**1990**). *Auditory Scene Analysis* (MIT, Cambridge, MA).

Bregman, A. S., and Rudnicky, A. I. (**1975**). ''Auditory segregation: stream or streams?,'' J. Exp. Psychol. **1**(3), 263–267.

Brown, G. J. (**1992**). ''Computational auditory scene analysis: A representational approach,'' University of Sheffield Research Reports, CS-92-22.

Brown, G. J., and Cooke, M. (**1994**). ''Computational auditory scene analysis,'' Comput. Speech Lang. **8**, 297–336.

Brown, G. J., and Cooke, M. (**1995**). ''Temporal synchronisation in a neural oscillator model of primitive auditory stream segregation,'' Proc. IJCAI Workshop on Computational Auditory Scene Analysis, Montreal, 40–47.

Cooke, M. P. (**1992**). ''An explicit time-frequency characterization of synchrony in an auditory model,'' Comput. Speech Lang. **6**, 153–173.

Creutzfeldt, O., Hellweg, F. C., and Schreiner, C. E. (**1980**). ''Thalamocortical transformation of responses to complex auditory stimuli,'' Exp. Brain Res. **39,** 87–104.

Darwin, C. J. (**1981**). ''Perceptual grouping of speech components differing in fundamental frequency and onset-time,'' Q. J. Exp. Psychol. **33**, 185–207.

Darwin, C. J., Hukin, R. W., and Al-Khatib, B. Y. (**1995**). ''Grouping in pitch perception: Evidence for sequential constraints,'' J. Acoust. Soc. Am. **98,** 880–885.

Deutsch, D. (**1975**). ''Two channel listening to musical scales,'' J. Acoust. Soc. Am. **57,** 1156–1160.

Dowling, W. J., Lung, K. M., and Herrbold, S. (**1987**). ''Aiming attention in pitch and time in the perception of interleaved melodies,'' Percept. Psychophys. **41**(6), 642–656.

Glasberg, B. R., and Moore, B. C. J. (**1990**). ''Derivation of auditory filter shapes from notched noise data,'' Hear. Res. **47**, 103–138.

Greenberg, S. (**1996**). ''Understanding speech understanding: towards a unified theory of speech perception,'' *Proceedings of the ESCA Workshop on the Auditory Basis of Speech Perception* (Keele, United Kingdom), pp. 1–8.

Hukin, R. W., and Darwin, C. J. (**1995**). ''Comparison of the effect of onset asynchrony on auditory grouping in pitch matching and vowel identification,'' Percept. Psychophys. **57**(2), 191–196.

Jones, M. R. (**1976**). ''Time, our lost dimension: Toward a new theory of perception, attention, and memory,'' Psychol. Rev. **83**(5), 323–355.

Kraus, N., McGee, T., Carrell, T., King, C., Littman, T., and Nicol, T. (**1994**). ''Discrimination of speechlike contrasts in the auditory thalamus and cortex,'' J. Acoust. Soc. Am. **96,** 2758–2768.

Llinas, R. R., and Pare, D. (**1991**). ''Commentary: Of dreaming and wakefulness,'' Neuroscience **44**(3), 521–535.

Luria, A. (**1980**). *Higher Cortical Functions in Man* (Basic, New York).

Meddis, R. (**1990**). ''Implementation details of a computational model of the inner hair-cell/auditory-nerve synapse,'' J. Acoust. Soc. Am. **87,** 1813–1816.

Meddis, R., and Hewitt, M. J. (**1991**). ''Virtual pitch and phase sensitivity of a computer model of the auditory periphery. I. Pitch identification,'' J. Acoust. Soc. Am. **89,** 2866–2882.

Moore, B. C. J., Glasberg, B. R., and Peters, R. W. (**1985**). ''Thresholds for the detection of inharmonicity in complex tones,'' J. Acoust. Soc. Am. **77,** 1861–1868.

Naatanen, R. (**1995**). ''The mismatch negativity: A powerful tool for cognitive neuroscience,'' Ear Hear. **16**(1), 7–18.

Patterson, R. D., Holdsworth, J., and Nimmo-Smith, I. (**1988**). ''SVOS Final Report: The Auditory Filterbank,'' APU Report 2341.

Suga, N. (**1996**). ''Basic acoustic patterns and neural mechanisms shared by humans and animals for auditory perception: a neuroethologist's view,'' *Proceedings of the ESCA Workshop on the Auditory Basis of Speech Perception* (Keele, United Kingdom) pp. 31–38.

Summerfield, Q. R., Haggard, M., Foster, J., and Gray, S. (**1984**). ''Perceiving vowels from uniform spectra: Phonetic exploration of an auditory aftereffect,'' Percept. Psychophys. **35**(3), 203–213.

van Noorden, L. P. A. S. (**1975**). ''Temporal coherence in the perception of tone sequences,'' Doctoral dissertation, Institute for Perception Research, P. O. Box 513, Eindhoven, NL.

Wang, D. L. (**1994**). ''Auditory stream segmentation based on oscillatory correlation,'' *Proceedings of the IEEE Workshop on Neural Networks for Signal Processing*, IEEE (Piscataway, NJ), pp. 624–632.

Warren, R. M. (**1982**). *Auditory Perception: A New Synthesis* (Pergamon, New York).

Musical pitch perception with electrical stimulation of the cochlea[a)]

Hugh J. McDermott and Colette M. McKay
Department of Otolaryngology, The University of Melbourne, c/o The Bionic Ear Institute, 384-388 Albert Street, East Melbourne, 3002, Australia

(Received 20 November 1995; revised 28 October 1996; accepted 6 November 1996)

Studies were undertaken to investigate the ability of a user of the Nucleus multi-electrode cochlear implant to judge pitch in the context of musical intervals. The subject had qualified as a musical instrument tuner before he received his implant, and was able to judge the intervals between electrical sensations with neither training nor the guidance of familiar melodies. The procedures used were interval estimation, and interval production by the method of adjustment. The pitch of the electrical stimulation was controlled by varying the pulse repetition rate, the active electrode position, or two combinations of these parameters. Further studies employed sinusoidally amplitude modulated pulse trains with varying modulation frequency. The results showed that rate or modulation frequency could convey musical pitch information over a limited range (approximately two octaves). The data were directly comparable with the relationship between musical intervals and frequency for normal hearing. The pitch related to electrode place varied in accordance with the tonotopic organization of the cochlea, and also appeared to be able to support musical intervals. When both place and rate varied together, the place-related pitch was generally dominant. In all cases, the judgement of intervals tended to diverge from their acoustic counterparts as the intervals became larger. [S0001-4966(97)04203-3]

PACS numbers: 43.66.Ba, 43.66.Fe, 43.66.Hg, 43.75.Cd [LLF]

INTRODUCTION

The study of how musical sounds are perceived through a cochlear implant is both interesting and informative. Now that advanced sound processing strategies (Wilson *et al.*, 1991; McDermott *et al.*, 1992) are providing many implant users with considerable ability to understand speech, research is broadening to address additional issues, including the perception of music (see, for example, Gfeller and Lansing, 1991) and other environmental sounds. One of the fundamental components of music is pitch, which can be operationally defined as that attribute of sound that carries melodic information. Investigation of pitch perception in a musical context has the potential to add significantly to the expanding body of knowledge about the percepts produced by electrical stimulation of the cochlea. It may also lead to the development of improved sound processors for cochlear implants that can enhance users' enjoyment and understanding of music. In particular, because the ability to recognize melodies depends on pitch perception, improving the way processors code aspects of sound signals that convey pitch information would most likely prove beneficial.

A special difficulty faced by the researcher in this area is that relatively few people have sufficient knowledge of musical terminology, or experience in judging musical pitch relationships. One solution to this problem (Pijl and Schwarz, 1995) is to make use of portions of familiar melodies as exemplars of pitch intervals (e.g., the first ascending interval in ''Twinkle, Twinkle, Little Star'' is a fifth). However, this imposes several constraints on the experimenter: first, only a few different intervals occur in the most easily recognized tunes; second, it is hard to isolate the pitch perceived for a specific interval from confounding effects, such as the rhythm or the overall pitch contour of the melody; and third, it is difficult to identify enough suitable tunes with which most implant users are familiar. Moreover, it is reasonable to doubt the accuracy of a person's memory for pitch intervals, even in the context of well-known melodies, particularly if he or she has endured a long period of auditory deprivation before receiving a cochlear implant. For example, Pijl and Schwarz (1995) reported that the only subject out of 17 implantees who was unable to recognize any of 30 rhythmically intact popular melodies had been deaf for 25 years prior to implantation.

In our laboratory, we have conducted small-scale studies of melody and pitch interval recognition with several implant users over a number of years. Recently, we have been fortunate to be able to work with one implant user who had received formal training as an instrument tuner. Currently he is the only implantee available locally who is able to judge pitch intervals reliably without specific training or the support of familiar melodies. The studies described below report the results obtained with this subject in experiments which investigated how pitch changed when several parameters of the electrical stimulation were varied.

Many previous psychophysical studies have reported on the effects of changing the rate of pulsatile stimulation or the intracochlear location to which it is delivered (Simmons, 1966; Bilger, 1977; Eddington *et al.*, 1978; Tong *et al.*, 1979; Hochmair-Desoyer *et al.*, 1981; Shannon, 1983; Dobie and Dillier, 1985; Tong and Clark, 1985; Townshend *et al.*,

[a)]Portions of these data were presented at the 131st meeting of the Acoustical Society of America, Indianapolis, Indiana, May 1996 [J. Acoust. Soc. Am. **99**, 2584(A) (1996)].

1987; Dorman *et al.*, 1990; Busby *et al.*, 1994; McDermott and McKay, 1995; Nelson *et al.*, 1995). When these parameters are varied, subjects are generally able to rank the sensations along a ''low-to-high'' or ''dull-to-sharp'' dimension, and usually describe the sounds as differing in pitch. The pitch increases with the rate of stimulation (delivered to a fixed location) up to a rate of about 200–1000 Hz. Beyond this value, which varies across electrodes and implantees, increases in the rate usually produce little or no change in the pitch. At very low rates, below about 50 Hz, subjects describe the sound as a buzz or flutter that does not seem to have a well-defined pitch. The smallest variation in rate that produces a change in pitch varies considerably across electrodes and among implantees, but is generally at least 2%. On the other hand, pitch variation is also perceived when the stimulation rate is held constant and the place of stimulation is changed by selecting different electrodes. This pitch generally corresponds with the tonotopicity of the cochlea, such that stimulation at apical locations gives rise to low-pitched sensations, while basal stimulation is perceived as high pitched.

More recent studies have investigated the pitch sensations produced by sinusoidally amplitude-modulated (SAM) pulse trains (McKay *et al.*, 1994). These stimuli, usually delivered to a single cochlear position, consist of a constant-rate pulse train in which the current levels are sinusoidally modulated within the dynamic range of hearing at that electrode position, such that all component pulses are audible. The pitch characteristics of SAM stimuli with varying modulation frequency are similar to those of constant-amplitude pulse trains with varying rate, at least for large modulation depths (see McKay *et al.*, 1995). The perceived pitch corresponds to the modulation frequency up to about 200–300 Hz, provided that the carrier rate is either much higher than (at least four times) the modulation frequency, or a constant multiple of the modulation frequency.

There are differences, however, between the pitch described by subjects in experiments of this sort and musical pitch as defined above. Changes in most stimulation parameters, including the site of delivery, rate, or SAM modulation frequency, often cause changes in subjective sound quality or timbre. Variations in some aspects of timbre are often described loosely as changes in pitch, and can also be ranked along a low-to-high dimension. To determine whether melodic pitch can be conveyed by controlling the parameters of electrical stimulation, it is helpful to perform experiments in which subjects respond in musical terms. With acoustic hearing, frequency ratios can be labeled as musical intervals by knowledgeable subjects. For example, a fifth corresponds nominally to a frequency ratio of 1.5:1, and an octave to a ratio of 2:1. In principle, a similar interval labeling scheme can be used for electrical stimulation using a cochlear implant. Data obtained in this way can be compared directly with the established attributes of normal hearing, providing a powerful insight into the pitch characteristics of intracochlear electrical stimulation.

A number of psychoacoustic experiments have been reported on musical pitch perception by normally hearing subjects. It is well known that very small frequency differences can be detected in sinusoids, and that subjects with some musical training can reliably adjust frequency ratios to a given interval. For example, Ward (1954), reporting on octave adjustments performed by nine musically trained subjects, found a mean intra-observer standard deviation of about 10 cents. (A cent is that frequency ratio corresponding to 1/100 of a semitone. In the standard equal-tempered musical scale, a semitone corresponds to a defined frequency ratio of close to 1.0595:1, and one cent corresponds to a ratio of 1.000 578:1.) However, performance with other types of stimuli can be significantly poorer. Burns and Viemeister (1976, 1981) investigated whether the modulation frequency of sinusoidally amplitude-modulated (SAM) noise could convey melodic pitch. They found that two musically trained subjects could adjust the modulation frequency to produce target intervals, but with standard deviations of approximately 50–100 cents, compared with an average standard deviation of 37 cents for the same tasks using pure tones. The results of these experiments imply that melodic pitch can be conveyed by temporal characteristics of an acoustic stimulus, even in the absence of spectral cues.

There appear to be few published reports on musical pitch perception by cochlear implantees. Moore and Rosen (1979) reported preliminary results obtained with one subject who had a single-channel extracochlear implant. The subject was able to recognize several well-known tunes, suggesting that melodic information was being conveyed by the temporal pattern of the stimulation. Similar observations have also been reported for other cochlear-implant designs (Simmons, 1966; Chouard, 1978; Eddington *et al.*, 1978; Hochmair-Desoyer *et al.*, 1981). Recently, Pijl and Schwarz (1995) described a series of experiments investigating musical pitch perception by a small number of users of the Nucleus Mini System 22 cochlear implant. The stimuli comprised pulse trains delivered to one electrode pair at a time; thus, pitch was controlled exclusively by variations in the pulse rate. The three most relevant experiments all required subjects to label a presented pitch interval as flat, in tune, or sharp, relative to a given target. The results were analyzed to estimate the pulse rate ratios corresponding most closely to the target intervals. In the first experiment, all stimuli were delivered to an apical electrode, and four intervals (300, 500, 700, and 900 cents) with different rates representing the lower ''notes'' (137, 145, 163, and 127 Hz, respectively) were presented. The mean responses for each of the three subjects were generally within 1 semitone (100 cents) of the correct response expected for each of the intervals. The remaining experiments used a similar procedure in which the target interval was always 700 cents. The second experiment required the subjects to label intervals which had been transposed by shifting the rate representing the lower note down one octave to 81 Hz (relative to the previous condition), and up one octave to 326 Hz. All subjects responded with rate ratios that became smaller as the lower note's rate was increased (with an average change of −120 cents/oct). The third experiment held the lower note's rate constant at 100

Hz, but changed the site of delivery from the apical electrode used previously to two positions shifted 4.50 mm and 9.75 mm in the basal direction. The mean responses for two of the subjects showed little effect of electrode position, although the third subject's responses showed a tendency toward smaller rate ratios for more-basal electrodes. However, subjects indicated that the tasks were least difficult and the sounds were most pleasant and ''musical'' for pulse trains delivered to the most-apical electrode at moderately low rates (around 100–200 Hz). Overall, the results of these experiments strongly support the assertion that temporal patterns can provide sufficient pitch information for accurate melodic interval recognition, at least for some implantees.

The specific objectives of the experiments reported below were to extend the results for pitch perception with varying rates of stimulation, and to investigate the pitch produced when the place of stimulation was varied, with either a constant rate, or a related change in rate. In addition, the pitch associated with SAM pulsatile stimulation was studied, with either a fixed carrier rate, or a constant ratio between the carrier rate and the modulation frequency. These fundamental parameters of pulsatile electrical stimulation are all of those that, on current knowledge, might be expected to convey adequate pitch information for recognition of musical melodies.

I. METHODS

A. Subject

The subject was a 36-year-old man who, in addition to being an enthusiastic amateur musician, had considerable experience both estimating and adjusting pitch while working as a qualified piano tuner. Having a serious visual impairment since birth, he had chosen to study instrument tuning in a formal course of 4 years duration provided by the Royal National Institute for the Blind in the United Kingdom. The techniques taught in this course included judgment of relative pitch, as well as interval tuning based on perception of beats (which may occur when two notes are sounded simultaneously). Thus he had some prior experience relevant to the psychophysical tasks described below, in which stimuli were always presented sequentially rather than simultaneously. His hearing loss was of mixed conductive and sensorineural origins, and progressed in both ears over a period of 25 years. Recurrent infections on the right side necessitated a radical mastoidectomy in 1991, and a cholesteatoma was surgically removed in May 1992. He had a cortical mastoidectomy on the left side early in 1992, and subsequently received a Nucleus Mini System 22 cochlear implant in that ear. Immediately prior to the implant surgery, a clinical evaluation yielded a response at only one frequency (120 dB HL at 750 Hz) within the limits of the audiometer. Postoperatively all of the electrodes of the implant were found to be functional, although the four most-basal electrodes are deactivated in his sound processor because they produce unpleasant sensations. The sound processor he uses currently is a SPECTRA-22 programmed with the SPEAK coding strategy, with which he obtains above average performance in speech recognition tests. For example, in a recent open-set test using recorded monosyllabic words presented by hearing alone, he achieved an average score of 74% whole words correct. He commenced involvement in the research reported below early in 1994.

B. Stimuli

The three electrical stimulation parameters investigated in the experiments were pulse repetition rate, frequency of SAM pulse trains, and location of the active electrode. All stimuli were presented as trains of biphasic pulses with an overall duration of 500 ms, and each pulse had a phase duration of 150 μs. The current levels were set to produce comfortable loudness for all stimuli. The electrodes were configured as bipolar pairs with a spacing between members of each pair of 2.25 mm (or 3 electrode rings); this is often referred to as the BP+2 mode (Patrick and Clark, 1991). The electrodes are numbered from 1 to 22 in a basal-to-apical direction, and each pair will be denoted below by the number of its more-basal member.

In the pulse rate experiments, a single electrode pair was used to deliver stimuli in which only the pulse repetition rate was varied. To determine whether the location of the electrode pair had a significant effect, three electrodes were tested: in the apical (electrode 19), middle (electrode 12), and basal (electrode 5) regions of the electrode array.

In the experiments investigating the effect of modulation frequency of SAM pulse trains, two types of stimuli were tested. In the first the carrier pulse rate was constant at 1200 Hz, and in the second a constant ratio of exactly 4:1 was maintained between the carrier rate and the modulation frequency. It was considered important to test both types of SAM stimuli to take account of sampling artifacts, similar to beats, which can occur when the carrier rate is not either a multiple of the modulation frequency, or very much higher than it (see McKay *et al.*, 1994). The modulation depth was set such that the ratio of the highest to the lowest currents in the SAM stimuli equalled the subject's dynamic range from comfortable to threshold loudness, which was measured using unmodulated pulse trains at the appropriate rate. The stimuli were delivered to electrodes 19, 12, and 5 in different trials, as in the pulse rate experiments.

In the electrode position experiments, a pulse train at a constant rate of 250 Hz was delivered to a selected electrode pair. The location of the active pair was varied among all positions between, and including, electrode 18 and electrode 6. In two further tests, the pulse rate and the electrode position were varied together, as described below.

C. Procedures

To determine the range of rates over which changes (presumably in pitch) could be discriminated by the subject, rate difference limens (DLs) were obtained on electrodes 5, 12, and 19. A two-alternative forced-choice procedure was used. The subject heard two stimuli of equal loudness at rates chosen by the experimenter, and was asked to indicate which had the higher pitch. For each reference rate tested, the rate of the comparison stimulus was varied, and the proportion of responses for the higher-rate stimulus having the higher pitch

was obtained. A total of 32 responses for each stimulus pair were collected. The response ratios were converted to z scores and interpolated logarithmically to find the rate difference corresponding to a response ratio of 75%. This rate difference, expressed as a percentage of the reference rate, was recorded as the difference limen. The same procedure was used to obtain DLs for modulation frequency with the two types of SAM stimuli.

The remaining experiments investigated musical pitch perception. Where possible, two complementary procedures were used to try to compensate for any systematic bias in the subject's responses. These were interval production and interval estimation.

In the production procedure, the subject heard a reference stimulus followed after a gap of 250 ms by a variable stimulus, and was asked to adjust the pitch of the variable stimulus to obtain the specified interval. The two stimuli repeated continually with a delay of 1.0 s between each repetition while the subject made the adjustment, using a multiturn, unmarked knob. The subject was instructed to approach the target pitch from both above and below before converging on a final setting. When pulse rate or modulation frequency was the varying parameter, the rate or frequency of the reference note was chosen randomly in each trial to prevent the subject from merely repeating a previous setting without judging the interval afresh. The reference rate or frequency was chosen from a set covering the range 60–160 Hz in 10-Hz steps. The intervals tested included minor thirds (nominal value: 300 cents), fourths (500 cents), fifths (700 cents), and octaves (1200 cents). Responses were obtained from at least 8, and usually 10, trials for each interval in each condition. Interval production could not be performed with varying electrode position, however, because position can be altered only by selecting the active electrode. Even adjacent electrodes were found to produce generally large changes in pitch, which made adjustment difficult. Furthermore, the abrupt changes in pitch perceived during adjustment would have permitted the subject to choose settings by counting the number of electrode steps encompassed by each interval, thus confounding the results. This problem did not occur in the rate production experiments because of the continuous relation between pitch perceived and stimulation rate.

In the estimation procedure, the subject heard two stimuli in sequence, separated by 500 ms of silence. The subject was asked to name the musical interval between the two sounds. He was told that he might hear any interval, including intervals that did not correspond exactly with those of the conventional musical scale, and that his response should describe as accurately as possible the interval that he heard. If necessary, he was permitted to hear the stimuli repeated before giving a response. Descending intervals were not tested, because, during a preliminary exploration, the subject reported that he was trying to imagine the higher note transposed one octave down, and then estimating the size of the complementary ascending interval. To avoid this complication, the pulse rate, modulation frequency, or electrode position of the second stimulus in each pair was constrained to be higher or more basal than that of the first, according to which parameter was being varied. Unison intervals were not tested.

In each estimation experiment, a set of 13 stimuli was constructed. For each trial, the two stimuli to be presented were selected at random from the set, subject to the constraint just mentioned. When pulse rate was the variable parameter, the 13 stimuli were based on all the semitones in one equal-tempered octave; i.e., the rates increased by a constant factor of 1.0595. The lowest rate in the set was 100 Hz, and the highest was 200 Hz. A similar stimulus set was used for the SAM pulse trains, in which the modulation frequency was the variable parameter. In these cases, all stimuli were delivered to electrode 12. When electrode position was the parameter under investigation, each of the stimuli in the set used one of the 13 electrodes between electrode 18 and electrode 6. In two tests, both the rate and the electrode position varied among the stimuli. A preliminary exploration showed that pitch perception was dominated by the place of stimulation, so in these experiments, the electrode position varied from apical to basal while the corresponding rates either increased or decreased. The stimulus set with increasing rates comprised the 13 equal-tempered semitones between 100 Hz (most apical electrode) and 200 Hz (most-basal electrode). The set with decreasing rates also encompassed one octave, with 200 Hz on the most-apical electrode, and 100 Hz on the most-basal electrode. Again, the stimuli were selected for each trial so that only ascending intervals were heard. For each stimulus set, one response was obtained for each of the 78 possible pairs of stimuli. The responses were recorded as the number of cents, rounded to the nearest 50, in the pitch interval.

It was considered important to equalize the loudnesses among the stimuli to minimize the influence of any loudness irregularities on the task of judging the pitch intervals. For the experiments involving varying rates on a single electrode, no significant loudness differences were apparent across the relatively small range of rates tested. However, when the electrode position varied within a stimulus set, large loudness differences would have occurred for a constant current level. Consequently, the loudness of each stimulus was balanced to that of a central reference stimulus on electrode 12. The method of adjustment was used, in which the subject heard the variable stimulus alternating continually with the reference, and adjusted the current level of the variable stimulus using an unmarked rotary knob to obtain approximately equal loudnesses. A final check was made by presenting all of the stimuli to be tested sequentially in groups of four to ensure that they were perceived as equally loud.

All stimuli were presented to the subject using a personal computer interfaced with a speech processor executing specifically designed software; they were not generated acoustically or processed by a speech-processing strategy. At no time was any training provided to the subject, nor any feedback as to the accuracy or consistency of his responses.

II. RESULTS

The difference limens for rate obtained on the three electrodes tested are listed in Table I. The results show values of

TABLE I. Difference limens for rate of pulsatile stimuli.

Electrode	Rate (Hz)	DL (%)
19	50	1.8
	100	7.5
	200	11.3
	300	11.3
	400	>40
12	50	1.5
	100	3.1
	150	3.8
	200	11.3
	250	>40
5	50	3.4
	100	4.4
	200	5.4
	300	9.4
	400	13.8
	500	>40

less than 15% for low rates, and a sharp increase in DL at a rate that varies somewhat among electrodes. In the context of musical intervals, these values can be compared with the frequency ratio corresponding to one semitone, which is 5.9% approximately. The DLs indicate that the range over which a semitone rate change would be discriminable is less than about two octaves.

The DL results for modulation frequency of the SAM stimuli (Table II) show similar characteristics. For each condition tested, the DL for 200-Hz modulation is higher than that for 100-Hz modulation. Most DLs are less than 5%, and only one is greater than 15% (200-Hz modulation with 1200-Hz carrier on electrode 19).

For unmodulated stimuli, the lowest rate at which the subject reported hearing a clear pitch, rather than ''roughness,'' was found to be close to 60 Hz on all electrodes tested. This and the DL data were used in establishing the range of rates employed in the pitch estimation and production procedures. As stated above, a range of 100–200 Hz was used in the estimation experiments, while in the production experiments the range of reference rates used was determined partly by the size of the target interval. For example, lower reference rates were selected for the largest target interval (one octave), so that the subject was less likely to try to adjust the rate in a region with large DLs.

TABLE II. Difference limens for modulation frequency of sinusoidally amplitude-modulated pulse trains.

Electrode	Carrier rate	Modulation frequency (Hz)	DL (%)
19	1200 Hz	100	3.5
		200	26.7
	$4\times f_M$	100	3.0
		200	9.4
12	1200 Hz	100	4.1
		200	4.2
	$4\times f_M$	100	1.7
		200	5.0
5	1200 Hz	100	3.5
		200	12.9
	$4\times f_M$	100	4.1
		200	5.5

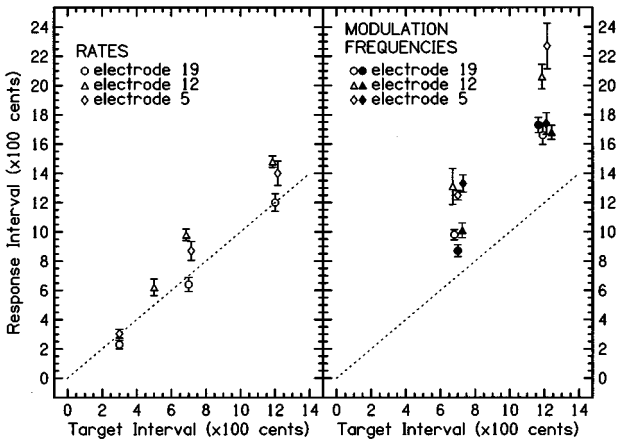

FIG. 1. Results of the interval production experiments for three electrodes. Each data point is the mean of at least eight trials, and the error bars represent plus and minus one standard error of the mean. The diagonal line indicates the pattern of results expected for acoustic frequencies and normal hearing. Left panel: unmodulated pulse trains with stimulation rate as the variable parameter. Right panel: sinusoidally amplitude-modulated pulse trains with modulation frequency as the variable parameter. Open symbols: carrier rate constant at 1200 Hz. Filled symbols: carrier rate maintained at four times the modulation frequency. Some symbols are offset horizontally for clarity.

Turning to the pitch interval production experiments, the averaged results with stimulation rate as the variable parameter are shown in the left panel of Fig. 1. All of the intervals produced are larger than, or very close to, their nominal equal-tempered values. For each condition, a *t*-test was applied to aid comparison of the production results with the target intervals. The responses that did not differ significantly from the targets ($p>0.05$) are for the three intervals tested on electrode 19, the smallest interval (500 cents) on electrode 12, and the smallest interval (300 cents) on electrode 5. The remaining four conditions, which include the larger intervals on the more-basal electrodes, resulted in responses significantly larger than the targets.

The results for SAM stimuli with variable modulation frequency are in the right panel of Fig. 1. All of the intervals produced with SAM stimuli are significantly larger than the targets, with the differences being generally greater than those for varying rates of unmodulated stimuli. No overall differences are evident between the results for the SAM stimuli having a fixed (1200-Hz) carrier rate compared with those having a constant ratio between the carrier and modulation frequencies. However, it is interesting that the subject noticed fluctuations in the sound quality, apparently similar to acoustic beats, only in the fixed carrier rate stimuli as he altered the modulation frequency.

The results for the interval estimation experiment with varying rates are plotted in Fig. 2 (left panel). Each data point is the average of all responses obtained for each presented interval (except for the three largest intervals, for which each estimate is plotted separately). The results for the smaller intervals are generally close to the values expected

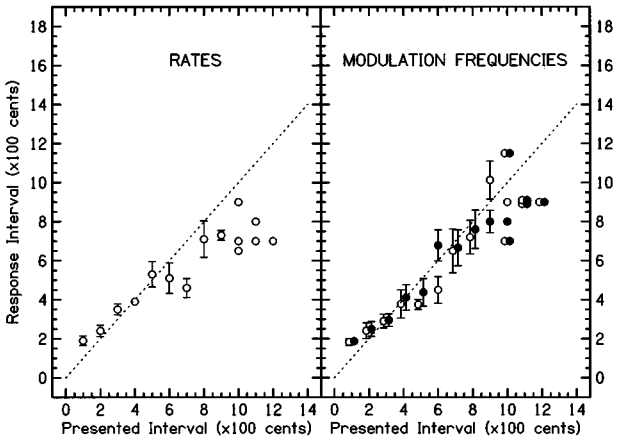

FIG. 2. Results of the interval estimation experiments for temporal pitch. For presented intervals between 100 and 900 cents, each data point is the mean of between 4 and 12 trials (see text), and the error bars represent plus and minus one standard error of the mean. For the remaining intervals (1000–1200 cents), each of the subject's responses is plotted individually. The diagonal line indicates the pattern of results expected for acoustic frequencies and normal hearing. Left panel: unmodulated pulse trains with stimulation rate as the variable parameter. Right panel: sinusoidally amplitude-modulated pulse trains with varying modulation frequency. Open symbols: carrier rate constant at 1200 Hz. Filled symbols: carrier rate maintained at four times the modulation frequency. Some symbols are offset horizontally for clarity.

nominally for normal hearing, and have relatively small standard errors. Clearly, however, the responses to the larger intervals are significantly smaller than expected. They also exhibit larger standard errors, but this may be a side effect of the different number of estimations obtained for each interval, as explained above. On the other hand, this trend is consistent with the subject's comments that larger intervals were more difficult to judge than smaller intervals.

A very similar pattern of responses was obtained for estimation using SAM stimuli (Fig. 2, right panel). Again, the judgments of the largest intervals are smaller than would be expected and exhibit greater variability. The tendency for the results to approach a plateau toward the largest intervals suggests that some response bias was occurring when the subject experienced particular difficulty forming a judgment. An examination of the individual responses seemed to confirm this, showing a tendency for the subject to avoid labeling any intervals as being larger than about a major sixth.

Figure 3 shows the results for interval estimation when electrode position was the varying parameter. In the left panel the results are for constant rate, in the center panel for increasing rates, and in the right panel for decreasing rates. Note that the abscissa represents the separation between the two electrodes used to present the interval; it does not indicate their location in the cochlea. As with the data of Fig. 2, a different number of responses are included in each average plotted. The results show a generally monotonic trend of increasing interval size with increasing electrode separation. Concurrent rate changes in the same direction did not seem to increase the size of the interval perceived, but they may have made the pitch more salient resulting in less variance in the subject's responses. Rate changes in the opposing direction resulted in a smaller overall change in pitch. However, in these two conditions the subject's responses were affected much more by changes in the place of stimulation than by changes in the rate.

III. DISCUSSION

Overall, the results for musical pitch perception mediated by rate of pulsatile stimulation support and extend those reported previously (Pijl and Schwarz, 1995). The pitch in-

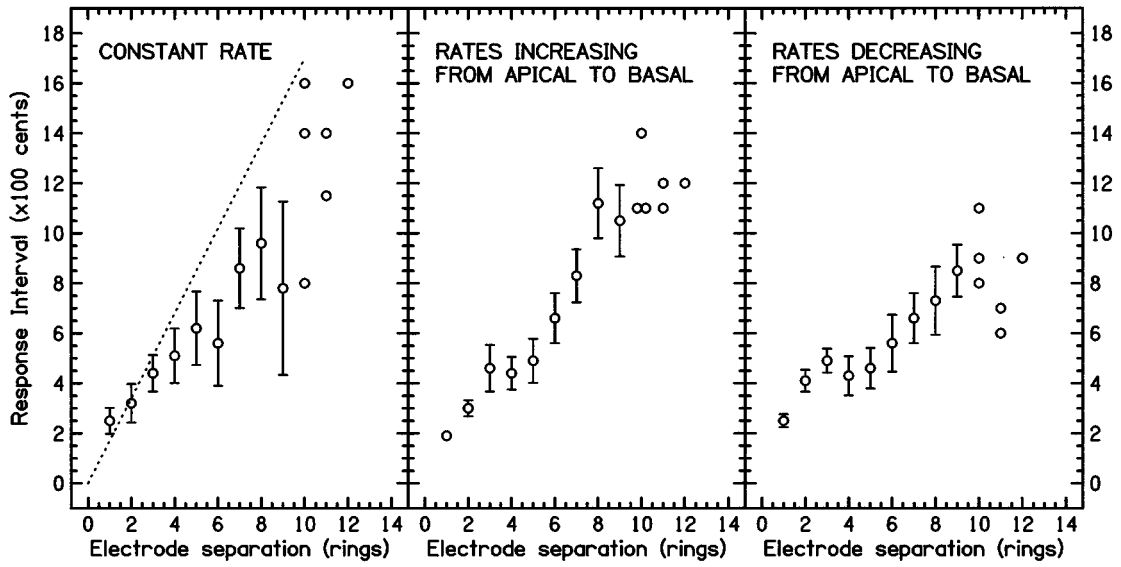

FIG. 3. Results of the interval estimation experiments for place-related pitch. For presented intervals between 100 and 900 cents, each data point is the mean of between 4 and 12 trials (see text), and the error bars represent plus and minus one standard error of the mean. For the remaining intervals (1000–1200 cents), each of the subject's responses is plotted individually. The electrode separation represented on the abscissa is in terms of the number of rings, which are spaced at intervals of 0.75 mm. Left panel: stimuli presented at a constant rate of 250 Hz. Center panel: stimuli with rate increasing from 100 to 200 Hz toward more basal electrode positions. Right panel: stimuli with rate decreasing from 200 to 100 Hz toward more basal electrode positions. The dotted line in the left panel indicates the approximate relationship between characteristic frequency of residual neurons and electrode position.

tervals produced by varying the modulation frequency of SAM pulse trains are comparable with those for rate, but diverge further from those expected for analogous acoustic stimuli and normal hearing, as discussed below. The results for varying place of stimulation are more difficult to interpret, but suggest that place of stimulation may be able to convey musical pitch in a similar fashion to the temporal parameters of stimulation.

The rate DL results are consistent with data previously published (e.g., Simmons, 1966; Bilger, 1977; McKay *et al.*, 1994), and show that stimulation rate is of limited utility for conveying a range of musical pitch sensations. The variation across electrodes could be an effect of nonuniform neural survival, differences in electric current distributions, or other factors. The results are comparable with those establishing the existence region for pitch when amplitude-modulated noise is presented to listeners with normal hearing (Burns and Viemeister, 1976). This suggests that the auditory system is capable of extracting pitch from the temporal aspects of either electrical or acoustic stimulation (in the absence of spectral cues) only up to about 300–600 Hz.

The pitch production results for rate indicate that a similar pitch interval is perceived for rate of electrical stimulation as for acoustic frequency in normal hearing. The closest similarity was obtained with electrode 19, perhaps because the relatively low place-related pitch of this apical electrode was in better concordance with the rate-related pitch. The data that differ significantly from their acoustic equivalents are all overadjustments. In this respect they are similar to the phenomenon observed in many subjects with normal hearing, who tend to select a frequency ratio greater than 2:1 when producing the interval of one octave (e.g., Ward, 1954; Dobbins and Cuddy, 1982), and similarly stretch other large intervals (Rakowski and Miskiewicz, 1985). However, the overadjustments in our data are much larger in many instances than those reported for normal hearing. It is noteworthy that these data are consistent with the corresponding pitch estimation results, which show that the perceived intervals tended to be smaller than the presented intervals (rate ratios), in those cases where they were not approximately equal.

These results can be compared directly with those reported by Pijl and Schwarz (1995), summarized earlier. In their data the size of the rate ratio perceived as the interval of a fifth decreased as the stimulation rate of the lower note was increased. The lowest rates they tested (81 and 100 Hz) are close to the corresponding mean rates used in our experiments (both production and estimation). Their results show that two of the three subjects selected a rate ratio of greater than 700 cents in these cases, consistent with the results obtained in our experiments. On the other hand, much of the data reported by Pijl and Schwarz was obtained with higher rates for the lower note, resulting in rate ratios that were often smaller than the equivalent frequency ratios expected for acoustic hearing. To verify this trend, we conducted an additional rate production experiment with our subject, using rates for the lower note in the range of 140–220 Hz (on electrode 5). A mean response of 570 cents was obtained for the fifth, in contrast to 870 cents for the lower rates, as shown in Fig. 1.

This apparent relation between perceived interval size (for a given rate ratio) and rate of the lower note, is counterintuitive, in that the rate-pitch DLs increase (usually steeply) at higher rates. One might expect that larger DLs would more likely lead to overadjustments in interval production experiments, as the subject would attempt to adjust the rate in a region where little change in pitch would result. Although Pijl and Schwarz did not report DL data in their paper, evidence from a melody recognition experiment (their Fig. 2) suggests that the two subjects who showed this unexpected trend most strongly would have had large DLs at the higher rates, in common with the majority of implantees. The authors speculated that the rate dependence of the pitch interval perceived may have been the result of differences in neural firing patterns between electrical and acoustic stimulation. At high electrical stimulation rates, the average neural spike rate may have been higher than would be expected for acoustic stimulation at the same frequencies. This assumes the electrical stimuli produced spikes on every pulse, while acoustic stimuli would have produced phase-locked neural responses, but without a spike for every period. The resulting conflict between actual and expected spike interval distributions would somehow result in a central interpretation of pitch that increased more rapidly with rate for electrical than for acoustic stimulation. However, the authors did not suggest any details of the underlying mechanism.

An alternative, and possibly more satisfactory, explanation for this phenomenon is as follows. The increase in DLs with stimulation rate indicates that the temporally encoded pitch is becoming less salient. On the other hand, the place-related pitch is present even at relatively high rates, and tends to dominate the percept when both place and rate of stimulation are varied (see Fig. 3). Evidence from the electrode insertion depth data (see below) implies that the place pitch of the most apical electrode is most likely somewhat higher (around 1000 Hz) than the highest discriminable rate pitch (around 200–500 Hz). Therefore, as the rate is increased, it is likely that the place pitch becomes relatively more salient, creating a rapid change in the quality of the percept as the rate enters the large-DL region. Such an interaction between rate and place pitches may induce subjects to choose smaller rate ratios at higher rates, as observed.

In another study, one user of the Ineraid cochlear implant was able to match the pitch of an acoustic signal in his unimplanted ear (which had usable low-frequency hearing) to that of a sine wave presented electrically to one electrode at a time (Dorman *et al.*, 1994). The matches were closest for the most-apical electrode (e.g., mean match of 135-Hz acoustic to 125-Hz electrical), and shifted to progressively higher acoustic frequencies for the same electrical frequency on more-basal electrodes (e.g., approximately 320-Hz acoustic for 125-Hz electrical on the most-basal electrode). To facilitate comparison with the results obtained in our experiment, we calculated from the published data the intervals encompassed by the acoustic frequencies which were matched to electrical frequencies in a given ratio. These intervals were approximately correct for stimuli delivered to

the most-apical electrode, but became smaller for more-basal electrodes. While it is possible that the subject had abnormal pitch perception in his unimplanted ear, it is interesting that this trend of decreasing interval size for more-basal electrodes is also evident in our results.

The results for SAM pulse trains show generally similar characteristics to those for rates of unmodulated stimuli. The interval production responses are all larger than the equivalent acoustic frequency ratios, especially for the larger intervals and the constant carrier rate condition. The responses that are closest to the equivalent acoustic ratios are those for the most-apical electrode tested, electrode 19. In a previous study (McKay *et al.*, 1994) it was found that the pitch of SAM pulse trains depended in a complex way on both the modulation frequency and the carrier frequency, as well as on indeterminate factors that were specific to each subject. The interval production data of Fig. 1 are not inconsistent with the reported results of that study.

The results of the pitch estimation experiments generally support and extend those of the production experiments. The tendency for the responses to approach a plateau for the larger presented intervals (e.g., Fig. 2) suggests that the subject had more difficulty judging pitch intervals when there was a large difference between the electrical parameters of the two ''notes.'' Most likely this was because there were distracting changes in qualities of the sensations other than pitch, such as timbre. For example, the subject described some sounds as ''crackly,'' and occasionally likened the two sounds forming an interval with two notes played on different stops of a pipe organ.

The interval estimates for changing place of stimulation indicate that the place-related pitch is more salient than the rate-related pitch when a rate change accompanies the place change. The slope of the data did not increase when a rate change in the same direction was combined with the place change (Fig. 3). However, when the rate change was reversed relative to the place change, the slope of the data was reduced, suggesting that although the place pitch is dominant, there is some interaction between the effects of rate and place variations. A previous study of the perceptual dissimilarities of combinations of electrode position and pulse rate (Tong *et al.*, 1983) also found the interaction between these two parameters to be small.

To interpret the place-related pitch in terms of its acoustic equivalent, the characteristic frequencies corresponding to the positions of the electrodes were estimated using a postoperative x ray of this subject's implant (Cohen *et al.*, 1996). The predicted pitch change was approximately 170 cents per electrode position, which is in broad agreement with the experimental results, at least for the smallest intervals (see Fig. 3). However, because the procedure relies on several assumptions and estimated parameter values, the calculated characteristic frequencies can be regarded only as approximations. For example, there is no way of specifying precisely which auditory neurons are most susceptible to stimulation from each electrode pair in our subject, nor how the residual neurons are distributed spatially along the cochlear spiral.

It is also possible that changing the place of stimulation resulted in an orderly change in some quality of the percept other than pitch (as narrowly defined here). If so, the data of Fig. 3 could be essentially ranking results consistent with those reported previously from experiments without a musical context (e.g., Busby *et al.*, 1994; Nelson *et al.*, 1995; McDermott and McKay, 1995). In general, a similar interpretation could be made of data obtained from any perceptual estimation experiment with a limited number of stimuli. It is unfortunate that, in the case of stimuli varying in electrode position, it was not possible to complement the pitch estimation results with production data, as explained earlier. However, some support for the assertion that the estimation data represent musical pitch (rather than the ranking of some other quality) can be found in the observed dominance of place pitch over rate pitch. If only temporal aspects of the signal were conveying musical pitch, the data plotted in Fig. 3 would be expected to follow the rate of stimulation (at least in direction of change) rather than the place, as was actually (and unexpectedly) the case. Nevertheless, further research is required to define more exactly the roles in pitch perception played by rate and place of stimulation, and to investigate their interactions.

Although the experimental data were obtained with computer-generated signals, it is also interesting to examine the appropriateness of the frequency to place mapping in the subject's sound processor. One question is whether the mapping would be expected to produce perceived intervals that are correct in terms of the corresponding acoustic frequency ratios. The SPECTRA-22 processor, programmed with the SPEAK sound coding strategy, assigns acoustic frequencies linearly for the apical half of the electrode array, and on a logarithmic scale for the basal half. This means that the frequency ratios for adjacent electrodes decrease along the lower-pitched electrodes, and then remain constant with increasing frequency. The constant-ratio region encompasses electrodes 5–14 inclusive, over which the equivalent acoustic pitch change would be approximately 250 cents per electrode position. For example, electrode 12 would deliver most stimulation for an input pure tone at 1890 Hz, and electrode 11 for 2170 Hz, which corresponds to an acoustic interval of 240 cents, or slightly more than a whole tone. This frequency-to-pitch function is steeper than the slope of the interval estimation results we obtained psychophysically. However, it does not necessarily follow that an unnaturally compressed range of pitch would be perceived when sounds are heard through the processor. Other differences between processed sounds and the experimental stimuli, such as activation of multiple electrodes, representation of spectral shape information, and the simultaneous presence of temporal features including periodic amplitude modulation, would be expected to affect the overall pitch perceived.

Finally, there is the issue of whether the experimental results can be generalized, given that this one subject has exceptional ability to judge musical pitch. For example, considering his etiology and medical history, there is the possibility that he still possesses operative hair cells. If so, it is conceivable that electrophonic mediation of the electrical stimulation could enhance his performance in extracting pitch, particularly from temporal properties of the stimulus

waveform. However, the evidence of the basic psychophysics indicates that he has no better than average abilities at discriminating either stimulation rates or electrode positions. (To compare his results with those of other users of the same implant, see McKay *et al.*, 1994; McDermott and McKay, 1995.) Therefore, it seems reasonable to assume that his exceptional abilities do not arise from any extraordinary functional characteristics at the peripheral level, but rather from his extensive pre-implant training and experience in closely related tasks.

IV. CONCLUSIONS

These experiments have investigated the ability of a musically trained cochlear implant user to judge the pitch of electrical stimuli. In this research, the term ''pitch'' is defined specifically as that attribute of a hearing sensation which conveys melodic information. It was found that the pitch perceived depended on the temporal properties of the stimulation and on the intracochlear location to which the stimulation was delivered. Stimulation rate, or modulation frequency of amplitude-modulated pulse trains, affected pitch in a way that was comparable with that of acoustic frequency in normal hearing. However, the pitch was relatively weak and could be varied only over a narrow range; in these respects it was similar to the pitch of amplitude-modulated noise heard acoustically. The place-related pitch varied in accordance with the tonotopic organization of the cochlea. When place and rate changes occurred in combination, the pitch was more affected by the place of stimulation, although the rate also had a slight effect.

To conclude, it is worthwhile considering how the results of the above experiments may be applied to the development of improved sound processing strategies for cochlear implants. The finding that musical pitch can be conveyed by controlling the rate of pulsatile stimuli delivered to a single electrode suggests that it may be effective to convert the estimated pitch of acoustic signals to pulse rate. Such a technique was employed in a series of processors developed previously for the Nucleus implant (Patrick and Clark, 1991). However, those processors were designed specifically to estimate the fundamental frequency of speech, and it is uncertain how they would perform with complex musical sounds. Furthermore, the place of stimulation varied rapidly, according to the estimated speech formant frequencies, possibly reducing the perceived salience of the rate-pitch cue. This probably explains the generally poor performance on musical perception tasks reported for some users of these processors (Gfeller and Lansing, 1991). A processor design more appropriate for musical sounds might involve controlling the rate at a fixed electrode position.

The two obvious limitations associated with the use of rate are the narrow pitch range (approximately two octaves in our experiments), and the difficulty of presenting multiple pitches simultaneously. It is possible that those problems could be overcome by distributing pulses across several electrodes (see, for example, McKay and McDermott, 1996). However, there is a need for further research into the perceptual effects of varying stimulation place to determine more conclusively whether it affects musical pitch directly, as our results seem to suggest, or whether it could be used more effectively to represent some other aspect of the acoustic signal, such as its spectral shape.

Another possibility for presenting multiple pitches at one or more electrode positions might be to use high-rate pulse trains modulated with complex waveforms (rather than the sine waves used in our experiments). Research is required to investigate whether implant users are able to perceive multiple frequency components within the modulation. Also, an assessment of the performance of the current sound processing strategy with musical sounds would be valuable. Because the SPEAK strategy distributes amplitude-modulated, constant-rate pulsatile stimuli across electrodes according to the spectral envelope of incoming acoustic signals, it is likely to provide implantees with better perception of music than its predecessors, as users' subjective appraisals have indicated (Skinner *et al.*, 1994). Clearly, however, there remains considerable scope for improving sound processor design.

ACKNOWLEDGMENTS

Special thanks are due to our subject, who devoted considerable time and patient effort to this research. We thank Professor Graeme Clark, Dr. Lawrie Cohen, and Pam Dawson, who also contributed significantly. Dr. Ed Burns and an anonymous reviewer made constructive suggestions on an earlier version of the manuscript. Financial support was provided by the Australian Research Council's Special Research Centre, ''The Human Communication Research Centre,'' and the Bionic Ear Institute.

Bilger, R. C. (**1977**). ''Psychoacoustic evaluation of present prostheses,'' Ann. Otol. Rhinol. Laryngol. **86** (Suppl. 38), 92–140.

Burns, E. M., and Viemeister, N. F. (**1976**). ''Nonspectral pitch,'' J. Acoust. Soc. Am. **60,** 863–869.

Burns, E. M., and Viemeister, N. F. (**1981**). ''Played-again SAM: Further observations on the pitch of amplitude-modulated noise,'' J. Acoust. Soc. Am. **70,** 1655–1660.

Busby, P. A., Whitford, L. A., Blamey, P. J., Richardson, L. M., and Clark, G. M. (**1994**). ''Pitch perception for different modes of stimulation using the Cochlear multiple-electrode prosthesis,'' J. Acoust. Soc. Am. **95,** 2658–2669.

Chouard, C-H. (**1978**). ''Multiple intracochlear electrodes for rehabilitation in total deafness,'' in *Otolaryngologic Clinics of North America*, Vol. 11, edited by M. E. Glassock (Sanders, Philadelphia).

Cohen, L. T., Xu, J., Xu, S. A., and Clark, G. M. (**1996**). ''Improved and simplified methods for specifying positions of the electrode bands of a cochlear implant array,'' Am. J. Otol. **17**, 859–865.

Dobbins, P. A., and Cuddy, L. L. (**1982**). ''Octave discrimination: An experimental confirmation of the ''stretched'' subjective octave,'' J. Acoust. Soc. Am. **72,** 411–415.

Dobie, R. A., and Dillier, N. (**1985**). ''Some aspects of temporal coding for single-channel electrical stimulation of the cochlea,'' Hearing Res. **18**, 41–55.

Dorman, M. F., Smith, L., McCandless, G., Dunnavant, G., Parkin, J., and Dankowski, K. (**1990**). ''Pitch scaling and speech understanding by patients who use the Ineraid cochlear implant,'' Ear Hear. **11**, 310–315.

Dorman, M. F., Smith, M., Smith, L., and Parkin, J. L. (**1994**). ''The pitch of electrically presented sinusoids,'' J. Acoust. Soc. Am. **95,** 1677–1679.

Eddington, D. K., Dobelle, W. H., Brackman, E. E., Brackman, D. E., Mladejovsky, M. G., and Parkin, J. L. (**1978**). ''Auditory prosthesis research with multiple-channel intracochlear stimulation in man,'' Ann. Otol. Rhinol. Laryngol. **87** (Suppl. 53), 5–39.

Gfeller, K., and Lansing, C. R. (**1991**). ''Melodic, rhythmic, and timbral perception of adult cochlear implant users,'' J. Speech Hear. Res. **34**, 916–920.

Hochmair-Desoyer, I. J., Hochmair, E. S., Burian, K., and Fischer, R. E. (**1981**). ''Four years of experience with cochlear prostheses,'' Med. Progr. Technol. **8**, 107–119.

McDermott, H. J., McKay, C. M., and Vandali, A. E. (**1992**). ''A new portable sound processor for the University of Melbourne/Nucleus Limited multielectrode cochlear implant,'' J. Acoust. Soc. Am. **91,** 3367–3371.

McDermott, H. J., and McKay, C. M. (**1995**). ''Pitch ranking with nonsimultaneous dual-electrode electrical stimulation of the cochlea,'' J. Acoust. Soc. Am. **96,** 155–162.

McKay, C. M., and McDermott, H. J. (**1996**). ''The perception of temporal patterns for electrical stimulation presented at one or two intracochlear sites,'' J. Acoust. Soc. Am. **100,** 1081–1092.

McKay, C. M., McDermott, H. J., and Clark, G. M. (**1994**). ''Pitch percepts associated with amplitude-modulated current pulse trains in cochlear implantees,'' J. Acoust. Soc. Am. **96,** 2664–2673.

McKay, C. M., McDermott, H. J., and Clark, G. M. (**1995**). ''Pitch matching of amplitude-modulated current pulse trains by cochlear implantees: The effect of modulation depth,'' J. Acoust. Soc. Am. **97,** 1777–1785.

Moore, B. C. J., and Rosen, S. M. (**1979**). ''Tune recognition with reduced pitch and interval information,'' Q. J. Exp. Psychol. **31**, 229–240.

Nelson, D. A., Van Tasell, D. J., Schroder, A. C., Soli, S., and Levine, S. (**1995**). ''Electrode ranking of ''place pitch'' and speech recognition in electrical hearing,'' J. Acoust. Soc. Am. **98,** 1987–1999.

Patrick, J. F., and Clark, G. M. (**1991**). ''The Nucleus 22-channel cochlear implant system,'' Ear Hear. **12**, Suppl. 3S–9S.

Pijl, S., and Schwarz, D. W. (**1995**). ''Melody recognition and musical interval perception by deaf subjects stimulated with electrical pulse trains through single cochlear implant electrodes,'' J. Acoust. Soc. Am. **98,** 886–895.

Rakowski, A., and Miskiewicz, A. (**1985**). ''Deviations from equal temperament in tuning isolated musical intervals,'' Arch. Acoust. **10**, 95–104.

Shannon, R. V. (**1983**). ''Multichannel electrical stimulation of the auditory nerve in man: I. Basic psychophysics,'' Hearing Res. **11**, 157–189.

Simmons, F. B. (**1966**). ''Electrical stimulation of the auditory nerve in man,'' Arch. Otolaryngol. **84**, 24–76.

Skinner, M. W., Clark, G. M., Whitford, L. A., Seligman, P. M., Staller, S. J., Shipp, D. B., Shallop, J. K., Everingham, C., Menapace, C. M., Arndt, P. L., Antognelli, T., Brimacombe, J. A., Pijl, S., Daniels, P., George, C. R., McDermott, H. J., and Beiter, A. L. (**1994**). ''Evaluation of a new spectral peak (SPEAK) coding strategy for the Nucleus 22-channel cochlear implant system,'' Am. J. Otol. **15** (Suppl. 2), 15–27.

Tong, Y. C., and Clark, G. M. (**1985**). ''Absolute identification of electric pulse rates and electrode positions by cochlear implant patients,'' J. Acoust. Soc. Am. **77,** 1881–1888.

Tong, Y. C., Black, R. C., Clark, G. M., Forster, I. C., Millar, J. B., O'Loughlin, B. J., and Patrick, J. F. (**1979**). ''A preliminary report on a multiple-channel cochlear implant operation,'' J. Laryngol. **93**, 679–695.

Tong, Y. C., Blamey, P. J., Dowell, R. C., and Clark, G. M. (**1983**). ''Psychophysical studies evaluating the feasibility of a speech processing strategy for a multiple-channel cochlear implant,'' J. Acoust. Soc. Am. **74,** 73–80.

Townshend, B., Cotter, N., van Compernolle, D., and White, R. L. (**1987**). ''Pitch perception by cochlear implantees,'' J. Acoust. Soc. Am. **82,** 106–115.

Ward, W. D. (**1954**). ''Subjective musical pitch,'' J. Acoust. Soc. Am. **26,** 369–380.

Wilson, B. S., Lawson, D. T., Finley, C. C., and Wolford, R. D. (**1991**). ''Coding strategies for multichannel cochlear prosthesis,'' Am. J. Otol. **12** (Suppl. 1), 55–60.

Dependence of frequency modulation detection on frequency modulation coherence across carriers: Effects of modulation rate, harmonicity, and roving of the carrier frequencies

Shigeto Furukawa and Brian C. J. Moore
Department of Experimental Psychology, University of Cambridge, Downing Street, Cambridge CB2 3EB, England

(Received 27 February 1996; accepted for publication 14 October 1996)

Furukawa and Moore [S. Furukawa and B. C. J. Moore, J. Acoust. Soc. Am. **100**, 2299–2312 (1996)] found that the detection of frequency modulation (FM) imposed on two inharmonically related carriers was better when the FM was coherent across carriers than when it was incoherent. Here, ''coherence'' refers to whether the pattern of frequency change over time was identical or different across carriers. The present paper was designed to explore three possible mechanisms underlying this effect. Thresholds were measured for the detection of a single cycle of sinusoidal FM imposed on two sinusoidal carriers. The FM of each carrier was equally detectable, as determined in preliminary experiments. A continuous pink-noise background was used to mask the outputs of auditory filters tuned between the two carrier frequencies. The modulation rate was either 2.5, 5, or 10 Hz. Three combinations of carrier frequencies were used, varying in the extent to which the carriers were harmonically related (1050 and 2069 Hz; 1100 and 2000 Hz; and 1100 and 1925 Hz). The carrier frequencies were either fixed at these values, or were randomly varied (roved) from one trial to another (±10%) keeping the frequency ratio constant. Performance for coherent FM was generally better than for incoherent FM. The effect of FM coherence was greater at the lowest modulation rate and was slightly greater when the carrier frequencies were fixed throughout a block of trials than when they were roved. For the two lowest modulation rates, the effect of FM coherence was greater for carriers that were (nearly) harmonically related. It is proposed that sensitivity to FM coherence depends partly on comparing patterns of phase locking to the carriers; this is done most effectively at low modulation rates. However, two other factors may play a small role. These are: sensitivity to the coherence of amplitude modulation induced in the auditory system by the FM (which is somewhat disrupted by roving the carrier frequencies); and sensitivity to fluctuations in the residue pitch evoked by the two carriers (the residue pitch being less salient for inharmonically related carriers). © *1997 Acoustical Society of America.* [S0001-4966(97)05402-7]

PACS numbers: 43.66.Fe, 43.66.Mk, 43.66.Nm [JWH]

INTRODUCTION

In order to segregate sounds from different sources presented simultaneously, the auditory system has to select appropriate frequency components that correspond to one sound source and to ''group'' them together to form one perceptual object. It has been suggested that several acoustical cues are available for auditory grouping [see Bregman (1990) for a review]. For example, the auditory system may group components changing in a correlated way in amplitude or frequency. This would imply the existence of one or more mechanisms sensitive to the pattern of changes across components. Several researchers have presented evidence suggesting sensitivity to the coherence of amplitude modulation (AM) across frequency (Hall *et al.*, 1984; Bregman *et al.*, 1985; Strickland *et al.*, 1989). However, evidence indicating sensitivity to the coherence of frequency modulation (FM) across frequencies has been more elusive. Here, coherence refers to whether the *pattern* of frequency changes over time is identical or not across frequencies. Note that in this definition, the modulation depths of the carriers are not necessarily the same, and the frequency ratio of the carriers does not necessarily stay constant (although the latter has often been the case in experiments on sensitivity to FM coherence). Essentially, coherence is defined in terms of whether the contour of changes is the same or different across frequencies.

Evidence for sensitivity to FM coherence has been sought using paradigms such as modulation detection/discrimination interference (Wilson *et al.*, 1990; Moore *et al.*, 1991; Carlyon, 1992, 1994), comodulation masking release (CMR) (Schooneveldt and Moore, 1988; Grose and Hall, 1990), CMR interference (Grose *et al.*, 1995), discrimination between coherent and incoherent FM (Grose and Hall, 1990; Carlyon, 1991), segregation of competing vowels (McAdams, 1989; Marin and McAdams, 1991; Summerfield and Culling, 1992; Chalikia and Bregman, 1993; Culling and Summerfield, 1995), effects of FM coherence on signal detectability (Cohen and Chen, 1992; Carlyon, 1994), and the shift of the first formant phoneme boundary (Gardner and Darwin, 1986). While some studies have been interpreted as indicating a weak sensitivity to FM coherence (Cohen and Chen, 1992; Chalikia and Bregman, 1993), the majority of studies have failed to indicate such sensitivity. These studies have been reviewed in an earlier paper (Furukawa and Moore, 1996).

A difficulty in experiments seeking evidence for mechanism(s) sensitive to FM coherence is how to eliminate cues other than FM coherence. One cue is mistuning from harmonicity. For example, when the carrier frequencies are harmonic, coherent frequency modulation preserves harmonicity or causes only a little inharmonicity, whereas incoherent modulation causes momentary inharmonicity. This could lead to perceptual differences between sounds with coherent and incoherent FM that should not be attributed to the coherence *per se*. To minimize this effect, the carrier frequencies must be chosen very carefully so that the degree of harmonicity does not provide cues to FM coherence. This can be done, for example, by ensuring that the carrier frequencies do not have a *simple* harmonic ratio in any condition, even momentarily.[1]

It is also important to eliminate within-channel cues which may arise from combination tones (CTs), particularly those of the type $2f_1 - f_2$. When two primary tones are both frequency modulated, the CT is also frequency modulated. However, the modulation depth of the CT is larger when the FM of the primaries is incoherent than when it is coherent. Thus, information about FM coherence can be obtained from the FM depth of the CT.

A further within-channel cue can arise from ''beating'' at the output of an auditory filter tuned between the carrier frequencies. ''Beating'' here is defined as the fluctuation in the envelope of the output of the filter caused by the interaction of the carriers. Two types of cue are potentially available in the pattern of beating. First, the relatively rapid fluctuations at a rate corresponding to the difference between the two carrier frequencies would be more regular for coherent FM than for incoherent FM. Second, the slower fluctuations in excitation level caused by the FM itself would be larger for incoherent modulation than for coherent modulation. For example, an increase in excitation level is produced by an increase in the lower carrier frequency and a decrease in the upper carrier frequency. When the two carriers are modulated in opposite phase this gives a larger overall change in excitation level than when they are modulated in phase. Hence, information about FM coherence might be obtained by attending to a single auditory filter tuned between the two carrier frequencies.

Furukawa and Moore (1996) investigated the ability to detect FM imposed on two inharmonically related carriers. The modulation on each carrier was equally detectable, as determined in preliminary experiments, and a pink-noise background was used to mask CTs and the outputs of auditory filters tuned between the two carriers. They found that detectability was generally better when the FM was coherent across carriers than when the FM was incoherent. Since the use of inharmonic carriers and the pink-noise background prevented listeners from using cues such as mistuning from harmonicity and within-channel cues, their results were taken to imply the existence of one or more mechanisms which are sensitive to the coherence of frequency changes across carrier frequencies. It is noteworthy that if the harmonicity and within-channel cues had influenced detectability, one would have expected better detectability for *incoherent* FM than for coherent FM: incoherent FM would give larger variation of harmonicity than coherent FM; the frequencies of CTs would have varied more for incoherent FM than for coherent FM; and the beating at the output of an auditory filter tuned between the carriers would have been larger for incoherent FM than for coherent FM.

Furukawa and Moore (1996) proposed three possible mechanisms for the effect of FM coherence on FM detection. One of them is that the effect relies on information about FM coded by phase locking. Moore and Sek (1995, 1996) and Sek and Moore (1995) have proposed that FM is coded by phase locking for low modulation rates and for carriers below 4–5 kHz; for modulation rates above about 10 Hz, only place information appears to be used. One of the experiments of Furukawa and Moore (1996) showed a greater effect of FM coherence for the lowest modulation rate tested (2.5 Hz) than for the highest rate (10 Hz), although the effect still remained at the highest rate. This result implies that sensitivity to FM coherence may rely partly or completely on a mechanism that uses phase-locking information, which cannot provide useful information about frequency change for relatively rapid modulation rates ($>$10 Hz).

A second possible mechanism for the effect of FM coherence is that the subjects partly based their judgements on the fluctuation of the ''pitch'' corresponding to the approximate fundamental frequency of the two carriers. This could have happened if the two carriers were fused perceptually, rather than being ''heard out.'' The pitch would fluctuate much more when the carriers were modulated coherently than when they were modulated incoherently. In Furukawa and Moore's experiments, the frequency ratio of the carriers was chosen to make the stimuli inharmonic, which would reduce the tendency for perceptual fusion compared to carriers that were harmonically related (Moore *et al.*, 1986; see Moore and Bacon, 1993, for a review). However, as will be discussed, the stimuli may not have been sufficiently inharmonic to be treated as such by the auditory system. If the carriers were fused perceptually, this could explain the effects of FM coherence. It seems unlikely that judgements were based *purely* on fluctuations in (residue) pitch, since if that were true, performance would have been poorer for the detection of incoherent FM on two carriers than for the detection of FM on a single carrier, but in fact this was not the case. Nevertheless, fluctuations in pitch may have played some role. In this study, we refer to this mechanism as the ''pitch-fluctuation mechanism.''

The perception of harmonicity and inharmonicity has been modeled using the concept of a harmonic sieve (Duifhuis *et al.*, 1982; Hartmann *et al.*, 1990). If a number of sinusoidal components in a complex sound all pass through a given sieve, then they are treated by the auditory system as all being part of a harmonic series. If one or more components do not pass through the sieve, then those components are treated as not belonging to the harmonic series. Moore *et al.* (1985a) investigated the size of the ''meshes'' in the hypothetical harmonic sieve. They showed that mistuning a single component in an otherwise harmonic complex sound can shift the pitch of the whole complex sound in the direction of the mistuning, if the amount of mistuning is less than about 3%. When the mistuning is increased beyond 3%, the

contribution of the mistuned component to the pitch of the sound declines. Thus, the mesh width was estimated to be about ±3% of the harmonic frequency, although the results indicate that the sieve does not operate in an all-or-none manner; the contribution of the mistuned harmonic declines progressively with increasing mistuning beyond 3%, rather than dropping abruptly. The carrier frequencies of 1100 and 2000 Hz used in Furukawa and Moore's (1996) experiments were mistuned by about 5% from two harmonic tones with frequencies of 1050 and 2100 Hz, respectively. On the basis of the data of Moore *et al.*, this should have been sufficient to ensure that the tones were treated as inharmonic by the auditory system. However, a recent experiment of Darwin *et al.* (1994) has shown that the harmonic sieve can be wider (up to about ±5%) when the complex sound is frequency modulated. Since Furukawa and Moore's (1996) stimuli were frequency modulated, the carrier frequencies of 1100 and 2000 Hz might have been treated as harmonic by the auditory system, and thus have been perceptually fused. In the present experiment, the role of harmonicity was investigated by systematically varying the degree to which the carriers were harmonically related.

A third possible explanation for the effect of FM coherence is that the auditory system is sensitive to the coherence of *amplitude* modulation across the outputs of the auditory filters. When two carriers are frequency modulated coherently, the AM is coherent across certain auditory filters and incoherent across others. For example, the AM is coherent for filters centered just below the two carrier frequencies, but is incoherent for filters centered just above one carrier and just below the other. Similarly, when the FM is incoherent across carriers, the AM is coherent for certain filters, and incoherent for others. Also, the outputs of auditory filters with CFs very close to the carrier frequency fluctuate at twice the rate of the FM. In order to explain the sensitivity to FM coherence in terms of sensitivity to AM coherence, it is necessary to assume that listeners select appropriate auditory filters (or, equivalently, regions of the excitation pattern) for comparison.

Since the lower side of the excitation pattern for a sinusoid is steeper than the upper side at moderate to high sound levels, FM would produce larger excitation level changes on the lower side of the pattern than on the upper side (Zwicker, 1952). It is possible that listeners select the region giving the largest changes in excitation level. Furukawa and Moore (1996) estimated the amount of AM at the outputs of the auditory filters due to the FM used in their experiments. They showed that for FM depths in the region of the FM detection threshold, the AM depth at the outputs of auditory filters with CFs around or above the carrier frequencies was small compared with that for filters with CFs just below the carrier frequencies. Based on this, Furukawa and Moore proposed an explanation for the effect of FM coherence, which depends on two assumptions: (1) when detecting FM on two carriers, the listener attends to auditory filters with CFs below the carrier frequencies, whose outputs give the largest FM-induced amplitude fluctuation; (2) the auditory system is more sensitive to coherent amplitude changes at the outputs of those auditory filters than to incoherent ones. Since the amplitude changes at the outputs of those filters are coherent when the FM is coherent across carriers, and incoherent when the FM is incoherent, coherent FM is expected to be more detectable than incoherent FM. We refer to this mechanism as the ''FM-induced-AM mechanism.''

Several variations of these two assumptions can be entertained. For example, the listener may attend to several filters whose outputs would not necessarily have the largest output fluctuation. Also, the auditory system may be more sensitive to incoherent AM than coherent AM. In that case, the listener should select auditory filters that would produce incoherent FM-induced AM when the FM is coherent across carriers to explain the results of Furukawa and Moore's experiment. However, such alternative assumptions do not affect the critical point of the FM-induced-AM mechanism, namely that, in the detection of FM on two carrier frequencies, the auditory system attends to selected regions on the excitation pattern and the detectability of the FM depends on the coherence of the AM at those regions of the pattern.

It is possible that more than one of these three suggested mechanisms (phase locking, pitch fluctuation, and FM-induced AM) plays a role in the dependence of FM detection on FM coherence. The experiment in this study attempted to examine the relative contribution of each one. As in the experiments of Furukawa and Moore (1996), the present experiment had two stages: In stage 1, psychometric functions were determined for the detection of FM on each of the two carrier frequencies, presented separately, using a two-alternative forced-choice (2AFC) method. These functions were used to determine equally detectable amounts of FM for the two carriers. In stage 2, using a 2AFC method and an adaptive procedure, detection thresholds were measured for FM imposed on both carriers with modulation depths that would be equally detectable when presented on each carrier separately.

The stimuli were varied along several dimensions. The modulation rate was varied to see if we could replicate the finding of the previous experiment that the effect of FM coherence was greater at very low rates. If so, this might indicate a role of phase locking in sensitivity to FM coherence, assuming that the proposal by Moore and Sek (1995, 1996) and Sek and Moore (1995) is correct. Second, the harmonicity of the carrier frequencies was varied, so as to vary the amount of perceptual fusion of the carriers. If the pitch-fluctuation mechanism plays an important role, we would expect the effect of FM coherence to be smallest when the carrier frequencies were least harmonic and therefore were least fused perceptually. Finally, in some conditions, the carrier frequencies were randomly varied for every stimulus presentation both within a trial of the 2AFC task and across trials. In stage 2 this was done keeping the ratio of the carrier frequencies constant. This random variation was introduced so as to disrupt the ability of listeners to attend to the auditory filters whose outputs changed the most; it prevented the listeners from selecting the appropriate filters using information obtained over a series of trials. If the FM-induced-AM mechanism plays an important role, then we would expect this random variation of the carrier frequencies to reduce the effect of FM coherence.

I. EXPERIMENT: STAGE 1

A. Method

1. Stimuli

In stage 1, only one carrier was presented, with a frequency of either 1100 or 2000 Hz. Note that this differs from our previous experiment (Furukawa and Moore, 1996), where both carriers were present, but only one was modulated. Only one carrier was presented in the present experiment, to avoid measuring detectability for each degree of harmonicity of the carriers (described in Sec. II). Although the presence of the other carrier could influence the detectability of FM on the target carrier, we assumed that this would not substantially affect the relative detectability of FM on the two carriers. Note that our main interest was in the *difference* in detectability for coherent and incoherent FM (as measured in stage 2).

The carrier frequency was either fixed throughout a block of trials (FIX condition), or randomly varied from one interval of a 2AFC trial to another with a uniform probability distribution over the range of $\pm 10\%$ of the nominal carrier frequency (ROV condition).

Each carrier had a level of 65 dB SPL and was gated on and off with 50-ms raised-cosine ramps. The part with steady amplitude had one cycle of sinusoidal frequency modulation, and the 50-ms ramps were unmodulated in frequency. Frequency modulation always started at a positive- or negative-going zero crossing. Modulation rates tested were 2.5, 5, and 10 Hz, giving durations for the steady amplitude of 400, 200, and 100 ms, respectively. The interstimulus interval in the 2AFC task was 500 ms. The instantaneous frequency, f_i, during the steady amplitude segment of a modulated carrier was:

$$f_i = f_c \pm \Delta f \sin(2\pi f_m t), \tag{1}$$

where f_c is the carrier frequency, Δf is the maximum frequency deviation, f_m is the modulator frequency, and t is time relative to the point when the modulation starts. The sign determined the starting direction of the modulation. When the sign was $+$, the modulation started upward in frequency; when the sign was $-$, the modulation started downward.

In summary, there were 24 conditions, comprising all possible combinations of two carrier frequencies, fixed or roving carriers, three modulation rates, and two modulation directions.

The signals were digitally generated at a sampling rate of 10 kHz, using a Masscomp 5400 computer system and a 16-bit digital-to-analog converter (DAC, model DA04H). The output of the DAC was low-pass filtered (Kemo, type VBF 8/03, 48 dB/oct) with a cutoff frequency of 4 kHz and mixed with a filtered (Kemo, type VBF 8/03, 48 dB/oct) pink noise with a passband from 100 to 2000 Hz and with a spectrum level of 25 dB at 1000 Hz. The choice of the level for the pink noise is described in Sec. II. The levels of the sinusoidal and noise stimuli were adjusted by manual attenuators. The stimuli were delivered to one earpiece of a Sennheiser HD 414 headset.

2. Procedure

A 2AFC task was used to measure the detectability of FM, where the subject's task was to indicate whether the first or the second stimulus in a pair was modulated in frequency. Psychometric functions were measured using the same procedure as described by Moore and Sek (1992). Five modulation depths were chosen for each subject on the basis of pilot experiments, so that the resulting detectability indices, d', were reasonably evenly spread over the range 0–2.5. The conditions (FIX or ROV, modulation rate, carrier frequency) except modulation direction were fixed within a block of 55 trials. The first five trials used the highest modulation depth and were treated as practice. The rest of a block consisted of 10 sub-blocks, each of which started with the highest modulation depth and decreased progressively to the lowest. This was done to avoid subjects ''loosing'' the detection cue (not knowing what to listen for) when the modulation depth was fixed at a low level (Moore and Sek, 1992). The ''easy'' stimulus every five trials reminded subjects what to listen for. Both modulation directions, upward and downward, were tested within a block of trials. The order of the modulation directions was random, but the number of upward and downward stimuli for each modulation depth was balanced in a block, except for the practice trials where the numbers of upward and downward stimuli were not balanced. Values of d' were calculated from 200 trials (i.e., 40 blocks) for each modulation depth and modulation direction, using standard tables (Hacker and Ratcliff, 1979). We refer to values of d' for the individual carriers obtained in this way as d'_{ind}.

Subjects were tested in a double-walled sound-attenuating chamber. Correct-answer feedback was provided by lights on the response box.

3. Subjects

Three subjects with normal hearing thresholds ($\leqslant$15 dB HL at frequencies between 250 and 8000 Hz) were used. One was author SF. The other two subjects were paid for their services. Subject SF was highly experienced in similar psychoacoustical experiments. All subjects were trained until their performance appeared to be stable. Performance was compared across blocks of 200 trials, and training continued until no consistent improvements were observed. This took about 6 h.

B. Results

The results are shown for each subject in Figs. 1 and 2. Each column shows the results for one modulation rate. Each row shows the results for one subject. Since the d'_{ind} values seemed to be linearly related to the squared modulation depth, as found by Moore and Sek (1992) and in our previous study (Furukawa and Moore, 1996), values of d'_{ind} are plotted as a function of $(100\Delta f/f_c)^2$ (i.e., the modulation depth expressed as a percentage and then squared) for each carrier frequency. Different symbols indicate the pattern of modulation direction and whether the carrier frequency was fixed or roved. Straight lines were fitted to the values of d' as a function of $(100\Delta f/f_c)^2$. The obtained slopes were used to

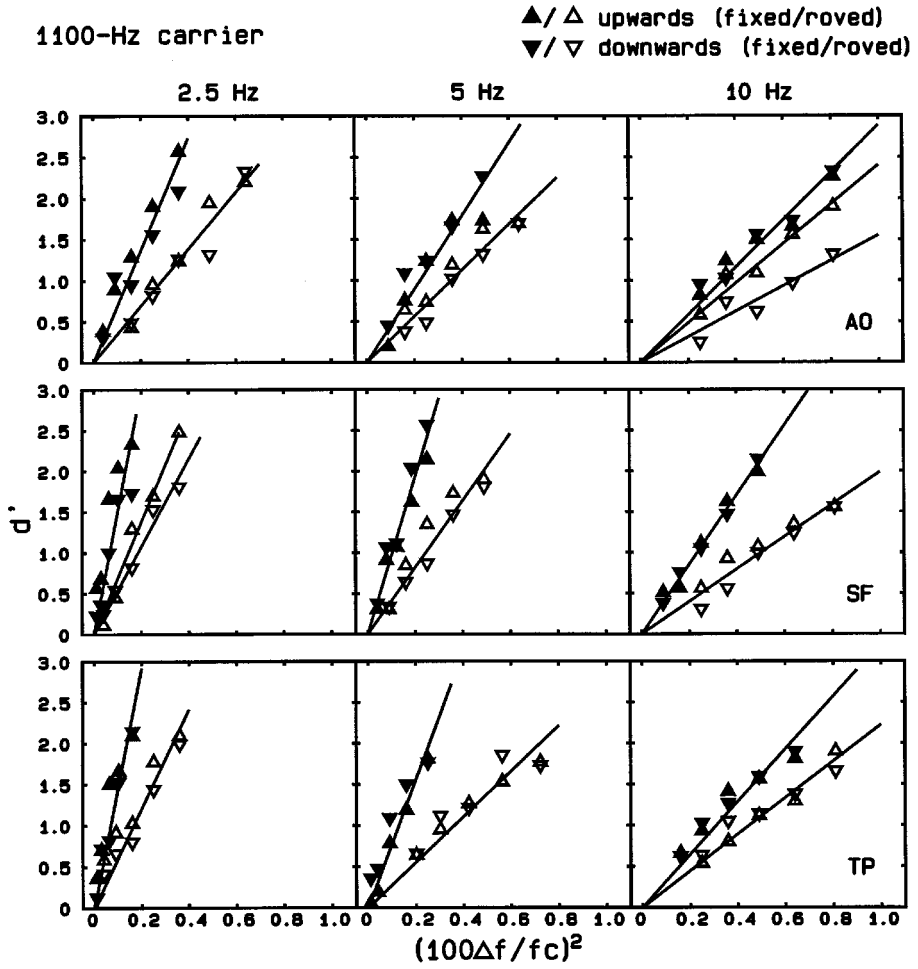

FIG. 1. Results of stage 1 for the 1100-Hz carrier, showing psychometric functions for the detection of FM. Detectability, d', is plotted as a function of the square of the maximum relative zero-to-peak frequency deviation (expressed as a percentage of the carrier frequency), $(100\Delta f/f_c)^2$. Up-pointing symbols indicate that the modulation started in the ''upward'' direction and down-pointing symbols indicate that the modulation started in the ''downward'' direction. Filled symbols show results for the FIX condition and open symbols show results for the ROV condition. Each column shows results for one modulation rate. Each row shows results for one subject. Best fitting lines to the data points are also shown (see text).

calculate the modulation depths used in stage 2, so as to give the same d' values for the two individual carriers.

In most cases a single straight line was fitted to the data for both modulation directions. However, sometimes the slopes of the fitted lines for the two modulation directions appeared to be somewhat different. The significance of the differences was tested by *t* tests, the variances of the slopes being estimated from the sum of the squared deviations of the data from each regression line (Snedecor and Cochran, 1967, p. 153). When the *t* tests showed that the slopes for the two modulation directions were different with a significance level of 1%, two separate lines were fitted to the data. The difference in the slopes indicates that the auditory system is not equally sensitive to FM with different modulation directions, as found in some previous studies (Tsumura *et al.*, 1973; Gardner and Wilson, 1979; Schouten, 1985, 1986; Carlyon and Stubbs, 1989; Demaney and Clément, 1995). To our knowledge, there is no theory to explain these effects of modulation direction. Significant differences in slope were found only in the ROV condition (subject AO: 1100-Hz carrier, 10-Hz rate; subject SF: 1100- and 2000-Hz carriers, 2.5 Hz). We have no explanation for this.

The FM was consistently more detectable for the FIX condition than for the ROV condition. Table I shows the ratios of the slopes of the psychometric functions for the FIX and ROV conditions. These ratios quantify the extent to which the roving disrupted performance; larger ratios indicate more disruption. The ratios are generally in the range 2–3, indicating that the roving had rather a large effect. However, the effect of roving on thresholds estimated from these data (for example, by comparing the FM depths needed to achieve a d' of 1) would be smaller, because the psychometric functions are linear when plotted as a function of $(100\Delta f/f_c)^2$. In fact, the ratio of thresholds is equal to the square root of the ratio of slopes. Hence, the ratios of thresholds are generally in the range 1.4–1.7.

The finding that there is an effect of roving is somewhat surprising. Moore and Sek (1994) have argued that FM at a 10-Hz rate is detected by combining information from all parts of the excitation pattern that are above absolute threshold. They found that a multichannel model based on this assumption accounted for their data much better than a model based on monitoring only a single point on the excitation pattern. If subjects do monitor all points on the exci-

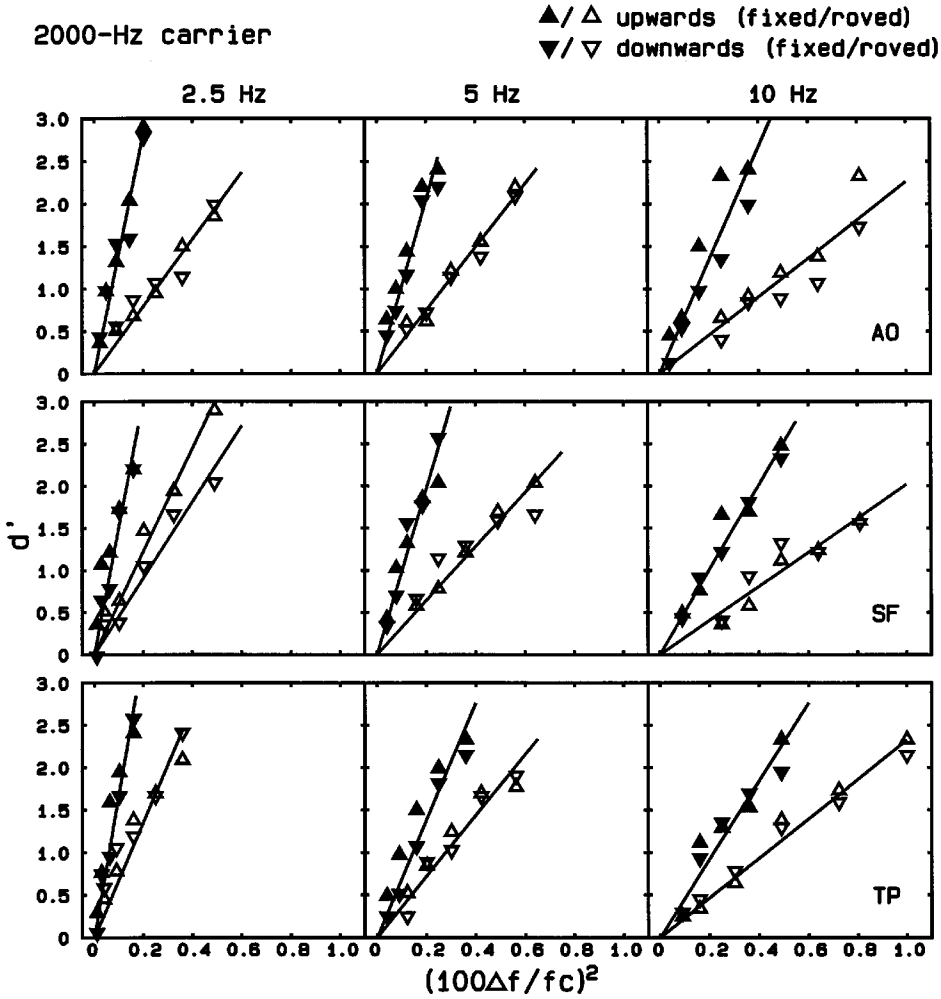

FIG. 2. As Fig. 1, but for the 2000-Hz carrier.

tation pattern, it is not clear why roving the carrier frequency has a disruptive effect. The appropriate channels to attend to should automatically be defined by the parts of the excitation pattern that are above absolute threshold. For lower modulation rates, FM may be detected using phase-locking information, as described earlier, but again, it is not clear why roving the carrier frequency should have an effect. The crucial factor is that the FM is coded by how the phase locking varies over time; the actual carrier frequency should be of little relevance.

Neither of the two postulated mechanisms for FM detection predicts an effect of roving the carrier frequency. It is possible that the effect reflects an attentional process. The changes in pitch produced by the roving are easily detectable and are highly salient compared with the small changes induced by the FM. This may make it hard to focus attention on the FM. It is noteworthy that comparable effects of roving the frequency have also been found in a task requiring the frequency discrimination of steady tones (Moore and Glasberg, 1990). However, the crucial point for this experiment is whether the effect of FM coherence on FM detection is affected by roving the carrier(s). Although an attentional effect may disrupt performance, the extent of the effect should be similar for coherent and incoherent FM in stage 2 of the experiment.

The performance of our subjects always improved with decreasing modulation rate. This result is consistent with the finding of the previous study (Furukawa and Moore, 1996) that, when only a single cycle of modulation was used, sensitivity to FM increased with decreasing modulation rate over the range 2–10 Hz.

TABLE I. Ratios of slopes of the psychometric functions for the FIX condition *re*: ROV conditions.

		Modulation rate (Hz)		
Subject	f_c (Hz)	2.5	5	10
AO	1100	1.98	1.59	1.46
	2000	3.55	2.74	2.95
SF	1100	2.45	2.36	2.14
	2000	2.83	3.06	2.49
TP	1100	2.42	2.81	1.45
	2000	2.48	1.92	1.99
Mean	1100	2.28	2.25	1.68
	2000	2.95	2.57	2.48

II. EXPERIMENT: STAGE 2

A. Method

1. Stimuli

Two carriers were presented simultaneously as in the previous experiment (Furukawa and Moore, 1996). Three combinations of carrier frequencies were used for stage 2: (1) 1050 and 2069 Hz (HAR condition; about 1:2 in frequency ratio); (2) 1100 and 2000 Hz (MID condition); (3) 1100 and 1925 Hz (INH condition; 4:7 in frequency ratio). These combinations of carrier frequencies were chosen so that the HAR condition had the most ''harmonic'' stimulus, and the INH condition had the most inharmonic stimulus. The harmonicity of the stimuli for the MID condition was intermediate between those for the HAR and INH condition. Carrier frequencies for the MID condition were the same as the ones used in the experiments of Furukawa and Moore (1996). The degree of mistuning from hypothetical octave stimuli was: for the HAR condition, about 0.74% and -0.74% from harmonic frequencies of 1042.3 and 2084.5 Hz, respectively; for the MID condition, 4.8% and -4.8% from harmonic frequencies of 1050 and 2100 Hz; and for the INH condition, about 6.7% and -6.7% from harmonic frequencies of 1031.3 and 2062.5 Hz. Note that for all combinations of carrier frequencies, the frequency was mistuned upward from hypothetical octave stimuli for the lower carrier and downwards for the higher carrier. The carrier frequencies for the HAR condition were not perfectly harmonic so as to reduce the salience of an additional cue which can occur when the carriers are perfectly harmonic, namely the markedly stronger mistuning caused by incoherent FM than by coherent FM (Carlyon, 1991, 1994). However, since the amount of mistuning for the HAR carriers was well within the tolerance of the harmonic sieve for both coherent and incoherent FM, the stimuli can be considered as ''harmonic'' (Moore *et al.*, 1985b, 1986).

It should be noted that since the modulation depth relative to the carrier frequency was not necessarily the same for the two carriers (see Sec. II A 1.2), the frequency ratio and degree of harmonicity varied throughout one presentation of a modulated stimulus even when the modulation was coherent. However, this variation of the frequency ratio was small because the modulation depth used in the experiment was generally small compared to differences in harmonicity between the conditions. It should also be noted that the frequency separation of the carriers on an ERB scale (Glasberg and Moore, 1990) varied slightly for the three conditions HAR, MID, and INH. However, all carriers were separated by at least 4.5 ERBs, which should have been sufficient to ensure that they were very well resolved (Moore and Ohgushi, 1993).

As in stage 1, the carrier frequencies were either fixed (FIX condition) or roved from one interval of a trial to another (ROV condition). This was done for all three harmonicity conditions. The frequency ratio between the two carriers was always kept constant throughout a block of trials, even when the carriers were roved in frequency.

The stimulus level for each carrier, the modulation rate and the stimulus duration were all the same as in stage 1. For the signal interval of a 2AFC trial, both of the carriers were modulated, whereas the other interval contained unmodulated carriers.

There were four patterns in the directions of frequency changes for the two carriers: modulation starting in the same direction for both carrier frequencies (upward for the higher carrier and upward for the lower carrier; downward for the higher carrier and downward for the lower carrier); and modulation starting in the opposite direction (upward for the higher carrier and downward for the lower carrier; downward for the higher carrier and upward for the lower carrier). These conditions are described by combinations of the symbols + and −, corresponding to the signs in Eq. (1). The first symbol refers to the higher carrier frequency and the second symbol to the lower one. For example, the symbol $\langle ++ \rangle$ indicates modulation starting upward for both carriers; the symbol $\langle +- \rangle$ indicates modulation starting upward for the higher carrier and downward for the lower carrier. Conditions with the same modulator starting directions ($\langle ++ \rangle$ or $\langle -- \rangle$) had coherent FM across frequencies, and conditions with opposite modulator starting directions ($\langle +- \rangle$ or $\langle -+ \rangle$) had incoherent FM.

In summary there were 72 conditions, comprising all possible combinations of three degrees of harmonicity, fixed or roving carriers, three modulation rates, and four patterns of direction of frequency change.

The same equipment was used to generate the stimuli as in stage 1. As in the previous stage, a band of pink noise with a passband from 100 to 2000 Hz and with a spectrum level of 25 dB at 1000 Hz was added to the carriers. This noise was used to remove within-channel cues associated with combination tones and with the outputs of auditory filters that respond to both carrier frequencies. The level of the pink noise was determined as follows: First, the excitation pattern produced by each carrier was calculated for the carrier frequencies used in the MID and FIX condition, using the procedure described by Glasberg and Moore (1990); second, we determined the range of CFs over which the excitation levels for the two carriers were different by less than 15 dB; finally, the level of the pink noise was chosen so that, over this range of CFs, the pink noise would produce an excitation level greater than or equal to that produced by either carrier alone. We assumed that if the excitation levels evoked by the two carriers differed by more than 15 dB, then effects due to within-channel interactions would be very small.

2. Procedure

As in stage 1, a 2AFC task was used to measure the detectability of FM. The modulation depth for each carrier was varied, on the basis of the results of stage 1, so that the modulation would always give the same d'_{ind} values for each of the two carriers. The value of d'_{ind} was decreased after three successive correct responses, and was increased after one wrong response. This procedure estimates the value of d'_{ind} giving 79.4% correct responses (Levitt, 1971). The change from increasing to decreasing modulation depth, or vice versa, defined a turnpoint, and each run continued until at least 12 turnpoints had occurred. The initial value of d'_{ind} was 3. Up to the first four turnpoints, d'_{ind} was multiplied (or

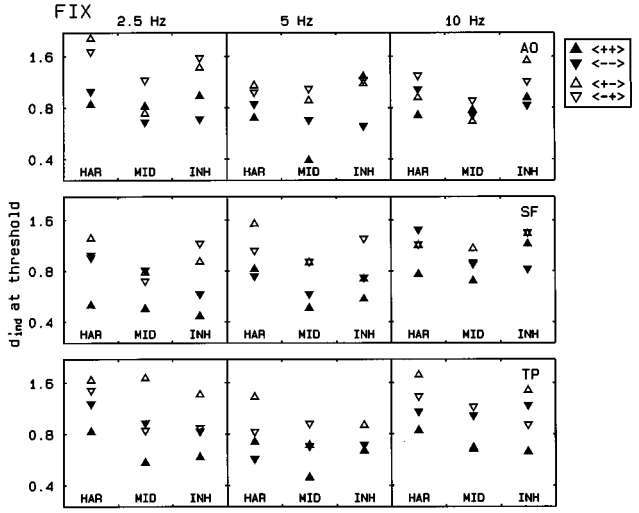

FIG. 3. Results of stage 2 for FIX condition. Detection thresholds for FM on the two carriers (d'_{ind}; see text) are plotted for each degree of harmonicity (HAR, MID, and INH). Different symbols indicate the pattern of modulation direction (see the key). Filled symbols indicate conditions with coherent FM, and open symbols indicate conditions with incoherent FM. Each row shows results for one subject. Each column shows results for one modulation rate.

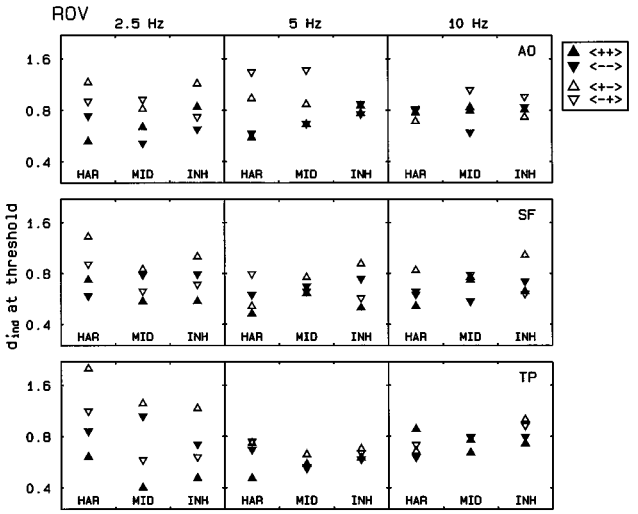

FIG. 4. As Fig. 3, but for the ROV condition.

divided) by the step size of 0.6. For the following eight turnpoints, the step size was 0.9. An estimate of the threshold value of d'_{ind} was obtained by geometrically averaging the values of d'_{ind} at the last eight turnpoints. At least three estimates of threshold were obtained for each condition. A set of three measurements was done successively. When the standard deviation of the logarithm (base 10) of those estimates exceeded 0.1, another three thresholds were measured separately from the first set of three measurements (at a different time). This happened about 50% of the time, and this prevalence did not vary markedly across conditions. Those three or six thresholds for each subject and condition were geometrically averaged to give an estimate of the value of d'_{ind} at threshold.

The condition (harmonicity, FIX or ROV, modulation rate, modulation direction) was fixed within a block of trials. The carrier frequencies were slightly different across conditions with different degrees of harmonicity. However, we assumed that the sensitivity to FM was approximately invariant over a small range of carrier frequencies. Hence, we used psychometric functions for the 1100-Hz carrier to estimate appropriate modulation depths for the 1050-Hz carrier and psychometric functions for the 2000-Hz carrier to estimate appropriate modulation depths for the 2069-Hz and 1925-Hz carriers. The same subjects were used as in stage 1.

B. Results

The results are shown in Figs. 3 (FIX condition) and 4 (ROV condition). Each column shows results for one modulation rate. Each row shows results for one subject. Within each panel, results are shown for each combination of modulation direction and each degree of harmonicity. Different symbols represent the patterns of modulation direction as indicated in the key. Thresholds for the detection of FM on two carriers are plotted on a logarithmic scale. Note that smaller values of d'_{ind} (corresponding to smaller modulation depths) indicate better performance.

In general, thresholds for coherent FM (filled symbols) are lower than for incoherent FM (open symbols), indicating that the detectability of FM on the two carrier frequencies is better when the FM is coherent across the carriers. This effect of FM coherence is most clear for the lowest modulation rate and least clear for the highest rate. This is consistent with our earlier results (Furukawa and Moore, 1996). The data are somewhat ''noisy,'' making it difficult to see a clear effect of harmonicity. The overall levels of performance were not markedly affected by whether the carrier frequencies were fixed or roved, although there was a trend for lower thresholds in the ROV condition. However, it should be remembered that the psychometric functions used to determine the values of d'_{ind} in the ROV condition were themselves determined using carriers that were roved.

A within-subjects analysis of variance (ANOVA) was conducted on the logarithms of the thresholds with factors modulation rate (three values), harmonicity (three values), roving (FIX or ROV), and modulation direction (four combinations). The effect of modulation rate was not significant, but the other main effects were significant: for harmonicity, $F(2,4)=9.69$, $p=0.029$; for roving $F(1,2)=140.58$, $p=0.007$; for modulation direction, $F(3,6)=12.65$, $p=0.005$. Mean thresholds were lower (better) for the MID harmonicity than for either HAR or INH. However, the effect was small, corresponding to a factor of about 1.15. Thresholds were lower for the ROV condition than for the FIX condition, but again the difference was small, corresponding to a factor of 1.22. Thresholds were lower for the conditions with coherent FM ($\langle++\rangle$ and $\langle--\rangle$) than for the conditions with incoherent FM ($\langle+-\rangle$ and $\langle-+\rangle$) by a factor of 1.38.

Since our interest was in the effect of FM coherence on FM detection, the ratios of thresholds for coherent and incoherent FM were calculated for each subject and condition (harmonicity, FIX or ROV, modulation rate). This was done

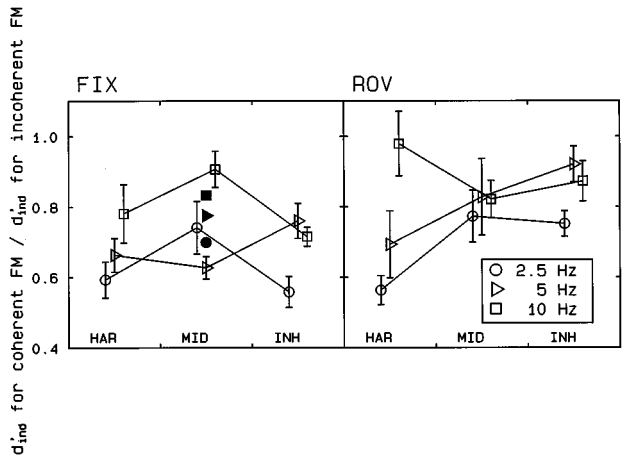

FIG. 5. Ratios of detection thresholds (d'_{ind}) for coherent and incoherent FM. The results were arithmetically averaged across subjects. The vertical lines show standard errors. Different symbols show ratios for different modulation rates. The ratios are plotted separately for each degree of harmonicity. The left panel shows results for the FIX condition, and the right panel shows results for the ROV condition. Filled symbols in the left panel show the ratios estimated by Furukawa and Moore (1996). See text for details.

by dividing the geometric average of thresholds for coherent FM (collapsing across $\langle++\rangle$ and $\langle--\rangle$) by that for incoherent FM (collapsing across $\langle+-\rangle$ and $\langle-+\rangle$). Figure 5 shows the (arithmetic) average of these ratios across subjects together with the standard errors. Ratios smaller than unity indicate that the detectability of FM is better for coherent FM than for incoherent FM. The smaller the ratio is, the larger the effect of FM coherence.

In all conditions, the mean ratio was below unity, indicating that coherent FM was more detectable than incoherent FM. In five cases out of six, the ratio was smallest for the 2.5-Hz modulation rate. The effect of harmonicity was not consistent across modulation rates and roving conditions. To assess the overall significance of the effects, a within-subjects ANOVA was conducted on the ratios, with factors modulation rate (three values), harmonicity (three values), and roving (FIX or ROV).

Significant main effects were found for modulation rate [$F(2,4)=13.3$, $p=0.017$] and roving [$F(1,2)=32.2$, $p=0.030$]. The interaction of modulation rate and harmonicity was also significant [$F(4,8)=5.2$, $p=0.024$]. The other main factor (harmonicity) and the interactions were not significant. The significant effect of modulation rate reflects the decrease in mean ratio with decreasing modulation rate (ratios of 0.85, 0.75, and 0.66 for rates of 10, 5, and 2.5 Hz, respectively). The significant effect of roving is due to the fact that the mean ratio for the ROV condition was somewhat larger than for the FIX condition (0.80 versus 0.705, respectively). The significant interaction of modulation rate and harmonicity reflects the fact that the mean ratio did not vary over the three harmonicities when the modulation rate was 10 Hz, while it varied with harmonicity when the modulation rate was 2.5 or 5 Hz. *Post hoc t* tests showed that, for the modulation rate 2.5 Hz, the ratio for the HAR condition was significantly smaller than that for the MID condition ($p<0.05$). For the 5-Hz rate, the ratio for the HAR condition was significantly smaller than that for the INH condition ($p<0.05$).

III. DISCUSSION

A. Comparison with our previous study

Our previous experiments (Furukawa and Moore, 1996) used conditions with fixed carrier frequencies of 1100 and 2000 Hz. Thus, the results of the previous study can be compared with the FIX and MID condition of the present study. However, caution is needed since the two studies used slightly different methods and procedures. Specifically, the present experiment presented only one carrier in stage 1, and used an adaptive procedure in stage 2, whereas the previous experiments always presented two carriers simultaneously, and measured psychometric functions in stage 2.

The filled symbols in Fig. 5 show ratios estimated from experiment 2 of Furukawa and Moore (1996, Table II). They were obtained by calculating reciprocals of the ratios of the slopes of the psychometric functions for coherent and incoherent FM. The ratios are fairly consistent across the two studies, although the present experiment showed slightly greater effects of modulation rate. Both studies gave ratios smaller than unity for all modulation rates, the ratio for the 10-Hz modulation rate being the largest of the three rates tested. A *t* test was used to estimate the significance of the differences in the ratios between the present and the previous experiments, separately for each modulation rate. There was no significant difference at any modulation rate.

B. Relative importance of the three postulated mechanisms

We consider now the implications of the results for the three mechanisms for sensitivity to FM coherence that were postulated in the introduction. Consider first the FM-induced-AM mechanism. Our prediction based on this mechanism was that roving the carrier frequencies should markedly reduce the effects of FM coherence, since the roving would make it more difficult for subjects to select the appropriate frequency channels (the ones showing the largest amounts of AM). In fact, the results did show an effect in the predicted direction; the effect of FM coherence was greater in the FIX condition than in the ROV condition. However, the difference between the FIX and ROV conditions was not very large. Furthermore, there was still a significant effect of FM coherence even in the ROV condition. At first sight, these results suggest that, while the FM-induced-AM mechanism may be partly responsible for the better detectability of coherent FM than of incoherent FM, it probably does not account for the whole of the effect. However, it is possible that even when the carrier frequencies were varied from one trial to another, listeners may still have been able to attend to the auditory filters with the largest fluctuation at their outputs. Further experiments are needed to assess the importance of the FM-induced-AM mechanism.

Consider now the postulated mechanism based on phase locking. It was predicted, on the basis of ideas proposed by Moore and Sek (1995, 1996) and Sek and Moore (1995), that

phase locking would play a large role in detection of FM at the 2.5-Hz modulation rate and a negligible role at the 10-Hz rate. If phase locking also plays a role in the effect of FM coherence, then this effect might be expected to be greatest at the lowest modulation rate. The results did, indeed, show this to be the case. However, as in our earlier experiments, the effects of FM coherence remained significant for a 10-Hz modulation rate. Thus, the results are consistent with the idea that phase-locking information is partly responsible for the dependence of FM detection on FM coherence.

It is worth pointing out that the duration of the stimuli used in the present experiment varied depending on modulation rate since only one cycle of FM was used. Thus, the duration was longer for the lower modulation rate. However, the results of an earlier experiment (Furukawa and Moore, 1996) showed that the effect of FM coherence at a given modulation rate did not depend on duration (number of modulator cycles). Thus, it appears that modulation rate rather than duration is the factor determining the size of the effect of FM coherence.

Consider now the possibility that the effects of FM coherence were caused by subjects basing their judgements on the fluctuation of the pitch of the two carriers. We argued that, if this were so, the effects of FM coherence should be greater for harmonic stimuli than for inharmonic stimuli, since the former would be more strongly fused. However, there was no significant overall effect of harmonicity on the ratios of thresholds for coherent and incoherent FM. The synchronous gating of the two carriers may have weakened any possible effects of harmonicity, but the harmonicity should still have had some effect on perceptual fusion (Moore *et al.*, 1986). Thus, the insignificant overall effect of harmonicity suggests that the effect of FM coherence on FM detection is not caused by subjects basing their judgments on the fluctuation of the residue pitch of the carriers.

The interaction of modulation rate and harmonicity was, however significant. This was mainly caused by the fact that the effect of FM coherence at the two lowest modulation rates (2.5 and 5 Hz) was greater (i.e., the ratios in Fig. 5 were lower) for the HAR condition than for other harmonicity conditions (MID for the 2.5-Hz rate and INH for the 5-Hz rate), whereas the effect for 10 Hz did not vary with harmonicity. This could be taken to indicate that perceptual fusion induced by harmonicity plays a role, but only for very low modulation rates. However, it may also be the case that the mechanism based on phase locking, which is assumed mainly to operate at very low modulation rates, treats harmonically related carriers in a special way; this may be a property of the mechanism for determining residue pitch (Moore, 1989) and is not necessarily related to perceptual fusion.

It is possible that subjects adopted different strategies in different conditions. Specifically, judgments could have been based on pitch fluctuation for coherent FM, but not for incoherent FM. If pitch fluctuation did play a role in the detection of coherent FM, then we would expect that thresholds for detecting coherent FM (Figs. 3 and 4) would be lower for condition HAR than for conditions MID or INH, owing to the greater perceptual fusion expected in condition HAR. However, the ANOVA on the threshold values, described earlier, revealed no significant interaction of harmonicity and modulation direction; $F(6, 12)=1.2$, $p=0.37$. This suggests that pitch fluctuations did not play a greater role in coherent than in incoherent conditions. For the coherent modulation, thresholds were not lower in condition HAR than in conditions MID or INH. This again suggests that the pitch fluctuation did not play an important role.

IV. SUMMARY

The following conclusions can be drawn from our results:

(1) When equally detectable amounts of FM were imposed on two widely separated carriers, thresholds for detecting the FM were lower when the FM was coherent across carriers than when it was incoherent. This is consistent with the results of our previous study (Furukawa and Moore, 1996) and indicates that the auditory system is sensitive to the coherence of FM across frequencies.

(2) Moore and Sek (1995, 1996) and Sek and Moore (1995) have suggested that the detection of FM at a 2.5-Hz rate depends mainly on changes in phase locking to the carrier rather than on changes in the excitation pattern. Our results showed that the effect of FM coherence on detectability was greater for a modulation rate of 2.5 Hz than for rates of 5 and 10 Hz. This is consistent with the results of our previous study (Furukawa and Moore, 1996). Thus, if Moore and Sek are correct, our results indicate that phase locking may play an important role in the effect of FM coherence on detectability of FM.

(3) Another possible explanation for the effect of FM coherence is that the carriers fuse perceptually, and judgements are based on the residue pitch that they evoke; coherently modulated carriers would give a larger change in pitch than incoherently modulated carriers. To test this idea, the harmonicity of the carrier frequencies was varied to control the degree of perceptual fusion. Harmonicity had no significant overall effect on the dependence of FM detection on FM coherence. This finding does not support the pitch-fluctuation hypothesis. However, for the lower modulation rates, the effect of FM coherence was somewhat greater for the harmonically related carriers, suggesting that judgments based on pitch fluctuation may play some role.

(4) Another possible explanation for the effect of FM coherence is that subjects are sensitive to the coherence of FM-induced AM at the outputs of the auditory filters whose outputs change the most, i.e., the filters with CFs just below the carrier frequencies. Such a mechanism would require selection of the appropriate filter outputs. To test this idea, we examined the effect of varying the carrier frequencies from trial to trial, keeping the frequency ratio fixed. This should make it more difficult to select the appropriate filters. The effect of FM coherence was somewhat smaller when the carriers were roved than when the frequencies were fixed within a block of trials. This is consistent with the idea that the auditory system is sensitive to the coherence of FM-induced AM. How-

ever, a significant effect of FM coherence occurred even when the carriers were roved.

ACKNOWLEDGMENTS

This work was supported by the Medical Research Council (U.K.). S. Furukawa was supported by the British Council and an ORS award. We thank Robert Carlyon for helpful discussions, and Robert Carlyon, Joseph Alcántara, Deborah Vickers, Brian Glasberg, and Marina Rose for comments on an earlier version of this paper. We also thank two anonymous reviewers for detailed helpful comments.

[1]The auditory system does not appear to treat pairs of tones as harmonically related when their frequencies do not form a simple ratio (such as 2:1, 3:2 or 5:4) or a consonant musical interval, even when the pairs do have a common fundamental in the audio range (Plomp and Levelt, 1965; Srulovicz and Goldstein, 1983). For example, sinusoids with frequencies of 1100 and 2000 Hz have a common fundamental frequency of 100 Hz, but they are not treated as harmonically related by the auditory system; they do not seem to form a consonant musical interval, and they do not give rise to a clear residue pitch.

Bregman, A. S. (**1990**). *Auditory Scene Analysis: The Perceptual Organization of Sound* (Bradford Books, MIT, Cambridge, MA).

Bregman, A. S., Abramson, J., Doehring, P., and Darwin, C. J. (**1985**). ''Spectral integration based on common amplitude modulation,'' Percept. Psychophys. **37,** 483–493.

Carlyon, R. P. (**1991**). ''Discriminating between coherent and incoherent frequency modulation of complex tones,'' J. Acoust. Soc. Am. **89,** 329–340.

Carlyon, R. P. (**1992**). ''The psychophysics of concurrent sound segregation,'' Philos. Trans. R. Soc. London, Ser. B **336,** 347–355.

Carlyon, R. P. (**1994**). ''Further evidence against an across-frequency mechanism specific to the detection of frequency modulation (FM) incoherence between resolved frequency components,'' J. Acoust. Soc. Am. **95,** 949–961.

Carlyon, R. P., and Stubbs, R. J. (**1989**). ''Detecting single-cycle frequency modulation imposed on sinusoidal, harmonic, and inharmonic carriers,'' J. Acoust. Soc. Am. **85,** 2563–2574.

Chalikia, M. H., and Bregman, A. S. (**1993**). ''The perceptual segregation of simultaneous vowels with harmonic, shifted, or random components,'' Percept. Psychophys. **53,** 125–133.

Cohen, M. F., and Chen, X. (**1992**). ''Dynamic frequency change among stimulus components: Effects of coherence on detectability,'' J. Acoust. Soc. Am. **92,** 766–772.

Culling, J. F., and Summerfield, Q. (**1995**). ''The role of frequency modulation in the perceptual segregation of concurrent vowels,'' J. Acoust. Soc. Am. **98,** 837–836.

Darwin, C. J., Ciocca, V., and Sandell, G. J. (**1994**). ''Effects of frequency and amplitude modulation on the pitch of a complex tone with a mistuned harmonic,'' J. Acoust. Soc. Am. **95,** 2631–2636.

Demany, L., and Clément, S. (**1995**). ''The perception of frequency peaks and troughs in wide frequency modulations, II. Effects of frequency register, stimulus uncertainty, and intensity,'' J. Acoust. Soc. Am. **97,** 2454–2459.

Duifhuis, H., Willems, L. F., and Sluyter, R. J. (**1982**). ''Measurement of pitch in speech: an implementation of Goldstein's theory of pitch perception,'' J. Acoust. Soc. Am. **71,** 1568–1580.

Furukawa, S., and Moore, B. C. J. (**1996**). ''Across-channel processes in frequency modulation detection,'' J. Acoust. Soc. Am. **100,** 2219–2312.

Gardner, R. B., and Darwin, C. J. (**1986**). ''Grouping of vowel harmonics by frequency modulation: Absence of effects of phonemic categorization,'' Percept. Psychophys. **40,** 183–187.

Gardner, R. B., and Wilson, J. P. (**1979**). ''Evidence for direction specific channels in the processing of frequency modulation,'' J. Acoust. Soc. Am. **66,** 704–709.

Glasberg, B. R., and Moore, B. C. J. (**1990**). ''Derivation of auditory filter shapes from notched-noise data,'' Hear. Res. **47, 103–138.**

Grose, J. H., Hall, J. W., and Mendoza, L. (**1995**). ''Perceptual organization in a comodulation masking release interference paradigm: Exploring the role of amplitude modulation, frequency modulation, and harmonicity,'' J. Acoust. Soc. Am. **97,** 3064–3071.

Grose, J. H., and Hall, J. W. (**1990**). ''The effect of modulation coherence on signal threshold in frequency-modulated noise bands,'' J. Acoust. Soc. Am. **88,** 703–710.

Hacker, M. J., and Ratcliff, R. (**1979**). ''A revised table of d' for M-alternative forced choice,'' Percept. Psychophys. **26,** 168–170.

Hall, J. W., Haggard, M. P., and Fernandes, M. A. (**1984**). ''Detection in noise by spectro-temporal pattern analysis,'' J. Acoust. Soc. Am. **76,** 50–56.

Hartmann, W. M., McAdams, S., and Smith, B. K. (**1990**). ''Hearing a mistuned harmonic in an otherwise periodic complex tone,'' J. Acoust. Soc. Am. **88,** 1712–1724.

Levitt, H. (**1971**). ''Transformed up–down methods in psychophysics,'' J. Acoust. Soc. Am. **49,** 467–477.

Marin, C. M. H., and McAdams, S. (**1991**). ''Segregation of concurrent sounds. II: Effects of spectral envelope tracing, frequency modulation coherence, and frequency modulation width,'' J. Acoust. Soc. Am. **89,** 341–351.

McAdams, S. (**1989**). ''Segregation of concurrent sounds. I: Effects of frequency modulation coherence,'' J. Acoust. Soc. Am. **86,** 2148–2159.

Moore, B. C. J. (**1989**). *An Introduction to the Psychology of Hearing* (Academic, London), 3rd ed.

Moore, B. C. J., and Bacon, S. P. (**1993**). ''Detection and identification of a single modulated component in a complex sound,'' J. Acoust. Soc. Am. **94,** 759–768.

Moore, B. C. J., and Glasberg, B. R. (**1990**). ''Frequency discrimination of complex tones with overlapping and nonoverlapping harmonics,'' J. Acoust. Soc. Am. **87,** 2163–2177.

Moore, B. C. J., and Ohgushi, K. (**1993**). ''Audibility of partials in inharmonic complex tones,'' J. Acoust. Soc. Am. **93,** 452–461.

Moore, B. C. J., and Sek, A. (**1992**). ''Detection of combined frequency and amplitude modulation,'' J. Acoust. Soc. Am. **92,** 3119–3131.

Moore, B. C. J., and Sek, A. (**1994**). ''Effects of carrier frequency and background noise on the detection of mixed modulation,'' J. Acoust. Soc. Am. **96,** 741–751.

Moore, B. C. J., and Sek, A. (**1995**). ''Effects of carrier frequency, modulation rate, and modulation waveform on the detection of modulation and the discrimination of modulation type (amplitude modulation versus frequency modulation),'' J. Acoust. Soc. Am. **97,** 2468–2478.

Moore, B. C. J., and Sek, A. (**1996**). ''Detection of frequency modulation at low modulation rates: Evidence for a mechanism based on phase locking,'' J. Acoust. Soc. Am. **100,** 2320–2331.

Moore, B. C. J., Glasberg, B. R., and Peters, R. W. (**1985a**). ''Relative dominance of individual partials in determining the pitch of complex tones,'' J. Acoust. Soc. Am. **77,** 1853–1860.

Moore, B. C. J., Peters, R. W., and Glasberg, B. R. (**1985b**). ''Thresholds for the detection of inharmonicity in complex tones,'' J. Acoust. Soc. Am. **77,** 1861–1967.

Moore, B. C. J., Glasberg, B. R., and Peters, R. W. (**1986**). ''Thresholds for hearing mistuned partials as separate tones in harmonic complexes,'' J. Acoust. Soc. Am. **80,** 479–483.

Moore, B. C. J., Glasberg, B. R., Gaunt, T., and Child, T. (**1991**). ''Across-channel masking of changes in modulation depth for amplitude- and frequency-modulated signals,'' Q. J. Exp. Psychol. **43A**, 327–347.

Plomp, R., and Levelt, W. J. M. (**1965**). ''Tonal consonance and critical bandwidth,'' J. Acoust. Soc. Am. **38,** 548–560.

Schooneveldt, G. P., and Moore, B. C. J. (**1988**). ''Failure to obtain comodulation masking release with frequency-modulated maskers,'' J. Acoust. Soc. Am. **83,** 2290–2292.

Schouten, M. E. H. (**1986**). ''Three-way identification of sweep tones,'' Percept. Psychophys. **40,** 359–361.

Schouten, M. E. H. (**1985**). ''Identification and discrimination of sweep tones,'' Percept. Psychophys. **37,** 369–376.

Sek, A., and Moore, B. C. J. (**1995**). ''Frequency discrimination as a function of frequency, measured in several ways,'' J. Acoust. Soc. Am. **97,** 2479–2486.

Snedecor, G. W., and Cochran, W. G. (**1967**). *Statistical Methods* (The Iowa State University Press, Ames, IA).

Srulovicz, P., and Goldstein, J. L. (**1983**). ''A central spectrum model: A synthesis of auditory-nerve timing and place cues in monaural communication of frequency spectrum,'' J. Acoust. Soc. Am. **73,** 1266–1276.
Strickland, E. A., Viemeister, N. F., Fantini, D. A., and Garrison, M. A. (**1989**). ''Within- versus cross-channel mechanisms in detection of envelope phase disparity,'' J. Acoust. Soc. Am. **86,** 2160–2166.
Summerfield, Q., and Culling, J. F. (**1992**). ''Auditory segregation of competing voices: Absence of effects of FM or AM coherence,'' Philos. Trans. R. Soc. London, Ser. B **336,** 357–366.
Tsumura, T., Sone, T., and Nimura, T. (**1973**). ''Auditory detection of frequency transition,'' J. Acoust. Soc. Am. **53,** 17–25.
Viemeister, N. F. (**1979**). ''Temporal modulation transfer functions based on modulation thresholds,'' J. Acoust. Soc. Am. **66,** 1364–1380.
Wilson, A. S., Hall, J. W., and Grose, J. H. (**1990**). ''Detection of frequency modulation (FM) in the presence of a second FM tone,'' J. Acoust. Soc. Am. **88,** 1333–1338.
Zwicker, E. (**1952**). ''Die Grenzen der Hörbarkeit der Amplitudenmodulation und der Frequenzmodulation eines Tones,'' Acustica **2,** 125–133.

Pitch strength of iterated rippled noise when the pitch is ambiguous

William A. Yost
Parmly Hearing Institute, Loyola University Chicago, 6525 North Sheridan Road, Chicago, Illinois 60626

(Received 25 June 1996; accepted for publication 29 October 1996)

Two versions of a cascade of delay, gain following delay, and add circuits were used to generate iterated rippled noise (IRN) stimuli. IRN stimuli produce a repetition pitch whose pitch strength relative to the noise percept can be varied by changing the type of circuit, the attenuation, or the number of iterations in the circuit. The repetition pitch of IRN is different when the delayed noise is subtracted (gain <0) rather than added (gain >0) to the undelayed noise. In the case of subtraction, IRN pitch is often ambiguous having two or more pitches. Listeners were asked to use pitch strength to discriminate between various pairs of IRN stimuli generated with different gains, different network circuits, and different number of iterations. For most conditions the gain was less than one. The data were described by a description based on an exponential function of the largest peak of the autocorrelation function of IRN stimuli [W. A. Yost, J. Acoust. Soc. Am. **100**, 511–518 (1996)] processed such that the spectral dominance region is emphasized. These results suggest that the strength of the pitch of IRN stimuli can be described by temporal processing mechanisms as might be revealed by autocorrelation. © *1997 Acoustical Society of America.* [S0001-4966(97)04103-9]

PACS numbers: 43.66.Hg, 43.66.Ki, 43.66.Lj, 43.66.Mk [JWH]

INTRODUCTION

Yost *et al.* (1996), Patterson *et al.* (1996), and Yost (1996b) argued that the strength of the pitch of iterated rippled noise (IRN) depends on the height of the first peak in the autocorrelation function of IRN stimuli.[1] Two networks, shown in Fig. 1, are used to generate IRN stimuli. In the ''add-original'' network, the delayed and added noise is added to the original waveform at each stage (iteration) of the process. In the ''add-same'' network, the delayed and added noise is added back to the previous summed waveform. We use the nomenclature of IRNO (d,g,n) for iterated rippled noise in the add-original configuration and IRNS (d,g,n) for iterated rippled noise in the add-same configuration, where d is the delay in ms, g is gain $(-1\leqslant g\leqslant 1)$, and n is the number of iterations. When $g<0$ (when the delayed noise is subtracted from the underlayed noise), the pitch of IRN stimuli is different than when the delayed noise is added $(g>0)$ to the undelayed noise [see Yost (1996a) for a review of the literature for cases involving addition and subtraction]. When $g>0$ (addition), the pitch of IRN stimuli is equal to $1/d$. When $g<0$ (subtraction), the pitch of IRN stimuli depends on the number of iterations. For $n<4$, the pitch is ambiguous having two values of approximately $1/d$ $\pm 10\%$, and when $n>4$ the pitch tends to e equal to $1/2d$ (see Yost, 1996a).

When $g>0$, all peaks in the autocorrelation function are positive and there are n peaks. When $g<0$, there are also n peaks in the autocorrelation function, but the first peak and its odd integer multiples are negative, while the remaining peaks at the even integer multiples are positive.[2] Yost (1996a) showed that if IRN stimuli are first processed (filtered) such that the spectral region of pitch dominance, which is between $3/d$ and $6/d$ [see Yost (1979,1996a), and Raatgever and Bilsen (1992) for a discussion of the spectral dominance region IRN stimuli] is emphasized, then the largest peaks in the autocorrelation function can be used to account for the pitch of IRN stimuli. That is, the reciprocal of the lags at which the largest peak(s) occurs indicate the pitch. Figure 2 shows three autocorrelation functions for IRNO (4, -1.0, $n=1,3,8$). As can be seen the largest peaks for $n=1$ are those near a lag of 4 ms (at lags of 4.4 and 3.6 ms), while the largest peak for $n=8$ is at a lag of 8 ms, and for $n=3$ peaks at lags of 3.6, 4.4, and 8 ms are all about equal. Thus, based on the reciprocal of the lags of these largest autocorrelation peaks the pitch of these IRNO stimuli should be 227 and 278 Hz when $n=1$, 125 Hz when $n=8$, and all three of these pitches might be the matched pitch of IRNO stimuli when $n=3$. This is what Yost (1996a) obtained [however, see Raatgever and Bilsen (1992) and Cohen *et al.* (1995) for a discussion of spectral models of IRN pitch]. The autocorrelation functions for IRNS stimuli are similar to those of IRNO stimuli, except that the heights of the peaks at integer multiples of d are smaller for IRNS than for IRNO stimuli.

In general, as the heights of the peaks increase the strength of the pitch of IRN stimuli increases. Thus, pitch strength increases as n increases and as g increases. In our previous paper (Yost, 1996b) we studied pitch strength discrimination for IRNO and IRNS stimuli when $g>0$. We found that discrimination performance could be accounted for by using the difference in the exponential of the height of the first peak in the autocorrelation functions for the two stimuli in the discrimination task. For the IRN stimuli of that study, the first peak was always the largest. The use of the exponential function was based on a magnitude estimation pitch strength experiment in which the perceived magnitude of pitch strength was described by an exponential function of

 0001-4966/97/101(3)/1644/5/$10.00

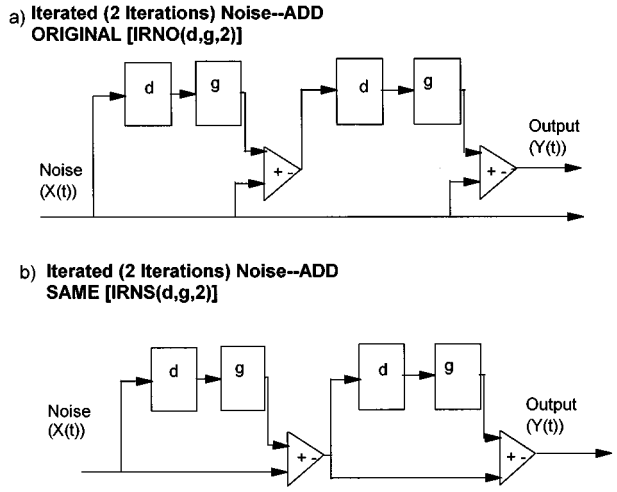

FIG. 1. Schematic diagrams of the delay (d), gain (g), and add networks used to generate various forms of IRN stimuli. (a) Shows the network which produces IRNO stimuli based on the delayed noise being added back to the original noise, and (b) shows the network which produces IRNS stimuli based on the delayed noise at one stage being added back to the delay and added waveform from the previous stage. The gain can be either positive (addition) or negative (subtraction). The notation of IRNO (d,g,n) or IRNS (d,g,n) is used where d is the delay in ms, g is gain ($-1 \leqslant g \leqslant 1$), and n is the number of iterations ($n=2$ in Fig. 1).

the height of the first peak in the autocorrelation function.

In the current study we measured pitch strength discrimination for IRNO and IRNS stimuli when $g<0$ (subtraction). We tested the assumption that discrimination performance would be based on the difference in the exponential functions of the heights of the largest peaks in the autocorrelation functions. We determined the heights of the autocorrelation functions based on filtering the IRN stimuli such that the spectral dominance region between $3/d$ and $6/d$ is emphasized (i.e., the filter is a bandpass filter with cutoffs at $3/d$ and $6/d$; Yost, 1996a).

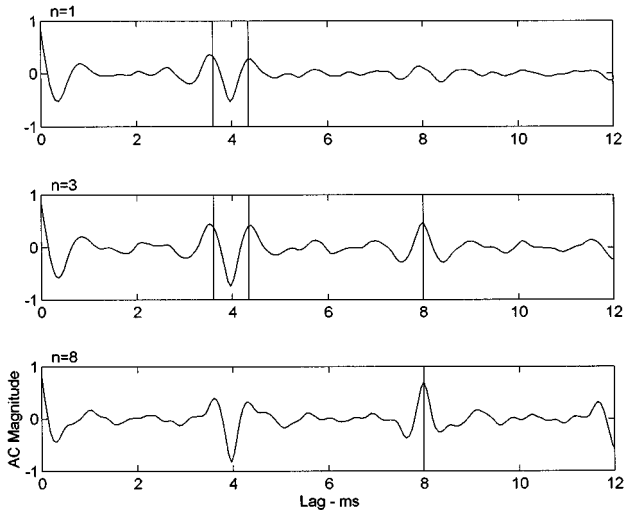

FIG. 2. The autocorrelation functions for three IRNO stimuli, IRNO (4, -1.0,1), IRNO (4,-1.0,3), IRNO (4,-1.0,8). The lags at which the largest positive peaks (marked by vertical lines) occur determine the pitch of IRN stimuli and the height of the peaks determine peak strength.

I. METHODS

Iterated noises were generated on a Tucker Davis Technologies (TDT) system using software delay lines. The waveforms had a Gaussian distribution of instantaneous amplitudes and were played out of 16-bit D-to-A converters at 50 000 samples/s into a 4000-Hz low-pass filter (rolloff of approximately 96 dB/octave). The signals were 500 ms in duration, shaped with a 20-ms $\cos^2$ gate, and presented diotically. The overall level of the stimuli was 70 dB SPL. In all experiments the overall level was roved across each stimulus presentation over a ± 6-dB range about 70 dB SPL (12-dB overall rove). The software delay lines implemented either a network for generating IRNO or IRNS stimuli. In this study the mean delay (d) was always 4 ms. However, because the pitch as well as the pitch strength changes as a function of n, the actual value of d used for each stimulus was randomly chosen form of range of delays ($d=8$, 6, 4.4, 4, 3.6, 3, 2 ms). This range of delays covers the pitch range from an octave above to an octave below 250 Hz the pitch of IRN stimuli when $d=4$ ms and $g>0$. The number of iterations ranged from 1 to 19 and $|g|$ ranged from 0.05 to 1.0. Six listeners with normal hearing participated in the study.

There were three separate experiments: pitch strength discrimination for IRNO stimuli for $g<0$, pitch strength discrimination for IRNS stimuli for $g<0$, and pitch strength discrimination between two IRNO stimuli, one generated with $g=1.0$ and one with $g=-1.0$. In the first two experiments, the listener was presented an IRN stimulus with a low number of iterations (n_l) or a stimulus with a higher number of iterations (n_h). The IRN stimulus generated with n_l was always generated with $g=-1.0$. The IRN stimulus generated with n_h was generated with one of five values of $g(-1.0<g<0)$. The comparisons were between $n_l=1$ and $n_h=3$ and 7; $n_l=3$ and $n_h=5$ and 9; and $n_l=9$ and $n_h=11$ and 16. For IRNO and IRNS stimuli, when $g=1.0$, the height of the first peak is $n/(n+1)$, while for IRNO stimuli the height of the second peak is $(n-1)/(n+1)$.[1] The decrease in the height of the autocorrelation peaks with decreasing g and increasing n is different for IRNO stimuli than it is for IRNS stimuli[1] (see Yost, 1996a). Thus, the five values of g for each comparison were chosen such that one value of g would yield the same height of the second peak for the two stimuli to be discriminated, two values of g would yield heights of the second peak that were greater for the n_h than for the n_l condition, and two values of g were chosen to yield heights of the second peak that were greater for the n_l condition than for the n_h condition.

In the third experiment we measured discrimination between IRNO stimuli for the case in which $g=1.0$ and $g=-1.0$ and such that n was the same for both stimuli. We used $n=1$, $n=3$, $n=5$, and $n=7$. The same randomization level and delay were used as described above.

For all experiments the listeners were presented pairs of these two IRN stimuli in random order and were instructed to indicate whether the pitch of the first or second IRN stimulus was stronger. No feedback was provided. The data were scored as the proportion of times the listeners choose that the pitch of the IRN stimulus generated with n_h (for the first two experiments) or with $g=1.0$ (for the third experiment) was stronger. This proportion was called PS and was

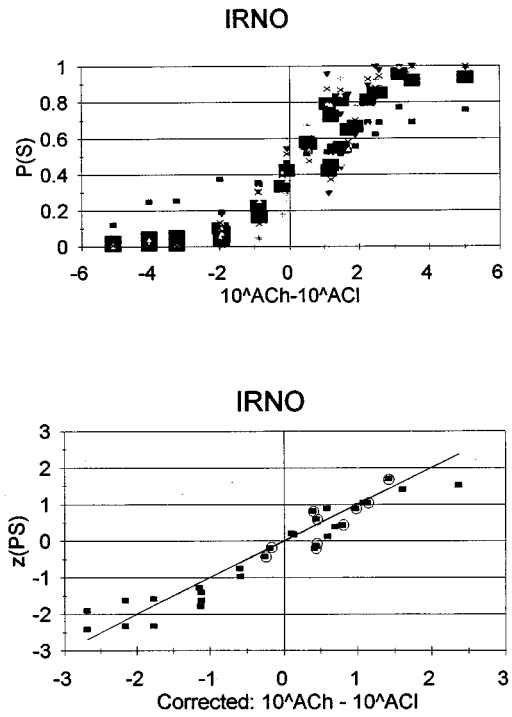

FIG. 3. On top, PS (percent of time the listener chooses the IRNO stimulus with n_h as having the stronger pitch) is shown as a function of the difference in the exponential functions of AC ($10^{\mathrm{ACh}}-10^{\mathrm{ACl}}$), where ACl is the height of first peak in the autocorrelation function for n_l and ACh is the height for n_h. The small data points are the data for each of the six listeners and the large squares are the average data. On the bottom is shown z(PS) (the z-score transform of PS) as a function of the difference in the exponential functions of AC divided by the slope of the linear regression (see text for additional clarification). On the bottom, the line fit to the data has zero intercept and unity slope. The data are for IRNO discriminations.

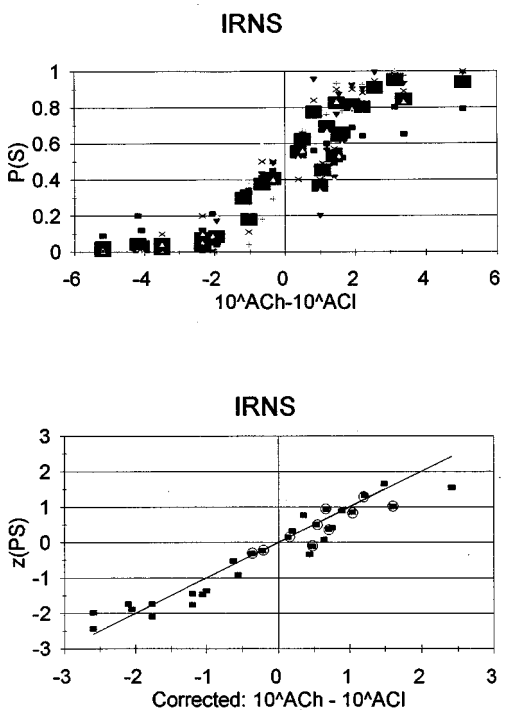

FIG. 4. Same as Fig. 3 except for IRNS discriminations.

based on five blocks of 50 trials obtained for each condition.

On each trial the autocorrelation function for both stimuli was computed after the stimuli had been filtered with a second order Butterworth bandpass filter with cutoffs at $3/d$ and $6/d$. The height of the largest peak for each of the two stimuli in the trial was stored for later analysis (the largest peak for lags greater than 1.75 ms were determined to avoid using a peak near a lag of zero which always produces the largest autocorrelation function peak).

II. RESULTS

The data for IRNO stimuli are shown at the top of Fig. 3 as PS (percent of time the listener chooses the IRNO stimulus with n_h as having the stronger pitch) as a function of the difference in the exponentials of the height of first peak in the autocorrelation functions, where ACl is the height of largest peak in the autocorrelation function for n_l and ACh is the height for n_h. The smaller data points are the data of the individual listeners (each symbol for a different listener) and the large squares are the mean values across listeners. The difference in the exponentials is based on the previous study by Yost (1996b). ACh and ACl were the average values of the largest peaks computed across trials from the stored values for each n and g used for each pair of stimuli to be discriminated. The data with circles around them are those conditions in which the largest peak in the autocorrelation function was almost always in the region of $d\pm10\%$. That is, these are the cases in which $n<4$ (see Fig. 2). For all of the other data the largest peak was almost always that at $2d$.

The form of the data at the top of Fig. 3 is that of a cumulative normal. Thus, as was done in our other study (Yost, 1996b), we computed the z scores for each PS [z(PS)] and replotted the data as z(PS) versus the difference of the exponentials. The data are well fit by a linear regression with a slope of 0.49 which accounts for 90% of the variance. Thus, the difference in the exponentials is proportional to the z scores with the proportionality constant being equal to the slope of the linear regression. Note that the data and the difference in the exponentials differ by a factor that is equal to the slope of the regression line. If we rescale the difference in the exponentials (the abscissa) by the slope of the regression line we obtain the graph at the bottom of Fig. 3, where ''corrected'' means corrected by the slope as just described. If these rescaled data are fit with a line with unity slope and zero intercept as shown in the bottom of Fig. 3, then 87% of the variance is accounted for. This exercise implies that $z(\mathrm{PS})=k(10^{\mathrm{ACh}}-10^{\mathrm{ACl}})$, where k is the slope of the linear regression between z(PS) and the difference in the exponentials. For the data of Fig. 3, k was 0.49.

Figure 4 shows the data in the same form as that used in Fig. 3 but for the case of the IRNS discrimination. For Fig. 4 the slope of the regression line is 0.50 and 83% of the variance is accounted for based on the unity slope and zero intercept fit.

If all of the data for each listener and each condition (IRNO and IRNS discrimination) were fit with a single regression line with a slope of 0.5 and a zero intercept, 80% of the variance was accounted for. This implies that to a good first approximation,

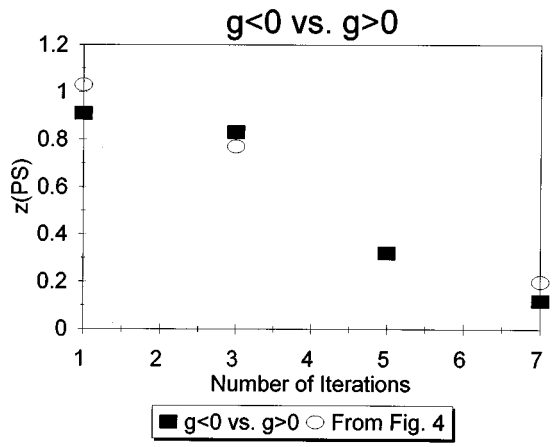

FIG. 5. Plot of $z(\mathrm{PS})$ as a function of the number of iterations (n) for conditions in which the discrimination was between IRNO stimuli generated with $g=1.0$ and $g=-1.0$ (the squares). The circles are data from Fig. 3 in which the largest peaks in the autocorrelation functions are nearly the same as those obtained based on discriminating $g=1.0$ from $g=-1.0$ (the squares).

$$z(\mathrm{PS})=(10^{\mathrm{ACh}}-10^{\mathrm{ACl}})/2, \tag{1}$$

can be used to account for the discrimination data. When each listener's data for each condition was fit with this same regression line (zero intercept and slope of 0.5) between 62% and 94% of the variance could be accounted for across the 12 conditions (six listeners by the two conditions). Thus, performance was based on the height of the largest peak in the autocorrelation function independent on which combination of type of circuit (IRNO or IRNS), delay, or gain was used.

As Yost (1996b) showed PS can also be translated to a d' value (d'_{PS}). Assuming a symmetric criterion for this type of two-alternative, forced-choice task, then (see McMillian and Creelman, 1987):

$$d'_{\mathrm{PS}}=\sqrt{2}z(mPS). \tag{2}$$

Equation (1) shows that: $z(\mathrm{PS})=(10^{\mathrm{ACh}}-10^{\mathrm{ACl}})/2$; thus:

$$d'_{\mathrm{PS}}=(10^{\mathrm{ACh}}-10^{\mathrm{ACl}})\sqrt{2} \tag{3}$$

will also fit the data as well as Eq. (1).

For some of the conditions for IRNO stimuli, a comparison was made between an IRNO stimulus with $n_h=3$ and one with $n_l=1$. For these discriminations and for one value of "g," the height of the largest peak for n_h was 0.5. When $g=1.0$ and $n=1$ there is only one peak and its height is also 0.5. Thus, comparing an IRNO stimulus with $g=1.0$ to one with $g=-1.0$ and $n=1$ would produce the same two heights of the largest peaks in the autocorrelation functions as occurred for $n_h=3$ vs $n_h=1$, with the appropriate gain for the IRNO stimulus generated with n_h. In both comparisons one of the IRNO stimuli is produced with $g=-1.0$ and $n=1$, while for one comparison the other IRNO stimulus was generated with $n=1$ and $g=1.0$ (producing an autocorrelation peak of 0.5) and for the other comparison the other stimulus was generated with $n=3$ and a gain such that the height of the largest autocorrelation peak was 0.5. Figure 5 shows the results (squares) for discriminations between two IRNO stimuli when $g=1.0$ and $g=-1.0$, and when n is equal for each stimulus. $z(\mathrm{PS})$ is based on the stimulus with $g=1.0$ and is shown as a function of "n" (the squares). Also shown (as circles) are data from Fig. 3 in which the heights of the largest peaks in the autocorrelation functions were on average close to those obtained when the discrimination was between $g=1.0$ and $g=-1.0$. When the comparison is between IRNO stimuli with the same largest peaks, performance is similar and the discriminability based on pitch strength decreases with increasing n when the discrimination is between stimuli generated with $g=1.0$ and $g=-1.0$.

III. DISCUSSION

These data appear to support the notion that the pitch strength of IRN stimuli depends on the largest peak in the autocorrelation function. That is, even when the autocorrelation functions have different number of peaks (differ in "n"), it is the height of the largest peak that appears to determine discriminations based on pitch strength. The data of this study are consistent with those obtained by Yost (1996b) when $g>0$. In this case the relationship between $z(\mathrm{PS})$ and the difference of the exponentials was also like that of Eq. (1). That is, for $g>0$ and $g<0$, $z(\mathrm{PS})=(10^{\mathrm{ACh}}-10^{\mathrm{ACl}})/2$, as long as AC is the height of the largest peak in the autocorrelation. These results and those of Fig. 5 indicate that it makes no difference how the stimuli are generated, it is the height of the largest peak that determines pitch strength discriminability, assuming the autocorrelation functions are based on emphasizing the spectral dominance region.

An autocorrelation model has been applied to these data. Since autocorrelation is the Fourier transform of the power spectrum of a stimulus, why not also consider a spectral model? In a series of papers we (Yost *et al.*, 1996; Patterson *et al.*, 1996; Yost, 1996b) have shown that there are many spectral aspects of IRN stimuli that are inconsistent with the results we have obtained based on the pitch strength of IRN stimuli, but these results have been consistent with our use of autocorrelation. A similar set of arguments can be applied to the simuli of this paper based on $g<0$. Thus, we (Yost *et al.*, 1996; Patterson *et al.*, 1996; Yost, 1996b) have commented that processing of the pitch strength of IRN stimuli is more consistent with a temporal processing mechanism, like autocorrelation, than with a purely spectral processing mechanism. However, a spectral model has not been developed to directly account for pitch-strength discrimination data such as those we have obtained (this paper and in Yost *et al.*, 1996; Patterson *et al.*, 1996; Yost, 1996b). Thus, it is possible that there might be a spectrally based model that could account for pitch-strength discrimination data, and deal with the spectral differences among the IRN stimuli. The series of papers cited above do support the use of an autocorrelation approach for accounting for discriminations based on pitch strength.

For $n=1$, Yost *et al.* (1978) have shown that the pitch strength of IRN stimuli was less for $g=-1.0$ than for $g=1.0$ as measured in a pitch discrimination experiment. The experiment involved discriminating between two IRN stimuli that differed in delay as a function of g. That is, when $|g|$ is near one the pitch difference (due to the change in delay)

could be detected, but as $|g|$ approaches zero both IRN stimuli become noisy and the pitch difference disappears. Yost *et al.* (1978) found that there was about a 2–3 dB difference in the threshold between cases in which $g=-1.0$ and $g=1.0$, with the pitch difference for the IRN stimuli generated with $g=-1.0$ being more difficult to discriminate. This 2–3 dB difference is consistent with the small difference in discrimination shown for the $n=1$ data of Fig. 5.

The data shown in Figs. 3 and 4 were based on using a filter for the IRN stimuli that emphasized the dominance spectral region between $3/d$ and $6/d$. As Yost (1979 and 1996a) has shown, the pitch of IRN stimuli, especially for $n<4$, can be accounted for when the stimuli are filtered in this matter. This is especially true when $n=1$, since without filtering there is no positive correlation and only a filter centered at approximately $4/d$ places the positive peaks in the autocorrelation function at approximately $d\pm10\%$ (Yost *et al.*, 1978).

In summary, the results of this study reinforce those of Yost *et al.* (1996), and Petterson *et al.* (1966), and Yost (1996b) showing that pitch strength of IRN stimuli may be determined by the largest peaks in the autocorrelation function. Previous work by these investigators has shown that the autocorrelation function can be viewed as a means of revealing the regularity in the fine structure of IRN stimuli. As such the use of the autocorrelation function for accounting for the pitch and pitch strength of IRN stimuli indicates that this stimulus might be processed in a temporal manner.

ACKNOWLEDGMENTS

This research was supported by a Program Project grant from the National Institute on Deafness and Other Communication Disorders (NIDCD) and a grant from the Air Force Office of Scientific Research (AFOSR). I would like to thank Dr. Sheryl Coombs, Dr. Dick Fay, Dr. Toby Dye, Dr. Bill Shofner, Dr. Greg Sandell and especially Dr. Stan Sheft for their advice regarding this research. I am grateful to Roy Petterson for the many discussions we have had regarding this work and our mutual interest in IRN stimuli.

[1]The Fourier transforms of the square of the magnitude of the transfer functions are given below in terms of the kth Dirac impulse function, $\delta(\Upsilon+kd)$ (for $k\leqslant n$). For the add-original network,

$$\{[g^k(1-g^{2(n-k+1)})]/(1-g^{2(n+1)})\}\delta(\Upsilon+kd),$$

and for the add-same network,

$$\left(\left\{\sum_{j=0}^{n-k}[(n!/(n-j)!j!)(n!/(n-j-k)!(j+k)!)g^{k+2j}]\right\}\Big/\left\{\sum_{j=0}^{n}[(n!/(n-j)!j!)g^j]^2\right\}\right)\delta(\Upsilon+kd).$$

These functions can be assumed to be the normalized autocorrelation functions of an ensemble average of infinitely wide wideband noise. The height of the peak in the function at lag kd is given by the term in front of the Dirac function, $\delta(\Upsilon+kd)$. In this paper we use the term autocorrelation function to refer to the normalized autocorrelation function.

[2]As Yost (1996a) points out, both a spectral-like and a temporal-like model can account for the pitch of IRN stimuli. However, since Yost *et al.* (1996), Patterson *et al.* (1996), and Yost (1996b) have all shown that the pitch strength of IRN stimuli can be accounted for by an autocorrelation analysis, but are inconsistent with a spectral analysis, this paper will consider primarily a temporal approach (as described by the autocorrelation analysis) for describing pitch strength discrimination.

Cohen, M. A., Grossberg, S., and Wyse, L. L. (**1995**). ''A spectral network model for pitch perception,'' J. Acoust. Soc. Am. **98,** 862–880.

Mc Millian, N. A., and Creelman, C. D. (**1991**). *Detection Theory: A User's Guide* (Cambridge U.P., New York).

Patterson, R. P., Handel, S., Yost, W. A., and Datta, A. J. (**1996**). ''The relative strength of tone and noise components of iterated rippled noise,'' J. Acoust. Soc. Am. **100**, 3286–3294.

Raatgever, J., and Bilsen, F. A. (**1992**). ''The pitch of anharmonic comb filtered noise reconsidered,'' in *Auditory Physiology and Perception*, edited by Y. Cazals, L. Demany, and K. Horner (Pergamon, Oxford).

Yost, W. A., Hill, R., and Perez-Falcon, T. (**1978**). ''Pitch and pitch discrimination of broadband signals with rippled power spectra,'' J. Acoust. Soc. Am. **63,** 1166–1173.

Yost, W. A. (**1979**). ''Models of the pitch and pitch strength of rippled noise,'' J. Acoust. Soc. Am. **66,** 400–411.

Yost, W. A. (**1996a**). ''Pitch of iterated rippled noise,'' J. Acoust. Soc. Am. **100,** 511–518.

Yost, W. A. (**1996b**). ''Pitch strength of iterated rippled noise,'' J. Acoust. Soc. Am. **100,** 3329–3335.

Yost, W. A., Patterson, R. D., and Sheft, S. (**1996**). ''A time domain description for the pitch strength of iterated rippled noise,'' J. Acoust. Soc. Am. **99,** 1066–1078.

Onset dominance in lateralization

Richard L. Freyman
Department of Communication Disorders, University of Massachusetts, Amherst, Massachusetts 01003

Patrick M. Zurek
Research Laboratory of Electronics, Massachusetts Institute of Technology, Cambridge, Massachusetts 02138

Uma Balakrishnan and Yuan-Chuan Chiang
Department of Communication Disorders, University of Massachusetts, Amherst, Massachusetts 01003

(Received 12 April 1993; revised 12 February 1996; accepted 21 October 1996)

Saberi and Perrott [Acustica **81**, 272–275 (1995)] found that the in-head lateralization of a relatively long-duration pulse train could be controlled by the interaural delay of the single pulse pair that occurs at onset. The present study examined this further, using an acoustic pointer measure of lateralization, with stimulus manipulations designed to determine conditions under which lateralization was consistent with the interaural onset delay. The present stimuli were wideband pulse trains, noise-burst trains, and inharmonic complexes, 250 ms in duration, chosen for the ease with which interaural delays and correlations of select temporal segments of the stimulus could be manipulated. The stimulus factors studied were the periodicity of the ongoing part of the signal as well as the multiplicity and ambiguity of interaural delays. The results, in general, showed that the interaural onset delay controlled lateralization when the steady state binaural cues were relatively weak, either because the spectral components were only sparsely distributed across frequency or because the interaural time delays were ambiguous. Onset dominance can be disrupted by sudden stimulus changes within the train, and several examples of such changes are described. Individual subjects showed strong left–right asymmetries in onset effectiveness. The results have implications for understanding how onset and ongoing interaural delay cues contribute to the location estimates formed by the binaural auditory system. [S0001-4966(97)01003-5]

PACS numbers: 43.66.Pn, 43.66.Qp [HSC]

INTRODUCTION

When two brief binaural sounds are presented within a few ms of one another such that a fused image is heard, the interaural time delay (ITD) of the earlier sound generally contributes substantially more to the image's lateral position than does the ITD of the later sound (Wallach *et al.*, 1949; Yost and Soderquist, 1984; Shinn-Cunningham *et al.*, 1993). The greater perceptual weight given the earliest arriving directional cues has been called the precedence effect (see Gardner, 1968; Blauert, 1984; and Zurek, 1987, for reviews).

The most dramatic demonstrations of the importance of the first-arriving wavefront come from both free-field and earphone studies in which directional cues at signal onset oppose those contained within the remainder of a relatively long sound (Thurlow *et al.*, 1965; Kunov and Abel, 1981; Abel and Kunov, 1983; Hartmann and Rakerd, 1989; Saberi and Perrott, 1995). Thurlow *et al.* (1965) demonstrated that if a pulse was presented from a loudspeaker 50° left of midline, and a 40- or 400-ms 1500-Hz tone was gated on synchronously with the pulse from a second loudspeaker at 10° right of midline, the tone's perceived location was shifted to the loudspeaker that produced the pulse (50° left). In a demonstration of the Franssen effect (Franssen, 1962), Hartmann and Rakerd (1989) presented the onset transient of a 500-Hz tone from one loudspeaker, then gated the initial transient off as the steady state portion was gated on from a second loudspeaker at a different location. Remarkably, for many conditions, the entire stimulus appeared to originate from the onset loudspeaker, even though the stimulus from the second loudspeaker continued uninterrupted until a response was made.

Using pure tones of at least 200-ms duration, Kunov and Abel (1981) delayed the tone to one earphone by between one-half and one full period, creating an ongoing phase lead (less than 180°) in the same ear that had the delayed onset. For short rise/fall times, lateralization was almost completely determined by the onset time disparity, rather than the ongoing phase disparity. Saberi and Perrott (1995) found that when a train of several hundred binaural pulse pairs having a time lead to one ear was preceded by a single pulse pair with a time lead to the opposite side, listeners often reported hearing the entire stimulus on the side of the onset lead. The effect was observed only for interpulse intervals (IPIs) of about 2 ms or less.

Some investigators have found that ongoing cues, not onset cues, are more important for lateralization. For example, Tobias and Schubert (1959), using a broadband noise with an ongoing lead to one ear and an onset-gating lead favoring the other ear, found that the ongoing delay dominated lateralization. Buell *et al.* (1991) found that ongoing delays are usually more influential than gating delays in the lateralization of low-frequency pure tones, except for conditions in which the ongoing tone is interaurally ambiguous. This finding of the importance of ambiguity in the steady

state stimulus may be related to the ''plausibility'' concept discussed by Hartmann and Rakerd (1989), who showed that onset transients control localization in a sound field when localization cues in the steady state stimulus are weak or implausible.

Zurek (1993) attempted to resolve some of the differences between the studies by looking at the nature of the interaural cues at onset, noting that Tobias and Schubert (1959) and Buell *et al.* (1991) used a gating delay, not a delay of the whole waveform. Zurek suggested that a gating delay, being an example of an envelope delay, is likely to be dominant only for high-frequency stimuli. A whole waveform delay, such as that used by Kunov and Abel (1981) and Abel and Kunov (1983), would be expected to be a stronger onset cue for low-frequency or broadband sounds. However, the method employed in those two studies required that the onset delays be of greater magnitude than the opposing ongoing delays, which could complicate comparisons of their relative strengths (Buell *et al.*, 1991). The type of pulse train stimuli used by Saberi and Perrott (1995) would seem to be very useful for assessing the relative potency of onset and ongoing cues, because the onset and ongoing delays are both waveform delays that are separately manipulable. The selection of stimuli for the current study exploited this property of this type of stimulus.

In the current study, binaural pairs of pulses or noise bursts were used as the onset stimulus, with interaural delays of 500 μs leading to the right or left. With the interaural onset delay fixed at these values, aspects of the ongoing stimulus, which was either a train of pulses or noise bursts or a tone complex, could be manipulated independently to identify which factors facilitate the dominance of onsets. The experiments focused primarily on the importance of ambiguity in the ongoing stimulus. Ambiguity appeared to be a requirement for the gating delay to control lateralization in the Buell *et al.* (1991) study. However, Saberi and Perrott's (1995) experiment with pulse trains demonstrated onset dominance in lateralization for stimuli with apparently straightforward ongoing interaural delays. Experiment 1 used trains of pulses with different patterns of interaural delay to study the importance of ambiguity in the steady-state stimulus. In experiment 2, trains of noise bursts and inharmonic tone complexes were used to manipulate patterns of interaural correlation and spectral density.

I. EXPERIMENT 1: LATERALIZATION OF PULSE TRAINS

A. Stimuli and rationale

Stimuli consisted of binaural pulse trains of the three types depicted schematically in Fig. 1. Individual electrical pulses were 50 μs in duration. In all cases, the initial, or ''onset,'' pulse pair will be distinguished from the remainder of the pulse train, which will be called the ''ongoing'' part of the train. In type 1 stimuli, pulse pairs with a 500-μs lead to one ear alternated with pairs having the same time lead favoring the other ear. In type 2 stimuli, a left- or right-leading pair alternated with a diotic pair in the ongoing part, and a pulse pair with a lead opposite to that of the nondiotic pair in the ongoing train was added at the beginning of the waveform. Type 3 stimuli were essentially the same kind used by Saberi and Perrott (1995): A train of pulse pairs with a consistent 500 μs lead to one ear was preceded by an initial pulse pair leading by 50 μs to the opposite ear (except when the IPI was 1 ms, in which case left and right ongoing delays were equivalent). For all three types, IPIs were 1, 2, 3, 4, and 5 ms, measured as the time between the onsets of adjacent pulse pairs (see markers in Fig. 1 for a 2-ms IPI). The total stimulus duration was always 250 ms.

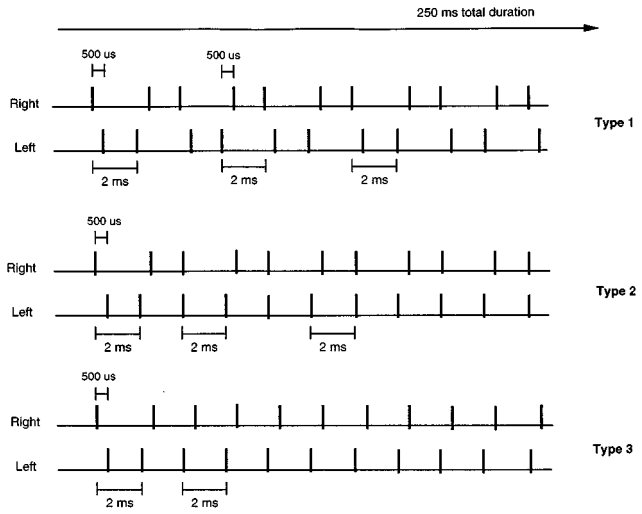

FIG. 1. Schematic diagram of the initial portion of the waveforms (amplitude as a function of time) delivered to the right and left earphones for three types of signals used in experiment 1. The three examples depicted have a 2-ms IPI and right-leading interaural onset delays. The entire set of stimuli varied with respect to IPI (1–5 ms). Half the conditions had right-leading onsets (as shown in the figure). In the other half the right and left channels were reversed. The interaural delays were always 500 μs favoring either the right or left ear.

The three types of stimuli were designed to determine the extent to which ambiguous interaural time disparities during the ongoing part of the train facilitate the dominance of onset delays. Type 1 trains had ambiguous interaural delays at all IPIs, whereas with type 3 trains, the only ambiguity arises from the complementary interaural delay at IPI minus 500 μs. If ambiguity is important, then one might expect that the onset delay would control lateralization at all IPIs for type 1 trains. However, for type 3 trains, the dominance of onsets should disappear as IPI is increased. Type 2 trains had ambiguous interaural delays at all IPIs but, unlike type 1, none of the delays matched that of the onset delay. Buell *et al.* (1991) suggested that the function of enhanced sensitivity to onset cues might be to select between competing ongoing delays, especially when the onset delay matches or is close to one of the ongoing delays. Extending that general idea to the current stimuli predicts a stronger influence of the onset delay in type 1 relative to type 2 pulse trains.

B. Procedures

Lateralization was measured using an interaural-delay based acoustic pointer that was alternated with the target pulse train. The pointer was a 50-ms burst of binaural white

noise. Subjects adjusted the ITD of the pointer until it appeared in the same intracranial position as the target. If the image separated into an initial click and steady-state sound, listeners were instructed to base their match on the steady-state sound. If multiple steady-state images were heard, listeners were instructed to base their match on the strongest image. To control the pointer ITD, subjects rotated the knob of a five-turn potentiometer, the position of which was read by an analog-to-digital (A/D) converter. Based on the A/D output, the pointer ITD was modified with 20-μs resolution over the range of $+800$ μs (right) to -800 μs (left) to control the intracranial lateral position of the image. Matching procedures were similar to those used by Buell *et al.* (1991), although their pointer was adjusted by varying interaural intensity rather than time differences. During each trial, subjects heard three presentations of the pointer alternating continuously with three presentations of the target stimulus. The onset-to-onset delay between presentations both within and between target and pointer was 500 ms. Subjects took as long as necessary to adjust the pointer until it appeared to be lateralized at the position of the target. By pressing a key on a response terminal, they had the opportunity to override the alternation between target and pointer and listen to either for an unlimited period. Another key produced a pause in the presentations. After making a tentative match, subjects occasionally found it helpful to check the match following a short pause before actually entering their final response. The mapping between the A/D output and the pointer ITD was shifted randomly after each trial, making it useless for subjects to return to specific knob positions on successive trials. Because we did not run a separate experiment mapping the noise-burst pointer to perceived lateral position, it is not possible to identify precisely the intercranial position of the pointer at any specified interaural delay. However, Blauert's (1983, p. 144) replotting of the lateralization data of Toole and Sayers (1965) suggests a linear relationship between ITD and extent of lateralization in the range of approximately $+/-600$ μs, with interaural delays of 500 μs producing about 75% of maximum lateralization toward the ear. A linear relationship would indicate that the extent of laterality of the pointer with a 250-μs delay is half that of the 500-μs delay.

Both target and pointer were synthesized on a 80386-based microcomputer and presented from a two-channel 16-bit D/A converter (TDT QDA2). The analog signals were low-pass filtered at 8.5 kHz (TTE J1390), attenuated (Charybdis), impedance transformed, and delivered to a matched set of TDH-39 earphones mounted in MX-41/AR cushions. The earphones had a flat response between approximately 500 and 6000 Hz, with a gradual attenuation below 500 Hz and a steeper attenuation above 6000 Hz. The target signals were presented at a 20-kHz D/A conversion rate, and the pointer at a 50-kHz rate, the latter providing the 20-μs resolution in pointer ITD. Signal levels were calibrated in a 6 cm^3 coupler using a sound level meter set on the ''fast'' response. Target signal levels ranged from 60 dB SPL for long IPIs to 65 dB SPL for short IPIs. The pointer was presented at 62 dB SPL.

Subjects listened to blocks of 11 trials, with the stimulus type fixed within a block. All five IPIs (from 1 to 5 ms) were presented within each block; five trials had right-leading onsets, as shown in Fig. 1; in another five, the entire stimulus was reserved, right to left, for a total of 10 trials. The eleventh stimulus was a diotic 250-ms pulse train with a 3-ms IPI. This stimulus was easy to match and provided a means of evaluating whether subjects could make consistent matches to a punctate, well defined target. The 11 stimuli were presented in random order within a block. Six repetitions of each block were distributed essentially evenly through a total of 18 blocks (6 matches×3 types). The earphones were refitted by the subjects after each block. The experiment was typically completed in three listening sessions.

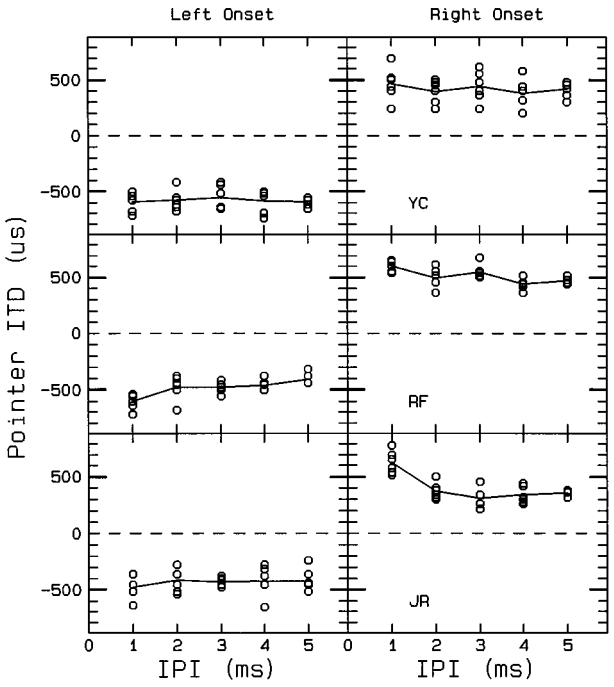

FIG. 2. Acoustic pointer matches for type 1 stimuli as a function of IPI for both left- and right-leading onset delays. Positive numbers indicate that the pointer led to the right, negative to the left. Results for the three subjects are shown. A data point indicates a single adjustment; solid lines connect means.

Listeners were three young adults with pure-tone air conduction thresholds of less than or equal to 15 dB HL (*re*: ANSI, 1989) at 0.25, 0.5, 1, 2, 3, 4, 6 kHz. Two of the subjects, RF and YC, were authors.

C. Results

Figures 2–4 display the raw matches for the three stimulus types for all three subjects. The pointer ITD (positive for right-leading, negative for left-reading) is plotted as a function of the IPI of the pulse train. For type 1 stimuli (Fig. 2), where the pulse pairs within a train alternated between left leading and right leading, the signals were matched on the side of the initial pulse pair for all IPIs. There was a tendency, especially for JR right onset and RF left onset, for the pointer ITD to become more central with increasing IPI.

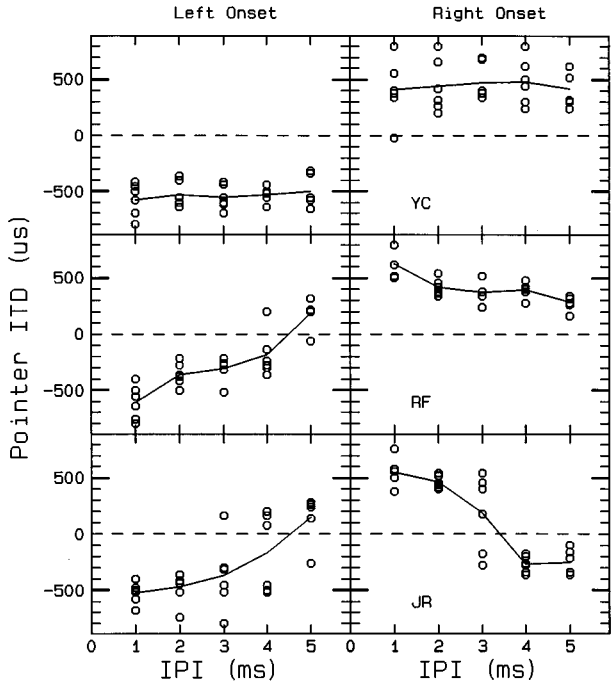

FIG. 3. As in Fig. 2, but with type 2 stimuli.

Figure 3 displays the results for the type 2 stimuli in which the ITDs in the ongoing train alternated between +500 and 0 μs or −500 and 0 μs. The influence of the onset (which opposed the right- or left-leading ongoing ITD) seemed to depend upon the subject and, for a given subject, upon the ear to which the first pulse pair led. For JR, the onset pulse pair was very influential at IPIs of 1 and 2 ms and weaker at 3 and 4, with variable or bimodal adjustments. With IPI=5 ms, the majority of matches were somewhere between the two ongoing ITDs being alternated. RF's data show a strong influence of the onset at the short IPIs and a relatively steady migration toward zero as the IPI was increased. An asymmetry in RF's data is quite noticeable, with the onset dominance stronger when the right ear received the onset lead. YC appeared to maintain a strong influence of the onset across the IPIs, although the variability of matches suggests a diffuse or variable image, or multiple images, particularly for right onset.

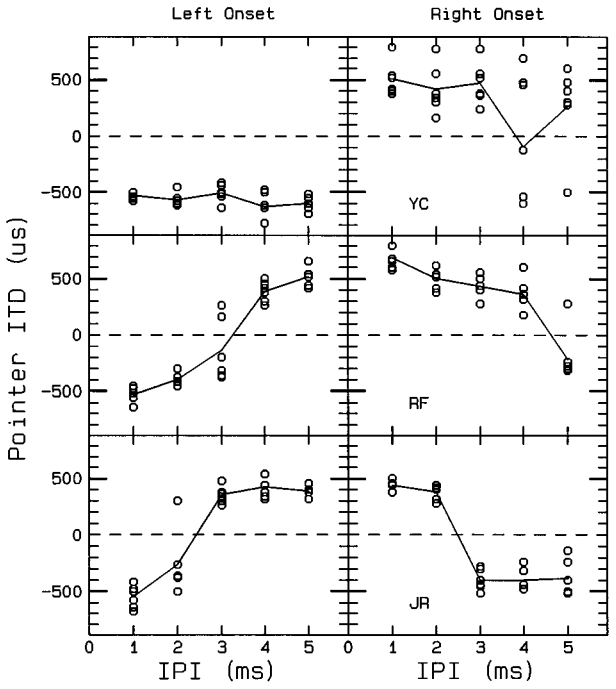

FIG. 4. As in Fig. 2, but with type 3 stimuli.

As shown in Fig. 4, the onset was least potent for type 3 stimuli as IPI increased, especially for JR and for RF left onset. YC lateralized the left-onset signals to the left but, as with the type 2 stimuli, did not lateralize the right-onset signals consistently. At IPIs of 4 and 5 ms, there were matches to both right and left. The bimodal pattern of responses observed for this and several other conditions (e.g., RF left onset at the 3-ms IPI) may reflect the presence of multiple or unstable images. The asymmetry for RF was again in favor of the right-leading onset. When the onset pulse pair led to the right, its influence on lateralization lasted through longer IPIs than in the opposite case. The origin of the asymmetry is not clear, but it should be noted that similar biases have been noted in sound field measurements of the precedence effect (Clifton and Freyman, 1989; Grantham, 1996).

From informal observation during listening to the type 3 stimuli, we suspect that the specific IPIs at which the image begins to follow the ongoing rather the onset ITD is not independent of the paradigm used to obtain the matches. The multiple repetitions of the target bursts during the matching procedures seemed to solidify the perception of a single image. For example, at some of the longer IPIs, split images were sometimes heard in the first one or two presentations of the target signals before a single stable image emerged. For the first author, the experience was similar to listening to the ''buildup'' of echo suppression that has been observed in sound field studies of the precedence effect (e.g., Clifton and Freyman, 1989; Freyman *et al.,* 1991; Grantham, 1996).

The mean pointer adjustments for the diotic control stimulus, based upon 18 matches across all conditions in experiment 1 were −17.4 μs (s.d.=27.4 μs) for JR, −1.1 μs (s.d.=22.6 μs) for RF, and −38.9 μs (s.d.=44.0 μs) for YC. Similar results were obtained in experiment 2. The reason for this relatively small but consistent bias to the left is not clear to us, but possibly involved small asymmetries in headphones or subjects' thresholds that affected the continuous-spectrum pointer differently than the diotic pulse train.

II. EXPERIMENT 2: NOISE BURSTS AND INHARMONIC COMPLEXES

A. Rationale

This experiment was an attempt to determine whether the existence of some degree of rivalry or ambiguity between ongoing interaural delays is required for the onset to contribute substantially to lateralization. For the type 1 stimuli in experiment 1, interaural cues in the ongoing train were completely ambiguous, and one of the ongoing ITDs was equal to the onset ITD. The results indicated that if the stimulus is gated on abruptly, the ambiguity is resolved in favor of the

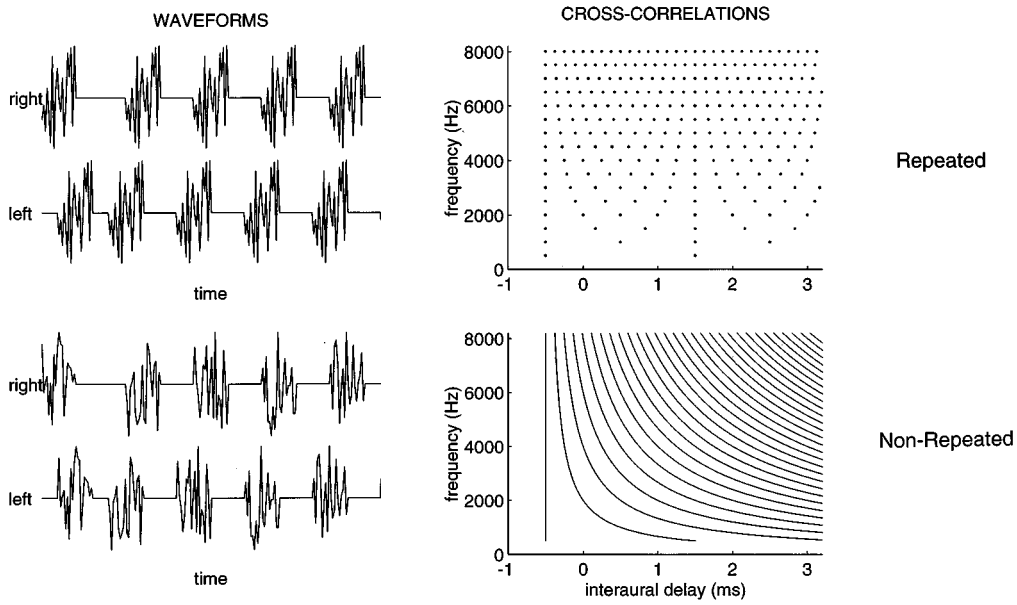

FIG. 5. First 10 ms of the waveforms (amplitude as a function of time) and cross correlation peaks for the repeated (top) and nonrepeated (bottom) burst conditions in experiment 2.

lead ear of the first pulse pair. One could think of the onset disparity as resolving the ambiguity, or ''tipping the scale'' (Buell *et al.*, 1991) in favor of the onset side. The type 2 signals were also interaurally ambiguous during the ongoing train, but the onset ITD did not correspond to either of the ongoing ITDs.

With the exception of the 1-ms IPI, which was completely ambiguous, in type 3 trains the ongoing part led consistently toward the ear opposite that to which the onset led. However, while the ongoing part of the type 3 stimulus shown in Fig. 1 is nominally left leading with a 500-μs ITD, it can also be considered right leading with a 1500-μs ITD, due to the 2-ms periodicity. The 500-μs ITD is generally thought to be a much stronger cue that the 1500-μs ITD because of its ''centrality,'' or proximity to zero (Stern *et al.*, 1988). Because of the difference in centrality between left- and right-leading delays, one would not normally think of the ongoing part of the type 3 pulse train shown in Fig. 1 as ambiguous. However, as demonstrated by Blodgett *et al.* (1956), some ability to use interaural correlation for lateralization extends to quite long delays (10–20 ms). Therefore, although the longer delay (IPI-500 μs) may be a weaker cue than the 500-μs delay, it might still influence lateralization, particularly if an initial pulse pair leads to that side. Note that for type 3 signals, as the IPI increases the difference in centrality between the two cues increases (one is fixed at 500 μs while the other is IPI-500 μs), which may explain why the effect tended to break down at the longer IPIs for type 3, but not type 1 stimuli, which continue to have bidirectional cues, even at long IPIs. For the moment at least, it is assumed that all three stimulus configurations in experiment 1 contain at least some degree of interaural ambiguity during the ongoing train, arising from the use of identical pulses in the train. To control the amount of ambiguity more directly, noise bursts and inharmonic complexes were used in this experiment instead of pulses.

B. Noise-burst train conditions

1. Stimuli

Stimuli were trains of 1-ms bursts of digitally synthesized Gaussian noise presented in two conditions. The trains had the same structure of nominal interaural delays as the type 3 stimuli used in the previous experiment, with a 2-ms IPI. However, they differed in the sequence of repetitions of individual tokens, resulting in different degrees of ambiguity and interaural correlation during the ongoing part of the train. The first 10 ms of the 250-ms stimuli are shown in the left side of Fig. 5. The example of right-leading onset, left-leading ongoing is shown. In the repeated burst condition, a single noise token was used throughout the train. Because all the tokens were identical for a given stimulus, these trains contained the same type of interaural ambiguity described above for pulses.

In the nonrepeated burst condition, the individual tokens were not repeated during the train. The bursts were correlated within pairs, but not between pairs. In the example shown, the interaural correlation during the ongoing part of the train is only left leading, eliminating any interaural ambiguity during the ongoing part of the train. Differences between the repeated and nonrepeated conditions can also be seen in the right side of Fig. 5, which displays peaks in the interaural cross correlation of the ongoing portion as a function of frequency. The cross correlation of the repeated burst stimulus has a straight trajectory in the frequency-delay (''F-tau'') plane at the nominal delay of -500 μs and a ''slipped-cycle'' trajectory at $+1500$ μs, due to the 2-ms periodicity. The nonrepeated burst stimulus has only one straight trajectory, which is at -500 μs.

For both kinds of stimuli, three different frozen noise-burst trains were created using different random number generator seeds (one of the three is shown in Fig. 5). Two subconditions were run, one with the abrupt opposing onset as

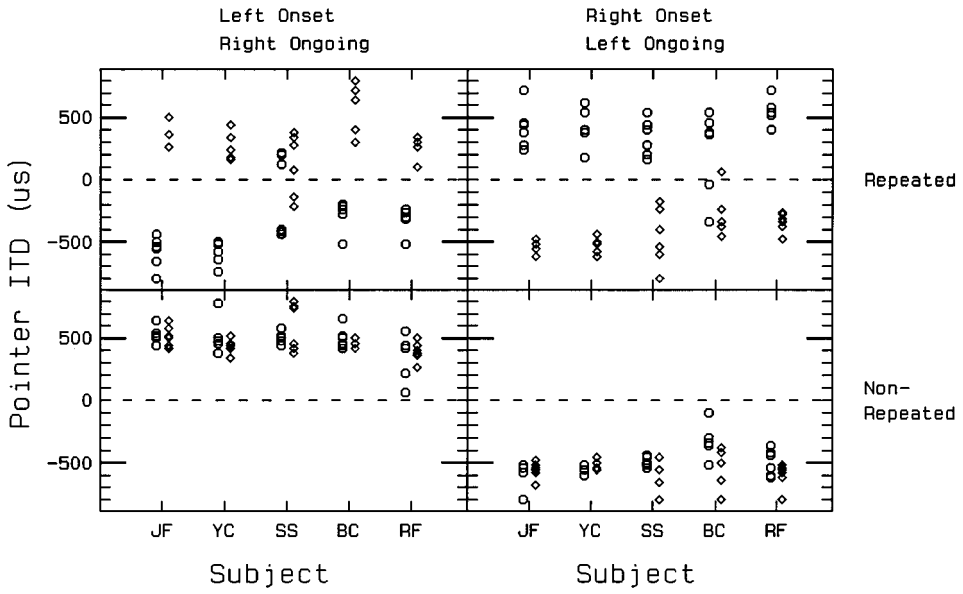

FIG. 6. Acoustic pointer matches for the repeated and nonrepeated burst conditions in experiment 2. Circles show results for trains with an abrupt opposing onset. Diamonds show matches for the same stimuli that had been gated on and off slowly with 125-ms linear rise and fall times.

shown in Fig. 5, and a second in which the ongoing part was presented with the opposing initial burst pair removed, and was gated on and off slowly with a 125-ms linear rise/fall time. This latter condition was presumed to indicate where the ongoing part of the sound would be lateralized in the absence of an abrupt onset.

2. Subjects and procedures

Subjects consisted of two listeners from experiment 1 and three additional normal-hearing listeners. Matching procedures were identical to those used in experiment 1. Subjects performed six matches for each of eight conditions (repeated or nonrepeated bursts×abrupt onset or gradual onset ×left leading or right leading) arranged in 12 blocks of 4 matches each.[1] The blocks, which consisted of both repeated and nonrepeated bursts for the left-onset right-ongoing and right-onset left-ongoing signals, also included the control stimulus with no delay used in experiment 1. Among the six matches obtained for a particular stimulus, each of the three tokens was presented twice.

All abrupt-onset signals were presented at 62 dB SPL. Attenuator settings for the gradual-onset signals were the same as for the abrupt-onset conditions, i.e., there was no compensation for any reduction in overall level that may have resulted from the gradual rise/fall times.

3. Results

The results are displayed in Fig. 6. Pointer adjustments for the abrupt-onset stimuli are represented by circles, and the data for the gradual-onset signals are represented by diamonds. Differences between the two should reveal the effect of the initial burst. The gradual-onset results (diamonds) for both the repeated and nonrepeated burst stimuli were as expected. They show, with a few exceptions (e.g., SS left onset), that the ongoing part of the stimulus was lateralized toward the side having the 500-μs ongoing time lead. The repeated burst signals gated on abruptly and preceded by an initial burst pair leading to the opposite side (circles) were almost always heard on the side of the onset lead. Again, the data from SS left onset, which show bimodal responses, were the most notable exception. In contrast, the results for the nonrepeated bursts with the abrupt opposing onsets indicate that lateralization judgments were always determined by the ongoing interaural differences, not the onsets.

The differences in results between the two conditions lead to a preliminary conclusion that the presence of ambiguity is necessary for an opposing onset delay to control the lateralization. When ambiguity is present in the form of interaural correlation in both the right- and left-leading directions (repeated bursts), the interaural onset delay dominates lateralization. When this ambiguity is not present (nonrepeated bursts), the onset delay has no effect.

This interpretation based on ambiguity must be evaluated in light of other possible explanations. For example, a second difference between the repeated and nonrepeated conditions is that the ongoing stimulus in the repeated condition is periodic with a discrete spectrum and tonal quality, while the nonrepeated condition has a continuous spectrum and noisy quality. The cross-correlation peak functions in Fig. 5 demonstrate the difference in spectrum. Hartmann and Rakerd (1989), when evaluating conditions where the Franssen effect did or did not occur, suggested that the density of the spectrum of the steady-state sound was an important factor. Hartmann (1983) had found that a densely distributed harmonic complex was easier to localize than a sparsely distributed complex when the signals were gating on slowly. Hartmann and Rakerd (1989) reasoned that the richer the directional cues from the steady-state location, the less likely that an initial broad-spectrum transient could dominate the localization. Similarly, in the current experiment, it is possible that onset cues dominate lateralization when the spectrum of the ongoing part of the sound is sparsely distributed,

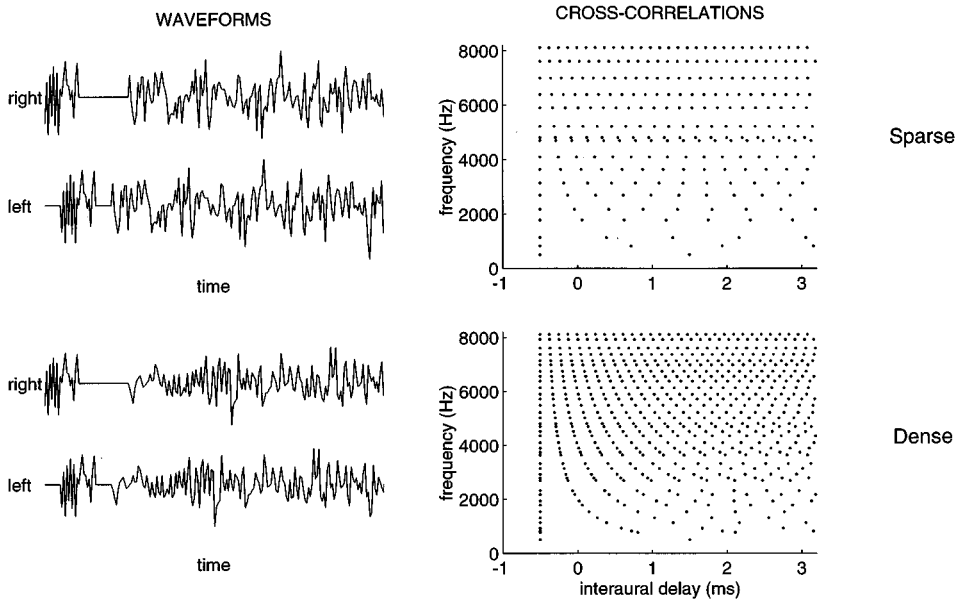

FIG. 7. Waveforms (first 10 ms) and cross correlation peaks for the sparse and dense inharmonic complex conditions in experiment 2.

while ongoing cues dominate when the spectrum of the ongoing part is also dense. The above conditions cannot distinguish between the two explanations, because ambiguity is a consequence of repetition, and repetition produces a discrete spectrum. While it is possible that both factors are involved, an attempt was made to sort out the relative importance of ambiguity and spectral density in two additional conditions described below.

C. Inharmonic tone complexes

1. Stimuli and procedures

Stimuli were 250-ms complexes of inharmonically related tones created by summing equal-amplitude sinusoids in sine phase within the frequency range of 500–8111 Hz with two different degrees of spectral density. The signal presented to the two ears was identical expect for a 500-μs time delay imposed on one channel. The use of inharmonic complexes insured that the interaural time delay was unambiguous. That is, a straight trajectory in the F-tau plane occurred at only one delay, the nominal interaural delay of 500 μs or -500 μs. As seen in the example in Fig. 5, top, for the repeated bursts, a harmonic spectral structure produces multiple straight trajectories in the F-tau plane because a delay of one full cycle at 500 Hz is the same time delay as two periods of 1000 Hz, three periods of 1500 Hz, etc. Thus, straight trajectories are seen (i.e., consistent correlation peaks across frequency) at delays separated by one period of the fundamental. If the tones in a complex are not harmonically related, no such consistency across frequency occurs except at the nominal interaural delay. Thus, inharmonic complexes have an unambiguous time delay.

Two types of complexes were created with different degrees of spectral density. The Sparse complex had a total of 17 components, approximately the same number of components as the repeated-burst trains over the same frequency range. The specific frequencies were 500, 820, 1125, 1776, 2171, 2689, 3133, 3634, 4092, 4687, 4800, 5212, 5890, 6375, 6892, 7600, and 8111 Hz. The sparse complex was a subset of the dense complex, which consisted of an additional 22 components for a total of 39. These were 500, 766, 820, 922, 1125, 1308, 1531, 1776, 1928, 2171, 2309, 2689, 2782, 2915, 3133, 3314, 3634, 3740, 3887, 4092, 4342, 4506, 4687, 4800, 5008, 5212, 5479, 5715, 5890, 6129, 6375, 6552, 6744, 6982, 7130, 7369, 7600, 7923, and 8111 Hz. The choice of specific frequencies was essentially arbitrary, and was modified several times after viewing the cross correlation functions before a final set was selected. The addition of sinewaves in phase produced an initial high-amplitude peak in the waveforms that was trimmed off digitally. The first 10 ms of the waveforms (right-leading onset, left-leading ongoing) and idealized cross-correlation peak functions of the ongoing stimuli are shown in Fig. 7. As shown, the ongoing waveforms (excluding the initial burst pair) are unambiguously left leading, and the cross-correlation functions reveal no straight trajectories except at the imposed interaural delay.

Like the noise-burst conditions in Sec. II B, two subsets of conditions were run. One included the 1-ms noise bursts from Sec. II B added 2 ms (onset to onset) in front of the ongoing complexes with a 500-μs interaural delay opposing the ongoing delay. The same three frozen noise waveforms from the repeated burst condition were used, one example of which is shown in Fig. 7. The power in the burst was adjusted to be equal to the average power in the ongoing stimulus. Because the power in the dense and sparse complexes was equivalent, the level of each component was lower in the dense complex. The other subset had a 125-ms rise/fall time imposed on the ongoing stimulus and had no onset noise bursts. Matching procedures were identical to those described in Sec. II B above.

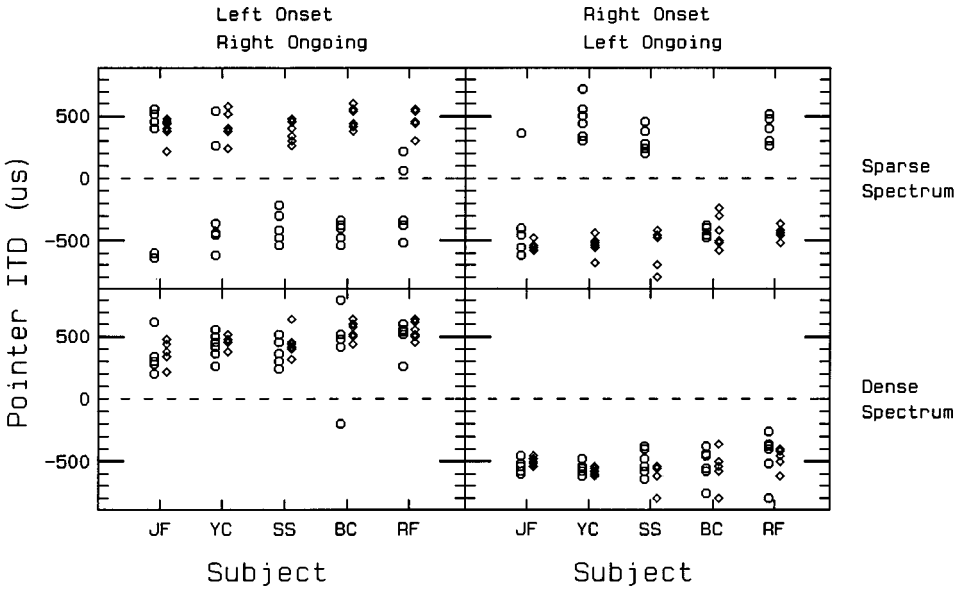

FIG. 8. Acoustic pointer matches for the sparse and dense inharmonic complex conditions in experiment 2. Legend as in Fig. 6.

2. Results

The primary question addressed by this experiment was whether an ongoing signal's vulnerability to dominance by the interaural onset delay is more closely related to interaural ambiguity or to spectral density. Lateralization of the gradual-onset stimuli (diamonds in Fig. 8) was consistently on the side of the ongoing interaural delay for both the sparse and dense complexes. The crucial condition was lateralization of the sparse complex with the abrupt opposing onset, with the dense complex acting as a control. The results displayed in Fig. 8 (circles) show that whereas the matches for the dense complex almost always followed the ongoing interaural delay, the matches for the sparse complex usually followed the interaural onset delay. There were some exceptions. Most of the matches from JF and BC right onset followed the lead ear of the ongoing part of the signal, and there were a few instances of matches on both sides of the head (e.g., RF, left onset). Still, it is clear that there were generally greater onset dominance for the sparse complex than the dense complex.

The results of this experiment should be interpreted cautiously because only two examples of complexes were compared, with many more choices of frequency components possible. Nevertheless, the preliminary conclusion is that the lateralization of a stimulus with sparsely distributed spectral components is more vulnerable to control by onset cues than is a spectrally richer stimulus. The presence of interaural ambiguity appears less important because lateralization of the sparse complex showed a great deal of onset dominance despite an apparent lack of interaural ambiguity in the signal. The consistency of onset dominance approaches, although it does not equal, that found for the repeated-burst condition from Sec. II B. The two conditions are similar in spectral density, but are different in ambiguity.

D. Introspective observations

Several other stimulus manipulations were explored by two subjects, RF and YC, who noted the gross laterality of the ongoing portions of the stimuli. Several of the manipulations are similar to those employed by Hafter and Buell (1990) in studies of interaural delay discrimination.

Long (5-s) pulse trains: We were interested in whether the onset's influence would hold over several seconds. When the steady-state portion of the type 1 stimulus shown in Fig. 1 (2-ms IPI) was extended for 5 s, both subjects heard the image remain on the side of the onset pulse pair throughout the 5 s period. When this duration was also used with type 3 signals and a 2-ms IPI, the image always switched from the onset to the ongoing side during the 5-s period. The rapidity of the switching was different for the two subjects and was consistent with the ear asymmetries observed earlier. For YC, the image for the right-onset condition switched fairly early and suddenly from right to left, while the image for the left-onset condition switched sides more slowly and after a few seconds. The reverse was true for RF, who observed the abrupt and early switching for the left-onset conditions.

Uncorrelated noise: We wondered whether a binaural pair of correlated 1-ms white noise bursts leading to one side could ''focus'' the image of an immediately following 250-ms noise burst that was binaurally uncorrelated. The answer was no. Both listeners could identify the leading ear of the onset burst, but the ongoing noise was heard throughout the head, presumably as it would be without the abrupt onset.

Pulse trains with gaps: Type 3 pulse trains with a 2-ms IPI were extended to approximately 400 ms. Approximately 100 ms after onset, one or more pulse pairs were removed, leaving gaps ranging from 4 to 32 ms, followed by a 300-ms trailing portion. With one pulse pair removed, both subjects reported the trailing portion to be on the side of the head favoring the ongoing lead, suggesting that the image lateralization had switched from the onset side following the gap. By 32 ms, the switching from the onset to the ongoing side was unequivocal and obvious.

Gaps filled with noise: The gap conditions just described were repeated, with a diotic white noise filling the gap. The rms voltage of the noise (computed from the digital signal,

before D/A conversion) was approximately 6 dB above that for the pulse train as a whole, and approximately 10 dB below the rms voltage of each individual pulse. For both subjects, the observations were relatively independent of the duration of the gap and noise. but did depend upon which ear received the onset pulse pair. For YC, when the onset pair led to the right, the image switched from right to left as with the unfilled gaps. However, when the onset favored the left, the image remained on the left following the gap. RF observed the opposite pattern, with the image either switching to, or remaining on, the right. These differences are consistent with the different biases shown by these two subjects in the lateral position measurements.

Sudden reduction in IPI: After 100 ms, the IPI of a type 3 pulse train was suddenly reduced from 3 ms to 2 ms and remained at the lower value for an additional 300 ms. Simultaneous with a pitch increase, both subjects heard the image switch from the side of the onset lead to that of the ongoing lead. The switching was obvious for both subjects for both left- and right-leading onsets.

Abrupt increase in intensity: After 100 ms, the level of a type 3 pulse train with 2-ms IPI was abruptly (between two pulse pairs) increased by 6 dB and remained at the higher level for 300 ms. RF heard the image switch from the side of the onset lead to that of the ongoing lead when it increased in loudness. YC reported the same phenomenon when the onset was on the right and the image switched to the left (her bias), but had difficulty lateralizing the signal in the opposite condition.

III. DISCUSSION

The results reported here support and extend previous results showing the importance of onsets in directional hearing. It was shown that the extent to which lateralization of 250-ms length signals is controlled by the interaural onset delay was determined by the configuration of the interaural delays and spectrum in the ongoing part of the signal. When the ongoing signal was a train of binaural pulse pairs with a delay of 500 μs that alternated between right leading and left leading (type 1), lateralization was determined by the lead at onset. For this type of signal, onset dominance did not decline as IPI was increased from 1 to 5 ms. In type 2 signals, the pulse pairs during the ongoing train alternated between 0 and 500-μs delay, with the initial pulse pair leading to the ear opposite the ongoing lead. The delay in the initial pulse pair contributed substantially to lateralization at short and medium IPIs, but the effect declined in two of three subjects as IPI increased to 5 ms. For type 3 signals, which had an initial pulse pair with an ITD opposing that during the ongoing part of the train, the onset delay was also most effective at the shorter IPIs, as was shown by Saberi and Perrott (1995). The extent of onset dominance with type 2 and type 3 trains is subject to substantial variability across listeners and, within listeners, there can be considerable left–right asymmetry. In experiment 2, the strong onset dominance observed for the type 3 pulse trains at the 2-ms IPI was replicated with trains of repeated noise bursts. However, there was no such onset dominance for nonrepeated bursts. In the second part of experiment 2, the interaural delay of an initial noise-burst pair generally dominated the lateralization of a 250-ms inharmonic complex with sparsely distributed spectral components, but the initial noise burst had almost no effect for an inharmonic complex with densely distributed components. Onset dominance is subject to a variety of disrupting agents, such as inserted gaps and changes in fundamental frequency and intensity. These findings are similar in many respects to the ''resetting'' phenomena observed for ITD discrimination with high-frequency pulse trains (Hafter and Buell, 1990).

Taken together, the results point to key stimulus features in the ongoing part of the stimulus that allow for onset cues to dominate lateralization for signals of 250-ms duration. Assuming that the onset cue itself is strong, then signals with ambiguous ongoing interaural cues, or ongoing cues that are only sparsely distributed across the frequency spectrum, will be susceptible to onset dominance in lateralization. Conversely, signals with spectrally rich and unambiguous ongoing interaural cues will not be subject to onset dominance.

The two factors of spectral density and ambiguity have been discussed in past work on the influence of onsets in localization. Hartmann and Rakerd (1989) suggested that the Franssen effect could not be observed for noise stimuli, although it could for tonal stimuli, because the steady-state sound in the noise signal was spectrally dense, having strong directional cues opposing the onset transient. Applying Hartmann and Rakerd's (1989) hypothesis to the current experiments predicts many of the results. The repeated burst and sparse inharmonic stimuli in experiment 2 were susceptible to onset dominance whereas the nonrepeated and dense inharmonic stimuli were not. Further, Hartmann and Rakerd's hypothesis predicts the reduction in the influence of onsets in experiment 1 for type 3 stimuli as IPI is increased, because this reduces the fundamental frequency and increases the density of spectral components.

This spectral explanation assumes that there is little effect of the reduced level in each frequency region that results from increasing IPIs or the density of the inharmonic complex. Rather, the important factor is either the total number of frequency channels stimulated, or perhaps the presence of spectral components at some key frequencies not stimulated by the shorter IPI pulse trains or the sparse complex, or, possibly, some other difference between the signals that we have yet to consider. Hartmann (1983) suggested that one advantage of having closely spaced spectral components is that, with several components interacting within the same auditory filter, localization would be enhanced by the resulting envelope fluctuations. Further testing with other sets of harmonic and inharmonic complexes should reveal more answers.

An alternative explanation for the effect of IPI had been proposed earlier in this paper, namely that longer IPIs created less ambiguity between competing ongoing delays. With type 3 stimuli the competing ongoing delays are 500 μs and IPI-500 μs. The latter delay was presumed to lose its effectiveness as IPI increases due to its lack of centrality relative to 500 μs. However, the finding in experiment 2 that the sparse inharmonic complex was often vulnerable to onset dominance suggests that the presence of an ongoing delay

consistent with the onset delay is not required. These results also suggest that the onset delay can control lateralization for stimuli that produce reasonably consistent lateralizations when there is no abrupt onset. Although a quantitative analysis of variability across matches was not conducted, Fig. 8 shows that lateralization of the gradual-onset stimuli (diamonds) was on the side of the ongoing delay in all cases, and no large differences in variability are apparent between the sparse and dense complexes. Yet, when an abrupt onset transient with an opposing delay was present, lateralization for the sparse complex was often controlled by the onset delay, whereas the dense complex was not.

The apparent importance of spectral density does not completely rule out a role for ambiguity in facilitating control by onsets.

Although the onset delay need not match an ongoing delay in order for the onset delay to influence lateralization, the presence of ambiguous cues in the ongoing part of the train does appear to increase the importance of onsets, consistent with the interpretation by Buell *et al.* (1991) of their results. In the current studies, the influence of onset cues was strongest for the type 1 train, which alternated between pulse pairs having equal and opposite ITDs. The onset's effects were least dependent on IPI with this stimulus type. Also, the lateralization for the repeated burst stimuli in experiment 2, where there was some degree of interaural ambiguity, showed somewhat more consistent onset dominance than the sparse inharmonic complex.

The results of the current experiments may shed additional light on differences in the past literature on the topic. As noted in the Introduction, Tobias and Schubert (1959) reported very little effect of onset cues. They used a broadband noise with an envelope-gating delay at stimulus onset that opposed an ongoing fine structure delay. Zurek (1993) pointed out that because Tobias and Schubert used only an envelope delay, not a whole waveform delay, the lateralization cue at the onset was weak. These problems were avoided in the current experiment, where both onset and ongoing delays were whole waveform delays. The results suggest, consistent with the sound field localization data of Hartmann and Rakerd (1989), that the lateralization of a spectrally dense signal with an unambiguous ongoing delay is not subject to dominance by onsets even if the onset cue itself if strong.

The interpretation based on spectral density predicts that a single pure tone should be quite vulnerable to the influence of onset cues. Indeed, Kunov and Abel (1981) and Abel and Kunov (1983) found that when low-frequency tones were gated on with short rise/fall times, onset delays dominated lateralization. The much stronger effects on onsets observed in those studies than by Buell *et al.* (1991) must relate to the type and relative strength of the onset cue itself (Buell *et al.*, 1991; Zurek, 1993). The importance of interaural ambiguity, as defined by the presence and relative centrality of competing delays, might be investigated further using low-frequency pure tones, because ambiguity varies with pure-tone frequency for a given interaural delay. For example, for a 500-Hz tone with a 500-μs lead favoring the left ear, the competing delays are -500 μs and 1500 μs. However, for a lower-frequency tone, say 200 Hz, the competing delays are -500 μs and 4500 μs, creating even less ambiguity. If ambiguity is of importance in facilitating onset dominance, lateralization of the 200-Hz tone would be expected to be less susceptible to control by onsets than the 500-Hz tone. Abel and Kunov (1983) investigated the effect of frequency on the importance of onsets, but did not test below 500 Hz.

The mechanisms through which interaural onset cues exert their influence over a period of at least 250 ms remain unclear. Processes related to the binaural adaptation phenomenon (Hafter and Dye, 1983) or theoretical inhibitory processes proposed to explain the precedence effect (Lindemann, 1986), may be invoked to weaken later cues, facilitating control by onsets. However, it is clear that later-arriving binaural information is not completely lost because, as the current results show, the configuration of ongoing interaural cues is of critical importance in determining the extent of onset dominance.

IV. CONCLUSIONS

An initial transient with an interaural delay can have a strong influence on the lateralization of a 250-ms broadband stimulus. The onset delay is able to control lateralization even when there is an apparently unambiguous ongoing delay and the ongoing part of the stimulus can be lateralized in the absence of and abrupt onset. Consistent with the previous literature, ambiguity of interaural cues in the ongoing part of the stimulus facilitates dominance by onsets. The sparseness of the spectral components in the ongoing part of the stimulus, a factor shown to be important for observing the Fransen effect (Hartmann and Rakerd, 1989), appears to also facilitate control by onsets in lateralization.

ACKNOWLEDGMENTS

This work was supported by Grant Nos. DC01625 and DC00100 from the National Institute on Deafness and other Communication Disorders and by Biomedical Research Support Grant No. RR07048-26. The authors would like to thank Jill Raney for her assistance in data collection, Kuan Chung-Huei, Shih Chia-Shiang, and Ning Wang for their technical assistance, and Barbara Shinn-Cunningham and the reviewers for comments on earlier versions of this article.

[1]Subjects YC and RF, who had participated in experiment 1, listened to the repeated and nonrepeated conditions as part of a larger stimulus set that was not included in the final version of this paper. Therefore, the order of conditions was somewhat different for them.

Abel, S. M., and Kunov, H. (**1983**). ''Lateralization based on interaural phase differences: Effects of frequency, amplitude, duration, and shape of rise/decay,'' J. Acoust. Soc. Am. **73,** 955–960.

ANSI (**1989**). ANSI S3.6-1989, ''Specification for audiometers'' (American National Standards Institute, New York).

Blauert, J. (**1983**). *Spatial Hearing* (MIT, Cambridge, MA).

Blodgett, H. C., Wilbanks, W. A., and Jeffress, L. A. (**1956**). ''Effect of large interaural time differences upon the judgment of sidedness,'' J. Acoust. Soc. Am. **28,** 639–643.

Buell, T. N., Trahiotis, C., and Bernstein, L. R. (**1991**). ''Lateralization of low-frequency tones: Relative potency of gating and ongoing interaural delays,'' J. Acoust. Soc. Am. **90,** 3077–3085.
Clifton, R. K., and Freyman, R. L. (**1989**). ''Effect of click rate and delay on breakdown of the precedence effect,'' Percept. Psychophys. **46,** 139–145.
Franssen, N. V. (**1962**). *Stereophony* (Philips Technical Library, Eindhoven, The Netherlands), English translation (1964).
Freyman, R. L., Clifton, R. K., and Litovsky, R. Y. (**1991**). ''Dynamic processes in the precedence effect,'' J. Acoust. Soc. Am. **90,** 874–884.
Gardner, M. B. (**1968**). ''Historical background of the Haas and/or precedence effect,'' J. Acoust. Soc. Am. **43,** 1243–1248.
Grantham, D. W. (**1996**). ''Left-right asymmetry in the buildup of echo suppression in normal-hearing adults,'' J. Acoust. Soc. Am. **99,** 118–123.
Hafter, E. R., and Dye, Jr., D. H. (**1983**). ''Detection of interaural differences of time in trains of high-frequency clicks as a function of interclick interval and number,'' J. Acoust. Soc. Am. **73,** 644–651.
Hartmann, W. M. (**1983**). ''Localization of sound in rooms,'' J. Acoust. Soc. Am. **74,** 1380–1391.
Hafter, E. R., and Buell, T. N. (**1990**). ''Restarting the adapted binaural system,'' J. Acoust. Soc. Am. **88,** 806–812.
Hartmann, W. M., and Rakerd, B. (**1989**). ''Localization of sound in rooms. IV: The Franssen effect,'' J. Acoust. Soc. Am. **86,** 1366–1373.
Kunov, H., and Abel, S. M. (**1981**). ''Effects of rise-decay time on the lateralization of interaurally delayed 1-kHz tones,'' J. Acoust. Soc. Am. **69,** 769–773.
Lindemann, W. (**1986**). ''Extension of a binaural cross-correlation model by contralateral inhibition. II. The law of the first wavefront,'' J. Acoust. Soc. Am. **80,** 1623–1630.
Saberi, K., and Perrott, D. R. (**1995**). ''Lateralization of click-trains with opposing onset and ongoing interaural delays,'' Acustica **81,** 272–275.
Shinn-Cunningham, B. G., Zurek, P. M., and Durlach, N. I. (**1993**). ''Adjustment and discrimination measurements of the precedence effect,'' J. Acoust. Soc. Am. **93,** 2923–2932.
Stern, R. M., Zeiberg, A. S., and Trahiotis, C. (**1988**). ''Lateralization of complex binaural stimuli: A weighted image model,'' J. Acoust. Soc. Am. **84,** 156–165.
Thurlow, W. R., Marten, A. E., and Bhatt, B. J. (**1965**). ''Localization aftereffects with pulse-tone and pulse-pulse stimuli,'' J. Acoust. Soc. Am. **37,** 837–842.
Tobias, J. V., and Schubert, E. R. (**1959**). ''Effective onset duration of auditory stimuli,'' J. Acoust. Soc. Am. **31,** 1595–1605.
Toole, F. E., and Sayers, McA. (**1965**). ''Lateralization judgments and the nature of binaural acoustic images,'' J. Acoust. Soc. Am. **37,** 319–324.
Wallach, H., Newman, E. B., and Rosenzweig, M. R. (**1949**). ''The precedence effect in sound localization,'' Am. J. Psychol. **52**, 315–336.
Yost, W. A., and Soderquist, D. R. (**1984**). ''The precedence effect: Revisited,'' J. Acoust. Soc. Am. **76,** 1377–1383.
Zurek, P. M. (**1987**). ''The precedence effect,'' in *Directional Hearing*, edited by W. A. Yost and G. Gourevitch (Springer-Verlag, New York), pp. 85–105.
Zurek, P. M. (**1993**). ''A note on onset effects in binaural hearing,'' J. Acoust. Soc. Am. **93,** 1200–1201.

Directivity of binaural noise reduction in spatial multiple noise-source arrangements for normal and impaired listeners

Jürgen Peissig[a] and Birger Kollmeier[b]
AG Medizinische Physik, FB Physik, Universität Oldenburg, D-26111 Oldenburg, Germany

(Received 3 April 1995; revised 19 June 1996; accepted 26 September 1996)

Speech reception thresholds (SRTs) were obtained for different azimuths of up to three interfering sound sources in a simulated (''virtual'') spatial arrangement. For the SRT measurements a fast subjective threshold assessment method was used. The reduction in SRT relative to the reference threshold caused by spatial separation of target and interference signal is called the intelligibility level difference (ILD). For normal listeners, the maximum ILD was achieved at 105° or 255° azimuth of a single noise source when the target emanated from the front (0° azimuth). The ILD decreased rapidly if the number of interfering signals was increased and if they were located on opposite sides of the head. When using continuous speech as interference, this decrease of ILD was less pronounced. These findings indicate that the binaural system can suppress interference from only one azimuthal region at a time and can utilize temporal pauses in the interference to suppress a second interference from a different direction. For eight sensorineural impaired listeners, the maximum attainable ILD for one interfering noise source was reduced in a way not predictable from the audiogram. The ability to exploit pauses in the signal of an interfering talker was also reduced. Hence, hearing-impaired listeners are handicapped in realistic spatial interference situations both by an increased monaural SRT and a reduced binaural noise reduction ability. [S0001-4966(97)04002-2]

PACS numbers: 43.66.Pn, 43.66.Sr, 43.71.Gv [RHD]

INTRODUCTION

Several studies have focused on the effect of binaural release from masking for specific narrow-band signals and speech (e.g., Hirsh, 1948; Cherry, 1953; Carhart *et al.*, 1969; Plomp and Mimpen, 1981; Kollmeier, 1990; Bronkhorst and Plomp, 1992). A typical condition for measuring speech intelligibility in the presence of spatially distributed noise sources is to use a target sound in front of the listener and one interfering noise source with varying direction of incidence relative to the listener's head. Plomp and Mimpen (1981), vom Hövel (1984), and Müller (1992) measured speech reception thresholds for this condition as a function of the difference in azimuthal angle between the target speech and the interfering noise. The reduction in speech reception threshold caused by separating the location of the interfering noise source from the location of the target sound is called the intelligibility level difference (ILD) and averages about 12 dB for noise sources from 105° to 120° or 240° to 255° azimuth (all azimuthal angles of sound incidence are given in degrees when viewed from above, where 0° denotes frontal incidence and 90° denotes directly to the right) (vom Hövel, 1984; Müller, 1992; Peissig, 1992; Peissig and Kollmeier, 1993).

Unfortunately, the case of several speakers interfering simultaneously and the ''effective'' directionality of binaural unmasking in this condition has not been studied thoroughly. In addition, the difference between the masking properties of continuous speech-simulating noise and one interfering speaker has not been considered in detail. Both effects are important for the investigation of the ''cocktail party effect,'' i.e., a listeners ability to suppress interfering sound components and to enhance the ''desired'' speaker (Cherry, 1953; Yost, 1991; Kollmeier, 1990). The current study therefore attempts to measure the influence of an increasing number of interfering noise sources while using both speech simulating noise and interfering continuous speech as spatially distributed maskers.

To separate the binaural effect, which is caused by interaural interaction in central auditory processing stages, from monaural effects (primarily caused by the head-shadow effect), the binaural intelligibility level difference (BILD) is obtained, i.e., the difference between listening with one ear and listening with both ears in a situation where a positive ILD occurs. In the configurations described above, the BILD averages about 6 dB in normal listeners. Thus, approximately half of the maximum effect of the ILD is accounted for by binaural interaction. The remainder is due to the head-shadow effect which results in an improved signal-to-noise ratio at the ''better'' ear. In an alternative approach, Bronkhorst and Plomp (1988) separated the relative contribution of interaural intensity differences and interaural phase differences and found that both interaural differences contribute about equally to the binaural unmasking effect in speech perception. Vom Hövel (1984) studied the influence of the diffuseness of the sound field and found that the maximum ILD reduces to approximately 3 dB if the noise is diffuse. Bronkhorst and Plomp (1992) measured the gain in intelligibility for various spatial configurations of multiple sound sources both with continuous noise and speech-envelope-modulated noise. They found an increase in speech reception thresholds (SRT) with an increasing number of

[a]Now at Sennheiser Electronic KG, Pf 100264, D-30900 Wedemark, Germany.
[b]Corresponding author.

 0001-4966/97/101(3)/1660/11/$10.00

noise sources. In addition, their hearing-impaired listeners exhibited less benefit from modulating the interfering noise than their normal listeners.

While most studies cited so far used speech as test material and speech intelligibility tests as measurement methods, the fundamental effects of binaural release from masking have been investigated mainly in signal detection experiments. Typically, noise maskers with various interaural relations were employed and sinusoidal test-tones had to be detected against a noisy background. The principal outcomes of these studies were summarized in a number of models of binaural signal processing that are reviewed by Colburn and Durlach (1978). These models were primarily based on neurophysiological evidence and psychophysical experiments on tone detection and localization or lateralization, and they were rarely applied to describing binaural effects in speech understanding. One exception is the work by vom Hövel (1984): He predicted speech reception thresholds in a variety of conditions with spatially distributed noise sources. To do so he used an ''Equalization and Cancellation'' (EC) mechanism proposed by Durlach (1972) to predict the noise reduction in each critical band in parallel. Based on the resulting spectrum of the noise and the target speech signal, respectively, he predicted speech intelligibility on the basis of the ''articulation index'' (Fletcher and Steinberg, 1929; Kryter, 1962). However, vom Hövel's experiments and theoretical calculations were restricted to the special case of one target sound source and one interfering noise source in an anechoic environment or in a completely diffuse acoustical environment.

Another important factor contributing to the ''effective'' benefit a listener might receive from binaural hearing in such a complex acoustical environment is the individual's hearing impairment. In hearing-impaired listeners, the binaural system is impaired in a rather variable and complex way (Durlach *et al.*, 1981; Kinkel and Kollmeier, 1992) and a reduction in ILD and BILD is observed that can not be predicted from the audiogram or any other audiological measure (Kollmeier, 1990). In addition, degraded speech reception in noise is observed even for monaural listening conditions (Plomp, 1986). The current study therefore tries to find out how many interfering noise sources can be ''canceled out'' simultaneously by the normal listener's auditory system and how hearing impairment affects this performance. Within this context it is important to know if normal listeners can utilize spectro-temporal ''gaps'' in the interfering signals in order to improve the intelligibility of the ''target'' speech signal located elsewhere and how this ability is reduced in hearing-impaired listeners.

I. METHOD

A. Subjects

Eight male young normal listeners aged between 25 and 32 years participated voluntarily in this study. They had clinically normal hearing (normal outer and middle ear function, normal pure tone audiogram) and reported no problems with their listening capabilities. They had some prior experience in other auditory tasks.

In the experiments with hearing-impaired listeners, four male and four female sensorineural hearing-impaired subjects participated voluntarily. All of them had some experience with speech perception tests and psychoacoustical tests from prior studies. Their clinical examination indicated normal middle ear function and sensorineural hearing loss. Their pure tone audiograms for left and right ears (bone conduction thresholds at 500 Hz and 4 kHz) are given in Table II.

B. Threshold estimation procedure

For estimating the speech reception threshold for a variety of (simulated) spatial noise configurations in an efficient way, a method of adjustment was used in combination with a subjective assessment of speech intelligibility. The validity of this method and the high correlation between speech reception thresholds estimated with such a ''subjective'' adustment method and ''objective'' conventional speech scoring methods was demonstrated by Wesselkamp (1994) and Kollmeier and Wesselkamp (1997). Similar findings were reported by Cox *et al.* (1991) for a related method. One out of two possible target sentences was presented to the subject after adding it to the background noise which was presented at a constant level. The subject's task was to adjust the level of the test sentence to a value which subjectively corresponded to 50% intelligibility of the sentence. The subject was instructed that 50% intelligibility corresponds to approximately half of the words being intelligible or the whole sentence being approximately half intelligible. The two possible target sentences were well known to the subjects. To adjust the ''subjective'' speech reception threshold, the subject was instructed to depress certain keys on a computer keyboard: One key resulted in a repetition of the sentence at the same level, another key resulted in a repetition of the sentence at a level increased by 1 dB, and a third key resulted in a repetition of the sentence at a level decreased by 1 dB. The fourth key was depressed by the subject as soon as the adjusted level corresponded to 50% intelligibility. A complete record of all trials and responses was stored automatically by the personal computer controlling the experiments. The initial level of each session was set to be well above the expected SRT obtained from pilot experiments. It was 4 dB (expressed as signal-to-noise ratio) for conditions with interfering talkers and -4 dB for interfering noise, respectively. After the termination of each measurement block for a given (simulated) spatial configuration, the last level was held as the initial level for the subsequent measurement block employing a similar configuration.

C. Target signal

Two different target sentences were employed: ''Ein kleiner Junge war der Sieger'' (a little boy was the winner) and ''Der Regen brachte die erhoffte Kühle'' (the rain brought the desired coolness). They are both samples of a German sentence intelligibility test (Göttinger Satztest developed by Wesselkamp *et al.*, 1992; see Kollmeier and Wesselkamp, 1997). The test material was recorded with a male speaker (Dr. Sotscheck, Berlin) who uttered the sentences in a normal conversational mode with a constant vocal effort.

D. Interfering signals

A speech-simulating noise was employed which was produced by a random superposition of all 524 target words of a digitized monosyllabic rhyme test recorded with the same male speaker (Dr. Sotscheck, Berlin, cf. Müller, 1992). For sythesizing the noise, each digitized word was repeated several times with a random pause between successive repetitions that varied between 0.5 and 1.5 s. These repeated words were added up in a digital buffer. Due to the random pauses employed, the resulting speech babble has no periodic envelope structure and sounds very similar to a continuous, speech-spectrum-shaped noise. For creating different virtual spatial arrangements of up to three different continuous interfering noise sources, three noncorrelated recordings of this speech-simulating noise were used.

For creating the virtual conditions with various numbers of interfering talkers, four recordings of different speakers (two male and two female) were stored separately. Each of the talkers read continuously from a different chapter of Lewis Carroll's ''Alice in Wonderland'' at a medium speech rate. During recording, the talkers were asked to maintain a constant talking effort and a constant average speech level which was helped by observing the volume control of the recording device.

E. Spatial configurations

To simulate different azimuthal angles of incidence for the target speech and the various interfering noise sources in an anechoic environment, a real-time convolution of the digitized material was performed with standard outer ear impulse responses for the respective azimuthal angle (Pösselt *et al.*, 1986). This operation converts monaurally recorded speech or noise signals into a stereophonic signal with the subjective impression of the selected angle of incidence when presented via headphone (Sennheiser HDA 200). The outer ear impulse responses employed had been measured with two miniature microphones inserted 5 mm into the blocked meatus of a representative human subject in an anechoic room in Bochum (Germany, see Pösselt *et al.*, 1986). They were corrected in the frequency domain with reference measurements using the same loudspeaker and miniature microphones. Only the impulse responses with zero elevation and an azimuth varying in steps of 5° were employed. They had a duration of 3.6 ms which corresponds to 90 samples at a rate of 25 kHz.

The virtual sound field consisting of one target speaker and up to three interfering sound sources located at different azimuthal positions was created as follows: First, stereophonic DAT recordings of the respective interfering sound source configuration were produced by summing up the respective stereophonic output signals of the various noise or interfering speech signals subsequent to the digital convolution described above. The same recording level was used for each respective simulated interfering sound source. During the experiments, the resulting stereophonic recording was added to the convolved recording of the target speaker at a variable signal-to-noise ratio.

In all test situations, the level of the interfering sound

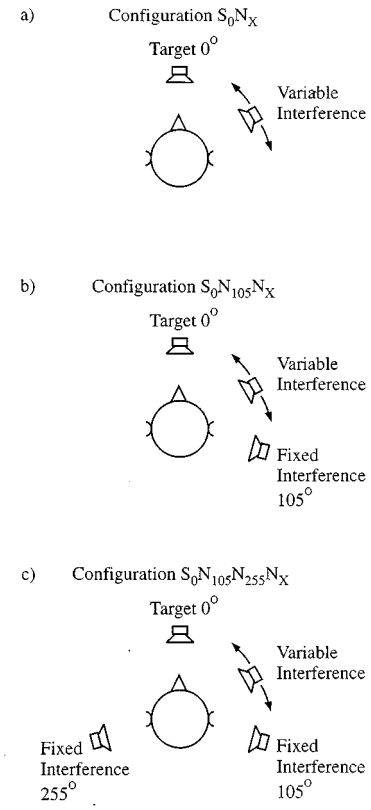

FIG. 1. Sketch of the simulated spatial arrangement of target speech and interfering noise sources as viewed from above. The target speaker is always located in front and one interfering sound source is located at a variable azimuthal angle. The number of additional interfering sound sources at a fixed azimuth is increased from top to bottom: (a) (upper panel) configuration S_0N_x, no fixed interfering sound source; (b) (center panel) configuration $S_0N_{105}N_x$, one interfering sound source at 105° azimuth; and (c) (lower panel) configuration $S_0N_{105}N_{255}N_x$, two interfering sound sources at 105° and 255° azimuth.

sources was adjusted to correspond to approximately 75 dB SPL for normal-hearing subjects. The level of the interference was measured with a true-rms voltmeter without frequency weighting and a ''fast'' time constant. In the case of the fluctuating speech level, the average speech level was approximately 10 dB below the peak speech level. The signal-noise (S/N) ratio for the various conditions was defined as the average speech level of the target talker in relation to the level of the variable interfering sound source. In the tests with hearing-impaired listeners, the level of the interfering noise had to be increased in order to partially compensate for the hearing loss. Therefore, the subjects were asked to adjust the level of the interfering sound to an intense but still comfortable loudness impression, e.g., the loudness impression at a lively cocktail party or at a crowded train station without moving trains. This increase in presentation level was maximally about 20 dB. In addition, patients with asymmetrical hearing loss were asked to adjust the interaural level difference of a noise emanating from 0° to yield a subjective localization corresponding to 0° azimuth. This procedure resulted in a maximum interaural level difference of about 10 dB. Hearing aid users among the hearing-impaired listeners participated in the tests without using their aid.

Figure 1 illustrates the different spatial configurations employed. The target signal always came from the front (0° azimuth). In the first condition [Fig. 1(a)], the azimuthal angle of incidence for one interfering sound source was varied from 0° to 360°. In the second condition [Fig. 1(b)], the location of the first interfering sound source was fixed at 105° and the location of the second interfering sound source varied from 0° to 360°. In the third condition [Fig. 1(c)], the location of the first and second interfering sound source was fixed at 105° and at 255°, respectively, and the location of the third interfering sound source varied from 0° to 360°. For all of these conditions, either speech-simulating continuous noise or different talkers were employed as interfering sound signals.

The notation of the different configurations is as follows: ''S_0'' stands for the target speech signal coming from 0° (in front of the listener) whereas ''N_x'' stands for a noise coming from x°. The position of an additional interfering noise source from a certain direction is indicated by adding another ''N'' to the description of the situation [for example, $S_0N_{105}N_{255}N_x$ stands for a signal coming from the front, two noise sources coming from 105° and 255°, and a third noise (the probe noise) coming from x°]. The positions of the fixed noise sources at 105° and 255° were selected because these directions yield the maximum intelligibility level difference in the situation with only one interfering noise source (see below).

F. Test conditions

For each subject and for each experimental condition, 17 directions of the varying interfering noise source were tested. The step size between successive directions was set to 15° for lateral incidence and 30° for frontal or rearward incidence. In order for the subjects to get accustomed to the experiment and to establish a constant criterion for 50% intelligibility, training was performed prior to data collection employing all 17 directions of the interfering sound source. For each configuration, the subjective assessment of 50% sentence intelligibility could be completed by experienced subjects within 4–10 s and was repeated at least four times. Since about 400 different configurations had to be tested with each normal-hearing subject, the total measurement time amounted to 4 h. Employing a conventional sentence intelligibility test would have resulted in a substantial increase in measurement time by at least a factor of 20. For the hearing-impaired listeners, a reduced number of configurations was tested both because of time limitations and because of their difficulties in performing the task when one or two continuous talkers were employed as interfering sounds.

II. RESULTS

A. Normal listeners

The first spatial configuration tested in this study employed one target speaker directly in front of the listener and one interfering signal with varying azimuth [configuration S_0N_x, Fig. 1(a)]. This configuration is similar to the one studied by a number of previous workers (e.g., Plomp and Mimpen, 1981; vom Hövel, 1984; Müller, 1992). Figure 2

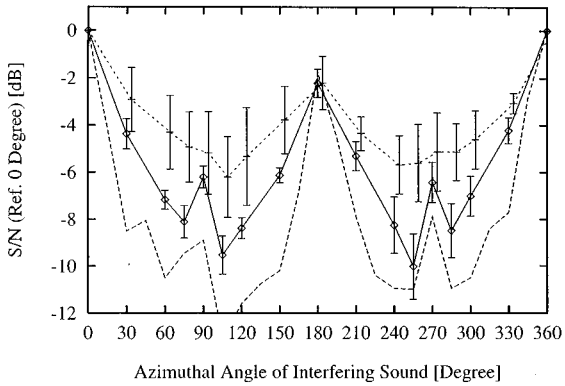

FIG. 2. Speech reception threshold for normal listeners (average values and standard deviations of subjectively adjusted thresholds) as a function of the azimuth of an interfering sound source [configuration S_0N_x, cf. Fig. 1(a)]. The diamonds connected with a solid line denote the results using continuous noise as interference while the crosses connected with a dashed line denote the results using one interfering talker. The ordinate denotes the subjectively assessed reception threshold individually related to the threshold in the reference condition S_0N_0 for 0° azimuth (Table I). The long-dashed line gives data reported by Müller (1992) using a speech intelligibility measurement task.

gives the speech reception thresholds as a function of the azimuthal angle of the interfering sound source which varies from 0° to 360°. The ordinate denotes the S/N ratio for 50% intelligibility after individually subtracting the S/N ratio obtained for 0° azimuth. Thus, the intelligibility level difference (ILD) is directly given as the negative value of the S/N ratio on the abscissa. The symbols denote average values and interindividual standard deviations for eight normal listeners. The diamonds connected with the solid line denote the results obtained for interfering continuous speech simulating noise whereas the crosses connected with the dashed line denote the results obtained for one interfering male speaker.

The average value and interindividual standard deviation of the reference signal-to-noise ratio for 0° azimuth is provided by Table I. The large interindividual standard deviation for the reference thresholds reflects the large variation in individual threshold criterion across the normal listeners. However, by relating the individually assessed speech reception threshold for each azimuth to the respective individual reference threshold, the impact of these variations in threshold criterion can be minimized. This can be concluded from the comparatively small interindividual standard deviations (less than 2 dB in most cases) in Fig. 2. Thus the measurement error for the speech reception thresholds as a function of azimuth obtained with our assessment method is comparable to the measurement error employing conventional

TABLE I. Average value and standard deviation of the signal-to-noise ratios (in dB) for normal-hearing subjects for the reference situation in the configurations considered here.

	Configuration		
Interfering sound	S_0N_0 (dB)	$S_0N_{105}N_0$ (dB)	$S_0N_{155}N_{255}N_0$ (dB)
Noise	−13.85±4.6	−11.90±4.5	−9.73±5.1
Speech	−30.83±7.0	−24.60±8.9	−17.71±8.4

speech intelligibility tests as performed by, e.g., Plomp and Mimpen (1981) and Müller (1992).

Figure 2 clearly shows that the subjects profit considerably from increasing the azimuthal angle between the target speaker and the interfering sound signal. The ILD is maximal for 105° and 255° azimuth amounting to 9.8 dB in the case of the continuous interfering noise and 6.2 dB in the case of one interfering continuous talker. Both curves are approximately symmetrical about the median plane, indicating that for our normal subjects both ears yield the same effect. Local maxima in the curves can be observed for 90° and 270°, where the interfering sound arrives directly from the right or from the left, respectively. This ILD decrease can be explained by an increased interaural cross talk for symmetrical configurations yielding a decreased head shadow effect: For azimuthal angles of 90° and 270° the ear opposite to the sound source and the ear directed toward the sound source are approximately aligned to the ''optical axis,'' i.e., the connection line between the sound source and the head which acts as a diffraction object. According to Babinet's theorem from wave optics,[1] an intensity maximum is observed on the symmetry axis behind a diffracting symmetrical object. Therefore, the interaural intensity difference and the binaural dissimilarity is smaller for the situation S_0N_{90} than for the situations S_0N_{75} or S_0N_{105} and the intelligibility level difference is thus decreased. This increased interaural cross-talk between the ears can also be observed in measured outer-ear transfer functions (e.g., Genuit, 1984; Kollmeier and Drüke, 1992).

In the condition employing a continuous male talker as interfering sound source (dashed line in Fig. 2), the subjects reported problems in adjusting the level of the target speaker to 50% intelligibility, because the intelligibility depended very much on the segment of the interfering speech that actually masked the target speaker. Therefore, the subjects needed more repetitions to assess the intelligibility in a reliable way and, in addition, both the intra- and interindividual standard deviations are higher in this situation than in the situation with the interfering continuous noise. The resulting reference threshold S_0N_0 is on the average 17 dB lower than for the condition with the continuous speech-simulating noise (Table I). Parts of this reduction in signal-to-noise ratio are due to the different level definitions for continuous noise (e.g., average level) and continuous speech (e.g., 10 dB below the peak speech level). The main part of this effect, however, is due to the subject's ability to utilize speech pauses and segments with less intensity of the interfering speech.

To compare the results obtained with the subjective assessment method of speech intelligibility with standard speech intelligibility measurement methods, the results obtained by Müller (1992) are included in Fig. 2 by the long-dashed line. He used a German monosyllabic rhyme test in the same experimental setup as described above, employing the same target speaker and the same speech-simulating continuous noise. Since this measurement method is very time consuming, he conducted a complete measurement only with two normal listeners. Qualitatively, there is a very good agreement between his speech reception thresholds and the

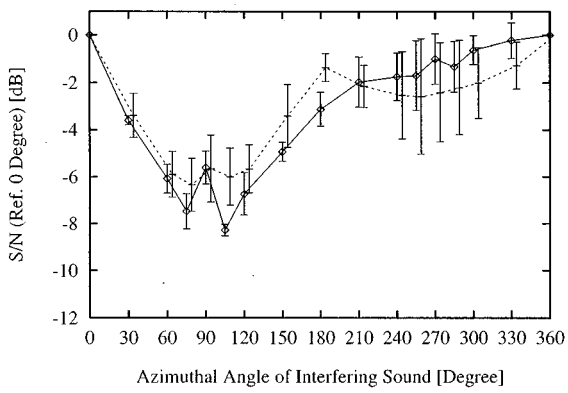

FIG. 3. Same as Fig. 2 using one additional fixed interfering sound source at 105° azimuth [condition $S_0N_{105}N_x$, cf. Fig. 1(b)].

subjective assessment method employed in this study. However, the ILD observed for the data from Müller (1992) is up to 4 dB larger than the ILD observed here. It seems that our subjects used a more conservative criterion to assess speech intelligibility in those acoustical situations where a large release from masking was achieved through some type of binaural processing.

Figure 3 gives the results for the situation $S_0N_{105}N_x$. The position of the variable interfering sound source is given on the abscissa. Again, the ordinate denotes the subjectively assessed speech reception threshold individually normalized to the threshold for the reference condition $S_0N_{105}N_0$. The average value and standard deviation of this reference threshold are also included in Table I. The diamonds connected with a solid line give the results for the interfering noise condition. The crosses connected with a dashed line give the results for the condition with two different interfering talkers.

For the condition with two interfering noise sources (solid line), the results are similar to those for one interfering noise source (solid line in Fig. 2) for azimuths between 0° and 180°. This indicates that a significant release from masking is achieved if both interfering sound sources are in the same hemicircle or even exhibit the same azimuthal angle. Note, however, that the reference threshold in situation $S_0N_{105}N_0$ is increased by approximately 2 dB in comparison to the reference threshold S_0N_0 (Table I) because the S/N ratio was defined as the difference between target speech level and level of the variable interfering noise source. In addition, the lowest threshold, which is obtained at an azimuthal angle of 105°, is about 3 dB higher, yielding a maximum ILD of 8.4 dB which is 1 dB less than for Fig. 2. If the second interfering noise source is in the left hemicircle (i.e., azimuthal angles between 180° and 360° in Fig. 3), the ILD decreases monotonically with increasing angle and no significant release from masking is obtained. It seems that the binaural system is not able to suppress two continuous noise sources simultaneously if they emanate from different sides of the head. Instead, it appears as if a substantial binaural release from masking can only be achieved if both continuous noise sources are close enough together to constitute a single effective interferer.

With two interfering talkers (dashed line) thresholds are

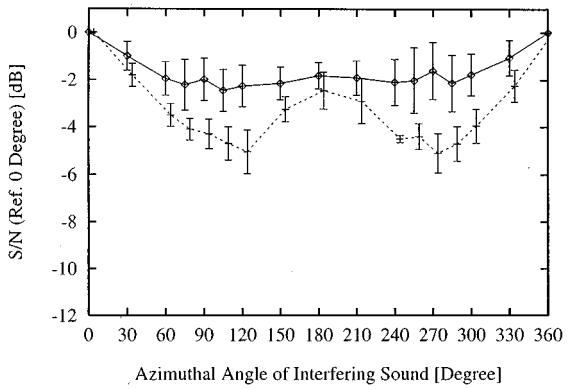

FIG. 4. Same as Fig. 2 using two additional fixed interfering sound sources at 105° and 255° azimuth [condition $S_0N_{105}N_{255}N_x$, Fig. 1(c)].

considerably higher than in the situation with one interfering talker both because of the additivity of masker energy and because pauses rarely occur simultaneously for both interfering talkers. In the reference situation $S_0N_{105}N_0$ this increase amounts to 6.2 dB (Table I). Nevertheless, approximately the same release from masking is obtained as for the situation with only one interfering speaker (Fig. 2) if both interfering sound sources are located within the same hemicircle (i.e., azimuthal angles from 0° to 180° in Fig. 3). In contrast to the situation with continuous noise, however, a small release from masking was still achieved when the second interfering speaker emanated from the side opposite that of the first interfering speaker (i.e., azimuthal angles from 180° to 360° in Fig. 3). In the situation $S_0N_{105}N_{255}$, for example, a clear decrease in the subjectively assessed threshold of 2.8 dB was obtained, whereas no such release of masking was obtained for continuous interfering noise sources. This effect is significant even though the standard deviations obtained for the situations with continuous interfering talkers are larger than in the situations with continuous noise. Probably, the pauses of one interfering talker can be utilized by the binaural system to reduce the interference from the other interfering talker. Thus, our findings suggest that the binaural system can only suppress interfering sound from one azimuthal region at a given time but is also able to exploit pauses or dips in one interfering sound source to ''switch'' the effective directionality of noise suppression towards a second sound source.

Figure 4 gives the results for the condition $S_0N_{105}N_{255}N_x$. Again the ordinate denotes the subjectively assessed speech reception threshold individually normalized to the threshold for the reference condition $S_0N_{105}N_{255}N_0$ (Table I). The diamonds connected with the solid line give the results for continuous speech-simulating noise as interference, whereas the crosses connected with the dashed line give the results for three different recording segments of the male speaker as continuous interfering talkers.

For the condition with three noise sources, the reference threshold is raised by approximately 2 dB in comparison to the situation with two interfering noise sources (see Table I). This is consistent with the increase of masking energy introduced by the additional noise source. As the position of the variable interfering noise source is changed from 0° to 360°, only a very small release from masking, with a maximum of about 2 dB, is achieved, virtually independent of the azimuth. It appears as if the binaural noise reduction system is already ''overloaded'' with the input from the two fixed continuous noise sources so that no binaural release from masking can be obtained with the third noise irrespective of its azimuthal angle.

When three talkers were used, the reference threshold is increased by 6.9 dB as compared to the situation with only two interfering talkers (Table I) which is due both to the addition of masking energy and to the reduction of pauses in the resulting masking signal. As the azimuthal angle of the third interfering talker is varied, a pronounced release from masking is achieved with a maximum of approximately 5 dB at 120° and 270°. Note that in these situations the interfering sound source with the variable position is close to a sound source with fixed position (i.e., 105° and 255°, respectively) so that the situation might be comparable to the condition with two interfering sound sources. The observed release from masking can thus be explained with the assumption that the binaural system suppresses the interference from one direction efficiently if a pause occurs in the interfering sound from another direction. Hence, the difference between the situation with continuous interfering noise (solid line) and continuous talkers (dashed lines) again seems to reflect the ability of the binaural system to utilize the pauses in order to switch the direction of maximum interference reduction.

B. Hearing-impaired listeners

In order to restrict the measurement time and to employ only situations that could be handled by naive listeners without excessive training, only the condition with one interfering continuous noise (S_0N_x) and with two fixed noise sources ($S_0N_{105}N_{255}N_x$) using both continuous noise and interfering talkers were employed. This set of conditions was also selected in order to observe three principal factors that were significant in the experiments with normal listeners: The first factor is the individual's maximum ILD. Thus the situation S_0N_x with continuous interfering noise was employed. The second factor is the number of interfering sound sources. Its effect can be assessed by comparing the condition with one interfering sound source and with three interfering sound sources. Hence, the situation $S_0N_{105}N_{255}N_x$ with continuous noise was employed. The third factor relevant for sensorineural hearing-impaired listeners is the difference between continuous speech and continuous noise as maskers in a complex acoustical situation. Therefore, the same conditions as above were tested using continuous talkers. Unfortunately, most of our hearing-impaired subjects were not able to subjectively assess intelligibility in the condition S_0N_x with one interfering talker in a reliable way because they confused the target talker and the interfering talker. Therefore, only results from the condition $S_0N_{105}N_{255}N_x$ with continuous talkers are reported here.

Table II gives the individual results for each of the eight hearing-impaired listeners. For each of the conditions employed, the individual reference threshold is reported as well as the maximum ILD obtained at certain azimuthal angles of

TABLE II. Bone-conduction hearing loss and performance in the various listening tasks for normal listeners (average values) and each of eight sensorineural-hearing-impaired listeners. For each of the three conditions S_0N_x (noise), $S_0N_{105}N_{255}N_x$ (noise), and $S_0N_{105}N_{255}N_x$ (speech), respectively, the reference thresholds (Ref. Thr.) are given including interindividual standard deviations for the normal group and intraindividual standard deviations for the hearing-impaired listeners. In addition, values of maximum obtained intelligibility level difference (Max. ILD) are given. For the condition S_0N_x, values for the interfering noise located both on the left and on the right hemicircle are reported, whereas only the larger of the two values is given for the condition $S_0N_{105}N_{255}N_x$. The hearing-impaired listeners are subdivided into three groups (G1, G2, and G3) according to their performance in the S_0N_x condition (* not measured, ** not measurable).

	Hearing loss				S_0N_x (noise)			$S_0N_{105}N_{255}N_x$			
	Left		Right		Ref. Thr.	Max. ILD		Noise		Speech	
Subject	500	4*k*	500	4*k*		left	right	Ref. Thr.	Max. ILD	Ref. Thr.	Max. ILD
	(dB HL)				(dB)			(dB)		(dB)	
ϕ Norm	0	0	0	0	−13.8±4.6	−10.0	−9.5	−9.7±5.1	−2.1	−17.7±8.4	−4.1
G1:											
ISDI	30	50	20	60	−11.2±1.1	−5.6	−7.0	*	*	**	**
PEZO	0	80	0	80	−10.2±1.4	−6.0	−7.5	−6.3±1.1	−3.1	−11.2±2.1	−3.8
GEMO	30	80	20	50	−11.7±1.2	−10.4	−8.8	−8.1±0.8	−2.9	−9.1±1.7	−2.3
G2:											
WOSH	10	60	10	70	−12.9±0.8	−4.9	−6.9	−10.2±1.5	−2.5	−10.9±1.8	−2.9
FRBU	50	40	60	50	−13.0±0.7	−6.8	−3.5	−7.2±1.1	−1.8	−5.9±1.4	−1.6
G3:											
ELWU	30	50	30	50	−13.0±0.9	−2.2	−3.4	−9.5±0.8	−1.5	−5.1±2.1	−0.6
HOBE	20	50	30	60	−13.5±1.3	−5.3	−5.0	−8.9±1.2	−1.4	**	**
GUSH	70	80	80	80	−9.0±1.4	−1.3	−1.0	−6.2±1.1	−0.0	**	**

the interfering sound. This angle was selected according to the maximum ILD of normal listeners in the comparable condition.

According to their performance in the various tasks depicted in Table II, the eight subjects were classified into three groups: group 1 (subjects ISDI, PEZO, and GEMO) only showed a slight degradation of performance in comparison to normal listeners. Their reference thresholds were only slightly higher than normal and the maximum ILD was comparatively large and symmetrical about 0° azimuth. Group 2 (subjects WOSH and FRBU) exhibited an asymmetric ILD in the S_0N_x condition with an asymmetry greater than 2 dB. Group 3 (subjects ELWU, HOBE, and GUSH) exhibited only a comparatively small, symmetric ILD which was less than 5.5 dB in the S_0N_x condition. Note that the amount and the configuration of the audiometric hearing loss is not directly related to the performance in the tasks reported here. The individual hearing-impaired listener's assignment to a specific subgroup therefore is based on performance in these tasks rather than on the audiogram.

In general, in the conditions with continuous interfering noise sources, all hearing-impaired subjects only exhibited an insignificant increase of the reference threshold in comparison to normal subjects. However, in the condition with three interfering continuous talkers ($S_0N_{105}N_{255}N_x$), all hearing-impaired listeners showed a significant increase in the reference threshold which reflects both their inability to profit from pauses in the masker and their difficulty in identifying the target speaker in the background of three competing talkers. For three hearing-impaired listeners (ISDI, HOBE, and GUSH) no stable threshold could be obtained for this configuration. Therefore, no threshold measurements are reported in Table II for these cases.

To illustrate the findings with hearing-impaired listeners in more detail, Figs. 5 and 6 give results typical for the subjects from the second group of hearing-impaired subjects (FRBU, Fig. 5) and the third group (subject ELWU, Fig. 6), respectively. The upper panels give the individual results for the situation S_0N_x with continuous noise. The average data from normal listeners (cf. Fig. 2) are included as dashed lines. For subject FRBU [Fig. 5(a)], the threshold is lower around 255° than around 105° (75° on either side of 180°). This effect might correspond to the asymmetry in the configuration of the subjects' hearing loss (Table II) which is 10 dB higher in the right ear. Note that the presentation levels at both ears were adjusted to partially compensate for this asymmetry. Despite this level adjustment, the patients' performance was worse when the interfering noise was presented from the right side (i.e., the side with the ''worse'' ear) than from the left side. One possible reason for this asymmetry is a different amount of nonlinear distortions in the internal acoustical representation produced by each ear. Any such distortion would interfere with a central noise reduction process and hence reduce the maximum benefit of binaural interaction in the respective subject. Specifically, the amplified noise presented to subject FRBU's ''worse'' ear might produce more distortion in the respective internal acoustical representation than if the same noise was presented to the ''better'' ear.

In contrast to subject FRBU, subject ELWU exhibits a symmetric but highly reduced ILD in the situation S_0N_x [Fig. 6(a)]. In the more complex situation $S_0N_{105}N_{255}N_x$ with continuous noise [Figs. 5(b) and 6(b)], both subjects show qualitatively similar results to normal listeners, i.e., they do not show any significant ILD. In addition, no significant ILD is observed for the configuration $S_0N_{105}N_{255}N_x$ with interfering

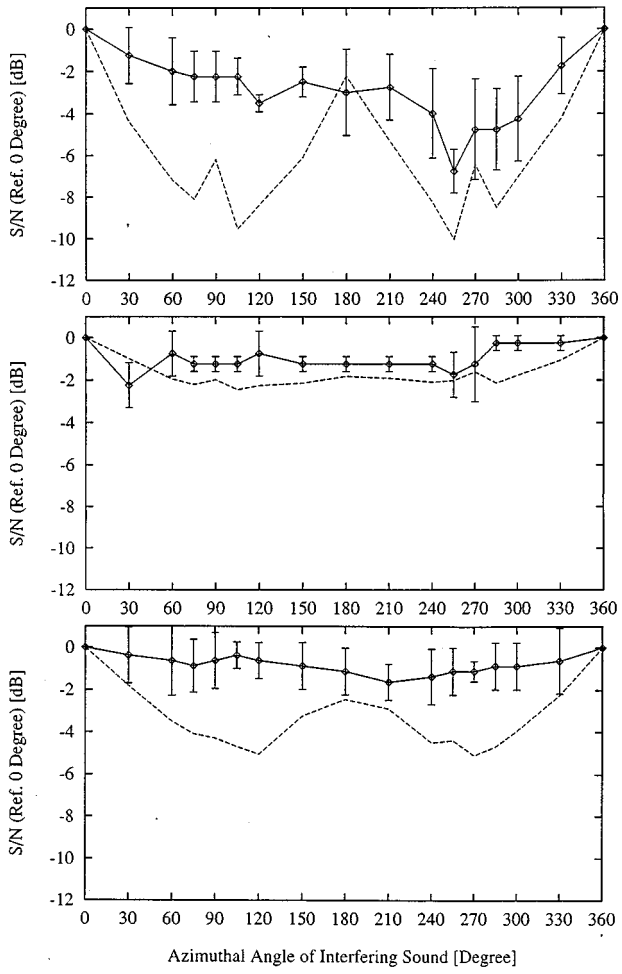

FIG. 5. Speech reception thresholds for the hearing-impaired listener FRBU as a function of the azimuth of an interfering sound source for different configurations of the interference plotted in a similar way as in Figs. 2 and 4. The diamonds connected with solid lines give the average values and intraindividual standard deviations of the subjectively adjusted thresholds. The dashed lines give the average result of normal listeners from Figs. 2 and 4. Upper panel: configuration S_0N_x [Figs. 1(a) and 2] using continuous noise as interference. Middle panel: configuration $S_0N_{105}N_{255}N_x$ [Figs. 1(c) and 4] using continuous noise as interference. Lower panel: configuration $S_0N_{105}N_{255}N_x$ [Figs. 1(c) and 4] using continuous talkers as interference.

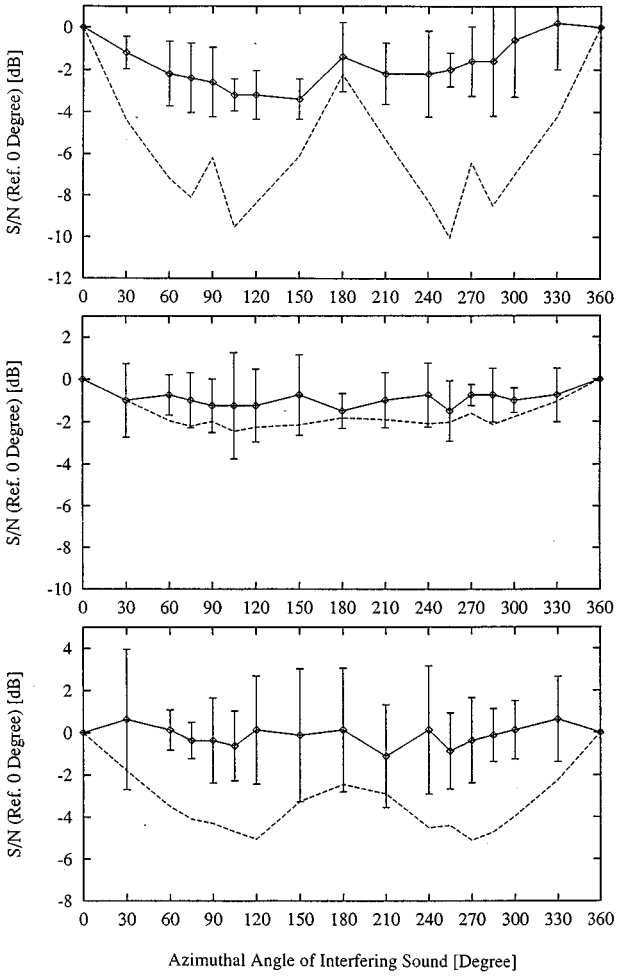

FIG. 6. Same as Fig. 5 for the hearing-impaired subject ELWU.

talkers [Figs. 5(c) and 6(c)]. This lack of ILD differs significantly from the results found in normal listeners (dashed curves). On the basis of the data shown in Fig. 5(a), a larger ILD would have been expected at least for subject FRBU for azimuths around 240°. One reason for the lack of ILD might be the subjects' difficulties in adjusting the speech to threshold in this configuration, which is also reflected in the large standard deviations. Another reason might be an inability to utilize the temporal pauses within the signals of the interfering talkers. This effect is well known from the literature (e.g., Bronkhorst and Plomp, 1992). It is also reflected in the fact that the reference threshold using speech interference is more elevated for hearing-impaired listeners in comparison to normal listeners than in the same configuration but using continuous noise (see Table II).

In summary, the hearing-impaired listeners tested in this study exhibit a moderate increase in reference thresholds (with the exception of the condition described last, where a substantial increase was observed) and a reduction of the maximum ILD that varies across subjects and does not systematically depend on the audiogram and the configuration and symmetry of the hearing loss.

III. DISCUSSION

A. Measurement method

The subjective assessment of speech intelligibility performed here is a very time-efficient method that qualitatively measures the same effects as lengthy speech intelligibility tests. Each subject requires on the average about 7 s to adjust the signal-to-noise ratio in a given situation. Even if this measurement is repeated four to eight times (as was done in this study), the measurement time is far less than the 20-min measurement time required for a complete speech reception threshold measurement by, e.g., Müller (1992). Hence, the reduction in measurement time amounts to about a factor of 20. It should be noted, however, that the subjectively assessed thresholds are highly dependent on the subject's criterion. Thus, comparatively large interindividual standard deviations of 5 dB for continuous noise maskers and 8 dB for continuous talkers as maskers are observed. This indicates that the absolute values of the assessed thresholds do not

exactly correspond to measured SRTs. However, if the subject's subjective criterion is eliminated by only considering the difference between two assessed thresholds for different configurations, the interindividual differences are drastically reduced to values below 1 dB. These deviations are at the same order of magnitude as the variability in the SRT data reported by, e.g., vom Hövel (1984) and Plomp and Mimpen (1981).

The maximum ILD obtained in the configuration S_0N_x amounts to about 10 dB with the method employed here, while vom Hövel (1984) obtained a maximum ILD of 13 dB at 120° azimuth, Plomp and Mimpen (1981) obtained 11 dB at 112.5°, and Müller (1992) obtained about 12 dB at 105°. The differences between all these values can on the one hand be attributed to the slightly different measurement configurations and test materials. However, the configuration employed by Müller (1992) was nearly identical with the one employed here. This indicates that the subjects have a more conservative criterion when subjectively assessing the maximum improvement in speech intelligibility in comparison with ''objective'' measurement methods. A similar observation was reported by Wesselkamp (1994) (cf. Kollmeier and Wesselkamp, 1997), who compared the assessed thresholds for short sentences from the ''Göttinger Satzverständlichkeitstest'' (Wesselkamp *et al.*, 1992) with the actual sentence reception threshold measured for each specific sentence. He found a high correlation between both measures (average correlation coefficient 0.78), but a much smaller range of subjectively assessed thresholds than ''objectively'' measured reception thresholds. Hence, the subjective intelligibility assessment methods appear to ''compress'' the maximum observable effect of varying an independent variable (e.g., azimuth of interfering sound source) on the observed speech intelligibility.

B. Influence of additional interfering sound sources

For a single interfering noise, the ILD is found to be maximal when the noise is at 105° and 255° azimuth, if the target sound emanates from the front (0° azimuth). The maximum ILD decreases significantly if the number of interfering sound sources is increased and the sources are located on both hemicircles. When continuous talkers are used as interfering sound sources instead of continuous noise, the negative effect of increasing the number of interfering sound sources is less pronounced. It should be noted that the release from masking for different azimuths of the interfering sound source reported here reflects the ''effective'' global performance of the auditory system. The relative contribution of different mechanisms to this global effect (e.g., head shadow effect also related to monaural hearing at the ''better'' ear and binaural interaction that utilizes interaural level and time differences) is not established here. Nevertheless, some conclusions can be drawn about the principles underlying human noise suppression in realistic, spatial situations with increasing complexity. For example, our findings provide evidence that the binaural system can only suppress one interfering sound source at a time and hence provides little or even no benefit if at least one additional sound source is present simultaneously with a sufficiently large separation in azimuthal angle. In this sense the binaural system operates like a two-sensor system known from spatial beam forming techniques in radar or acoustic signal processing. In these systems, a certain attenuation and delay between both inputs is applied at each frequency in order to minimize the sensitivity to one spatial direction and provide a high sensitivity to another spatial direction. These elements also are the basic ingredients of current models of binaural interaction developed on the basis of psychoacoustical data [e.g., the EC theory of Durlach (1972), or all models based on the Jeffress (1948) model]. Therefore, the current findings are compatible with the model of vom Hövel (1984) who described speech intelligibility in simple spatial configurations by a bank of EC models at different frequencies and an articulation-index (AI)-based speech intelligibility prediction at the output of the EC processors.

Another aspect of our findings has not yet been described with any of these binaural models, i.e., the ability of the binaural system to switch the direction of maximum attenuation rapidly from one interfering sound source to the other, thus exploiting the temporal pauses of interfering talkers. This ability requires that within each frequency band the signal-to-noise ratio can be optimized by rapidly changing the processing strategy by, e.g., altering the interaural attenuation and delay for each frequency. This switching of binaural processing strategy was studied in various psychoacoustical experiments that provided evidence of a binaural ''sluggishness'' (cf. Grantham and Wightman, 1979; Kollmeier and Gilkey, 1990). From these measurements it can be estimated that a binaural noise reduction strategy can be changed with time constants of approximately 100–200 ms, which might be still sufficient to utilize pauses in the envelope of a single talker in an efficient way. These time constants of binaural sluggishness seem to be adapted very well to the most prominent average modulation rate of speech of about 4 Hz.

C. Effect of hearing impairment

Sensorineural hearing-impaired listeners show a reduction in maximum ILD. The ILDs for interfering noise on the left or right side can differ substantially. The exact type and degree of this reduction varies considerably among subjects and cannot easily be related to the audiogram. Since some hearing-impaired subjects do not profit significantly from a spatial separation between target sound and interference (i.e., neither from monaural headshadow effect nor from the binaural differences across ears), one can not separate the influence of both effects on the current data. In addition, hearing-impaired listeners obtain less benefit from pauses in the interference, i.e., if continuous talkers are employed as interfering sound sources instead of continuous noise. Thus it appears that sensorineural-impaired listeners are handicapped in realistic communication situations with background noise in two ways: first, the minimum signal-to-noise ratio required to understand speech is elevated for each individual ear. This effect is even more severe if a fluctuating background noise or an interfering talker is present. Second,

the binaural release from masking is impaired so that they receive less benefit from spatial separation between the target sound source and the interfering noise source. This reduction in binaural advantage holds especially for fluctuating maskers where hearing-impaired listeners have more difficulty in using the pauses of the interfering noise to suppress the remaining noise. Thus a substantial effort should be made to assist hearing-impaired listeners in noisy situations (e.g., the typical ''cocktail-party situation''). Assistive devices should therefore not only aim to restore the listening capabilities at each ear separately, but should also try to restore the noise suppression ability of the normal listener in spatial situations and should utilize binaural cues to enhance signal processing performance (see Kollmeier, 1997, for a review).

IV. CONCLUSIONS

(1) The speech assessment method employed here provides a rapid and valid measure of the normal and hearing-impaired listeners' speech reception capability for various acoustical situations. If threshold differences are evaluated, the same qualitative results are obtained as for lengthy SRT measurements.

(2) The normal listener's binaural system is capable of suppressing interference from one azimuth at a time. It can utilize pauses in one interfering source (e.g., speech pauses) to suppress the interference from a second source at a different azimuth. However, the maximum release from masking decreases rapidly as the number of interfering sound sources and their respective azimuthal separation increases.

(3) Sensorineural hearing-impaired listeners exhibit a decrease in ILD and a reduced ability to exploit pauses in the interfering sound. Hence, they are handicapped in realistic spatial interference situations both by an increased monaural speech reception threshold and a decreased binaural noise reduction ability.

(4) The type and amount of reduction in binaural noise suppression ability varies across hearing-impaired subjects and cannot easily be predicted from the audiogram.

ACKNOWLEDGMENTS

This work was supported by BMBF PT AUG. Thanks to B. C. J. Moore, A. Bronkhorst, W. A. Yost, and two anonymous reviewers for improving a previous draft of the paper. Thanks to U. Vriesen-Lippke and A. Sievers for typing the manuscript.

[1]Babinet's theorem states that the diffraction pattern produced by a shading object (for example, a circular obstacle) is the same as the one produced by the ''negative'' of the shading object (e.g., a circular hole). The reason for this theorem is that the combination of both objects produces a complete shade. Thus both diffraction patterns have to add up to zero if they are combined in a coherent way. In the case of a diffracting sphere, for example, a maximum in the diffraction pattern always occurs exactly on the symmetry axis pointing opposite to the direction of incidence. Hence, a very small intensity difference is observed between the central points on both sides of the sphere pointing toward the direction of incidence and pointing opposite to it.

Bronkhorst, A. W., and Plomp, R. (**1988**). ''The effect of head-induced interaural time and level differences on speech intelligibility in noise,'' J. Acoust. Soc. Am. **83,** 1508–1516.

Bronkhorst, A. W., and Plomp, R. (**1992**). ''Effect of multiple speechlike maskers on binaural speech recognition in normal and impaired hearing,'' J. Acoust. Soc. Am. **92,** 3132–3139.

Carhart, R., Tillman, T. W., and Greetis, E. S. (**1969**). ''Perceptual masking in multiple sound backgrounds,'' J. Acoust. Soc. Am. **45,** 694–703.

Cherry, E. C. (**1953**). ''Some experiments on the recognition of speech, with one and two ears,'' J. Acoust. Soc. Am. **25,** 975–979.

Colburn, H. S., and Durlach, N. I. (**1978**). ''Models of binaural interaction,'' in *Handbook of Perception, Vol. IV*, edited by E. C. Carterette and M. P. Friedman: (Academic, New York), pp. 467–518.

Cox, R. M., Alexander, and G. C., Rivera, I. M. (**1991**). ''Comparison of objective and subjective measures of speech intelligibility in elderly hearing-impaired listeners,'' J. Speech Hear. Res. **34**, 904–915.

Durlach, N. I. (**1972**). ''Binaural signal detection: Equalization and cancellation theory,'' in *Foundations of Modern Auditory Theory*, edited by J. V. Tobias (Academic, New York), Vol. 2, pp. 363–462.

Durlach, N. I., Thompson, C. L., and Colburn, H. S. (**1981**). ''Binaural interaction in impaired listeners. A review of past research,'' Audiology **20**, 181–211.

Fletcher, H., and Steinberg, J. C. (**1929**). ''Articulation testing methods.'' Bell Syst. Tech. J. **8**, 806–854.

Genuit, K. (**1984**). ''Ein Modell zur Beschreibung der Außenohrübertragungseigenschaften,'' Dissertation, Technische Hochschule Aachen.

Grantham, D. W., and Wightman, F. L. (**1979**). ''Detectability of a pulsed tone in the presence of a masker with time-varying interaural correlation,'' J. Acoust. Soc. Am. **65,** 1509–1517.

Hirsh, I. J. (**1948**). ''The influence of interaural phase on interaural summation and inhibition,'' J. Acoust. Soc. Am. **22,** 536–544.

Jeffress, L. A. (**1948**). ''A place theory of sound localization,'' J. Comp. Physiol. Psychol. **61**, 468–486.

Kinkel, M., and Kollmeier, B. (**1992**). ''Binaurales Hören bei Normal-und Schwerhörigen II: Analyse der Ergebnisse,'' Audiol. Akust. **31**, 22–33.

Kollmeier, B. (**1990**). ''Meßmethodik, Modellierung und Verbesserung der Verständlichkeit von Sprache,'' Habilitationsschrift, Universität Göttingen.

Kollmeier, B. (**1997**). ''Signal Processing for Hearing Aids Employing Binaural Cues,'' in *Binaural and Spatial Hearing* edited by R. H. Gilkey and T. R. Anderson (Erlbaum, Hillsdale, NJ), pp. 753–775.

Kollmeier, B., and Drüke, G. (**1992**). ''Richtungsabhängige Freifeldentzerrung von Audiometrie-Kopfhörern mit digitaler Echtzeit-Filterung,'' in *Medizinische Physik '92*, edited by J. Roth (DGMP, Basel), pp. 296–297.

Kollmeier, B., and Gilkey, R. H. (**1990**). ''Binaural forward and backward masking: Evidence for sluggishness in binaural detection,'' J. Acoust. Soc. Am. **87,** 1709–1719.

Kollmeier, B., and Wesselkamp, M. (**1997**). ''Development and evaluation of a German sentence test for objective and subjective speech intelligibility assessment,'' submitted to J. Acoust. Soc. Am.

Kryter, K. D. (**1962**). ''Methods for the calculation and use of the Articulation Index,'' J. Acoust. Soc. Am. **34,** 1689–1697.

Müller, C. (**1992**). ''Perzeptive Analyse und Weiterentwicklung eines Reimtestverfahrens für die Sprachaudiometrie,'' Dissertation, Universität Göttingen, Germany.

Peissig, J. (**1992**). ''Binaurale Hörgerätestrategien in komplexen Störschallsituationen,'' Fortschr.-Ber. VDI Reihe 17 Nr. 88 (VDI-Verlag, Düsseldorf).

Peissig, J., and Kollmeier, B. (**1993**). ''Richtcharakteristik des binauralen Hörsystems bei Normal- und Schwerhörigen,'' in *Fortschritte der Akustik-DAGA '93* (DPG Verlag, Bad Honnef), pp. 744–747.

Plomp, R. (**1986**). ''A signal-to-noise ratio model for the speech-perception threshold of the hearing impaired,''J. Speech Hear. Res. **29,** 146–154.

Plomp, R., and Mimpen, A. M. (**1981**). ''Effect of the orientation of the speaker's head and the azimuth of a noise source on the speech-reception threshold for sentences,'' Acustica **48,** 325–328.

Pösselt, C., Schröter, J., Opitz, M., Divenji, P. L., and Blauert, J. (**1986**). ''Generation of binaural signals for research and home entertainment,'' in *Proceedings of the 12th International Congress on Acoustics*, Toronto, Vol. 1, B1–6.

vom Hövel, H. (**1984**). ''Zur Bedeutung der Übertragungseigenschaften des Außenohres sowie des binauralen Hörsystems bei gestörter Sprachübertragung,'' Ing. Dissertation, RWTH Aachen 1984.

Wesselkamp, M. (**1994**). ''Messung und Modellierung der Verständlichkeit von Sprache,'' Dissertation, Universität Göttingen.
Wesselkamp, M., Kliem, K., and Kollmeier, B. (**1992**). ''Erstellung eines optimierten Satztestes in deutscher Sprache,'' in *Moderne Verfahren der Sprachaudiometrie*, edited by B. Kollmeier (Median-Verlag, Heidelberg), pp. 330–343.
Yost, W. A. (**1991**). ''Auditory Image Perception and Analysis: The Basis for Hearing,'' Hear. Res. **56,** 8–18.

A new approach to comparing binaural masking level differences at low and high frequencies[a)]

Steven van de Par and Armin Kohlrausch
Institute for Perception Research (IPO), P.O. Box 513, NL-5600 MB Eindhoven, The Netherlands

(Received 27 December 1995; revised 6 September 1996; accepted 28 September 1996)

A new experimental technique for studying binaural processing at high frequencies is introduced. Binaural masking level differences (BMLDs) for the conditions N_0S_π and $N_\pi S_0$ were measured for a tonal signal in narrow-band noise at 125, 250, and 4000 Hz. In addition, ''transposed'' stimuli were generated, which were centered at 4000 Hz, but were designed to preserve within the envelope the temporal ''fine-structure'' information available at the two lower frequencies. The BMLDs measured with the 125-Hz transposed stimuli were essentially the same as BMLDs from the regular 125-Hz condition. The transposed 250-Hz stimuli generally produced smaller BMLDs than the stimuli centered at 250 Hz, but the pattern of results as a function of masker bandwidth was the same. The patterns of results from the transposed stimuli are different from those of the 4000-Hz condition and, consistent with the low-frequency masker data, generally show higher BMLDs. The results indicate that the mechanisms underlying binaural processing at low and high frequencies are similar, and that frequency-dependent differences in BMLDs probably reflect the inability of the auditory system to encode the temporal fine structure of high-frequency stimuli. © *1997 Acoustical Society of America.* [S0001-4966(97)04102-7]

PACS numbers: 43.66.Pn, 43.66.Ba, 43.66.Dc [RHD]

INTRODUCTION

It is well known that for broadband noise maskers, binaural masking level differences (BMLDs) resulting from the comparison of an N_0S_π condition (the noise masker, N, and the signal, S, have an interaural phase of 0 and π, respectively) with an N_0S_0 condition are much larger at low frequencies than at high frequencies (Durlach, 1964; Metz *et al.*, 1968). At low frequencies, BMLDs are approximately 15 dB, while at frequencies above about 2 kHz they are only 2–3 dB.

When narrow-band noise maskers instead of broadband maskers are used, the BMLDs are generally much larger, both at low and at high frequencies (Metz *et al.*, 1968; Zurek and Durlach, 1987). In this case, BMLDs at low frequencies can be as high as 25 dB, while at high frequencies they can amount to 15 dB.

There are two mechanisms that could account for the differences between low- and high-frequency BMLDs (e.g., Zurek and Durlach, 1987):

(1) With increasing frequency, the auditory filter bandwidth increases. It is a general rule that the maximum rate of fluctuations within a noise band is proportional to its bandwidth. For a broadband masker, therefore, the rate of changes in interaural time and intensity differences at the outputs of the auditory filter increases with increasing signal frequency. This increased rate is detrimental for binaural unmasking, if one assumes that the auditory system is not able to follow these rapid changes (Perrott and Musicant, 1977; Grantham and Wightman, 1978; Grantham, 1984; Bernstein and Trahiotis, 1992).

(2) With increasing frequency, the responses of the inner hair cells show a decrease in phase locking (Palmer and Russell, 1986). Therefore, at frequencies above about 1.5 kHz, the fine-structure information of the input waveform is gradually lost. As a result, interaural time differences which are present in the fine structure of the waveform are no longer present in the activity of the auditory nerve. Therefore, at high frequencies the binaural system has access only to the interaural intensity differences in the envelope of the stimulus.[1]

Although no interaural time differences in the *fine structure* of high-frequency stimuli can be exploited by the auditory system, several studies have shown that the auditory system is able to process interaural time differences that are available in the *envelope* of high-frequency stimuli. Henning (1974) tested the detectability of an interaural delay in a 300-Hz amplitude modulated high-frequency sinusoid and found that performance was as good as with a 300-Hz pure tone. McFadden and Pasanen (1976) measured the minimal interaural delay needed for lateralization of noise bands of several bandwidths and for two-tone complexes as a function of frequency separation and depth of modulation. They found that: ''In many conditions of listening, sensitivity to interaural time differences at high frequencies compares favorably with the sensitivity at low frequencies.''

The ability of the auditory system to process interaural time delays in the envelope of high-frequency stimuli such as presented in these studies suggests that this ability is also exploited in high-frequency binaural masking experiments. However, it is not possible to relate the results from these experiments directly to the difference in the results for low- and high-frequency BMLDs. Apart from the different experimental approach (lateralization versus binaural detection),

[a)]Portions of the data included in this paper were presented at the 10th International Symposium on Hearing in Irsee, Germany, 1994.

the specific stimulus properties do not allow a direct comparison of low- and high-frequency data because the internal representation after transformation in the inner hair cells (half-wave rectification and low-pass filtering) is different. Therefore, the question remains whether the difference in the size of BMLDs with frequency is a result of the loss of information contained in the fine structure of a stimulus in the auditory periphery prior to the binaural processing or whether it is the result of different binaural processing capabilities at low and high frequencies.

A first attempt to study binaural unmasking at high frequencies with specific emphasis on envelope structure was performed by Bernstein and Trahiotis (1992). They added a sinusoid to the envelopes of high-frequency narrow bands of noise. While the noise was in phase, the sinusoid was either homophasic or antiphasic. Subjects had to distinguish between intervals containing the homophasic and the antiphasic sinusoid. With this approach the rate of fluctuation of interaural intensity differences (IIDs) and the inherent rate of fluctuations of the envelope could be adjusted independently by changing the frequency of the sinusoid and the bandwidth of the noise, respectively. The results indicated that there is a rate limitation for the processing of dynamically changing IIDs such as proposed by Grantham (1984).

The experiments of this paper are intended to link the ideas on envelope processing at high frequencies with signal properties in a typical binaural masking experiment in a more direct way. We report the results of experiments with a special type of high-frequency stimulus which contains ''fine structure'' also after the first stages of peripheral transduction (basilar membrane filtering and hair-cell transduction). This property is achieved by encoding in the envelope of a 4-kHz carrier the information that is available after the transformation of a low-frequency stimulus through a simple hair-cell model. The temporal information, now presented in the high-frequency channel, is in principle identical to the low-frequency information. Using this technique, the role of fine structure for binaural processing at high and low frequencies can be compared directly.

The results for transposed stimuli are compared with BMLDs obtained with conventional high- and low-frequency stimuli, where the high-frequency stimuli are in the same spectral range as the transposed stimuli. A comparison of the BMLDs for transposed stimuli with those for high-frequency stimuli will indicate whether the additional envelope information affects binaural interaction at high frequencies. If the properties of binaural processing are the same at low and high frequencies, we would expect that the transposed and low-frequency stimuli give very similar BMLDs. In the next section we will explain the calculation of the transposed stimuli and discuss the properties of these stimuli.

I. TRANSPOSED STIMULI

In the following example, the procedure is described for the generation of a transposed stimulus in an N_0S_π condition. The first step is to generate a conventional low-frequency stimulus. Portions of low-frequency stimuli are shown in panel A of Fig. 1. The interval ranging from 0.0–0.1 s shows the time function of a diotic reference stimulus

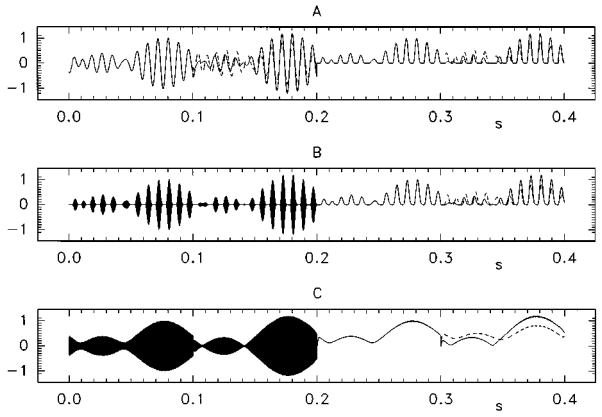

FIG. 1. An example of three different N_0S_π stimuli before and after peripheral processing. Panel A shows a 125-Hz stimulus, panel B shows a transposed stimulus, and panel C shows a 4-kHz stimulus. The intervals 0.0–0.1 s show the N_0 masker alone, the intervals 0.1–0.2 s show the N_0 masker plus the S_π signal at a signal-to-noise ratio of −10 dB, the intervals 0.2–0.3 s show the masker after peripheral processing, and the intervals 0.3–0.4 s show the combined masker and signal after peripheral processing.

(N_0) which is a noise masker with 25-Hz bandwidth centered at 125 Hz. In the interval ranging from 0.1–0.2 s, a dichotic test stimulus (N_0S_π) is shown, with an S_π signal added to the N_0 masker with a signal-to-noise ratio of −10 dB. The two curves in this interval represent the signals at the right and left ear. Comparing the two curves we find interaural time delays in the form of different timings of the zero crossings and we find interaural intensity differences in the form of differences between the envelopes, e.g., at t equals 0.17 s.

The interval ranging from 0.2–0.4 s shows the signals from the first half of panel A, after being processed by a stage that simulates properties of the auditory periphery. These are modeled by half-wave rectifying the input signal and, subsequently, low-pass filtering at 500 Hz. We assume that the signals in the interval 0.2–0.4 s are a reasonable description for the low-frequency stimuli at the level of the inner hair cell.

Multiplying the processed waveforms by a high-frequency carrier (4 kHz in the present experiments), we obtain a ''transposed'' stimulus as shown in panel B. The reference stimulus (noise alone) is plotted in the 0.0–0.1-s interval, the dichotic test stimulus in the interval from 0.1–0.2 s. In the interval 0.2–0.4 s, this transposed stimulus is shown after being processed by the first stages of the auditory periphery. We can now see that with our description of the auditory periphery, essentially the same temporal information is available for the transposed stimulus as for the initial low-frequency stimulus in panel A. The two conditions differ, however, by the center frequency of the auditory channel, through which this information is provided to the binaural processor.

The signals for a standard N_0S_π condition at 4 kHz are shown in panel C. Here, the masker is a 25-Hz-wide noise centered at 4 kHz and the signal is a 4-kHz sinusoid. We see that no information about the stimulus fine structure is present after the peripheral transduction. However, there are interaural differences present in the envelopes of the waveform. By comparing panels B and C, one sees that, with a

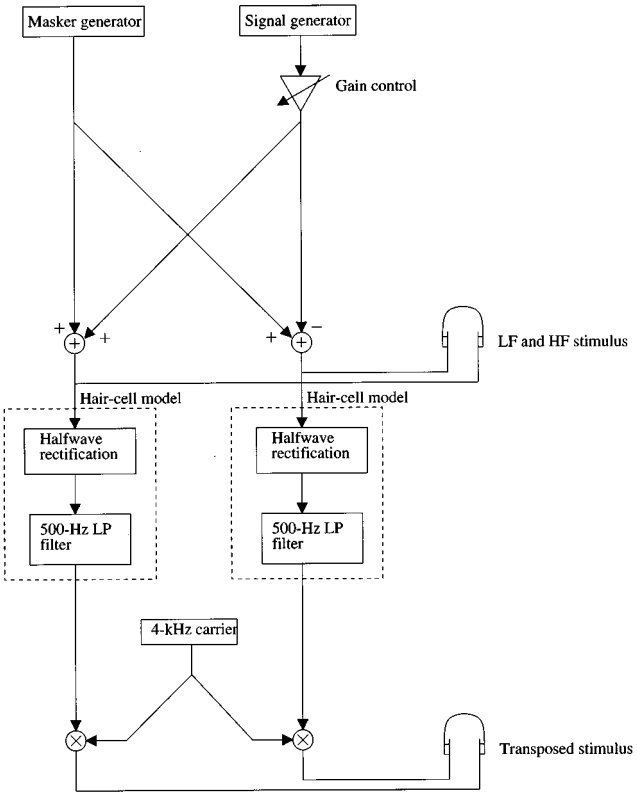

FIG. 2. A schematic overview of the transposed N_0S_π stimulus generation. The scheme starts at the top with the masker and signal generation, followed by a gain control of the signal and the summation and subtraction of the masker and signal. At this point the stimulus for a conventional N_0S_π condition is obtained. This stimulus is then transformed by a simple hair-cell model and multiplied by a 4 kHz carrier resulting in a transposed stimulus.

conventional high-frequency stimulus less information about temporal details is available for any central processing stage following the peripheral transduction.

In Fig. 2 the generation of a transposed N_0S_π stimulus is shown schematically. Since these stimuli will be used in a forced-choice procedure, the transposed stimuli will be either noise alone or noise plus signal. In the upper part of this figure a conventional low-frequency stimulus is generated. The signal-to-noise ratio of the stimulus is adjusted with the gain control. The low-frequency stimulus is then used as an input to generate a transposed stimulus, as is shown in the lower part of Fig. 2. When we discuss the signal-to-noise ratio of a transposed stimulus we will be referring to the signal-to-noise ratio of the underlying low-frequency stimulus.[2]

The hair-cell model that is used in the generation of the transposed stimuli consists of a half-wave rectifier and a second order low-pass filter at 500 Hz. For our purposes these are the important signal-processing characteristics of the inner hair cells. The adaptive and compressive properties of the inner hair cells are not included since we can expect these properties to affect the low-frequency and transposed stimulus similarly once they are transformed by the inner hair cells in the cochlea. The 500-Hz low-pass filter serves as a means to limit the bandwidth of the half-wave rectified signal such that after the multiplication with the 4-kHz carrier, only high-frequency (>1.5 kHz) auditory filters are excited.

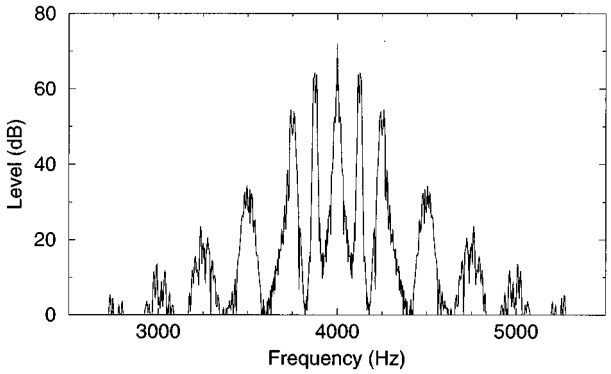

FIG. 3. The spectrum of a 25-Hz-wide 125-Hz transposed stimulus. Most of the stimulus energy is around 4 kHz. The spectrum of the original low-frequency stimulus now occurs at 4125 Hz and the mirror image of that spectrum is at 3875 Hz. Additional peaks in the spectrum occur with spacings of 250 Hz.

The spectrum of a transposed noise band is shown in Fig. 3. The average spectral level is highest around the carrier frequency (4 kHz) and decreases at both sides of the maximum. The spectrum of the original noise band is represented in the two side bands that have a spectral distance from the carrier frequency equal to the center frequency of the noise band. Additional peaks are found at regular intervals of multiples of twice the center frequency of the noise band. More details about the spectrum of the transposed stimulus are given in the Appendix. In our experiments the stimulus energy that was present below frequencies of 1.5 kHz was at least 70 dB lower than the total amount of energy in the stimulus spectrum for all conditions that were measured. Since we presented stimuli at a sound pressure level of about 70 dB, the low-frequency energy was below absolute threshold and could not lead to any binaural cues. This implies that subjects could only use binaural cues at high frequencies where, generally, binaural detection is observed to be worse than at low frequencies.

The introduction of a signal in a transposed stimulus not only leads to changes in the stimulus spectrum near the center frequency of the transposed stimulus, but also to changes in the more remote residual spectral parts. In this respect, the transposed stimulus differs from a conventional high-frequency stimulus. However, an analysis of the transposed stimuli shows that the off-frequency spectral parts are not likely to lead to a better binaural detection than the central part of the spectrum and that therefore the extra spectral components in the transposed stimulus do not affect binaural detection (cf. Appendix). To test this, the spectrum of 125-Hz transposed stimuli was bandpass filtered such that only the central three or five peaks remained.[3] Thresholds for an N_0S_π condition with and without bandpass filtering were measured for subject SP at narrow and broadband conditions. Differences between the conditions were no larger than 1.7 dB, suggesting that the additional spectral components have very little effect on the detection thresholds.

II. EXPERIMENT I

A. Procedure

A three-interval forced-choice procedure with adaptive signal-level adjustment was used to determine masked thresholds. The three masker intervals of 400-ms duration were separated by pauses of 200 ms. A signal of 300-ms duration was added in the temporal center to one of these intervals. The subject's task was to indicate which of the three intervals contained the signal. Feedback was provided to the subject after each trial.

The signal level was adjusted according to a two-down one-up rule (Levitt, 1971). The initial step size for adjusting the level was 8 dB. After each second reversal of the level track, the step size was halved until a step size of 1 dB was reached. The run was then continued for another eight reversals. From the level of these last eight reversals the median was calculated and used as a threshold value. At least four threshold values were obtained and averaged for each parameter value and subject.

Seven subjects participated in this experiment. They were all laboratory colleagues, except for one subject, and had experience in (monaural) masking experiments.

B. Stimuli

All stimuli were generated digitally and converted to analog signals with a two-channel, 16-bit D/A converter at a sampling rate of 32 kHz. The signals were presented to the subjects over Telephonics TDH-49P headphones at a sound pressure level of 70 dB.

The 400-ms masker samples for the low- and high-frequency stimuli were obtained by randomly selecting a segment from a 2000-ms bandpass-noise buffer. The band-limited noise buffer was created in the frequency domain by generating a flat spectrum within the passband and randomizing the phases. After an inverse Fourier transform, the noise buffer of 2000 ms was obtained. The 300-ms signals were sinusoids with a frequency equal to the center frequency of the noise masker. In order to avoid spectral splatter, the signal and the maskers were gated with 50-ms raised-cosine ramps.[4] Thresholds are expressed as signal-to-overall-noise level.

In this first experiment, BMLDs were obtained by measuring and comparing N_0S_0 and N_0S_π thresholds. Thresholds were measured for maskers with a center frequency of 125 Hz, 250 Hz, and 4 kHz, and bandwidths of 5, 10, 25, 50, 100, and 250 Hz. In addition, a bandwidth of 500 Hz was used for center frequencies of 250 Hz and 4 kHz. Transposed stimuli were obtained from the low-frequency conditions with 125- and 250-Hz center frequencies.

C. Results

Results for the N_0S_0 conditions were very similar across subjects, and therefore only the mean N_0S_0 thresholds are shown in Fig. 4. The symbols in the left panel indicate average results of five subjects for 125 Hz (○), 125-Hz transposed (□), and 4 kHz (◇). Up to a bandwidth of 100 Hz, the three curves are rather similar. Between 100- and 250-Hz bandwidth, the thresholds in the 125-Hz condition seem to decrease more rapidly than in the other two other conditions. This result can be attributed to the fact that the critical bandwidth is narrowest for the 125-Hz condition and that a part of the energy of the 250-Hz-wide masker is filtered out.

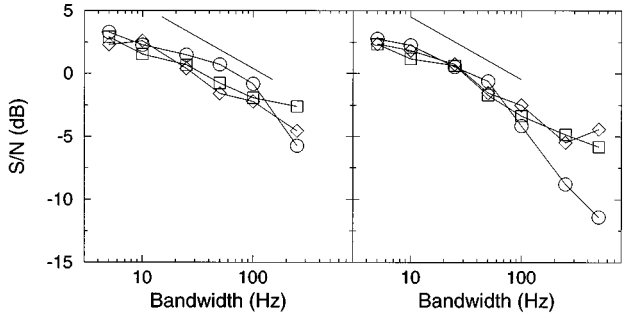

FIG. 4. The N_0S_0 thresholds as a function of masker bandwidth. The left panel shows thresholds for 125 Hz (○), 125-Hz transposed (□), and 4 kHz (◇). The right panel shows thresholds for 250 Hz (○), 250-Hz transposed (□), and 4 kHz (◇). Thresholds are the average of five subjects and are indicated as signal-to-overall-noise level ratio.

The right panel shows average data for the center frequencies 250 Hz (○), 250-Hz transposed (□), and 4 kHz (◇). The data are again averages for five subjects. Three of these subjects also contributed to the data in the left panel. For these conditions the curves are parallel up to a bandwidth of 100 Hz. At wider bandwidths, the 250-Hz curve lies significantly below the two other curves. The 250-Hz transposed and the 4-kHz curves are nearly identical, just as the two corresponding curves in the left panel. These data suggest that monaural processing is similar at low and high frequencies, as long as the auditory filter bandwidth does not affect the stimuli.

With increasing masker bandwidth, thresholds decrease for all conditions. Except for the low-frequency data at large masker bandwidths this is not due to the auditory filter bandwidth but to the variability in the overall stimulus level caused by the fluctuations in the masker envelope (Bos and de Boer, 1966). With a masker of finite length this variability is largest at the narrowest bandwidths. On the basis of the noise statistics it can be shown that the variability in stimulus energy decreases with 1.5 dB/oct (Green and Swets, 1974). If signal detection depends on an energy cue, thresholds can be expected to decrease with 1.5 dB per doubling of the masker bandwidth. The auxiliary lines in the left and right panels of Fig. 4 decrease with this slope and correspond well with the slope in the measured data. In a similar way, a decrease with increasing bandwidth of the signal-to-overall-noise ratio has been reported previously for subcritical bandwidths by several authors (e.g., de Boer, 1962; Weber, 1978; Kidd *et al.*, 1989).

The BMLDs for the N_0S_π condition for center frequencies of 125 Hz, 125-Hz transposed and 4 kHz are shown in Fig. 5. The panels show the individual results of the five observers and at the bottom right, the average of all subjects. The symbol with the error bars indicates the average of the standard deviations over all bandwidths. It is calculated separately for each individual observer and for each stimulus type. In the panel with the average of all observers the stan-

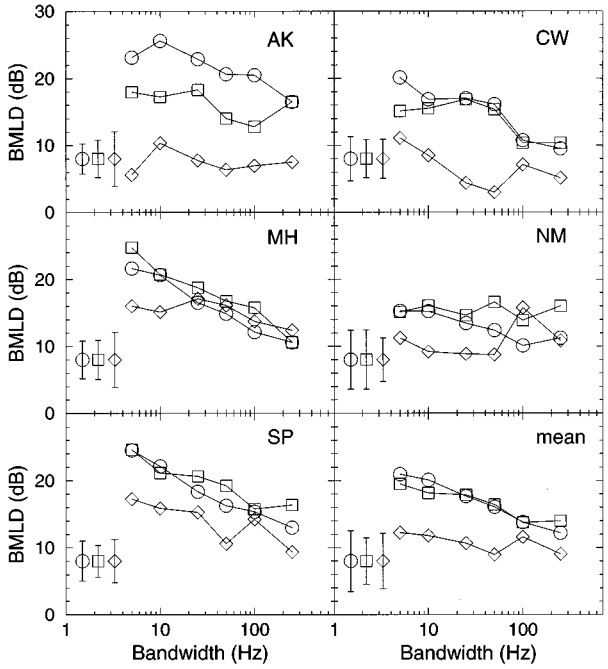

FIG. 5. The N_0S_π BMLDs as a function of masker bandwidth for 125 Hz (○), 125-Hz transposed (□), and 4 kHz (◇). Five panels show data for individual subjects; the panel at the bottom right shows the average of the five subjects. In the bottom right panel, the three symbols with error bars indicate the averaged standard deviation of the mean BMLD for the individual subjects for the three conditions. In all other panels the three symbols with error bars indicate the averaged standard deviation of repeated measurements.

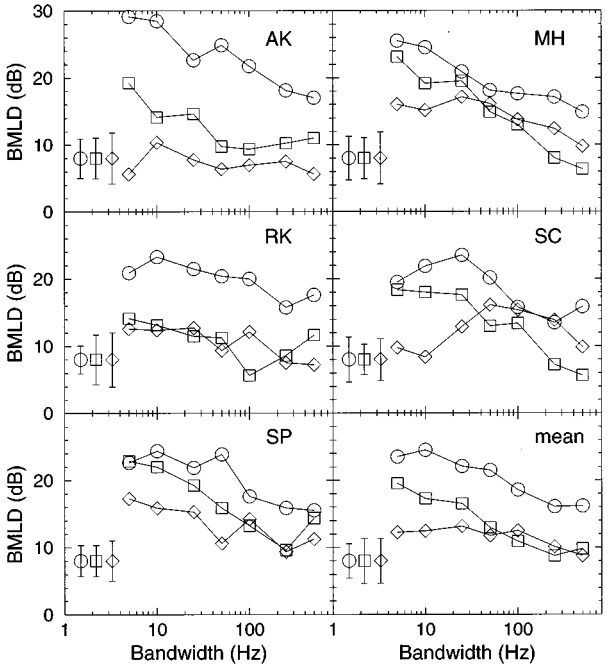

FIG. 6. The N_0S_π BMLDs as a function of masker bandwidth for 250 Hz (○), 250-Hz transposed (□), and 4 kHz (◇). Five panels show data for individual subjects; the panel at the bottom right shows the average of the five subjects.

dard deviation between observers is displayed by the error bars.

In general, we can see that the BMLDs for the 125-Hz and the 125-Hz transposed conditions are larger than BMLDs for the 4-kHz condition. The results also indicate that there is a substantial intersubject variance. However, the BMLDs for the transposed condition show a remarkable similarity with the 125-Hz BMLDs for most subjects. Only for subject AK is there a clear overall difference and for subject NM there is a difference at larger bandwidths. For this subject transposed BMLDs are even larger than the 125-Hz BMLDs. The averaged BMLDs of the five subjects (bottom right panel) again show that transposed BMLDs are very similar to the 125-Hz BMLDs. Furthermore, they are always larger than the 4-kHz BMLDs.

The results for the N_0S_π condition for center frequencies of 250 Hz, 250-Hz transposed, and 4 kHz are shown in Fig. 6. Again, the data from individual subjects are plotted, and the bottom right panel shows the average of all subjects.

Also for the 250-Hz and the 250-Hz transposed BMLDs there is a large variance among subjects. In general, we can see that the BMLDs for the 250-Hz condition are larger than those for the 4-kHz condition. The results are consistent with similar data of Zurek and Durlach (1987).

The BMLDs for the transposed condition show less similarity with the 250-Hz BMLDs than was the case in the comparable situation at 125 Hz. Comparing the 250-Hz transposed BMLDs with the 4-kHz BMLDs at small bandwidths up to 25 Hz, we see that the transposed BMLDs are larger for most subjects. For larger bandwidths the transposed BMLDs are generally not higher than the 4-kHz BMLDs except for subject AK. The averaged BMLDs of the five subjects in Fig. 6 (bottom right panel) show that transposed BMLDs are larger than 4-kHz BMLDs at bandwidths below 50 Hz.

III. EXPERIMENT II

A. Stimuli and method

This second experiment is very similar to the first, except that the binaural condition is $N_\pi S_0$ instead of N_0S_π. Measurements were performed for 125 Hz, 125-Hz transposed, and 4 kHz. Four of the five previous subjects participated in this experiment.

The rationale for this experiment is that at low frequencies, BMLDs for $N_\pi S_0$ are smaller than for N_0S_π (Metz *et al.*, 1968; Kohlrausch, 1986). If the processing of the transposed stimuli is similar to that of the underlying low-frequency stimuli, a similar difference in size of the BMLDs should exist between transposed N_0S_π and $N_\pi S_0$ conditions.

In Fig. 7, a plot, comparable to that in Fig. 1, is shown for the $N_\pi S_0$ condition. For the low-frequency and the transposed conditions (panels A and B), the fine structure of the waveform is essentially out of phase as a result of the antiphasic masker. This leads to a fundamentally different situation for the two reference stimuli (masker alone), N_0 and N_π. For the N_0 stimulus, the waveforms after peripheral transduction are identical, yielding an interaural correlation of 1. For the N_π stimulus, the correlation is smaller even after an internal delay to the stimulus in one of the ears. Thus, in the internal representation, the N_π stimulus never

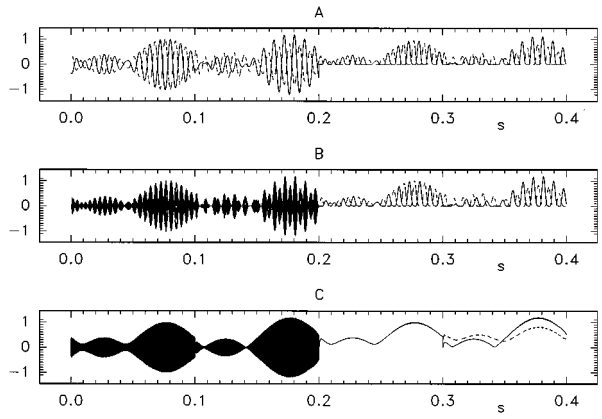

FIG. 7. An example of three different $N_\pi S_0$ stimuli before and after peripheral processing. Panel A shows a 125-Hz stimulus, panel B shows a transposed stimulus, and panel C shows a 4-kHz stimulus. The intervals 0.0–0.1 s show the N_π masker alone, the intervals 0.1–0.2 s show the N_π masker plus the S_0 signal at a signal-to-noise ratio of −10 dB, the intervals 0.2–0.3 s show the masker after peripheral processing, and the intervals 0.3–0.4 s show the combined masker and signal after peripheral processing.

reaches an interaural correlation of 1. This may be one of the reasons for the smaller BMLDs for the $N_\pi S_0$ condition.

B. Results

The BMLDs for the $N_\pi S_0$ condition for center frequencies of 125 Hz, 125-Hz transposed, and 4 kHz are shown in Fig. 8. The first four panels show the data for the individual subjects. The bottom left panel is the average of all subjects for the $N_\pi S_0$ condition and the bottom right panel is the average for the same group of subjects for the $N_0 S_\pi$ condition.

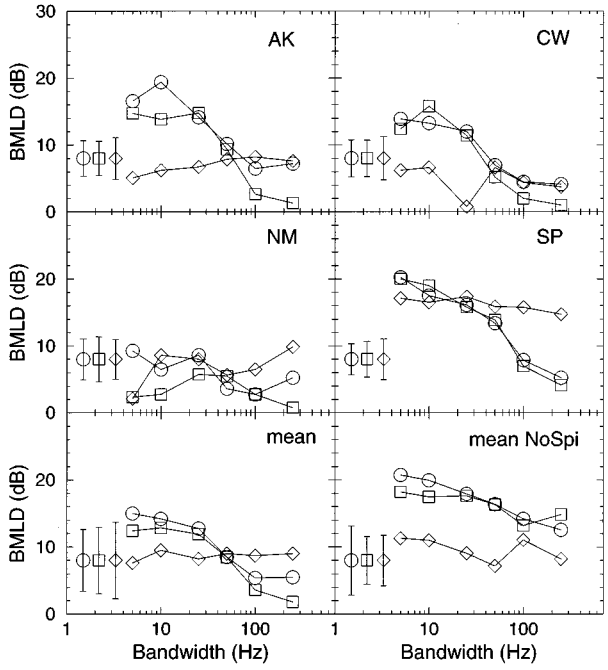

FIG. 8. The $N_\pi S_0$ BMLDs as a function of masker bandwidth for 125 Hz (○), 125-Hz transposed (□), and 4 kHz (◇). The top four panels show data for individual subjects; the bottom left panel shows the average of the four subjects. In addition, the bottom right panel shows BMLDs for the same four subjects for the $N_0 S_\pi$ condition.

The 125-Hz and the 125-Hz transposed $N_\pi S_0$ BMLDs again show a large variance among subjects. However, the two types of BMLDs are very similar for each individual subject. We can see that the BMLDs for the 125-Hz conditions are not always larger than those for the 4-kHz condition. Especially at the larger bandwidths the reverse is found for three of the four subjects. The averaged BMLDs of the four subjects in Fig. 8 also show that transposed BMLDs are larger than 4-kHz BMLDs up to 50-Hz masker bandwidths and that the opposite is true at larger bandwidths.

Comparing the averaged results in Fig. 5 for the 125-Hz and the 125-Hz transposed conditions we see that, in general, the BMLDs are larger for the $N_0 S_\pi$ condition than the corresponding BMLDs for the $N_\pi S_0$ condition. For the 4-kHz condition, on the other hand, $N_0 S_\pi$ and $N_\pi S_0$ BMLDs are rather similar. This is expected because at 4 kHz binaural processing has to rely on information present in the envelopes, which are indentical for the $N_0 S_\pi$ and the $N_\pi S_0$ conditions.

IV. DISCUSSION

The central question of this study is whether the difference between low- and high-frequency BMLDs is caused by the loss of fine structure information in the auditory periphery, prior to the binaural processing, or is due to poorer binaural processing at high frequencies. With the transposed stimuli we are able to provide the binaural processor with dichotic stimuli that contain similar temporal information in a high-frequency channel as is usually available in a low-frequency channel. If binaural processing capabilities are comparable at low and high frequencies, we expect very similar BMLDs for both types of stimuli.

We found nearly identical BMLDs for the 125-Hz low-frequency and the 125-Hz transposed conditions for both $N_0 S_\pi$ and $N_\pi S_0$ (cf. Figs. 5 and 8). The dependence on bandwidth is very similar and the tendency for low-frequency $N_\pi S_0$ BMLDs to be considerably smaller than $N_0 S_\pi$ BMLDs is also observed for the corresponding transposed conditions. A striking result is that low-frequency and transposed $N_\pi S_0$ BMLDs at bandwidths above 50 Hz are smaller than the high-frequency BMLDs at 4 kHz (Fig. 8). Thus, the notion that low-frequency BMLDs are larger than high-frequency BMLDs is not always true and, apparently, the additional fine-structure information in the transposed stimulus can affect binaural processing negatively in the case of $N_\pi S_0$.

Returning to the central question of this study, the similarity between the 125-Hz and the transposed 125-Hz BMLDs suggests that the information that was coded in the envelope of the 4-kHz carrier and the information present in the 125-Hz waveform is indeed processed similarly. This is in line with the assumption of Colburn and Esquissaud (1976).

For the 250-Hz data shown in Fig. 6 there is not such a clear correspondence between the transposed and low-frequency stimuli. On average the transposed BMLDs are

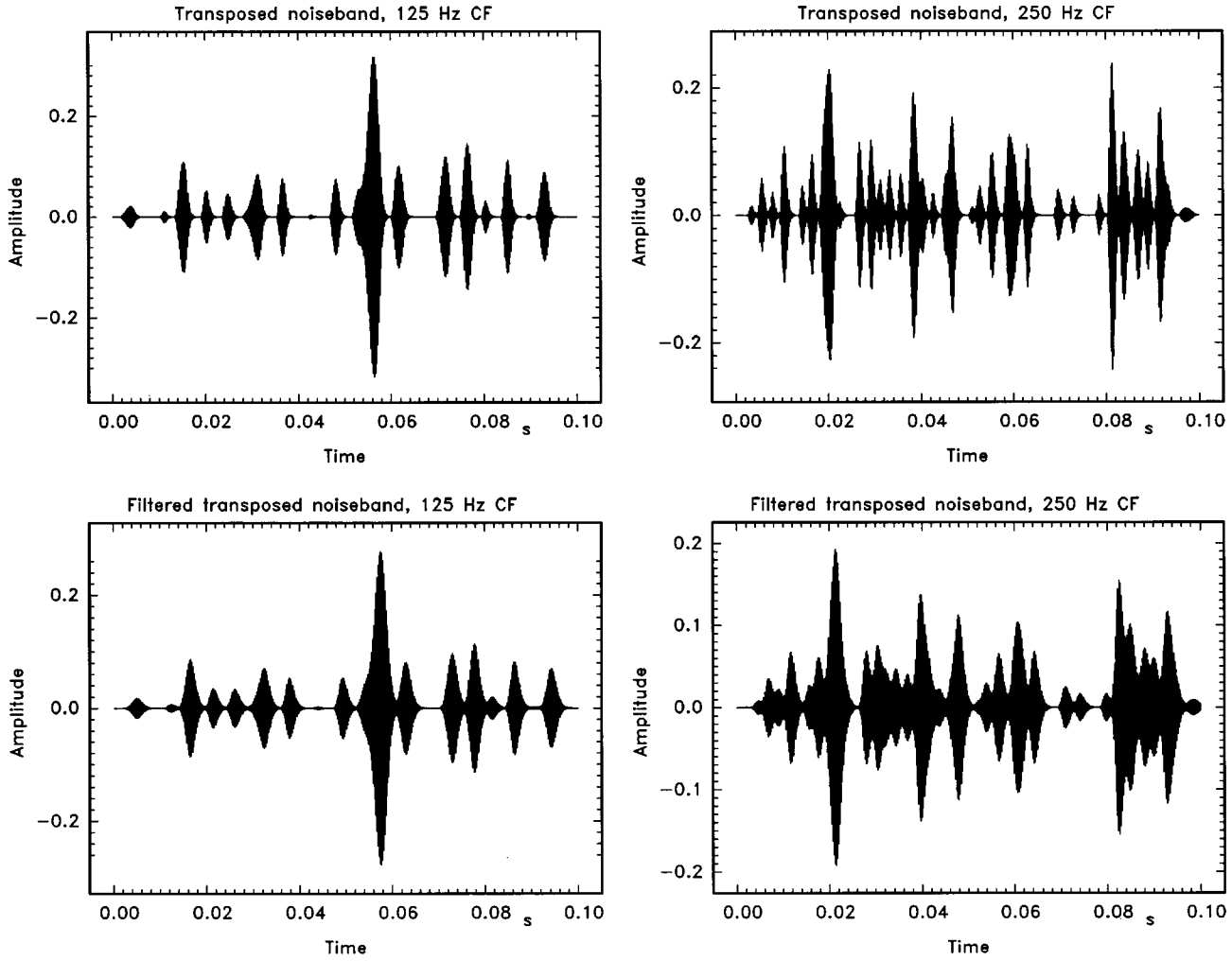

FIG. 9. The waveforms of a 50-Hz-wide band of noise at 125 Hz (left panels) and 250 Hz (right panels) after transposition to 4 kHz. These two conditions are shown before (top panels) and after filtering with a gammatone filter at 4 kHz with an ERB of 456 Hz.

6.5 dB smaller than the low-frequency BMLDs. Nevertheless, we can see that for the 250-Hz case there is a clear increase of transposed BMLDs with respect to 4-kHz BMLDs at the narrowest bandwidths. This shows that the addition of the extra envelope information can still improve binaural processing.

One could argue that for the 250-Hz transposed data, binaural processing at the wider bandwidths is hampered by the rate of interaural time and intensity fluctuations which increases with masker bandwidth. For the corresponding low-frequency condition the auditory filter limits this rate to about 50 Hz which could account for the more efficient processing of these low-frequency stimuli. However, from the study by Bernstein and Trahiotis (1992), it appears that such a rate limitation does only become effective at rates above 160 Hz, which implies that this can not have played an important role in our stimuli. In addition, for the comparable situation at 125 Hz, there is no difference between the low-frequency and the transposed stimuli, even at the large bandwidths.

Another reason could be that the auditory filter at 4 kHz modifies the envelope of the 250-Hz transposed stimulus. The central three bands of the stimulus span a total bandwidth that is comparable to the auditory filter bandwidth at 4 kHz. For a 125-Hz transposed condition this bandwidth is approximately half that of the 250-Hz transposed stimulus. The effect of filtering a 125-Hz and a 250-Hz transposed stimulus with a gammatone filter centered at 4 kHz and an ERB of 456 Hz is shown in Fig. 9. It is clear that as a result of this filter, the minima in the envelope of the waveform are less wide and have a less steep flank. For the 125-Hz transposed stimulus this effect is less prominent. These effects may explain the lack of correspondence between transposed and low-frequency BMLDs at 250 Hz.

As mentioned before, for 125-Hz conditions and for 125-Hz transposed conditions, $N_\pi S_0$ BMLDs are smaller than $N_0 S_\pi$ BMLDs. An explanation for this difference is related to the fact that for the $N_\pi S_0$ condition the waveforms at both ears are essentially out of phase. The time lag associated with this phase difference is 4 ms for a low-frequency stimulus centered at 125 Hz. This is large with respect to the time lags that occur in daily life as a result of the spatial separation of the ears. In models of binaural processing it has therefore been assumed that the auditory system cannot process these large time differences very efficiently (Langford and Jeffress, 1964; Colburn, 1977).

TABLE I. The decorrelation factor γ which is used in the EC theory is calculated for several bandwidths. This factor appears in the formula for the $N_\pi S_0$ BMLD. The average BMLDs for all subjects are used to derive γ. The second and third columns show γ values for the 125-Hz and the 125-Hz transposed condition, respectively.

Bandwidth (Hz)	Low freq. γ	Transposed γ
5	0.95	0.91
10	0.94	0.93
25	0.92	0.90
50	0.76	0.76
100	0.48	0.18
250	0.52	−0.30

Another explanation for the difference between low-frequency N_0S_π and $N_\pi S_0$ BMLDs can be given on the basis of the equalization and cancellation (EC) model by Durlach (1972). In the EC model it is assumed that in the equalization stage an internal delay is selected such that optimal noise reduction is obtained after the cancellation stage, with the limitation that the internal delay may not be longer than the length of half a signal cycle.

For an $N_\pi S_0$ stimulus, the equalization step will delay the waveforms in one of the two ears by half a period of the central component of the masker spectrum. When the bandwidth of the N_π masker is very small, the improvement of the signal-to-noise ratio after the cancellation step will be very large. However, when the bandwidth increases, the autocorrelation function of the N_π masker will be more damped and the cancellation step will not result in such a large improvement of the signal-to-noise ratio. Therefore, the difference between the $N_\pi S_0$ and N_0S_π BMLDs is predicted to increase with increasing masker bandwidth.

Using the EC theory, we can directly calculate the amount of decorrelation through the internal delay applied in the equalization step. According to this theory, the difference Δ in BMLD between N_0S_π and $N_\pi S_0$ is given by

$$\Delta = 10 \log\left(\frac{k-\gamma}{k-1}\right). \tag{1}$$

Here, k is a factor that represents internal errors of the signal representation and γ represents the masker decorrelation through internal delay. If we adjust k such that the N_0S_π BMLDs are predicted correctly, we can use the above formula to derive the value for γ from the $N_\pi S_0$ BMLDs. The result of such a calculation is shown in Table I for the 125-Hz and the 125-Hz transposed conditions.

While for bandwidths up to 25 Hz the γ values are above 0.9 for both conditions, they decrease for the larger bandwidths. This provides support for the idea that an increase in bandwidth leads to a decrease in the correlation of the *internally delayed* N_π masker. In this respect it is interesting to note that the γ values for the 125-Hz condition remain constant for the largest masker bandwidths, which probably reflects the bandwidth of the 125-Hz auditory filter. On the other hand, the γ values for the 125-Hz transposed condition decrease further even for larger bandwidths. Since the transposed stimuli are centered at 4 kHz, the auditory filter bandwidth is no limiting factor for bandwidths up to 250 Hz.

This argument about differences between N_0S_π and $N_\pi S_0$ is not applicable to standard high-frequency conditions. Here, only the envelope is available for binaural processing, which has an interaural envelope correlation of 1 for the N_π reference interval. Therefore, in contrast to the 125-Hz $N_\pi S_0$ condition, binaural processing of an N_π masker at 4 kHz does not have to rely on an internal delay. This may explain the larger BMLDs for the 4-kHz $N_\pi S_0$ condition as compared to the 125-Hz and 125-Hz transposed conditions at larger bandwidths.

V. SUMMARY

Our results show that for high carrier frequencies, introducing fine-structure information, normally available at low frequencies, in the envelope can improve as well as hamper binaural processing with respect to a situation where such fine structure is not available. Both for N_0S_π and $N_\pi S_0$, the results for the 125-Hz and 125-Hz transposed conditions are very similar, suggesting very similar binaural processing at high and low frequencies. These data suggest that most of the differences between low-frequency and high-frequency binaural detection can be explained by the frequency-dependent loss of fine-structure information prior to the binaural processor.

ACKNOWLEDGMENTS

We want to thank all our subjects for participating in our experiments, which meant spending some of their valuable time in the listening booth. We thank Tino Trahiotis for discussions that influenced the interpretations presented here. Furthermore, we thank Andrew Oxenham, Adrian Houtsma, Reinier Kortekaas, and Professor T. Huckin and the reviewers for their valuable comments on earlier drafts of this paper.

APPENDIX: Transposed stimulus properties

In this Appendix, the spectrum of the transposed stimulus is studied in detail and an analysis is made of the binaural spectrum detection performance that is expected if subjects are assumed to listen to one of the off-frequency bands of the transposed stimulus spectrum.

For the generation of a transposed masker stimulus, first a narrow-band noise is generated and half-wave rectified. In Fig. A1 the spectrum of this half-wave rectified narrow-band noise is shown. The structure of this spectrum can be understood when we first consider the spectrum of strongly clipped noise (cf. Lawson and Uhlenbeck, 1950). A strongly clipped noise, $c_g(t)$, is obtained from a narrow-band Gaussian noise, $g(t)$, by defining that $c_g(t)=1$ for $g(t)\geqslant 0$, and $c_g(t)=-1$ for $g(t)<0$. Using this definition for $c_g(t)$, the half-wave-rectified waveform, $h_g(t)$, can be written as

$$h_g(t) = \tfrac{1}{2}(1+c_g(t))g(t). \tag{A1}$$

When this equation is transformed to the frequency domain, we obtain

$$H_g(\omega) = \tfrac{1}{2}G(\omega) + \frac{1}{4\pi}C_g(\omega)\otimes G(\omega). \tag{A2}$$

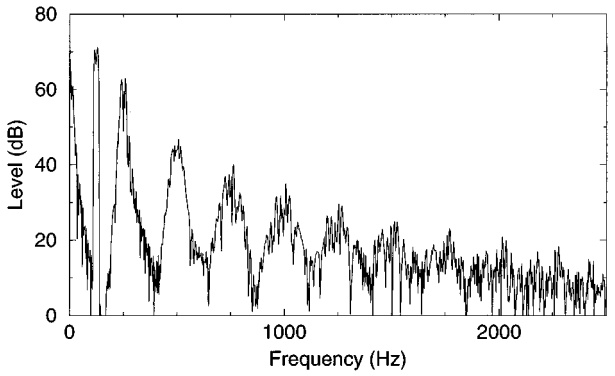

FIG. A1. The spectrum of a 25-Hz-wide 125-Hz half-wave rectified band of noise. Most of the stimulus energy is near 0 Hz. The spectrum of the noise band can be found at it original place. Additional peaks in the spectrum are at the even harmonics of the noise band.

The first term in this equation shows that the original noise spectrum, $G(\omega)$, comes back in the spectrum of the half-wave-rectified noise. In order to understand the second term in Eq. (A2) we have to analyze the spectrum of the strongly clipped noise, $C_g(\omega)$. This spectrum comprises a somewhat smeared version of $G(\omega)$ plus additional spectral bands centered at the odd harmonics of the center frequency of $G(\omega)$. The spectral level of these spectral bands decreases with increasing frequency (cf. Lawson and Uhlenbeck, 1950). Since $G(\omega)$ overlaps with one band from $C_g(\omega)$, the spectrum of $h_g(t)$ contains a smoothed triangular peak around $\omega=0$ with a bandwidth proportional to the bandwidth of g. And since C_g has peaks at every *odd* harmonic, we will, after convolution, find peaks in the spectrum of h_g at the *even* harmonic frequencies.

In the following step in the transposed stimulus generation, the high-frequency portions of the spectrum are attenuated by a 500-Hz low-pass filter. After multiplication with the 4-kHz carrier, the resulting spectrum is symmetrical around 4 kHz and its energy density decreases with increasing spectral distance from the carrier frequency. The spectrum of this transposed stimulus is shown in Fig. 3.

When the spectra of a transposed masker and a transposed masker plus signal are compared, differences can be found in all frequency bands in the spectrum. In order to find out whether the binaural system might benefit from listening to one of the sidebands of the transposed spectrum, some further analysis was done. It was assumed that at high frequencies, binaural detection can be described by the subject's sensitivity to a decrease in the envelope correlation due to the addition of the signal (Bernstein and Trahiotis, 1996). For this purpose the interaural envelope correlation for each sideband was calculated separately and compared to the envelope correlation of the central three and the central five spectral components. We found that the envelope correlation in none of the sidebands changed more than in the central spectral part and therefore we do not expect that detection can benefit from separately listening to these sidebands.

[1]In order to show how the loss of fine structure may impair binaural detection we assume that at low frequencies, effectively, the full waveform is processed in a correlator, while at high frequencies the envelope of the waveform is processed. Under these assumptions we obtain a 3 dB *smaller* BMLD at high frequencies. Note that when the covariance is used instead of the correlation, the BMLD at high frequencies should be 3.6 dB *larger* compared to low frequencies (cf. van de Par and Kohlrausch, 1995).

[2]Due to the nonlinear interaction between the signal and the masker in a transposed stimulus, it is not possible to separate the signal energy from the masker energy. In order to get an estimate of the signal-to-masker ratio for a transposed stimulus we calculated the quantity $(E_{m+s}-E_m)/E_m$, where E_m and E_{m+s} are the energies of the transposed masker and of the transposed masker plus signal, respectively. We found that the average value of this quantity is very close to the signal-to-masker ratio of the underlying low-frequency stimulus.

[3]Due to the bandpass filtering that was applied for this set of experiments the time that was needed to calculate one trial for our experiments increased by several seconds. Therefore, no bandpass filtering was applied in the rest of the experiments.

[4]Initially, ramps of 20 ms were used. These were found not to be sufficiently long to avoid audible spectral splatter. Some subjects reported hearing the on- and offsets of the signal for the narrow-band N_0S_0 conditions. Using the 50-ms ramps instead increased the thresholds for these subjects to a level comparable to that of other subjects.

Bernstein, L. R., and Trahiotis, C. (**1992**). ''Detection of antiphasic sinusoids added to the envelopes of high-frequency bands of noise,'' Hear. Res. **62**, 157–165.

Bernstein, L. R., and Trahiotis, C. (**1996**). ''On the use of the normalized correlation as an index of interaural envelope correlation ,'' J. Acoust. Soc. Am. **100,** 1754–1763.

de Boer, E. (**1962**). ''Note on the critical bandwidth,'' J. Acoust. Soc. Am. **34,** 985–986.

Bos, C. E., and de Boer, E. (**1966**). ''Masking and discrimination,'' J. Acoust. Soc. Am. **39,** 708–715.

Colburn, H. S. (**1977**). ''Theory of binaural interaction based on auditory-nerve data. II. Detection of tones in noise,'' J. Acoust. Soc. Am. **61,** 525–533.

Colburn, H. S., and Esquissaud, P. (**1976**). ''An auditory-nerve model for interaural time discrimination of high-frequency complex stimuli,'' J. Acoust. Soc. Am. **59,** S23.

Durlach, N. I. (**1964**). ''Note on binaural masking level differences at high frequencies,'' J. Acoust. Soc. Am. **36,** 576–581.

Durlach, N. I. (**1972**). ''Binaural signal and detection: Equalization and cancellation theory,'' in *Foundations of Modern Auditory Theory, Vol. II*, edited by J. V. Tobias (Academic, New York).

Grantham, D. W. (**1984**). ''Discrimination of dynamic interaural intensity differences,'' J. Acoust. Soc. Am. **76,** 71–76.

Grantham, D. W., and Wightman, F. L. (**1978**). ''Detectability of varying interaural temporal differences,'' J. Acoust. Soc. Am. **63,** 511–523.

Green, D. M., and Swets, J. A. (**1974**). *Signal Detection Theory and Psychophysics* (Wiley, New York); reprinted by Krieger, New York.

Henning, G. B. (**1974**). ''Detectability of interaural delay in high-frequency complex waveforms,'' J. Acoust. Soc. Am. **55,** 84–90.

Kidd, G., Mason, C. R., Brantley, M. A., and Owen, G. A. (**1989**). ''Roving-level tone-in-noise detection,'' J. Acoust. Soc. Am. **86,** 1310–1317.

Kohlrausch, A. (**1986**). ''The influence of signal duration, signal frequency and masker duration on binaural masking level differences,'' Hear. Res. **23**, 267–273.

Langford, T. L., and Jeffress, L. A. (**1964**). ''Effect of noise crosscorrelation on binaural signal detection,'' J. Acoust. Soc. Am. **36,** 1455–1458.

Lawson, J. L., and Uhlenbeck, G. E. (**1950**). *Threshold Signals* (McGraw-Hill, London).

Levitt, H. (**1971**). ''Transformed up-down methods in psychoacoustics,'' J. Acoust. Soc. Am. **49,** 467–477.

McFadden, D., and Pasanen, E. G. (**1976**). ''Lateralization at high frequencies based on interaural time differences,'' J. Acoust. Soc. Am. **59,** 634–639.

Metz, P. J., von Bismarck, G., and Durlach, N. I. (**1968**). ''Further results on binaural unmasking and the EC model. II. Noise bandwidth and interaural phase,'' J. Acoust. Soc. Am. **43,** 1085–1091.

Palmer, A. R., and Russell, I. J. (**1986**). ''Phase-locking in the cochlear nerve of the guinea pig and its relation to the receptor potential of the inner hair cells,'' Hear. Res. **24**, 1–15.

van de Par, S., and Kohlrausch, A. (**1995**). ''Analytical expressions for the envelope correlation of certain narrowband stimuli,'' J. Acoust. Soc. Am. **98,** 3157–3169.

Perrott, D. R., and Musicant, A. D. (**1977**). ''Minimum auditory movement angle: Binaural localization of moving sound sources,'' J. Acoust. Soc. Am. **62,** 1463–1466.

Weber, D. L. (**1978**). ''Suppression and critical bands in band-limiting experiments,'' J. Acoust. Soc. Am. **64,** 141–150.

Zurek, P. M., and Durlach, N. I. (**1987**). ''Masker-bandwidth dependence in homophasic and antiphasic tone detection,'' J. Acoust. Soc. Am. **81,** 459–464.

Interaction of noise-induced permanent threshold shift and age-related threshold shift

John H. Mills, Flint A. Boettcher, and Judy R. Dubno
Department of Otolaryngology and Communicative Sciences, Medical University of South Carolina, Charleston, South Carolina 29425-2242

(Received 3 March 1996; revised 13 September 1996; accepted 9 October 1996)

Current medical-legal practices as well as an international standard (ISO 1999) assume the permanent threshold shifts produced by exposure to noise add (in dB) to the threshold shifts caused by increased chronological age (presbyacusis). This assumption, known as the additivity rule, was tested in an animal model. Mongolian gerbils, born and raised in a quiet vivarium, were exposed at age 18 months to a 3.5-kHz pure tone for 1 h at 113 dB SPL. At 6-weeks post-exposure, permanent threshold shifts in the exposed ear were approximately 20 dB in the 4- to 8-kHz region. Thresholds in the nonexposed, control ear were unaffected by the exposure. Animals were then allowed to age in the quiet vivarium until age 36 months and then were retested. Thus in a given animal, aging-only effects were assessed in one ear (internal control) and noise-plus-aging effects were assessed in the other (test) ear. A second control was mean age-related threshold shift measured in 48 gerbils who were born and raised in the quiet vivarium. This group is referred to as a non-noise-exposed population (population control). Using the additivity rule, predictions with either the internal or population control significantly overestimated noise-plus-aging effects. Use of the ISO 1999 compression factor reduced the overestimations by 0–5 dB. The intensity rule produced the most accurate predictions. These results suggest that the interaction of noise-induced permanent threshold shift and age-related threshold shift is not straightforward and that current medical-legal methods using the additivity rule overestimate the contribution of ''noise effects.'' © *1997 Acoustical Society of America.* [S0001-4966(97)04903-5]

PACS numbers: 43.66.Sr [JWH]

INTRODUCTION

A medical–legal topic of longstanding interest is the interaction between hearing loss produced by exposure to noise and hearing loss produced by the effects of aging. Oftentimes, the focus of the interest is the allocation of hearing loss (Dobie, 1993) into two categories. One category is the hearing loss produced by exposure to industrial noise or to a series of industrial noises experienced over a working lifetime of a given individual or group. The second category is the hearing loss produced by the combined effects of aging (presbyacusis), nonindustrial noise exposures (socioacusis), and disease processes which cause hearing loss (nosoacusis). Although there is a large amount of literature on the interaction of noise and other nonacoustic variables (for reviews see Humes, 1984; Boettcher *et al.*, 1987), most of the available data on noise-aging interactions come from retrospective analyses of human epidemiologic data (Burns and Robinson, 1970; Macrae, 1971, 1991; Bies and Hansen, 1990).

According to current medical–legal procedures used in most of the United States (see Dobie, 1993), noise-induced threshold shifts are additive (in dB) with threshold shifts produced by the aging process. In an international standard, ISO 1999, the combined effect of noise and aging is defined by the formula

$$\mathrm{HL} = \mathrm{ARPTS} + \mathrm{NIPTS} - (\mathrm{ARPTS})(\mathrm{NIPTS})/120, \qquad (1)$$

where HL is the hearing level, ARPTS is the age-related permanent threshold shift, NIPTS is the noise-induced permanent threshold shift, and the third term is a compression factor which is to be applied when the threshold shifts exceed 40 dB. Data to support the validity of current medical–legal practices are not consistent, including the application of Eq. (1) from ISO 1999 to individuals or groups (Bies and Hansen, 1990; Macrae, 1991; see also Dobie, 1993; Mills *et al.*, 1996).

An alternative to the human epidemiologic approach to assess noise-aging interactions is the use of an animal model where the noise exposures are quantitatively evaluated and under experimenter control, where socioacusic and nosoacusic effects are eliminated or minimized, and where presbyacusic effects are quantitatively assessed (Mills, 1992; Mills *et al.*, 1990a; Shone *et al.*, 1991). Here, we test the accuracy of current medical-legal and ISO 1999 procedures in two ways. First, we examine the combined effects of noise and aging in ''old'' gerbils who were exposed at a young age in only one ear. Thus, in a given animal we assess aging effects in one ear (control) and noise-plus-aging effects in the other ear (test). A second control is the mean age-related threshold shift of 48 gerbils who were born and reared in a quiet environment and not exposed to noise. Thus in the first case, each animal serves as its own (internal) control whereas in the second case, the control is a ''large'' non-noise-exposed aged population.

I. METHODS

A. Experimental subjects

Subjects were 14 Mongolian gerbils born and reared in a quiet vivarium. Each animal was 18 months old at the onset

of the experiment and had no history of hearing loss or impacted ears. Seven animals completed the entire experiment. Six animals developed impacted ears or health problems and were eliminated during the course of the 26- to 30-month experiment. One animal developed a severe sensorineural hearing loss in the control ear and is used as an extreme example of individual variations in control or nonexposed ears.

B. Control subjects

A second control was the mean age-related threshold shift measured at 36 months in 48 animals who were born and reared in a vivarium where the ambient A-weighted sound levels rarely exceeded 40 dB. This group of control subjects is referred to as a non-noise exposed population or population control. Mean age-related hearing levels of gerbils at age 36 months correspond to those of human males age 60–65 yr and human females age 65–70 yr (see Mills *et al.*, 1990a). Variance in the population control is dramatic (see Mills *et al.*, 1990a). Some animals do not respond at 80 dB SPL, whereas other animals have nearly normal auditory sensitivity from 1 to 16 kHz. Variability of this magnitude is truly remarkable given that the variables most pertinent to the production of hearing loss are under experimenter control, i.e., age, diet, medications, environment, and absence of exposure to noise.

C. Auditory brain-stem responses (ABR)

ABR testing was performed under anesthesia using a combination of ketamine (35 mg/kg) and xylazine (8 mg/kg). Each subject was tested pre-exposure, six weeks after a monaural exposure to a 3.5-kHz pure tone (113 dB SPL, 1 h), and 18 months following exposure. Stimuli were Gaussian tone pips (1.8 ms, 0.7 ms rise–fall, 1–16 kHz in octave intervals, 200 signal presentations). Activity was recorded with customized needle electrodes at the vertex and behind each pinna. Additional details are given elsewhere (Mills *et al.*, 1990a).

D. Exposure to intense sound

The monaural exposure to a pure tone of 3.5 kHz (113 dB SPL, 1 h) was selected because pilot data indicated that it would produce permanent threshold shifts of approximately 20 dB in the 4- to 8-kHz region in the test ear and that it would have little, if any, measurable effect on the contralateral (control) ear. During the exposure, animals were anesthetized as during the ABR testing. A supplemental dose of ketamine was administered if needed.

II. RESULTS

Mean ABR thresholds of the control and exposed ears are shown in Fig. 1 [panels (A), (B), and (C)]. Vertical bars indicate standard errors. The mean pre-exposure thresholds at age 18 months [panel (A)] are not significantly different in the control (aging-only ear) and test ear (aging plus noise). ABR thresholds six weeks after the monaural exposure to the intense pure tone are shown in panel B. Thresholds of the

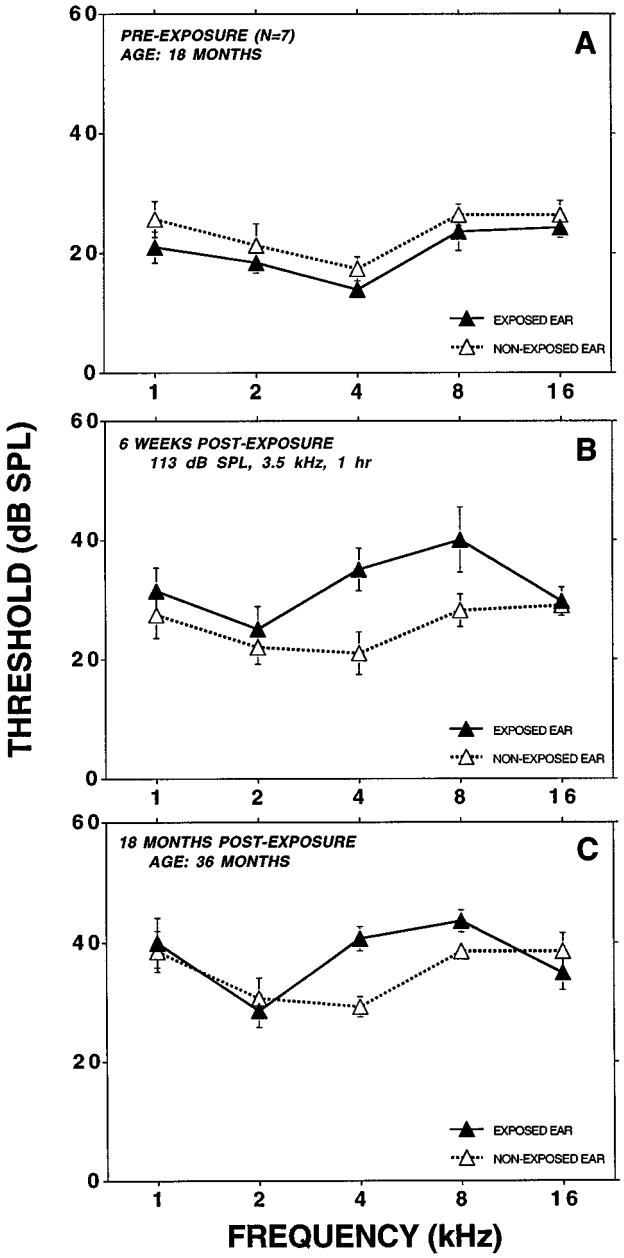

FIG. 1. Auditory thresholds of Mongolian gerbils estimated from auditory brainstem responses. Panel (A) shows mean pre-exposure thresholds in the control ear and in the test ear when the animals were 18 months old. Panel (B) shows mean thresholds measured 6 weeks after termination of the exposure to an intense pure tone (3.5 kHz, 113 dB SPL, 1 h). Panel (C) shows mean thresholds measured when the animals reached the age of 36 months or about 18 months after the pre-exposure audiograms of panel (A).

nonexposed or control ear are virtually identical with those shown in panel (A), indicating the monaural exposure had no measurable effect on the control (contralateral) ear. Thresholds in the exposed ear have increased 15–20 dB at 4 and 8 kHz. These threshold shifts are assumed to be permanent inasmuch as very little, if any, recovery occurs after the first 6 weeks following an intense exposure (Miller *et al.*, 1963). Panel (C) compares mean thresholds for the exposed and control ears when the animals have reached the age of 36 months. Thresholds of the control and exposed ears are not significantly different except at 4 and 8 kHz.

The permanent threshold shift (PTS) produced by the

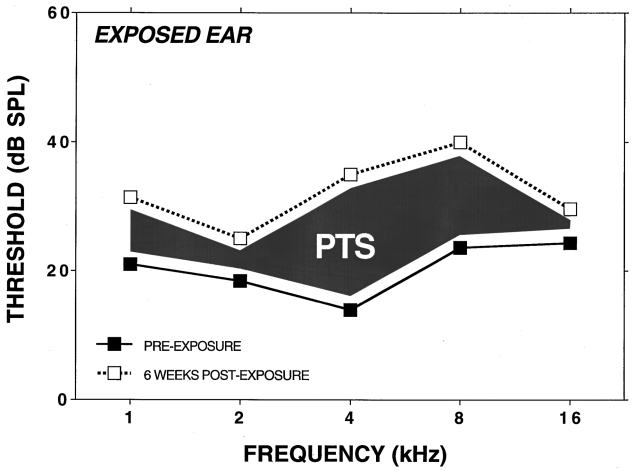

FIG. 2. Permanent threshold shift (PTS) in the exposed ear 6 weeks after exposure to the intense pure tone [data replotted from Fig. 1 panels (A) and (B)].

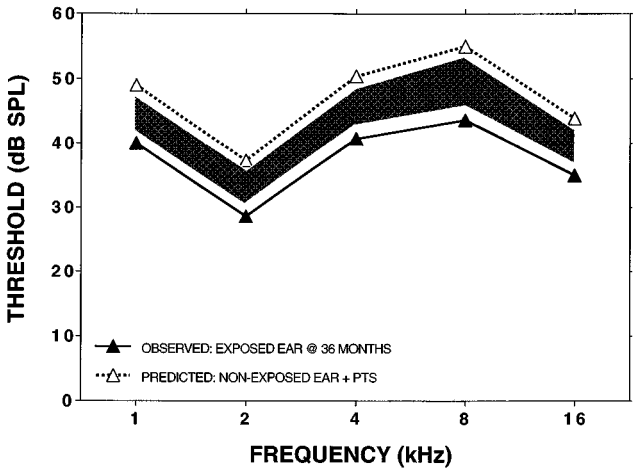

FIG. 4. Predicted and observed values of the combined effect of aging and noise. Observed values are from Fig. 1(C). Predicted values are the mean threshold shifts of Fig. 2 added (in dB) to the age-related threshold of Fig. 3.

monaural exposure is shown in Fig. 2. PTS is defined as the difference in the exposed ear between the preexposure thresholds [panel (A) of Fig. 1] and thresholds assessed 6 weeks after the exposure [panel (B) of Fig. 1]. PTS shown here is used in the predictions given in Figs. 4 and 6.

Age-related threshold shift is shown in Fig. 3 and is calculated as the difference between thresholds measured in the control ear at age 36 months [panel (C) of Fig. 1] and at 18 months [panel (A) of Fig. 1]. The age-related threshold shift shown here is used in the predictions shown in Fig. 4.

Figure 4 compares the observed and predicted effects of noise plus aging. The observed value is that measured in the exposed ear of the animals at age 36 months [Fig. 1(C)]. The predicted value is the PTS of Fig. 2 added (in dB) to the age-related threshold of Fig. 3. Note that the observed value is approximately 10–15 dB less than the predicted value. In this comparison of predicted and observed effects, it is important to stress that the control or nonexposed ear is an internal control, i.e., the exposed ear and the control ear are from the same animal.

As a second control, hearing levels of a group of animals are compared in Fig. 5 to hearing levels of exposed and unexposed ears [from Fig. 1, panel (C)]. Note on this figure that the hearing loss associated with aging in a large control group exceeds the combined effect of aging and noise exposure observed with a small experimental group of animals. This observation reflects the large variance seemingly inherent to age-related hearing loss in the Mongolian gerbil. Variance in the population control is substantially larger than the variance in the noise-aging ears. Standard deviations were 12.2 and 14.7 dB at 4 and 8 kHz, respectively, for the population group of 48 gerbils. In contrast, the standard deviations were 9.5 and 5.5 dB at 4 and 8 kHz, respectively, in the exposed ear of the experimental group. At 1 and 2 kHz standard deviations were similar in the two groups.

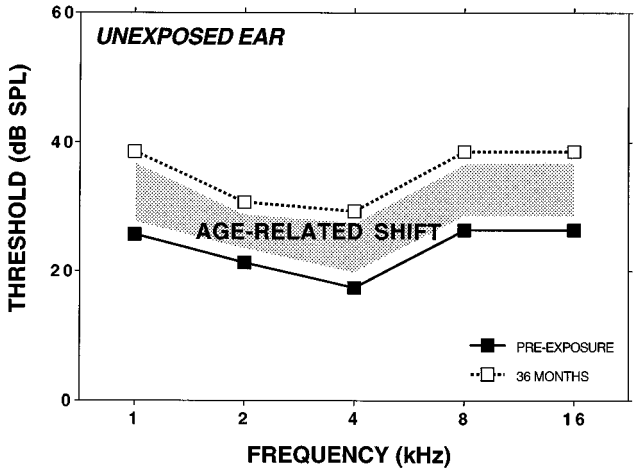

FIG. 3. Age-related threshold shift in the nonexposed ear at age 36 months [data from Fig. 1 panels (A) and (C)].

In Fig. 6 data of the non-noise-exposed population are used in combination with the PTS data (Fig. 2) to obtain a predicted value of the combined effects of noise and aging. The use of a non-noise-exposed population in estimating or separating noise-induced threshold shift from age-related threshold shift is the medical–legal procedure routinely used with humans. Note in Fig. 6 that the predicted value, i.e., PTS added to population control, exceeds the measured value by 10–25 dB depending upon frequency. Indeed, the disparity between predicted and observed values is substantially larger using a population control group than internal controls.

The disparities observed between predicted and observed values shown in Figs. 4 and 6 do not reflect the ''compression factor'' of Eq. (1) from ISO 1999. Use of this ''compression factor'' is recommended by ISO 1999 when the combined effect of noise plus aging exceed approximately 40 dB. When the ISO compression factor is applied to the predicted noise-plus-aging threshold shifts of Figs. 4 and 6, the disparities between observed and predicted values as great as 10–25 dB are reduced by approximately 5 dB.

Data for an exceptional animal are shown in Fig. 7. This subject was excluded from the mean data because of the unusually large threshold shift incurred in the control or non-noise-exposed ear. Note that the exposed and control ears are

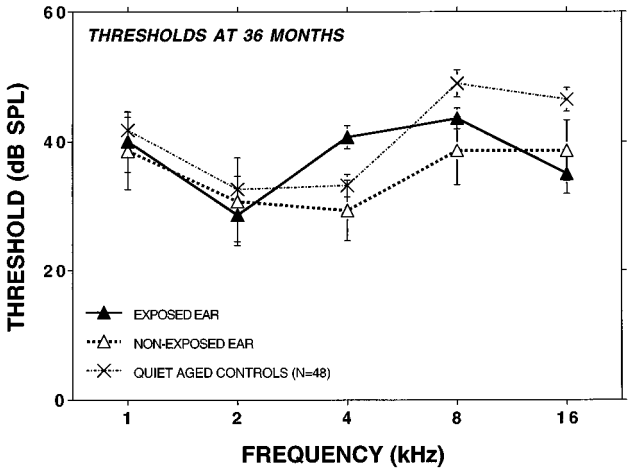

FIG. 5. Hearing levels of a large sample ($N=48$, age 36 months) of quiet-aged gerbils. This sample is referred to as a population control group of non-noise-exposed animals and is compared on this figure to the hearing levels of the exposed and unexposed ears from Fig. 1.

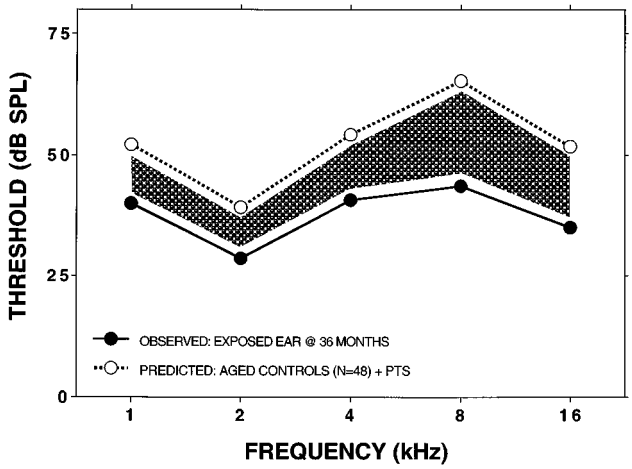

FIG. 6. Predicted and observed values of the combined effect of aging and noise using a non-noise-exposed population. To obtain the predicted value, thresholds of quiet-aged control animals from Fig. 5 are added (in dB) to the PTS of Fig. 2.

very similar pre-exposure and 6-weeks post-exposure; however, at age 36 months the control ear is clearly poorer than the noise-exposed ear. It is quite likely that the control ear did not respond to the test signals, but that the responses observed arose from the noise-exposed ear because the test signals crossed over either by bone or air conduction. Application of the additivity rule or the procedures of ISO 1999 to the data for this individual produces estimates of the combined effects of noise and aging that have little correspondence to observed values. In other words, use of data of individuals rather than groups produces very large errors.

There are alternatives to the ''additivity in dB'' and ISO 1999 methods for estimating the combined effects of age-related threshold shift and noise-induced threshold shift. One alternative is the intensity rule (Ward *et al.*, 1959; Mills *et al.*, 1981; Mills, 1992), which has been used successfully for combining noise-induced threshold shifts from different noise exposures. For example, an exposure produces a threshold shift of 20 dB at 4 kHz. Another independent exposure produces a 20 dB threshold shift at 4 kHz. When these two formerly independent exposures are combined, the intensity rule predicts a threshold shift at 4 kHz of 23 dB rather than 26 dB by an equal pressure rule or 40 dB by additivity in dB. Variations on the intensity rule are the modified power rule (Humes and Jesteadt, 1991) and the model of Bies and Hansen (1990).

Predictions of the intensity rule have been applied to the data of Figs. 2 and 3 and are shown in Fig. 8. Note that by using the intensity rule (or modified power law with an exponent of 1.0), the correspondence between predicted and observed effects is substantially improved compared to those shown in Figs. 4 and 6 using additivity in dB. Indeed, predictions using the intensity rule are within ± 1 standard deviation of observed values.

III. DISCUSSION

According to current medical-legal methods and an international standard (ISO 1999) for estimating noise-induced hearing loss in humans, threshold shifts produced by exposure to noise add (in dB) to threshold shifts produced by aging. Current results with experimental animals (Mongolian gerbils) do not support the application of these methods either to group data or to data of individuals. Using these methods, the combined effects of noise plus aging were overestimated. Use of the compression factor from the ISO 1999 standard reduced the overestimations by 0–5 dB. Use of the intensity rule produced the best correspondence between predicted and observed values.

Overestimations of noise-plus-aging effects may reflect at least two factors. One factor is the variance of hearing levels in aging gerbils. With experimenter control of acoustics, diet, temperature, humidity, and nosoacusis, hearing levels in 36-month gerbils range from normal (relative to 6- to 8-month animals) to no reliable responses at the maximum output available, 85 dB SPL. Clearly, variance of this magnitude in the control group complicates the assessment of noise-induced hearing loss and the allocation of a hearing loss in a 36-month animal into an aging component and a noise component. With humans, the situation may be even

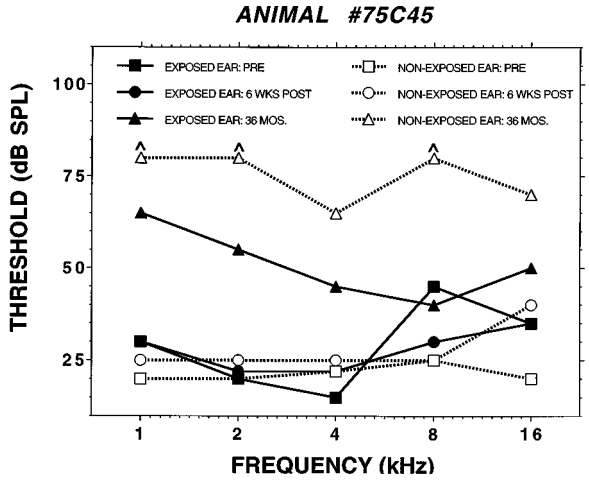

FIG. 7. Data for one animal showing pre-exposure, 6-week post-exposure, and 36-month measurements for the control and exposed ears.

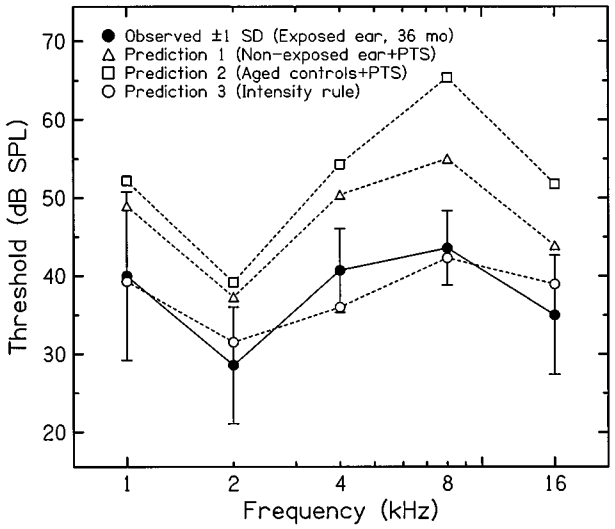

FIG. 8. Predictions of the intensity rule are compared with predictions from the internal control (Fig. 4), the population control (Fig. 6), and observed values.

more complicated since acoustics and a seemingly endless list of other variables are qualitatively and quantitatively unknown and unidentified.

A second factor contributing to the overestimation of noise-plus-aging effects may be the type of noise exposure, i.e., short-duration, high-level versus long-duration, low-moderate level. Previous results using gerbils supported the ''additivity in dB'' hypothesis when the exposure was 720 days at an A-weighted sound level of 85 dB (Mills *et al.*, 1990b). Furthermore, the intensity rule and its variants were not supported by these long-duration results. Other data (Mills, 1992) have suggested an order/sequence effect. That is, an intense pure-tone exposure followed by a wideband noise at a moderate level produced significantly more PTS than a wideband noise followed by an intense pure tone. Other order/sequence effects include the interactions between aminoglycosides and noise, as well as interactions between impulse noise and continuous noise (see Boettcher *et al.*, 1987 for a review). It is quite likely that the interaction between noise and aging effects is confounded by these factors as well as by variance in the non-noise-exposed population. In other words, the allocation of a hearing loss in an older individual into a noise component and an aging component is not straightforward.

IV. SUMMARY AND CONCLUSIONS

Mongolian gerbils, born and raised in a quiet vivarium, were exposed monaurally at age 18 months to a 3.5-kHz pure tone (1 h, 113 dB SPL). Six weeks after the exposure permanent threshold shifts in the exposed ear were approximately 20 dB in the 4- to 8-kHz region. Thresholds in the nonexposed, control ear, were unaffected by the pure-tone exposure. Animals were then allowed to age in the quiet vivarium until age 36 months when thresholds were assessed again. Thus in a given animal aging effects were assessed in one ear (internal control) and noise-plus-aging effects in the other ear. A second control was the mean age-related threshold shift measured at 36 months in 48 gerbils who were born and reared in the quiet vivarium. This group is referred to as a non-noise exposed population (population control). Predictions of the combined effects of noise and aging were made by using current medical–legal procedures and the recommendations of an international standard (ISO 1999) wherein it is assumed that changes in auditory thresholds due to aging add (in dB) to changes in auditory thresholds due to the effects of noise. Predictions using both internal and population controls significantly overestimated the hearing loss measured in the exposed/aging ear. Use of the ISO 1999 compression factor reduced the overestimations by only 0–5 dB. The most accurate predictions were achieved by using the intensity rule and its variants. These data suggest that the interaction of noise effects and aging effects is not straightforward and that current medical–legal procedures using the additivity rule may overestimate the contribution of noise effects to the hearing loss measured in older subjects.

ACKNOWLEDGMENTS

Supported in part by research Grant No. P01 DC00422 from the National Institute on Deafness and Other Communication Disorders, National Institutes of Health, and in part by a Deafness Research Foundation grant to FAB. The authors wish to thank Barbara L. Schmiedt for technical assistance.

Bies, D. A., and Hansen, C. H. (**1990**). ''An alternative mathematical description of the relationship between noise exposure and hearing loss,'' J. Acoust. Soc. Am. **88,** 2743–2754.

Boettcher, F. A., Henderson, D., Gratton, M. A., Danielson, R. W., and Byrne, C. D. (**1987**). ''Synergistic interactions of noise and other ototraumatic agents,'' Ear Hear. **8**, 192–212.

Burns, W., and Robinson, D. W. (**1970**). *Hearing and Noise in Industry* (Her Majesty's Stationary Office, London).

Dobie, R. A. (**1993**). *Medical-Legal Evaluation of Hearing Loss* (van Nostrand Reinhold, New York).

Humes, L. E. (**1984**). ''Noise-induced hearing loss as influenced by other agents and by some physical characteristics of the individual,'' J. Acoust. Soc. Am. **76,** 1318–1329.

Humes, L. E., and Jesteadt, W. (**1991**). ''Modeling the interactions between noise exposure and other variables,'' J. Acoust. Soc. Am. **90,** 182–188.

International Organization for Standards (**1990**). ''Acoustics: Determination of Occupational Noise Exposure and Estimation of Noise-Induced Hearing Impairment,'' ISO 1999 (Geneva).

Macrae, J. H. (**1971**). ''Noise-induced hearing loss and presbyacusis,'' Audiology **10**, 323–333.

Macrae, J. H. (**1991**). ''Presbycusis and noise-induced permanent threshold shift,'' J. Acoust. Soc. Am. **90,** 2513–2516.

Miller, J. D., Watson, C. S., and Covell, W. (**1963**). ''Deafening effects of noise on the cat,'' Acta Otolaryngol. Suppl. **176**, 1–91.

Mills, J. H. (**1992**). ''Noise-induced hearing loss: Effects of age and existing hearing loss,'' in *Noise-Induced Hearing Loss*, edited by A. Dancer, D. Henderson, R. Salvi, and R. Hamernik (Mosby-Yearbook, St. Louis), pp. 237–245.

Mills, J. H., Gilbert, R., and Adkins, W. Y. (**1981**). ''Temporary threshold shifts produced by wideband noise,'' J. Acoust. Soc. Am. **70,** 390–396.

Mills, J. H., Schmiedt, R. A., and Kulish, L. F. (**1990a**). ''Age-related changes in auditory potentials of Mongolian gerbil,'' Hear. Res. **46**, 201–210.

Mills, J. H., Schmiedt, R. A., and Adams, J. C. (**1990b**). ''Combined effects of noise and presbyacusis,'' in *International Congress on Noise as a Public Health Hazard*, edited by B. Berglund and T. Lindvall (Swedish Council for Building Research, Stockholm), Vol. 3, pp. 137–142.

Mills, J. H., Lee, F. S., Boettcher, F. A., and Dubno, J. R. (**1996**). ''Interactions between age-related and noise-induced hearing loss,'' in *Scientific Basis of Noise-Induced Hearing Loss*, edited by A. Axelsson, H. Borchgrevink, R. Hamernik, P. Hellstrom, D. Henderson, and R. Salvi (Thieme, New York), pp. 193–212.

Shone, G., Altschuler, R. A., Miller, J. M., and Nuttall, A. L. (**1991**). ''The effect of noise exposure on the aging ear,'' Hear. Res. **56**, 173–178.

Ward, W. D., Glorig, A., and Sklar, D. L. (**1959**). ''Temporary threshold shift from octave-band noise: applications to DRC's,'' J. Acoust. Soc. Am. **31,** 522–528.

Pitch and loudness estimation for single and multiple pulse per period electric pulse rates by cochlear implant patients

P. A. Busby and G. M. Clark
Department of Otolaryngology, University of Melbourne, Parkville, 3052, Victoria, Australia

(Received 3 March 1996; revised 31 July 1996; accepted 20 August 1996)

Numerical estimates of loudness and pitch for electric pulse rates were obtained from 14 patients using the 22 electrode cochlear implant manufactured by Cochlear Limited. Six patients were postlinguistically deafened adults, and eight patients were adults and children who became deaf very early in life. Comparisons were made between two types of pulse rate patterns. The SPP pulse pattern presented a single pulse every period, the inverse of the pulse rate. The MPP pulse pattern presented multiple pulses in the first half of the period, using a rate of 1000 pulses/s, with no stimulation in the second half of the period. The pulse rates used for the SPP and MPP pulse patterns were 71.4–500 pulses/s, which corresponded to periods of 14–2 ms. For the SPP pulse pattern, the total number of pulses over the duration of the stimulus increased with increases in pulse rate, while for the MPP pulse pattern, the total number of pulses remained constant. Pitch and loudness estimates were obtained from the postlinguistically deafened patients for the SPP and MPP pulse patterns, and from the early-deafened patients for the MPP pulse pattern. Loudness estimates for the SPP pulse pattern increased with increases in pulse rate for all postlinguistically deafened patients. Loudness estimates for the MPP pulse pattern decreased with increases in pulse rate for three of the six postlinguistically deafened patients and for six of the eight early-deafened patients. For the other patients (three postlinguistically deafened and two early-deafened), loudness estimates marginally increased with increases in pulse rate. Pitch estimates for the SPP and MPP pulse patterns increased with increases in pulse rate for the six postlinguistically deafened patients. For the early-deafened patients, pitch estimates for the MPP pulse patterns increased with increases in pulse rate for only five of the eight patients. For the other three early-deafened patients, pitch estimates were similar to the loudness estimates and decreased with increases in pulse rate. [S0001-4966(97)02402-8]

PACS numbers: 43.66.Ts, 43.66.Mk, 43.66.Hg, 43.64.Me [JWH]

INTRODUCTION

Postlinguistically deafened cochlear implant patients are generally able to perceive pitch related differences in electric pulse rates in the range from about 50 to 300–500 pulses/s (Eddington *et al.*, 1978; Lim and Tong, 1989; Pfingst, 1988; Pfingst *et al.*, 1994; Shannon, 1983, 1993; Tong *et al.*, 1983; Townshend *et al.*, 1987). In studies using numerical estimation, pitch increases with increases in pulse rate up to 300–500 pulses/s and does not markedly change at higher rates (Lim and Tong, 1989; Shannon, 1983, 1993; Tong *et al.*, 1983). Results from pulse rate discrimination (Eddington *et al.*, 1978; Pfingst, 1988; Pfingst *et al.*, 1994; Townshend *et al.*, 1987) and pulse rate identification (Lim and Tong, 1989; Tong and Clark, 1985) studies have been consistent with these findings in that performance has been markedly poorer at higher rates (>300–500 pulses/s) than at lower rates. There has, however, been considerable variability in performance across patients. For instance, Townshend *et al.* (1987) noted that the upper limit of pulse rate, above which discrimination performance became markedly poorer, ranged from about 200–1000 pulses/s across the three patients tested. Similarly, Pfingst (1988) reported a wide range of values in difference limens for pulse rate discrimination across patients and implant prostheses. In addition, it has been shown that pulse rate perception is dependent on the loudness of the stimuli. Poor performance for pitch ranking (Townshend *et al.*, 1987) and pulse rate discrimination (Pfingst *et al.*, 1994) has been reported using electric stimulation levels close to hearing threshold, with improved performance with increases in stimulation levels.

It has also been reported that loudness increases with increases in electric pulse rate when the same electric stimulation levels are used for the pulse rates tested (Eddington *et al.*, 1978; Pfingst *et al.*, 1994; Shannon, 1983; Tong *et al.*, 1983). To minimize the possible influences of loudness cues on pulse rate perception, Tong *et al.* (1983) proposed a pulse rate pattern where multiple pulses were presented in the first half of each period with no stimulation in the second half of the period. This compares with the standard pulse rate pattern where a single pulse is presented every period. Figure 1 shows these two types of pulse patterns for a 100-pulses/s signal. For the single pulse per period (SPP) pattern, a single biphasic pulse is presented every 10 ms. For the multiple pulses per period (MPP) pattern, five biphasic pulses are presented, using a rate of 1000 pulses/s, in the first 5 ms of the 10-ms period followed by 5 ms of silence. The overall periodic rate of the MPP pattern is the same as that of the SPP pattern. The total number of pulses over the duration of the stimulus increases with increases in pulse rate for the SPP pulse pattern, but is constant for the MPP pulse pattern. Therefore, the total charge delivered increases with increases in pulse rate for the SPP pulse pattern, assuming constant

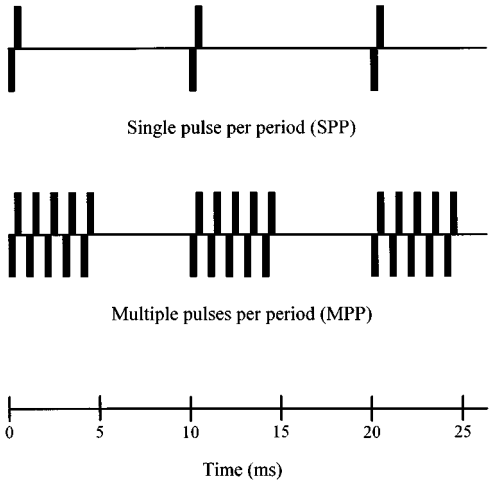

FIG. 1. The SPP and MPP pulse rate patterns for a 100-pulses/s signal. The SPP pattern consists of a single biphasic pulse every 10-ms period. The MPP pattern consists of multiple biphasic pulses, at 1000 pulses/s, in the first half of every 10-ms period. For the MPP pattern, five pulses are presented for the 100-pulses/s signal.

current amplitude and pulse duration. For the MPP pulse pattern, the total charge delivered is constant over pulse rate. Tong *et al.* (1983) showed that loudness increased with increases in pulse rate for SPP stimuli, while for MPP stimuli the variation in loudness was considerably smaller. Also, the size of the dynamic range between hearing threshold and comfortable listening level was similar for the SPP and MPP pulse patterns. Pitch ratio estimations for the two types of pulse rate patterns were similar, and the pulse rate difference limens for SPP and MPP stimuli were also similar. However, data were collected from only one postlinguistically deafened adult in Melbourne, who used a prototype prosthesis of ten electrodes.

In this report we describe the results of pitch and loudness estimation studies using SPP and MPP pulse rate patterns. Data were collected from six postlinguistically deafened adults, and from eight adults and children who became deaf very early in life. The patients were implanted with the 22-electrode cochlear implant manufactured by Cochlear Limited. The first aim was to determine whether the pitch and loudness percepts for the SPP and MPP pulse rate patterns, as reported in the one patient by Tong *et al.* (1983) and described above, were repeatable with a larger group of postlinguistically deafened patients. The second aim was to determine whether the performance of the early-deafened patients was similar to that of the postlinguistically deafened patients. It is not clear whether similar levels of performance would be recorded for the two groups of patients. For instance, we have previously shown that some early-deafened patients have been less successful in pulse rate discrimination, as difference limens were 71%–105% at 200 pulses/s for three from a group of ten patients tested (Busby *et al.*, 1992). For the other seven early-deafened patients, difference limens were 15%–29% at 200 pulses/s, which were within the range of those for postlinguistically deafened patients, 3%–40% at 200 pulses/s (Lim and Tong, 1989; Tong *et al.*, 1982; Townshend *et al.*, 1987).

The results from the current study would also indicate the usefulness of using MPP pulse rate patterns in studies of pitch perception by early-deafened patients. We are particularly interested in conducting comparative studies using different sets of stimuli to determine the reliability of pitch estimation procedures for this group of patients. One set would consist of the electrodes along the 22-electrode array of the Cochlear Limited prosthesis. Another set could be the MPP pulse rates used by Tong *et al.* (1983) and in the current study. It would be important to minimize any loudness related cues when using pulse rate stimuli so that performance was predominantly dependent on pitch perception. Therefore, the MPP rates may be a useful pulse rate pattern to use as a stimulus set. In these comparative studies, differences in patient performance across the different sets of stimuli could be used to indicate patient reliability in the pitch estimation procedures. In particular, poor performance in pitch estimation for electrodes along the array but good performance in pitch estimation for MPP pulse rates would suggest some difficulties in the perception of a tonotopic order of pitch for electrodes, and that this result was probably not related to the pitch estimation procedure. This finding would contrast with the tonotopic order of pitch for electrodes recorded in postlinguistically deafened adults (Busby *et al.*, 1994).

I. METHOD

A. Patients and electrical stimulation hardware

The histories of the six postlinguistically deafened adults (P1–P6) and the eight early-deafened patients (ED1–ED8), consisting of three adults and five children, are summarized in Table I. Note that P3 is the same patient used in the previous study using SPP and MPP pulse rate patterns (Tong *et al.*, 1983). The etiologies of deafness for the early-deafened patients were Usher's syndrome (ED2 and ED3), meningitis (ED6), and unknown (ED1, ED4, ED5, ED7, and ED8). All patients had a profound-to-total bilateral sensorineural hearing loss prior to implantation. The patients were implanted with the Cochlear Limited prosthesis of 22 electrodes (Clark *et al.*, 1987). The electrode array was fully inserted in the scala tympani for most patients except P2, P3, ED6, ED7, and ED8, where there were 1–4 electrodes external to the scala. The 10-electrode prototype device used by P3 was replaced with the 22-electrode prosthesis. The ages of the patients at the time of surgery were 42–66 years for P1–P6, and 8–20 years for ED1-ED8. Prior to data collection, P1–P6 had been using their prostheses for 6–11 years and ED1–ED8 had been using their prostheses for 1–7 years. The patients were selected on the basis of their availability for the study and all had participated in previous psychophysical studies.

The residual auditory neurones were activated using biphasic current pulses with the same pulse duration in the two phases. The duration of each pulse was 200 μs/phase. The current was equal but in opposite directions in the two phases with the negative phase leading. The Cochlear Limited prosthesis can deliver electric current between approximately 15 and 1500 μA. This range is converted to a scale of

TABLE I. Summary of patient histories.

Patient	Age (years)	Age at confirmation of profound-total hearing loss (years)	Cause of deafness	Age at implantation (years)	Duration of implant use (years)
P1	50	27	Acoustic trauma	44	6
P2	73	38	Progressive, otosclerosis	66	7
P3	63	46	Acoustic trauma	52	11
P4	49	41	Unknown progressive and acoustic trauma	42	6
P5	54	41	Unknown progressive	47	7
P6	58	35	Progressive, otosclerosis	52	6
ED1	22	1.0	Unknown congenital	18	4
ED2	21	0.5	Usher's syndrome	15	7
ED3	21	1.5	Usher's syndrome	20	1
ED4	15	0.8	Unknown congenital	14	1
ED5	14	1.5	Unknown congenital	8	6
ED6	14	2.0	Meningitis	8	6
ED7	14	1.3	Unknown congenital	12	2
ED8	12	0.8	Unknown congenital	8	4

238 levels with approximately a 2.5% increase in current for each level (Skinner *et al.*, 1991), although there are some variations across individual prostheses. The actual current delivered to the individual prostheses used by the patients were determined using calibration tables supplied by Cochlear Limited. These values are expressed in dB (*re*: 1 μA) in this report.

Bipolar stimulation was used for all patients. For most patients, except P4 and ED8, the two electrodes of the bipolar pair were separated by one electrode, which corresponds to ''BP+1'' in the Cochlear Limited clinical procedures. For P4 and ED8, the two electrodes were separated by two electrodes, corresponding to ''BP+2'' in the clinical procedures. The term ''electrode'' describes the basal member of the bipolar pair. Stimulation was on electrode 14 for all patients, where electrodes are numbered 22–1 in an apical-basal direction.

B. Procedure

1. SPP and MPP stimuli

Seven SPP stimuli were used, where a single pulse was presented at the following rates: 71.4, 83, 100, 125, 166.7, 250, and 500 pulses/s. These correspond to pulse periods of 14, 12, 10, 8, 6, 4, and 2 ms. The same pulse rates were used for the seven MPP stimuli. It was important to use periods which were even-numbered integers in order to accurately configure the MPP stimuli. The multiple pulses of the MPP stimuli were delivered at 1000 pulses/s, one pulse every 1 ms. The number of pulses presented in the MPP stimuli during the first half of each period were: 7, 6, 5, 4, 3, 2, and 1 pulse; for the rates of 71.4, 83, 100, 125, 166.7, 250, and 500 pulses/s, respectively. Note that the MPP and SPP stimuli at 500 pulses/s were equivalent as a single pulse was presented every 2 ms.

Two sets of stimuli were constructed. The first set consisted of all the SPP and MPP pulse rates and there were 14 stimuli in the set. The second set consisted of only the seven MPP pulse rates. The duration of each stimulus was fixed at 500 ms. The current levels used for each patient and each set of stimuli were separately determined, and were fixed at the one level for all the stimuli in the set in order to measure variations in loudness for the different stimuli. These levels were determined using the procedures described in the next section.

2. Threshold and comfortable listening level estimation

For each patient and set of stimuli, the current level was initially adjusted to a maximum comfortable listening level using a MPP stimulus at 250 pulses/s. The comfortable listening level was determined using the ascending–descending technique used in our previous study (Busby *et al.*, 1994). Current was increased until stimulation became too loud or uncomfortable and it was then decreased to a level which produced the comfortable listening level. In order to avoid uncomfortably loud sensations for the other stimuli in the set, each stimulus was then separately presented. If stimulation became too loud or uncomfortable, the current level was decreased to a level producing a comfortable listening level. The current level used in testing, therefore, provided a comfortable listening level for the stimulus that produced the loudest sensation. As can be seen in Figs. 2–4, the pulse rate and pulse rate pattern (SPP or MPP) that produced the loudest sensations were not the same across patients.

The range of usable hearing was also measured for the SPP and MPP pulse rate patterns at 250 pulses/s. The Hughson–Westlake ascending technique (Carhart and Jerger, 1959) was used to measure thresholds. The comfortable listening levels were measured using the ascending–descending procedure described in the preceding paragraph. The range of usable hearing was the difference, in dB, between threshold and the comfortable listening level.

3. Pitch and loudness estimation

Estimates of pitch and loudness were separately obtained. A single interval numerical estimation procedure was

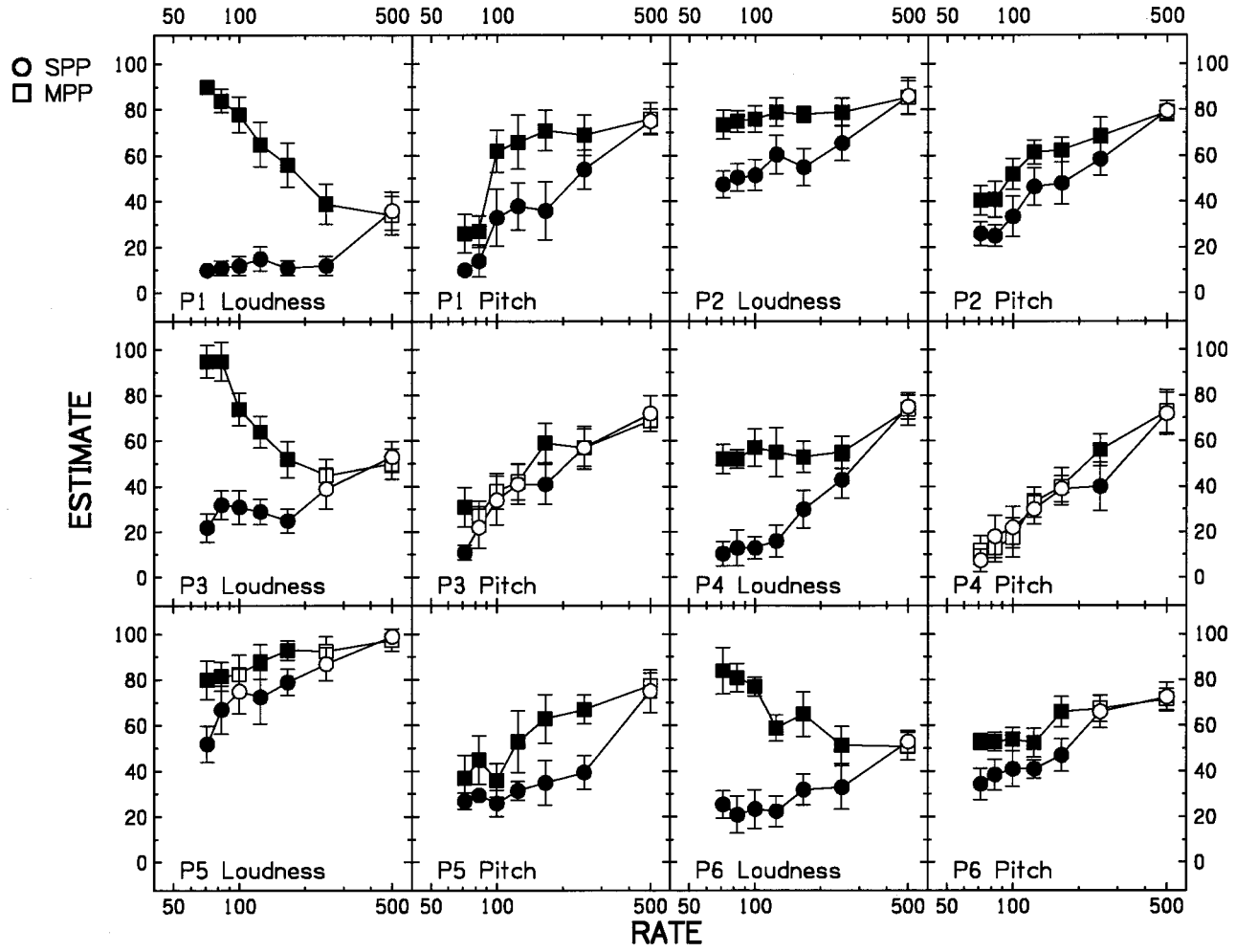

FIG. 2. Loudness and pitch estimates for SPP (circles) and MPP (squares) stimuli by the six postlinguistically deafened adults (P1–P6). Each set of two graphs shows the loudness and pitch estimates for each patient separately. The error bars indicate ±1 standard deviation around the means. The filled symbols indicate a significant difference in estimates between the SPP and MPP stimuli at the same pulse rate.

used, similar to that used in our previous study of pitch estimation for stimulation on different electrodes using the Cochlear Limited prosthesis (Busby *et al.*, 1994). The patient was instructed to assign a number in the range of 1–100 to the pitch or loudness of a single presentation. For pitch estimation, a low pitch was assigned a low number and a high pitch was assigned a high number. Similarly for loudness estimation, a soft sound was assigned a low number and a loud sound was assigned a high number. The numerical scales and written descriptions were displayed on a sheet of paper for reference. The patient was also advised that the numerical scales could be expanded in either direction, if required.

Data were collected from P1–P6 using the two sets of stimuli: SPP and MPP pulse rates in the first set and MPP pulse rates alone in the second set. Data were collected from ED1–ED8 for only the second set of stimuli: MPP pulse rates alone. For the set of SPP and MPP stimuli, two blocks of stimuli were presented for loudness estimation and two blocks for pitch estimation. In a single block, each SPP and MPP stimulus was presented five times each in random order and the number of items was 70 (14 stimuli×5 presentations). Therefore, a total of ten estimates of loudness and pitch were obtained for each SPP and MPP stimulus. For the set of MPP stimuli alone, usually a single block was separately presented for pitch and loudness estimation. In each block, each MPP stimulus was presented ten times each in random order, and the number of items was 70 (7 stimuli×10 presentations). For most early-deafened patients, however, it was necessary to use two blocks of 35 items (7 stimuli×5 presentations) so that the time taken for data collection was reduced and interest in the task was maintained. In all cases, ten estimates of loudness and pitch were obtained for each MPP stimulus. Data were not collected from the early-deafened patients for the set of SPP and MPP stimuli because it was difficult to maintain interest in the task, especially as they generally found the pitch estimation demanding. This suggested that pitch percepts may not have been very salient for these patients. In the case of loudness estimation, the early-deafened patients had less difficulty in performing the task. As to be described in the Results section, it is possible that some of the early-deafened patients may not have been able to reliably estimate pitch as the pitch and loudness estimates were similar (Fig. 4). Because the early-deafened patients found the pitch estimation task difficult and that we wished to conduct further psychophysical

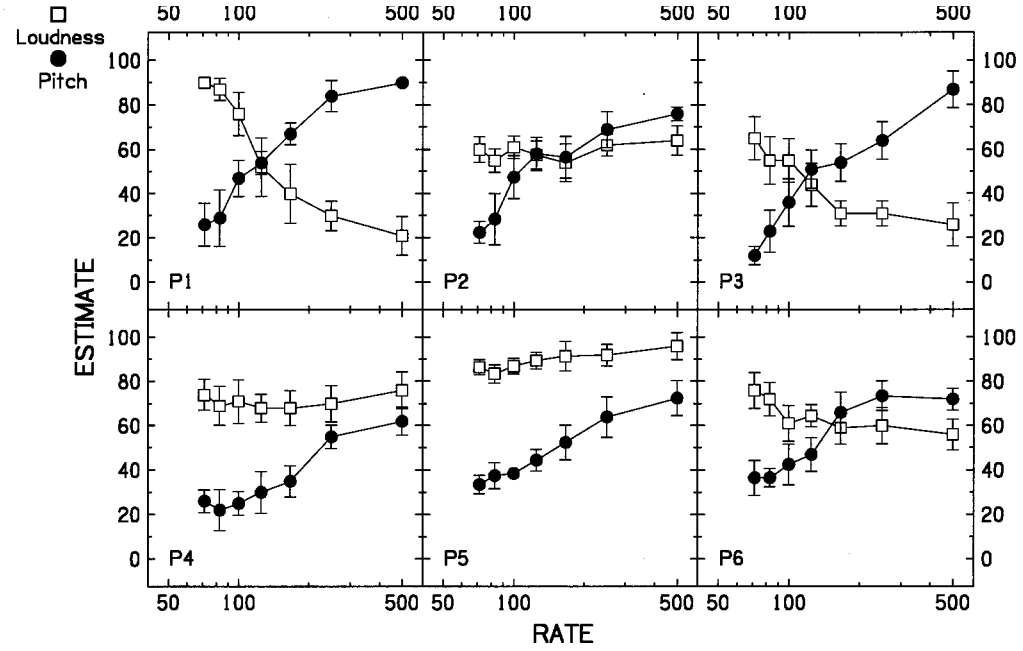

FIG. 3. Loudness and pitch estimates for MPP stimuli by the six postlinguistically deafened adults (P1–P6). Each graph shows the loudness (unfilled squares) and pitch (filled circles) estimates for each patient separately. The error bars indicate ±1 standard deviation around the means.

studies with these patients, it was decided not to test the early-deafened patients using the first set of stimuli of SPP and MPP pulse rates.

Two to three sessions of training in pitch and loudness estimation were given to the postlinguistically deafened adults prior to data collection, and two to six sessions to the early-deafened patients. The amount of training was primarily dependent on the ability of the patients to estimate the pitch of the different stimuli. Some patients found the pitch estimation task difficult because of the concurrent variations in the loudness of the stimuli. A small amount of training was provided in loudness estimation as all patients found this

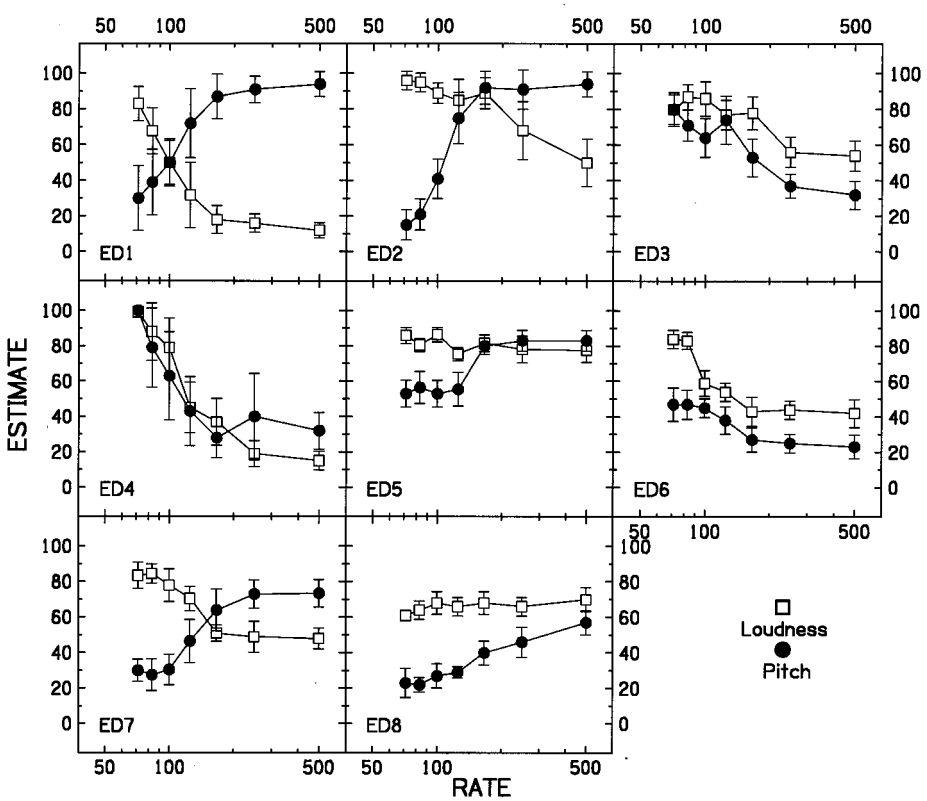

FIG. 4. Loudness and pitch estimates for MPP stimuli by the eight early deafened patients (ED1–ED8). Each graph shows the loudness (unfilled squares) and pitch (filled circles) estimates for each patient separately. The error bars indicate ±1 standard deviation around the means.

a relatively easy task. Data were collected over one to two sessions after training.

C. Data analysis

The loudness and pitch data from the postlinguistically deafened adults (P1–P6) were analyzed using three procedures to examine differences between the SPP and MPP pulse patterns. First, the data were analyzed to determine whether the estimates for the two pulse patterns at each pulse rate were significantly different from each other. Separate *t* tests (assuming unequal variances) were conducted on the loudness and pitch estimates at each pulse rate, each patient separately. Second, the data were analyzed to determine whether changes in estimates as a function of pulse rate were significantly different for the two pulse patterns. Separate two-way ANOVAs were conducted on the pitch and loudness data for each patient to assess whether the interaction between pulse pattern and pulse rate was significant. A significant interaction would indicate that the changes in estimates over pulse rate differed for the two pulse patterns. Third, a cumulative d' was calculated to determine the relative range of loudness and pitch estimates across pulse rates for each of the two pulse rate patterns. The d' between two successive pulse rates, i and j, for each pulse pattern was calculated using

$$d'_{i:j} = (M_i - M_j)/[(V_i + V_j + \cdots + V_n)/n]^{1/2}, \quad (1)$$

where M_i and V_i are the mean and variance of the estimate for pulse rate i, and M_j and V_j are the mean and variance of the estimate for pulse rate j. Note that the average variance was used as the variances were not the same across all pulse rates (Busby *et al.*, 1994).

Differences between the two pulse patterns in the current levels which elicited thresholds and comfortable listening levels for the postlinguistically deafened patients were analyzed using paired *t* tests. Also analyzed using the same procedure were differences in the ranges of usable hearing. For comparisons between postlinguistically deafened and early-deafened patient groups, a *t* test was used to determine whether the range of usable hearing for the MPP pulse pattern was different for the two patient groups. Note that it was not appropriate to compare the threshold and comfortable listening levels as the mode of stimulation was not the same across all patients.

II. RESULTS

The loudness and pitch estimation data from P1–P6 for the first set of stimuli, consisting of all the SPP and MPP pulse rates, are shown in Fig. 2. The filled symbols indicate significant differences between the estimates for the SPP and MPP pulse patterns at each pulse rate, and the unfilled symbols indicate no significant difference.

For P1–P6, loudness estimates for the MPP stimuli were significantly higher ($p<0.004$) than those for the SPP stimuli at the rates of 71.4–250 pulses/s (Fig. 2), except in three cases where the estimates were not significantly different: P5 at 100 pulses/s [$t(17)=1.83$, $p=0.085$], and P3 and P5 at 250 pulses/s [$t(17)=1.69$, $p=0.110$ and $t(17)=1.82$, $p=0.087$, respectively]. There were no significant differences in loudness estimates for the SPP and MPP stimuli at 500 pulses/s ($p>0.33$) for all patients. The interaction between pulse rate and pulse pattern was significant ($p<0.001$) for all patients, indicating that the changes in estimates as a function of pulse rate were different for the two pulse patterns. For the SPP stimuli, loudness estimates increased with increases in pulse rate for all patients, although there were some plateau effects at low rates. These plateau regions in the loudness estimates were most apparent for three patients, P1, P3, and P6, where there was also a decrease in loudness estimates with increases in pulse rate for the MPP stimuli. For the MPP stimuli, loudness estimates marginally increased with increases in pulse rate for P2, P4, and P5. For these three patients, the size of the increase in loudness estimates for the MPP stimuli over the range of pulse rates was considerably less than that for the SPP stimuli, as shown by the smaller cumulative d' values for the MPP pattern compared to the SPP pattern (Table II). For the other three patients (P1, P3, and P6), loudness estimates for the MPP stimuli markedly decreased with increases in pulse rate. Also for these three patients, the absolute size of the cumulative d' values were larger for the MPP pattern than for the SPP pattern (Table II).

TABLE II. Cumulative d' values for loudness and pitch estimates from the postlinguistically deafened patients.

	Loudness estimates		Pitch estimates	
Patient	SPP	MPP	SPP	MPP
P1	5.54	−7.19	7.20	5.69
P2	5.26	2.08	7.59	6.08
P3	4.61	−6.13	7.11	5.02
P4	9.44	2.96	7.92	8.02
P5	5.58	2.57	7.27	4.26
P6	3.74	−4.41	5.73	3.48

For four patients (P1, P2, P5, and P6), pitch estimates for the MPP stimuli were significantly higher ($p<0.021$) than those for the SPP stimuli at the rates of 71.4–250 pulses/s (Fig. 2), except in one case where the estimates were not significantly different: P6 at 250 pulses/s [$t(17)=0.52$, $p=0.61$]. For the other two patients (P3 and P4), pitch estimates for the MPP stimuli were not significantly different ($p>0.093$) from those for the SPP stimuli at the rates of 71.4–250 pulses/s, except in three cases where the estimates for the MPP stimuli were significantly higher than those for the SPP stimuli: P3 at 71.4 and 166.7 pulses/s [$t(11)=6.79$, $p<0.0001$ and $t(18)=4.60$, $p=0.0002$, respectively] and P4 at 250 pulses/s [$t(15)=4.00$, $p=0.0012$]. There were no significant differences in pitch estimates for the SPP and MPP stimuli at 500 pulses/s ($p>0.29$) for all patients. Pitch estimates increased with increases in pulse rate for both SPP and MPP stimuli. In all cases, a significant interaction ($p<0.001$) between pulse rate and pulse pattern was recorded which indicated that the changes in estimates for the two pulse patterns as a function of pulse rate were significantly different. The range of pitch estimates, as shown by the cumulative d' values, was greater for the SPP pattern than for the MPP pattern for most patients (Table II). The one exception was

P4, where the cumulative d' values were similar for the two pulse patterns. The average difference in cumulative d' values between the SPP and MPP patterns was 1.71.

The loudness estimation data from P3 in this study, using the 22-electrode prosthesis, differed from those previously obtained from the same patient using the 10-electrode prototype prosthesis (Tong *et al.*, 1983). For pitch estimation, the results from the two studies were similar. There were some methodological differences between the two studies. Common ground stimulation was used in the previous study, where a single electrode is activated and the other electrodes on the array are connected together to serve as the return path for the current. In the present study, bipolar stimulation was used. It is possible that the distribution of current in the cochlea could differ for these two modes of stimulation (Black *et al.*, 1983; Busby *et al.*, 1994). The upper limits of pulse rate used for the SPP and MPP stimuli were 1000 and 200 pulses/s, respectively, differing from the current study where the upper limit was 500 pulses/s. For pitch estimation in the previous study, a ratio estimation procedure was used. Tong *et al.* (1983) reported that loudness estimates were higher for the MPP stimuli than for the SPP stimuli at the same pulse rate, and the range in estimates over the pulse rates tested for the MPP stimuli was considerably less than that for the SPP stimuli. This differed from the current study where the absolute range in loudness estimates was considerably greater for the MPP stimuli than for the SPP stimuli (Fig. 2 and Table II). In the previous study, there was also a tendency for loudness estimates for the MPP stimuli to decrease with increases in pulse rate, although this was only apparent on three of the four electrodes tested. However, the size of the decrease in loudness estimates was considerably less than that recorded in the current study. For pitch estimation in the previous study, the estimates for the MPP and SPP stimuli were qualitatively similar as was also the case in the current study.

Figure 3 shows the loudness and pitch estimation data for P1–P6 for the second set of stimuli, consisting of only MPP pulse rates. The pattern of results was qualitatively, but not quantitatively, similar to that recorded for the MPP stimuli in the first set, consisting of MPP and SPP stimuli, described above (Fig. 2). For P2, P4, and P5, loudness estimates were constant or increased slightly with increases in pulse rate. Loudness estimates decreased with increases in pulse rate for P1, P3, and P6. For all patients, pitch estimates increased with increases in pulse rate.

Figure 4 shows the loudness and pitch estimation data for ED1–ED8 for the second set of stimuli, consisting of only MPP pulse rates. Loudness estimates decreased with increases in pulse rate for most early-deafened patients; the exceptions were ED5 and ED8 where the estimates were similar across pulse rates. The decrease in loudness estimates was most marked for ED1 and ED4, where estimates approached threshold at 500 pulses/s.

Pitch estimates increased with increases in pulse rate for five early-deafened patients: ED1, ED2, ED5, ED7, and ED8 (Fig. 4). Note that in the case of ED2, ED5, and ED7, a plateau in pitch estimates at rates above 125–166.7 pulses/s was recorded. A decrease in pitch estimates with increases in pulse rate was recorded for the other three early-deafened patients: ED3, ED4, and ED6. For these three patients, the pitch estimates followed a pattern similar to the loudness estimates. In the case of ED4, there was a very close correspondence between loudness and pitch estimates, and these estimates were significantly different at only two pulse rates: 250 pulses/s [$t(10)=-2.60$, $p=0.027$] and 500 pulses/s [$t(13)=-4.64$, $p=0.0005$]. It is possible that these patients were not able to effectively estimate pitch and gave numerical estimates primarily according to the loudness of the stimuli.

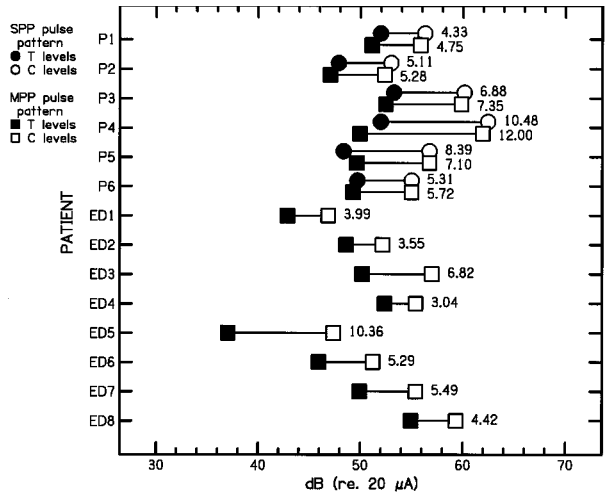

FIG. 5. Threshold, comfortable listening levels, and dynamic ranges for SPP and MPP stimuli, in dB (re: 1 μA). Thresholds (T) are shown by filled symbols and comfortable listening levels (C) are shown by unfilled symbols. The SPP stimuli are shown by circles and MPP stimuli are shown by squares. The dynamic range is given by the numerical values next to each set of T and C levels for each patient.

Figure 5 shows the thresholds and comfortable listening levels for the SPP and MPP pulse patterns at 250 pulses/s for all patients. The numerical values indicate the ranges of usable hearing. The comfortable listening levels were significantly higher for SPP stimuli than for MPP stimuli [$t(5)=-2.87$, $p=0.035$]. There were no significant differences for thresholds [$t(5)=-1.35$, $p=0.230$] and the ranges of usable hearing [$t(5)=-0.77$, $p=0.480$]. As far as any difference between the postlinguistically deafened and early-deafened patient groups is concerned, there was no significant difference in the ranges of usable hearing for the MPP pulse pattern [$t(10)=1.24$, $p=0.24$].

III. DISCUSSION

The results from this study showed that, first, loudness estimates for the MPP stimuli decreased with increases in pulse rate for three of the six postlinguistically deafened patients (Figs. 2 and 3 and Table II) and for six of the eight early-deafened patients (Fig. 4). For the other patients, loudness estimates for the MPP stimuli marginally increased with increases in pulse rate. For the SPP stimuli, loudness estimates increased with increases in pulse rate for all six postlinguistically deafened patients (Fig. 2 and Table II). Second, pitch estimates for the SPP and MPP stimuli increased with increases in pulse rate for all six postlinguistically deafened

patients (Figs. 2 and 3 and Table II). For the early-deafened patients, however, increases in pitch estimates for the MPP stimuli with increases in pulse rate were only recorded for five of the eight patients (Fig. 4).

The loudness estimates for the MPP stimuli revealed two distinct patterns of results across patients. This suggests that there may possibly be two different mechanisms involved in loudness coding for MPP pulse patterns which are exemplified by these results. In the case where loudness estimates increased marginally or were relatively constant across pulse rates, loudness coding could be dependent on the total electrical charge per unit of time. The total charge delivered by the MPP pulse patterns was the same across pulse rates for a time constant of 14 ms for the stimuli used in this study. Thus, a temporal integration process with time constants of about 14 ms, or in multiples of 14 ms, would result in similar loudness percepts across pulse rates. In the case where loudness estimates decreased with increases in pulse rate, loudness coding could be dependent on the number of pulses presented each period. The number of pulses presented in the first half of each period decreased with increases in pulse rate; where at 71.4 pulses/s, seven pulses were presented in the initial 7 ms, while at 500 pulses/s, one pulse was presented in the initial 1 ms. Thus, a short-term temporal integration process related to the number of closely spaced pulses would result in a decrease in loudness with increases in pulse rate.

A short-term temporal integration process related to the number of closely spaced pulses could be due to the activity of the peripheral auditory nerve fibers in response to electrical stimulation using biphasic pulses. Butikopfer and Lawrence (1979) showed that when myelinated nerve fibers are stimulated with a series of closely spaced pulses, the membrane voltage does not return to zero after each pulse and additional pulses increase the depolarization of the membrane. In cochlear implant patients, Eddington *et al.* (1995) have reported that thresholds for a single biphasic pulse are reduced when the pulse is closely preceded by another pulse which is subthreshold. Similar findings were also recorded by White *et al.* (1984) in two out of three patients tested. For stimulation at suprathreshold levels, McKay and McDermott (1996) showed a progressive increase in loudness percepts as the time interval between two pulses was reduced from 4 to less than 1 ms, for two out of four patients tested. This was recorded using two pulse stimuli at pulse rates of 50 and 250 pulses/s. Therefore, it may be that a series of closely spaced pulses may be more effective at stimulating the residual auditory fibers than single pulses that are more widely spaced in some cases. The decrease in loudness estimates with decreases in the number of pulses per period for the MPP stimuli, which was recorded for several patients, would be consistent with this interpretation. In the current study, however, the number of pulses per period and the duration of the silent period between these closely spaced pulses were not independently varied. It would be useful in further studies to examine the interactions between these two variables on loudness percepts produced by the MPP pulse pattern. This would also provide further information about the possible mechanism of loudness coding in cochlear implant patients.

It is also possible that these differences between patients in loudness estimates for the MPP stimuli could reflect on the consequences of neural damage and/or degeneration in the auditory pathway. Loudness estimates for the MPP stimuli decreased with increases in pulse rate for most of the early deafened patients. For these patients, it is possible that the morphological and physiological characteristics of the auditory pathway may have been adversely affected by the early onset of profound deafness and long-term sound deprivation, although the extent of neural degeneration is unclear (Harrison *et al.*, 1991; King and Moore, 1991; Moore, 1990; Snyder *et al.*, 1990). Other possible variables for these differences between patients could be differences in the number of surviving dendrites and ganglion cells, the number of myelinated fibers, the site of neural excitation, and the distance between the stimulating electrodes and the auditory nerve fibers (White *et al.*, 1984).

As far as the loudness estimation data from P1–P6 for the SPP pulse pattern are concerned, the results from this study (Fig. 2) confirm the previous findings that, at the same electric stimulation level, loudness increases with increases in pulse rate for biphasic pulsatile stimulation (Eddington *et al.*, 1978; Pfingst *et al.*, 1994; Shannon, 1983, 1993; Tong *et al.*, 1983).

The pitch estimates for the SPP and MPP stimuli increased with increases in pulse rate for all six postlinguistically deafened patients (Figs. 2 and 3). The results for the SPP pulse pattern were consistent with those previously reported (Lim and Tong, 1989; Shannon, 1983, 1993; Tong *et al.*, 1983). For the MPP pattern, the results from the six postlinguistically deafened patients generally confirm the previous findings recorded with one patient (Tong *et al.*, 1983). As far as the early-deafened patients are concerned, pitch estimates for the MPP pulse pattern increased with increases in pulse rate for only five of the eight patients (Fig. 4). For the other three patients (ED3, ED4, and ED6), pitch estimates were similar to the loudness estimates, suggesting that these three patients may not have been able to effectively estimate pitch and gave estimates based on the loudness of the stimuli. Alternatively, these patients may have had considerable difficulty in estimating pitch in the presence of variations in the loudness of the stimuli. Also, it has been shown that pitch sensations can be dependent on the loudness levels used (Townshend *et al.*, 1987), thus the decrease in pitch estimates with increases in pulse rates may have also been influenced by the loudness of the stimuli. Note that possible interactions between pitch and loudness could have also influenced the pitch estimation results for all patients as loudness varied as a function of pulse rate in all cases. In future studies, it would be important to balance the loudness of the SPP and MPP stimuli so that variations in pitch as a function of pulse rate for the two pulse patterns could be more effectively measured.

The results from this study indicate that the MPP pulse rate pattern may be a useful stimulus set to use in pitch estimation studies for some early-deafened patients. As suggested in the Introduction, the results from pitch estimation studies for MPP stimuli can be compared with those from pitch estimation studies for stimulation on different elec-

trodes along the array. Poor performance in pitch estimation for electrodes but good performance for MPP pulse rates may indicate some difficulties in the perception of a tonotopic order of pitch for the electrodes which was not related to the pitch estimation procedure. However, in order to effectively use the MPP pulse patterns in this type of study, it would be important to obtain loudness estimates for the same set of stimuli. In the case of patients like ED3, ED4, and ED6, where the loudness and pitch estimates were similar, the MPP pulse patterns may be of limited value in these studies of pitch estimation. For the other five early-deafened patients in this study, the results indicted that this pulse pattern would be a useful stimulus set to use in these comparative studies. The MPP pulse rates may also be useful in training early-deafened patients in pitch estimation procedures as more than one percept (pitch and loudness) could possibly vary within the stimulus set.

ACKNOWLEDGMENTS

This work was supported by the National Health and Medical Research Council of Australia. The authors wish to thank Mark Harrison for assistance in software development, Ray Watson (Department of Statistics, University of Melbourne) for statistical advice, Mark White and Rob Shepherd for their constructive comments on the data, and the patients for their participation. The comments from the two reviewers on earlier drafts of this paper were also very helpful.

Black, R. C., Clark, G. M., Tong, Y. C., and Patrick, J. F. (**1983**). ''Current distributions in cochlear stimulation,'' Ann. N.Y. Acad. Sci. **405,** 137–145.

Busby, P. A., Tong, Y. C., and Clark, G. M. (**1992**). ''Psychophysical studies using a multiple-electrode cochlear implant in patients who were deafened early in life,'' Audiology **31**, 95–111.

Busby, P. A., Whitford, L. A., Blamey, P. J., Richardson, L. M., and Clark, G. M. (**1994**). ''Pitch perception for different modes of stimulation using the Cochlear multiple-electrode prosthesis,'' J. Acoust. Soc. Am. **95,** 658–669.

Butikopfer, R., and Lawrence, P. D. (**1979**). ''Electrocutaneous nerve stimulation: II. Stimulus waveform selection,'' IEEE Trans. Biomed. Eng. **26,** 69–75.

Carhart, R., and Jerger, J. (**1959**). ''Preferred method for clinical determination of pure tone thresholds,'' J. Speech Hear. Disord. **24**, 330–345.

Clark, G. M., Blamey, P. J., Busby, P. A., Dowell, R. C., Franz, B. K., Musgrave, G. N., Nienhuys, T. G., Pyman, B. C., Roberts, S. A., Tong, Y. C., Webb, R. L., Kuzma, M. E., Money, D. K., Patrick, J. F., and Seligman, P. M. (**1987**). ''A multiple-electrode intracochlear implant for children,'' Arch. Otol. **113**, 825–828.

Eddington, D. K., Dobelle, W. H., Brackman, D. E., Mladejovsky, M. G., and Parkin, J. L. (**1978**). ''Auditory prostheses research with multiple channel intracochlear stimulation in man,'' Ann. Otol. Rhinol. Laryngol. **87** (Suppl. 53), 5–39.

Eddington, D. K., Long, C. J., Rubinstein, J. T., and Whearty, M. E. (**1995**). ''Minimizing nonsimultaneous interactions,'' Proc. 1995 Conference on Implantable Auditory Prostheses, Asilomar, CA, p. 22.

Harrison, R. V., Nagasawa, A., Smith, D. W., Stanton, S., and Mount, R. J. (**1991**). ''Reorganization of auditory cortex after neonatal high frequency cochlear hearing loss,'' Hear Res. **54**, 11–19.

King, A. J., and Moore, D. R. (**1991**). ''Plasticity of auditory maps in the brain,'' Trends Neurosci. **14**, 31–37.

Lim, H. H., and Tong, Y. C. (**1989**). ''Pitch scaling, difference limens and identification of electrical pulse rates on multichannel cochlear implant patients-implications on temporal processing,'' Proc. Ann. Int. Conf. IEEE Eng. Med. Biol. Soc. **11**, 1065–1066.

McKay, C. M., and McDermott, H. J. (**1996**). ''The effect on pitch and loudness of major interpulse intervals within modulated current pulse trains in cochlear implantees,'' J. Acoust. Soc. Am. **99,** 2584.

Moore, D. R. (**1990**). ''Auditory brainstem of the ferret: bilateral cochlear lesions in infancy do not affect the number of neurons projecting from the cochlear nucleus to the inferior colliculus,'' Dev. Brain Res. **54**, 125–130.

Pfingst, B. E. (**1988**). ''Comparisons of psychophysical and neurophysiological studies of cochlear implants,'' Hear. Res. **34**, 243–252.

Pfingst, B. E., Holloway, L. A., Poopat, N., Subramanya, A. R., Warren, M. F., and Zwolan, T. A. (**1994**). ''Effects of stimulus level on nonspectral frequency discrimination by human subjects,'' Hear. Res. **78**, 197–209.

Shannon, R. V. (**1983**). ''Multichannel electrical stimulation of the auditory nerve in man. I. Basic psychophysics,'' Hear. Res. **11**, 157–189.

Shannon, R. V. (**1993**). ''Psychophysics,'' in *Cochlear Implants: Audiological Foundations*, edited by R. S. Tyler (Singular, San Diego), pp. 357–388.

Skinner, M. W., Holden, L. K., Holden, T. A., Dowell, R. C., Seligman, P. M., Brimacombe, J. A., and Beiter, A. L. (**1991**). ''Performance of postlinguistically deaf adults with the wearable speech processor (WSP III) and mini speech processor (MSP) of the Nucleus multi-electrode cochlear implant,'' Ear Hear. **12**, 3–22.

Snyder, R. L., Rebscher, S. J., Cao, K., Leake, P. A., and Kelly, K. (**1990**). ''Chronic intracochlear electrical stimulation in the neonatally deafened cat. I: Expansion of central representation,'' Hear. Res. **50**, 7–34.

Tong, Y. C., and Clark, G. M. (**1985**). ''Absolute identification of electric pulse rates and electrode positions by cochlear implant patients,'' J. Acoust. Soc. Am. **77**, 188l–1888.

Tong, Y. C., Blamey, P. J., Dowell, R. C., and Clark, G. M. (**1983**). ''Psychophysical studies evaluating the feasibility of a speech processing strategy for a multiple-channel cochlear implant,'' J. Acoust. Soc. Am. **74,** 73–80.

Tong, Y. C., Clark, G. M., Blamey, P. J., Busby, P. A., and Dowell, R. C. (**1982**). ''Psychophysical studies for two multiple-channel cochlear implant patients,'' J. Acoust. Soc. Am. **71,** 153–160.

Townshend, B., Cotter, N., Van Compernolle, D., and White, R. L. (**1987**). ''Pitch perception by cochlear implant subjects,'' J. Acoust. Soc. Am. **82,** 106–115.

White, M. W., Merzenich, M. M., and Gardi, J. N. (**1984**). ''Multichannel cochlear implants. Channel interactions and processor design,'' Arch. Otol. **110**, 493–501.

Integrality in the perception of tongue root position and voice quality in vowels

John Kingston
Linguistics Department, South College, University of Massachusetts, Amherst, Massachusetts 01003

Neil A. Macmillan
Psychology Department, Brooklyn College of the City University of New York, Brooklyn, New York 11210

Laura Walsh Dickey,[a] Rachel Thorburn, and Christine Bartels
Linguistics Department, South College, University of Massachusetts, Amherst, Massachusetts 01003

(Received 5 December 1995; revised 25 June 1996; accepted 23 October 1996)

In English and a large number of African and Southeast Asian languages, voice quality along a tense–lax dimension covaries with advancement of the tongue root in vowels: a laxer voice quality co-occurs with a more advanced tongue root. As laxing the voice increases energy in the first harmonic relative to higher ones and advancing the tongue root lowers F_1, the acoustic consequences of these two articulations may integrate perceptually into a higher-level perceptual property, here called spectral ''flatness.'' Two Garner-paradigm experiments evaluated this interaction across nearly the entire range of tense–lax voice qualities and a narrow range of F_1 values. The acoustic consequences of laxness and advanced tongue root integrated into spectral flatness for tenser and laxer but not for intermediate voice qualities. Detection-theoretic models developed in earlier work proved highly successful in representing the perceptual interaction between these dimensions. © *1997 Acoustical Society of America.* [S0001-4966(97)03203-7]

PACS numbers: 43.71.An, 43.71.Es, 43.71.Hw, 43.70.Fq [RAF]

INTRODUCTION

That minimally contrasting speech sounds differ along multiple dimensions challenges both phoneticians and psychophysicists. Phoneticians are challenged to explain why some patterns of multiple differences recur across languages but others do not. Psychophysicists are challenged to explain how the array of differences between sounds influences internal representations or processes in the listener. However, neither challenge can be met in a sufficiently general way alone. General psychophysical models of how an external stimulus relates to an internal category are one way of explaining why some arrays of differences recur across languages, and patterns that recur across languages reveal some of those psychophysical processes and representations which are likely to arise naturally in response to stimuli.

The specific questions addressed by this paper are: (1) do the many differences between minimally contrasting speech sounds interact perceptually?; (2) if they do, how do they interact? and finally; (3) does the way in which they interact contribute to explaining why these patterns recur across languages? Answers to all these questions require explicit and general psychophysical models of these interactions.

The phonetic and psychophysical challenges are taken up in turn below.

A. The phonetic challenge

Previous work examining perceptual interactions among arrays of differences that recur across languages has examined the multiple differences between vowels contrasting for height (Kingston, 1991; Hoemeke and Diehl, 1994; Kingston and Macmillan, 1995) and intervocalic stops contrasting for [voice] (Parker *et al.*, 1986; Kluender *et al.*, 1988; Diehl and Kingston, 1991; Kingston and Diehl, 1995; Diehl *et al.*, submitted). Here, the focus is on the interaction between a source and a filter property of vowels, specifically, between voice quality and the position of the tongue root.

Vowels articulated with advanced tongue root (ATR) are often also produced with a lax or breathy voice quality, whereas vowels articulated with retracted tongue root (RTR) are often produced with a tense or creaky voice quality. This covariation of voice quality with the position of the tongue root is observed in many but not all[1] languages in East and West Africa in which vowels harmonize for ATR/RTR [Hall *et al.*, 1974; Lindau, 1975, 1978, 1979; Jackson, 1988; see Denning, 1989, for an extensive literature review and Jacobsen (1978, 1980) for a more specific discussion of such facts in DhoLuo and other Nilotic languages].

An essentially similar pattern of covariation can be also be observed in the historical development of many Mon–Khmer languages of Southeast Asia, in which higher vowels have developed diachronically in syllables which originally had breathy or lax voice, while lower vowels developed in originally tense (or modal) voiced syllables (see Huffman, 1976 for a review). As raising the tongue body frequently entails advancing the tongue root as well (Perkell, 1969; Jackson, 1988), the Mon–Khmer pattern is fundamentally similar to that observed in the African languages.

Finally, tense vowels in American English have laxer voice qualities than their lax counterparts (Bloedel, 1994). Differences in tongue position between tense and lax vowels

[a]Now at the Max Planck Institut für Psycholinguistik, PB 130, Nijmegen, NL 6500 AH, The Netherlands.

resemble those between vowels contrasting for (ATR): lax vowels in English are produced with more retracted tongue roots than tense vowels (Perkell, 1969; Jackson, 1988), and Baer *et al.* (1988) report greater hyoglossus contraction, which will retract the tongue root, in lax than tense vowels. Thus, voice quality and tongue root position covary in a similar way in this language as in Southeast Asian and African languages described above.

There are two strong and thus easily falsified ways to explain these patterns of covariation between the position of the tongue root or body and the tension of the vocal folds. Voice quality could vary with tongue root position because one articulation is linked physiologically to the other. Alternatively, these articulations could be covaried by speakers because their acoustic consequences enhance one another's perceptual effects. (A third, far less easily falsified, and thus inherently weaker kind of explanation will be laid out after these two stronger kinds are developed.) These two explanations are not mutually exclusive: speakers may exaggerate the covariation between physiologically linked articulations in order to enhance the perceptual effects of each's acoustic consequences. They are laid out separately below to show how each might be falsified.

One way in which voice quality may depend physiologically on tongue root position is if the aryepiglottal ligament and membrane, which connect the tongue root to the arytenoid cartilages via the epiglottis, cause the arytenoids to slide forward slightly and/or rock slightly apart, slackening or separating the vocal folds enough to lax the voice, when the tongue's root is advanced or its body raised.[2] However, vocal fold tension cannot always depend physiologically on tongue root or body position because it is independently controlled in some languages; for example, in Dinka, a Nilotic language of Kenya, vowels may contrast independently for tense versus lax voice quality and advanced versus retracted tongue root position (Denning, 1989).

The perceptual explanation for covariation of voice quality and tongue root position is consistent with this independent control. The perceptual explanation is most compeling if the covarying articulations' acoustic correlates are similar enough psychoacoustically to integrate into higher-level perceptual properties. In this case, the contrast is enhanced because both articulations' correlates evoke the same psychoacoustic property, not simply because the minimally contrasting phonemes differ in more than one way. Laxing the voice increases energy in the first harmonic at the expense of higher ones and advancing the tongue root lowers F_1. Tense voice and a retracted tongue root have the opposite acoustic effects. The two articulations may thus be deliberately covaried in order to depress or elevate the energy concentration in the vowel's spectrum. This overall effect on energy distribution in the vowel's spectrum will be referred to henceforth as spectral ''flatness.'' [3] This perceptual explanation also extends readily to the covariation of lax or breathy voice with higher tongue positions in the Mon–Khmer languages and tenser vowel qualities in English because higher or tenser lingual articulations also lower F_1.

Independent contrast of voice quality and tongue root position like that observed in Dinka is not, furthermore, a problem for the perceptual explanation, which requires that the two articulations be independently controlled. Such control allows speakers to use the articulations as independent contrasts or to combine them in order to enhance a single contrast.

The most direct means of falsifying the perceptual explanation is to show that the perceptual integration of the acoustic consequences of the two articulations simply does not occur, that they instead remain perceptually separate.

In recent work using part of the paradigm used here, Li and Pastore (1995) have shown that whereas two source properties, F_0 and spectral tilt, of vowel-like stimuli do integrate, the source property spectral tilt remains perceptually separate from a filter property, namely the number of peaks in the filter spectrum. Li and Pastore go on to argue that source and filter properties should in principle not integrate because they convey different kinds of information; according to Li and Pastore, source properties convey speaker identity and other paralinguistic information, whereas filter properties convey the linguistic content of the message. This functional explanation for the separability that Li and Pastore found between source and filter properties is clearly wrong, e.g., the source property F_0 conveys linguistic contrasts of tone and intonation. Moreover, voice quality is contrastive in many languages of Africa and Southeast Asia. Nonetheless, Li and Pastore's psychoacoustic claim may still be correct. Perhaps, the common independence of source and filter variation—one can sing the same vowel at different pitches or different vowels at the same pitch—is sufficient for listeners to keep their acoustic consequences separate.

Fowler (1996) argues for source–filter separability on the grounds that their articulatory origins are independent. She argues, specifically, that because the F_0 perturbations caused by vowel (height) or consonant (voice) contrasts are articulatorily independent of the control of F_0 to convey tone or intonation contrasts, these effects on this source property can all be kept perceptually separate.

The demonstration below that the acoustic consequences of varying tongue root position and voice quality do after all integrate perceptually is accordingly of some general interest for models of speech perception, and disconfirms the claims of both Li and Pastore and Fowler that source and filter properties should remain perceptually separate.

Consider now the third, less easily falsified explanation for covariation between articulations. Any combination of multiple difference articulations could make a minimal contrast easier to perceive, on the principle that more than one difference makes a contrast easier to detect reliably than just a single difference. And it is also possible that listeners can readily learn an association between differences from the simple fact of their covariation, and that those differences need neither cohere psychoacoustically nor share a common articulatory origin. Their covariation may instead be quite arbitrary. For discussion of this kind of systematic if arbitrary covariation, see Ohala (1981).[4]

The difficulty with this kind of explanation is its weakness; if even arbitrary covariation is readily learned, then it is very difficult to falsify such a hypothesis. A relatively weak means of falsification would be to show that languages differ

far less from one another in what patterns of covariation they allow than a theory allowing arbitrary covariation would predict. If instead properties which are not acoustically similar covary in languages just as often as acoustically similar ones do, then this weaker sort of explanation would be sufficient to explain the facts. At present, too little is known and there is substantial dispute regarding the extent to which languages differ from one another in this regard (see Kingston and Diehl, 1994, 1995; and Nearey, 1995, for discussion and opposing points of view). This kind of explanation is more surely falsified by the fact that integration occurs with nonspeech analogues (Kingston and Diehl, 1995; Diehl *et al.*, submitted), for which no arbitrary association could have been learned; see the papers cited for fuller discussion.

B. The psychophysical challenge

What is needed to meet the psychophysical challenge is: (1) a paradigm for assessing perceptual interactions between the multiple stimulus dimensions; and (2) a way to model the responses obtained from observers with that paradigm which will show whether variation along one dimension influences perception of differences along another, and if so, quantifying that influence.

The Garner paradigm (Garner, 1974) was devised as a test of perceptual interaction, or *integrality*, used here to refer to the degree to which an observer's perception of one dimension of a multidimensional stimulus is influenced by the value of another, physically orthogonal dimension: Integrality contrasts with *separability*, in which the percept of one dimension does not influence the percept of the other. To apply the paradigm, a stimulus array is constructed by varying two stimulus dimensions orthogonally and listeners are required to classify various subarrays from the array.

Our previous work used a detection-theoretic model of performance in the Garner paradigm tasks (Kingston and Macmillan, 1995; Macmillan and Kingston, 1995; also Kingston and Diehl, 1995; Diehl *et al.*, submitted) to investigate perceptual integration of the acoustic correlates of pairs of potentially independent articulations. That model is also used to interpret the two experiments reported here, and to test our principal hypothesis: that the acoustic correlates of voice quality and tongue root position integrate perceptually into the flatness property.

With respect to voice quality, this hypothesis was tested quite generally, in that the stimulus arrays used in the two experiments spanned a range from very tense to very lax voice qualities. On the other hand, the range of F_1 frequencies used to simulate differences in tongue root position was confined to a rather narrow range of intermediate values. Nonetheless, this is the part of the range that is of interest, for if any vowels contrast in a language for tongue root position, it is the mid vowels (Hall *et al.*, 1974), and these vowels have F_1 values in the intermediate range used here. One might even expect that variation in voice quality could alter the flatness percept only when the vowel's F_1 is neither especially high nor low, because the more extreme F_1 values saturate the effect.

The interval between adjacent stimuli along each dimension was kept small, to a just noticeable difference, so that variation in accuracy could be used to assess the perceptual interaction between voice quality and tongue root position. Detection theory was used to construct perceptual representations of the stimulus array, and to quantify the extent to which varying one dimension distorts the percept of the other.

I. METHODS

A. Stimuli

The two experiments used similar ranges of F_1 values, but differed in what part of the voice quality continuum was paired with F_1: in the TENSE experiment, voice quality ranged from very tense to the middle of the tense–lax continuum, whereas in the LAX experiment, voice quality ranged from the middle of the tense–lax continuum to very lax. Overlap between the lax stimuli in the TENSE experiment and the tense stimuli in the LAX experiment allowed us to combine the two experiments' results in mapping the perceptual interaction between F_1 and laxness over virtually the entire tense–lax continuum.

All stimuli were synthesized with the KLSYN88 terminal analogue synthesizer (as implemented in Sensyn; Klatt and Klatt, 1990; see also Maddieson and Ladefoged, 1985; and Huffman, 1987 for data on the phonetics of voice quality contrasts). Variation in tongue root position was implemented through manipulation of F_1, and variation in voice quality (VQ) through manipulation of the percentage or quotient of the glottal cycle in which the glottis was open (OQ) and the overall tilt of the source spectrum (ST). ST is expressed in terms of the number of additional dB the source spectrum's intensity has fallen off by 3 kHz, beyond the default fall-off of -6 dB/octave. The two parts of Table I below list the four values employed for each parameter in the two experiments (see also Fig. 1). Advancement of the tongue root varies inversely (right-to-left in this table) with F_1 and is coded by the letters A–D. Laxness of the voice varies directly with OQ and ST (bottom-to-top) and is coded by the numbers 1–8.[5]

The steps along each dimension were approximately a just-noticeable difference (jnd) at 70%–80% correct, and were determined by extensive pretesting of the stimuli with the listeners from whom the data were collected. Note that a smaller range of F_1 values, with smaller steps between adjacent values was used in the TENSE than the LAX experiment. The other synthesis parameters (listed in the Appendix) were set so as to create a syllable of the shape [bVb], whose vowel was mid to high back in quality, i.e., ranging from [ɔ] as in ''baulk'' or [ʌ] as in ''buck'' to [ʊ] as in ''book.'' The vowel's steady state varied across the values in Table I.

To undermine our listeners' ability to memorize particular stimulus tokens and thus prevent them from responding to dimensions other than those varied systematically, three different variants of each stimulus were created in which the peak amplitude in the vowel's steady-state relative to the rest of the stimulus was 59, 60, or 61 dB. Each variant occurred equally often but randomly in a block of trials.

TABLE I. The 4×4 stimulus arrays used in the TENSE (bottom) and LAX (top) experiments, with the manipulated parameter values in the vowel steady states: *A* to *D*=F_1 values, and 1 to 4 and 5 to 8=Ten(se) to Int(ermediate) and Int to Lax *VQ* values for the TENSE and LAX experiments, respectively.

	LAX *VQ*		F_1			
			Advanced			Retracted
	Open quotient %	Spectral tilt dB	470	484	499	514
Lax	90	−23	*A*8	*B*8	*C*8	*D*8
	72	−17	*A*7	*B*7	*C*7	*D*7
	54	−11	*A*6	*B*6	*C*6	*D*6
Int	42	−7	*A*5	*B*5	*C*5	*D*5
	TENSE *VQ*		F_1			
			Advanced			Retracted
	Open quotient	Spectral tilt	450	477	506	536
Int	53	−11	*A*4	*B*4	*C*4	*D*4
	39	−6	*A*3	*B*3	*C*3	*D*3
	33	−4	*A*2	*B*2	*C*2	*D*2
Ten	29	−3	*A*1	*B*1	*C*1	*D*1

B. Listeners

Two different groups of eight listeners were recruited from the undergraduate student population at the University of Massachusetts, Amherst. In each experiment, listeners were chosen from a larger pool of 10–12 listeners tested. To participate in the experiment a listener was required, within 5–6 h of pretesting, to reach 70%–80% correct in classifying stimuli that differed by a single step along a single dimension for both the F_1 and *VQ* dimensions. No listener in the TENSE experiment participated in the LAX experiment. None reported any speech or hearing pathology, and all were native speakers of English. All were paid for their time. As all listeners went through at least two 2-h pretesting sessions, and were trained on each task (see Sec. II D below for task descriptions) before any data were collected, they can be considered to be well practiced with the stimuli and procedures.

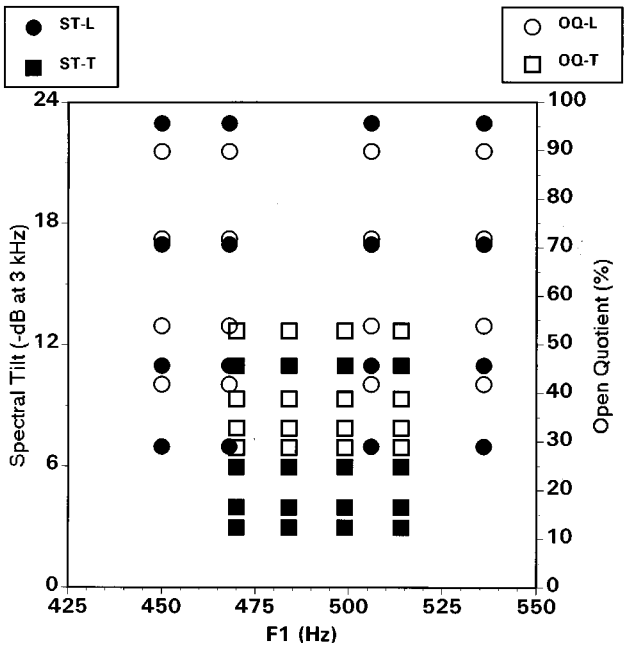

FIG. 1. Values of F_1 in Hz (horizontal axis) against spectral tilt in number of dB down at 3 kHz (left axis, filled symbols) and against open quotient in percent (right axis, open symbols) for the TENSE experiment (squares) and the LAX experiment (circles).

C. Procedures

In all tasks in both experiments, a single stimulus was presented on each trial, and the listener gave one of two responses. The listener also made a confidence judgment, on a 1–4 scale, where 1 indicated guessing, 4 certainty, and 2 and 3 intermediate levels of confidence. In all tasks, feedback as to the correct response was given at the end of the trial. A trial included the stimulus, a 2000-ms interval to give the response, a rapid triplet of tones to prompt the confidence judgment, 1500 ms to make the confidence judgment, a 500-ms feedback light, and then 2000 ms before the next trial began.

Listeners sat in a quiet room in partial isolation from other listeners in their group of four. They heard the stimuli binaurally through TDH-49 headphones, and were allowed to adjust the stimulus level individually to a comfortable and clearly audible value. They responded and gave confidence judgments by pushing appropriate buttons on a four-button response box. In addition to their responses and confidence judgments, reaction times to the responses were also recorded, to 1-ms accuracy.[6] Listeners were instructed to respond as accurately as possible, but were also told that puzzling over their answer would not help so they should also respond quickly.

In the LAX experiment, which was run first, a block of trials consisted of 16 orienting trials in which the stimuli

alternated systematically between the values relevant to the task tested in that block, followed by 96 test trials in which stimuli were presented in random order. All stimuli occurred equally often. One such block was run for tasks in which two stimulus types had to be classified, and two consecutive blocks were run for those in which four had to be. As the first six test trials were treated as further practice and were omitted from scoring, performance is assessed on the basis of 45 trials/stimulus/listener for each task in that experiment. The TENSE experiment used shorter blocks: 12 alternating orienting trails followed by 66 randomly ordered test trials. However, each condition was run twice, once early in the series of days allotted to that task type and once late. Again, two-stimulus blocks were run just once, and four-stimulus tasks twice. As the first 6 test trials in every block were again omitted from scoring, performance is assessed in the TENSE experiment from 60 trials/stimulus/listener in each task, an increase of one-third over the LAX experiment.

Each block lasted 9–12 min. Listeners heard 7–9 such blocks within each of three 1.5–2 h sessions per week. Each experiment required some 6–8 weeks to complete after initial jnd determination and training were complete.

D. Classification tasks

In both experiments, listeners classified stimuli from all 2×2 subarrays of adjacent stimuli in the 4×4 arrays; an example subarray from the TENSE experiment is stimuli *A*3, *B*3, *A*2, *B*2, and an example from the LAX experiment is stimuli C8, D8, C7, D7. In a block of trials, stimuli were classified according to one of the three rules or ''tasks'' ordinarily run in the Garner paradigm. In two of the tasks, just two stimuli were presented in a block of trials: (1) in *single-dimension* fixed classification tasks, stimuli were classified according to differences along just a single dimension, e.g., *A*3 vs *A*2 or *C*8 vs *D*8; and (2) in *correlated* fixed classification tasks, stimuli were classified according to correlated differences along both dimensions, e.g., *A*2 vs *B*3 or *C*8 vs *D*7. In the third task, *roving* classification, all four stimuli were presented in a block and were categorized according to their differences along one dimension, ignoring the other, e.g. *C*8 and *D*8 vs *C*7 and *D*7, or *A*2 and *A*3 vs *B*2 and *B*3.[7]

There are 12 single-dimension tasks along each dimension of the 4×4 array used in each experiment, e.g., for *VQ* differences *B*1 vs *B*2 (TENSE experiment) or *B*7 vs *B*8 (LAX experiment) and for F_1 differences *A*4 vs *B*4 (TENSE) or *C*6 vs *D*6 (LAX). In the correlated tasks, F_1 and tenseness of *VQ* could covary either ''negatively,'' e.g., *C*1 vs *D*2 (TENSE) or *A*7 vs *B*8 (LAX), or ''positively,'' e.g., *A*4 vs *B*3 (TENSE) or *C*6 vs *D*5 (LAX); there are nine such tasks for each correlation polarity in each 4×4 array. There are also nine roving classification tasks for each dimension in each 4×4 array, e.g., for *VQ* in the TENSE experiment, *A*2 and *B*2 vs *A*3 and *B*3 or for F_1 in the LAX experiment, *B*5 and *B*6 vs *C*5 and *C*6.

Both experiments began with the fixed classification tasks; single-dimension and correlated variants were run on alternate days. The roving classification tasks were run after all the fixed classification tasks were complete. At the beginning of each of these two phases in each experiment, listeners were trained for a day or two on the characteristics of the new tasks before any data were collected. To pseudorandomize task order, the eight listeners in each experiment were divided into two groups of four each and the tasks were run in one order for one group and in the opposite order for the other. In addition, the order in which 2×2 subarrays were run within a day was systematically mixed.

II. PSYCHOPHYSICAL ANALYSIS

A. Parallelogram models of mean integrality

1. Two-stimulus, fixed classification

As in our previous work (Kingston and Macmillan, 1995), detection theory (Green and Swets, 1966; Macmillan and Creelman, 1991) was used to model differences in our listeners' performance across tasks. The stimuli were designed to be imperfectly discriminable (70%–80% correct in single-dimension classification), and the principal measure was how accurately listeners sorted the stimuli into the classes defined by each task.

Detection theory assumes that the observer's accuracy can be represented as a map of the stimulus space onto a *decision space*, which in this application is taken to have two dimensions. Each stimulus has an average location in the space, but various sources of noise produce trial-to-trial variability on both dimensions, and the stimuli's perceptual values thus form bivariate distributions of response likelihood. In performing a specific task, the observer divides the space into regions corresponding to each response.

Because d' is a measure of the perceptual distance between the means of the corresponding distributions, in units of their standard deviation,[8] the d' values from the fixed classification tasks for a particular 2×2 subarray can be used to construct a quadrilateral representing the perceptual map of those four stimuli onto the decision space. The lengths of the sides of the quadrilateral are equal to the d' values for the four single-dimension classifications, the lengths of the diagonals to the d' values for the two correlated classifications. When the differences in performance on parallel single-dimension classifications are small (see Sec. III B below for assessment), the corresponding d' values can be averaged, so that the resulting quadrilateral is a parallelogram, as sketched in Fig. 2.

Figure 2 shows two possible maps from the stimulus to decision space. In these maps, points represent the means of the distributions, and circles contours of equal likelihood (a circle is the correct shape, for any likelihood, if the distributions are equal variance, uncorrelated, bivariate normal). The top panel's rectangular arrangement of the means in the decision space maps the case in which the perceptual value of a stimulus on one dimension does not depend on its value on the other, and the dimensions are *separable*. In the lower panel, the means of the distributions are no longer arranged rectangularly, and the value of a stimulus on one dimension does depend on its value on the other. Maddox (1992) labeled this particular violation of independence ''mean-shift integrality''; we have adopted the shorter term ''mean integrality'' (Kingston and Macmillan, 1995; Macmillan and

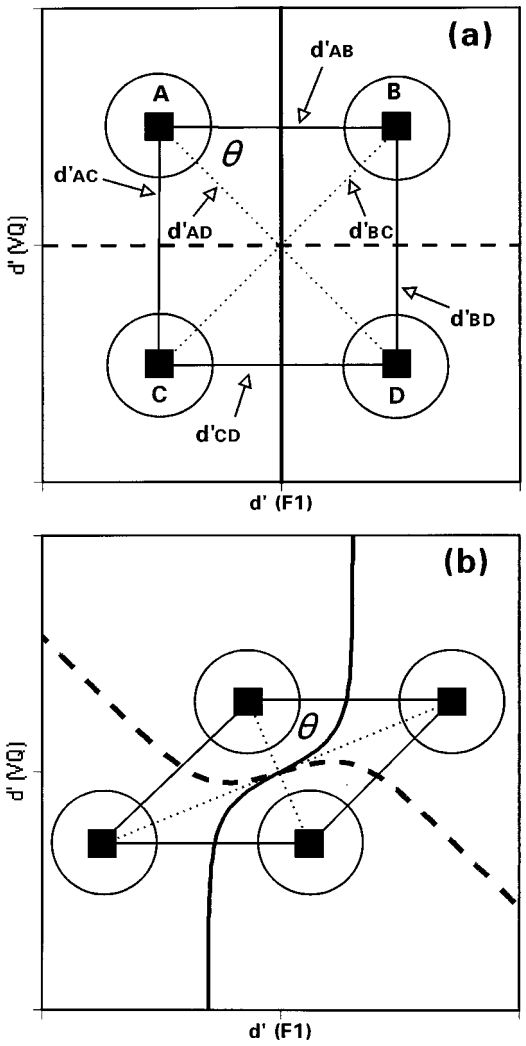

FIG. 2. (a) Rectangular versus (b) nonrectangular parallelograms for separable and mean-integral dimensions, respectively. θ represents the upper lefthand angle, which is used to estimate the degree of mean integrality. Thin, solid lines making up the sides of the parallelograms represent single-dimension d' values, thin, dotted lines the correlated d' values, as indicated in (a). Optimal criteria for the roving classification task are represented by thick lines: solid for F_1 and dashed for VQ.

Kingston, 1995). Comparing the two panels of this figure reveals that it is the (in)equality of the diagonals of the parallelogram, i.e., (in)equality of performance on the two correlated tasks in a 2×2 subarray, that determines whether the stimulus dimensions are perceptually separable or mean integral. The parallelogram representation permits calculation of a statistic that reflects the degree of mean integrality: the size of the angle of one of the parallelogram's corners; the angle in the upper left-hand corner was arbitrarily chosen. This value, referred to as θ, is 90° when the stimulus dimensions are perceptually separable but deviates from this value when they are integral. It is less than 90° when the negatively correlated task is easier than the positively correlated and greater than 90° when the difference in correlated difficulty is reversed.

According to Garner's (1974) original conception, dimensions are *separable* when classification of stimuli in which the two dimensions are correlated is no easier than single-dimension classification, and classification of stimuli with respect to one dimension while the other is roved irrelevantly is no harder than single dimension. Dimensions are integral when correlated classification is better, a *redundancy gain*, and roving classification worse, a *filtering loss*, than single-dimension classification.

In using the difference between performance on the two correlated tasks to indicate integrality, our model differs essentially from Garner's. Our models (Kingston and Macmillan, 1995; Macmillan and Kingston, 1995), following the analysis of Ashby and Townsend (1986), predict that average correlated performance will exceed average single-dimension even for the rectangular arrangement of the stimuli in the decision space, i.e., when the dimensions are separable. Simple geometric calculations show that mean correlated performance will always exceed mean single-dimension performance, but that the amount of the excess depends on both θ and the ratio of sides of the parallelogram sides.[9]

2. Filtering loss in roving classification predicted from mean integrality

The parallelogram representation can be used to predict performance on roving classification. In making this prediction, an optimal criterion is assumed, one composed of the locus of points with a likelihood ratio of 1, representing the case in which observations are equally likely to arise from either pair of distributions. (Optimal criteria are represented by thick lines in Fig. 2.) Under this assumption, no filtering loss is predicted with separable dimensions, because the optimal criterion is the same for roving classification as for single-dimension classification: a vertical or horizontal line perpendicular to the relevant dimension and parallel to the irrelevant dimension of the perceptual rectangle [Fig. 2(a)].

However, when the parallelogram is not a rectangle and the dimensions are instead mean integral [Fig. 2(b)], the optimal criteria in roving classification are no longer perpendicular to the stimulus dimensions. Instead, the optimal criterion for, say, roving classification by F_1 differences [thick solid line in Fig. 2(b)] approaches the perpendicular bisector of the line between the means of response distributions at the top of the parallelogram for large positive values of VQ, passes through the center of gravity of the parallelogram, and approaches the perpendicular bisector of the line between the means of the response distributions at the bottom of the parallelogram for large negative values of VQ. The criterion for roving classification by VQ differences [thick dashed line in Fig. 2(b)] similarly passes through the parallelogram's center of gravity and approaches the bisectors of the right and left sides of the parallelogram for large positive and negative values of F_1.

According to these optimal rules, roving classification should not be as good as in the corresponding single-dimension conditions. The size of the decline in performance resulting from mean integrality can be predicted for any parallelogram (Macmillan and Kingston, 1995): the magnitude of the predicted decline increases as θ diverges from 90°, and the effect is greatest when the two single-dimension sensitivities are equal.

TABLE II. Mean d' (se) across listeners for single-dimension *VQ* classification. In this and all subsequent tables, a space separates the results of the LAX experiment at the top from those of the TENSE experiment at the bottom.

	Low	F_1 level		High
VQ pair	*A*	*B*	*C*	*D*
7–8	1.72 (0.33)	1.30 (0.24)	1.26 (0.25)	0.96 (0.31)
6–7	3.10 (0.27)	2.73 (0.21)	2.69 (0.30)	3.14 (0.49)
5–6	1.52 (0.39)	0.98 (0.34)	0.53 (0.14)	0.14 (0.07)
3–4	3.07 (0.25)	3.21 (0.28)	2.63 (0.28)	2.13 (0.31)
2–3	1.18 (0.26)	1.98 (0.31)	1.98 (0.25)	1.05 (0.17)
1–2	1.15 (0.19)	1.62 (0.20)	1.50 (0.19)	1.44 (0.19)

Garner (1974) also predicts a decline in performance in roving classification as compared to fixed classification for integral dimensions, but for different reasons. In his model, irrelevant variation of one of two integral dimensions *interferes* with the observer's ability to detect that stimuli actually have the same value with respect to the relevant dimension. In other words, integrality interferes with ''filtering'' out of the perceptual effects of a stimulus value for the irrelevant dimension in judging its value for the relevant one. Moreover, Garner's model predicts filtering losses will be equally large for all the stimuli in the array, whereas the parallelogram model predicts an asymmetry: with the perceptual map in Fig. 2(b), filtering loss will be greater for stimuli *A* and *D* than for *B* and *C*. The extent of this asymmetry increases with the degree of mean integrality.

3. Testability of accuracy models

Assuming that the same perceptual representation underlies decisions in all tasks run with a particular 2×2 subarray and that decision criteria are optimal, performance in one correlated and both roving classifications can be predicted from performance in the single-dimension tasks and the other correlated condition. In addition, the more mean integral the dimensions are, the greater filtering loss for stimuli along the shorter than the longer diagonal in roving classification, so measuring this asymmetry serves as a further test of the model. The method introduced by Marascuilo (1970) for determining whether two d' values differ significantly from one another is also used throughout the following discussion in assessing the model's representation of these data, at the level of individual listeners.

B. Response times and their relation to perceptual distance

In most applications of the Garner paradigm, differences in task performance and thus the separable-integral question are assessed in terms of differences in response time (RT) rather than accuracy because the stimuli in single-dimension classification differ by many jnds rather than just one. Although the use of RTs leads naturally to interpretation of the results in terms of processes rather than the representations, Ashby, Maddox, and their colleagues (Ashby and Maddox, 1994; Ashby *et al.*, 1994) have recently put forward the ''RT-distance hypothesis''; time to respond in classifying a single stimulus is an inverse function of its distance from the criterion. The RT-distance hypothesis predicts that RTs and d' values correlate inversely, a prediction tested below.

III. RESULTS

A. Performance as a function of dimensions, tasks and subarrays

1. Accuracy

Tables II and III show mean performance on single-dimension classification for *VQ* and F_1, respectively, for each 2×2 subarray in the two experiments. The differences in performance in classifying individual stimulus pairs for differences on these dimensions are to some extent a function of their physical separation in the stimulus parameter space: differences in the voice quality parameters account for 22.4% of the variance in performance on *VQ* classification and differences in F_1 for 37.5% of the variance on F_1 classification. Preliminary stimulus evaluation clearly overestimated jnds for some stimulus pairs. An advantage of our detection-theoretic approach (Sec. III B) is that exactly equal perceptual spacing is unnecessary.

Table IV shows the results of the roving classification task for both *VQ* and F_1 differences. Performance varies between 2×2 subarrays in essentially the same way as in single-dimension classification, but comparison with Tables II and III shows a noticeable decline: for *VQ* differences roving performance is 0.67 of single-dimension in the TENSE experiment and 0.53 in the LAX experiment; for F_1 differences these proportions are 0.61 and 0.77, respectively.

Performance on the positively and negatively correlated tasks is displayed separately in each pair of cells in Table V.

TABLE III. Mean d' (se) across listeners for single-dimension F_1 classification.

		F_1 pair		
VQ level		*A*–*B*	*B*–*C*	*C*–*D*
Lax	8	2.23 (0.38)	1.70 (0.19)	2.88 (0.43)
	7	3.29 (0.48)	2.74 (0.37)	2.61 (0.39)
	6	1.76 (0.37)	2.84 (0.48)	2.52 (0.42)
	5	2.94 (0.60)	2.31 (0.41)	2.87 (0.40)
	4	2.02 (0.28)	1.05 (0.23)	0.93 (0.19)
	3	2.08 (0.20)	2.52 (0.21)	1.77 (0.28)
	2	2.69 (0.25)	1.97 (0.22)	1.21 (0.25)
Tense	1	2.85 (0.25)	1.67 (0.26)	1.14 (0.22)

TABLE IV. Mean d' (se) across listeners for VQ and F_1 roving classification.

	F_1 pair					
	$A-B$		$B-C$		$C-D$	
VQ pair	VQ	F_1	VQ	F_1	VQ	F_1
7–8	0.94 (0.38)	3.25 (0.46)	1.05 (0.21)	2.17 (0.35)	0.70 (0.12)	2.18 (0.39)
6–7	1.47 (0.20)	1.56 (0.23)	1.08 (0.25)	1.19 (0.36)	1.57 (0.11)	1.57 (0.33)
5–6	0.50 (0.21)	1.17 (0.25)	0.47 (0.18)	1.87 (0.32)	0.18 (0.11)	2.90 (0.48)
3–4	2.47 (0.29)	0.90 (0.21)	2.17 (0.28)	0.44 (0.11)	1.77 (0.32)	0.52 (0.09)
2–3	0.68 (0.16)	1.60 (0.21)	1.06 (0.19)	1.59 (0.17)	0.79 (0.11)	0.85 (0.15)
1–2	0.58 (0.12)	1.77 (0.19)	0.83 (0.12)	1.30 (0.26)	1.13 (0.15)	0.95 (0.17)

Performance is noticeably better when tenseness of voice quality correlates positively with F_1 than when these dimensions correlate negatively, except for intermediate voice qualities (row pairs 3–4 and 5–6).

2. Correlation between accuracy and response times

The correlation between mean RTs and d' values across all tasks and subarrays is -0.79, indicating a very strong tendency for more accurate responses to be faster. A straight line fitted to a plot of mean RT values against mean d' values indicates that RT is reduced 85 ms for each unit increase in d'; this line accounts for 62% of the variance in RT values. These results thus accord well with Ashby and Maddox's RT-distance hypothesis.

B. Parallelogram models of fixed classification

Parallelogram representations of the data for each 2×2 subarray are displayed in Fig. 3. In each panel, the vertical sides of the parallelogram have length d'_{VQ} (the average d' in the two VQ fixed classifications for the same subarray) and the other two sides have length d'_{F_1} (the average d' in the two F_1 fixed classifications). The correlated d' values correspond to the diagonals of the parallelogram. Iteration was used to find the value of θ that provided the best fit to all six d' values.

The extent to which the correlated and single-dimension data fit the same parallelogram is one test of the model. Each observed and predicted d' was converted to proportion correct $p(c)$ (assuming no bias) and the rms error computed; rms errors are listed next to the value of θ in each panel of Fig. 3. By this measure, the fit of the parallelogram model was good: in $p(c)$ units, rms errors averaged just 0.020 in the LAX experiment and 0.011 in the TENSE experiment. The halving of the error in the latter probably resulted from the one-third increase in the number of trials per point and the more extensive pretesting and training of listeners.

The appropriateness of fitting a parallelogram (rather than an irregular quadrilateral) can be assessed, by comparing d' values for parallel single-dimension tasks, because fitting a parallelogram assumes they should be equally easy. As there are nine 2×2 subarrays to which parallelograms could be fit and eight listeners in each experiment, each allows 72 comparisons for each dimension, VQ and F_1. Assuming $\alpha=0.05$, in the TENSE experiment, d' values for parallel VQ tasks were significantly different four (6%) times, and for F_1 eight (11%) times; in the LAX experiment, there were eight (11%) significant differences for both VQ and F_1. (If $\alpha=0.10$, these scores are 7, 11, 9, and 17, respectively.) Therefore, in just under 10% of the cases overall, the parallelogram assumption is incorrect (if $\alpha=0.10$, this rises to just over 15%). Violations do not cluster in any region in either $F_1\times VQ$ array. This success suggests that the parallelogram models provide a good fit to the data.

The observed values of θ, the degree of mean integrality, are either less than or greater than 90°, indicating mean integrality of F_1 and VQ. In the TENSE experiment, 24/72 (33%) comparisons of positively versus negatively correlated d' values were significantly different at $\alpha=0.05$, an additional 5 more at $\alpha=0.10$ [total 29 (40%)], and in the LAX experiment, 31 (43%) were significantly different at $\alpha=0.05$, an additional 2 more at $\alpha=0.10$ [total 33 (46%)].

As would be expected from the figure (but from not any *a priori* theorizing), the dimensions integrate quite differently at more tense or lax than at intermediate voice quali-

TABLE V. Mean d' (se) across listeners for positively and negatively correlated classification.

	F_1 pair					
	$A-B$		$B-C$		$C-D$	
VQ pair	Positive	Negative	Positive	Negative	Positive	Negative
7–8	3.80 (0.34)	2.15 (0.36)	4.10 (0.26)	3.57 (0.22)	3.71 (0.37)	1.45 (0.40)
6–7	3.80 (0.33)	0.57 (0.27)	4.51 (0.03)	0.61 (0.32)	4.27 (0.16)	1.06 (0.40)
5–6	1.45 (0.40)	3.86 (0.28)	3.28 (0.40)	4.28 (0.09)	2.72 (0.54)	3.73 (0.27)
3–4	2.73 (0.29)	3.62 (0.24)	2.29 (0.23)	3.71 (0.22)	1.79 (0.24)	3.15 (0.31)
2–3	3.32 (0.22)	2.99 (0.25)	3.45 (0.20)	2.07 (0.24)	2.87 (0.27)	1.13 (0.21)
1–2	3.98 (0.09)	2.20 (1.31)	3.43 (0.20)	1.09 (0.15)	2.50 (0.23)	1.27 (0.20)

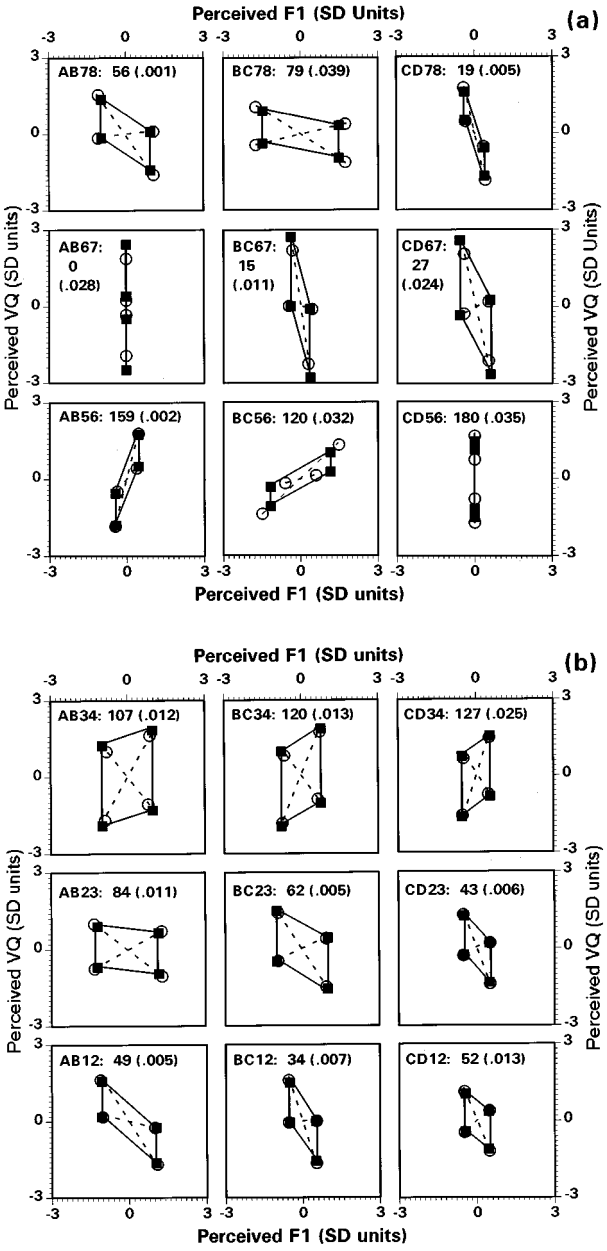

FIG. 3. Parallelograms fitted to single-dimension (filled squares) and correlated (open circles) classification data for each 2×2 subarray in the 4×4 arrays of the (a) LAX and (b) TENSE experiment. The letter–number pairs identifying each subarray denote their F_1 and VQ values, respectively. Solid lines represent the sides and dashed lines the diagonals of the parallelograms. The first number listed after the identifier is the θ (in degrees) for the parallelogram that best fits the two estimates. The rms errors in parentheses represent the discrepancy, in units of proportion (correct), between the baseline and correlated estimates of the locations of the corners of the parallelogram.

ties. The value of θ is systematically less than 90° for the more extreme voice qualities but greater than 90° for the intermediate ones: row pairs 1–2, 2–3 and 6–7, 7–8 [Fig. 3(a), AB67-CD78, Fig. 3(b) AB12–CD23] versus row pairs 3–4 and 5–6 [Fig. 3(a) AB56-CD56, Fig. 3(b), AB34–CD34]. Significant differences in positively versus negatively correlated d' values are also rarer for the intermediate than extreme voice qualities: in the TENSE experiment, row pairs 1–2 and 2–3 yielded 13/27 (48%) and 7 (26%) significant differences (α=0.05), respectively, whereas row pair 3–4 yielded only 3 (11%), and in the LAX experiment, row pair 5–6 yielded only 6 (22%) significant differences, whereas row pairs 6–7 and 7–8 yielded 19 (70%) and 6 (22%), respectively. VQ and F_1 are apparently more separable at intermediate than extreme voice qualities, although they are more nearly separable at the laxest voice qualities, too.

That θ>90° for the tenser and laxer voice qualities indicates that stimuli in which tenseness and F_1 covary positively are easier to classify at the two ends of the voice quality continuum. However, for intermediate voice qualities the direction of mean integrality is reversed with respect to either tenser or laxer voice qualities, because *negative* covariation between tenseness and F_1 makes classification easier in this part of the continuum. These reversals compared to more extreme voice qualities are far stronger in the LAX than TENSE experiment, despite the overlap in voice quality parameters values for the intermediate voice qualities in the two 4×4 arrays (see Table I and Fig. 1). In summary, our listeners apparently integrate F_1 and VQ differences in the predicted way, i.e., into the perceptual property called ''flatness'' at the more tense and lax extremes, but not in the middle of the tense–lax continuum.

C. Using the parallelograms to predict roving classification performance

1. Predicted versus observed filtering loss

Mean integrality predicts that performance on roving classification will be worse than that on single-dimension classification. When d' values obtained in roving classification are compared to the mean d' values obtained in the analogous single-dimension classifications, in the TENSE experiment 13/72 (18%) cases of VQ roving classification showed a significant (α=0.05) filtering loss as did 19 (26%) cases of F_1 classification; in the LAX experiment, significant filtering losses were obtained in 15 (21%) and 18 (25%) cases of VQ and F_1 roving classification, respectively. Overall, significant filtering losses were obtained in 23% of the cases. (At α=0.10, 18, 21, 19, and 20 cases, respectively, of significant filtering were obtained, a total of 27% overall.)

The loss predicted from the degree of mean integrality [in proportion correct $p(c)$ units] is listed in Table VI, together with the discrepancy between the observed and predicted loss. Predicted losses and discrepancies are listed for each dimension within each 2×2 subarray separately.

The magnitude of the predicted loss tends to be small, averaging in the TENSE experiment just 0.017 for F_1 and 0.018 for VQ and in the LAX experiment just 0.047 for F_1 and 0.060 for VQ. The amount of loss beyond that predicted from mean integrality is by contrast relatively large, in the TENSE experiment averaging 0.111 for F_1 and 0.081 for VQ and in the LAX experiment 0.048 for F_1 and 0.050 for VQ. Thus, the parallelogram model accounts for about 15% of the filtering loss in the TENSE experiment and about 52% in the LAX experiment. The additional loss may arise because roving variation along the irrelevant dimension increases the stimulus's variability and thus the listener's uncertainty about its value for the relevant dimension. This *variance integrality* is very like the interference to which

TABLE VI. Predicted loss in roving classification from mean integrality, and the discrepancy (in parentheses) between predicted and observed loss [both in $p(c)$ units]. A negative predicted loss indicates that roving is expected to be easier than single-dimension classification. A positive discrepancy indicates a loss greater than predicted, a negative one a lesser loss than predicted. Each 2×2 subarray is represented by a pair of cells, one above the other, representing predicted loss and discrepancies for the two dimensions of classification, cf. Table IV.

Exp.	VQ pair	Relevant dimension	F_1 pair A:B	B:C	C:D
LAX	7:8	F_1	0.017 (−0.050)	0.005 (0.036)	0.033 (0.017)
		VQ	0.021 (0.071)	−0.001 (0.070)	0.083 (−0.007)
	6:7	F_1	0.121 (0.001)	0.117 (0.070)	0.086 (0.035)
		VQ	0.112 (0.047)	0.124 (0.075)	0.084 (0.059)
	5:6	F_1	0.035 (0.157)	0.003 (0.114)	0.007 (0.001)
		VQ	0.084 (0.048)	0.010 (0.068)	0.026 (0.022)
TENSE	3:4	F_1	0.006 (0.169)	0.021 (0.220)	0.022 (0.172)
		VQ	0.002 (0.031)	0.012 (0.035)	0.015 (0.053)
	2:3	F_1	−0.007 (0.114)	0.010 (0.067)	0.024 (0.084)
		VQ	−0.001 (0.163)	0.018 (0.113)	0.028 (0.096)
	1:2	F_1	0.017 (0.094)	0.039 (0.044)	0.017 (0.034)
		VQ	0.028 (0.115)	0.045 (0.082)	0.015 (0.042)

Garner attributed any filtering loss (see also Maddox, 1992, on ''variance-shift integrality'') and will be explored in a subsequent paper.

2. Asymmetries in roving classification

The parallelogram model not only predicts a filtering loss in roving classification when the stimulus dimensions are mean integral but also a greater loss for the stimuli at the ends of the shorter than the longer diagonal. This asymmetry should furthermore be a function of θ's deviation from 90°.

Tables VII and VIII list d' values calculated separately for the stimuli along the two diagonals of each parallelogram for roving classification by VQ and F_1 differences, respectively. If the parallelograms in Fig. 3 correspond to the listener's perceptual representation of the stimuli in the 2×2 subarrays across tasks, then the differences in performance in roving classification between stimuli along the positive and negative diagonals should be in the same direction as the differences in the corresponding correlated tasks (Table V). This prediction holds for both dimensions because stimuli along the diagonals must be assigned to different classes in both roving classifications. The prediction is strongly upheld. In roving classification for F_1 differences (Table VIII), the asymmetries correspond to those in the correlated tasks in every 2×2 subarray in both experiments. The correspondence is nearly as good in roving classification for VQ differences (Table VII), where only 1 out of 18 2×2s shows the opposite asymmetry in roving than correlated classification: $C-D$×5–6 in the LAX experiment. In addition, the size of the asymmetry between positive and negative performance in roving classification correlates well with the deviation of θ from 90°: the correlation is 0.81 for F_1 and VQ differences combined, 0.87 for F_1 alone, and 0.77 for VQ alone. These results strongly support the contention that listeners employ the same perceptual representation in roving as fixed classification.

IV. DISCUSSION

The results of these experiments mix both a psychophysical and a phonetic loss among many wins.

Among the psychophysical wins can be counted the evidence that listeners use the same perceptual representations in roving as fixed classification, the very successful fit of the parallelogram models, the close agreement between RTs and accuracy, which qualitatively supports Ashby and Maddox's (1994) RT-distance hypothesis, and similarity in the listen-

TABLE VII. Mean d' (se) across listeners for positively and negatively correlated pairs in roving classification for VQ differences.

VQ pair	F_1 pair $A-B$ Positive	$A-B$ Negative	$B-C$ Positive	$B-C$ Negative	$C-D$ Positive	$C-D$ Negative
7–8	1.23 (0.37)	1.00 (0.45)	2.16 (0.45)	0.48 (0.25)	2.16 (0.28)	−0.07 (0.27)
6–7	3.15 (0.30)	0.41 (0.20)	2.51 (0.38)	0.27 (0.24)	3.01 (0.46)	0.49 (0.15)
5–6	0.10 (0.17)	1.01 (0.48)	0.64 (0.19)	0.77 (0.31)	0.65 (0.26)	−0.15 (0.25)
3–4	2.24 (0.29)	3.01 (0.28)	1.95 (0.36)	2.78 (0.29)	1.64 (0.30)	2.10 (0.38)
2–3	1.36 (0.22)	0.28 (0.20)	1.88 (0.26)	0.86 (0.24)	1.73 (0.20)	0.39 (0.18)
1–2	1.84 (0.31)	−0.26 (0.15)	1.51 (0.27)	0.19 (0.14)	1.60 (0.24)	0.71 (0.18)

TABLE VIII. Mean d' (se) across listeners for positively and negatively correlated stimulus pairs in roving classification for F_1.

	F_1 pair					
	$A-B$		$B-C$		$C-D$	
VQ pair	Positive	Negative	Positive	Negative	Positive	Negative
7–8	3.30 (0.40)	3.14 (0.41)	2.79 (0.33)	1.93 (0.35)	3.13 (0.44)	1.61 (0.33)
6–7	3.42 (0.31)	0.70 (0.27)	2.90 (0.28)	0.72 (0.28)	2.56 (0.34)	0.69 (0.37)
5–6	0.49 (0.18)	2.75 (0.46)	1.39 (0.35)	2.61 (0.45)	2.67 (0.46)	3.02 (0.41)
3–4	0.52 (0.29)	1.55 (0.24)	0.24 (0.22)	1.42 (0.18)	0.29 (0.29)	1.39 (0.29)
2–3	2.46 (0.30)	1.34 (0.29)	2.55 (0.26)	0.95 (0.20)	1.70 (0.26)	0.41 (0.12)
1–2	2.91 (0.24)	1.14 (0.22)	2.06 (0.34)	0.81 (0.26)	1.95 (0.26)	0.31 (0.17)

ers' responses to the overlapping portions of the two experiments' stimulus arrays. The most serious loss was that the parallelogram model substantially underestimated the filtering loss, especially in the TENSE experiment.

The principal phonetic win is finding the predicted direction of mean integrality at the extreme voice qualities, where positive correlation between tenseness and F_1 enhanced discriminability. For two-thirds of the stimuli in both experiments, voice quality and tongue root position apparently integrate perceptually into the property flatness. However, flatness differences clearly do not predict performance at intermediate voice qualities, as shown by the marked reversals in the direction of mean integrality there compared to laxer or tenser voice qualities.

A closer examination of the acoustics of the stimuli and their relation to listeners' performance hints at the basis for these reversals but does not explain them away. A useful acoustic correlate of flatness is the intensity differences (in

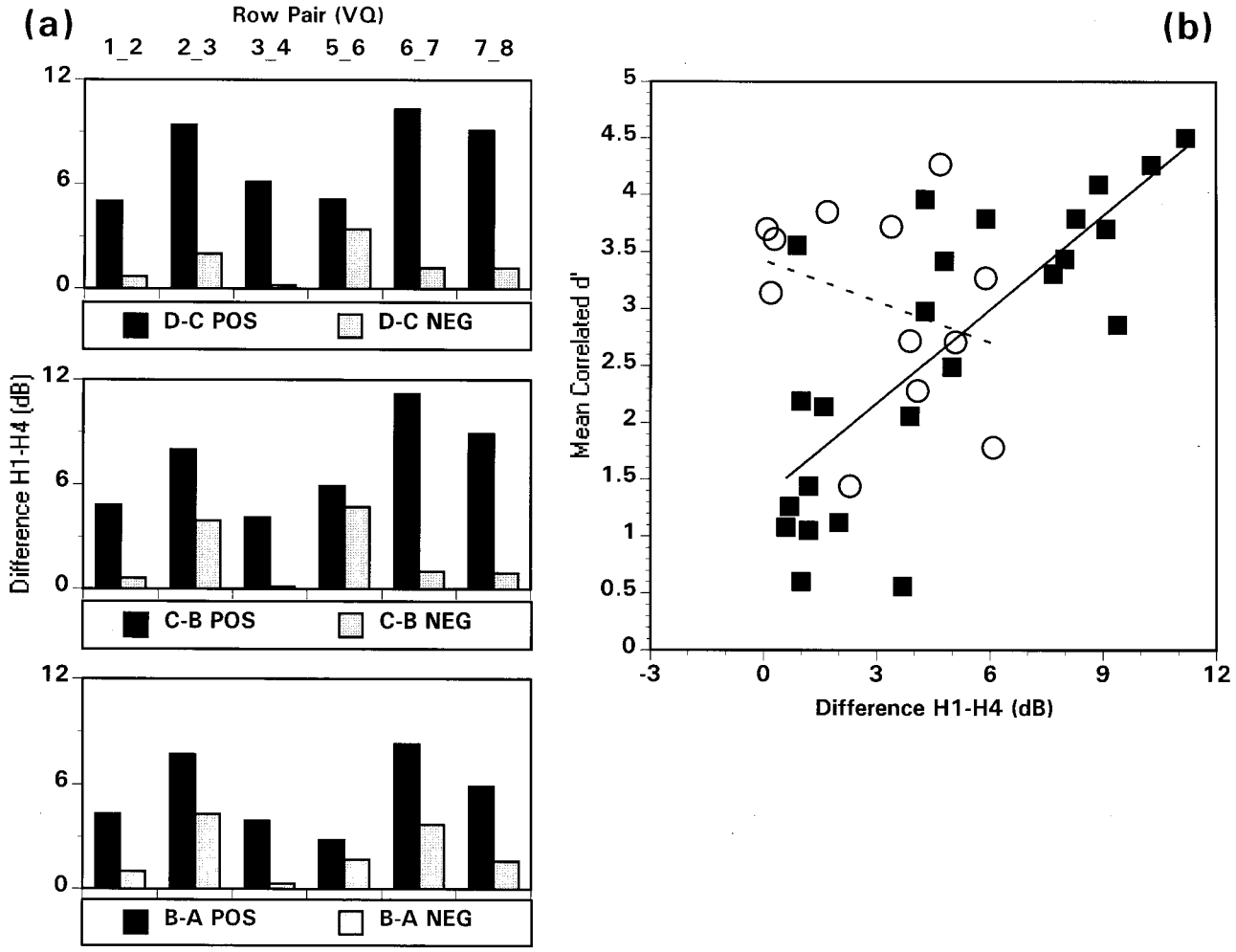

FIG. 4. (a) Difference between positively (black bars) and negatively (gray bars) correlated stimuli in the intensity difference between the first and fourth harmonics (H_1-H_4), in dB; F_1 decreases from top-to-bottom. (b) Mean d' values by differences in H_1-H_4. Stimulus pairs with extreme, i.e., tenser and laxer voice qualities (row pairs: 1–2, 2–3, 6–7, and 7–8) are plotted with filled squares, those with *intermediate* voice qualities (3–4 and 5–6) are plotted with open circles. A separate line is fitted to the *extreme* (solid) and intermediate (dashed) data in each case.

dB) between the first and fourth (H_1-H_4) harmonics, extracted from 1024 point (102.4 ms) FFTs centered on each vowel's midpoint (the center of gravity of the 0–1 kHz frequency interval in this spectrum was a similar measure). A laxer voice quality raises the intensity of H_1 relative to higher harmonics and a more advanced tongue root lowers F_1; the latter will affect H_4's intensity particularly, as that harmonic was closest in frequency to F_1. Thus, H_1-H_4 will be larger the flatter the vowel, and if flatness differences influence the listeners' performance then vowel pairs which differ more in this (or an analogous flatness measure such as center of gravity) should be easier to classify.

Figure 4(a) is a plot of magnitude of the difference in H_1-H_4 values between the members of positively versus negatively correlated vowel pairs in the two experiments, and shows that in all cases the positively correlated stimuli differ more than the negatively correlated ones in their H_1-H_4 values. This figure also shows, however, that the difference in magnitude is uniformly smaller at the intermediate (3–4 and 5–6) voice qualities than at tenser or laxer extremes. These smaller differences predict that if listeners were attending to flatness differences, performance on the negatively correlated task should be closer to that on the positively correlated task; i.e., weaker mean integrality or even separability should have been obtained at intermediate voice qualities. Fewer significant differences between positively and negatively correlated performance were found for intermediate voice than extreme voice qualities, but a problem remains.

By this acoustic measure, mean integrality should have been weaker for stimuli in the 5–6 row pair of the LAX experiment than in the overlapping 3–4 row pair in the TENSE experiment, but the results were quite the reverse. Not only was more evidence of separability obtained in the 3–4 row pair but the 5–6 row pair yielded exceptionally strong evidence of mean integrality in the *opposite* direction; i.e., θ values were markedly greater than 90°.

Figure 4(b), which plots mean d' values in the correlated tasks against the corresponding H_1-H_4 differences, shows the independence of correlated performance from flatness differences in another way. When just the mean d' values for extreme stimulus pairs (row pairs: 1–2, 2–3, 6–7, and 7–8; filled figures and solid line) are regressed against these differences, the percentage of variance accounted for is 58.9%. Mean d' increases by 0.274 units for each dB increase in the H_1-H_4 difference between the members of a stimulus pair. On the other hand, less than 1% of the variance is accounted for by the dashed line fitted to mean d' by H_1-H_4 differences for the intermediate voice qualities (row pairs: 3–4 and 5–6, open figures and dashed line).

This acoustic exploration shows that listeners probably only attend to flatness in judging these stimuli at the two ends of the voice quality continuum but not in its middle. These results furthermore predict that languages in which voice quality covaries with tongue root position would use either tense or lax extremes, because it is at the extremes that the flatness differences are greatest.[10] Because the acoustic correlates of voice quality differences interact with those of tongue root advancement so as to enhance the distinctiveness of vowels, their deliberate covariation is advantageous to speakers (and listeners).

Further work on the perceptual interaction between the acoustic correlates of voice quality and tongue root position is currently underway, to address some of the questions left unanswered in the current paper, and in hopes of turning what remain losses into wins. A subsequent paper will report how varying the range of variation of the relevant dimension, in complete identification of all four values of that dimension, affects accuracy compared to the two values that had to be identified in single-dimension fixed classification. Examining identification of the entire range of stimuli in an array may shed light on the reversal of mean integrality in the middle of the voice quality continuum. That paper will also examine the effects on filtering loss of increasing the range of irrelevant variation from just two to four values, and will thereby provide an account of variance integrality.

ACKNOWLEDGMENTS

We gratefully acknowledge the support for the work reported here obtained through Grant No. R-29-DC01708-2 from the National Institute of Deafness and Communicative Disorders, National Institutes of Health to the first author, and Grant No. DBS92-12043 from the National Science Foundation to the second author. Preliminary versions of this work were presented at the 127th and 129th meetings of the Acoustical Society of America (Thorburn *et al.*, 1994; Walsh *et al.*, 1995), at the 13th International Congress of Phonetic Sciences, Stockholm (Kingston *et al.*, 1995), to the Sound Seminar in the Linguistics Department, University of Massachusetts, and to the Linguistics Research group at AT&T Bell Laboratories; the comments of the audiences at all these presentations contributed positively to the preparation of this paper. In addition, the comments of our colleague José Benkí were very helpful at all stages in the writing of this paper. Finally, the comments of Keith Johnson and an anonymous reviewer have substantially improved this paper.

APPENDIX

Tables AI and AII below list the parameters that did not vary across the stimuli used in stimuli. Table AI shows the amplitude of voicing (AV) and F_0 profile, and Table AII the formant frequencies. A plateau occurs between points specified for the same value in adjacent cells in these tables, linear interpolation between points specified for different values in adjacent cells.

TABLE AI. Profile for amplitude of voicing (AV) and F_0 parameters for the stimuli used in both experiment I and experiment II. The middle row indicates roughly the correspondence of the inflection points in these profiles with the segments of the utterance.

Time (ms)	0	10	80	90	270	280	355	365
AV (dB)	0	48	48	60	60	48	48	0
Segments		*b*			*V*			*b*
Time (ms)		0	80	115	180	280		365
F_0 (Hz)		120	120	140	140	120		120

TABLE AII. Profiles of open quotient (OQ) in percent of glottal cycle, spectral tilt ($-$dB @ 3 kHz), formant frequencies for F_1-F_6, and corresponding bandwidths.

Time (ms)	0	75	115	245	280	365
OQ (%)	75	75			75	75
ST ($-$dB)	39	39	see Table I		39	39
F_1 (Hz)	180	180			180	180
F_2	700	700	1070	1070	700	700
F_3	1900	1900	2300	2300	1900	1900
F_4	3100	3100	3400	3400	3100	3100
F_5			3700			
F_6			4990			
Segments		*b*		*V*		*b*
Time (ms)	0	75	90	265	280	365
B_1 (Hz)	500	500	60	60	500	500
B_2	1000	1000	90	90	1000	1000
B_3	1000	1000	150	150	1000	1000
B_4	1000	1000	200	200	1000	1000
B_5	1500	1500	200	200	1500	1500
B_6			4000			

[1]Local (1995) reports that in Kalenjin (another Nilotic language) the pattern of covariation described above is reversed: a laxer voice quality occurs with retracted tongue root and vice versa. This counterexample does not nonetheless undermine the case made here, as a great many languages have been reported to have the pattern of covariation for which we seek an explanation. And in contrast to Local's description of Kalenjin, Tucker (1966) describes the advanced tongue root vowels as being produced with breathy voice and the retracted tongue root vowels with creaky voice in the Nandi–Kipsigis dialect of Kalenjin, and Hall *et al.* (1974) also report creaky voice as a correlate of the retracted tongue root vowels in the Elgyeo dialect. Although both reports rely on impressionistic rather than instrumental evidence, the difference between these descriptions and Local's suggests that at least some speakers of Kalenjin produce the more common covariation between tongue root position and voice quality.

[2]Another physiological linkage is the connection between the hyoid bone and the superior edges and superior cornua of the thyroid laminae. It is hard to imagine, however, how pulling the cornua forward when the hyoid bone is advanced in the tongue root would lax the voice.

[3]''Flat(ness)'' is obviously used here in a different sense than that of Jakobson *et al.* (1952) feature (flat), which represented the perceptual effect of the lowering of the second and higher formant frequencies brought about by the secondary articulations, labialization, velarization, or pharyngealization. See also Ohala (1985).

[4]We are grateful to Keith Johnson for making clear the necessity of discussing this third kind of explanation.

[5]Despite the large range of voice qualities used in each experiment, no listener reported, during the course of the experiment nor in debriefing afterwards, that any stimuli were unnatural or nonspeech-like.

[6]The clock started with the beginning of the stimulus, so RTs include the 365 ms of the stimulus. Also, any responses $\leqslant$100 ms or $\geqslant$2800 ms were excluded from the evaluation of speed or accuracy of response.

[7]Single-dimension fixed classification corresponds to the baseline task in traditional Garner nomenclature, and roving classification to the selective attention task; the correlated task is the same. The more revealing names used here are based on nomenclature introduced by Durlach *et al.* (1989).

[8]The d' value is expressed in standard deviation units because it is calculated from the z-score equivalents of the hit and false alarm proportions; see Macmillan and Creelman (1991).

[9]The 60–120° range of θ's predicts better mean correlated performance only if all four sides of the parallelogram are equal; i.e., the sides ratio as well as θ determine whether mean correlated performance will exceed single dimension performance (see Ashby and Townsend, 1986; Maddox, 1992; Macmillan and Kingston, submitted, for discussion and exemplification).

[10]Perhaps the Kalenjin speakers examined by Local (1995) use the middle of the voice quality continuum and may therefore reverse the direction of covariation observed elsewhere.

Ashby, F. G., Boynton, G., and Lee, W. W. (**1994**). ''Categorization response time with multidimensional stimuli,'' Percept. Psychophys. **55,** 11–27.

Ashby, F. G., and Maddox, W. T. (**1994**). ''A response time theory of separability and integrality in speeded classification,'' J. Math. Psychol. **38,** 423–466.

Ashby, F. G., and Townsend, J. T. (**1986**). ''Varieties of perceptual independence,'' Psychol. Rev. **93**, 154–179.

Baer, T., Alfonso, P. J., and Honda, K. (**1988**). ''Electromyography of tongue muscles during vowels in /əpVp/ environment,'' Ann. Bull. Res. Inst. Logoped. Phoniat., University of Tokyo, **7**, 7–18.

Bloedel, S. L. (**1994**). ''An analysis of the acoustic correlates of breathy phonation in the speech of adult men and women and pre-pubescent males,'' M.S. thesis, University of Wisconsin, Madison.

Denning, K. (**1989**). ''The diachronic development of phonological voice quality,'' Ph.D. dissertation, Stanford University.

Diehl, R. L., and Kingston, J. (**1991**). ''Phonetic covariation as auditory enhancement: The case of the [+voice]/[−voice] distinction,'' Perilus **15**, 139–143.

Diehl, R. L., Kingston, J., and Castleman, W. A. (**submitted**). On the internal perceptual structure of distinctive features: The [voice] distinction, J. Acoust. Soc. Am.

Durlach, N. I., Tan, H. Z., Macmillan, N. A., Rabinowitz, W. R., and Braida, L. D. (**1989**). ''Resolution in one dimension with random variations in background dimensions,'' Percept. Psychophys. **46,** 293–296.

Fowler, C. A. (**1996**). ''Listeners do hear sounds, not tongues,'' J. Acoust. Soc. Am. **99,** 1730–1741.

Garner, W. R. (**1974**). *The Processing of Information and Structure* (Erlbaum, Potomac, MD).

Green, D. M., and Swets, J. A. (**1966**). *Signal Detection Theory and Psychophysics* (Wiley, New York).

Hall, B. L., Hall, R. M. R., Pam, M. D., Myers, A., Antell, S. A., and Cherono, G. K. (**1974**). ''African vowel harmony systems from the vantage point of Kalenjin,'' Afrika und Übersee **57**, 241–267.

Hoemeke, K., and Diehl, R. L. (**1994**). ''Perception of vowel height: The role of $F1$-$F0$ distance,'' J. Acoust. Soc. Am. **96**, 661–674.

Huffman, F. E. (**1976**). ''The register problem in fifteen Mon–Khmer languages,'' in *Austroasiatic Studies I, Oceanic Linguistics Publication 15*, edited by P. N. Jenner, L. C. Thompson, and S. Starosta (University Press of Hawaii, Honolulu), pp. 575–590.

Huffman, M. K. (**1987**). ''Measures of phonation type in Hmong,'' J. Acoust. Soc. Am. **81,** 495–504.

Jackson, M. T. T. (**1988**). ''Phonetic Theory and Cross-Linguistic Variation in Vowel Production,'' University of California, Los Angeles, Working Papers in Phonetics No. 71.

Jacobsen, L. C. (**1978**). ''DhoLuo Vowel Harmony: A Phonetic Investigation,'' Univ. California, Los Angeles, Working Papers in Phonetics, No. 43.

Jacobsen, L. C. (**1980**). ''Voice quality harmony in Western Nilotic languages,'' in *Issues in Vowel Harmony*, edited by R. M. Vago (John Benjamins B. V., Amsterdam).

Jakobson, R., Fant, G., and Halle, M. (**1952**). *Preliminaries to Speech Analysis* (MIT, Cambridge, MA).

Kingston, J. (**1991**). ''Integrating articulations in the perception of vowel height,'' Phonetica **48**, 149–179.

Kingston, J., and Diehl, R. L. (**1994**). ''Phonetic knowledge,'' Language **70**, 419–454.

Kingston, J., and Diehl, R. L. (**1995**). ''Intermediate properties in the perception of distinctive feature values,'' in *Papers in Laboratory Phonology IV: Phonology and Phonetic Evidence*, edited by B. Connell and A. Arvaniti (Cambridge U.P., Cambridge, U.K.), pp. 7–27.

Kingston, J., and Macmillan, N. A. (**1995**). ''Integrality of nasalization and F_1 in vowels in isolation and before oral and nasal consonants: A detection-theoretic application of the Garner paradigm,'' J. Acoust. Soc. Am. **97,** 1261–1285.

Kingston, J., Walsh, L. J., Bartels, C. Thorburn, R., and Macmillan, N. A. (**1995**). ''Integrating voice quality and tongue root position in perceiving vowels,'' in *Proceedings of the 13th International Congress of Phonetic Sciences*, edited by K. Elenius and P. Branderud, Vol. 2 (Stockholm), pp. 514–517.

Klatt, D. H., and Klatt, L. (**1990**). ''Analysis, synthesis, and perception of voice quality variations among female and male talkers,'' J. Acoust. Soc. Am. **87,** 820–857.

Kluender, K. R., Diehl, R. L., and Wright, B. A. (**1988**). ''Vowel-length differences before voiced and voiceless consonants: an auditory explanation,'' J. Phon. **16**, 153–169.

Li, X., and Pastore, R. E. (**1995**). ''Perceptual constancy of a global spectral property: Spectral slope discrimination,'' J. Acoust. Soc. Am. **98,** 1956–1968.

Lindau, M. (**1975**). ''Features for Vowels,'' Univ. California, Los Angeles, Working Papers in Phonetics, No. 30.

Lindau, M. (**1978**). ''Vowel features,'' Language **54**, 541–563.

Lindau, M. (**1979**). ''The feature 'expanded','' J. Phon. **7**, 163–176.

Local, J. K. (**1995**). ''Making sense of dynamic, non-segmental phonetics,'' in *Proceedings of the 13th International Congress of Phonetic Science*, edited by K. Elenius and P. Branderud, Vol. 3 (Stockholm), pp. 2–9.

Macmillan, N. A., and Creelman, C. D. (**1991**). *Detection Theory: A User's Guide* (Cambridge U.P., New York).

Macmillan, N. A., and Kingston, J. (**1995**). ''Integrality, separability, and configurality: The psychophysics of the Garner paradigm,'' in *Fechner Day 95*, edited by C.-A. Possamai (Intl. Soc. Psycho-Physics, Cassis, France), pp. 243–248.

Macmillan, N. A., and Kingston, J. (**submitted**). ''Integrality, separability, and configurality: The psychophysics of the Garner paradigm,'' Psychol. Rev. (submitted).

Maddieson, I., and Ladefoged, P. (**1985**). '' 'Tense' and 'lax' in four minority languages of China,'' J. Phon. **13**, 433–454.

Maddox, W. T. (**1992**). ''Perceptual and decisional separability,'' in *Multidimensional Models of Perception and Cognition*, edited by F. G. Ashby (Erlbaum, Hillsdale, NJ), pp. 147–180.

Marascuilo, L. A. (**1970**). ''Extensions of the significance test for one-parameter signal detection hypotheses,'' Psychometricka **35**, 237–243.

Nearey, T. M. (**1995**). ''A double-weak view of trading relations: Comments on Kingston and Diehl,'' in *Papers in Laboratory Phonology IV: Phonology and Phonetic Evidence*, edited by B. Connell and A. Arvaniti (Cambridge U.P., Cambridge, U.K.), pp. 28–40.

Ohala, J. J. (**1981**). ''The listener as a source of sound change,'' in *Papers from the Parasession on Language and Behavior*, edited by C. S. Masek, R. A. Hendrick, and M. F. Miller (Chicago Linguistic Society, Chicago), pp. 178–203.

Ohala, J. S. (**1985**). ''Around flat,'' in *Phonetic Linguistics*,'' edited by V. Fromkin (Academic, Orlando).

Perkell, J. S. (**1969**). *Physiology of Speech Production: Results and Implications of a Quantitative Cineradiographic Study* (MIT, Cambridge, MA).

Thorburn, R., Walsh, L. J., Macmillan, N. A., and Kingston, J. (**1994**). ''Components of integrality in the perception of voice quality and tongue root position,'' J. Acoust. Soc. Am. **95,** 2871(A).

Tucker, A. N. (**1966**). *Linguistic Analyses: The Non-Bantu Languages of North-East Africa* (Oxford U.P., London).

Walsh (Dickey), L., Bartels, C., Thorburn, R., Kingston, J., and Macmillan, N. A. (**1995**). ''Laxness integrates with F_1 (Usually, but not always, negatively),'' J. Acoust. Soc. Am. **97,** 3421(A).

Meteorology and elephant infrasound at Etosha National Park, Namibia

David Larom and Michael Garstang
Department of Environmental Sciences, University of Virginia, Charlottesville, Virginia 22903

Malan Lindeque
Ministry of Environment and Tourism, Directorate of Resource Management, Private Bag 13306, Windhoek, Namibia

Richard Raspet
National Center for Physical Acoustics, University of Mississippi, University, Mississippi 38677

Mark Zunckel, Yvonne Hong, Kevin Brassel, and Sean O'Beirne
Atmospheric Impacts Management, CSIR, Ematek, P.O. Box 395, Pretoria 0001, Republic of South Africa

Frank Sokolic
Department of Geographical and Environmental Sciences, University of Natal, Durban 4001, Republic of South Africa

(Received 22 November 1995; accepted for publication 6 October 1996)

Measured vertical profiles of temperature and wind are used to model infrasound propagation over a representative high savanna habitat typically occupied by the African elephant, *Loxodonta africana*, to predict calling distance and area as a function of the meteorological variables. The profiles were measured up to 300 m above the surface by tethered balloon-borne instruments in Etosha National Park, Namibia, during the late dry season. Continuous local surface layer measurements of wind and temperature at 5 and 10 m provide the context for interpreting the boundary layer profiles. The fast field program (FFP) was used to predict the directionally dependent attenuation of a 15-Hz signal under these measured atmospheric conditions. The attenuation curves are used to estimate elephant infrasonic calling range and calling area. Directionality and calling range are shown to be controlled by the diurnal cycle in wind (shear) and temperature. Low-level nocturnal radiative temperature inversions and low surface wind speeds make the early evening the optimum time for the transmission of low-frequency sound at Etosha, with range at a maximum and directionality at a minimum. As the night progresses, a nocturnal low-level wind maximum (jet) forms, reducing upwind range and calling area. The estimated calling area drops rapidly after sunrise with the destruction of the inversion. Daytime calling areas are usually less than 50 km^2, while early evening calling areas frequently exceed 200 km^2 and are much less directional. This marked diurnal cycle will be present in any dry savanna climate, with variations due to local topography and climate. Calling range and low-frequency sound propagation cannot be effectively understood without knowledge of meteorological controls. [S0001-4966(97)01803-1]

PACS numbers: 43.80.Ev, 43.80.Jz, 43.80.Ka, 43.64.Tk [FD]

INTRODUCTION

The use of low-frequency sound by terrestrial mammals has been most clearly documented for the African (*Loxodonta africana*) and the Asian elephants (*Elephas maximus*).[1–3] *L. africana* employs infrasonic calls with fundamental frequencies of 14–35 Hz for several vital purposes, including reproduction and herd assemblage. Most of the acoustic energy of these calls is concentrated at the fundamental frequency. To date, Langbauer *et al.*[4] have performed the only field experiment aimed at determining the range of the elephant's infrasonic calls. They demonstrated that elephants responded to the playback of recorded infrasonic calls from distances of 1.2 and 2 km. Playback stimuli, because of limitations of the loudspeakers used, were broadcast at only half the amplitude (−6 dB) of the known actual strongest elephant calls. In the simplest approximation, the 6-dB reduction corresponds to a halving of the effective broadcast distance, suggesting that the strongest elephant calls were in fact audible to conspecifics at least 4 km away. This extrapolation, however, assumes that the playback sound will propagate with essentially no excess attenuation or enhancement due to surface effects or meteorological conditions.

Martin[5] observed apparent coordinated movements of herds in Zimbabwe, and hypothesized that elephants can communicate over distances up to 5 km under conditions where visual and olfactory signals are not possible. Garstang *et al.*[6] suggested that, under optimum atmospheric conditions, elephants could communicate over ranges in excess of 10 km. Calculated acoustic enhancement was greatest for the lowest of two frequencies modeled (15 and 30 Hz) and occurred when inversions of temperature of more than 20-m

height were present under calm or low wind speed conditions. The combination of a near surface inversion with low wind speeds occurs most frequently in the early evening over the elevated African savannas. Such evenings occur more often in the dry season or during dry periods. Garstang *et al.*[6] thus showed that there are pronounced diurnal (and perhaps larger scale) fluctuations in the range over which low-frequency sound is transmitted.

The report of Garstang *et al.*[6] was, however, based upon idealized atmospheric temperature profiles and examined neither the detailed time variations of actual observed profiles nor the effects of wind velocity or wind shear. The present study uses measured vertical profiles of temperature and wind to model infrasound propagation over a representative high savanna habitat at the end of the southern African dry season. These observations were taken by tethered balloon at Okaukuejo (19° S latitude, 16° E longitude) in the Etosha National Park, Namibia, as part of the 45-day Southern African Fire–Atmosphere Research Initiative (SAFARI) experiment (M. O. Andreae, personal communication). The profiles are used as input to the fast field program (FFP) to predict the acoustic attenuation. The calling area of a 15-Hz signal is estimated as a function of specified meteorological controls. The results strengthen Garstang *et al.*'s[6] prediction that the early evening is an optimum time for long distance communication, but show that range, direction, and calling area are strongly influenced by the diurnal evolution of the changes of near-surface thermal and kinematic structure of the atmosphere. The present paper delineates the complexity of this evolution and of the consequent acoustic fields.

I. THE AIR NEAR THE GROUND

A. Large-scale considerations

The Etosha National Park lies on the western escarpment of southern Africa at a mean elevation of about 1100 m, immediately east of the Skeleton Coast and northeast and northwest of the Namib and Kalahari deserts, respectively. The weather and climate of the region are dominated by the subtropical anticyclone. The large-scale atmospheric subsidence typical of anticyclonic circulations is amplified by the Benguela current, which flows northwards from Antarctica, and by upwelling of cold bottom water. Both factors create extremely cold sea surface temperatures of 14 °C–15 °C along the west coast of southern Africa. This cools the air above, suppressing atmospheric convection and vertical moisture transport. Humidity and cloudiness are therefore suppressed. Mean annual rainfall at Okaukuejo is about 360 mm, with pronounced wet (November–April) and dry seasons (May–October). The SAFARI experiment took place during the end of the 1992 dry season, as a prolonged and severe drought was ending; 3.2 mm of rain fell on 28 September. Light rain was measured on 10 October, and a trace of precipitation was measured on 9 and 11 October.

Precipitation in this and similar dry African savanna climates is typically in the form of brief thundershowers. The skies clear rapidly after these convective storms. Even during the rainy season, days with continuous cloud cover or high humidity are rare. High solar insolation during the day and rapid radiative cooling at night are thus the norm for most of the year. Temperatures at the soil–air interface often exceed 40 °C at solar noon. As the day progresses and the sun lowers, the ground begins to cool. Atmospheric water vapor is an important greenhouse gas buffering the nighttime cooling by absorption and emission of long wave radiation. Since humidity at Etosha is low, radiative cooling is rapid and air–surface interface temperatures often fall below 15 °C before sunrise. This diurnal oscillation in surface temperatures gives rise to very pronounced nocturnal temperature inversions; temperatures may rise by as much as 10 °C from the surface to 50-m elevation. Conversely, daytime surface temperatures are high but drop rapidly with height.

Nocturnal inversions form prior to sunset and persist until just after dawn under these conditions. The surface layer is frictionally decoupled from the deeper atmosphere with calm or near calm winds and little or no turbulence. Winds above the surface layer, however, accelerate in response to reduced surface friction and large scale pressure gradients. Continued nocturnal cooling causes the cold surface air to accelerate downslope, even if the slopes are very mild. The combined accelerations result in strong wind shear and change in wind direction across the boundary between the cold surface and the warmer overlying air. Later in the evening, mechanical turbulence induced by this wind shear mixes the air between the layers, reducing and elevating the early evening inversion.

B. Atmospheric surface layer

1. Solar and terrestrial radiation and surface temperatures

Global radiation measurements taken over 40 days of the 45-day field experiment show that close to 50% of the days were clear, 25% partly cloudy, and 25% cloudy. On the clear days the net outgoing long wave radiation (long wave losses from the surface+long wave radiation received from the atmosphere) exceeds the incoming short wave radiation (global short wave) (1-albedo) from shortly before sunset until shortly after sunrise. In response to the radiative balance, the atmosphere near the surface cools rapidly after 1600 Local Solar Time [Local Solar Time (LST) is used because of the solar control of radiative cooling and heating of the surface], commonly displaying a cooling rate of about −1.3 °C/h, as shown in Fig. 1. Air temperatures at 10 m above the ground reach maximum temperatures on clear days of 30 °C around 1400 LST. Cooling over the next 14 h produces a drop of over 18 °C, yielding a near-surface air temperature below 12 °C. After sunrise soil and air temperatures rise rapidly to their daytime maxima.

2. Surface wind

The pronounced diurnal cycle in temperature is reflected in measurements of wind speed and direction. Figure 2 shows a typical diurnal sequence of wind speed and direction. Fifteen days of the experiment show a similar structure. High daytime wind speeds and a northeasterly wind direction typify the dominant circulation associated with the southern African continental anticyclone (anticyclones rotate counter-

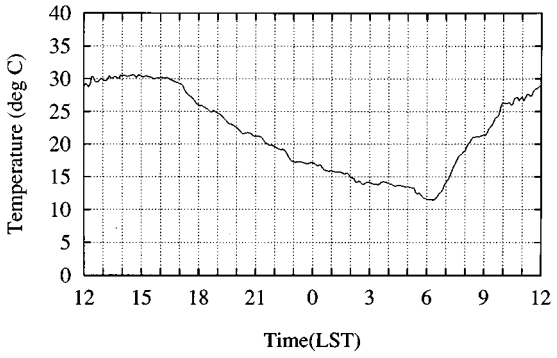

FIG. 1. Air temperature at Okaukuejo, Etosha National Park, Namibia at 10 m, 22–23 September 1992. *X* axis: Local Standard Time (LST). *Y* axis: Air temperature in degrees centigrade.

clockwise in the southern hemisphere). At night, wind speeds decrease greatly, due to the decoupling of the stable nocturnal atmospheric boundary layer from the free atmosphere above. The light southerly winds are due to drainage flow from low mountains to the south.

Mean daily (24 h) wind speeds are low, averaging 2.5 and 3.5 m s^{-1}, respectively, at 5 and 10 m. Mean hourly wind speeds show a pronounced semi-diurnal signature, with the lowest wind speeds occurring an hour after sunrise and sunset. The strongest winds (>4 m/s) occur over a 6-h period centered on solar noon. The greatest frequency of calm and winds between 0 and 1 m/s occurs between the hours of 1900

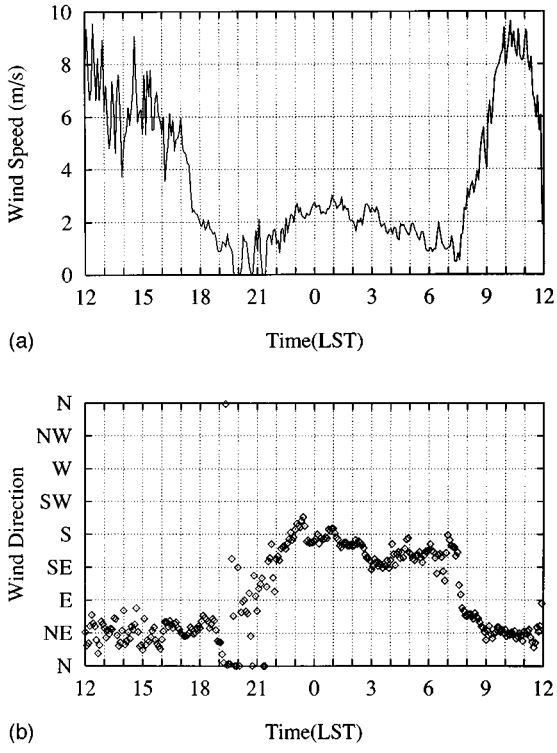

FIG. 2. (a) Wind speed at Okaukuejo, Etosha National Park, Namibia, at 10 m, 17–18 September 1992. *X* axis: Local Standard Time (LST). *Y* axis: Wind speed in m/s. (b) Wind direction at Okaukuejo, Etosha National Park, Namibia, at 10 m, 17–18 September 1992. *X* axis as for (a). *Y* axis: Wind direction (direction from which wind is coming). Letters (N, NE, etc.) depict wind direction with respect to true north.

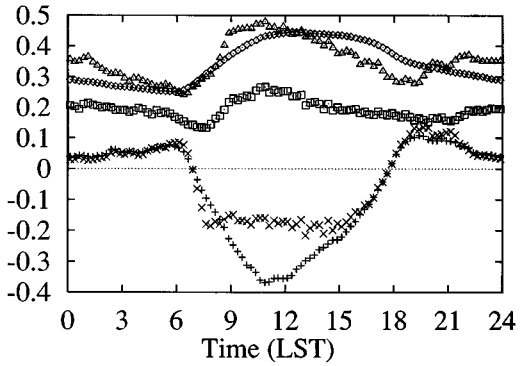

FIG. 3. Diurnal march of the average values of extrapolated surface temperature, T_0 (◇:°C*10^{-2}), temperature gradient dT/dz (+: °C/m), wind speed U at 10 m (△: m s^{-1}*10^{-1}), wind shear dU/dz (□: s^{-1}) and gradient Richardson number R_i (*x*: dimensionless). *X* axis: Local Standard Time (LST). *Y* axis: Value of the above-mentioned variables in the indicated units.

and 2100 at both 5 m and 10 m above the ground, with a secondary peak at sunrise. Five minute average wind speeds of 2 m/s or less occur about 40% of the time at 5 m and at about half this frequency at 10 m.

3. Temperature, wind gradients, and stability

Figure 3 shows the hourly average values of the extrapolated surface temperature (T_0), 10-m wind speed (U), wind shear (dU/dz), temperature gradient (dT/dz), and the gradient Richardson number (R_i). Here T_0, dU/dz, dT/dz, and R_i are calculated from the continuous tower measurements at 5 and 10 m. All of the variables show a response to daytime heating and nighttime cooling. The temperature gradient reaches a maximum shortly after sunset (1800 LST), decreases through the night, and rises to a secondary maximum just before sunrise (0600 LST). An opposite trend is found in the shear of the horizontal wind (dU/dz). Lowest shears are seen just after sunrise and sunset.

The effects of temperature lapse rates and wind shear are combined in the gradient Richardson number:

$$R_i = \frac{g}{\theta_0}\,\frac{d\theta/dz}{|dU/dz|^2},$$

where $\theta_0 = T_0(1000/890)^{0.286}$ is the surface potential temperature, and $d\theta/dz = dT/dz + 0.0098$ °C/m is the gradient of the potential temperature. Here, R_i is an index of atmospheric stability ($R_i > 0$ for a stable atmosphere, $R_i < 0$ for an unstable atmosphere). Since low-frequency sound transmission is optimized under stable atmospheric conditions with a positive temperature gradient and little or no wind shear, R_i may be a useful proxy for calling range or calling area.[7]

The diurnal progression of R_i in Fig. 3 indicates that conditions are unstable during the day but rapidly rise to maximum stability shortly after sunset. Stability follows a similar path to the temperature lapse, decreasing but remaining stable through the night, and rising to a secondary maximum before sunrise. Conditions quickly become unstable after sunrise.

TABLE I. Date, start time, and end time of tethersonde runs and number of soundings performed during SAFARI-92 in Okaukuejo, Namibia.[8]

Date	Start	End	Number of soundings
–09-14-92	0615	0900	4
–09-15-92	0630	0800	3
–09-16-92	0615	1000	5
09-16-92–09-17-92	1800	0900	8
09-17-92–09-18-92	1730	0900	8
09-18-92–09-19-92	1800	1000	8
09-19-92–09-20-92	1715	0900	11
09-20-92–	1800		1
09-21-92–09-22-92	1800	0615	3
09-22-92–09-23-92	1700	0900	5
09-23-92–09-24-92	1700	1000	11
09-25-92–09-26-92	1700	0900	11
09-26-92–	1715		1
09-27-92	1745	1900	2
09-28-92–09-29-92	1700	0700	8
09-30-92–10-01-92	1700	0815	11
10-01-92–10-02-92	1715	0900	8
10-02-92–	1700	1800	2
10-03-92	1900	2000	2
10-04-92–	1815		1
Total number of soundings			113

C. Atmospheric boundary layer

Under nonprecipitating conditions the atmospheric boundary layer may be defined as that part of the atmosphere above the surface layer in which the effects of the surface, such as surface friction and surface heating or cooling, are clearly discernible. The free atmosphere lies above the atmospheric boundary layer. The atmospheric boundary layer responds to surface heating, growing to a maximum height over land of 1200–1500 m above the surface soon after midday. Vertical profiles of temperature, humidity, pressure, and horizontal wind speed and direction were taken through the surface and boundary layers, by means of a tethered balloon system described by Zunckel *et al.*[8] A rate of ascent of the tethered balloon instrument package of about 1 m/s provides high vertical resolution of the measured fields. Table I shows the number of soundings and time intervals during the day for 113 soundings taken during the field experiment. Of the 113 soundings, all but 8 reached a height of greater than 100 m, and 65 exceeded 300 m. Soundings were made through the night on 12 occasions. Table II summarizes observed inversion strength and height just before and following sunset and sunrise. Adiabatic ($dT/dz=-9.8$ °C/km) to superadiabatic ($dT/dz<-9.8$ °C/km) conditions prevailed during the day, in response to strong convective mixing above the hot surface. On clear evenings when radiative cooling was greatest, near-surface inversions formed and decayed rapidly. Inversion conditions, in which cold dense air close to the ground is overlain by a warmer, less dense layer of air, effectively decouple the deeper atmosphere from the surface layer. Air that was frictionally slowed by the ground and by vegetation is now separated from the surface by a layer of cold air. This frictional decoupling, combined with the downslope flow of cold air and inertial accelerations from the Coriolis force, produces a low-level nocturnal jet.[9–12]

Figure 4 shows the evolution of the low-level thermal and wind speed fields during a representative night (19–20 September 1992). The data are given as contour plots with time represented on the x axis and height above ground on the y axis. The contour plots were constructed from interpolation of tethered balloon soundings taken at 1610, 1702, 1800, 2000, 2200, 0020, 0410, 0500, 0600, and 0802 LST. After 1700 LST, wind speeds decrease to less than 2 m s^{-1} throughout the boundary layer, and a low-level temperature inversion forms. After 2200 the nocturnal jet begins to form; by 2300 it is well established. During this time period, strong

TABLE II. Characteristics of tethersonde temperature profiles measured at various times of day during SAFARI-92 in Okaukuejo, Namibia. Asterisks (*) indicate that inversion strength and height may have been greater; balloon was unable to ascend further. Inversion strength≡maximum temperature in sounding −1.5 m temperature. Inversion height≡height of highest temperature reading (after Zunckel *et al.*[8]).

	Average inversion strength (°C/km)	Inversion strength range (°C)	Inversion height (m)	Inversion height range (m)
1600	No inversion			
1700	0.47	0.05–1.67	~20	
1800	2.13	0.38–3.88	59	33–139
2000	4.83	0.77–9.35	96	80–137
0500	4.49*	0.68–10.85*	102	30–240
0600	5.93	2.16–13.05	128	63–227
0700	3.22	1.34–7.52*	130	30–485
0800	2.56	0.57–5.70	131	30–480

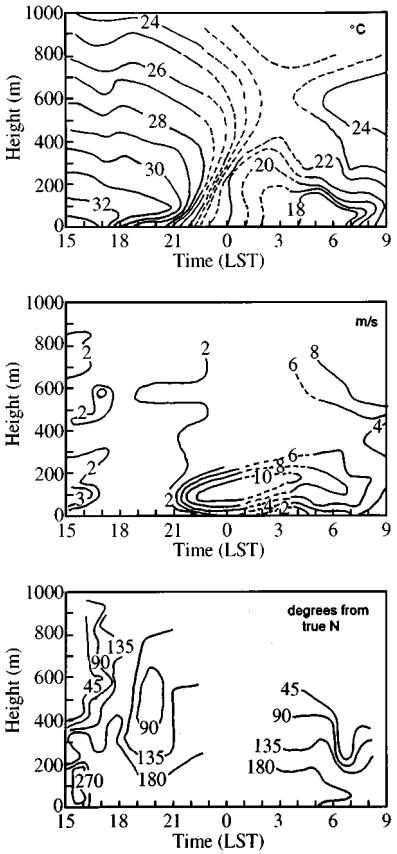

FIG. 4. Contours of temperature in °C (top), wind speed in m/s (middle) and wind direction in degrees from true north (bottom), for 19–20 September 1992. Constructed from the tethersonde profiles of Fig. 6. X axis: Local Standard Time. Y axis: Height above ground in m (after Zunckel *et al.*[8]).

low-level wind shear generated by the jet mixes cold low-level air with warmer air above, lessening the temperature gradient and raising the height of the inversion. From 0000 until the demise of the jet after sunrise, vigorous mixing produced by the jet, together with radiative cooling of the ground, induces a uniform cooling rate of approximately 1 °C h^{-1} in the lowest 200 m. Above this height the unmixed warmer air remains, forming an elevated inversion which persists 2 h or more after sunrise.

This temporal evolution of the thermal and velocity fields in the atmospheric boundary layer is common and widespread over the savannas of southern Africa. Since the low-level temperature gradient and wind shear are the main atmospheric controls on low-frequency sound propagation,[6] it is to be expected that there will be a strong diurnal cycle in the range and directionality of calls made by animals employing infrasound for long-distance communication. This hypothesis is explored in the following section.

II. OPTIMUM CONDITIONS FOR LOW-FREQUENCY SOUND TRANSMISSION

There are numerous computational and analytic solutions which predict atmospheric sound propagation based upon the vertical profiles of temperature and wind velocity. Most of these, however, assume that sound travels in rays.[13] This assumption applies only for high-frequency sound propagation in the atmosphere and is unsuitable for infrasonic frequencies. The present study uses a numerical solution of the acoustic wave equation to predict attenuation in a thermally and velocity stratified medium above an impedance surface. The solution is a fast field program or FFP, first developed for underwater sound propagation and modified for atmospheric propagation by Raspet *et al.*[14] and Lee *et al.*[15] A detailed description of this modified FFP is given by Franke and Swenson,[16] and its employment as a tool to predict the attenuation of elephant infrasonic calls is described by Garstang *et al.*[6] In brief, the assumption of a radially symmetric velocity field enables wind shear to be incorporated into a cylindrically symmetric, Helmholtz equation,

$$\frac{\partial^2 p}{\partial r^2}+\frac{1}{r}\frac{\partial p}{\partial r}+\frac{\partial^2 p}{\partial z^2}=\frac{2}{r}\,\delta(r)\,\delta(z-z_s),$$

where p=pressure, r=horizontal distance from the source, z_s=source height, and z=receiver height. The solution employs a Hankel transform to reduce the Helmholtz equation to a form of Bessel's equation in the transformed domain. The transformed equation is solved by analogy to the ''telegrapher's equations,'' with branch points and poles on the real axis avoided by the introduction of an ''artificial attenuation.'' The integral in the wave number space is approximated by a sum, and a single fast Fourier transform (FFT) yields $p(r,z)$.

Garstang *et al.*,[6] in a study of low-frequency sound transmission, found that the presence of atmospheric inversions of temperature enhanced transmission, while adiabatic and superadiabatic lapse rates significantly attenuated the signal. These results were, however, based upon simplified inversion structures, and the atmosphere was assumed to be at rest. The characterization of acoustic fields in an atmosphere in motion, using measured temperature and wind profiles, is considerably more complex.

In an atmosphere in motion, the direction of greatest range of low-frequency sound transmission may not be directly downwind. High positive wind shear causes the outwardly propagating acoustic waves to interact strongly with the ground; this absorbs energy and degrades the signal. A more intuitive explanation, though not strictly accurate for low frequencies, may be made by thinking of sound in terms of rays. Moderate wind shear will cause sound to bend downward, bringing extra rays to the receiver. However, strong wind shear causes multiple-bounce rays. Since each bounce absorbs energy, propagation directly downwind is not optimum. Maximum calling range can thus occur at an angle (less than 90°) from directly downwind. Further complicating this argument is the fact that, for a real sounding in which backing or veering (decrease or increase of wind direction with height) are present, ''downwind'' is an abstraction rather than a physical reality. Variation of wind speed and direction with height will produce asymmetric fluctuations in range and direction of propagation of the sound waves.

In the real atmosphere, particularly under the conditions studied in the Etosha National Park at the end of the dry season, marked changes in the thermal and velocity fields are seen over the diurnal cycle (Figs. 3 and 4). A numerical solution to the acoustic wave equation in the form of the fast field program (FFP), also applied and described in detail by Garstang *et al.*,[6] is used to calculate the attenuation of 15-Hz sound as a function of the vertical profiles of temperature and of the component of the wind speed in the direction of propagation. These directional predictions of acoustic fields are then used to find the optimal times to predict the range, and to characterize the temporal evolution and variability of elephant calling.

A. Nocturnal enhancement

The atmosphere will have no influence on surface-to-surface sound propagation above a certain height. A conservative minimum height of 300 m was chosen.[17] Based on this consideration, 65 of the 113 tethered balloon profiles were used as input for the FFP. The other profiles did not reach a height of 300 m. Decibel attenuation contours for each profile were obtained by calculating the directionally dependent attenuation in 24 increments of 15°. A separate FFP run was required for each direction, necessitating 24 runs for each profile. Attenuation contours were plotted for a frequency of 15 Hz. The complex impedance was calculated by FFP, using Attenborough's four-parameter model[18] and an estimated flow resistivity of 500 000 mks rayls/m. Calling ranges for higher frequencies or softer ground may be expected to be smaller.

Human hearing compared to that of elephants is very poor at low frequencies. Hearing thresholds are approximately 93 dB (all dB references are re 20 μPa rms at 1 m) at 15 Hz and 70 dB at 30 Hz. Elephant hearing at these same frequencies is markedly better.[19] A study by Heffner and

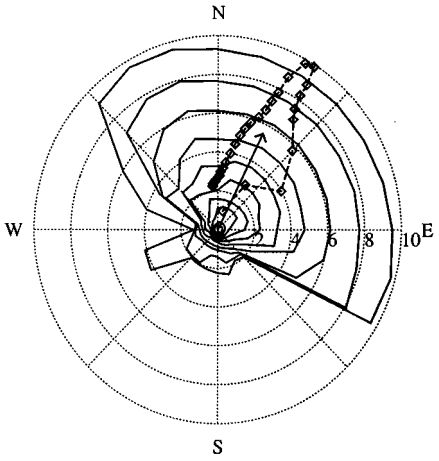

FIG. 5. Attenuation contours (closed solid lines) and wind hodograph (--□--) for 2200 LST, 19 September 1992. Contours are plotted in −3-dB increments from the innermost (−40 dB) to the outermost (−67 dB). Points on the wind hodograph give the terminus of the velocity vector in 25-m height increments from ground level to 300 m. Arrow indicates average wind in the first 300 m above the ground. Numbers (2,4,6, etc.) indicate both the distance in km from the source (for the attenuation contours) and the wind speed in m/s (for the hodograph and average wind arrow). Letters (N,E,S,W) show direction of wind and of sound propagation, with respect to true north.

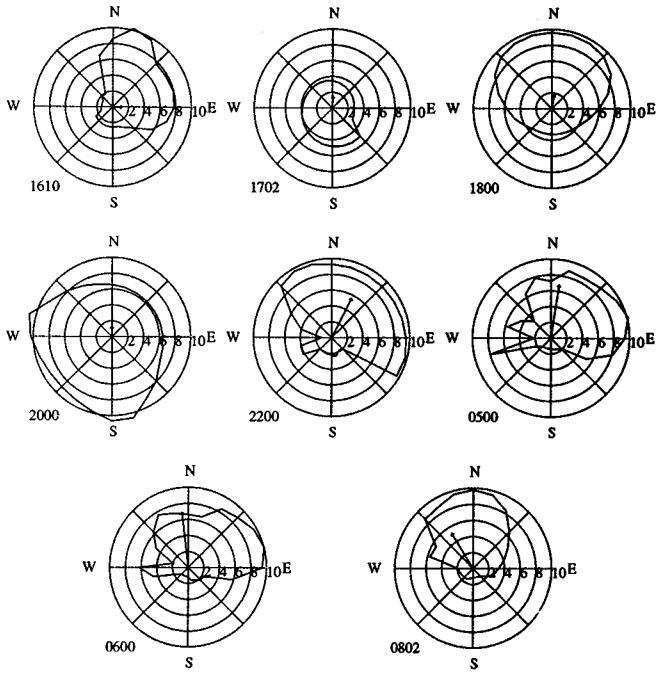

FIG. 6. The −67-dB attenuation contour predicted via FFP (irregular closed line depicting range in km) and mean wind in first 300 m (arrow: space in m s^{-1}) from tethered balloon soundings made on 19–20 September 1992 in Okaukuejo, Namibia. Time of sounding (LST) is given in lower left of each plot. Letters and numbers as in Fig. 5.

Heffner[20] gives the elephant hearing threshold at 16 Hz as 65 dB. This approximates to 68 dB at 15 Hz, rapidly improving to 43 dB at 30 Hz. However, these results are from one 7-year-old Indian elephant. The lowest reasonable threshold for a full grown African elephant was assumed to be 50 dB. Because the present study is primarily concerned with the diurnal variation in calling range and calling area, rather than the absolute magnitudes thereof, substitution of a greater or lesser value will not invalidate our conclusions.

The most intense elephant infrasonic signal reported in the literature is 117 dB.[3] With a sound level of 117 dB and a hearing threshold of 50 dB, an estimate of calling range is given by 117 dB+attenuation=50 dB. For the present study, the calling range is therefore defined as that range at which the attenuation is −67 dB. Figure 5 depicts a typical set of attenuation contours (for 2200 LST, 19 September 1992). The temperature and wind fields yielding these contours are given in Fig. 4. Contours are plotted in −3-dB increments from the innermost (−40 dB) to the outermost (−67 dB). The main features of Fig. 5 are present in many other sounding contours. There is a marked asymmetry, with degraded calling range ''upwind'' and enhanced range ''downwind.'' The sharp drop in range from NW to W and from E to SE is likely due to a combination of strong wind shear and change in wind direction with height. It may also in part be an artifact of the authors' simplifying assumption that the calling range is defined by the first radius at which the attenuation drops below −67 dB. In some profiles, the attenuation will drop below −67 dB and then rise above −67 dB at a greater distance from the source. Examination of these regions of ''anomalous propagation''[21] is deferred to a future study.

Figure 5 shows that the range of propagation downwind from the source is roughly five times greater than the range upwind. The innermost contours are nearly circular, moving outwards the contours first become extended in the downwind direction and then broaden considerably in the crosswind direction. The shapes become increasingly jagged with higher attenuation. These irregularities of shape are largely due to the fluctuations in the measured wind and temperature fields. Since these fluctuations do not persist in time, the irregularities in the contours are not relevant; the general elliptical shape is the important factor. The range of maximum and minimum low-frequency sound propagation is not directly upwind or downwind, for reasons previously stated.

B. Case study of combined thermal and kinematic controls

Figure 6 depicts the temporal evolution of the −67-dB contours of a 15-Hz signal over the night of 19–20 September 1992. These are used as an estimate of elephant calling range and calling area. At 1610 LST, a nearly adiabatic temperature gradient of −9.0 °C/km is combined with winds of approximately 2 m s^{-1} (Fig. 4). The winds are westerly to 150 m and highly variable from 150–300 m. This yields a very directional contour; the calling range is less than 2 km in the ''upwind'' direction and 8–10 km ''downwind.'' The region of extended range (>6 km) is concentrated in the quadrant from north to east.

An hour later (Fig. 4), ground cooling has commenced and a 40-m-thick layer of 32 °C air underlies the adiabatic zone. Winds have shifted to southerly and lessened slightly with the commencement of drainage flow from the hills to the south, and the range is 3–5 km in all directions. At 1800 the wind is essentially the same, but a temperature inversion of 2.7 °C strength and height of 42 m has formed. This en-

hances the range to over 9 km ''downwind,'' but shortens it to 3 km ''upwind.'' Although the minimum and maximum ranges are similar to those given by the 1610 sounding, the area covered is greater due to the broader shape. The zone in which the range is greater than 6 km now extends of over 180 ° from E to N to W, as opposed to the 90° of the 1610 sounding. This broad zone of extended range is characteristic of nocturnal soundings.

By 2000 the wind speeds are below 2 m s^{-1}. Wind shear is nonexistent or very mild above 2 m. The inversion has grown to 3 °C strength and 64-m height. This is the optimum calling time; the range goes beyond 10 km in two lobes to the west and south, and everywhere exceeds 6 km. (This is a typical evening optimum: in the most pronounced cases, the range was 10 km or more in all directions.[7]) By 2200 the southerly jet has set in, and the inversion has grown to 6 °C strength and 221 m height. Strong wind shear has greatly decreased the upwind range; over the 180° from SE to N to NW, the range mostly exceeds 9 km, while from NW to S to SE it is seldom over 2 km.

Over the rest of the night, the inversion becomes elevated. The low-level wind shear remains strong and the winds stay southerly. No attenuation contours were plotted for 0200, 0410, or 0700 as the soundings did not reach to 300 m. From 0500 to 0600 (approximately sunrise) to 0802, the wind remains southerly to 150 m, but the 300 m winds back to northeasterly, their characteristic daytime direction. This directional shear may explain why the 0500 and 0600 range plots are highly asymmetric, lacking the rough bilateral symmetry of the previous contour fields. For these two soundings, the elevated inversion is underlain by a 100- to 150-m-thick layer of air of constant temperature or of a near-adiabatic temperature gradient. Again, this is due to mechanical mixing caused by the strong wind shear.

Around sunrise (0600), the jet begins to break up as the onset of ground heating causes thermal convection and mixing. The low-level wind shear becomes confined to the lowest 30 m as the velocity begins to be mixed more evenly through the boundary layer. This, combined with the lessening of the elevated inversion, gives rise to a more confined range contour. At 0802, the shape is similar to the 1610 contour; the zone of extended range is concentrated in a narrow lobe downwind and there is severe attenuation upwind.

C. Characterization of range plots

Due to the extreme directionality and irregularity of many of the range plots generated for the 65 soundings, it is difficult to characterize the degree of enhancement or attenuation of long-range infrasonic calling. The simplest indicator is the calling area A, the area enclosed within the −67-dB contour. Figure 7 depicts the temporal evolution of A. Each of the 65 usable soundings is represented by a single data point. Four temporal regions can be defined. The first region, 1600–1830 LST, is a time of rapid growth in A. The optimum calling time is 1830–2030, with A mostly exceeding 200 km^2. After 2030, A collapses rapidly to 150 km^2 and then shrinks slowly until sunrise at 0600. From then until 0900, A again diminishes rapidly to its daytime value, typically well below 50 km^2.

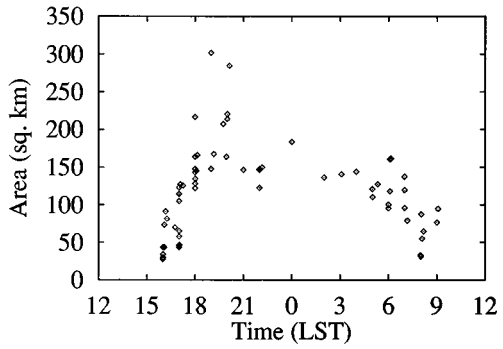

FIG. 7. Area (in square kilometers) covered by −67-dB attenuation contour as a function of time of day, for 65 tethered balloon soundings from 16 September to 4 October 1992. *X* axis: Local Standard Time. *Y* axis: Area in km^2.

Figure 7 shows that the case study of Fig. 6 is typical; although a nocturnal jet does not form every night, it forms with sufficient frequency that the trends in expansion and contraction of range in the case study are mirrored in Fig. 7. The following sequence of atmospheric controls and resultant calling range is hypothesized as a model of the diurnal cycle in calling area:

(i) 1600–1830: Rapid growth of A from 50 to 200 km^2 as winds die and the nocturnal inversion begins to form.
(ii) 1830–2030: Optimum time due to strong temperature gradients and low winds. A over 200 km^2.
(iii) After 2030: Collapse of A to below 150 km^2 due to onset of nocturnal jet.
(iv) 2030–0600: Slow diminishing of A from 150 to 125 km^2 as jet stabilizes and the inversion becomes elevated.
(v) 0600–0900: Second collapse to below 50 km^2 as solar radiation heats the ground, destroying the inversion and jet.
(vi) 0900–1600: Range below 50 km^2, perhaps much less.

III. CONCLUSIONS

The results of this paper are based on numerical predictions of 15-Hz signal propagation under measured atmospheric velocity and temperature profiles. Comparison with actual temporal patterns in elephant calling and reception is addressed in detail by Larom *et al.*[7] A study of 14 radio-collared and microphoned elephants in Zimbabwe[22] shows a late afternoon peak in loud, low-frequency elephant calls. This peak is caused by a pattern of late afternoon treks to water by elephants in this area, during the dry season. These treks require coordinated movements of each herd, necessitating calls. The timing is thought to be due to a combination of thirst at the end of a hot day, avoidance of predation of elephant calves by nocturnal predators, and transmission conditions considerably improved from midday. Further exploration of the role that atmospheric controls play in calling behavior will require a field study combining atmospheric measurements with simultaneous observation of elephants.

The vertical profiles of wind and temperature have strong and complex effects on ground-to-ground infrasound propagation at Etosha National Park. The formation of the

nocturnal temperature inversion in the early evening and its breakup with sunrise leads to a diurnal cycle in calling range, with a doubling or tripling of range after sunset. Optimal conditions occur one to two hours after sunset when winds are lowest and the inversion strongest. Shallow southerly gravity flow sets in later and is overlain by an easterly or southerly jet. This increase of wind during the night leads to a steady degradation and increased directionality of calling range as the night progresses. The increased wind shear also introduces mixing and weakens the temperature inversion, further degrading calling, until sunrise. However, the calling range at any time during the night is likely to be better than during the day, when adiabatic to superadiabatic temperature lapse rates combine with high ground-level winds, creating conditions highly detrimental to ground-to-ground low-frequency communication.

Infrasound propagation responds to the interactions between atmospheric thermal and velocity fields. In the dry, high-pressure-dominated atmosphere of the subtropics, thermal controls will exhibit a pronounced and predictable diurnal cycle. Wind velocity will exhibit a more complex cycle strongly influenced at night by topography. Even modest slopes of the ground surface will result in cold air drainage. During the early evening, stratification due to surface cooling will decouple the cold surface air from the warmer air above. Winds at the surface will die and calm or near calm conditions will prevail. Strong but shallow inversions with no wind will maximize low-frequency sound transmission during this part of the early evening. Both the range and the area over which low-frequency sound is transmitted will be maximized at this time. The calling area reaches a maximum and effects of directionality are at a minimum. Once drainage flow sets in, wind velocity becomes a factor and infrasound transmission becomes subject to the effects of both thermal stratification (now weaker) and wind shear. Both range and direction are affected and a marked directionality of propagation appears. Towards the end of the night, drainage flow may cease as cold air pools to capacity and the effects of air motion once again decline. Depending on local topography, this can lead to a second period of optimum low-frequency sound transmission conditions about dawn. Differences in relief and changing large-scale meteorological fields can disrupt the simple thermal response, which may be seen over a perfectly featureless and level plain. The thermal and velocity structure of the near surface atmosphere have a pronounced influence on low-frequency sound transmission at Okaukuejo. Any interpretation or application of low-frequency sound transmissions must take account of these temporal and spatial changes in calling range. No general conclusions can be drawn from observations of sound transmissions without concurrent attention being paid to the prevailing atmospheric conditions. Conversely, observations of low-frequency sound transmissions or communication can be effectively interpreted given only basic knowledge of atmospheric conditions and knowledge of the time of day of the infrasound observations. Similarly, any applied use of infrasound in the field should take account of atmospheric conditions which either enhance or interfere with the transmission of low-frequency sound.

ACKNOWLEDGMENTS

This paper draws upon the dissertation work of Mr. Larom at the University of Virginia. The field work for this study was carried out under the framework of the Southern African Fire–Atmosphere Research Initiative (SAFARI). The field work was supported by Grant ATM92-07924 and the analytical work by Grant ATM-9529315 from the National Science Foundation to the University of Virginia.

[1] K. Payne, W. R. Langbauer, Jr., and E. M. Thomas, ''Infrasonic calls of the Asian elephant (*Elephas maximus*),'' Behav. Ecol. Sociobiol. **18**, 297–301 (1986).

[2] W. R. Langbauer, Jr., K. B. Payne, K. B. R. A. Charif, and E. M. Thomas, ''Response of captive African elephants to playback of low-frequency calls,'' Can. J. Zool. **67**, 2604–2607 (1989).

[3] J. H. Poole, K. B. Payne, W. R. Langbauer, Jr., and C. J. Moss, ''The social contexts of some very low frequency calls of African elephants,'' Behav. Ecol. Sociobiol. **22**, 385–392 (1988).

[4] W. R. Langbauer, Jr., K. Payne, R. A. Charif, L. Rapaport, and F. Osborn, ''African elephants respond to distant playbacks of low-frequency conspecific calls,'' J. Exp. Biol. **157**, 35–46 (1991).

[5] R. B. Martin, ''Aspects of elephant social organization,'' Rhodesia Sci. News **12**, 184–187 (1978).

[6] M. Garstang, D. Larom, R. Raspet, and M. Lindeque, ''Atmospheric controls on elephant communication,'' J. Exp. Biol. **198**, 939–951 (1995).

[7] D. L. Larom, M. Garstang, K. Payne, R. Raspet, and M. Lindeque, ''The influence of surface atmospheric conditions on the range and area reached by animal vocalizations,'' J. Exp. Biol. (in press).

[8] M. Zunckel, Y. Hong, K. Brassel, and S. O'Beirne, ''Characteristics of the nocturnal boundary layer: Okaukuejo, Namibia during SAFARI-92,'' J. Geophys. Res. **101**, 23757–23766 (1996).

[9] A. K. Blackadar, ''Boundary layer wind maxima and their significance for the growth of nocturnal inversions,'' Bull. Am. Meteorol. Soc. **38**, 283–290 (1957).

[10] J. Holton, ''The diurnal boundary layer wind oscillation above sloping terrain,'' Tellus **19**, 199–205 (1967).

[11] S. Greco, S. Ulanski, M. Garstang, and S. Houston, ''Low-level nocturnal wind accelerations over the Central Amazon Basin,'' Bound. Layer Meteor. **58**, 91–115 (1992).

[12] M. Zunckel, G. Held, R. A. Preston-Whyte, and A. Joubert, ''Low-level wind maxima and the transport of pyrogenic products over southern Africa,'' J. Geophys. Res. **101**, 23745–23756 (1996).

[13] J. L. Spiesberger and K. M. Fristrup, ''Passive localization of calling animals and sensing of their acoustic environment using acoustic tomography,''Am. Nat. **135**, 107−153 (1990).

[14] R. Raspet, S. W. Lee, E. Kuester, D. C. Chang, W. F. Richards, R. Gilbert, and N. Bong, ''Fast-field program for a layered medium bounded by complex impedance surfaces,'' J. Acoust. Soc. Am. **77**, 345–352 (1985).

[15] S. W. Lee, N. Bong, W. F. Richards, and R. Raspet, ''Impedance formulation of the fast field program for acoustic wave propagation in the atmosphere,'' J. Acoust. Soc. Am. **79**, 628–634 (1986).

[16] S. J. Franke and G. W. Swenson, ''A brief tutorial on the Fast Field Program (FFP) as applied to sound propagation in the air,'' Appl. Acoust. **27**, 203–215 (1989).

[17] S. J. Franke, C. Shaffer, R. Raspet, and C. H. Liu, ''Application of the Fast Field Program to blast noise prediction,'' Proc. 3rd Intl. Symp. Long Range Sound Propagation and Coupling Into the Ground, University of Mississippi, 28–30 March (1988), pp. 243–260.

[18] L. Attenborough, ''Acoustical impedance models for outdoor ground surfaces,'' J. Sound. Vib. **99**, 521–544 (1985).

[19] N. S. Yeowart and M. J. Evans, ''Thresholds of audibility for very low-frequency pure tones,'' J. Acoust. Soc. Am. **55**, 814–818 (1974).

[20] R. Heffner and H. Heffner, ''Hearing in the elephant (*Elephas maximus*),'' J. Comp. Physiol. Psychol. **96**, 926–944 (1982).

[21] A. D. Pierce, *Acoustics: An Introduction to Its Physical Principles and Applications* (McGraw-Hill, New York, 1981).

[22] W. R. Langbauer, R. Charif, R. Martin, K. Payne, and L. Osborn, ''Long-range monitoring of elephant movements and vocalizations'' (in preparation).

Snapping shrimp noise near Gladstone, Queensland

Mark L. Readhead
Maritime Operations Division, Aeronautical and Maritime Research Laboratory, Defence Science and Technology Organisation, P.O. Box 44, Pyrmont, NSW, 2009, Australia

(Received 16 April 1996; accepted for publication 21 September 1996)

The intensity of the noise generated by snapping shrimp between 0.6 and 12.5 kHz was measured from Auckland Wharf to the end of the dredged channel leading into Gladstone, Queensland, Australia, and on a route out across to the edge of the Great Barrier Reef. The noise was recorded about every nautical mile within the channel and every 5 miles across the reef. Water depths varied between 11.5 and 58 m, with sites ranging from just a few meters from piers to 82 km from the mainland. Intense snapping shrimp noise was found at all sites and was the dominant source of ambient noise. Within the channel the noise exceeded that which would be expected from wind generated noise during sea state 7. Across the reef the noise levels were lower, but still exceeded that from sea state 3 wind generated noise. Comparison is made with other published snapping shrimp noise spectra which show differences in both level and shape. [S0001-4966(97)03502-9]

PACS numbers: 43.80.Ka, 43.50.Cb [FD]

INTRODUCTION

Snapping shrimp (*Alpheus* and *Synalpheus spp.*) are commonly found on sea bottoms composed of rock, shell, coral, or other sheltering materials, in waters of less than 55-m depth where the water temperature exceeds 11 °C for the greater part of the year.[1] By snapping closed its large claw the shrimp makes a loud impulsive click with a broad frequency response from tens of hertz to hundreds of kilohertz. The sound has been identified with snapping shrimp by placing several in a vessel of water in the laboratory.[1] When the shrimp gather in large numbers, the superposition of their sound impulses leads to a sustained background noise resembling a distinctive frying noise.[1,2]

Previous reports indicate that snapping shrimp noise is common in Australian waters. To determine the extent of the problem for inshore sonar operations, a survey was conducted to measure the distribution of snapping shrimp noise within and near a typical harbor, specifically in the vicinity of Gladstone, Queensland, Australia.

I. SURVEY LOCATION

The route of the survey was from alongside Auckland Wharf in Gladstone harbor, out along the dredged channel to the farther pair of channel markers, S1 and S2, showing the approach to Gladstone harbor. Over much of this route the pairs of markers occurred at regular intervals of 0.6 nautical miles and measurements were taken between each second pair, that is, each 1.2 nautical miles (Fig. 1). Next to Auckland Wharf the water depth was 11.5 m, but over the rest of this portion of the route the water depth only varied between 15.7 and 15.8 m.

A large portion of the intended route across Curtis Channel to the edge of the Great Barrier Reef was not covered due to inclement weather. However, a section from 23° 54.6′ S and 152° 1.2′ E to 24° 1.3′ S and 152° 42.9′ E was measured (Fig. 2). Here the water depth was quite variable, ranging between 32 and 58 m.

II. EXPERIMENTAL PROCEDURE

The hydrophone used to detect the snapping shrimp noise was an omnidirectional Clevite CH17 attached to the end of a 30-m coaxial cable. At the other end of the cable was a passive filter to reduce the intensity of the incoming signal below 2 kHz and prevent low-frequency overloading of the recorder input stage. The signal was amplified with a Maritime Operations Division designed and built low-noise preamplifier with 40 dB of gain, and recorded with a Sony Walkman WM60 audio professional recorder using TDK SA-X90 tapes.

The hydrophone, cable, and passive filter combination were calibrated using the comparison method,[3] yielding a sensitivity varying between −207 and −197 dB *re*: 1 V/μPa over the frequency range from 630 to 12 500 Hz. The preamplifier was calibrated with a Hewlett-Packard 3562A dynamic signal analyzer, using a sinusoidal signal slowly swept from 100 Hz to 20 kHz. The response of the analogue tape

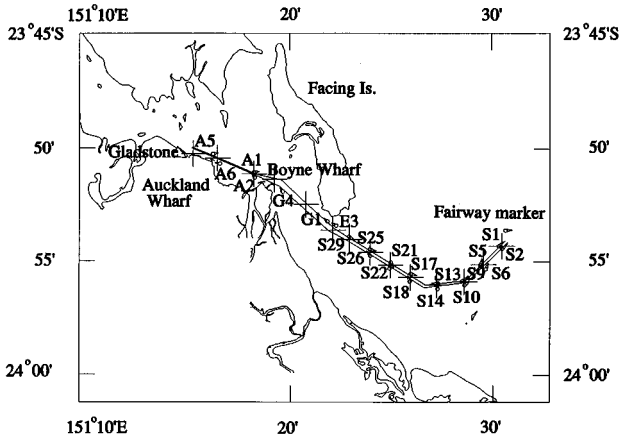

FIG. 1. Gladstone harbor and channel sample locations. The sample locations are marked with a cross. Those beacons from Auckland wharf to the fairway marker which were close to the sample sites are shown. Also marked is the dredged approach channel to the harbor.

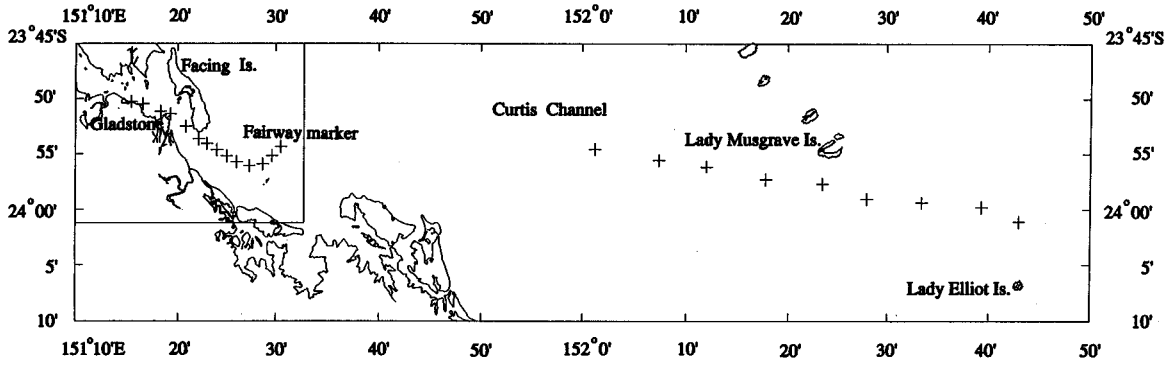

FIG. 2. Sample locations across Curtis Channel to the edge of the Great Barrier Reef off Gladstone. The crosses mark the sample locations.

recorder was flat to within ±3 dB between 40 Hz and 15 kHz, and had a dynamic range of 58 dB. The recording system, from preamplifier to tape recorder and tape, were calibrated by feeding in a known signal from a Maritime Operations Division designed and built pink noise generator, using a noise level of −130 dB *re*: 1 V^2/Hz at 1 kHz, which was similar to the level of snapping shrimp noise as output by the hydrophone. This calibration signal was laid down on the tape after every few recordings in order to correct for any possible drift in recording gain. As a check on possible tape recording distortion, pink noise signals from −130 to −100 dB *re*: 1 V^2/Hz at 1 kHz were recorded and played back into a Hewlett-Packard 3562A dynamic signal analyzer. Even though the most intense of these signals was some 40 dB greater than the snapping shrimp intensities recorded off Gladstone, there was no sign of distortion for any of them.

At each survey site the hydrophone was lowered to a depth of 3 m and the incoming noise was recorded for 5 min. During the recording the incoming sound was monitored to confirm that the distinctive frying noise associated with snapping shrimp was what was being recorded. The calibration signal from the pink noise generator was laid down on the tape after every few recordings.

The data were analyzed using B&KNOISE, a software package written by Tavener.[4] It is intended to be used in conjunction with a Brüel & Kjaer 2131 spectrum analyzer, which it controls according to input choices made by the user. The spectrum analyzer was set to linearly average the noise recorded in one third octave bands centred from 630 to 12 500 Hz, using 8 samples of 16 s each. Further details of the equipment, its calibration and the analysis procedure are given in a DSTO report.[5]

III. RESULTS

Figures 3 and 4 show the noise spectra from 630 to 12 500 Hz at selected stations in Gladstone harbor, its approach channel, and across Curtis Channel. The noise levels were higher in the harbor and dredged channel than further out across the reef, and generally decreased with distance from the harbor wharfs.

In Fig. 5 the average noise spectrum levels have been given for all the measurements from Gladstone harbor and its approach channel, and Curtis Channel. Also shown are the noise spectra to be expected from wind noise in sea states of approximately 3 and 7 on the Beaufort scale.[6] Within the harbor and dredged channel the noise exceeded that which would be expected from wind generated noise during a sea state of 7. Across Curtis Channel the noise levels were lower, but still exceeded that from sea state 3 wind generated noise.

Figure 6 shows the noise spectrum level at 5 kHz and water depth versus distance along the survey route from Auckland Wharf. This diagram allows the variation of intensity with location to be seen at one representative frequency. In the shallower water the level is higher, although rather variable. These variations do not correspond to different water depths, which were mostly between 15.7 and 15.8 m, but presumably to the density of snapping shrimp colonies as habitats change. Across Curtis Channel, where the water depth was greater, the noise intensities are lower and more uniform, even though the depth was varying more. The gap in the noise spectrum level for distances between 30 and 84

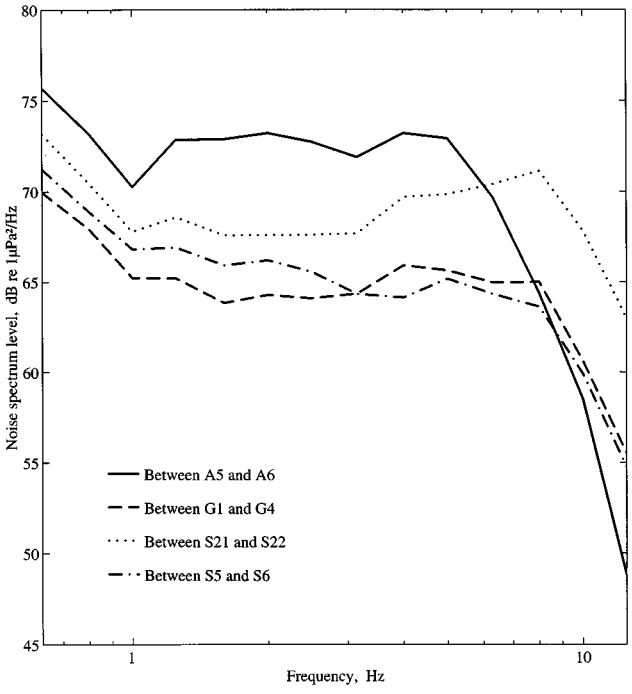

FIG. 3. Noise spectra recorded in Gladstone harbor and channel: between A5 and A6 beacons; between G1 and G4 beacons; between S21 and S22 beacons; between S5 and S6 beacons.

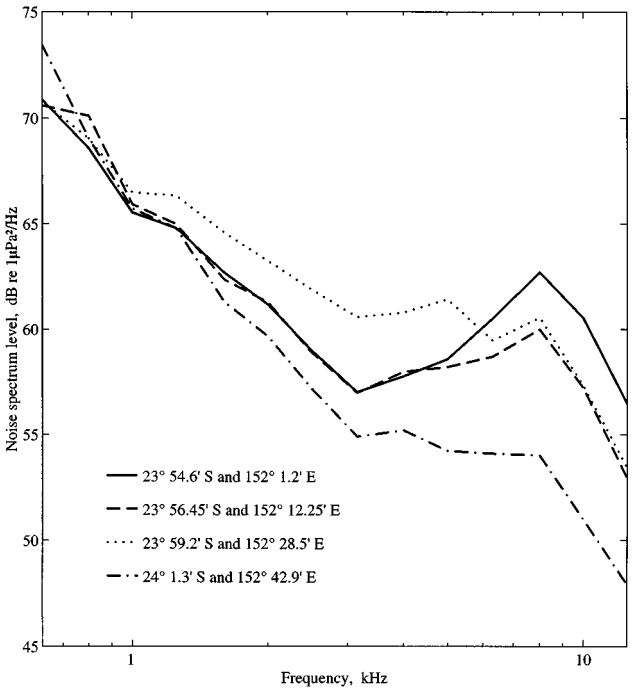

FIG. 4. Noise spectra recorded across Curtis Channel: between 23° 54.6″ S and 152° 1.2″ E, and 24° 1.3″ S and 152° 42.9″ E.

km corresponds to that portion of the reef over which no readings were taken.

IV. COMPARISONS WITH OTHER DATA

Data collected at other locations[1,2,7] are shown in Figs. 7 and 8. The data labeled ''Cowley Beach'' were recorded by

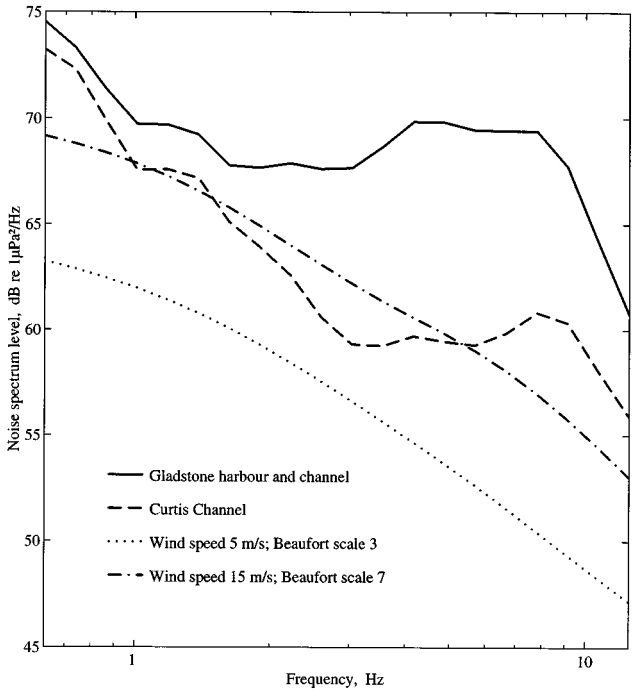

FIG. 5. Average noise spectra recorded in Gladstone harbor and channel, and across Curtis Channel. Also shown are the curves for noise generated by winds of 5 and 15 m/s.

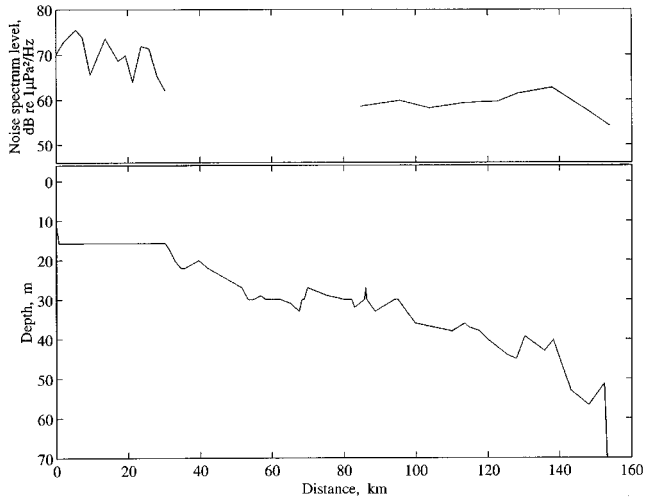

FIG. 6. Noise spectrum level at 5 kHz along the survey route. Also shown is the water depth along the route.

Cato and Bell[7] in a region where rock and coral outcrops were evident in a water depth of about 6 m off Cowley Beach, near Innisfail in Queensland. About 1 km away in 20-m water depth, where the bottom was muddy, they found the noise to be ''very much lower... and not sufficiently above background noise from other sources to make a reliable estimate of its spectral levels.'' Hence, off Cowley Beach they recorded noise levels both exceeding and less than those off Gladstone.

Cato and Bell[7] also took readings from Jones Bay within Sydney Harbour, and these data are also shown in Fig. 7. In this case the levels are somewhat higher than those from Cowley Beach, and hence are greater than those from Gladstone.

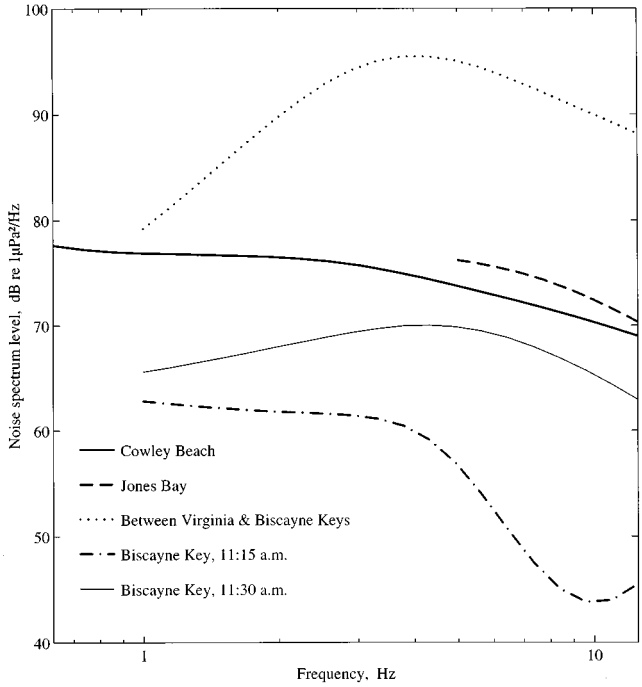

FIG. 7. Noise spectra recorded at sites in Queensland and New South Wales, Australia,[7] and in Florida.[2]

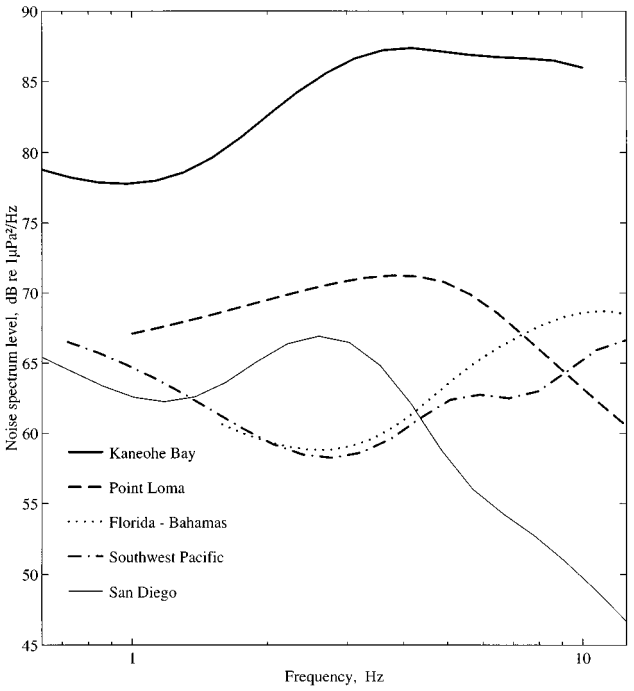

FIG. 8. Noise spectra recorded at sites in Hawaii and California, the Florida–Bahamas area, and the southwest Pacific.[1]

Three sets of data of Widener[2] are presented. The highest level reported came from the end of a pier between Virginia and Biscayne Keys, Florida, in 3-m water depth. The author noted that the noise sources were distributed; the hydrophone was not located near a concentrated source and the data showed no temporal variation from 1 h before sunrise to 2 h after sunset. The levels greatly exceed those near Gladstone.

A little over a mile away, off the lighthouse on Biscayne Key, Widener[2] measured the snapping shrimp spectra over a 25-min period. Two of his curves are reproduced in Fig. 7, having been recorded 15 min apart. Not only are the noise levels between 13 and 47 dB less than off the pier, but change by 2–22 dB over this short time interval at the same site. The spectra at the two times are significantly different. Nevertheless, the levels are broadly similar to those recorded off Gladstone.

Five sets of results of Everest *et al.*[1] are shown in Fig. 8. The spectrum for Kaneohe Bay, Hawaii, is the average of two very consistent spectra taken about a meter from a pier close to shrimp living in the fowling material on the nearby pilings. The authors noted that 7 m away the noise spectrum level was 10 dB lower. Even so, the spectrum level is substantially higher than those measured off Gladstone.

The curve labeled ''Point Loma'' is the average of 21 stations over shrimp beds off San Diego, California. The curve is similar to that recorded within Gladstone harbor and its approach channel. A very different spectral shape came from averaging 23 stations in the Florida–Bahamas area. Its shape is similar to that obtained from 15 stations near Funafuti, Tuvalu; Guadalcanal, Solomon Islands; and Noumea, New Caledonia. Both curves are unlike any of the others.

The fifth curve is the average of nine sets of readings in San Diego Yacht Harbor. The authors noted that although the shrimp noise was prominent, the spectrum was quite different in shape from that obtained with the same equipment off Point Loma, just a few kilometers away. They suggest that the difference may be because the species found in this harbor are not found in outside areas. The spectral shape is also different from that for the Gladstone data.

Not only do the noise levels in Figs. 7 and 8 show significant variability, but the spectral shapes are quite different. In the present study the average fall between 630 Hz and 12.5 kHz was 17 dB, from 73 to 56 dB *re*: 1 μ Pa^2/Hz across Curtis Channel. Within Gladstone harbor and its approach channel, the fall was 14 dB, from 75 to 61 dB *re*: 1 μPa^2/Hz. This decline exceeded some of the other data, but was similar to that for San Diego and one of the sets from near Biscayne Key.

A rapid decline was also apparent between 8 and 12.5 kHz. Across Curtis Channel the average fall was 5 dB, from 61 to 56 dB *re*: 1 μPa^2/Hz. Within Gladstone harbor and its approach channel a fall of 8 dB occurred, from 69 to 61 dB *re*: 1 μPa^2/Hz. This decline also exceeded some of the other data, but was similar to that for Point Loma, San Diego, and one of the sets from near Biscayne Key.

V. CONCLUSION

At all sites surveyed within Gladstone harbor, its approaches, and across Curtis Channel to the edge of the Great Barrier Reef, snapping shrimp produced a dominant and persistent source of noise. This was not restricted to sites around piers and pilings, where other reported measurements were made, but occurred up to 82 km from the mainland. The noise levels were higher in the shallow waters of the harbor and its channel, than across Curtis Channel. They exceeded levels which would be expected from wind generated noise during sea states of 7 and 3, respectively.

Differences in the level and shape of the noise spectra in the Gladstone area, compared to other areas in Australia and overseas, may be attributable not only to the density of snapping shrimp present, but to different species. There are no data relating spectral shape to species, or the species present in the areas surveyed. More work is required to identify those species present and to elucidate any consequential spectral variations, preferably with equipment recording over a broader frequency band.

ACKNOWLEDGMENTS

The author wishes to thank Neil Tavener of the Defence Science and Technology Organization, and CPO Paul Ukhoff of the Royal Australian Navy for their assistance with the measurements off Gladstone. Dr. Doug Cato, Mrs. Helen Lawless, Mr. Mark Savage, Mrs. Sandra Tavener, and Mr. Jim Thompson, all of the Defence Science and Technology Organization, provided their expertise in the calibration of the equipment and the planning and analysis of the experiments.

[1] F. A. Everest, R. W. Young, and M. W. Johnson, ''Acoustical characteristics of noise produced by snapping shrimp,'' J. Acoust. Soc. Am. **20**, 137–142 (1948).
[2] M. W. Widener, ''Ambient-noise levels in selected shallow water off Miami, Florida,'' J. Acoust. Soc. Am. **42**, 904–905 (1967)
[3] R. J. Bobber, *Underwater Electroacoustic Measurements* (Peninsula, Los Altos, 1988).
[4] S. Tavener, ''Manual for the program B&KNOISE'' (version 2.0), General Document DSTO-GD-0023, DSTO Aeronautical and Maritime Research Laboratory, Melbourne, 1995.
[5] M. Readhead, ''The distribution of snapping shrimp noise near Gladstone, Queensland,'' Technical Report DSTO-TR-0047 DSTO Aeronautical and Maritime Research Laboratory, Melbourne, 1994.
[6] D. H. Cato, ''Review of ambient noise in the ocean: non biological sources,'' Bull. Austral. Acoust. Soc. **6**, 31–36 (1978).
[7] D. H. Cato and M. J. Bell, ''Ultrasonic ambient noise in Australian shallow waters at frequencies up to 200 kHz,'' Technical Report MRL-TR-91-23, Materials Research Laboratory, Maribyrnong, Vic., 1992.

The combination of echolocation emission and ear reception enhances directional spectral cues of the big brown bat, *Eptesicus fuscus*

Janine M. Wotton and Rick L. Jenison[a)]
Departments of Neurophysiology and Psychology, University of Wisconsin, Madison, Wisconsin 53706

David J. Hartley[b)]
Medical Sciences Program, Indiana University, Bloomington, Indiana 47405

(Received 24 May 1996; accepted for publication 29 October 1996)

The acoustic information used by bats is produced by a combination of the properties of the sound emission and the reception at the eardrum. The potential localization cues used by bats can only be fully revealed when the magnitude spectra of the emission and the external ear are convolved to produce the echolocation combination magnitude spectra. The spatially dependent changes in the magnitude spectra of the echolocation combination of *Eptesicus fuscus* are described. The emission and external ear magnitude spectra act together to enhance the potential localization cues. In the echolocation combination, the spectral peaks are sharpened and there is greater contrast in intensity between peaks and notches when compared to the spectra of the ear alone. The spectral localization cues in the echolocation combination appear to be restricted to a cone of space of approximately $\pm 30°$. © *1997 Acoustical Society of America.* [S0001-4966(97)04503-7]

PACS numbers: 43.80.Ka, 43.80.Lb, 43.66.Qp [FD]

INTRODUCTION

Mammalian pinnae act as spatially dependent filters for sounds (e.g., human—Middlebrooks, 1992; Shaw, 1974, 1982; Searle *et al.*, 1975; Wightman and Kistler, 1989a, 1989b; cat—Musicant *et al.*, 1990; Rice *et al.*, 1992; ferret—Carlile, 1990; bats—Fuzessery, 1996; Wotton *et al.*, 1995) and the information produced by this filtering is known to be used, at least by humans, to localize the elevation of sound sources (Kistler and Wightman, 1992; Wightman and Kistler, 1989b). The localization cues are encoded as systematic spectral changes in the acoustical transfer functions (measured at the eardrum) with changes in sound source position (Wightman and Kistler, 1989a). One problem in interpreting the information provided by these changes in the spectra is that the source spectrum is usually unknown (Middlebrooks and Green, 1991; Wightman and Kistler, 1993).

Most mammals listen passively to the sounds in their environment and do not generally have information about the original spectrum of the sound at the source. However, some mammals use an active means of listening called biosonar or echolocation. These animals emit a sound that probes the environment and returns as an echo and thus both the original source spectrum and the changes in the spectrum are known. For example, echolocating bats emit a high-frequency signal that returns to them as an echo reflected from an object. Bats use the acoustic information contained in the echoes to detect and localize objects. It is assumed that bats also use spectral cues imposed by the shape of the external ear on the echoes to localize objects (e.g., Fuzessery, 1986; Grinnell, 1963; Guppy and Coles, 1988; Jen and Chen, 1988; Obrist *et al.*, 1993).

The measurements of bat ear directionality indicate that the spatial information is not uniform over all possible positions. The interaural intensity differences (IID) of several bat species are quite linear with azimuth only over a limited range of about $\pm 30°$ or 40° (Jen and Chen, 1988; Shimozawa *et al.*, 1974). The external ear transfer functions of *Eptesicus fuscus* contain systematic notches and peaks that appear over a limited range in both azimuth (about $\pm 30°$) and elevation (about $+30°$ to $-40°$) (Wotton *et al.*, 1995). The predictable changes in IID or spectral shape seem to be most reliable in the frontal field of bats for a restricted range of locations.

The signal emitted by bats also has directional properties (e.g., Hartley and Suthers, 1987, 1989, 1990; Schnitzler and Grinnell, 1977) and therefore must be considered in determining the directional information available to the bat. Shimozawa *et al.* (1974) measured the IID of two bat species which use a frequency modulated (FM) emission (*Myotis grisescens* and *Myotis lucifugus*) to four pure tones (35, 55, 75, and 95 kHz). They also measured the directionality of the bats' emission at these frequencies and thus were able to describe the directionality of the echolocation system. They found that the combined (ear and emission) echolocation directionality was sharper over a 180° range of positions (in azimuth) than the directionality of either the ear or emission alone. The echolocation system directional information was best between $\pm 30°$ or 40° in azimuth.

Two different bats (*Rhinolophus ferrumequinum* and *Pteronotus parnelli*) which use a constant frequency (CF) component in their emission have also been the subjects of echolocation directionality studies. Fuzessery *et al.* (1992) combined the ear directionality of *Pteronotus* for three pure tones (30, 60, and 90 kHz) with the directionality of the

[a)]Address reprint requests to: Rick Jenison, Department of Psychology, University of Wisconsin, 1202 W. Johnson St., Madison, WI 53706.
[b)]Current address: Microsoft Corporation, 1 Microsoft Way, Redmond, WA.

emission at the same frequencies. The echolocation system as a whole was more directional for the center of the frontal azimuthal field ($\pm 26°$) than the ear directionality alone indicated. They suggested that although *Pteronotus* can detect objects in the lateral field, it may only use the frontal field for a more detailed analysis of objects.

Grinnell and Schnitzler (1977) conducted the only study using behavioral measures of the directionality of hearing by a bat (*Rhinolophus*). This bat showed sensitivity decreases of about 45 dB from the midline to the side and very sharp decreases below the horizon. These behavioral measurements were combined with the measurements of the CF emission directionality made by Schnitzler and Grinnell (1977). The directionality of the echolocation system had a very sharp, fairly symmetrical drop in echo effectiveness at angles greater than 30° from the midline for both azimuth and elevation (Grinnell and Schnitzler, 1977). They suggested that all useful echoes for this bat would probably originate at angles of less than 30° or 40°.

The directionality of the echolocation system of the FM bat *Eptesicus* in azimuth was calculated by Simmons *et al.* (1995) using IID data for four pure tones (25, 40, 60, and 80 kHz) from Jen and Chen (1988) and emission data from Hartley and Suthers (1989). At the three higher frequencies, the directional information is sharpest (within 3-dB directional gain) in the range from about 25° to 40° on the ipsilateral side to 10° on the contralateral side. The drop in intensity on the contralateral side is rapid and quite large, the signal is attenuated by almost 20 dB at 25° contralateral. At 25 kHz the sensitivity (3-dB directional gain) is much broader extending from 65° ipsilateral to 30° contralateral.

These studies, which all used a few discrete pure tones to determine echolocation directionality, suggest that the bats have a restricted spatial region in which the directional information is greatest. Although a series of a few pure-tone stimuli can demonstrate the frequency dependence of directional reception, it cannot show the spatial filtering properties of the external ear for broadband sounds having a continuous spectrum. Details that are necessary for vertical localization in other animals, such as spectral peaks or notches, can only be detected if many, very closely spaced frequencies are tested (Musicant *et al.*, 1990). To understand the directional effects of the external ear of an FM bat on sonar echoes, it is essential to use a broadband signal which contains the full range of frequencies occurring in the emission. This, in combination with the directional information of the entire emission spectrum, can demonstrate the available cues for object localization. We have used available data for the FM bat *Eptesicus* to combine the spectral filtering properties of the external ear (Wotton *et al.*, 1995) with the directional properties of the emission for the entire frequency range of the emission (Hartley and Suthers, 1989). We expect that the bat's emission and external ear have evolved to enhance localization information and that this information will be contained in a restricted region of the frontal field. The combination of ear and emission data should contain more precise directional information than either ear or emission alone.

The particular features of the sound spectrum thought to provide mammalian vertical information are contentious. Some authors place great emphasis on spectral peaks (e.g., Blauert, 1969/1970; Humanski and Butler, 1988), while others attribute the notch with special importance (e.g., Bloom, 1977; Hebrank and Wright, 1974; Rice *et al.*, 1992), and some authors treat all spectral changes as equally important (e.g., Wightman and Kistler, 1989b; Middlebrooks, 1992). One feature of spectral change which is implicit in the discussion of these cues is a change in gradient, that is, the rate of change in the magnitude of portions of the spectrum. According to Lehky and Sejnowski (1990), as a tuning curve becomes steeper, the change in a stimulus parameter required to elicit a response becomes smaller. They therefore suggest that steep tuning curve slopes correspond to fine discriminability (Lehky and Sejnowski, 1990). A change in spectral gradient could be a potent cue for localization, for example, small changes in the frequency or magnitude of a notch could dramatically alter the slope of the sides of the notch. Clearly, as the gradient become steeper, then the magnitude difference between neighboring frequencies also increases, which may improve the detectability of spectral differences. We intend to examine all of these features of the spectrum and determine how the combination of emission and ear spectra alter potential cues for localization.

I. METHODS

A. Emission measurement

The procedure to measure the directionality of the emission of *Eptesicus* was previously described in detail in Hartley and Suthers (1987, 1989). Briefly, the bat was anaesthetized and suspended in an echo-attenuating chamber. The head was fixed in place by a steel rod cemented to the skull and locked into a holder. The head was oriented with the eye-nostril line aligned horizontally. Echolocation emissions were elicited from awake bats by brain stimulation (Suga and Schlegel, 1972). The emissions were recorded by two microphones (Bruel and Kjaer, model 4135) each placed 32 cm from the bat. One microphone positioned directly in front of the bat was stationary and designated the reference microphone and the second microphone was moved in azimuth (range 0° to 90°) and elevation ($+80°$ to $-80°$) in 10° steps. Ten emission were averaged at each moving microphone position. The ratio of the output at the moving microphone to that of the reference was taken as the ratio of the spectrum magnitudes calculated in dB SPL. The recorded spectra at each position ranged from 20 to 80 kHz. The echolocation emissions of the two bats recorded were very similar (Hartley and Suthers, 1989); the spectra from one bat were available for this study.

B. External ear measurements

The procedure for measuring the external ear transfer functions of *Eptesicus* was described in detail in Wotton *et al.* (1995), and is therefore only briefly summarized here. The sound-pressure levels at the position of the eardrum were measured as the azimuth and elevation of a sound source were varied. The head of a dead bat was cut in an oblique sagittal section to expose the eardrum of one ear. A microphone (Bruel and Kjaer, model 4138) and coupler were

inserted from the middle ear side to replace the eardrum. The head was fixed in position and was oriented such that the median sagittal plane corresponded to 0° azimuth and the eye-nostril plane to 0° in elevation. A condenser loudspeaker attached to a moveable frame was positioned 45 cm from the ear. The sound stimulus was a wideband FM sweep (100–10 kHz) with a short duration (0.5 ms). At each loudspeaker location, sound passing through the ear was recorded at the microphone and digitally sampled (RC Electronics, Inc. ISC-16; sampling rate 500 kHz). The data were averaged (128 sweeps) in real time to improve the signal to noise ratio. The sound source was moved around the head in 5° steps in an azimuthal range of 70° ipsilateral to 25° or 30° contralateral and an elevation range of +65° to 70°, without changing the radial distance to the ear. A free-field reference measure of sound-pressure level was made of the microphone and coupler without the head and ear attached. The transfer functions for each position were calculated by dividing the cross spectral density of the reference free-field measurement and the external ear measurement by the spectral density of the reference free field measurement (ILS Signal Technology, Inc.). The magnitude spectrum for each transfer function was calculated in dB SPL for ears B and C from Wotton *et al.* (1995).

C. Echolocation combination

The ear (ear B) and emission spectra were convolved (added in dB) to produce the echolocation combination over the frequency range 20–80 kHz, at each of the corresponding spatial locations, resulting in 112 positions ranging in azimuth from 0° to +70° and in elevation from +60° to −70° in 10° steps. The echolocation combination was also calculated for ear C to verify the validity of the results. All analyses were done using Matlab software (Mathworks, Inc.).

II. RESULTS

To conserve space the results of both ears are not shown, all figures display the results obtained using ear B and the results from ear C are reported briefly.

A. Echolocation directionality in elevation

Figure 1 is a set of shaded contour plots showing the spectral changes across all elevations in the range +60° to 70° at the single azimuth 0°, for all frequencies from 20 to 80 kHz for the emission (A), the ear (B), and the combined echolocation system (C). The measurements are at 10° intervals and the intervening points have been interpolated. The shading corresponds to relative intensity, with dark regions being areas of low intensity and white regions of highest intensity. The first contour line encircles the region of maximum intensity and the remaining contour lines are plotted at 3-dB decrements in intensity.

B. Emission

Most of the energy in the emission, of Fig. 1(A), is directed below the horizon between about 0° and −40° or

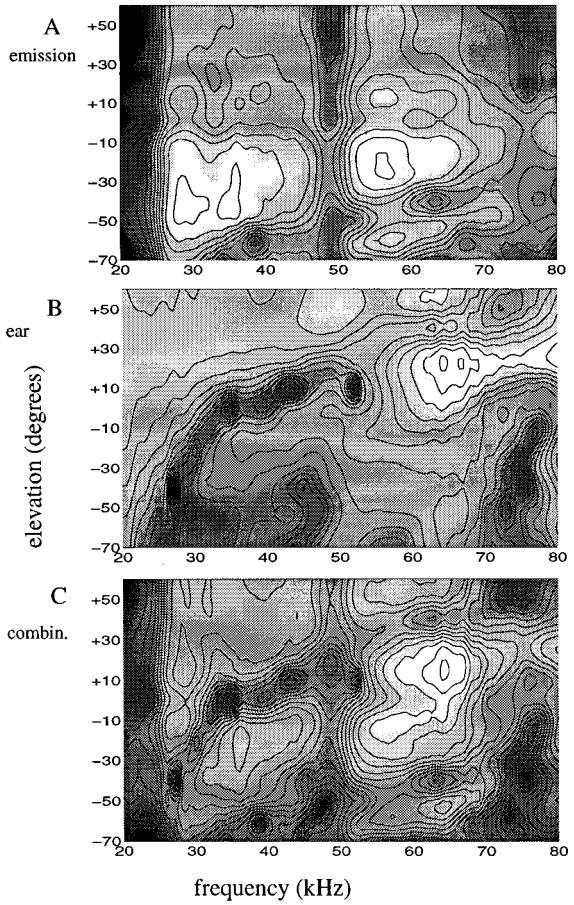

FIG. 1. Shaded contour plots of the magnitude spectra of the emission (A), the external ear (B), and the echolocation combination (C). Each panel shows the frequency at all elevations (from +60° to −70° in 10° steps) at 0° in azimuth. The shading corresponds to relative intensity, with white being the most intense and darkening with decreases in intensity. The first contour encircles the greatest intensity and the remaining contours are plotted in 3-dB decrements.

−50°. Two distinct bands of energy can be seen, the first from about 25 to about 47 kHz and the second from about 51 to 70 kHz [Fig. 1(A)].

C. External ear

Figure 1(B) shows clearly the presence of a notch (local minima), in the magnitude spectra of the external ear transfer functions, which changes systematically in frequency (from about 50 to 30 kHz) with changes in elevation. This notch is referred to as the primary notch. The prominent peak (local maxima) between about 60 and 70 kHz, referred to as the main peak hereafter, is also clearly visible. Both the primary notch and main peak are present for a restricted range of elevations. The primary notch appears between about +10° and −40° and the main peak between +30° and −10°. The intensity at about 50 kHz is low at most elevations below +30°.

D. Combination pattern

Figure 1(C) shows the echolocation combination pattern, the primary notch and main peak are both still visible and appear to be more prominent, with regions of greater contrast

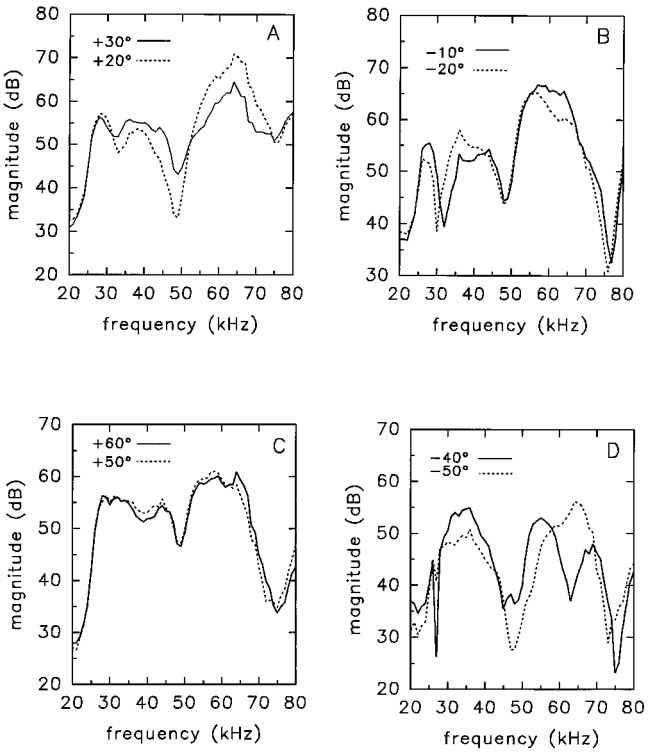

FIG. 2. Each panel compares the magnitude spectra of the echolocation combination at two different elevations (panel A: +30° and +20°; panel B: −10° and −20°; panel C: +60° and +50°; panel D: −40° and −50°) at 0° in azimuth.

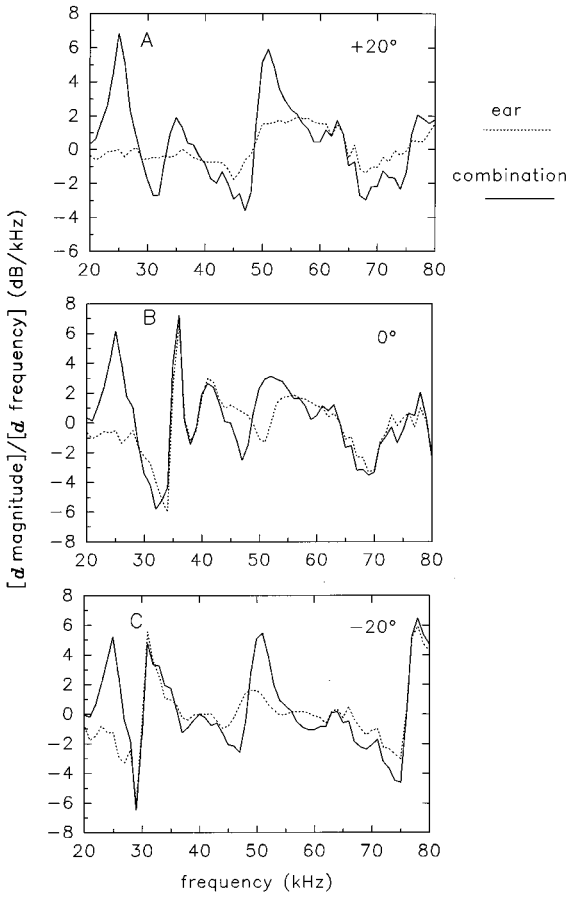

FIG. 3. The spectral gradient (∂ magnitude/∂ frequency) as a function of frequency is shown for the external ear and the echolocation combination at three different elevations (panel A: +20°; panel B: 0°; panel C: −20°).

in intensity surrounding both the peak and notch. This is evident in the closer spacing of the contours near the boundaries of the peak and notch. The primary notch still shifts in frequency from about 50 to 30 kHz but all locations in the echolocation combination also have a deep stationary notch at 50 kHz. The range of elevations in the combination pattern for which the primary notch is present is increased to about +20° to −40°, and for the main peak it is increased to about +30° to −30°. The elevation range for the primary notch in the echolocation combination for ear C was about +10° to −40° and for the main peak about +30° to −40°.

Within ±−30° in elevation, the differences between combination echolocation spectra are clear and reveal cues that the bat might use to distinguish between two elevations. Comparison of the combination echolocation spectra at +20° and +30° in elevation (at 0° in azimuth) reveal large differences, particularly between the frequency range of 50–65 kHz [Fig. 2(A)]. A comparison of elevations −10° and −20° display differences mainly in the primary notch frequency in the range of 30–40 kHz [Fig. 2(B)]. However, there is very little difference between the spectra at positions +50° and +60° in elevation [Fig. 2(C)]. Comparison of echolocation spectra at −40° and −50° reveals large differences in the spectra, but the frequency of the primary notch is the same in both functions [Fig. 2(D)]. This is true for Fig. 2(A) as well. The spectral difference in Fig. 2(D) is introduced almost entirely by the emission because both ear spectra are very similar at these elevations.

E. Information enhancement

The main peak and primary notch information appear to be enhanced in the echolocation combination compared to the ear alone. The spectral gradients (magnitude change with respect to frequency change) were calculated for the ear and the echolocation combination. Figure 3 displays the gradients at each frequency for the echolocation combination and for the ear at three different elevations (+20°, 0°, −20°) at 0° azimuth. In all plots, the gradients between about 45 and 55 kHz are greater for the echolocation combination. The rate of intensity change between the main peak at about 60–70 kHz and the drop to a notch at 50 kHz is greater in the echolocation combination, and thus the contrast in intensity is enhanced. Similarly, all plots show that the gradients between 20 and 30 kHz are greater in the echolocation combination which might narrow the width of the primary notch and its lower adjacent peak for the lower elevations.

To facilitate direct comparison, the magnitude of the ear spectra and the combination echolocation spectra were made more similar (as judged by eye), by adding 60 dB to the ear spectra at elevations +20° and 0° and 65 dB at elevation −20°. Figure 4 displays this comparison of echolocation combination spectra and ear plus 60/65 dB spectra at these three elevations (+20°, 0°, −20°) at 0° in azimuth. At all elevations, but particularly at +20°, the difference between the spectra is greatest in the range of 45–55 kHz with the

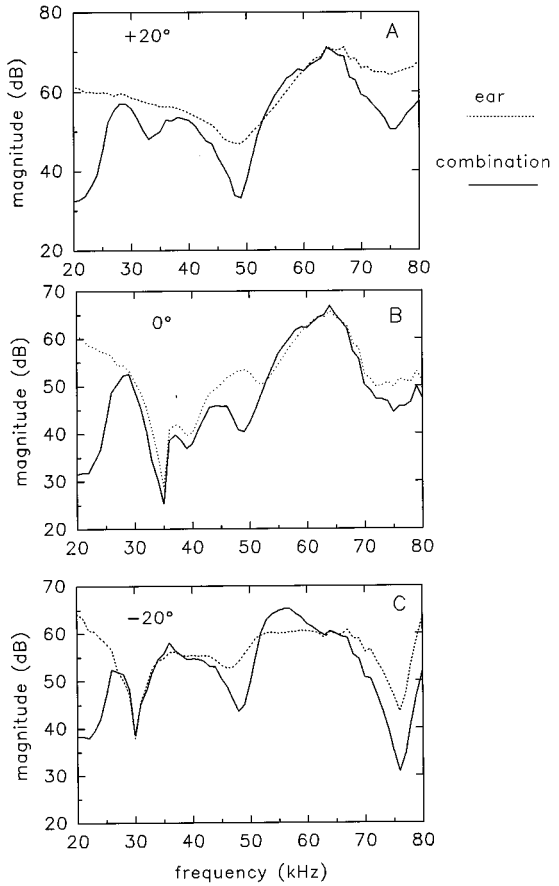

FIG. 4. The magnitude spectra of the echolocation combination compared to the magnitude spectra of the ear plus 60 dB at elevation +20° (panel A) and 0° (panel B). Panel C compares the magnitude spectra of the echolocation combination and the ear plus 65 dB.

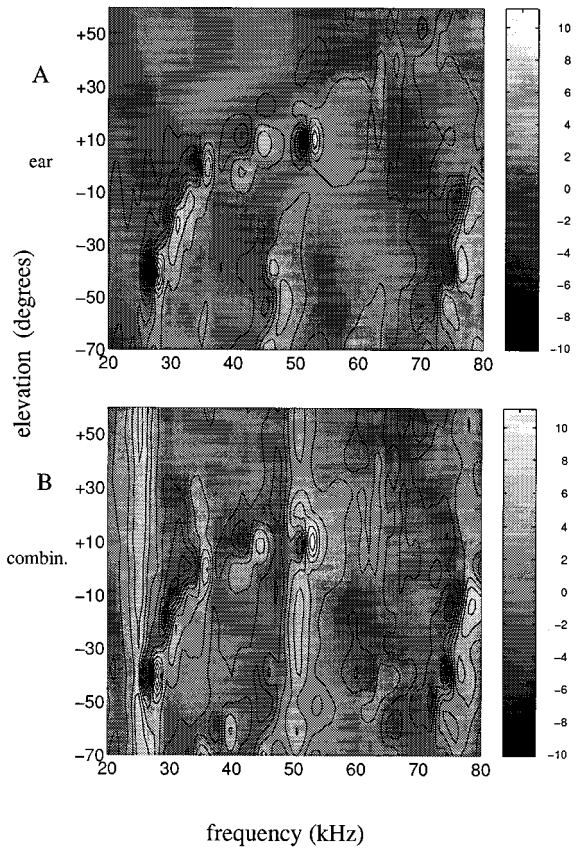

FIG. 5. The spectral gradient (∂ magnitude/∂ frequency) as a function of frequency is interpolated for the external ear (A) and the echolocation combination (B) for the full range of elevations (+60° to −70°).

echolocation combination dropping sharply at about 50 kHz. This greatly increases the intensity difference between this frequency region and the main peak region between 60 and 70 kHz [Fig. 4(A), (B), (C)]. All elevations have a much sharper peak between 20 and 30 kHz in the echolocation combination, presumably due to the roll-off of the emission at around 25 kHz. At 0°, there is a slight difference in the primary notch depth at about 37 kHz between the two spectra, with the echolocation combination having a slightly deeper notch [Fig. 4(B)]. At −20°, the primary notch depths at about 32 kHz are very similar but the peaks (between 20 and 30 kHz and between 35 and 40 kHz) adjacent to the primary notch are sharper in the echolocation combination [Fig. 4(C)]. These peaks, referred to as adjacent peaks, are enhanced in the echolocation combination thereby increasing the intensity contrast between the primary notch and surrounding frequencies [Fig. 4(C)].

Figure 5 shows the gradient change over the full range of elevations (+60° to +70°) at 0° in azimuth for the ear [Fig. 5(A)] and the echolocation combination [Fig. 5(B)]. The shading corresponds to the relative change in magnitude with frequency, with the brightest white being set at +11 dB/kHz and the darkest black at −10 dB/kHz. Both plots use the same scale of color coding and the contour lines are drawn at 2-dB/kHz decrements. In both plots there are regions of large positive and negative gradients which shift in frequency (between about 50 and 25 kHz) with changes in elevation. These regions are pronounced in the echolocation combination, between about +30° and −40°, and in the ear plots, between +10° and −40°, and correspond to the frequency shift of the primary notch. In the echolocation combination there are two bands of large positive gradients at around 25 and 50 kHz which are present for all elevations. The increased gradient between 20 and 30 kHz in the echolocation combination is probably due to the sharp roll-off of the emission at around 25 kHz and thus does not seem to be direction dependent. However, this lower-frequency peak does act to enhance nearby features, such as the notch, which are direction dependent. Similarly, the increased gradient between 45 and 55 kHz is probably due to the harmonic structure of the emission. However, there are bands of increased gradient between 40 and 50 kHz in the ear at lower elevations [Fig. 5(A)] and these are greatly enhanced in the echolocation combination [Figs. 3 and 5(B)].

To verify this result with a different set of ear transfer functions, the gradients were calculated for ear C and echolocation combination of ear C. The gradients were increased particularly in the 45–55 kHz and 20–30 kHz regions, acting to enhance the difference between the primary notch and the adjacent peaks.

Figure 6 shows the intensity of a single frequency (either 40 kHz or 80 kHz) at all elevations (+60° to −70°) and all azimuths (0° to +70°) as shaded 3-dB contour plots. The

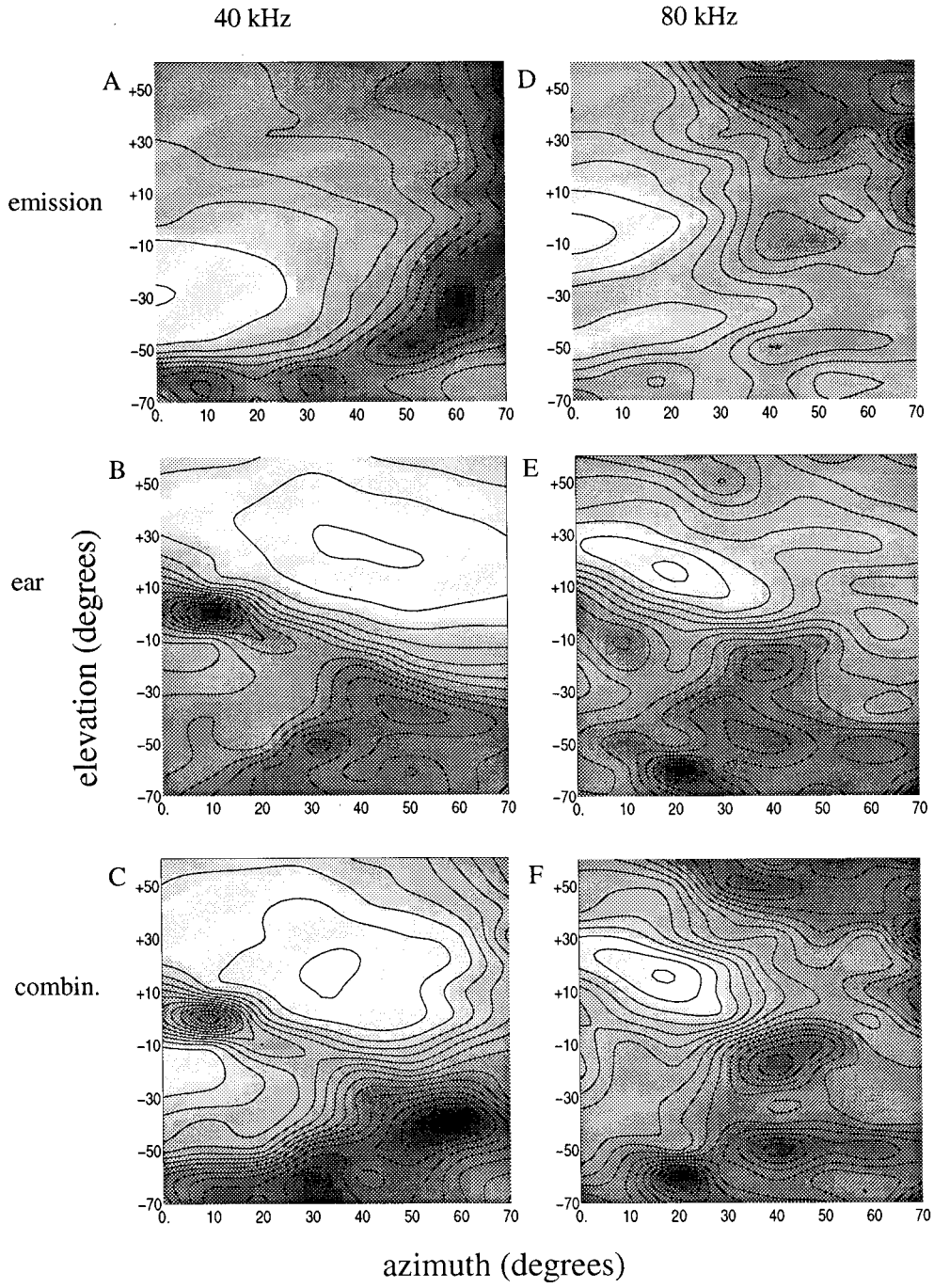

FIG. 6. Shaded contour plots at 40 kHz (A, B, C) and 80 kHz (D, E, F) as a function of elevation (+60° to −70°) and azimuth (0° to +70°) for the emission (panels A and D), the external ear (B and E), and the echolocation combination (C and F). The shading corresponds to relative intensity and the contours are plotted at 3-dB decrements.

directionality of the emission is symmetrical around the midline (Hartley and Suthers, 1989) and thus the emission contours shown in Fig. 6 display only half the space contained in the intensity contours. For both frequencies, the contours encircle smaller regions of space for the echolocation combination than for either the emission or the ear alone, indicating that the echolocation combination is more directional. As frequency is increased, all conditions show smaller regions encircled by 3-dB contours. The contours around the acoustic axis (position of greatest intensity) are closer to each other in the echolocation combination than for either the ear or emission alone. At each frequency (40 or 80 kHz) this sharpening of the gradient of intensity change can be seen best near the acoustic axis.

A shift in the position of greatest intensity (acoustic axis) is visible in Fig. 6. The emission plots reveal that as frequency is increased, the elevation of the greatest intensity is increased [Fig. 6(A) and (D)]. Both the ear and combination plots show that the acoustic axis is more lateral at 40 kHz compared with the acoustic axis for 80 kHz [Fig. 6(B) and (E), and Fig. 6(C) and (F)]. Only two frequencies have been displayed here but there is a general trend across all

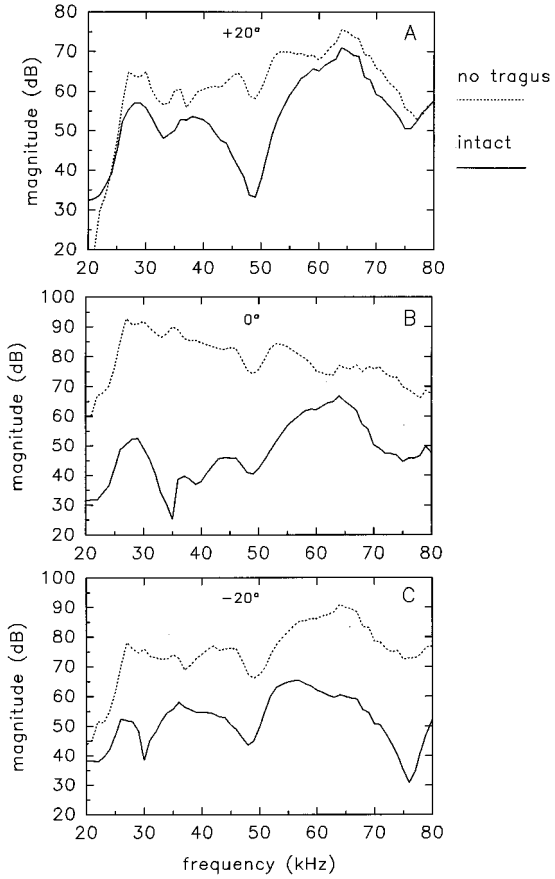

FIG. 7. The magnitude spectra of the intact echolocation combination compared to the magnitude spectra of the no tragus echolocation spectra at three elevations (panel A: +20°; panel B: 0°; panel C: −20°) at 0° azimuth.

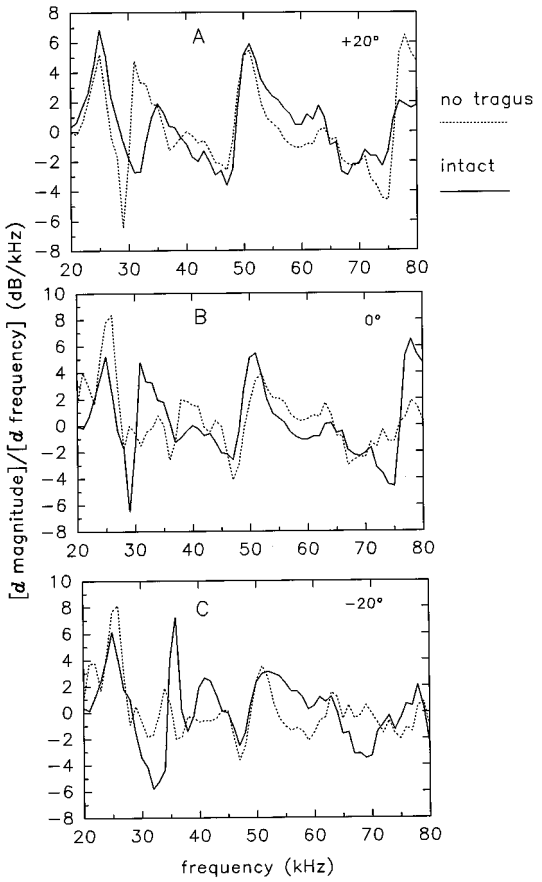

FIG. 8. The gradient of magnitude change as a function of frequency is shown for the intact echolocation combination and the no tragus echolocation combination at three different elevations (panel A: +20°; panel B: 0°; panel C: −20°) at 0° azimuth.

frequencies (with a few anomalies) for an increase in elevation with frequency for the acoustic axes of the emission, ear, and echolocation combination. The ear and echolocation combination show an azimuthal shift of the acoustic axis toward the midline with an increase in frequency.

F. Tragus

The ear (ear B) used to calculate the combination was measured before and after the tragus was removed. Figure 7 shows the magnitude spectra of the echolocation of the intact ear combination (emission plus ear) and the no tragus combination (emission plus ear). At +20°, the main peak region is similar for both conditions, although the notch at 50 kHz is more pronounced in the intact condition [Fig. 7(A)]. At 0° and −20° there are differences across the entire spectra with the largest differences in spectral shape in the region of 25–50 kHz [Fig. 7(B) and (C)]. The spectra are much flatter in the no tragus combination condition.

The gradients of the intensity change of the intact combined echolocation system are compared with the gradients for the combined echolocation system with no tragus in Fig. 8. At +20° the main difference is between about 27 and 35 kHz [Fig. 8(A)]. At 0° the biggest differences in the gradients are in the region 27–37 kHz [Fig. 8(B)] which is the region of the primary notch and its adjacent peaks in the intact combination [Fig. 7(B)]. At −20° the biggest differences are in the region between 25 and 40 kHz [Fig. 8(C)]. The intact combination has a sharp notch at about 32 kHz with adjacent peaks at about 25 kHz and 40 kHz [Fig. 7(C)]. The gradients of the intact combination are steeper and sharper, particularly for the elevations 0° and −20° [Fig. 8(B) and (C)].

G. Azimuth

Although not the primary focus of the paper, we briefly describe data on the azimuthal component of the echolocation combination. The primary notch and peak information are also restricted in azimuth. Figure 9 is a set of shaded frequency contour plots showing the range of azimuthal positions from 0° to +70° at a single elevation 0° for the echolocation combination. The combined echolocation plot shows that the primary notch is present for a restricted range of azimuths, from 0° to about +20°. The main peak in the echolocation combination is present for a limited azimuthal range (about 0° to +30° or +40°). The echolocation combination for ear C also showed a restricted azimuthal range for the main peak and primary notch (about 0° to +30° or +40°).

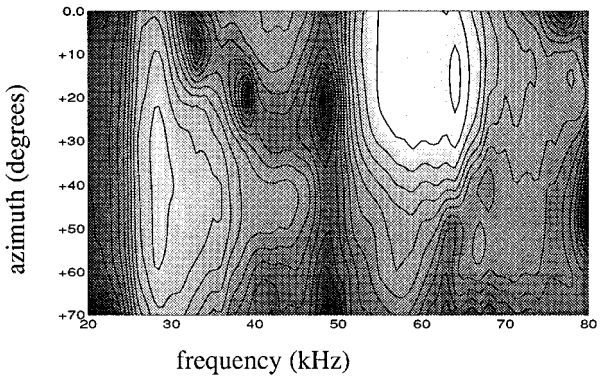

FIG. 9. Shaded contour plot of the magnitude spectra of the echolocation combination at all azimuths (0° to +70° intervals of 10°) at the elevation 0°. The shading corresponds to relative intensity and the contours are plotted in 3-dB decrements.

III. DISCUSSION

A. Echolocation directionality in elevation

The putative localization cues contained in the external ear transfer functions and in the echolocation combination are restricted in elevation. For the external ear, the primary notch is prominent between +10° and −40° in elevation and the main peak between about +30° and −10°. This range has been extended in the echolocation combination; the primary notch is prominent between +20° and −40° and the main peak between +30° and −30°.

Figure 2 reveals the spectral information available to distinguish different elevations. Within the ±30° range in elevation, locations separated by 10° have large spectral differences [Fig. 2(A) and (B)]. There are clear differences between elevations +20° and +30° in the magnitude of the main peak around 65 kHz, the notch at 50 kHz, and the rate of change between the lowest intensity of the notch and highest intensity of the peak. These differences could provide the bat with information to distinguish the two positions. However, the differences are very small for two positions higher in elevation (+50° and 60°) and might not provide enough information for the bat to discriminate between these locations [Fig. 2(C)]. The frequency of the primary notch could be used to distinguish two elevations below the horizon, as a comparison of the spectra at −10° and −20° shows [Fig. 2(B)]. At more extreme positions such as −40° and −50° the frequency of the primary notch is the same [Fig. 2(D)]. If bats are able to discriminate between these locations, they presumably must use the spectral differences at the higher frequencies. The spectral differences between these two positions were largely introduced by differences between the emission spectra. Perhaps the emission gradient information provides more elevation information than that provided by the ears for the lower elevations. Figure 1 shows that the emission is largely directed below the horizon but for the ear measurements there is little acoustic energy at extremely low elevations.

Behavioral measures of the vertical acuity of *Eptesicus* (Wotton and Simmons, in preparation) reveal that bats have a similar difference angle acuity (between 3° and 4°) for objects within the ±30° elevation range. However, their performance at lower elevations is significantly worse (between 6° and 8°) and at higher elevations the bats would not discriminate the angle difference at the largest angle tested (21°). The bats appear to have a zone of about ±30° in which they display best angular discrimination performance and this coincides with the zone of elevation for which the putative localization cues are available.

Moore *et al.* (1989) found that spectral peak cues are more salient to human listeners than notches in stationary stimuli; however, for moving stimuli a change in the frequency of a notch is detectable even for narrow notches. Similarly, the bat may be able to detect a change in frequency of the notch as the target changes in elevation. The change in frequency is from approximately 50 to 30 kHz over about 50° to 60° in elevation which corresponds to 1 kHz for 2.5°–3°. The vertical acuity of *Eptesicus* is about 3°–3.5° (Lawrence and Simmons, 1982a), and therefore, if the frequency resolution of this bat is 1 kHz or less, then this notch cue could be perceptually relevant. Roverud and Rabitoy (1994) estimate that *Eptesicus* is able to resolve tone steps within an FM signal that are separated by about 450 Hz or more. Thus, the changes in the frequency of the notch in the echolocation combination should be perceptually available to the bat.

The frequency of a notch in a signal, in the range of 50–35 kHz, influences the ability of *Eptesicus* to discriminate between two signals from sound sources at elevations between +5° and −10° (Wotton *et al.*, 1996). The bats are unable to discriminate, a signal with the notch from another signal with no-notch, at only one sound source elevation. The sound source elevation at which the discrimination cannot be performed is changed when the frequency of the notch in the signal is changed. Although this does not show that the notch is necessarily a localization cue, it does indicate that the frequency of the primary notch and/or adjacent peaks influence the bat's behavior in this elevation range.

B. Information enhancement

Comparisons of the ear spectra with the combination echolocation spectra (Fig. 4) show that the peak and notch information appear to be enhanced in the combination condition. The intensity difference between the main peak and the notch at 50 kHz is increased and the rate of change between the main peak and this notch is also increased (Figs. 3 and 5). The contrast between the primary notch and the surrounding frequencies is enhanced. This is achieved by sharpening small adjacent peaks on either side of the notch, especially the lower-frequency peak (below 30 kHz), which causes steep changes in intensity from the peaks to the tip of the primary notch [Fig. 1(B) and (C), in Figs. 3, 4, and 5]. In addition, the elevation range of the main peak is extended to lower elevations [Fig. 1(B) and (C)] which provides greater contrast between the intensities of the primary notch and the notch at 50 kHz.

The emission of *Eptesicus* is an FM sweep from about 100 to 25 kHz usually composed of 2 or 3 harmonics. The frequencies of the first harmonic sweep from about 55/50 to 25 kHz (Menne, 1988; Simmons *et al.*, 1979). There is sub-

stantial individuality in the emission of *Eptesicus*, with variation in the beginning and ending frequencies of the harmonics (Masters *et al.*, 1991; Obrist, 1995). Sometimes the harmonics can overlap slightly in frequency, but often there is little or no overlap and there may even be a gap between the first and second harmonics (Masters *et al.*, 1991). Sonograms of the emission show that there is less energy at the beginning and end of the harmonics (e.g., Hartley and Suthers, 1989; Simmons, 1989). Figure 1(A) displays a pronounced notch at about 50 kHz in the emission spectra which probably coincides with the beginning of the first harmonic and the end of the second. The change in the magnitude of the echolocation combination in this frequency region is therefore probably largely due to the harmonic structure of the emission.

The echolocation combination of *Eptesicus* is particularly well suited to revealing changes in gradient because spectral features change in magnitude and/or frequency. The FM emission ''interrogates'' the contours of each frequency; thus changes in magnitude will be revealed progressively as the emission sweeps through all the frequencies in order. The main peak is fixed in frequency between 60 and 70 kHz but changes in intensity, there is also a notch fixed at about 50 kHz that changes in intensity. A change in intensity of either of these features will alter the gradient between them. The primary notch moves down in frequency from about 50 kHz, so the change in frequency relative to the fixed main peak causes a change in gradient. At lower elevations, the primary notch moves further down in frequency and smaller peaks, adjacent on either side of the notch, appear. The gradient of the primary notch can therefore be compared to the main peak or to the adjacent peaks at these lower elevations.

Signals can vary in the rate of change in frequency (FM) or amplitude (AM). The ability of humans to detect glides in frequency or amplitude is very similar, but thresholds tend to be smaller when both types of glides are combined (Dooley and Moore, 1988). Similarly, Moore and Sek (1992) found that signals of mixed frequency and amplitude modulation (AM) were more detectable than AM signals alone. Effectively, the echolocation combination is composed of both types of sweep; the changes in magnitude across time are imposed on an FM emission. Rapid changes in level created by steep gradients between peaks and notches are imposed on the temporal structure of the emission. The combination of glide types should provide more information to the bat than the FM sweep alone.

The region of space encircled by the 3-dB contours decreases with increases of frequency for all conditions (Fig. 6). This has also been reported for other bat ears (e.g., Jen and Chen, 1988; Fuzessery and Pollak, 1985) and cat ears (e.g., Phillips *et al.*, 1982), for the emission of bats (Hartley and Suthers, 1989), and for the echolocation combination (Shimozawa *et al.*, 1974; Fuzessery *et al.*, 1992). The acoustic axes of the ear and of the combination shift toward the midline with increases in frequency, which has also been found for bat ears (Jen and Chen, 1988; Obrist *et al.*, 1993) and for the echolocation combination (Shimozawa *et al.*, 1974; Fuzessery *et al.*, 1992). The frequencies chosen for Fig. 6 (40 and 80 kHz) are close to those plotted for the ear of *Eptesicus* by Jen and Chen (1988) (45 and 85 kHz) and the position of the acoustic axes in Fig. 6(B) and (D) are very similar to their plots.

The contour plots at a single frequency show that the echolocation combination is more directional than either the emission or ear alone (Fig. 6). The acoustic axes of the ear and of the emission are not spatially coincident and the interaction of these different regions of high intensity produces a smaller, high intensity region of space for the echolocation combination. The echolocation combination therefore would provide more directional information than either a broadband noise signal combined with the external ear or the emission combined with pinnaless heads. As expected, the ear and emission have evolved to combine in such a way to provide more precise directional information. Similar results have been found for other species of bats (e.g., Fuzessery *et al.*, 1992; Shimozawa *et al.*, 1974) indicating that it is important to consider both the ear and the emission in determining the directional information available to bats.

Further evidence of the cooperative action of the ear and emission is that spectral cues seem to be enhanced. *Eptesicus* appears to have a region or cone of best focus in the echolocation combination. Although information from more extreme positions is available, it may not be sufficient to accurately localize or identify a target, and thus bats may need to turn to put the object in the cone of focus.

C. Tragus influence

The external ear transfer functions measured after removal of the tragus showed that the frequency of the main peak above the horizon was largely unaffected, but the change in frequency of the primary notch was greatly disrupted (Wotton *et al.*, 1995). Figure 7(A) compares the intact and no tragus echolocation combinations at three elevations and shows that the frequency range from 20 to 50 kHz is especially affected by tragus removal for all positions. The main peak region (between 60 and 70 kHz) at elevation $+20°$ is very similar in spectral shape between the two conditions. At $0°$ and $-20°$ there are large spectral differences across the whole frequency range, but these are particularly pronounced between 25 and 50 kHz. Comparison of the gradients of the intact and the no tragus echolocation combinations shows that the frequency region of the primary notch and the adjacent peaks (25–50 kHz) are smeared in the no tragus echolocation combination [Fig. 8(B)].

The spectral gradients are sharper in the intact ear combination compared to the no tragus combination, especially near and below the horizon. Similarly, the gradients are sharper in the intact echolocation combination compared to the intact ear alone condition. It seems that the combination of three elements, the emission, the pinna, and the tragus, all act together to sharpen the spectral gradients in the intact echolocation combination. The interaction of sounds with the pinna and tragus may provide bats with elevation information (Grinnell and Grinnell, 1965; Simmons and Grinnell, 1988; Wotton *et al.*, 1995) and apparently this information is enhanced by the addition of the emission.

If the change in frequency of the primary notch and/or the adjacent peaks are elevation cues, then distortion of the

tragus should interfere with localization. When the tragi of both ears of *Eptesicus* are glued to the side of the head, the bat's ability to discriminate vertical angles near (Lawrence and Simmons, 1982a) and below the horizon (Wotton and Simmons, in preparation) is greatly perturbed. However, bending the tragus does not alter the bat's ability to discriminate vertical angles above the horizon (Wotton and Simmons, in preparation). The spectral information below the horizon is altered across the entire spectrum by tragus removal, but the most prominent information in the intact echolocation combination is contained in the 25–50 kHz region. It is not clear that bats must necessarily be using the notch and/or adjacent peaks to discriminate locations below the horizon, but this is the most obvious cue available in the intact combination and removed in the no tragus combination. It seems likely that the bats are using information contained in the frequency range of the main peak (60–70 kHz) to determine the location of a target above the horizon because this appears to be the only portion of the spectrum which is relatively intact after tragus removal.

D. Azimuth

Studies of the echolocation directionality for pure tones indicated that several bat species, including *Eptesicus*, have a region of about $\pm 25°$ or 40° in azimuth in which directional information is most useful (Shimozawa *et al.*, 1974; Fuzessery *et al.*, 1992; Grinnell and Schnitzler, 1977; Simmons *et al.*, 1995). Figure 9 shows that the primary notch and main spectral peak in the echolocation combination are restricted to a similar range on the ipsilateral side. Thus, for *Eptesicus*, both the broad IID cues and the specific spectral changes are limited to a frontal cone of space approximately $\pm 30°$ in azimuth and elevation. Although the external ear primary notch and main peak are present between azimuths 0° and $-20°$ or $-30°$ (Wotton *et al.*, 1995), the attenuation of frequencies above 40 kHz in the echolocation combination is high for these contralateral positions and thus only the lowest frequencies are likely to be useful (Simmons *et al.*, 1995). This greatly limits the use of fine spectral changes to provide information about contralateral locations. On the ipsilateral side the information provided by notches and peaks in the spectra is available and potentially useful.

Humans, by contrast, do not show such a limited range of best directionality. Human ears are positioned approximately at 90° with respect to the midline and so a sound source moving from directly opposite one ear to the other would move almost 180°. The region of space in front of human ears is essentially the same as the frontal field of the head. However, bat ears are positioned on the top of the head and face forward, thus a sound source moving from one *Eptesicus* ear to the other would move about 60°–80°. Sound sources moving beyond this region would move behind the ears. For the bat, the region in front of the ears might best be described as the frontal ear field, which is considerably smaller than the frontal field of the head.

E. ''Matching'' emission and external ear

Ear and emission measurements were not made at the same distances and thus are not perfectly matched. The emission was measured at 32 cm and the highest frequency recorded was 80 kHz. The ear measurements were made at a greater distance (45 cm) but still include frequencies up to 100 kHz. If the high frequencies were altered by attenuation at the greater distance of the ear measurement, then this should be ameliorated by restricting the frequency range between 20 and 80 kHz. These echolocation combination descriptions should apply best to targets within about 30–50 cm of the bat. Within this range the bat has probably detected and identified the target (Simmons, 1989) and must now accurately locate and track the target in order to catch it. At closer distances, the bats include more high-frequency components in the emission (Simmons, 1989) and the echolocation combination would need to include these and compensate for any attenuation of these high frequencies in the ear measurement. At greater distances, the higher frequencies are produced less (Simmons, 1989) and attenuated more (Lawrence and Simmons, 1982b), and this needs to be considered for echolocation directionality estimates beyond about 50 cm.

Bats display spectral individuality in measurements of both the external ear and emission (Wotton *et al.*, 1995; Masters *et al.*, 1991; Obrist, 1995), and therefore the echolocation combination might also be expected to differ slightly between bats. For example, the frequency of the primary notch differs, between ears B and C, for different elevations but both echolocation combinations retain the same general features. Although the exact frequencies of spectral features may differ, the main features in the echolocation combination are the same for different ears. Here, we have displayed the results of combining one bat's ear with another bat's emission and it seems likely that the best match, with the greatest enhancement of information, will exist for the emission and ear of the same bat.

IV. CONCLUSION

The echolocation directionality of *Eptesicus* is best in a restricted region of space approximately a cone of about $\pm 30°$. This cone of best directional focus exists for both information based on IID measurements (Simmons *et al.*, 1995) and on fine spectral localization cues. Localization cues are enhanced in the combination, the peaks are sharpened, and there is a greater contrast in intensity between peaks and notches. The combination of the ear and emission information should enhance the discriminability of target location.

ACKNOWLEDGMENTS

This research was supported by the grant NIH Training Program in Hearing (T32 DC00045) to J.M.W. and NIH Grant No. DC02804 to R.L.J. We would like to thank the two anonymous reviewers for their suggestions which improved this manuscript. Thanks also to James A. Simmons for initiating this collaboration.

Blauert, J. (**1969**). ''Sound localization in the median plane,'' Acustica **22,** 205–213.

Bloom, P. J. (**1977**). ''Creating source elevation illusions by spectral manipulation,'' J. Audio Eng. Soc. **25**, 560–565.

Carlile, S. (**1990**). ''The auditory periphery of the ferret. II: The spectral transformations of the external ear and their implications for sound localization,'' J. Acoust. Soc. Am. **88,** 2196–2204.
Dooley, G. J., and Moore, B. C. J. (**1988**). ''Duration discrimination of steady and gliding tones: A new method for estimating sensitivity to rate of change,'' J. Acoust. Soc. Am. **84,** 1332–1337.
Fuzessery, Z. M. (**1986**). ''Speculations on the role of frequency in sound localization,'' Brain Behav. Evolution **28**, 95–108.
Fuzessery, Z. M. (**1996**). ''Monaural and binaural spectral cues created by the external ears of the pallid bat,'' Hearing Res. **95**, 1–17.
Fuzessery, Z. M., and Pollak, G. D. (**1985**). ''Determinants of sound location selectivity in bat inferior colliculus: A combined dichotic and free-field stimulation study,'' J. Neurophysiol. **54,** 757–781.
Fuzessery, Z. M., Hartley, D. J., and Wenstrup, J. J. (**1992**). ''Spatial processing within the mustache bat echolocation system: Possible mechanisms for optimization,'' J. Comp. Physiol. A **170**, 57–71.
Grinnell, A. D. (**1963**). ''The neurophysiology of audition in bats: directional localization and binaural interaction,'' J. Physiol. (London) **167,** 97–113.
Grinnell, A. D., and Grinnell, V. S. (**1965**). ''Neural correlates of vertical localization by echolocating bats,'' J. Physiol. (London) **181,** 830–851.
Grinnell, A. D., and Schnitzler, H.-U. (**1977**). ''Directional sensitivity of echolocation in the horseshoe bat, *Rhinolophus ferrumequinum.* II: Behavioral directionality of hearing,'' J. Comp. Physiol. A **116**, 63–76.
Guppy, A., and Coles, R. B. (**1988**). ''Acoustical and neural aspects of hearing in the Australian gleaning bats, *Macroderma gigas* and *Nyctophilus gouldi*,'' J. Comp. Physiol. A **162**, 653–668.
Hartley, D. J., and Suthers, R. A. (**1987**). ''The sound emission pattern and the acoustical role of the noseleaf in the echolocating bat, *Carollia perspicillata*,'' J. Acoust. Soc. Am. **82,** 1892–1900.
Hartley, D. J., and Suthers, R. A. (**1989**). ''The sound emission pattern of the echolocating bat, *Eptesicus fuscus*,'' J. Acoust. Soc. Am. **85,** 1348–1351.
Hartley, D. J., and Suthers, R. A. (**1990**). ''Sonar pulse radiation and filtering in the mustached bat, *Pteronotus parnellii rbiginosus*,'' J. Acoust. Soc. Am. **87,** 2756–2772.
Hebrank, J., and Wright, D. (**1974**). ''Spectral cues used in the localization of sound sources on the median plane,'' J. Acoust. Soc. Am. **56,** 1829–1834.
Humanski, R. A., and Butler, R. A. (**1988**). ''The contribution of the near and far ear toward localization of sound in the sagittal plane,'' J. Acoust. Soc. Am. **83,** 2300–2310.
Jen, P. H-S., and Chen, D. (**1988**). ''Directionality of sound pressure transformation at the pinna of echolocating bats,'' Hearing Res. **34**, 101–118.
Kistler, D. J., and Wightman, F. L. (**1992**). ''A model of head-related transfer functions based on principal components analysis and minimum-phase reconstruction,'' J. Acoust. Soc. Am. **91,** 1637–1647.
Lawrence, B. D., and Simmons, J. A. (**1982a**). ''Echolocation in bats: The external ear and perception of the vertical positions of targets,'' Science **218,** 481–483.
Lawrence, B. D., and Simmons, J. A. (**1982b**). ''Measurements of atmospheric attenuation at ultrasonic frequencies and the significance for echolocation by bats,'' J. Acoust. Soc. Am. **71,** 585–590.
Lehky, S. R., and Sejnowski, T. J. (**1990**). ''Neural model of stereoacuity and depth interpolation based on a distributed representation of stereo disparity,'' J. Neurosci. **10,** 2281–2299.
Masters, W. M., Jacobs, S. C., and Simmons, J. A. (**1991**). ''The structure of echolocation sounds used by the big brown bat *Eptesicus fuscus*: some consequences for echo processing,'' J. Acoust. Soc. Am. **89,** 1402–1413.
Menne, D. (**1988**). ''Is the structure of bat echolocation calls an adaptation to the mammalian hearing system?,'' J. Acoust. Soc. Am. **83,** 2447–2449.
Middlebrooks, J. C. (**1992**). ''Narrow-band sound localization related to external ear acoustics,'' J. Acoust. Soc. Am. **92,** 2607–2624.
Middlebrooks, J. C., and Green, D. M. (**1991**). ''Sound localization by human listeners,'' Annu. Rev. Psychol. **42,** 135–159.
Moore, B. C. J., and Sek, A. (**1992**). ''Detection of combined frequency and amplitude modulation,'' J. Acoust. Soc. Am. **92,** 3119–3131.
Moore, B. C. J., Oldfield, S. R., and Dooley, G. J. (**1989**). ''Detection and discrimination of spectral peaks and notches at 1 and 8 kHz,'' J. Acoust. Soc. Am. **85,** 820–836.
Musicant, A. D., Chan, J. C. K., and Hind, J. E. (**1990**). ''Direction-dependent spectral properties of cat external ear: New data and cross-species comparisons,'' J. Acoust. Soc. Am. **87,** 757–781.
Obrist, M. K. (**1995**). ''Flexible bat echolocation: the influence of individual, habitat and conspecifics on sonar signal design,'' Behav. Ecol. Sociobiol. **36**, 207–219.
Obrist, M. K., Fenton, M. B., Eger, J. L., and Schlegel, P. A. (**1993**). ''What ears do for bats: A comparative study of pinna sound pressure transformation in Chiroptera,'' J. Exp. Biol. **180**, 119–152.
Phillips, D. P., Calford, M. B., Pettigrew, J. D., Aitkin, L. M., and Semple, M. N. (**1982**). ''Directionality of sound pressure transformation at the cat's pinna,'' Hearing Res. **8**, 13–28.
Rice, J. J., May, B. J., Spirou, G. A., and Young, E. D. (**1992**). ''Pinna-based spectral cues for sound localization in cat,'' Hearing Res. **58**, 132–152.
Roverud, R. C., and Rabitoy, E. R. (**1994**). ''Complex sound analysis in the FM bat *Eptesicus fuscus*, correlated with structural parameters of frequency modulated signals,'' J. Comp. Physiol. A **174**, 567–573.
Schnitzler, H.-U., and Grinnell, A. D. (**1977**). ''Directional sensitivity of echolocation in the horseshoe bat, *Rhinolophus ferrumequinum.* I. Directionality of sound emission,'' J. Comp. Physiol. **116**, 51–61.
Searle, C. L., Braida, L. D., Cuddy, D. R., and Davis, M. F. (**1975**). ''Binaural pinna disparity: Another auditory localization cue,'' J. Acoust. Soc. Am. **57,** 448–455.
Shaw, E. A. G. (**1972**). ''Transformation of sound pressure level from the free field to the eardrum in the horizontal plane,'' J. Acoust. Soc. Am. **56,** 1848–1861.
Shaw, E. A. G. (**1982**). ''External ear response and sound localization,'' in Localization of Sound: Theory and Applications, edited by R. Gatehouse (Amphora, Groton, CT), pp. 30–41.
Shimozawa, T., Suga, N., Hendler, P., and Schuetze, S. (**1974**). ''Directional sensitivity of echolocation system in bats producing frequency-modulated signals,'' J. Exp. Biol. **60**, 53–69.
Simmons, J. A. (**1989**). ''A view of the world through the bat's ear: The formation of acoustic images in echolocation,'' Cognition **33**, 155–199.
Simmons, J. A., and Grinnell, A. D. (**1988**). ''The performance of echolocation: Acoustic images perceived by echolocating bats,'' in *Animal Sonar Systems*, edited by P. Nachtigall (Plenum Press, New York), pp. 353–385.
Simmons, J. A., Fenton, M. B., and O'Farrell, M. J. (**1979**). ''Echolocation and pursuit of prey by bats,'' Science **203,** 16–21.
Simmons, J. A., Saillant, P. A., Wotton, J. M., Haresign, T., Ferragamo, M. J., and Moss, C. F. (**1995**). ''Composition of biosonar images for target recognition by echolocating bats,'' Neural Networks **8**, 1239–1261.
Suga, N., and Schlegel, P. (**1972**). ''Neural attenuation of responses to emitted sounds in echolocating bats,'' Science **177,** 82–84.
Wightman, F. L., and Kistler, D. J. (**1989a**). ''Headphone simulation of free-field listening I. Stimulus synthesis,'' J. Acoust. Soc. Am. **85,** 858–867.
Wightman, F. L., and Kistler, D. J. (**1989b**). ''Headphone simulation of free-field listening. II: Psychophysical validation,'' J. Acoust. Soc. Am. **85,** 868–878.
Wightman, F. L., and Kistler, D. J. (**1993**). ''Sound localization,'' in *Human Psychophysics*, edited by W. A. Yost, A. N. Popper, and R. R. Fay (Springer-Verlag, New York), pp. 155–192.
Wotton, J. M., and Simmons, J. A. (**in preparation**). ''Spectral cues and the perception of the vertical position of targets by the big brown bat, *Eptesicus fuscus*.''
Wotton, J. M., Haresign, T., and Simmons, J. A. (**1995**). ''Spatially dependent acoustic cues generated by the external ear of the big brown bat, *Eptesicus fuscus*,'' J. Acoust. Soc. Am. **98,** 1423–1445.
Wotton, J. M., Haresign, T., Ferragamo, M. J., and Simmons, J. A. (**1996**). ''The influence of sound source elevation and external ear notch cues on the discrimination of spectral notches by the big brown bat, *Eptesicus fuscus*,'' J. Acoust. Soc. Am. **100,** 1764–1776.

An investigation of penetration depth control using parallel opposed ultrasound arrays and a scanning reflector

Eduardo G. Moros,[a] Xiaobing Fan, and William L. Straube
Radiation Oncology Center, Washington University School of Medicine, St. Louis, Missouri 63108

(Received 16 April 1996; accepted for publication 17 October 1996)

A theoretical study of penetration depth control in superficial hyperthermia utilizing parallel opposed linear ultrasound arrays and a double-faced (V-shaped) scanning reflector is presented. This is a dual array system (DAS), where one array operates at a low frequency and the other at a high frequency (1 and 5 MHz, respectively in this study). The arrays are positioned facing each other and both are aimed at a double-faced scanning reflector which distributes the energy over the scanned surface. Each reflecting surface is angled at 45° with respect to the sound propagation direction so that both beams are deflected in the same direction toward the treatment volume. The system was designed to be compatible for combined operation with a medical linear accelerator for the delivery of simultaneous thermoradiotherapy. It is demonstrated that by varying the excitation magnitude of one array relative to the other, it is possible to control the magnitude of absorbed energy as a function of depth, and thus improved control of the heating pattern in all three spatial dimensions is obtained. This improvement is demonstrated with bio-heat transfer simulations which show how penetration depth control translates into control of temperature distributions. The simulations also show that the DAS is able to produce more uniform temperature distributions in highly perfused tissue. © *1997 Acoustical Society of America.* [S0001-4966(97)04403-2]

PACS numbers: 43.80.Sh, 43.80.Vi [FD]

INTRODUCTION

It has been shown that properly applied hyperthermia (tumor temperatures above 41.5 °C for 45–60 min) can significantly enhance the therapeutic effects of radiation therapy by increasing local tumor regression rate and prolonging the duration of regression (Myerson *et al.*, 1990; Oleson *et al.*, 1993; Kapp and Cox, 1995). However, the induction of adequate hyperthermia has proven to be problematic in the clinical setting. Several factors responsible for decreasing the potential for delivering adequate treatments have been identified, such as improper thermal and absorbed power tumor coverages, insufficient number of temperature sensors, and inadequate equipment. It is widely accepted that further technological advancements aimed at overcoming these factors will improve thermal doses and therefore clinical outcome.

Another possible way to improve clinical outcome is by combining the therapies so that the net biological effect is increased. Traditionally, clinical trials combining radiotherapy and hyperthermia have been performed in a sequential fashion. However, it is known from *in vitro* and *in vivo* experiments that the simultaneous delivery of these therapies enhances cell killing due to increased thermal radiosensitization (Dewey, 1994). Although cell killing is augmented, a net therapeutic gain is only possible if heating is localized to the target volume. This is because normal tissues can also be radiosensitized by elevated temperatures which may increase the risk for complications. A recent phase I clinical trial using commercial heating technology, however, showed no additional complications of simultaneous over sequential thermoradiotherapy (Moros *et al.*, 1995a; Myerson *et al.*, 1996). A phase II dose escalation trial is ongoing.

Our current objective is to design and develop superficial ultrasonic heating systems with (1) power deposition control, and (2) that are compatible for delivering hyperthermia simultaneously with external beam radiation therapy. Power deposition control is necessary to improve time–temperature distributions within target volumes and to more effectively spare normal tissues. The scanning ultrasound reflector linear array system (SURLAS) introduced by Moros *et al.* (1995b) was designed with these objectives in mind. Simulations and experimental studies showed that the SURLAS can induce uniform temperature distributions in superficial target volumes, that it can control lateral distribution of power deposition, and that it can operate concurrently with a medical linear accelerator (Moros *et al.*, 1995b, 1996a, 1996b). However, this design did not provide a way for controlling heating as a function of depth into tissue; in other words, it lacked penetration depth control. In this article, a new design is introduced—an ultrasound applicator that uses parallel opposed arrays and a double-faced (V-shaped) scanning reflector—that offers control of power penetration depth in addition to lateral control of power deposition and compatibility with simultaneous therapy. Penetration depth control is achieved by controlling the relative power output of a low-frequency array relative to that of a geometrically opposed high-frequency array. We have named this design a dual array system or DAS.

The advantages of inducing ultrasound hyperthermia with different frequency transducers or multifrequency applicators have previously been reported in theoretical and experimental studies as well as in preliminary clinical experience (Anhalt *et al.*, 1993; Hynynen, 1993; Moros *et al.*,

[a]Electronic mail: moros_eg@rophys.wustl.edu

1993). Hynynen (1993) briefly discussed that depth of heating can be varied on line by controlling the amplitudes of different frequency transducers or by time multiplexing between the first and third harmonic frequencies. He presented *in vivo* results showing feasibility. The group at the University of Arizona experienced improvements in temperature distributions in superficial human lesions using a combination of low (1.0–2.0 MHz) and high (4.0 MHz) frequency transducers in their modified scanned focused ultrasound system. They were able to vary depth of heating by moving the transducers in the direction perpendicular to the patient's surface (*Z* direction). They planned on implementing independent amplitude control of the different frequency transducers to alleviate the need of moving the transducers in that direction (Anhalt *et al.*, 1993). Theoretically, it has been shown that therapeutic penetration in superficial hyperthermia is strongly dependent on maximum temperature, frequency, and acoustic absorption of tissue (Moros *et al.*, 1993). These authors recommended treatment delivery techniques for single-frequency applicators and showed the need for a clinical system able to operate over a range of frequencies. The DAS design incorporates high- and low-frequency arrays for concurrent dual frequency insonation. This approach allows real time control of depth of heating.

As mentioned above, the DAS evolved from the SURLAS, and consequently, many of the design considerations and the studies already performed for the SURLAS also applied to the DAS. The reader is referred to these studies for further details on design feasibility, choices and constraints, the relationship between array element size and temperature distributions, and experimental data (Moros *et al.*, 1995b, 1996a, 1996b). For the sake of completeness, however, the most important design features are briefly summarized, namely, array element size and choice of frequencies.

The smallest element size possible is desired to minimize the thickness of coupling water a radiation beam must pass through during simultaneously treatment.This is especially important in the case of electron beams (Moros *et al.*, 1995b). However, the element size is also dictated by tumor size, minimum frequency, and most importantly, power requirements; hence, a compromise must be reached. An optimization study relating these parameters was performed from which the element sizes used in this paper were selected (Moros *et al.*, 1996a). As alluded to above, dual frequency operation can be achieved using different frequency transducers or by time multiplexing between the first and third harmonic frequencies of a given array (Hynynen, 1993). The former approach is preferred because it offers concomitant dual frequency and more net acoustic power for heating. The particular choice of frequencies for the low- and high-frequency arrays is mostly based on clinical experience. On one hand, frequencies below 1 MHz are very penetrating in soft tissues and are more likely to cause induced or referred pain when nonfocused beams are employed (Anhalt *et al.*, 1993). On the other hand, frequencies above 5 MHz heat very superficial tissues. Thus, the combination of 1 and 5 MHz for the DAS is justifiable on practical grounds for the present study.

This paper presents a systematic theoretical study of penetration depth control for the DAS design using acoustic and bio-heat transfer numerical models. It is shown that the DAS can produce more uniform temperature distributions in highly perfused tissue with a good degree of penetration depth control. Characteristic ultrasonic power patterns and temperature distributions are presented. The effects of tissue perfusion and skin temperature on temperature distributions are also considered.

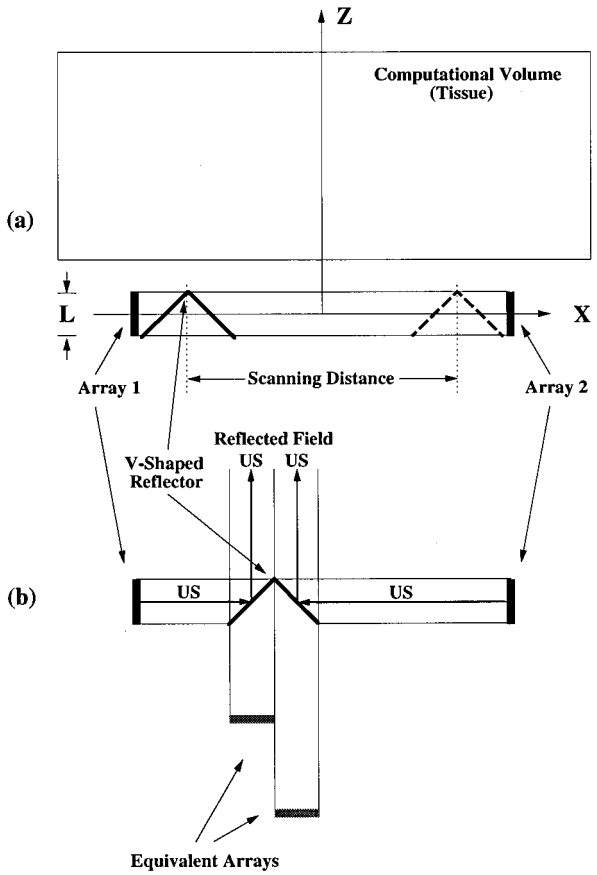

FIG. 1. (a) Schematic diagram of dual array system (DAS) showing the parallel opposed arrays and the V-shaped scanning reflector. Also shown is the coordinate system used in the simulations. (b) Illustration of the equivalent arrays technique used in the ultrasound field calculations.

I. MATERIALS AND METHODS

A. System design

The basic components of the proposed DAS for external superficial simultaneous thermoradiotherapy consists of two planar ultrasound arrays of the same size and geometrically opposing each other, and a double-faced, V-shaped reflector which scans between the arrays (Fig. 1). The reflecting surface makes 45° angles with respect to the sound propagation so that both beams are deflected in the same direction toward tissue. Each linear array is assumed to be made from a single rectangular piezo-electric crystal electrically divided into equal size square elements. The two arrays have the same number of elements and have separate driving rf sources. The magnitude of the input power to each individual array element is controllable. A schematic diagram of the basic design and of the coordinate system used in this article is

shown in Fig. 1. As shown in this figure, the arrays are aligned parallel to the Y axis, the reflector scans along the X axis, and the reflected ultrasound propagates in the positive Z direction.

Simulations were performed for two general cases. In the first case both arrays operated at the same frequency. These simulations were done to demonstrate the advantages of two opposing arrays (as in the DAS) versus a single array (as in the SURLAS). In the second case the arrays were operated at different frequencies to allow penetration depth control. As discussed in the previous section the high and low frequencies were selected based on clinical experience. Hence, one array operated at 1 MHz and the other at 5 MHz. Assuming plane wave behavior and a linear acoustic attenuation in tissues of 5 Np/m/MHz, this frequency combination should allow 50% power penetration depths (the depth at which the absorbed power is 50% of the skin value) from 1.5 to 7 cm deep. Moros *et al.* (1996a) performed computer simulations of the SURLAS for three tumor size categories: $5\times5\times5$ cm^3, $10\times10\times3.5$ cm^3, and $15\times15\times2$ cm^3. In this study, the $10\times10\times3.5$ cm^3 tumor was selected to illustrate the advantages of the DAS. From clinical experience it is known that to induce temperature elevations in a tumor above 43 °C, an average acoustic intensity level of 1 W/cm^2 is required (Corry *et al.*, 1982). Therefore, the tumor size selected for the simulations requires an average acoustic power output of 100 W. Given that square transducer elements can produce a maximum of about 10 W/cm^2 (Benkeser *et al.*, 1989), a minimum total array area of 10 cm^2 would be required for the average clinical situation. Bearing in mind that it is desirable to use the smallest element size possible (Moros *et al.*, 1996a), we chose the DAS arrays to have ten 1-cm^2 elements each for a total of 20 cm^2 of total surface area to ensure sufficient power output. This element size was used when both arrays operated at the same frequency. In the depth of heating control study with dual frequency, however, the size of the array elements was larger. This was found to be necessary to obtain uniform temperature distributions because of the differences in frequency (penetration) and power level between the arrays. Consequently, arrays with five 2-cm^2 elements were used in the penetration depth control simulation study.

B. Ultrasound field calculations

The ultrasound fields generated by the arrays and then reflected from the scanning reflector are very time consuming to compute exactly. Therefore, equivalent arrays were simulated instead. An equivalent array is one that produces an ultrasound field without reflection in effect equal to the reflected ultrasound field [Fig. 1(b)]. This is because a symmetric beam which is deflected by a specular surface at an angle of incidence of 45° is identical to the original unreflected beam except for the change in propagation direction. This approximation was first introduced by Moros *et al.* (1996b) and, it is refined here and extended to parallel opposed arrays.

The complex acoustic pressure field due to a planar array is given by

$$p(x,y,z)=\frac{j\rho ck}{2\pi}\sum_{n=1}^{N} u_n \int_{s_n}\frac{e^{-jkr_n}}{r_n}ds_n, \tag{1}$$

where $j=\sqrt{-1}$, ρ is the density of the tissue, c is the speed of sound in tissue, k is the real wavenumber, N is the total number of array elements, u_n is the source excitation magnitude of nth element, r_n is the distance from a point on the nth element to the field point of interest, and s_n is the area of the nth element. The integral can be evaluated numerically by two-dimensional integration (i.e., Zemanek, 1971) or by computational CPU saving techniques such as that of Ocheltree and Frizzell (1989). The average steady-state power deposition due to acoustic pressure in an attenuating medium is given by

$$q(x,y,z)=\mu\frac{|p(x,y,z)|^2}{Z}e^{-2\alpha z}, \tag{2}$$

where μ is the absorption coefficient, α is the attenuation coefficient, and $Z=\rho c$ is the impedance of the medium. The power deposition generated by parallel opposed arrays with the scanning dual-faced reflector is given by

$$Q(x,y,z)=\frac{1}{N_s}\sum_{n_s=1}^{N_s}[q_1(x+x_1,y,z+z_1) + q_2(x+x_2,y,z+z_2)], \tag{3}$$

where N_s is the total number of discrete locations of the scanning reflector, q_1 and q_2 are the local power deposition generated by each array, $x_1=-SD/2+(n_s-1)\cdot\Delta s-L/2$, $x_2=-SD/2+(n_s-1)\cdot\Delta s+L/2$, $z_1=(n_s-1)\cdot\Delta s$, $z_2=(N_s-n_s)\cdot\Delta s$, where Δs is the grid spacing, SD is the scanning distance [Fig. 1(a)], and L is the height of array (the size of the individual square elements). Notice that the center of the reflector starts scanning at $X=-SD/2$.

C. Temperature model

The three-dimensional steady-state temperature distributions due to ultrasound power deposition were calculated using the bio-heat transfer equation of Pennes (1948). The finite difference technique was employed to discretize the tissue volume and a successive over-relaxation (SOR) technique was applied to solve the equation (for further details see Moros *et al.*, 1993). The tissue medium was assumed homogeneous and isotropic. Unless otherwise specified, the following tissue properties were used as nominal values: thermal conductivity of 0.5 W/cm °C, specific heat of blood of 4000 J/kg °C, and a blood perfusion rate of 5 kg/m^3 s. Likewise, the skin temperature boundary condition and all the internal temperature boundary conditions were set equal to 37 °C. The input power to each array was adjusted so that the maximum temperature induced in the target volume was 45 °C.

D. Simulations

In ultrasound hyperthermia, water is used as a coupling medium between the sound sources (transducers) and the skin of the patient. Our simulations assumed a 2-cm-thick water coupling bolus between the upper edge of the arrays

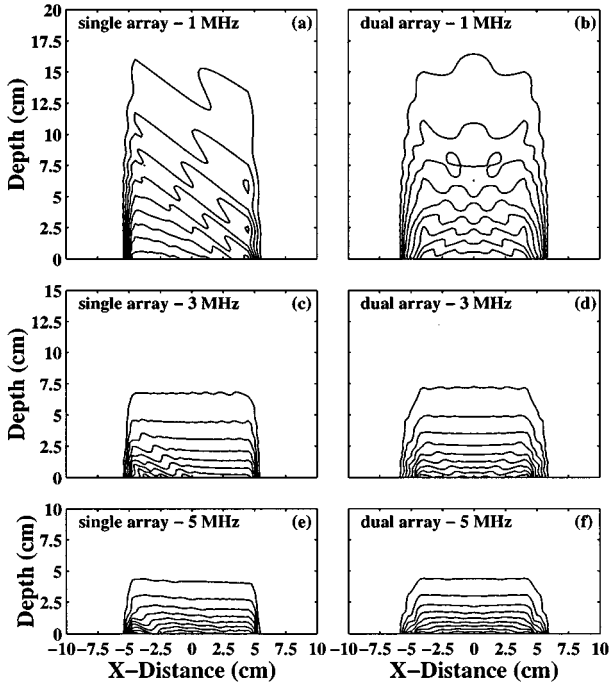

FIG. 2. Contour plots for the central plane ($Y=0$) of the ultrasound power fields (a,c,e) produced by the SURLAS; and ultrasound power fields (b,d,f) produced by the DAS operating at a single frequency. The operating frequency used in the simulation was (a,b) 1 MHz; (c,d) 3 MHz; and (e,f) 5 MHz. The isopower contour are plotted every 10% beginning with 10% (outer contour).

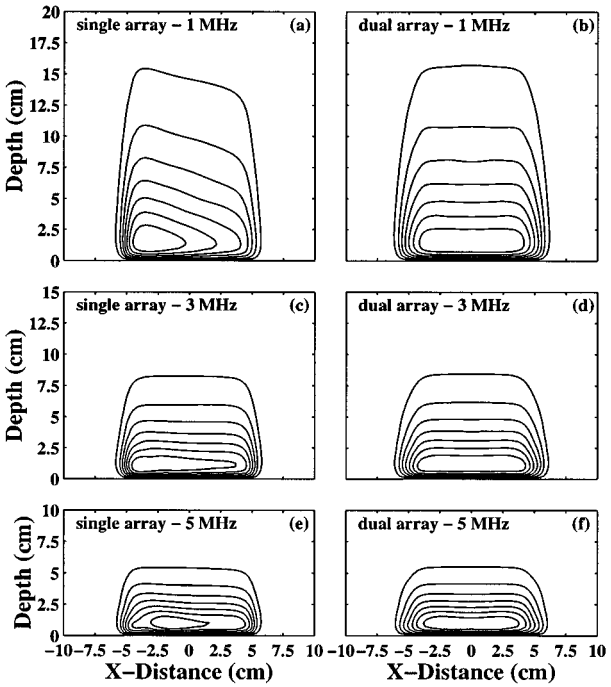

FIG. 3. Contour plots for the central plane ($Y=0$) of the temperature distributions (a,c,e) produced by the SURLAS; and temperature distributions (b,d,f) produced by the DAS operating at a single frequency. The operating frequency used in the simulation was (a,b) 1 MHz; (c,d) 3 MHz; and (e,f) 5 MHz. The isotherms are drawn at 1 °C increments beginning with the 38 °C isotherm (outer contour).

[Fig. 1(a)] and skin surface, that is, the skin surface starts at $Z=(L/2)+2$ cm. The speed of sound and the density were assumed to be 1500 m/s and 1000 kg/m^3, respectively. These values are commonly used for both water and tissue media. Power deposition from scattered ultrasound was neglected and therefore, the attenuation (μ) and absorption (α) coefficients of tissue were assumed identical, and equal to 5 Np/m/MHz (Moros and Hynynen, 1992). It was also assumed that the amount of energy that missed the reflector due to beam divergence was negligible (Moros *et al.*, 1996a).

The ultrasound fields were only calculated within the tissue region [Fig. 1(a)] that absorbs the reflected ultrasound. The computational volumes for all simulations were chosen so that there were approximately 5 cm between the target and the boundaries in the X and Y directions. In most cases, the depth dimension in the Z direction was chosen so that there were approximately 5 cm between the 10% isopower contours and the deepest boundary. Therefore, the calculation volume used depended on the tumor size and the effective operating frequency. A grid spacing of 0.25 cm was used in all the numerical simulations (Moros *et al.*, 1996a).

Penetration depth control with the DAS was studied by varying the relative power levels of one array with respect to the other. Array 1 and array 2 (Fig. 1) operated at 1 and 5 MHz, respectively. Both acoustic and temperature fields were computed using the following ratios of source excitation magnitudes (u_n^1/u_n^2): (a) 0.8/0.2; (b) 0.7/0.3; (c) 0.6/0.4; (d) 0.5/0.5; (e) 0.4/0.6; and (f) 0.3/0.7, where u_n^1 and u_n^2 are the source excitation magnitudes for arrays 1 and 2, respectively. These imply the following radiated power ratios $[(u_n^1/u_n^2)^2]$: (a) 16/1; (b) 5.4/1; (c) 2.3/1; (d) 1/1; (e) 1/2.3; (f) 1/5.4.

II. RESULTS

Comparison of ultrasound fields and temperature distributions between the previous single-array single-frequency system design (SURLAS: Moros *et al.*, 1995b, 1996a) and the proposed dual-frequency dual-array system (the DAS) are presented first. Ultrasound field distributions on a center plane ($Y=0$) generated by a SURLAS are shown in Fig. 2(a), (c), and (e); and generated by the DAS are shown in Fig. 2(b), (d), and (f) for the operating frequencies 1, 3, and 5 MHz, respectively. The corresponding temperature distributions are shown in Fig. 3. It can be easily seen that the ultrasound field and temperature distribution induced by the DAS are more uniform along the scan direction for the operating frequency of 1 MHz. At higher frequencies (3 and 5 MHz), the ultrasound fields and temperature distributions generated by the SURLAS are closer to the those obtained by the DAS, but the DAS still induces more uniform distributions. As expected, the depth of heating is decreased as the frequency is increased. For the results obtained by the DAS, the distal depth of 43 °C isotherms on the center plane ($Y=0$) were located at 3.6, 2.5, and 1.9 cm for the frequencies 1, 3, and 5 MHz, respectively.

Results showing the capability of the DAS to control the depth and pattern of heating are presented next. Figure 4 shows the ultrasound field distributions obtained by different combinations of the source excitation magnitudes for each array. The corresponding temperature distributions are

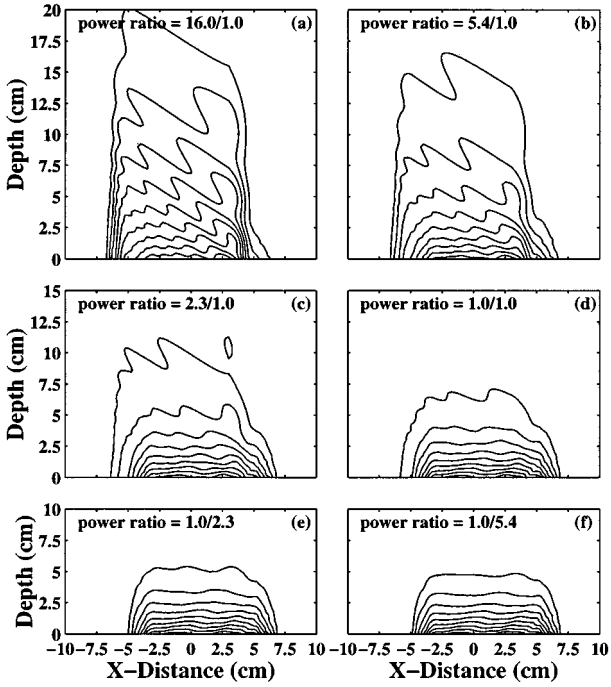

FIG. 4. Contour plots for the central ($Y=0$) of the ultrasound power fields obtained by the proposed system with dual frequency. The operating frequency was 1 and 5 MHz for the left-hand side and the right-hand side array, respectively. The radiated power ratio $[(u_n^1/u_n^2)^2]$ in each case was: (a) 16/1; (b) 5.4/1; (c) 2.3/1; (d) 1/1; (e) 1/2.3; and (f) 1/5.4. The isopower contour are plotted every 10% beginning with 10% (outer) contour.

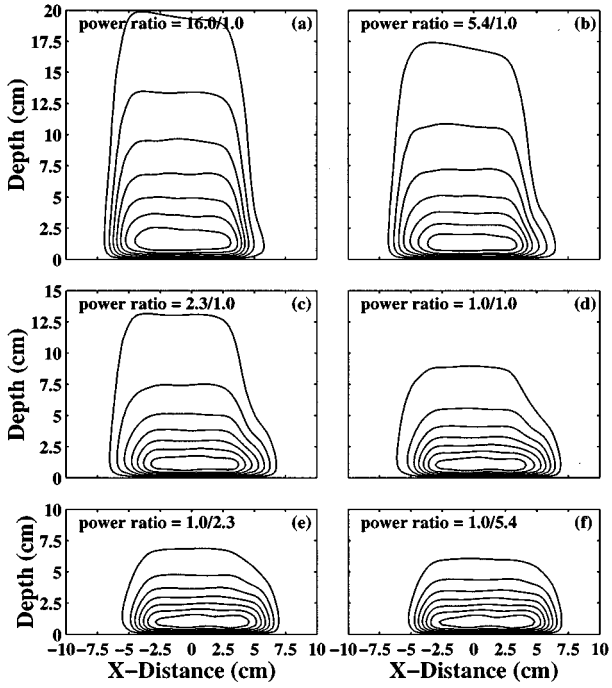

FIG. 5. Contour plots for the central ($Y=0$) temperature distributions obtained by the proposed system with dual frequency. The operating frequency was 1 and 5 MHz for the left-hand side and the right-hand side array, respectively. The radiated power ratio $[(u_n^1/u_n^2)^2]$ in each case was: (a) 16/1; (b) 5.4/1; (c) 2.3/1; (d) 1/1; (e) 1/2.3; and (f) 1/5.4. The isotherms are drawn at 1 °C increments beginning with the 38 °C isotherms (outer contour).

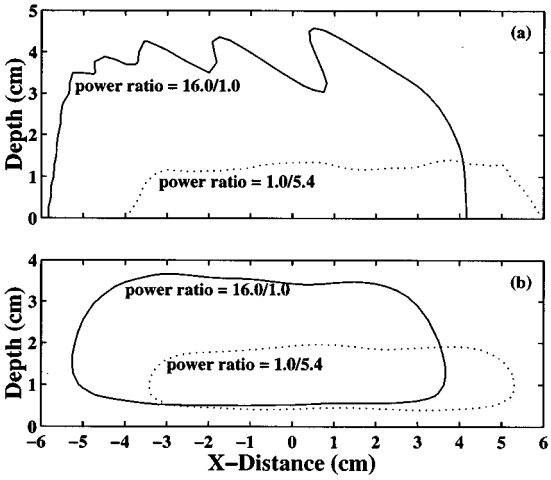

FIG. 6. (a) Comparison of the 50% isopower contours for power ratios $[(u_1^n/u_n^2)^2]$ 16/1 and 1/5.4. These are cases (a) (solid line) and (f) (dotted line) in Fig. 4. (b) Comparison of the 43 °C isotherms for power ratios $[(u_n^1/u_n^2)^2]$ 16/1 and 1/5.4. These are cases (a) (solid line) and (f) (dotted line) in Fig. 5.

shown in Fig. 5. Note that the source excitation magnitude is the same for all the elements in each array. The radiated power ratios $[(u_n^1/u_n^2)^2]$ for Figs. 4(a)–(f) and 5(a)–(f) are those given above. The lower-frequency array (array 1) is located on the left-hand side of each graph. It can be easily seen that the heating pattern and the depth of heating varies for different power ratio values. Notice that the temperature patterns for cases 5(a) and 5(f) are similar to those obtained with the SURLAS [Fig. 3(a) and (f)]. This is expected at high- and low-power ratios since most of the heating is induced predominantly from one array (i.e., one frequency). However, the ultrasound fields and temperature distributions for intermediate power ratios shown in Figs. 4(b)–(e) and 5(b)–(e) can only be obtained with a dual-frequency system such as the DAS. To more clearly illustrate how the heating pattern can be varied, the 50% isopower contours of Fig. 4(a) and (f) are plotted together in Fig. 6(a), and the 43 °C isotherms (the volume enclosed by the 43 °C surface could be considered as the therapeutic volume) of Fig. 5(a) and (f) are plotted in Fig. 6(b). In Fig. 6(a), notice the change in the depth of the 50% isopower contour from 1.5 to 4.0 cm, approximately. The respective change in depth of the 43 °C isotherms was from 2.0 to 3.7 cm, approximately. Also, notice in Fig. 6(b) that the area enclosed by the isotherm produced with the highest-power ratio is about twice the area enclosed by the isotherm produced with the lowest-power ratio. These results illustrate how a tumor with uneven depth could be treated with the DAS with the proper combination of source excitation magnitudes as a function of reflector position. Another important characteristic of both the power and temperature patterns induced by the DAS is the shift of approximately 1 cm from the center to the side of the array emitting the most power. This is because toward the edges of the scanning window the ultrasound field is only contributed to by one array [Fig. 1(a)] and only by part of the field of that array (Moros *et al.*, 1996b). Penetration depth results are summarized in Fig. 7 which plots isopower contour depth versus isopower contour value for cases (a)–(f) of Fig. 4, and

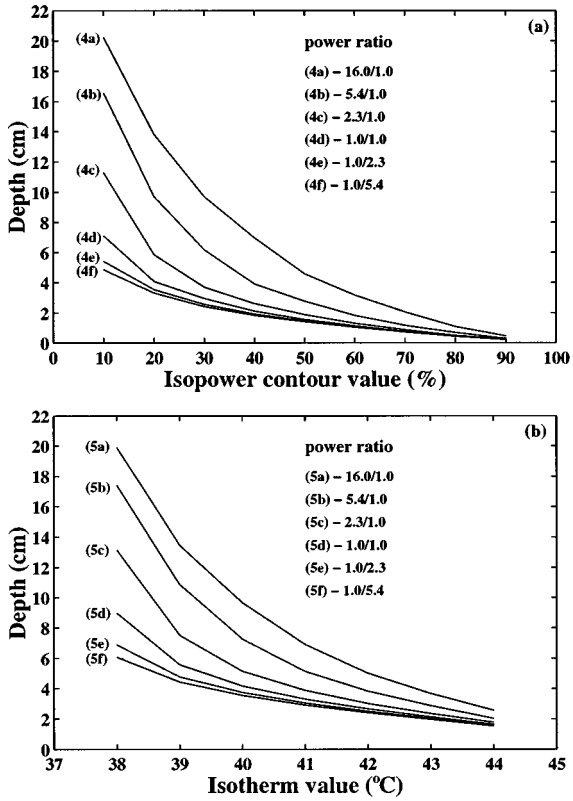

FIG. 7. (a) Distal depth of isopower contours at the central plane ($Y=0$) as a function of percentage of maximum power deposition values for cases (a)–(f) in Fig. 4. (b) Distal depth of isotherms at the central plane ($Y=0$) as a function of the isotherm value for cases (a)–(f) in Fig. 5.

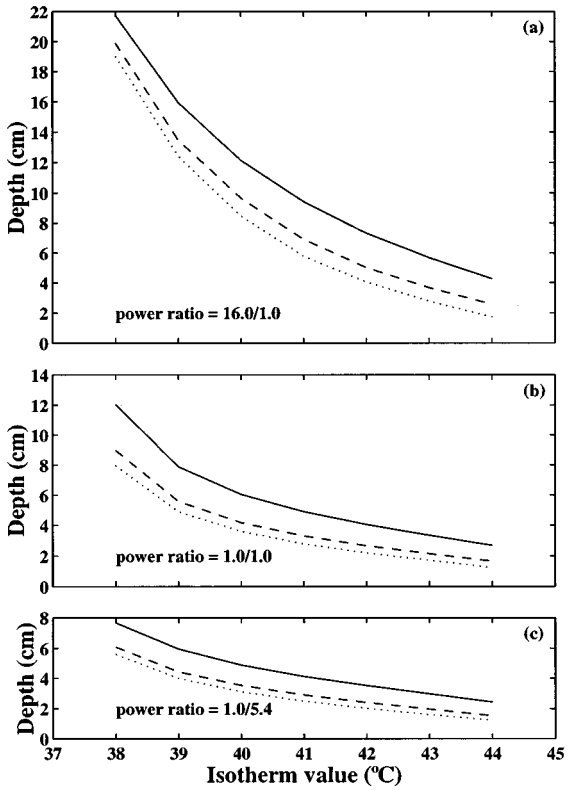

FIG. 8. Distal depth of isotherms at the central plane ($Y=0$) produced by the DAS as a function of temperature for the power ratio $[(u_n^1/u_n^2)^2]$ of (a) 16/1; (b) 1/1; and (c) 1/5.4. The perfusion rates used in the simulations were: 1 (solid line), 5 (dashed line), and 10 kg/m^3 s (dotted line).

distal depth of isotherms versus temperature for cases (a)–(f) of Fig. 5. It can be seen that as the power level for the high/low-frequency array (5 MHz/1 MHz) increases/decreases, the isopower contours and the distal isotherms move closer to the skin surface. For example, along the centerline, the depth of the 25% isopower contour varied from 11.8 to 2.9 cm (depth range of 8.9 cm), and the distal depth of the 42 °C isotherm moves from 5.0 to 2.4 cm.

In the above simulations, the blood perfusion rate was 5 kg/m^3 s which is 5–10 times the normal value for resting muscle (Chato, 1985). This perfusion value gives conservative isotherm depth estimates. The effect of tissue perfusion rate on the temperature distribution was studied for the DAS. Figure 8 shows the distal isotherm depths ($Y=0$ plane) as a function of isotherm value for perfusion rates of 1, 5, and 10 kg/m^3 s. The radiated power ratios $[(u_n^1/u_n^2)^2]$ used in the simulations were: (a) 16/1; (b) 1/1; and (c) 1/5.4. Notice that the depth of a given isotherm varies with perfusion by more than 2 cm for the power ratio 16/1, and more than 1 cm for the power ratio 1/5.4. Also, as expected, the isotherms become shallower the higher the blood perfusion.

Finally, the effect of skin temperature on the temperature field distribution for the DAS is presented in Fig. 9 where isotherm contours (42, 43, and 44 °C) are plotted at three power ratios: (a) 16/1; (b) 1/1; and (c) 1/5.4. When the skin temperature was changed from 37 °C to 20 °C, the isotherms were shifted about 2–4 mm deeper. Except for these relatively small shifts the heating patterns were virtually unchanged.

III. DISCUSSION

From the single-frequency simulation results, it was shown that the DAS design can produce more uniform temperature distribution than the original SURLAS design in tissue with high perfusion rates. The improvements are mainly the result of a more uniform power deposition pattern induced when two parallel opposed arrays are used instead of just one. The additional array forces the acoustic field to be symmetric about the plane $X=0$, and thus natural nonuniformities in the field are smoothed. The improvements are especially noticeable for the low-frequency case (1 MHz) where the near-field–far-field transition for a 1-cm^2 square element is less than 2 cm from the array surface, and therefore, a highly nonuniform field is convoluted. The additional array also doubles the available power that can be used either to increase the scanning distance or to minimize the height of the array (L) to further minimize attenuation of electron beams during simultaneous thermoradiatherapy (Moros *et al.*, 1995b).

It was also demonstrated that penetration depth control can be accomplished with the dual frequency DAS by adjusting the power levels to each array. By increasing/decreasing the power level of the low-/high-frequency array, the depth of a given isopower contour can be moved deeper into tissue. The reverse action will move the isopower contour toward

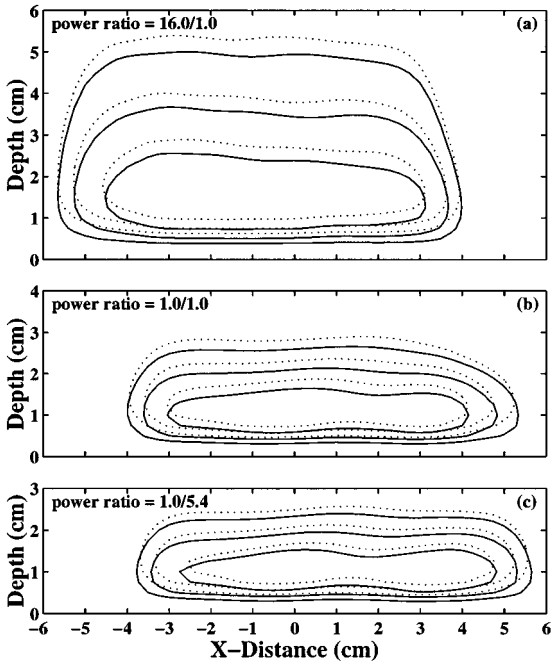

FIG. 9. Contour plots of temperature distributions produced by the DAS for the power ratio $[(u_n^1/u_n^2)^2]$ of (a) 16/1; (b) 1/1; and (c) 1/5.4 for two skin temperature boundary conditions: 37 °C (solid line) and 20 °C (dotted line). The isotherms are drawn at 1 °C increments beginning with the 42 °C isotherm (outer contour).

the skin. The acoustic simulations suggested that the 50% power penetration depth can be moved as much as 3.2 cm. This is a very significant degree of control for superficial therapy applications. The capability of controlling depth of heating is very important in superficial hyperthermia because tumors come in many different sizes and shapes, with varying depths, perfusion patterns, and acoustic properties, and may be near or in contact with bony structures or air cavities. These tumor characteristics demand a system with highly controllable power deposition in all three dimensions. It should be mentioned that the single array in the SURLAS could be driven at the first and third harmonic frequencies using time multiplexing to control penetration depth. However, reduced radiating area, time multiplexing, and a reduced transducer efficiency at the third harmonic would greatly reduce power availability (Moros and Hynynen, 1992), and thus, limiting treatment to very small tumors. The DAS design offers approximately four times the power offered by a single array device running at the first and third harmonics.

In the case of dual frequency insonation with the DAS, power deposition in tissues at both ends of the scanning distance results from ultrasound reflected only from one of the arrays. This induces a heating pattern that is shifted off the center toward the side of the array emitting higher power. The magnitude of the shift is dependent on the power ratio and it is more evident for the array with larger element size. The offset can be of up to 1 cm for the array with 2-cm square elements. The shifting of the power deposition pattern is not necessarily a disadvantage since it can be compensated for by proper manipulation of power levels and/or scanning speed, or the scanning window can be blocked to further shape the field aperture.

As alluded to above, the height of the arrays for the DAS can be made smaller relative to the SURLAS' because the total transducer area required to treat the same tumor size can be reduced by up to a factor of 2. This is to say that for a given array element size (L) the DAS is able to treat tumors with larger surface areas, or for a given tumor size, it needs less radiating area. This is important because in practice the smallest possible height is desirable in order to minimize the amount of attenuating/scattering water-equivalent medium that a photon or an electron beam must pass through before entering the target volume. In the case of electron beams, the deepest possible therapeutic dose depth is strongly dependent on the combined height of the arrays and the coupling bolus. The DAS design, therefore, should allow the treatment of deeper tumors with simultaneous thermoradiotherapy.

Finally, we showed that tissue blood perfusion rate has an impact on the depth and pattern of heating. The change in heating depth could be more than 2 cm for perfusion rates between 1 and 10 kg/m^3 s. However, from the results presented already it can be said that change of 2 cm in penetration depth due to perfusion can be adequately managed with a dual frequency DAS. Finally, the effect of skin temperature on temperature distributions is relatively small and limited to the first few millimeters (1–4 mm) of tissue for all power ratios (Fig. 9).

IV. CONCLUDING REMARKS

In this paper we introduced a new hyperthermia applicator design using a dual-frequency dual-array approach with a scanning double-faced reflector. This design was named the DAS. The DAS design evolved from a previous single-frequency single-array applicator design (the SURLAS). Both applicators were specifically developed for the application of simultaneous thermoradiotherapy with external radiation beams. The most important new feature of the DAS is its ability to control penetration depth—an ability which is needed in superficial hyperthermia systems. To study this feature, models were developed and simulations performed. The simulations demonstrated that by varying the excitation magnitude of a low-frequency array relative to the magnitude of a high-frequency array it is possible to control the distribution of absorbed acoustic energy as a function of depth into tissue. Therefore, we conclude that the heating pattern can be controlled in all three spatial dimensions with the DAS. Other advantages of the DAS were discussed as well, such as increased power availability and improved temperature uniformity. A physical prototype is now under development in our laboratory.

ACKNOWLEDGMENTS

This work was supported by DHHS/NCI Grant No. R29-CA63121 and a Biomedical Engineering Research Grant from the Whitaker Foundation, Washington, DC.

Anhalt, D. P., Hynynen, K., Roemer, R. B., Nathanson, S. M., Stea, B., and Cassady, J. R. **(1993)**. ''Scanned ultrasound hyperthermia for treating superficial disease,'' in *Hyperthermic Oncology 1992*, edited by E. W. Gerner and T. C. Cetas (Arizona Board of Regents), Vol. 2, pp. 191–192.

Benkeser, P. J., Frizzell, L. A., Goss, S. A., and Cain, C. A. (**1989**).''Analysis of a multielement ultrasound hyperthermia applicator,'' IEEE Trans. Ultrason. Ferroelectr. Freq. Control **UFFC-36,** 319–324.

Chato, J. C. **(1985)**. ''Selected thermophysical properties of biological materials,'' in *Heat Transfer in Medicine and Biology, Analysis and Applications*, edited by A. Shitzer and R. C. Eberhart, Vol. 2 (Plenum, New York).

Corry, P. M., Barlogie, B., Tilchen, E. J., and Armour, E. P. **(1982)**. ''Ultrasound-induced hyperthermia for the treatment of human superficial tumors,'' Int. J. Radiat. Oncol. Biol. Phys. **8**, 1225–1229.

Dewey, W. C. **(1994)**. ''Arrhenius relationships from the molecule and cell to the clinic,'' Int. J. Hyperthermia **10**, 457–483.

Hynynen, K. **(1993)**. ''Advanced ultrasound hyperthermia techniques,'' in *Hyperthermic Oncology 1992*, edited by E. W. Gerner and T. C. Cetas (Arizona Board of Regents, Tucson, Arizona), Vol. 2, pp. 25–29.

Kapp, D. S., and Cox, R. S. **(1995)**. ''Thermal treatment parameters are most predictive of outcome in patients with single tumor nodules per treatment field in recurrent adenocarcinoma of the breast,'' Int. J. Radiat. Oncol. Biol. Phys. **33**, 887–899.

Moros, E. G., and Hynynen, K. A. (**1992**).''Comparison of theoretical and experimental ultrasound field distributions in canine muscle tissue *in vivo*,'' Ultrasound Med. Biol. **18**, 81–92.

Moros, E. G., Myerson, R. J., and Straube, W. (**1993**).''Aperture size to therapeutic volume relation for a multielement ultrasound system—determination of applicator adequacy for superficial hyperthermia,'' Med. Phys. **20,** 1399–1409.

Moros, E. G., Straube, W. L., and Myerson, R. J. (**1996a**).''A reflected-scanned ultrasound system for external simultaneous thermoradiotherapy,'' IEEE Trans. Ultrason. Ferroelectr. Freq. Control **43,** 441–449.

Moros, E. G., Straube, W. L., and Myerson, R. J. **(1996b)**. ''Potential for power deposition conformability using reflected-scanned planar ultrasound,'' Int. J. Hyperthermia, **12**, 723–736.

Moros, E. G., Straube, W. L., Klein, E. E., Maurath, J., and Myerson, R. J. **(1995a)**. ''Clinical system for simultaneous external superficial microwave hyperthermia and Cobalt-60 radiation,'' Int. J. Hyperthermia **11**, 11–26.

Moros, E. G., Straube, W. L., Klein, E. E., Yousaf, M., and Myerson, R. J. **(1995b)**. ''Simultaneous delivery of electron beam therapy and ultrasound hyperthermia using scanning reflectors: A feasibility study,'' Int. J. Radiat. Oncol. Biol. Phys. **31**, 893–904.

Myerson, R. J., Perez, C. A., Emami, B., Straube, W., Kuske, R. R., Leybovich, L., and Von Gerichten, D. **(1990)**. ''Tumor control in long-term survivors following superficial hyperthermia,'' Int. J. Radiat. Oncol. Biol. Phys. **18**, 1123–1129.

Myerson, R. J., Moros, E. G., Straube, W. L., Emami, B., Lee, H. K., and Taylor, M. E. **(1996)**. ''Feasibility and tolerance of simultaneous external radiation and superficial hyperthermia,'' in *Hyperthermic Oncology 1996*, edited by C. Franconi, G. Arcangeli, and R. Cavaliere (Tor Vergata, Rome, Italy), Vol. 2, pp. 167–169.

Ocheltree, K. B., and Frizzell, L. A. (**1989**).''Sound field calculation for rectangular sources,'' IEEE Trans. Ultrason. Ferroelectr. Freq. Control **36,** 242–248.

Oleson, J. R., Samulski, T. V., Leopold, K. A., Clegg, S. T., Dewhirst, M., Dodge, R. K., and George, S. L. **(1993)**. ''Sensitivity of hyperthermia trails outcomes to temperature and time: Implications for thermal goals of treatment,'' Int. J. Radiat. Oncol. Biol. Phys. **25**, 289–290.

Pennes, H. H. **(1948)**. ''Analysis of tissue and aerial blood temperature in the resting human forearm,'' J. Appl. Physiol. **1**, 93–122.

Zemanek, J. (**1971**).''Beam behavior within the nearfield of a vibrating piston,'' J. Acoust. Soc. Am. **49,** 181–191.

LETTERS TO THE EDITOR

This Letters section is for publishing (a) brief acoustical research or applied acoustical reports, (b) comments on articles or letters previously published in this Journal, and (c) a reply by the article author to criticism by the Letter author in (b). Extensive reports should be submitted as articles, not in a letter series. Letters are peer-reviewed on the same basis as articles, but usually require less review time before acceptance. Letters cannot exceed four printed pages (approximately 3000–4000 words) including figures, tables, references, and a required abstract of about 100 words.

A change of subscripts of the stimulus placements for a four-point sampling method

Chan F. Lam
Department of Biometry and Epidemiology, Medical University of South Carolina, Charleston, South Carolina 29425

John H. Mills and Judy R. Dubno
Department of Otolaryngology and Communicative Sciences, Medical University of South Carolina, Charleston, South Carolina 29425

(Received 4 September 1996; accepted for publication 10 October 1996)

Because the variance parameter, σ, in a cumulative normal function is not the same as the spread parameter, S, of a logistic function, the subscripts of the four stimulus placements of Eq. (3), and thereafter, of Lam *et al.* [J. Acoust. Soc. Am. **99**, 3689–3693 (1996)] should be X_{12}, X_{27}, X_{73}, and X_{88}. © *1997 Acoustical Society of America.* [S0001-4966(97)03403-6]

PACS numbers: 43.66.Yw [JWH]

In a recent article by Lam *et al.* (1996), a four-point stimulus placement method for the efficient estimation of a psychometric function was presented.

For parameter estimation purposes, instead of a cumulative Gaussian function, a logistic function in the form of Eq. (1) was used:

$$P(X)=\alpha+(1-\alpha)\frac{1}{1+e^{-(X-M)/S}}, \tag{1}$$

where M and S are the threshold and spread parameters, and α is the false alarm.

Because the σ parameter in a cumulative normal function is not the same as the S parameter of a logistic function, the placements of the four points (X_2, X_{16}, X_{84}, X_{98}) shown in Eq. (3) of Lam *et al.* (1996) should be (where the subscript p of X_p denotes the stimulus level with p% of a correct response):

$$X_2=M-3.89S, \quad X_{16}=M-1.66S,$$
$$X_{84}=M+1.66S, \quad X_{98}=M+3.89S. \tag{2}$$

However, through computer simulation, the estimated parameter values of M and S from data using Eqs. (2) are very similar to those obtained from Eqs. (3):

$$X_{12}=M-2S, \quad X_{27}=M-S,$$
$$X_{73}=M+S, \quad X_{88}=M+2S, \tag{3}$$

In the computer simulation, Eq. (1), with α=0, $M = 0$, and $S = 0.5885$, was used to calculate $P(X_p)$ for different values of p specified in either Eqs. (2) (X_2, X_{16}, X_{84}, X_{98}) or Eqs. (3) (X_{12}, X_{27}, X_{73}, X_{88}). A (0,1) uniform random number was generated and compared to the corresponding values of $P(X_p)$. If the random number was smaller than $P(X_p)$, the trial was counted as a correct response. Fifty trials per point were used to determine the percent correct responses of each of the four stimuli [Eqs. (2) or Eqs. (3)]. The parameters M and S of the simulated percent correct responses were then estimated by nonlinear regression using Eq. (1). This process was repeated 1000 times, each using Eqs. (2) and Eqs. (3). The means and variances of the estimated M and S are listed in Table I. The estimated M and S from placements given by Eqs. (2) and Eqs. (3) are very similar to each other and to the known parameter values. Thus, the subscripts of the four stimulus placements of Eqs. (3), and thereafter, of Lam *et al.* (1996) should be those shown in Eqs. (3) in this Letter to the Editor.

TABLE I. Mean and variance of the estimated M and S.

Stimulus locations	$\overline{M}$	$\overline{S}$	σ_M	σ_S
X_2, X_{16}, X_{84}, X_{98} [Eqs. (2)]	0.0004	0.5844	0.0243	0.0079
X_{12}, X_{27}, X_{73}, X_{88} [Eqs. (3)]	0.0029	0.5844	0.0011	0.0067

ACKNOWLEDGMENT

The authors would like to express their sincere thanks to Dr. J. L. Hall of Lucent Bell Laboratories for pointing out the correct subscripts of the stimulus values.

Lam, C. F., Mills, J. H., and Dubno, J. R. (**1996**). ''Placement of observations for the efficient estimation of a psychometric function,'' J. Acoust. Soc. Am. **99,** 3689–3693.

Inherent background coefficients for submerged cylindrical shells

Myoung-Seon Choi, Young-Sang Joo, and Jong-Po Lee
Nondestructive Evaluation Team, Korea Atomic Energy Research Institute, P.O. Box 105, Yusong, Taejon 305-600, Korea

(Received 27 June 1996; accepted for publication 7 October 1996)

The scattering of sound waves by an empty, cylindrical, elastic shell in a fluid is considered in the resonance regime. A long-standing difficulty in the application of the resonance scattering theory is that an exact expression of the acoustical background has been elusive to find over the years. The exact expression, named the *inherent* background coefficient, is presented here. The coefficient is uniquely determined by the generalized fluid-loading-parameter and leads to the impenetrable background coefficient in appropriate limit. Numerical calculations show that it describes the background for a shell of arbitrary thickness and material correctly over the entire frequency range.
 [S0001-4966(97)03003-8]

PACS numbers: 43.20.Fn, 43.30.Gv, 43.40.Ey [CBB]

INTRODUCTION

Since the advent of the acoustic resonance scattering theory (RST),[1] a number of models for the acoustical background, which is often required to isolate the resonance feature of a target, have been presented with limited success in applicability to target geometry and frequency range. They involve the impenetrable (i.e., rigid or soft) backgrounds,[1,2] the intermediate background by Murphy *et al.*,[3,4] the midway background by Ayres and Gaunaurd,[5] the liquid shell background by Veksler,[6] the hybrid background by Werby[7] and Gaunaurd,[8] and the matched asymptotic background by Norris and Vasudevan.[9] However, an exact expression of the acoustical background for any penetrable target had been elusive to find over the past two decades.

Recently, the present authors proposed a general approach to an exact and simple expression of the acoustical background named the *inherent* background coefficient.[10] But, in the work, the inherent background coefficient only for a spherical shell was shown explicitly. In the present study, the approach has been applied to acoustic wave scattering from an empty cylindrical elastic shell in a fluid. This study is two dimensional, limited to normal incidence on an infinite cylindrical shell. The inherent background coefficient is determined uniquely by generalization of the fluid-loading-parameter (also called the null frequency)[9,11–13] which has provided a rough separation for thin shells between the low frequency, heavy fluid-loading regime in which the shells act more like a pressure release surface, and higher frequencies where the fluid loading is weak and the shells are more like a rigid target. The inherent background coefficient leads to the rigid or soft background coefficient in appropriate limit. Also, it is numerically shown that the inherent background coefficient describes the acoustical background for a shell of arbitrary thickness and material correctly over the entire frequency range.

I. SCATTERING COEFFICIENT

For an empty cylindrical elastic shell of outer radius a and inner radius b (thus thickness $d=a-b$) insonified normally by a plane sound wave of unit amplitude, the scattering form function is given by the Rayleigh normal mode (also called partial wave) series,[14,15]

$$f(x_1,\theta)=\sum_{n=0}^{\infty} f_n(x_1,\theta)=\sum_{n=0}^{\infty}\frac{2}{\sqrt{\pi i x_1}}\varepsilon_n R_n\cos(n\theta), \tag{1}$$

where ε_n is the Neumann factor ($\varepsilon_0=1$, $\varepsilon_n=2$ for $n\geqslant 1$), and R_n is a coefficient from the five boundary conditions (three at the outer surface and two at the inner surface of the shell). The scattering coefficient R_n has a form of fractional expression of the 5×5 determinants: $R_n=B_n/D_n$. The elements of these determinants B_n and D_n, listed in Ref. 15, contain the cylindrical Bessel and outgoing Hankel functions (J_n, Y_n, and H_n), and their derivatives (J_n', Y_n', and H_n') with respect to the argument x_i ($\equiv k_i a$, $i=1,L,T$) or y_i ($\equiv k_i b$, $i=L,T$), where k_1 is the wave number of the incident wave in the outer fluid and $k_{L,T}$ are those of longitudinal and transverse waves in the shell. The dimensionless frequencies of the elastic bulk waves are linearly related to that of the incident wave by $x_{L,T}=x_1(C_1/C_{L,T})$ and $y_{L,T}=x_{L,T}(1-h)$, where C_1 and $C_{L,T}$ are the velocities of the incident wave and the elastic bulk waves and h is the ratio of thickness to outer radius of shell, i.e., $h=d/a$.

By expanding the secular determinants, B_n and D_n, with respect to their first column, the scattering coefficient is given as

$$R_n=-\frac{x_1J_n'(x_1)-F_nJ_n(x_1)}{x_1H_n'(x_1)-F_nH_n(x_1)}, \tag{2}$$

where $F_n=-(\rho_1/\rho_2)x_T^2D_n^{11}/D_n^{21}$, ρ_1 and ρ_2 are material densities of the outer fluid and the shell, and D_n^{11} and D_n^{21} are the 4×4 minor determinants of the first two nonvanishing elements in the first column of D_n. The function F_n, called the modal surface admittance, depends on the density ratio of the outer fluid to the shell and the characteristics of the elastic bulk waves in the shell. By taking advantage of the fluid-loading-parameter, $\Omega\equiv(\rho_1/\rho_2)/h$,[9,11–13] the following func-

tion G_n can be defined; $G_n \equiv F_n/\Omega = -hx_T^2 D_n^{11}/D_n^{21}$. This function G_n is independent of the density ratio explicitly but still depends on the velocity ratio of the incident sound wave to the elastic bulk waves, their frequency, and the relative shell thickness.

II. INHERENT BACKGROUND COEFFICIENT

In our previous work on spherical shells,[10] it was shown that, within the function G_n, there are two interacting contributions: one is a nonresonant component which is a constant (independent of frequency) and corresponds to the *inherent* background coefficient, the other is a resonant component which is significant at and near resonance frequencies and is small off resonances. These two components interact over almost all frequencies; thus, the constant component seldom manifests itself. But, it was found by the present authors that, when shear waves in an elastic shell are neglected, like in the liquid-shell background by Veksler,[6] the constant component reveals itself furtively near zero frequency.

As shown in Ref. 6, the modal surface admittance (divided by the fluid-loading-parameter) for an empty cylindrical *liquid* shell is expressed as

$$G_n^{(L)} = hx_L \frac{J_n(y_L)Y_n'(x_L) - J_n'(x_L)Y_n(y_L)}{J_n(y_L)Y_n(x_L) - J_n(x_L)Y_n(y_L)}. \tag{3}$$

By substituting the approximate expressions of Bessel functions for x $(=x_L$ or $y_L) \ll 1$, $J_n(x) = x^n/(2^n n!)$, $Y_{n=0}(x) = (2/\pi)\ln x$, and $Y_{n\geqslant 1}(x) = -(n-1)!(2/x)^n/\pi$ into Eq. (3), the values of the function $G_n^{(L)}$ near zero frequency are given as follows:

for $n=0$

$$G_n^{(L)}(0^+) = \frac{-h}{\ln(1-h)}, \tag{4a}$$

and for $n \geqslant 1$

$$G_n^{(L)}(0^+) = nh\frac{1+(1-h)^{2n}}{1-(1-h)^{2n}}. \tag{4b}$$

Therefore, the constant component of F_n is determined by $F_n^{(L)}(0^+) = \Omega G_n^{(L)}(0^+)$. By replacing the function F_n in Eq. (2) with its constant component $F_n^{(L)}(0^+)$, the inherent background coefficient is obtained:

$$R_n^{(b)} = -\frac{x_1 J_n'(x_1) - F_n^{(L)}(0^+)J_n(x_1)}{x_1 H_n'(x_1) - F_n^{(L)}(0^+)H_n(x_1)}. \tag{5}$$

Although $F_n^{(L)}(0^+)$ was obtained in the zero frequency limit, the inherent background coefficient of Eq. (5) is applicable in all frequencies because the constant component of F_n is independent of frequency.

Figure 1 shows the graphical plots of $G_n^{(L)}(0^+)$ for the lowest six $(n=0-5)$ partial waves as a function of h. For thin shells with $h \ll 1$, $G_n^{(L)}(0^+) \approx 1$ and then $F_n^{(L)}(0^+)$ reduces to the fluid-loading-parameter Ω. Therefore, it can be said that $G_n^{(L)}(0^+)$ of Eq. (4) plays the role of a modal correction factor for a thick shell, which indicates deviations from the fluid-loading-parameter for thin shells. This implies that $F_n^{(L)}(0^+)$ can be defined as a generalized fluid-loading-parameter. For cylinders with $h \approx 1$, $G_n^{(L)}(0^+) \approx n$. And, from Eq. (5), it is easily shown that the inherent background for a shell, which is determined uniquely by the generalized fluid-loading-parameter for the shell, leads to the soft background in the low-frequency regime of $x_1 \ll F_n^{(L)}(0^+)$ and to the rigid background in the high-frequency regime of $x_1 \gg F_n^{(L)}(0^+)$.

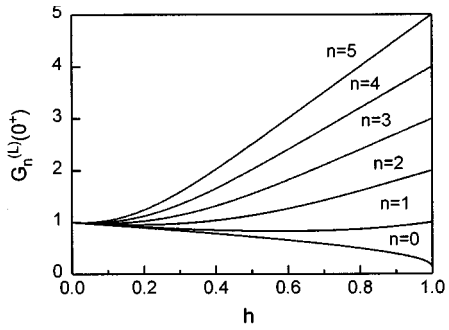

FIG. 1. $G_n^{(L)}(0^+)$ of the first six $(n=0-5)$ partial waves plotted as a function of relative shell-thickness h.

III. NUMERICAL CALCULATIONS

The modal scattering and inherent background form functions, $f_n(x_1,\theta)$ and $f_n^{(b)}(x_1,\theta)$, are now examined for the region of $x_1 = 0-20$ in the backscattering direction $(\theta=\pi)$. The background form function $f_n^{(b)}(x_1,\pi)$ is obtained by using $R_n^{(b)}$ of Eq. (5) instead of R_n in Eq. (1) and the total form functions, $f(x_1,\pi)$ and $f^{(b)}(x_1,\pi)$, are obtained by summing the modal form functions up to $n=25$. All calculations are performed for empty stainless steel shells in water and the calculation step size of $\Delta x_1 = 0.01$ is used. The material properties of the pertinent substances are as follows: $\rho_1 = 1.0$ g cm^{-3}, $\rho_2 = 7.9$ g cm^{-3}, $C_1 = 1480$ m s^{-1}, $C_L = 5780$ m s^{-1}, and $C_T = 3090$ m s^{-1}.

Figure 2 shows moduli and phases of the total backscattering form functions of the inherent backgrounds for the 2% and 99% thick shells, as well as those of the impenetrable backgrounds. For the 2% thick shells, the modulus is similar to that for the soft background. But, with increasing frequency, the phase undergoes a transition from that for the soft background to that for the rigid background. For the 99% thick shells, the inherent background resembles the rigid background, although there is a slight difference particularly in the moduli. Of course, the deviations from the impenetrable backgrounds are attributed to the refracted waves into the shells. As have been pointed out in a number of previous works,[4,5,7–9] the trends to shell thickness and to frequency, such as in the above observations, are the most important characteristics that proper backgrounds for shells have to possess. In order that the inherent background is utilized as the exact background for a shell, however, it should be made sure that their modal form functions coincide with each other except for the domain where resonances take place and thus all the resonances are isolated cleanly by subtracting the inherent background from the shell response. These requirements have been checked for each partial wave. For example, Fig. 3 shows the isolated resonances of the

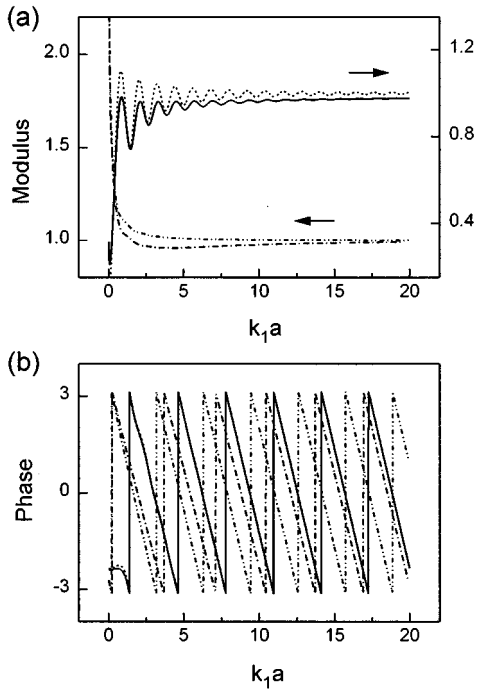

FIG. 2. (a) Moduli and (b) phases (in radians) of the total backscattering form functions of the inherent backgrounds for the 2% (dash-and-dot line) and 99% (solid line) thick, empty, stainless steel shells in water, as well as those of the rigid (dotted line) and soft (dash-and-two-dots line) backgrounds.

lowest six ($n=0-5$) partial waves for the 2% thick shells. As has been usually used in the RST, each resonance is identified by two indexes (n,l). The first index n defines the order of resonance and the second index l defines the type of resonance. For this case, only one type ($l=2$) of resonance, which corresponds to the lowest symmetric Lamb wave,[6,16] is shown in the given frequency region. In any partial wave, we can see that the inherent background isolates the resonance cleanly.

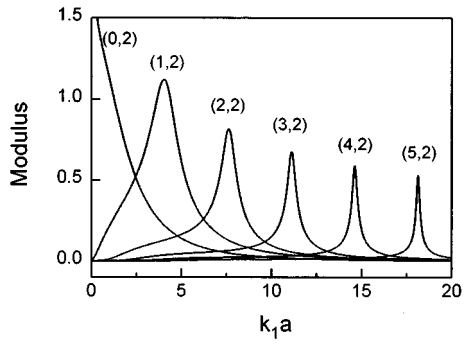

FIG. 3. Moduli of the residual backscattering form functions, $|f_n-f_n^{(b)}|$, of the lowest six ($n=0-5$) partial waves for the 2% thick, empty, stainless steel shells in water.

IV. CONCLUSIONS

The inherent background coefficient of Eq. (5), which is determined uniquely by the generalized fluid-loading-parameter from Eq. (4), describes the background for empty cylindrical shells correctly over the entire frequency range. The inherent background seems to have no limitation in applicability to shell thickness or composition because it emerges from a physical concept. Future works will show that this concept is applicable to the problems of acoustic wave scattering by very complicated targets such as layered shells.

ACKNOWLEDGMENTS

This investigation has been supported by the Advisory Committee for Nuclear Technology Development, Korea Atomic Energy Research Institute. The authors would like to thank Prof. Herbert Überall and Dr. Louis R. Dragonette for their helpful discussion held at the Naval Research Laboratory on 15 September 1995.

[1] L. Flax, L. R. Dragonette, and H. Überall, ''Theory of elastic resonance excitation by sound scattering,'' J. Acoust. Soc. Am. **63**, 723–731 (1978).
[2] G. C. Gaunaurd and M. F. Werby, ''Acoustic resonance scattering by submerged elastic shells,'' Appl. Mech. Rev. **43**, 171–208 (1990).
[3] J. D. Murphy, E. D. Breitenbach, and H. Überall, ''Resonance scattering of acoustic waves from cylindrical shells,'' J. Acoust. Soc. Am. **64**, 677–683 (1978).
[4] J. D. Murphy, J. George, A. Nagl, and H. Überall, ''Isolation of the resonance component in acoustic scattering from fluid-loaded elastic spherical shells,'' J. Acoust. Soc. Am. **65**, 368–373 (1979).
[5] V. M. Ayres and G. C. Gaunaurd, ''Acoustic resonance scattering by viscoelastic objects,'' J. Acoust. Soc. Am. **81**, 301–311 (1987).
[6] D. N. Veksler, ''Intermediate background in problems of sound waves scattering by elastic shells,'' Acustica **76**, 1–9 (1992).
[7] M. F. Werby, ''The acoustical background for a submerged elastic shell,'' J. Acoust. Soc. Am. **90**, 3279–3287 (1991).
[8] G. C. Gaunaurd, ''Hybrid background coefficients to isolate the resonance spectrum of submerged shells,'' J. Acoust. Soc. Am. **92**, 1981–1984 (1992).
[9] A. N. Norris and N. Vasudevan, ''Acoustic wave scattering from thin shell structures,'' J. Acoust. Soc. Am. **92**, 3320–3336 (1992).
[10] M.-S. Choi and Y.-S. Joo, ''Theory of the background amplitudes in acoustic resonance scattering,'' J. Acoust. Soc. Am. (to be published).
[11] D. G. Crighton, A. D. Dowling, J. E. Ffowcs Williams, M. Heckl, and F. G. Leppington, *Modern Methods in Analytical Acoustics: Lecture Notes* (Springer-Verlag, New York, 1992), pp. 510–523.
[12] N. Norris and D. A. Rebinsky, ''Acoustic coupling to membrane waves on elastic shells,'' J. Acoust. Soc. Am. **95**, 1809–1829 (1994).
[13] D. A. Rebinsky and A. N. Norris, ''Benchmarking acoustic coupling theory for elastic shells of arbitrary shape,'' J. Acoust. Soc. Am. **98**, 2368–2371 (1995).
[14] P. Ugincius and H. Überall, ''Creeping-wave analysis of acoustic scattering by elastic cylindrical shell,'' J. Acoust. Soc. Am. **43**, 1025–1034 (1968).
[15] P. L. Marston and N. H. Sun, ''Backscattering near the coincidence frequency of a thin cylindrical shell: Surface wave properties from elasticity theory and an approximate ray synthesis,'' J. Acoust. Soc. Am. **97**, 771–783 (1995).
[16] M. Talmant, G. Quentin, J. L. Rousselot, J. V. Subrahmanyam, and H. Überall, ''Acoustic resonance of thin cylindrical shells and the resonance scattering theory,'' J. Acoust. Soc. Am. **84**, 681–688 (1988).

Erratum: "The attenuation and dispersion of sound in water containing multiply interacting air bubbles" [J. Acoust. Soc. Am. 99, 3412–3430 (1996)]

C. Feuillade
Naval Research Laboratory, Stennis Space Center, Mississippi 39529-5004

(Received 28 October 1996; accepted for publication 10 November 1996)

[S0001-4966(97)00603-6]

PACS numbers: 43.30.Es, 43.30.Jx, 43.30.Ky, 43.30.Ft, 43.10.Vx [JHM]

I am indebted to Z. Ye for bringing to my attention an error in Fig. 4. An initial computational attempt to evaluate Eq. (30), and determine the sound speed in water containing bubbles of uniform radius, involved iterating the value of the complex wave number k appearing in the integral in the denominator of the expression. Upon repeating these calculations, a minor programming error was detected. Correcting the error yields Fig. A (shown here), which compares the resulting predicted attenuation coefficient with data from one of the experimental cases of Silberman [J. Acoust. Soc. Am. **29**, 925–933 (1957)]. Careful checking of other programs showed that the error was not propagated into succeeding calculations. The error, which occurs in the data comparison section of the paper, affects only one example, and has no consequences beyond Fig. 4. This is because the iterative method of solution was not subsequently used, and neither the substantive data analysis nor the conclusions of the paper depend upon it.

The iterative method of solution was not pursued in the paper because problems were suspected in using the macroscopic properties of bubbly water to describe microscopic processes between individual bubbles. Indeed, in Fig. A, the divergence of the solid line from the data points below the resonance frequency appears to confirm this anticipation.

I would also like to clarify another issue which arises in the alternative approximate method subsequently used to evaluate Eq. (30) and make comparisons with data. This equated k with the propagation wave number for pure water (k is not generally defined to represent this quantity in the paper), and truncated the integral at a finite upper bound R representing the radius of a spherical ''region of collective interaction'' around each bubble. For all of the data cases analyzed, the value of $k_0 R \ll 1$ (where k_0 is the wave number at resonance). For most of the data points the condition $kR<1$ is also satisfied, and in every case the data points lie well below the frequency region where the integral becomes oscillatory and the approximation breaks down. This method produces consistent results, as Table I indicates in the paper, and has the advantage of allowing the total number of bubbles involved in the collective interaction at each locality to be estimated.

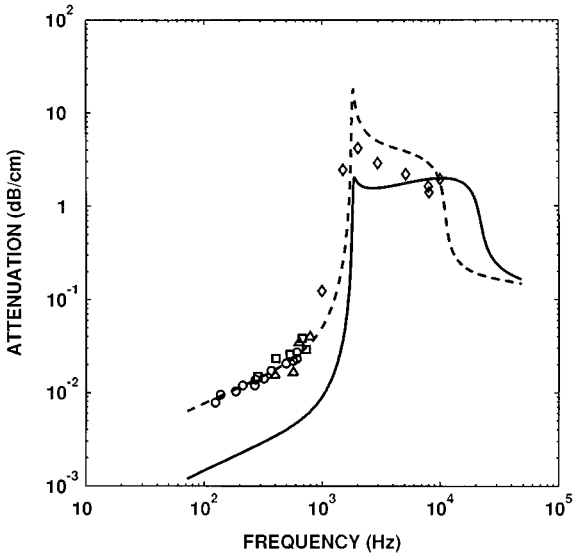

FIG. A. Attenuation coefficient as a function of frequency. The data are taken from Silberman [J. Acoust. Soc. Am. **29**, 925–933 (1957)]. The air volume fraction β=0.22%. The data points are for bubbles of radius: 1.77 mm (◇); 1.83 mm (○); 2.07 mm (□); 2.44 mm (△). The dashed line shows the theoretical attenuation coefficient predicted for bubbles of radius 1.77 mm using the classic theory of acoustic propagation in bubbly water. The solid line shows the theoretical attenuation coefficient predicted by Eq. (30) for 1.77-mm bubbles, evaluated using an iterative procedure.

 0001-4966/97/101(3)/1746/1/$10.00

Erratum: "A composite model for rough bottom scattering" [J. Acoust. Soc. Am. 100, 2797(A) (1996)]

Yevgeniy Y. Dorfman and Ira Dyer
Department of Ocean Engineering, Massachusetts Institute of Technology, Cambridge, Massachusetts 02139

(Received 18 November 1996; accepted for publication 18 November 1996)

[S0001-4966(97)00703-0]

PACS numbers: 43.30.Hw, 43.10.Vx

Instead of Kuryanov on line 4 of the abstract the name should be Caruthers and Novarini.

Erratum: "On acoustic attenuation by swimbladder fish" [J. Acoust. Soc. Am. 100, 669–672 (1996)]

Zhen Ye
Ocean Acoustics, Institute of Ocean Sciences, Sidney, British Columbia V8L 4B2, Canada

(Received 5 September 1996; accepted for publication 11 November 1996)

[S0001-4966(97)00803-5]

PACS numbers: 43.30.Xm, 43.30.Ft, 43.30.Gv, 43.10.Vx [JHM]

The legends in Fig. 1 and Fig. 2 should be exchanged. Dr. Sam McClatchie is thanked for useful communications.

 0001-4966/97/101(3)/1747/1/$10.00

Erratum: "Perception of asynchronous and conflicting visual and auditory speech" [J. Acoust. Soc. Am. 100, 1777–1786 (1996)]

Dominic W. Massaro, Michael M. Cohen, and Paula M. T. Smeele
Department of Psychology, University of California, Santa Cruz, California 95064

(Received 5 November 1996; accepted for publication 18 November 1996)

[S0001-4966(97)02103-6]

PACS numbers: 43.71.An, 43.72.Ja, 43.71.Ma, 43.10.Vx [RAF]

The affiliation of one of the authors, Paula M. T. Smeele, was omitted. Her affiliation is:
Department of Industrial Design Engineering,
Delft University of Technology, 2628 BX Delft, The Netherlands.

 0001-4966/97/101(3)/1748/1/$10.00